FUNCTIONAL HETEROGENEITIES IN BIOMEMBRANES

EDITED BY: Rainer A. Böckmann, Robert Ernst and Falk Nimmerjahn
PUBLISHED IN: Frontiers in Cell and Developmental Biology,
Frontiers in Physiology and Frontiers in Immunology

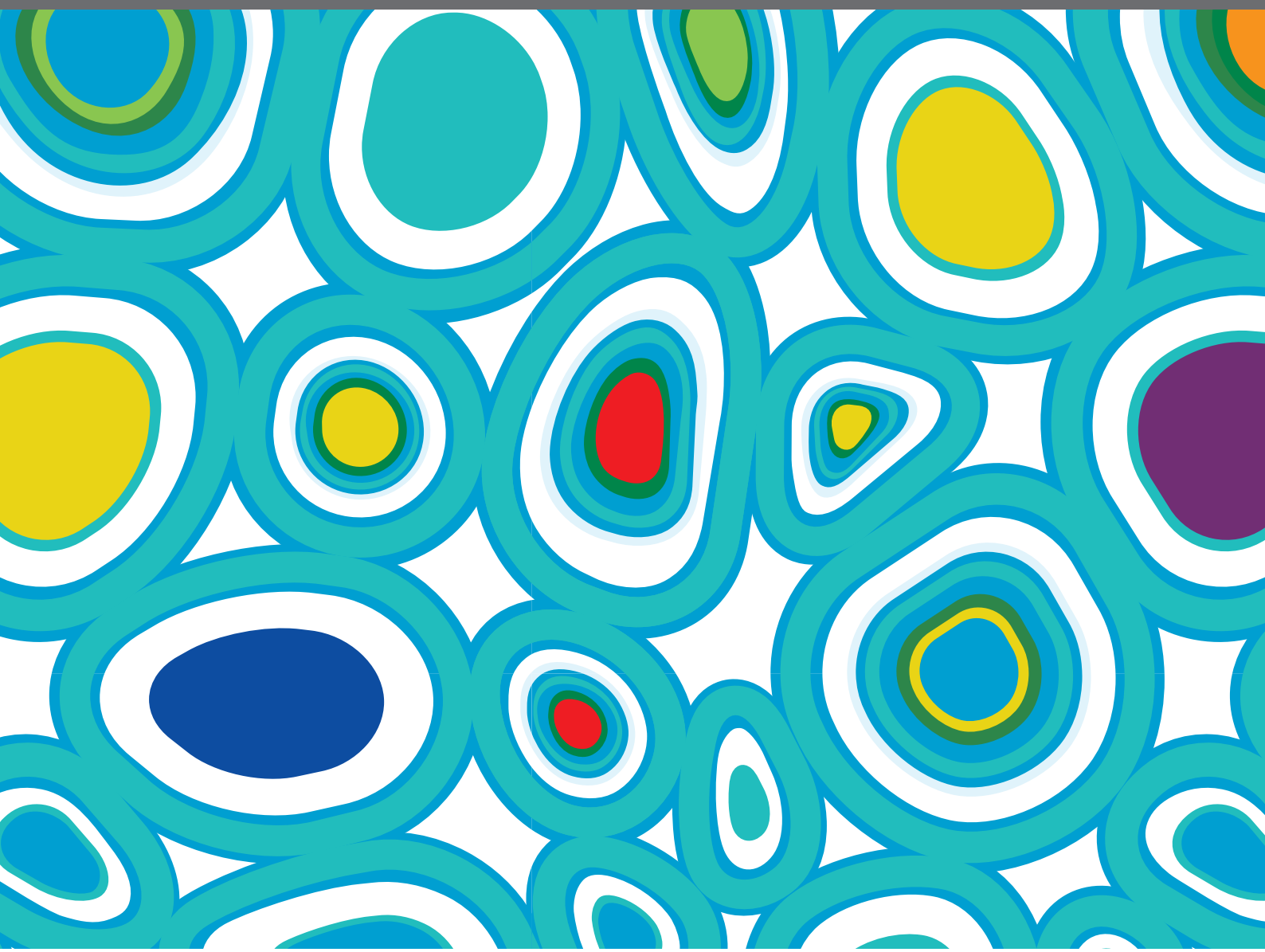

frontiers Research Topics

frontiers

ISSN 1664-8714
ISBN 978-2-88971-248-9
DOI 10.3389/978-2-88971-248-9

About Frontiers

Frontiers is more than just an open-access publisher of scholarly articles: it is a pioneering approach to the world of academia, radically improving the way scholarly research is managed. The grand vision of Frontiers is a world where all people have an equal opportunity to seek, share and generate knowledge. Frontiers provides immediate and permanent online open access to all its publications, but this alone is not enough to realize our grand goals.

Frontiers Journal Series

The Frontiers Journal Series is a multi-tier and interdisciplinary set of open-access, online journals, promising a paradigm shift from the current review, selection and dissemination processes in academic publishing. All Frontiers journals are driven by researchers for researchers; therefore, they constitute a service to the scholarly community. At the same time, the Frontiers Journal Series operates on a revolutionary invention, the tiered publishing system, initially addressing specific communities of scholars, and gradually climbing up to broader public understanding, thus serving the interests of the lay society, too.

Dedication to Quality

Each Frontiers article is a landmark of the highest quality, thanks to genuinely collaborative interactions between authors and review editors, who include some of the world's best academicians. Research must be certified by peers before entering a stream of knowledge that may eventually reach the public - and shape society; therefore, Frontiers only applies the most rigorous and unbiased reviews.
Frontiers revolutionizes research publishing by freely delivering the most outstanding research, evaluated with no bias from both the academic and social point of view. By applying the most advanced information technologies, Frontiers is catapulting scholarly publishing into a new generation.

What are Frontiers Research Topics?

Frontiers Research Topics are very popular trademarks of the Frontiers Journals Series: they are collections of at least ten articles, all centered on a particular subject. With their unique mix of varied contributions from Original Research to Review Articles, Frontiers Research Topics unify the most influential researchers, the latest key findings and historical advances in a hot research area! Find out more on how to host your own Frontiers Research Topic or contribute to one as an author by contacting the Frontiers Editorial Office: frontiersin.org/about/contact

FUNCTIONAL HETEROGENEITIES IN BIOMEMBRANES

Topic Editors:
Rainer A. Böckmann, University of Erlangen Nuremberg, Germany
Robert Ernst, Saarland University, Germany
Falk Nimmerjahn, University of Erlangen Nuremberg, Germany

Citation: Böckmann, R. A., Ernst, R., Nimmerjahn, F., eds. (2021). Functional Heterogeneities in Biomembranes Lausanne: Frontiers Media SA. doi: 10.3389/978-2-88971-248-9

Table of Contents

frontiers in Cell and Developmental Biology

ORIGINAL RESEARCH
published: 15 November 2019
doi: 10.3389/fcell.2019.00281

More Favorable Palmitic Acid Over Palmitoleic Acid Modification of Wnt3 Ensures Its Localization and Activity in Plasma Membrane Domains

*Yagmur Azbazdar[1,2], Ozgun Ozalp[1,2], Erdinc Sezgin[3], Sapthaswaran Veerapathiran[4], Anna L. Duncan[5], Mark S. P. Sansom[5], Christian Eggeling[3,6,7], Thorsten Wohland[4,8], Ezgi Karaca[1,2] and Gunes Ozhan[1,2]**

[1] Izmir Biomedicine and Genome Center (IBG), Dokuz Eylul University Health Campus, Inciralti-Balcova, Izmir, Turkey, [2] Izmir International Biomedicine and Genome Institute (IBG-Izmir), Dokuz Eylul University, Inciralti-Balcova, Izmir, Turkey, [3] MRC Human Immunology Unit, Weatherall Institute of Molecular Medicine, University of Oxford, Oxford, United Kingdom, [4] Department of Biological Sciences and Center for BioImaging Sciences, National University of Singapore, Singapore, Singapore, [5] Department of Biochemistry, University of Oxford, Oxford, United Kingdom, [6] Department of Super-Resolution Microscopy, Institute for Applied Optics and Biophysics, Friedrich-Schiller-University Jena, Jena, Germany, [7] Department of Biophysical Imaging, Leibniz Institute of Photonic Technology e.V., Jena, Germany, [8] Department of Chemistry, National University of Singapore, Singapore, Singapore

OPEN ACCESS

Edited by:
Rainer A. Böckmann, University of Erlangen Nuremberg, Germany

Reviewed by:
Marek Cebecauer, J. Heyrovsky Institute of Physical Chemistry (ASCR), Czechia
Andreas Heuer, University of Münster, Germany
Ingela Parmryd, University of Gothenburg, Sweden

***Correspondence:**
Gunes Ozhan
gunes.ozhan@ibg.edu.tr

Specialty section:
This article was submitted to Membrane Physiology and Membrane Biophysics, a section of the journal Frontiers in Cell and Developmental Biology

Received: *01 August 2019*
Accepted: *31 October 2019*
Published: *15 November 2019*

Citation:
Azbazdar Y, Ozalp O, Sezgin E, Veerapathiran S, Duncan AL, Sansom MSP, Eggeling C, Wohland T, Karaca E and Ozhan G (2019) More Favorable Palmitic Acid Over Palmitoleic Acid Modification of Wnt3 Ensures Its Localization and Activity in Plasma Membrane Domains. Front. Cell Dev. Biol. 7:281. doi: 10.3389/fcell.2019.00281

While the lateral organization of plasma membrane components has been shown to control binding of Wnt ligands to their receptors preferentially in the ordered membrane domains, the role of posttranslational lipid modification of Wnt on this selective binding is unknown. Here, we identify that the canonical Wnt is presumably acylated by palmitic acid, a saturated 16-carbon fatty acid, at a conserved serine residue. Acylation of Wnt3 is dispensable for its secretion and binding to Fz8 while it is essential for Wnt3's proper binding and domain-like diffusion in the ordered membrane domains. We further unravel that non-palmitoylated Wnt3 is unable to activate Wnt/β-catenin signaling either in zebrafish embryos or in mammalian cells. Based on these results, we propose that the lipidation of canonical Wnt, presumably by a saturated fatty acid, determines its competence in interacting with the receptors in the appropriate domains of the plasma membrane, ultimately keeping the signaling activity under control.

Keywords: ordered plasma membrane domain, lipid raft, Wnt/β-catenin pathway, structural modeling, acylation, palmitoylation

INTRODUCTION

Wnt/β-catenin signaling, the so-called canonical Wnt pathway, regulates a broad range of biological processes during embryonic development, adult tissue homeostasis and tissue regeneration (Huang and He, 2008; Clevers and Nusse, 2012; Ozhan and Weidinger, 2014). Aberrant Wnt signaling is related to various types of cancer, congenital defects and degenerative diseases (Logan and Nusse, 2004; Clevers, 2006; Nusse and Clevers, 2017). Wnts are lipid- and sugar-modified morphogens that play critical roles in cells through engagement of a receptor complex that includes Frizzled (Fz) and low-density lipoprotein receptor-related protein 5/6 (LRP 5/6). Wnt/β-catenin signaling is kept in the OFF-state in the absence of an active canonical Wnt ligand, leading to phosphorylation of β-catenin in the cytoplasm by the destruction complex and its proteasomal degradation (Angers and Moon, 2009; MacDonald et al., 2009). Transition from the Wnt-OFF- to the Wnt-ON-state is

initiated by the binding of a canonical Wnt ligand to a canonical Fz receptor and the co-receptor low-density lipoprotein receptor-related protein 5/6 (Lrp5/6) (Angers and Moon, 2009). The formation of Wnt-receptor complex triggers a series of cellular events that include phosphorylation and endocytosis of Lrp5/6, recruitment of the cytoplasmic proteins Disheveled (Dvl) and Axin to the receptor complex, inhibition of the destruction complex, stabilization of cytoplasmic β-catenin and translocation of stabilized β-catenin to the nucleus where it interacts with the transcription factors of the lymphoid enhancer-binding factor (Lef) and T cell factor (Tcf) family to activate gene expression (Kikuchi and Yamamoto, 2007; Yamamoto et al., 2008; Niehrs and Shen, 2010).

A key step underlying initiation of the pathway is the binding of canonical Wnt ligands to their receptor complexes at the plasma membrane. The plasma membrane contains ordered membrane domains, conventionally referred to as membrane (lipid) rafts, that are highly dynamic membrane regions characterized by the selective recruitment of saturated lipids, sterols and specific lipid-anchored proteins (Simons and Ikonen, 1997; Sezgin et al., 2017b). These ordered structures generate compact transient platforms for ligand-receptor interaction and receptor clustering, and are critical in signal transduction pathways including the canonical Wnt signaling (Simons and Toomre, 2000; Jury et al., 2007; Midgley et al., 2013; Ozhan et al., 2013; Dinic et al., 2015; Guven-Maiorov et al., 2015; Sezgin et al., 2017b; Agarwal et al., 2018; Badawy et al., 2018). In contrast to the scattered distribution of the canonical pathway receptor Fz8 and the coreceptor Lrp6 throughout the membrane, the membrane-bound Wnt pathway modulator Lypd6 becomes localized to the ordered membrane domains and ensures via direct physical interaction that Lrp6 is phosphorylated in these domains to activate signaling (Yamamoto et al., 2008; Sakane et al., 2010; Ozhan et al., 2013). Our recent work has unraveled the influence of the immediate plasma membrane environment on the canonical Wnt–receptor interaction by showing that canonical Wnt selectively binds to its pool of receptors in the ordered domains and this domain-specific binding is necessary for downstream signaling activity (Sezgin et al., 2017b). Nevertheless, the link between lipid modifications of Wnt and its preferential binding to specific membrane regions has remained elusive.

Wnt proteins are extensively modified through glycosylation and acylation at the post-translational level. Mutations introduced at N-linked glycosylation sites of different Wnt proteins suggest that glycosylation plays critical roles in Wnt folding and subsequent secretion (Mason et al., 1992; Komekado et al., 2007; Kurayoshi et al., 2007). In contrast to glycosylation, acylation is essential for Wnt activity (Willert and Nusse, 2012). Initially, mass spectrometric analysis of the purified mouse Wnt3a (mWnt3a) exhibited two different acyl group modifications, i.e., a thioester-linked palmitic acid at a conserved cysteine (C77 in murine Wnt3a) and an oxyester-linked palmitoleic acid at a conserved serine (S209 in murine Wnt3a) (Willert et al., 2003; Takada et al., 2006). In the later published high-resolution structure of *Xenopus* Wnt8 (xWnt8) in complex with the extracellular cysteine-rich domain (CRD) of mouse Fz8 (Protein Data Bank [PDB] id: 4F0A), the conserved serine was found to be acylated, suggesting this serine as a consensus acylation site across all Wnts (Janda et al., 2012; Willert and Nusse, 2012). In this study, the chemical identity of the lipid linked to xWnt8 could not be unambiguously detected by mass spectrometry (Janda et al., 2012).

The role of lipid modifications in secretion and functionality of Wnt has also been studied in several Wnt proteins by mutating conserved acylation sites (Kurayoshi et al., 2007; Franch-Marro et al., 2008; Tang et al., 2012; Luz et al., 2014). Mutagenesis of the conserved serine Wnt acylation sites (S209 in mWnt3a and S239 in *Drosophila* Wingless [Wg]) consistently abolished Wnt function in different species (Takada et al., 2006; Franch-Marro et al., 2008). Yet, the amount of Wnt secreted from mWnt3aS209A mutant was dramatically reduced when compared to Wnt secreted from WgS239A mutant. Mutation introduced at the conserved serine residue of zebrafish Wnt8a reduced both its secretion and signaling capability (Luz et al., 2014). On the contrary, mWnt1 and mWnt3a without any lipid adducts were secreted but non-functional (Doubravska et al., 2011). Therefore, the impact of acylation on the secretion of different types of Wnts is still a matter of debate.

Another ambiguity in the literature emanates from the influence of acylation on protein binding to the plasma membrane. S acylation typically by a saturated 16-carbon fatty acid, i.e., palmitoylation, determines the ability of soluble proteins to associate with the membrane and membrane-associated proteins and targets them into ordered membrane domains, suggesting a link between order preference and signaling activation (Levental et al., 2010). Thus, acylation of a canonical Wnt ligand by a monounsaturated fatty acid (Takada et al., 2006) appears to strongly contradict Wnt's membrane binding and activation of signaling preferentially in the ordered domains (Zhai et al., 2004; Ozhan et al., 2013; Sezgin et al., 2017a).

To address all the above-mentioned open questions, here we address the type and influence of the lipid modification on the ability of canonical Wnt ligand in binding to the plasma membrane and activation of Wnt/β-catenin signaling. To this end, we have conformationally analyzed the accessible palmitoleic acid (PAM; 16:1) and palmitic acid (PLM, 16:0) structures (deposited in the PDB). Upon comparing the acquired PAM/PLM coordinates with the fatty acid present in the crystal structure of xWnt8-mouse:Fz8-CRD, we have shown that the fatty acid molecule within the xWnt8-mouse:Fz8-CRD complex is conformationally closest to a PLM molecule bound to the human acyloxyacyl hydrolase (PDB id: 5W78). Based on this, we have constructed the atomistic models of Fz8-CRD bound to PAM and PLM, which has demonstrated that only Wnt8's acylation by PLM is conformationally permissive. To further investigate the functional role of acylation in zebrafish Wnt3, a canonical Wnt ligand, we have generated a point mutation in the conserved serine at position 212, namely S212 (homologous to S209 in mWnt3a). Our data have shown that this specific acylation of Wnt3 ligand is not essential for its secretion and physical interaction with its receptor Fz8 at the plasma membrane. It is, however, required for Wnt's localization to the ordered domains of the plasma membrane, where the ligand selectively binds to its receptors and co-internalizes with the receptor complex. Using Imaging Total Internal Reflection

Fluorescence Correlation Spectroscopy (ITIR-FCS) diffusion law, we have demonstrated that acylation is indispensable for the domain-like diffusion of Wnt3 in the ordered membrane regions, and for Wnt3 to activate canonical Wnt signaling in both zebrafish embryos and mammalian cells. In the light of these findings, here we propose that the acylation of Wnt3 ligand with a saturated palmitic acid ensures its partitioning into the ordered membrane domains and the downstream canonical Wnt signaling activity. Overall, by using a prominent combination of computational and experimental work, we underscore the significance of Wnt acylation, presumably by a palmitic acid, in receptor targeting within the ordered domains and subsequent signaling activation.

MATERIALS AND METHODS

Analysis of the Available PAM/PLM Conformations

The 24 PAM and 195 PLM ligands deposited in the Protein Data Bank (https://www.rcsb.org) were aligned on the fatty acid provided within the PDB entry 4F0A (Janda et al., 2012). The alignment was carried out with the fitting program ProFit where 4F0A's fatty acid carbons were used as a reference (Martin and Porter, 2009). For each case, obtained fit distributions (expressed in Å) were binned into 20 with the standard histogram building option of Matlab (The MathWorks, 2018). To remove the statistical bias, the occurrence frequencies obtained with this analysis were normalized by the size of the data set. The normalized distributions were interpreted as the probability density for being conformationally close to 4F0A's ligand (**Figure 1D**).

Modeling the Interatomic Contacts Formed Between PAM/PLM and Mouse Frizzled 8

In 4F0A, the fatty acid ligand spans Fz8-CRD's hydrophobic channel formed by GLN71, PHE72, PRO74, ILE78, MET122, TYR125, PHE127, PRO130 where the fatty acid's first carbon C1 is within <7 Å of GLN71 and TRP129. The latter amino acid secures the fatty acid covalently linked to Wnt. Taken this information as a basis, two modeling scenarios were constructed. In the first one, the optimal PAM coordinates (including its hydrogens) were obtained via ligand expo rscb (http://ligand-expo.rcsb.org, **Figure S6**). Then, the topology and parameter files of these ligands were obtained by PRODRG (http://prodrg1.dyndns.org/) (Schuttelkopf and van Aalten, 2004). These templates were used as a reference to add missing atoms of 4F0A's PAM within the integrative modeling platform HADDOCK (van Zundert et al., 2016). After proper addition of the missing atoms, PAM interactions with Fz8 were reconstructed under the effect of the interaction information listed above. The same procedure was repeated with the same starting structures, this time by supplying PLM topology and parameter files to define the ligand. The relevant restraint files, topologies and outcomes of the runs are provided under https://github.com/ezgikaraca/Wnt-acylation.

Modeling the Interatomic Contacts Formed Between PLM and Zebrafish Frizzled 8

The homology model of the zebrafish Fz8 was constructed by using mouse Fz8 as a template within i-Tasser (https://zhanglab.ccmb.med.umich.edu/I-TASSER/) (Yang et al., 2015). After obtaining zebrafish Fz8 structure, its PLM interacting residues were determined by using structural comparison with the mouse Fz8, i.e., GLN66, PHE67, PRO 69, LEU70, ILE73, LEU116, MET117, TYR120, PHE122 (**Figure S4**). These residues were kept in contact with the relevant PLM atoms while the zebrafish Fz8-PLM interaction was refined in HADDOCK. Here the PLM topology and coordinates were taken from the previous modeling step (https://github.com/ezgikaraca/Wnt-acylation).

Transgenic Fish Lines

Transgenic zebrafish (*Danio rerio*) line Tg(*7xTcfF-Xla.Siam*:nlsmCherry) was outcrossed to wild type zebrafish and sorted as described previously (Moro et al., 2012). This line was used as a reporter of Wnt/ß-catenin signaling activity.

Cell Culture

HEK293T cells were grown in Dulbecco's Modified Eagle Medium (DMEM) supplemented with 10% fetal bovine serum (FBS) at 37°C in 5% (v/v) CO_2 humidified environment. SH-SY5Y cells were obtained from ATCC (Manassas, VA, USA) and grown in DMEM/F12 supplemented with 10% FBS, 1% L-glutamine and 1% non-essential amino acids.

Cloning of Zf wt Wnt3-GFP, Zf Wnt3S212A-GFP, and Zf FLAG-Fz8a

Total RNA was isolated from 24 h-post-fertilization (hpf) zebrafish embryos using Direct-zol RNA Kit (Zymo Research, Irvine, CA) and cDNA was synthesized with iScript reverse transcriptase (Biorad, Hercules, CA) using a 1:1 mixture of oligodT and random primers. For (-RT) controls, iScript RT was replaced with water. For zebrafish (Zf) wt Wnt3-GFP, PCR was performed using 1 μL cDNA with the forward primer 5′-GATCTCCACCATGGATTTGTACCTGGTT GGATT-3′ and the reverse primer 5′-GAATTCTTTACATGTA TGTACGTCGTAGACC-3′. PCR product was digested with BglII and EcoRI and ligated into pCS2P+ vector that has EGFP. Zf Wnt3S212A-GFP was generated by site-directed mutagenesis at Zf wt Wnt3-GFP using overlap extension PCR. The following primers were used for the first round of PCR: forward1 5′-AGATCTCCACCATGGATTTGTACCTGGT TGGATT-3 with reverse1 5′-ACTTCACAGCTGCCAGCCAG-3′ and forward2 5′-CTGGCTGGCAGCTGTGAAGT-3′ with reverse2 5′ GAATTCTTTACATGTATGTACGTCGTAGACC-3′. The second round of PCR was conducted by using the purified PCR product of the first round of PCR as the template and the primers forward1 with reverse2. The purified PCR product of the second round of PCR was digested with BglII and EcoRI and ligated into pCS2P+ vector that has EGFP. Zf Fz8a was amplified with the following primers: forward 5′-AGAATTCAACCACCATGGAG TGCTACCT-3′ and reverse 5′- GGATCCTCAGACTTGGGACA AAGGC-3′. PCR product was digested with EcoRI and BamHI and ligated into p3xFLAG-CMV-7.1 vector. Successful cloning was verified by restriction digestion and agarose gel electrophoresis.

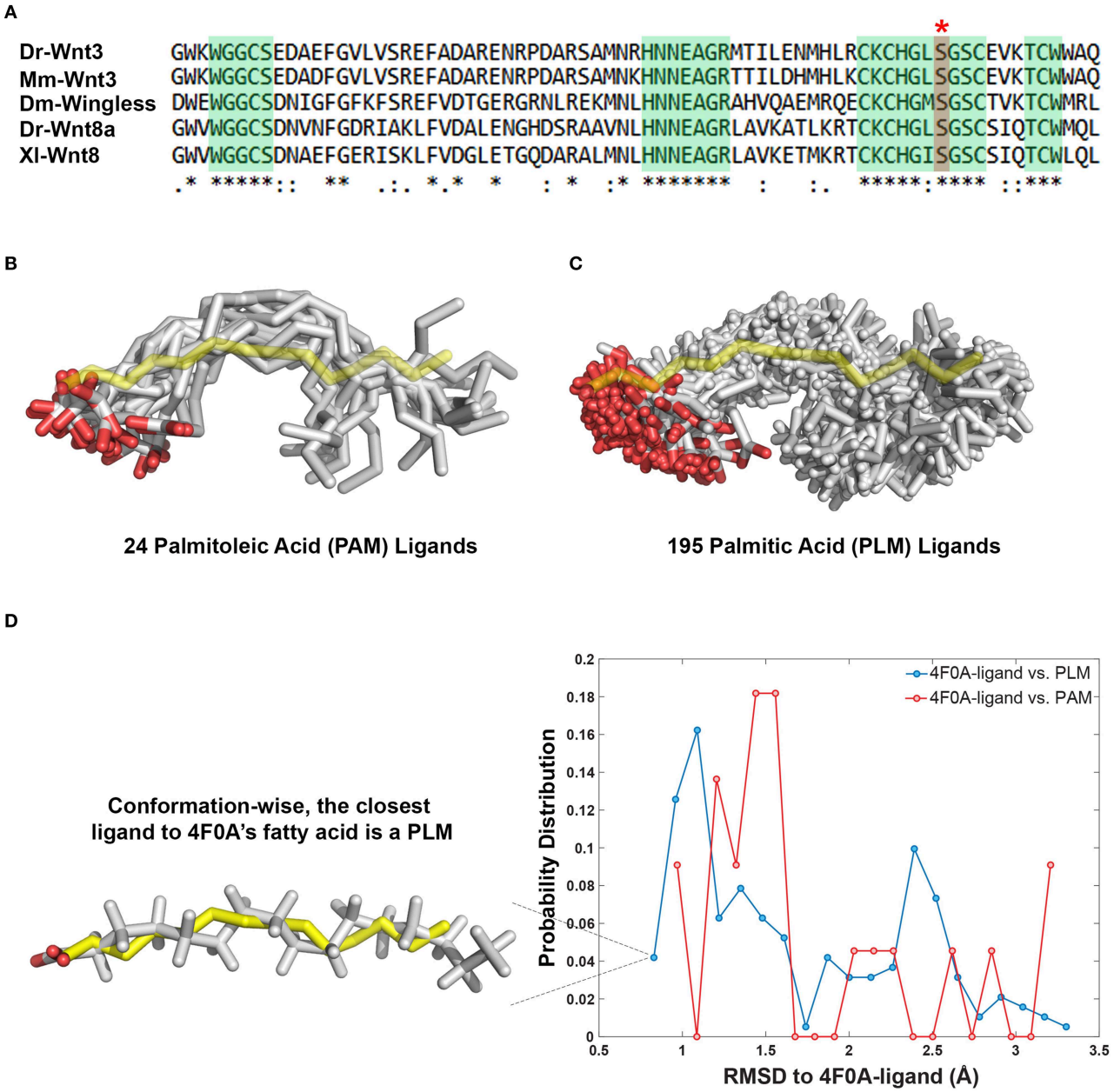

FIGURE 1 | PAM and PLM can adopt a diverse range of conformations. **(A)** Protein multiple sequence alignment covering a region conserved between two canonical Wnt ligands (Wnt3 and Wnt8) of vertebrates and Wingless (Wg) of *Drosophila*. A conserved serine amino acid (red marked column with asterisk) has been shown to be acylated in various ligands. Consensus sequences are marked in green. Dr *Danio rerio*, Mm, *Mus musculus*, Dm, *Drosophila melanogaster,* and Xl *Xenopus laevis*. **(B,C)** Structurally characterized **(B)** PAM and **(C)** PLM conformations downloaded from PDB (depicted in white sticks) aligned on the backbone of 4F0A's fatty acid (represented in yellow sticks). **(D)** The probability density distributions of being conformationally close to 4F0A's ligand. The closeness measure used is the Root-mean-square deviation (RMSD) from 4F0A's ligand, calculated over its carbon atoms. Available PLM ligand conformers have a higher probability to be <1 Å away from 4F0A's ligand. The closest ligand to 4F0A's ligand is a PLM molecule, which is depicted as an inset.

Capped Sense mRNA Synthesis, Microinjection, and Whole-Mount *in situ* Hybridization

Capped sense RNAs of wt Wnt3-GFP and Wnt3S212A-GFP were synthesized with mMessage mMachine Kit (Thermo Fisher Scientific, Waltham, MA, USA). For DRM flotation assay and qPCR, 1 ng of mRNA was injected into one-cell zebrafish embryos and embryos were fixed at 6 hpf in 4% paraformaldehyde (PFA) dissolved in PBS overnight. For whole-mount *in situ* hybridization (WMISH), 200 pg mRNA was

injected into one-cell zebrafish embryos and embryos were fixed at either 50% epiboly or 24 hpf in 4% PFA overnight. WMISH was performed with *mCherry*, *sp5l* or *foxg1a* and *her5* antisense RNA probes as described previously (Jowett and Lettice, 1994).

Quantitative PCR (qPCR)

Capped sense RNA (wt Wnt3-GFP, Wnt3S212A-GFP or membrane-bound GFP as control) was injected into one-cell zebrafish embryos. RNA was isolated from injected embryos at 7 hpf using Direct-zol RNA kit and cDNA was synthesized with iScript reverse transcriptase (RT). 1:1 mixture of oligodT and random primers were used and qPCR was performed in triplicates using *rpl13a* primers for normalization to determine relative gene expression levels. qPCR was performed using GoTaq qPCR master mix (Promega, Madison, WI, USA) at Applied Biosystems 7500 Fast Real Time PCR Machine (Foster City, CA, USA). The following primers were used for qPCR: *mCherry* forward 5′GAACGGCCACGAGTTCGAGA-3′, *mCherry* reverse 5′CTTGGAGCCGTACATGAACTGAGG-3′, Zf *sp5l* forward 5′-GCTTCACGCAGGTGTGGAT-3′, Zf *sp5l* reverse 5′-TTCT GGAGATGAGCTGGGAGT-3′, Zf *rpl13a* forward 5′-TCTG GAGGACTGTAAGAGGTATGC-3′ and Zf *rpl13a* reverse 5′-AGACGCACAATCTTGAGAGCAG-3′.

Transfection and Luciferase Assay

SH-SY5Y cells were seeded on 24-well plates and transfected in triplicates with 200 ng of wt Wnt3-GFP or Wnt3S212A-GFP or 75 ng of membrane-bound GFP as control together with 20 ng of firefly luciferase reporter pGL3 BAR (Biechele and Moon, 2008) and 5 ng of renilla luciferase reporter pGL4.73 hRLuc/SV40 (Promega, Madison, WI, USA) using Fugene HD Transfection Reagent (1 μg/1 μL, Promega). Twenty-four hours after transfection, reporter activity was measured using the dual luciferase reporter assay kit (Promega, Madison, WI, USA). Statistical analysis was performed using Student's *t*-test. Error bars represent SD, where $^{***}p < 0.001$, $^{**}p < 0.01$, and $^{*}p < 0.05$. HEK293T cells were transfected with wt Wnt3-EGFP or S212A Wnt3-EGFP by electroporation using the Neon® Transfection System (Invitrogen, Singapore) according to the manufacturer's protocol. The transfected cells were incubated for ∼24 h, washed with Hank's Balanced Salt Solution (HBSS; Invitrogen, Singapore) twice, and imaged using imaging medium (Phenol red free DMEM + 10% FBS). For cholesterol extraction measurements, 3 mM methyl-β-cyclodextrin (MßCD; Sigma-Aldrich) dissolved in HBSS was added to cells and incubated for 15 min. The treated cells were then washed with HBSS twice and measured in imaging medium.

DRM Flotation

Capped sense RNAs of wt Wnt3-GFP or Wnt3S212A-GFP injected into one-cell zebrafish embryos. Embryos were processed for detergent-resistant membrane (DRM) flotation protocol at 7 hpf. Embryos were collected in 1.5 mL test tubes, washed with ice-cold 1X TNE buffer (50 mM Tris [pH 7.4], 150 mM NaCl, and 2 mM EDTA). Embryos were lysed in 400 μL 1X TNE buffer containing phosphatase inhibitor (PI; Roche, Basel, Switzerland), protease inhibitor cocktail (PIC; Sigma-Aldrich, St. Louis, MO, USA) and 1% Triton X-100. Samples were then passed 20 times through a 26G needle, incubated on ice for 30 min and centrifuged at 4°C at 3,000 g for 5 min. Four hundred microliters of supernatant was homogenously mixed with 800 μL of OptiPrep Density Gradient Medium (60%, Sigma-Aldrich). Gradients were prepared by overlaying this mixture gently with 1,680 μL of 30% OptiPrep in 1X TNE and 720 μL of 5% Optiprep in 1X TNE (Sezgin et al., 2017a). Samples were ultracentrifuged at 226,800 g (45,000 rpm) for 6 h at 4°C using a type 90 Ti rotor in an Optima L-100 XP ultracentrifuge. Eight fractions were collected as 400 μL each. Proteins were precipitated by mixing the samples with 10% TCA and incubating for 15 min at −20°C. Samples were then centrifuged at 17,000 g at 4°C for 1 h. After centrifugation, supernatant was discarded, pellet was dissolved in sample loading dye and western blotting was performed.

Co-immunoprecipitation (CoIP)

HEK293T cells were seeded in 6-well plates. Cells were transfected with Zf wt Wnt3-GFP or ZfWnt3S212A-GFP together with Zf FLAG-Fz8a. Forty-eight hours after transfection, cells were washed with ice-cold PBS and lysed with NOP buffer [10 mM Hepes KOH pH 7.4, 150 mM NaCl, 2 mM EDTA, 10% glycerol, 1% NP40 (Igepal CA-630, Sigma-Aldrich)]. Samples were passed 20 times through a 21G needle and centrifuged at 300 g for 5 min at 4°C. Supernatant was precipitated with Dynabeads using Dynabeads Protein G Co-Immunoprecipitation Kit (Thermo Fisher Scientific) according to the kit protocol.

Secretion Assay

HEK293T cells were seeded in 10-cm culture plates. Cells were transfected with Zf wt Wnt3-GFP or ZfWnt3S212A-GF. Membrane-bound GFP and secreted GFP and were used as negative and positive controls, respectively. The day cells reached 100% confluence was accepted as day 0. Media was collected at day 2, 4, and 6, filtered with Minisart filters with a pore size of 0.2 μm (Merck, Burlington, MA, USA) and media was concentrated with Amicon Ultra-4 Centrifugal Filter Unit (Merck, Burlington, MA, USA). The viability and continuous growth of the collected cells was verified by MTT [3-(4,5-Dimethylthiazol-2-yl)-2,5-Diphenyltetrazolium Bromide] assay (**Figure S5**). For MTT assay, cells were seeded in a 96-well plate (5,000 cells/100 μL). 15 microliters of MTT reagent (5 mg/ml) was added onto the cells at 80% confluence (day-1), day 0, 2, 4, and 6. After 4 h incubation, media were removed and 100 μL of DMSO was added into each well. Cells were incubated for 30 min in dark. Absorbances were recorded at 570 nm. Samples were immunoprecipitated with an anti-GFP (see below) antibody using Dynabeads™ Protein G, prepared with 5X loading dye and processed for western blotting.

Western Blotting

Samples were dissolved in 5X loading dye and separated by SDS gel electrophoresis by running on 10% acrylamide-bisacrylamide gel. Proteins were transferred to polyvinylidene fluoride (PVDF) membrane (GE Healthcare Life science, Chicago, IL, USA). Membrane blots was blocked in 5% milk powder for 45 min

at room temperature (RT). Following antibodies were used at the indicated dilutions for membrane incubation. Primary antibodies: rabbit anti-GFP [(D5.1) XP, 1: 1000; Cell Signaling Technology, Danvers, MA, USA] rabbit anti-TfR2 (1:2000; Abcam, Cambridge, UK), mouse anti-Caveolin1 (1:2000; BD Transduction Laboratories, Franklin Lakes, NJ, USA) and anti-DDDDK tag antibody (ab1162, Abcam). Secondary antibodies: rabbit IgG HRP-linked F(ab′)2 fragment from donkey (1: 2500; GE Healthcare Bio-Sciences) and mouse IgG HRP Linked F(ab′)2 fragment from sheep (1:2500; GE Healthcare Bio-Sciences).

ITIR-FCS Measurements and Imaging FCS Diffusion Law

To investigate the membrane organization and dynamics of Wnt3 and its acylation site mutant, Imaging Total Internal Reflection Fluorescence Correlation Spectroscopy (ITIR-FCS) was performed on HEK293T cells transfected with wt Wnt3-EGFP or S212A Wnt3-EGFP. The transfected cells were mounted on an Olympus Inverted epi-fluorescence microscope IX83 with motorized TIRF illumination combiner (cell^TIRF/IX3-MITICO, Olympus). The cells were illuminated with 100 μW of a 488 nm laser (Olympus Cell Lasers), which was reflected to the back focal plane of an Olympus UApoN 100x/1.49 oil immersion objective using a ZT 405/488/561/640rpc (Chroma Technology, USA) dichroic mirror. The fluorescence signal was collected by the same objective and then was filtered using a quad band ZET 405/488/561/647m emission filter for TIRF applications (Chroma Technology, USA), and directed to an Andor iXon3 X-9388 EMCCD camera (128 × 128 pixels, 24 μm pixel size). All measurements were performed at 37°C and 5% CO_2 by fitting an incubator with an objective heater (Live Cell Instrument, CU-109, Chamlide, Seoul, Korea) and a CO_2/Air gas chamber (Live Cell Instrument, FC-5, Chamlide, Seoul, Korea) to the stage of the TIRF microscope. TIRF mode was achieved by adjusting the incident angle of illumination using the Olympus Xcellence software, thereby illuminating only the cell membrane. For data acquisition, a 21 × 21 pixel region was chosen in the center of the cell (sample plane of 5 × 5 μm^2), and 50,000 frames were acquired at 3 ms exposure. The obtained stacks were analyzed using the ImFCS plugin (http://www.dbs.nus.edu.sg/lab/BFL/imfcs_image_j_plugin.html) for Image J. Analysis of the intensity fluctuations was achieved via autocorrelation functions (ACF curves), which were fitted using equation (1) to obtain diffusion coefficient and number of particles maps. The ImFCS diffusion law (τ_D vs. A_{eff}) was plotted to obtain the τ_0 values which gives information about membrane organization and dynamics of the probe.

$$G(\tau) = \sum_{i}^{N_d} \alpha_i \left[\frac{\operatorname{erf}\left(p(\tau)\right) + \frac{\left(\exp -\left(p(\tau)\right)^2 - 1\right)}{\sqrt{\pi}\, p(\tau)}}{\operatorname{erf}\left(p(0)\right) + \frac{\left(\exp -\left(p(0)\right)^2 - 1\right)}{\sqrt{\pi}\, p(0)}} \right]^2 \left[1 + \left(\frac{F_t}{1 - F_t} \right) \exp\left(-\frac{\tau}{t_f} \right) \right] + G_\infty; \quad (1)$$

Where $p(\tau) = \frac{a}{\sqrt{4D\tau + \omega_0^2}}$ and $\alpha_i = \frac{B_i^2 \langle N_i \rangle}{\sum_i \left(B_i \langle N_i \rangle\right)^2}$

Here $G(\tau)$ is the temporal autocorrelation function containing N_d diffusive components, $\langle N_i \rangle$ represents the average number of particles in the detection area, B_i represents the brightness of component i, F_t is the fraction of particles in triplet state, a is the pixel size, t_f is the average time molecules spend in the triplet state, G_∞ is the convergence of G (τ) at long lag times and ω_0 is the $1/e^2$ radius of the Gaussian approximation of the microscope's point spread function (PSF). The fitting parameters are N, D, F_t, t_f, and G_∞.

The FCS diffusion law provides information on sub-resolution structures of membrane organization by measuring the dependence of the diffusion time of membrane probes at various observation areas (Wawrezinieck et al., 2005). The FCS diffusion law plot is generated by plotting the diffusion time (τ_D) of a probe vs. the transverse area of the confocal volume. Freely diffusing particles exhibit a linear relationship between τ_D and the observation area, while particles undergoing hindered diffusion due to confinement in membrane domains or particles undergoing hop diffusion due to meshwork compartmentalization in the cell membranes display non-linear transitions in the FCS diffusion law plots (Sezgin et al., 2017a). Positive, negative and zero intercept (τ_0) values indicate hindered diffusion with domain confinement, meshwork compartmentalized hop diffusion and free diffusion, respectively.

The FCS diffusion law can be implemented in imaging FCS (ImFCS), a camera based modality of FCS (Kannan et al., 2006; Sankaran et al., 2013), on either a Total Internal Reflection Fluorescence Microscope (TIRF) (Kannan et al., 2007) or a Single Plane Illumination Microscope (SPIM) (Wohland et al., 2010; Singh et al., 2013). In the ImFCS diffusion law, only a single measurement is required since various observation areas (A_{eff}) can be achieved by software binning of pixels post acquisition, and convoluting the detection area with the PSF (Bag et al., 2016; Veerapathiran and Wohland, 2018). So, for a of pixel side length a, the observation area is $A_{eff} = a^2 \otimes \mathrm{PSF}$. The ACFs for each observation area was calculated and fitted to obtain the diffusion time (τ_D) in a given observation area. The ImFCS diffusion law was then plotted and fitted with the Equation (2) to obtain the τ_0 value, and inverse slope of the plot would yield the effective diffusion coefficient (D_{eff}).

$$\tau_D(A_{eff}) = \tau_0 + \frac{A_{eff}}{D_{eff}} \quad (2)$$

Molecular Dynamics: Potential of Mean Force Calculations

Bilayers were constructed using insane (the MARTINI tool available at: cgmartini.nl/images/tools/insane/insane.py). Lipid parameters used were from Martini 2.1. The pulling simulations were performed using GROMACS version 4.6 (www.gromacs.org), with the MARTINI forcefield (Monticelli et al., 2008; de Jong et al., 2013), a pulling rate of 10 nm/ns and a pulling force constant of 10 kJ/mol/nm^2. Starting positions for umbrella-sampling simulations were extracted from the pulling simulations spaced at distances of 0.1 nm (or 0.05 nm for the 10 lowest distance windows) along the reaction co-ordinate. Each umbrella sampling simulation was run for 1 μs, with a harmonic

restraint of 1,000 kJ/mol/nm^2 applied between the center of mass of lipid phosphate moieties and the lipidated Ser187 center of mass. The potential of mean force was extracted from the umbrella sampling simulations using the Weighted Histogram Analysis Method (WHAM) provided by the GROMACS g_wham tool (Hub et al., 2013). Periodic boundary conditions were applied, and a time step of 20 fs was used in all simulations. The temperature was maintained at 323 K using a Berendsen thermostat (Berendsen et al., 1984), and the pressure at 1 bar using a Berendsen barostat, and compressibility 5×10^{-6} bar. For both the temperature and pressure, a coupling constant of 4 ps was used for all simulations. In all simulations, the reaction field coulomb type was used with a switching function from 0.0 to 1.2 nm, and the Lennard Jones interactions were cutoff at 1.2 nm with a switching function applied from 0.9 nm. The LINCS algorithm was used to constrain covalent bonds to their equilibrium values (Hess et al., 1997).

RESULTS

PAM and PLM Can Adopt a Diverse Range of Conformations

The Wnt proteins constitute a large family of secreted signaling molecules that are highly conserved among vertebrates. They are, however, less conserved between vertebrates and invertebrates while still exhibiting apparent orthologous relationships (Miller, 2002; Willert and Nusse, 2012) (**Figure 1A**). Another shared feature of Wnt proteins is the presence of a conserved serine amino acid that is palmitoylated (**Figure 1A**). Earlier, this palmitoylation was demonstrated to project from the conserved serine, located at the tip of Wnt's thumb into an extended groove within Fz8-CRD (Janda et al., 2012). As previous studies produced an ambiguity on the type of Wnt acylation due to experimental limitations (Takada et al., 2006; Janda et al., 2012), we initially set out to reveal whether the zebrafish canonical Wnt3 ligand is modified with a monounsaturated PAM or a saturated PLM at its conserved serine residue. For this purpose, we extracted PAM and PLM ligands from the PDB and aligned them on the resolved fatty acid structure of xWnt8-mouse Fz8-CRD complex (PDB id: 4F0A). This conformational analysis revealed that these both PLM and PAM flex into a diverse range of conformations (**Figures 1B,C**). It also highlighted that, unlike stated in the literature (Takada et al., 2006; Nile et al., 2017; Lee et al., 2019), both PAM and PLM could fold into a kinked conformation. Strikingly, among all published fatty acid coordinates, PLM has the highest probability to be the closest to 4F0A's fatty acid conformation (**Figure 1D**). Taken together with the ambiguities in determining the fatty acid type bound to the mouse Fz8 (Janda et al., 2012), we propose that 4F0A's fatty acid could very well be a PLM. This is also supported by the unrestrictive electron density of 4F0A's fatty acid ligand (**Figure S1**) (Janda et al., 2012). We also carried out potential of mean force calculations of PAM and PLM with pure membranes to predict their binding profile differences. Here, we simulated PAM and PLM binding to two different membranes with saturated or unsaturated lipids. These simulations did not reflect any difference between PAM or PLM membrane binding (**Figure S2**), suggesting that the fatty acid type is not a defining factor in the molecule's direct contact with the plasma membrane.

PLM Modified Wnt Permits Conformationally Viable Fz8-PLM Interaction

Next, we tested if PAM/PLM affects the binding of Wnt to Fz8. To this end, we designed two modeling scenarios, probing the structural differences between mouse Fz8-PAM and mouse Fz8-PLM interactions. For this, we constructed the atomistic models of mouse Fz8-PAM and mouse Fz8-PLM by using 4F0A's Fz8-fatty acid binding mode as a template (see section Materials and Methods, **Figure 2A**). Our Fz8-PAM and Fz8-PLM models unravel the following findings: (1) Both ligands are competent to reside along Fz8's hydrophobic channel. (2) However, only in the case of PLM the oxygen atoms of the fatty acid are close enough to be covalently linked to Ser187 of xWnt8 (compare **Figures 2B,C** and **Figure S3**). (3) Moreover, PLM induces a 6% increase in the buried surface area across the Fz8-fatty acid surface. Expanding on these observations, we generated the first structural model of zebrafish Fz8-PLM complex (see Materials and Methods) and PLM turned out to be compatible with zebrafish Fz8, similar to mouse Fz8. The critical residues of PLM interacting with the zebrafish Fz8 are highlighted in **Figure S4**. These results indicate that even though free PAM/PLM can interact with Fz8 in a similar manner, only Fz8-PLM is conformationally competent with Wnt's acylation.

Acylation of Wnt3 at the Conserved Serine Residue (S212) Is Not Necessary for Its Secretion and Interaction With Its Receptor

To test the influence of acylation on canonical Wnt function, we first aimed to determine whether the lack of acylation alters Wnt secretion and interaction with its receptor. To this purpose, we cloned the wild-type zebrafish Wnt3 into a pCS2P+ expression vector that has EGFP, termed as wt Wnt3-GFP (**Figure 3A**, top). By introducing a point mutation in zebrafish Wnt3 gene corresponding to the conserved serine residue at position 212 (S212), we generated a mutant Wnt3 which we termed as Wnt3S212A-GFP and has its serine replaced by alanine (**Figure 3A**, bottom). Then, to test whether lack of this acylation on Wnt3 has an influence on its secretion, we transfected HEK293T cells with wt Wnt3-GFP or Wnt3S212A-GFP with membrane-bound GFP (GFP:GPI) as negative and secreted GFP as positive control alongside. When we compared the secreted and total produced levels of the proteins, both wt Wnt3 and mutant Wnt3, albeit reduced, were found to be secreted into the media (**Figure 3B**). This reduction in secretion level could also be due to the lower growth rate of cells transfected with the mutant Wnt3 (**Figure S5**). Secreted GFP used as control was detected in the media, whereas membrane-bound GFP control was not (**Figure 3B**). Finally, to understand how S212 acylation of Wnt3 affects its physical interaction to

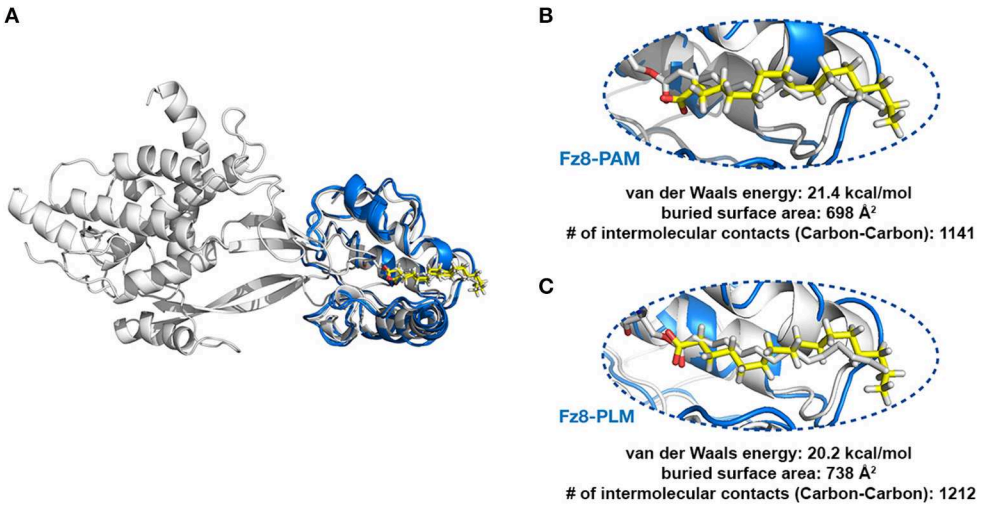

FIGURE 2 | PLM modified Wnt permits conformationally viable Fz8-PLM interaction. **(A)** xWnt8-Fz8-PAM complex is depicted in white. xWnt8-Fz8 are represented in cartoon, where PAM is denoted in sticks. Modeled PAM and PLM ligands (including the previously missing atoms we added) are represented in yellow sticks. **(B)** A close-up into the Fz8-PAM interactions. Modeled PAM cannot be aligned on the oxygen atoms of 4F0A's fatty acid. **(C)** PLM can direct its oxygen atoms without any problems to the serine that is modified.

Fz8 receptor, we co-expressed wt Wnt3-GFP or Wnt3S212A-GFP with Zf FLAG-Fz8a. Both wt and mutant Wnt3, which exclusively represent the exogenously expressed proteins, coimmunoprecipitated (coIPed) with the exogenously expressed receptor Fz8a (**Figure 3C**). These collected data suggest that acylation of zebrafish Wnt3 at the conserved serine residue is dispensable for its secretion and binding to its receptor Fz8 at the plasma membrane.

Acylation of Wnt3 Facilitates Its Partitioning Into More Ordered Plasma Membrane Environments

We have previously shown that the canonical Wnt ligand preferably interacts with its receptors residing in the ordered membrane environments and undergoes cholesterol and saturated lipid-dependent domain-like diffusion at the plasma membrane (Sezgin et al., 2017a). To examine the impact of S212 acylation on Wnt binding to its receptor complex, we performed subcellular fractionation and subsequent membrane flotation assay on zebrafish embryos injected with the capped sense RNAs of wt *Wnt3-GFP* or *Wnt3S212A-GFP*. We found that wt *Wnt3* was enriched in the detergent resistant membrane (DRM) fractions marked by DRM marker Caveolin1. Though not being definitive, DRM enrichment shows a propensity of the molecules to partition into the ordered domains of the plasma membrane (Brown and London, 1998; Magee and Parmryd, 2003; Lingwood and Simons, 2007) (**Figure 4A**, compare third row to the first row). *Wnt3S212A-GFP*, however, significantly shifted from the DRMs toward the detergent soluble phases of the membrane marked by the transmembrane receptor Transferrin-receptor 2 (Tfr2) (**Figure 4A**, compare fourth row to the second row. Eighty-five percent of wt Wnt3 detected in DRMs and only 16% of Wnt3S212A detected in DRMs). To substantiate our findings obtained via *in vitro* DRM analysis with a less harsh, more sensitive and more accurate approach, we employed the Imaging Total Internal Reflection Fluorescence Correlation Spectroscopy (ITIR-FCS) diffusion law. In ITIR-FCS, due to internal reflection, an evanescent wave of light illuminates only the cell membrane and, unlike confocal-based FCS, the intracellular signals are not detected. Moreover, since it is a camera-based method, the fast diffusion that originates from the intracellular signal cannot be recorded, resulting in recording of signals coming almost exclusively from the plasma membrane. The diffusion behavior of molecules on the membrane can be investigated by analyzing the τ_0 intercept values of the ImFCS diffusion law plots : a near zero intercept ($\tau_0 \leq \pm 0.2$ s) indicates free diffusion, a positive intercept ($\tau_0 > +0.2$ s) indicates domain confined diffusion due to membrane domains and a negative intercept ($\tau_0 < -0.2$ s) indicates hop-diffusion due to cytoskeleton compartmentalization (See Materials and Methods section). We expressed wt Wnt3-GFP or Wnt3S212A-GFP in HEK293T cells and evaluated the τ_0 value (**Figure 4B**). Our analyses revealed that wt Wnt3-EGFP undergoes domain-like diffusion (τ_0-value of 1.66 s $\pm$ 0.28 s) whereas Wnt3S212A-GFP shows reduced domain confinement with a lower y-axis intercept (τ_0-value of 0.71 s $\pm$ 0.25 s). On extraction of cholesterol using 3 mM MßCD, τ_0 converges to free diffusion at the plasma membrane for the mutant (τ_0-value of 0.16 s $\pm$ 0.1 s), indicating the importance of acylation of Wnt3 at S212 for its association to membrane domains on the membrane (**Figure 4C** and **Table 1**). These data collectively show that acylation of Wnt3 is necessary for its proper binding in the ordered environments and its domain-confined diffusion at the plasma membrane.

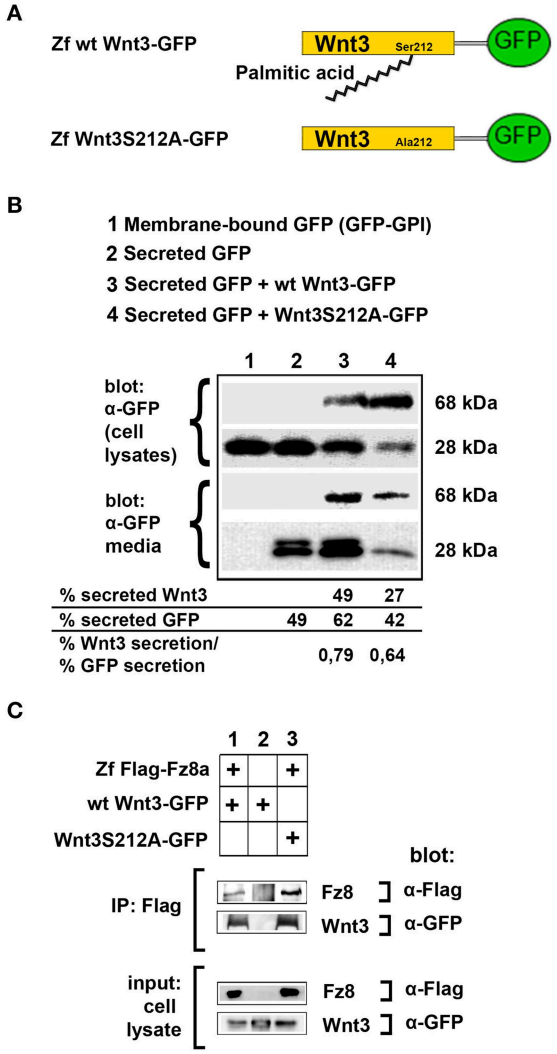

FIGURE 3 | Acylation of Wnt3 at the conserved serine residue (S212) is not necessary for its secretion and interaction with its receptor. **(A)** Domain structure of C-terminally GFP-tagged wild-type (Zf wt Wnt3-GFP) and mutant (zf Wnt3S121A-GFP) zebrafish Wnt3. Palmitic acid is attached to the conserved serine residue. Palmitoylation is supposed not to occur in the mutant construct where serine is replaced by alanine. **(B)** Secretion assay for wt and mutant Wnt3 proteins and western blot of input (cell lysates) and collected media. Both wt Wnt3-GFP and Wnt3S121A-GFP are detected in the media collected from HEK293T cells transfected with corresponding constructs. Secreted and total produced levels of the proteins were calculated and used for comparisons. Membrane-bound GFP (GFP:GPI) and secreted GFP are used as negative (non-secretory protein) and positive (secretory protein) controls, respectively. Forty-nine, sixty-two, and forty-two percent of total GFP were secreted from cells transfected with secreted (sec) GFP, sec GFP+ wt Wnt3-GFP and sec GFP+ Wnt3S212A-GFP, respectively. Forty-nine and twenty-seven percent of Wnt3 were secreted from cells transfected with sec GFP+ wt Wnt3-GFP and sec GFP+ Wnt3S212A-GFP, respectively. Ratios of secreted Wnt3 to secreted GFP were 0.79 and 0.64 for wt Wnt and Wnt3S212A, respectively. Percentages represent mean of three independent experiments. **(C)** Coimmunoprecipitation of wt and mutant Wnt3 proteins with Frizzled8 receptor. Both wt Wnt3-GFP and Wnt3S121A-GFP coIP with Zf FLAG-Fz8a in HEK293T cells. wt Wnt3-GFP does not bind to Dynabeads non-specifically. Three independent experiments were performed.

Acylation of Wnt3 Is Essential for Activation of Canonical Wnt Signaling

To investigate whether acylation of Wnt3 at the conserved serine influences Wnt/β-catenin signaling activity, we injected the capped sense RNAs of wt *Wnt3-GFP* or *Wnt3S212A-GFP* into 1-cell zebrafish embryos. While wt *Wnt3-GFP* efficiently suppressed eye formation at 24 hpf, a distinctive phenotype caused by enhanced Wnt/ß-catenin signaling (Lekven et al., 2001; Ozhan et al., 2013), *Wnt3S212A-GFP* overexpression did not exhibit any phenotypic alteration as compared to control (**Figure 5A**). Next to directly test the specificity of this effect on Wnt/β-catenin signaling, we exploited a transgenic zebrafish reporter of Wnt/ß-catenin signaling Tg(*7xTcf-Xla.Siam*:nlsm-Cherry^{ia}) (Moro et al., 2012). In contrast to strong activation of the reporter by wt *Wnt3-GFP* in embryos at both gastrula (50% epiboly) and organogenesis (24 hpf) stages, *Wnt3S212A-GFP* overexpression had no detectable effect on the reporter activity as shown by both WMISH at both stages and qPCR at the gastrula stage (**Figure 5B**, first and second columns, left; **Figure 5C**, left). *Wnt3S212A-GFP* appeared to reduce the expression of the direct Wnt/ß-catenin target gene *sp5l* (Weidinger et al., 2005) as detectable by WMISH and qPCR at the gastrula stage (**Figure 5B**, second column, right; **Figure 5C**, right). This reduction could be due to a potential dominant negative effect of the mutation. During vertebrate gastrulation, Wnt/β-catenin signaling is required for induction of posterior neural fates in neuroectodermal patterning (Lekven et al., 2001). wt *Wnt3-GFP* overexpression thus reduced the anterior neuroectodermal fates, as evidenced by complete elimination of the telencephalon marker *foxg1a* at organogenesis while the midbrain-hindbrain boundary marker *her5* is preserved (**Figure 5B**, rightmost column). On the contrary, *Wnt3S212A-GFP* expressing embryos appeared indifferent to the control (**Figure 5B**, first column, right). Next we tested the activity of the wt and mutant Wnt3 constructs in mammalian cells and found that Wnt3S212A-GFP, similarly to zebrafish embryos, was unable to activate on Wnt/β-catenin signaling in SH-SY5Y cells as evidenced by the activation of the pBAR reporter of Tcf/Lef-mediated transcription (**Figure 5D**). Thus, we conclude that acylation of Wnt3 at the conserved serine residue is required for Wnt3 to activate canonical Wnt signaling.

DISCUSSION

The dynamic lateral heterogeneity in the plasma membrane is known to control the formation of canonical Wnt-receptor complex by ensuring that the Wnt ligand preferentially binds to its receptors in ordered membrane environments where it activates downstream signaling pathway (Sezgin et al., 2017a). However, whether the posttranslational lipid modifications of Wnt influence this preferential binding remained to be understood. Our study uncovers the role of a specific lipid modification, acylation with a saturated fatty acid, of canonical Wnt ligand in regulation of its interactions with

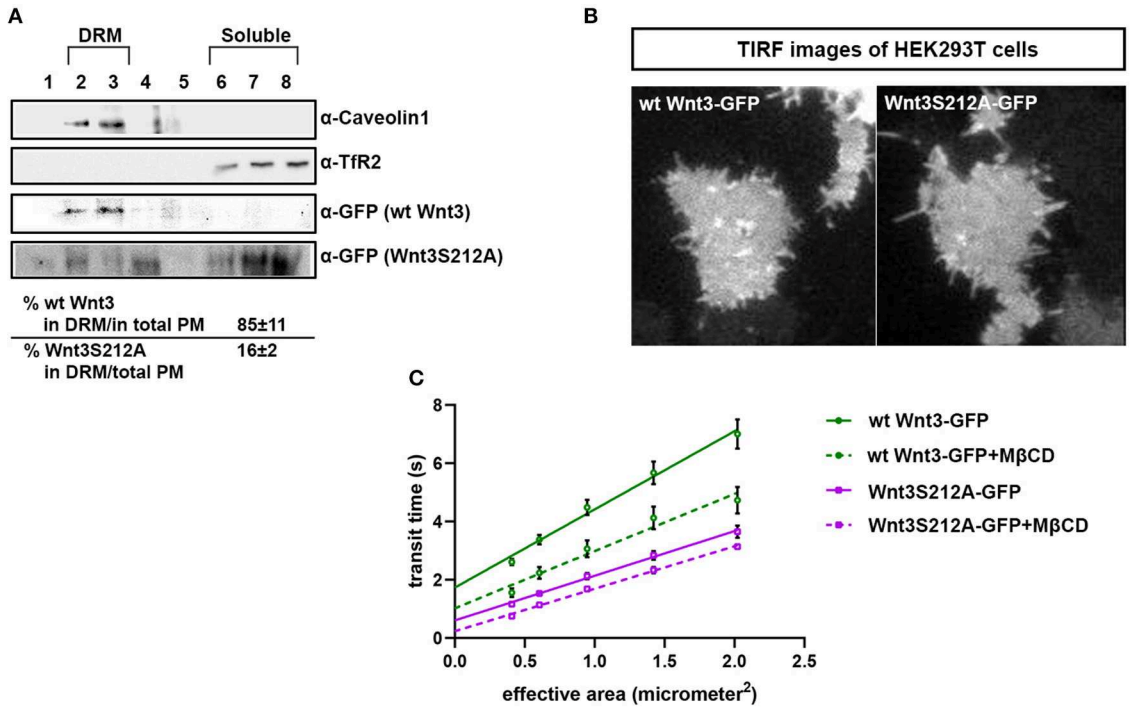

FIGURE 4 | Acylation of Wnt3 facilitates its partitioning into more ordered plasma membrane environments. **(A)** Membrane flotation assay for wt and mutant Wnt constructs. Western blots show soluble and detergent-resistant fractions of plasma membranes derived from zebrafish embryos injected with 1 ng capped sense RNA of wt *Wnt3-GFP* or *Wnt3S212A-GFP*. DRMs and soluble fractions are marked by endogenous TfR2 and Caveolin-1 (Cav1), respectively. All Wnt proteins are detected by their GFP tags. Eighty-five percent of wt Wnt3-GFP is detected in the DRM fractions while only sixteen percent of mutant Wnt3S212A-GFP is detected in DRMs with the rest of it shifting to soluble phases. Percentages represent mean ± standard deviation (SD) of three independent experiments. **(B)** TIRF images of HEK293T cells expressing wt Wnt3-GFP and Wnt3S212A-GFP **(C)** ITIR-FCS measurements. Signal is recorded from the basolateral membrane of the cells and correlated with different bin size to form varying observation areas. The diffusion time positively correlates with the size of the area and determines the diffusion mode of the molecule as free or hindered. wt Wnt3-GFP undergoes domain-like diffusion (positive y-axis intercept) while Wnt3S212A-GFP tends to diffuse freely after cholesterol extraction. MβCD, methyl-β-cyclodextrin. Transit time and SD are obtained from three independent experiments.

TABLE 1 | Y-axis intercept (τ_0 values) for the ImFCS diffusion law of wt Wnt3 and Wnt3S212A mutant in HEK293 cells.

	Untreated	3 mM MßCD
wt-Wnt3	1.66 ± 0.28 s	0.78 ± 0.19 s
Wnt3S212A	0.71 ± 0.25 s	0.16 ± 0.1 s

the receptor complex within the ordered membrane regions. Our computational, biochemical and biophysical data together suggest that (i) the canonical Wnt3 ligand is acylated at a conserved serine residue presumably with a saturated fatty acid PLM, (ii) this acylation, while being dispensable for its secretion and interaction with the Fz8 receptor, (iii) is essential for its proper partitioning into the ordered membrane domains, (iv) where Wnt can activate downstream canonical Wnt signaling. Therefore, the acylation appears to assist canonical Wnt in associating with the proper domains of the plasma membrane where it can activate the signaling.

Palmitoylation serves an essential function in protein activation through modifying hydrophobicity and conformation, and ultimately determining the protein's subcellular localization and function (Smotrys and Linder, 2004). Acylation of mWnt3a has been proposed to occur through addition of a palmitoleic acid, a monounsaturated fatty acid, to a conserved serine residue (Takada et al., 2006). This, however, does not properly align with (1) the preferential binding of the canonical Wnt ligand to its receptor complex in the ordered membrane domains (Sezgin et al., 2017a) and (2) the influence of steric preference for a saturated fatty acid on Wnt's domain confinement and signaling activity. In this work, the authors also speculated that the kinked nature of the unsaturated fatty acid, PAM is essential to its packing into the interior of small lipid particles (Takada et al., 2006). Other studies have likewise assumed that due to its unsaturated nature, only PAM exerts a kinked conformation, whereas PLM adopts a linear one (Nile et al., 2017; Lee et al., 2019). Lee et al. (2019) have further argued that the cavity of human Porcupine protein, a member of the membrane-bound O-acyl transferases catalyzing the posttranslational fatty acylation of Wnts, is likely to recognize the kink in the unsaturated fatty acyl substrate. Our thorough analysis of the available PAM and PLM conformers, however, has demonstrated that both ligands span a diverse range of conformations, from linear to kinked (**Figure 1**); excluding the possibility that binding of PAM or PLM is driven by shape selectivity. Thus, we suggest that Porcupine's cavity easily

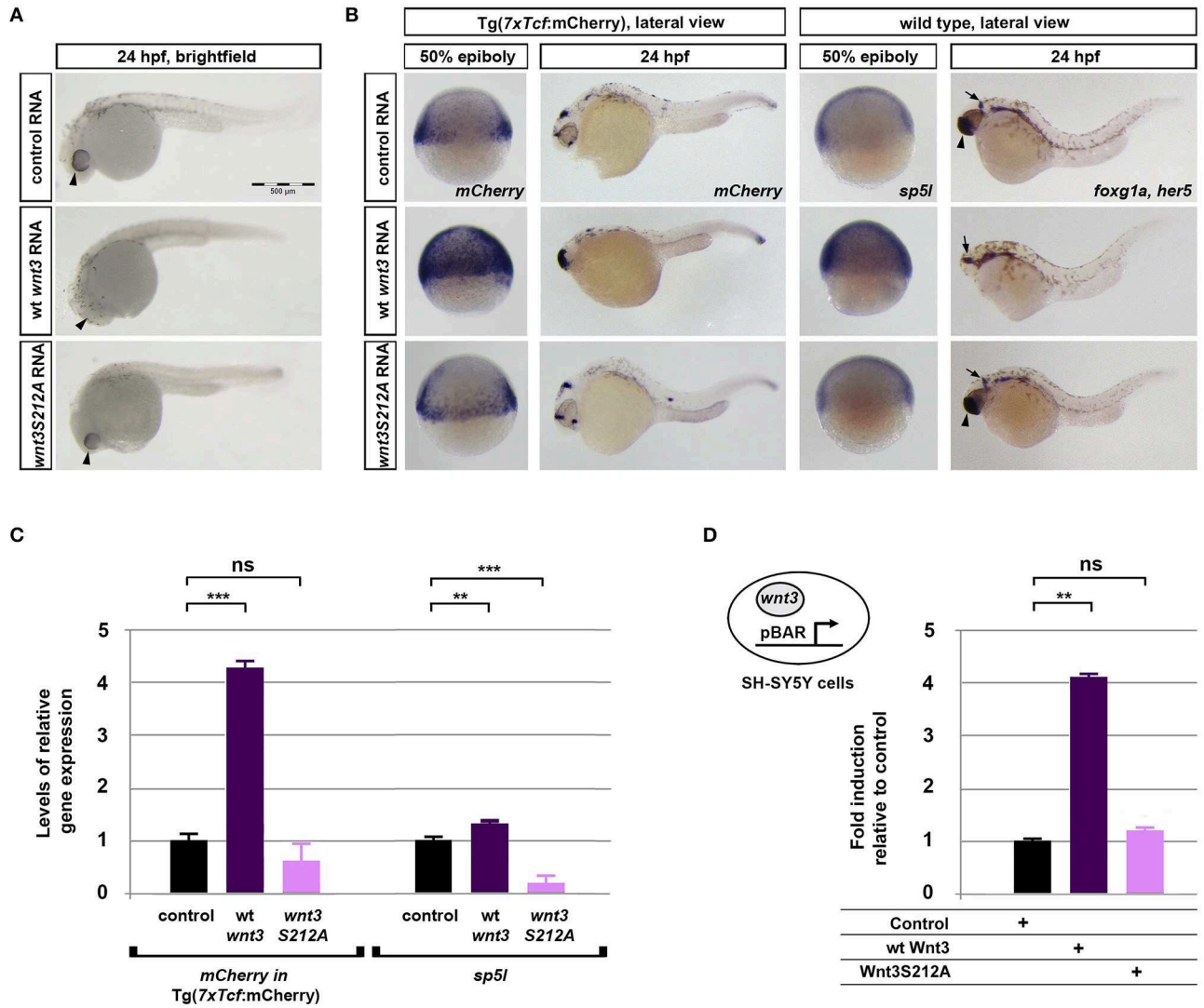

FIGURE 5 | Acylation of Wnt3 is essential for activation of canonical Wnt signaling. **(A)** Morphological phenotypes at 24 hpf of embryos injected with capped sense RNA of *Wnt3-EGFP* (200 pg, 53/56 embryos) or *Wnt3(S212A)-EGFP* (200 pg, 46/49 embryos). **(B)** Whole mount *in situ* hybridization (WMISH) showing the loss of capacity in *Wnt3(S212A)-EGFP* (200 pg) capped sense RNA to activate canonical Wnt signaling. First and second columns left: *mCherry* WMISH shows upregulation of signaling in the transgenic Tg(*7xTcf-Xla.Siam:nlsm-Cherry*^{ia}) canonical Wnt/ß-catenin reporter embryos by *Wnt3-EGFP* (36/36) but not by *Wnt3(S212A)-EGFP* (32/33). Second column right: Direct Wnt/ß-catenin target gene *sp5l* is upregulated by *Wnt3-EGFP* (30/32) but not by *Wnt3(S212A)-EGFP* (29/32). Rightmost column: *Wnt3-EGFP* (33/34), but not *Wnt3(S212A)-EGFP* (36/36), completely abolishes the telencephalon, marked by *foxg1a* (arrowhead), while the midbrain-hindbrain boundary, marked by *her5* (arrow), is preserved. **(C)** Expression levels of *mCherry* in transgenic Tg(7xTcf-Xla.Siam:nlsm-Cherry^{ia}) and *sp5l* in wt embryos injected with capped sense RNAs of *Wnt3-EGFP* (200 pg) or *Wnt3(S212A)-EGFP* (200 pg) and determined by qPCR. Four independent experiments were performed. **(D)** Average and SD of the mean (error bars) values of pBAR luciferase reporter activity monitoring Wnt/ß-catenin signaling activity (normalized to renilla luciferase activity) in SH-SY5Y cells transfected with wt Wnt3-GFP or Wnt3S212A-GFP. wt Wnt3-GFP significantly activated the reporter whereas Wnt3S212A-GFP did not. Statistical significance was evaluated using unpaired *t*-test. ***$p < 0.001$, **$p < 0.01$, and n.s., non-significant. Error bars represent SD. Three independent experiments were performed.

allows a saturated fatty acyl chain such as PLM to fit in by taking its shape.

While the structural basis of a lipid-modified Wnt recognition by Fz has been resolved, the full atomistic details of this lipid modification has remained unclear (Janda et al., 2012). The fact that Janda et al. could not unambiguously determine the chemical identity of the lipid bound to mouse Fz8 by mass spectrometry (Janda et al., 2012) induces an open discussion platform whether there is any inherent molecular specificity encoded in Fz8 toward PAM or PLM. In this work, we present the first structural evidence that mouse Fzd8 prefers to bind to PLM instead of PAM since only PLM could adopt a conformation compatible with the stereochemical features Wnt modification, while not entirely excluding the possibility that Wnt3 could also

be modified by PAM. We believe that the saturation of this lipid facilitates binding of Wnt in the ordered domains of the plasma membrane where saturated lipids are enriched. A promising question would be to compare how differently Wnt ligands with saturated and unsaturated lipid modifications behave in binding to the membrane domains. PLM binding is also endorsed by the increased buried surface area, indicating a tighter interaction with Fz8. In addition, transferring these findings to an analogous zebrafish system reveals the zebrafish Fz8 amino acids that are potentially critical to its interaction with a PLM molecule. Thus, it will be very interesting to further test how these amino acids influence binding of Fz8 to the PLM of Wnt3.

Independent studies on mWnt1 and mWnt3a showed that secretion of lipid-deficient Wnts were significantly reduced and these mutants displayed significantly less signaling activity than wild-type Wnts (Takada et al., 2006; Galli and Burrus, 2011; Gao and Hannoush, 2014). In contrast, the same ligands without lipidic adducts at their conserved serine residues were found to be secreted normally and showed no significant differences in their abilities to bind the Wnt receptor Fz4 as compared to their wild-type counterparts (Doubravska et al., 2011). These acyl-deficient Wnts, however, were not able to activate signaling, implying that acylation is indispensable for proper activation of the canonical Wnt pathway (Doubravska et al., 2011). Similarly, *Drosophila* Wg mutant WgS239A, where acylation is prevented due to replacement of its conserved serine residue with an alanine, was shown to be secreted normally into the media of *Drosophila* S2 cells, but displayed poor signaling activity (Franch-Marro et al., 2008). A recent work has likewise reported that mutation of the conserved acylation site of xWnt8 or mWnt1 interferes neither with its secretion into the culture medium when expressed in HEK293 or Expi293 cells nor with its interaction with the Fz receptor (Speer et al., 2019). The ability of several non-acylated Wnts including xWnt8S187A, mWnt1S224A and hWnt3aS209A to activate signaling varied significantly and even contrasted for mWnt1S224A between *in vitro* and *in vivo*, arguing that, acylation dependence varies between different Wnt ligands and that this dependence can even be regulated in a biological context-dependent manner (Speer et al., 2019). Our results show that S212 acylation of zebrafish Wnt3 presumably with a saturated fatty acid, while reducing its secretion, is largely dispensable for its secretion and binding to its receptor Fz8 at the plasma membrane, but is essential for activation of signaling. Thus, we believe that, the role of acylation in protein secretion, receptor interaction and pathway activation varies between Wnt ligands, so it needs to be elucidated for each ligand individually and compared in different cellular contexts. Individual and context-dependent characterization of Wnt ligands will also yield important information on how to modulate Wnt signaling activity in different types of cancers. Moreover, Janda et al. reported that cysteine 55 (C55) residue of XWnt8 does not serve as a lipidation site but is rather engaged in a disulfide bond (Janda et al., 2012). Given the major role of lipidation in Wnt signaling, more work is required to elucidate whether indeed C80 in zebrafish Wnt3, the cysteine residue analogous to C55 in XWnt8 and C77 in mouse Wnt3a, is not lipidated.

Although Wnt/β-catenin signaling pathway have been extensively explored for the development of new drugs that inhibit canonical Wnt signaling, so far, no drugs have been approved to target the pathway (Zimmerman et al., 2012; Anastas and Moon, 2013; Bao et al., 2013; Kahn, 2014; Nusse and Clevers, 2017; Krishnamurthy and Kurzrock, 2018). A considerable amount of drugs that has entered the clinical trials consist of antibodies that target Fz CRDs at the plasma membrane (Gurney et al., 2012; Lee et al., 2015; Le et al., 2015; Tran and Zheng, 2017; Krishnamurthy and Kurzrock, 2018; Zeng et al., 2018). However, the fact that these antibodies target Fz receptors ubiquitously in a domain-independent manner contradicts the fact that the receptor pool, which can be activated by ligand binding, localizes in the ordered membrane domains (Sezgin et al., 2017a). In addition to domain-dependent activation of the receptor pool by the Wnt ligand, we show that acylation of Wnt is necessary for signaling, rendering domain-specific receptor targeting even more important for drug development strategies. Our study reveals that acylation of canonical Wnt ligand is critical for regulation of signaling activity via controlling the ligand's physical interactions with the receptor and the plasma membrane. Considering the major differences between the plasma membranes of healthy and cancer cells, novel therapies based on targeting the cancer cell membrane in a lipid-specific manner is very likely to constitute a promising approach for anticancer drug development. One such approach would be to modify candidate Fz CRD inhibitor molecules with proper lipid groups such as PLM to target them specifically to the Fz receptors residing in the ordered membrane domains and this way to convert them into more potent therapeutic agents to inhibit abnormal Wnt signaling.

DATA AVAILABILITY STATEMENT

The datasets generated for this study can be found in the https://github.com/ezgikaraca/Wnt-acylation.

ETHICS STATEMENT

The animal study was reviewed and approved by Dokuz Eylul University-Izmir International Biomedicine and Genome Institute-Animal Experiments Local Ethics Committee.

AUTHOR CONTRIBUTIONS

GO, YA, ES, and EK designed the experiments. YA and GO performed the biochemical and developmental experiments (**Figures 3**, **4A**, **5** and **Figure S5**). OO and EK conducted the structural modeling experiments (**Figures 1**, **2** and **Figures S1, S3, S4, S6**). SV performed the biophysical experiments (**Figures 4B,C**). AD performed the molecular dynamics experiments (**Figure S2**). MS, CE, and TW contributed reagents and materials analysis tools. GO, ES, and EK wrote the manuscript. All authors contributed to the discussion.

ACKNOWLEDGMENTS

We thank Izmir Biomedicine and Genome Center Vivarium-Zebrafish Core Facility and Optical Imaging Core Facility for providing zebrafish care and microscope facility support, respectively. ES is funded by Newton-Katip Celebi Fund (grant number 352333122). SV is supported by Research Scholarship from National University of Singapore. TW acknowledges funding by the Singapore Ministry of Education (MOE2016-T3-1-005). MS and AD are supported by the BBSRC (grant number BB/R00126X/1) and Pembroke College, Oxford (BTP Fellowship); simulations were performed on ARCHER. MS lab is funded by Wellcome Trust (grant number 208361/Z/17/Z). AD would like to thank George Hedger for instructive discussions. GO Lab is funded by EMBO Installation Grant (grant number 3024). This work has been supported by the bilateral grant of British Council and Scientific and Technological Research Council of Turkey (TUBITAK) with the program name Newton-Katip Celebi Fund (TUBITAK grant number 217Z141). ES and CE are funded by Wolfson Foundation, the Medical Research Council (MRC, grant number MC_UU_12010/unit programmes G0902418 and MC_UU_12025), MRC/BBSRC/EPSRC (grant number MR/K01577X/1) and Wellcome Trust (grant ref 104924/14/Z/14) for microscope facility usage and general lab and staff support. EK acknowledges Alexander von Humboldt Foundation Return Fellowship.

SUPPLEMENTARY MATERIAL

The Supplementary Material for this article can be found online at: https://www.frontiersin.org/articles/10.3389/fcell.2019.00281/full#supplementary-material

REFERENCES

Agarwal, S. R., Gratwohl, J., Cozad, M., Yang, P. C., Clancy, C. E., and Harvey, R. D. (2018). Compartmentalized cAMP signaling associated with lipid raft and non-raft membrane domains in adult ventricular myocytes. *Front. Pharmacol.* 9:332. doi: 10.3389/fphar.2018.00332

Anastas, J. N., and Moon, R. T. (2013). WNT signalling pathways as therapeutic targets in cancer. *Nat. Rev. Cancer* 13, 11–26. doi: 10.1038/nrc3419

Angers, S., and Moon, R. T. (2009). Proximal events in Wnt signal transduction. *Nat. Rev. Mol. Cell Biol.* 10, 468–477. doi: 10.1038/nrm2717

Badawy, S. M. M., Okada, T., Kajimoto, T., Hirase, M., Matovelo, S. A., Nakamura, S. I., et al. (2018). Extracellular alpha-synuclein drives sphingosine 1-phosphate receptor subtype 1 out of lipid rafts, leading to impaired inhibitory G-protein signaling. *J. Biol. Chem.* 293, 8208–8216. doi: 10.1074/jbc.RA118.001986

Bag, N., Ng, X. W., Sankaran, J., and Wohland, T. (2016). Spatiotemporal mapping of diffusion dynamics and organization in plasma membranes. *Methods Appl. Fluoresc.* 4:034003. doi: 10.1088/2050-6120/4/3/034003

Bao, J., Lee, H. J., and Zheng, J. J. (2013). Genome-wide network analysis of Wnt signaling in three pediatric cancers. *Sci. Rep.* 3:2969. doi: 10.1038/srep02969

Berendsen, H. J. C., Postma, J. P. M., van Gunsteren, W. F., Di Nola, A., and Haak, J. R. (1984). Molecular dynamics with coupling to an external bath. *J. Chem. Phys.* 81, 3684–3690. doi: 10.1063/1.448118

Biechele, T. L., and Moon, R. T. (2008). Assaying beta-catenin/TCF transcription with beta-catenin/TCF transcription-based reporter constructs. *Methods Mol. Biol.* 468, 99–110. doi: 10.1007/978-1-59745-249-6_8

Brown, D. A., and London, E. (1998). Functions of lipid rafts in biological membranes. *Annu. Rev. Cell Dev. Biol.* 14, 111–136. doi: 10.1146/annurev.cellbio.14.1.111

Clevers, H. (2006). Wnt/beta-catenin signaling in development and disease. *Cell* 127, 469–480. doi: 10.1016/j.cell.2006.10.018

Clevers, H., and Nusse, R. (2012). Wnt/beta-catenin signaling and disease. *Cell* 149, 1192–1205. doi: 10.1016/j.cell.2012.05.012

de Jong, D. H., Singh, G., Bennett, W. F., Arnarez, C., Wassenaar, T. A., Schafer, L. V., et al. (2013). Improved parameters for the martini coarse-grained protein force field. *J. Chem. Theory Comput.* 9, 687–697. doi: 10.1021/ct300646g

Dinic, J., Riehl, A., Adler, J., and Parmryd, I. (2015). The T cell receptor resides in ordered plasma membrane nanodomains that aggregate upon patching of the receptor. *Sci. Rep.* 5:10082. doi: 10.1038/srep10082

Doubravska, L., Krausova, M., Gradl, D., Vojtechova, M., Tumova, L., Lukas, J., et al. (2011). Fatty acid modification of Wnt1 and Wnt3a at serine is prerequisite for lipidation at cysteine and is essential for Wnt signalling. *Cell Signal.* 23, 837–848. doi: 10.1016/j.cellsig.2011.01.007

Franch-Marro, X., Wendler, F., Griffith, J., Maurice, M. M., and Vincent, J. P. (2008). *In vivo* role of lipid adducts on Wingless. *J. Cell Sci.* 121, 1587–1592. doi: 10.1242/jcs.015958

Galli, L. M., and Burrus, L. W. (2011). Differential palmit(e)oylation of Wnt1 on C93 and S224 residues has overlapping and distinct consequences. *PLoS ONE* 6:e26636. doi: 10.1371/journal.pone.0026636

Gao, X., and Hannoush, R. N. (2014). Single-cell imaging of Wnt palmitoylation by the acyltransferase porcupine. *Nat. Chem. Biol.* 10, 61–68. doi: 10.1038/nchembio.1392

Gurney, A., Axelrod, F., Bond, C. J., Cain, J., Chartier, C., Donigan, L., et al. (2012). Wnt pathway inhibition via the targeting of Frizzled receptors results in decreased growth and tumorigenicity of human tumors. *Proc. Natl. Acad. Sci. U.S.A.* 109, 11717–11722. doi: 10.1073/pnas.1120068109

Guven-Maiorov, E., Keskin, O., Gursoy, A., VanWaes, C., Chen, Z., Tsai, C. J., et al. (2015). The architecture of the TIR domain signalosome in the toll-like receptor-4 signaling pathway. *Sci. Rep.* 5:13128. doi: 10.1038/srep13128

Hess, B., Bekker, H., Berendsen, H. J. C., and Fraaije, J. G. E. M. (1997). A linear constraint solver for molecular simulations. *J. Comp. Chem.* 18, 1463–1472.

Huang, H., and He, X. (2008). Wnt/beta-catenin signaling: new (and old) players and new insights. *Curr. Opin. Cell Biol.* 20, 119–125. doi: 10.1016/j.ceb.2008.01.009

Hub, J. S., de Groot, B. L., and van der Spoel, D. (2013). g_wham—a free weighted histogram analysis implementation including robust error and autocorrelation estimates. *J. Chem. Theory Comput.* 6, 3713–3720. doi: 10.1021/ct100494z

Janda, C. Y., Waghray, D., Levin, A. M., Thomas, C., and Garcia, K. C. (2012). Structural basis of Wnt recognition by Frizzled. *Science* 337, 59–64. doi: 10.1126/science.1222879

Jowett, T., and Lettice, L. (1994). Whole-mount in situ hybridizations on zebrafish embryos using a mixture of digoxigenin- and fluorescein-labelled probes. *Trends Genet.* 10, 73–74. doi: 10.1016/0168-9525(94)90220-8

Jury, E. C., Flores-Borja, F., and Kabouridis, P. S. (2007). Lipid rafts in T cell signalling and disease. *Semin. Cell Dev. Biol.* 18, 608–615. doi: 10.1016/j.semcdb.2007.08.002

Kahn, M. (2014). Can we safely target the WNT pathway? *Nat. Rev. Drug Discov.* 13, 513–532. doi: 10.1038/nrd4233

Kannan, B., Guo, L., Sudhaharan, T., Ahmed, S., Maruyama, I., and Wohland, T. (2007). Spatially resolved total internal reflection fluorescence correlation microscopy using an electron multiplying charge-coupled device camera. *Anal. Chem.* 79, 4463–4470. doi: 10.1021/ac0624546

Kannan, B., Har, J. Y., Liu, P., Maruyama, I., Ding, J. L., and Wohland, T. (2006). Electron multiplying charge-coupled device camera based fluorescence correlation spectroscopy. *Anal. Chem.* 78, 3444–3451. doi: 10.1021/ac0600959

Kikuchi, A., and Yamamoto, H. (2007). Regulation of Wnt signalling by receptor-mediated endocytosis. *J. Biochem.* 141, 443–451. doi: 10.1093/jb/mvm061

Komekado, H., Yamamoto, H., Chiba, T., and Kikuchi, A. (2007). Glycosylation and palmitoylation of Wnt-3a are coupled to produce an active form of Wnt-3a. *Genes Cells* 12, 521–534. doi: 10.1111/j.1365-2443.2007.01068.x

Krishnamurthy, N., and Kurzrock, R. (2018). Targeting the Wnt/beta-catenin pathway in cancer: update on effectors and inhibitors. *Cancer Treat Rev.* 62, 50–60. doi: 10.1016/j.ctrv.2017.11.002

Kurayoshi, M., Yamamoto, H., Izumi, S., and Kikuchi, A. (2007). Post-translational palmitoylation and glycosylation of Wnt-5a are necessary for its signalling. *Biochem J.* 402, 515–523. doi: 10.1042/BJ20061476

Le, P. N., McDermott, J. D., and Jimeno, A. (2015). Targeting the Wnt pathway in human cancers: therapeutic targeting with a focus on OMP-54F28. *Pharmacol. Ther.* 146, 1–11. doi: 10.1016/j.pharmthera.2014.08.005

Lee, C. J., Rana, M. S., Bae, C., Li, Y., and Banerjee, A. (2019). In vitro reconstitution of Wnt acylation reveals structural determinants of substrate recognition by the acyltransferase human porcupine. *J. Biol. Chem.* 294, 231–245. doi: 10.1074/jbc.RA118.005746

Lee, H. J., Bao, J., Miller, A., Zhang, C., Wu, J., Baday, Y. C., et al. (2015). Structure-based discovery of novel small molecule wnt signaling inhibitors by targeting the cysteine-rich domain of frizzled. *J. Biol. Chem.* 290, 30596–30606. doi: 10.1074/jbc.M115.673202

Lekven, A. C., Thorpe, C. J., Waxman, J. S., and Moon, R. T. (2001). Zebrafish wnt8 encodes two wnt8 proteins on a bicistronic transcript and is required for mesoderm and neurectoderm patterning. *Dev. Cell* 1, 103–114. doi: 10.1016/S1534-5807(01)00007-7

Levental, I., Lingwood, D., Grzybek, M., Coskun, U., and Simons, K. (2010). Palmitoylation regulates raft affinity for the majority of integral raft proteins. *Proc. Natl. Acad. Sci. U.S.A.* 107, 22050–22054. doi: 10.1073/pnas.1016184107

Lingwood, D., and Simons, K. (2007). Detergent resistance as a tool in membrane research. *Nat. Protoc.* 2, 2159–2165. doi: 10.1038/nprot.2007.294

Logan, C. Y., and Nusse, R. (2004). The Wnt signaling pathway in development and disease. *Annu. Rev. Cell Dev. Biol.* 20, 781–810. doi: 10.1146/annurev.cellbio.20.010403.113126

Luz, M., Spannl-Muller, S., Ozhan, G., Kagermeier-Schenk, B., Rhinn, M., Weidinger, G., et al. (2014). Dynamic association with donor cell filopodia and lipid-modification are essential features of Wnt8a during patterning of the zebrafish neuroectoderm. *PLoS ONE* 9:e84922. doi: 10.1371/journal.pone.0084922

MacDonald, B. T., Tamai, K., and He, X. (2009). Wnt/beta-catenin signaling: components, mechanisms, and diseases. *Dev. Cell* 17, 9–26. doi: 10.1016/j.devcel.2009.06.016

Magee, A. I., and Parmryd, I. (2003). Detergent-resistant membranes and the protein composition of lipid rafts. *Genome Biol.* 4:234. doi: 10.1186/gb-2003-4-11-234

Martin, A. C. R., and Porter, C. T. (2009). *ProFit Version 3.1*. London: University College London. Available online at: http://www.bioinf.org.uk/software/profit/index.html

Mason, J. O., Kitajewski, J., and Varmus, H. E. (1992). Mutational analysis of mouse Wnt-1 identifies two temperature-sensitive alleles and attributes of Wnt-1 protein essential for transformation of a mammary cell line. *Mol. Biol. Cell* 3, 521–533. doi: 10.1091/mbc.3.5.521

Midgley, A. C., Rogers, M., Hallett, M. B., Clayton, A., Bowen, T., Phillips, A. O., et al. (2013). Transforming growth factor-beta1 (TGF-beta1)-stimulated fibroblast to myofibroblast differentiation is mediated by hyaluronan (HA)-facilitated epidermal growth factor receptor (EGFR) and CD44 co-localization in lipid rafts. *J. Biol. Chem.* 288, 14824–14838. doi: 10.1074/jbc.M113.451336

Miller, J. R. (2002). The Wnts. *Genome Biol.* 3:1028. doi: 10.1186/gb-2002-3-10-reviews1028

Monticelli, L., Kandasamy, S. K., Periole, X., Larson, R. G., Tieleman, D. P., and Marrink, S. J. (2008). The MARTINI coarse-grained force field: extension to proteins. *J. Chem. Theory Comput.* 4, 819–834. doi: 10.1021/ct700324x

Moro, E., Ozhan-Kizil, G., Mongera, A., Beis, D., Wierzbicki, C., Young, R. M., et al. (2012). *In vivo* Wnt signaling tracing through a transgenic biosensor fish reveals novel activity domains. *Dev. Biol.* 366, 327–340. doi: 10.1016/j.ydbio.2012.03.023

Niehrs, C., and Shen, J. (2010). Regulation of Lrp6 phosphorylation. *Cell Mol. Life Sci.* 67, 2551–2562. doi: 10.1007/s00018-010-0329-3

Nile, A. H., Mukund, S., Stanger, K., Wang, W., and Hannoush, R. N. (2017). Unsaturated fatty acyl recognition by Frizzled receptors mediates dimerization upon Wnt ligand binding. *Proc. Natl. Acad. Sci. U.S.A.* 114, 4147–4152. doi: 10.1073/pnas.1618293114

Nusse, R., and Clevers, H. (2017). Wnt/beta-catenin signaling, disease, and emerging therapeutic modalities. *Cell* 169, 985–999. doi: 10.1016/j.cell.2017.05.016

Ozhan, G., Sezgin, E., Wehner, D., Pfister, A. S., Kuhl, S. J., Kagermeier-Schenk, B., et al. (2013). Lypd6 enhances Wnt/beta-catenin signaling by promoting Lrp6 phosphorylation in raft plasma membrane domains. *Dev. Cell* 26, 331–345. doi: 10.1016/j.devcel.2013.07.020

Ozhan, G., and Weidinger, G. (2014). "Restoring tissue homeostasis: Wnt signaling in tissue regeneration after acute injury," in *Wnt Signaling in Development and Disease: Molecular Mechanisms and Biological Functions,* eds S. P. Hoppler and R. T. Moon (Hoboken, NJ: John Wiley & Sons, Inc.). doi: 10.1002/9781118444122.ch26

Sakane, H., Yamamoto, H., and Kikuchi, A. (2010). LRP6 is internalized by Dkk1 to suppress its phosphorylation in the lipid raft and is recycled for reuse. *J. Cell Sci.* 123, 360–368. doi: 10.1242/jcs.058008

Sankaran, J., Bag, N., Kraut, R. S., and Wohland, T. (2013). Accuracy and precision in camera-based fluorescence correlation spectroscopy measurements. *Anal. Chem.* 85, 3948–3954. doi: 10.1021/ac303485t

Schuttelkopf, A. W., and van Aalten, D. M. (2004). PRODRG: a tool for high-throughput crystallography of protein-ligand complexes. *Acta Crystallogr. D Biol. Crystallogr.* 60, 1355–1363. doi: 10.1107/S0907444904011679

Sezgin, E., Azbazdar, Y., Ng, X. W., Teh, C., Simons, K., Weidinger, G., et al. (2017a). Binding of canonical Wnt ligands to their receptor complexes occurs in ordered plasma membrane environments. *FEBS J.* 284, 2513–2526. doi: 10.1111/febs.14139

Sezgin, E., Levental, I., Mayor, S., and Eggeling, C. (2017b). The mystery of membrane organization: composition, regulation and roles of lipid rafts. *Nat. Rev. Mol. Cell Biol.* 18, 361–374. doi: 10.1038/nrm.2017.16

Simons, K., and Ikonen, E. (1997). Functional rafts in cell membranes. *Nature* 387, 569–572. doi: 10.1038/42408

Simons, K., and Toomre, D. (2000). Lipid rafts and signal transduction. *Nat. Rev. Mol. Cell Biol.* 1, 31–39. doi: 10.1038/35036052

Singh, A. P., Krieger, J. W., Buchholz, J., Charbon, E., Langowski, J., and Wohland, T. (2013). The performance of 2D array detectors for light sheet based fluorescence correlation spectroscopy. *Opt. Express* 21, 8652–8668. doi: 10.1364/OE.21.008652

Smotrys, J. E., and Linder, M. E. (2004). Palmitoylation of intracellular signaling proteins: regulation and function. *Annu. Rev. Biochem.* 73, 559–587. doi: 10.1146/annurev.biochem.73.011303.073954

Speer, K. F., Sommer, A., Tajer, B., Mullins, M. C., Klein, P. S., and Lemmon, M. A. (2019). Non-acylated Wnts can promote signaling. *Cell Rep.* 26, 875–883. doi: 10.1016/j.celrep.2018.12.104

Takada, R., Satomi, Y., Kurata, T., Ueno, N., Norioka, S., Kondoh, H., et al. (2006). Monounsaturated fatty acid modification of Wnt protein: its role in Wnt secretion. *Dev. Cell* 11, 791–801. doi: 10.1016/j.devcel.2006.10.003

Tang, X., Wu, Y., Belenkaya, T. Y., Huang, Q., Ray, L., Qu, J., et al. (2012). Roles of N-glycosylation and lipidation in Wg secretion and signaling. *Dev. Biol.* 364, 32–41. doi: 10.1016/j.ydbio.2012.01.009

The MathWorks (2018). *MATLAB and Statistics Toolbox Release.* Natick, MA.

Tran, F. H., and Zheng, J. J. (2017). Modulating the wnt signaling pathway with small molecules. *Protein Sci.* 26, 650–661. doi: 10.1002/pro.3122

van Zundert, G. C. P., Rodrigues, J., Trellet, M., Schmitz, C., Kastritis, P. L., Karaca, E., et al. (2016). The HADDOCK2.2 web server: user-friendly integrative modeling of biomolecular complexes. *J. Mol. Biol.* 428, 720–725. doi: 10.1016/j.jmb.2015.09.014

Veerapathiran, S., and Wohland, T. (2018). The imaging FCS diffusion law in the presence of multiple diffusive modes. *Methods* 140–141, 140–150. doi: 10.1016/j.ymeth.2017.11.016

Wawrezinieck, L., Rigneault, H., Marguet, D., and Lenne, P. F. (2005). Fluorescence correlation spectroscopy diffusion laws to probe the submicron cell membrane organization. *Biophys. J.* 89, 4029–4042. doi: 10.1529/biophysj.105.067959

Weidinger, G., Thorpe, C. J., Wuennenberg-Stapleton, K., Ngai, J., and Moon, R. T. (2005). The Sp1-related transcription factors sp5 and sp5-like act downstream of Wnt/beta-catenin signaling in mesoderm and neuroectoderm patterning. *Curr. Biol.* 15, 489–500. doi: 10.1016/j.cub.2005.01.041

Willert, K., Brown, J. D., Danenberg, E., Duncan, A. W., Weissman, I. L., Reya, T., et al. (2003). Wnt proteins are lipid-modified and can act as stem cell growth factors. *Nature* 423, 448–452. doi: 10.1038/nature01611

Willert, K., and Nusse, R. (2012). Wnt proteins. *Cold Spring Harb. Perspect. Biol.* 4:a007864. doi: 10.1101/cshperspect.a007864

Wohland, T., Shi, X., Sankaran, J., and Stelzer, E. H. (2010). Single plane illumination fluorescence correlation spectroscopy (SPIM-FCS) probes inhomogeneous three-dimensional environments. *Opt. Express* 18, 10627–10641. doi: 10.1364/OE.18.010627

Yamamoto, H., Sakane, H., Michiue, T., and Kikuchi, A. (2008). Wnt3a and Dkk1 regulate distinct internalization pathways of LRP6 to tune the activation of beta-catenin signaling. *Dev. Cell* 15, 37–48. doi: 10.1016/j.devcel.2008.04.015

Yang, J., Yan, R., Roy, A., Xu, D., Poisson, J., and Zhang, Y. (2015). The I-TASSER Suite: protein structure and function prediction. *Nat. Methods* 12, 7–8. doi: 10.1038/nmeth.3213

Zeng, C. M., Chen, Z., and Fu, L. (2018). Frizzled receptors as potential therapeutic targets in human cancers. *Int. J. Mol. Sci.* 19:E1543. doi: 10.3390/ijms19051543

Zhai, L., Chaturvedi, D., and Cumberledge, S. (2004). Drosophila wnt-1 undergoes a hydrophobic modification and is targeted to lipid rafts, a process that requires porcupine. *J. Biol. Chem.* 279, 33220–33227. doi: 10.1074/jbc.M403407200

Zimmerman, Z. F., Moon, R. T., and Chien, A. J. (2012). Targeting Wnt pathways in disease. *Cold Spring Harb. Perspect. Biol.* 4:a008086. doi: 10.1101/cshperspect.a008086

Conflict of Interest: The authors declare that the research was conducted in the absence of any commercial or financial relationships that could be construed as a potential conflict of interest.

frontiers in Cell and Developmental Biology

REVIEW
published: 15 April 2020
doi: 10.3389/fcell.2020.00253

The Emerging Role of the Mammalian Glycocalyx in Functional Membrane Organization and Immune System Regulation

*Leonhard Möckl**

Department of Chemistry, Stanford University, Stanford, CA, United States

All cells in the human body are covered by a dense layer of sugars and the proteins and lipids to which they are attached, collectively termed the "glycocalyx." For decades, the organization of the glycocalyx and its interplay with the cellular state have remained enigmatic. This changed in recent years. Latest research has shown that the glycocalyx is an organelle of vital significance, actively involved in and functionally relevant for various cellular processes, that can be directly targeted in therapeutic contexts. This review gives a brief introduction into glycocalyx biology and describes the specific challenges glycocalyx research faces. Then, the traditional view of the role of the glycocalyx is discussed before several recent breakthroughs in glycocalyx research are surveyed. These results exemplify a currently unfolding bigger picture about the role of the glycocalyx as a fundamental cellular agent.

Keywords: glycocalyx, membrane organization, cancer, immune system, cancer immune therapy, immunosynapse, siglecs, KRAS

OPEN ACCESS

Edited by:
Falk Nimmerjahn,
University of Erlangen Nuremberg, Germany

Reviewed by:
Vincenzo Desiderio,
Second University of Naples, Italy
Zhong Yao,
University of Toronto, Canada

***Correspondence:**
Leonhard Möckl
lmoeckl@stanford.edu

Specialty section:
This article was submitted to Cellular Biochemistry, a section of the journal Frontiers in Cell and Developmental Biology

Received: *24 January 2020*
Accepted: *25 March 2020*
Published: *15 April 2020*

Citation:
Möckl L (2020) The Emerging Role of the Mammalian Glycocalyx in Functional Membrane Organization and Immune System Regulation. Front. Cell Dev. Biol. 8:253. doi: 10.3389/fcell.2020.00253

INTRODUCTION

Every cell in the human body – endothelial cells, immune cells, muscle cells, blood cells, neurons, and all the others – exhibit a glycocalyx. "Glycocalyx" literarily translates to "sweet husk." "Sweet" indicates its key building units – various sugars (or monosaccharides) like glucose, mannose, galactose, and many others. "Husk" points toward the location of these sugars – they reside extracellularly on the cell membrane, surrounding the cell like a cloak. The sugars in the glycocalyx are connected with each other in a plethora of ways, forming sugar conjugates or "glycans." Their sizes range from few to tens of thousands of monosaccharide units. Glycans are either free or linked to proteins, which creates glycoproteins and proteoglycans, or lipids, which creates glycolipids. The term "glycocalyx" is thus an umbrella term for the entirety of free glycans, glycoproteins, proteoglycans, and glycolipids present on the cell surface (**Figure 1**).

The glycocalyx has been connected to a variety of fundamental cellular and organismic events such as blastocyst implantation, embryonic development, leukocyte adhesion, or viral and bacterial infections (Matrosovich et al., 2004; Lipowsky, 2012; Weber et al., 2014; Constantinou et al., 2015; Stanley and Cummings, 2015; Formosa-Dague et al., 2018). Given the omnipresence of the glycocalyx in the human body and the importance of the processes it has been connected to, one might assume that its functional role has been investigated and understood in detail. This

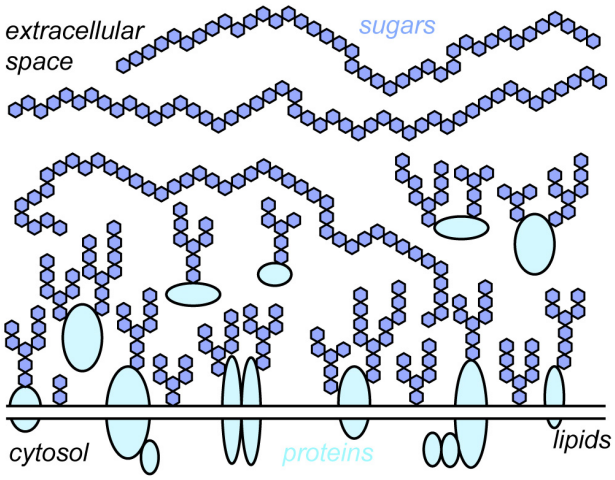

FIGURE 1 | Schematic depiction of the glycocalyx. The glycocalyx is a central constituent of any cell, consisting of sugars and the proteins and lipids to which they are attached. For simplicity, the different sugars found within the glycocalyx are depicted with the same symbol (blue hexagons). Note that the depiction is roughly to scale, i.e., membrane proteins are buried under sugars.

is, however, not the case. In contrast, the glycocalyx has been surprisingly elusive. For many decades, it was assumed that the glycocalyx merely forms a protective layer on the cell surface with no regulative potential. In retrospect, this might seem a bit surprising: The glycocalyx resides directly at the periphery of the cell and forms the interface of the cell with the extracellular space. Thus, it seems reasonable to assume that it is involved in the many processes that are related to the cell membrane.

However, there is a simple reason for the remarkable elusiveness of the glycocalyx: The glycocalyx confronts any researcher with an incredible complexity at all levels, from synthesis all the way to structural organization (see sections "From Monosaccharides to Glycopolymers" and "Biosynthesis of Glycocalyx Components"). Because of this, traditional methods to study biological systems are of very limited use when applied to the glycocalyx (see section "Problems Specific to Glycocalyx Research and Approaches to Solve Them"). Therefore, for a long time, the picture of the glycocalyx was very incomplete as tools for its detailed investigation were not available. Specifically, the prominent size of the glycocalyx – typically several 10 s to few 100 s of nanometers and thus typically burying even large membrane proteins – was underestimated for a long time.

This situation dramatically changed in recent years. Novel tools to image, model, characterize, and manipulate the glycocalyx precisely have brought it into the spotlight of biochemical and medical research. Rather than a passive coat, the glycocalyx is an active player in cell biology, chiefly involved in a range of vital cellular processes.

In this review, I will first give a brief, general introduction to fundamental concepts in glycocalyx biology. Then, I will discuss some roles that were traditionally assigned to the glycocalyx before presenting breakthrough discoveries that have revolutionized this traditional view in recent years.

FUNDAMENTALS OF GLYCOCALYX BIOLOGY

From Monosaccharides to Glycopolymers

The key component of the glycocalyx are sugars or monosaccharides. They are also referred to as carbohydrates as they were initially identified as hydrates of carbon, $C_x(H_2O)_y$. However, this name does not capture the true chemistry of sugars well. Rather, sugars can be considered polyhydroxylated carbonyl compounds. For example, glucose is an aldo-hexose, i.e., a six-membered chain of carbon atoms, where the first carbon exhibits a carbonyl group and the other five groups each carry a hydroxyl group. Fructose is a keto-hexose: Here, the second carbon atom in the chain carries the carbonyl group. Thus, the positioning of the carbonyl group and the orientation of the hydroxyl group at the chiral carbon atoms determines the monosaccharide structure. For example, glucose, galactose, and mannose are all aldo-hexoses, which differ only in the orientation of one hydroxyl group (**Figure 2A**, top row), emphasizing the importance of stereochemistry in glycobiology.

In solution, monosaccharides exist as a mixture between an open, chain-like form and a cyclic form. The latter is formed by an intramolecular ring closure reaction where a hydroxyl group reacts with the carbon atom carrying the carbonyl group, typically forming five- or six-membered rings with four or five carbon atoms and one oxygen atom. The ratio of open and closed form depends on the structure of the sugar, but the closed form is usually energetically more stable and thus prevalent. The carbon derived from the carbonyl group is called "anomeric carbon." Dependent on the orientation of the hydroxyl group at the anomeric carbon, the monosaccharide exists either in the α- or β-anomer. Via ring opening and reclosing, the two anomers can interchange. For a detailed overview of the intriguing chemistry of sugars, see the literature (Lindhorst, 2007).

Figure 2A depicts the most common sugars found in the human body and their pictorial representations according to the symbol nomenclature for glycans (SNFG) (Varki et al., 2015; Neelamegham et al., 2019). As mentioned above, stereochemistry plays a central role in glycobiology. The second aspect that determines monosaccharide identity are chemical modifications such as oxidation of hydroxyl groups, *N*-acetylation, sulfation, and many more. The resulting complexity already at the level of individual monosaccharides is remarkable.

The complexity of monosaccharides is, however, just a small hint at the complexity of oligo- and polysaccharides, i.e., glycoconjugates of several to many monosaccharide units. For example, let's consider the formation of a disaccharide that consist of two glucose units. The glyosidic bond is formed by the anomeric carbon of the first glucose unit and any hydroxyl group of the other glucose unit. As each of the two units can exist in the α- or β-anomer, there are already 19 disaccharides consisting of two glycose units. Moving to slightly larger hexasaccharides that may include all the sugars found in the human body, the number of possible isomers

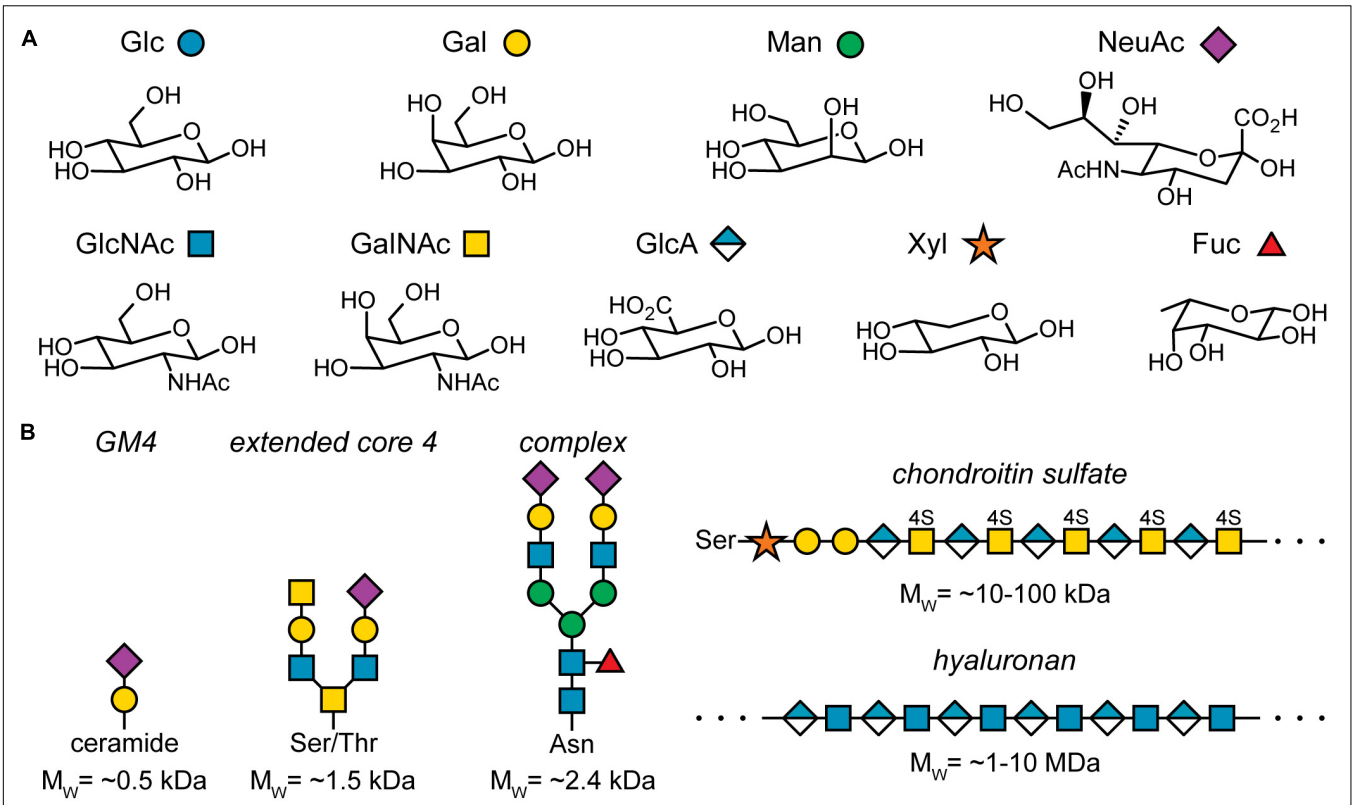

FIGURE 2 | Important sugars found in humans and examples of sugar conjugates found in the glycocalyx. **(A)** Common sugars found in humans and their pictorial representation according to the symbol nomenclature for glycans (SNFG). Note that this list is not exhaustive. Glc, glucose; Gal, galactose; Man, mannose; NeuAc, *N*-acetylneuraminic acid; GlcNAc, *N*-acetylglucosamine; GalNAc, *N*-acetylgalactosamine; GlaA, glucuronic acid; Xyl, xylose; Fuc, fucose. **(B)** Five examples for sugar conjugates found in the glycocalyx: GM4, a glycolipid; an extended core 4 *O*-glycosylation structure; the core structure of complex *N*-glycosylation; a side chain found in chondroitin sulfate; hyaluronan or hyaluronic acid. For simplicity, the linkage chemistry of the glycosidic bond between each monosaccharide is not specified.

is at least 1.05×10^{12} (Laine, 1994), compared to 4096 hexanucleotides and approximately 86 million hexapeptides. Of course, not all of these possible hexasaccharide structures are realized, but the number of distinct glycoconjugates structures in the body, ranging from small conjugates of just a few hundred Da to polymers of several MDa, is still enormous (**Figure 2B**) (Marino et al., 2010; Gagneux et al., 2015; Stanley and Cummings, 2015).

A common way to organize glycocalyx components into major classes is to consider whether they are attached to another biomolecule or if they are free. If a glycan is attached to a lipid anchor, the resulting conjugate is called glycolipid. If one or more glycans are attached to a protein, a further differentiation is typically made: In case the glycan portion are oligosaccharides of approximately 3 to 20 monosaccharides, the resulting conjugate is called glycoprotein. In case the attached glycans are long, polymeric chains, leading to a significant sugar content, the resulting conjugate is called proteoglycan. Finally, free glycans are usually polymers, and thus, they are called glycopolymers.

Notably, the two major classes of glycoproteins are divided according to the attachment of the glycan to the protein: If the glycan is attached via a nitrogen atom of an asparagine side chain, one speaks of *N*-glycosylation and *N*-glycans. If the glycan is attached via an oxygen atom of a serine or threonine side chain, one speaks of *O*-glycosylation and *O*-glycans.

Biosynthesis of Glycocalyx Components

The biosynthesis of glycocalyx components occurs at many places in the cell and is a complex, interlaced process. Considering the numerous in-depth reviews devoted to this topic (Spiro, 2002; Breton et al., 2006; Moremen et al., 2012; Krasnova and Wong, 2016), I will only briefly discuss it here.

For glycoproteins and glycolipids, biosynthesis is performed in the endoplasmic reticulum (ER) and the Golgi apparatus (secretory pathway). The newly synthesized protein chain is usually inserted cotranslationally into the ER. Inside the ER, the peptide chain is folded. The glycosylation procedure of the folded protein chain is dependent on the glycosylation type: *N*-glycans are preassembled and transferred as a whole onto the peptide chain inside the ER. During maturation in the Golgi apparatus, they can be further modified. For *O*-glycosylation, only a single sugar is attached in the ER, and further sugars are added stepwise in the Golgi apparatus. Glycans on glycolipids are stepwise assembled in the Golgi apparatus as well. After the synthesis is finished, the final products

are packaged into secretory granules, transported to the cell membrane, and secreted.

Some glycocalyx components are not synthesized via the ER-Golgi apparatus pathway. For example, the assembly of hyaluronic acid takes place directly at the membrane by integral membrane proteins, hyaluronan synthases. Activated sugars are added to the glycopolymer chain while it is secreted into the extracellular space (Toole, 2004; Weigel and Deangelis, 2007).

The many enzymes that take part in glycan synthesis within the ER and Golgi apparatus are positioned within the secretory pathway according to the reaction they catalyze. It is, however, worth noting that many of these enzymes have a broad substrate and reaction spectrum and that they are constantly shuttled back and forth within the secretory pathway (Bieberich, 2014). Moreover, the availability of donor molecules for glycosylations, usually activated monosaccharides, strongly depend on the cellular metabolism (Lau et al., 2007). As the metabolic state of the cell is altered in cancer, this link between the cellular metabolism and the glycocalyx state directly hints at remodeling of the glycocalyx upon oncogenic events (Pavlova and Thompson, 2016; Deberardinis and Chandel, 2020). Indeed, many relations between tumor metabolism, the glycocalyx, and the cellular state have been uncovered, for example the key role of the mucin Muc1 in hypoxia survival (for a discussion of mucins, see section "The Glycocalyx Controls Cell Morphology") (Yin et al., 2007; Chaika et al., 2012). These discoveries may be the first steps toward a unified concept linking tumor metabolism and glycocalyx state.

Taken together, glycan synthesis is regulated, but exhibits significant stochastic components, which contribute to the observed structural diversity of the synthesized glycoconjugates (Müller et al., 2016; Varki, 2017). The totality of glycosylated species of an organism or even of a single cell, the "glycome," is thus of staggering complexity.

Problems Specific to Glycocalyx Research and Approaches to Solve Them

As a result of the complexity of the glycocalyx at all levels, its investigation is not trivial. Many unique problems that need to be solved in order to study the glycocalyx can be named, however, three issues form the basis of the challenge:

- The glycocalyx exhibits lateral dimensions of typically several 10 s to few 100 s of nm. Its size is therefore below or close to the diffraction limit of light, which is at approximately 250 nm. Thus, the dimension of the glycocalyx can only rarely be determined with conventional optical microscopy, and fine structures are not accessible. The second major microscopy method used to study biological systems, electron microscopy, necessitates elaborate sample preparation, and reports in literature are conflicting if and how the required procedures affect the result (Ebong et al., 2011; Hegermann et al., 2016; Chevalier et al., 2017). Moreover, electron microscopy typically provides no information on the molecular identity of the imaged species. Considering the huge number of tightly packed glycans and glycoconjugates found within the glycocalyx, this is particularly unfortunate.
- The components of the glycocalyx are secondary gene products. Thus, their structure is not directly encoded in the genome, rather, it is a product of many interdependent biosynthetic pathways and furthermore subject to the metabolic state of the cell (Lau et al., 2007). Also, the enzymes involved frequently exhibit overlapping specificities. Consequently, classical genetic methods to label the glycocalyx or to identify regulatory networks during synthesis via knockouts are largely unusable.
- The difference between two monosaccharides can be as subtle as the orientation of a single functional group, but the chemical and biological effect is often tremendous. This drastically impedes specific labeling of the glycocalyx as any labeling approach must be able to precisely distinguish two glycoconjugates that are structurally almost identical.

In addition, the design of model systems, which has proven to be very beneficial for DNA and protein research, is much more challenging for glycoconjugates. Due to the intricate stereochemistry and the large number of functional groups, the synthesis of glycoconjugates is not trivial. However, pioneering work by the labs of Peter Seeberger, Geert-Jan Boons, Chi-Huey Wong, and many others, has significantly simplified this problem, and many glycoconjugates can be synthesized automatically nowadays (Schmaltz et al., 2011; Wang et al., 2013; Hahm et al., 2017; Budhadev et al., 2019; Guberman and Seeberger, 2019).

The three key challenges of glycocalyx biology fundamentally still persist, however, many inroads toward at least partially addressing them have been found. For example, if the structure of glycoconjugates in the glycocalyx are more of interest than their specific localization on the cell membrane, mass spectrometry is an excellent tool to address such questions (Pan et al., 2011; Han and Costello, 2013).

Several strategies exist to label glycocalyx components. Naturally occurring glycan-binding proteins, called lectins, have been used successfully to address individual glycan structures for various applications, however, they can suffer from low affinities or low specificities (Rudiger and Gabius, 2001; Lehmann et al., 2006; Smith and Cummings, 2013; Whelan and Bell, 2015). The creation of antibodies against glycan structures has been challenging as purification of the target glycoconjugates from a complex biological mixture at high yields is demanding. However, with recent advances in glycan synthesis (see above), it can be expected that glycan antibodies become more easily accessible (Paschinger et al., 2005; Broecker et al., 2015).

A unique approach to label specific glycocalyx components is called metabolic labeling. In this approach, cells or whole organisms are supplied with a precursor molecule, which is internalized by the cell(s) and used for glycocalyx synthesis (Keppler et al., 1995; Laughlin and Bertozzi, 2007; Baskin et al., 2010). Critically, the precursor molecule exhibits an unnatural modification, which is attached in such a way that the precursor is processed normally by the cellular biosynthetic machinery: The modification is "invisible" to the cell. Thus, the modified precursor is inserted into glycocalyx components, and the

unnatural modification can be chemically addressed to attach, for example, fluorophores. Due to the bioorthogonal nature of the employed unnatural modifications, e.g., azido groups, this targeting is compatible with the requirements of living cells and organisms. This approach provides excellent specificity and high degrees of labeling and is thus very powerful. Its main drawback is that it currently only allows for targeting of individual sugars such as sialic acids or GalNAc, not reporting on the glycan structure the labeled sugar is part of.

Visualization of the glycocalyx with fluorescence microscopy is desirable as it enables to make use of the currently available and future specific labeling chemistry. This allows to assess the organization of glycocalyx components with known molecular identity. However, conventional optical microscopy is largely inapt to provide detailed insights into glycocalyx structure and dimensions due to the small size of the glycocalyx. One solution to this problem is to use super-resolution microscopy, which allows for resolutions of 10–20 nm (Moerner, 2012; Von Diezmann et al., 2017). Recently, this method has been used in combination with metabolic labeling or lectin-based staining to successfully visualize and investigate the glycocalyx in cultured cells (Letschert et al., 2014; Jiang et al., 2015; Chen et al., 2016; Möckl et al., 2019). In general, single-molecule methods seem to be valuable tools to address questions in glycocalyx research due to their unprecedented resolution and specificity (Lakshminarayanan et al., 2018).

The three key challenges of glycocalyx biology mentioned at the beginning of this section were roadblocks for a long time and prevented the appreciation of the glycocalyx as a vital cellular component. Significant process has been made over the last years to address them, but even though our understanding of the glycocalyx has improved considerably, these issues are not resolved, and further work is required.

FUNCTIONS TRADITIONALLY ATTRIBUTED TO THE GLYCOCALYX

Even though the functional role of the glycocalyx for cell and membrane biology was underestimated for a long time, it would be incorrect to assume that the glycocalyx was considered to have no relevant biological purpose at all. Several functions were attributed to the glycocalyx for decades. Special attention has been paid to the endothelial glycocalyx, which lines blood vessels, in medical contexts.

The first identified function of the glycocalyx was probably protection. The glycocalyx is a dense, gel-like meshwork that surrounds the cell, constituting a physical barrier for any object to enter the cell. For example, the glycocalyx was identified to play an important role to prevent the entry of pathogens into the cell. Consequently, bacteria and viruses employ tailored mechanisms to infect (Bomsel and Alfsen, 2003; Mcguckin et al., 2011). Similarly, in the context of nanomedicine, it has been shown that the endothelial glycocalyx acts as a barrier for nanoparticle entry (Gromnicova et al., 2016; Möckl et al., 2017; Uhl et al., 2017). Also, undesired leukocyte adhesion is prevented by the endothelial glycocalyx (Lipowsky, 2012).

The endothelial glycocalyx is continuously in contact with the blood stream and acts as a vital mechanosensor on endothelial cells. Specifically, long proteoglycans with strong glycosylation such as heparan sulfate or chondroitin sulfate are involved in this process. Often, the image of wind brushing through trees is used: In this analogy, the "wind" of the blood stream acts on the proteoglycan "trees" of the glycocalyx, bending them, which creates a torque that is transferred to the inside of the cells. This leads to various intracellular responses such as release of the vasodilator nitric oxide, actin cytoskeleton rearrangement, and cell polarization (Florian et al., 2003; Thi et al., 2004; Pahakis et al., 2007; Zeng et al., 2018). Notably, interruption of the blood flow due to, e.g., ischemia/reperfusion, both pathological or due to surgery, causes substantial shedding of the endothelial glycocalyx, which leads to severe adverse effects (Rehm et al., 2007; Annecke et al., 2011).

Regarding glycocalyx regulation and organization, galectins and the galectin lattice were identified early as important agents. Galectins are a class of proteins that bind to β-galactosides, e.g., the abundant glycocalyx disaccharide *N*-acetyllactosamine (Johannes et al., 2018). Galectins exhibit either two binding sites for β-galactosides or self-assemble. Thus, they can bind multiple glycans, interconnecting them and the proteins to which they are attached. This leads to clustering of the bound glycocalyx components and formation of the so called "galectin lattice." Consequently, receptor internalization and diffusion change, causing alterations in cellular signaling (Nieminen et al., 2007; Möckl et al., 2015), which can be also artificially induced to precisely tune the strength of lattice formation (Möckl et al., 2016).

However, it seems like significant parts of the extraordinarily complex galectin story are yet to be discovered. For example, it was recently shown that galectin-1 is shuttled to the nucleus, where it is part of morphogenesis regulation (Bhat et al., 2016). Galectin-3 has been implicated in such diverse cellular processes as organization of the primary cilium, apoptosis attenuation, and endocytosis (Furtak et al., 2001; Koch et al., 2010; Harazono et al., 2014). Interestingly, apoptosis attenuation requires heterodimerization with Bax, a protein that exhibits intriguing allostery (Jiang et al., 2016). Moreover, galectin-3 interacts with the master regulator KRAS, which, if mutated, is one of the main driver of various cancer types (Shalom-Feuerstein et al., 2008). Finally, lectins are also employed by highly pathogenic bacteria such as *Mycobacterium tuberculosis*, *Pseudomonas aeruginosa*, and uropathogenic *Escherichia coli* to facilitate cell adhesion and entry (Mitchell et al., 2002; Imberty et al., 2008; Hartmann and Lindhorst, 2011; Kolbe et al., 2019).

Considering that galectins are both glycocalyx organizing proteins and involved in a variety of cellular processes, it appears as if the glycocalyx can act as "storage compartment" for galectins and potentially other proteins. Upon triggering events, they are released and translocated into the cell, where they fulfill their respective function. This glycocalyx-controlled axis of cellular organization has

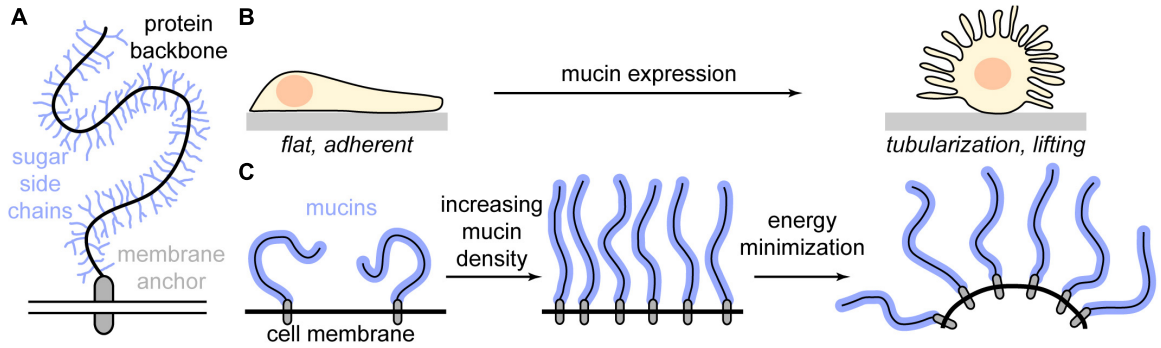

FIGURE 3 | The influence of mucins on cell morphology. **(A)** Schematic depiction of a mucin. Mucins have a bottlebrush structure: A heavily *O*-glycosylated protein backbone is attached to the membrane via a membrane anchor. **(B)** Increased mucin density on the cell membrane causes a fundamental change in cell morphology from a flat, adherent phenotype to strong membrane tubularization and cell lifting. **(C)** At low densities, mucins adopt a compact mushroom phenotype. When the mucin density increases above a threshold, the mucins extend to a polymer brush. The increased order imposes an entropic penalty on the system, which is reduced via bending of the membrane, giving the mucins more orientational degrees of freedom.

likely significant impact on the state of the cell, but it is currently not understood.

THE NEW VIEW OF THE GLYCOCALYX

The Glycocalyx Controls Cell Morphology

Cell membranes can adopt a variety of morphologies. Specifically, tubular extensions have been known for decades (Kolata, 1975). Initially, it was suspected that their main role is to increase the cell-surface area, e.g., for secretion and absorption. More recent investigations showed, however, that these protrusions or membrane tubules contribute to various processes. They are relevant in such diverse areas as antigen surveillance (Jung et al., 2016), tissue development (Bischoff et al., 2013), cell signaling (Ramirez-Weber and Kornberg, 1999; Rustom et al., 2004), and vesicle formation during cancer progression (Al-Nedawi et al., 2008; Antonyak et al., 2011; Becker et al., 2016).

Intriguingly, the mechanisms that are responsible for the formation of membrane tubules were poorly understood until recently. It was hypothesized that cytoskeletal filaments push out these protrusions (Tricarico et al., 2017), but the detailed processes were not clear. One reason for this can be traced back to the challenge of creating model glycocalyces of various dimensions with exact genetic control.

Precisely this problem was addressed by a study in 2018, which introduced a method to express the mucin Muc1 with well-defined sizes in model cells (Shurer et al., 2018). Mucins are an important component of the glycocalyx and specifically relevant in the context of cancer (**Figure 3A**) (Kufe, 2009). They exhibit a protein backbone which is mainly composed of many tandem repeats of characteristic amino acid sequences, collectively referred to as "mucin domains." As each domain is heavily glycosylated, whole mucins, which can exhibit persistence lengths of several microns, regularly carry more than 50% glycosylation content by mass and sometimes up to 85% (Patton et al., 1995; Felder et al., 2014; Das et al., 2015). This strong glycosylation makes mucins effectively inert to conventional proteases, severely hampering their investigation. However, a recently identified mucin-selective proteinase has overcome this limitation, which will be certainly highly beneficial for the study of mucins (Malaker et al., 2019).

The difficulty to express defined glycocalyx components is convincingly exemplified by mucins: The use of a conventional expression strategy leads to expression of mucins with a broad size distribution, typically smaller than intended, and with low yield. Using a tailored transposon-based approach, however, Shurer et al. (2019) were able to express Muc1 in model cells with high yield, precise size control, and narrow size distributions.

Building on their foundational earlier work, the group of Matt Paszek went on to study the effect of the glycocalyx on membrane morphology (Shurer et al., 2019). Strikingly, they observed that MCF10A cells, which show almost no membrane tubules when untreated, undergo massive tubularization of the membrane when mucins are expressed (**Figure 3B**). This effect was specific to the glycocalyx, as expression of a membrane protein without glycosylation did not induce tubularization. Considering that cancer cells frequently overexpress mucins and usually exhibit a depolarized, migratory, and tubulated phenotype, the results by Shurer et al. (2019) also provide highly relevant insights into the relationship of membrane biophysics and cancer progression.

To understand the physical mechanisms behind the tubularization of the membrane, Shurer et al. (2019) conducted a detailed theoretical analysis using a polymer brush model of the glycocalyx. Upon increasing mucin concentration in the membrane, the coiled, rather compact mucins start to interact. To avoid each other, they stretch out, forming a polymer brush ("mushroom-to-brush transition"). Bending the membrane reduces the energy of the system as each mucin gains more conformational freedom, increasing spontaneous curvature (**Figure 3C**). Strikingly, Shurer et al. (2019) determined the energy required to "push out" a membrane tube in the brush regime is maximally a few pN and decreases well below 1 pN for high mucin densities. At the same time, the cytoplasmic pressure required to maintain a spherical membrane bleb sharply

increases and becomes quickly unphysiological. Since a single polymerizing actin filament exerts approximately 1 pN of force, the theoretical analysis explains why at a certain mucin density, membrane tubularization is the only relevant cellular phenotype.

Importantly, Shurer et al. (2019) showed that this effect is not limited to mucins. Using live synovial tissue extracted from equine carpus, they demonstrated that the same phenotype can be observed in synoviocytes. Synoviocytes are specialized cells responsible for hyaluronic acid synthesis. They exhibit a strongly tubularized membrane, very similar to the genetically modified mucin expressing cells. As treatment with hyaluronidase, degrading hyaluronic acid, completely abolished membrane tubularization, Shurer et al. (2019) verified that membrane tubularization is not specific to mucin expression, but can equally be introduced by other polymeric glycocalyx components.

It should be emphasized that this regulation of cell membrane morphology is an excellent example for an important motive: The glycocalyx frequently (although not exclusively) acts via physical interactions. Steric effects, molecular crowding, electrostatic effects (e.g., repulsion of sulfated sugars and counter ion trapping), multivalency effects, size exclusion, and others are phenomena which play a key role in glycocalyx biology (Kuo et al., 2018; Gandhi et al., 2019). Characteristically, each instance of the listed phenomena exerts only a small force on the system, but due to the large dimensions of the glycocalyx, many small forces add up to a significant total force, having a considerable effect on the cellular state.

The Glycocalyx Is Involved in the Regulation of Membrane Protein Diffusion

Diffusion of membrane proteins, its regulation, and its interplay with membrane composition is one of the most important aspects of membrane biology (Jacobson et al., 1987, 2019; Pluhackova and Böckmann, 2015), and numerous models have been developed to describe this key process (Singer and Nicolson, 1972; Henderson and Unwin, 1975; Robertson, 1981). One model specifically addresses the interplay between membrane proteins and the cytoskeleton: The picket-fence model (Kusumi and Sako, 1996). This model proposes that "pickets," i.e., abundant membrane proteins, bind the "fence," i.e., the cytoskeleton close to the cell membrane, which establishes membrane domains that, for example, affect membrane protein diffusion.

In a recent study from the lab of Sergio Grinstein, an excellent candidate for a picket was identified, and the relevance of the glycocalyx was impressively shown (Freeman et al., 2018). Freeman et al. (2018) focused on phagocytosis regulation in macrophages. They showed that pickets and fences mediate receptor diffusion, functionally changing phagocytosis at a subcellular level.

In their study, Freeman et al. (2018) identified CD44 as a bona fide picket. CD44 is highly abundant in the membrane of bone-marrow-derived macrophages ($\sim 10^6$ copies per cell) and has been described earlier to be involved in various cellular contexts (Goodison et al., 1999). As shown in **Figure 4A**, CD44 binds intracellularly to the cortical actin cytoskeleton via linker proteins such as ezrin and others. Notably, CD44 exhibits another binding mode: Extracellularly, it engages with the key glycocalyx component hyaluronic acid. Thus, CD44 acts as picket and the cortical actin cytoskeleton as well as hyaluronan on the extracellular side as fences. Together, the three components form a superstructure which define membrane domains, regulating the diffusion of membrane proteins (**Figure 4B**).

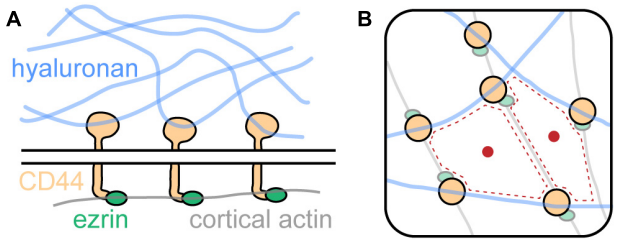

FIGURE 4 | The picket-fence model and its influence onto membrane protein diffusion. **(A)** CD44, an abundant transmembrane protein, binds the glycocalyx component hyaluronic acid with its extracellular domain. Intracellularly, it engages with the cortical actin cytoskeleton via ezrin and other linker proteins. **(B)** Hyaluronan, CD44, and cortical actin demarcate membrane domains (red dotted line) that regulate diffusion of membrane proteins (red dot).

Freeman et al. (2018) showed that each component of the superstructure is required for efficient diffusion control. Knockout of CD44 significantly increased diffusivity of membrane proteins. A synthetic construct consisting of the transmembrane domain of FcR and ezrin fused together was used to investigate the role of actin binding. The construct showed significantly increased diffusivity when actin binding of ezrin was disrupted via a point mutation in the ezrin domain. Finally, overexpression of hyaluronic acid synthase 3 greatly reduced membrane protein diffusion. Thus, the three components of the picket-fence structure (CD44, hyaluronan, and cortical actin) act together in regulation of membrane protein diffusion.

Importantly, the regulation of membrane protein diffusivity has a substantial effect on subcellular organization and phagocytosis by the studied macrophages. Freeman et al. (2018) found that migrating macrophages break down the CD44-hyaluronan-actin superstructure at the leading edge of the cell, but not at the trailing end. This causes higher receptor mobility at the leading edge, allowing for receptor clustering and initiation of phagocytosis in the area of the macrophage that is closest to, for example, a pathogen that needs to be engulfed.

In addition, this study also suggests a regulative potential of membrane proteins back on the glycocalyx: The interaction of a single CD44 molecule with hyaluronan is weak, but due to the huge number of CD44-hyaluronan binding events, the long hyaluronan molecules are firmly engaged. This was verified by investigating the interaction between *Salmonella typhimurium* bacteria with either wild-type or CD44-deficient macrophages. Immobile bacteria bound much more readily to CD44-deficient macrophages than to wild-type macrophages, suggesting that absence of CD44 causes a reduction of

hyaluronan on the cell surfaces. Fascinatingly, motile bacteria bound equally well to both wild-type and CD44-deficinet macrophages. This indicates that the force generated by the bacterium is sufficient to penetrate the glycocalyx, which was corroborated by centrifugation experiments using opsonized beads: CD44-deficinet macrophages would bind much more beads than wild-type macrophages when no force was applied, but both macrophages types would bind similar amounts of beads when the beads were pressed onto the cell surface via centrifugation.

The Glycocalyx Is Functionally Relevant for Cancer Development at All Stages

Over decades, evidence has accumulated that point toward a key role of the glycocalyx in cancer development and progression (Ohtsubo and Marth, 2006; Pinho and Reis, 2015; Tarbell and Cancel, 2016). For example, rewiring of the cellular metabolism via the Warburg effect characteristically changes glycosylation of membrane proteins (Dennis et al., 2009; Heiden et al., 2009). This changed glycosylation causes alterations in protein behavior, e.g., increased membrane residence times via prolonged engagement with the galectin lattice (Rudd et al., 1999; Lau et al., 2007). As a result, cellular signaling is shifted, ultimately modifying cellular behavior. Other studies have shown that the cancer glycocalyx acts as a mechanosensor in flow-regulated invasion (Qazi et al., 2013, 2016; Moran et al., 2019).

Tumor cells have turned against the healthy cells of the body and must therefore survive in a hostile environment. Specifically, formation of metastases is complicated: Circulating tumor cells are sought to be removed from the blood stream, and uncontrolled adhesion of circulating cells is challenging. Several recent findings have established that physical characteristics of the cancer glycocalyx play a major role in these processes, directly priming tumor cells for adhesion and prolonged survival.

Paszek et al. (2014) studied the effect of glycocalyx thickness on integrin-mediated cellular adhesion, growth, and survival. They showed that, perhaps paradoxically at first sight, a thick glycocalyx strongly increases integrin-mediated adhesion via formation of large adhesion plaques that firmly anchor the cell to the substrate, e.g., the extracellular matrix (ECM). This effect can, however, be explained via a kinetic trap model: Upon activation, integrins undergo a conformational change, causing them to extend 15–20 nm from the cell surface (Campbell and Humphries, 2011; Dai et al., 2015). Thus, a thin glycocalyx of approximately 10 nm height does not hinder the interaction of integrins with the ECM (**Figure 5A**). In contrast, a thick glycocalyx of several tens of nm largely prevents the interaction of integrins with the ECM. If, however, an interaction is established at some point, integrin activation will predominantly occur at the already established site of interaction. If active integrins detach from the ECM, they will likely not leave the interaction area due to the thick glycocalyx around. Thus, the thick glycocalyx primes strong integrin-mediated adhesion due to kinetic funnels or traps (**Figure 5B**). Strikingly, Paszek et al. (2014) found that large, bulky glycoproteins and proteoglycans such as mucins are strongly expressed on many circulating tumor cells, which emphasizes the direct clinical relevance of the revealed mechanism.

A study by Woods et al. (2017) took this idea *in vivo*. Here, mammary carcinoma cells bearing either short (∼3 nm) or long (∼90 nm) synthetic glycopolymers were injected into the tail veins of mice. The synthetic glycopolymers emulate cell-surface mucins and feature a special lipid anchor that leads to storage of the synthetic glycoproteins in intracellular vesicles. Thus, instead of degradation, the glycopolymers are recycled back to the cell surface for many days, enabling long-term studies (Woods et al., 2015). After 15 days, the mice were sacrificed and the lungs, where the injected cells migrated, were excised. The tumor burden was severely increased when the injected cells carried the long form of the synthetic glycopolymer compared to the short form. In accordance with the study by Paszek et al. (2014) and Woods et al. (2017) found that the long synthetic glycopolymer stimulated integrin-FAK mechanosensing, emphasizing the relevance of integrin-mediated tumor cell adhesion and survival.

In a recent investigation conducted by the labs of W. E. Moerner and Carolyn Bertozzi, the dimensions and nanoscale architecture of the glycocalyx was investigated with super-resolution microscopy (Möckl et al., 2019). The increased resolution allowed for direct quantification of glycocalyx dimensions from the cell membrane up. This approach was used to monitor changes in glycocalyx height upon two key oncogenic events: Epithelial-to-mesenchymal transition (EMT) and proto-oncogene activation, in this case the expression of $KRAS^{G12D}$, one of the most prevalent oncogenic mutations known (Kalluri and Weinberg, 2009; Cox et al., 2014). They found that upon both oncogenic events, glycocalyx height significantly increased. As both EMT and $KRAS^{G12D}$ trigger a multitude of signaling cascades, Möckl et al. (2019) went on to identify mediator genes for the effect of $KRAS^{G12D}$ on the glycocalyx. Transcriptomic analysis revealed several promising hits, among which the galactosyltransferase *GALNT7* was most striking: In patients suffering from pancreatic adenocarcinoma, a tumor type in which *KRAS* carries an activating mutation more than 90% of the time, *GALNT7* was strongly correlated with patient survival, suggesting a relation between *KRAS* and *GALNT7*. Indeed, in $KRAS^{G12D}$ expressing cells, siRNA-mediated knockdown of GALNT7 caused a strong reduction in glycocalyx height, indicating that *GALNT7* is indeed a single-gene mediator of the effect of oncogenic *KRAS* onto the glycocalyx. Considering the studies by Paszek et al. (2014) and Woods et al. (2017), these findings strongly suggest that cancer cells actively remodel their glycocalyx from the first oncogenic events on, which fosters tumor progression, metastasis, and survival (**Figure 5C**).

The Glycocalyx Is a Key Player in Immune System Regulation and Checkpoint Inhibition

The previous sections described recent significant findings that ascertain the central role of the glycocalyx for cell morphology determination, membrane organization, and cancer progression. Each of these investigations can be readily transferred to

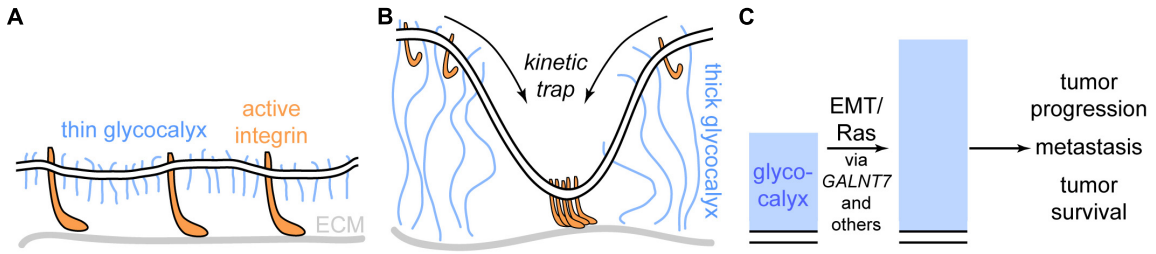

FIGURE 5 | The cancer glycocalyx in integrin-mediated cell survival and its alteration upon oncogenic events. **(A)** Cells adhere to extracellular matrix (ECM) components via integrins. If the glycocalyx is thin, the integrins extend beyond the glycocalyx. **(B)** A thick glycocalyx as frequently expressed by cancer cells extends significantly further into the extracellular space than active integrins. As a result, interactions between integrins and the ECM are not possible in most areas of the cell surface, however, hotspots of integrin-ECM-binding are created via a kinetic funnel. **(C)** Upon proto-oncogenic events such as epithelial-to-mesenchymal transition (EMT) or oncogenic *RAS* activation (e.g., $KRAS^{G12D}$), the height of the glycocalyx increases, which fosters tumor progression and survival. The oncogenic effect is mediated by mediators such as *GALNT7* and others.

therapeutic applications. In addition, recent studies from the lab of Carolyn Bertozzi have started to explore the potential of the glycocalyx in therapy and specifically cancer immunotherapy.

One of the hallmarks of cancer is immune evasion (Bhatia and Kumar, 2014). Normally, uncontrolled cell proliferation is recognized and terminated, but in cancer, this is no longer the case. Cancer immunotherapy therefore seeks to stimulate the immune system in order to reinstall its normal response to fight the cancer (Scott et al., 2012). This can be achieved in various ways, e.g., by using antibodies that block pathways responsible for reduced immune system activity.

The glycocalyx component that mainly constitutes the relevance of the glycocalyx for immune system regulation is sialic acid. Sialic acids are an abundant monosaccharide in the glycocalyx. Among the many cellular and organismic processes they are involved in, their role as "marker of self" is of special importance (Paulson et al., 2012; Varki and Gagneux, 2012; Blaum et al., 2015), and many studies have impressively shown the importance of sialic acids and sialic acid-binding receptors on the cell membrane, termed "siglecs" (short for sialic acid-binding immunoglobulin-type lectins, belonging to the family of I-type lectins) (Crocker et al., 2007; Jandus et al., 2014; Läubli et al., 2014). In accordance with this picture, many cancer cells overexpress sialylated proteins and lipids and their membrane, and it could be shown that this overexpression is directly involved in immune system downregulation, enabling the cancer cell to evade the attack by immune cells (Hudak et al., 2014; Boligan et al., 2015).

This strategy to dodge the immune system is very efficient. For example, one immunotherapeutic strategy to treat breast cancer is to employ a monoclonal antibody, known as Trastuzumab (Tras). Tras binds to the overexpressed cancer cell surface protein human epidermal growth factor receptor 2 (HER2) and induces an immune response which leads to internalization and downregulation of HER2 (Bange et al., 2001). Furthermore, Tras binds to FCγRIII (also known as CD16), which is expressed on natural killer (NK) cells. Thus, Tras is able to link NK cells to cancer cells, prolonging the interaction time and increasing NK cell-mediated cancer cell killing. However, the situation is more complex. 74% of breast cancer patients show HER2 expression, but only the patient group with highest HER2 levels (∼20%) respond to treatment at all (Lee et al., 2011). Even more puzzling, less than 20% of this patient group shows a response to Tras alone. Even combination therapies exhibit just 50 to 80% response (Bartsch et al., 2007).

Xiao et al. (2016) showed that the reason for this inefficient action of Tras is mediated by the cancer glycocalyx. It presents sialylated species to siglecs on immune cells, for example NK cells. Siglecs contain cytosolic immunoreceptor tyrosine-based inhibition motifs (ITIMs) and immunoreceptor tyrosine-based switch motifs (ITSMs). Upon binding of sialylated species on the cancer cell, SHP1 and -2 (short for Src homology 2 domain-containing protein tyrosine phosphatase 1 and 2) are recruited and activated, which causes a reduction in NK cell activity (**Figure 6A**). Furthermore, the binding of NK cell-activating receptors such as NK-activating receptor natural killer group 2D (NKG2D) is disrupted by hypersialylation of cancer cell glycans. Therefore, treatment with Tras may remove HER2 from the picture, but if the sialic acid- and siglec-mediated inhibition is strong enough, the patient will not show a response to Tras. Thus, sialic acids and siglecs contribute to drug resistance.

This observation directly raises the possibility to target the cancer sialome for more efficient treatment. However, broad, unspecific desialylation would lead to severe side effects due to the omnipresence of sialic acid in the organism. Thus, Xiao et al. (2016) engineered a Tras-sialidase conjugate, called T-Sia, which selectively desialylates the cancer cell. This caused enhanced activity of Tras-mediated NK cell cytotoxicity, resulting in higher potency against cells with low HER2 levels compared to treatment with Tras alone.

Recently, a smaller, improved version of T-Sia was developed by Gray et al. (2019), called T-Sia 2.0, shown in **Figure 6B**. The older T-Sia showed unwanted Tras-independent activity, which was caused by the affinity of the *Vibrio cholerae* derived sialidase to polyvalent substrates like cell surfaces due to the presence of lectin domains. T-Sia 2.0 employs a sialidase from *Salmonella typhimurium*, which significantly reduces Tras-independent cell desialylation. This strongly enhanced the cytotoxicity and specificity of T-Sia 2.0. Similar to T-Sia, T-Sia 2.0 binds to HER2 in the immunosynapse, where it removes

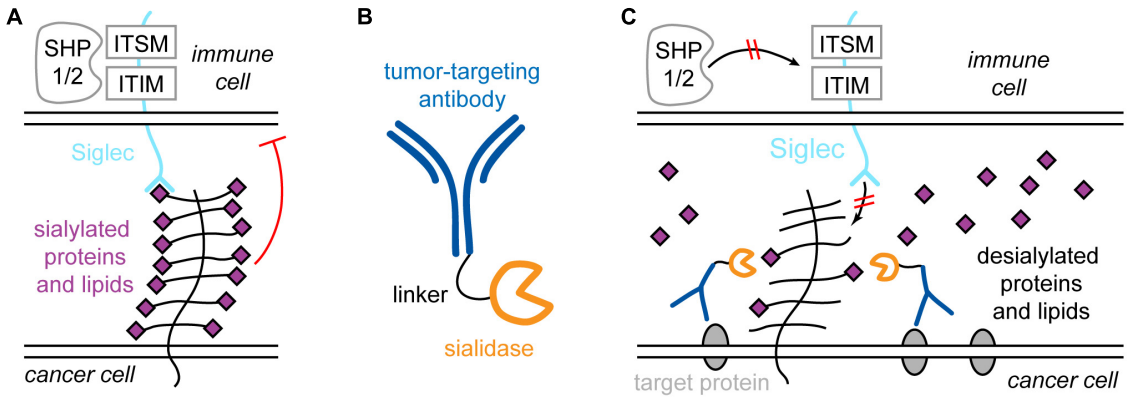

FIGURE 6 | Siglecs and sialic acid in immune system regulation and specific targeting of the cancer sialome for treatment strategies. **(A)** Sialylated proteins of lipids on the cancer cell bind to siglec receptors on immune cells, e.g., natural killer (NK) cells. Siglecs contain immunoreceptor tyrosine-based inhibition motifs (ITIMs) and immunoreceptor tyrosine-based switch motifs (ITSMs), which recruit phosphatases such as Src homology 2 domain-containing protein tyrosine phosphatase 1 and 2 (SHP1 and -2), which causes activity reduction of the NK cell. **(B)** The antibody-sialidase conjugate T-Sia 2.0 to specifically desialylate cancer cells. **(C)** T-Sia 2.0 binds to membrane proteins characteristically overexpressed by the cancer. The sialidase causes desialylation of the cancer, which abolishes binding of NK cell siglecs and prevents NK cell downregulation.

sialic acids from sialylated proteins and lipids, which prevents siglecs on the immune cell from binding and restores the interaction of NK cell-activating receptors such as NKG2D with their ligands. Consequently, SHP1/2 is not recruited to the ITIM and ITSM domains of siglecs, and the immune cell activity is not downregulated (**Figure 6C**). Due to the improved activity and specificity of T-Sia 2.0, it was possible to study the effect of targeted cancer cell desialylation *in vivo* using a syngeneic orthotopic HER2 + breast cancer model. Treatment with T-Sia 2.0 delayed tumor growth and enhanced immune cell infiltration and activation, leading to prolonged survival. Therefore, targeted desialylation of cancer cells was established as a promising strategy to overcome glyco-immune checkpoints *in vivo*.

DISCUSSION AND OUTLOOK

Until recently, the glycocalyx was recognized as a cellular structure with important functions, but it was generally not assumed that the glycocalyx is an agent that is capable to fundamentally determine the cellular and organismic state. This view changed dramatically when a series of breakthrough studies over the last few years established the glycocalyx as an organelle with significant regulative potential. We now know that the glycocalyx is functionally involved at the core of cellular events of high relevance for both health and disease – from membrane organization all the way to cancer progression. Moreover, these research efforts did not halt at a mere description of the role of the glycocalyx, but also showed that the glycocalyx is an invaluable clinical target.

The glycocalyx is a fascinating melting pot of chemistry, physics, biology, and medicine. Its astounding molecular and structural complexity is deeply rooted in the diversity of carbohydrate chemistry. This complexity translates to cellular effects that touch upon various areas of cell biology: Signaling, metabolism, immunity, cell migration, adhesion, and proliferation, and many more. Finally, the complexity of the glycocalyx also frequently unites into one entity, become a force acting almost exclusively via physical forces.

Even though recent discoveries have revolutionized our view of the glycocalyx, a long way is now in front of us. New approaches need to be found to determine the detailed architecture of the glycocalyx, to understand the interplay between glycocalyx and cellular state, and to monitor its dynamic changes upon key cellular events in health and disease.

Establishing the tools required will allow for passing the first glimpses into a deeper, integrated understanding of the communication between the glycocalyx and the cell that we have acquired so far. We are yet to discover the most fascinating aspects of glycocalyx biology: The age of the glycocalyx has just began.

AUTHOR CONTRIBUTIONS

LM wrote the manuscript.

FUNDING

Partial support from the National Institute of General Medical Sciences (grant No. R35GM118067) is gratefully acknowledged.

ACKNOWLEDGMENTS

The author thanks W. E. Moerner, Carolyn Bertozzi, Kayvon Pedram, and Anna-Karin Gustavsson, all Stanford University, for valuable discussions and proofreading the manuscript.

REFERENCES

Al-Nedawi, K., Meehan, B., Micallef, J., Lhotak, V., May, L., Guha, A., et al. (2008). Intercellular transfer of the oncogenic receptor EGFrvIII by microvesicles derived from tumour cells. *Nat. Cell Biol.* 10, 619–U624.

Annecke, T., Fischer, J., Hartmann, H., Tschoep, J., Rehm, M., Conzen, P., et al. (2011). Shedding of the coronary endothelial glycocalyx: effects of hypoxia/reoxygenation vs ischaemia/reperfusion. *Br. J. Anaesth.* 107, 679–686. doi: 10.1093/bja/aer269

Antonyak, M. A., Li, B., Boroughs, L. K., Johnson, J. L., Druso, J. E., Bryant, K. L., et al. (2011). Cancer cell-derived microvesicles induce transformation by transferring tissue transglutaminase and fibronectin to recipient cells. *Proc. Natl. Acad. Sci. US A.* 108, 4852–4857. doi: 10.1073/pnas.1017667108

Bange, J., Zwick, E., and Ullrich, A. (2001). Molecular targets for breast cancer therapy and prevention. *Nat. Med.* 7, 548–552. doi: 10.1038/87872

Bartsch, R., Wenzel, C., and Steger, G. G. (2007). Trastuzumab in the management of early and advanced stage breast cancer. *Biol. Target. Ther.* 1, 19–31.

Baskin, J. M., Dehnert, K. W., Laughlin, S. T., Amacher, S. L., and Bertozzi, C. R. (2010). Visualizing enveloping layer glycans during zebrafish early embryogenesis. *Proc. Natl. Acad. Sci. U.S.A.* 107, 10360–10365. doi: 10.1073/pnas.0912081107

Becker, A., Thakur, B. K., Weiss, J. M., Kim, H. S., Peinado, H., and Lyden, D. (2016). Extracellular vesicles in cancer: cell-to-cell mediators of metastasis. *Cancer Cell* 30, 836–848. doi: 10.1016/j.ccell.2016.10.009

Bhat, R., Belardi, B., Mori, H., Kuo, P. W., Tam, A., Hines, W. C., et al. (2016). Nuclear repartitioning of galectin-1 by an extracellular glycan switch regulates mammary morphogenesis. *Proc. Natl. Acad. Sci. U.S.A.* 113, E4820–E4827.

Bhatia, A., and Kumar, Y. (2014). Cellular and molecular mechanisms in cancer immune escape: a comprehensive review. *Exp. Rev. Clin. Immunol.* 10, 41–62. doi: 10.1586/1744666x.2014.865519

Bieberich, E. (2014). Synthesis, processing, and function of N-glycans in N-glycoproteins. *Adv. Neurobiol.* 9, 47–70.

Bischoff, M., Gradilla, A. C., Seijo, I., Andres, G., Rodriguez-Navas, C., Gonzalez-Mendez, L., et al. (2013). Cytonemes are required for the establishment of a normal Hedgehog morphogen gradient in *Drosophila epithelia*. *Nat. Cell Biol.* 15, 1269–U1240.

Blaum, B. S., Hannan, J. P., Herbert, A. P., Kavanagh, D., Uhrin, D., and Stehle, T. (2015). Structural basis for sialic acid-mediated self-recognition by complement factor H. *Nat. Chem. Biol.* 11, 77–82. doi: 10.1038/nchembio.1696

Boligan, K. F., Mesa, C., Fernandez, L. E., and Von Gunten, S. (2015). Cancer intelligence acquired (CIA): tumor glycosylation and sialylation codes dismantling antitumor defense. *Cell. Mol. Life Sci.* 72, 1231–1248. doi: 10.1007/s00018-014-1799-5

Bomsel, M., and Alfsen, A. (2003). Entry of viruses through the epithelial barrier: pathogenic trickery. *Nat. Rev. Mol. Cell Biol.* 4, 57–68. doi: 10.1038/nrm1005

Breton, C., Snajdrova, L., Jeanneau, C., Koca, J., and Imberty, A. (2006). Structures and mechanisms of glycosyltransferases. *Glycobiology* 16, 29R–37R. doi: 10.1093/glycob/cwj016

Broecker, F., Anish, C., and Seeberger, P. H. (2015). Generation of monoclonal antibodies against defined oligosaccharide antigens. *Methods Mol. Biol.* 1331, 57–80. doi: 10.1007/978-1-4939-2874-3_5

Budhadev, D., Saxby, K., Walton, J., Davies, G., Tyler, P. C., Schworer, R., et al. (2019). Using automated glycan assembly (AGA) for the practical synthesis of heparan sulfate oligosaccharide precursors. *Organ. Biomol. Chem.* 17, 1817–1821. doi: 10.1039/c8ob02756k

Campbell, I. D., and Humphries, M. J. (2011). Integrin Structure, Activation, and Interactions. *Cold Spring Harb. Perspect. Biol.* 3:a004994. doi: 10.1101/cshperspect.a004994

Chaika, N. V., Gebregiworgis, T., Lewallen, M. E., Purohit, V., Radhakrishnan, P., Liu, X., et al. (2012). MUC1 mucin stabilizes and activates hypoxia-inducible factor 1 alpha to regulate metabolism in pancreatic cancer. *Proc. Natl. Acad. Sci. U.S.A.* 109, 13787–13792. doi: 10.1073/pnas.1203339109

Chen, J. L., Gao, J., Zhang, M., Cai, M. J., Xu, H. J., Jiang, J. G., et al. (2016). Systemic localization of seven major types of carbohydrates on cell membranes by dSTORM imaging. *Sci. Rep.* 6:30247.

Chevalier, L., Selim, J., Genty, D., Baste, J. M., Piton, N., Boukhalfa, I., et al. (2017). Electron microscopy approach for the visualization of the epithelial and endothelial glycocalyx. *Morphologie* 101, 55–63. doi: 10.1016/j.morpho.2017.04.001

Constantinou, P. E., Morgado, M., and Carson, D. D. (2015). Transmembrane mucin expression and function in embryo implantation and placentation. regulation of implantation and establishment of pregnancy in mammals: tribute to 45 year anniversary of roger V. *Shorts Mater. Recogn. Preg.* 216, 51–68. doi: 10.1007/978-3-319-15856-3_4

Cox, A. D., Fesik, S. W., Kimmelman, A. C., Luo, J., and Der, C. J. (2014). Drugging the undruggable RAS: mission possible? *Nat. Rev. Drug Discover.* 13, 828–851. doi: 10.1038/nrd4389

Crocker, P. R., Paulson, J. C., and Varki, A. (2007). Siglecs and their roles in the immune system. *Nat. Rev. Immunol.* 7, 255–266. doi: 10.1038/nri2056

Dai, A., Ye, F., Taylor, D. W., Hu, G. Q., Ginsberg, M. H., and Taylor, K. A. (2015). The Structure of a full-length membrane-embedded integrin bound to a physiological ligand. *J. Biol. Chem.* 290, 27168–27175. doi: 10.1074/jbc.m115.682377

Das, S., Majhi, P. D., Al-Mugotir, M. H., Rachagani, S., Sorgen, P., and Batra, S. K. (2015). Membrane proximal ectodomain cleavage of MUC16 occurs in the acidifying Golgi/post-Golgi compartments. *Sci. Rep.* 5:9759.

Deberardinis, R. J., and Chandel, N. S. (2020). We need to talk about the Warburg effect. *Nat. Metab.* 2, 127–129. doi: 10.1038/s42255-020-0172-2

Dennis, J. W., Nabi, I. R., and Demetriou, M. (2009). Metabolism, cell surface organization, and disease. *Cell* 139, 1229–1241. doi: 10.1016/j.cell.2009.12.008

Ebong, E. E., Macaluso, F. P., Spray, D. C., and Tarbell, J. M. (2011). Imaging the endothelial glycocalyx in vitro by rapid freezing/freeze substitution transmission electron microscopy. *Arteriosc. Thromb. Vasc. Biol.* 31, 1908–1915. doi: 10.1161/atvbaha.111.225268

Felder, M., Kapur, A., Gonzalez-Bosquet, J., Horibata, S., Heintz, J., Albrecht, R., et al. (2014). MUC16 (CA125): tumor biomarker to cancer therapy, a work in progress. *Mol. Cancer* 13:129. doi: 10.1186/1476-4598-13-129

Florian, J. A., Kosky, J. R., Ainslie, K., Pang, Z. Y., Dull, R. O., and Tarbell, J. M. (2003). Heparan sulfate proteoglycan is a mechanosensor on endothelial cells. *Circul. Res.* 93, E136–E142.

Formosa-Dague, C., Castelain, M., Martin-Yken, H., Dunker, K., Dague, E., and Sletmoen, M. (2018). The role of glycans in bacterial adhesion to mucosal surfaces: how can single-molecule techniques advance our understanding? *Microorganisms* 6:39. doi: 10.3390/microorganisms6020039

Freeman, S. A., Vega, A., Riedl, M., Collins, R. F., Ostrowski, P. P., Woods, E. C., et al. (2018). Transmembrane pickets connect cyto- and pericellular skeletons forming barriers to receptor engagement. *Cell* 172, 305–317.

Furtak, V., Hatcher, F., and Ochieng, J. (2001). Galectin-3 mediates the endocytosis of beta-1 integrins by breast carcinoma cells. *Biochem. Biophys. Res. Commun.* 289, 845–850. doi: 10.1006/bbrc.2001.6064

Gagneux, P., Aebi, M., and Varki, A. (2015). "Evolution of glycan diversity," in *Essentials of Glycobiology*, eds A. Varki, R. D. Cummings, J. D. Esko, P. Stanley, G. W. Hart, M. Aebi, et al. (Cold Spring Harbor, NY: Cold Spring Harbor Laboratory Press).

Gandhi, J. G., Koch, D. L., and Paszek, M. J. (2019). Equilibrium modeling of the mechanics and structure of the cancer glycocalyx. *Biophys. J.* 116, 694–708. doi: 10.1016/j.bpj.2018.12.023

Goodison, S., Urquidi, V., and Tarin, D. (1999). CD44 cell adhesion molecules. *J. Clin. Pathol. Mol. Pathol.* 52, 189–196. doi: 10.1136/mp.52.4.189

Gray, M., Stanczak, M. A., Xiao, H., Pijnenborg, J. F., Mantuano, N. R., Malaker, S. A., et al. (2019). Targeted desialylation overcomes glyco-immune checkpoints and potentiates the anticancer immune response in vivo. *ChemRxiv*. [Preprint]. ChemRxiv.8187146.v2.

Gromnicova, R., Kaya, M., Romero, I. A., Williams, P., Satchell, S., Sharrack, B., et al. (2016). Transport of gold nanoparticles by vascular endothelium from different human tissues. *Plos One* 11:e0161610. doi: 10.1371/journal.pone.0161610

Guberman, M., and Seeberger, P. H. (2019). Automated glycan assembly: a perspective. *J. Am. Chem. Soc.* 141, 5581–5592. doi: 10.1021/jacs.9b00638

Hahm, H. S., Schlegel, M. K., Hurevich, M., Eller, S., Schuhmacher, F., Hofmann, J., et al. (2017). Automated glycan assembly using the Glyconeer 2.1 synthesizer. *Proc. Natl. Acad. Sci. U.S.A.* 114, E3385–E3389.

Han, L., and Costello, C. E. (2013). Mass spectrometry of glycans. *Biochem. Mosco.* 78, 710–720.

Harazono, Y., Kho, D. H., Balan, V., Nakajima, K., Zhang, T. P., Hogan, V., et al. (2014). Galectin-3 leads to attenuation of apoptosis through Bax heterodimerization in human thyroid carcinoma cells. *Oncotarget* 5, 9992–10001.

Hartmann, M., and Lindhorst, T. K. (2011). The bacterial lectin fimh, a target for drug discovery-carbohydrate inhibitors of type 1 fimbriae-mediated bacterial adhesion. *Eur. J. Organ. Chem.* 2011, 3583–3609. doi: 10.1002/ejoc.201100407

Hegermann, J., Lunsdorf, H., Ochs, M., and Haller, H. (2016). Visualization of the glomerular endothelial glycocalyx by electron microscopy using cationic colloidal thorium dioxide. *Histochem. Cell Biol.* 145, 41–51. doi: 10.1007/s00418-015-1378-3

Heiden, M. G. V., Cantley, L. C., and Thompson, C. B. (2009). Understanding the warburg effect: the metabolic requirements of cell proliferation. *Science* 324, 1029–1033. doi: 10.1126/science.1160809

Henderson, R., and Unwin, P. N. T. (1975). Three-dimensional model of purple membrane obtained by electron microscopy. *Nature* 257:28. doi: 10.1038/257028a0

Hudak, J. E., Canham, S. M., and Bertozzi, C. R. (2014). Glycocalyx engineering reveals a Siglec-based mechanism for NK cell immunoevasion. *Nat. Chem. Biol.* 10, 69–U111.

Imberty, A., Chabre, Y. M., and Roy, R. (2008). Glycomimetics and glycodendrimers as high affinity microbial anti-adhesins. *Chem. Eur. J.* 14, 7490–7499. doi: 10.1002/chem.200800700

Jacobson, K., Ishihara, A., and Inman, R. (1987). Lateral diffusion of proteins in membranes. *Ann. Rev. Physiol.* 49, 163–175.

Jacobson, K., Liu, P., and Lagerholm, B. C. (2019). The lateral organization and mobility of plasma membrane components. *Cell* 177, 806–819. doi: 10.1016/j.cell.2019.04.018

Jandus, C., Boligan, K. F., Chijioke, O., Liu, H., Dahlhaus, M., Demoulins, T., et al. (2014). Interactions between Siglec-7/9 receptors and ligands influence NK cell-dependent tumor immunosurveillance. *J. Clin. Investigat.* 124, 1810–1820. doi: 10.1172/jci65899

Jiang, H., English, B. P., Hazan, R. B., Wu, P., and Ovryn, B. (2015). Tracking surface glycans on live cancer cells with single-molecule sensitivity. *Angew. Chem. Int. Ed.* 54, 1765–1769. doi: 10.1002/anie.201407976

Jiang, Z. Y., Zhang, H. S., and Bockmann, R. A. (2016). Allostery in BAX protein activation. *J. Biomol. Struct. Dynam.* 34, 2469–2480. doi: 10.1080/07391102.2015.1119731

Johannes, L., Jacob, R., and Leffler, H. (2018). Galectins at a glance. *J. Cell Sci.* 131:jcs208884. doi: 10.1242/jcs.208884

Jung, Y. M., Riven, I., Feigelson, S. W., Kartvelishvily, E., Tohya, K., Miyasaka, M., et al. (2016). Three-dimensional localization of T-cell receptors in relation to microvilli using a combination of superresolution microscopies. *Proc. Natl. Acad. Sci. U.S.A.* 113, E5916–E5924.

Kalluri, R., and Weinberg, R. A. (2009). The basics of epithelial-mesenchymal transition. *J. Clin. Investigat.* 119, 1420–1428. doi: 10.1172/jci39104

Keppler, O. T., Stehling, P., Herrmann, M., Kayser, H., Grunow, D., Reutter, W., et al. (1995). Biosynthetic modulation of sialic acid-dependent virus-receptor interactions of two primate polyoma viruses. *J. Biol. Chem.* 270, 1308–1314. doi: 10.1074/jbc.270.3.1308

Koch, A., Poirier, F., Jacob, R., and Delacour, D. (2010). Galectin-3, a novel centrosome-associated protein, required for epithelial morphogenesis. *Mol. Biol. Cell* 21, 219–231. doi: 10.1091/mbc.e09-03-0193

Kolata, G. B. (1975). Microvilli: a major difference between normal and cancer cells? *Science* 188, 819–820. doi: 10.1126/science.188.4190.819

Kolbe, K., Veleti, S. K., Reiling, N., and Lindhorst, T. K. (2019). Lectins of mycobacterium tuberculosis-rarely studied proteins. *Beilst. J. Organ. Chem.* 15, 1–15. doi: 10.3762/bjoc.15.1

Krasnova, L., and Wong, C. H. (2016). Understanding the chemistry and biology of glycosylation with glycan synthesis. *Ann. Rev. Biochem.* 85, 599–630. doi: 10.1146/annurev-biochem-060614-034420

Kufe, D. W. (2009). Mucins in cancer: function, prognosis and therapy. *Nat. Rev. Cancer* 9, 874–885. doi: 10.1038/nrc2761

Kuo, J. C. H., Gandhi, J. G., Zia, R. N., and Paszek, M. J. (2018). Physical biology of the cancer cell glycocalyx. *Nat. Phys.* 14, 658–669. doi: 10.1038/s41567-018-0186-9

Kusumi, A., and Sako, Y. (1996). Cell surface organization by the membrane skeleton. *Curr. Opin. Cell Biol.* 8, 566–574. doi: 10.1016/s0955-0674(96)80036-6

Laine, R. A. (1994). A calculation of all possible oligosaccharide isomers both branched and linear yields 1.05x10(12) structures for a reducing hexasaccharide - the isomer-barrier to development of single-method saccharide sequencing or synthesis systems. *Glycobiology* 4, 759–767. doi: 10.1093/glycob/4.6.759

Lakshminarayanan, A., Richard, M., and Davis, B. G. (2018). Studying glycobiology at the single-molecule level. *Nat. Rev. Chem.* 2, 148–159. doi: 10.1038/s41570-018-0019-5

Lau, K. S., Partridge, E. A., Grigorian, A., Silvescu, C. I., Reinhold, V. N., Demetriou, M., et al. (2007). Complex N-glycan number and degree of branching cooperate to regulate cell proliferation and differentiation. *Cell* 129, 123–134. doi: 10.1016/j.cell.2007.01.049

Läubli, H., Pearce, O. M. T., Schwarz, F., Siddiqui, S. S., Deng, L. Q., Stanczak, M. A., et al. (2014). Engagement of myelomonocytic siglecs by tumor-associated ligands modulates the innate immune response to cancer. *Proc. Natl. Acad. Sci. U.S.A.* 111, 14211–14216. doi: 10.1073/pnas.1409580111

Laughlin, S. T., and Bertozzi, C. R. (2007). Metabolic labeling of glycans with azido sugars and subsequent glycan-profiling and visualization via Staudinger ligation. *Nat. Protoc.* 2, 2930–2944. doi: 10.1038/nprot.2007.422

Lee, A. H. S., Key, H. P., Bell, J. A., Hodi, Z., and Ellis, I. O. (2011). Breast carcinomas with borderline (2+) HER2 immunohistochemistry: percentage of cells with complete membrane staining for HER2 and the frequency of HER2 amplification. *J. Clin. Pathol.* 64, 490–492. doi: 10.1136/jcp.2011.089177

Lehmann, F., Tiralongo, E., and Tiralongo, J. (2006). Sialic acid-specific lectins: occurrence, specificity and function. *Cell. Mol. Life Sci.* 63, 1331–1354. doi: 10.1007/s00018-005-5589-y

Letschert, S., Gohler, A., Franke, C., Bertleff-Zieschang, N., Memmel, E., Doose, S., et al. (2014). Super-resolution imaging of plasma membrane glycans. *Angew. Chem. Int. Ed.* 53, 10921–10924. doi: 10.1002/anie.201406045

Lindhorst, T. K. (2007). *Essentials of Carbohydrate Chemistry and Biochemistry*. Weinheim: Viley-VCH.

Lipowsky, H. H. (2012). The endothelial glycocalyx as a barrier to leukocyte adhesion and its mediation by extracellular proteases. *Ann. Biomed. Eng.* 40, 840–848. doi: 10.1007/s10439-011-0427-x

Malaker, S. A., Pedram, K., Ferracane, M. J., Bensing, B. A., Krishnan, V., Pett, C., et al. (2019). The mucin-selective protease StcE enables molecular and functional analysis of human cancer-associated mucins. *Proc. Natl. Acad. Sci. U.S.A.* 116, 7278–7287. doi: 10.1073/pnas.1813020116

Marino, K., Bones, J., Kattla, J. J., and Rudd, P. M. (2010). A systematic approach to protein glycosylation analysis: a path through the maze. *Nat. Chem. Biol.* 6, 713–723. doi: 10.1038/nchembio.437

Matrosovich, M. N., Matrosovich, T. Y., Gray, T., Roberts, N. A., and Klenk, H. D. (2004). Neuraminidase is important for the initiation of influenza virus infection in human airway epithelium. *J. Virol.* 78, 12665–12667. doi: 10.1128/jvi.78.22.12665-12667.2004

Mcguckin, M. A., Linden, S. K., Sutton, P., and Florin, T. H. (2011). Mucin dynamics and enteric pathogens. *Nat. Rev. Microbiol.* 9, 265–278. doi: 10.1038/nrmicro2538

Mitchell, E., Houles, C., Sudakevitz, D., Wimmerova, M., Gautier, C., Perez, S., et al. (2002). Structural basis for oligosaccharide-mediated adhesion of *Pseudomonas aeruginosa* in the lungs of cystic fibrosis patients. *Nat. Struct. Biol.* 9, 918–921. doi: 10.1038/nsb865

Möckl, L., Hirn, S., Torrano, A. A., Uhl, B., Brauchle, C., and Krombach, F. (2017). The glycocalyx regulates the uptake of nanoparticles by human endothelial cells in vitro. *Nanomedicine* 12, 207–217. doi: 10.2217/nnm-2016-0332

Möckl, L., Horst, A. K., Kolbe, K., Lindhorst, T. K., and Brauchle, C. (2015). Microdomain formation controls spatiotemporal dynamics of cell-surface glycoproteins. *Chembiochem* 16, 2023–2028. doi: 10.1002/cbic.201500361

Möckl, L., Lindhorst, T. K., and Brauchle, C. (2016). Artificial formation and tuning of glycoprotein networks on live cell membranes: a single-molecule tracking study. *Chemphyschem* 17, 829–835. doi: 10.1002/cphc.201500809

Möckl, L., Pedram, K., Roy, A. R., Krishnan, V., Gustavsson, A. K., Dorigo, O., et al. (2019). Quantitative super-resolution microscopy of the mammalian glycocalyx. *Dev. Cell* 50, 57–72. doi: 10.1016/j.devcel.2019.04.035

Moerner, W. E. (2012). Microscopy beyond the diffraction limit using actively controlled single molecules. *J. Micro.* 246, 213–220. doi: 10.1111/j.1365-2818.2012.03600.x

Moran, H., Cancel, L. M., Mayer, M. A., Qazi, H., Munn, L. L., and Tarbell, J. M. (2019). The cancer cell glycocalyx proteoglycan glypican-1 mediates interstitial flow mechanotransduction to enhance cell migration and metastasis. *Biorheology* 56, 151–161. doi: 10.3233/bir-180203

Moremen, K. W., Tiemeyer, M., and Nairn, A. V. (2012). Vertebrate protein glycosylation: diversity, synthesis and function. *Nat. Rev. Mol. Cell Biol.* 13, 448–462. doi: 10.1038/nrm3383

Müller, C., Despras, G., and Lindhorst, T. K. (2016). Organizing multivalency in carbohydrate recognition. *Chem. Soc. Rev.* 45, 3275–3302. doi: 10.1039/c6cs00165c

Neelamegham, S., Aoki-Kinoshita, K., Bolton, E., Frank, M., Lisacek, F., Lutteke, T., et al. (2019). Updates to the symbol nomenclature for glycans guidelines. *Glycobiology* 29, 620–624. doi: 10.1093/glycob/cwz045

Nieminen, J., Kuno, A., Hirabayashi, J., and Sato, S. (2007). Visualization of galectin-3 oligomerization on the surface of neutrophils and endothelial cells using fluorescence resonance energy transfer. *J. Biol. Chem.* 282, 1374–1383. doi: 10.1074/jbc.m604506200

Ohtsubo, K., and Marth, J. D. (2006). Glycosylation in cellular mechanisms of health and disease. *Cell* 126, 855–867. doi: 10.1016/j.cell.2006.08.019

Pahakis, M. Y., Kosky, J. R., Dull, R. O., and Tarbell, J. M. (2007). The role of endothelial glycocalyx components in mechanotransduction of fluid shear stress. *Biochem. Biophys. Res. Commun.* 355, 228–233. doi: 10.1016/j.bbrc.2007.01.137

Pan, S., Chen, R., Aebersold, R., and Brentnall, T. A. (2011). Mass spectrometry based glycoproteomics-from a proteomics perspective. *Mol. Cell. Proteom.* 10:R110.003251.

Paschinger, K., Fabini, G., Schuster, D., Rendic, D., and Wilson, I. B. H. (2005). Definition of immunogenic carbohydrate epitopes. *Acta Biochim. Polon.* 52, 629–632. doi: 10.18388/abp.2005_3422

Paszek, M. J., Dufort, C. C., Rossier, O., Bainer, R., Mouw, J. K., Godula, K., et al. (2014). The cancer glycocalyx mechanically primes integrin-mediated growth and survival. *Nature* 511, 319–325. doi: 10.1038/nature13535

Patton, S., Gendler, S. J., and Spicer, A. P. (1995). The epithelial mucin, MUC1, of milk, mammary gland and other tissues. *Biochim. Biophys. Acta Rev. Biomembr.* 1241, 407–423. doi: 10.1016/0304-4157(95)00014-3

Paulson, J. C., Macauley, M. S., and Kawasaki, N. (2012). Siglecs as sensors of self in innate and adaptive immune responses. *Glycobiol. Immu. Res.* 1253, 37–48. doi: 10.1111/j.1749-6632.2011.06362.x

Pavlova, N. N., and Thompson, C. B. (2016). The Emerging hallmarks of cancer metabolism. *Cell Metab.* 23, 27–47. doi: 10.1016/j.cmet.2015.12.006

Pinho, S. S., and Reis, C. A. (2015). Glycosylation in cancer: mechanisms and clinical implications. *Nat. Rev. Cancer* 15, 540–555. doi: 10.1038/nrc3982

Pluhackova, K., and Böckmann, R. A. (2015). Biomembranes in atomistic and coarse-grained simulations. *J. Phys. Cond. Matter* 27:323103. doi: 10.1088/0953-8984/27/32/323103

Qazi, H., Palomino, R., Shi, Z. D., Munn, L. L., and Tarbell, J. M. (2013). Cancer cell glycocalyx mediates mechanotransduction and flow-regulated invasion. *Integrat. Biol.* 5, 1334–1343. doi: 10.1039/c3ib40057c

Qazi, H., Shi, Z. D., Song, J. W., Cancel, L. M., Huang, P., Zeng, Y., et al. (2016). Heparan sulfate proteoglycans mediate renal carcinoma metastasis. *Int. J. Cancer* 139, 2791–2801. doi: 10.1002/ijc.30397

Ramirez-Weber, F. A., and Kornberg, T. B. (1999). Cytonemes: cellular processes that project to the principal signaling center in *Drosophila* imaginal discs. *Cell* 97, 599–607.

Rehm, M., Bruegger, D., Christ, F., Conzen, P., Thiel, M., Jacob, M., et al. (2007). Shedding of the endothelial glycocalyx in patients undergoing major vascular surgery with global and regional ischemia. *Circulation* 116, 1896–1906. doi: 10.1161/circulationaha.106.684852

Robertson, J. D. (1981). Membrane structure. *J. Cell Biol.* 91:189.

Rudd, P. M., Wormald, M. R., Stanfield, R. L., Huang, M. D., Mattsson, N., Speir, J. A., et al. (1999). Roles for glycosylation of cell surface receptors involved in cellular immune recognition. *J. Mol. Biol.* 293, 351–366. doi: 10.1006/jmbi.1999.3104

Rudiger, H., and Gabius, H. J. (2001). Plant lectins: occurrence, biochemistry, functions and applications. *Glycoconj. J.* 18, 589–613.

Rustom, A., Saffrich, R., Markovic, I., Walther, P., and Gerdes, H. H. (2004). Nanotubular highways for intercellular organelle transport. *Science* 303, 1007–1010. doi: 10.1126/science.1093133

Schmaltz, R. M., Hanson, S. R., and Wong, C. H. (2011). Enzymes in the synthesis of glycoconjugates. *Chem. Rev.* 111, 4259–4307. doi: 10.1021/cr200113w

Scott, A. M., Wolchok, J. D., and Old, L. J. (2012). Antibody therapy of cancer. *Nat. Rev. Cancer* 12, 278–287.

Shalom-Feuerstein, R., Plowman, S. J., Rotblat, B., Ariotti, N., Tian, T. H., Hancock, J. F., et al. (2008). K-Ras nanoclustering is subverted by overexpression of the scaffold protein Galectin-3. *Cancer Res.* 68, 6608–6616. doi: 10.1158/0008-5472.can-08-1117

Shurer, C. R., Colville, M. J., Gupta, V. K., Head, S. E., Kai, F., Lakins, J. N., et al. (2018). Genetically encoded toolbox for glycocalyx engineering: tunable control of cell adhesion, survival, and cancer cell behaviors. *ACS Biomater. Sci. Eng.* 4, 388–399. doi: 10.1021/acsbiomaterials.7b00037

Shurer, C. R., Kuo, J. C. H., Roberts, L. M., Gandhi, J. G., Colville, M. J., Enoki, T. A., et al. (2019). Physical principles of membrane shape regulation by the glycocalyx. *Cell* 177, 1757–1770.

Singer, S. J., and Nicolson, G. L. (1972). The fluid mosaic model of the structure of cell membranes. *Science* 175, 720–731. doi: 10.1126/science.175.4023.720

Smith, D. F., and Cummings, R. D. (2013). Application of microarrays for deciphering the structure and function of the human glycome. *Mol. Cell. Proteom.* 12, 902–912. doi: 10.1074/mcp.r112.027110

Spiro, R. G. (2002). Protein glycosylation: nature, distribution, enzymatic formation, and disease implications of glycopeptide bonds. *Glycobiology* 12, 43r–56r. doi: 10.1093/glycob/12.4.43r

Stanley, P., and Cummings, R. (2015). "Structures common to different glycans," in *Essentials of Glycobiology*, eds A. Varki, R. D. Cummings, J. D. Esko, P. Stanley, G. W. Hart, M. Aebi, et al. (Cold Spring Harbor, NY: Cold Spring Harbor Laboratory Press).

Tarbell, J. M., and Cancel, L. M. (2016). The glycocalyx and its significance in human medicine. *J. Int. Med.* 280, 97–113. doi: 10.1111/joim.12465

Thi, M. M., Tarbell, J. M., Weinbaum, S., and Spray, D. C. (2004). The role of the glycocalyx in reorganization of the actin cytoskeleton under fluid shear stress: a "bumper-car" model. *Proc. Natl. Acad. Sci. U.S.A.* 101, 16483–16488. doi: 10.1073/pnas.0407474101

Toole, B. P. (2004). Hyaluronan: from extracellular glue to pericellular cue. *Nat. Rev. Cancer* 4, 528–539. doi: 10.1038/nrc1391

Tricarico, C., Clancy, J., and D'souza-Schorey, C. (2017). Biology and biogenesis of shed microvesicles. *Small GTPases* 8, 220–232. doi: 10.1080/21541248.2016.1215283

Uhl, B., Hirn, S., Immler, R., Mildner, K., Mockl, L., Sperandio, M., et al. (2017). The endothelial glycocalyx controls interactions of quantum dots with the endothelium and their translocation across the blood-tissue border. *ACS Nano* 11, 1498–1508. doi: 10.1021/acsnano.6b06812

Varki, A. (2017). Biological roles of glycans. *Glycobiology* 27, 3–49. doi: 10.1093/glycob/cww086

Varki, A., Cummings, R. D., Aebi, M., Packer, N. H., Seeberger, P. H., Esko, J. D., et al. (2015). Symbol nomenclature for graphical representations of glycans. *Glycobiology* 25, 1323–1324.

Varki, A., and Gagneux, P. (2012). Multifarious roles of sialic acids in immunity. *Glycobiol. Immun. Respons.* 1253, 16–36. doi: 10.1111/j.1749-6632.2012.06517.x

Von Diezmann, A., Shechtman, Y., and Moerner, W. E. (2017). Three-dimensional localization of single molecules for super resolution imaging and single-particle tracking. *Chem. Rev.* 117, 7244–7275. doi: 10.1021/acs.chemrev.6b00629

Wang, Z., Chinoy, Z. S., Ambre, S. G., Peng, W. J., Mcbride, R., De Vries, R. P., et al. (2013). A general strategy for the chemoenzymatic synthesis of asymmetrically branched n-glycans. *Science* 341, 379–383. doi: 10.1126/science.1236231

Weber, T., Chandrasekaran, V., Stamer, I., Thygesen, M. B., Terfort, A., and Lindhorst, T. K. (2014). Switching of bacterial adhesion to a glycosylated surface by reversible reorientation of the carbohydrate ligand. *Angew. Chem. Int. Ed.* 53, 14583–14586. doi: 10.1002/anie.201409808

Weigel, P. H., and Deangelis, P. L. (2007). Hyaluronan synthases: a decade-plus of novel glycosyltransferases. *J. Biol. Chem.* 282, 36777–36781. doi: 10.1074/jbc.r700036200

Whelan, D. R., and Bell, T. D. M. (2015). Image artifacts in single molecule localization microscopy: why optimization of sample preparation protocols matters. *Sci. Rep.* 5:7924.

Woods, E. C., Kai, F., Barnes, J. M., Pedram, K., Pickup, M. W., Hollander, M. J., et al. (2017). A bulky glycocalyx fosters metastasis formation by promoting G1 cell cycle progression. *eLife* 6:e25752.

Woods, E. C., Yee, N. A., Shen, J., and Bertozzi, C. R. (2015). Glycocalyx engineering with a recycling glycopolymer that increases cell survival in vivo. *Angew. Chem. Int. Ed.* 54, 15782–15788. doi: 10.1002/anie.201508783

Xiao, H., Woods, E. C., Vukojicic, P., and Bertozzi, C. R. (2016). Precision glycocalyx editing as a strategy for cancer immunotherapy. *Proc. Natl. Acad. Sci. U.S.A.* 113, 10304–10309. doi: 10.1073/pnas.1608069113

Yin, L., Kharbanda, S., and Kufe, D. (2007). Mucin 1 oncoprotein blocks hypoxia-inducible factor 1 alpha activation in a survival response to hypoxia. *J. Biol. Chem.* 282, 257–266. doi: 10.1074/jbc.m610156200

Zeng, Y., Zhang, X. F., Fu, B. M. M., and Tarbell, J. M. (2018). The role of endothelial surface glycocalyx in mechanosensing and transduction. *Mol. Cell. Tissue Eng. Vascul. Syst.* 1097, 1–27. doi: 10.1007/978-3-319-96445-4_1

Conflict of Interest: The author declares that the research was conducted in the absence of any commercial or financial relationships that could be construed as a potential conflict of interest.

frontiers in Physiology

ORIGINAL RESEARCH
published: 16 April 2020
doi: 10.3389/fphys.2020.00250

Membrane Thinning Induces Sorting of Lipids and the Amphipathic Lipid Packing Sensor (ALPS) Protein Motif

Niek van Hilten[1], *Kai Steffen Stroh*[2] *and Herre Jelger Risselada*[1,2]*

[1] *Leiden Institute of Chemistry, Leiden University, Leiden, Netherlands,* [2] *Institute for Theoretical Physics, Georg August University Göttingen, Göttingen, Germany*

Heterogeneities (e.g., membrane proteins and lipid domains) and deformations (e.g., highly curved membrane regions) in biological lipid membranes cause lipid packing defects that may trigger functional sorting of lipids and membrane-associated proteins. To study these phenomena in a controlled and efficient way within molecular simulations, we developed an external field protocol that artificially enhances packing defects in lipid membranes by enforcing local thinning of a flat membrane region. For varying lipid compositions, we observed strong thinning-induced depletion or enrichment, depending on the lipid's intrinsic shape and its effect on a membrane's elastic modulus. In particular, polyunsaturated and lysolipids are strongly attracted to regions high in packing defects, whereas phosphatidylethanolamine (PE) lipids and cholesterol are strongly repelled from it. Our results indicate that externally imposed changes in membrane thickness, area, and curvature are underpinned by shared membrane elastic principles. The observed sorting toward the thinner membrane region is in line with the sorting expected for a positively curved membrane region. Furthermore, we have demonstrated that the amphipathic lipid packing sensor (ALPS) protein motif, a known curvature and packing defect sensor, is effectively attracted to thinner membrane regions. By extracting the force that drives amphipathic molecules toward the thinner region, our thinning protocol can directly quantify and score the lipid packing sensing of different amphipathic molecules. In this way, our protocol paves the way toward high-throughput exploration of potential defect- and curvature-sensing motifs, making it a valuable addition to the molecular simulation toolbox.

Keywords: membrane thinning, lipid sorting, protein sorting, membrane deformation, membrane curvature, lipid packing, curvature sensing

OPEN ACCESS

Edited by:
Rainer A. Böckmann, University of Erlangen Nuremberg, Germany

Reviewed by:
Jeffery Klauda, University of Maryland College Park, United States
Richard Walter Pastor, National Institutes of Health (NIH), United States

***Correspondence:**
Herre Jelger Risselada
herre.risselada@uni-goettingen.de

Specialty section:
This article was submitted to Membrane Physiology and Membrane Biophysics, a section of the journal Frontiers in Physiology

Received: *17 January 2020*
Accepted: *05 March 2020*
Published: *16 April 2020*

Citation:
van Hilten N, Stroh KS and Risselada HJ (2020) Membrane Thinning Induces Sorting of Lipids and the Amphipathic Lipid Packing Sensor (ALPS) Protein Motif. Front. Physiol. 11:250. doi: 10.3389/fphys.2020.00250

1. INTRODUCTION

Biological membranes are highly dynamic and heterogeneous lipid bilayer barriers that physically separate the functional compartments of cells (McMahon and Gallop, 2005). The role of membrane curvature in the spatial organization of membrane-associated proteins (Hatzakis et al., 2009; Bhatia et al., 2010; Antonny, 2011; Singh et al., 2012; Nguyen et al., 2017; Nepal et al., 2018; Bhaskara et al., 2019) and the membrane's local lipid composition (Derganc, 2007; Jiang and Powers, 2008; Sorre et al., 2009; Tian and Baumgart, 2009; Baumgart et al., 2011; Callan-Jones et al., 2011; Baoukina et al., 2018; Harayama and Riezman, 2018; Woodward et al., 2018) (and *vice versa*!) are well-established. One important driving force that underlies these phenomena are lipid packing defects.

Positive membrane curvature (the outer leaflets of vesicles) and surface tension both increase the exposure of alkyl chains to solvents via increased formation of packing defects. This results in an increased attractive stress at the oil-water interface, as evident from lateral pressure profiles (see **Figure S1A** and Ollila et al., 2009; Nepal et al., 2018). Proteins or lipids can reduce or even nullify the energetic cost associated with defect formation depending on their intrinsic molecular shape (Risselada and Marrink, 2009; Pinot et al., 2014; Baoukina et al., 2018) and amphipathicity (Ouberai et al., 2013; Vanni et al., 2013). They consequently reduce the elastic energy associated with membrane bending. Therefore, provided that the concomitant enthalpic gain is bigger than the entropic loss of demixing, lipids or proteins are effectively attracted toward the curved region of the membrane (i.e., curvature sensing).

Although the field's focus has been mostly on membrane curvature, lipid packing defects are a more general phenomenon. Due to the heterogeneity of biological membranes, there are many irregularities that may cause disturbances of the local lipid packing in a similar fashion to curvature; e.g., the edges of lipid nanodomains ("rafts") (Schäfer and Marrink, 2010; Nickels et al., 2015; Belička et al., 2017; Park and Im, 2018), membrane junctions [e.g., membrane fusion intermediates (Risselada et al., 2014; Tsai et al., 2014; Smirnova et al., 2019), and transmembrane proteins (Lee, 2003; Corradi et al., 2018)]. In these three examples, the difference in chemical potential imposed by the membrane inhomogeneity alters its surrounding membrane environment, and this has interesting consequences for biological functionality.

To date, simulation tools that can study and quantify lipid packing defect-induced sorting in both a controlled and computationally efficient way are still lacking. Existing setups/protocols are based on perforated vesicles (Risselada and Marrink, 2009), membrane tethers (Baoukina et al., 2018), or buckled membranes (Elías-Wolff et al., 2018, 2019). However, all of these setups are based on local differences in membrane curvature, and they involve the simulation of relatively large, complex, and computationally expensive systems. Local differences in lipid packing can alternatively result from local differences in membrane thickness rather than membrane curvature. Conveniently, a strong but gradual change in membrane thickness can be confined to a few nanometers only. This results in a very steep "packing defect" gradient. Therefore, a sensing protocol based on local differences in thickness has the potential to (i) substantially reduce the size of the simulation box and (ii) better emphasize differences in defect sensing because of a larger sorting force (steep gradient).

To this aim, we have designed a protocol that exerts an external force on a user-defined section of a flat bilayer membrane to locally decrease its thickness. When a membrane is squeezed, lipid tails get exposed to the water phase because they must expand laterally (xy) to conserve their volume with a decreasing z-component. These lipid packing defects are comparable to the scenario imposed by (i) surface tension, (ii) protein-induced negative hydrophobic mismatch (Milovanovic et al., 2015), (iii) and the outer monolayers of vesicles (positive membrane curvature). This allows one to study the properties of a membrane that, in terms of lipid packing defects, *behaves like* it is positively curved but that has an actual membrane curvature of zero. We have illustrated that our thinning protocol can be used as a convenient proxy for scoring positive curvature-induced sorting and sensing in the absence of its conjugated negative membrane curvature and in a much smaller simulation box. Moreover, our thinning protocol is extremely adaptive, tunable, and easy to set up. As a proof of principle, we have demonstrated strong thinness-induced sorting of four biorelevant lipids and the amphipathic ALPS protein motif; this is in line with theory as well as previous simulations and experiments.

2. METHODS

2.1. Simulation Details

All simulations were performed using the MARTINI force field for coarse-grained (CG) molecular dynamics (MD) (Marrink et al., 2007), and the version used was version 2.0 in GROMACS 2019.3 (Abraham et al., 2015). A 20 fs time step was used. The compressibility was set to $4.5 \cdot 10^{-5}$ bar^{-1}. The temperature was coupled to 310 K by the velocity rescaling thermostat (Bussi et al., 2007) ($\tau_T = 1$ ps). Van der Waals and coulomb interactions were described by shifted potentials that gradually switched off with interaction distances exceeding 0.9 and zero, respectively. For both potentials, a 1.2 nm neighbor list cut-off was used. The neighbor list was updated every 10 simulation steps.

2.2. Thinning Protocol

A module was added to the GROMACS 2019.3 source code to exert an inward-directed harmonic force F_z (with user-defined force constant k, see Equation 1) on lipid tail beads within a lateral section of a lipid bilayer, resulting in effective thinning of the membrane in that area. See **Figure 1A** for a schematic representation of the protocol.

$$\vec{F}_z = d \cdot C \cdot k \cdot \left(\frac{D}{2} - |z| \right) \tag{1}$$

The value D determines the minimal membrane thickness: F_z only acts on lipid tail beads that are more than $\frac{D}{2}$ from the center (which is at $z = 0$) of the bilayer, as controlled by d. Constant d also directs the force to the center of the bilayer.

$$d = \begin{cases} 1 & \text{if } z > \frac{D}{2} \quad \textbf{(upper leaflet)} \\ 0 & \text{if } -\frac{D}{2} < z < \frac{D}{2} \quad \textbf{(within minimal membrane thickness)} \\ -1 & \text{if } z < -\frac{D}{2} \quad \textbf{(lower leaflet)} \end{cases} \tag{2}$$

The scaling factor C depends on the particle's x-coordinate. The simulation box is split into three zones–the centered "thin" zone, with user-defined length A_{thin}, flanked by two "buffer" zones with user-defined length A_{buffer} and the "normal" zones–that are connected through the periodic boundaries in the x-direction (**Figure 1A**). Constant C linearly scales from 1 (in the thin zone) to 0 (in the normal zone).

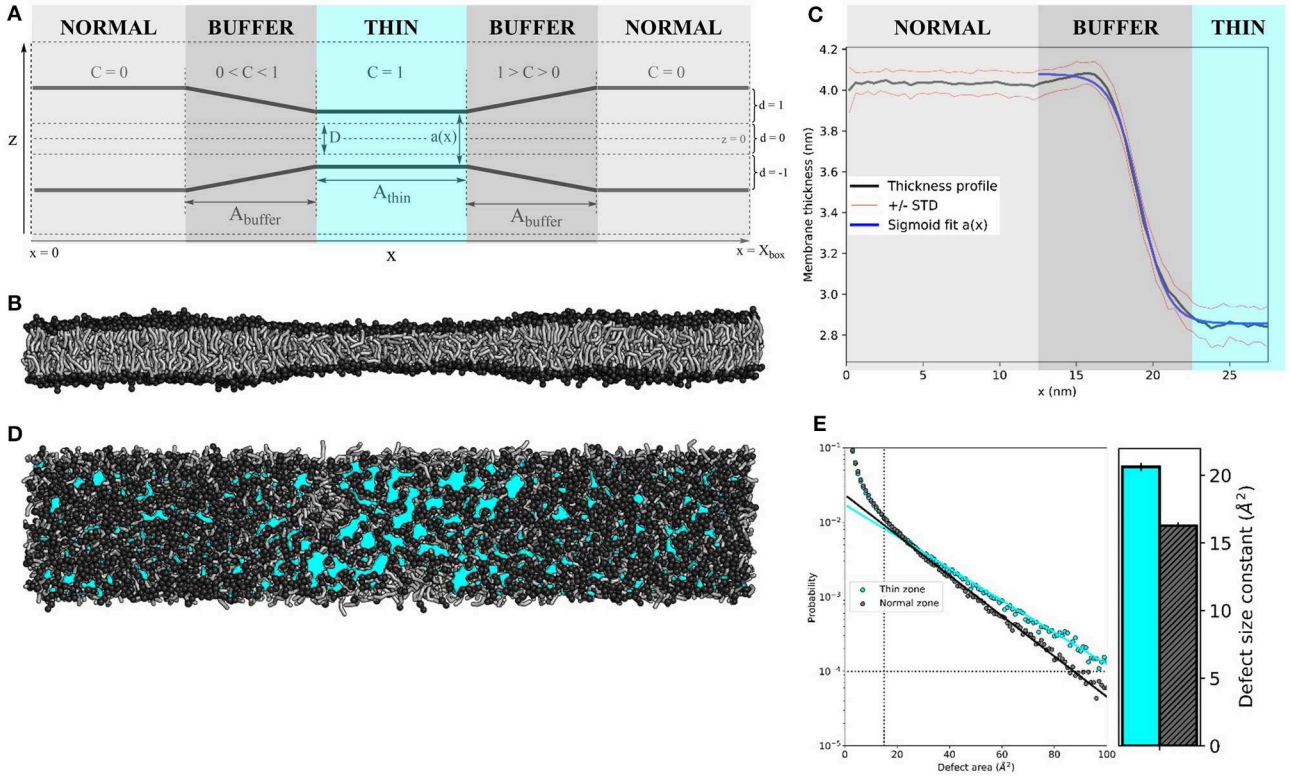

FIGURE 1 | Membrane thinning induces lipid packing defects. **(A)** Schematic representation of the thinning protocol setup. Parameters correspond to those in Equations (1–4). **(B)** Side view of applying the thinning protocol to a 55 × 10 nm^2 POPC membrane. **(C)** The average thickness profile for the same 55x10 nm^2 POPC membrane (black line), symmetrized around the center of the thin zone. Red lines indicate the one standard deviation (STD) interval. Blue line is the sigmoid fit $a(x)$ (see Equation 4). **(D)** Top view of the 55 × 10 nm^2 POPC membrane. Cyan patches depict lipid packing defects (visualized by PackMem (Gautier et al., 2018). **(E)** Quantification of lipid packing defects in the thin (cyan) and normal zones (black). The block-averaged defect size constants in the bar plot (right) equate to the inverse of the slope of the linear fit to the probability distribution (left). The vertical and horizontal dotted lines indicate the minimal values for curve fitting (area $A = 15$ Å^2 and probability $p(A) = 10^{-4}$, as recommended by the PackMem authors (Gautier et al., 2018).

$$C = \begin{cases} 1 & \text{if } \frac{X_{box}-A_{thin}}{2} \le x \le \frac{X_{box}+A_{thin}}{2} \quad \textbf{(thin zone)} \\ \frac{\left|\frac{X_{box}+A_{thin}}{2}+A_{buffer}-x\right|}{A_{buffer}} & \text{if } \frac{X_{box}+A_{thin}}{2} < x \le \frac{X_{box}+A_{thin}}{2}+A_{buffer} \quad \textbf{(buffer zone)} \\ \frac{\left|\frac{X_{box}-A_{thin}}{2}-A_{buffer}-x\right|}{A_{buffer}} & \text{if } \frac{X_{box}-A_{thin}}{2}-A_{buffer} < x \le \frac{X_{box}-A_{thin}}{2} \quad \textbf{(buffer zone)} \\ 0 & \text{if } x < \frac{X_{box}-A_{thin}}{2}-A_{buffer} \quad \textbf{(normal zone)} \\ 0 & \text{if } x > \frac{X_{box}+A_{thin}}{2}+A_{buffer} \quad \textbf{(normal zone)} \end{cases} \tag{3}$$

For all simulations in this paper, the thinning parameters were set to $k = 20$ kJ nm^{-2} mol^{-1}, $D = 1$ nm and $A_{thin} = A_{buffer} = 10$ nm. We exaggerated the size of the normal and thin zones for the sake of visual clarity.

2.3. Lipid Mixing Simulations

The *insane* python script (Wassenaar et al., 2015) was used to generate a 50 × 10 × 10 nm^3 simulation box with bilayers of varying composition in the XY-plane: pure 16:0–18:1 PC (POPC), 70 mol% POPC with 30 mol% 16:0–18:1 PE (POPE), 70 mol% POPC with 30 mol% cholesterol, 70 mol% POPC with 30 mol% lysophosphatidylcholine (LysoPC, PPC in MARTINI) or 70 mol% POPC with 30 mol% 16:0–18:2 PC (PLiPC, PIPC in MARTINI) in explicit MARTINI water. After steepest descent minimization, a 2 μs NPT equilibration was performed with semiisotropic pressure coupling by the Berendsen barostat (Berendsen et al., 1984) to a reference pressure of 1 bar. Coupling of the membrane to overall tensionless conditions via a single pressure bath is ambiguous because of the heterogeneous nature of the system. It is important that the simulation box can accommodate for the extra membrane area that is created when the thin zone is being compressed. Our goal was to achieve tensionless conditions for the normal zone. To this aim, for each lipid composition, short runs with Berendsen surface tension

coupling ($\tau_P = 2$ ps) to lateral pressures ranging from 25 to 50 mN/m were performed to find the surface tension at which the membrane thickness of the normal zones matches the thickness of the corresponding tensionless membranes obtained from a normal unbiased simulation (**Figure S2**). At the respective calibrated surface tension coupling settings, the membranes slightly expand in the x-direction to an equilibrium box length of 55 nm for pure POPC (see **Table S1** for details). A reference pressure of 1 bar was used in the z-direction. We performed five replicas (with random initial velocities) of 20 ns equilibration followed by 4 μs production runs for each lipid composition.

2.4. Umbrella Sampling of the ALPS Protein Motif

A CG model of the amphipathic lipid packing sensor (ALPS) motif of the ArfGAP1 protein was built from the atomistic MD-refined structure by González-Rubio et al. (2011) with the *martinize* python script (Monticelli et al., 2008). Based on the peptide's hydrogen bonding pattern, a helical secondary structure was assigned to all residues by DSSP (Kabsch and Sander, 1983). The backbone angle parameters of the central region of the peptide (GWSSFTTG) were relaxed to MARTINI's default values for loop regions ($k = 20$ kJ rad^{-2} mol^{-1}, angle $= 96°$) to allow for some flexibility, which is known to play a role in membrane interactions (González-Rubio et al., 2011). Still, we should note that the MARTINI model does not fully capture changes in the secondary structure. Since our focus was on ALPS' amphipathicity, we deemed an aphipathic helical structure to sufficiently capture its characteristics. However, our general method is not limited to coarse-grained simulations only, and, in principle, allows for the incorporation of dynamic changes in the secondary structure via atomistic simulations.

After energy minimization, the CG ALPS peptide was placed in the middle of the thin zone of the aforementioned 55×10 nm^2 pure POPC membrane. Following 200 ns of NPT equilibration (protein restrained), the center of mass (COM) of the peptide was pulled in the x-direction from the center of the thin zone ($x \approx 27.5$ nm) to the center of the normal zone ($x \approx 5.5$ nm), while leaving the y- and z-coordinates unrestrained. From this trajectory, 111 frames were extracted with the x-coordinate decreasing with 0.2 nm steps. Each of these frames was NPT equilibrated for 50 ns and run for 100 ns with a harmonic potential ($k = 10^3$ kJ nm^{-2} mol^{-1}) to restrict the x-coordinate of the peptide's COM to that of the respective umbrella window. The free energy profile $F(x)$ was calculated from the 111 umbrella sampling production run data using the weighted histogram analysis method (WHAM) (Kumar et al., 1992) to unbias the probability distributions, as implemented in GROMACS (Hub et al., 2010).

3. RESULTS

3.1. Membrane Thinning Causes Lipid Packing Defects

The setup of the thinning protocol is depicted schematically in **Figure 1A** (see Method section for details). Applying this protocol to a 55×10 nm^2 pure POPC bilayer ($k = 20$ kJ nm^{-2} mol^{-1}, $D = 1$ nm and $A_{thin} = A_{buffer} = 10$ nm) yields an hourglass-shaped membrane (**Figure 1B**). We measured the membrane thickness (the distance between amine headgroup beads of opposing membrane leaflets) over 10 μs of simulation and symmetrized the data around the center of the simulation box (**Figure 1C**). The average thickness was 4.03 ± 0.06 nm for the normal zone, which closely matches the thickness of a well-equilibrated MARTINI POPC membrane without thinning (4.08 ± 0.05 nm, see **Table S1**). The average thickness of the thin zone was 2.85 ± 0.09 nm. At the edge of the buffer zone (around $x = 15$ nm), we observed a slight overshoot (1Å) in the thickness profile. Such overshoots were observed before in the context of protein nanopores with a mismatched hydrophobic thickness (Marelli, 2012; Garcia-Fandiño et al., 2016). The thickness profile in the buffer zone as a function of the x-coordinate can be described by a sigmoid function $a(x)$ (see Equation 4), which neatly falls within one standard deviation (STD) interval (**Figure 1C**). For our setup, $L = -1.22$ nm, $\kappa = -19.14$ nm^{-1}, $x_0 = 1.11$ nm, and $b = 4.08$ nm.

$$a(x) = \frac{L}{1 + e^{-\kappa(x - x_0)}} + b \tag{4}$$

We used PackMem (Gautier et al., 2018) to visualize and quantify the lipid packing defects that arise upon membrane thinning. In **Figure 1D**, cyan patches depict regions of the membrane where the hydrophobic lipid tails are exposed to water. Quantification was performed on 4,000 snapshots from a 400 ns simulation of a 10×10 nm^2 POPC membrane with and without applying the thinning protocol (PackMem's recommended settings). As expected, the block-averaged defect size constant is higher in the thin membrane than in the normal membrane (**Figure 1E**; 20.62 ± 0.31 vs. 16.28 ± 0.23 Å^2, respectively). This indicates that there is a significantly higher probability of finding greater lipid packing defects in a thin POPC membrane than in normally thick POPC membrane.

3.2. Thinness-Induced Lipid Sorting

With the thinning protocol in hand, we proceeded to test whether the induced lipid packing defects in a POPC membrane would lead to sorting when mixing in other lipids (**Figure 2A**). Starting with random distributions of 30 mol% POPE, cholesterol, LysoPC or PLiPC, we tracked the lipid positions over five replicas of 4 μs simulations (**Figure 2B**, see trajectory movies in **Supplementary Material**). We found that both POPE and cholesterol partition away from the thin zone of the membrane: both concentrations more than halved (**Figure 2C**). In contrast, we found that both LysoPC (only one lipid tail) and PLiPC (doubly unsaturated) were strongly enriched in the thin zone of our squeezed membrane (**Figure 2C**).

3.3. Thinness-Induced Sorting of the Curvature Sensing ALPS Protein Motif

Finally, we investigated protein sorting along the thinning gradient of our POPC membrane. One of the best studied curvature sensing protein motifs is the α-helical ALPS (Bigay

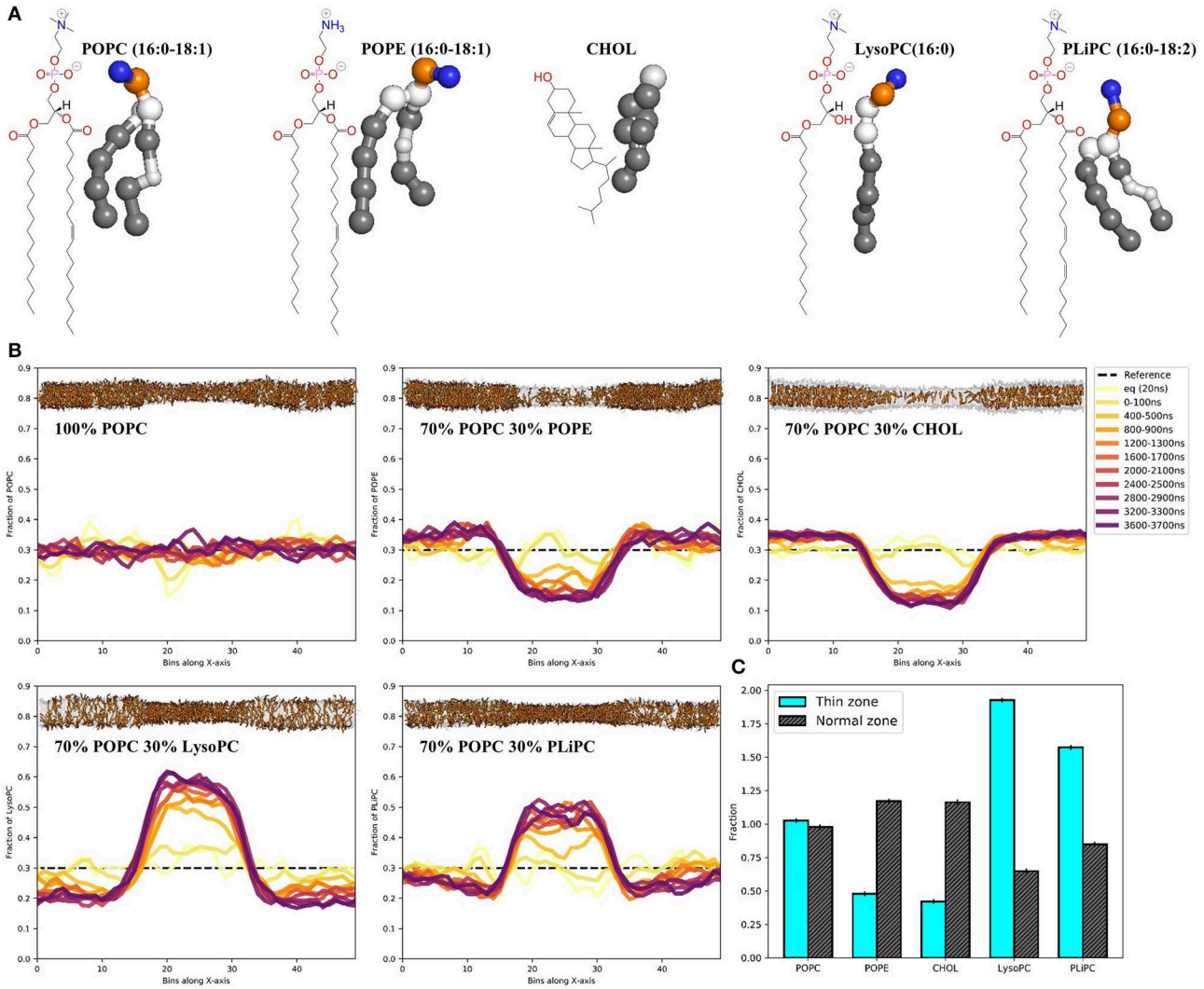

FIGURE 2 | Membrane thinning induces lipid sorting. **(A)** Chemical structures and MARTINI's coarse-grained representations of POPC, POPE, CHOL, LysoPC, and PLiPC. **(B)** Histograms of the POPC, POPE, CHOL, LysoPC, and PLiPC content in 50 bins along the x-axis over 4 μs of simulation. Data are averages over five replica runs. As a reference, the black dashed line depicts the initial distribution of 30 mol%. Membrane snapshots show the final configuration, with 70 mol% POPC in transparent gray and 30 mol% of mixed-in lipid in orange. The full trajectories are provided as movies in the **Supplementary Material. (C)** Quantification of lipid mixing after 4 μs of simulation for every lipid composition in the thin zone (cyan) and the normal zone (black). Data is normalized to 30 mol%.

et al., 2005; Drin et al., 2007; Mesmin et al., 2007; González-Rubio et al., 2011; Vanni et al., 2014; Doucet et al., 2015). This 20–40 residue motif comprises regularly distributed hydrophobic residues that can favorably complement the lipid packing defects that arise at positive membrane curvature (Vanni et al., 2013). Recent simulations of a similar ALPS motif showed effective sensing of defects up to $\approx$ 115 Å^2 (Wildermuth et al., 2019), which is exactly the regime of defect sizes that our thinning protocol can controllably induce. Hence, we set out to quantify the attractive force acting on the ALPS peptide toward the lipid packing defects in the thin membrane region.

Hereto, we performed umbrella sampling of the ALPS motif of ArfGAP1 along the 10 nm buffer zone of the same 55 × 10 nm^2 POPC membrane we described before (**Figure 3A**). This yielded the free energy profile $F(x)$ with respect to the x-coordinate of the position in the box (**Figure 3B**, see **Figure S3** for histogram). The slope $\frac{dF(x)}{dx}$ of a linear fit to this energy profile in the buffer zone describes the average attractive force on the peptide toward the thin region of the membrane. For the ALPS motif in the current setup, this force equals 6.89 kJ mol^{-1} nm^{-1}, or 11.44 pN. One can interpret this value as a measure for the ability of the peptide to sense lipid packing defects.

Combining the $F(x)$ profile with the thickness profile $a(x)$ (**Figure 1C**, Equation 4) yields the free energy as a function of the membrane thickness $F(a)$ (**Figure 3C**, see **Supplementary Material** for the derivation of the required Jacobian transformation). From this, we could conclude that ALPS indeed favors the thinner section of the membrane due

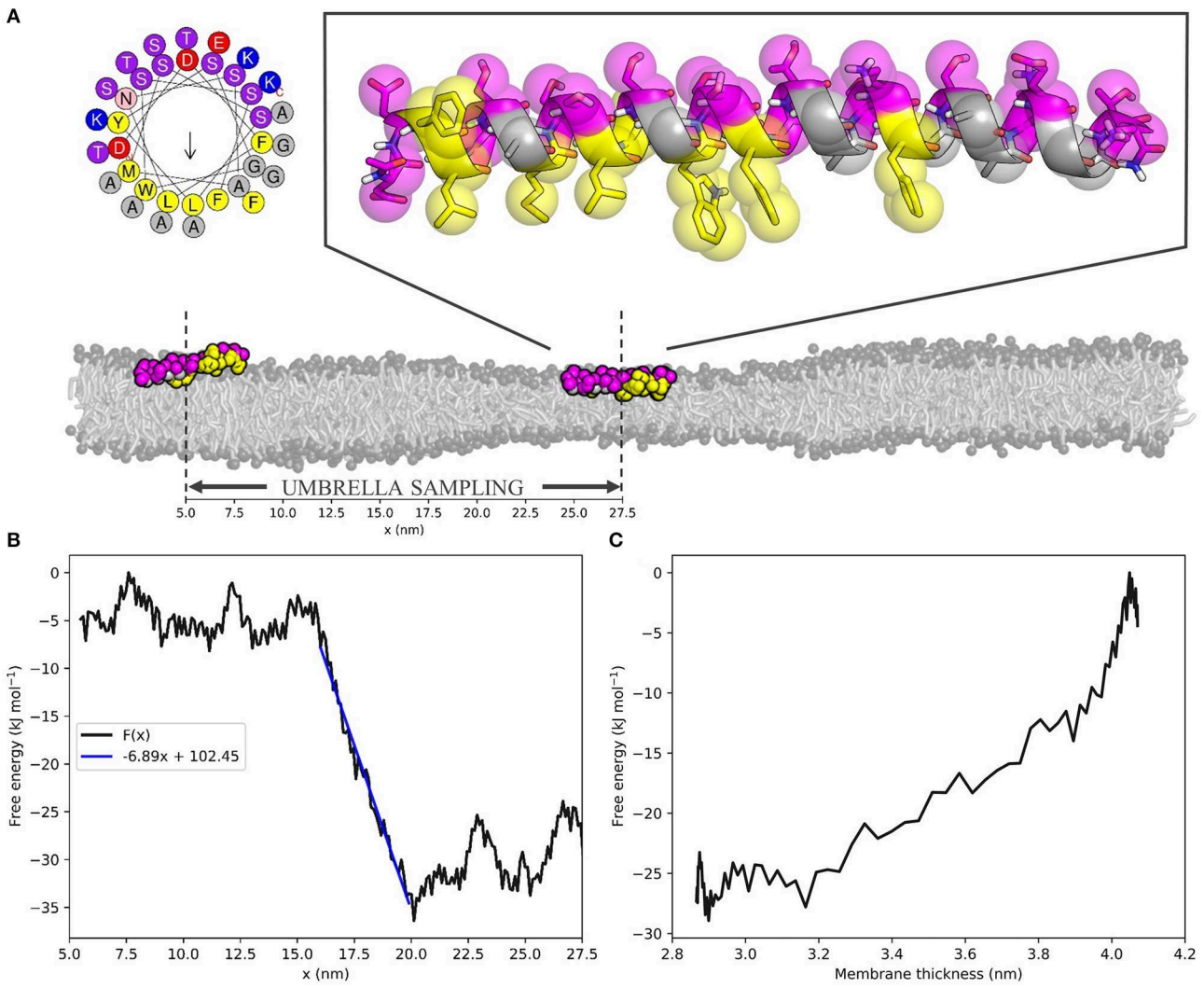

FIGURE 3 | The ALPS peptide is attracted toward the thin zone of the membrane. **(A)** Top left; helical wheel representation of the ALPS peptide [generated with HELIQUEST (Gautier et al., 2008)]. Top right; atomistic starting configuration of ALPS, as adapted from González-Rubio et al. (2011) and overlayed MARTINI beads. Hydrophobic and hydrophilic residues are shown in yellow and magenta, respectively. Bottom; initial ($x \approx 27.5$ nm) and final ($x \approx 5.5$ nm) membrane positions on the squeezed 55 × 10 nm^2 POPC membrane used for umbrella sampling. Scale indicates x-coordinates. **(B)** ALPS free energy profile $F(x)$ as a function of the x-coordinate. Blue line is the linear fit of the buffer zone, which' slope $\frac{dF(x)}{dx}$ yields the effective force that acts on the peptide. **(C)** ALPS' membrane thickness-dependent free energy $F(a)$, calculated for the buffer zone (see **Supplementary Material** for derivation).

to its ability to sense lipid packing defects. The free energy difference $\Delta F(a)$ between the thin and the normal zone was roughly 25 kJ mol^{-1}, or 10 k_BT, which is in the same range as the experimental binding free energy of helical amphipathic peptides to membranes (He and Lazaridis, 2013). This result underlines that the "curvature"-sensing ability of the ALPS motif (and arguably many other proteins) actually boils down to lipid packing defect sensing, and this is consistent with previous simulations (Vanni et al., 2013).

4. DISCUSSION

We here presented a protocol for controlled thinning of lipid membranes in MD simulations. Although we performed our simulations with the MARTINI model for CGMD simulations, we should note that our protocol is not at all restricted to coarse-grained systems. We can imagine that, for most applications, the thickness gradient in the buffer zone of the membrane would be the main region of interest. Therefore, one could choose to only simulate that specific area. This would reduce the box dimensions to a system size that is feasible to simulate in atomistic detail (10 × 10 × 10 nm^3 vs. the current 50 × 10 × 10 nm^3, for our setup). Since the current work's main goal was to explain the principle of an external thinning potential, we here chose to exaggerate the size of the normal and thin zones for the sake of clarity.

We showed that induced thin zones bear lipid packing defects (**Figures 1D,E**), comparable to, e.g., membrane regions with a positive curvature. Because of the hydrophobic nature of the thin

zone (it is under a net surface tension), it attracts surfactants that are better able to shield the hydrophobic tail region from the water interface. These surfactants generally form membranes with an inherently weaker oil-water surface tension, as evident from their lateral pressure profiles (**Figure S1B**). As a proof of principle, we illustrated that this way of inducing lipid packing defects can strongly affect the sorting of four different biorelevant lipids (**Figures 2B,C**). We observed that POPE and cholesterol partitioned *away* from the thin zone of the membrane. With respect to POPC, POPE has a headgroup ($N(CH_3)_3$ vs. NH_3) that can form inter-molecular hydrogen bonds, thus resulting in stronger homogeneous attractions. This increased homogeneous headgroup attraction is implicitly modeled by the MARTINI model (Marrink et al., 2007) and we indeed observed an increase in POPE headgroup self-interaction upon thinning (**Figure S4**). Intuitively, POPE sorts away from the thin zone since increased spacing between lipid headgroups is less favorable. It is noteworthy that stronger homogeneous headgroup attractions also increase the surface hydrophobicity of the membrane because this decreases (competitive) heterogeneous interactions with water. As a consequence, PE headgroups have a reduced ability to compensate for the energetic cost associated with the oil-water interface (**Figure S1B**). This effective increase in surface hydrophobicity simultaneously dictates the molecules' effective shape via the first moment of the pressure profile, which translates into a more negative spontaneous curvature within membrane elasticity models. In line with this shape argument, POPE sorts away from the thin zone where lipid packing defects mimic a positively curved membrane.

Although cholesterol behaved very similarly to POPE in our simulations, additional underlying driving forces are present. Since cholesterol both thickens a POPC membrane and increases its elastic modulus (the membrane becomes "stiffer") (Daily et al., 2014), diffusing away from the thin zone reduces the equilibrium work required for thinning. In contrast, PE headgroups in fact significantly "soften" lipid membranes within this model, as evident by an increase in bending modulus (Bubnis et al., 2016). Yet, partitioning within the thin zone is unfavorable because PE simultaneously increases surface hydrophobicity.

Conversely, but according to the same principles, LysoPC and PLiPC were *enriched* in the thin zone. For LysoPC, this result is effectively explained by the spontaneous curvature argument (lysolipids decrease surface hydrophobicity because of their small hydrophobic tail volume) and the notion that lysolipids both thin and soften the membrane. The enrichment of the thin zone with PLiPC lipids largely arises from the fact that their highly unsaturated tails are effectively less hydrophobic because alkenes are slightly more hydrophilic than alkanet. As a consequence, PLiPC reduces the hydrophobicity of the membrane surface, as evident by the lateral pressure profile (see **Figure S1B**). Additionally, PLiPC favors more disordered phases (Pinot et al., 2014) because of its decreased tendency to shield the (less) hydrophobic tails from the water phase. Since membrane thinning reduces lipid order, it is not surprising that PLiPC concentration are elevated in the thin zone.

Qualitatively, our results are consistent with curvature-induced lipid sorting toward regions of a positive membrane curvature (Risselada and Marrink, 2009; Boyd et al., 2017; Baoukina et al., 2018; Elías-Wolff et al., 2018, 2019). For symmetry reasons, sorting in simulations based on membrane curvature are based on a competition between both positive and negative curvature, which can make it hard to distinguish e.g., positive curvature depletion from negative curvature enrichment. Since our system only includes one of both conditions, it can help to deconvolute these effects. For example, PLiPC does not show a pronounced preference for the inner or outer leaflet in small 20 nm-sized lipid vesicles (Risselada and Marrink, 2009), yet we observed a strong sorting toward the thin membrane region. Furthermore, since externally pulled membrane tethers are likely under an additional tension, both curvature and tension driven sorting may occur simultaneously (Baoukina et al., 2018). In such a scenario, differences in the adopted composition between the two monolayers in a tether can alternatively be due to differences in relative stretch between the monolayers.

Beyond lipid sorting effects, we showed that inducing membrane thinning induces sorting of the "curvature" sensing ALPS motif (**Figures 3B,C**). Umbrella sampling of the ALPS peptide along the buffer zone of the squeezed membrane yielded a free energy difference of $\approx 10\ k_BT$ over a relative decrease in thickness of ≈ 1.1 nm. These obtained values are similar to the binding free energies that were experimentally determined for such peptides (He and Lazaridis, 2013). The slope of the free energy profile along the buffer zone equates to the attractive (or repulsive) force on the peptide toward the thin zone of the membrane. For ALPS, this attractive force was estimated to be about 11 pN–a substantial biomolecular force close to, for example, the force exerted by a neuronal SNARE complex (Gao et al., 2012). Such a force allows for direct, quantitative measuring of lipid packing sensing ability and could be exploited to validate, score, and rank the sensing ability of amphipathic molecules. Since the obtained free energy gradient, $\frac{dF(x)}{dx}$, is rather linear, it already suffices to restrict sampling to only a handful of points along the buffer zone, or obtain $\frac{dF(x)}{dx}$ even from a single simulation. Hence, $\frac{dF(x)}{dx}$ is simply the average force acting against the umbrella potential. This means that our protocol can serve as a very efficient way to both quantify and score protein sorting effects.

Taken together, we have shown that our thinning protocol is able to induce lipid and protein sorting in line with theory and previous simulations and experiments. Since the driving force (sensing lipid packing defects) for such thinning-induced sorting is the same as in, for example, membrane curvature and membrane junctions, our protocol can serve as a proxy for studying such phenomena *in silico*. Moreover, and for the first time, it allowed us to "measure" the attractive force acting on the ALPS sensor motif toward lipid packing defects. Finally, because of the protocol's efficient and tunable nature, it enables high-throughput scoring of lipid packing-induced sorting effects of virtually any amphipathic molecule.

DATA AVAILABILITY STATEMENT

The code used in this study can be found at https://github.com/nvanhilten/thinning_protocol.

AUTHOR CONTRIBUTIONS

NH and HR designed the experiments and implemented the thinning protocol code. NH performed all MD simulations and analyzed the data. KS contributed to the free energy calculations. NH and HR wrote the manuscript.

FUNDING

This work was funded by the NWO Vidi (the Netherlands), the DFG grant number RI2791/2-1 (Germany), and the SAW-Verfahren of the Leibniz Society (Germany). We thank the Dutch Research Organization NWO (Cartesius@Surfsara) and the HLRN Göttingen/Berlin for the provided computational resources.

ACKNOWLEDGMENTS

We thank Patrick F. J. Fuchs for sharing the atomistic MD-refined ALPS peptide structure with us. Jeroen Methorst is thanked for useful discussions and technical assistance.

SUPPLEMENTARY MATERIAL

The Supplementary Material for this article can be found online at: https://www.frontiersin.org/articles/10.3389/fphys.2020.00250/full#supplementary-material

REFERENCES

Abraham, M. J., Murtola, T., Schulz, R., Páll, S., Smith, J. C., Hess, B., et al. (2015). GROMACS: High performance molecular simulations through multi-level parallelism from laptops to supercomputers. *Soft. X* 1–2:19–25. doi: 10.1016/j.softx.2015.06.001

Antonny, B. (2011). Mechanisms of membrane curvature sensing. *Annu. Rev. Biochem*. 80, 101–123. doi: 10.1146/annurev-biochem-052809-155121

Baoukina, S., Ingolfsson, H. I., Marrink, S. J., and Tieleman, D. P. (2018). Curvature-induced sorting of lipids in plasma membrane tethers. *Adv. Theory Simul.* 1:1800034. doi: 10.1002/adts.201800034

Baumgart, T., Capraro, B. R., Zhu, C., and Das, S. L. (2011). Thermodynamics and mechanics of membrane curvature generation and sensing by proteins and lipids. *Annu. Rev. Phys. Chem*. 62, 483–506. doi: 10.1146/annurev.physchem.012809.103450

Belička, M., Weitzer, A., and Pabst, G. (2017). High-resolution structure of coexisting nanoscopic and microscopic lipid domains. *Soft Matter* 13, 1823–1833. doi: 10.1039/C6SM02727J

Berendsen, H. J. C., Postma, J. P. M., van Gunsteren, W. F., Di Nola, A., and Haak, J. R. (1984). Molecular dynamics with coupling to an external bath. *J. Chem. Phys*. 81, 3684–3690. doi: 10.1063/1.448118

Bhaskara, R. M., Grumati, P., Garcia-Pardo, J., Kalayil, S., Covarrubias-Pinto, A., Chen, W., et al. (2019). Curvature induction and membrane remodeling by FAM134B reticulon homology domain assist selective ER-phagy. *Nat. Commun*. 10:2370. doi: 10.1038/s41467-019-10345-3

Bhatia, V. K., Hatzakis, N. S., and Stamou, D. (2010). A unifying mechanism accounts for sensing of membrane curvature by BAR domains, amphipathic helices and membrane-anchored proteins. *Semin. Cell Dev. Biol*. 21, 381–390. doi: 10.1016/j.semcdb.2009.12.004

Bigay, J., Casella, J. F., Drin, G., Mesmin, B., and Antonny, B. (2005). ArfGAP1 responds to membrane curvature through the folding of a lipid packing sensor motif. *EMBO J*. 24, 2244–2253. doi: 10.1038/sj.emboj.7600714

Boyd, K. J., Alder, N. N., and May, E. R. (2017). Buckling under pressure: Curvature-based lipid segregation and stability modulation in cardiolipin-containing bilayers. *Langmuir* 33, 6937–6946. doi: 10.1021/acs.langmuir.7b01185

Bubnis, G., Risselada, H. J., and Grubmüller, H. (2016). Exploiting lipid permutation symmetry to compute membrane remodeling free energies. *Phys. Rev. Lett*. 117:188102. doi: 10.1103/PhysRevLett.117.188102

Bussi, G., Donadio, D., and Parrinello, M. (2007). Canonical sampling through velocity rescaling. *J. Chem. Phys*. 126:014101. doi: 10.1063/1.2408420

Callan-Jones, A., Sorre, B., and Bassereau, P. (2011). Curvature-driven lipid sorting in biomembranes. *Cold Spring Harb. Perspect. Biol*. 3:a004648. doi: 10.1101/cshperspect.a004648

Corradi, V., Mendez-Villuendas, E., Ingólfsson, H. I., Gu, R.-X., Siuda, I., Melo, M. N., et al. (2018). Lipid-protein interactions are unique fingerprints for membrane proteins. *ACS Cent. Sci*. 4, 709–717. doi: 10.1021/acscentsci.8b00143

Daily, M. D., Olsen, B. N., Schlesinger, P. H., Ory, D. S., and Baker, N. A. (2014). Improved coarse-grained modeling of cholesterol-containing lipid bilayers. *J. Chem. Theory Comput*. 10, 2137–2150. doi: 10.1021/ct401028g

Derganc, J. (2007). Curvature-driven lateral segregation of membrane constituents in Golgi cisternae. *Phys. Biol*. 4, 317–324. doi: 10.1088/1478-3975/4/4/008

Doucet, C. M., Esmery, N., de Saint-Jean, M., and Antonny, B. (2015). Membrane curvature sensing by amphipathic helices is modulated by the surrounding protein backbone. *PLoS ONE* 10:e0137965. doi: 10.1371/journal.pone.0137965

Drin, G., Casella, J. F., Gautier, R., Boehmer, T., Schwartz, T. U., and Antonny, B. (2007). A general amphipathic alpha-helical motif for sensing membrane curvature. *Nat. Struct. Mol. Biol*. 14, 138–146. doi: 10.1038/nsmb1194

Elias-Wolff, F., Lindén, M., Lyubartsev, A. P., and Brandt, E. G. (2018). Computing curvature sensitivity of biomolecules in membranes by simulated buckling. *J. Chem. Theory Comput*. 14, 1643–1655. doi: 10.1021/acs.jctc.7b00878

Elias-Wolff, F., Lindén, M., Lyubartsev, A. P., and Brandt, E. G. (2019). Curvature sensing by cardiolipin in simulated buckled membranes. *Soft Matter*. 15, 792–802. doi: 10.1039/C8SM02133C

Gao, Y., Zorman, S., Gundersen, G., Xi, Z., Ma, L., Sirinakis, G., et al. (2012). Single reconstituted neuronal SNARE complexes zipper in three distinct stages. *Science* 337, 1340–1343. doi: 10.1126/science.1224492

Garcia-Fandino, R., Pineiro, n., Trick, J. L., and Sansom, M. S. P. (2016). Lipid bilayer membrane perturbation by embedded nanopores: a simulation study. *ACS Nano* 10, 3693–3701. doi: 10.1021/acsnano.6b00202

Gautier, R., Bacle, A., Tiberti, M. L., Fuchs, P. F., Vanni, S., and Antonny, B. (2018). PackMem: A versatile tool to compute and visualize interfacial packing defects in lipid bilayers. *Biophys. J*. 115, 436–444. doi: 10.1016/j.bpj.2018.06.025

Gautier, R., Douguet, D., Antonny, B., and Drin, G. (2008). HELIQUEST: a web server to screen sequences with specific alpha-helical properties. *Bioinformatics* 24, 2101–2102. doi: 10.1093/bioinformatics/btn392

Gonzalez-Rubio, P., Gautierd, R., Etchebest, C., and Fuchs, P. F. J. (2011). Amphipathic-lipid-packing-sensor interactions with lipids assessed by atomistic molecular dynamics. *Biochim. Biophys. Acta, Biomembr*. 1808, 2119–2127. doi: 10.1016/j.bbamem.2011.05.006

Harayama, T., and Riezman, H. (2018). Understanding the diversity of membrane lipid composition. *Nat. Rev. Mol. Cell Biol*. 19:281. doi: 10.1038/nrm.2017.138

Hatzakis, N. S., Bhatia, V. K., Larsen, J., Madsen, K. L., Bolinger, P. Y., Kunding, A. H.,et al. (2009). How curved membranes recruit amphipathic helices and protein anchoring motifs. *Nat. Chem. Biol*. 5, 835–841. doi: 10.1038/nchembio.213

He, Y., and Lazaridis, T. (2013). Activity determinants of helical antimicrobial peptides: a large-scale computational study. *PLoS ONE* 8:e66440. doi: 10.1371/journal.pone.0066440

Hub, J. S., de Groot, B. L., and van der Spoel, D. (2010). g_wham-a free weighted histrogram analysis implementation including robust error and autocorrelation estimates. *J. Chem. Theory Comput*. 6, 3713–3720. doi: 10.1021/ct100494z

Jiang, H., and Powers, T. R. (2008). Curvature-driven lipid sorting in a membrane tubule. *Phys. Rev. Lett*. 101:018103. doi: 10.1103/PhysRevLett.101.018103

Kabsch, W., and Sander, C. (1983). Dictionary of protein secondary structure: Pattern recognition of hydrogen-bonded and geometrical features. *Biopolymers* 22, 2577–2637. doi: 10.1002/bip.360221211

Kumar, S., Rosenberg, J. M., Bouzida, D., Swendsen, R. H., and Kollman, P. A. (1992). THE weighted histogram analysis method for free-energy calculations on biomolecules. I. The method. *J. Comput. Chem*. 13, 1011–1021. doi: 10.1002/jcc.540130812

Lee, A. G. (2003). Lipid-protein interactions in biological membranes: a structural perspective. Biochim. Biophys. Acta, 1612, 1–40. doi: 10.1016/S0005-2736(03)00056-7

Marelli, G. (2012). Minimal models for lipid membranes: local modifications around fusion objects (Ph.D. thesis). Georg August University, Göttingen, Germany

Marrink, S. J., Risselada, H. J., Yefimov, S., Tieleman, D. P., and de Vries, A. H. (2007). The martini force field: Coarse grained model for biomolecular simulations. *J. Phys. Chem. B*. 111, 7812–7824. doi: 10.1021/jp071097f

McMahon, H. T., and Gallop, J. L. (2005). Membrane curvature and mechanisms of dynamic cell membrane remodelling. *Nature* 438, 590–596. doi: 10.1038/nature04396

Mesmin, B., Drin, G., Levi, S., Rawet, M., Cassel, D., Bigay, J., and Antonny, B. (2007). Two lipid-packing sensor motifs contribute to the sensitivity of ArfGAP1 to membrane curvature. *Biochemistry* 46, 1779–1790. doi: 10.1021/bi062288w

Milovanovic, D., Honigmann, A., Koike, S., Göttfert, F., Pähler, G., Junius, M., et al. (2015). Hydrophobic mismatch sorts SNARE proteins into distinct membrane domains. *Nat. Commun*. 6:6984. doi: 10.1038/ncomms6984

Monticelli, L., Kandasamy, S. K., Periole, X., Larson, R. G., Tieleman, D. P., and Marrink, S.-J. (2008). The MARTINI coarse-grained force field: extension to proteins. *J. Chem. Theory Comput*. 4, 819–834. doi: 10.1021/ct700324x

Nepal, B., Leveritt, J., and Lazaridis, T. (2018). Membrane curvature sensing by amphipathic helices: insights from implicit membrane modeling. *Biophys. J*. 114, 2128–2141. doi: 10.1016/j.bpj.2018.03.030

Nguyen, N., Shteyn, V., and Melia, T. J. (2017). Sensing membrane curvature in macroautophagy. *J. Mol. Biol*. 429, 457–472. doi: 10.1016/j.jmb.2017.01.006

Nickels, J. D., Cheng, X., Mostofian, B., Stanley, C., Lindner, B., Heberle, F. A., et al. (2015). Mechanical properties of nanoscopic lipid domains. *J. Am. Chem. Soc*. 137, 15772–15780. doi: 10.1021/jacs.5b08894

Ollila, O. H. S., Risselada, H. J., Louhivuori, M., Lindahl, E., Vattulainen, I., and Marrink, S. J. (2009). 3D pressure field in lipid membranes and membrane-protein complexes. *Phys. Rev. Lett*. 102:078101. doi: 10.1103/PhysRevLett.102.078101

Ouberai, M. M., Wang, J., Swann, M. J., Galvagnion, C., Guilliams, T., Dobson, C. M., et al. (2013). α-synuclein senses lipid packing defects and induces lateral expansion of lipids leading to membrane remodeling. *J. Biol. Chem*. 288, 20883–20895. doi: 10.1074/jbc.M113.478297

Park, S., and Im, W. (2018). Quantitative characterization of cholesterol partitioning between binary bilayers. *J. Chem. Theory Comput*. 14, 2829–2833. doi: 10.1021/acs.jctc.8b00140

Pinot, M., Vanni, S., Pagnotta, S., Lacas-Gervais, S., Payet, L.-A., Ferreira, T., et al. (2014). Polyunsaturated phospholipids facilitate membrane deformation and fission by endocytic proteins. *Science* 345, 693–697. doi: 10.1126/science.1255288

Risselada, H. J., and Marrink, S. J. (2009). Curvature effects on lipid packing and dynamics in liposomes revealed by coarse grained molecular dynamics simulations. *Phys. Chem. Chem. Phys*. 11, 2056–2067. doi: 10.1039/b818782g

Risselada, H. J., Smirnova, Y., and Grubmüller, H. (2014). Free energy landscape of rim-pore expansion in membrane fusion. *Biophys. J*. 107, 2287–2295. doi: 10.1016/j.bpj.2014.08.022

Schäfer, L. V., and Marrink, S. J. (2010). Partitioning of lipids at domain boundaries in model membranes. *Biophys. J*. 99, L91-L93. doi: 10.1016/j.bpj.2010.08.072

Singh, P., Mahata, P., Baumgart, T., and Das, S. L. (2012). Curvature sorting of proteins on a cylindrical lipid membrane tether connected to a reservoir. *Phys. Rev. E: Stat. Nonlinear Soft Matter Phys*. 85:051906. doi: 10.1103/PhysRevE.85.051906

Smirnova, Y. G., Risselada, H. J., and Müller, M. (2019). Thermodynamically reversible paths of the first fusion intermediate reveal an important role for membrane anchors of fusion proteins. *Proc. Natl Acad. Sci. U.S.A*. 116, 2571–2576. doi: 10.1073/pnas.1818200116

Sorre, B., Callan-Jones, A., Manneville, J. B., Nassoy, P., Joanny, J. F., Prost, J., et al. (2009). Curvature-driven lipid sorting needs proximity to a demixing point and is aided by proteins. *Proc. Natl. Acad. Sci. U.S.A*. 106, 5622–5626. doi: 10.1073/pnas.0811243106

Tian, A., and Baumgart, T. (2009). Sorting of lipids and proteins in membrane curvature gradients. *Biophys. J*. 96, 2676–2688. doi: 10.1016/j.bpj.2008.11.067

Tsai, H. H., Chang, C. M., and Lee, J. B. (2014). Multi-step formation of a hemifusion diaphragm for vesicle fusion revealed by all-atom molecular dynamics simulations. *Biochim. Biophys. Acta* 1838, 1529–1535. doi: 10.1016/j.bbamem.2014.01.018

Vanni, S., Hirose, H., Barelli, H., Antonny, B., and Gautier, R. (2014). A sub-nanometre view of how membrane curvature and composition modulate lipid packing and protein recruitment. *Nat. Commun*. 5:4916. doi: 10.1038/ncomms5916

Vanni, S., Vamparys, L., Gautier, R., Drin, G., Etchebest, C., Fuchs, P. F., et al. (2013). Amphipathic lipid packing sensor motifs: probing bilayer defects with hydrophobic residues. *Biophys. J*. 104, 575–584. doi: 10.1016/j.bpj.2012.11.3837

Wassenaar, T. A., Ingolfsson, H. I., Bockmann, R. A., Tieleman, D. P., and Marrink, S. J. (2015). Computational lipidomics with insane: a versatile tool for generating custom membranes for molecular simulations. *J. Chem. Theor. Comput*. 11, 2144–2155. doi: 10.1021/acs.jctc.5b00209

Wildermuth, K. D., Monje-Galvan, V., Warburton, L. M., and Klauda, J. B. (2019). Effect of membrane lipid packing on stable binding of the ALPS peptide. *J. Chem. Theory Comput*. 15, 1418–1429. doi: 10.1021/acs.jctc.8b00945

Woodward, X., Stimpson, E. E., and Kelly, C. V. (2018). Single-lipid tracking on nanoscale membrane buds: the effects of curvature on lipid diffusion and sorting. *Biochim. Biophys. Acta Biomembr*. 1860, 2064–2075. doi: 10.1016/j.bbamem.2018.05.009

Conflict of Interest: The authors declare that the research was conducted in the absence of any commercial or financial relationships that could be construed as a potential conflict of interest.

frontiers in Cell and Developmental Biology

REVIEW
published: 28 April 2020
doi: 10.3389/fcell.2020.00285

Membrane Compartmentalization and Scaffold Proteins in Leukocyte Migration

Guerric P. B. Samson[1] *and Daniel F. Legler*[1,2,3]*

[1] *Biotechnology Institute Thurgau at the University of Konstanz, Kreuzlingen, Switzerland,* [2] *Faculty of Biology, University of Konstanz, Konstanz, Germany,* [3] *Theodor Kocher Institute, University of Bern, Bern, Switzerland*

Leukocyte migration across vessels into and within peripheral and lymphoid tissues is essential for host defense against invading pathogens. Leukocytes are specialized in sensing a variety of guidance cues and to integrate environmental stimuli to navigate in a timely and spatially controlled manner. These extracellular signals must be transmitted across the leukocyte's plasma membrane in a way that intracellular signaling cascades enable directional cell movement. Therefore, the composition of the membrane in concert with proteins that influence the compartmentalization of the plasma membrane or contribute to delineate intracellular signaling molecules are key in controlling leukocyte navigation. This becomes evident by the fact that mislocalization of membrane proteins is known to deleteriously affect cellular functions that may cause diseases. In this review we summarize recent advances made in the understanding of how membrane cholesterol levels modulate chemokine receptor signaling and hence leukocyte trafficking. Moreover, we provide an overview on the role of membrane scaffold proteins, particularly tetraspanins, flotillins/reggies, and caveolins in controlling leukocyte migration both *in vitro* and *in vivo*.

Keywords: leukocyte migration, membrane compartmentalization, scaffold proteins, flotillin/reggie, tetraspanin, caveolin

OPEN ACCESS

Edited by:
Falk Nimmerjahn, University of Erlangen–Nuremberg, Germany

Reviewed by:
Ritva Tikkanen, University of Giessen, Germany
Katalin Szaszi, St. Michael's Hospital, Canada

***Correspondence:**
Daniel F. Legler
daniel.legler@bitg.ch

Specialty section:
This article was submitted to Cellular Biochemistry, a section of the journal Frontiers in Cell and Developmental Biology

Received: *23 January 2020*
Accepted: *02 April 2020*
Published: *28 April 2020*

Citation:
Samson GPB and Legler DF (2020) Membrane Compartmentalization and Scaffold Proteins in Leukocyte Migration. Front. Cell Dev. Biol. 8:285. doi: 10.3389/fcell.2020.00285

INTRODUCTION

Cell migration is essential for a number of physiological and pathophysiological processes, such as embryogenesis, organogenesis, tissue homeostasis, but also cancer malignancy. In host defense, guided cell locomotion and positioning critically contributes to wound healing and cellular immune responses. Leukocytes are professional migratory cells that are able to sense various guidance cues and to integrate external signals to navigate through different types of tissue and to cross blood and lymph vessels (Nourshargh et al., 2010). Important guidance cues are provided by the chemokine network. Locally produced chemokines can form gradients *in situ* that migrating cells can sense through cognate chemokine receptors (Hughes and Nibbs, 2018). Chemokine receptors belong to the class A of G-protein coupled receptors (GPCRs) and possess seven α-helical domains that span the plasma membrane and are connected by extracellular and intracellular loops (Legler and Thelen, 2018; Lämmermann and Kastenmüller, 2019). Chemokine binding to the receptor

induces conformational changes that markedly rearrange the positions of the transmembrane helices particularly at the cytoplasmic surface of the plasma membrane allowing G-protein coupling and signal transduction (Legler and Thelen, 2018; Weis and Kobilka, 2018). Chemokine receptors couple to heterotrimeric G-proteins of the G_i class and their activation promotes the exchange of GTP for GDP on the Gα-subunit resulting in its dissociation from the βγ-subunits (**Figure 1**). Notably, members of the small GTPase family transmit downstream signals and thereby link chemokine receptor activation to actin cytoskeleton rearrangements required for the induction of cell polarity and locomotion. Members of the Rho family GTPases, namely Rac1 (Benvenuti et al., 2004), RhoA (Pertz et al., 2006), and Cdc42 (Lämmermann et al., 2009), translocate to the plasma membrane upon activation (Collins, 2003). In general, Rac1 is known to control actin polymerization at the leading edge, while RhoA regulates myosin contraction at the rear of a migrating cell (Pertz et al., 2006; MacHacek et al., 2009).

As guided cell migration depends on extracellular signals that must be transmitted across the plasma membrane, it became obvious that the organization of the plasma membrane and membrane compartmentalization influence the cell's ability to sense extracellular cues and to migrate. One of the most prominent concept for membrane compartmentalization refers to as the "lipid raft" hypothesis first described in 1988 (Simons and Van Meers, 1988) proposing that specialized subcompartments or microdomains of the lipid bilayer of the membrane control different cellular functions such as receptor endocytosis and signaling (Simons and Ikonen, 1997). In the 1990s, different membrane residing scaffold protein families were discovered, that affect the composition of the membrane (**Figure 2**). Proteins of the tetraspanin family integrate into the membrane through four transmembrane domains, whereas the flotillin/reggie family represent small cytoplasmic proteins that are hooked to the membrane by means of fatty acid oxidation (Seigneuret et al., 2001; Ficht et al., 2019). Finally, proteins of the caveolin (cav) family penetrate from the cytoplasmic site into the membrane through a hairpin-like structure and are further anchored into the membrane through palmitoylation/myristoylation (Dietzen et al., 1995; **Figure 2**). Briefly, tetraspanins have the ability to interact with other members of their family or with partner proteins such as integrins, adhesion molecules or signaling receptors to form "tetraspanin enriched microdomains" or "TEMs" (Hemler, 2005). The flotillin/reggie family consists of two members, flotillin-1 (flot1), also known as reggie-2, and flotillin-2 (flot2)/reggie-1 (Bickel et al., 1997; Schulte et al., 1997). Flotillins are known to hetero-dimerize and to assemble into larger complexes to act as scaffold (Langhorst et al., 2007; Neumann-Giesen et al., 2007). For example, in T cells, flotillins were shown to pre-assembly in caps to stabilize the immunological synapse and to as scaffold for the T cell receptor (TCR) machinery (Slaughter et al., 2003; Langhorst et al., 2006; Compeer et al., 2018). Members of the cav family are best known for the formation of cave-like membrane structures termed caveolae, membrane invaginations involved in endocytosis and signaling (Lefkir et al., 2003; Collins et al., 2012; Sotgia et al., 2012; Wang et al., 2015). In this review, we summarize the current understanding how cholesterol modulates chemokine receptor signaling and how membrane scaffold proteins regulate leukocyte migration.

MEMBRANE MICRODOMAINS, LIPID RAFTS AND CHOLESTEROL

Amphiphilic phospholipids represent the major building block of lipid bilayers of vertebrate membranes. Phospholipids are composed of a hydrophilic phosphate head and two hydrophobic fatty acid tails, which vary in length and saturation and thereby account for the broad range of phospholipid species (Simons and Toomre, 2000). The fatty acyl groups of the phospholipids influence the membrane fluidity and hence the lateral mobility of membrane associated proteins (Krapf, 2018). In addition, cell membranes also contain the sterol cholesterol. Cholesterol molecules preferentially interact with saturated fatty acyl groups of phospholipids and thereby shift the membrane structure from a heterogeneous fluid membrane with high mobility to a more rigid and stiff membrane with lipid and protein patches (Legler et al., 2017). The original concept of "lipid raft" or "membrane microdomains" (Simons and Ikonen, 1997) has been further developed and refined. Although direct microscopic visualization of lipids rafts at millisecond rates still remains challenging (Klymchenko and Kreder, 2014; Sezgin et al., 2017; Kinoshita et al., 2018), recent new biophysical techniques confirmed the presence of such domains in cells and provided new insights in to the cell membrane heterogeneity (Sezgin et al., 2017). In addition, studies on crystal structures of proteins clearly revealed that cholesterol molecules can directly interact with membrane associated scaffold proteins. Notably, solving the crystal structure of the tetraspanin CD81 revealed a cholesterol-binding pocket at the cavity between the four transmembrane helices situated at the inner leaflet of the membrane (Zimmerman et al., 2016). Importantly, the presence of cholesterol within the cavity keeps CD81 in a closed conformation. Molecular dynamics analysis revealed that cholesterol dissociation from the binding pocked results in an open conformation of CD81 that facilitates a tetraspanin-dependent transport of CD19 to the cell surface (Zimmerman et al., 2016). These findings are in line with an earlier study showing that membrane cholesterol contributes to the organization of tetraspanin microdomains (Charrin et al., 2003). More generally, this property of cholesterol to modulate the mode of action of tetraspanins not only affects protein transport [e.g., CD81:CD19 (Zimmerman et al., 2016); CD9:MHCII (Silvie et al., 2003; Rocha-Perugini et al., 2009; Banse et al., 2018)], but also malaria or cytomegalovirus infection [through CD81 (Silvie et al., 2003; Rocha-Perugini et al., 2009; Banse et al., 2018)], and cell migration as described later. Similarly, early electron microscopy studies identified an important role of cholesterol for the assembly of caveolae (Rothberg et al., 1992) whose major constituent, caveolin-1, contributes to dendritic cell migration as discussed in a subsequent paragraph.

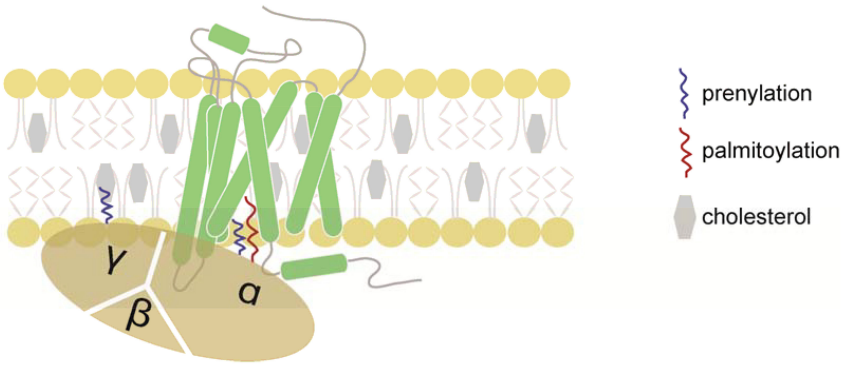

FIGURE 1 | Schematic representation of a chemokine receptor and its associated heterotrimeric G-protein. Chemokine receptors belong to the GPCR family and possess seven-transmembrane domains. Chemokines initiate chemokine receptor activation by binding to the N-terminus and extracellular loops of the receptor. Once the chemokine is tethered to the receptor, the N-terminus enters the binding pocket where it interacts with the transmembrane domains of the chemokine receptor. The presence of cholesterol is critical for the stability of the chemokine receptor. Upon ligand binding, the receptor promotes the exchange of GDP for GTP on the Gα-subunit, resulting in the dissociation of the Gα- from the Gβγ-subunits and downstream signaling. The Gα- and Gγ-subunits are post-transcriptionally lipidated facilitating their association with the plasma membrane.

ROLE OF CHOLESTEROL IN CHEMOKINE RECEPTOR CRYSTALLIZATION, SIGNALING AND LEUKOCYTE MIGRATION

Chemokine receptor activation is initiated by the binding of the chemokine to the extracellular N-terminus and extracellular loops of the receptors (**Figure 1**). Once the chemokine is tethered to its cognate receptor, its unstructured N-terminus is capable to enter the binding pocket where it interacts with the transmembrane bundles of the receptor. This leads to the rearrangement of the seven transmembrane helices of the receptor resulting in profound conformational changes across the plasma membrane (Kufareva et al., 2017; Legler and Thelen, 2018). Attempts to crystalize chemokine receptors, and GPCRs in general, revealed that addition of cholesterol is necessary to stabilize the receptor during the solubilization, purification, and crystallization processes (Wu et al., 2010; Qin et al., 2015). Evidence for a direct physical interaction between cholesterol and a GPCR has first been noted in the crystal structure of the β_2-adrenergic receptor, where two cholesterol molecules were found to directly interact with a receptor monomer (Cherezov et al., 2007). Although chemokine receptors do not possess a consensus cholesterol binding motifs as many other GPCRs (Hanson et al., 2008; Thelen and Legler, 2018), chemokine receptors (i.e., CXCR4, CCR2, CCR5, and CCR7) had to be reconstituted into lipidic cubic phases containing at least 10% cholesterol prior to successful crystallization (Wu et al., 2010; Qin et al., 2015; Zheng et al., 2016, 2017; Jaeger et al., 2019). Importantly, cholesterol inclusion was shown to increase chemokine binding to solubilized CXCR4 (Babcock et al., 2003; Palmesino et al., 2016). By contrast, cholesterol depletion in cells reversibly inhibited ligand binding to the chemokine receptor CCR5 and resulted in attenuated signal transduction and cell migration (Mañes et al., 2000; Signoret et al., 2005). A regulatory role for cholesterol in chemokine receptor function derive from the discovery that CCR5 and CXCR4 serve as co-receptors for human immunodeficiency virus (HIV) infection and that cholesterol is essential for the budding and fusion of the virus envelope with the host plasma membrane (Hug et al., 2000; Simons and Ehehalt, 2002). In fact, the HIV glycoprotein gp120 binds to CXCR4 and CCR5 in cholesterol-enriched domains of the host cell (Mañes et al., 2000; Ono and Freed, 2001). The notion that changes in cholesterol levels in dendritic cells regulate their migratory capacity (Hauser et al., 2016) has gained significant attention. In fact, exposing dendritic cells to danger signals led to a marked downregulation of key enzymes involved in cholesterol biosynthesis, while proteins controlling cholesterol efflux were upregulated. Simultaneously, theses danger signals were shown to provoke oligomerization of the chemokine receptor CCR7 resulting in a pro-migratory dendritic cell phenotype (Hauser et al., 2016). Moderately modulating cholesterol levels using cholesterol lowering drugs not only affected CCR7 oligomerization, but also chemokine-driven migration (Hauser et al., 2016). By contrast, a complete depletion of cellular cholesterol interfered with the stability of the receptor manifested by impaired chemokine binding to the receptor and hampered chemotactic cell behavior (Nguyen and Taub, 2002). Molecularly, cholesterol-dependent CCR7 oligomerization enabled the activation of an additional oligomer-dependent Src kinase signal transduction pathway aside the classical G-protein-dependent signaling pathway. This conjoint signaling is possible as in a CCR7 dimer (or tetramer) scenario, one (or two) receptor-mer(s) are able to couple to the heterotrimeric G-protein, while the other (two) receptor-mer(s) interact with the Src kinase. Notably, Src is able to pre-associate with oligomeric CCR7, which upon chemokine activation, phosphorylates the receptor and creates a docking site for SH2-domain-bearing signaling molecules (Hauser et al., 2016). It is interesting to note that the α- and γ-subunits of heterotrimeric G-proteins, as well as Src, undergo lipid

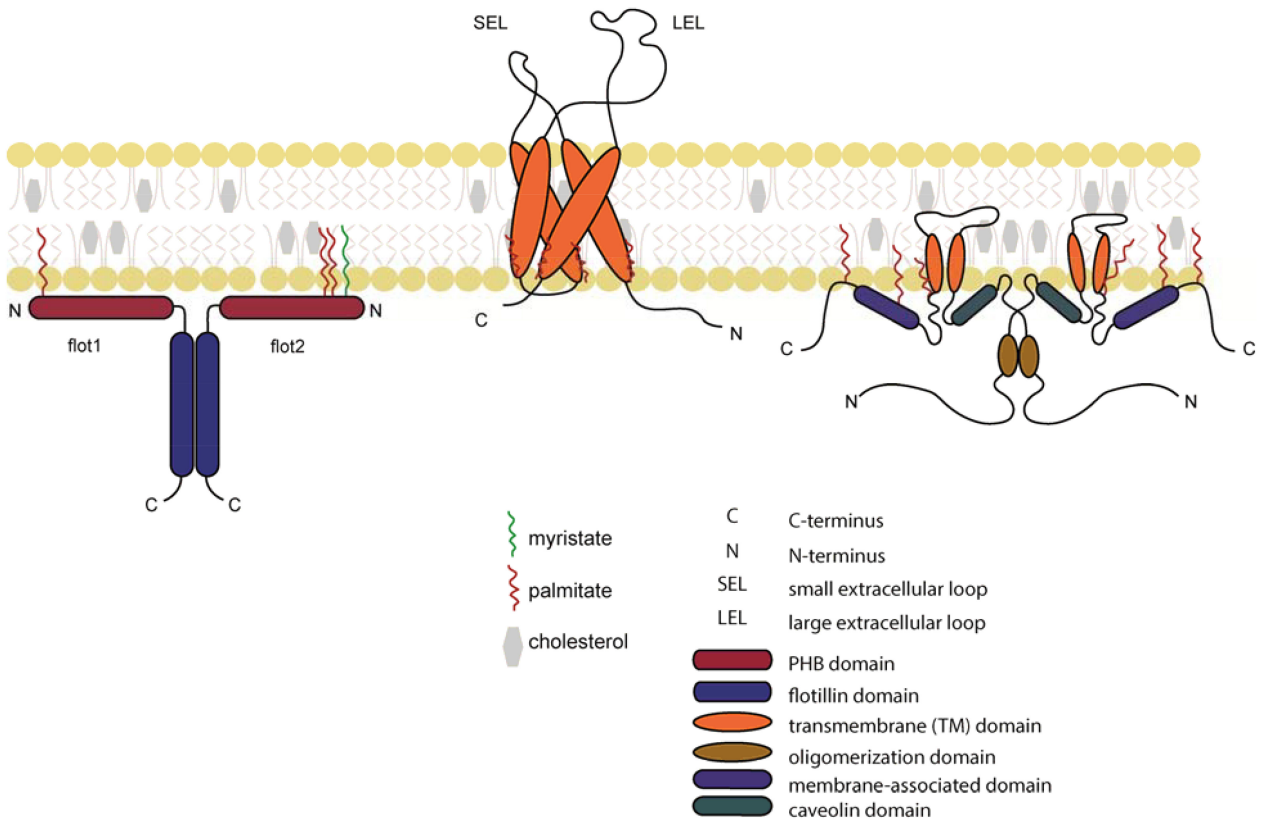

FIGURE 2 | Schematic representation of flotillin, tetraspanin, and caveolin in the lipid bilayer. Flotillins are associated at the cytosolic leaflet of the plasma membrane through its N-terminal PHB domain. Membrane association is further assured through myristoylation (green) and palmitoylation (red). Flotillins form hetero-mers through specialized intracellular flotillin domains. Tetraspanins are composed of four transmembrane α-helices and two extracellular domains: the SEL (small extracellular loop) and the LEL (large extracellular loop). Tetraspanins are palmitoylated at a conserved CXXC motif in their transmembrane domains. Caveolins form hairpin loops that are inserted into the plasma membrane. Both N- and C-termini face the cytoplasmic side of the membrane.

modification facilitating their association with cholesterol-rich membrane domains.

Interestingly, CXCR4 was found to form monomers, dimers and nanoclusters on T cells that own distinct lateral mobility characteristics (Martínez-Muñoz et al., 2018). Ligand binding was further shown to modulate CXCR4 dynamics leading to enhanced nanoclustering of the receptor that is controlled by the cortical actin, which in turn correlated with the strength of CXCR4 signaling. Consequently, cells expressing CXCR4 mutants with deficits in nanocluster formation showed impaired chemokine-driven signaling and leukocyte migration, both *in vitro* and *in vivo* (Martínez-Muñoz et al., 2018). Although not formally shown in this study, it is tempting to speculate that cholesterol molecules, by modulating the stiffness of membranes, are involved in controlling the lateral mobility of CXCR4 and the formation of nanoclusters.

Beside the above described role of plasma membrane cholesterol, altered extracellular cholesterol levels are observed under certain pathological conditions. High cholesterol levels in the blood (hypercholesterolemia) is a common risk factor for coronary heart diseases (Tall and Yvan-Charvet, 2015). Deposition of cholesterol in the subendothelial layer is effectively narrowing and hardening arteries leading to atherosclerosis. Importantly, cholesterol accumulation in atherosclerotic plaques gives rise to the formation of cholesterol crystals, which induce complement-dependent inflammasome activation (Samstad et al., 2014) and production of inflammatory chemokines (CCL2, CCL3, and CCL5), which results in leukocyte recruitment and a CCR2-driven chronic inflammatory disorder (Boring et al., 1998). Moreover, in a mouse model for atherosclerosis, namely in apolipoprotein E (ApoE)-deficient mice, cholesterol deposits and local dermal inflammation were observed to coincide with skin resident dendritic cells possessing a systemically reduced migratory behavior (Angeli et al., 2004). As dendritic cell emigration from the skin relies on CCR7-guided migration, it is tempting to speculate that extracellular cholesterol is

TABLE 1 | Expression level of scaffold proteins in various leukocyte subsets.

Scaffold protein		Leukocyte subset	Expression level*	References
flotillin	flot1	neutrophils	+++	Ludwig et al., 2010
		monocytes	++	Ludwig et al., 2010
		T cells	++	Ficht et al., 2019
		dendritic cells	++	–
	flot2	neutrophils	+++	–
		monocytes	++	–
		T cells	++	–
		dendritic cells	++	–
caveolin	cav1	dendritic cells	++	Oyarce et al., 2017
tetraspanin	CD9	monocytes	+++	Schenk et al., 2013
		dendritic cells	+++	Rocha-Perugini et al., 2017
	CD81	monocytes	++	Dijkstra et al., 2008
		dendritic cells	++	Mantegazza et al., 2004
	CD63	dendritic cells	++	Mantegazza et al., 2004
	CD82	dendritic cells	+++	Mantegazza et al., 2004
	CD37	dendritic cells	+++	Jones et al., 2016
				Gartlan et al., 2013
	CD151	T cells	++	Zelman-Toister et al., 2016

**Expression level based on ImmGen Microarray database (++>80; +++>800)*

taken up by dendritic cells and integrated into the plasma membrane where it interferes with CCR7 oligomerization and signaling. Pre-clinical studies using statins, which inhibit the HMG-CoA reductase to block cholesterol *de novo* synthesis, in ApoE-deficient mice revealed a marked regression of atherosclerosis through a CCR7-dependent emigration of foam cells from plaques (Feig et al., 2011) supporting this hypothesis.

ROLE OF FLOTILLINS IN LEUKOCYTE MIGRATION

The ubiquitously conserved membrane organizing proteins flotillin-1 (flot1), also known as reggie-2, and flotillin-2 (flot2)/reggie-1 have been reported as important regulators of leukocyte activities (Giri et al., 2007; Langhorst et al., 2007; Otto and Nichols, 2011; Guillaume et al., 2013; Bodin et al., 2014). The reggie proteins were originally described to be upregulated on goldfish retinal ganglion cells after nerve injury and subsequent axon regeneration (Schulte et al., 1997). Simultaneously, flotillins were identified as lipid raft proteins of detergent-resistant membrane fractions of marine lung tissue that float in sucrose density gradients (Bickel et al., 1997). Flotillins are also expressed at different levels in many leukocyte subsets, including neutrophils, monocytes, T cells and dendritic cells (**Table 1**). Both flot1 and flot2 possess N-terminal fatty acid modifications close to the prohibitin homology (PHB) domain (**Figure 2**) that allow their association with the plasma membrane and a direct interaction with F-actin (Langhorst et al., 2007; Guillaume et al., 2013; Bodin et al., 2014). Particularly, flotillins pile in actin-driven mobile membranes, such as lamellipodia and ruffles (Guillaume et al., 2013). The C-terminal part of flotillins contain an α-helical region required for their hetero-oligomerization, stabilization and lipid rafts association (Langhorst et al., 2007; Guillaume et al., 2013; Bodin et al., 2014). As flotillins are involved in cell-cell contacts (Guillaume et al., 2013; Bodin et al., 2014) and are able to interact with the actomyosin cytoskeleton of leukocytes (Ludwig et al., 2010), flotillins are predestinated to contribute to cell adhesion and migration processes. In neutrophils, both flotillins were found to interact with the adhesion molecule P-selectin glycoprotein ligand 1 (PSGL-1; Rossy et al., 2009). Upon chemokine stimulation, neutrophils polarized and flotillins together with other lipid raft associated signaling molecules (i.e., CD43 and ezrin/radixin/moesin proteins) accumulated at the cell's uropod. Notably, the redistribution of flotillins preceded the one of CD43 and the ezrin/radixin/moesin proteins and required the integrity of the actin cytoskeleton, but not actin-myosin contraction (Rossy et al., 2009), suggesting that flotillins actively participate in neutrophil polarization. Spurred by these observations, Ludwig and colleagues found that flot1-deficient neutrophils and monocytes failed to efficiently migrate to inflammatory sites *in vivo* (Ludwig et al., 2010). *Ex vivo* analysis revealed that uropod formation and myosin IIa activity are compromised in flot1-deficient neutrophils (Ludwig et al., 2010).

In T cells, flotillins also accumulate at the uropod upon exposure to chemotactic signals. Moreover, flotillins in these cells were shown to bind to actin and to regulate the actin cytoskeleton (Langhorst et al., 2007; Neumann-Giesen et al., 2007), suggesting that flotillins are required for optimal T cell migration. Recently, Ficht and colleagues demonstrated that migrating $CD8^+$ T cells retrieved from flot1-deficient mice indeed displayed significant altered shape changes and motility *in vitro* and *in vivo* (Ficht et al., 2019). Surprisingly, $CD8^+$ T cell homing to lymphoid organs was comparable in wild-type and flot1-deficient mice (Ficht et al., 2019).

BOX 1 | Role of tetraspanins in antigen presentation. Orchestrated leukocyte migration is essential to launch innate and adaptive immune responses. Homing of dendritic cells to draining lymph nodes and the presentation of peripherally acquired antigens derived from pathogens to T cells conjointly dictate the quality of an adaptive immune response. Importantly, T cells migrate within lymph nodes in search for cognate antigens presented by dendritic cells. Hence the role of tetraspanins in leukocyte migration must also be discussed in the light of antigen presentation by major histocompatibility complex (MHC) molecules. Notably, many tetraspanins expressed by dendritic cells not only influence their ability to migrate but also influence antigen presentation. In fact, CD9, CD53, CD81, CD151, and CD37 were shown to associate with MHCII molecules on the cell surface of dendritic cells to augment antigen presentation (Angelisová et al., 1994; Szöllósi et al., 1996; Engering and Pieters, 2001; Saiz et al., 2018). Other members of the tetraspanin family, namely, CD63 and CD82, regulate antigen processing, MHCII biosynthesis and/or transport to the cell surface (Hammond et al., 1998; Mantegazza et al., 2004; Untemaehrer et al., 2007; Saiz et al., 2018). Several members of the tetraspanin family (CD37, CD53, CD63, CD81, and CD82) are expressed by human antigen presenting cells (Escola et al., 1998; Hammond et al., 1998; Van Den Hoorn et al., 2012) and have therefore been proposed as potential target candidates for treating inflammation and immune-mediated chronic diseases (Jin et al., 2018). More information on the role of tetraspanins in antigen presentation can be found in a recent review by Saiz et al. (2018).

BOX 2 | Role of scaffold proteins and cancer. Cancer progression and metastasis formation are clearly linked to migration. Although not discussed in this review, it is important to note that the expression of the three families of scaffold proteins discussed in this review are implicated in cancer. Enhanced expression of flot2 was detected in samples of breast cancer and mice lacking flot2 expression showed a significantly reduced tumorigenicity and metastatic capability (Berger et al., 2013). This finding is in line with other studies that proposed the presence of flotillins as a marker for poor prognosis in breast cancer (Banning et al., 2014; Ou et al., 2017), melanoma (Liu et al., 2015), and gastric cancer (Zhu et al., 2013). Similarly, high expression of the tetraspanin CD151 has been proposed as a maker for poor prognosis in a number of metastatic tumors (Franco et al., 2010; Voss et al., 2011; Deng et al., 2012; Kwon et al., 2012; Lee et al., 2013; Li et al., 2013; Sachs et al., 2014; Yu et al., 2018; Jiang et al., 2019). The role of CD9 in cancer remains controversial and seems to vary among different cancer types. Despite promising results obtained in pre-clinical mouse models (Beckwith et al., 2015), CD37 is the only targeted tetraspanin that has moved to clinical studies (de Winde et al., 2017). CD37 is highly expressed in malignant B cells, but not on solid tumors, which makes it suitable for immunotherapy (de Winde et al., 2017). Reduced or absent expression of cav-1 strongly correlated with a poor prognosis in cancer patients. This was attributed to altered signaling in tumor cells and changes in the metabolic tumor environment as reviewed elsewhere (Martinez-Outschoorn et al., 2015).

In conclusion, flot1 emerges to play a critical role in myeloid cell migration by facilitating cell polarization, whereas in $CD8^+$ T cell migration flot1 plays an unexpectedly minor role. The contribution of flot2, i.e., using flot2-deficient mice, in leukocyte migration has not been studied yet. Further studies are hence mandatory to decipher the precise role of the two flotillin proteins in the migratory behavior of different leukocyte subsets.

ROLE OF CAVEOLIN-1 IN DENDRITIC CELL MIGRATION

The cav family constitutes of three isoforms, namely cav-1, cav-2, and cav-3, of which cav-1 is best characterized. The two splicing variants of cav-1, cav-1α, and cav-1β (Okamoto et al., 1998), not only localizes at the plasma membrane, but also at endomembranes, such as the ER, the Golgi, endosomes, and mitochondria, as well as at lipid droplets (Parton and Howes, 2010). Cav-1 is constituted of an N-terminal domain, followed by a scaffold domain, an integral membrane domain and a C-terminal domain (Root et al., 2015). The integral membrane domain includes two α-helices, which are connected by a linker region forming a U-shaped conformation that penetrates deep into the lipid bilayer of the membrane (Rui et al., 2014). Major post-translational modifications, including phosphorylations at the N-terminal domain (on tyrosine14 and serine80) and palmitoylations on three cysteine residues located at the C-terminal domain (Krishna and Sengupta, 2019), not only anchor cav-1 in the membrane but also facilitates cav oligomerization and cholesterol transport (Monier et al., 1996; Okamoto et al., 1998). Although cav proteins are predominately expressed in epithelial cells, endothelial cells, fibroblasts, and adipocytes, they are also present in leukocytes (Harris et al., 2002; Tomassian et al., 2011; **Table 1**). Importantly, cav-1 was reported to be upregulated in dendritic cells upon exposure to pathogen-derived danger signals (Oyarce et al., 2017). Pathogen encountering also provokes the induction of CCR7 and subsequent migration of dendritic cells to the draining lymph where the dendritic cells present pathogen-derived antigens to T cells to launch an adaptive immune response (Hauser and Legler, 2016). Notably, cav-1-deficient dendritic cells migrate significantly less towards the CCR7 chemokine ligand CCL21 compared to cav-1 proficient cells (Oyarce et al., 2017). Interestingly, the intrinsic random cell motility was not affected in dendritic cells lacking cav-1 (Oyarce et al., 2017), suggesting that cav-1 contributes to directional cell locomotion. Mechanistically, danger signal challenged dendritic cells retrieved from wild-type mice possessed significantly more actin-rich protrusions and filopodia than cav-1-deficient cells. In addition, CCR7-driven activation of the GTPases Rac1, known to promote actin protrusions, was impaired in dendritic cells lacking cav-1 (Oyarce et al., 2017). Collectively, this study suggests that cav-1 control chemokine-mediated Rac1 activation, cytoskeleton rearrangement and migration of dendritic cells *in vitro* and *in vivo*.

ROLE OF TETRASPANINS IN LEUKOCYTE MIGRATION

The family of tetraspanins, also known as the transmembrane 4 superfamily (TM4SF), comprises 34 members in mammals that are highly conserved among species (Adell et al., 2004; Huang et al., 2005). Tetraspanins are composed of four transmembrane domains, a small and large extracellular loop (termed SEL and LEL, respectively), and two intracellular tail domains (Seigneuret et al., 2001; Levy and Shoham, 2005; **Figure 2**). The LEL domain accounts for most interactions with environmental stimuli, while the cytoplasmic regions are linked to cytoskeletal and signaling molecules. The four transmembrane domains are quite flexible and facilitates the formation of the so-called tetraspanin webs or tetraspanin-enriched microdomains (TEMs) by neighboring

tetraspanins (Kitadokoro et al., 2001; Hemler, 2005; Levy and Shoham, 2005; Seigneuret, 2006). Generally, tetraspanin webs act as important signaling platforms that control signaling, cell invasion, cell–cell fusion, cell adhesion, antigen presentation (**Box 1**), as well as cell migration.

Members of the tetraspanin family relevant for leukocyte migration, including information on the expression level, are listed in **Table 1**. In T cells, the tetraspanin CD151 was shown to form complexes with integrins (VLA-4 and LFA-1), and its activation was found to augment chemokine-mediated actin polymerization and migration *in vitro* (Zelman-Toister et al., 2016). Monocytes express the tetraspanins CD9 and CD81, and their cross-linking by specific antibodies was shown to significantly improve their ability to migrate across endothelial monolayers *in vitro* (Dijkstra et al., 2008; Schenk et al., 2013). Immature dendritic cells were shown to express the tetraspanins CD9, CD63, CD81, CD82, and CD151, of which CD9 and CD81 are mostly expressed at the cell surface, whereas CD63, CD82, and CD151 also localize in intracellular organelles (Mantegazza et al., 2004). Antibody-mediated cross-linking of CD9, CD63, CD81, and CD82 substantially enhanced immature dendritic cell migration *in vitro* towards the inflammatory chemokines CCL3 and CCL15, while cross-linking CD151 showed no effect (Mantegazza et al., 2004). Interestingly, cross-linking CD81 on mature, danger signal challenged dendritic cells inhibited their *in vitro* migration abilities towards the lymph-node homing chemokine CCL21 (Nattermann et al., 2006). Using gene-targeted mice revealed that CD9-deficient dendritic cells migrated readily towards CCL21 *in vitro* and migrated from the skin to inguinal lymph nodes *in vivo* (Rocha-Perugini et al., 2017). Collectively, these studies provide evidence that the tetraspanin CD9 contributes to, but is dispensable for dendritic cell migration. By contrast, migration of dendritic cells from the skin to draining lymph nodes in a contact sensitization model (FITC skin painting) was impaired in mice lacking CD37 (Gartlan et al., 2013), while mice lacking CD82 display the opposite phenotype (Jones et al., 2016). Both CD37 and CD82-deficient dendritic cells lack cellular projections. Nevertheless, $CD37^{-/-}$ dendritic cells poorly spread under low shear flow conditions on fibronectin, while $CD82^{-/-}$ dendritic cells showed increased cell spreading (Jones et al., 2016). Interestingly, immature dendritic cells, defined as $CD37^{hi}CD82^{lo}$ (as found in the skin), are highly motile cells owing a limited ability to activate naive T cells, while matured dendritic cells, defined as $CD37^{lo}CD82^{hi}$ (which have been exposed to pathogens and homed to lymph nodes), are less motile but show a well-orchestrated antigen presentation machinery to efficiently activate naive T cells (Jones et al., 2016). These observations strengthen the notion that leukocyte migration, cell–cell interaction and antigen presentation are interconnected processes than conjointly regulate immunity (see **Box 1**).

Mechanistic insights into how tetraspanins regulate cell migration are sparse. However, dendritic cells and neutrophils lacking CD37 have deficits in actin polymerization, cell spreading and polarization, which can partially be attributed to deregulated Rac1 activation and accelerated β_2-integrin internalization, which conjointly result in impaired cell adhesion (Jones et al., 2016). Generally speaking, the family of tetraspanins play versatile roles in modulating various leukocyte functions, including migration. More to that, a single member of the tetraspanin family fulfills distinct functions that depend on subcellular localization, the differentiation stage of the cell, as well as on the environmental context the cell is navigating through.

CONCLUSION AND OUTLOOK

Accumulated evidence underpins the critical role of cellular cholesterol in regulating chemokine receptor signaling and functions. Particularly, the presence of cholesterol is essential for chemokine receptor stability, ligand binding, and hence receptor function. Moreover, recent advances indicate that pathogen-derived danger signals modulate cholesterol levels in dendritic cells, which in turn affects their migratory capacities. Similarly chemokine receptor nanocluster, which is presumably regulated by cholesterol, emerges to control the signaling strength and consequently lymphocyte migration. The three membrane scaffold protein families have in common that they contribute to the formation, organization and maintenance of specialized membrane compartments. Flotillins redistribute in migrating leukocytes. Notably, while chemokine-driven cell polarization and spatio-temporal redistribution of flotillins are observed in myeloid cells and lymphocytes, flotillins are fundamentally required for directional myeloid cell migration, but seem to be dispensable for T cell migration *in vivo*. This suggests that different leukocyte subsets possess alternative adaptation modes for efficient cell migration. Caveolin-1 controls chemokine-driven Rac1 activation to promote cytoskeleton rearrangements and migration of dendritic cells *in vitro* and *in vivo*. Several tetraspanins, CD37 and CD82 in particular, play a role in regulating leukocyte migration although the molecular mechanism(s) are far from being fully understood. Further studies are required for a more comprehensive understanding of how membrane compartmentalization and membrane scaffold proteins control cell migration in general. This becomes evident by the fact that these scaffold proteins also affect cancer cell migration and metastasis formation as briefly summarized in **Box 2**. In general, new knowledge will be key to understand how membrane compartments in concert with membrane-associated or – spanning proteins orchestrated cell migration in health and disease.

AUTHOR CONTRIBUTIONS

GS prepared the figures. Both authors wrote the manuscript.

FUNDING

This work is supported by the Swiss National Science Foundation (grant number 189144), the Thurgauische Stiftung für Wissenschaft und Forschung, and the State Secretariat for Education, Research and Innovation (all to DL).

REFERENCES

Adell, T., Gamulin, V., Peroviæ-Ottstadt, S., Wiens, M., Korzhev, M., Müller, I. M., et al. (2004). Evolution of metazoan cell junction proteins: the scaffold protein MAGI and the transmembrane receptor tetraspanin in the demosponge *Suberites domuncula*. *J. Mol. Evol.* 59, 41–50. doi: 10.1007/s00239-004-2602-2

Angeli, V., Llodrá, J., Rong, J. X., Satoh, K., Ishii, S., Shimizu, T., et al. (2004). Dyslipidemia associated with atherosclerotic disease systemically alters dendritic cell mobilization. *Immunity* 21, 561–574. doi: 10.1016/j.immuni.2004.09.003

Angelisová, P., Hilgert, I., and Horejsí, V. (1994). Association of four antigens of the tetraspans family (CD37, CD53, TAPA-1, and R2/C33) with MHC class II glycoproteins. *Immunogenetics* 39, 249–256. doi: 10.1007/BF00188787

Babcock, G. J., Farzan, M., and Sodroski, J. (2003). Ligand-independent dimerization of CXCR4, a principal HIV-1 coreceptor. *J. Biol. Chem.* 278, 3378–3385. doi: 10.1074/jbc.M210140200

Banning, A., Kurrle, N., Meister, M., and Tikkanen, R. (2014). Flotillins in receptor tyrosine kinase signaling and cancer. *Cells* 3, 129–149. doi: 10.3390/cells3010129

Banse, P., Moeller, R., Bruening, J., Lasswitz, L., Kahl, S., Khan, A. G., et al. (2018). CD81 receptor regions outside the large extracellular loop determine hepatitis C virus entry into hepatoma cells. *Viruses* 10:E207. doi: 10.3390/v10040207

Beckwith, K. A., Byrd, J. C., and Muthusamy, N. (2015). Tetraspanins as therapeutic targets in hematological malignancy: a concise review. *Front. Physiol.* 6:91. doi: 10.3389/fphys.2015.00091

Benvenuti, F., Hugues, S., Walmsley, M., Ruf, S., Fetler, L., Popoff, M., et al. (2004). Requirement of Rac1 and Rac2 expression by mature dendritic cells for T cell priming. *Science* 305, 1150–1153. doi: 10.1126/science.1099159

Berger, T., Ueda, T., Arpaia, E., Chio, I. I. C., Shirdel, E. A., Jurisica, I., et al. (2013). Flotillin-2 deficiency leads to reduced lung metastases in a mouse breast cancer model. *Oncogene* 32, 4989–4994. doi: 10.1038/onc.2012.499

Bickel, P. E., Scherer, P. E., Schnitzer, J. E., Oh, P., Lisanti, M. P., and Lodish, H. F. (1997). Flotillin and epidermal surface antigen define a new family of caveolae-associated integral membrane proteins. *J. Biol. Chem.* 272, 13793–13802. doi: 10.1074/jbc.272.21.13793

Bodin, S., Planchon, D., Rios Morris, E., Comunale, F., and Gauthier-Rouviere, C. (2014). Flotillins in intercellular adhesion - from cellular physiology to human diseases. *J. Cell Sci.* 127, 5139–5147. doi: 10.1242/jcs.159764

Boring, L., Gosling, J., Cleary, M., and Charo, I. F. (1998). Decreased lesion formation in CCR2-/- mice reveals a role for chemokines in the initiation of atherosclerosis. *Nature* 394, 894–897. doi: 10.1038/29788

Charrin, S., Manié, S., Thiele, C., Billard, M., Gerlier, D., Boucheix, C., et al. (2003). A physical and functional link between cholesterol and tetraspanins. *Eur. J. Immunol.* 33, 2479–2489. doi: 10.1002/eji.200323884

Cherezov, V., Rosenbaum, D. M., Hanson, M. A., Rasmussen, S. G. F., Thian, F. S., Kobilka, T. S., et al. (2007). High-resolution crystal structure of an engineered human β2-adrenergic G protein-coupled receptor. *Science* 318, 1258–1265. doi: 10.1126/science.1150577

Collins, B. M., Davis, M. J., Hancock, J. F., and Parton, R. G. (2012). Structure-based reassessment of the caveolin signaling model: do caveolae regulate signaling through caveolin-protein interactions? *Dev. Cell* 23, 11–20. doi: 10.1016/j.devcel.2012.06.012

Collins, R. N. (2003). 'Getting it on' - GDI displacement and small GTPase membrane recruitment. *Mol. Cell* 12, 1064–1066. doi: 10.1016/S1097-2765(03)00445-3

Compeer, E. B., Kraus, F., Ecker, M., Redpath, G., Amiezer, M., Rother, N., et al. (2018). A mobile endocytic network connects clathrin-independent receptor endocytosis to recycling and promotes T cell activation. *Nat. Commun.* 9:1597. doi: 10.1038/s41467-018-04088-w

de Winde, C. M., Elfrink, S., and van Spriel, A. B. (2017). Novel Insights into Membrane Targeting of B Cell Lymphoma. *Trends Cancer* 3, 442–453. doi: 10.1016/j.trecan.2017.04.006

Deng, X., Li, Q., Hoff, J., Novak, M., Yang, H., Jin, H., et al. (2012). Integrin-associated CD151 drives ErbB2-evoked mammary tumor onset and metastasis. *Neoplasia* 14, 678–689. doi: 10.1593/neo.12922

Dietzen, D. J., Hastings, W. R., and Lublin, D. M. (1995). Caveolin is palmitoylated on multiple cysteine residues. Palmitoylation is not necessary for localization of caveolin to caveolae. *J. Biol. Chem.* 270, 6838–6842. doi: 10.1074/jbc.270.12.6838

Dijkstra, S., Kooij, G., Verbeek, R., van der Pol, S. M. A., Amor, S., Geisert, E. E., et al. (2008). Targeting the tetraspanin CD81 blocks monocyte transmigration and ameliorates EAE. *Neurobiol. Dis.* 31, 413–421. doi: 10.1016/j.nbd.2008.05.018

Engering, A., and Pieters, J. (2001). Association of distinct tetraspanins with MHC class II molecules at different subcellular locations in human immature dendritic cells. *Int. Immunol.* 13, 127–134. doi: 10.1093/intimm/13.2.127

Escola, J. M., Kleijmeer, M. J., Stoorvogel, W., Griffith, J. M., Yoshie, O., and Geuze, H. J. (1998). Selective enrichment of tetraspan proteins on the internal vesicles of multivesicular endosomes and on exosomes secreted by human B-lymphocytes. *J. Biol. Chem.* 273, 20121–20127. doi: 10.1074/jbc.273.32.20121

Feig, J. E., Shang, Y., Rotllan, N., Vengrenyuk, Y., Wu, C., Shamir, R., et al. (2011). Statins promote the regression of atherosclerosis via activation of the CCR7-dependent emigration pathway in macrophages. *PLoS One* 6:e28534. doi: 10.1371/journal.pone.0028534

Ficht, X., Ruef, N., Stolp, B., Samson, G. P. B., Moalli, F., Page, N., et al. (2019). *In vivo* function of the lipid raft protein flotillin-1 during CD8+ T cell-mediated host surveillance. *J. Immunol.* 203, 2377–2387. doi: 10.4049/jimmunol.1900075

Franco, M., Muratori, C., Corso, S., Tenaglia, E., Bertotti, A., Capparuccia, L., et al. (2010). The tetraspanin CD151 is required for Met-dependent signaling and tumor cell growth. *J. Biol. Chem.* 285, 38756–38764. doi: 10.1074/jbc.M110.145417

Gartlan, K. H., Wee, J. L., Demaria, M. C., Nastovska, R., Chang, T. M., Jones, E. L., et al. (2013). Tetraspanin CD37 contributes to the initiation of cellular immunity by promoting dendritic cell migration. *Eur. J. Immunol.* 43, 1208–1219. doi: 10.1002/eji.201242730

Giri, B., Dixit, V. D. D., Ghosh, M. C. C., Collins, G. D. D., Khan, I. U. U., Madara, K., et al. (2007). CXCL12-induced partitioning of flotillin-1 with lipid rafts plays a role in CXCR4 function. *Eur. J. Immunol.* 37, 2104–2116. doi: 10.1002/eji.200636680

Guillaume, E., Comunale, F., Do Khoa, N., Planchon, D., Bodin, S., Gauthier-Rouviere, C., et al. (2013). Flotillin microdomains stabilize cadherins at cell–cell junctions. *J. Cell Sci.* 126, 5293–5304. doi: 10.1242/jcs.133975

Hammond, C., Denzin, L. K., Pan, M., Griffith, J. M., Geuze, H. J., and Cresswell, P. (1998). The tetraspan protein CD82 is a resident of MHC class II compartments where it associates with HLA-DR, -DM, and -DO molecules. *J. Immunol.* 161, 3282–3291.

Hanson, M. A., Cherezov, V., Griffith, M. T., Roth, C. B., Jaakola, V.-P., Chien, E. Y. T., et al. (2008). A specific cholesterol binding site is established by the 2.8 Å structure of the human β2-adrenergic receptor. *Structure* 16, 897–905. doi: 10.1016/j.str.2008.05.001

Harris, J., Werling, D., Hope, J. C., Taylor, G., and Howard, C. J. (2002). Caveolae and caveolin in immune cells: distribution and functions. *Trends Immunol.* 23, 158–164. doi: 10.1016/s1471-4906(01)02161-5

Hauser, M. A., and Legler, D. F. (2016). Common and biased signaling pathways of the chemokine receptor CCR7 elicited by its ligands CCL19 and CCL21 in leukocytes. 99, 1–14. doi: 10.1189/jlb.2MR0815-380R

Hauser, M. A., Schaeuble, K., Kindinger, I., Impellizzieri, D., Krueger, W. A., Hauck, C. R., et al. (2016). Inflammation-induced CCR7 oligomers form scaffolds to integrate distinct signaling pathways for efficient cell migration. *Immunity* 44, 59–72. doi: 10.1016/j.immuni.2015.12.010

Hemler, M. E. (2005). Tetraspanin functions and associated microdomains. *Nat. Rev. Mol. Cell Biol.* 6, 801–811. doi: 10.1038/nrm1736

Huang, S., Yuan, S., Dong, M., Su, J., Yu, C., Shen, Y., et al. (2005). The phylogenetic analysis of tetraspanins projects the evolution of cell-cell interactions from unicellular to multicellular organisms. *Genomics* 86, 674–684. doi: 10.1016/j.ygeno.2005.08.004

Hug, P., Lin, H.-M. J., Korte, T., Xiao, X., Dimitrov, D. S., Wang, J. M., et al. (2000). Glycosphingolipids promote entry of a broad range of human immunodeficiency virus type 1 isolates into cell lines expressing CD4, CXCR4, and/or CCR5. *J. Virol.* 74, 6377–6385. doi: 10.1128/jvi.74.14.6377-6385.2000

Hughes, C. E., and Nibbs, R. J. B. (2018). A guide to chemokines and their receptors. *FEBS J.* 285, 2944–2971. doi: 10.1111/febs.14466

Jaeger, K., Bruenle, S., Weinert, T., Guba, W., Muehle, J., Miyazaki, T., et al. (2019). Structural basis for allosteric ligand recognition in the human CC chemokine receptor 7. *Cell* 178:1222-1230.e10. doi: 10.1016/j.cell.2019.07.028

Jiang, L., Zhang, X., Geradts, J., Wei, Q., Hochwald, S., Xu, H., et al. (2019). Expression of tetraspanins NET-6 and CD151 in breast cancer as a potential tumor biomarker. *Clin. Exp. Med.* 19, 377–384. doi: 10.1007/s10238-019-00554-x

Jin, Y., Takeda, Y., Kondo, Y., Tripathi, L. P., Kang, S., Takeshita, H., et al. (2018). Double deletion of tetraspanins CD9 and CD81 in mice leads to a syndrome resembling accelerated aging. *Sci. Rep.* 8:5145. doi: 10.1038/s41598-018-23338-x

Jones, E. L., Wee, J. L., Demaria, M. C., Blakeley, J., Ho, P. K., Vega-Ramos, J., et al. (2016). Dendritic cell migration and antigen presentation are coordinated by the opposing functions of the tetraspanins CD82 and CD37. *J. Immunol.* 196, 978–987. doi: 10.4049/jimmunol.1500357

Kinoshita, M., Suzuki, K. G. N., Murata, M., and Matsumori, N. (2018). Evidence of lipid rafts based on the partition and dynamic behavior of sphingomyelins. *Chem. Phys. Lipids* 215, 84–95. doi: 10.1016/j.chemphyslip.2018.07.002

Kitadokoro, K., Bordo, D., Galli, G., Petracca, R., Falugi, F., Abrignani, S., et al. (2001). CD81 extracellular domain 3D structure: insight into the tetraspanin superfamily structural motifs. *EMBO J.* 20, 12–18. doi: 10.1093/emboj/20.1.12

Klymchenko, A. S., and Kreder, R. (2014). Fluorescent probes for lipid rafts: from model membranes to living cells. *Chem. Biol.* 21, 97–113. doi: 10.1016/j.chembiol.2013.11.009

Krapf, D. (2018). Compartmentalization of the plasma membrane. *Curr. Opin. Cell Biol.* 53, 15–21. doi: 10.1016/j.ceb.2018.04.002

Krishna, A., and Sengupta, D. (2019). Interplay between membrane curvature and cholesterol: role of Palmitoylated Caveolin-1. *Biophys. J.* 116, 69–78. doi: 10.1016/j.bpj.2018.11.3127

Kufareva, I., Gustavsson, M., Zheng, Y., Stephens, B. S., and Handel, T. M. (2017). What do structures tell us about chemokine receptor function and antagonism? *Annu. Rev. Biophys.* 46, 175–198. doi: 10.1146/annurev-biophys-051013-022942

Kwon, M. J., Park, S., Choi, J. Y., Oh, E., Kim, Y. J., Park, Y. H., et al. (2012). Clinical significance of CD151 overexpression in subtypes of invasive breast cancer. *Br. J. Cancer* 106, 923–930. doi: 10.1038/bjc.2012.11

Lämmermann, T., and Kastenmüller, W. (2019). Concepts of GPCR-controlled navigation in the immune system. *Immunol. Rev.* 289, 205–231. doi: 10.1111/imr.12752

Lämmermann, T., Renkawitz, J., Wu, X., Hirsch, K., Brakebusch, C., and Sixt, M. (2009). Cdc42-dependent leading edge coordination is essential for interstitial dendritic cell migration. *Blood* 113, 5703–5710. doi: 10.1182/blood-2008-11-191882

Langhorst, M. F., Reuter, A., Luxenhofer, G., Boneberg, E.-M., Legler, D. F., Plattner, H., et al. (2006). Preformed reggie/flotillin caps: stable priming platforms for macrodomain assembly in T cells. *FASEB J.* 20, 711–713. doi: 10.1096/fj.05-4760fje

Langhorst, M. F., Solis, G. P., Hannbeck, S., Plattner, H., and Stuermer, C. A. O. O. (2007). Linking membrane microdomains to the cytoskeleton: regulation of the lateral mobility of reggie-1/flotillin-2 by interaction with actin. *FEBS Lett.* 581, 4697–4703. doi: 10.1016/j.febslet.2007.08.074

Lee, D., Suh, Y. L., Park, T. I., Do, I. G., Seol, H. J., Nam, D. H., et al. (2013). Prognostic significance of tetraspanin CD151 in newly diagnosed glioblastomas. *J. Surg. Oncol.* 107, 646–652. doi: 10.1002/jso.23249

Lefkir, Y., Chassey, B., Dubois, A., Bogdanovic, A., Brady, R., Destaing, O., et al. (2003). The AP-1 Clathrin-adaptor is reguired for lysosomal enzymes sorting and biogenesis of the contractile vacuole complex in dictyostelium Cells. *Mol. Biol. Cell* 14, 1835–1851. doi: 10.1091/mbc.E02

Legler, D. F., Matti, C., Laufer, J. M., Jakobs, B. D., Purvanov, V., Allmen, E. U., et al. (2017). Modulation of chemokine receptor function by cholesterol: new prospects for pharmacological intervention. *Mol. Pharmacol.* 91, 331–338. doi: 10.1124/mol.116.107151

Legler, D. F., and Thelen, M. (2018). New insights in chemokine signaling. *F1000Res.* 7:95. doi: 10.12688/f1000research.13130.1

Levy, S., and Shoham, T. (2005). The tetraspanin web modulates immune-signalling complexes. *Nat. Rev. Immunol.* 5, 136–148. doi: 10.1038/nri1548

Li, Q., Yang, X., Xu, F., Sharma, C., Wang, H.-X., Knoblich, K., et al. (2013). Tetraspanin CD151 plays a key role in skin squamous cell carcinoma. *Oncogene* 32, 1772–1783. doi: 10.1038/onc.2012.205

Liu, R., Xie, H., Luo, C., Chen, Z., Zhou, X., Xia, K., et al. (2015). Identification of FLOT2 as a novel target for microRNA-34a in melanoma. *J. Cancer Res. Clin. Oncol.* 141, 993–1006. doi: 10.1007/s00432-014-1874-1

Ludwig, A., Otto, G. P., Riento, K., Hams, E., Fallon, P. G., and Nichols, B. J. (2010). Flotillin microdomains interact with the cortical cytoskeleton to control uropod formation and neutrophil recruitment. *J. Cell Biol.* 191, 771–781. doi: 10.1083/jcb.201005140

MacHacek, M., Hodgson, L., Welch, C., Elliott, H., Pertz, O., Nalbant, P., et al. (2009). Coordination of Rho GTPase activities during cell protrusion. *Nature* 461, 99–103. doi: 10.1038/nature08242

Mañes, S., del Real, G., Lacalle, R. A., Lucas, P., Gómez-Moutón, C., Sánchez-Palomino, S., et al. (2000). Membrane raft microdomains mediate lateral assemblies required for HIV-1 infection. *EMBO Rep.* 1, 190–196. doi: 10.1093/embo-reports/kvd025

Mantegazza, A. R., Barrio, M. M., Moutel, S., Bover, L., Weck, M., Brossart, P., et al. (2004). CD63 tetraspanin slows down cell migration and translocates to the endosomal-lysosomal-MIICs route after extracellular stimuli in human immature dendritic cells. *Blood* 104, 1183–1190. doi: 10.1182/blood-2004-01-0104

Martínez-Muñoz, L., Rodríguez-Frade, J. M., Barroso, R., Sorzano, C. ÓS., Torreño-Pina, J. A., Santiago, C. A., et al. (2018). Separating actin-dependent chemokine receptor nanoclustering from dimerization indicates a role for clustering in CXCR4 signaling and function. *Mol. Cell* 71:873. doi: 10.1016/j.molcel.2018.08.012

Martinez-Outschoorn, U. E., Sotgia, F., and Lisanti, M. P. (2015). Caveolae and signalling in cancer. *Nat. Rev. Cancer* 15, 225–237. doi: 10.1038/nrc3915

Monier, S., Dietzen, D. J., Hastings, W. R., Lublin, D. M., and Kurzchalia, T. V. (1996). Oligomerization of VIP21-caveolin in vitro is stabilized by long chain fatty acylation or cholesterol. *FEBS Lett.* 388, 143–149. doi: 10.1016/0014-5793(96)00519-4

Nattermann, J., Zimmermann, H., Iwan, A., Von Lilienfeld-Toal, M., Leifeld, L., Nischalke, H. D., et al. (2006). Hepatitis C virus E2 and CD81 interaction may be associated with altered trafficking of dendritic cells in chronic hepatitis C. *Hepatology* 44, 945–954. doi: 10.1002/hep.21350

Neumann-Giesen, C., Fernow, I., Amaddii, M., and Tikkanen, R. (2007). Role of EGF-induced tyrosine phosphorylation of reggie-1/flotillin-2 in cell spreading and signaling to the actin cytoskeleton. *J. Cell Sci.* 120, 395–406. doi: 10.1242/jcs.03336

Nguyen, D. H., and Taub, D. (2002). Cholesterol is essential for macrophage inflammatory protein 1β binding and conformational integrity of CC chemokine receptor 5. *Blood* 99, 4298–4306. doi: 10.1182/blood-2001-11-0087

Nourshargh, S., Hordijk, P. L., and Sixt, M. (2010). Breaching multiple barriers: leukocyte motility through venular walls and the interstitium. *Nat. Rev. Mol. Cell Biol.* 11, 366–378. doi: 10.1038/nrm2889

Okamoto, T., Schlegel, A., Scherer, P. E., and Lisanti, M. P. (1998). Caveolins, a family of scaffolding proteins for organizing 'preassembled signaling complexes' at the plasma membrane. *J. Biol. Chem.* 273, 5419–5422. doi: 10.1074/jbc.273.10.5419

Ono, A., and Freed, E. O. (2001). Plasma membrane rafts play a critical role in HIV-1 assembly and release. *Proc. Natl. Acad. Sci. U.S.A.* 98, 13925–13930. doi: 10.1073/pnas.241320298

Otto, G. P., and Nichols, B. J. (2011). The roles of flotillin microdomains - endocytosis and beyond. *J. Cell Sci.* 124, 3933–3940. doi: 10.1242/jcs.092015

Ou, Y.-X., Liu, F.-T., Chen, F.-Y., and Zhu, Z.-M. (2017). Prognostic value of Flotillin-1 expression in patients with solid tumors. *Oncotarget* 8, 52665–52677. doi: 10.18632/oncotarget.17075

Oyarce, C., Cruz-Gomez, S., Galvez-Cancino, F., Vargas, P., Moreau, H. D., Diaz-Valdivia, N., et al. (2017). Caveolin-1 expression increases upon maturation in dendritic cells and promotes their migration to lymph nodes thereby favoring the induction of CD8+ T cell responses. *Front. Immunol.* 8:1794. doi: 10.3389/fimmu.2017.01794

Palmesino, E., Apuzzo, T., Thelen, S., Mueller, B., Langen, H., and Thelen, M. (2016). Association of eukaryotic translation initiation factor eIF2B with fully solubilized CXCR4. *J. Leukoc. Biol.* 99, 971–978. doi: 10.1189/jlb.2MA0915-415R

Parton, R. G., and Howes, M. T. (2010). Revisiting caveolin trafficking: the end of the caveosome. *J. Cell Biol.* 191, 439–441. doi: 10.1083/jcb.201009093

Pertz, O., Hodgson, L., Klemke, R. L., and Hahn, K. M. (2006). Spatiotemporal dynamics of RhoA activity in migrating cells. *Nature* 440, 1069–1072. doi: 10.1038/nature04665

Qin, L., Kufareva, I., Holden, L. G., Wang, C., Zheng, Y., Zhao, C., et al. (2015). Crystal structure of the chemokine receptor CXCR4 in complex with a viral chemokine. *Science* 347, 1117–1122. doi: 10.1126/science.1261064

Rocha-Perugini, V., Lavie, M., Delgrange, D., Canton, J., Pillez, A., Potel, J., et al. (2009). The association of CD81 with tetraspanin-enriched microdomains is not essential for Hepatitis C virus entry. *BMC Microbiol* 9:111. doi: 10.1186/1471-2180-9-111

Rocha-Perugini, V., Martínez Del Hoyo, G., González-Granado, J. M., Ramírez-Huesca, M., Zorita, V., Rubinstein, E., et al. (2017). CD9 regulates major histocompatibility complex class II trafficking in monocyte-derived dendritic Cells. *Mol. Cell. Biol.* 37:e00202-17. doi: 10.1128/MCB.00202-17

Root, K. T., Plucinsky, S. M., and Glover, K. J. (2015). Recent progress in the topology, structure, and oligomerization of caveolin: a building block of caveolae. *Curr. Top. Membr.* 75, 305–336. doi: 10.1016/bs.ctm.2015.03.007

Rossy, J., Schlicht, D., Engelhardt, B., and Niggli, V. (2009). Flotillins interact with PSGL-1 in neutrophils and, upon stimulation, rapidly organize into membrane domains subsequently accumulating in the uropod. *PLoS One* 4:e5403. doi: 10.1371/journal.pone.0005403

Rothberg, K. G., Heuser, J. E., Donzell, W. C., Ying, Y. S., Glenney, J. R., and Anderson, R. G. W. (1992). Caveolin, a protein component of caveolae membrane coats. *Cell* 68, 673–682. doi: 10.1016/0092-8674(92)90143-Z

Rui, H., Root, K. T., Lee, J., Glover, K. J., and Im, W. (2014). Probing the U-shaped conformation of caveolin-1 in a bilayer. *Biophys. J.* 106, 1371–1380. doi: 10.1016/j.bpj.2014.02.005

Sachs, N., Secades, P., Van Hulst, L., Song, J. Y., and Sonnenberg, A. (2014). Reduced susceptibility to two-stage skin carcinogenesis in mice with epidermis-specific deletion of CD151. *J. Invest. Dermatol.* 134, 221–228. doi: 10.1038/jid.2013.280

Saiz, M. L., Rocha-Perugini, V., and Sánchez-Madrid, F. (2018). Tetraspanins as organizers of antigen-presenting cell function. *Front. Immunol.* 9:1074. doi: 10.3389/fimmu.2018.01074

Samstad, E. O., Niyonzima, N., Nymo, S., Aune, M. H., Ryan, L., Bakke, S. S., et al. (2014). Cholesterol crystals induce complement-dependent inflammasome activation and cytokine release. *J. Immunol.* 192, 2837–2845. doi: 10.4049/jimmunol.1302484

Schenk, G. J., Dijkstra, S., van het Hof, A. J., van der Pol, S. M. A., Drexhage, J. A. R., van der Valk, P., et al. (2013). Roles for HB-EGF and CD9 in multiple sclerosis. *Glia* 61, 1890–1905. doi: 10.1002/glia.22565

Schulte, T., Paschke, K. A., Laessing, U., Lottspeich, F., and Stuermer, C. A. (1997). Reggie-1 and reggie-2, two cell surface proteins expressed by retinal ganglion cells during axon regeneration. *Development* 124, 577–587.

Seigneuret, M. (2006). Complete predicted three-dimensional structure of the facilitator transmembrane protein and hepatitis C virus receptor CD81: conserved and variable structural domains in the tetraspanin superfamily. *Biophys. J.* 90, 212–227. doi: 10.1529/biophysj.105.069666

Seigneuret, M., Delaguillaumie, A., Lagaudrière-Gesbert, C., and Conjeaud, H. (2001). Structure of the tetraspanin main extracellular domain: a partially conserved fold with a structurally variable domain insertion. *J. Biol. Chem.* 276, 40055–40064. doi: 10.1074/jbc.M105557200

Sezgin, E., Levental, I., Mayor, S., and Eggeling, C. (2017). The mystery of membrane organization: composition, regulation and roles of lipid rafts. *Nat. Rev. Mol. Cell Biol.* 18, 361–374. doi: 10.1038/nrm.2017.16

Signoret, N., Hewlett, L., Wavre, S., Pelchen-Matthews, A., Oppermann, M., and Marsh, M. (2005). Agonist-induced endocytosis of CC chemokine receptor 5 is clathrin dependent. *Mol. Biol. Cell* 16, 902–917. doi: 10.1091/mbc.e04-08-0687

Silvie, O., Rubinstein, E., Franetich, J. F., Prenant, M., Belnoue, E., Rénia, L., et al. (2003). Hepatocyte CD81 is required for *Plasmodium falciparum* and *Plasmodium yoelii* sporozoite infectivity. *Nat. Med.* 9, 93–96. doi: 10.1038/nm808

Simons, K., and Ehehalt, R. (2002). Cholesterol, lipid rafts, and disease. *J. Clin. Invest.* 110, 597–603. doi: 10.1172/JCI16390

Simons, K., and Ikonen, E. (1997). Functional rafts in cell membranes. *Nature* 387, 569–572. doi: 10.1038/42408

Simons, K., and Toomre, D. (2000). Lipid rafts and signal transduction. *Nat. Rev. Mol. Cell Biol.* 1, 31–39. doi: 10.1038/35036052

Simons, K., and Van Meers, G. (1988). Lipid sorting in epithelial cells. *Biochemistry* 27, 6197–6202. doi: 10.1021/bi00417a001

Slaughter, N., Laux, I., Tu, X., Whitelegge, J., Zhu, X., Effros, R., et al. (2003). The flotillins are integral membrane proteins in lipid rafts that contain TCR-associated signaling components: implications for T-cell activation. *Clin. Immunol.* 108, 138–151. doi: 10.1016/S1521-6616(03)00097-4

Sotgia, F., Martinez-Outschoorn, U. E., Howell, A., Pestell, R. G., Pavlides, S., and Lisanti, M. P. (2012). Caveolin-1 and cancer metabolism in the tumor microenvironment: markers, models, and mechanisms. *Annu. Rev. Pathol.* 7, 423–467. doi: 10.1146/annurev-pathol-011811-120856

Szöllósi, J., Horejsí, V., Bene, L., Angelisová, P., and Damjanovich, S. (1996). Supramolecular complexes of MHC class I, MHC class II, CD20, and tetraspan molecules (CD53, CD81, and CD82) at the surface of a B cell line JY. *J. Immunol.* 157, 2939–2946.

Tall, A. R., and Yvan-Charvet, L. (2015). Cholesterol, inflammation and innate immunity. *Nat. Rev. Immunol.* 15, 104–116. doi: 10.1038/nri3793

Thelen, M., and Legler, D. F. (2018). Membrane lipid environment: potential modulation of chemokine receptor function. *Cytokine* 109, 72–75. doi: 10.1016/j.cyto.2018.02.011

Tomassian, T., Humphries, L. A., Liu, S. D., Silva, O., Brooks, D. G., and Miceli, M. C. (2011). Caveolin-1 orchestrates TCR synaptic polarity, signal specificity, and function in CD8 T cells. *J. Immunol.* 187, 2993–3002. doi: 10.4049/jimmunol.1101447

Untemaehrer, J. J., Chow, A., Pypaert, M., Inaba, K., and Mellman, I. (2007). The tetraspanin CD9 mediates lateral association of MHC class II molecules on the dendritic cell surface. *Proc. Natl. Acad. Sci. U.S.A.* 104, 234–239. doi: 10.1073/pnas.0609665104

Van Den Hoorn, T., Paul, P., Janssen, L., Janssen, H., and Neefjes, J. (2012). Dynamics within tetraspanin pairs affect MHC class II expression. *J. Cell Sci.* 125, 328–339. doi: 10.1242/jcs.088047

Voss, M. A., Gordon, N., Maloney, S., Ganesan, R., Ludeman, L., McCarthy, K., et al. (2011). Tetraspanin CD151 is a novel prognostic marker in poor outcome endometrial cancer. *Br. J. Cancer* 104, 1611–1618. doi: 10.1038/bjc.2011.80

Wang, Z., Wang, N., Liu, P., Peng, F., Tang, H., Chen, Q., et al. (2015). Caveolin-1, a stress-related oncotarget, in drug resistance. *Oncotarget* 6, 37135–37150. doi: 10.18632/oncotarget.5789

Weis, W. I., and Kobilka, B. K. (2018). The molecular basis of G protein–coupled receptor activation. *Annu. Rev. Biochem.* 87, 897–919. doi: 10.1146/annurev-biochem-060614-033910

Wu, B., Chien, E. Y. T., Mol, C. D., Fenalti, G., Liu, W., Katritch, V., et al. (2010). Structures of the CXCR4 chemokine GPCR with small-molecule and cyclic peptide antagonists. *Science* 330, 1066–1071. doi: 10.1126/science.1194396

Yu, Y., Liang, C., Wang, S., Zhu, J., Miao, C., Hua, Y., et al. (2018). CD151 promotes cell metastasis via activating TGF-β1/smad signaling in renal cell carcinoma. *Oncotarget* 9, 13313–13323. doi: 10.18632/oncotarget.24028

Zelman-Toister, E., Bakos, E., Cohen, S., Zigmond, E., Shezen, E., Grabovsky, V., et al. (2016). CD151 Regulates T-cell migration in health and inflammatory bowel disease. *Inflamm. Bowel Dis.* 22, 257–267. doi: 10.1097/MIB.0000000000000621

Zheng, Y., Han, G. W., Abagyan, R., Wu, B., Stevens, R. C., Cherezov, V., et al. (2017). Structure of CC chemokine receptor 5 with a potent chemokine antagonist reveals mechanisms of chemokine recognition and molecular mimicry by HIV. *Immunity* 46, 1005–1017.e5. doi: 10.1016/j.immuni.2017.05.002

Zheng, Y., Qin, L., Zacarías, N. V. O., De Vries, H., Han, G. W., Gustavsson, M., et al. (2016). Structure of CC chemokine receptor 2 with orthosteric and allosteric antagonists. *Nature* 540, 458–461. doi: 10.1038/nature20605

Zhu, Z., Wang, J., Sun, Z., Sun, X., Wang, Z., and Xu, H. (2013). Flotillin2 expression correlates with HER2 levels and poor prognosis in gastric cancer. *PLoS One* 8:e62365. doi: 10.1371/journal.pone.0062365

Zimmerman, B., Kelly, B., Mcmillan, B. J., Seegar, T. C. M., Dror, R. O., Kruse, A. C., et al. (2016). Crystal structure of a full-length human tetraspanin reveals a cholesterol-binding pocket. *Cell* 167, 1041–1051. doi: 10.1016/j.cell.2016.09.056

Conflict of Interest: The authors declare that the research was conducted in the absence of any commercial or financial relationships that could be construed as a potential conflict of interest.

frontiers in Cell and Developmental Biology

REVIEW
published: 28 April 2020
doi: 10.3389/fcell.2020.00284

Interleaflet Coupling of Lipid Nanodomains – Insights From *in vitro* Systems

*Maria J. Sarmento, Martin Hof and Radek Šachl**

J. Heyrovský Institute of Physical Chemistry of the Czech Academy of Sciences, Dolejškova, Prague, Czechia

The plasma membrane is a complex system, consisting of two layers of lipids and proteins compartmentalized into small structures called nanodomains. Despite the asymmetric composition of both leaflets, coupling between the layers is surprisingly strong. This can be evidenced, for example, by recent experimental studies performed on phospholipid giant unilamellar vesicles showing that nanodomains formed in the outer layer are perfectly registered with those in the inner leaflet. Similarly, microscopic phase separation in one leaflet can induce phase separation in the opposing leaflet that would otherwise be homogeneous. In this review, we summarize the current theoretical and experimental knowledge that led to the current view that domains are – irrespective of their size – commonly registered across the bilayer. Mechanisms inducing registration of nanodomains suggested by theory and calculations are discussed. Furthermore, domain coupling is evidenced by experimental studies based on the sparse number of methods that can resolve registered from independent nanodomains. Finally, implications that those findings using model membrane studies might have for cellular membranes are discussed.

Keywords: domain registration, interleaflet coupling, membrane asymmetry, nanodomains, plasma membranes, phase separation, biomembranes

OPEN ACCESS

Edited by:
Falk Nimmerjahn, University of Erlangen Nuremberg, Germany

Reviewed by:
Pushpendra Singh, Johns Hopkins University, United States
Steven Michael Claypool, Johns Hopkins University, United States

***Correspondence:**
Radek Šachl
radek.sachl@jh-inst.cas.cz

Specialty section:
This article was submitted to Cellular Biochemistry, a section of the journal Frontiers in Cell and Developmental Biology

Received: *23 January 2020*
Accepted: *02 April 2020*
Published: *28 April 2020*

Citation:
Sarmento MJ, Hof M and Šachl R (2020) Interleaflet Coupling of Lipid Nanodomains – Insights From in vitro Systems. Front. Cell Dev. Biol. 8:284. doi: 10.3389/fcell.2020.00284

INTRODUCTION

Plasma membranes are composed of two layers of lipids and proteins in close contact with each other. They are in fact so close that the individual layers cannot be viewed as two independent units. In literature, this physical phenomenon is known as interleaflet coupling (Devaux and Morris, 2004; Collins, 2008; Kiessling et al., 2009; May, 2009; Fujimoto and Parmryd, 2017) and has in the past been evidenced through experiments showing that the physical properties of one layer

Abbreviations: AFM, atomic force microscopy; CHO cells, Chinese hamster ovary cells; Chol, cholesterol; DiphyPC, 1,2-diphytanoyl-*sn*-glycero-3-phosphocholine; DLPC, 1,2-dilauroyl-*sn*-glycero-3-phosphocholine; DOPC, 1,2-dioleoyl-*sn*-glycero-3-phosphocholine; DPPC, 1,2-dipalmitoyl-*sn*-glycero-3-phosphocholine; DSPC, 1,2-distearoyl-*sn*-glycero-3-phosphocholine; DUPC, 1,2-diundecanoyl-*sn*-glycero-phosphocholine; FCS, fluorescence correlation spectroscopy; FLCS, fluorescence lifetime correlation spectroscopy; FRAP, fluorescence recovery after photobleaching; FRET, Förster resonance energy transfer; GPI, glycosylphosphatidylinositol; GPMV, giant plasma membrane vesicle; GSL, glycosphingolipids; GUV, giant unilamellar vesicle; L_d, liquid-disordered; L_o, liquid-ordered; LUV, large unilamellar vesicle; MC-FRET, Förster resonance energy transfer analyzed by Monte Carlo simulations; MD, molecular dynamic; MIET, metal induced energy transfer; NBD-DOPE, 1,2-dioleoyl-*sn*-glycero-3-phosphoethanolamine (7-nitro-2-1,3-benzoxadiazol-4-yl); OMPC, 1-oleoyl-2-myristoyl-*sn*-glycero-3-phosphocholine; PC, phosphatidylcholine; PE, phosphatidylethanolamine; PIP, phosphatidylinositol phosphate; PIP_2, phosphatidylinositol 4,5-bisphosphate; PLL, poly-L-lysine; POPC, 1-palmitoyl-2-oleoyl-*sn*-glycero-3-phosphocholine; POPE, 1-palmitoyl-2-oleoyl-*sn*-glycero-3-phosphoethanolamine; POPG, 1-palmitoyl-2-oleoyl-*sn*-glycero-3-phospho-(1′-rac-glycerol); PS, phosphatidylserine; SANS, small-angle neutron scattering; SPB, supported phospholipid bilayer; Sph, sphingomyelin; SOPC, 1-stearoyl-2-oleoyl-*sn*-glycero-3-phosphocholine; T_m, melting temperature; TMD, transmembrane domain.

can modulate the physical state of the opposing leaflet (Chiantia and London, 2012; Heberle et al., 2016).

Importantly, biological membranes are not homogeneous. They contain small heterogeneities, also known as lipid nanodomains (Eggeling et al., 2009; Owen et al., 2012), with different physico-chemical properties in respect to the surrounding bulk membrane (Cebecauer et al., 2018). Although lipid nanodomains of similar size have even been detected in synthetic model membranes consisting of only two different types of lipids (Koukalová et al., 2017), they are still difficult to detect and characterize due to their small size (<200 nm) (Cebecauer et al., 2018). Consequently, liquid-ordered (L_o; see **Box 1**) microdomains (>200 nm) have been extensively used as suitable models for plasma membrane nanodomains, despite their significantly larger size, less dynamic behavior, and increased membrane order (Dietrich et al., 2001; Mouritsen and Bagatolli, 2015; Cebecauer et al., 2018). Interestingly, microdomains formed in one leaflet of free-standing vesicles have always been found in perfect alignment with the microdomains formed in the opposing layer, implying the presence of interleaflet coupling (Garg et al., 2007; Kiessling et al., 2009; Blosser et al., 2015). Furthermore, shear stress experiments performed on supported phospholipid bilayers (SPBs) show that the pressure required to deregister (de-couple) microdomains increases with the decrease in domain size (Blosser et al., 2015). This observation suggests that biologically more relevant nanodomains are also perfectly registered (Garg et al., 2007; Kiessling et al., 2009; Blosser et al., 2015). As shown below in this review, recent Förster resonance energy transfer analyzed by Monte Carlo simulations (MC-FRET) experiments confirm this hypothesis (Vinklárek et al., 2019).

Additionally, plasma membranes are asymmetric (Devaux and Morris, 2004), with most glycosphingolipids (GSL), sphingomyelins (Sph), and phosphatidylcholines (PC) being found in the outer leaflet, whereas phosphatidylinositol phosphates (PIPs), phosphatidylserines (PS), and phosphatidylethanolamines (PE) are mainly localized in the inner leaflet (Bretscher, 1972; Devaux, 1991; Harayama and Riezman, 2018). Although this membrane asymmetry had been recognized a long time ago, asymmetric model membranes only began to be used recently. This is probably due to limitations on the preparation methods and the limited stability of the induced asymmetry. Nevertheless, experiments performed on these systems have clearly shown that the presence of domains in one layer is capable of inducing the formation of registered domains in the other leaflet (Collins and Keller, 2008; Wan et al., 2008; Kiessling et al., 2009; Wang and London, 2018) and that the final strength of interleaflet coupling depends on the actual conditions of the membrane. Not surprisingly, coupling is often mentioned in connection with signal transduction across the plasma membrane (Iwabuchi et al., 2010; Wernick et al., 2010; Bergan et al., 2012; Skotland and Sandvig, 2019), which can be triggered by clustering of receptors (i.e., formation of membrane nanodomains) in the outer leaflet and transfer of information to the inner leaflet (Klokk et al., 2016).

Characterization of coupling in simpler model systems has proved to be a convenient tool to understand the underlying mechanisms that ultimately lead to domain registration. Keeping this in mind, in this review we first discuss the mechanisms suggested to cause interleaflet coupling, potentially resulting in domain registration. In the following section, we have summarized the experimental evidence that contributed to the current understanding that the level of interleaflet coupling is neither negligible nor strong. It is instead moderate yet enough to universally register lipid domains irrespective of their size. Since the characterization of nanodomains' interleaflet organization requires the use of sophisticated biophysical approaches and up-to-date techniques, we have paid significant attention to the principles based on which the most important techniques can detect domain registration. At the end of the review, we discuss the implications that the discoveries on model systems might have for our overall understanding of the organization and function of the plasma membrane in living cells. Moreover, and despite the sparse evidence, we attempt at discussing how proteins might contribute to lipid nanodomain registration and how these protein–lipid interactions can ultimately be of great significance for signal transduction across different biological membranes.

THEORETICAL FRAMEWORK: MECHANISMS LEADING TO NANODOMAIN REGISTRATION

Line Tension

It has been shown by X-ray diffraction that L_o domains are thicker than the surrounding liquid-disordered (L_d) phase (see **Box 1**) (Gandhavadi et al., 2002), meaning that in principle there is a hydrophobic mismatch between the acyl chains of

BOX 1 | Lateral segregation of lipids resulting in membrane heterogeneity.

Depending on the temperature and lipid composition, a lipid bilayer may be present in several phases. *Liquid-disordered phase*, L_d, usually encountered above the melting temperature (T_m) of the bilayer is characterized by high lipid mobility with maximal rotational and translational freedom, low lipid packing and disordered acyl chains. By lowering the temperature below the T_m, the bilayer freezes into a *solid (gel) phase*, *S*, for which low lipid mobility, high lipid packing and membrane order are typical. In some conditions, usually in bilayers containing cholesterol, *liquid-ordered phase*, L_o, may be formed. With regard to the mobility of individual lipids, this phase rather resembles the L_d phase, with only slightly reduced diffusion of lipids in comparison to the actual L_d. In contrast, membrane order and lipid packing are more similar to the *S* phase.

Due to limited miscibility of some lipids, a bilayer can separate into several co-existing phases, resulting in membrane heterogeneity. Depending on the size of these heterogeneities, they are termed as *micro- or nanodomains*. In this work and in analogy to (Cebecauer et al., 2018) we define nanodomain as "any compartmentalization within a lipid membrane that has an estimated 'diameter equivalent' within the range of 4–200 nm." Since the nanodomain of 4 nm diameter contains only 100 lipids, it cannot be viewed as a single phase, i.e., a region of space throughout which all physical properties of a material are essentially uniform.

different phases, with the ones in the L_o phase being more exposed to the hydrophilic environment. This gives rise to line tension, which can be understood as energy stored into a unit length of the domain boundary. For instance, for a 0.5 nm difference in the thickness of the two phases, the line tension would theoretically rise to about 6 k_BT nm^{-1} (Tien, 1974; Galimzyanov et al., 2015). However, such high value has never been observed experimentally, since lipid re-distribution assures a smooth transition between phases and the consequent decrease in the line tension (panel D in **Figure 1**) (Baumgart et al., 2003; Esposito et al., 2007; Akimov et al., 2009).

As shown by Galimzyanov et al. (2015), line tension alone is sufficient to drive registration of nanodomains. However, the efficiency of this process decreases with the increase in nanodomain size (Galimzyanov et al., 2017). In fact, minimal line tension is reached when nanodomains get into registration with a slight shift (∼4 nm) relative to each other (Galimzyanov et al., 2015). This effect is universal, since it does not require any special lipid component in the membrane. Theoretically, the line tension disappears completely if nanodomains get into antiregistration. However, the amounts of L_o and L_d phases would need to match perfectly (**Figure 2**). Naturally, this condition is hardly achievable for an actual membrane, which explains why antiregistration has so far only been observed *in silico* (Perlmutter and Sachs, 2011; Galimzyanov et al., 2015; Williamson and Olmsted, 2015b).

Interestingly, surface tension, which can be induced for instance by bending or swelling of the lipid bilayer, cannot drive domain registration (Akimov et al., 2009; Galimzyanov et al., 2015). In fact, lipid domain registration occurs rather independently of the surface tension applied onto the membrane. Nevertheless, it influences the energy balance of the whole process (Frolov et al., 2006; Akimov et al., 2007; García-Sáez et al., 2007). Specifically, increasing surface tension leads to greater energy storage at the domain boundaries, which in turn favors the coalescence of domains and the subsequent increase of the domain size (Ayuyan and Cohen, 2008; Akimov et al., 2009).

Membrane Undulations

It follows from theoretical considerations based on continuum theory that the line tension alone is not enough to register nanodomains larger than 38 nm in radius (Galimzyanov et al., 2017). Galimzyanov et al. (2017) identified thermal membrane

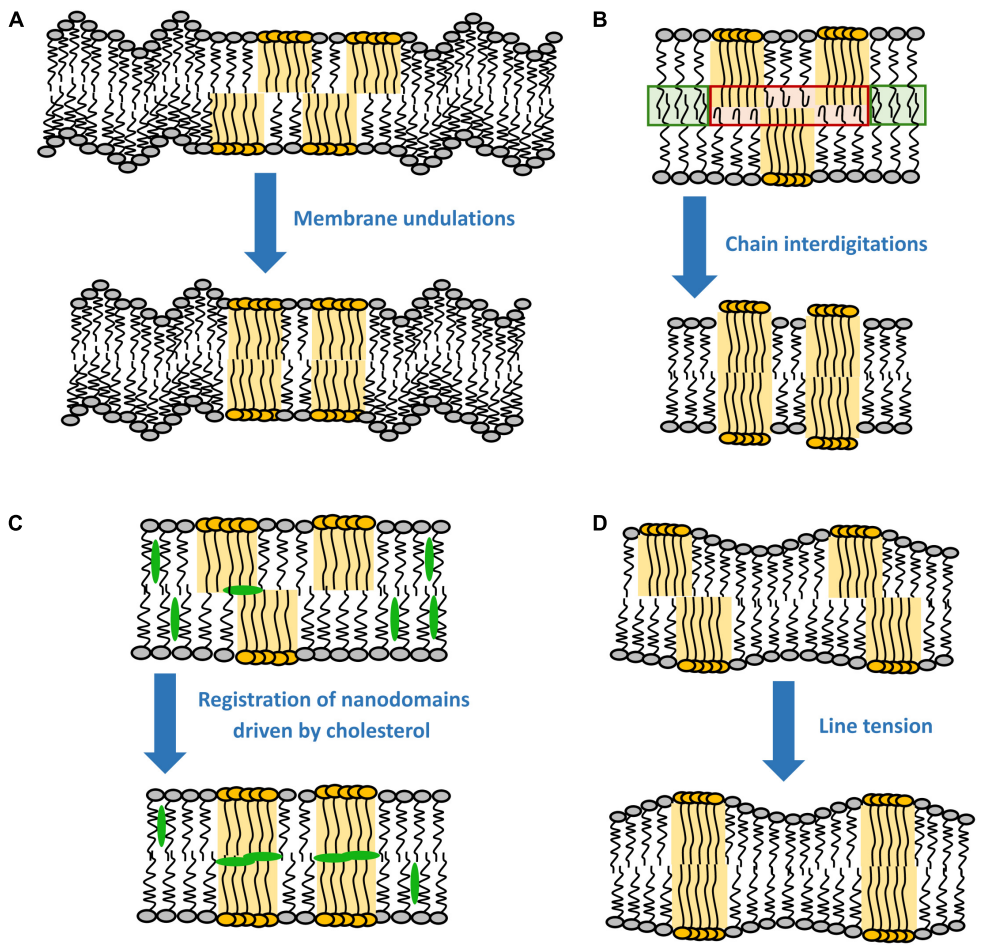

FIGURE 1 | Most probable driving forces for the registration of nanodomains. **(A)** Membrane undulations, **(B)** chain interdigitations, **(C)** registration of nanodomains by cholesterol, and **(D)** line tension.

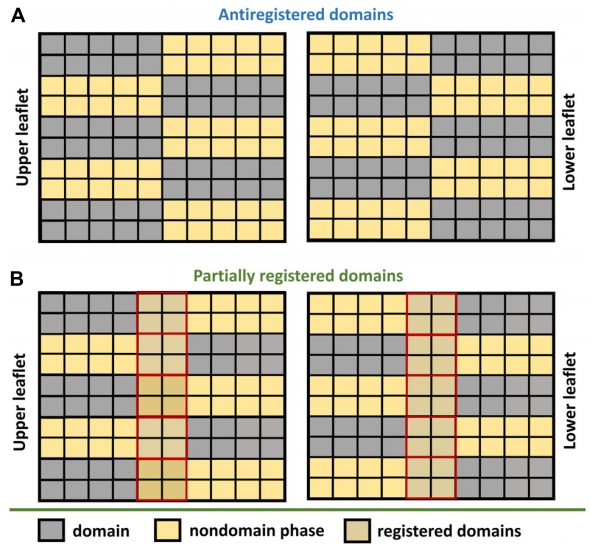

FIGURE 2 | Domain anti-registration versus partial registration. **(A)** Domains are classified as antiregistered when the domains localized in one leaflet (gray squares) are aligned with the nondomain region in the other leaflet (yellow squares). Such an arrangement is possible only if the domain and nondomain subregions occupy an equal area of the bilayer. **(B)** Higher amount of one of the regions inevitably leads to transversal overlap between the domain and nondomain subregions (yellow-gray squares surrounded by solid red).

undulations as an additional energy source contributing to robust coupling of nanodomains for a broad spectrum of nanodomain sizes (panel A in **Figure 1**). It is known that L_o domains have approximately 2–3 times higher bending rigidity than the surrounding L_d phase (Khelashvili et al., 2013; Kollmitzer et al., 2015). Because such stiff parts of both leaflets cannot undulate with the same efficiency as the remaining L_d phase, membrane undulations drive the stiff regions into the same bilayer locations, causing registration of domains. According to recent experimental work on SPBs, the resulting energy gain is about 0.016 $k_BT\ nm^{-2}$ (Blosser et al., 2015). Since the gain in the coupling energy increases with the increase in the nanodomain area, undulations primarily act on the registration of larger domains, although they are still able to co-localize nanodomains as small as 10 nm in radius (Haataja, 2017). This behavior is thus utterly the opposite to the line tension, which mainly drives registration of smaller domains (see section "Line Tension"). Interestingly, the efficiency of the undulations varies significantly with the wavelength of the fluctuations, the most efficient being in the ultraviolet region and then rapidly declining with the increase in the wavelength (Galimzyanov et al., 2017).

Undulations represent a robust mechanism of domain registration, being resistant to external influences. For instance, a surface tension as high as 10 $nN\ m^{-1}$, which is able to rupture a lipid bilayer (Evans et al., 2003), has only a modest effect on the coupling energy. This is mainly because the tension is only able to supress fluctuations with longer wavelengths, which do not contribute to domain registration (Galimzyanov et al., 2017). Similarly, undulations are only slightly affected by a solid membrane support, which is known to hamper collective motion of lipids in both leaflets and slow down motion of individual lipids (Sonnleitner et al., 1999; Przybylo et al., 2006; Garg et al., 2007). Although the theoretical framework for membrane undulations predicts the membrane support to not influence the coupling energy that governs domain registration (Galimzyanov et al., 2017), recent atomic force microscopy (AFM) experiments performed on various membrane supports indicate that it may significantly affect interleaflet coupling of lipid domains (see section "Imaging").

Chain Interdigitation

Even though acyl chain interdigitation is often suggested in literature as a plausible mechanism for interleaflet coupling, its importance has not yet been sufficiently confirmed (May, 2009; Nickels et al., 2015b; Fujimoto and Parmryd, 2017; Skotland and Sandvig, 2019) (panel B in **Figure 1**). In principle, interdigitation is expected to fuel registration of nanodomains because the ability of acyl chains to penetrate (interdigitate) into the opposing leaflet is considerably better if the L_d phase faces a similar L_d environment in the opposing leaflet. Interdigitation will be hampered if the disordered phase faces an ordered one, in which the acyl chains cannot penetrate. Therefore, chain interdigitation should be thermodynamically favorable due to the overall entropy increase of the acyl chains. Interestingly, the energy of the interaction between leaflets (0.1–10 $k_BT\ nm^{-2}$) is similar to the energy that would have to be paid in order to prevent chain interdigitation (Szleifer et al., 1990; Collins, 2008; May, 2009).

In practice, a couple of experiments support the hypothesis that chain interdigitation is important, although not required, for interleaflet coupling. It has been shown by fluorescence correlation spectroscopy (FCS) that the presence of long chain Sph (C24:0) in the outer membrane leaflet slows down lipid diffusion within the inner leaflet composed of 1,2-dioleoyl-*sn*-glycero-3-phosphocholine (DOPC) (Chiantia and London, 2012). Similarly, molecular dynamics (MD) simulations indicate that long chain Sph can penetrate deeply into the opposing leaflet, strongly interacting with neighboring lipids (Róg et al., 2016). Recently, it has also been proposed that chain interdigitation might even have biological significance. Skotland and Sandvik (2019) suggest in their perspective article that toxin-induced clustering of long chain Sph in the outer leaflet could be used to transmit the signal into the inner leaflet, through interdigitation of Sph molecules and their consequent coupling to the lipids with short tails from the inner leaflet. From MD simulations, the strongest of these interactions was observed to be between Sph (18:0/24:0) and PS (16:0/18:1), a well-known signaling lipid (Llorente et al., 2013).

Despite these interesting findings that rather support interdigitation as one of the main coupling mechanisms, there are experiments questioning this concept. For instance, Horner et al. (2013) measured the intermonolayer viscosity of fluorescent probes with both short and long acyl chains and found out that the viscosity was independent of the acyl chain length. This result would in principle rule out interdigitation as one of the main coupling mechanisms. Further supporting this hypothesis,

Chiantia and London (2012) have demonstrated by FCS that interleaflet coupling of diffusion does not necessarily require lipids with long acyl chains, but rather occurs in the presence of lipids containing one saturated acyl chain [such as 1-palmitoyl-2-oleoyl-*sn*-glycero-3-phosphocholine (POPC), which is abundant in cellular membranes]. For example, substitution of DOPC by 1-oleoyl-2-myristoyl-*sn*-glycero-3-phosphocholine (OMPC) led to a significant increase in the coupling of diffusion across the bilayer (Chiantia and London, 2012). This suggests that, instead of chain interdigitation, the physical proximity and possible interaction between acyl chains of complementary leaflets at the bilayer midplane can play a more general role, in which strong interdigitation would be the extreme case. In this way, stretching of a saturated acyl chain of, e.g., POPC would also allow a more effective interaction with the slow moving Sph in the outer leaflet (when compared with DOPC), reducing its diffusion and ultimately resulting in interleaflet coupling.

Additional insight into the whole problematics has been provided by MD simulations. First, the simulations do not support complementarity between short chains in one layer and long chains in the opposite layer as the source of interleaflet coupling (Capponi et al., 2016). Second, it has been shown that the acyl chains can move very fast and exhibit a disordered character (Lu et al., 1995). Particularly the oleoyl chains of DOPC can bend back to the interface, thereby reducing the electron density close to the membrane midplane (Chiu et al., 1999). A higher density of terminal methyl groups was found for POPC in comparison to DOPC lipids (Chiu et al., 1999). Moreover, the determined average distance between terminal segments of both leaflets is significantly smaller for bilayers with one saturated chain than for a DOPC bilayer (Chiantia and London, 2012). Nuclear magnetic resonance (NMR) experiments have confirmed that the methylene groups do penetrate into the opposing leaflet and that the chain mobility is only partially affected by the opposing leaflet (Xu and Cafiso, 1986; Lu et al., 1995). Due to the disordered chain ends, the entire surface at which both layers meet appears very rough, much rougher than the side surfaces of the acyl chains close to their headgroups. Therefore, the lipid mobility is mainly determined by interlayer friction and much less by intralayer viscosity (Horner et al., 2013).

In summary, recent experimental and theoretical findings suggest that interdigitation is not required to interleaflet-couple lipid nanodomains. On the other hand, close contacts and frequent interactions of acyl chains belonging to opposing leaflets seem to play a more relevant role. The degree of mixing across the bilayer midplane thus depends on the length of both *sn*-1 and *sn*-2 acyl chains, the presence of double bonds, and acyl chain asymmetry (Capponi et al., 2016). Although these interactions across the midplane appear significant, their importance still needs to be confirmed by detailed MD simulations, and possibly by experimental work.

Cholesterol

In the past, it has been often suggested that cholesterol flip-flop, i.e., the rapid exchange of cholesterol between the two leaflets, can significantly contribute to domain registration (Hamilton, 2003). The proposed mechanism would result primarily from the fact that cholesterol can move significantly faster in the disordered phase in comparison to the ordered one (Risselada and Marrink, 2008). Therefore, higher cholesterol flip-flop rates are monitored if less/more ordered domains in one leaflet are matched with less/more ordered domains in the other leaflet. In contrast, cholesterol movement will be confined to only one leaflet in case of nonmatching domains. However, and although the contribution of cholesterol flip-flop to the overall coupling energy might seem considerable, by far it does not reach the contributions reported for the remaining coupling mechanisms (see the sub-sections above) (May, 2009). Thus, cholesterol flip-flop can be presently excluded as a plausible mechanism for nanodomain registration.

Yet, according to a recent coarse grain simulation study by Thallmair et al. (2018), cholesterol might still be involved in lipid domain registration, but in a slightly different manner. This study identified an intermediate state of cholesterol, in which it is sandwiched between the leaflets. This state would be responsible for increased correlations in lipid densities between the two leaflets, resulting in a weak repulsion of L_o domains and a small attraction of the remaining liquid disordered phase, thereby promoting domain registration (panel C in **Figure 1**). Although this finding agrees well with another simulation study (Weiner and Feigenson, 2018), it still requires experimental confirmation.

EXPERIMENTAL EVIDENCE FOR THE REGISTRATION OF MICRO- AND NANODOMAINS

Microdomains have immense practical advantage over much smaller nanodomains, mostly thanks to their adequate size for conventional fluorescence microscopy. More sophisticated approaches had to be developed to enable lipid domain detection and characterization at the nanoscale (Eggeling et al., 2009; Heberle et al., 2016; Šachl et al., 2016; Koukalová et al., 2017). Nevertheless, studying the registration of these nanodomains is even more challenging, since high resolution is, in principal, required not in two but in all three directions simultaneously. The choice of approach to be used for this purpose is thus very limited. In this section, we summarize the most important contributions of the techniques that, from our standpoint, contributed the most to our understanding of interleaflet coupling in model membranes.

Imaging

Direct visualization of lipid domain registration can be accomplished by AFM-based approaches or several different variations of fluorescence microscopy. It requires, however, the ability to detect a third intermediate state that might arise from having a domain in one leaflet without a counterpart in the opposing layer. In practice, this is accomplished by measuring the height of an SPB (thickness) with AFM or the fluorescence intensity arising from both leaflets in a fluorescence microscopy experiment (**Figure 3**).

Due to its high 3D resolution, AFM has been the most used imaging tool to study interleaflet coupling. The general coupling

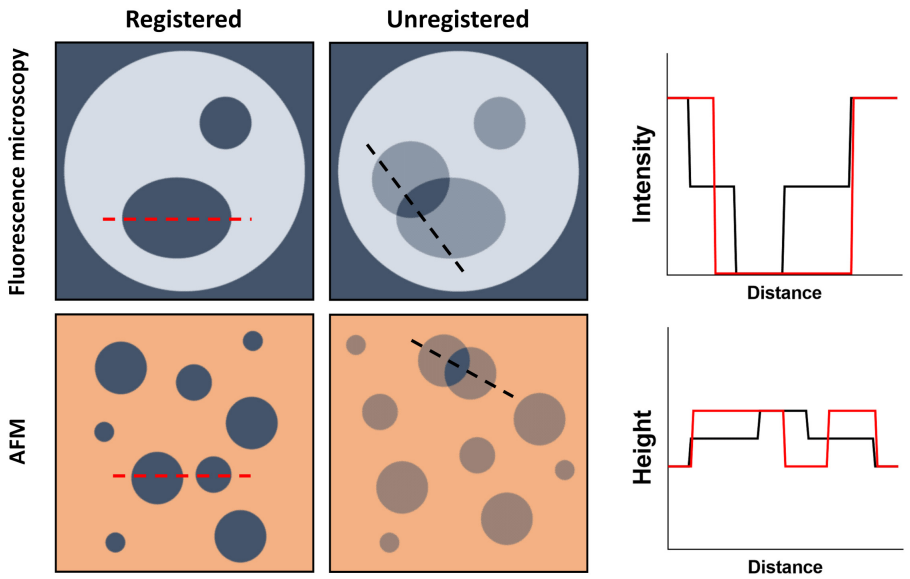

FIGURE 3 | Schematic representation of the direct visualization of lipid domains by fluorescence microscopy and AFM. **(Top)** Domain formation within GUVs can be assessed by fluorescence microscopy if, for example, a lipid dye with no affinity for the domains is used. For registered domains, the bulk membrane fluorescence is recorded while the domains have no intensity. Unregistered domains would present half the fluorescence intensity of the bulk membrane whenever there is no corresponding domain within the opposing leaflet. **(Bottom)** Using AFM, L_o nanodomains, for example, can be detected by measuring the height of the bilayer, since they will be thicker than the bulk membrane. Unregistered domains would however present an intermediate membrane height resulting from the opposing bulk membrane not contributing to the thickness increase.

of both lipid monolayers has been studied by tracking the temperature-induced phase transition of the bilayer (thickness). Several studies reported two transition temperatures instead of one, meaning that both leaflets would respond independently (uncoupled) to variations in temperature (Keller et al., 2005; Seeger et al., 2009). However, it is now evident that interleaflet coupling in supported bilayers greatly depends on the SPB preparation conditions and the strength of the interaction between the solid support and the proximal leaflet (type of and distance from the support). It was shown, for example, that by increasing the preparation temperature of 1-palmitoyl-2-oleoyl-*sn*-glycero-3-phosphoethanolamine (POPE)/1-palmitoyl-2-oleoyl-*sn*-glycero-3-phospho-(1′-rac-glycerol) (POPG) SPBs (assembled on mica by vesicle fusion), it is possible to couple both monolayers and thus obtain a single-phase transition for the bilayer, accompanied by the formation of registered domains (Seeger et al., 2009). Interestingly, assembling the same bilayer onto a silicon oxide solid support always resulted in a single temperature-induced phase transition independently of the preparation procedure, pointing to coupling of both leaflets (Seeger et al., 2010).

It is then expected that studying micro- and nanodomain interleaflet coupling in SPBs will also be affected by the same additional contingencies. Indeed, Lin et al. (2006) have shown that using three distinct preparation procedures to form 1,2-dilauroyl-*sn*-glycero-3-phosphocholine (DLPC)/1,2-distearoyl-*sn*-glycero-3-phosphocholine (DSPC) supported bilayers resulted in different patterns of DSPC-enriched gel domain registration: all registered (1.8 nm above the DLPC surroundings), all unregistered (1.2 nm above), and registered/unregistered (1.8 and 1.1 nm above, respectively). Apart from the preparation protocol, the distance (d) at which the bilayers are assembled onto the support also seems to greatly interfere with the degree of domain registration, as clearly demonstrated by Garg et al. (2007). In their work, 1-stearoyl-2-oleoyl-*sn*-glycero-3-phosphocholine (SOPC):eggSph:Chol (1:1:1) SPBs were prepared using a solid support (d = 15 Å) or a hydrophilic polymer cushion at d = 30 Å or d = 58 Å. Using epifluorescence microscopy, the authors show that complete registration of L_o domains across the bilayer could only be achieved when the bilayer was sufficiently decoupled from the solid support, in this case at 58 Å (Garg et al., 2007).

Although a systematic study of interleaflet coupling at different lipid compositions is still missing, several imaging studies have over the years retrieved pertinent information on particular aspects of domain registration. For example, DOPC:Sph supported bilayers contain domains that extend 1 nm over the bulk fluid membrane (Rinia et al., 2001). However, intermediate heights are also detected, suggesting that domains in both monolayers are independent from each other and thus uncoupled. Interestingly, when cholesterol is included in the bilayer [DOPC:Sph (1:1) + 25 mol% Chol], these intermediate height levels are no longer detected and the domains appear 0.8 nm above the overall membrane, indicating that cholesterol is involved in L_o domain registration (Rinia et al., 2001). Since cholesterol flip-flop is already excluded as a possible mechanism for cholesterol-induced interleaflet coupling (May, 2009), these results tend to support coarse grain simulations showing that

cholesterol might be sandwiched between both leaflets and by that promote domain registration (see section "Cholesterol") (Thallmair et al., 2018; Weiner and Feigenson, 2018).

Nevertheless, moving from SPBs to free-standing bilayer models, and thus avoiding the effect of the support, seems to result in more consistent data. In 1,2-diphytanoyl-*sn*-glycero-3-phosphocholine (DiphyPC)/1,2-dipalmitoyl-*sn*-glycero-3-phosphocholine (DPPC)/Chol vesicles (different compositions along a tie-line), as well as cell-derived giant plasma membrane vesicles (GPMVs), lipid domains appear always in-register along the bilayer normal (Cornell et al., 2018). In practice, no intermediate fluorescence intensity levels were observed, confirming the interleaflet coupling of the domains both in giant unilamellar vesicles (GUVs) and GPMVs (Cornell et al., 2018). Similar results were obtained in GUVs composed of DLPC/DPPC/Chol (Korlach et al., 1999). Furthermore, when directly compared, vesicles and SPBs present a very different behavior. Contrary to what is observed in GUVs, phase-separated SPBs composed of DOPC:DPPC:Chol and DOPC:brainSph:Chol are static and do not couple across the bilayer over an experimental timescale of 2–3 h (Stottrup et al., 2004).

Overall, most fluorescence microscopy and AFM data show that micro- and nanodomains in both leaflets are coupled across the bilayer both in free-standing vesicles and in SPBs where the support does not play a significant role.

Shear Stress Experiments

The aim of a shear stress experiment is to measure the shear that is required to move microdomains in an SPB out of registry (Blosser et al., 2015). The shear is applied by a hydrodynamic flow above the lipid bilayer. A 10 μm large domain in an SPB that is 1 nm apart from the solid surface is exposed to an effective friction that is approximately 1,000 times larger than the interleaflet friction (Bayerl and Bloom, 1990; Kiessling and Tamm, 2003). Consequently, the collective motion of the lipids in the lower leaflet is inhibited and remains hindered even when the shear is applied.

Shear stress experiments show that the shear required to deregister domains increases with the decrease in domain size (Blosser et al., 2015). This suggests that nanodomains (<200 nm diameter) must be registered. However, since the experiments were carried out in a relatively narrow range of domain sizes (1.5–6 μm), interleaflet coupling of lipid domains at the nanoscale is solely inferred by extrapolating these results across a wider size range. Nevertheless, this consideration is fairly useful as it allows at least a partial characterization of the nanodomains, which is generally difficult due to their small size.

Förster Resonance Energy Transfer Analyzed by Monte Carlo Simulations

As described above, studying interleaflet coupling of nanodomains requires high spatial resolution to allow the distinction of registered and unregistered domains within the membrane. Recently, we have shown that MC-FRET fulfills such requirements (Vinklárek et al., 2019). In the past, we have mainly used the method to determine the size of nanodomains and the total area occupied by these lipid domains (Šachl et al., 2015; Amaro et al., 2016; Koukalová et al., 2017). However, when an appropriate donor/acceptor pair is used, MC-FRET can also resolve interleaflet coupled from independent nanodomains. More specifically, MC-FRET relies on the use of fluorescently labeled lipids (which act as either donors or acceptors for energy transfer) with high affinity for the nanodomains (**Figure 4**) (Šachl et al., 2011, 2012). Thus, in the presence of these nanodomains, both donors and acceptors accumulate locally, leading to an efficient FRET process. Importantly, if the donor/acceptor pair is selected so that its Förster radius matches the thickness of the lipid bilayer, FRET will occur not only within the same leaflet but also across the membrane, from one leaflet to the other (**Figure 5**) (Vinklárek et al., 2019). These FRET events along the membrane normal make it then possible to study interleaflet coupling of nanodomains, since their frequency depends on the spatial interleaflet organization of the domains.

As shown on **Figure 5**, the outcome of an MC-FRET measurement is the time-resolved fluorescence decay of donors recorded in the presence of acceptors (Valeur, 2001). As a rule of thumb, the average lifetime of the donors is shorter and the decay faster the more often FRET occurs. Importantly, the decay becomes significantly faster when nanodomains are formed, with the extent to which this happens depending on their interleaflet arrangement: the highest when nanodomains are registered and the lowest in case of anti-registration (**Figure 5**). The shape of the decay thus contains information not only about the nanodomain size (expressed in terms of nanodomain radius R_D) and the total area occupied by the nanodomains but also on their interleaflet coupling.

Using this method, we were able to show that nanodomains found in DOPC/Chol/SM bilayers containing 10 mol% of oxidized phospholipids are registered for a broad range of nanodomain sizes ranging from 10 to 160 nm (Vinklárek et al., 2019). The possibilities that the nanodomains in each monolayer were independent of each other, anti-registered or in partial registration were clearly excluded. Therefore, this work represents the first experimental evidence that nanodomains, like microdomains, are registered in free-standing bilayers for a broad spectrum of nanodomain sizes. Additionally, it is worth noting that MC-FRET is not limited to symmetric bilayers. Studies are underway which could demonstrate that MC-FRET can be used to study formation of nanodomains individually in each leaflet.

Diffusion Techniques

Lipid domain coupling across the membrane implies that any hinderance in lipid diffusion (due to nanodomain formation) in one leaflet must be accompanied by an equivalent effect in the opposing layer. In principle, diffusion techniques such as FCS or single-particle tracking (SPT) can be used to retrieve reliable information on the extent of domain registration if both leaflets can be measured independently. This can be achieved by either preparing asymmetric bilayers with distinct labeled lipids in each layer or by obstructing lipid diffusion in one side of the bilayer and tracking how it translates to the opposing leaflet. A good example is the use of FCS to measure lipid diffusion on

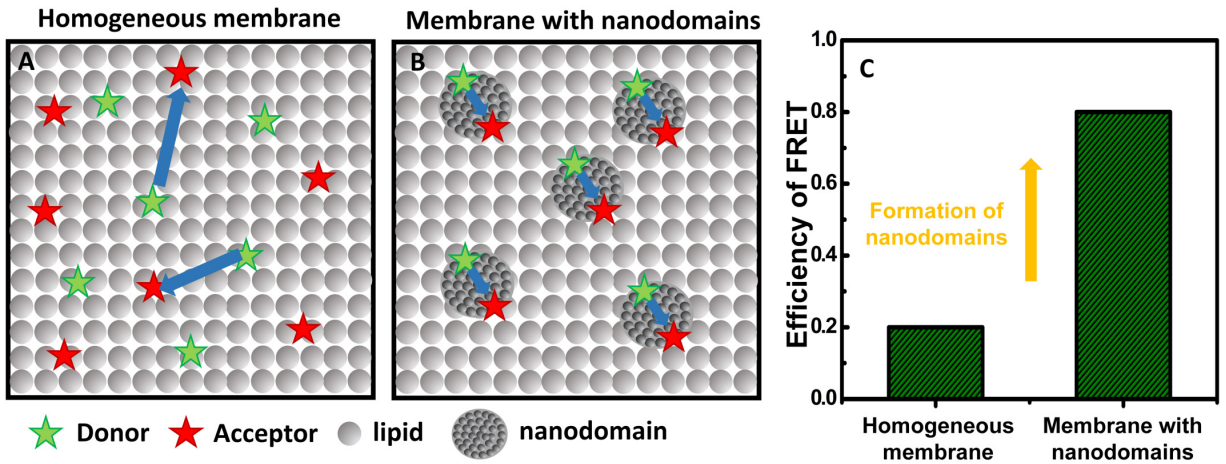

FIGURE 4 | Basic principles of MC-FRET for detection of nanodomains. **(A)** At a sufficiently high acceptor concentration in the bilayer, FRET between donors (green stars) and acceptors (red stars) occurs. **(B)** If donors and acceptors with high affinity for nanodomains are used, the presence of nanodomains leads to accumulation of donors and acceptors in the nanodomains, and consequently to a more efficient FRET. **(C)** The efficiency of FRET on a homogeneous vs a heterogeneous membrane with nanodomains.

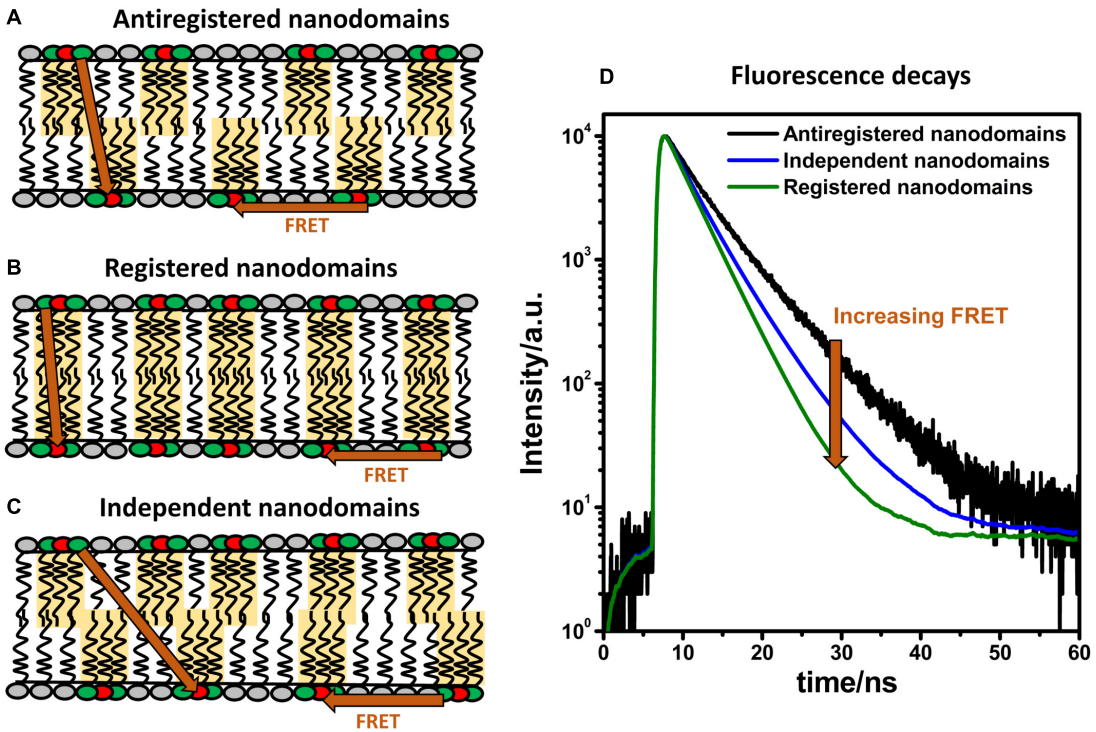

FIGURE 5 | FRET and domain registration. In a lipid bilayer, FRET (indicated by orange arrows) occurs within the same leaflet (intra-FRET) but also from one leaflet to the other one (inter-FRET). The efficiency of FRET, measured by time-resolved spectroscopy, depends on mutual organization of nanodomains. The efficiency of FRET is the lowest when nanodomains are in antiregistration **(A)**, intermediate when they are independent **(B)**, and the highest when the nanodomains are registered **(C)**. Time-resolved fluorescence decays of donors in the presence of acceptors shown on panel **(D)** report on the kinetics of deexcitation and contain information about the size and concentration of nanodomains and their interleaflet organization.

asymmetric vesicles with the inner leaflet composed of PC lipids [labeled with 1,2-dioleoyl-*sn*-glycero-3-phosphoethanolamine (7-nitro-2-1,3-benzoxadiazol-4-yl), NBD-DOPE] and the outer leaflet comprising Sph (labeled with Atto647-Sph) (Chiantia and London, 2012). In this study, the authors tested DOPC, OMPC, POPC, and SOPC (increasing T_m) in the inner layer and brain Sph (shorter chain and weak interdigitation), milk Sph (longer chain and strong interdigitation), and synthetic C24:0 Sph on

the outer leaflet. The presence of Sph decreases the diffusion within the outer leaflet and can then be used to study if and how this decrease translates to a slower lateral diffusion within the inner leaflet, i.e., to understand if the leaflets are coupled (see section "Chain Interdigitation" for details on interdigitation). While the above-mentioned FCS study required the formation of bilayers which are selectively labeled either in the inner or outer layer, fluorescence lifetime correlation spectroscopy (FLCS) (Kapusta et al., 2007) allows to simultaneously monitor the diffusion in both layers labeled with the same fluorescently labeled lipid analog. The main requirement for such FLCS experiment is to create a difference in the fluorescence lifetime of the dye when located in one of the two lipid layers. One possibility is to use potassium iodide to reduce the fluorescence lifetime in one layer, which might in turn change the diffusion properties of that layer (Vácha et al., 2009; Otosu and Yamaguchi, 2019). Metal induced energy transfer (MIET) represents a more universal approach. Here, the lipid bilayers are adsorbed onto an indiumtinoxide-covered glass (Benda et al., 2006; Przybylo et al., 2006). More recently, graphene has also been used as the "metal" layer yielding distinct lifetime differences between both layers (Ghosh et al., 2019). Although no systematic experiments on interleaflet coupling were performed so far, we believe that the combination of FLCS with MIET will be a useful tool to quantify interleaflet coupling.

Apart from using asymmetric bilayers, binding of proteins and polymers has been used to hinder lipid diffusion in one leaflet and study interleaflet coupling. For example, binding of poly-L-lysine (PLL) to one leaflet of a planar lipid bilayer was shown by FCS to decrease lipid diffusion and to attract a PLL-bound slow-diffusing patch on the opposing leaflet, resulting in nanodomain registration (Horner et al., 2009). In a different approach using wide-field single molecule fluorescence imaging, pinning of an SOPC bilayer through polymer-tethered phospholipids, and thus hindering the diffusion of the proximal leaflet, also resulted in a slower diffusion of the lipopolymer-free leaflet (Deverall et al., 2008). Overall, nanodomain interleaflet coupling, as seen by different diffusion techniques, appears to result from the balance between the freedom of the membrane to undulate and the energy required to maintain the domains in-register across the bilayer.

Small-Angle Neutron Scattering

Together with the approaches described above, neutron scattering has been extensively used to study lipid domain formation at the nanoscale (Czeslik et al., 1997; Nicolini et al., 2004; Pencer et al., 2005, 2006, 2007a,b; Hirai et al., 2006; Masui et al., 2006, 2008; Krivanek et al., 2008; Vogtt et al., 2010; Heberle et al., 2013). Since neutrons are mainly scattered by their interaction with atomic nuclei (Pabst et al., 2010), the scattering process has very different sensitivities for isotopes of the same element. Thus, an obvious advantage over fluorescence techniques is the minimal perturbation that results from not using probes to address, for example, membrane lateral organization. In biomolecular studies, such as lipid domain formation, hydrogen and deuterium are the most used isotopes, with coherent neutron scattering lengths of −3.742 and −6.674 fm, respectively (Marquardt et al., 2015). In general terms, this scattering contrast forms the basis of any small-angle neutron scattering (SANS) experiment and can be optimized by either varying the hydrogen/deuterium ratio of the buffer and/or by selectively deuterating specific parts of a particular component of the studied system (Pan et al., 2013). In membrane organization studies, both the headgroup and the acyl chains can be labeled.

Nevertheless, studying nanodomain formation with SANS greatly depends on matching the scattering from the solvent and the lipid vesicles and on enhancing the contrast between the domain and nondomain phases. Otherwise, the contrast between the bulk solution and the vesicles would overwhelm any signal arising from lipid domain formation (Pan et al., 2013). Therefore, the main goal of a typical SANS experiment is to obtain a strong scattering signal arising from the contrast between the bulk membrane and the lipid nanodomains. This is frequently achieved by deuterating a specific lipid species with high affinity for the nanodomains, e.g., the acyl chain of the lipid with the highest melting temperature. In this way, the scattering signal would depend only on the size, composition, and shape of the nanodomains. For comprehensive reviews on the use of SANS to detect nanodomain formation (see Pan et al., 2013; Marquardt et al., 2015).

Recently, SANS has also been shown to be suitable for addressing coupling of nanodomains across the bilayer (Nickels et al., 2015a; Heberle et al., 2016; Heberle and Pabst, 2017; Eicher et al., 2018). The experimental strategy often used is based on rendering one of the phases invisible to neutrons by contrast matching (either the nanodomains or the bulk membrane) and on comparing the bilayer thicknesses and bending moduli of both homogeneous and heterogeneous vesicles. Using this strategy, Nickels et al. (2015a) were able to demonstrate that L_d nanodomains (∼13 nm) within POPC/DSPC/Chol large unilamellar vesicles (LUVs; 60 nm) were in-register across the bilayer. By contrast matching the L_o phase of the phase-separated vesicles, the resulting scattering signal allowed the determination of the thickness and the bending modulus of only L_d nanodomains. The obtained values were identical to the ones obtained for the bulk L_d phase of the homogeneous vesicles, confirming interleaflet coupling and the concomitant registration of the nanodomains. Since the L_o phase was not contributing to the scattering wave in this case, domain antiregistration would alternatively result in bilayer thickness values corresponding to a monolayer (only the L_d leaflet would be detected) and higher bending modulus of the L_d nanodomains, since they would be across the L_o phase on the opposing leaflet. Similar strategies have also shown, e.g., that disordered inner leaflets can fluidize ordered nanodomains within the outer layer (Heberle et al., 2016) and that intrinsic lipid curvature (e.g., POPE) can play a role in coupling both leaflets (Eicher et al., 2018). Since both these studies use asymmetric bilayers, they are discussed in more detail in section "Domain Registration in Asymmetric Bilayers."

Molecular Dynamic Simulations

Although computer sciences have recently experienced unprecedented development, computational power is still very limited for applications related to nanodomain coupling.

Most importantly, the recently available computational power does not allow (1) to include enough lipid molecules into an atomistic simulation to simulate multiple domains at the same time; and (2) to simulate domain registration for a sufficiently long time. Despite these shortcomings, MD simulations represent an important complementary approach in domain studies, because they can, apart from the above-mentioned continuum theories (see section "Membrane Undulations"), provide a detailed molecular view.

To better demonstrate the limitations of MD simulations, let us assume a simulation box that contains a bilayer in which each leaflet contains five nanodomains with 10 nm radius occupying in total 50% of the bilayer surface. Under these conditions, the entire box contains approximately 8,700 lipid molecules, out of which 440 molecules belong to just one nanodomain. Furthermore, a molecule needs approximately 11 μs to fully cross a nanodomain and 90 μs to reach the other end of the box. The possibilities of an atomistic simulation are clearly determined by considering a typical simulation which runs for around 3 μs and contains about 512 lipids (Enkavi et al., 2019).

Scientists usually overcome this limitation by using coarse grain simulations, which inevitably lead to less accurate results. Together with the difficulties to account for macroscopic phenomena (such as membrane undulations) in the simulations, this may explain why nanodomain antiregistration has mainly been observed by *in silico* approaches (Stottrup et al., 2004; Crane et al., 2005; Stevens, 2005; Lin et al., 2006; Bennun et al., 2007; Perlmutter and Sachs, 2011; Williamson and Olmsted, 2015a,b). Specifically, Perlmutter and Sachs (2011) studied registration of nanodomains by coarse grain simulations in various mixtures of saturated (di-16:0 or di-20:0) and unsaturated (di-18:2) lipids with cholesterol. They observed almost perfect antiregistration in the mixtures that contained the same amounts of L_o and L_d phases. As shown on **Figure 2**, perfect antiregistration is only possible in such mixtures, leading to the release of stress enforced onto the membrane by hydrophobic mismatch. If the L_o content is higher or lower than the L_d, it inevitably leads at least to partial phase overlap or to a better mixing of the saturated and unsaturated lipids, resulting in the suppression of phase separation (Perlmutter and Sachs, 2011). Interestingly, when the authors increased the content of L_o phase, they observed some regions with L_o/L_o overlap but also increased mixing of saturated with unsaturated lipids at domain boundaries. On the other hand, when the content of L_d was higher than the content of L_o, frequent registration of L_d regions was detected. In a different work, long-term domain antiregistration has also been observed by Stevens, who reported transbilayer matching of lipids with short tails with those possessing long tails (Stevens, 2005). In other cases, antiregistered nanodomains were found only as metastable structures during nucleation of nanodomains and the consequent formation of the final equilibrium state comprising registered nanodomains (Williamson and Olmsted, 2015a,b).

In contrast to the above mentioned work based on coarse grain simulations, Javanainen et al. (2017) performed atomistic MD simulations on an experimentally well characterized binary system of DPPC and cholesterol. The simulation was 1.3 μs long and contained 1,000 lipids. A phase diagram for this system is available and predicts the coexistence of L_o and L_d phases at approximately 10 to 20 mol% of cholesterol and temperatures slightly above the transition temperature of DPPC. Importantly, the authors observed the formation of nanodomains with 5 nm radius and a strong correlation in lipid chain ordering indicative of domain registration. Similarly, registered nanodomains were observed in a coarse grain simulation of a DPPC/DOPC/Chol (64/16/20) bilayer (Thallmair et al., 2018). In this work, cholesterol sandwiched between the leaflets was suggested to contribute to the registration of nanodomains. In addition, using both coarse-grained and all-atom MD simulations of membranes composed of DPPC, cholesterol and 1,2-diundecanoyl-*sn*-glycero-phosphocholine (DUPC; including variations on the position of the double bonds), Zhang and Lin (2019) have also shown L_o domain registration depending on the position of the acyl chain *cis* double bonds. Given the great diversity of simulation results, it seems that more atomistic simulations will need to be carried out, especially for the membranes that are according to coarse grain simulations prone to the formation of antiregistered nanodomains.

DOMAIN REGISTRATION IN ASYMMETRIC BILAYERS

Despite the existence of protocols for preparation of asymmetric vesicles, studies focusing on interleaflet coupling of nanodomains in asymmetric bilayers are rare. Interesting work has been carried out on the extent to which the properties of one leaflet are influenced by the different properties of the opposing leaflet. Kiessling et al. (2006) showed more than a decade ago that L_o microdomains in one layer induce phase-separation in the opposing layer composed of porcine brain PC, PE, PS, and cholesterol. However, the same domains are not enough to form domains in the opposite leaflet consisting solely of POPC and cholesterol. Similarly, Collins and Keller (2008) demonstrated that asymmetric bilayers composed of varying amounts of DiphyPC, DPPC, and cholesterol, in which only one leaflet has a composition that drives phase-separation, can either be microscopically phase-separated, or homogeneous, depending on the ratio between the three lipids. Recently, Heberle et al. (2016) performed SANS experiments on asymmetric vesicles where the outer leaflet was composed of DPPC and the inner leaflet of POPC. The authors managed to show that the order of the outer leaflet gel domains was significantly decreased by coupling to the inner leaflet POPC. In contrast, the DPPC gel domains did not alter the packing density of the POPC inner leaflet. Remarkably, experiments performed by Wang and London (2018) indicate that increasing the ability of the outer leaflet to form L_o phase by itself (e.g., increasing the high-T_m PC content) decreases the inhibition of L_o domain formation in the outer leaflet by inner leaflet lipids.

Based on these experiments, it seems that both the chemical composition and temperature are important parameters that govern interleaflet coupling. Wan et al. (2008) showed that interleaflet coupling strongly depends on intrinsic chain melting temperatures (thereby on the chemical composition

and temperature) and to a much lesser extent on the specific headgroup classes. Interestingly, it follows from a recent work by Eicher et al. (2018) that interleaflet coupling is also mediated by bilayer curvature. In this work, the authors prepared asymmetric LUVs where the inner and outer leaflets were composed of POPE and POPC, respectively. Strong coupling was demonstrated by cooperative melting and similar packing of both inner and outer leaflets. In contrast, when the composition of both leaflets was reversed, i.e., the inner leaflet contained POPC and the outer one POPE, the melting transition became broad and the coupling disappeared. The authors interpreted their results by a less convenient arrangement of POPE in the latter case, which – despite its conical shape was forced to reside in the outer layer. These data thus provide evidence for curvature-mediated interleaflet coupling in asymmetric bilayers.

Overall, the above mentioned experimental results suggest that some degree of interleaflet coupling indeed exists but is not very strong. If both layers showed no coupling or were only weakly coupled, they would have to be completely independent of each other. Nearly all the above experimental results speak against this conclusion. On the other hand, very strong coupling would predict that – irrespective of bilayer composition – both layers would need to behave as one single unit with a sharp melting temperature roughly corresponding to an intermediate value for both leaflets. This is evidently not the case. Therefore, the level of interleaflet coupling must be intermediate. This is concomitant with the observed characteristic behavior which includes: considerable sensitivity of coupling to external parameters such as temperature, and a strength of coupling that is dependent on acyl chain composition, packing of individual leaflets, bilayer curvature and the overall chemical composition of the lipid bilayer.

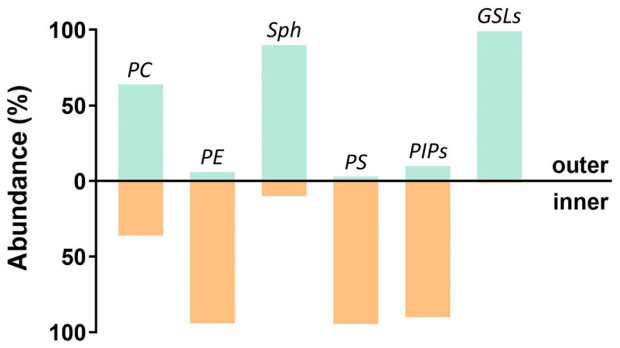

FIGURE 6 | Plasma membrane asymmetry. Schematic representation of the plasma membrane lipid composition. Distribution in both leaflets is depicted as a percentage of the total lipid class. Based on (Zachowski, 1993; Lingwood, 2011; Fujimoto and Parmryd, 2017).

IMPLICATIONS FOR CELLULAR MEMBRANES

Cell membranes are much more complex when compared to model membranes (**Figure 6**). They contain not only a larger amount of different lipids, but also proteins that can have a significant influence on the resulting strength of interleaflet coupling. Nevertheless, the experiments performed on model systems show that coupling is strong enough, even in the absence of proteins, to induce domain registration in a wide range of domain sizes. Except for a few MD simulations and experimental AFM studies (Rinia et al., 2001; Stevens, 2005; Lin et al., 2006; Garg et al., 2007; Perlmutter and Sachs, 2011), micro- as well as nanodomains in symmetric bilayers have been mostly found in registration. Such behavior obviously requires an effective mechanism that can register domains irrespective of their size. So far, two mechanisms have been identified as being the most efficient: membrane undulations and line tension, which complement each other (see sections "Line Tension" and "Membrane Undulations" for details). On the other hand, the importance of acyl chain interdigitation as an efficient coupling mechanism has not yet been fully established, as discussed in section "Chain Interdigitation."

It can be expected that in cellular membranes the differences in lipid packing and order between nanodomains and the remaining bulk membrane will be less pronounced than in model membranes. Nevertheless, we have recently reported that nanodomains with subtle differences to their surroundings are also formed in model systems and that these nanodomains are interleaflet coupled (Koukalová et al., 2017). This implies that large differences between the physical properties of the nanodomain and non-domain parts are generally not required, and that domain registration could be a part of biological membranes as well. Since cell membranes also oscillate and contain areas with increased line tension, the mechanism by which such in-register domains are formed in cellular membranes can hypothetically be based on similar principles, although other mechanisms are also very likely to contribute.

It should not be overlooked that biological membranes are asymmetric, contrasting with the most used model systems (**Figure 6**). Synthetic asymmetric membranes emerged as a completely new type of membrane mimetics about 10 years ago and have since become very popular. Experiments performed in recent years have shown that interleaflet coupling is strong, but not always strong enough that domains formed in one layer would induce formation of domains in the other layer of generally different composition. Cases have been reported where the presence of lipid domains in one layer resulted in different effects within the opposing layer: (1) formation of domains (Garg et al., 2007; Collins and Keller, 2008; Kiessling et al., 2009), (2) formation of areas of reduced lipid mobility (Chiantia and London, 2012), or (3) no change detected (Eicher et al., 2018). These results indicate that individual leaflets interact, but the final equilibrium state depends on temperature, acyl chain composition, packing of individual leaflets, bilayer curvature, and the overall chemical composition.

The conditions where a small change in one or more physical parameters can modulate the strength of coupling seem ideal for lipid domain registration to play a non-negligible role within cell

membranes. For instance, it has been suggested that interleaflet coupling could be used to transmit signals from the outer to the inner membrane leaflet. This mechanism has often been discussed in connection with signaling pathways initiated by the binding of protein ligands to the outer layer (Klokk et al., 2016; Skotland and Sandvig, 2019). Probably the best-known examples are the binding of Cholera toxin to ganglioside GM_1 (Wernick et al., 2010), Shiga toxin to globotriaosylceramide Gb_3 (Johannes and Römer, 2010; Bergan et al., 2012), and the binding of lectins to GSL (Wang et al., 2009; Russo et al., 2016; Ledeen et al., 2018). Moreover, the virus SV40 is known to multivalently bind GM_1 (Ewers et al., 2010). In the case of Cholera toxin, it has been shown experimentally that its binding to GM_1 induces formation of L_o nanodomains (Štefl et al., 2012). The presence of such regions with impeded mobility of lipids and proteins is sufficient to dynamically segregate proteins into these regions (Nicolau et al., 2006). The existence of such regions, with possible registration across the bilayer, could therefore facilitate nanoscale protein–protein interactions and be important for many signaling cascades.

Nevertheless, the mechanism through which lipid nanodomain formation in one leaflet is then transferred to the opposing lipid layer ultimately leading to signal transduction across the membrane in living cells is still not yet clear. More specifically, both peripheral and transmembrane proteins, due to their abundance and function, are bound to play a role in the overall process. One example is the influence the actin cytoskeleton seems to have in the organization of outer plasma membrane lipids and GPI-anchored proteins. Although the experimental evidence is still sparse, lipid pinning of inner plasma membrane lipids (and other proteins) by the cytoskeleton has been suggested to be involved in the transduction process. In general, pinning accounts for the reduced or absent mobility of membrane components, which in turn alters the mixing entropy of the membrane and could lead to phase separation. MD simulations have shown that immobile molecules can act as obstacles to the diffusion of the remaining mobile membrane components, ultimately resulting in the formation of in register nanodomains (Fischer et al., 2012). At the plasma membrane of living cells, the actin cytoskeleton has been shown to interact directly with negatively charged lipids such as phosphatidylinositol 4,5-bisphosphate (PIP_2), reducing their mobility and inducing the formation of GM_1-containing L_o nanodomains in the outer leaflet (Dinic et al., 2013; Fujimoto and Parmryd, 2017). This explains why, in plasma membrane blebs lacking actin cytoskeleton filaments, the fraction of these GM_1-containing L_o domains significantly decreases (Dinic et al., 2013). It is worth noting that pinning, or reduced lipid mobility due to protein binding, also occurs within the outer plasma membrane leaflet. As previously stated, the most studied case is the cross-linking of GM_1 and the consequent formation of L_o patches frequently including GPI-anchored proteins – the so-called rafts (Dinic et al., 2013; Fujimoto and Parmryd, 2017). Interestingly, some studies seem to indicate that upon cross-linking (pinning), GM_1 acyl chains might stretch and increase the contacts with inner leaflet lipids at the bilayer midplane (Spillane et al., 2014; Sun et al., 2015). This, as discussed in section "Chain Interdigitation," would definitely favor registration of nanodomains formed through, e.g., binding of cholera toxin to the outer leaflet GM_1 molecules. The importance of membrane midplane interactions became even more evident in a very comprehensive study by Raghupathy et al. (2016). Using a combination of FCS, fluorescence recovery after photobleaching (FRAP), and anisotropy measurements in CHO cells, as well as lipidomics and atomistic MD simulations, the authors show that not only long saturated acyl chains are required to patch GPI-anchored proteins but also PS molecules with long acyl chains at the inner plasma membrane leaflet are required for domain interleaflet coupling. Moreover, MD simulations showed that immobilizing long saturated acyl chains, irrespectively of the leaflet, stabilizes cholesterol-dependent transbilayer interactions within patches of the membrane with biophysical properties characteristic of a L_o phase (Raghupathy et al., 2016). This work is in great alignment with the results obtained in model systems, reinforcing the role of membrane midplane interactions in nanodomain registration (see sections "Chain Interdigitation" and "Cholesterol"). Apart from protein–lipid interactions, also cell adhesion to biological or non-biological surfaces has been shown to induce lipid nanodomain registration (Gordon et al., 2008). In this case, interaction with the surface leads to an increased stiffness and decreased fluctuations at the contact regions. In other words, cell adhesion could promote lipid demixing and domain formation in the outer membrane leaflet. As discussed in sections "Line Tension" and "Membrane Undulations," a local increase in line tension and decreased undulations could then induce the formation of nanodomains in the opposing leaflet, even if the lipid composition is not prone to phase-separate (Gordon et al., 2008).

In addition to peripheral proteins, also transmembrane proteins have been suggested to help forming and stabilizing lipid nanodomains across the membrane, thus being intimately involved in interleaflet coupling and signal transduction. Recently, using a mean-filed lattice-based model, Bossa et al. (2019) suggest that the effect of introducing a transmembrane domain (TMD) within the membrane very much depends on the strength of the lipid–protein interactions. The authors show that, if the interactions are weak, lipids get diluted by the TMD and no domains are formed. If, on the other hand, the interaction strength is in the range of lipid–lipid interactions (responsible for domain formation), then the TMD has the ability to couple the domains across the bilayer (Bossa et al., 2019). Nevertheless, the most common effect of incorporating a TMD within a membrane is the possible hydrophobic mismatch and the consequent increase in line tension. However, since transmembrane proteins have frequently very important and conserved functions (such as membrane receptor), cells have evolved to decrease this energetic penalty, by properly modulating the orientation of the TMDs. For example, negatively charged lipids (e.g., PS and PIP_2) of the inner plasma membrane leaflet associate mainly with positive regions of TMDs, in order to accommodate the local protein charge and hydrophobic thickness (von Heijne and Gavel, 1988; Gafvelin et al., 1997; Lin and London, 2014; Nickels et al., 2015b). Besides charge, also the thickness of TMDs seems to be adjusted to membrane asymmetry and involved in lipid domain

coupling. It has been suggested that thin TMDs (rich in Ala/Gly) might be more easily incorporated into ordered and tightly packed domains than thicker TMDs rich in Leu/Phe. Indeed, Lorent et al. (2019) have recently shown that plasma membrane TMDs are in general asymmetric. Specifically, to avoid great perturbations of the outer, tightly packed, plasma membrane leaflet, exoplasmic portions of TMDs tend to be thinner. This observation suggests that, by keeping the asymmetry, TMDs could, in principle, couple ordered lipid nanodomains on the exoplasmic leaflet (e.g., containing GM_1) with more fluid patches at the cytoplasmic leaflet (e.g., containing PIP_2), thus assuring direct and efficient signal transduction. In addition, recent MD simulations also show that by migrating to lipid domain boundaries, transmembrane proteins are able to reduce the line tension in 25–35%, once again suggesting the energetic balance resulting from having a TMD within the membrane might indeed stabilize the lipid domains and their registration (Bandara et al., 2019).

In conclusion, it should be noted that this review focused mainly on domain interleaflet coupling induced by lipids in protein-free bilayers. It is clear, however, that particular membrane proteins can play a significant role in nanodomain coupling. Specially, transmembrane proteins can act as transducers of lipid assembly, by not only influencing interleaflet coupling and nanodomain registration but also by modulating the size of these domains (Yethiraj and Weisshaar, 2007), attracting some lipids/proteins (Anderson and Jacobson, 2002; Marsh, 2008) or influencing mechanistic properties of lipid bilayers that are responsible for nanodomain coupling (see section "Theoretical Framework: Mechanisms Leading to the Nanodomain Registration"). Despite a clear significance of proteins for lipid domain interleaflet coupling, the literature on this topic is very limited. On the other hand, significant attention was paid to the formation of the so-called lipid shells around proteins (see Marsh, 2008 for a comprehensive summary). These shells can be characterized as regions with reduced lipid mobility and specific lipid order and composition. Nevertheless, and despite its biological importance, this field is relatively unexplored and should deserve more attention in the near future.

Overall, the purpose of this review was to provide the reader with a comprehensive biophysical view of the problematics of interleaflet coupling. So far, biophysical studies show that interleaflet coupling is strong enough to drive registration of lipid domains of any physically relevant size and that the strength of coupling depends on the specific conditions in which the membrane is currently found. Based on this knowledge, it seems likely that interleaflet coupling can play a significant role in cell membrane lateral organization and processes related to signal transduction across the membrane.

AUTHOR CONTRIBUTIONS

MS and RŠ conceived the idea and wrote the manuscript with the help of MH.

FUNDING

MH acknowledges GAČR grant 19-26854X. RŠ acknowledges GAČR grant 18-04871S. MS acknowledges European structural and investments funds in the frame of operational program research development and education: Project No. CZ.02.2.69/0.0/0.0/16_027/0008355.

REFERENCES

Akimov, S. A., Hlaponin, E. A., Bashkirov, P. V., Boldyrev, I. A., Mikhalyov, I. I., Telford, W. G., et al. (2009). Ganglioside GM1 increases line tension at raft boundary in model membranes. *Biochem. Suppl. Ser. A Membr. Cell Biol.* 3, 216–222. doi: 10.1134/S1990747809020159

Akimov, S. A., Kuzmin, P. I., Zimmerberg, J., and Cohen, F. S. (2007). Lateral tension increases the line tension between two domains in a lipid bilayer membrane. *Phys. Rev. E Stat. Nonlin. Soft Matter. Phys.* 75:011919. doi: 10.1103/PhysRevE.75.011919

Amaro, M., Šachl, R., Aydogan, G., Mikhalyov, I. I., Vácha, R., and Hof, M. (2016). GM1 ganglioside inhibits β-amyloid oligomerization induced by sphingomyelin. *Angew. Chem. Int. Ed.* 55, 9411–9415. doi: 10.1002/anie.201603178

Anderson, R. G. W., and Jacobson, K. (2002). Cell biology: a role for lipid shells in targeting proteins to caveolae, rafts, and other lipid domains. *Science* 296, 1821–1825. doi: 10.1126/science.1068886

Ayuyan, A. G., and Cohen, F. S. (2008). Raft composition at physiological temperature and pH in the absence of detergents. *Biophys. J.* 94, 2654–2666. doi: 10.1529/BIOPHYSJ.107.118596

Bandara, A., Panahi, A., Pantelopulos, G. A., Nagai, T., and Straub, J. E. (2019). Exploring the impact of proteins on the line tension of a phase-separating ternary lipid mixture. *J. Chem. Phys.* 150:204702. doi: 10.1063/1.5091450

Baumgart, T., Hess, S. T., and Webb, W. W. (2003). Imaging coexisting fluid domains in biomembrane models coupling curvature and line tension. *Nature* 425, 821–824. doi: 10.1038/nature02013

Bayerl, T. M., and Bloom, M. (1990). Physical properties of single phospholipid bilayers adsorbed to micro glass beads. A new vesicular model system studied by 2H-nuclear magnetic resonance. *Biophys. J.* 58, 357–362. doi: 10.1016/s0006-3495(90)82382-1

Benda, A., Fagul'ová, V., Deyneka, A., Enderlein, J., and Hof, M. (2006). Fluorescence lifetime correlation spectroscopy combined with lifetime tuning: new perspectives in supported phospholipid bilayer research. *Langmuir* 22, 9580–9585. doi: 10.1021/la061573d

Bennun, S. V., Longo, M. L., and Faller, R. (2007). Molecular-scale structure in fluid-gel patterned bilayers: stability of interfaces and transmembrane distribution. *Langmuir* 23, 12465–12468. doi: 10.1021/la701370t

Bergan, J., Dyve Lingelem, A. B., Simm, R., Skotland, T., and Sandvig, K. (2012). Shiga toxins. *Toxicon* 60, 1085–1107. doi: 10.1016/j.toxicon.2012.07.016

Blosser, M. C., Honerkamp-Smith, A. R., Han, T., Haataja, M., and Keller, S. L. (2015). Transbilayer colocalization of lipid domains explained via measurement of strong coupling parameters. *Biophys. J.* 109, 2317–2327. doi: 10.1016/j.bpj.2015.10.031

Bossa, G. V., Gunderson, S., Downing, R., and May, S. (2019). Role of transmembrane proteins for phase separation and domain registration in asymmetric lipid bilayers. *Biomolecules* 9:303. doi: 10.3390/biom9080303

Bretscher, M. S. (1972). Asymmetrical lipid bilayer structure for biological membranes. *Nat. New Biol.* 236, 11–12. doi: 10.1038/newbio236011a0

Capponi, S., Freites, J. A., Tobias, D. J., and White, S. H. (2016). Interleaflet mixing and coupling in liquid-disordered phospholipid bilayers. *Biochim. Biophys. Acta Biomembr.* 1858, 354–362. doi: 10.1016/j.bbamem.2015.11.024

Cebecauer, M., Amaro, M., Jurkiewicz, P., Sarmento, M. J., Šachl, R., Cwiklik, L., et al. (2018). Membrane lipid nanodomains. *Chem. Rev.* 118, 11259–11297. doi: 10.1021/acs.chemrev.8b00322

Chiantia, S., and London, E. (2012). Acyl Chain length and saturation modulate interleaflet coupling in asymmetric bilayers: effects on dynamics and structural order. *Biophys. J.* 103, 2311–2319. doi: 10.1016/j.bpj.2012.10.033

Chiu, S. W., Jakobsson, E., Subramaniam, S., and Scott, H. L. (1999). Combined Monte Carlo and molecular dynamics simulation of fully hydrated dioleyl and palmitoyl-oleyl phosphatidylcholine lipid bilayers. *Biophys. J.* 77, 2462–2469. doi: 10.1016/s0006-3495(99)77082-7

Collins, M. D. (2008). Interleaflet coupling mechanisms in bilayers of lipids and cholesterol. *Biophys. J.* 94, L32–L34. doi: 10.1529/biophysj.107.124362

Collins, M. D., and Keller, S. L. (2008). Tuning lipid mixtures to induce or suppress domain formation across leaflets of unsupported asymmetric bilayers. *Proc. Natl. Acad. Sci. U.S.A.* 105, 124–128. doi: 10.1073/pnas.0702970105

Cornell, C. E., Skinkle, A. D., He, S., Levental, I., Levental, K. R., and Keller, S. L. (2018). Tuning length scales of small domains in cell-derived membranes and synthetic model membranes. *Biophys. J.* 115, 690–701. doi: 10.1016/j.bpj.2018.06.027

Crane, J. M., Kiessling, V., and Tamm, L. K. (2005). Measuring lipid asymmetry in planar supported bilayers by fluorescence interference contrast microscopy. *Langmuir* 21, 1377–1388. doi: 10.1021/la047654w

Czeslik, C., Erbes, J., and Winter, R. (1997). Lateral organization of binary-lipid membranes—Evidence for fractal-like behaviour in the gel-fluid coexistence region. *Europhys. Lett.* 37, 577–582. doi: 10.1209/epl/i1997-00193-6

Devaux, P. F. (1991). Static and dynamic lipid asymmetry in cell membranes. *Biochemistry* 30, 1163–1173. doi: 10.1021/bi00219a001

Devaux, P. F., and Morris, R. (2004). Transmembrane asymmetry and lateral domains in biological membranes. *Traffic* 5, 241–246. doi: 10.1111/j.1600-0854.2004.00170.x

Deverall, M. A., Garg, S., Lüdtke, K., Jordan, R., Rühe, J., and Naumann, C. A. (2008). Transbilayer coupling of obstructed lipid diffusion in polymer-tethered phospholipid bilayers. *Soft Matter* 4, 1899–1908. doi: 10.1039/b800801a

Dietrich, C., Bagatolli, L. A., Volovyk, Z. N., Thompson, N. L., Levi, M., Jacobson, K., et al. (2001). Lipid rafts reconstituted in model membranes. *Biophys. J.* 80, 1417–1428. doi: 10.1016/s0006-3495(01)76114-0

Dinic, J., Ashrafzadeh, P., and Parmryd, I. (2013). Actin filaments attachment at the plasma membrane in live cells cause the formation of ordered lipid domains. *Biochim. Biophys. Acta Biomembr.* 1828, 1102–1111. doi: 10.1016/j.bbamem.2012.12.004

Eggeling, C., Ringemann, C., Medda, R., Schwarzmann, G., Sandhoff, K., Polyakova, S., et al. (2009). Direct observation of the nanoscale dynamics of membrane lipids in a living cell. *Nature* 457, 1159–1162. doi: 10.1038/nature07596

Eicher, B., Marquardt, D., Heberle, F. A., Letofsky-Papst, I., Rechberger, G. N., Appavou, M.-S., et al. (2018). Intrinsic curvature-mediated transbilayer coupling in asymmetric lipid vesicles. *Biophys. J.* 114, 146–157. doi: 10.1016/j.bpj.2017.11.009

Enkavi, G., Javanainen, M., Kulig, W., Róg, T., and Vattulainen, I. (2019). Multiscale simulations of biological membranes: the challenge to understand biological phenomena in a living substance. *Chem. Rev.* 119, 5607–5774. doi: 10.1021/acs.chemrev.8b00538

Esposito, C., Tian, A., Melamed, S., Johnson, C., Tee, S. Y., and Baumgart, T. (2007). Flicker spectroscopy of thermal lipid bilayer domain boundary fluctuations. *Biophys. J.* 93, 3169–3181. doi: 10.1529/biophysj.107.111922

Evans, E., Heinrich, V., Ludwig, F., and Rawicz, W. (2003). Dynamic tension spectroscopy and strength of biomembranes. *Biophys. J.* 85, 2342–2350. doi: 10.1016/S0006-3495(03)74658-X

Ewers, H., Römer, W., Smith, A. E., Bacia, K., Dmitrieff, S., Chai, W., et al. (2010). GM1 structure determines SV40-induced membrane invagination and infection. *Nat. Cell Biol.* 12, 11–18. doi: 10.1038/ncb1999

Fischer, T., Jelger Risselada, H., and Vink, R. L. C. (2012). Membrane lateral structure: the influence of immobilized particles on domain size. *Phys. Chem. Chem. Phys.* 14, 14500–14508. doi: 10.1039/c2cp41417a

Frolov, V. A. J., Chizmadzhev, Y. A., Cohen, F. S., and Zimmerberg, J. (2006). "Entropic traps" in the kinetics of phase separation in multicomponent membranes stabilize nanodomains. *Biophys. J.* 91, 189–205. doi: 10.1529/biophysj.105.068502

Fujimoto, T., and Parmryd, I. (2017). Interleaflet coupling, pinning, and leaflet asymmetry — major players in plasma membrane nanodomain formation. *Front. Cell. Dev. Biol.* 4:155. doi: 10.3389/fcell.2016.00155

Gafvelin, G., Sakaguchi, M., Andersson, H., and Von Heijne, G. (1997). Topological rules for membrane protein assembly in eukaryotic cells. *J. Biol. Chem.* 272, 6119–6127. doi: 10.1074/jbc.272.10.6119

Galimzyanov, T. R., Kuzmin, P. I., Pohl, P., and Akimov, S. A. (2017). Undulations drive domain registration from the two membrane leaflets. *Biophys. J.* 112, 339–345. doi: 10.1016/j.bpj.2016.12.023

Galimzyanov, T. R., Molotkovsky, R. J., Bozdaganyan, M. E., Cohen, F. S., Pohl, P., and Akimov, S. A. (2015). Elastic membrane deformations govern interleaflet coupling of lipid-ordered domains. *Phys. Rev. Lett.* 115:088101. doi: 10.1103/PhysRevLett.115.088101

Gandhavadi, M., Allende, D., Vidal, A., Simon, S. A., and McIntosh, T. J. (2002). Structure, composition, and peptide binding properties of detergent soluble bilayers and detergent resistant rafts. *Biophys. J.* 82, 1469–1482. doi: 10.1016/S0006-3495(02)75501-X

García-Sáez, A. J., Chiantia, S., and Schwille, P. (2007). Effect of line tension on the lateral organization of lipid membranes. *J. Biol. Chem.* 282, 33537–33544. doi: 10.1074/jbc.M706162200

Garg, S., Rühe, J., Lüdtke, K., Jordan, R., and Naumann, C. A. (2007). Domain registration in raft-mimicking lipid mixtures studied using polymer-tethered lipid bilayers. *Biophys. J.* 92, 1263–1270. doi: 10.1529/biophysj.106.091082

Ghosh, A., Sharma, A., Chizhik, A. I., Isbaner, S., Ruhlandt, D., Tsukanov, R., et al. (2019). Graphene-based metal-induced energy transfer for sub-nanometre optical localization. *Nat. Photonics* 13, 860–865. doi: 10.1038/s41566-019-0510-7

Gordon, V. D., Deserno, M., Andrew, C. M. J., Egelhaaf, S. U., and Poon, W. C. K. (2008). Adhesion promotes phase separation in mixed-lipid membranes. *EPL* 84:48003. doi: 10.1209/0295-5075/84/48003

Haataja, M. P. (2017). Lipid domain co-localization induced by membrane undulations. *Biophys. J.* 112, 655–662. doi: 10.1016/j.bpj.2016.12.030

Hamilton, A. D. (2003). Fast flip-flop of cholesterol and fatty acids in membranes: implications for membrane transport proteins. *Curr. Opin. Lipidol.* 14, 263–271. doi: 10.1097/01.mol.0000073507.41685.9b

Harayama, T., and Riezman, H. (2018). Understanding the diversity of membrane lipid composition. *Nat. Rev. Mol. Cell Biol.* 19, 281–296. doi: 10.1038/nrm.2017.138

Heberle, F. A., Marquardt, D., Doktorova, M., Geier, B., Standaert, R. F., Heftberger, P., et al. (2016). Subnanometer structure of an asymmetric model membrane: interleaflet coupling influences domain properties. *Langmuir* 32, 5195–5200. doi: 10.1021/acs.langmuir.5b04562

Heberle, F. A., and Pabst, G. (2017). Complex biomembrane mimetics on the sub-nanometer scale. *Biophys. Rev.* 9, 353–373. doi: 10.1007/s12551-017-0275-5

Heberle, F. A., Petruzielo, R. S., Pan, J., Drazba, P., Kučerka, N., Standaert, R. F., et al. (2013). Bilayer thickness mismatch controls domain size in model membranes. *J. Am. Chem. Soc.* 135, 6853–6859. doi: 10.1021/ja3113615

Hirai, M., Hirai, H., Koizumi, M., Kasahara, K., Yuyama, K., and Suzuki, N. (2006). Structure of raft-model membrane by using the inverse contrast variation neutron scattering method. *Phys. Rev. B Condens. Matter* 38, 868–870. doi: 10.1016/j.physb.2006.05.129

Horner, A., Akimov, S. A., and Pohl, P. (2013). Long and short lipid molecules experience the same interleaflet drag in lipid bilayers. *Phys. Rev. Lett.* 110:268101. doi: 10.1103/PhysRevLett.110.268101

Horner, A., Antonenko, Y. N., and Pohl, P. (2009). Coupled diffusion of peripherally bound peptides along the outer and inner membrane leaflets. *Biophys. J.* 96, 2689–2695. doi: 10.1016/j.bpj.2008.12.3931

Iwabuchi, K., Nakayama, H., Iwahara, C., and Takamori, K. (2010). Significance of glycosphingolipid fatty acid chain length on membrane microdomain-mediated signal transduction. *FEBS Lett.* 584, 1642–1652. doi: 10.1016/j.febslet.2009.10.043

Javanainen, M., Martinez-Seara, H., and Vattulainen, I. (2017). Nanoscale membrane domain formation driven by cholesterol. *Sci. Rep.* 7:1143.

Johannes, L., and Römer, W. (2010). Shiga toxins from cell biology to biomedical applications. *Nat. Rev. Microbiol.* 8, 105–116. doi: 10.1038/nrmicro2279

Kapusta, P., Wahl, M., Benda, A., Hof, M., and Enderlein, J. (2007). Fluorescence lifetime correlation spectroscopy. *J. Fluoresc.* 17, 43–48.

Keller, D., Larsen, N. B., Møller, I. M., and Mouritsen, O. G. (2005). Decoupled phase transitions and grain-boundary melting in supported phospholipid bilayers. *Phys. Rev. Lett.* 94:025701. doi: 10.1103/PhysRevLett.94.025701

Khelashvili, G., Kollmitzer, B., Heftberger, P., Pabst, G., and Harries, D. (2013). Calculating the bending modulus for multicomponent lipid membranes in different thermodynamic phases. *J. Chem. Theory Comput.* 9, 3866–3871. doi: 10.1021/ct400492e

Kiessling, V., Crane, J. M., and Tamm, L. K. (2006). Transbilayer effects of raft-like lipid domains in asymmetric planar bilayers measured by single molecule tracking. *Biophys. J.* 91, 3313–3326. doi: 10.1529/biophysj.106.091421

Kiessling, V., and Tamm, L. K. (2003). Measuring distances in supported bilayers by fluorescence interference-contrast microscopy: polymer supports and SNARE proteins. *Biophys. J.* 84, 408–418. doi: 10.1016/s0006-3495(03)74861-9

Kiessling, V., Wan, C., and Tamm, L. K. (2009). Domain coupling in asymmetric lipid bilayers. *Biochim. Biophys. Acta Biomembr.* 1788, 64–71. doi: 10.1016/j.bbamem.2008.09.003

Klokk, T. I., Kavaliauskiene, S., and Sandvig, K. (2016). Cross-linking of glycosphingolipids at the plasma membrane: consequences for intracellular signaling and traffic. *Cell. Mol. Life Sci.* 73, 1301–1316. doi: 10.1007/s00018-015-2049-1

Kollmitzer, B., Heftberger, P., Podgornik, R., Nagle, J. F., and Pabst, G. (2015). Bending rigidities and interdomain forces in membranes with coexisting lipid domains. *Biophys. J.* 108, 2833–2842. doi: 10.1016/j.bpj.2015.05.003

Korlach, J., Schwille, P., Webb, W. W., and Feigenson, G. W. (1999). Characterization of lipid bilayer phases by confocal microscopy and fluorescence correlation spectroscopy. *Proc. Natl. Acad. Sci. U.S.A.* 96, 8461–8466. doi: 10.1073/pnas.96.15.8461

Koukalová, A., Amaro, M., Aydogan, G., Gröbner, G., Williamson, P. T. F., Mikhalyov, I., et al. (2017). Lipid driven nanodomains in giant lipid vesicles are fluid and disordered. *Sci. Rep.* 7:5460. doi: 10.1038/s41598-017-05539-y

Krivanek, R., Jeworrek, C., Czeslik, C., and Winter, R. (2008). Composition fluctuations in phospholipid-sterol vesicles - A small-angle neutron scattering study. *Z. Phys. Chem.* 222, 1679–1692. doi: 10.1524/zpch.2008.5433

Ledeen, R. W., Kopitz, J., Abad-Rodríguez, J., and Gabius, H. J. (2018). Glycan chains of gangliosides: functional ligands for tissue lectins (siglecs/galectins). *Prog. Mol. Biol. Transl. Sci.* 156, 289–324. doi: 10.1016/bs.pmbts.2017.12.004

Lin, Q., and London, E. (2014). The influence of natural lipid asymmetry upon the conformation of a membrane-inserted protein (perfringolysin O). *J. Biol. Chem.* 289, 5467–5478. doi: 10.1074/jbc.M113.533943

Lin, W. C., Blanchette, C. D., Ratto, T. V., and Longo, M. L. (2006). Lipid asymmetry in DLPC/DSPC-supported lipid bilayers: a combined AFM and fluorescence microscopy study. *Biophys. J.* 90, 228–237. doi: 10.1529/biophysj.105.067066

Lingwood, C. A. (2011). Glycosphingolipid functions. *Cold Spring Harb. Perspect. Biol.* 3:a004788. doi: 10.1101/cshperspect.a004788

Llorente, A., Skotland, T., Sylvänne, T., Kauhanen, D., Róg, T., Orłowski, A., et al. (2013). Molecular lipidomics of exosomes released by PC-3 prostate cancer cells. *Biochim. Biophys. Acta Mol. Cell Biol. Lipids* 1831, 1302–1309. doi: 10.1016/j.bbalip.2013.04.011

Lorent, J., Ganesan, L., Rivera-Longsworth, G., Sezgin, E., Levental, K., Lyman, E., et al. (2019). The molecular and structural asymmetry of the plasma membrane. *bioRxiv [Preprint]* doi: 10.1101/698837

Lu, D., Vavasour, I., and Morrow, M. R. (1995). Smoothed acyl chain orientational order parameter profiles in dimyristoylphosphatidylcholine-distearoylphosphatidylcholine mixtures: a 2H-NMR study. *Biophys. J.* 68, 574–583. doi: 10.1016/s0006-3495(95)80219-5

Marquardt, D., Heberle, F. A., Nickels, J. D., Pabst, G., and Katsaras, J. (2015). On scattered waves and lipid domains: detecting membrane rafts with X-rays and neutrons. *Soft Matter* 11, 9055–9072. doi: 10.1039/c5sm01807b

Marsh, D. (2008). Protein modulation of lipids, and vice-versa, in membranes. *Biochim. Biophys. Acta* 1778, 1545–1575. doi: 10.1016/j.bbamem.2008.01.015

Masui, T., Imai, M., and Urakami, N. (2006). Microdomain formation in model biomembranes. *Phys. B Condens. Matter* 385–386, 821–823. doi: 10.1016/j.physb.2006.06.099

Masui, T., Urakami, N., and Imai, M. (2008). Nano-meter-sized domain formation in lipid membranes observed by small angle neutron scattering. *Eur. Phys. J. E* 27, 379–389. doi: 10.1140/epje/i2008-10400-x

May, S. (2009). Trans-monolayer coupling of fluid domains in lipid bilayers. *Soft Matter* 5, 3148–3156. doi: 10.1039/b901647c

Mouritsen, O. G., and Bagatolli, L. A. (2015). Lipid domains in model membranes: a brief historical perspective. *Essays Biochem.* 57, 1–19. doi: 10.1042/bse0570001

Nickels, J. D., Cheng, X., Mostofian, B., Stanley, C., Lindner, B., Heberle, F. A., et al. (2015a). Mechanical properties of nanoscopic lipid domains. *J. Am. Chem. Soc.* 137, 15772–15780. doi: 10.1021/jacs.5b08894

Nickels, J. D., Smith, J. C., and Cheng, X. (2015b). Lateral organization, bilayer asymmetry, and inter-leaflet coupling of biological membranes. *Chem. Phys. Lipids* 192, 87–99. doi: 10.1016/j.chemphyslip.2015.07.012

Nicolau, D. V., Burrage, K., Parton, R. G., and Hancock, J. F. (2006). Identifying optimal lipid raft characteristics required to promote nanoscale protein-protein interactions on the Plasma Membrane. *Mol. Cell. Biol.* 26, 313–323. doi: 10.1128/mcb.26.1.313-323.2006

Nicolini, C., Thiyagarajan, P., and Winter, R. (2004). Small-scale composition fluctuations and microdomain formation in lipid raft models as revealed by small-angle neutron scattering. *Phys. Chem. Chem. Phys.* 6, 5531–5534. doi: 10.1039/b408928f

Otosu, T., and Yamaguchi, S. (2019). Reduction of glass-surface charge density slows the lipid diffusion in the proximal leaflet of a supported lipid bilayer. *J. Chem. Phys.* 151:025102. doi: 10.1063/1.5103221

Owen, D. M., Williamson, D. J., Magenau, A., and Gaus, K. (2012). Sub-resolution lipid domains exist in the plasma membrane and regulate protein diffusion and distribution. *Nat. Commun.* 3:1256. doi: 10.1038/ncomms2273

Pabst, G., Kučerka, N., Nieh, M. P., Rheinstädter, M. C., and Katsaras, J. (2010). Applications of neutron and X-ray scattering to the study of biologically relevant model membranes. *Chem. Phys. Lipids* 163, 460–479. doi: 10.1016/j.chemphyslip.2010.03.010

Pan, J., Heberle, F. A., Petruzielo, R. S., and Katsaras, J. (2013). Using small-angle neutron scattering to detect nanoscopic lipid domains. *Chem. Phys. Lipids* 170–171, 19–32. doi: 10.1016/j.chemphyslip.2013.02.012

Pencer, J., Anghel, V. N. P., Kučerka, N., and Katsaras, J. (2006). Scattering from laterally heterogeneous vesicles. I. Model-independent analysis. *J. Appl. Crystallogr.* 39, 791–796. doi: 10.1107/S0021889806035163

Pencer, J., Anghel, V. N. P., Kučerka, N., and Katsaras, J. (2007a). Scattering from laterally heterogeneous vesicles. III. Reconciling past and present work. *J. Appl. Crystallogr.* 40, 771–772. doi: 10.1107/S0021889807024624

Pencer, J., Mills, T. T., Kucerka, N., Nieh, M. P., and Katsaras, J. (2007b). Small-angle neutron scattering to detect rafts and lipid domains. *Methods Mol. Biol.* 398, 231–244. doi: 10.1007/978-1-59745-513-8_16

Pencer, J., Mills, T., Anghel, V., Krueger, S., Epand, R. M., and Katsaras, J. (2005). Detection of submicron-sized raft-like domains in membranes by small-angle neutron scattering. *Eur. Phys. J. E* 18, 447–458. doi: 10.1140/epje/e2005-00046-5

Perlmutter, J. D., and Sachs, J. N. (2011). Interleaflet interaction and asymmetry in phase separated lipid bilayers: molecular dynamics simulations. *J. Am. Chem. Soc.* 133, 6563–6577. doi: 10.1021/ja106626r

Przybylo, M., Sykora, J., Humpolickova, J., Benda, A., Zan, A., and Hof, M. (2006). Lipid diffusion in giant unilamellar vesicles is more than 2 times faster than in supported phospholipid bilayers under identical conditions. *Langmuir* 22, 9096–9099. doi: 10.1021/la061934p

Raghupathy, R., Anupama Ambika, Anilkumar Polley, A., Singh, P. P., Yadav, M., Johnson, C., et al. (2016). Transbilayer lipid interactions mediate nanoclustering of lipid- anchored proteins. *Cell* 161, 581–594. doi: 10.1016/j.cell.2015.03.048.Transbilayer

Rinia, H. A., Snel, M. M. E., Van Der Eerden, J. P. J. M., and De Kruijff, B. (2001). Visualizing detergent resistant domains in model membranes with atomic force microscopy. *FEBS Lett.* 501, 92–96. doi: 10.1016/s0014-5793(01)02636-9

Risselada, H. J., and Marrink, S. J. (2008). The molecular face of lipid rafts in model membranes. *Proc. Natl. Acad. Sci. U.S.A.* 105, 17367–17372. doi: 10.1073/pnas.0807527105

Róg, T., Orłowski, A., Llorente, A., Skotland, T., Sylvänne, T., Kauhanen, D., et al. (2016). Interdigitation of long-chain sphingomyelin induces coupling of membrane leaflets in a cholesterol dependent manner. *Biochim. Biophys. Acta Biomembr.* 1858, 281–288. doi: 10.1016/j.bbamem.2015.12.003

Russo, D., Parashuraman, S., and D'Angelo, G. (2016). Glycosphingolipid–protein interaction in signal transduction. *Int. J. Mol. Sci.* 17:1732. doi: 10.3390/ijms17101732

Šachl, R., Amaro, M., Aydogan, G., Koukalová, A., Mikhalyov, I. I., Boldyrev, I. A., et al. (2015). On multivalent receptor activity of GM1 in cholesterol containing membranes. *Biochim. Biophys. Acta Mol. Cell Res.* 1853, 850–857. doi: 10.1016/j.bbamcr.2014.07.016

Šachl, R., Bergstrand, J., Widengren, J., and Hof, M. (2016). Fluorescence correlation spectroscopy diffusion laws in the presence of moving nanodomains. *J. Phys. D Appl. Phys.* 49:114002. doi: 10.1088/0022-3727/49/11/114002

Šachl, R., Humpolíčková, J., Štefl, M., Johansson, L. B. -Å., and Hof, M. (2011). Limitations of electronic energy transfer in the determination of lipid nanodomain sizes. *Biophys. J.* 101, L60–L62.

Šachl, R., Johansson, L. B. -Å., and Hof, M. (2012). Förster resonance energy transfer (FRET) between heterogeneously distributed probes: application to lipid nanodomains and pores. *Int. J. Mol. Sci.* 13, 16141–16156. doi: 10.3390/ijms131216141

Seeger, H. M., Di Cerbo, A., Alessandrini, A., and Facci, P. (2010). Supported lipid bilayers on mica and silicon oxide: comparison of the main phase transition behavior. *J. Phys. Chem. B* 114, 8926–8933. doi: 10.1021/jp1026477

Seeger, H. M., Marino, G., Alessandrini, A., and Facci, P. (2009). Effect of physical parameters on the main phase transition of supported lipid bilayers. *Biophys. J.* 97, 1067–1076. doi: 10.1016/j.bpj.2009.03.068

Skotland, T., and Sandvig, K. (2019). The role of PS 18:0/18:1 in membrane function. *Nat. Commun.* 10:2752.

Sonnleitner, A., Schütz, G. J., and Schmidt, T. (1999). Free Brownian motion of individual lipid molecules in biomembranes. *Biophys. J.* 77, 2638–2642. doi: 10.1016/s0006-3495(99)77097-9

Spillane, K. M., Ortega-Arroyo, J., De Wit, G., Eggeling, C., Ewers, H., Wallace, M. I., et al. (2014). High-speed single-particle tracking of gm1 in model membranes reveals anomalous diffusion due to interleaflet coupling and molecular pinning. *Nano Lett.* 14, 5390–5397. doi: 10.1021/nl502536u

Štefl, M., Šachl, R., Humpolíčková, J., Cebecauer, M., Macháò, R., Koláøová, M., et al. (2012). Dynamics and size of cross-linking-induced lipid nanodomains in model membranes. *Biophys. J.* 102, 2104–2113. doi: 10.1016/j.bpj.2012.03.054

Stevens, M. J. (2005). Complementary matching in domain formation within lipid bilayers. *J. Am. Chem. Soc.* 127, 15330–15331. doi: 10.1021/ja043611q

Stottrup, B. L., Veatch, S. L., and Keller, S. L. (2004). Nonequilibrium behavior in supported lipid membranes containing cholesterol. *Biophys. J.* 86, 2942–2950. doi: 10.1016/s0006-3495(04)74345-3

Sun, H., Chen, L., Gao, L., and Fang, W. (2015). Nanodomain formation of ganglioside GM1 in lipid membrane: effects of cholera toxin-mediated cross-linking. *Langmuir* 31, 9105–9114. doi: 10.1021/acs.langmuir.5b01866

Szleifer, I., Ben-Shaul, A., and Gelbart, W. M. (1990). Chain packing statistics and thermodynamics of amphiphile monolayers. *J. Phys. Chem.* 94, 5081–5089. doi: 10.1021/j100375a060

Thallmair, S., Ingólfsson, H. I., and Marrink, S. J. (2018). Cholesterol flip-flop impacts domain registration in plasma membrane models. *J. Phys. Chem. Lett.* 9, 5527–5533. doi: 10.1021/acs.jpclett.8b01877

Tien, H. T. (1974). *Bilayer Lipid Membranes (BLM): Theory and Practice*. New York, NY: M. Dekker.

Vácha, R., Siu, S. W. I., Petrov, M., Böckmann, R. A., Barucha-Kraszewska, J., Jurkiewicz, P., et al. (2009). Effects of alkali cations and halide anions on the DOPC lipid membrane. *J. Phys. Chem. A* 113, 7235–7243. doi: 10.1021/jp809974e

Valeur, B. (2001). *Molecular Fluorescence: Principles and Applications*, ed. W.-V. V. GmbH Weinheim (Hoboken, NJ: Wiley). doi: 10.1002/3527600248

Vinklárek, I. S., Vel'as, L., Riegerová, P., Skála, K., Mikhalyov, I., Gretskaya, N., et al. (2019). Experimental evidence of the existence of interleaflet coupled nanodomains: an MC-FRET study. *J. Phys. Chem. Lett.* 10, 2024–2030. doi: 10.1021/acs.jpclett.9b00390

Vogtt, K., Jeworrek, C., Garamus, V. M., and Winter, R. (2010). Microdomains in lipid vesicles: structure and distribution assessed by small-angle neutron scattering. *J. Phys. Chem. B* 114, 5643–5648. doi: 10.1021/jp101167n

von Heijne, G., and Gavel, Y. (1988). Topogenic signals in integral membrane proteins. *Eur. J. Biochem.* 174, 671–678. doi: 10.1111/j.1432-1033.1988.tb14150.x

Wan, C., Kiessling, V., and Tamm, L. K. (2008). Coupling of cholesterol-rich lipid phases in asymmetric bilayers. *Biochemistry* 47, 2190–2198. doi: 10.1021/bi7021552

Wang, J., Lu, Z.-H., Gabius, H.-J., Rohowsky-Kochan, C., Ledeen, R. W., and Wu, G. (2009). Cross-linking of GM1 ganglioside by galectin-1 mediates regulatory T cell activity involving TRPC5 channel activation: possible role in suppressing experimental autoimmune encephalomyelitis. *J. Immunol.* 182, 4036–4045. doi: 10.4049/jimmunol.0802981

Wang, Q., and London, E. (2018). Lipid structure and composition control consequences of interleaflet coupling in asymmetric vesicles. *Biophys. J.* 115, 664–678. doi: 10.1016/j.bpj.2018.07.011

Weiner, M. D., and Feigenson, G. W. (2018). Presence and role of midplane cholesterol in lipid bilayers containing registered or antiregistered phase domains. *J. Phys. Chem. B* 122, 8193–8200. doi: 10.1021/acs.jpcb.8b03949

Wernick, N. L. B., Chinnapen, D. J. F., Cho, J. A., and Lencer, W. I. (2010). Cholera toxin: an intracellular journey into the cytosol by way of the endoplasmic reticulum. *Toxins* 2, 310–325. doi: 10.3390/toxins2030310

Williamson, J. J., and Olmsted, P. D. (2015a). Nucleation of symmetric domains in the coupled leaflets of a bilayer. *Soft Matter* 11, 8948–8959. doi: 10.1039/c5sm01328c

Williamson, J. J., and Olmsted, P. D. (2015b). Registered and antiregistered phase separation of mixed amphiphilic bilayers. *Biophys. J.* 108, 1963–1976. doi: 10.1016/j.bpj.2015.03.016

Xu, Z. C., and Cafiso, D. S. (1986). Phospholipid packing and conformation in small vesicles revealed by two-dimensional 1H nuclear magnetic resonance cross-relaxation spectroscopy. *Biophys. J.* 49, 779–783. doi: 10.1016/s0006-3495(86)83705-5

Yethiraj, A., and Weisshaar, J. C. (2007). Why are lipid rafts not observed in vivo? *Biophys. J.* 93, 3113–3119. doi: 10.1529/biophysj.106.101931

Zachowski, A. (1993). Phospholipids in animal eukaryotic membranes: transverse asymmetry and movement. *Biochem. J.* 294, 1–14. doi: 10.1042/bj2940001

Zhang, S., and Lin, X. (2019). Lipid acyl chain cis double bond position modulates membrane domain registration/anti-registration. *J. Am. Chem. Soc.* 141, 15884–15890. doi: 10.1021/jacs.9b06977

Conflict of Interest: The authors declare that the research was conducted in the absence of any commercial or financial relationships that could be construed as a potential conflict of interest.

frontiers in Cell and Developmental Biology

REVIEW
published: 28 April 2020
doi: 10.3389/fcell.2020.00277

Phospholipids of the Plasma Membrane – Regulators or Consequence of Cell Polarity?

*Michael P. Krahn**

Department of Medical Cell Biology, Medical Clinic D, University Hospital of Münster, Münster, Germany

Cell polarity is a key feature of many eukaryotic cells, including neurons, epithelia, endothelia and asymmetrically dividing stem cells. Apart from the specific localization of proteins to distinct domains of the plasma membrane, most of these cells exhibit an asymmetric distribution of phospholipids within the plasma membrane too. Notably, research over the last years has revealed that many known conserved regulators of apical-basal polarity in epithelial cells are capable of binding to phospholipids, which in turn regulate the localization and to some extent the function of these proteins. Conversely, phospholipid-modifying enzymes are recruited and controlled by polarity regulators, demonstrating an elaborated balance between asymmetrically localized proteins and phospholipids, which are enriched in certain (micro)domains of the plasma membrane. In this review, we will focus on our current understanding of apical-basal polarity and the implication of phospholipids within the plasma membrane during the cell polarization of epithelia and migrating cells.

Keywords: cell polarity, phospholipids, phosphoinositide, phosphatidic acid, plasma membrane

OPEN ACCESS

Edited by:
Falk Nimmerjahn, University of Erlangen Nuremberg, Germany

Reviewed by:
Agnieszka Swiatecka-Urban, University of Pittsburgh, United States
Manisha Sharma, Vanderbilt University, United States

***Correspondence:**
Michael P. Krahn
Michael.Krahn@uni-muenster.de;
Michael.Krahn@ukmuenster.de

Specialty section:
This article was submitted to Cellular Biochemistry, a section of the journal Frontiers in Cell and Developmental Biology

Received: *30 January 2020*
Accepted: *31 March 2020*
Published: *28 April 2020*

Citation:
Krahn MP (2020) Phospholipids of the Plasma Membrane – Regulators or Consequence of Cell Polarity? Front. Cell Dev. Biol. 8:277. doi: 10.3389/fcell.2020.00277

INTRODUCTION

One of the fundamental prerequisites for the function of epithelial cells is the polarization along their apical-basal axis. This apical-basal polarity is established and regulated by a set of highly conserved polarity determinants (**Table 1**), which act in antagonizing fashions in order to keep the balance between the apical and the basolateral plasma membrane domain. Notably, most key determinants of this epithelial apical-basal polarity also regulate anterior-posterior polarity in the zygote of *Caenorhabditis elegans* and the oocyte of *Drosophila* as well as front-rear polarity in migrating cells (for review see St Johnston and Ahringer, 2010; Tepass, 2012; Rodriguez-Boulan and Macara, 2014; Campanale et al., 2017).

In order to achieve this balance, polarity determinants cluster in apical and basolateral polarity complexes: In particular, the PAR/aPKC-complex and the Crumbs complex determine the apical plasma membrane domain, whereas the Scribble (Scrb)/Discs Large (Dlg)/Lethal (2) Giant Larvae (Lgl) complex together with the kinases PAR-1 and LKB1 (PAR-4 in *C. elegans*) substantiate the (baso-) lateral domain (**Figure 1**). The core components of the PAR/aPKC complex are the scaffolding proteins PAR-3 (Bazooka in *Drosophila*) and PAR-6 (PAR-6α/β/γ in mammals) and the Serine/Threonine kinase aPKC (atypical protein kinase C, Protein Kinase Cζ and ι in mammals). Furthermore, PAR-6 is regulated by the small GTPase Cdc42, which dynamically associates with the PAR-complex too.

TABLE 1 | Summary of conserved polarity regulators and their reported phospholipid-binding capacity.

Mammalian	*Drosophila*	*C. elegans*	Phospholipid-binding
Apical			
PAR-3	Bazooka	PAR-3	PI(4,5)P2, PI(3,4,5)P3
PAR-6	PAR-6	PAR-6	–
PKCζ/ι	aPKC	PKC-3	–
Cdc42	Cdc42	Cdc42	PS
Rac1	Rac1	Rac-2	PA, PI(4,5)P2, PI(3,4,5)P3
Tiam1	–	–	PI(3,4)P2, PI(4,5)P2, PI(3,4,5)P3
PTEN	PTEN	DAF-18	PI(4,5)P2, (PS, PC)
Annexin-2	–	–	PI(4,5)P2
Crb1/2/3	Crb	Crb-1	–
Pals1	Stardust	Magu-2	–
PATJ	PATJ	Mpz-1	–
Basolateral			
Llgl	Lgl	Lgl-1	PI(4)P, PI(4,5)P2
Dlg1	Dlg	Dlg-1	–
Scrb	Scrb	Let-413	–
MARK3	PAR-1	PAR-1	PS, PA, PI(4)P
LKB1	LKB1	PAR-4	PA

Within the Crumbs (Crb)-complex, the transmembrane protein Crb is stabilized in the plasma membrane by its adaptor protein Pals1 (Stardust in *Drosophila*), which in turn recruits the adaptor proteins Pals1-associated tight junction protein (PATJ) and Lin-7 to the complex (reviewed by Bulgakova and Knust, 2009). However, several studies demonstrated a crosstalk between these two apical complexes, indicating that their composition is highly dynamic and depends on the cell type, differentiation status and other stimuli of the epithelium (Hurd et al., 2003b; Gao and Macara, 2004; Lemmers et al., 2004; Penkert et al., 2004; Sotillos et al., 2004; Wang et al., 2004; Kempkens et al., 2006; Krahn et al., 2010a; Sen et al., 2015; Whitney et al., 2016). The basolateral localized Scrb, Dlg and Lgl are scaffolding proteins which function as a module to determine basolateral plasma membrane domain and to regulate the assembly of cell–cell contacts. Notably, deletion of these components results not only in polarity defects, but also in tissue overgrowth (in *Drosophila* and to some extent in vertebrates), leading to the identification of these proteins as tumor suppressors (reviewed by Stephens et al., 2018).

In order to mutually exclude apical and basolateral determinants, aPKC phosphorylates Lgl and PAR-1, which subsequently dissociate from the plasma membrane in the aPKC-active apical zone of epithelia and apical-basal polarized neural stem cells (neuroblasts) of *Drosophila* (Betschinger et al., 2003; Plant et al., 2003; Hurov et al., 2004; Suzuki et al., 2004; Wirtz-Peitz et al., 2008; Doerflinger et al., 2010). Conversely, PAR-1 phosphorylates PAR-3 and aPKC, displacing them from the basolateral cortex (Benton and St Johnston, 2003; Hurd et al., 2003a; Krahn et al., 2009). In *Drosophila* neuroblasts, aPKC also excludes the adaptor protein Miranda and the Notch inhibitor Numb from the basal cortex by phosphorylation, thereby controlling asymmetric cell division (Smith et al., 2007; Atwood and Prehoda, 2009).

Phospholipids are a major component of biological membranes and not only responsible for dynamic membrane fluctuations but also function as signaling hubs (for review see Liu et al., 2013; Schink et al., 2016; Yang et al., 2018; Kay and Fairn, 2019). Phosphatidylcholine (PC), phosphatidylethanolamine (PE), phosphatidylserine (PS) and sphingomyelin are most frequent and constitute the framework of biological membranes, stabilized by cholesterol. However, the less abundant phosphatidic acid (PA) and phosphoinositides (PI) have been found to play crucial roles in recruiting membrane-associated proteins and function as signaling hubs. Moreover, the accumulation of distinct phospholipids (in particular of the PI family) is a characteristic feature of different cellular compartments, targeting phospholipid-binding proteins to these compartments. An overview of the generation and metabolism of the main phospholipids discussed in this review is given in **Figure 2**.

PROTEIN–PHOSPHOLIPID INTERACTIONS

Several distinct lipid-binding domains have been identified in proteins (reviewed by Varnai et al., 2017): for instance, Pleckstrin homology (PH) domains and Epsin N-terminal homology (ENTH) domains bind preferentially to PI(4,5)P2 and PI(3,4,5)P3. FYVE domains target endosomal proteins to PI(3)P-enriched endosomes. C1 domains in PKCs bind to diacylglycerol, which activates the kinase and C2 domains recognize acidic phospholipids. However, over the last years, an increasing amount of proteins, which do not contain a distinct lipid-binding domain, have been described to directly associate with phospholipids. Mapping the interaction domains, positively charged motifs have been identified in many of these proteins, including polarity regulators. These motifs are mostly composed of a stretch of positively charged Lysines and Arginines in the primary sequence but might also result from a three-dimensional clustering of more distant located amino acids upon protein folding. Due to their positive charge, these motifs interact electrostatically with the negatively charged phospholipids of the inner leaflet of the plasma membrane (reviewed in Li et al., 2014). Phenylalanine, Tryptophan and Leucin adjacent to positively charged amino acids further enhance the association with phospholipids (Heo et al., 2006). In contrast to the above-mentioned distinct lipid-binding domains, the affinity of polybasic motifs to particular phospholipids is diverse and (currently) hard (if not impossible) to predict if no three-dimensional structure of the protein is available. Calculation of a lipid-binding index of the primary protein sequence of a candidate protein might help to identify potential membrane binding sites (Brzeska et al., 2010), which subsequently needs be tested experimentally. However, three-dimensional polybasic motifs are not revealed by these predictions, which are based on the primary sequence. Due to structural differences of the head group of the phospholipids (**Figure 2**), the

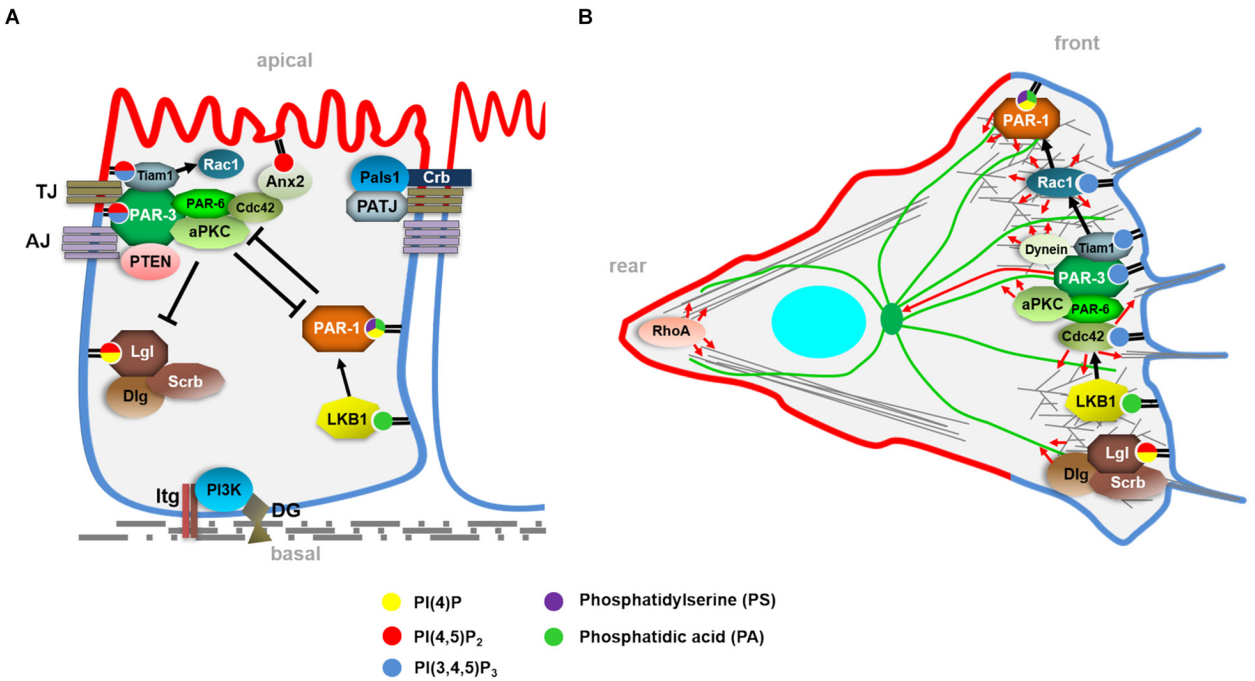

FIGURE 1 | (A) Simplified scheme of a differentiated epithelial cell with apical-basal polarity regulators and their described phospholipid interaction. Apical-basal polarization starts with the recruitment and activation of PI3-Kinase to focal adhesions (Integrin-complexes) and to the Dystroglycan complex, determining the basal side of the epithelial cell. Subsequently, the PAR/aPKC-complex (PAR-3, PAR-6, aPKC) is localized to the Tight Junctions (TJ) by PAR-3. PAR-3 also recruits PTEN, which catalyzes the turn over from PI(3,4,5)P3 to PI(4,5)P2. Furthermore, PAR-3 binds the Rac1 activator Tiam1 and PAR-6/aPKC target Cdc42 to the complex. Together and partly in redundancy with the second TJ-associated complex, the Crb-complex (Crb, Pals1, and PATJ), the PAR/aPKC complex determines the PI(4,5)P2-enriched apical plasma membrane domain, which is counterbalanced by the basolateral cell polarity regulators. Here, the Lgl/Dlg/Scrb-module and the kinase LKB1/PAR-1 also exhibit phospholipid-binding capacities, which are essential for their localization and function. **(B)** Polarity complexes and phospholipids regulating cell migration. In contrast to apical-basal polarity, migrating cells exhibit a front-rear polarity with apical and basolateral polarity regulators localizing at the leading edge, regulating cell protrusions (lamellipodia in particular via Rac1 and filopodia via Cdc42) by modulating the actin cytoskeleton (gray fibers) or affecting microtubules (green fibers).

three-dimensional protein structure surrounding the polybasic motif might distinguish between PS, PA and the family of phosphoinositides. For the later, taking in account the charge density/concentration as well as its abundance in the plasma membrane (Balla, 2013), PI(4)P and PI(4,5)P2 are obviously the most targeted phosphoinositides (Gambhir et al., 2004). However, even short polybasic motifs might be as specific for one particular phospholipid as a specific lipid binding domain, e.g., the binding of the polybasic tail of LKB1 to PA is magnitudes higher than to PI(4,5)P2 and PI(3,4,5)P3 (Dogliotti et al., 2017).

APICAL VERSUS BASOLATERAL POLARITY: THE PAR-COMPLEX AND ITS ANTAGONISTS

The scaffolding protein PAR-3 is essential for the initial establishment of apical-basal polarity by targeting PAR-6 and aPKC to the apical junctions. PAR-3 itself can be recruited to the adherens- and tight junctions by Cadherins (Harris and Peifer, 2005; Iden et al., 2006; Kullmann and Krahn, 2018b), Nectins (or the Nectin-like protein Echinoid in *Drosophila*) (Takekuni et al., 2003; Wei et al., 2005; Kullmann and Krahn, 2018b) and Junctional Adhesion molecule (JAM-A) (Ebnet et al., 2001). However, the correct subcellular localization of PAR-3 can also be accomplished by a conserved polybasic motif within the C-terminal part of the protein (Krahn et al., 2010b; Horikoshi et al., 2011; Ahmed and Macara, 2017; Kullmann and Krahn, 2018b). This Lysine/Arginine rich "lipid binding" motif binds to PI(4)P, PI(4,5)P2, and PI(3,4,5)P3 with highest affinity to the triphosphorylated PI. Deletion or mutation of this motif alone does not affect membrane localization of the full length protein, as the N-terminal oligomerization domain functions in redundancy to the lipid-binding motif in targeting PAR-3 to the apical junctions in *Drosophila* epithelial cells and neuroblasts (Kullmann and Krahn, 2018b). However, disturbed oligomerization together with impaired lipid-binding abolishes PAR-3 membrane association, which can be rescued by either PI(4,5)P2- or PI(3,4,5)P3-specific PH domains (Krahn et al., 2010b; Kullmann and Krahn, 2018b). Notably, plasma membrane association of PAR-3 is essential to prevent its proteasomal degradation (Kullmann and Krahn, 2018b). In *Drosophila* follicular epithelial cells, PI(4,5)P2 and not PI(3,4,5)P3 seems to be the phospholipid for correct apical PAR-3 localization, as depletion of the PI(4,5)P2-producing enzyme results in a mislocalization of PAR-3 to the basolateral membrane (but still

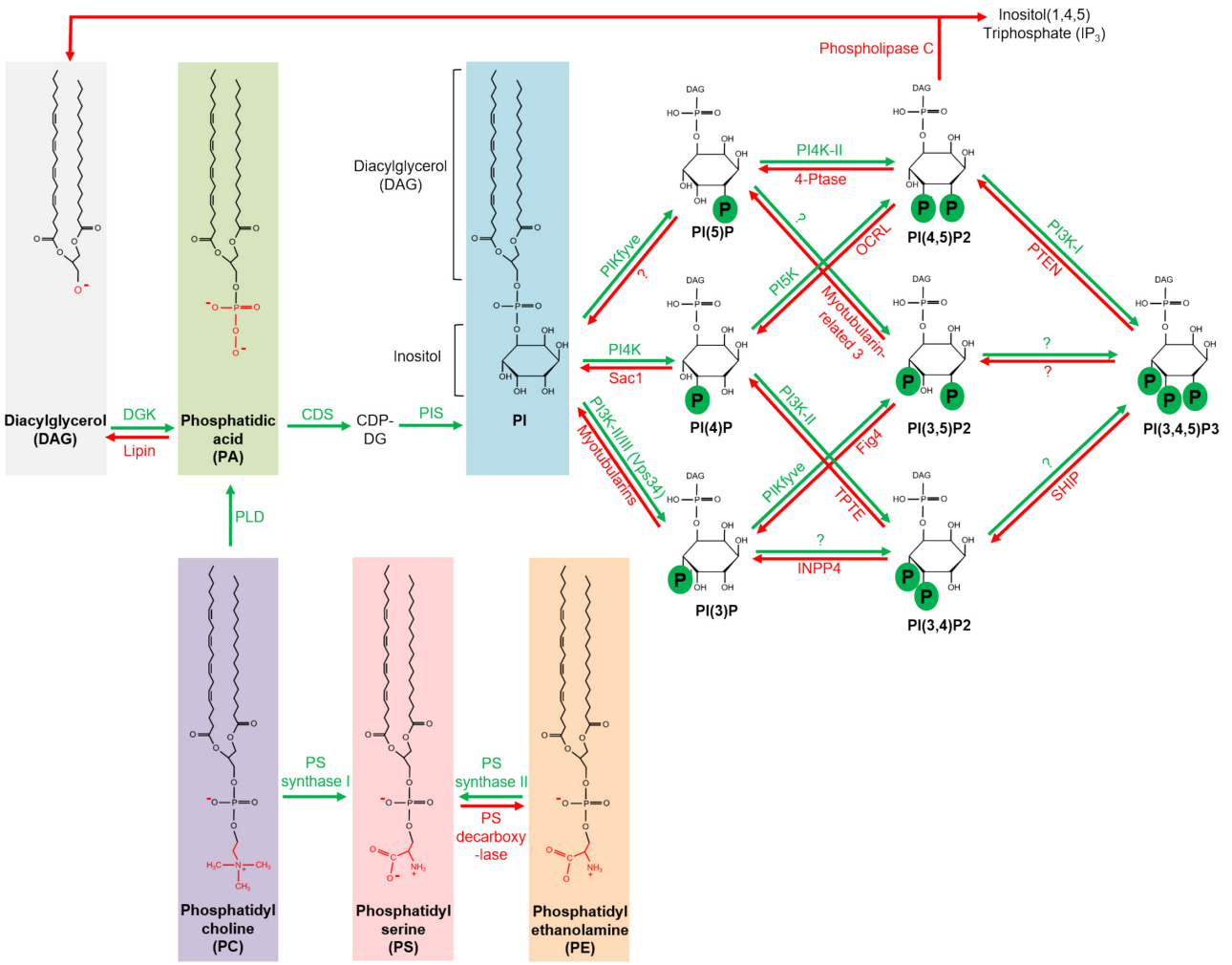

FIGURE 2 | Metabolism of major phospholipids implicated in cell polarity. DGK, diacylglycerol kinase. CDP-DG, cytidine diphosphate diacylglycerol. CDS, CDP-diacylglycerol synthase. FIG4, FIG4 phosphoinositide 5-phosphatase. FYVE-type zinc finger containing. INPP4, inositol polyphosphate-4-phosphatase. OCRL, OCRL inositol polyphosphate 5-phosphatase. PIKfyve, phosphoinositide kinase. PIS, PI synthase. PTEN, phosphatase and tensin homolog. SHIP, Src homology 2 (SH2) domain containing inositol polyphosphate 5-phosphatase. TPTE, transmembrane phosphatase with tensin homology.

remains membrane-associated) (Claret et al., 2014). Although the PDZ-domains of PAR-3 seem to have some phospholipid binding affinity (Wu et al., 2007; Yu and Harris, 2012), deletion of these domains do not affect membrane targeting in *Drosophila* epithelia *in vivo* (Krahn et al., 2010b; McKinley et al., 2012; Kullmann and Krahn, 2018b).

In epithelia and neuroblasts, PAR-3 is displaced from the basolateral membrane upon phosphorylation by laterally localized PAR-1 at two conserved Serines, one of which is located near the lipid binding motif (Benton and St Johnston, 2003). Subsequently to PAR-1 mediated phosphorylation, 14-3-3 adaptor proteins bind to phosphorylated PAR-3, which presumably blocks the lipid-binding domain, resulting in a membrane displacement of PAR-3 at PAR-1 active sites (Benton and St Johnston, 2003; Hurd et al., 2003a; Krahn et al., 2009).

Similar to the reciprocal regulation of PAR-1 versus PAR-3/aPKC, Lgl is phosphorylated by aPKC, which results in a displacement of Lgl from the cortex in epithelia and *Drosophila* neural stem cells (Betschinger et al., 2003; Plant et al., 2003; Wirtz-Peitz et al., 2008). Strikingly, the highly conserved aPKC-phosphorylation domain of Lgl was recently identified as a polybasic motif, which targets the protein to the plasma membrane by electrostatic interactions with phospholipids, in particular PI(4,5)P2 and PI(4)P (Dong et al., 2015). Phosphorylation of Lgl by aPKC attenuates the positive charge of this domain, thus inhibiting its interaction with phospholipids and displacing Lgl from the membrane (Bailey and Prehoda, 2015; Dong et al., 2015). In a similar mechanism, aPKC displaces Miranda and Numb from the plasma membrane (Bailey and Prehoda, 2015), which is essential for asymmetric cell division of neuroblasts. Both proteins contain polybasic motifs, too, with at least one internal aPKC-phosphorylation site, which blocks the interaction with phospholipids once it is phosphorylated. However, several other aPKC-phosphorylation

sites have been identified in Miranda and Numb *in vitro* (Smith et al., 2007; Atwood and Prehoda, 2009). Although they are not situated in the polybasic motif, these sites partly contribute to aPKC-mediated membrane displacement of the proteins. This observation suggests either a stepwise phosphorylation, in which the critical polybasic motif phosphorylation site is only phosphorylated after a conformational change upon phosphorylation of the other critical sites. Or phosphorylation of residues outside the polybasic motif result in changes in protein folding so that the polybasic motif is masked by other domains of the protein itself or any of its interaction partners (which might be bound upon this particular phosphorylation event too). Three-dimensional modeling is needed to further understand the molecular mechanisms underlying these protein-membrane interactions. Notably, hypoxia reduces phosphoinositides in the inner leaflet of the PM, resulting in a decreased association of Lgl and Numb with the plasma membrane (Dong et al., 2015). This seems to be even more intriguing, as hypoxia is a key feature of rapidly proliferating tumor cells, which eventually lose their apical-basal polarity and cell-cell adhesion to become migratory.

In epithelial cells, not only proteins are asymmetrically distributed: PAR-3 at the apical junctions recruits the phosphatase PTEN, which converts PI(3,4,5)P3 to PI(4,5)P2 (von Stein et al., 2005; Feng et al., 2008), thereby supporting the segregation of apical enrichment of PI(4,5)P2 and basolateral PI(3,4,5)P3 in the plasma membrane (Martin-Belmonte et al., 2007). Strikingly, these PIs themselves function as polarity regulators: PI(4,5)P2 recruits Annexin-2 to the apical membrane, which assembles and activates Cdc42 and aPKC (Martin-Belmonte et al., 2007). Addition of PI(4,5)P2 to the basolateral domain in a three-dimensional cell culture model mistargets apical junctional markers to the basolateral membrane and vice versa: The addition of PI(3,4,5)P3 to the apical membrane domain recruits basolateral polarity markers to the ectopic PI(3,4,5)P3 microdomains. Conversely, inhibition of PTEN or PI3K results in polarity defects and disturbed lumen formation in three-dimensional cell culture models. In *Drosophila* tracheae and MDCK cysts, apical enriched PI(4,5)P2 together with RhoA recruits the Formin Diaphanous, which induces the formation of Actin cables necessary for apical secretion and thus tubulogenesis/lumen formation (Rousso et al., 2013). Furthermore, the authors showed that the PI(4,5)P2 producing PIP5K Skittles (in *Drosophila*) is apically localized and contributes to this process. These results indicate that PI(4,5)P2 and PI(3,4,5)P3 function as regulators of apical-basal polarity by specifically recruiting apical or basolateral polarity determinants.

Moreover, the asymmetric enrichment of phospholipids seems to be one of the first cues during the establishment of polarity: Peng et al. (2015) recently demonstrated that during polarization and lumen formation of MDCK cysts in a three-dimensional ECM matrix, PI3K (in particular, the p110δ isoform) is stabilized by Dystroglycan (DG) at the basal cell-matrix contact. Expression of p110δ is induced by ECM components and production of PI(3,4,5)P3 by p110δ is essential for the apical-basal polarization of the cell. Consequently, inhibition of p110δ with specific inhibitors results in an inverted polarity of the epithelial cells. Thus, phospholipid polarity and protein polarity are highly interconnected and regulate each other in order to accomplish apical-basal polarization of epithelial cells. Notably, this interaction between polarity proteins and phospholipids is also essential during oriented cell division: The junctional adhesion molecule JAM-A mediates the generation of PI(3,4,5)P3 by PI3K via an Cdc42-dependent pathway thus controlling the planar positioning of the mitotic spindle, which is tethered to the PI(3,4,5)P3-enriched cell poles by dynactin (Tuncay et al., 2015). Similar to protein polarity regulators, phospholipid polarity seems to be conserved throughout evolution and different forms of polarity: In anterior-posterior polarized *C. elegans* zygotes, PI(4,5)P2 accumulates asymmetrically at the anterior cortex, where it regulates actin assembly and the asymmetric localization of the anterior polarity proteins PAR-3, PAR-6 and PKC3 (aPKC) (Scholze et al., 2018). Conversely, downregulation of PAR-3, but not of the posterior determinant PAR-2, results in disturbed anterior PI(4,5)P2 accumulation.

Cdc42 IS RECRUITED TO THE PLASMA MEMBRANE BY PHOSPHOLIPIDS FOR FULL ACTIVATION

Cdc42 regulates a variety of cellular functions, including Actin dynamics and endocytosis, by which Cdc42 controls apical-basal polarity as well as cell migration. Notably, Cdc42 is one of the "oldest" polarity regulators in evolution as direct homologs can not only be identified in humans, flies and worms, but also in yeast.

Apart from its activation via membrane-bound Annexin-2, Cdc42 itself binds directly to PS via a polybasic motif at its C-terminus, and PS controls its asymmetric localization in budding yeast (Fairn et al., 2011; Das et al., 2012; Haupt and Minc, 2017). Furthermore, PS and GTPase activation of Cdc42 are essential for nano-clustering of the protein in budding yeast (Sartorel et al., 2018). Given the importance of Cdc42 in cell polarity it is likely that this interaction with phospholipids is also essential for apical-basal polarity of epithelial cells. However, it is still unclear whether or how PS-enriched microdomains within distinct plasma membrane domains contribute to asymmetric localization of proteins in epithelial cells.

THE Crb-COMPLEX AND PHOSPHOLIPIDS

None of the two essential adaptor proteins of the Crb complex (Pals1 and PATJ) have been linked to phospholipids. However, Crb regulates phospholipid polarity by antagonizing the activity of PI3K in *Drosophila* epithelial cells, thus preventing apical conversion of PI(4,5)P2 to PI(3,4,5)P3 (Chartier et al., 2011). Interestingly, this seems to be one of the major functions of Crb as the polarity defects of *crb*-mutant embryos can be rescued to some extent by overexpression of PTEN or inhibition of PI3K. This fits with the hypothesis that Crb determines the apical [PI(4,5)P2-enriched] plasma membrane domain whereas PI(3,4,5)P3 in a positive feedback activation loop with Rac1

supports lateral membrane growth. Reciprocal activation of Rac1 and PI(3,4,5)P3 and their role in lateral membrane determination has also been shown for mammalian epithelial cells (Gassama-Diagne et al., 2006; Liu K.D. et al., 2007; Jeanes et al., 2009).

Apart from the canonical members of the Crb complex, several proteins have been linked to this complex biochemically. One important regulator of the complex is Angiomotin, whose expression is low in differentiated epithelia but becomes upregulated in migratory epithelial cells. Angiomotin binds to a PDZ domain of PATJ, disturbing its interaction with Crb-Pals1 (Wells et al., 2006). Notably, this process seems to be regulated by binding of Angiomotin to several phospholipids, with the highest affinity to PI(4)P, thereby targeting the Angiomotin/PATJ complex to recycling endosomes and thus disrupting the TJ, a prerequisite for cell migration (Heller et al., 2010). Therefore, phospholipid-binding of Angiomotin is a key regulatory mechanism of TJ/polarity disassembly during epithelial dedifferentiation (e.g., EMT), qualifying Angiomotin as an oncogene in some cancer types (reviewed by Lv et al., 2017).

POSTTRANSLATIONAL MODIFICATIONS REGULATE PLASMA MEMBRANE LOCALIZATION OF LATERAL POLARITY REGULATORS

Apart from the classical polarity complex Scribble/Dlg/Lgl, two conserved protein kinases localize to the lateral plasma membrane: PAR-1 and LKB1 (PAR-4 in *C. elegans*). Whereas PAR-1 antagonizes the PAR/aPKC complex (see above) and regulates microtubule dynamics (summarized by McDonald, 2014), LKB1 functions as a master kinase, phosphorylating the T-loop of several kinases of the AMPK (AMP-dependent Kinase) family, including PAR-1 (Lizcano et al., 2004). Consequently, phosphorylation of these kinases by LKB1 results in their full activation.

PAR-1 contains a C-terminal Kinase associated-1 (KA1) domain, which regulates the kinase activity of PAR-1 by auto-inhibition (Elbert et al., 2005). However, in 2006 the KA1 domain had already been identified as the region responsible for membrane association of the protein (Goransson et al., 2006). Later it became clear that this domain facilitates direct binding to PI(4)P, PS and PA (Moravcevic et al., 2010). Similar to polybasic motifs, positively charged Lysines/Arginines located at the outside of the folded KA1 domain are responsible for binding to negatively charged phospholipids. Mutation of these residues abolishes membrane association of PAR-1 in cell culture (Moravcevic et al., 2010). In the zygote of *C. elegans*, mutation of these residues displaces PAR-1 from the cortex (Ramanujam et al., 2018). Interestingly, similar to Lgl, phosphorylation of PAR-1 by PKC-3 (in worms) or aPKC (in *Drosophila* and mammals) results in a dissociation of PAR-1 from the membrane, providing a molecular mechanism for the aPKC < > PAR-1 exclusion (Hurov et al., 2004; Suzuki et al., 2004; Ramanujam et al., 2018). However, the aPKC-phosphorylation site is not located in the phospholipid-binding KA1-domain, suggesting an indirect effect of aPKC-mediated phosphorylation as discussed above for Miranda and Numb. Moreover, PAR-1 is phosphorylated outside the KA1 domain by several other kinases, and 14-3-3 adaptor proteins bind to phosphorylated PAR-1, displacing it from the membrane (Benton et al., 2002; Goransson et al., 2006). Consequently, the mutation of all phosphorylation sites results in a strictly membrane-association of PAR-1 (Goransson et al., 2006). Given the broad phospholipid binding of PAR-1 (Moravcevic et al., 2010), specific localization of PAR-1 might be rather accomplished by unspecific binding to the entire plasma membrane followed by apical exclusion (via the PAR/aPKC complex) than by selective targeting to the lateral plasma membrane domain.

LKB1 regulates an immense number of cellular processes, including energy metabolisms (via phosphorylating AMPK) and apical-basal/anterior-posterior polarity (by activating PAR-1 and AMPK). LKB1 has long been assumed to be a constitutively active kinase once it is associated with its co-factors Mo25 and SRADα. However, over the last years, several posttranslational modifications have been described (reviewed in Kullmann and Krahn, 2018a). Apart from a C-terminal farnesylation, which facilitates only transient membrane association, LKB1 contains a C-terminal polybasic motif adjacent to the farnesylated Cysteine, which directly binds to PA with a high specificity (Dogliotti et al., 2017). Mutation of this motif abolishes membrane association and severely decreases the kinase activity of LKB1 and the addition of PA-enriched micelles to recombinant LKB1 kinase complex increases its activity *in vitro*, and overexpression of Phospholipase D, one of the enzymes producing PA, results in an enhanced LKB1 activity in cell culture (Dogliotti et al., 2017). Notably, PDZGEF, a guanine exchange factor for Rap, also binds to PA (and other phospholipids) via a polybasic motif (Consonni et al., 2014). PDZGEF functions downstream of LKB1 to polarize intestinal epithelial cells by activating Ezrin via Rap2A (Gloerich et al., 2012). This suggests that PA-enriched microdomains in the PM function as signaling hubs, assembling several components of a distinct polarization pathway. However, it still remains unclear whether PA is enriched in distinct (micro)domains of the plasma membrane in apical-basal polarized epithelial cells. A possible hint comes from migrating epithelial cells, in which PA is enriched at the rear rather than at the leading edge (Ferraz-Nogueira et al., 2014), which would be in contradiction to the proposed role of LKB1 at the leading edge of migrating cancer cells (Zhang S. et al., 2008).

PHOSPHOLIPIDS AND POLARITY REGULATORS IN MIGRATING CELLS

In migrating (epithelial) cells, cell-cell adhesion molecules are downregulated or internalized and apical-basal polarity is converted into a front-rear polarity (**Figure 1B**). Now, the former apical PAR/aPKC complex accumulates at the leading edge (at least in isolated cells), being essential for collective cell migration as well as migration of fibroblasts (Etienne-Manneville, 2008; Schmoranzer et al., 2009; Mayor and Etienne-Manneville, 2016). However, in contrast to the apical domain of epithelial cells, the

leading edge in migrating cells is characterized by accumulation of PI(3,4,5)P3, and conversion of PI(4,5)P2 to PI(3,4,5)P3 at the leading edge triggers the activation of Actin regulators in order to organize lamellipodia for forward movement of the cell. Like the majority of PM-localized small GTPases, the Actin cytoskeleton regulators Rho, Rac, and Cdc42 have been found to contain polybasic motifs by which they bind to PI(4,5)P2 and PI(3,4,5)P3 (Heo et al., 2006). The interplay and feedback loops between these phospholipids and Actin regulators is essential for cell migration (Maree et al., 2012). In order to prevent hydrolysis of PI(3,4,5)P3 to PI(4,5)P2, PI(3,4,5)P3 at the leading edge and PTEN at the rear edge are mutually exclusive, at least in *Dictyostelium discoideum* (Matsuoka and Ueda, 2018). Here, targeting of PTEN to the plasma membrane via interaction of its N-terminus with PI(4,5)P2 is essential for chemotaxis (Iijima et al., 2004), although PTEN also exhibits a C2 domain, which associates with PC and PS-enriched liposomes *in vitro* (Lee et al., 1999). This is in contrast to the situation in epithelial cells, where PTEN colocalizes and associates with apical-junctional PAR-3, which is found at the leading edge in migrating cells, far away from PTEN. One explanation could be that in epithelial cells, the border between PI(4,5)P2-enriched apical domain and PI(3,4,5)P3-accumulation at the basolateral domain might be below the resolution limit for current studies – in migrating cells, both poles (and thus PTEN and PAR-3) are spatially clearly separated.

Apart from its implication in Cdc42/Rac1-dependent Actin turnover, the PAR-complex also regulates microtubule dynamics and centrosome positioning in migrating cells via PAR-3/Dynein and Cdc42/PAR-6-activated aPKC (Etienne-Manneville, 2008; Schmoranzer et al., 2009). Disturbed aPKC activity does not affect front-rear polarity, but rather results in a random migration of the cell, whereas knockdown of PAR-3 leads to abolished cell migration in fibroblasts. However, it is still unclear whether PI(4,5)P2 or PI(3,4,5)P3-binding of PAR-3 is essential for its localization at the leading edge and its role during cell migration.

At the leading edge, Cdc42 and Rac1 regulate the polymerization, turnover and branching of Actin, thereby enhancing the formation of lamellipodia and filopodia (summarized by Sit and Manser, 2011). Mechanistically, the binding of the polybasic tail of Rac1 to PA, PI(4,5)P2 and PI(3,4,5)P3 results in the establishment of Rac1-nanoclusters, which are essential for the formation of lamellipodia (Remorino et al., 2017; Maxwell et al., 2018). One of the Rac1 activators, the GEF Tiam1, is recruited to the plasma membrane by PAR-3 in polarized and migrating epithelial cells (Chen and Macara, 2005; Pegtel et al., 2007). Interestingly, Tiam1 itself contains two PH-domains, which are capable of binding to PI(3,4)P2, PI(4,5)P2, and PI(3,4,5)P3 and thus tether Tiam1 to the plasma membrane, which is essential for its Rac1 activating function (Michiels et al., 1997; Ceccarelli et al., 2007). In contrast to Rac/Cdc42, Rho is active at the rear edge, supporting the establishment of focal adhesions and Actin stress fibers as well as inducing cell contractility by activating Myosin. Apart from their direct binding to phospholipids, numerous activating [Guanine Nucleotide Exchange factors (GEFs)] and inactivating [GTPase activating proteins (GAPs)] factors for small GTPases of the Rho family contain a BAR domain, which is activated by PM curvatures (reviewed in de Kreuk and Hordijk, 2012).

Similar to the PAR/aPKC-complex, the lateral polarity regulators Scribble/Dlg/Lgl and LKB1/PAR-1 are also essential for directed cell migration (reviewed by McDonald, 2014; Stephens et al., 2018). Like for PAR-3, it is not yet clear whether phospholipid-binding of the lateral polarity proteins (Lgl, PAR-1, LKB1) affects their function in this process. Notably, these "lateral" polarity complexes also accumulate at the leading edge, thus overlapping with the "apical" complex PAR/aPKC (at least in collective cell migration). This raises the question whether and why the mutual exclusion of aPKC – Lgl and aPKC/PAR-3 – PAR-1 described above does not occur at this subcellular compartment or whether the leading edge is further composed of microdomains with distinct polarity protein composition (and particular phospholipid enrichment).

PI(4,5)P2 TARGETS POLARIZED VESICLE TRAFFICKING

In migrating cells not only the polarization of Actin/Myosin dynamics is regulated by phospholipids of the plasma membrane – Thapa et al. (2012) described PI(4,5)P2 to be essential for the delivery of Integrins to the leading edge, where they are essential for the establishment of nascent focal adhesions, facilitating extension of the lamellipodium. Notably, the authors identified an interaction of the enzyme responsible for PI(4,5)P2 production, PI(4)P-5-Kinase type 1C, with the Integrin adaptor protein Talin to be essential for this process. Thus, although PI(3,4,5)P3 has been supposed to be the critical leading-edge PI, spatial and temporally regulated production of PI(4,5)P2 at the leading edge is essential to mediate the delivery of vesicles to sites of newly formed cell-matrix contacts. This vesicle delivery is accomplished by the exocyst complex, which is targeted to the plasma membrane by direct binding of its components Exo70 and Sec3 to PI(4,5)P2 (He et al., 2007; Liu J. et al., 2007; Moore et al., 2007; Zhang X. et al., 2008). Polarized vesicle delivery by the exocyst complex is also essential for apical-basal polarity (reviewed by Polgar and Fogelgren, 2018).

Interestingly, the polarity protein PAR-3 functions as an exocyst receptor (via SEC8) at the TJ, and the exocyst binding domain was mapped to the polybasic motif of PAR-3, which also mediates binding to phospholipids (Ahmed and Macara, 2017). Disruption of the PAR-3-exocyst interaction disturbs delivery of lateral transmembrane proteins (e.g., *E*-cadherin) und thus strongly affects apical-basal polarity. One interesting question would be whether PAR-3 can simultaneously bind to both, phospholipids and exocyst, or whether these bindings are mutually exclusive. Nevertheless, this study identified PAR-3 as a key gatekeeper for vesicle docking at the border of apical versus basolateral delivery, similar to its role in recruiting PTEN in order to separate PI(3,4,5)P3 and PI(4,5)P2-enriched membrane domains (see above). In the future, it would be interesting to test whether PAR-3 at the leading edge also functions as an exocyst receptor for the delivery of focal-adhesion proteins in migrating cells.

CONCLUDING REMARKS

Emerging evidences suggest a critical role of phospholipids in regulating polarity proteins' localization and function in polarized epithelial and migrating (epithelial and non-epithelial) cells and vice versa: Polarity proteins regulate the accumulation of distinct phospholipids in different membrane compartments by localizing the respective enzymes, e.g., PI3K accumulation at focal adhesions or PTEN targeting at apical junctions (von Stein et al., 2005; Martin-Belmonte et al., 2007; Feng et al., 2008; Peng et al., 2015). Thereby, the apical-basal polarity of phospholipids [PI(4,5)P2 apical, PI(3,4,5)P3 basolateral] is established and regulated. In contrast, there are increasing reports of phospholipids regulating the localization and function of polarity regulators suggest that phospholipid polarity is not only a simple consequence of protein polarity but both modules are affecting each other: Disturbed or manipulated phospholipid polarity results in mislocalization of proteins and impaired apical-basal polarity (e.g., Gassama-Diagne et al., 2006; Martin-Belmonte et al., 2007; Claret et al., 2014) and deletion/mutation of phospholipid-binding motifs in polarity regulators leads to mislocalization of these proteins and disturbed polarity (Moravcevic et al., 2010; Bailey and Prehoda, 2015; Dong et al., 2015; Dogliotti et al., 2017; Kullmann and Krahn, 2018b). Taken together, both mechanisms, phospholipid-regulated protein localization and – function and protein-directed phospholipids accumulation, are essential for cell polarization and probably affect each other reciprocally so that it is rather a positive feedback circuit than a simple cause-consequence relationship.

One complication in our understanding of these processes is that most polarity regulators bind to several phospholipids although with different affinities, which mostly have been tested *in vitro*. In many cases, it is still not fully understood which particular phospholipid(s) is/are essential for targeting of the polarity regulator to the plasma membrane. Furthermore, several phospholipids, in particular PA, PS, and PI(4)P have not been shown to be asymmetrically enriched in distinct (micro)domains of the plasma membrane in polarized epithelial cells. Nonetheless, their interaction with polarity regulators is essential for polarized localization of the proteins. One explanation is that other factors, such as displacement from the plasma membrane at other domains (as shown for Lgl, Numb, PAR-1 and Miranda) or binding of interaction partners masking the lipid-binding motif (as supposed for PAR-3), contribute to the correct targeting of polarity regulators.

Another obstacle is the current technical limitations: Some phospholipid-probes are not absolutely specific for one distinct phospholipid but also bind to several others with lower affinities, which might be enough to mask microdomains in the plasma membrane, in particular if the concentration of the phospholipid of interest is magnitudes lower than others. Secondly, the principle of probes itself is critical because (over)expression of these lipid-binding domains themselves may disturb the phospholipid composition of membranes and block targeting of polarity regulators. Enhanced sensitivity of microscopy techniques combined with super resolution/single molecule imaging and improved fluorochromes might diminish this problem in the future.

AUTHOR CONTRIBUTIONS

MK conceived and wrote the manuscript.

FUNDING

This work was funded by the German Research Foundation (DFG) via the Comprehensive Research Center (CRC) 1438, project A05.

REFERENCES

Ahmed, S. M., and Macara, I. G. (2017). The Par3 polarity protein is an exocyst receptor essential for mammary cell survival. *Nat. Commun.* 8:14867. doi: 10.1038/ncomms14867

Atwood, S. X., and Prehoda, K. E. (2009). aPKC phosphorylates Miranda to polarize fate determinants during neuroblast asymmetric cell division. *Curr. Biol.* 19, 723–729. doi: 10.1016/j.cub.2009.03.056

Bailey, M. J., and Prehoda, K. E. (2015). Establishment of par-polarized cortical domains via phosphoregulated membrane motifs. *Dev. Cell* 35, 199–210. doi: 10.1016/j.devcel.2015.09.016

Balla, T. (2013). Phosphoinositides: tiny lipids with giant impact on cell regulation. *Physiol. Rev.* 93, 1019–1137. doi: 10.1152/physrev.00028.2012

Benton, R., Palacios, I. M., and St Johnston, D. (2002). *Drosophila* 14-3-3/PAR-5 is an essential mediator of PAR-1 function in axis formation. *Dev. Cell* 3, 659–671. doi: 10.1016/s1534-5807(02)00320-9

Benton, R., and St Johnston, D. (2003). *Drosophila* PAR-1 and 14-3-3 inhibit Bazooka/PAR-3 to establish complementary cortical domains in polarized cells. *Cell* 115, 691–704. doi: 10.1016/s0092-8674(03)00938-3

Betschinger, J., Mechtler, K., and Knoblich, J. A. (2003). The Par complex directs asymmetric cell division by phosphorylating the cytoskeletal protein Lgl. *Nature* 422, 326–330. doi: 10.1038/nature01486

Brzeska, H., Guag, J., Remmert, K., Chacko, S., and Korn, E. D. (2010). An experimentally based computer search identifies unstructured membrane-binding sites in proteins: application to class I myosins, PAKS, and CARMIL. *J. Biol. Chem.* 285, 5738–5747. doi: 10.1074/jbc.M109.066910

Bulgakova, N. A., and Knust, E. (2009). The Crumbs complex: from epithelial-cell polarity to retinal degeneration. *J. Cell Sci.* 122, 2587–2596. doi: 10.1242/jcs.023648

Campanale, J. P., Sun, T. Y., and Montell, D. J. (2017). Development and dynamics of cell polarity at a glance. *J. Cell Sci.* 130, 1201–1207. doi: 10.1242/jcs.188599

Ceccarelli, D. F., Blasutig, I. M., Goudreault, M., Li, Z., Ruston, J., Pawson, T., et al. (2007). Non-canonical interaction of phosphoinositides with pleckstrin homology domains of Tiam1 and ArhGAP9. *J. Biol. Chem.* 282, 13864–13874. doi: 10.1074/jbc.m700505200

Chartier, F. J., Hardy, E. J., and Laprise, P. (2011). Crumbs controls epithelial integrity by inhibiting Rac1 and PI3K. *J. Cell Sci.* 124, 3393–3398. doi: 10.1242/jcs.092601

Chen, X., and Macara, I. G. (2005). Par-3 controls tight junction assembly through the Rac exchange factor Tiam1. *Nat. Cell Biol.* 7, 262–269. doi: 10.1038/ncb1226

Claret, S., Jouette, J., Benoit, B., Legent, K., and Guichet, A. (2014). PI(4,5)P2 produced by the PI4P5K SKTL controls apical size by tethering PAR-3 in *Drosophila* epithelial cells. *Curr. Biol.* 24, 1071–1079. doi: 10.1016/j.cub.2014.03.056

Consonni, S. V., Brouwer, P. M., van Slobbe, E. S., and Bos, J. L. (2014). The PDZ domain of the guanine nucleotide exchange factor PDZGEF directs binding to phosphatidic acid during brush border formation. *PLoS One* 9:e98253. doi: 10.1371/journal.pone.0098253

Das, A., Slaughter, B. D., Unruh, J. R., Bradford, W. D., Alexander, R., Rubinstein, B., et al. (2012). Flippase-mediated phospholipid asymmetry promotes fast Cdc42 recycling in dynamic maintenance of cell polarity. *Nat. Cell Biol.* 14, 304–310. doi: 10.1038/ncb2444

de Kreuk, B. J., and Hordijk, P. L. (2012). Control of Rho GTPase function by BAR-domains. *Small GTPases.* 3, 45–52. doi: 10.4161/sgtp.18960

Doerflinger, H., Vogt, N., Torres, I. L., Mirouse, V., Koch, I., Nusslein-Volhard, C., et al. (2010). Bazooka is required for polarisation of the *Drosophila* anterior-posterior axis. *Development* 137, 1765–1773. doi: 10.1242/dev.045807

Dogliotti, G., Kullmann, L., Dhumale, P., Thiele, C., Panichkina, O., Mendl, G., et al. (2017). Membrane-binding and activation of LKB1 by phosphatidic acid is essential for development and tumour suppression. *Nat. Commun.* 8:15747. doi: 10.1038/ncomms15747

Dong, W., Zhang, X., Liu, W., Chen, Y. J., Huang, J., Austin, E., et al. (2015). A conserved polybasic domain mediates plasma membrane targeting of Lgl and its regulation by hypoxia. *J. Cell Biol.* 211, 273–286. doi: 10.1083/jcb.201503067

Ebnet, K., Suzuki, A., Horikoshi, Y., Hirose, T., Meyer, M., Zu Brickwedde, K., et al. (2001). The cell polarity protein ASIP/PAR-3 directly associates with junctional adhesion molecule (JAM). *EMBO J.* 20, 3738–3748. doi: 10.1093/emboj/20.14.3738

Elbert, M., Rossi, G., and Brennwald, P. (2005). The yeast par-1 homologs kin1 and kin2 show genetic and physical interactions with components of the exocytic machinery. *Mol. Biol. Cell* 16, 532–549. doi: 10.1091/mbc.e04-07-0549

Etienne-Manneville, S. (2008). Polarity proteins in migration and invasion. *Oncogene* 27, 6970–6980. doi: 10.1038/onc.2008.347

Fairn, G. D., Hermansson, M., Somerharju, P., and Grinstein, S. (2011). Phosphatidylserine is polarized and required for proper Cdc42 localization and for development of cell polarity. *Nat. Cell Biol.* 13, 1424–1430. doi: 10.1038/ncb2351

Feng, W., Wu, H., Chan, L. N., and Zhang, M. (2008). Par-3-mediated junctional localization of the lipid phosphatase PTEN is required for cell polarity establishment. *J. Biol. Chem.* 283, 23440–23449. doi: 10.1074/jbc.M802482200

Ferraz-Nogueira, J. P., Diez-Guerra, F. J., and Llopis, J. (2014). Visualization of phosphatidic acid fluctuations in the plasma membrane of living cells. *PLoS One* 9:e102526. doi: 10.1371/journal.pone.0102526

Gambhir, A., Hangyas-Mihalyne, G., Zaitseva, I., Cafiso, D. S., Wang, J., Murray, D., et al. (2004). Electrostatic sequestration of PIP2 on phospholipid membranes by basic/aromatic regions of proteins. *Biophys. J.* 86, 2188–2207. doi: 10.1016/s0006-3495(04)74278-2

Gao, L., and Macara, I. G. (2004). Isoforms of the polarity protein par6 have distinct functions. *J. Biol. Chem.* 279, 41557–41562. doi: 10.1074/jbc.m403723200

Gassama-Diagne, A., Yu, W., ter Beest, M., Martin-Belmonte, F., Kierbel, A., Engel, J., et al. (2006). Phosphatidylinositol-3,4,5-trisphosphate regulates the formation of the basolateral plasma membrane in epithelial cells. *Nat. Cell Biol.* 8, 963–970. doi: 10.1038/ncb1461

Gloerich, M., ten Klooster, J. P., Vliem, M. J., Koorman, T., Zwartkruis, F. J., Clevers, H., et al. (2012). Rap2A links intestinal cell polarity to brush border formation. *Nat. Cell Biol.* 14, 793–801. doi: 10.1038/ncb2537

Goransson, O., Deak, M., Wullschleger, S., Morrice, N. A., Prescott, A. R., and Alessi, D. R. (2006). Regulation of the polarity kinases PAR-1/MARK by 14-3-3 interaction and phosphorylation. *J. Cell Sci.* 119, 4059–4070. doi: 10.1242/jcs.03097

Harris, T. J., and Peifer, M. (2005). The positioning and segregation of apical cues during epithelial polarity establishment in *Drosophila*. *J. Cell Biol.* 170, 813–823. doi: 10.1083/jcb.200505127

Haupt, A., and Minc, N. (2017). Gradients of phosphatidylserine contribute to plasma membrane charge localization and cell polarity in fission yeast. *Mol. Biol. Cell* 28, 210–220. doi: 10.1091/mbc.E16-06-0353

He, B., Xi, F., Zhang, X., Zhang, J., and Guo, W. (2007). Exo70 interacts with phospholipids and mediates the targeting of the exocyst to the plasma membrane. *EMBO J.* 26, 4053–4065. doi: 10.1038/sj.emboj.7601834

Heller, B., Adu-Gyamfi, E., Smith-Kinnaman, W., Babbey, C., Vora, M., Xue, Y., et al. (2010). Amot recognizes a juxtanuclear endocytic recycling compartment via a novel lipid binding domain. *J. Biol. Chem.* 285, 12308–12320. doi: 10.1074/jbc.M109.096230

Heo, W. D., Inoue, T., Park, W. S., Kim, M. L., Park, B. O., Wandless, T. J., et al. (2006). PI(3,4,5)P3 and PI(4,5)P2 lipids target proteins with polybasic clusters to the plasma membrane. *Science* 314, 1458–1461. doi: 10.1126/science.1134389

Horikoshi, Y., Hamada, S., Ohno, S., and Suetsugu, S. (2011). Phosphoinositide binding by par-3 involved in par-3 localization. *Cell Struct. Funct.* 36, 97–102. doi: 10.1247/csf.11005

Hurd, T. W., Fan, S., Liu, C. J., Kweon, H. K., Hakansson, K., and Margolis, B. (2003a). Phosphorylation-dependent binding of 14-3-3 to the polarity protein Par3 regulates cell polarity in mammalian epithelia. *Curr. Biol.* 13, 2082–2090. doi: 10.1016/j.cub.2003.11.020

Hurd, T. W., Gao, L., Roh, M. H., Macara, I. G., and Margolis, B. (2003b). Direct interaction of two polarity complexes implicated in epithelial tight junction assembly. *Nat. Cell Biol.* 5, 137–142. doi: 10.1038/ncb923

Hurov, J. B., Watkins, J. L., and Piwnica-Worms, H. (2004). Atypical PKC phosphorylates PAR-1 kinases to regulate localization and activity. *Curr. Biol.* 14, 736–741. doi: 10.1016/j.cub.2004.04.007

Iden, S., Rehder, D., August, B., Suzuki, A., Wolburg-Buchholz, K., Wolburg, H., et al. (2006). A distinct PAR complex associates physically with VE-cadherin in vertebrate endothelial cells. *EMBO Rep.* 7, 1239–1246. doi: 10.1038/sj.embor.7400819

Iijima, M., Huang, Y. E., Luo, H. R., Vazquez, F., and Devreotes, P. N. (2004). Novel mechanism of PTEN regulation by its phosphatidylinositol 4,5-bisphosphate binding motif is critical for chemotaxis. *J. Biol. Chem.* 279, 16606–16613. doi: 10.1074/jbc.m312098200

Jeanes, A., Smutny, M., Leerberg, J. M., and Yap, A. S. (2009). Phosphatidylinositol 3'-kinase signalling supports cell height in established epithelial monolayers. *J. Mol. Histol.* 40, 395–405. doi: 10.1007/s10735-010-9253-y

Kay, J. G., and Fairn, G. D. (2019). Distribution, dynamics and functional roles of phosphatidylserine within the cell. *Cell Commun. Signal.* 17:126. doi: 10.1186/s12964-019-0438-z

Kempkens, O., Medina, E., Fernandez-Ballester, G., Ozuyaman, S., Le Bivic, A., Serrano, L., et al. (2006). Computer modelling in combination with in vitro studies reveals similar binding affinities of *Drosophila* Crumbs for the PDZ domains of Stardust and DmPar-6. *Eur. J. Cell Biol.* 85, 753–767. doi: 10.1016/j.ejcb.2006.03.003

Krahn, M. P., Buckers, J., Kastrup, L., and Wodarz, A. (2010a). Formation of a Bazooka-Stardust complex is essential for plasma membrane polarity in epithelia. *J. Cell Biol.* 190, 751–760. doi: 10.1083/jcb.201006029

Krahn, M. P., Egger-Adam, D., and Wodarz, A. (2009). PP2A antagonizes phosphorylation of Bazooka by PAR-1 to control apical-basal polarity in dividing embryonic neuroblasts. *Dev. Cell* 16, 901–908. doi: 10.1016/j.devcel.2009.04.011

Krahn, M. P., Klopfenstein, D. R., Fischer, N., and Wodarz, A. (2010b). Membrane targeting of Bazooka/PAR-3 is mediated by direct binding to phosphoinositide lipids. *Curr. Biol.* 20, 636–642. doi: 10.1016/j.cub.2010.01.065

Kullmann, L., and Krahn, M. P. (2018a). Controlling the master-upstream regulation of the tumor suppressor LKB1. *Oncogene* 37, 3045–3057. doi: 10.1038/s41388-018-0145-z

Kullmann, L., and Krahn, M. P. (2018b). Redundant regulation of localization and protein stability of DmPar3. *Cell. Mol. Life Sci.* 75, 3269–3282. doi: 10.1007/s00018-018-2792-1

Lee, J. O., Yang, H., Georgescu, M. M., Di Cristofano, A., Maehama, T., Shi, Y., et al. (1999). Crystal structure of the PTEN tumor suppressor: implications for its phosphoinositide phosphatase activity and membrane association. *Cell* 99, 323–334.

Lemmers, C., Michel, D., Lane-Guermonprez, L., Delgrossi, M. H., Medina, E., Arsanto, J. P., et al. (2004). CRB3 binds directly to Par6 and regulates the morphogenesis of the tight junctions in mammalian epithelial cells. *Mol. Biol. Cell* 15, 1324–1333. doi: 10.1091/mbc.e03-04-0235

Li, L., Shi, X., Guo, X., Li, H., and Xu, C. (2014). Ionic protein-lipid interaction at the plasma membrane: what can the charge do? *Trends Biochem. Sci.* 39, 130–140. doi: 10.1016/j.tibs.2014.01.002

Liu, J., Zuo, X., Yue, P., and Guo, W. (2007). Phosphatidylinositol 4,5-bisphosphate mediates the targeting of the exocyst to the plasma membrane for exocytosis in mammalian cells. *Mol. Biol. Cell* 18, 4483–4492. doi: 10.1091/mbc.e07-05-0461

Liu, K. D., Datta, A., Yu, W., Brakeman, P. R., Jou, T. S., Matthay, M. A., et al. (2007). Rac1 is required for reorientation of polarity and lumen formation through a PI 3-kinase-dependent pathway. *Am. J. Physiol. Renal Physiol.* 293, F1633–F1640.

Liu, Y., Su, Y., and Wang, X. (2013). Phosphatidic acid-mediated signaling. *Adv. Exp. Med. Biol.* 991, 159–176. doi: 10.1007/978-94-007-6331-9_9

Lizcano, J. M., Goransson, O., Toth, R., Deak, M., Morrice, N. A., Boudeau, J., et al. (2004). LKB1 is a master kinase that activates 13 kinases of the AMPK subfamily, including MARK/PAR-1. *EMBO J.* 23, 833–843. doi: 10.1038/sj.emboj.7600110

Lv, M., Shen, Y., Yang, J., Li, S., Wang, B., Chen, Z., et al. (2017). Angiomotin family members: oncogenes or tumor suppressors? *Int. J. Biol. Sci.* 13, 772–781. doi: 10.7150/ijbs.19603

Maree, A. F., Grieneisen, V. A., and Edelstein-Keshet, L. (2012). How cells integrate complex stimuli: the effect of feedback from phosphoinositides and cell shape on cell polarization and motility. *PLoS Comput. Biol.* 8:e1002402. doi: 10.1371/journal.pcbi.1002402

Martin-Belmonte, F., Gassama, A., Datta, A., Yu, W., Rescher, U., Gerke, V., et al. (2007). PTEN-mediated apical segregation of phosphoinositides controls epithelial morphogenesis through Cdc42. *Cell* 128, 383–397. doi: 10.1016/j.cell.2006.11.051

Matsuoka, S., and Ueda, M. (2018). Mutual inhibition between PTEN and PIP3 generates bistability for polarity in motile cells. *Nat. Commun.* 9:4481. doi: 10.1038/s41467-018-06856-0

Maxwell, K. N., Zhou, Y., and Hancock, J. F. (2018). Rac1 nanoscale organization on the plasma membrane is driven by lipid binding specificity encoded in the membrane anchor. *Mol. Cell. Biol.* 38:e00186-18. doi: 10.1128/MCB.00186-18

Mayor, R., and Etienne-Manneville, S. (2016). The front and rear of collective cell migration. *Nat. Rev. Mol. Cell Biol.* 17, 97–109. doi: 10.1038/nrm.2015.14

McDonald, J. A. (2014). Canonical and noncanonical roles of Par-1/MARK kinases in cell migration. *Int. Rev. Cell Mol. Biol.* 312, 169–199. doi: 10.1016/B978-0-12-800178-3.00006-3

McKinley, R. F., Yu, C. G., and Harris, T. J. (2012). Assembly of Bazooka polarity landmarks through a multifaceted membrane-association mechanism. *J. Cell Sci.* 125, 1177–1190. doi: 10.1242/jcs.091884

Michiels, F., Stam, J. C., Hordijk, P. L., van der Kammen, R. A., Ruuls-Van Stalle, L., Feltkamp, C. A., et al. (1997). Regulated membrane localization of Tiam1, mediated by the NH2-terminal pleckstrin homology domain, is required for Rac-dependent membrane ruffling and C-Jun NH2-terminal kinase activation. *J. Cell Biol.* 137, 387–398. doi: 10.1083/jcb.137.2.387

Moore, B. A., Robinson, H. H., and Xu, Z. (2007). The crystal structure of mouse Exo70 reveals unique features of the mammalian exocyst. *J. Mol. Biol.* 371, 410–421. doi: 10.1016/j.jmb.2007.05.018

Moravcevic, K., Mendrola, J. M., Schmitz, K. R., Wang, Y. H., Slochower, D., Janmey, P. A., et al. (2010). Kinase associated-1 domains drive MARK/PAR1 kinases to membrane targets by binding acidic phospholipids. *Cell* 143, 966–977. doi: 10.1016/j.cell.2010.11.028

Pegtel, D. M., Ellenbroek, S. I., Mertens, A. E., van der Kammen, R. A., de Rooij, J., and Collard, J. G. (2007). The Par-Tiam1 complex controls persistent migration by stabilizing microtubule-dependent front-rear polarity. *Curr. Biol.* 17, 1623–1634. doi: 10.1016/j.cub.2007.08.035

Peng, J., Awad, A., Sar, S., Komaiha, O. H., Moyano, R., Rayal, A., et al. (2015). Phosphoinositide 3-kinase p110delta promotes lumen formation through the enhancement of apico-basal polarity and basal membrane organization. *Nat. Commun.* 6:5937. doi: 10.1038/ncomms6937

Penkert, R. R., DiVittorio, H. M., and Prehoda, K. E. (2004). Internal recognition through PDZ domain plasticity in the Par-6-Pals1 complex. *Nat. Struct. Mol. Biol.* 11, 1122–1127. doi: 10.1038/nsmb839

Plant, P. J., Fawcett, J. P., Lin, D. C., Holdorf, A. D., Binns, K., Kulkarni, S., et al. (2003). A polarity complex of mPar-6 and atypical PKC binds, phosphorylates and regulates mammalian Lgl. *Nat. Cell Biol.* 5, 301–308. doi: 10.1038/ncb948

Polgar, N., and Fogelgren, B. (2018). Regulation of cell polarity by exocyst-mediated trafficking. *Cold Spring Harb. Perspect. Biol.* 10:a031401. doi: 10.1101/cshperspect.a031401

Ramanujam, R., Han, Z., Zhang, Z., Kanchanawong, P., and Motegi, F. (2018). Establishment of the PAR-1 cortical gradient by the aPKC-PRBH circuit. *Nat. Chem. Biol.* 14, 917–927. doi: 10.1038/s41589-018-0117-1

Remorino, A., De Beco, S., Cayrac, F., Di Federico, F., Cornilleau, G., Gautreau, A., et al. (2017). Gradients of Rac1 nanoclusters support spatial patterns of Rac1 signaling. *Cell Rep.* 21, 1922–1935. doi: 10.1016/j.celrep.2017.10.069

Rodriguez-Boulan, E., and Macara, I. G. (2014). Organization and execution of the epithelial polarity programme. *Nat. Rev. Mol. Cell Biol.* 15, 225–242. doi: 10.1038/nrm3775

Rousso, T., Shewan, A. M., Mostov, K. E., Schejter, E. D., and Shilo, B. Z. (2013). Apical targeting of the formin Diaphanous in *Drosophila* tubular epithelia. *eLife* 2:e00666. doi: 10.7554/eLife.00666

Sartorel, E., Unlu, C., Jose, M., Massoni-Laporte, A., Meca, J., Sibarita, J. B., et al. (2018). Phosphatidylserine and GTPase activation control Cdc42 nanoclustering to counter dissipative diffusion. *Mol. Biol. Cell* 29, 1299–1310. doi: 10.1091/mbc.E18-01-0051

Schink, K. O., Tan, K. W., and Stenmark, H. (2016). Phosphoinositides in control of membrane dynamics. *Annu. Rev. Cell Dev. Biol.* 32, 143–171. doi: 10.1146/annurev-cellbio-111315-125349

Schmoranzer, J., Fawcett, J. P., Segura, M., Tan, S., Vallee, R. B., Pawson, T., et al. (2009). Par3 and dynein associate to regulate local microtubule dynamics and centrosome orientation during migration. *Curr. Biol.* 19, 1065–1074. doi: 10.1016/j.cub.2009.05.065

Scholze, M. J., Barbieux, K. S., De Simone, A., Boumasmoud, M., Suess, C. C. N., Wang, R., et al. (2018). PI(4,5)P2 forms dynamic cortical structures and directs actin distribution as well as polarity in Caenorhabditis elegans embryos. *Development* 145:dev169144. doi: 10.1242/dev.169144

Sen, A., Sun, R., and Krahn, M. P. (2015). Localization and function of Pals1-associated tight junction protein in *Drosophila* is regulated by two distinct apical complexes. *J. Biol. Chem.* 290, 13224–13233. doi: 10.1074/jbc.M114.629014

Sit, S. T., and Manser, E. (2011). Rho GTPases and their role in organizing the actin cytoskeleton. *J. Cell Sci.* 124, 679–683. doi: 10.1242/jcs.064964

Smith, C. A., Lau, K. M., Rahmani, Z., Dho, S. E., Brothers, G., She, Y. M., et al. (2007). aPKC-mediated phosphorylation regulates asymmetric membrane localization of the cell fate determinant Numb. *EMBO J.* 26, 468–480. doi: 10.1038/sj.emboj.7601495

Sotillos, S., Diaz-Meco, M. T., Caminero, E., Moscat, J., and Campuzano, S. (2004). DaPKC-dependent phosphorylation of Crumbs is required for epithelial cell polarity in *Drosophila*. *J Cell Biol.* 166, 549–557. doi: 10.1083/jcb.200311031

St Johnston, D., and Ahringer, J. (2010). Cell polarity in eggs and epithelia: parallels and diversity. *Cell* 141, 757–774. doi: 10.1016/j.cell.2010.05.011

Stephens, R., Lim, K., Portela, M., Kvansakul, M., Humbert, P. O., and Richardson, H. E. (2018). The scribble cell polarity module in the regulation of cell signaling in tissue development and tumorigenesis. *J. Mol. Biol.* 430, 3585–3612. doi: 10.1016/j.jmb.2018.01.011

Suzuki, A., Hirata, M., Kamimura, K., Maniwa, R., Yamanaka, T., Mizuno, K., et al. (2004). aPKC acts upstream of PAR-1b in both the establishment and maintenance of mammalian epithelial polarity. *Curr. Biol.* 14, 1425–1435. doi: 10.1016/j.cub.2004.08.021

Takekuni, K., Ikeda, W., Fujito, T., Morimoto, K., Takeuchi, M., Monden, M., et al. (2003). Direct binding of cell polarity protein PAR-3 to cell-cell adhesion molecule nectin at neuroepithelial cells of developing mouse. *J. Biol. Chem.* 278, 5497–5500. doi: 10.1074/jbc.c200707200

Tepass, U. (2012). The apical polarity protein network in *Drosophila* epithelial cells: regulation of polarity, junctions, morphogenesis, cell growth, and survival. *Annu. Rev. Cell Dev. Biol.* 28, 655–685. doi: 10.1146/annurev-cellbio-092910-154033

Thapa, N., Sun, Y., Schramp, M., Choi, S., Ling, K., and Anderson, R. A. (2012). Phosphoinositide signaling regulates the exocyst complex and polarized integrin trafficking in directionally migrating cells. *Dev. Cell* 22, 116–130. doi: 10.1016/j.devcel.2011.10.030

Tuncay, H., Brinkmann, B. F., Steinbacher, T., Schurmann, A., Gerke, V., Iden, S., et al. (2015). JAM-A regulates cortical dynein localization through Cdc42 to control planar spindle orientation during mitosis. *Nat. Commun.* 6:8128. doi: 10.1038/ncomms9128

Varnai, P., Gulyas, G., Toth, D. J., Sohn, M., Sengupta, N., and Balla, T. (2017). Quantifying lipid changes in various membrane compartments using lipid binding protein domains. *Cell Calcium* 64, 72–82. doi: 10.1016/j.ceca.2016.12.008

von Stein, W., Ramrath, A., Grimm, A., Muller-Borg, M., and Wodarz, A. (2005). Direct association of Bazooka/PAR-3 with the lipid phosphatase PTEN

reveals a link between the PAR/aPKC complex and phosphoinositide signaling. *Development* 132, 1675–1686. doi: 10.1242/dev.01720

Wang, Q., Hurd, T. W., and Margolis, B. (2004). Tight junction protein Par6 interacts with an evolutionarily conserved region in the amino terminus of PALS1/stardust. *J. Biol. Chem.* 279, 30715–30721. doi: 10.1074/jbc.m401930200

Wei, S. Y., Escudero, L. M., Yu, F., Chang, L. H., Chen, L. Y., Ho, Y. H., et al. (2005). Echinoid is a component of adherens junctions that cooperates with DE-Cadherin to mediate cell adhesion. *Dev. Cell* 8, 493–504. doi: 10.1016/j.devcel.2005.03.015

Wells, C. D., Fawcett, J. P., Traweger, A., Yamanaka, Y., Goudreault, M., Elder, K., et al. (2006). A Rich1/Amot complex regulates the Cdc42 GTPase and apical-polarity proteins in epithelial cells. *Cell* 125, 535–548. doi: 10.1016/j.cell.2006.02.045

Whitney, D. S., Peterson, F. C., Kittell, A. W., Egner, J. M., Prehoda, K. E., and Volkman, B. F. (2016). Crumbs binding to the Par-6 CRIB-PDZ module is regulated by Cdc42. *Biochemistry* 55, 1455–1461. doi: 10.1021/acs.biochem.5b01342

Wirtz-Peitz, F., Nishimura, T., and Knoblich, J. A. (2008). Linking cell cycle to asymmetric division: Aurora-A phosphorylates the Par complex to regulate Numb localization. *Cell* 135, 161–173. doi: 10.1016/j.cell.2008.07.049

Wu, H., Feng, W., Chen, J., Chan, L. N., Huang, S., and Zhang, M. (2007). PDZ domains of Par-3 as potential phosphoinositide signaling integrators. *Mol. Cell* 28, 886–898. doi: 10.1016/j.molcel.2007.10.028

Yang, Y., Lee, M., and Fairn, G. D. (2018). Phospholipid subcellular localization and dynamics. *J. Biol. Chem.* 293, 6230–6240. doi: 10.1074/jbc.r117.000582

Yu, C. G., and Harris, T. J. (2012). Interactions between the PDZ domains of Bazooka (Par-3) and phosphatidic acid: in vitro characterization and role in epithelial development. *Mol. Biol. Cell* 23, 3743–3753. doi: 10.1091/mbc.E12-03-0196

Zhang, S., Schafer-Hales, K., Khuri, F. R., Zhou, W., Vertino, P. M., and Marcus, A. I. (2008). The tumor suppressor LKB1 regulates lung cancer cell polarity by mediating cdc42 recruitment and activity. *Cancer Res.* 68, 740–748. doi: 10.1158/0008-5472.CAN-07-2989

Zhang, X., Orlando, K., He, B., Xi, F., Zhang, J., Zajac, A., et al. (2008). Membrane association and functional regulation of Sec3 by phospholipids and Cdc42. *J. Cell Biol.* 180, 145–158. doi: 10.1083/jcb.200704128

Conflict of Interest: The author declares that the research was conducted in the absence of any commercial or financial relationships that could be construed as a potential conflict of interest.

frontiers in Cell and Developmental Biology

ORIGINAL RESEARCH
published: 19 May 2020
doi: 10.3389/fcell.2020.00350

Localization Preference of Antimicrobial Peptides on Liquid-Disordered Membrane Domains

*Juanjuan Su[1], Siewert J. Marrink[1] and Manuel N. Melo[2]**

[1] Molecular Dynamics Group, Groningen Biomolecular Sciences and Biotechnology Institute and Zernike Institute for Advanced Materials, University of Groningen, Groningen, Netherlands, [2] Multiscale Modeling Lab, Instituto de Tecnologia Química e Biológica António Xavier, Universidade Nova de Lisboa, Oeiras, Portugal

We performed coarse-grained simulations of the antimicrobial peptides Magainin-2, BP100, MSI-103, and MSI-78 on a phase-separated membrane to study their preference for the different domains. All the peptides displayed a clear preference for the liquid-disordered (Ld) phase over the liquid-ordered (Lo) one. For BP100, MSI-103, and MSI-78 there was a further preference of the peptides for the domain interface. The peptides' preference toward the disordered phase was shown to reflect a penalization of lipid–lipid interaction enthalpy in the Lo phase, when in the vicinity of peptides. Similar results were observed at the two studied concentrations, although Ld phase saturation at the higher concentration drove some of the peptide excess to the Lo phase. Magainin-2 and MSI-103 were found to dimerize, in agreement with available experimental data. Interestingly, at high concentrations of Magainin-2 toroidal pores spontaneously formed in the Ld phase. We performed additional simulations to characterize this phenomenon, which is likely related to Magainin-2's membranolytic action.

Keywords: antimicrobial peptides, phase separation, liquid-ordered, liquid-disordered, pore, coarse-grain, molecular dynamics, enthalpy

OPEN ACCESS

Edited by:
Rainer A. Böckmann, University of Erlangen Nuremberg, Germany

Reviewed by:
Alan Marc Grossfield, University of Rochester, United States
Lianghui Gao, Beijing Normal University, China

****Correspondence:***
Manuel N. Melo
m.n.melo@itqb.unl.pt

Specialty section:
This article was submitted to Cellular Biochemistry, a section of the journal Frontiers in Cell and Developmental Biology

Received: *22 January 2020*
Accepted: *20 April 2020*
Published: *19 May 2020*

Citation:
Su J, Marrink SJ and Melo MN (2020) Localization Preference of Antimicrobial Peptides on Liquid-Disordered Membrane Domains. Front. Cell Dev. Biol. 8:350. doi: 10.3389/fcell.2020.00350

INTRODUCTION

Membrane lipid heterogeneity is crucial for various processes in living cells. Functions attributed to the membrane lipidome range from specific integral protein solvation (Contreras et al., 2011) to signaling (Forrester et al., 2004; Golub et al., 2004) to formation of spatial domains of different local composition (Simons and Toomre, 2000). Commonly used model systems are bilayers composed of ternary mixtures of cholesterol, saturated, and unsaturated lipids, which yield a rich phase behavior at physiological temperatures (Feigenson, 2006). Over a range of component concentrations these ternary mixtures laterally separate into a liquid-ordered (Lo) phase, enriched in the saturated lipid and cholesterol, and a liquid-disordered (Ld) one, enriched in the unsaturated lipid (Veatch and Keller, 2003; Marsh, 2009; Dewitt and Dunn, 2015). While such lipid segregation has not been observed at large scales in cellular membranes, the phase-separated ternary mixture

model is still relevant, as there is plenty evidence of heterogeneity in lipid distribution, both in physiological membranes (Van Meer et al., 2008; Fadeel and Xue, 2009) and in complex models thereof (Ingólfsson et al., 2014). Understanding the interplay between membrane proteins and such heterogeneous surroundings is central to shedding light on the function of both proteins and the associated lipids.

An important class of proteins interacting with lipid membranes is formed by antimicrobial peptides (AMPs). Antimicrobial peptides are typically short cationic peptides and diverse both in sequence and structure (Epand and Vogel, 1999; Yeaman and Yount, 2003). The amphipathic α-helical structured AMPs are particularly abundant and widespread in nature (Oren and Shai, 1998). Their net cationicity and amphipathic character facilitates their incorporation into the negatively charged microbial membranes. The activity of AMPs has been observed to depend critically on the composition of target cell membranes. Many studies focus on model membranes containing negatively charged lipids, mimicking the bacterial membrane composition and allowing the characterization of the electrostatic component of the interactions between the cationic peptides and the host's membranes (Epand et al., 2010; Polyansky et al., 2010; Wadhwani et al., 2012). At the same time, the disruption of cholesterol-containing homogeneous membranes by AMPs has attracted some interest since many of these peptides are able to kill fungi, protozoa, and enveloped viruses—all of which have sterol-rich membranes (Raghuraman and Chattopadhyay, 2004; Verly et al., 2008; Ramamoorthy et al., 2010). However, only a limited number of experimental studies have looked at AMPs interacting with phase-separated heterogeneous membranes (Brender et al., 2012; McHenry et al., 2012).

In this work, we use molecular dynamics (MD) simulations to study the interactions of four AMPs—Magainin-2, BP100, MSI-103, and MSI-78—with phase-separated model membranes composed of cholesterol, a saturated lipid (di-palmitoyl phosphatidylcholine; DPPC), and a polyunsaturated lipid (di-linoleyl phosphatidylcholine; DLiPC). The four peptides were selected to represent different sizes and charge densities, although all four share the same α-helical secondary structure and cationic nature, both typical of AMPs (**Figure 1**). Magainin-2 (23 residues) has a low net charge (+3), while MSI-78 has a similar length (22 residues) but a much higher cationic charge (+9); MSI-78 has also been experimentally investigated by McHenry et al. (2012) on phase-separated lipid membranes. BP100 has the highest charge density (+6 over 11 residues). MSI-103 (+7, 21 residues) is a somewhat intermediate example, and also the only one of the peptides that has an entirely synthetic origin (Strandberg et al., 2008), all others being either naturally occurring AMPs or inspired by AMPs that are.

We use the Martini coarse-grained force field (Marrink et al., 2007), widely used in simulations of phase-separating bilayers (Risselada and Marrink, 2008; Bennett and Tieleman, 2013). Previous simulation studies using this model have shown a preference of other compounds—transmembrane proteins (Schäfer et al., 2011; Domański et al., 2012), sugars (Moiset et al., 2014), aliphatics (Barnoud et al., 2014; Rossi et al., 2014), and drugs (Muddana et al., 2012)—to partition into the Ld phase, or to adsorb at the domain boundaries, sometimes leading to domain remodeling. Here, our aim is to ascertain the phase preference of AMPs and to explain the driving forces behind it.

MATERIALS AND METHODS

Force Field and Simulated Systems

In this work, we employed Martini version 2.2 for our lipids, cholesterol, and peptide parameters (Marrink et al., 2007; Monticelli et al., 2008; de Jong et al., 2013; Melo et al., 2015). The representation of the simulation box, peptides and lipids is shown in **Figure 1**. We used the Avogadro software (Hanwell et al., 2012) to build the initial atomistic structures of each peptide, assuming an entirely α-helical secondary structure. The coarse-grained Martini structures were obtained using the *martinize.py* script. The simulated bilayers were composed of DPPC, DLiPC, and cholesterol at a 42:28:30 ratio, for a total of 3628 lipids. A membrane patch was first equilibrated in water for 2.3 μs until equilibrium Lo/Ld phase separation was reached, following the pioneering work of Risselada and Marrink (2008). A rectangular patch shape of large aspect ratio was chosen so that phase domains could easily become continuous with themselves across the periodicity in the y direction, thus reducing the phase interface line tension. Each AMP was added to a separate copy of this patch, placed at the surface of the membrane. Two peptide-to-lipid (P:L) ratios were employed: 1:200 and 1:20. All systems were made charge neutral by addition of the appropriate amount of chloride ions. At the highest concentration case, peptides were added to both sides of the membrane, in equal numbers, to prevent bilayer disruption due to sheer tension mismatch. Prior to production runs, peptide orientation and depth were equilibrated for at least 200 ns under the following adsorption protocol (adapted from Su et al., 2018): first and last backbone particles (also called "beads") of each peptide were restrained in the xy plane with a harmonic potential of 3000 kJ mol^{-1} nm^{-2} to prevent lateral diffusion and untimely peptide–peptide association. A harmonic restraint in z (5000 kJ mol^{-1} nm^{-2}) was further applied on the peptides, pulling them to a distance of 1.4 nm from the bilayer center, and preventing dissociation into the aqueous phase. This setup allowed the peptides to rotate parallel to the bilayer plane to optimally face the bilayer, without getting trapped in pre-equilibrium aggregates. Production runs then proceeded without any restraint on the peptides for a minimum of 60 μs, with configurations saved for analysis every 30 ns.

Simulation Parameters

All the simulations were performed using the GROMACS software (Hess et al., 2008) version 4.6.7 or version 5.1 when the use of flat-bottom restraining potentials was needed. Periodic boundary conditions were used. The temperature was coupled (coupling time 1.0 ps) to T = 295 K, using the Berendsen thermostat (Berendsen et al., 1984). The pressure was coupled using the Berendsen barostat (Berendsen et al., 1984) (coupling time of 0.5 ps and compressibility of 4.5×10^{-5}), using a semi-isotropic coupling scheme in which the lateral and perpendicular

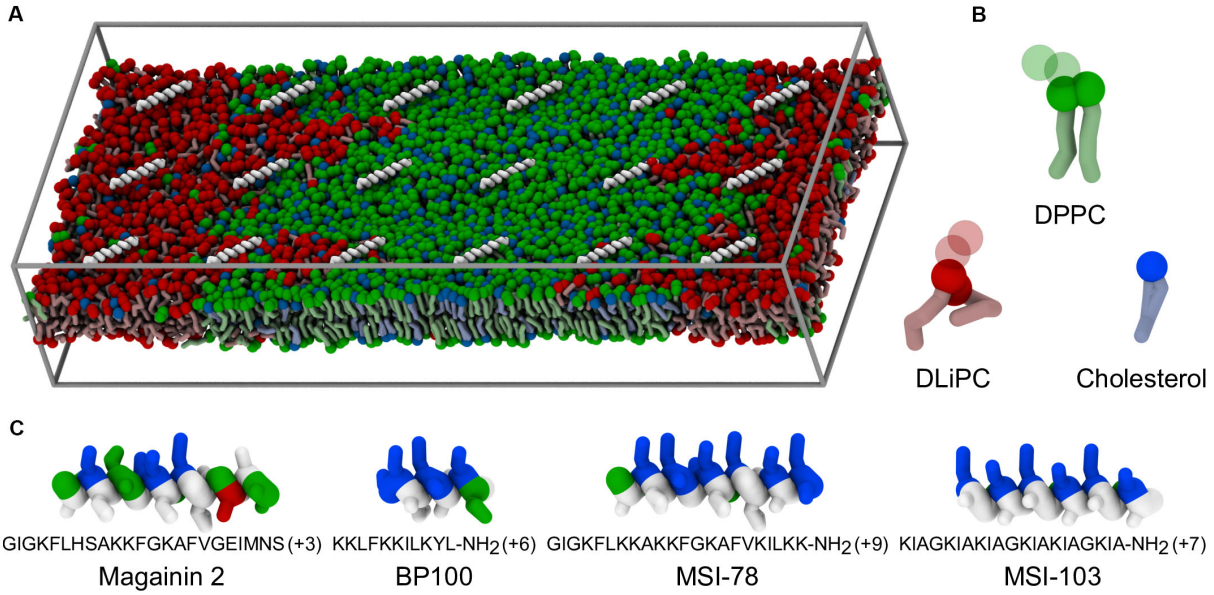

FIGURE 1 | Coarse-grained representation of simulation box, peptides, and lipids. **(A)** Example of starting system configuration, showing the initial placement of low concentrations of MSI-78. The box size was of 47 nm × 19 nm × 10 nm. Components follow the representation scheme of the remaining panels, with the exceptions that, for clarity, peptides are shown only as white backbones and the charged particles of the phospholipid headgroups (phosphate and choline) are omitted; solvent is also not shown. **(B)** Representation of the coarse-grain structure of the used lipids. Full spheres highlight the polar coarse-grain particles (glycerol in the phospholipids, hydroxyl moiety in cholesterol); translucent spheres indicate the charged phospholipid particles not depicted in **(A)**. **(C)** Coarse-grain structure of the studied α-helical peptides, colored according to residue polarity/charge (apolar: white, polar: green, acidic: red, basic: blue) and highlighting their amphipathic nature.

pressures were coupled independently at 1 bar, corresponding to a tension-free state of the membrane. Non-bonded interactions were computed as Lennard-Jones (LJ) potentials, switched to zero from 0.9 to 1.2 nm (pair-list update frequency of once per 10 steps). Electrostatics were calculated as Coulombic interactions with an implicit dielectric screening constant of 15, shifted to zero from 0 nm to the same 1.2 nm cutoff. A time step of 30 fs was used.

Buckling Restraints

Membrane buckling can be expected to occur, independently of peptide presence, in these systems with large box vectors. To dampen it, one glycerol bead of each lipid was position-restrained in the z direction with a weak (300 kJ mol^{-1} nm^{-2}) quadratic potential. This strategy, also successfully applied to more complex membranes (Ingólfsson et al., 2014), allows the use of a box size of smaller height without the risk of direct interaction between peptides and lipids of adjacent periodic images in z. In a reference simulation, we used as an alternative a flat-bottomed potential restraint of 1000 kJ mol^{-1} nm^{-2}, confining glycerol moieties to a xy slab of defined (4 nm) vertical thickness. This potential, available since GROMACS version 5.0, is harmonic at the slab edges but zero throughout. It therefore only acts on particles leaving the slab region, allowing the headgroups to move freely toward the bilayer core and even flip-flop.

Analysis

The analyses focus on the last 20 μs of each production simulation and extensively employ the NumPy (van der Walt et al., 2011), scikit-learn (Pedregosa et al., 2012), scikit-image (van der Walt et al., 2014), and MDAnalysis (Michaud-Agrawal et al., 2011; Gowers et al., 2016) Python packages. Values are reported as averages over those 20 μs, with 95% confidence intervals estimated using a bootstrap procedure with 1000 resamplings. Underestimation of uncertainty due to time-correlated data was corrected for by bootstrap-resampling a lower number of datapoints, proportionally to the integrated autocorrelation time of the observation (expressed in number of frames). As an example: for the 666 data points in the analyzed 20 μs at a rate of 30 ns/frame, for an observation with an integrated autocorrelation time of 2 frames, bootstrap resamplings were only done for 333 data points. All the measured values on which analysis was performed are included as a **Supplementary Data** archive. The Python code used to generate such datasets is included in the same archive.

Phase Assignment and Peptide Depth

To identify different domains, a phase-assignment algorithm (Jefferys et al., 2014) was implemented. In this algorithm lipid positions were flattened in z and smoothed using a Gaussian kernel with a 1.0 nm standard deviation. The first lipid tail beads (particles C1A and C1B) of DPPC and DLiPC were used to represent each species. The smoothed signal was sampled on a point grid of 1 × 1 Å spacing. The phase domain interfaces were determined by subtracting the DPPC signal from the DLiPC signal and running the result through the scikit-image Canny edge-detection filter. Analysis edge effects due to box periodicity were avoided by including beads of the neighboring periodic

images and extending the phase assignment region by 2 nm in each direction. **Figure 2** schematizes the analysis of a system in the presence of low concentrations of BP100.

To quantify the domain preference of the AMPs, peptide backbone beads were assigned to each of three possible regions: Ld, Lo, or interface, based on their *z*-flattened *xy* position. Beads were considered interfacial if within a 1.5 nm radius of an interface grid point. This radius was chosen for corresponding to a phosphate–phosphate distance that includes at least the first two neighbor shells; robustness of results to this choice was tested with radii from 1.2 to 2.0 nm (**Supplementary Figure 4**). Remaining backbone beads were considered to be in the Ld (resp. Lo) region if they were closest to a cell of that type. The counts of assigned backbone beads were normalized by the expected counts in each respective region given a random peptide distribution, which amounts to a normalization by region area fraction and global peptide density. The resulting value represents the ratio of enrichment of each region relative to a random peptide distribution.

The depth of peptides inserted into the membrane was measured as the *z*-distance of backbone beads to the center-of-mass of the phosphate beads of lipids within a 2 nm *xy* radius.

Enthalpy Decomposition

The GROMACS package allows for the decomposition of interaction energies between defined groups. These groups, however, cannot be dynamically updated throughout the simulation, making the GROMACS tools unsuited to decomposing energies based on phase location criteria. To this end we implemented the Martini force-field nonbonded energy functions in Python and were then able to calculate nonbonded interactions between dynamic groups. We recreated the coulombic and LJ interaction potentials as per **Supplementary Equation 1** through **6**. Potential shapes were confirmed to be accurate by comparison to the debug output of the GROMACS mdrun program, which allows the inspection of the potential shapes used during simulation in tabulated numerical form. We focused energy analysis on the interactions between peptides, lipids, and solvent, discriminating the location of each peptide residue (based on the backbone bead location of said residue) as either Ld, Lo, or interfacial. As a further test of the accurate reproduction of nonbonded energies by our in-house code, a 20-frame trajectory segment was analyzed and the phase-discriminated peptide–lipid and peptide–solvent nonbonded energies were summed for the three considered phases. The resulting sum compared very well to the non-discriminated values calculated by the GROMACS package, with a maximum absolute difference of 8×10^{-3} kJ mol^{-1} and a maximum relative difference of 3 ppm, likely attributable to the differences in order of floating point operations (**Supplementary Figure 5**). The decomposition code is included in the **Supplementary Data**, archive alongside the dataset produced with it and scripts for further processing into the data presented here.

To estimate the enthalpic impact of peptide adsorption on lipid interactions a second discrimination was performed: lipids were classified as either Ld, interfacial, or Lo (depending on the closest phase-assignment grid point to the lipid's phosphate bead), and as near to or far from a peptide depending on whether any of the lipid's particles are within the 1.2 nm interaction cutoff of any peptide particles. Interfacial lipids were not considered for purposes of energy discrimination. Energies were calculated between each of the four discriminated groups (Ld/Lo, near/far) and the non-discriminated groups of all lipids, peptides, and solvent. Energies were normalized by the number of near/far lipid molecules and by the number of peptide residues in the respective Ld/Lo region—see more details in the accompanying **Supplementary Figure 2**.

Enthalpy decomposition was processed independently for each leaflet. Because cholesterol molecules can undergo flip-flop in the simulation's timescale, they further had to be frame-by-frame dynamically assigned to each leaflet; a leaflet's cholesterols were defined to be those with their hydroxyl bead within 2 nm of any of the leaflet's lipid phosphate beads.

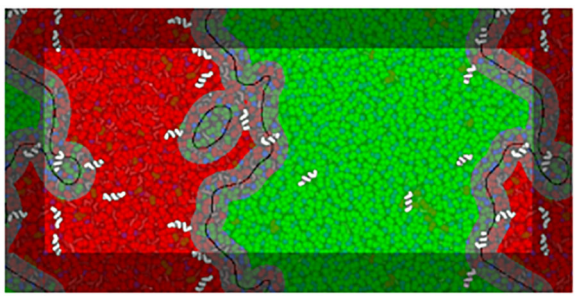

FIGURE 2 | Example of interface analysis on a frame of a BP100 simulation at low peptide concentrations (matching the respective panel in **Figure 3**). A visualization of the analysis is overlaid on a representation of the system configuration, peptides being shown above the overlay for clarity. Black lines trace the identified interface phase boundaries, with a 1.5 nm contour—the interface region—in gray. The Lo and Ld domains are shown in translucent green and red, respectively. The interface lines are depicted with a thickness proportional to the width of the phase assignment grid spacing (1 Å).

Cluster Size Determination

To quantify oligomerization order, a 0.6 nm cutoff-based neighborhood graph between backbone beads was constructed. However, to still be able to have meaningful results at high peptide densities, where chance contacts are frequent, the following rules were employed: (i) two peptides are in contact, and establish a cluster, if at least three of each peptide's backbone beads are neighbors to any of the other peptide's backbone beads; (ii) a peptide is part of a cluster if at least three of its backbone beads are neighbors to at least three backbone beads of the cluster's peptides (regardless if the contacted beads are all from a single peptide in the cluster or from multiple ones); and (iii) two clusters with peptides in common are considered a single cluster. These criteria were tuned to match visual assignments in representative cases, by favoring the counting of side-by-side peptide oligomerization as cluster-forming relative to weaker-bound situations (such as when two peptides meet in a T formation). Cluster size distributions are presented not as the

number of clusters of each order, which visually inflates the contribution of low-order clusters, but as the fraction of total peptides taking part in clusters of each order.

RESULTS

Peptide Oligomerization

Figure 3 shows the lateral organization of the peptides after 60 μs simulation time, at 1:200 and 1:20 P:L ratios. Focusing at the level of peptide–peptide interactions, the oligomerization behavior clearly differs between Magainin-2—mostly a dimer—and the other AMPs—mostly monomers. The oligomerization state is quantified in **Figure 4**, showing a much broader size distribution for Magainin-2, with a peak for the dimeric state regardless of concentration. This is in good agreement with the experimental observation of Magainin-2 dimer formation (Mukai et al., 2002; Wakamatsu et al., 2002). We observed MSI-103 to also dimerize, transiently and to a low extent (12%) at high concentrations (**Figures 3F**, **4**–inset), in line with experimental evidence of environment-dependent MSI-103 aggregation (Toke et al., 2004). MSI-78 and BP100 have an even lower dimerization propensity, reaching only 9% and 3% rates of dimerization, respectively, at high concentrations. Although there is no direct experimental evidence that this is indeed their preferred oligomerization state, MSI-78 and BP100 have cationic charge densities higher than those of either Magainin-2 or the weakly-dimerizing MSI-103. BP100 or MSI-78 aggregation is therefore an unlikely event, consistent with our observations, and supported by the overall agreement of simulated Magainin-2/MSI-103 oligomerization with experimental data. Because AMP oligomerization is dependent, at least in part, on charge interactions, the observed agreement with experimental behavior validates our use of Martini's coarse electrostatics and of a simplified ionic environment with only neutralizing ions.

Peptide Phase Localization

According to the experimental data of McHenry et al. (2012), MSI-78 has a preference for the Ld phase. Our simulations display the same behavior, as can be inferred from **Figure 3**. In fact, one can observe that all four AMPs prefer the Ld phase. The affinity for the disordered domain does not seem to be the same for all peptides, though. Magainin-2 is virtually absent from the ordered phase at low concentrations, whereas MSI-103 seems to distribute more homogeneously. **Figure 5** shows the quantification of these observations over the last 20 μs of each trajectory. Indeed, at low concentrations there is a preference of all peptides for the Ld phase over the Lo one. It is the interfacial region, however, that is the most enriched, for all peptides but Magainin-2.

At high concentrations, and for all peptides, the enrichment ratio of each region is brought closer to 1 (**Figure 5B**). This seems to indicate that the preferred regions (interface and/or Ld) get saturated and the excess peptide is forced into the remaining phases. In the particular case of MSI-78 the preference for the interface region over the Ld phase becomes reduced. This may be related to some degree of lowering of line tension by MSI-78,

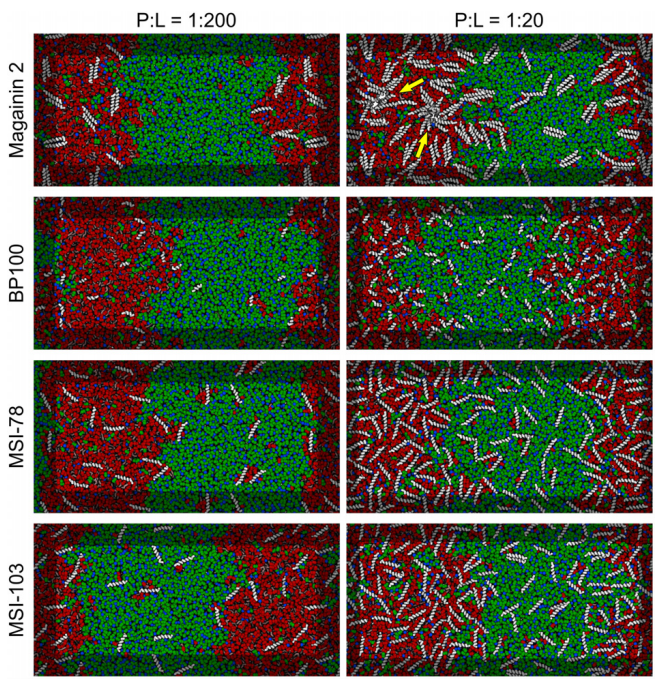

FIGURE 3 | Partitioning behavior of antimicrobial peptides. Snapshots of simulations at 60 μs at low (P:L = 1:200, **left column**) and high (P:L = 1:20, **right column**) peptide concentrations. DPPC, DLiPC, and cholesterol are colored in green, red, and blue, respectively. Backbones of each peptide are shown in white (peptide names are indicated at the left of the panels). Two star-shaped aggregates can be seen for Magainin-2 in the Ld phase where pores were observed to form (indicated by yellow arrows).

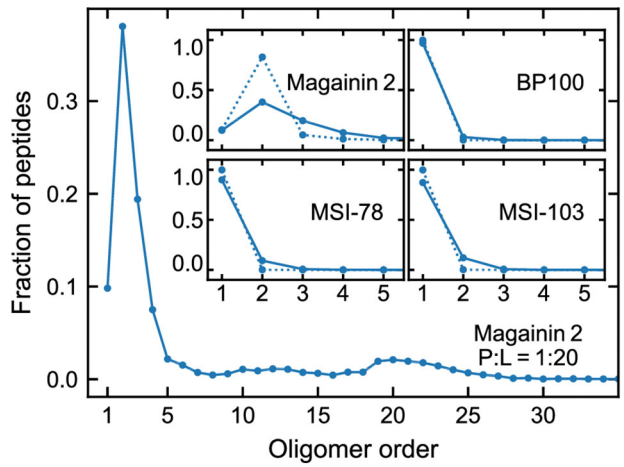

FIGURE 4 | Oligomerization preference of each peptide, analyzed over the last 20 μs of simulation and expressed as the fraction of the total peptide per oligomer order. Main plot: distribution for Magainin-2 at high (P:L = 1:20) concentrations. Insets: distributions for all the peptides, at P:L ratios of 1:200 (dotted line) and 1:20 (full line), with plots focused on low oligomerization numbers.

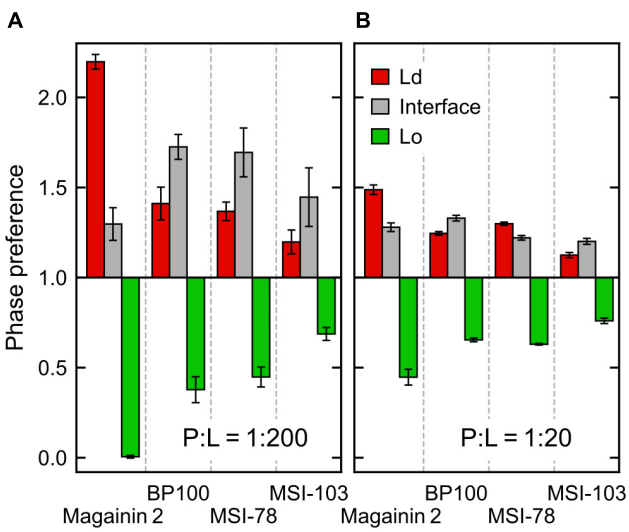

FIGURE 5 | Ratio of peptide enrichment in each region relative to a random distribution. **(A)** At low (P:L = 1:200) peptide concentration; and **(B)** at high (P:L = 1:20) peptide concentration.

as also visible in **Figure 3** and in the relative phase areas, discussed below.

The above phase preference observations are mostly independent of the chosen radius for interface definition, but the preference values themselves are not (**Supplementary Figure 3**): analysis at a narrower radius yields a higher interfacial preference, presumably due to less averaging being performed over the depleted region of the Lo phase.

At low AMP concentrations phase areas are mostly unchanged by peptide type, with relative values around 33%, 20%, and 47% for Ld, interface, and Lo phases, respectively (see the detailed data in **Supplementary Figure 3**). High peptide concentrations bring about area changes only for the cases of MSI-78 and MSI-103. For both peptides there is an increase of the interface area, which reflects a lowering of the Ld–Lo line tension also visible in **Figure 3**. Interestingly, under MSI-78 the interface grows mostly at the expense of the Lo phase, whereas for MSI-103 it grows at the expense of both Ld and Lo phases (**Supplementary Figure 4**).

Driving Forces

The concentration of peptides in any given region is clearly entropically unfavorable. We set out to identify the enthalpic forces driving this phenomenon. In case of transmembrane helices, it has been shown (Schäfer et al., 2011) that the main driving force for sorting of the peptides to the Ld phase is caused by changes in lipid–lipid enthalpy: the transmembranar peptides are essentially incompatible with the ordered nature of the Lo phase and disturb the tight packing of saturated lipids and cholesterol; this leads to an enthalpic driving force for sorting into the Ld domains. In case of the surface-adsorbed AMPs, one might expect little difference in the enthalpy of peptide interaction with either phase because DPPC and DLiPC have identical headgroups. However, a direct inspection of the peptide interaction enthalpies does show a difference between Ld-adsorbed and Lo-adsorbed peptide potential energy (**Figure 6A**). Furthermore, and contrary to what would be expected from the peptide localization preferences, it is the Lo-adsorbed state that is the most energetically favorable—even if the peptides interact with shallower adsorptions (**Figure 6B**). We can rationalize this enthalpic preference as likely stemming from the increased density of peptide–lipid interactions in the more compact Lo-phase, but this does not explain the peptide preference for the Ld/interface regions over Lo. We then monitored the effect of peptide presence on lipid–lipid interactions.

Energy discrimination, plotted in detail in **Supplementary Figure 2**, shows that the presence of peptides mostly leads to more favorable global interactions by nearby lipids, regardless of phase. In other words, even though peptides prefer the Ld phase, lipids would enthalpically rather have a peptide adsorbed on the Lo phase than to have no peptide at all (exceptions are the cases of Magainin-2 at low concentrations—for which there is also a large a measured error—and BP100, also at low concentrations). A main contributor to this is the aforementioned favorable peptide–lipid interactions. However, peptide adsorption can be seen to always come at a cost to lipid–lipid interactions: comparison between lipids in-contact and not-in-contact with peptides shows that in both phases lipid–lipid interactions become significantly weakened in the presence of peptides, and more so in the Lo phase. Lipid–solvent interactions seem to be largely insensitive to peptide presence.

These observations point to the effect that makes it overall enthalpically advantageous for a peptide to move from the Lo phase to the Ld phase: it makes lipid–lipid interactions more favorable in the Lo phase by an amount of energy that more than compensates for both the weaker lipid–lipid interactions (**Supplementary Figure 2**) and weaker peptide–lipid

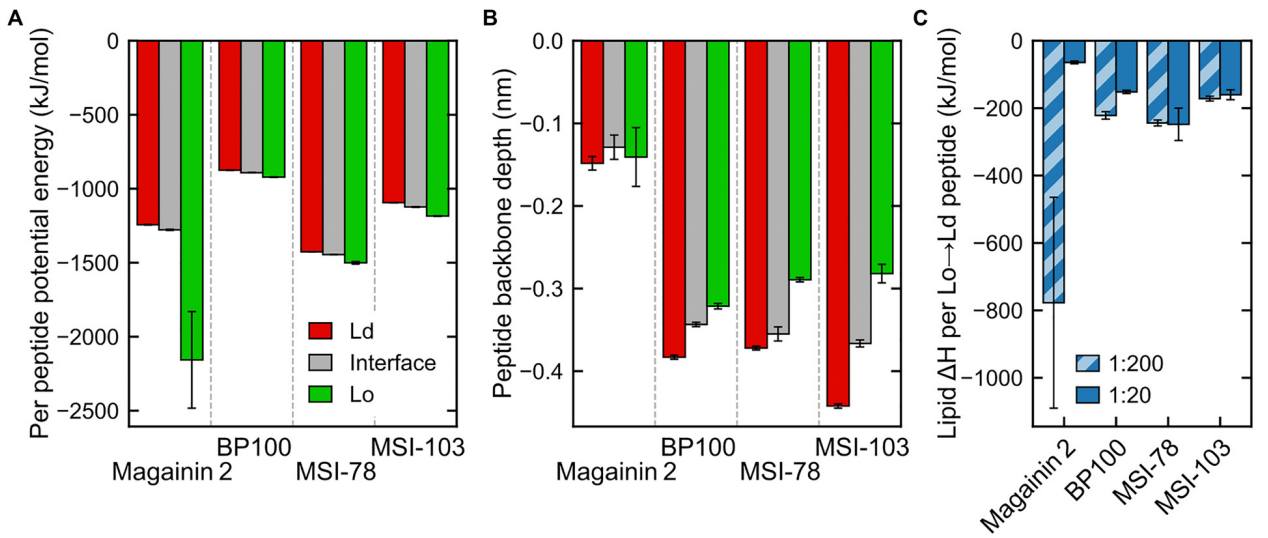

FIGURE 6 | Interaction energies and penetration depths across domains (for panels **(A,B)** only data for the less concentrated systems, P:L = 1:200, is shown—see **Supplementary Figure 1** for a side-by-side comparison with measured energies/depths at both peptide concentrations). **(A)** Total peptide nonbonded interaction potential energy in each region, averaged by the number of peptides in that region (intrapeptide nonbonded contributions excluded). **(B)** Peptide backbone in-depth position, expressed as the z-position difference to the average of nearby phosphate beads, for each region. **(C)** Difference in global lipid–lipid potential energy per peptide moved from the Lo region to the Ld region, at both concentrations. The very low numbers of Magainin-2 visiting the Lo phase at low concentrations (see **Figure 5**) introduce a large uncertainty in the measured value.

interactions (**Figure 6A**) in the Ld phase. This then yields the negative enthalpies in **Figure 6C** in the order of hundreds of kJ mol^{-1} per peptide that justify why the peptides can accumulate so clearly against the entropic tendency. Interestingly, the impact of lipid–lipid interactions occurs even though the AMPs are mostly adsorbed on the bilayer surface, and not transmembranar as previously studied transmembrane helices (Schäfer et al., 2011; Lin and Gorfe, 2019) that become phase-sorted by similar driving forces.

The argument of enthalpic competition between the Lo-lipid packing and peptide adsorption further explains why the peptides display a preference for the phase interface over even the Ld phase: at the interface the energetic cost of disrupting Lo-lipid packing is already partly paid for; peptides can then interact with Lo-lipids to some extent, and therefore have a lower global interaction energy, without incurring in the lipid–lipid energetic penalty that drives them away from the Lo phase.

Higher AMP concentrations, for the most part, did not bring about changes in the energetic driving forces. Enthalpy analysis indicates that the increase of AMP accumulation in the Lo phase with concentration results indeed from overcrowding of the Ld phase: overall peptide interactions in the Ld phase become more unfavorable at high concentrations, when compared to Lo (**Supplementary Figure 1C**).

Magainin-2 Pore Formation at High Concentrations

At high P:L ratios two Magainin-2 pores were observed to spontaneously form in the Ld phase (**Figure 3**). From the peptide's mechanistic point of view, this is an expected event (Ludtke et al., 1996). However, it is a significant observation with the Martini model because coarse-grain simulation of AMP pore formation often requires promoting the insertion step—either by multiscale approaches (Rzepiela et al., 2010), the self-assembly of membranes with peptides (Cruz et al., 2013; Balatti et al., 2017), or the pre-insertion of peptides (Woo and Wallqvist, 2011; Balatti et al., 2017). Successful descriptions of AMP insertion and pore formation from unbiased atomistic simulations (Leontiadou et al., 2006; Wang et al., 2016) show that these are observable in the microsecond scale, and therefore reachable by the faster Martini model. The reasons behind the difficulty of simulating pore phenomena with Martini are not entirely clear, although it has been pointed out that defects hardly form in Martini membranes, even during lipid flip-flop or crossing by polar moieties (Bennett and Tieleman, 2011). Indeed, Martini membranes covered with Magainin-2 will sooner buckle and bud than form pores (Woo and Wallqvist, 2011). In our simulations at high peptide densities membrane buckling was prevented by the application of a restraining potential in the z direction on the lipid headgroups; tension was further balanced by having equal amounts of peptide on each leaflet. Under this light, we believe that the extreme Magainin-2-induced buckling observed by others (Woo and Wallqvist, 2011) is probably a consequence of the reluctance of the Martini model for pore formation: once we removed membrane buckling as an energy outlet, we were able to readily observe pore formation. Furthermore, preventing a large membrane from naturally buckling may introduce additional pore-inducing tension. This factor alone, however, cannot explain why pore formation was only observed for Magainin-2 when all AMPs were simulated under buckling restraints.

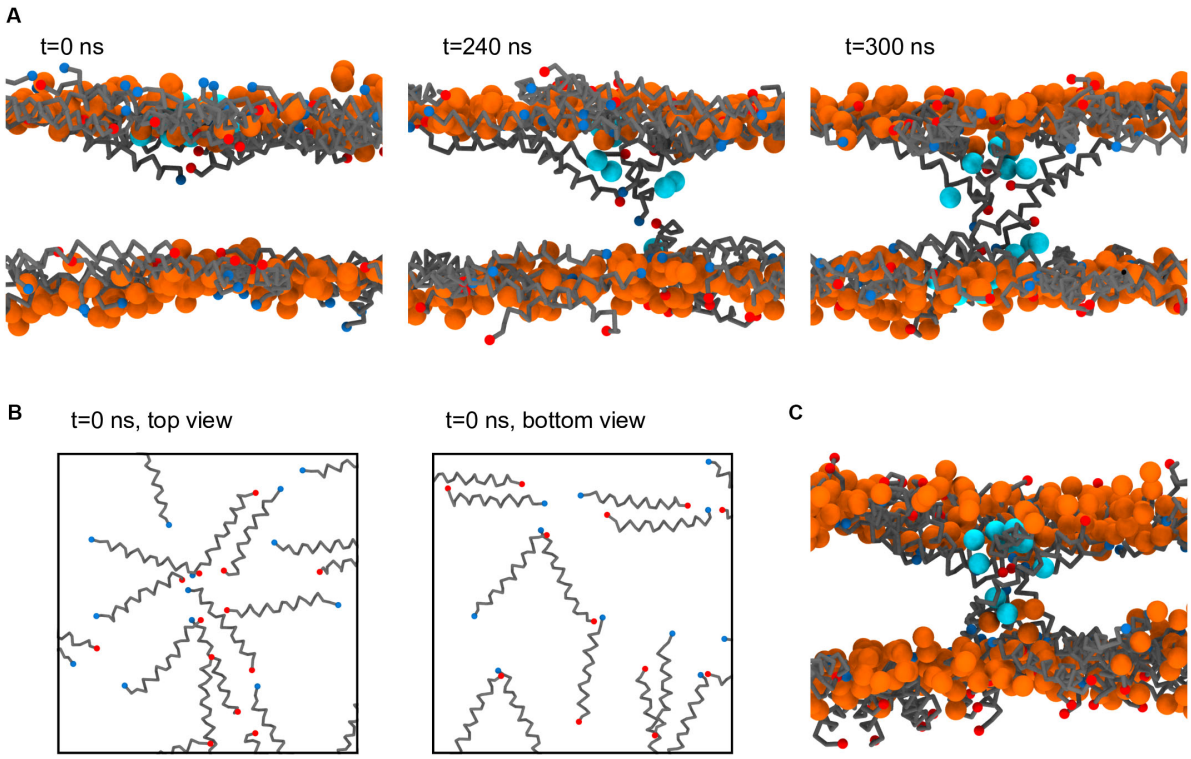

FIGURE 7 | Process of Magainin-2 pore formation. **(A)** Three side-view snapshots depicting peptide internalization from the top leaflet, contact with the bottom leaflet, and establishment of a stable pore (see the main text for more detail). Label times are relative to the beginning of internalization, with t = 0 corresponding to 7.8 μs simulation time; for this system buckling was prevented by restraining vertical headgroup movement; the view at t = 300 ns is rotated by 180° around the z axis relative to the other two panels. **(B)** Top and bottom leaflet views of the peptide organization at t = 0, for the same system as in **(A)**. **(C)** Pore structure obtained in a membrane held flat by a flat-bottomed potential, as opposed to the headgroup restraints in **(A,B)**. Peptide backbones are depicted in gray, with blue and red N and C termini, respectively; lipids are shown only as their phosphate bead, in orange (these are mostly, but not entirely, DLiPC lipids, since the pores formed in the Ld phase); the water beads closest to the pore core are shown in cyan; for clarity, all other system components were hidden, and in **(B)** the phosphate beads were also not shown.

Another possibly relevant aspect of how the observed pores formed has to do with (i) the careful pre-simulation peptide placement/adsorption protocol (Su et al., 2018), which prevented untimely peptide association and (ii) the gradual and spontaneous concentration of peptides in the Ld phase, which prevented the artifactual introduction of tension when peptides are forced together with unfavorable contacts.

Figure 7A depicts a step-by-step formation of one of the Magainin-2 pores. Preceding pore formation Magainin-2 dimers, mostly antiparallel, assemble in one of the leaflets in a roughly radial fashion (**Figure 7B**). For both pores, formation involved the incursion of top leaflet peptides into the bottom leaflet. Two-to-three peptides, of mixed orientation and of different dimers, penetrate simultaneously end-first into the bilayer core (the mixed N- and C-terminal orientations presumably stabilizing the terminal charges), dragging water beads along. Peptides from the bottom leaflet then tilt inward to meet the incoming top-leaflet peptides, after which the pore is established. In both cases, after the initial radial aggregation, the process was quite fast, with the first peptide becoming transmembranar within 300 ns. Once inserted, peptide organization is tilted and no longer dimeric. The pore structure is also dynamic, with peptides frequently exchanging between the adsorbed and internalized states. However, no peptides were observed to fully translocate and adopt the adsorbed configuration in the opposing leaflet; there were, at most, cases where transmembrane peptides cross the membrane all the way and become anchored closer to the opposing leaflet than the starting leaflet. Regardless of peptide dynamics, once formed the pores themselves were stable for the remainder of the run (extended over 60 μs after pore formation) and were able to conduct water.

As stated, the observation of Magainin-2 pore formation seems to have been facilitated by the restriction of lipid headgroup movement in the out-of-membrane-plane direction. Naturally, this raises concern about the significance of the pore structure since such potentials prevent the lipid headgroups from accompanying the internalizing peptides, as is expected to occur for toroidal pore models (Ludtke et al., 1996; Leontiadou et al., 2006). To test the influence of this bias we employed a different method to restrict membrane buckling, namely a flat-bottomed potential (see Materials and Methods). Under the less biasing flat-bottomed potential two Magainin-2 pores were also observed to form (**Figure 7C**), confirming that it is not the specific restriction of headgroup movement that is promoting

pore formation. The final structure of these pores is quite similar to the pores obtained with the headgroup restraints, with peptides inserted in a tilted, monomeric fashion. Incidentally, though the membrane is allowed to become somewhat distorted near the pores when using the flat-bottomed potential, headgroups still do not completely follow the peptides into the bilayer core. This behavior may be connected to the lack of membrane defects under the Martini model during lipid flip-flop (Bennett and Tieleman, 2011). Similar pore formation occurred for both types of potentials, even though flat-bottomed potentials controlled buckling without imposing nearly as much bias as harmonic position restraints. System restraining energies, before pore formation, were of 38.9 ± 0.5 kJ mol^{-1} for the flat-bottomed case vs. 3106.4 ± 5.7 kJ mol^{-1} for the harmonic case. Upon pore formation flat-bottomed energies remained unchanged (38.5 ± 0.6 kJ mol^{-1}) but harmonic ones dropped to 3068.8 ± 2.0 kJ mol^{-1}, suggesting that in this case lipid restraints may drive pore formation more directly.

DISCUSSION

In this work we were able to observe and assign the molecular bases for AMP preference for disordered phases. This extends and complements available experimental studies, in which a preference of AMPs for the Ld phase could be inferred, but only from indirect evidence (McHenry et al., 2012). Our findings show that AMPs disrupt lipid–lipid interactions in both phases, but mostly in the Lo phase. This ultimately causes the AMPs to locate in the Ld phase, even though the AMPs themselves do establish more favorable interactions in the Lo phase. The observed further preference of AMPs for the phase interface is a corollary of these energetic considerations. The relative depletion of Magainin-2 and MSI-78 at the interface, on the other hand, were interesting observations and merit further research. The choice of studied peptides and lipid mixture focused the scope of our conclusions on α-helical AMPs, on a particular phase separation condition. Future work on AMPs of different predominant secondary structure, on membrane with different degrees of lipid saturation, could shed light on other aspects of phase preference.

In addition to Ld phase preference, in the case of Magainin-2 pores were also observed to spontaneously form there. The definition of the conditions required for this observation opens the door to a much more detailed characterization of determinants of pore formation in the simulation of membrane-active peptides.

Our observation of AMP accumulation in the Ld phase supports the view that phase preference can potentiate AMP activity by promoting localized high-density peptide regions in the membrane (McHenry et al., 2012). Still, extrapolation of these conclusions to the much more complex bacterial or eukaryotic membranes, where sharp phase separation seems unlikely (Ingólfsson et al., 2014), should be done with caution.

DATA AVAILABILITY STATEMENT

The datasets generated from measurements on the performed simulations, on which analysis was performed, are included as a **Supplementary Data** archive.

AUTHOR CONTRIBUTIONS

JS performed simulations. SM and MM designed the research. MM performed the analysis. All authors wrote the manuscript.

FUNDING

MM acknowledges the financial support by Project LISBOA-01-0145-FEDER-007660 (Microbiologia Molecular, Estrutural e Celular) funded by FEDER funds through COMPETE2020—Programa Operacional Competitividade e Internacionalização (POCI) and by national funds through FCT–Fundação para a Ciência e a Tecnologia.

SUPPLEMENTARY MATERIAL

The Supplementary Material for this article can be found online at: https://www.frontiersin.org/articles/10.3389/fcell.2020.00350/full#supplementary-material

REFERENCES

Balatti, G. E., Ambroggio, E. E., Fidelio, G. D., Martini, M. F., and Pickholz, M. (2017). Differential interaction of antimicrobial peptides with lipid structures studied by coarse-grained molecular dynamics simulations. *Molecules* 22:1775. doi: 10.3390/molecules22101775

Barnoud, J., Rossi, G., Marrink, S. J., and Monticelli, L. (2014). Hydrophobic compounds reshape membrane domains. *PLoS Comput. Biol.* 10:e1003873. doi: 10.1371/journal.pcbi.1003873

Bennett, W. F. D., and Tieleman, D. P. (2011). Water defect and pore formation in atomistic and coarse-grained lipid membranes: pushing the limits of coarse graining. *J. Chem. Theory Comput.* 7, 2981–2988. doi: 10.1021/ct200291v

Bennett, W. F. D., and Tieleman, D. P. (2013). Computer simulations of lipid membrane domains. *Biochim. Biophys. Acta Biomembr.* 1828, 1765–1776. doi: 10.1016/j.bbamem.2013.03.004

Berendsen, H. J. C., Postma, J. P. M., van Gunsteren, W. F., DiNola, A., and Haak, J. R. (1984). Molecular dynamics with coupling to an external bath. *J. Chem. Phys.* 81, 3684–3690. doi: 10.1063/1.3474951

Brender, J. R., McHenry, A. J., and Ramamoorthy, A. (2012). Does cholesterol play a role in the bacterial selectivity of antimicrobial peptides? *Front. Immunol.* 3:195. doi: 10.3389/fimmu.2012.00195

Contreras, F. X., Ernst, A. M., Wieland, F., and Brügger, B. (2011). Specificity of intramembrane protein-lipid interactions. *Cold Spring Harb. Perspect. Biol.* 3:a004705. doi: 10.1101/cshperspect.a004705

Cruz, V. L., Ramos, J., Melo, M. N., and Martinez-Salazar, J. (2013). Bacteriocin AS-48 binding to model membranes and pore formation as revealed by coarse-grained simulations. *Biochim. Biophys. Acta Biomembr.* 1828, 2524–2531. doi: 10.1016/j.bbamem.2013.05.036

de Jong, D. H., Singh, G., Bennett, W. F., Arnarez, C., Wassenaar, T. A., Schäfer, L. V., et al. (2013). Improved parameters for the martini coarse-grained

protein force field. *J. Chem. Theory Comput.* 9, 687–697. doi: 10.1021/ct300646g

Dewitt, B. N., and Dunn, R. C. (2015). Interaction of cholesterol in ternary lipid mixtures investigated using single-molecule fluorescence. *Langmuir* 31, 995–1004. doi: 10.1021/la503797w

Domański, J., Marrink, S. J., and Schäfer, L. V. (2012). Transmembrane helices can induce domain formation in crowded model membranes. *Biochim. Biophys. Acta Biomembr.* 1818, 984–994. doi: 10.1016/j.bbamem.2011.08.021

Epand, R. F., Maloy, W. L., Ramamoorthy, A., and Epand, R. M. (2010). Probing the "charge cluster mechanism" in amphipathic helical cationic antimicrobial peptides. *Biochemistry* 49, 4076–4084. doi: 10.1021/bi100378m

Epand, R. M., and Vogel, H. J. (1999). Diversity of antimicrobial peptides and their mechanisms of action. *Biochim. Biophys. Acta Biomembr.* 1462, 11–28. doi: 10.1016/s0005-2736(99)00198-4

Fadeel, B., and Xue, D. (2009). The ins and outs of phospholipid asymmetry in the plasma membrane: roles in health and disease. *Crit. Rev. Biochem. Mol. Biol.* 44, 264–277. doi: 10.1080/10409230903193307

Feigenson, G. W. (2006). Phase behavior of lipid mixtures. *Nat. Chem. Biol.* 2, 560–563.

Forrester, J. S., Milne, S. B., Ivanova, P. T., and Brown, H. A. (2004). Computational lipidomics: a multiplexed analysis of dynamic changes in membrane lipid composition during signal transduction. *Mol. Pharmacol.* 65, 813–821. doi: 10.1124/mol.65.4.813

Golub, T., Wacha, S., and Caroni, P. (2004). Spatial and temporal control of signaling through lipid rafts. *Curr. Opin. Neurobiol.* 14, 542–550. doi: 10.1016/j.conb.2004.08.003

Gowers, R. J., Linke, M., Barnoud, J., Reddy, T. J. E., Melo, M. N., Seyler, S. L., et al. (2016). "MDAnalysis: a Python package for the rapid analysis of molecular dynamics simulations," in *Proceedings of the 15th Python in Science Conference*, eds S. Benthall, and S. Rostrup (Austin, TX: SciPy), 98–105.

Hanwell, M. D., Curtis, D. E., Lonie, D. C., Vandermeersch, T., Zurek, E., and Hutchison, G. R. (2012). Avogadro: an advanced semantic chemical editor, visualization, and analysis platform. *J. Cheminform.* 4:17. doi: 10.1186/1758-2946-4-17

Hess, B., Kutzner, C., van der Spoel, D., and Lindahl, E. (2008). GROMACS 4: algorithms for highly efficient, load-balanced, and scalable molecular simulation. *J. Chem. Theory Comput.* 4, 435–447. doi: 10.1021/ct700301q

Ingólfsson, H. I., Melo, M. N., van Eerden, F. J., Arnarez, C., Lopez, C. A., Wassenaar, T. A., et al. (2014). Lipid organization of the plasma membrane. *J. Am. Chem. Soc.* 136, 14554–14559. doi: 10.1021/ja507832e

Jefferys, E., Sansom, M. S. P., and Fowler, P. W. (2014). NRas slows the rate at which a model lipid bilayer phase separates. *Faraday Discuss.* 169, 209–223. doi: 10.1039/c3fd00131h

Leontiadou, H., Mark, A. E., and Marrink, S. J. (2006). Antimicrobial peptides in action. *J. Am. Chem. Soc.* 128, 12156–12161.

Lin, X., and Gorfe, A. A. (2019). Understanding membrane domain-partitioning thermodynamics of transmembrane domains with potential of mean force calculations. *J. Phys. Chem. B* 123, 1009–1016. doi: 10.1021/acs.jpcb.8b10148

Ludtke, S. J., He, K., Heller, W. T., Harroun, T. A., Yang, L., and Huang, H. W. (1996). Membrane pores induced by magainin. *Biochemistry* 35, 13723–13728.

Marrink, S. J., Risselada, H. J., Yefimov, S., Tieleman, D. P., and de Vries, A. H. (2007). The MARTINI force field: coarse grained model for biomolecular simulations. *J. Phys. Chem. B* 111, 7812–7824. doi: 10.1021/jp071097f

Marsh, D. (2009). Cholesterol-induced fluid membrane domains: a compendium of lipid-raft ternary phase diagrams. *Biochim. Biophys. Acta Biomembr.* 1788, 2114–2123. doi: 10.1016/j.bbamem.2009.08.004

McHenry, A. J., Sciacca, M. F., Brender, J. R., and Ramamoorthy, A. (2012). Does cholesterol suppress the antimicrobial peptide induced disruption of lipid raft containing membranes? *Biochim. Biophys. Acta Biomembr.* 1818, 3019–3024. doi: 10.1016/j.bbamem.2012.07.021

Melo, M. N., Ingólfsson, H. I., and Marrink, S. J. (2015). Parameters for martini sterols and hopanoids based on a virtual-site description. *J. Chem. Phys.* 143:243152. doi: 10.1063/1.4937783

Michaud-Agrawal, N., Denning, E. J., Woolf, T. B., and Beckstein, O. (2011). MDAnalysis: a toolkit for the analysis of molecular dynamics simulations. *J. Comput. Chem.* 32, 2319–2327. doi: 10.1002/jcc.21787

Moiset, G., López, C. A., Bartelds, R., Syga, L., Rijpkema, E., Cukkemane, A., et al. (2014). Disaccharides impact the lateral organization of lipid membranes. *J. Am. Chem. Soc.* 136, 16167–16175. doi: 10.1021/ja505476c

Monticelli, L., Kandasamy, S. K., Periole, X., Larson, R. G., Tieleman, D. P., and Marrink, S. J. (2008). The MARTINI coarse-grained force field: extension to proteins. *J. Chem. Theory Comput.* 4, 819–834. doi: 10.1021/ct700324x

Muddana, H. S., Chiang, H. H., and Butler, P. J. (2012). Tuning membrane phase separation using nonlipid amphiphiles. *Biophys. J.* 102, 489–497. doi: 10.1016/j.bpj.2011.12.033

Mukai, Y., Matsushita, Y., Niidome, T., Hatekeyama, T., and Aoyag, H. (2002). Parallel and antiparallel dimers of magainin 2: their interaction with phospholipid membrane and antibacterial activity. *J. Pept. Sci.* 8, 570–577. doi: 10.1002/psc.416

Oren, Z., and Shai, Y. (1998). Mode of action of linear amphipathic α-helical antimicrobial peptides. *Biopolymers* 47, 451–463. doi: 10.1002/(SICI)1097-0282(1998)47:6<451::AID-BIP4>3.0.CO;2-F

Pedregosa, F., Varoquaux, G., Gramfort, A., Michel, V., Thirion, B., Grisel, O., et al. (2012). Scikit-learn: machine learning in python. *J. Mach. Learn. Res.* 12, 2825–2830.

Polyansky, A. A., Ramaswamy, R., Volynsky, P. E., Sbalzarini, I. F., Marrink, S. J., and Efremov, R. G. (2010). Antimicrobial peptides induce growth of phosphatidylglycerol domains in a model bacterial membrane. *J. Phys. Chem. Lett.* 1, 3108–3111.

Raghuraman, H., and Chattopadhyay, A. (2004). Interaction of melittin with membrane cholesterol: a fluorescence approach. *Biophys. J.* 87, 2419–2432. doi: 10.1529/biophysj.104.043596

Ramamoorthy, A., Lee, D. K., Narasimhaswamy, T., and Nanga, R. P. (2010). Cholesterol reduces pardaxin's dynamics-a barrel-stave mechanism of membrane disruption investigated by solid-state NMR. *Biochim. Biophys. Acta Biomembr.* 1798, 223–227. doi: 10.1016/j.bbamem.2009.08.012

Risselada, H. J., and Marrink, S. J. (2008). The molecular face of lipid rafts in model membranes. *Proc. Natl. Acad. Sci. U.S.A.* 104, 17367–17372. doi: 10.1073/pnas.0807527105

Rossi, G., Barnoud, J., and Monticelli, L. (2014). Polystyrene nanoparticles perturb lipid membranes. *J. Phys. Chem. Lett.* 5, 241–246. doi: 10.1021/jz402234c

Rzepiela, A. J., Sengupta, D., Goga, N., and Marrink, S. J. (2010). Membrane poration by antimicrobial peptides combining atomistic and coarse-grained descriptions. *Faraday Discuss.* 144, 431–443. doi: 10.1039/b901615e

Schäfer, L. V., de Jong, D. H., Holt, A., Rzepiela, A. J., de Vries, A. H., Poolman, B., et al. (2011). Lipid packing drives the segregation of transmembrane helices into disordered lipid domains in model membranes. *Proc. Natl. Acad. Sci. U.S.A.* 108, 1343–1348. doi: 10.1073/pnas.1009362108

Simons, K., and Toomre, D. (2000). Lipid rafts and signal transduction. *Nat. Rev. Mol. Cell. Biol.* 1, 31–39.

Strandberg, E., Kanithasen, N., Tiltak, D., Bürck, J., Wadhwani, P., Zwernemann, O., et al. (2008). Solid-state NMR analysis comparing the designer-made antibiotic MSI-103 with its parent peptide PGLa in lipid bilayers. *Biochemistry* 47, 2601–2616. doi: 10.1021/bi701944r

Su, J., Thomas, A. S., Grabietz, T., Landgraf, C., Volkmer, R., Marrink, S. J., et al. (2018). The N-terminal amphipathic helix of Pex11p self-interacts to induce membrane remodelling during peroxisome fission. *Biochim. Biophys. Acta Biomembr.* 1860, 1292–1300. doi: 10.1016/j.bbamem.2018.02.029

Toke, O., O'Connor, R. D., Weldeghiorghis, T. K., Maloy, W. L., Glaser, R. W., Ulrich, A. S., et al. (2004). Structure of (KIAGKIA)3 aggregates in phospholipid bilayers by solid-state NMR. *Biophys. J.* 87, 675–687. doi: 10.1529/biophysj.103.032714

van der Walt, S., Colbert, S. C., and Varoquaux, G. (2011). The NumPy array: a structure for efficient numerical computation. *Comput. Sci. Eng.* 13, 22–30.

van der Walt, S., Schönberger, J. L., Nunez-Iglesias, J., Boulogne, F., Warner, J. D., Yager, N., et al. (2014). scikit-image: image processing in Python. *PeerJ.* 2:e453. doi: 10.7717/peerj.453

Van Meer, G., Voelker, D. R., and Feigenson, G. W. (2008). Membrane lipids: where they are and how they behave. *Nat. Rev. Mol. Cell. Biol.* 9, 112–124. doi: 10.1038/nrm2330

Veatch, S. L., and Keller, S. L. (2003). Separation of liquid phases in giant vesicles of ternary mixtures of phospholipids and cholesterol. *Biophys. J.* 85, 3074–3083. doi: 10.1016/S0006-3495(03)74726-2

Verly, R. M., Rodrigues, M. A., Daghastanli, K. R., Denadai, A. M., Cuccovia, I. M., Bloch, C Jr, et al. (2008). Effect of cholesterol on the interaction of the amphibian antimicrobial peptide DD K with liposomes. *Peptides* 29, 15–24. doi: 10.1016/j.peptides.2007.10.028

Wadhwani, P., Epand, R. F., Heidenreich, N., Bürck, J., Ulrich, A. S., and Epand, R. M. (2012). Membrane-active peptides and the clustering of anionic lipids. *Biophys. J.* 103, 265–274. doi: 10.1016/j.bpj.2012.06.004

Wakamatsu, K., Takeda, A., Tachi, T., and Matsuzaki, K. (2002). Dimer structure of magainin 2 bound to phospholipid vesicles. *Biopolymers* 64, 314–327. doi: 10.1002/bip.10198

Wang, Y., Chen, C. H., Hu, D., Ulmschneider, M. B., and Ulmschneider, J. P. (2016). Spontaneous formation of structurally diverse membrane channel architectures from a single antimicrobial peptide. *Nat. Commun.* 7:13535. doi: 10.1038/ncomms13535

Woo, H.-J., and Wallqvist, A. (2011). Spontaneous buckling of lipid bilayer and vesicle budding induced by antimicrobial peptide magainin 2: a coarse-grained simulation study. *J. Phys. Chem. B* 115, 8122–8129. doi: 10.1021/jp2023023

Yeaman, M. R., and Yount, N. Y. (2003). Mechanisms of antimicrobial peptide action and resistance. *Pharmacol. Rev.* 55, 27–55. doi: 10.2174/0929866053405959

Conflict of Interest: The authors declare that the research was conducted in the absence of any commercial or financial relationships that could be construed as a potential conflict of interest.

frontiers in Cell and Developmental Biology

ORIGINAL RESEARCH
published: 12 June 2020
doi: 10.3389/fcell.2020.00337

Liquid-Ordered Phase Formation by Mammalian and Yeast Sterols: A Common Feature With Organizational Differences

*Alena Khmelinskaia[1†‡], Joaquim M. T. Marquês[1‡], André E. P. Bastos[1], Catarina A. C. Antunes[1], Andreia Bento-Oliveira[1], Silvia Scolari[2], Gerson M. da S. Lobo[1], Rui Malhó[3], Andreas Herrmann[2], H. Susana Marinho[1] and Rodrigo F. M. de Almeida[1]**

[1] Centro de Química Estrutural, Faculdade de Ciências, Universidade de Lisboa, Lisbon, Portugal, [2] Department of Biology, Molecular Biophysics, Humboldt-Universität zu Berlin, Berlin, Germany, [3] Faculdade de Ciências, BioISI, Universidade de Lisboa, Lisbon, Portugal

OPEN ACCESS

Edited by:
Rainer A. Böckmann, University of Erlangen–Nuremberg, Germany

Reviewed by:
Erdinc Sezgin, Karolinska Institutet (KI), Sweden
Martin Hof, J. Heyrovsky Institute of Physical Chemistry (ASCR), Czechia

***Correspondence:**
Rodrigo F. M. de Almeida
rfalmeida@fc.ul.pt

†Present address:
Alena Khmelinskaia, Institute for Protein Design, University of Washington, Seattle, WA, United States

‡These authors have contributed equally to this work

Specialty section:
This article was submitted to Cellular Biochemistry, a section of the journal Frontiers in Cell and Developmental Biology

Received: 31 January 2020
Accepted: 17 April 2020
Published: 12 June 2020

Citation:
Khmelinskaia A, Marquês JMT, Bastos AEP, Antunes CAC, Bento-Oliveira A, Scolari S, Lobo GMdS, Malhó R, Herrmann A, Marinho HS and de Almeida RFM (2020) Liquid-Ordered Phase Formation by Mammalian and Yeast Sterols: A Common Feature With Organizational Differences. Front. Cell Dev. Biol. 8:337. doi: 10.3389/fcell.2020.00337

Here, biophysical properties of membranes enriched in three metabolically related sterols are analyzed both *in vitro* and *in vivo*. Unlike cholesterol and ergosterol, the common metabolic precursor zymosterol is unable to induce the formation of a liquid ordered (l_O) phase in model lipid membranes and can easily accommodate in a gel phase. As a result, Zym has a marginal ability to modulate the passive membrane permeability of lipid vesicles with different compositions, contrary to cholesterol and ergosterol. Using fluorescence-lifetime imaging microscopy of an aminostyryl dye in living mammalian and yeast cells we established a close parallel between sterol-dependent membrane biophysical properties *in vivo* and *in vitro*. This approach unraveled fundamental differences in yeast and mammalian plasma membrane organization. It is often suggested that, in eukaryotes, areas that are sterol-enriched are also rich in sphingolipids, constituting highly ordered membrane regions. Our results support that while cholesterol is able to interact with saturated lipids, ergosterol seems to interact preferentially with monounsaturated phosphatidylcholines. Taken together, we show that different eukaryotic kingdoms developed unique solutions for the formation of a sterol-rich plasma membrane, a common evolutionary trait that accounts for sterol structural diversity.

Keywords: ergosterol, cholesterol, zymosterol, fluorescence lifetime imaging microscopy, fluorescence spectroscopy, plasma membrane, lipid-lipid interactions, sterol-rich domain

INTRODUCTION

Ergosterol (Erg) and cholesterol (Chol) are the major sterols in yeast (fungi) and mammalian (animal) cell membrane, respectively. These two sterols share several properties, namely the ability to increase the order of fluid model membranes and to induce the formation of ordered domains when mixed with certain lipids, such as phosphatidylcholines (PCs) with either one or two saturated acyl chains (Ipsen et al., 1990; Vist and Davis, 1990; De Almeida et al., 2003; Silva et al., 2006; Hsueh et al., 2007). Zymosterol (Zym) is a biosynthetic precursor of both Chol and Erg in the Blöch pathway (Megha et al., 2006). Notably, all three molecules have very small structural differences (**Scheme 1**). Zym is, by proportion, only the fourth main sterol present in the plasma membrane

of *Saccharomyces cerevisiae* wild-type (*wt*) cells (Pedroso et al., 2009) but is known to accumulate in certain *S. cerevisiae* mutant strains, such as *erg6*Δ and *erg2*Δ*erg6*Δ cells (Munn et al., 1999; Guan et al., 2009), where its levels raise several-fold becoming a major sterol (Munn et al., 1999; Heese-Peck et al., 2002; Valachovic et al., 2006; Dupont et al., 2011). Despite the changes in sterol profile, the total sterol content in plasma membrane extracts remains essentially unchanged in *erg6*Δ cells (Daum et al., 1999; Abe and Hiraki, 2009; Dupont et al., 2011). Erg and Chol are known to regulate cell membrane permeability (Subczynski et al., 1989; Mukhopadhyay et al., 2002). Yeast cells with deletions in Erg biosynthesis-related genes frequently exhibit increased membrane permeability (Kaur and Bachhawat, 1999; Mukhopadhyay et al., 2002; Folmer et al., 2008) when compared to *wt* cells, which has been attributed to modifications in the sterol profile (Kaur and Bachhawat, 1999), and the consequent altered membrane fluidity (Abe and Hiraki, 2009), or instability of ordered domains (Mukhopadhyay et al., 2002). In fact, Erg and Chol have been considered crucial for the formation of a subset of membrane lipid domains described as being in a liquid ordered (l_o) phase, due to their ability to establish tight interactions with sphingolipids (Simons and Vaz, 2004; Klose et al., 2010). Although both Chol and Erg form l_o phases, their respective two kingdoms present fundamental differences in their membrane lipid organization, namely the transient nature and nanoscopic scale of the lipid domains in mammalian cells (Sezgin et al., 2017) versus stable large membrane compartments in yeast (Malinsky and Opekarova, 2016; Athanasopoulos et al., 2019; Zahumensky and Malinsky, 2019). Another distinctive feature is the leaflet distribution of either Chol or Erg: whereas for Chol the literature is not consensual in the evidence for its preferential location in the outer/inner leaflet or its even distribution (Steck and Lange, 2018), regarding Erg interleaflet partition recent results point toward a possible preferential location in the inner leaflet (Solanko et al., 2018). Such feature possibly relates with the presence of sphingolipid-enriched gel-like domains, under physiological conditions, in the plasma membrane of yeast (Aresta-Branco et al., 2011). So far, the ability of Zym to form an l_o phase has not been directly assessed and its biophysical properties are still poorly understood, both *in vitro* and *in vivo*. Yet, it is known that yeast strains defective in Erg biosynthesis, e.g., *erg2*Δ, *erg6*Δ, or *erg2*Δ*erg6*Δ are sensitive to weak organic acids (Mollapour et al., 2004) and a wide variety of drugs (Kaur and Bachhawat, 1999; Emter et al., 2002) to

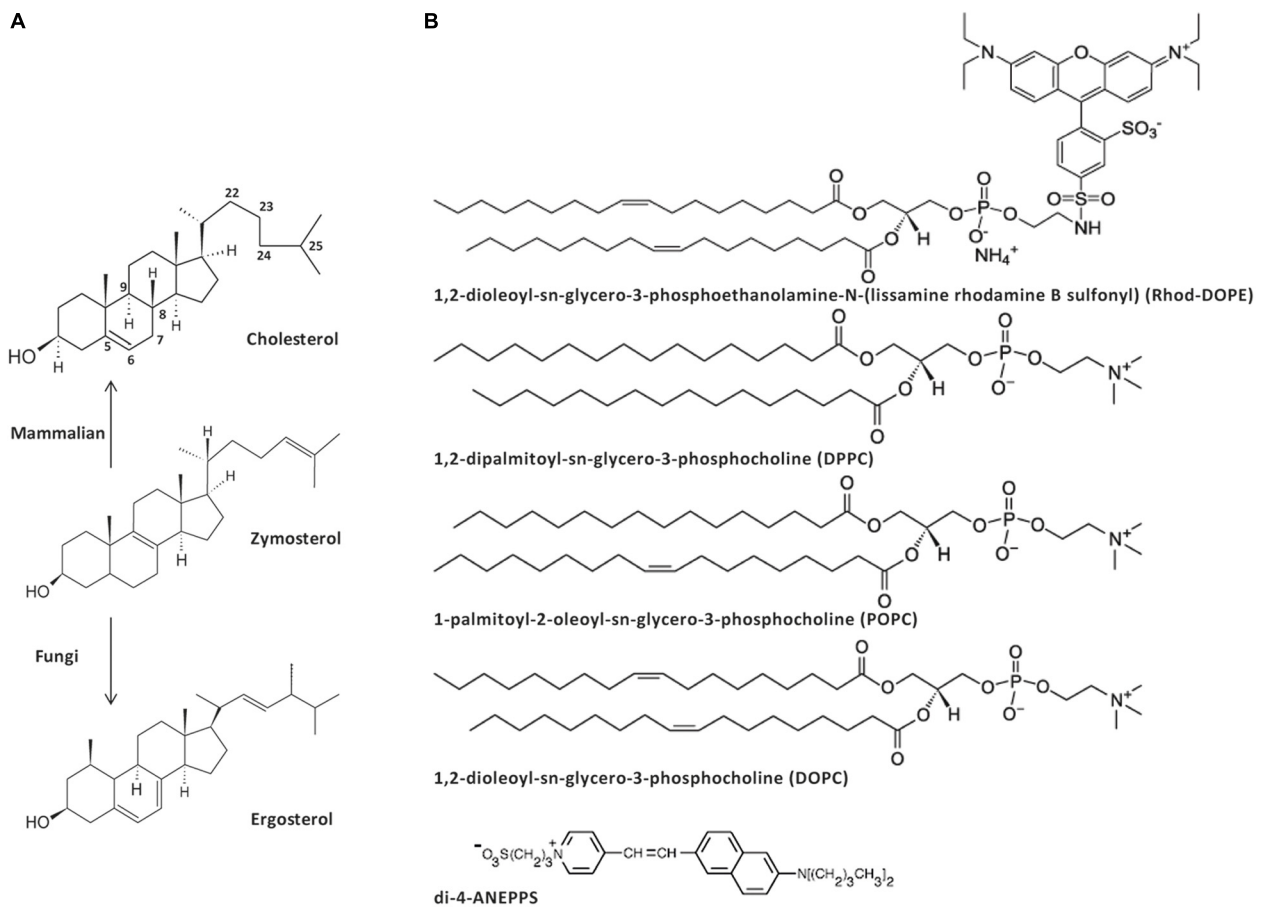

SCHEME 1 | Structure of the sterols **(A)**, phospholipids and dyes **(B)** used in this work. Zymosterol is a biosynthetic precursor of both cholesterol, the major sterol in the plasma membrane of animal cells, and ergosterol, the major sterol in the plasma membrane of fungi.

which increased passive diffusion across the plasma membrane is, most likely, determinant (Emter et al., 2002). Consequently, a comprehensive characterization of Zym biophysical properties can help understanding the underlying causes for Erg and Chol selection as the major sterols, respectively, in fungi and animals.

The present work aimed at assessing the ability of metabolically related sterols (Chol, Erg, and Zym) to form l_o lipid domains and at gaining further insight into the lipid composition of such domains in living cells. We found that, unlike Chol and Erg, Zym can be incorporated to similar extents in both gel and fluid phase PC bilayers without significantly compromising gel-phase dense packing, as shown by the maintenance of a very low permeability, and its inability to efficiently form an l_o phase. Thus, we hypothesize that l_o phase formation ability of fungi and mammalian sterols is a convergent evolutionary trait that results in their selective enrichment over Zym (and possibly other sterol precursors). However, whereas in mammalian cells there is a clear biophysical similarity to sphingomyelin (or saturated PC)/chol model membranes, it seems that in *S. cerevisiae* cells sterol-enriched membrane domains bear more resemblance with monounsaturated PC/Erg model mixtures. This might explain fundamental differences between mammalian and fungal cell membrane organization.

MATERIALS AND METHODS

Chemicals and Yeast Strains

1,2-dipalmitoyl-*sn*-glycero-3-phosphocholine (DPPC), 1,2-dioleoyl-*sn*-glycero-3-phosphocholine (DOPC), 1-palmitoyl-2-oleoyl-*sn*-glycero-3-phosphocholine (POPC), and N-(lissamine Rhodamine B sulfonyl)-1,2-dioleoyl-*sn*-3-phosphatidylethanolamine (Rhod-DOPE) were purchased from Avanti Polar Lipids (Alabaster, AL, United States). Chol, Erg, Ludox (colloidal silica diluted to 50 weight% in water), CCCP (carbonyl cyanide *m*-chlorophenyl hydrazine), FCCP (carbonyl cyanide-4-(trifluoromethoxy)phenylhydrazone) and pyranine were purchased from Sigma-Aldrich (St. Louis, MO, United States). Zym was purchased from Avanti or from Steraloids, yielding the same results. Di-4-ANEPPS was purchased from Invitrogen (Madrid, Spain). Valinomycin was purchased from EMD Chemical Inc. (San Diego, CA, United States). Yeast extract, bactopeptone, yeast nitrogen base, and agar were obtained from Difco (Detroit, MI, United States). Solvents for lipid and probe stock solutions were spectroscopic grade. Other reagents were of the highest purity available.

Saccharomyces cerevisiae BY4741 (*wt*) cells (genotype *MATa his3*Δ1 *leu2*Δ0 *met15*Δ0 *ura3*Δ0) and *erg6*Δ cells (BY4741*; MATa his3*Δ1 *leu2*Δ0 *met15*Δ0 *ura3*Δ0 *YML008c:*kanMX4) were obtained from EUROSCARF (Frankfurt, Germany). Chinese Hamster Ovary (CHO)-K1 cells were obtained from American Type Culture Collection.

Media and Growth Conditions

Saccharomyces cerevisiae cells were cultured as described previously (Aresta-Branco et al., 2011). Briefly, cells were grown overnight at 30°C in synthetic complete medium (SC) containing 2% (w/v) glucose, 0.68% (w/v) yeast nitrogen base and amino acids as indicated in Pedroso et al. (2009). Cells were inoculated at an A_{600} of 0.15 and, after incubation for 5–6 h, cells in mid-exponential phase were harvested at an A_{600} = 0.6.

CHO-K1 cells were grown in Dulbecco's modified Eagle's medium (PAN Biotech, Aidenbach, Germany) without phenol red and supplied with 2 mM L-Glutamine, 10% FBS and 5% PS (complete medium) and incubated at 37°C and 5% CO_2. About 48 h prior to experiment cells were plated into 35 mm Matek dishes till 80–90% confluence.

Cell Preparation

Harvested yeast cells (*wt*, *erg6*Δ) were washed twice with sterile water and then suspended in 100 mM sodium dihydrogen phosphate, 100 mM sodium chloride, 1 mM EDTA, pH 7.4 buffer solution (fluorescence buffer). The probe di-4-ANEPPS was added from a concentrated methanol stock solution to the cells at a final concentration of 1 μM and incubated for 5 min, at room temperature (24°C). After incubation, the cells were centrifuged and resuspended in the fluorescence buffer. For CCCP treatment, cells were incubated with CCCP [20 μM (Grossmann et al., 2007) in buffer] throughout imaging.

CHO-K1 cells were washed twice in fluorescence buffer prior to imaging and treatments. The probe was diluted 10× in fluorescence buffer. Cell staining with 0.1 μM di-4-ANEPPS was then carried out for 5–40 min at 24°C. To allow for intracellular membrane staining the treatment was prolonged to 90 min. Cells were then washed twice with fluorescence buffer prior to imaging. For methyl-β-cyclodextrin (MβCD) treatment, before staining CHO cells were incubated with MβCD (5 mM) for 1 min at 4°C, which removes approximately 12 mol% of Chol from the plasma membrane (Scolari et al., 2009).

Vesicles Preparation

Multilamellar vesicles (MLVs) containing the appropriate lipids, as well as di-4-ANEPPS when used, were prepared by previously described methods (Bastos et al., 2012). The lipid was hydrated by the addition of 1 mL of HEPES buffer (10 mM, NaCl 150 mM pH 7.4), previously heated above the main transition temperature (T_m) of the lipids. The MLV suspension was slowly cooled down and kept in the dark at 4°C. Before measurement, the liposomes suspension was slowly brought to room temperature. All the procedures involving Erg and Zym were performed in the dark. Large unilamellar vesicles (LUVs) with ca. 100 nm diameter were obtained by MLV extrusion (Bastos et al., 2012).

Giant unilamellar vesicles (GUVs) were prepared by electroformation in titanium chambers as previously described (Stockl et al., 2010; Marques et al., 2015). The lipid film in the titanium chambers was hydrated with 700 μL of 250 mM sucrose solution, with 15 mM NaN_3, 280 mOsm/kg in MilliQ water, sealed and connected to the signal generator and subjected to the sequence of signals described in Marques et al. (2015). In case of DPPC-containing mixtures, the chambers were equilibrated with a block heater at 60°C throughout electroformation, and the sucrose buffer was previously heated to that temperature. The vesicle suspension was kept at room

temperature (24°C) in the dark until use. The osmolality of the solutions used in GUV preparation/observation was checked with a 3300 cryo-osmometer (Advanced Instruments, Norwood, MA, United States).

DPPC, DOPC and POPC concentrations in stock solutions (chloroform) were determined by phosphorus analysis (McClare, 1971). Probe concentrations were determined spectrophotometrically: ε (Rhod-DOPE, λ_{max} = 559 nm, chloroform) = 95 × 10^3 M^{-1} cm^{-1}; ε(di-4-ANEPPS, λ_{max} = 497 nm, methanol) = 42 × 10^3 M^{-1} cm^{-1}; ε(*t*-PnA, λ_{max} = 300 nm, ethanol) = 89 × 10^3 M^{-1} cm^{-1} (Johnson and Spence, 2010).

Sterol concentrations in stock solutions (chloroform) were determined by gravimetry.

Confocal Fluorescence Microscopy of GUVs

An aliquot (100 μL) of GUV suspension was added to a chamber of an eight-well plastic plate with glass-like coverslip bottom (Ibidi GmbH, Germany). A volume of 150 μL of glucose buffer (250 mM glucose, 5.8 mM Na_2HPO_4, 5.8 mM NaH_2PO_4) 300 mOsm/kg, pH 7.2, in MilliQ water was added, forcing the GUVs to precipitate in the bottom of the chamber. GUVs were observed with a Leica SP-E confocal inverted microscope (Leica Microsistemas, Lisbon, Portugal) using the 488 nm excitation line at <20% laser intensity and operating in the mode 1024 × 1024, 400 Hz. A ×63 HCX PL APO oil immersion (NA = 1.4) objective (Leica) was used. Thin Z-optical sections (≈ 0.6–0.8 μm thick) were acquired and 3D projections of GUV hemispheres obtained using Leica software. Rhod-DOPE was the probe used to label the GUVs and was co-dissolved with the lipids at a probe/lipid ratio of 1:500. At least three independent GUV preparations were used for each mixture, showing consistent phase behavior among all GUVs and between samples.

Absorption and Fluorescence Measurements and Data Analysis

Spectrophotometric absorption measurements were performed on a Jasco V-560 (Tokyo, Japan) double beam spectrophotometer.

Fluorescence measurements were carried out on a Horiba Jobin Yvon Flurolog 3.22 spectrofluorometer at 24°C described previously (Aresta-Branco et al., 2011).

The probe/lipid ratio used with di-4-ANEPPS was 1:500, for a total lipid concentration of 0.4 mM and at least three independent samples were analyzed. For steady-state spectra the bandwidths were 4 nm in both excitation and emission. The spectra representing the median are shown. Other details are given with the results.

For time-resolved measurements by the single photon counting technique, a nanoLED N-460 (Horiba Jobin Yvon) was used for the excitation of di-4-ANEPPS, and the emission wavelength was set to 610 nm with a bandwidth of 15 nm. Other conditions were as described in Bastos et al. (2012). Data analysis was performed as previously described (Bastos et al., 2012; Khmelinskaia et al., 2014).

Briefly, a normalized fluorescence intensity decay is described by a sum of exponentials, i.e.,

$$I(t) = \sum_{i=1}^{n} \alpha_i exp(-t/\tau_i) \quad (1)$$

where α_i and τ_i are the normalized amplitude and the lifetime of component *i*, respectively. The (intensity-weighted) mean fluorescence lifetime is given by

$$< \tau >= \sum \alpha_i \tau_i^2 / \sum \alpha_i \tau_i \quad (2)$$

and the amplitude-weighted average lifetime is defined as

$$\bar{\tau} = \sum \alpha_i \tau_i \quad (3)$$

Two exponentials were required to describe di-4-ANEPPS decays (plus a scattering factor). All the data represents the mean ± standard deviation of at least three independent samples.

Confocal Microscopy and FLIM of Living Cells Labeled With di-4-ANEPPS

Intensity images as well as fluorescence lifetime imaging microscopy (FLIM) measurements were taken in the confocal mode using an Olympus Fluoview, 1000 (Olympus, Tokyo, Japan) equipped with a time-resolved LSM upgrade kit (PicoQuant GmbH, Berlin, Germany) and a x60 (1.35 N.A.) UPlanSApo oil immersion objective (Olympus). Di-4-ANEPPS was excited at 488 nm using the corresponding line of a multiline argon laser and was detected in the range of 565–665 nm. Images with a frame size of 512 × 512 pixels were acquired. For FLIM measurements, di-4-ANEPPS was excited at 440 nm using a pulsed-laser diode. Fluorescence was detected by a single photon avalanche photodiode (SPAD) and a 620 ± 30 nm bandpass filter was used. Further details of the experimental settings and data analysis can be found in **Supplementary Note 3**. For every single cell the average lifetime <τ> and the amplitude weighted lifetime $\bar{\tau}$ were calculated using equations 2 and 3. The values reported in **Table 2** are the average of 30–100 cells of at least three independent experiments. The fluorescence lifetime of the probe was independent of the incubation time. The quality of the fitting was judged by the distribution of the residuals and the χ^2 value.

Water Permeability Assay

For the water permeability studies, unlabeled MLVs were prepared in Tris–HCl 5 mM, pH 7.0, 100 mM sucrose buffer (isotonic buffer). The liposomes contained an additional 4 mol% of dicetylphosphate (Sigma-Aldrich), to stabilize the suspension (Bittman and Blau, 1976).

Isotonic MLV suspensions were diluted approximately 1/20 (0.123 mL added to 2.5 mL) in hypotonic buffer (Tris–HCl 5 mM, pH 7.0). The transfer of MLVs from an isotonic sucrose solution into a hypotonic solution, accompanied by a reduction of the suspension turbidity, was monitored overtime by measuring the time dependence of absorbance at 550 nm (Bittman and Blau, 1976) for 5 min (Jasco V-560, Easton, MD, United States). All the data represents the mean ± standard deviation of at least

TABLE 1 | Zym is unable to regulate the passive permeability of lipid bilayers in contrast to Erg and Chol.

	$\Delta(1/A_{550\ nm})$/min		IF_{510nm} (a.u.)/min
Sterol	**DPPC**	**DPPC/DOPC**	**DPPC/DOPC**
–	0.022 ± 0.001	0.187 ± 0.011	−0.263 ± 0.035
Erg	0.120 ± 0.001	0.081 ± 0.012	−0.091 ± 0.031
Zym	0.023 ± 0.005	0.155 ± 0.012	−0.157 ± 0.028
Chol	0.062 ± 0.001	0.082 ± 0.007	−0.074 ± 0.021

Passive permeability to water is expressed as a variation of MLV suspension absorbance at 550 nm [$\Delta(1/A_{550\ nm})$/min] when transferred to hypotonic buffer. Passive permeability to potassium/proton is expressed as a variation of pyranine fluorescence intensity at 510 nm over time [$IF_{510\ nm}$(a.u.)/min]. Each sterol was added in equimolar proportion to the lipid mixture.

three independent samples. For more details see **Supplementary Note 1** and **Supplementary Figure S2**.

K^+/H^+ Exchange Assay

LUV of equimolar DPPC/DOPC and DPPC/DOPC/sterol mixtures were prepared in HEPES 20 mM, K_2SO_4 100 mM, pH 7.4 with 0.5 mM pyranine (K-Pyr-buffer). The excess pyranine was removed by gel filtration in a Sephadex G-25 column equilibrated in K-buffer (HEPES 20 mM, K_2SO4 100 mM, pH 7.4 buffer) and the LUVs with encapsulated pyranine were collected.

The effect of sterol on the potassium permeability of the lipid vesicles was monitored by measuring the variation in fluorescence intensity of membrane impermeable pyranine, as described elsewhere (Coutinho et al., 2004). Further experimental details can be found under **Supplementary Note 2** and **Supplementary Figure S3**. For a quantitative comparison between sterols, the initial slope of the curves was calculated, as a measure of bilayer permeability to potassium (**Table 1**). All the data represents the mean ± standard deviation of at least four independent samples. Only samples with the same final gradient were selected for analysis, i.e., with the same qualitative behavior of fluorescence intensity and similar final relative emission intensity.

RESULTS

Zym Is Unable to Support Liquid Ordered/Liquid Disordered Phase Coexistence

In order to directly evaluate the ability of Zym to induce the coexistence of liquid/liquid domains, Erg or Zym were incorporated into GUVs containing equimolar ratios of the saturated lipid DPPC and the unsaturated lipid DOPC, and their behaviors were compared to that of the DOPC/DPPC binary mixture. DOPC/DPPC/Chol system labeled with the same fluorescent lipid analog, Rhod-DOPE, has been previously studied in detail (De Almeida et al., 2007). This probe has been shown to preferentially label the liquid disordered (l_d) phase versus gel (De Almeida et al., 2007), Chol-induced l_o (De Almeida et al., 2005), and Erg-induced l_o (Bastos et al., 2012) domains.

For the binary equimolar mixture of DPPC and DOPC, the confocal microscopy images showed a Rhod-DOPE distribution with bright, unsaturated lipid-enriched and dark, saturated lipid-enriched domains (**Figure 1A**). In this binary mixture the domains observed correspond to gel (dark) and l_d (bright) phase coexistence, with relative areas in agreement with the phase diagram for this mixture (De Almeida et al., 2007). The domains are irregularly shaped, as characteristic for gel/fluid coexistence, in contrast to l_d/l_o phase coexistence which leads to round-shaped domains (Dietrich et al., 2001). In addition, if Chol is added to form a ternary 1:1:2 (molar ratio) mixture, the vesicles are completely in l_o state, whereas for the 1:1:1 equimolar proportion it is well known that l_d/l_o phase separation occurs (**Supplementary Figure S1A**) (Veatch and Keller, 2003; De Almeida et al., 2007).

In the case of Erg, our results also indicate a clear l_d/l_o phase coexistence for the lipid composition DOPC/DPPC/Erg (1:1:1, molar ratio) (**Figure 1B** and **Supplementary Figure S1B**), as a single dark round l_o domain is observed. Indeed, GUVs with similar proportions of DOPC/DPPC/Erg have previously been reported to present a bright l_d phase, rich in unsaturated lipid (DOPC), coexisting with dark l_o domains, rich in saturated lipid (DPPC) and Erg (Beattie et al., 2005).

For the DOPC/DPPC/Zym (1:1:2, molar ratio) (**Figure 1C** and **Supplementary Figure S1D**), non-round gel phase domains, similar to those found in DOPC/DPPC vesicles (**Figure 1A**), were clearly observed. This indicates that Zym, unlike Chol and Erg, does not have the ability to promote the formation of coexisting l_d/l_o phases from a pre-existing l_d/gel situation. Since an estimation of the gel area fraction from visual inspection of several GUVs reveals no marked differences on the fraction of gel and l_d phases with or without Zym, the partition of this sterol among the two phases seems to be similar. Analogous

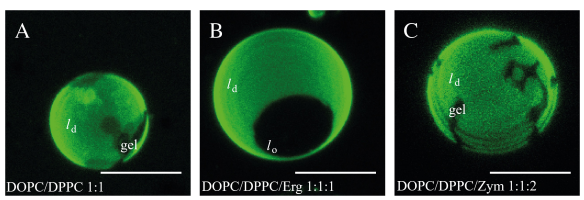

FIGURE 1 | Zym does not promote the formation of coexisting l_d/l_o liquid phases. Confocal microscopy images of GUVs of **(A)** DOPC/DPPC (1:1 molar ratio), **(B)** DOPC/DPPC/Erg (1:1:1 molar ratio), **(C)** DOPC/DPPC/Zym (1:1:2 molar ratio) at 23°C, labeled with Rhod-DOPE (0.2 mol%). Scale bar = 5 μm.

results were obtained for equimolar mixtures (1:1:1 molar ratio) of DOPC/DPPC/Zym (**Supplementary Figure S1C**).

Zym Is Unable to Affect the Passive Permeability of Lipid Bilayers

One major difference between gel and l_d phase with direct and vital biological significance is membrane passive permeability, which is known to be modulated by sterols (Scheidt et al., 2013). Thus, passive permeability to water (**Supplementary Note 1** and **Supplementary Figure S2**) and to ions (**Supplementary Note 2** and **Supplementary Figure S3**) was studied in lipid vesicles formed by binary and ternary mixtures containing each of the metabolically related sterols (DPPC/sterol 2:1 and DPPC/DOPC/sterol 1:1:1 molar ratio, respectively).

A higher permeability to water is expressed as a higher rate of increase of liposomal volume (**Table 1**). DPPC and DPPC/DOPC (1:1 molar ratio) show opposite behavior: while the highly organized DPPC (gel phase) is quite impermeable to water, the presence of a DOPC-rich fluid phase and the associated packing defects at the interface between coexisting gel and l_d domains (Clerc and Thompson, 1995) in DPPC/DOPC (1:1 molar ratio) mixtures at room temperature lead to the highest permeability of all the MLVs tested.

The incorporation of Erg or Chol increased the water permeability of the DPPC bilayer (**Supplementary Figure S2A** and **Table 1**). Erg had a stronger effect than Chol on bilayer permeability, while Zym had a negligible effect. This typical behavior of Chol and Erg is assigned to the formation of the l_o phase which, although ordered, has a higher fluidity than the gel phase and a higher passive permeability (Bittman and Blau, 1976).

An opposite effect was observed for DPPC/DOPC mixtures – the incorporation of an equimolar proportion of sterol reduces the water permeability of the bilayer (**Supplementary Figure S2B** and **Table 1**). The effect was higher for Erg and Chol in comparison to Zym. Although for binary mixtures the intrinsic bulk permeability of the DPPC-rich phase became higher in the presence of sterol, we found that overall the permeability significantly decreased for DPPC/DOPC membranes containing Chol or Erg. By fluidizing gel domains (**Figure 1**), the interaction between lipids at the domain interface is facilitated and the mismatch between ordered and disordered phases is reduced, resulting in a decrease of lipid bilayer permeability relatively to gel/l_d domain interfaces (Cordeiro, 2018; Kirsch and Böckmann, 2019). More specifically, an equimolar proportion of Chol in DPPC/DOPC bilayers corresponds to a l_d/l_o phase coexistence (De Almeida et al., 2007) and the interface between two liquid phases is much less prone to packing defects than that between a gel and l_d phase, that would be present in the absence of sterol. The same explanation holds for the observation of a similar effect on permeability when Erg is present in DPPC/DOPC vesicles and is consistent with the l_d/l_o phase coexistence observed in GUVs (**Figure 1**). Thus, permeability of domain interfaces is a crucial factor for the total passive permeability in ternary mixtures. The small effect of Zym, as it is incapable of fluidizing the gel phase through l_o formation, supports that it accommodates well between the tightly packed phospholipids, most probably by adopting a highly planar structure.

Comparable results to those obtained for water permeability were observed for the bilayer permeability to monovalent cations reported by the fluorescence intensity kinetics of the pH-sensitive probe pyranine (**Table 1** and **Supplementary Figure S3**). In DPPC/DOPC mixtures, the incorporation of an equimolar proportion of sterol reduced the K^+/H^+ exchange rate, but the effect of the l_o-promoting sterols, Chol and Erg, was much stronger when compared to Zym.

Overall, these results support that the formation of l_o domains promoted by Erg and Chol is directly related to the control of membrane passive permeability in highly heterogeneous membranes. Additionally, our experiments highlight that l_o domains, with properties halfway between l_d and gel, are important for reducing passive permeability at the interfaces between membrane domains.

Erg, Chol and Zym Distinctly Affect the Dielectric Properties of Phospholipid Bilayers

Sterols, in particular Chol, are known to increase the membrane dipole potential when mixed with phospholipids (Haldar et al., 2012). Hence we tested the effect of each sterol on the membrane dipole potential and its connection to l_o phase. Due to its complex photophysics, di-4-ANEPPS is responsive to changes in polarity or membrane potential and hydration (Loew et al., 1992; Loew, 1996; Amaro et al., 2017). The well-established excitation ratiometric method (Haldar et al., 2012) with this dye was thus used to assess the membrane dipole potential in binary systems (**Figure 2A**). Representative excitation and emission spectra of di-4-ANEPPS incorporated into the different systems under study are shown in **Supplementary Figure S4**.

When added to fluid POPC, neither Erg nor Zym had pronounced effects on the dipole potential, whereas Chol induced a modest but noticeable increase (**Figure 2A**). For Erg and Chol the results are in full agreement with a study performed using a similar probe, di-8-ANEPPS (Haldar et al., 2012). In the presence of a DPPC gel phase, Erg had the lowest effect on membrane dipole potential, whereas Chol affected it the most. Despite differing in the induced membrane potential, both Chol and Erg are consensual l_o-forming/"raft-promoting" sterols. Thus, a very high membrane dipole potential is a particular feature of Chol-enriched domains but cannot be directly related to the l_o phase forming ability of sterols.

Next, we analyzed the sterol-induced spectral shift of di-4-ANEPPS emission by Erg and Zym (**Figure 2B**), which relates to the hydration layer and the solvent relaxation in the vicinity of the lipid bilayer (Loew, 1996). For Chol, the spectral shifts obtained are much larger for saturated gel phase lipids, such as DPPC or sphingomyelin, than for unsaturated l_d phase lipids, such as POPC or DOPC (Bastos et al., 2012). When comparing Erg and Zym in POPC/sterol mixtures, blue-shifts of emission are large even for low Zym, whereas for Erg, the blue-shift is small when l_d phase still persists (Erg $<$ 30 mol%), increasing more steeply when the

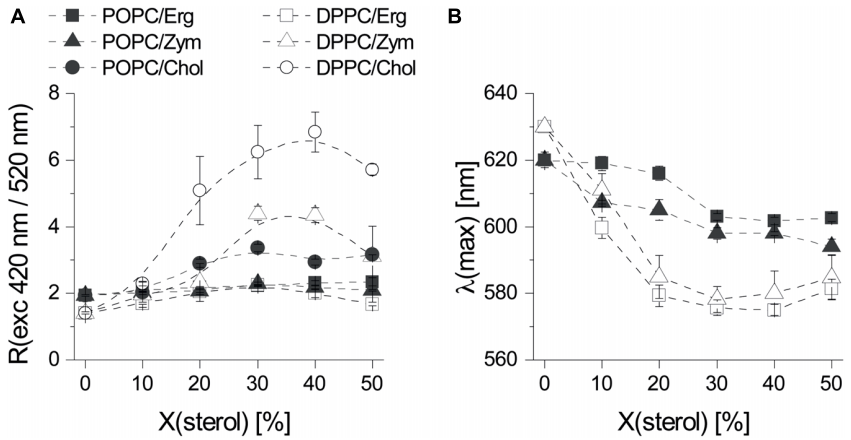

FIGURE 2 | The three sterols Erg, Chol, and Zym induce distinct biophysical changes in phospholipid bilayers. **(A)** Fluorescence excitation ratio, R_{ex}, as a function of sterol mole fraction in POPC and DPPC MLVs. R_{ex} is defined as the ratio of fluorescence emission intensity of di-4-ANEPPS arising from excitation at 420 nm divided by the one arising from excitation at 520 nm. **(B)** Influence of Erg and Zym on the polarity at the membrane/water interface expressed as the sterol induced shift of the wavelength of maximum emission intensity of di-4-ANEPPS as a function of sterol mole fraction in POPC/sterol and DPPC/sterol binary mixtures. The values are the mean ± S.D. of at least three independent experiments. Probe:lipid ratio 1:500.

system approaches the full l_o state. This possibly derives from Zym's homogeneous distribution throughout the membrane, affecting membrane properties globally, whereas the effect of Erg on membrane hydration depends on its concentration and hence the proportion of l_d to l_o. Although the sterol-induced spectral shift follows the same trend in DPPC mixtures with Erg and Zym, the difference between the shifts in a gel versus an l_d PC bilayer is larger in the case of Erg. Moreover, the absolute magnitude of the emission blue-shift is generally larger for Chol- than for Erg-containing lipid bilayers (Bastos et al., 2012).

Zym Is Unable to Discriminate Gel and l_d Phases

In a previous study (Bastos et al., 2012) we have shown that di-4-ANEPPS fluorescence properties respond specifically to sterol type and levels, as well as to sterol-phospholipid interactions. Similarly, the fluorescence lifetime of di-4-ANEPPDHQ, a probe of the same family, is considerably higher in lipid vesicles containing Chol (Amaro et al., 2017) and, in addition, the removal of Chol from the plasma membrane of mammalian cells with MβCD leads to the decrease of the lifetime of this probe (Owen et al., 2006). Moreover, these fluorescent probes can be very efficiently excited with visible light with absorption maximum close to the wavelength of common pulsed excitation lasers used in time-resolved fluorescence microscopy, in opposition to other polarity and sterol sensitive dyes e.g., of the family of Laurdan (Golfetto et al., 2013; Mazeres et al., 2017).

To ensure that di-4-ANEPPS mainly reports on sterol dependent properties, we analyzed its fluorescence intensity decays in LUVs made of binary mixtures comprising a PC, either the fully saturated 16:0 DPPC (gel phase forming) or the mono-unsaturated 16:0,18:1Δ^{9c} POPC (l_d phase forming), and each sterol. The parameters obtained from the analysis of such decays are shown in **Table 2**. Notably, intensity-weighted mean fluorescence lifetime $<\tau>$ of di-4-ANEPPS in saturated lipid (DPPC) or unsaturated lipid (POPC) bilayers devoid of any sterol was similar (≈ 1.8 ns and 1.9 ns, respectively) [**Figure 3** and Bastos et al. (2012)]. The results in **Figure 3** show that all three sterols increase $<\tau>$ of di-4-ANEPPS. This indicates a higher quantum yield of the probe in sterol-enriched phases. Moreover, the membrane/water partition coefficient of di-4-ANEPPS previously determined for the POPC/Erg binary system was higher (∼ 2.1×) for an l_o membrane than for an l_d membrane (Bastos et al., 2012) and its quantum yield was found to be larger when incorporated in the l_o phase (Khmelinskaia et al., 2014).

In the presence of Chol and Zym, $<\tau>$ was longer than for the same Erg mole fractions, in agreement with the spectral emission blue-shifts previously discussed (**Figure 2B**). However, when comparing the results obtained for DPPC and POPC, it is obvious that Chol and Erg have a much stronger effect in the gel phase lipid, since $<\tau>$ of di-4-ANEPPS had a higher increase in vesicles with DPPC than with POPC. On the other hand, Zym showed a unique behavior since $<\tau>$ obtained in DPPC or POPC vesicles containing this sterol largely overlapped. This observation, in good agreement with the approximately equal surface area of each phase in DOPC:DPPC:Zym and DOPC/DPPC GUVs (**Figure 1** and **Supplementary Figure S1**), suggests that Zym is not able to discriminate gel and l_d phase phospholipids and seems to be equally well accommodated in both phases. The behavior of di-4-ANEPPS $<\tau>$ (**Figure 3**), regardless of the maximum value reached in each particular case, is similar for the Chol and Erg mixtures with DPPC, reaching a plateau slightly before the system is completely in l_o phase (≈ 30 mol% sterol) (Sankaram and Thompson, 1991; Hsueh et al., 2005; Silva et al., 2006), which is consistent with a preference of

TABLE 2 | The molecular environment reported by di-4-ANEPPS is comparable in living cell membranes and model systems containing the same major sterol in a similar fraction.

Sterol	System	α_1	τ_1 (ns)	α_2	τ_2 (ns)	$\bar{\tau}$ (ns)	$<\tau>$ (ns)
Erg	*S. cerevisiae wt* PM	0.40	1.50	0.60	2.95	2.37	2.58
	POPC/Erg (7:3)	0.41	1.53	0.59	2.77	2.26	2.42
	[#] DPPC/Erg (7:3)	0.50	1.50	0.50	3.90	2.70	3.24
Zym	*S. cerevisiae erg6*Δ PM	0.60	1.79	0.40	3.60	2.47	2.76
	DPPC/Zym (9:1)	0.65	1.70	0.35	3.51	2.33	2.64
	DPPC/Zym (8:2)	0.50	2.21	0.50	3.86	3.03	3.25
	POPC/Zym (9:1)	0.47	1.90	0.43	3.05	2.32	2.55
	POPC/Zym (8:2)	0.46	2.02	0.54	3.45	2.81	2.98
Chol	CHO-K1 PM	0.27	2.39	0.73	4.65	4.04	4.27
	CHO-K1 IM	0.41	1.99	0.59	4.27	3.35	3.72
	[#] DPPC/Chol (7:3)	0.23	2.09	0.77	4.50	4.01	4.22
	[#] PSM/Chol (7:3)	0.24	1.75	0.76	4.74	4.03	4.43
	[#] POPC/Chol (6:4)	0.43	2.02	0.57	3.57	2.92	3.12

Fluorescence intensity decay parameters of di-4-ANEPPS incorporated in yeast (S. cerevisiae) and mammalian (CHO-K1) cells, and in LUVs of different compositions containing Chol, Erg or Zym, at 24°C. The fluorescence intensity decays measured both in cells by FLIM (30–100 cells in three independent experiments) and in LUVs suspensions by fluorescence spectroscopy (at least three independent experiments) were described by the sum of two exponentials, with amplitudes α_1 and α_2 and lifetimes τ_1 and τ_2. $\bar{\tau}$ is the amplitude-weighted average fluorescence lifetime and $<\tau>$ is the intensity-weighted mean fluorescence lifetime (Eqs. 1–3). [#]Values from Bastos et al. (2012).

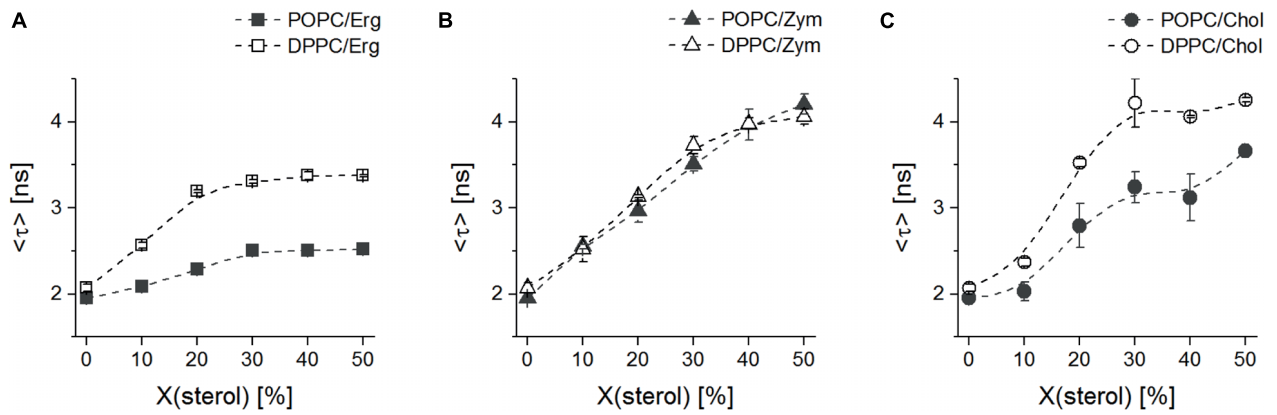

FIGURE 3 | The l_o-promoting sterols Erg and Chol induce clearly distinct changes in lipid properties in saturated (DPPC) versus unsaturated (POPC) phospholipids. Mean fluorescence lifetime $<\tau>$ of di-4-ANEPPS in binary mixtures of MLVs with Erg **(A)**, Zym **(B)** or Chol **(C)** and DPPC (open symbols) or POPC (solid symbols), as a function of sterol mole fraction, at 24°C. The values are the mean ± S.D. of at least three independent experiments. Probe:lipid ratio 1:500.

the probe for the sterol-enriched l_o phase. In contrast, the trend of di-4-ANEPPS $<\tau>$ is approximately linear in the case of Zym, without reaching a clear plateau, indicating the absence of a phase separation and of l_o phase formation. The linear trend up to 40/50 mol% Zym is indicative of the efficient incorporation of this sterol into the membrane, despite the lack of marked changes in domain organization and membrane permeability shown above. It should be noted that, in the case of Erg, the sterol solubility limit might have been transposed, particularly when mixed with POPC. Nonetheless, both DPH (1,6-diphenylhexatriene) fluorescence anisotropy in POPC/Erg liposomes (Silva et al., 2006) and the mean temperature of one broad endotherm component of DPPC/Erg mixtures (Mannock et al., 2010) increase up to 40 mol% of the sterol. Moreover, no Erg crystallites were detected at molar proportions as high as 50 mol% in the same DPPC/Erg mixtures (Mannock et al., 2010). The solubility of Chol in both saturated and monounsaturated phosphocholine bilayers, on the other hand, is unarguably higher than 50 mol% (Huang et al., 1999).

Sterol Type and Fraction Dictate the Molecular Environment Reported by di-4-ANEPPS in Living Cell Membranes

Finally, we analyzed living systems naturally containing different sterols in their plasma membrane: mammalian CHO-K1 cells (Chol-containing), *wt* (Erg-containing) and *erg6*Δ (Zym-enriched in comparison to *wt*; no Erg) *S. cerevisiae* cells. The single mutant *erg6*Δ was used instead of the double mutant *erg6*Δ*erg2*Δ, with higher levels of Zym, since double mutants in the Erg biosynthetic pathway have a slower

growth rate and exhibit a lower total sterol content than their progenitors (Barton et al., 1975). Cells were labeled with di-4-ANEPPS and FLIM experiments were conducted (**Figure 4**) to analyze both the plasma membrane and the intracellular membranes of individual cells (**Supplementary Note 3**, **Supplementary Figures S5, S6** and **Supplementary Table S1**). Importantly, since Erg seems to preferentially localize in the inner leaflet (Solanko et al., 2018), di-4-ANNEPS is suitable to probe these Erg-enriched regions not only because, as di-4-ANEPPDHQ, its fluorescence properties are sensitive to medium polarity, membrane potential and hydration, but also because of its ability to flip flop and distribute across both membrane leaflets as a non-charged and short-chained probe, in comparison with the double positively charged di-4-ANEPPDHQ. As the cellular environment is highly complex, to better understand how sterol structure defines biophysical properties of the plasma membrane in eukaryotes, and what simple lipid mixtures may reflect sterol-dependent properties as reported by di-4-ANEPPS fluorescence intensity decay parameters, we compared the cellular results with those in model membranes.

In CHO-K1 cells, a significant difference between the average fluorescence lifetime $<\tau>$ of di-4-ANEPPS in the plasma membrane (4.27 ± 0.09 ns) and intracellular membranes (3.72 ± 0.20 ns) was observed (**Figures 4A,D** and **Supplementary Figures S5, S6A, S7D**). As $<\tau>$ of di-4-ANEPPS is sensitive to sterol levels (see **Supplementary Notes 4, 5**), this difference of $<\tau>$ is most probably due to the lower content of Chol in intracellular membranes than in the plasma membrane, a general feature of mammalian cells (Simons and Vaz, 2004; Owen et al., 2006). These results are in perfect concordance with previous observations for di-4-ANEPPDHQ in HEK293 cells, where longer lifetimes were obtained in the plasma membrane in opposition to intracellular membranes (Owen et al., 2006). Similarly, the labeling of mammalian, *Drosophila* Kc and *Dictyostelium* AX2 cells with Laurdan probes also revealed a lower polarity of the plasma membrane lipid environment in contrast to intracellular membranes (Mazeres et al., 2017).

Interestingly, in CHO-K1 cells $<\tau>$ of di-4-ANEPPS was much longer (about 63%) than in *wt S. cerevisiae* plasma membrane (2.58 ± 0.07 ns), which is in very good agreement with the previously measured value in living *wt* yeast cells

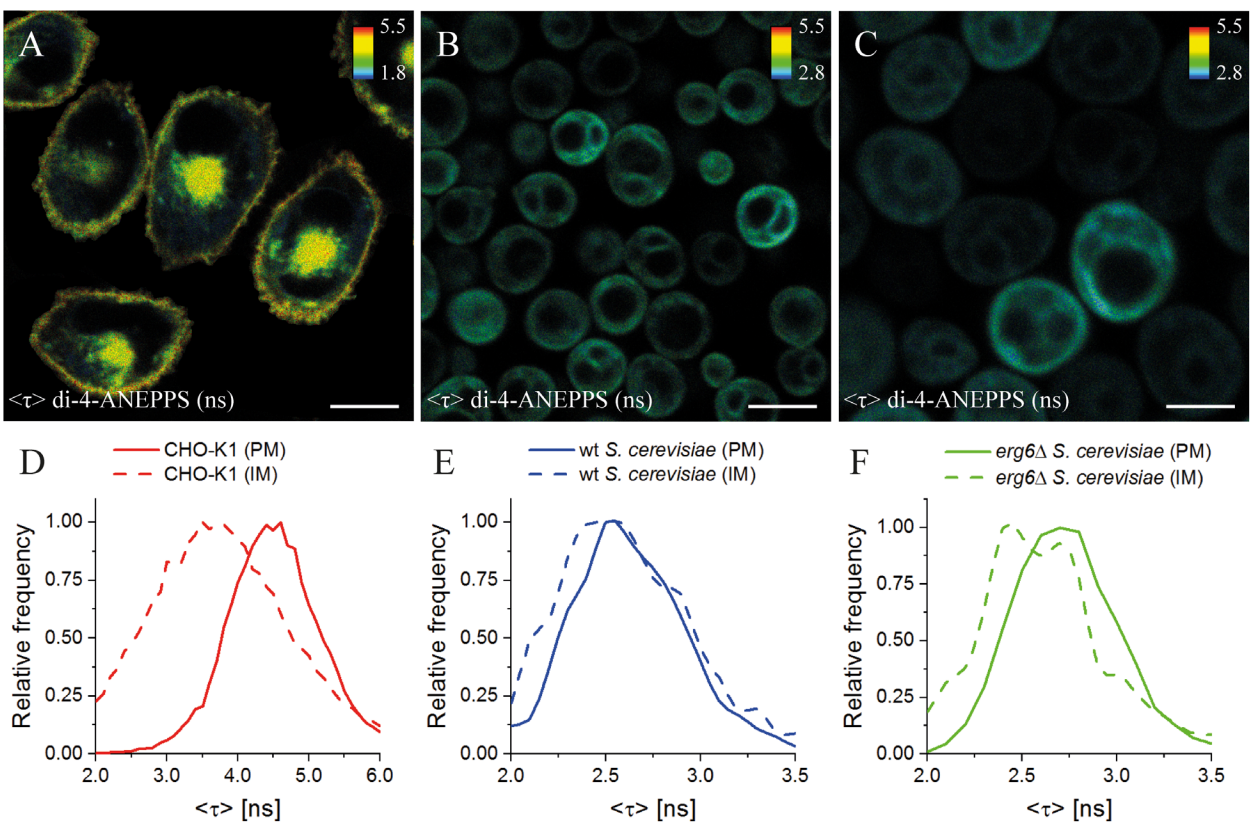

FIGURE 4 | Mean fluorescence lifetime $<\tau>$ of di-4-ANEPPS unravels significant differences in lipid membrane organization between mammalian and yeast cells. FLIM images of mammalian (CHO-K1, **A**), *wt* **(B)** and *erg6*Δ **(C)** *S. cerevisiae* cells. The inset color bars give the $<\tau>$ range in ns used in the respective image. Scale bar corresponds to 10 μm for **(A,B)**, 5 μm for **(C)**. Frequency histograms of $<\tau>$ **(D–F)** corresponding to the plasma membrane, PM (solid lines), or intracellular membrane, IM (dashed lines), for each cell type are shown. The corresponding regions of interest can be found in **Supplementary Figure S5**.

in mid-exponential phase in suspension (2.55 ± 0.06 ns) (Santos et al., 2017; **Figures 4B,E**). This may be compared with our observations in model membranes, where it was shown that Erg had a smaller ability to increase di-4-ANEPPS $<\tau>$ than Chol (**Table 2**). Interestingly, membrane organization as judged from $<\tau>$ of di-4-ANEPPS in vesicles containing either saturated PC or palmitoylsphingomyelin (PSM)/Chol lipids resembled most that of CHO-K1 cells, while membrane organization in POPC/Erg vesicles resembled that of *S. cerevisiae* cells. These results point to a fundamental difference in how to model sterol-enriched regions of mammalian and yeast cell membranes.

To study the influence of sterol profile on membrane properties reported by di-4-ANEPPS $<\tau>$, *S. cerevisiae erg6*Δ cells were also analyzed, in which Erg is absent and the level of Zym is about four to seven-fold higher than in the *wt* strain (Zinser et al., 1993; Pedroso et al., 2009; Dupont et al., 2011). Despite the fact that Erg is no longer present, and Zym becomes one of the major cellular sterols (Heese-Peck et al., 2002; Guan et al., 2009; Dupont et al., 2011), no significant differences have been found in the levels of other major membrane lipids (Guan et al., 2009). At a first glance, FLIM images (**Figures 4B,C**) suggest a similar di-4-ANEPPS fluorescence lifetime in both *wt* and *erg6*Δ yeast strains. However, the frequency histograms (**Figures 4E,F**) point to a slightly longer $<\tau>$ of di-4-ANEPPS in *erg6*Δ cells (**Supplementary Figure S4E**; see also **Supplementary Figure S7**). This slight increase may be related to the higher Zym content of the mutant cells' plasma membrane, as mentioned above. This would mean that in the presence of the main sterol of the plasma membrane in this strain, the probe would present a $<\tau>$ value similar to the one in the presence of Erg. In fact, that sterol is cholesta-5,7,24-trienol, which was found to accumulate in membrane regions resistant to detergent extraction in Erg6p defective mutants, at levels identical to those of Erg in *wt* cells (Eisenkolb et al., 2002).

The fluorescence intensity decays of di-4-ANEPPS contain more information than the average fluorescence lifetime $<\tau>$, namely the pre-exponentials and the fluorescence lifetimes of the two exponential components that describe each fluorescence intensity decay. These parameters were collected from all analyzed cells and the average values are given in **Table 2**. A noticeable difference is found in the value of τ_2 between *wt* and *erg6*Δ, despite the small difference between $<\tau>$ of the probe in those yeast strains – $\tau_{2\,wt}$ = 2.95 ns and $\tau_{2\,erg6\Delta}$ = 3.60 ns (**Figure 5**). The mutant strain value is more similar to the one obtained in model membranes containing Zym than Erg (**Table 2**). Comparing the lifetimes measured in yeast to those measured in CHO cells, both τ_2 and $<\tau>$ were clearly longer in the mammalian cells, as in the model systems containing Chol compared to Erg and Zym.

Cell membranes are highly complex and dynamic, and their large number of components could conceivably influence di-4-ANEPPS measurements. Nevertheless, a good parallel could be drawn between the measured fluorescence lifetime components and amplitudes in mammalian and yeast cells of varied sterol profile and the model systems of closer sterol composition.

DISCUSSION

Recent studies in both yeast and mammalian cells have challenged the hypothesis that the main role of sterols is solely to generate l_d/l_o lateral membrane heterogeneity (Souza et al., 2011). FLIM results and the high sterol content of eukaryotic plasma membranes suggest that an l_o-like phase may actually correspond to a major area of the cell membrane (Owen et al., 2006; De Almeida and Joly, 2014; Kilin et al., 2015). These diverse perspectives can be reconciled by hypothesizing that while not all sterols are able to form l_o phase, the ability to form such phases in membrane model systems seems to be a common underlying feature of the main sterols of eukaryotic organisms. Here, we tested this hypothesis by a biophysical approach, in which physiologically relevant membrane properties in model systems containing the fungal and mammalian major sterols, Erg and Chol, were assessed. The measurements obtained with a probe suitable to report on sterol-dependent properties were directly compared to those performed in cell membranes of yeast and mammalian cells having different plasma membrane sterol profiles. Moreover, we made a parallel study of the last common biosynthetic precursor to Erg and Chol in the Blöch pathway, Zym.

The formation of l_o phase, a feature common to Erg and Chol, is a determining factor in lateral lipid organization of model membranes used in the present study. Previous observations on lipid monolayers upon sterol incorporation showed a steep increase of both DPPC and PSM monolayer condensation up to ≈ 30 mol% Chol, after which a plateau is reached (Hac-Wydro et al., 2014). At this composition, DPPC/Chol and PSM/Chol bilayers are 100% in l_o (Sankaram and Thompson, 1991; De Almeida et al., 2003). The plateau is not a result of the sterol solubility limit, i.e., for Chol in PC membranes this limit is much larger than 30 mol% (Huang et al., 1999; Mannock et al., 2010). For Zym, however, a slower and approximately linear increase in condensation was observed along all the composition range, i.e., up to 50 mol%, which can be explained by the inability of Zym to form a new phase analogous to the l_o phase found in lipid bilayer membranes. Those results for Zym-containing monolayers can be paralleled to the approximately linear increase in the $<\tau>$ of di-4-ANEPPS up to ca. 50 mol% of this sterol in binary mixtures with a fluid or gel PC presented in this work.

Crucial membrane biophysical features are imprinted by the major sterol component, one of the most important being, apparently, the ability to form an l_o phase or the lack of this ability. This feature has important consequences for biologically relevant properties, such as membrane passive permeability to water and univalent cations studied in this work. The hypersensitivity of Erg biosynthetic mutant cells to stress situations, such as dehydration (Dupont et al., 2011), univalent metal cations (Welihinda et al., 1994; Pagani et al., 2007; Ruotolo et al., 2008) and high saline conditions (Kodedova and Sychrova, 2015), could be related to the higher passive permeability of their cell membrane compared to the Erg-containing *wt* cells. In fact, increased permeability to small dyes such as Rhodamine 6G is a phenotypic feature of *erg6*Δ cells (Mukhopadhyay et al., 2002). Moreover, *erg6*Δ cells exhibit higher plasma membrane

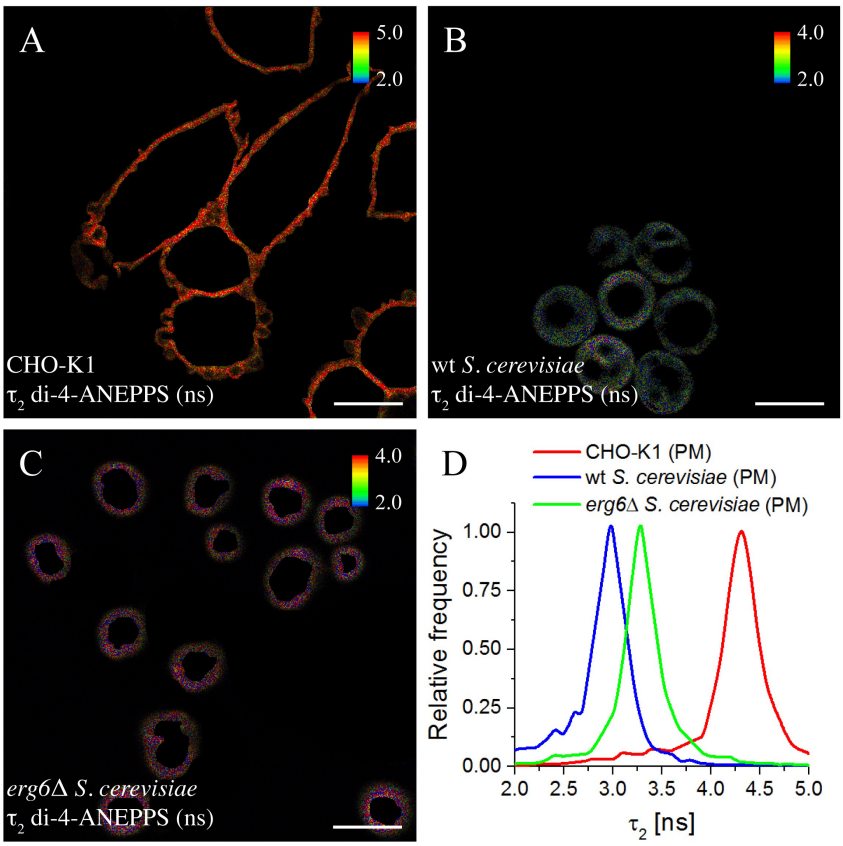

FIGURE 5 | Long lifetime component τ_2 of the fluorescence decay of di-4-ANEPPS is highly sensitive to changes in sterol-dependent properties of membranes. FLIM images of ROIs of the plasma membrane (PM) of CHO-K1 cells **(A)**, *wt* **(B)**, and *erg6*Δ *S. cerevisiae* cells **(C)**. The inset color bars give the long lifetime component τ_2 range in ns used in the respective image. Scale bar = 10 μm. **(D)** Frequency histograms of τ_2 corresponding to the FLIM images shown.

permeability to H_2O_2 and, thus, are more sensitive to this molecule (Branco et al., 2004), which can, at least in part, be explained by our observation that membranes lacking l_o-forming sterols are more permeable to water and ions.

Previously, it has been hypothesized that sterols and sphingolipids have co-evolved to provide an optimal interaction between the two lipid groups (Guan et al., 2009). Although in mammalian cells sphingolipids and Chol are present in the same plasma membrane leaflet, in yeast there is evidence that Erg predominates in the inner leaflet whereas sphingolipids accumulate in the outer one. Thus, while in mammalian plasma membrane sphingolipid/Chol interactions are easily established in order to dominate the global properties of the membrane, in yeast plasma membrane Erg/sphingolipid interactions are not as likely to occur and therefore their contribution for the overall membrane properties seems more limited. Analysis of the double mutant yeast strain *elo3*Δ*erg6*Δ, with defects both in sphingolipid and sterol biosynthesis, revealed an important role of the methyl group at carbon 24 of the side chain of Erg for its interaction with sphingolipids (Eisenkolb et al., 2002). The Erg precursor Zym lacks this methyl group, but interestingly so does Chol. Thus, this methyl group should not be responsible for the driving force conferring Erg (and Chol) the ability to induce the formation of an l_o phase, but should be important for the stability of the fungal membrane. Conversely, the double bond at C-6 (**Scheme 1**), which is a common structural feature between Erg and Chol and absent in Zym, would, according to our results, likely be required for their l_o-forming ability. On the other hand, a saturated acyl chain is a distinctive feature of Chol and could therefore be important for the significant increase in membrane dipole potential that only Chol could convey to the membrane (**Figure 2**). Thus, it appears that during the evolutionary process a fine-tuning of the structure of sterols, which confers e.g., variable tilt and orientation toward the acyl chains of phospholipids (Rog and Pasenkiewicz-Gierula, 2003; Rog et al., 2008), may have occurred, leading to the selection of Erg as the sterol that could preferentially associate with lipids present in yeast membranes, and Chol as the sterol that would perform a similar function in mammals. The observation that a yeast strain where Chol replaces Erg is even more sensitive to weak organic acids than *erg6*Δ (Souza et al., 2011) strengthens the hypothesis formulated above. In further support, Erg does not affect the di-4-ANEPPS $<\tau>$ in mixtures with PSM, whereas the longest $<\tau>$ was achieved when Chol was mixed with this same sphingolipid (Bastos et al., 2012), one of the most abundant in mammalian cells but absent in fungi.

Indeed, the probe di-4-ANEPPS is sensitive to sterol content and type, more than to membrane fluidity (Amaro et al., 2017). Factors influencing the fluorescence decay of di-4-ANEPPS include hydrogen bonds, both from hydration water and others mainly in the region of the phospholipid headgroups, which define the probe microenvironment (Loew, 1996; M'baye et al., 2008). Although some photophysical parameters of di-4-ANEPPS can be different between pure DPPC and POPC environments, the factors that govern the average fluorescence lifetime defined by the chemical environment of the probe are relatively similar, as the fluorophore is accommodated between the phosphocholine and the ester polar groups of the phospholipids (Celli and Gratton, 2010; Golfetto et al., 2013; Timr et al., 2014; Amaro et al., 2017). In fact, in PC/Chol mixtures, the general polarization values of di-4-ANEPPDHQ do not correlate with lipid packing as it is the case for Laurdan. Instead, they are influenced by the presence of Chol (Amaro et al., 2017). Thus, any changes in the di-4-ANEPPS $<\tau>$ in binary lipid bilayers of DPPC or POPC with increasing sterol concentrations are mostly attributed to sterol structural and dynamic features (Galván-Hernández et al., 2020) reflected on the membrane biophysical properties which of course, are also dependent on the lipid species interacting with the sterol (Bastos et al., 2012). Altogether, these features suggest that the probe reports preferentially the properties of sterol-enriched domains in more complex environments, such as that of a cellular membrane. In fact, the amplitude-weighted average fluorescence lifetime of di-4-ANEPPS was shown to correlate remarkably with the glycerophospholipid/Erg ratio along germination of *Neurospora crassa* asexual spores (Santos et al., 2018). Our study showed that di-4-ANEPPS fluorescence intensity decay parameters and $<\tau>$ in living cells can be recapitulated by membrane model systems of similar sterol composition. This happens for Chol containing membranes and CHO cells and for Erg-containing membrane and *wt* yeast cells. Moreover, the differences between *wt* and *erg6*Δ yeast cells can be related to the Zym ability to increase $<\tau>$ of the probe to a larger extent than Erg. However, these results also indicate that a longer $<\tau>$ of di-4-ANEPPS cannot be directly associated to the presence of l_o domains in yeast, as Zym is unable to induce the formation of this phase. The similarity between di-4-ANEPPS $<\tau>$ in *S. cerevisiae* cells and in POPC/Erg vesicles could indicate that the fraction of l_d-like domains is higher in yeast than in CHO-K1 cells. However, several studies suggest that the plasma membrane of *S. cerevisiae* is considerably ordered, containing both l_o and gel domains (Klose et al., 2010; Aresta-Branco et al., 2011; Malinsky et al., 2013). Therefore, an alternative depiction of *S. cerevisiae* membrane organization that conciliates its ordered character with the relatively low di-4-ANEPPS $<\tau>$ is required. In multicomponent membranes, each domain type is enriched in certain lipids, but also contains minor fractions of other components. Thus, the l_o domains in yeast may contain a higher fraction of unsaturated phospholipids than their mammalian counterpart. On one hand, this hypothesis is consistent with the recent proposal that only ca. 20 mol% of Erg is localized in the outer leaflet of the plasma membrane (Solanko et al., 2018). Consequently, sphingolipids would be mainly forming Erg-depleted domains, whilst Erg-containing regions in the outer leaflet would largely correspond to a POPC/Erg (ca. 70:30 mole fraction) mixture, which is in fair agreement with the glycerophospholipid/Erg ratio in the outer leaflet calculated from the composition reported for the plasma membrane of *S. cerevisiae,* i.e., considering ca. 20 mol% Erg in the outer leaflet (Solanko et al., 2018). On the other hand this hypothesis also agrees with the fluorescence lifetime of di-4-ANEPPS in CHO-K1 cells, which indicates that in these cells sterol-enriched membrane regions are mainly formed by saturated lipids (sphingomyelin) and Chol. Indeed, the average lifetime $<\tau>$ obtained in the plasma membrane of CHO-K1 cells is identical to the ones observed for either DPPC/Chol or PSM/Chol (70:30 mole fraction), typical l_o phase forming mixtures, but not for POPC/Chol. In contrast, for *wt S. cerevisiae* cells, the membrane properties as reported by di-4-ANEPPS $<\tau>$ present closer similarity with POPC/Erg vesicles, rather than with DPPC/Erg. Consistently with these observations, the anisotropy of DPH in *wt* yeast cells ($<r> \sim 0.15$) (Aresta-Branco et al., 2011) is almost coincident with the one obtained in POPC/Erg mixtures containing more than 20 mol% Erg ($<r> \sim 0.14$) (Arora et al., 2004) whereas the higher anisotropy values determined in DPPC/Chol mixtures (Arora et al., 2004) correlate with those measured in CHO cells (Carreira, 2019). Taken together, these results support the seemingly different microdomain organization in yeast and animal cells: in yeast, a significant fraction of the saturated lipids are segregated into Erg-depleted gel domains that may act as diffusion barriers, stabilizing larger and less dynamic membrane compartments (Clay et al., 2014; Marques et al., 2015), while the Erg-rich l_o phase contains a large fraction of monounsaturated lipids; in mammalians, such gel domains, apart from cells with pathological levels of ceramide or glucosylceramide (Varela et al., 2014, 2017), have never been reported and saturated lipids are a major component of the Chol-rich phase.

CONCLUSION

We compared the properties of Erg, Chol and Zym-containing membranes both in living cells and model membranes. This allowed us to extend our understanding of the importance of sterol-dependent membrane biophysical properties in eukaryotes. By establishing the ability to form l_o phase as the major common biophysical property of Erg and Chol that is not shared by Zym, our results may provide a general framework to a more insightful interpretation of observations both in model systems and cellular membranes.

As Zym is a biosynthetic precursor of both Chol and Erg, it is tempting to extrapolate our main conclusions to sterol selection during organism evolution. We hypothesize that sterol evolution in fungi and animals was divergent in terms e.g., of solvent dynamics and dipole potential, but was convergent in the l_o phase promoting aptitude. This model can be a useful framework for the interpretation of biological outcomes related to membrane-sterol alterations.

DATA AVAILABILITY STATEMENT

The datasets generated for this study are available on request to the corresponding author.

AUTHOR CONTRIBUTIONS

AK, JM, AB, CA, AB-O, SS, GL and RM performed the experiments and analyzed the data. AH and HM provided scientific and technical expertise to research, reviewed and edited the manuscript. HM and RA designed the project. AK, JM, AB, CA, SS, and RA designed the experimental work and wrote the manuscript. RA supervised and coordinated the research.

FUNDING

This work was supported by the Fundação para a Ciência e a Tecnologia (FCT), Portugal through research grants PTDC/BBB-BQB/6071/2014 and PTDC/QUI-BIQ/104311/2008, which included fellowships to AB, CA, and JM and Centro de Química Estrutural research unit (UIDB/00100/2020). AK was a recipient of a scholarship from Fundação Amadeus Dias/UL (2010).

ACKNOWLEDGMENTS

The authors thank Dr. Kristina Ganzinger and Prof. Tim Liedl for proofreading the manuscript.

SUPPLEMENTARY MATERIAL

The Supplementary Material for this article can be found online at: https://www.frontiersin.org/articles/10.3389/fcell.2020.00337/full#supplementary-material

REFERENCES

Abe, F., and Hiraki, T. (2009). Mechanistic role of ergosterol in membrane rigidity and cycloheximide resistance in *Saccharomyces cerevisiae*. *Biochim. Biophys. Acta* 1788, 743–752. doi: 10.1016/j.bbamem.2008.12.002

Amaro, M., Reina, F., Hof, M., Eggeling, C., and Sezgin, E. (2017). Laurdan and Di-4-ANEPPDHQ probe different properties of the membrane. *J. Phys. D Appl. Phys.* 50:134004. doi: 10.1088/1361-6463/aa5dbc

Aresta-Branco, F., Cordeiro, A. M., Marinho, H. S., Cyrne, L., Antunes, F., and De Almeida, R. F. (2011). Gel domains in the plasma membrane of *Saccharomyces cerevisiae*: highly ordered, ergosterol-free, and sphingolipid-enriched lipid rafts. *J. Biol. Chem.* 286, 5043–5054. doi: 10.1074/jbc.m110.154435

Arora, A., Raghuraman, H., and Chattopadhyay, A. (2004). Influence of cholesterol and ergosterol on membrane dynamics: a fluorescence approach. *Biochem. Biophys. Res. Commun.* 318, 920–926. doi: 10.1016/j.bbrc.2004.04.118

Athanasopoulos, A., Andre, B., Sophianopoulou, V., and Gournas, C. (2019). Fungal plasma membrane domains. *FEMS Microbiol. Rev.* 43, 642–673.

Barton, D. H., Gunatilaka, A. A., Jarman, T. R., Widdowson, D. A., Bard, M., and Woods, R. A. (1975). Biosynthesis of terpenes and steroids. X. The sterols of some yeast mutants doubly defective in ergosterol biosynthesis. *J. Chem. Soc. Perkin.* 1, 88–92.

Bastos, A. E., Marinho, H. S., Cordeiro, A. M., De Soure, A. M., and De Almeida, R. F. (2012). Biophysical properties of ergosterol-enriched lipid rafts in yeast and tools for their study: characterization of ergosterol/phosphatidylcholine membranes with three fluorescent membrane probes. *Chem. Phys. Lipids* 165, 577–588. doi: 10.1016/j.chemphyslip.2012.06.002

Beattie, M. E., Veatch, S. L., Stottrup, B. L., and Keller, S. L. (2005). Sterol structure determines miscibility versus melting transitions in lipid vesicles. *Biophys. J.* 89, 1760–1768. doi: 10.1529/biophysj.104.049635

Bittman, R., and Blau, L. (1976). Kinetics of solute permeability in phospholipid vesicles. *J. Chem. Educ.* 53, 259–261.

Branco, M. R., Marinho, H. S., Cyrne, L., and Antunes, F. (2004). Decrease of H2O2 plasma membrane permeability during adaptation to H2O2 in *Saccharomyces cerevisiae*. *J. Biol. Chem.* 279, 6501–6506. doi: 10.1074/jbc.m311818200

Carreira, A. C. (2019). *Sphingosine-Induced Alterations in Membrane Biophysical Properties: Biological Relevance in the Pathophysiology of Human Disease*. Doctoral thesis, Universidade de Lisboa, Lisbon.

Celli, A., and Gratton, E. (2010). Dynamics of lipid domain formation: fluctuation analysis. *Biochim. Biophys. Acta* 1798, 1368–1376. doi: 10.1016/j.bbamem.2009.12.002

Clay, L., Caudron, F., Denoth-Lippuner, A., Boettcher, B., Buvelot Frei, S., Snapp, E. L., et al. (2014). A sphingolipid-dependent diffusion barrier confines ER stress to the yeast mother cell. *eLife* 3:e01883.

Clerc, S. G., and Thompson, T. E. (1995). Permeability of dimyristoyl phosphatidylcholine/dipalmitoyl phosphatidylcholine bilayer membranes with coexisting gel and liquid-crystalline phases. *Biophys. J.* 68, 2333–2341. doi: 10.1016/s0006-3495(95)80415-7

Cordeiro, R. M. (2018). Molecular structure and permeability at the interface between phase-separated membrane domains. *J. Phys. Chem. B* 122, 6954–6965. doi: 10.1021/acs.jpcb.8b03406

Coutinho, A., Silva, L., Fedorov, A., and Prieto, M. (2004). Cholesterol and ergosterol influence nystatin surface aggregation: relation to pore formation. *Biophys. J.* 87, 3264–3276. doi: 10.1529/biophysj.104.044883

Daum, G., Tuller, G., Nemec, T., Hrastnik, C., Balliano, G., Cattel, L., et al. (1999). Systematic analysis of yeast strains with possible defects in lipid metabolism. *Yeast* 15, 601–614. doi: 10.1002/(SICI)1097-0061(199905)15:7(601:AID-YEA390(3.0.CO;2-N

De Almeida, R. F., Borst, J., Fedorov, A., Prieto, M., and Visser, A. J. (2007). Complexity of lipid domains and rafts in giant unilamellar vesicles revealed by combining imaging and microscopic and macroscopic time-resolved fluorescence. *Biophys. J.* 93, 539–553. doi: 10.1529/biophysj.106.098822

De Almeida, R. F., Fedorov, A., and Prieto, M. (2003). Sphingomyelin/phosphatidylcholine/cholesterol phase diagram: boundaries and composition of lipid rafts. *Biophys. J.* 85, 2406–2416. doi: 10.1016/s0006-3495(03)74664-5

De Almeida, R. F., and Joly, E. (2014). Crystallization around solid-like nanosized docks can explain the specificity, diversity, and stability of membrane microdomains. *Front. Plant Sci.* 5:72. doi: 10.3389/fpls.2014.00072

De Almeida, R. F., Loura, L. M., Fedorov, A., and Prieto, M. (2005). Lipid rafts have different sizes depending on membrane composition: a time-resolved fluorescence resonance energy transfer study. *J. Mol. Biol.* 346, 1109–1120. doi: 10.1016/j.jmb.2004.12.026

Dietrich, C., Bagatolli, L. A., Volovyk, Z. N., Thompson, N. L., Levi, M., Jacobson, K., et al. (2001). Lipid rafts reconstituted in model membranes. *Biophys. J.* 80, 1417–1428. doi: 10.1016/s0006-3495(01)76114-0

Dupont, S., Beney, L., Ferreira, T., and Gervais, P. (2011). Nature of sterols affects plasma membrane behavior and yeast survival during dehydration. *Biochim. Biophys. Acta* 1808, 1520–1528. doi: 10.1016/j.bbamem.2010.11.012

Eisenkolb, M., Zenzmaier, C., Leitner, E., and Schneiter, R. (2002). A specific structural requirement for ergosterol in long-chain fatty acid synthesis mutants important for maintaining raft domains in yeast. *Mol. Biol. Cell* 13, 4414–4428. doi: 10.1091/mbc.e02-02-0116

Emter, R., Heese-Peck, A., and Kralli, A. (2002). ERG6 and PDR5 regulate small lipophilic drug accumulation in yeast cells via distinct mechanisms. *FEBS Lett.* 521, 57–61. doi: 10.1016/s0014-5793(02)02818-1

Folmer, V., Pedroso, N., Matias, A. C., Lopes, S. C., Antunes, F., Cyrne, L., et al. (2008). H2O2 induces rapid biophysical and permeability changes in the plasma membrane of *Saccharomyces cerevisiae*. *Biochim. Biophys. Acta* 1778, 1141–1147. doi: 10.1016/j.bbamem.2007.12.008

Galván-Hernández, A., Kobayashi, N., Hernández-Cobos, J., Antillón, A., Nakabayashi, S., and Ortega-Blake, I. (2020). Morphology and dynamics of domains in ergosterol or cholesterol containing membranes. *Biochim. Biophys. Acta* 1862:183101. doi: 10.1016/j.bbamem.2019.183101

Golfetto, O., Hinde, E., and Gratton, E. (2013). Laurdan fluorescence lifetime discriminates cholesterol content from changes in fluidity in living cell membranes. *Biophys. J.* 104, 1238–1247. doi: 10.1016/j.bpj.2012.12.057

Grossmann, G., Opekarova, M., Malinsky, J., Weig-Meckl, I., and Tanner, W. (2007). Membrane potential governs lateral segregation of plasma membrane proteins and lipids in yeast. *EMBO J.* 26, 1–8. doi: 10.1038/sj.emboj.7601466

Guan, X. L., Souza, C. M., Pichler, H., Dewhurst, G., Schaad, O., Kajiwara, K., et al. (2009). Functional interactions between sphingolipids and sterols in biological membranes regulating cell physiology. *Mol. Biol. Cell* 20, 2083–2095. doi: 10.1091/mbc.e08-11-1126

Hac-Wydro, K., Wydro, P., and Flasinski, M. (2014). The comparison of zymosterol vs cholesterol membrane properties–the effect of zymosterol on lipid monolayers. *Colloids Surf. B Biointerfaces* 123, 524–532. doi: 10.1016/j.colsurfb.2014.09.054

Haldar, S., Kanaparthi, R. K., Samanta, A., and Chattopadhyay, A. (2012). Differential effect of cholesterol and its biosynthetic precursors on membrane dipole potential. *Biophys. J.* 102, 1561–1569. doi: 10.1016/j.bpj.2012.03.004

Heese-Peck, A., Pichler, H., Zanolari, B., Watanabe, R., Daum, G., and Riezman, H. (2002). Multiple functions of sterols in yeast endocytosis. *Mol. Biol. Cell* 13, 2664–2680. doi: 10.1091/mbc.e02-04-0186

Hsueh, Y. W., Chen, M. T., Patty, P. J., Code, C., Cheng, J., Frisken, B. J., et al. (2007). Ergosterol in POPC membranes: physical properties and comparison with structurally similar sterols. *Biophys. J.* 92, 1606–1615. doi: 10.1529/biophysj.106.097345

Hsueh, Y. W., Gilbert, K., Trandum, C., Zuckermann, M., and Thewalt, J. (2005). The effect of ergosterol on dipalmitoylphosphatidylcholine bilayers: a deuterium NMR and calorimetric study. *Biophys. J.* 88, 1799–1808. doi: 10.1529/biophysj.104.051375

Huang, J., Buboltz, J. T., and Feigenson, G. W. (1999). Maximum solubility of cholesterol in phosphatidylcholine and phosphatidylethanolamine bilayers. *Biochim. Biophys. Acta* 1417, 89–100. doi: 10.1016/s0005-2736(98)00260-0

Ipsen, J. H., Mouritsen, O. G., and Bloom, M. (1990). Relationships between lipid membrane area, hydrophobic thickness, and acyl-chain orientational order. The effects of cholesterol. *Biophys. J.* 57, 405–412. doi: 10.1016/s0006-3495(90)82557-1

Johnson, I., and Spence, M. T. Z. (2010). The Molecular probes handbook - a guide to fluorescent probes and labeling technologies. 11th edition, *Life Technologies*, 480–600.

Kaur, R., and Bachhawat, A. K. (1999). The yeast multidrug resistance pump, Pdr5p, confers reduced drug resistance in erg mutants of *Saccharomyces cerevisiae*. *Microbiology* 145(Pt 4), 809–818. doi: 10.1099/13500872-145-4-809

Khmelinskaia, A., Ibarguren, M., De Almeida, R. F. M., Lopez, D. J., Paixao, V. A., Ahyayauch, H., et al. (2014). Changes in membrane organization upon spontaneous insertion of 2-hydroxylated unsaturated fatty acids in the lipid bilayer. *Langmuir* 30, 2117–2128. doi: 10.1021/la403977f

Kilin, V., Glushonkov, O., Herdly, L., Klymchenko, A., Richert, L., and Mely, Y. (2015). Fluorescence lifetime imaging of membrane lipid order with a ratiometric fluorescent probe. *Biophys. J.* 108, 2521–2531. doi: 10.1016/j.bpj.2015.04.003

Kirsch, S. A., and Böckmann, R. A. (2019). Coupling of membrane nanodomain formation and enhanced electroporation near phase transition. *Biophys. J.* 116, 2131–2148. doi: 10.1016/j.bpj.2019.04.024

Klose, C., Ejsing, C. S., Garcia-Saez, A. J., Kaiser, H. J., Sampaio, J. L., Surma, M. A., et al. (2010). Yeast lipids can phase-separate into micrometer-scale membrane domains. *J. Biol. Chem.* 285, 30224–30232. doi: 10.1074/jbc.m110.123554

Kodedova, M., and Sychrova, H. (2015). Changes in the sterol composition of the plasma membrane affect membrane potential, salt tolerance and the activity of multidrug resistance pumps in *Saccharomyces cerevisiae*. *PLoS One* 10:e0139306. doi: 10.1371/journal.pone.0139306

Loew, L. M. (1996). Potentiometric dyes: imaging electrical activity of cell membranes. *Pure Appl. Chem.* 68, 1405–1409. doi: 10.1351/pac199668071405

Loew, L. M., Cohen, L. B., Dix, J., Fluhler, E. N., Montana, V., Salama, G., et al. (1992). A naphthyl analog of the aminostyryl pyridinium class of potentiometric membrane dyes shows consistent sensitivity in a variety of tissue, cell, and model membrane preparations. *J. Membr. Biol.* 130, 1–10.

Malinsky, J., and Opekarova, M. (2016). New insight into the roles of membrane microdomains in physiological activities of fungal cells. *Int. Rev. Cell Mol. Biol.* 325, 119–180. doi: 10.1016/bs.ircmb.2016.02.005

Malinsky, J., Opekarova, M., Grossmann, G., and Tanner, W. (2013). Membrane microdomains, rafts, and detergent-resistant membranes in plants and fungi. *Annu. Rev. Plant Biol.* 64, 501–529. doi: 10.1146/annurev-arplant-050312-120103

Mannock, D. A., Lewis, R., and Mcelhaney, R. N. (2010). A calorimetric and spectroscopic comparison of the effects of ergosterol and cholesterol on the thermotropic phase behavior and organization of dipalmitoylphosphatidylcholine bilayer membranes. *Biochim. Biophys. Acta* 1798, 376–388. doi: 10.1016/j.bbamem.2009.09.002

Marques, J. T., Cordeiro, A. M., Viana, A. S., Herrmann, A., Marinho, H. S., and De Almeida, R. F. M. (2015). Formation and properties of membrane-ordered domains by phytoceramide: role of sphingoid base hydroxylation. *Langmuir* 31, 9410–9421. doi: 10.1021/acs.langmuir.5b02550

Mazeres, S., Fereidouni, F., and Joly, E. (2017). Using spectral decomposition of the signals from laurdan-derived probes to evaluate the physical state of membranes in live cells. *F1000Res* 6:763. doi: 10.12688/f1000research.11577.2

M'baye, G., Mely, Y., Duportail, G., and Klymchenko, A. S. (2008). Liquid ordered and gel phases of lipid bilayers: fluorescent probes reveal close fluidity but different hydration. *Biophys. J.* 95, 1217–1225. doi: 10.1529/biophysj.107.127480

McClare, C. W. (1971). An accurate and convenient organic phosphorus assay. *Anal. Biochem.* 39, 527–530. doi: 10.1016/0003-2697(71)90443-x

Megha, Bakht, O., and London, E. (2006). Cholesterol precursors stabilize ordinary and ceramide-rich ordered lipid domains (lipid rafts) to different degrees. Implications for the Bloch hypothesis and sterol biosynthesis disorders. *J. Biol. Chem.* 281, 21903–21913. doi: 10.1074/jbc.m600395200

Mollapour, M., Fong, D., Balakrishnan, K., Harris, N., Thompson, S., Schuller, C., et al. (2004). Screening the yeast deletant mutant collection for hypersensitivity and hyper-resistance to sorbate, a weak organic acid food preservative. *Yeast* 21, 927–946. doi: 10.1002/yea.1141

Mukhopadhyay, K., Kohli, A., and Prasad, R. (2002). Drug susceptibilities of yeast cells are affected by membrane lipid composition. *Antimicrob. Agents Chemother.* 46, 3695–3705. doi: 10.1128/aac.46.12.3695-3705.2002

Munn, A. L., Heese-Peck, A., Stevenson, B. J., Pichler, H., and Riezman, H. (1999). Specific sterols required for the internalization step of endocytosis in yeast. *Mol. Biol. Cell* 10, 3943–3957. doi: 10.1091/mbc.10.11.3943

Owen, D. M., Lanigan, P. M. P., Dunsby, C., Munro, I., Grant, D., Neil, M. A. A., et al. (2006). Fluorescence lifetime imaging provides enhanced contrast when imaging the phase-sensitive dye di-4-ANEPPDHQ in model membranes and live cells. *Biophys. J.* 90, L80–L82.

Pagani, M. A., Casamayor, A., Serrano, R., Atrian, S., and Arino, J. (2007). Disruption of iron homeostasis in *Saccharomyces cerevisiae* by high zinc levels: a genome-wide study. *Mol. Microbiol.* 65, 521–537. doi: 10.1111/j.1365-2958.2007.05807.x

Pedroso, N., Matias, A. C., Cyrne, L., Antunes, F., Borges, C., Malho, R., et al. (2009). Modulation of plasma membrane lipid profile and microdomains by H2O2 in *Saccharomyces cerevisiae*. *Free Radic. Biol. Med.* 46, 289–298. doi: 10.1016/j.freeradbiomed.2008.10.039

Rog, T., and Pasenkiewicz-Gierula, M. (2003). Effects of epicholesterol on the phosphatidylcholine bilayer: a molecular simulation study. *Biophys. J.* 84, 1818–1826. doi: 10.1016/s0006-3495(03)74989-3

Rog, T., Vattulainen, I., Jansen, M., Ikonen, E., and Karttunen, M. (2008). Comparison of cholesterol and its direct precursors along the biosynthetic pathway: effects of cholesterol, desmosterol and 7-dehydrocholesterol on saturated and unsaturated lipid bilayers. *J. Chem. Phys.* 129:154508. doi: 10.1063/1.2996296

Ruotolo, R., Marchini, G., and Ottonello, S. (2008). Membrane transporters and protein traffic networks differentially affecting metal tolerance: a genomic phenotyping study in yeast. *Genome Biol.* 9, R67.

Sankaram, M. B., and Thompson, T. E. (1991). Cholesterol-induced fluid-phase immiscibility in membranes. *Proc. Natl. Acad. Sci. U.S.A.* 88, 8686–8690. doi: 10.1073/pnas.88.19.8686

Santos, F. C., Fernandes, A. S., Antunes, C. A. C., Moreira, F. P., Videira, A., Marinho, H. S., et al. (2017). Reorganization of plasma membrane lipid domains during conidial germination. *Biochim. Biophys. Acta* 1862, 156–166. doi: 10.1016/j.bbalip.2016.10.011

Santos, F. C., Lobo, G. M., Fernandes, A. S., Videira, A., and De Almeida, R. F. M. (2018). Changes in the biophysical properties of the cell membrane are involved in the response of Neurospora crassa to staurosporine. *Front. Physiol.* 9:1375. doi: 10.3389/fphys.2018.01375

Scheidt, H. A., Meyer, T., Nikolaus, J., Baek, D. J., Haralampiev, I., Thomas, L., et al. (2013). Cholesterol's aliphatic side chain modulates membrane properties. *Angew Chem.* 52, 12848–12851. doi: 10.1002/anie.201306753

Scolari, S., Engel, S., Krebs, N., Plazzo, A. P., De Almeida, R. F., Prieto, M., et al. (2009). Lateral distribution of the transmembrane domain of influenza virus hemagglutinin revealed by time-resolved fluorescence imaging. *J. Biol. Chem.* 284, 15708–15716. doi: 10.1074/jbc.m900437200

Sezgin, E., Levental, I., Mayor, S., and Eggeling, C. (2017). The mystery of membrane organization: composition, regulation and roles of lipid rafts. *Nat. Rev. Mol. Cell Biol.* 18, 361–374. doi: 10.1038/nrm.2017.16

Silva, L., Coutinho, A., Fedorov, A., and Prieto, M. (2006). Competitive binding of cholesterol and ergosterol to the polyene antibiotic nystatin. A fluorescence study. *Biophys. J.* 90, 3625–3631. doi: 10.1529/biophysj.105.075408

Simons, K., and Vaz, W. L. (2004). Model systems, lipid rafts, and cell membranes. *Annu. Rev. Biophys. Biomol. Struct.* 33, 269–295. doi: 10.1146/annurev.biophys.32.110601.141803

Solanko, L. M., Sullivan, D. P., Sere, Y. Y., Szomek, M., Lunding, A., Solanko, K. A., et al. (2018). Ergosterol is mainly located in the cytoplasmic leaflet of the yeast plasma membrane. *Traffic* 19, 198–214. doi: 10.1111/tra.12545

Souza, C. M., Schwabe, T. M., Pichler, H., Ploier, B., Leitner, E., Guan, X. L., et al. (2011). A stable yeast strain efficiently producing cholesterol instead of ergosterol is functional for tryptophan uptake, but not weak organic acid resistance. *Metab. Eng.* 13, 555–569. doi: 10.1016/j.ymben.2011.06.006

Steck, T. L., and Lange, Y. (2018). Transverse distribution of plasma membrane bilayer cholesterol: Picking sides. *Traffic* 19, 750–760. doi: 10.1111/tra.12586

Stockl, M., Nikolaus, J., and Herrmann, A. (2010). Visualization of lipid domain-specific protein sorting in giant unilamellar vesicles. *Methods Mol. Biol.* 606, 115–126. doi: 10.1007/978-1-60761-447-0_10

Subczynski, W. K., Hyde, J. S., and Kusumi, A. (1989). Oxygen permeability of phosphatidylcholine–cholesterol membranes. *Proc. Natl. Acad. Sci. U.S.A.* 86, 4474–4478. doi: 10.1073/pnas.86.12.4474

Timr, S., Bondar, A., Cwiklik, L., Stefl, M., Hof, M., Vazdar, M., et al. (2014). Accurate determination of the orientational distribution of a fluorescent molecule in a phospholipid membrane. *J. Phys. Chem. B* 118, 855–863. doi: 10.1021/jp4067026

Valachovic, M., Bareither, B. M., Shah Alam, B. M., Eckstein, J., Barbuch, R., Balderes, D., et al. (2006). Cumulative mutations affecting sterol biosynthesis in the yeast *Saccharomyces cerevisiae* result in synthetic lethality that is suppressed by alterations in sphingolipid profiles. *Genetics* 173, 1893–1908. doi: 10.1534/genetics.105.053025

Varela, A. R. P., Da Silva, A., Fedorov, A., Futerman, A. H., Prieto, M., and Silva, L. C. (2014). Influence of intracellular membrane pH on sphingolipid organization and membrane biophysical properties. *Langmuir* 30, 4094–4104. doi: 10.1021/la5003397

Varela, A. R. P., Ventura, A. E., Carreira, A. C., Fedorov, A., Futerman, A. H., Prieto, M., et al. (2017). Pathological levels of glucosylceramide change the biophysical properties of artificial and cell membranes. *Phys. Chem. Chem. Phys.* 19, 340–346. doi: 10.1039/c6cp07227e

Veatch, S. L., and Keller, S. L. (2003). Separation of liquid phases in giant vesicles of ternary mixtures of phospholipids and cholesterol. *Biophys. J.* 85, 3074–3083. doi: 10.1016/s0006-3495(03)74726-2

Vist, M. R., and Davis, J. H. (1990). Phase equilibria of cholesterol/dipalmitoylphosphatidylcholine mixtures: 2H nuclear magnetic resonance and differential scanning calorimetry. *Biochemistry* 29, 451–464. doi: 10.1021/bi00454a021

Welihinda, A. A., Beavis, A. D., and Trumbly, R. J. (1994). Mutations in LIS1 (ERG6) gene confer increased sodium and lithium uptake in *Saccharomyces cerevisiae*. *Biochim. Biophys. Acta* 1193, 107–117. doi: 10.1016/0005-2736(94)90339-5

Zahumensky, J., and Malinsky, J. (2019). Role of MCC/eisosome in fungal lipid homeostasis. *Biomolecules* 9:305. doi: 10.3390/biom9080305

Zinser, E., Paltauf, F., and Daum, G. (1993). Sterol composition of yeast organelle membranes and subcellular distribution of enzymes involved in sterol metabolism. *J. Bacteriol.* 175, 2853–2858. doi: 10.1128/jb.175.10.2853-2858.1993

Conflict of Interest: The authors declare that the research was conducted in the absence of any commercial or financial relationships that could be construed as a potential conflict of interest.

frontiers in Immunology

REVIEW
published: 30 June 2020
doi: 10.3389/fimmu.2020.01320

Impact of Plasma Membrane Domains on IgG Fc Receptor Function

Sibel Kara[1], *Lukas Amon*[2], *Jennifer J. Lühr*[2,3], *Falk Nimmerjahn*[1,4,5], *Diana Dudziak*[2,4,5,6] *and Anja Lux*[1,4]*

[1] Department of Biology, Institute of Genetics, Friedrich-Alexander University Erlangen-Nürnberg (FAU), Erlangen, Germany, [2] Laboratory of Dendritic Cell Biology, Department of Dermatology, University Hospital Erlangen, Friedrich-Alexander University Erlangen-Nürnberg (FAU), Erlangen, Germany, [3] Division of Nano-Optics, Max-Planck Institute for the Science of Light, Erlangen, Germany, [4] Medical Immunology Campus Erlangen (MICE), Friedrich-Alexander University Erlangen-Nürnberg (FAU), Erlangen, Germany, [5] Deutsches Zentrum Immuntherapie (DZI), Erlangen, Germany, [6] Comprehensive Cancer Center Erlangen-European Metropolitan Area of Nürnberg (CCC ER-EMN), Erlangen, Germany

OPEN ACCESS

Edited by:
Claudia Kemper,
National Heart, Lung, and Blood Institute (NHLBI), United States

Reviewed by:
Maurizio Sorice,
Sapienza University of Rome, Italy
Erdinc Sezgin,
Karolinska Institutet (KI), Sweden
Ilya Levental,
University of Texas Health Science Center at Houston, United States

***Correspondence:**
Anja Lux
anja.lux@fau.de

Specialty section:
This article was submitted to Molecular Innate Immunity, a section of the journal Frontiers in Immunology

Received: 12 March 2020
Accepted: 26 May 2020
Published: 30 June 2020

Citation:
Kara S, Amon L, Lühr JJ, Nimmerjahn F, Dudziak D and Lux A (2020) Impact of Plasma Membrane Domains on IgG Fc Receptor Function. Front. Immunol. 11:1320. doi: 10.3389/fimmu.2020.01320

Lipid cell membranes not only represent the physical boundaries of cells. They also actively participate in many cellular processes. This contribution is facilitated by highly complex mixtures of different lipids and incorporation of various membrane proteins. One group of membrane-associated receptors are Fc receptors (FcRs). These cell-surface receptors are crucial for the activity of most immune cells as they bind immunoglobulins such as immunoglobulin G (IgG). Based on distinct mechanisms of IgG binding, two classes of Fc receptors are now recognized: the canonical type I FcγRs and select C-type lectin receptors newly referred to as type II FcRs. Upon IgG immune complex induced cross-linking, these receptors are known to induce a multitude of cellular effector responses in a cell-type dependent manner, including internalization, antigen processing, and presentation as well as production of cytokines. The response is also determined by specific intracellular signaling domains, allowing FcRs to either positively or negatively modulate immune cell activity. Expression of cell-type specific combinations and numbers of receptors therefore ultimately sets a threshold for induction of effector responses. Mechanistically, receptor cross-linking and localization to lipid rafts, i.e., organized membrane microdomains enriched in intracellular signaling proteins, were proposed as major determinants of initial FcR activation. Given that immune cell membranes might also vary in their lipid compositions, it is reasonable to speculate, that the cell membrane and especially lipid rafts serve as an additional regulator of FcR activity. In this article, we aim to summarize the current knowledge on the interplay of lipid rafts and IgG binding FcRs with a focus on the plasma membrane composition and receptor localization in immune cells, the proposed mechanisms underlying this localization and consequences for FcR function with respect to their immunoregulatory capacity.

Keywords: type I FcR, type II FcR, FcγR, CLR, cell membrane, lipid rafts, membrane, membrane localization

INTRODUCTION

Fc receptors (FcR) for immunoglobulin G (IgG) are cell surface receptors widely expressed on cells of both, the innate and the adaptive immune system. Based on distinct mechanisms of IgG binding, these IgG FcRs are currently classified as either type I Fc receptors (classical FcγR) or type II FcRs, which belong to the sugar-binding C-type lectin receptors [reviewed in (1)]. Upon ligand binding, receptors of both families have been shown to induce immune cell activation and cell-type specific effector responses via initiation of distinct intracellular signaling pathways. Ligand-induced cross-linking of multiple receptors facilitating the recruitment of intracellular signaling components was consequently proposed to be a crucial part of receptor function especially for type I Fc receptors [reviewed in (2)]. Since organized membrane microdomains, i.e., lipid rafts, are known to be enriched for signaling components [summarized in (3)], the question arises to what extent IgG FcR function in immune cells is affected by specified membrane domains or the composition of the plasma membrane in general.

THE CELL MEMBRANE IS A HIGHLY COMPLEX LIPID BILAYER

Biomembranes are a prerequisite for cell formation and cell survival as the cellular envelope establishes a biological barrier between intracellular and extracellular space. In more detail, they maintain energy storage, protect the cell from pathogens, are the site for cell-to-cell recognition, and are involved in almost all signaling and membrane trafficking processes by allowing both, active as well as passive transport of molecules into and out of the cell [summarized in (4–7)]. The plasma membrane is likely the most intensely studied biomembrane. In general, it consists of a lipid bilayer composed of a huge variety of different lipids that can be of either amphiphilic or hydrophobic nature, and a multitude of embedded membrane proteins (**Figure 1**) [for specialized review articles see (4, 8, 9)].

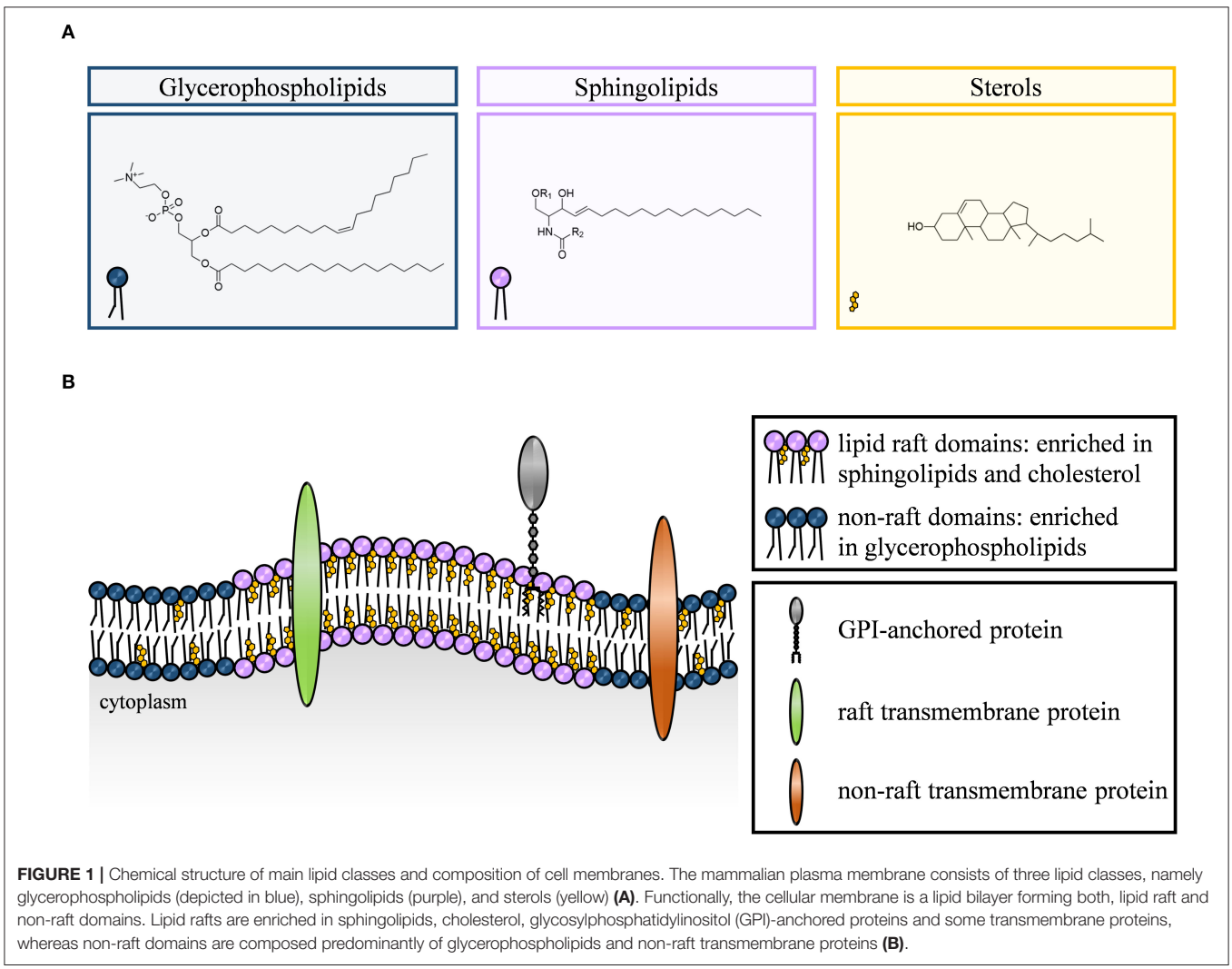

FIGURE 1 | Chemical structure of main lipid classes and composition of cell membranes. The mammalian plasma membrane consists of three lipid classes, namely glycerophospholipids (depicted in blue), sphingolipids (purple), and sterols (yellow) **(A)**. Functionally, the cellular membrane is a lipid bilayer forming both, lipid raft and non-raft domains. Lipid rafts are enriched in sphingolipids, cholesterol, glycosylphosphatidylinositol (GPI)-anchored proteins and some transmembrane proteins, whereas non-raft domains are composed predominantly of glycerophospholipids and non-raft transmembrane proteins **(B)**.

Structure and Function of Lipid Classes

The lipid composition of the plasma membrane of eukaryotic cells is based on three lipid classes, namely glycerophospholipids, sphingolipids, and sterols.

Glycerophospholipids (e.g., phosphatidylcholine or phosphatidylglycerol) are the predominant lipid component of mammalian plasma membranes and provide their basic framework. Distinct members of this lipid class also operate as second messengers or serve as precursors for the generation of second messengers. A glycerol backbone linked to two hydrophobic fatty acid chains and a phosphate group connected to a hydrophilic alcohol head group are the structural features of glycerophospholipids. Additional structural variations of this lipid species are based on modifications of the head group and the fatty acid chain length, degree of saturation, and linkage to glycerol (4, 10–13).

In comparison to glycerophospholipids, sphingolipids are much less frequent components of lipid cell membranes. However, together with cholesterol, they greatly contribute to the heterogeneity of plasma membrane organization. The common structural feature of sphingolipids is a ceramide core with an amphiphilic sphingosine backbone in turn providing the framework to form more complex sphingolipids such as sphingomyelin or gangliosides (4, 9, 14). Sphingolipids play a critical role both as structural components within membranes as well as bioactive signaling molecules. In this respect, they regulate numerous cellular processes that range from cell growth, differentiation and apoptosis (15, 16) to cytoskeletal reorganization (17, 18).

In recent years, many studies focused on the role of cholesterol in the plasma membrane as a modulator of structural integrity, membrane organization, and fluidity (3, 19, 20). With an amount of up to 40% of all membrane lipids, cholesterol is a major component of mammalian cell membranes (21, 22). It consists of a hydrophilic head group linked to a hydrophobic rigid steroid ring system which serves as a spacer between bulky sphingolipids and promotes the formation of distinct dynamic clusters with higher ordering, i.e., lipid rafts (3).

From Fluid Mosaic Model to Highly Complex Plasma Membranes

In 1972, Singer and Nicolson postulated the fluid mosaic model of the cell membrane, describing the structure of the plasma membrane as a mosaic of phospholipids, cholesterol, proteins, and carbohydrates. According to this model, the lipid membrane is a neutral two-dimensional solvent, crowded with randomly distributed membrane proteins (23). The fluid mosaic model was based on the observation that most physiological phospholipids have low melting temperatures, suggesting them to preferentially remain in liquid disordered phases. Many studies in the last decades have further refined this model and suggested that mammalian membranes contain very small and dynamic lipid domains with much higher melting temperatures that exist in a liquid ordered phase (24–26) The distribution of liquid ordered and disordered phases subsequently leads to transient formation of membrane nano- or microdomains, so-called lipid rafts that further shape the physical properties of the plasma membrane. Such compartmentalization subsequently facilitates segregation or aggregation of membrane proteins and signaling molecules within these distinct domains thus affecting their biological function (4, 9, 12, 27, 28). It is important to emphasize that both, the lipids in the plasma membrane as well as anchored membrane proteins exhibit a bilateral asymmetric architecture. This asymmetry seems to be required to compensate for membrane perturbations and facilitates membrane reorganization, trafficking and signaling (4, 29, 30). Asymmetry is a consequence of differential distribution of saturated and unsaturated lipids in the plasma membrane bilayer, in which saturated lipids seem to be located exclusively in the exoplasmic leaflet (30, 31). In contrast, heterogeneous cholesterol distribution between the inner and outer leaflet is still debated (21, 22, 32, 33). Membrane bilayer assymetry is further proposed to be modulated by long chain sphingolipids (34).

Lipid Rafts: Multifunctional Communication Platforms in Health and Disease

Lipid rafts are small, tightly packed and highly organized but dynamic membrane domains enriched in cholesterol and sphingolipids. The lipid raft hypothesis proposes that organized domains are fluid at physiological temperatures, facilitating lateral diffusion of proteins and lipids within the domain as well as of the raft itself. Furthermore, select interactions between cholesterol, saturated, and glycosylated lipids are involved in the recruitment of other lipids and proteins, e.g., glycosylphosphatidylinositol (GPI)-anchored and acylated or palmitoylated transmembrane proteins (9, 35–39).

From a functional perspective, lipid rafts are debated to be involved in sorting of membrane proteins, protein trafficking, membrane partitioning, and signaling (28, 40–43). In this respect, immunological synapses formed as interfaces between activated lymphocytes and their cognate antigen presenting cells have been hypothesized to be an example of organized raft domains within the immune system (44–46). Furthermore, lipid rafts are also discussed to play a crucial role in hematopoietic stem cell homing (47–49), mobilization (47, 50, 51), and differentiation (52–54). Moreover, many studies indicate lipid rafts to be involved in various diseases, e.g., HIV-1 infection including a role in virus budding (55, 56), cancer (57), or neurodegenerative disorders such as prion diseases (58), and Alzheimer's (59, 60).

Lipid Composition of Immune Cells

In the last years, evolutionary details have been gathered about the lipidome of mammalian tissues, e.g., cortex, brain, heart, kidney, muscle, or liver (61, 62) and mammary breast cancer cells (63, 64). But despite the fact that the lipid membrane plays a crucial role in many processes involved in immune cell function, information on the composition of immune cell membranes is surprisingly scarce. Recently, novel approaches allow for the detailed analysis of plasma membrane lipids by lipidomics, a method based on sensitive high-throughput mass spectrometry (65–67). Lipidomics analysis

revealed, for example, that the membrane lipid composition of leukocytes is characterized by sizable amounts of cholesterol and phosphatidylcholine. However, the observed amounts were lower than in neurons or epithelial cells (38). A study by Leidl et al. provided more detailed information on the lipidome of primary human peripheral blood leukocytes including neutrophils, monocytes, and lymphocytes. Accordingly, elevated amounts of ceramide and cholesterol but diminished phosphatidylcholine and sphingomyelin levels were identified in human neutrophils in comparison to monocytes. Lymphocytes exhibited an even lower content of phosphatidylcholine and sphingomyelin in contrast to monocytes and reduced levels of ceramide and cholesterol as compared to neutrophils. Thus, the authors propose monocytes and to a lesser degree lymphocytes to possess more fluid and neutrophils more rigid membrane features (65). In addition, the lipidome of human monocyte-derived DCs (moDCs) has been analyzed in both resting cells and in cells stimulated with the pro-inflammatory cytokine interleukin 17A (IL-17A). IL-17A appears to remodel the lipid metabolism by increasing the phospholipid and cholesterol content in moDCs and facilitates the formation of foamy rather than resting cells. Consequently, Salvatore et al. suggest that IL-17A activated lipid-rich moDCs might be involved in atherosclerosis (68).

Differences in the lipid membrane composition of immune cells have also been observed with respect to the sialic acid containing gangliosides [summarized in (69)]. For example, GM3 is the sole ganglioside found in the membrane of hematopoietic stem cells (70), dendritic cells [summarized in (71)], macrophages (72, 73), and monocytes (72, 74). In contrast, mast cells (75, 76), B cells (77, 78), and T cells (78–80) possess GM1, GM3 as well as GD3 in their cell membranes. Furthermore, neutrophils contain GM1 and GM3, but no GD3 (81–83), whereas NK cells display GM1 and GD3, but lack GM3 (79, 80).

Although these kinds of analysis provide detailed information about the individual lipid species contributing to membrane formation, it is difficult to predict physical properties of membranes from the lipid composition alone. Nevertheless, it became increasingly clear that specific properties of immune cells such as cell rolling and adhesion to endothelial cells are indeed affected by the lipid cell membrane composition (84–87).

Membrane composition and lipid rafts have also been shown to impact many different families of immune receptors including toll-like receptors (TLR) (88, 89), B cell receptors (90–92) and T cell receptors (93, 94), while negatively regulating elements such as transmembrane phosphatases by exclusion from lipid rafts (9). It is however much less clear to what extent lipid cell membranes influence the immunoregulatory function of the diverse family of IgG binding FcRs, both with respect to ligand binding as well as intracellular signal transduction.

CHARACTERISTICS, EXPRESSION AND SIGNALING OF TYPE I FC RECEPTORS

Classical FcγRs, or type I Fc receptors, interact with the fragment crystallizable (Fc) of IgG and thereby provide the crucial link between the soluble effector molecules of an adaptive immune response and innate immune effector cells. In a cell-type dependent manner, FcγR can trigger a multitude of different IgG effector functions including the uptake of IgG-coated pathogens by phagocytic cells, enhancement of antigen-presentation by dendritic cells (DCs), innate immune cell activation, and production of inflammatory mediators or killing of IgG coated target cells by antibody-dependent cytotoxicity (ADCC). In turn, FcγR expression on B cells is involved in modulation of adaptive immune responses and induction of apoptosis [summarized in (2)]. In humans, these various functions are maintained by a family of different FcγRs (FcγRIa/CD64A, FcγRIIa/CD32A, FcγRIIb/CD32B, FcγRIIIa/CD16A, and FcγRIIIb/CD16B) whose members are characterized by distinct expression profiles, IgG binding capacity and intracellular signaling potentials.

Expression Patterns of Type I Fc Receptors

One major layer of complexity in FcγR biology is cell-type specific expression of different FcγRs. As summarized in **Table 1**, typical examples of the latter include neutrophils expressing FcγRIIa and FcγRIIIb (and FcγRI upon activation), classical monocytes expressing FcγRIa, FcγRIIa, and FcγRIIb, and non-classical monocytes expressing FcγRIIa, FcγRIIb, and FcγRIIIa. FcγRIIa is also found on eosinophils that may express FcγRI upon stimulation, basophils that strongly co-express FcγRIIb and mast cells co-expressing FcγRIIb and FcγRIIIa (95, 96). Human DCs have been shown to express predominantly FcγRIIa/b and FcγRIa (97, 98) in a presumably DC subtype specific manner while expression of FcγRIIIa is still under discussion (99, 100). In contrast, NK cells exclusively express FcγRIIIa while FcγRIIb is the only FcγR found on B cells (95). While T cells largely lack FcγR expression there is accumulating data suggesting that select T helper cell subsets may express the inhibitory FcγRIIb [reviewed in (95, 101)].

Structure of FcγRs

The human FcγR family is predominantly composed of type I transmembrane proteins (**Figure 2**). The only known exception is FcγRIIIb that is anchored to the cell membrane via a glycosylphosphatidyl-inositol (GPI) tail (102). Otherwise, the FcγR α-chain is composed of an aminoterminal extracellular domain involved in binding IgG, a transmembrane-spanning domain and a carboxyterminal intracellular domain. With the exception of FcγRIIa, activating FcγRs require the association with the FcεRγ chain (short FcRγ) for cell surface expression (103–105), a signaling competent accessory chain originally discovered for its role in expression and function of the IgE FcR (FcεR) (106). The FcγR-FcεRγ chain complex assembles by non-covalent interactions of the respective transmembrane domains and is indispensable for cell surface expression as well as the immunomodulatory FcγR functions (107).

Classification of FcγRs According to Affinity for IgG or Intracellular Signaling

Based on their affinity for IgG, the high-affinity FcγRIa can be distinguished from the low-to-medium affinity FcγRII and FcγRIII family members. Consequently, FcγRIa is able to interact with monomeric IgG (108), whereas FcγRIIa/b and FcγRIIIa/b

TABLE 1 | Expression pattern of type I and type II Fc receptors on human immune cell populations (*induced upon cell activation, ‡ monocyte subpopulations not distinguished, n.d., not determined).

		Plasmacytoid DCs	Conventional DCs	Macrophages	Mast cells	Basophils	Eosinophils	Neutrophils	NK cells	Non – classical monocytes	Classical monocytes	T cells	B cells
Type I	FcγRIa	–	+	+	*+	–	*+	*+	–	–	+	–	–
	FcγRIIa	+	+	+	+	+	+	+	–	+	+	–	–
	FcγRIIb	+	+	+	+	+	–	+	–	+	+	–	+
	FcγRIIIa	–	–	+	+	–	–	–	+	+	–	–	–
	FcγRIIIb	–	–	–	–	–	–	+	–	–	–	–	–
Type II	Dectin-1	+	+	+	+	n.d.	+	+	–	+	+	+	+
	DC-SIGN	–	+/–	+	n.d.	–	–	–	n.d.	–	–	–	–
	FcεRII	n.d.	n.d.	*+	n.d.	n.d.	*+	*+	n.d.	‡+	‡+	*+	+

require multiple IgG molecules in complex, i.e., IgG immune complexes (IgG-IC) typically obtained by IgG recognizing their cognate antigens. The resulting multivalency of the interaction is able to compensate for a reduced affinity of an individual interaction (109, 110).

Alternatively, human FcγRs can be grouped by their intracellular signaling potential, i.e., what type of intracellular signaling pathway they are able to initiate. Due to the presence of an intracellular immunoreceptor tyrosine activation motif (ITAM), three activating FcγRs are recognized (FcγRIa, FcγRIIa, and FcγRIIIa). Within these receptors, the ITAM is either encoded by the cytoplasmic domain of the ligand-binding FcγR α-chain (as is the case for FcγRIIa) or is part of the accessory FcεRγ chain (FcγRIa and FcγRIIIa). In contrast, the FcγRIIb α-chain contains an immunoreceptor tyrosine based inhibitory motif (ITIM) rendering it an inhibitory receptor [reviewed in (2)]. The GPI-linked FcγRIIIb, which is only found in humans, is a signaling-deficient FcγR since it neither contains an intracellular domain nor interacts with FcεRγ. However, it plays a major role for capture of IgG immune complexes and co-operates with FcγRIIa for induction of signaling (111–113).

Intracellular Signaling of FcγRs

Albeit FcγR pose a quite diverse receptor family with respect to expression and structural composition, their intracellular signaling pathways are surprisingly similar. Upon IgG recognition, the intracellular ITAMs of activating FcγRs are phosphorylated by kinases of the SRC family enabling recruitment of SYK kinases. Downstream signaling includes activation of phosphoinositide 3-kinase (PI3K), which causes the release of intracellular calcium via activation of phospholipase Cγ (PLCγ). In addition, FcγRs trigger the mitogen-activated protein kinase (MAPK) pathway via ras and raf. Since most immune cells co-express both, activating and inhibitory FcγRs, IgG-IC binding will also initiate intracellular inhibitory signaling via FcγRIIB. Upon phosphorylation of ITIMs, phosphatases, e.g., SRC-homology-2-domain-containing inositol-5-phosphatase (SHIP) are recruited that interfere with the activating pathways by reducing the activation of ras and by hydrolysis of phosphoinositide intermediates [summarized in (114)]. Accordingly, activating and inhibitory FcγRs cooperate in setting a threshold for immune cell activation.

PROPERTIES AND EXPRESSION OF TYPE II FC RECEPTORS

Type I and type II Fc receptors share the ability to bind to IgG Fc but their mode of interaction differs. Based on the composition of the coupled bi-antennary Fc glycan, type I Fc receptors recognize IgG Fc in an open protein conformation at equimolar rate. In contrast, closed conformation recognition via type II receptors enables the binding of two Fc fragments at the same time (1, 115). So far, the identified type II Fc receptors belong to the super family of C-type lectins receptors (CLRs).

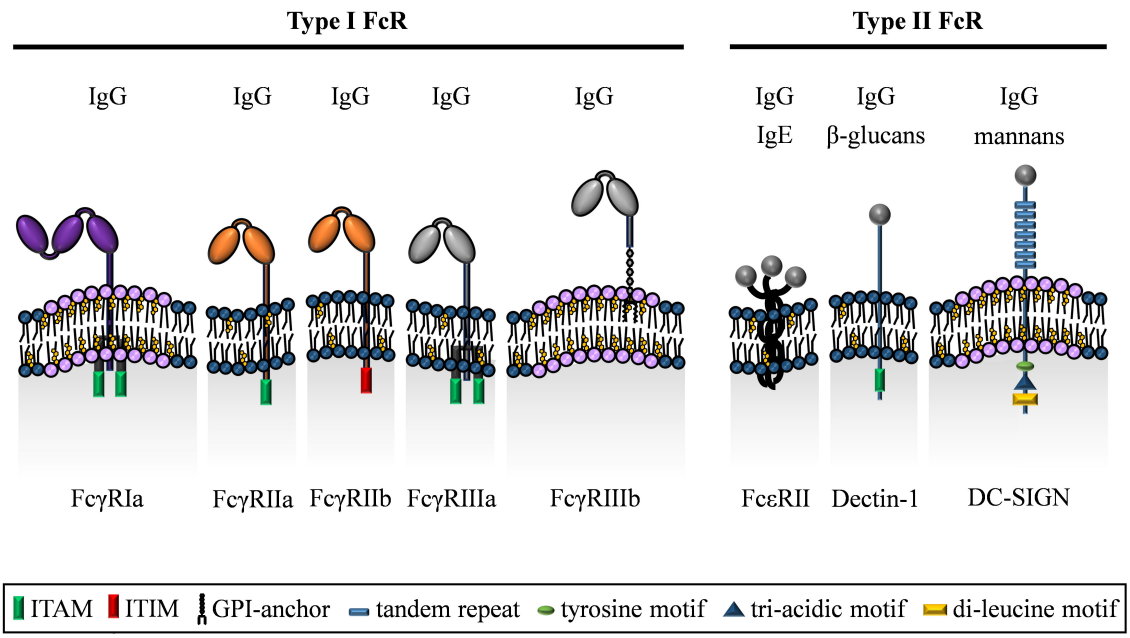

FIGURE 2 | The family of IgG binding type I and type II Fc receptors. The Fc receptors for IgG can be distinguished by their distinct binding mechanisms into either type I FcRs (classical FcγR) or type II FcRs (C-type lectin receptors). With respect to signal transduction, FcγRIa, FcγRIIa, FcγRIIIa, and Dectin-1 signal via ITAM domains in their cytoplasmic tail or on the associated FcεRγ chain. In contrast, the only inhibitory receptor FcγRIIb carries an ITIM domain in its cytoplasmic region. In addition, the GPI-linked FcγRIIIb lacks an intracellular signaling domain, but has a crucial role in binding of IgG immune complexes and enhances signaling upon cross-linking with other FcγRs. Besides, FcεRII has a short cytoplasmic region, whereas DC-SIGN exhibits a cytoplasmic domain including tyrosine, di-leucine and tri-acidic motifs. In addition to recognizing IgG, Dectin-1 and DC-SIGN are known to bind other ligands including defined sugar moieties.

Classification of C-Type Lectin Receptors

The classification of CLRs was first established to separate Ca^{2+}-dependent (C-type) from independent lectins [reviewed in (116)] where all Ca^{2+}-dependent lectins share an intrinsic carbohydrate recognition domain (CRD) allowing for binding of foreign and endogenous carbohydrate ligands (117). Owing to conserved residue motifs and the unique folding of the CRD, it was termed C-type lectin domain, which is the defining hallmark feature of all CLR family members (116). However, sequence analysis identified new CLRs able to recognize other ligands then carbohydrates including exogenous and endogenous protein side chains, glycosphingolipids and inorganic ligands in an Ca^{2+}-dependent or -independent manner [for specialized review articles see (118–120)]. Therefore, not all CLRs are classical pattern recognition receptors. Today, the CLR super family comprises more than one thousand soluble or membrane bound members (119).

Besides the C-type lectin domain, membrane bound CLRs are further dissected into type I and type II CLRs (not to be confused with type I and type II FcRs) depending on the localization of the N-terminus. They further differ in their intracellular motifs responsible for receptor internalization, cycling and signaling [summarized in (121)]. Because of this complexity, here we will focus only on the three so far described type II FcRs, DC-SIGN (CD209), Dectin-1 (CLEC7A) and Fcε receptor II (FcεRII; CD23) characterized by the ability to bind immunoglobulins (**Figure 2**) although this is a current matter of debate (119, 122–125).

Dendritic-Cell-Specific ICAM-3 Grabbing Non-integrin (DC-SIGN)

DC-SIGN is a type II CLR carrying an extracellular, C-terminal CRD, followed by seven complete and one incomplete tandem repeats and a hydrophobic, intracellular N-terminus. The latter is including tyrosine-, di-leucine and tri-acidic motifs, which are involved in internalization and shuttling (120, 121, 126, 127). DC-SIGN is specifically expressed on moDCs and macrophage subpopulations including alveolar macrophages (128, 129) (**Table 1**). In addition, expression of DC-SIGN on conventional DCs is also proposed (130). Following ligand recognition, it was demonstrated that DC-SIGN is rapidly internalized to late endosomes and lysosomes (127). The highly conserved Glu-Pro-Asn CRD motif facilitates the recognition of structures containing several mannose- and fucose-residue bearing ligands from pathogens, allergens, or endogenous molecules (120). One of the most prone antigens recognized by DC-SIGN is the HIV glycoprotein gp120 (126, 131, 132).

Signaling mediated via DC-SIGN is independent of immunoreceptor tyrosine-based motifs and does not lead to major modulations of immune cell activation by itself. DC-SIGN rather co-operates and fine-tunes the signaling of other receptors, e.g., TLRs (120). In this respect, high mannose ligands were found to foster the assembly of LSP1, KSR1, and CNK ultimately boosting the transcription of CXCL8, IL-12, IL-6, and IL-10 promoters via ras, raf-1 (133) and the NF-κB p65 subunit (133, 134). In contrast, fucose-rich ligands only allowed

for DC-SIGN association with LSP1 leading to production of IL-10 in a raf-1 independent manner and negatively influenced transcription of IL-6 and IL-12 (133). Finally, the DC-SIGN agonist Salp15 was found to negatively regulate the production of TNFα, IL-6 and IL-12 via ras and raf-1 dependent activation of MEK (135).

Besides the carbohydrate binding capacity, DC-SIGN has been originally described to be important for the emigration of moDCs from vascular endothelium (128). Moreover, DC-SIGN is a key player in establishing contacts between DCs and resting T cells (136). Besides this multitude of functions, DC-SIGN was identified as the first receptor being able to bind sialylated IgG. Sialylated IgG Fc, which is a component of intravenous immunoglobulin G (IVIg) preparations (137), was demonstrated to bind to DC-SIGN on macrophages and thereby mediate anti-inflammatory responses *in vivo* (138, 139). Thus, sialylated IgG Fc may comprise the therapeutically active component in IVIg preparations even though the exact mechanisms are still subject of debate (124, 137, 140, 141).

Dendritic-Cell-Associated C-Type Lectin 1 (Dectin-1)

Dectin-1 serves as a prototypic model for CLR pattern recognition receptors as its functions range from pathogen recognition to the initiation of signaling and uptake of bound material. Thus, Dectin-1 facilitates the recognition of β-1,3- and β-1,6-glucans in the defense against fungi in a Ca^{2+}-independent manner (142–144). It was recently also shown to recognize annexins on apoptotic cells in mice, thereby contributing to self-tolerance (145) albeit it remains to be determined if this finding can be translated to the human system. Karsten et al. showed that IgG1 immune complexes counteract C5a receptor signaling via FcγRIIb and Dectin-1 (146). Even though this study does not demonstrate direct IgG binding to Dectin-1, it has subsequently been suggested that Dectin-1 may recognize the core-fucose residue of the IgG sugar moiety (123).

As summarized in **Table 1**, Dectin-1 is widely expressed on human innate cells including both monocyte populations, conventional and plasmacytoid DCs, macrophages, neutrophils, eosinophils and mast cells. In addition, B cells and a subpopulation of T cells have also been suggested to express Dectin-1 (142, 143, 147, 148).

Full length Dectin-1 is composed of an extracellular C-terminus carrying a single CRD followed by a stalk region, the transmembrane domain and an intracellular N-terminus carrying an ITAM motif (149, 150). Smaller spliced isoforms of Dectin-1 lacking, e.g., the stalk region are expressed in a cell-type specific manner (142, 149, 151, 152).

Following ligand recognition, Dectin-1 has been shown to recruit syk via its hemITAM (single tyrosine based ITAM) motif initiating the production of reactive oxygen species, act in the activation of the NLRP3 inflammasome and the canonical p65 NF-κB pathway (120, 153–155). Comparable to DC-SIGN, Dectin-1 was also found to foster the syk-independent Raf-1 pathway (133). Finally, Dectin-1 signaling can synergize with MyD88 dependent TLR signaling in the induction of NF-κB (150).

The Low Affinity IgE Receptor FcεRII (CD23)

FcεRII (or CD23) is a type II CLR carrying an extracellular C-terminal CRD, a stalk region important for CD23 oligomerization, another extracellular region of yet unknown function, one single hydrophobic membrane domain and a short cytoplasmic N-terminus (156, 157). Thus, FcεRII is the only Fc receptor not belonging to the immunoglobulin superfamily (156). Described ligands for FcεRII are IgE, CD21, CD11b, CD11c, but also IgG (1, 158, 159). FcεRII is thought to be expressed on B cells, T cells, polymorphonuclear leukocytes including eosinophils and neutrophils, monocytes, follicular DCs as well as epithelial and stromal cells (156, 160–165) (**Table 1**).

Structure and function of FcεRII strongly differ from the high affinity IgE receptor FcεRI as it consists of a single amino acid chain, is not associated with the FcεRγ chain and is found in trimers on the cell surface (164, 166, 167). Ligation of FcεRII on B cells downregulates IgE production in the latter (156). FcεRII can also be released from the cell surface by metalloproteinases to exert cytokine-like activities while maintaining its IgE binding activity (168). These soluble FcεRII:IgE complexes can then interact with surface bound IgE receptors, thereby positively acting on survival and differentiation of B cells (169–171). Furthermore, soluble FcεRII was found to ligate CD11b and CD11c thereby promoting NF-κB dependent inflammatory responses by human monocytes including nitric oxide production, cAMP synthesis and cytokine production (172).

Depending on external environmental stimuli, FcεRII exists in two isoforms differing in their amino-terminal sequence and transcriptional start sites (156). While FcεRIIa is constitutively expressed on B cells, FcεRIIb expression may be induced and foster antigen retention following binding instead of processing and endocytosis (156). Membrane-bound FcεRII was further described to be involved in B cell selection and affinity maturation (173). This is mediated by autocrine upregulation of FcγRIIb following binding of sialylated Fc domains to FcεRII, thereby increasing the threshold for BCR signaling (173).

In summary, DC-SIGN, Dectin-1, and FcεRII are considered to be type II Fc receptors due to their capacity to interact with immunoglobulins. All of them belong to the superfamily of CLRs unified by the structural feature of the C-type lectin domain. Nevertheless, it has at least to be noted that the IgG binding capability of DC-SIGN and FcεRII has recently been challenged (125).

TYPE I FC RECEPTORS DIFFERENTIALLY LOCALIZE WITHIN THE CELL MEMBRANE

Circulating human immune cells exhibit different FcγR expression patterns, enabling the cells to implement cell-type specific regulatory functions [reviewed in (2)]. In recent years,

many studies focused on the role of lipid rafts in modulation of FcγR activity.

FcγRIa

Several studies indicate that FcγRIa is predominantly located within lipid rafts (174–176). In myeloid cell lines, high amounts of FcγRIa are detected in detergent-resistant membrane fractions. Moreover, imaging studies of primary human monocytes show co-localization of FcγRIa with GM1 (monosialotetrahexosylganglioside) ganglioside, a marker (177) that predominantly partitions to lipid rafts. According to a study by Beekman et al., this localization is proposed to be independent of FcγRIa cross-linking (174). In accordance, a more detailed imaging study focusing on the mechanism of FcγRIa membrane localization, identifies patching of FcγRIa and the membrane-associated protein 4.1G (178, 179) in absence of ligand binding (175). Cross-linking of FcγRIa induces cytoplasmic serine phosphorylation and dissociation from 4.1G enabling FcγRIa to remain in lipid rafts. The authors propose that 4.1G plays a crucial role in targeting FcγRIa to lipid rafts in a serine phosphorylation dependent manner (175). Association of FcγRIa with lipid rafts is indeed important for FcγRIa function, e.g., in contributing to antimicrobial activity (176) or involvement in the secretion of TNF family cytokines (175). Cholesterol depletion is a common experimental method to disrupt lipid raft organization [reviewed in (40, 180)] and has been shown to alter FcγRIa arrangement in the cell membrane (174). With respect to IgG binding, cholesterol depletion results in a diminished capability of FcγRIa to recognize monomeric IgG, while interaction with IgG immune complexes is unaltered. Cross-linking induced signal transduction seems therefore not to be affected by FcγRIa relocalization to lipid rafts (174).

FcγRIIa

Activating FcγRIIa is the most studied FcγR with respect to membrane localization and its underlying mechanisms. However, consistency of the data is complicated by the use of different experimental model systems. FcγRIIa is widely expressed on innate immune cells (including neutrophils and both monocyte subsets). These cell types may also express the closely related inhibitory FcγRIIb (95, 96). This further complicates interpretation of data because of high homology of the extracellular domains. Consequently, many available monoclonal antibodies are not able to discriminate between FcγRIIa and FcγRIIb (181). Regardless of these open questions it was suggested, that FcγRIIa is dispersed in the cell membrane and is localized to lipid raft domains upon IgG-mediated cross-linking (182–184) (**Figure 3**). Of note, lipid raft localization is apparently not simply a consequence of FcγRIIa cross-linking. In fact, interaction with IgG correlates with FcγRIIa localization as both, lipid raft disruption as well as receptor mutants with abolished lipid raft re-localization show decreased IgG binding (185–187) and IgG immune complex phagocytosis (186). However, data regarding phagocytosis is controversial, since García-García et al. show a more pronounced uptake in absence of lipid raft localization (188).

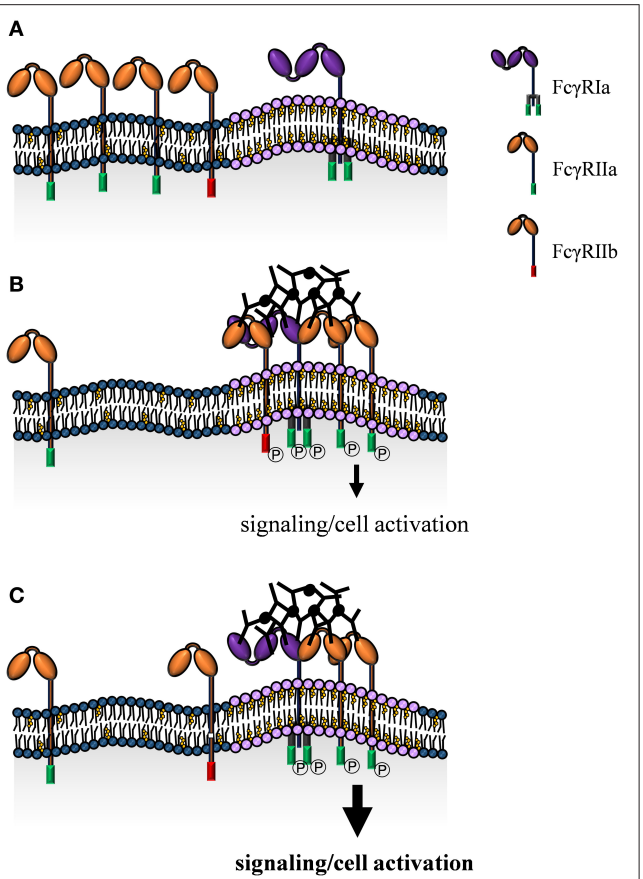

FIGURE 3 | Model of FcγR localization and receptor clustering in the cell membrane. Classical monocytes express the activating FcγRIa and FcγRIIa and the inhibitory FcγRIIb with distinct membrane localizations. FcγRIa is predominantly confined to cholesterol-rich lipid raft domains, while FcγRIIa and FcγRIIb are found in non-raft regions in absence of IgG immune complexes **(A)**. Upon IgG immune complex binding FcγRIIa/b are recruited to lipid rafts. Close proximity to each other and to signaling components concentrated at lipid raft domains, enables ITAM/ITIM phosphorylation and induction of intracellular signaling cascades **(B)**. Exclusion of FcγRIIb from lipid rafts due to a mutation in the transmembrane domain causes enhanced activatory signaling **(C)**.

Upon receptor cross-linking, intracellular signaling is triggered by phosphorylation of ITAMs and recruitment of intracellular signaling molecules. Lipid raft localization indeed seems to enhance FcγRIIa phosphorylation (184, 189, 190) and increasing sphingolipid-cholesterol-rich membrane rafts causes FcγRIIa clustering and phosphorylation even in absence of IgG (191). Furthermore, cholesterol depletion is consistent with abolished association of cross-linked FcγRIIa with low density detergent resistant membranes and abrogates FcγRIIa tyrosine phosphorylation (189). In contrast, Barabe et al. observed prominent FcγRIIa localization in non-raft domains in human primary neutrophils even upon cross-linking-induced clustering of FcγIIa. According to this study, only a small portion of FcγRIIa rearranges in rafts, where it is degraded in a short period of time. Interestingly, this can be prevented by cholesterol

depletion. Nevertheless, this neither results in diminished tyrosine phosphorylation nor calcium release, indicating that the integrity of cholesterol-rich raft domains and therefore translocation of FcγRIIa in lipid rafts seems not to be critical for FcγRIIa-mediated signal transduction (192) or cellular effector functions such as superoxide generation (183). This conclusion is in part supported by García-García et al. showing FcγRIIa-induced syk activation independent of lipid rafts. Of note, the same authors also propose NF-κB activation to be dependent on lipid rafts (188).

Mechanistically, some studies propose palmitoylation of a cytoplasmic cysteine residue to be responsible for FcγRIIa membrane localization to ordered domains (185, 187, 193). However, this was not confirmed by García-García et al., who instead suggest the transmembrane domain to be crucial for receptor localization (188). In any case, phosphorylation of the FcγRIIa ITAM seems not to be involved mechanistically in lipid raft recruitment (183, 194).

FcγRIIb

The inhibitory receptor FcγRIIb is mainly expressed on B cells and monocytes and plays a crucial role in modulating activating immune receptors and thereby immune cell activation essentially preventing autoimmune diseases. There is convincing data that lipid raft localization of FcγRIIb is initiated by ligand binding (195) and seems to be critical for receptor function. In fact, FcγRIIb with a specific mutation in the transmembrane domain (Ile232Thr) is not able to localize to lipid rafts and is associated with an increased susceptibility for autoimmune diseases due to attenuated negative regulation of immune cells (196, 197) (**Figure 3**). Mechanistically, cross-linking of the B cell receptor and FcγRIIb enhances FcγRIIb recruitment to lipid rafts (195), where B cell receptor signaling induces transphosphorylation of FcγRIIb (196). The extent of this tyrosine phosphorylation is a decisive indicator for distribution of the receptor within organized domains. Accordingly, the magnitude of inhibition of B cell receptor signaling corresponds to the level of FcγRIIb recruitment within lipid rafts (196). These findings are further supported by imaging studies of living cells using confocal as well as total internal reflection fluorescence (TIRF) microscopy in combination with fluorescence resonance energy transfer (FRET) that not only show co-localization of the B cell receptor and FcγRIIb in lipid rafts, but also destabilization of the complex and inhibition of immune synapse formation upon receptor cross-linking (198).

FcγRIIIa

Albeit FcγRIIIa is found to be expressed on NK cells and a small monocyte subpopulation, so-called non-classical monocytes, the membrane localization of FcγRIIIa has only been studied in NK cells. For this cell type, cellular fractionation as well as confocal microscopy revealed that FcγRIIIa preferentially resides in non-raft membrane regions in resting cells compared to enhanced localization in lipid rafts upon cell stimulation (199, 200). Cross-linking with IgG leads to recruitment of FcγRIIIa to lipid rafts, induction of intracellular signaling (200) and actin-dependent internalization of FcγRIIIa (201). Further supporting the importance of lipid raft association, FcγRIIIa signaling is inhibited in response to chemical disruption of organized domains even upon co-stimulation of NK cells (200). Mechanistically, FcγRIIIa redistribution to organized domains seems to be dependent on PLC activity (201). Lou et al. even suggested the presence of a positive feedback loop of receptor cross-linking, raft aggregation and signal transduction. In turn, killer cell immunoglobulin-like receptors (KIR) negatively affect formation and rearrangement of organized domains through (SHP-1 induced) dephosphorylation of signaling molecules and diminished cell polarization (202). Therefore, it was suggested that polarization and consequently FcγRIIIa relocalization to lipid rafts is indeed required to initialize FcγRIIIa signaling (200).

FcγRIIIb

Lipid-lipid interactions in highly organized raft domains contribute to the recruitment of GPI-anchored proteins (25). The only member of the FcγR family that is inserted into lipid rafts by a GPI linker is FcγRIIIb, which is exclusively expressed on the cell surface of neutrophils (203). Membrane fractionation experiments determined that FcγRIIIb indeed partitions in high density sphingolipid and cholesterol-rich membrane domains (204). Strikingly, signal transduction can be initialized by clustering of the GPI-anchored FcγRIIIb itself in absence of any characteristic signaling motifs (26) and is even enhanced upon cross-linking of FcγRIIIb with other receptors, e.g., FcγRIIa (205). The function of membrane anchored FcγRIIIb in signal transduction is however ambiguous. Besides activating intracellular signaling, FcγRIIIb is strikingly able to affect cell death (206). Recently, Yang et al. demonstrated that SHP-2 phosphorylation induced upon neutrophil activation by FcγRIIIb cross-linking results in reorganization within lipid rafts and causes a delay in activation-induced cell death (206). Thus, lipid raft association is crucial for receptor function since enhancement of FcγRIIa signaling is abrogated upon replacement of the FcγRIIIb lipid anchor with a transmembrane domain (207). On the other hand, it has been shown that cholesterol depleting reagents attenuate FcγRIIIb function resulting in upregulated activation of intracellular signaling molecules (203, 204).

MODULATION OF TYPE II FC RECEPTOR FUNCTION BY THE LIPID CELL MEMBRANE

In comparison to type I FcRs, information about the role of membrane domains on type II FcR localization and function is scarce.

Dectin-1

When it comes to pathogen recognition, signaling and the production of anti-microbial mediators such as reactive oxygen species via pattern recognition receptors, a phagocytic cell has to distinguish between soluble antigens released by pathogens in the distance and direct contact. This is particularly important when the target pattern recognition receptor can function as a

monomer as is the case for Dectin-1, which does not require oligomerization for its activity *in vitro* [reviewed in (150)]. Hence, the question arises how Dectin-1 can distinguish between single microbial products and direct pathogen contact. This issue was resolved by Goodridge et al. providing evidence for the formation of a phagocytic membrane area. In contrast to soluble Dectin-1 ligands, particulate Dectin-1 target structures are able to induce Dectin-1 clusters and initiate signaling (208). Dectin-1 cluster formation in defined membrane areas can therefore be considered paramount to initiate direct anti-microbial programs only when needed. Xu et al. provided additional evidence supporting an impact of lipid membrane domains on Dectin-1. Sorting of Dectin-1 into lipid raft domains following stimulation with β-glucans coincides with the recruitment of syk and PLCγ2, while disruption of lipid rafts impairs the uptake of zymosan particles, signaling and cytokine production of murine bone-marrow derived DCs (209). As Dectin-1 was found to associate with FcγRIIb upon IgG immune complex binding (146) and FcγRIIb is localized to lipid rafts upon ligand-induced cross-linking (195) this further points toward an important role of organized microdomains for Dectin-1 activity.

DC-SIGN

The priming of naïve T cell responses in secondary lymphoid organs requires the establishment of contact between DCs and T cells (210), a process which involves DC-SIGN (136). Once contact is established, communication takes place in a nanoscale area termed the immunological synapse (211). This microdomain concentrates molecules and ligands needed for a productive interaction and shaping of T cell immunity (211, 212). Following TCR and CD28 ligation, rafts are recruited to the contact area thereby enriching molecules responsible for signaling and contact maintenance (213). While the MHC:TCR interaction takes place in the inner zone of the formed synapse, outer zone adhesion molecules such as integrins maintain DC:T cell contact and sorting of these two molecule classes may be achieved by size exclusion of integrins to the inner zone (211, 213).

Initial studies on DC-SIGN neither assessed its localization within the cell membrane, nor the contribution of membrane domains for receptor function. In 2004, Cambi et al. first provided evidence for organization of DC-SIGN in membrane nanodomains likely to represent lipid rafts. Furthermore, these DC-SIGN assemblies were found to be important for binding and uptake of virus particles in moDCs (214). In a different study, DC-SIGN was found to form nanoscale clusters in living cells. These clusters localize to defined membrane areas and show little exchange with the surrounding membrane and are therefore assumed to be of stable nature (215). Furthermore, active movement of DC-SIGN clusters is observed with concentration at endocytosis sites (215). Therefore, the authors hypothesized that DC-SIGN is indeed organized in microdomain clusters, which move from the pathogen recognition site to the location of endocytosis (215). Finally, lipid raft localization of DC-SIGN was confirmed by co-precipitation with downstream signaling molecules upon receptor cross-linking (216).

FcεRII

The assembly of B cell receptor containing lipid rafts is a crucial component of B cell development and activity (90, 91, 217). Even though data on the localization of FcεRII within defined membrane domains are so far lacking, the importance of FcεRII expressed on B cells was recently demonstrated. During the process of affinity maturation, ligation of FcεRII by IgG induces the upregulation of FcγRIIb thereby raising the threshold for BCR signaling (173). However, if this involves coalescence of FcεRII, the BCR and FcγRIIb within lipid rafts has to be determined.

CLINICAL IMPLICATIONS OF PLASMA MEMBRANE MANIPULATION FOR FCR FUNCTION

Based on the crucial role of the plasma membrane and its organized domains for many cellular processes, drugs altering the plasma membrane lipid composition, structure or function have been developed for, e.g., malignant, metabolic, cardiovascular, or neurodegenerative disorders (218, 219). One example for such a drug, the compound azurin, has recently been shown to decrease the plasma membrane order of cancer cells upon uptake thereby attenuating cell signaling and subsequently tumor cell growth (220). In addition, plasma membrane altering functions have been described for established therapeutics such as lovastatin, a cholesterol-reducing drug applied in the treatment of hypercholesterinemia (221, 222), or non-steroidal anti-inflammatory drugs (NSAIDs) used to treat inflammatory disorders which were shown to cause membrane softening and re-organization of membrane associated proteins (223, 224). Assuming that FcγR function is indeed regulated by the plasma membrane lipid environment, it is very likely that these drugs may alter FcγR and thus IgG activity. Of note, this may not only affect immune cells but also non-immune cells which can also express FcRs [summarized in (225)]. For instance, human endothelial cells express both DC-SIGN (226, 227) and FcγRIIb (228, 229) which is involved in trafficking of maternal IgG (230) or clearance of small IgG immune complexes in liver sinusoids (231). Furthermore, FcγRs have been identified on cells of the human central nervous system including neurons and microglia, i.e., brain specific phagocytic cells. Microglia express all types of FcγR (232) which are also found to be upregulated under inflammatory conditions (233). Neurons express FcγRIa and FcγRIIb that are involved in IgG uptake and induce the release of neurotransmitters (234). Taken together, it is reasonable to speculate that a treatment with drugs affecting the plasma membrane might also affect FcR dependent effector functions of IgG on immune and non-immune cells *in vivo*. More research identifying these potential systemic drug side-effects will be required to understand this in more detail in the future.

CONCLUDING REMARKS

Lipid cell membranes are highly complex mixtures of different lipids and proteins that can interact with and influence each

other. Moreover, lateral heterogeneity of membranes including the formation of organized microdomains, i.e., lipid rafts, have previously been shown to affect a number of receptors expressed on immune cells. It is therefore reasonable to assume that distinct membrane localization is also involved in the modulation of FcR function. However, the respective experimental data is both, incomplete (e.g., with respect to FcR expression on different cell types or impact of membrane domains on FcR-IgG interactions and subsequent effector functions) and partially inconsistent. One possible explanation for the observed inconsistencies might be the use of various cell lines with possibly divergent membrane compositions in relation to primary cells. Furthermore, different experimental approaches might also affect the results and interpretation of the data. For example, cold non-ionic detergent extraction was once widely used to investigate the membrane structure of organized domains and their function [reviewed in (26, 235, 236)]. It was later, however, demonstrated that detergents diminish the lateral complexity of membranes. Therefore, detergent-resistant membrane structures seem to be artificial and not reflecting the native structure of lipid rafts in living cells [reviewed in (237)]. In recent years, membrane manipulation has gained popularity in analysis of complex membrane compositions and the significance of organized domains. The most commonly used method to manipulate cellular membranes is based on cholesterol depletion by chemical reagents. Nevertheless, targeting cholesterol with various chemicals to disrupt lipid raft organization seems to differentially affect the cell membrane necessitating cautiousness when interpreting experimental data. Furthermore, the biological effects of these chemicals have not been investigated in great detail [reviewed in (40, 180)]. In addition, present technical advances in the field of high-resolution microscopy allow analyzing the impact of native cell membranes, especially lipid rafts, on the localization of membrane receptors such as FcRs in relevant cellular contexts. One, however, must be aware that fixation of samples for microscopy might alter receptor location and plasma membrane structure (238, 239). In conclusion, future research will need to clarify the role of lipid cell membranes and organized membrane domains for type I and type II FcR function and hopefully allow implementing some of these findings for developing novel therapeutic avenues to enhance or suppress FcR dependent effector functions.

AUTHOR CONTRIBUTIONS

AL and DD drafted the manuscript. SK, LA, JL, and AL wrote the manuscript. FN and DD revised the manuscript. All authors critically reviewed the manuscript.

FUNDING

This work was supported by the Deutsche Forschungsgesellschaft (DFG) project grant RTG1962 to DD and AL. DD was further supported by IZKF-A80. AL was supported by Emerging Talent Initiative of the Friedrich-Alexander University Erlangen-Nürnberg. AL and FN are supported by the DFG-FOR 2886 TPB2. FN was further supported by DFG-TRR130-P13. DD and FN were supported by CRC1181-TPA07 and by the Friedrich-Alexander University Erlangen-Nürnberg Emerging Fields Initiative Big-Thera.

REFERENCES

1. Pincetic A, Bournazos S, DiLillo DJ, Maamary J, Wang TT, Dahan R, et al. Type I and type II Fc receptors regulate innate and adaptive immunity. *Nat Immunol.* (2014) 15:707–16. doi: 10.1038/ni.2939
2. Nimmerjahn F, Ravetch JV. Fcgamma receptors as regulators of immune responses. *Nat Rev Immunol.* (2008) 8:34–47. doi: 10.1038/nri2206
3. Ouweneel AB, Thomas MJ, Sorci-Thomas MG. The ins and outs of lipid rafts: functions in intracellular cholesterol homeostasis, microparticles, and cell membranes. *J Lipid Res.* (2020) 61:676–86. doi: 10.1194/jlr.TR119000383
4. Simons K, Sampaio JL. Membrane organization and lipid rafts. *Cold Spring Harb Perspect Biol.* (2011) 3:a004697. doi: 10.1101/cshperspect.a004697
5. Yang NJ, Hinner MJ. Getting across the cell membrane: an overview for small molecules, peptides, and proteins. *Methods Mol Biol.* (2015) 1266:29–53. doi: 10.1007/978-1-4939-2272-7_3
6. Shi Y, Cai M, Zhou L, Wang H. The structure and function of cell membranes studied by atomic force microscopy. *Semin Cell Dev Biol.* (2018) 73:31–44. doi: 10.1016/j.semcdb.2017.07.012
7. Gerle C. Essay on biomembrane structure. *J Membr Biol.* (2019) 252:115–30. doi: 10.1007/s00232-019-00061-w
8. Engelman DM. Membranes are more mosaic than fluid. *Nature.* (2005) 438:578–80. doi: 10.1038/nature04394
9. Sezgin E, Levental I, Mayor S, Eggeling C. The mystery of membrane organization: composition, regulation and roles of lipid rafts. *Nat Rev Mol Cell Biol.* (2017) 18:361–74. doi: 10.1038/nrm.2017.16
10. Fahy E, Subramaniam S, Brown HA, Glass CK, Merrill AH Jr, Murphy RC, et al. A comprehensive classification system for lipids. *J Lipid Res.* (2005) 46:839–61. doi: 10.1194/jlr.E400004-JLR200
11. Bleijerveld OB, Houweling M, Thomas MJ, Cui Z. Metabolipidomics: profiling metabolism of glycerophospholipid species by stable isotopic precursors and tandem mass spectrometry. *Anal Biochem.* (2006) 352:1–14. doi: 10.1016/j.ab.2006.02.016
12. van Meer G, Voelker DR, Feigenson GW. Membrane lipids: where they are and how they behave. *Nat Rev Mol Cell Biol.* (2008) 9:112–24. doi: 10.1038/nrm2330
13. Lorent JH, Levental KR, Ganesan L, Rivera-Longsworth G, Sezgin E, Doktorova MD, et al. The mammalian plasma membrane is defined by transmembrane asymmetries in lipid unsaturation, leaflet packing, and protein shape. *bioRxiv.* (2020) 2020:698837. doi: 10.1101/698837
14. Futerman AH, Hannun YA. The complex life of simple sphingolipids. *EMBO Res.* (2004) 5:777–82. doi: 10.1038/sj.embor.7400208
15. Bartke N, Hannun YA. Bioactive sphingolipids: metabolism and function. *J Lipid Res.* (2009) 50:S91–6. doi: 10.1194/jlr.R800080-JLR200
16. Yabu T, Shiba H, Shibasaki Y, Nakanishi T, Imamura S, Touhata K, et al. Stress-induced ceramide generation and apoptosis via the phosphorylation and activation of nSMase1 by JNK signaling. *Cell Death Differ.* (2015) 22:258–73. doi: 10.1038/cdd.2014.128
17. Chichili GR, Rodgers W. Cytoskeleton-membrane interactions in membrane raft structure. *Cell Mol Life Sci.* (2009) 66:2319–28. doi: 10.1007/s00018-009-0022-6
18. Adada M, Canals D, Hannun YA, Obeid LM. Sphingolipid regulation of ezrin, radixin, and moesin proteins family: implications for cell dynamics. *Biochim Biophys Acta.* (2014) 1841:727–37. doi: 10.1016/j.bbalip.2013.07.002
19. Maxfield FR, van Meer G. Cholesterol the central lipid of mammalian cells. *Curr Opin Cell Biol.* (2010) 22:422–9. doi: 10.1016/j.ceb.2010.05.004

20. Subczynski WK, Pasenkiewicz-Gierula M, Widomska J, Mainali L, Raguz M. High cholesterol/low cholesterol: effects in biological membranes: a review. *Cell Biochem Biophys.* (2017) 75:369–85. doi: 10.1007/s12013-017-0792-7
21. Steck TL, Lange Y. Transverse distribution of plasma membrane bilayer cholesterol: picking sides. *Traffic.* (2018) 19:750–60. doi: 10.1111/tra.12586
22. Pinkwart K, Schneider F, Lukoseviciute M, Sauka-Spengler T, Lyman E, Eggeling C, et al. Nanoscale dynamics of cholesterol in the cell membrane. *J Biol Chem.* (2019) 294:12599–609. doi: 10.1074/jbc.RA119.009683
23. Singer SJ, Nicolson GL. The fluid mosaic model of the structure of cell membranes. *Science.* (1972) 175:720–31. doi: 10.1126/science.175.4023.720
24. Harder T, Simons K. Caveolae, DIGs, and the dynamics of sphingolipid-cholesterol microdomains. *Curr Opin Cell Biol.* (1997) 9:534–42. doi: 10.1016/S0955-0674(97)80030-0
25. Simons K, Ikonen E. Functional rafts in cell membranes. *Nature.* (1997) 387:569–72. doi: 10.1038/42408
26. Brown DA, London E. Functions of lipid rafts in biological membranes. *Annu Rev Cell Dev Biol.* (1998) 14:111–36. doi: 10.1146/annurev.cellbio.14.1.111
27. Jacobson K, Mouritsen OG, Anderson RG. Lipid rafts: at a crossroad between cell biology and physics. *Nat Cell Biol.* (2007) 9:7–14. doi: 10.1038/ncb0107-7
28. Coskun U, Simons K. Membrane rafting: from apical sorting to phase segregation. *FEBS Lett.* (2010) 584:1685–93. doi: 10.1016/j.febslet.2009.12.043
29. van Meer G. Dynamic transbilayer lipid asymmetry. *Cold Spring Harb Perspect Biol.* (2011) 3:a004671. doi: 10.1101/cshperspect.a004671
30. Raghupathy R, Anilkumar AA, Polley A, Singh, Yadav M, Johnson C, et al. Transbilayer lipid interactions mediate nanoclustering of lipid-anchored proteins. *Cell.* (2015) 161:581–94. doi: 10.1016/j.cell.2015.03.048
31. Levental I, Levental KR, Heberle FA. Lipid rafts: controversies resolved, mysteries remain. *Trends Cell Biol.* (2020) 30:341–53. doi: 10.1016/j.tcb.2020.01.009
32. Mondal M, Mesmin B, Mukherjee S, Maxfield FR. Sterols are mainly in the cytoplasmic leaflet of the plasma membrane and the endocytic recycling compartment in CHO cells. *Mol Biol Cell.* (2009) 20:581–8. doi: 10.1091/mbc.e08-07-0785
33. Liu SL, Sheng R, Jung JH, Wang L, Stec E, O'Connor MJ, et al. Orthogonal lipid sensors identify transbilayer asymmetry of plasma membrane cholesterol. *Nat Chem Biol.* (2017) 13:268–74. doi: 10.1038/nchembio.2268
34. Courtney KC, Pezeshkian W, Raghupathy R, Zhang C, Darbyson A, Ipsen JH, et al. C24 sphingolipids govern the transbilayer asymmetry of cholesterol and lateral organization of model and live-cell plasma membranes. *Cell Rep.* (2018) 24:1037–49. doi: 10.1016/j.celrep.2018.06.104
35. Pike LJ. Rafts defined: a report on the keystone symposium on lipid rafts and cell function. *J Lipid Res.* (2006) 47:1597–8. doi: 10.1194/jlr.E600002-JLR200
36. Lingwood D, Simons K. Lipid rafts as a membrane-organizing principle. *Science.* (2010) 327:46–50. doi: 10.1126/science.1174621
37. Resh MD. Covalent lipid modifications of proteins. *Curr Biol.* (2013) 23:R431–5. doi: 10.1016/j.cub.2013.04.024
38. Levental I, Veatch S. The continuing mystery of lipid rafts. *J Mol Biol.* (2016) 428(Pt. A):4749–64. doi: 10.1016/j.jmb.2016.08.022
39. Kusumi A, Fujiwara TK, Tsunoyama TA, Kasai RS, Liu AA, Hirosawa KM, et al. Defining raft domains in the plasma membrane. *Traffic.* (2020) 21:106–37. doi: 10.1111/tra.12718
40. Simons K, Toomre D. Lipid rafts and signal transduction. *Nat Rev Mol Cell Biol.* (2000) 1:31–9. doi: 10.1038/35036052
41. Schuck S, Simons K. Polarized sorting in epithelial cells: raft clustering and the biogenesis of the apical membrane. *J Cell Sci.* (2004) 117(Pt. 25):5955–64. doi: 10.1242/jcs.01596
42. Sezgin E, Levental I, Grzybek M, Schwarzmann G, Mueller V, Honigmann A, et al. Partitioning, diffusion, and ligand binding of raft lipid analogs in model and cellular plasma membranes. *Biochim Biophys Acta.* (2012) 1818:1777–84. doi: 10.1016/j.bbamem.2012.03.007
43. Mollinedo F, Gajate C. Lipid rafts as signaling hubs in cancer cell survival/death and invasion: implications in tumor progression and therapy. *J Lipid Res.* (2020) 61:611–35. doi: 10.1194/jlr.TR119000439
44. Owen DM, Gaus K, Magee AI, Cebecauer M. Dynamic organization of lymphocyte plasma membrane: lessons from advanced imaging methods. *Immunology.* (2010) 131:1–8. doi: 10.1111/j.1365-2567.2010.03319.x
45. Ritter AT, Angus KL, Griffiths GM. The role of the cytoskeleton at the immunological synapse. *Immunol Rev.* (2013) 256:107–17. doi: 10.1111/imr.12117
46. Wu W, Shi X, Xu C. Regulation of T cell signalling by membrane lipids. *Nat Rev Immunol.* (2016) 16:690–701. doi: 10.1038/nri.2016.103
47. Lapidot T, Kollet O. The brain-bone-blood triad: traffic lights for stem-cell homing and mobilization. *Hematol Am Soc Hematol Educ Prog.* (2010) 2010:1–6. doi: 10.1182/asheducation-2010.1.1
48. Shirvaikar N, Marquez-Curtis LA, Janowska-Wieczorek A. Hematopoietic stem cell mobilization and homing after transplantation: the role of MMP-2, MMP-9, and MT1-MM. *Biochem Res Int.* (2012) 2012:685267. doi: 10.1155/2012/685267
49. Ratajczak MZ, Adamiak M. Membrane lipid rafts, master regulators of hematopoietic stem cell retention in bone marrow and their trafficking. *Leukemia.* (2015) 29:1452–7. doi: 10.1038/leu.2015.66
50. Greenbaum AM, Link DC. Mechanisms of G-CSF-mediated hematopoietic stem and progenitor mobilization. *Leukemia.* (2011) 25:211–7. doi: 10.1038/leu.2010.248
51. Bonig H, Papayannopoulou T. Hematopoietic stem cell mobilization: updated conceptual renditions. *Leukemia.* (2013) 27:24–31. doi: 10.1038/leu.2012.254
52. Seita J, Weissman IL. Hematopoietic stem cell: self-renewal versus differentiation. *Wiley Interdiscip Rev Syst Biol Med.* (2010) 2:640–53. doi: 10.1002/wsbm.86
53. Takehara M, Takagishi T, Seike S, Oishi K, Fujihara Y, Miyamoto K, et al. *Clostridium perfringens* alpha-toxin impairs lipid raft integrity in neutrophils. *Biol Pharm Bull.* (2016) 39:1694–700. doi: 10.1248/bpb.b16-00444
54. Karbanova J, Lorico A, Bornhauser M, Corbeil D, Fargeas CA. Prominin-1/CD133: lipid raft association, detergent resistance, and immunodetection. *Stem Cells Transl Med.* (2018) 7:155–60. doi: 10.1002/sctm.17-0223
55. Ono A. Relationships between plasma membrane microdomains and HIV-1 assembly. *Biol Cell.* (2010) 102:335–50. doi: 10.1042/BC20090165
56. Dubrovsky L, Ward A, Choi SH, Pushkarsky T, Brichacek B, Vanpouille C, et al. Inhibition of HIV replication by apolipoprotein A-I binding protein targeting the lipid rafts. *mBio.* (2020) 11:e02956-19. doi: 10.1128/mBio.00234-20
57. Staubach S, Hanisch FG. Lipid rafts: signaling and sorting platforms of cells and their roles in cancer. *Expert Rev Proteomics.* (2011) 8:263–77. doi: 10.1586/epr.11.2
58. Pinheiro TJ. The role of rafts in the fibrillization and aggregation of prions. *Chem Phys Lipids.* (2006) 141:66–71. doi: 10.1016/j.chemphyslip.2006.02.022
59. Vetrivel KS, Thinakaran G. Membrane rafts in Alzheimer's disease beta-amyloid production. *Biochim Biophys Acta.* (2010) 1801:860–7. doi: 10.1016/j.bbalip.2010.03.007
60. Cordy JM, Hooper NM, Turner AJ. The involvement of lipid rafts in Alzheimer's disease. *Mol Membr Biol.* (2006) 23:111–22. doi: 10.1080/09687860500496417
61. Khrameeva E, Kurochkin I, Bozek K, Giavalisco P, Khaitovich P. Lipidome evolution in mammalian tissues. *Mol Biol Evol.* (2018) 35:1947–57. doi: 10.1093/molbev/msy097
62. Hussain G, Wang J, Rasul A, Anwar H, Imran A, Qasim M, et al. Role of cholesterol and sphingolipids in brain development and neurological diseases. *Lipids Health Dis.* (2019) 18:26. doi: 10.1186/s12944-019-0965-z
63. Doria ML, Cotrim Z, Macedo B, Simoes C, Domingues, Helguero L, et al. Lipidomic approach to identify patterns in phospholipid profiles and define class differences in mammary epithelial and breast cancer cells. *Breast Cancer Res Treat.* (2012) 133:635–48. doi: 10.1007/s10549-011-1823-5
64. Kim HY, Lee KM, Kim SH, Kwon YJ, Chun YJ, Choi HK. Comparative metabolic and lipidomic profiling of human breast cancer cells with different metastatic potentials. *Oncotarget.* (2016) 7:67111–28. doi: 10.18632/oncotarget.11560
65. Leidl K, Liebisch G, Richter D, Schmitz G. Mass spectrometric analysis of lipid species of human circulating blood cells. *Biochim Biophys Acta.* (2008) 1781:655–64. doi: 10.1016/j.bbalip.2008.07.008
66. Ejsing CS, Sampaio JL, Surendranath V, Duchoslav E, Ekroos K, Klemm RW, et al. Global analysis of the yeast lipidome by quantitative

shotgun mass spectrometry. *Proc Natl Acad Sci USA*. (2009) 106:2136–41. doi: 10.1073/pnas.0811700106
67. Shevchenko A, Simons K. Lipidomics: coming to grips with lipid diversity. *Nat Rev Mol Cell Biol.* (2010) 11:593–8. doi: 10.1038/nrm2934
68. Salvatore G, Bernoud-Hubac N, Bissay N, Debard C, Daira, Meugnier E, et al. Human monocyte-derived dendritic cells turn into foamy dendritic cells with IL-17A. *J Lipid Res.* (2015) 56:1110–22. doi: 10.1194/jlr.M054874
69. Zhang T, de Waard AA, Wuhrer M, Spaapen RM. The role of glycosphingolipids in immune cell functions. *Front Immunol.* (2019) 10:90. doi: 10.3389/fimmu.2019.00090
70. Giebel B, Corbeil D, Beckmann J, Hohn J, Freund D, Giesen K, et al. Segregation of lipid raft markers including CD133 in polarized human hematopoietic stem and progenitor cells. *Blood.* (2004) 104:2332–8. doi: 10.1182/blood-2004-02-0511
71. Puryear WB, Gummuluru S. Role of glycosphingolipids in dendritic cell-mediated HIV-1 trans-infection. *Adv Exp Med Biol.* (2013) 762:131–53. doi: 10.1007/978-1-4614-4433-6_5
72. Delannoy C, Rombouts Y, Groux-Degroote S, Holst S, Coddeville B, Harduin-Lepers A, et al. Glycosylation changes triggered by the differentiation of monocytic THP-1 cell line into macrophages. *J Proteome Res.* (2017) 16:156–69. doi: 10.1021/acs.jproteome.6b00161
73. Mobarak E, Håversen L, Manna M, Rutberg M, Levin M, Perkins R, et al. Glucosylceramide modifies the LPS-induced inflammatory response in macrophages and the orientation of the LPS/TLR4 complex *in silico*. *Sci Rep.* (2018) 8:13600. doi: 10.1038/s41598-018-31926-0
74. Gracheva EV, Samovilova NN, Golovanova NK, Andreeva ER, Andrianova IV, Tararak EM, et al. Activation of ganglioside GM3 biosynthesis in human monocyte/macrophages during culturing *in vitro*. *Biochemistry.* (2007) 72:772–7. doi: 10.1134/S0006297907070127
75. Zuberbier T, Guhl S, Hantke T, Hantke C, Welker, Grabbe J, et al. Alterations in ganglioside expression during the differentiation of human mast cells. *Exp Dermatol.* (1999) 8:380–7. doi: 10.1111/j.1600-0625.1999.tb00386.x
76. Ren S, Kambe N, Du Z, Li Y, Xia HZ, Kambe M, et al. Disialoganglioside GD3 is selectively expressed by developing and mature human mast cells. *J Allergy Clin Immunol.* (2001) 107:322–30. doi: 10.1067/mai.2001.112272
77. Erdmann M, Wipfler D, Merling A, Cao Y, Claus C, Kniep B, et al. Differential surface expression and possible function of 9-O- and 7-O-acetylated GD3 (CD60 b and c) during activation and apoptosis of human tonsillar B and T lymphocytes. *Glycocon J.* (2006) 23:627–38. doi: 10.1007/s10719-006-9000-5
78. Wipfler D, Srinivasan GV, Sadick H, Kniep B, Arming S, Willhauck-Fleckenstein M, et al. Differentially regulated expression of 9-O-acetyl GD3 (CD60b) and 7-O-acetyl-GD3 (CD60c) during differentiation and maturation of human T and B lymphocytes. *Glycobiology.* (2011) 21:1161–72. doi: 10.1093/glycob/cwr050
79. Reivinen J, Holthofer H, Miettinen A. O-acetyl GD3 ganglioside in human peripheral blood T lymphocytes. *Int Immunol.* (1994) 6:1409–16. doi: 10.1093/intimm/6.9.1409
80. Kniep B, Claus C, Peter-Katalinic J, Monner DA, Dippold W, Nimtz M. 7-O-acetyl-GD3 in human T-lymphocytes is detected by a specific T-cell-activating monoclonal antibody. *J Biol Chem.* (1995) 270:30173–80. doi: 10.1074/jbc.270.50.30173
81. Karlsson A, Miller-Podraza H, Johansson, Karlsson KA, Dahlgren C, Teneberg S. Different glycosphingolipid composition in human neutrophil subcellular compartments. *Glycocon J.* (2001) 18:231–43. doi: 10.1023/A:1013183124004
82. Iwabuchi K, Nagaoka I. Lactosylceramide-enriched glycosphingolipid signaling domain mediates superoxide generation from human neutrophils. *Blood.* (2002) 100:1454–64. doi: 10.1182/blood.V100.4.1454.h81602001454_1454_1464
83. Sheriff A, Gaipl US, Franz S, Heyder, Voll RE, Kalden JR, et al. Loss of GM1 surface expression precedes annexin V-phycoerythrin binding of neutrophils undergoing spontaneous apoptosis during *in vitro* aging. *Cytometry A.* (2004) 62:75–80. doi: 10.1002/cyto.a.20090
84. Leitinger B, Hogg N. The involvement of lipid rafts in the regulation of integrin function. *J Cell Sci.* (2002) 115(Pt. 5):963–72.
85. Kiely JM, Hu Y, Garcia-Cardena G, Gimbrone MA Jr. Lipid raft localization of cell surface E-selectin is required for ligation-induced activation of phospholipase C gamma. *J Immunol.* (2003) 171:3216–24. doi: 10.4049/jimmunol.171.6.3216
86. Setiadi H, McEver R. Clustering endothelial E-selectin in clathrin-coated pits and lipid rafts enhances leukocyte adhesion under flow. *Blood.* (2008) 111:1989–98. doi: 10.1182/blood-2007-09-113423
87. Oh H, Mohler ER III, Tian A, Baumgart T, Diamond SL. Membrane cholesterol is a biomechanical regulator of neutrophil adhesion. *Arterioscler Thromb Vasc Biol.* (2009) 29:1290–7. doi: 10.1161/ATVBAHA.109.189571
88. Koberlin MS, Heinz LX, Superti-Furga G. Functional crosstalk between membrane lipids and TLR biology. *Curr Opin Cell Biol.* (2016) 39:28–36. doi: 10.1016/j.ceb.2016.01.010
89. Varshney P, Yadav V, Saini N. Lipid rafts in immune signalling: current progress and future perspective. *Immunology.* (2016) 149:13–24. doi: 10.1111/imm.12617
90. Cheng C, Dykstra ML, Mitchell RN, Pierce SK. A role for lipid rafts in B cell antigen receptor signaling and antigen targeting. *J Exp Med.* (1999) 190:1549–60. doi: 10.1084/jem.190.11.1549
91. Gupta N, DeFranco AL. Visualizing lipid raft dynamics and early signaling events during antigen receptor-mediated B-lymphocyte activation. *Mol Biol Cell.* (2003) 14:432–44. doi: 10.1091/mbc.02-05-0078
92. Gold MR, Reth MG. Antigen receptor function in the context of the nanoscale organization of the B cell membrane. *Annu Rev Immunol.* (2019) 37:97–123. doi: 10.1146/annurev-immunol-042718-041704
93. Mitchell JS, Kanca O, McIntyre BW. Lipid microdomain clustering induces a redistribution of antigen recognition and adhesion molecules on human T lymphocytes. *J Immunol.* (2002) 168:2737–44. doi: 10.4049/jimmunol.168.6.2737
94. Simons K, Gerl MJ. Revitalizing membrane rafts: new tools and insights. *Nat Rev Mol Cell Biol.* (2010) 11:688–99. doi: 10.1038/nrm2977
95. Hogarth M, Anania JC, Wines BD. The FcgammaR of humans and non-human primates and their interaction with IgG: implications for induction of inflammation, resistance to infection and the use of therapeutic monoclonal antibodies. *Curr Top Microbiol Immunol.* (2014) 382:321–52. doi: 10.1007/978-3-319-07911-0_15
96. Kerntke C NF, Biburger M. There is (Scientific) strength in numbers: a comprehensive quantification of Fc gamma receptor numbers on human and murine peripheral bloot leukocytes. *Front Immunol.* (2020) 11:118. doi: 10.3389/fimmu.2020.00118
97. Fanger NA, Wardwell K, Shen L, Tedder TF, Guyre M. Type I (CD64) and type II (CD32) Fc gamma receptor-mediated phagocytosis by human blood dendritic cells. *J Immunol.* (1996) 157:541–8.
98. Guilliams M, Bruhns, Saeys Y, Hammad H, Lambrecht BN. The function of Fcgamma receptors in dendritic cells and macrophages. *Nat Rev Immunol.* (2014) 14:94–108. doi: 10.1038/nri3582
99. Piccioli D, Tavarini S, Borgogni E, Steri V, Nuti S, Sammicheli C, et al. Functional specialization of human circulating CD16 and CD1c myeloid dendritic-cell subsets. *Blood.* (2007) 109:5371–9. doi: 10.1182/blood-2006-08-038422
100. Collin M, Bigley V. Human dendritic cell subsets: an update. *Immunology.* (2018) 154:3–20. doi: 10.1111/imm.12888
101. Nimmerjahn F. Keeping T-he killers at Bay via Fcgammariib. *Immunity.* (2020) 52:9–11. doi: 10.1016/j.immuni.2019.12.012
102. Kurosaki T, Ravetch JV. A single amino acid in the glycosyl phosphatidylinositol attachment domain determines the membrane topology of Fc gamma RIII. *Nature.* (1989) 342:805–7. doi: 10.1038/342805a0
103. Wirthmueller U, Kurosaki T, Murakami MS, Ravetch JV. Signal transduction by Fc gamma RIII (CD16) is mediated through the gamma chain. *J Exp Med.* (1992) 175:1381–90. doi: 10.1084/jem.175.5.1381
104. Miller KL, Duchemin AM, Anderson CL. A novel role for the Fc receptor gamma subunit: enhancement of Fc gamma R ligand affinity. *J Exp Med.* (1996) 183:2227–33. doi: 10.1084/jem.183.5.2227
105. Brandsma AM, Hogarth M, Nimmerjahn F, Leusen JH. Clarifying the confusion between cytokine and Fc receptor "Common Gamma Chain". *Immunity.* (2016) 45:225–6. doi: 10.1016/j.immuni.2016.07.006
106. Perez-Montfort R, Kinet J, Metzger H. A previously unrecognized subunit of the receptor for immunoglobulin E. *Biochemistry.* (1983) 22:5722–8. doi: 10.1021/bi00294a007

107. Blazquez-Moreno A, Park S, Im W, Call MJ, Call ME, Reyburn HT. Transmembrane features governing Fc receptor CD16A assembly with CD16A signaling adaptor molecules. *Proc Natl Acad Sci USA*. (2017) 114:E5645–54. doi: 10.1073/pnas.1706483114
108. Bruhns, PB, Iannascoli B, England, Mancardi DA, Fernandez N, Jorieux S, et al. Specificity and affinity of human Fcgamma receptors and their polymorphic variants for human IgG subclasses. *Blood*. (2009) 113:3716–25. doi: 10.1182/blood-2008-09-179754
109. Lux A, Yu X, Scanlan CN, Nimmerjahn F. Impact of immune complex size and glycosylation on IgG binding to human FcgammaRs. *J Immunol*. (2013) 190:4315–23. doi: 10.4049/jimmunol.1200501
110. Nesspor TC, Raju TS, Chin CN, Vafa O, Brezski RJ. Avidity confers FcgammaR binding and immune effector function to aglycosylated immunoglobulin G1. *J Mol Recognit*. (2011) 25:147–54. doi: 10.1002/jmr.2155
111. Hundt M, Schmidt RE. The glycosylphosphatidylinositol-linked Fc gamma receptor III represents the dominant receptor structure for immune complex activation of neutrophils. *Eur J Immunol*. (1992) 22:811–6. doi: 10.1002/eji.1830220327
112. Selvaraj P, Fifadara N, Nagarajan S, Cimino A, Wang G. Functional regulation of human neutrophil Fc gamma receptors. *Immunol Res*. (2004) 29:219–30. doi: 10.1385/IR:29:1-3:219
113. Chuang FY, Sassaroli M, Unkeless JC. Convergence of Fc gamma receptor IIA and Fc gamma receptor IIIB signaling pathways in human neutrophils. *J Immunol*. (2000) 164:350–60. doi: 10.4049/jimmunol.164.1.350
114. Nimmerjahn F. Activating and inhibitory FcgammaRs in autoimmune disorders. *Semin Immunopathol*. (2006) 28:305–19. doi: 10.1007/s00281-006-0052-1
115. Sondermann P, Huber R, Oosthuizen V, Jacob U. The 3.2-A crystal structure of the human IgG1 Fc fragment-Fc gammaRIII complex. *Nature*. (2000) 406:267–73. doi: 10.1038/35018508
116. Zelensky AN, Gready JE. The C-type lectin-like domain superfamily. *FEBS J*. (2005) 272:6179–217. doi: 10.1111/j.1742-4658.2005.05031.x
117. Drickamer K. Demonstration of carbohydrate-recognition activity in diverse proteins which share a common primary structure motif. *Biochem Soc Trans*. (1989) 17:13–5. doi: 10.1042/bst0170013
118. Lehmann CH, Heger L, Heidkamp GF, Baranska A, Luhr JJ, Hoffmann A, et al. Direct delivery of antigens to dendritic cells via antibodies specific for endocytic receptors as a promising strategy for future therapies. *Vaccines*. (2016) 4:8. doi: 10.3390/vaccines4020008
119. Brown GD, Willment JA, Whitehead L. C-type lectins in immunity and homeostasis. *Nat Rev Immunol*. (2018) 18:374–89. doi: 10.1038/s41577-018-0004-8
120. Sancho D, Reis e Sousa C. Signaling by myeloid C-type lectin receptors in immunity and homeostasis. *Annu Rev Immunol*. (2012) 30:491–529. doi: 10.1146/annurev-immunol-031210-101352
121. Figdor CG, van Kooyk Y, Adema GJ. C-type lectin receptors on dendritic cells and Langerhans cells. *Nat Rev Immunol*. (2002) 2:77–84. doi: 10.1038/nri723
122. Osorio F, Reis e Sousa C. Myeloid C-type lectin receptors in pathogen recognition and host defense. *Immunity*. (2011) 34:651–64. doi: 10.1016/j.immuni.2011.05.001
123. Manabe Y, Marchetti R, Takakura Y, Nagasaki M, Nihei W, Takebe T, et al. The core fucose on an IgG antibody is an endogenous ligand of dectin-1. *Angew Chem Int Ed Engl*. (2019) 58:18697–702. doi: 10.1002/anie.201911875
124. Yu X, Vasiljevic S, Mitchell DA, Crispin M, Scanlan CN. Dissecting the molecular mechanism of IVIg therapy: the interaction between serum IgG and DC-SIGN is independent of antibody glycoform or Fc domain. *J Mol Biol*. (2013) 425:1253–8. doi: 10.1016/j.jmb.2013.02.006
125. Temming AR, Dekkers G, van de Bovenkamp FS, Plomp HR, Bentlage AEH, Szittner Z, et al. Human DC-SIGN and CD23 do not interact with human IgG. *Sci Res*. (2019) 9:9995. doi: 10.1038/s41598-019-46484-2
126. Curtis BM, Scharnowske S, Watson AJ. Sequence and expression of a membrane-associated C-type lectin that exhibits CD4-independent binding of human immunodeficiency virus envelope glycoprotein gp120. *Proc Natl Acad Sci USA*. (1992) 89:8356–60. doi: 10.1073/pnas.89.17.8356
127. Engering A, Geijtenbeek TB, van Vliet SJ, Wijers M, van Liempt E, Demaurex N, et al. The dendritic cell-specific adhesion receptor DC-SIGN internalizes antigen for presentation to T cells. *J Immunol*. (2002) 168:2118–26. doi: 10.4049/jimmunol.168.5.2118
128. Geijtenbeek TB, Krooshoop DJ, Bleijs DA, van Vliet SJ, van Duijnhoven GC, Grabovsky V, et al. DC-SIGN-ICAM-2 interaction mediates dendritic cell trafficking. *Nat Immunol*. (2000) 1:353–7. doi: 10.1038/79815
129. Tailleux L, Pham-Thi N, Bergeron-Lafaurie A, Herrmann JL, Charles, Schwartz O, et al. DC-SIGN induction in alveolar macrophages defines privileged target host cells for mycobacteria in patients with tuberculosis. *PLoS Med*. (2005) 2:e381. doi: 10.1371/journal.pmed.0020381
130. Watchmaker B, Lahl K, Lee M, Baumjohann D, Morton J, Kim SJ, et al. Comparative transcriptional and functional profiling defines conserved programs of intestinal DC differentiation in humans and mice. *Nat Immunol*. (2014) 15:98–108. doi: 10.1038/ni.2768
131. Geijtenbeek TB, Kwon DS, Torensma R, van Vliet SJ, van Duijnhoven GC, Middel J, et al. DC-SIGN, a dendritic cell-specific HIV-1-binding protein that enhances trans-infection of T cells. *Cell*. (2000) 100:587–97. doi: 10.1016/S0092-8674(00)80694-7
132. Kwon DS, Gregorio G, Bitton N, Hendrickson WA, Littman DR. DC-SIGN-mediated internalization of HIV is required for trans-enhancement of T cell infection. *Immunity*. (2002) 16:135–44. doi: 10.1016/S1074-7613(02)00259-5
133. Gringhuis SI, den Dunnen J, Litjens M, van der Vlist M, Wevers B, Bruijns SC, et al. Dectin-1 directs T helper cell differentiation by controlling noncanonical NF-kappaB activation through Raf-1 and Syk. *Nat Immunol*. (2009) 10:203–13. doi: 10.1038/ni.1692
134. Gringhuis SI, den Dunnen J, Litjens M, van Het Hof B, van Kooyk Y, Geijtenbeek TB. C-type lectin DC-SIGN modulates Toll-like receptor signaling via Raf-1 kinase-dependent acetylation of transcription factor NF-kappaB. *Immunity*. (2007) 26:605–16. doi: 10.1016/j.immuni.2007.03.012
135. Hovius JW, de Jong MA, den Dunnen J, Litjens M, Fikrig E, van der Poll T, et al. Salp15 binding to DC-SIGN inhibits cytokine expression by impairing both nucleosome remodeling and mRNA stabilization. *PLoS Pathog*. (2008) 4:e31. doi: 10.1371/journal.ppat.0040031
136. Geijtenbeek TB, Torensma R, van Vliet SJ, van Duijnhoven GC, Adema GJ, van Kooyk Y, et al. Identification of DC-SIGN, a novel dendritic cell-specific ICAM-3 receptor that supports primary immune responses. *Cell*. (2000) 100:575–85. doi: 10.1016/S0092-8674(00)80693-5
137. Schwab I, Nimmerjahn F. Intravenous immunoglobulin therapy: how does IgG modulate the immune system? *Nat Rev Immunol*. (2013) 13:176–89. doi: 10.1038/nri3401
138. Anthony RM, Wermeling F, Karlsson MC, Ravetch JV. Identification of a receptor required for the anti-inflammatory activity of IVIG. *Proc Natl Acad Sci USA*. (2008) 105:19571–8. doi: 10.1073/pnas.0810163105
139. Anthony RM, Kobayashi T, Wermeling F, Ravetch JV. Intravenous gammaglobulin suppresses inflammation through a novel T(H)2 pathway. *Nature*. (2011) 475:110–3. doi: 10.1038/nature10134
140. Kaneko Y, Nimmerjahn F, Ravetch JV. Anti-inflammatory activity of immunoglobulin G resulting from Fc sialylation. *Science*. (2006) 313:670–3. doi: 10.1126/science.1129594
141. Schwab I, Lux A, Nimmerjahn F. Reply to - IVIG pluripotency and the concept of Fc-sialylation: challenges to the scientist. *Nat Rev Immunol*. (2014) 14:349. doi: 10.1038/nri3401-c2
142. Willment JA, Marshall AS, Reid DM, Williams DL, Wong SY, Gordon S, et al. The human beta-glucan receptor is widely expressed and functionally equivalent to murine Dectin-1 on primary cells. *Eur J Immunol*. (2005) 35:1539–47. doi: 10.1002/eji.200425725
143. Olynych TJ, Jakeman DL, Marshall JS. Fungal zymosan induces leukotriene production by human mast cells through a dectin-1-dependent mechanism. *J Allergy Clin Immunol*. (2006) 118:837–43. doi: 10.1016/j.jaci.2006.06.008
144. Brown GD, Gordon S. Immune recognition. a new receptor for beta-glucans. *Nature*. (2001) 413:36–7. doi: 10.1038/35092620
145. Bode K, Bujupi F, Link C, Hein T, Zimmermann S, Peiris D, et al. Dectin-1 binding to annexins on apoptotic cells induces peripheral immune tolerance via NADPH oxidase-2. *Cell Res*. (2019) 29:4435–46.e9. doi: 10.1016/j.celrep.2019.11.086
146. Karsten CM, Pandey MK, Figge J, Kilchenstein R, Taylor R, Rosas M, et al. Anti-inflammatory activity of IgG1 mediated by Fc galactosylation and association of FcgammaRIIB and dectin-1. *Nat Med*. (2012) 18:1401–6. doi: 10.1038/nm.2862

147. Park HY, Yoon HK, Kim JY, Park SK. Heat-killed *Saccharomyces cerevisiae*, a dectin-1 agonist, selectively induces IgG4 production by human B cells. *Immune Netw.* (2018) 18:e46. doi: 10.4110/in.2018.18.e46
148. Taylor R, Brown GD, Reid DM, Willment JA, Martinez-Pomares L, Gordon S, et al. The beta-glucan receptor, dectin-1, is predominantly expressed on the surface of cells of the monocyte/macrophage and neutrophil lineages. *J Immunol.* (2002) 169:3876–82. doi: 10.4049/jimmunol.169.7.3876
149. Yokota K, Takashima A, Bergstresser R, Ariizumi K. Identification of a human homologue of the dendritic cell-associated C-type lectin-1, dectin-1. *Gene.* (2001) 272:51–60. doi: 10.1016/S0378-1119(01)00528-5
150. Brown GD. Dectin-1: a signalling non-TLR pattern-recognition receptor. *Nat Rev Immunol.* (2006) 6:33–43. doi: 10.1038/nri1745
151. Hermanz-Falcon, Arce I, Roda-Navarro, Fernandez-Ruiz E. Cloning of human DECTIN-1, a novel C-type lectin-like receptor gene expressed on dendritic cells. *Immunogenetics.* (2001) 53:288–95. doi: 10.1007/s002510100326
152. Willment JA, Gordon S, Brown GD. Characterization of the human beta -glucan receptor and its alternatively spliced isoforms. *J Biol Chem.* (2001) 276:43818–23. doi: 10.1074/jbc.M107715200
153. Rosas M, Liddiard K, Kimberg M, Faro-Trindade I, McDonald JU, Williams DL, et al. The induction of inflammation by dectin-1 *in vivo* is dependent on myeloid cell programming and the progression of phagocytosis. *J Immunol.* (2008) 181:3549–57. doi: 10.4049/jimmunol.181.5.3549
154. Hernanz-Falcon P, Joffre O, Williams DL, Reis e Sousa C. Internalization of Dectin-1 terminates induction of inflammatory responses. *Eur J Immunol.* (2009) 39:507–13. doi: 10.1002/eji.200838687
155. Goodridge HS, Shimada T, Wolf AJ, Hsu YM, Becker CA, Lin X, et al. Differential use of CARD9 by dectin-1 in macrophages and dendritic cells. *J Immunol.* (2009) 182:1146–54. doi: 10.4049/jimmunol.182.2.1146
156. Acharya M, Borland G, Edkins AL, Maclellan LM, Matheson J, Ozanne BW, et al. CD23/FcepsilonRII: molecular multi-tasking. *Clin Exp Immunol.* (2010) 162:12–23. doi: 10.1111/j.1365-2249.2010.04210.x
157. Bettler B, Maier R, Ruegg D, Hofstetter H. Binding site for IgE of the human lymphocyte low-affinity Fc epsilon receptor (Fc epsilon RII/CD23) is confined to the domain homologous with animal lectins. *Proc Natl Acad Sci USA.* (1989) 86:7118–22. doi: 10.1073/pnas.86.18.7118
158. Bajorath J, Aruffo A. Structure-based modeling of the ligand binding domain of the human cell surface receptor CD23 and comparison of two independently derived molecular models. *Protein Sci.* (1996) 5:240–7. doi: 10.1002/pro.5560050207
159. Bournazos S, Ravetch JV. Fcgamma receptor function and the design of vaccination strategies. *Immunity.* (2017) 47:224–33. doi: 10.1016/j.immuni.2017.07.009
160. Armitage RJ, Goff LK, Beverley C. Expression and functional role of CD23 on T cells. *Eur J Immunol.* (1989) 19:31–5. doi: 10.1002/eji.1830190106
161. Vella A, Bellavite, Adami A, Ortolani R, Benoni G, Carletto A, et al. Expression of FcepsilonII/CD23 on human neutrophils isolated from rheumatoid arthritis patients. *Inflammation.* (1999) 23:471–9. doi: 10.1023/A:1021969127489
162. Capron M, Truong MJ, Aldebert D, Gruart V, Suemura M, Delespesse G, et al. Eosinophil IgE receptor and CD23. *Immunol Res.* (1992) 11:252–9. doi: 10.1007/BF02919131
163. Vercelli D, Jabara HH, Lee BW, Woodland N, Geha RS, Leung DY. Human recombinant interleukin 4 induces Fc epsilon R2/CD23 on normal human monocytes. *J Exp Med.* (1988) 167:1406–16. doi: 10.1084/jem.167.4.1406
164. Delespesse G, Sarfati M, Hofstetter H, Suter U, Nakajima T, Peleman R, et al. Structure, function and clinical relevance of the low affinity receptor for IgE. *Immunol Invest*. (1988) 17:363–87. doi: 10.3109/08820138809049845
165. Yamaoka KA, Arock M, Issaly F, Dugas N, Le Goff L, Kolb J. Granulocyte macrophage colony stimulating factor induces Fc epsilon RII/CD23 expression on normal human polymorphonuclear neutrophils. *Int Immunol.* (1996) 8:479–90. doi: 10.1093/intimm/8.4.479
166. Kraft S, Kinet J. New developments in FcepsilonRI regulation, function and inhibition. *Nat Rev Immunol.* (2007) 7:365–78. doi: 10.1038/nri2072
167. Kilmon MA, Shelburne AE, Chan-Li Y, Holmes KL, Conrad DH. CD23 trimers are preassociated on the cell surface even in the absence of its ligand, IgE. *J Immunol.* (2004) 172:1065–73. doi: 10.4049/jimmunol.172.2.1065
168. Lemieux GA, Blumenkron F, Yeung N, Zhou, Williams J, Grammer AC, et al. The low affinity IgE receptor (CD23) is cleaved by the metalloproteinase ADAM10. *J Biol Chem.* (2007) 282:14836–44. doi: 10.1074/jbc.M608414200
169. Cairns JA, Gordon J. Intact, 45-kDa (membrane) form of CD23 is consistently mitogenic for normal and transformed B lymphoblasts. *Eur J Immunol.* (1990) 20:539–43. doi: 10.1002/eji.1830200312
170. Gordon J, Rowe M, Walker L, Guy G. Ligation of the CD23, p45 (BLAST-2,EBVCS) antigen triggers the cell-cycle progression of activated B lymphocytes. *Eur J Immunol.* (1986) 16:1075–80. doi: 10.1002/eji.1830160908
171. Liu YJ, Mason DY, Johnson GD, Abbot S, Gregory CD, Hardie DL, et al. Germinal center cells express bcl-2 protein after activation by signals which prevent their entry into apoptosis. *Eur J Immunol.* (1991) 21:1905–10. doi: 10.1002/eji.1830210819
172. Rezzonico R, Chicheportiche R, Imbert V, Dayer JM. Engagement of CD11b and CD11c β2 integrin by antibodies or soluble CD23 induces IL-1β production on primary human monocytes through mitogen-activated protein kinase–dependent pathways. *Blood.* (2000) 95:3868–77. doi: 10.1182/blood.V95.12.3868.012k43_3868_3877
173. Wang TT, Maamary J, Tan GS, Bournazos S, Davis CW, Krammer F, et al. Anti-HA glycoforms drive b cell affinity selection and determine influenza vaccine efficacy. *Cell.* (2015) 162:160–9. doi: 10.1016/j.cell.2015.06.026
174. Beekman JM, van der Linden JA, van de Winkel JG, Leusen JH. FcgammaRI (CD64) resides constitutively in lipid rafts. *Immunol Lett.* (2008) 116:149–55. doi: 10.1016/j.imlet.2007.12.003
175. Gibson AW, Li X, Wu J, Baskin JG, Raman C, Edberg JC, et al. Serine phosphorylation of FcgammaRI cytoplasmic domain directs lipid raft localization and interaction with protein 4.1G. *J Leukoc Biol.* (2012) 91:97–103. doi: 10.1189/jlb.0711368
176. Serezani CH, Aronoff DM, Sitrin RG, Peters-Golden M. FcgammaRI ligation leads to a complex with BLT1 in lipid rafts that enhances rat lung macrophage antimicrobial functions. *Blood.* (2009) 114:3316–24. doi: 10.1182/blood-2009-01-199919
177. Day CA, Kenworthy AK. Functions of cholera toxin B-subunit as a raft cross-linker. *Essays Biochem.* (2015) 57:135–45. doi: 10.1042/bse0570135
178. Chen L, Wang T, Wang Y, Zhang J, Qi Y, Weng H, et al. Protein 4.1G regulates cell adhesion, spreading, and migration of mouse embryonic fibroblasts through the beta1 integrin pathway. *J Biol Chem.* (2016) 291:2170–80. doi: 10.1074/jbc.M115.658591
179. Parra M, Gascard, Walensky LD, Snyder SH, Mohandas N, Conboy JG. Cloning and characterization of 4.1G (EPB41L2), a new member of the skeletal protein 4.1 (EPB41) gene family. *Genomics.* (1998) 49:298–306. doi: 10.1006/geno.1998.5265
180. Bieberich E. Sphingolipids and lipid rafts: Novel concepts and methods of analysis. *Chem Phys Lipids.* (2018) 216:114–31. doi: 10.1016/j.chemphyslip.2018.08.003
181. Veri MC, Gorlatov S, Li H, Burke S, Johnson S, Stavenhagen J, et al. Monoclonal antibodies capable of discriminating the human inhibitory Fcgamma-receptor IIB (CD32B) from the activating Fcgamma-receptor IIA (CD32A): biochemical, biological and functional characterization. *Immunology.* (2007) 121:392–404. doi: 10.1111/j.1365-2567.2007.02588.x
182. Strzelecka-Kiliszek A, Korzeniowski M, Kwiatkowska K, Mrozinska K, Sobota A. Activated FcgammaRII and signalling molecules revealed in rafts by ultra-structural observations of plasma-membrane sheets. *Mol Membr Biol.* (2004) 21:101–8. doi: 10.1080/09687680310001639094
183. Katsumata O, Hara-Yokoyama M, Sautes-Fridman C, Nagatsuka Y, Katada T, Hirabayashi Y, et al. Association of FcgammaRII with low-density detergent-resistant membranes is important for cross-linking-dependent initiation of the tyrosine phosphorylation pathway and superoxide generation. *J Immunol.* (2001) 167:5814–23. doi: 10.4049/jimmunol.167.10.5814
184. Kwiatkowska K, Frey J, Sobota A. Phosphorylation of FcgammaRIIA is required for the receptor-induced actin rearrangement and capping: the role of membrane rafts. *J Cell Sci.* (2003) 116(Pt. 3):537–50. doi: 10.1242/jcs.00254
185. Bournazos S, Hart S, Chamberlain LH, Glennie MJ, Dransfield I. Association of FcgammaRIIa (CD32a) with lipid rafts regulates ligand binding activity. *J Immunol.* (2009) 182:8026–36. doi: 10.4049/jimmunol.0900107

186. Vieth JA, Kim MK, Pan XQ, Schreiber AD, Worth RG. Differential requirement of lipid rafts for FcgammaRIIA mediated effector activities. *Cell Immunol.* (2010) 265:111–9. doi: 10.1016/j.cellimm.2010.07.011
187. Vieth JA, Kim MK, Glaser D, Stiles K, Schreiber AD, Worth RG. FcgammaRIIa requires lipid rafts, but not co-localization into rafts, for effector function. *Inflamm Res.* (2013) 62:37–43. doi: 10.1007/s00011-012-0548-1
188. Garcia-Garcia E, Brown EJ, Rosales C. Transmembrane mutations to FcgammaRIIA alter its association with lipid rafts: implications for receptor signaling. *J Immunol.* (2007) 178:3048–58. doi: 10.4049/jimmunol.178.5.3048
189. Kwiatkowska K, Sobota A. The clustered Fcgamma receptor II is recruited to Lyn-containing membrane domains and undergoes phosphorylation in a cholesterol-dependent manner. *Eur J Immunol.* (2001) 31:989–98. doi: 10.1002/1521-4141(200104)31:4<989::AID-IMMU989>3.0.CO;2-V
190. Abdel Shakor AB, Kwiatkowska K, Sobota A. Cell surface ceramide generation precedes and controls FcgammaRII clustering and phosphorylation in rafts. *J Biol Chem.* (2004) 279:36778–87. doi: 10.1074/jbc.M402170200
191. Kulma M, Kwiatkowska K, Sobota A. Raft coalescence and FcgammaRIIA activation upon sphingomyelin clustering induced by lysenin. *Cell Signal.* (2012) 24:1641–7. doi: 10.1016/j.cellsig.2012.04.007
192. Barabe F, Rollet-Labelle E, Gilbert C, Fernandes MJ, Naccache SN, Naccache H. Early events in the activation of Fc gamma RIIA in human neutrophils: stimulated insolubilization, translocation to detergent-resistant domains, degradation of Fc gamma RIIA. *J Immunol.* (2002) 168:4042–9. doi: 10.4049/jimmunol.168.8.4042
193. Barnes NC, Powell MS, Trist HM, Gavin AL, Wines BD, Hogarth M. Raft localisation of FcgammaRIIa and efficient signaling are dependent on palmitoylation of cysteine 208. *Immunol Lett.* (2006) 104:118–23. doi: 10.1016/j.imlet.2005.11.007
194. Mansfield J, Hinkovska-Galcheva V, Borofsky MS, Shayman JA, Boxer LA. Phagocytic signaling molecules in lipid rafts of COS-1 cells transfected with FcgammaRIIA. *Biochem Biophys Res Commun.* (2005) 331:132–8. doi: 10.1016/j.bbrc.2005.02.191
195. Aman MJ, Tosello-Trampont AC, Ravichandran K. Fc gamma RIIB1/SHIP-mediated inhibitory signaling in B cells involves lipid rafts. *J Biol Chem.* (2001) 276:46371–8. doi: 10.1074/jbc.M104069200
196. Kono H, Kyogoku C, Suzuki T, Tsuchiya N, Honda H, Yamamoto K, et al. FcgammaRIIB Ile232Thr transmembrane polymorphism associated with human systemic lupus erythematosus decreases affinity to lipid rafts and attenuates inhibitory effects on B cell receptor signaling. *Hum Mol Genet.* (2005) 14:2881–92. doi: 10.1093/hmg/ddi320
197. Floto RA, Clatworthy MR, Heilbronn KR, Rosner DR, MacAry A, Rankin A, et al. Loss of function of a lupus-associated FcgammaRIIb polymorphism through exclusion from lipid rafts. *Nat Med.* (2005) 11:1056–8. doi: 10.1038/nm1288
198. Sohn HW, Pierce SK, Tzeng SJ. Live cell imaging reveals that the inhibitory FcgammaRIIB destabilizes B cell receptor membrane-lipid interactions and blocks immune synapse formation. *J Immunol.* (2008) 180:793–9. doi: 10.4049/jimmunol.180.2.793
199. Galandrini R, Tassi I, Mattia G, Lenti L, Piccoli M, Frati L, et al. SH2-containing inositol phosphatase (SHIP-1) transiently translocates to raft domains and modulates CD16-mediated cytotoxicity in human NK cells. *Blood.* (2002) 100:4581–9. doi: 10.1182/blood-2002-04-1058
200. Kondadasula SV, Roda JM, Parihar R, Yu J, Lehman A, Caligiuri MA, et al. Colocalization of the IL-12 receptor and FcgammaRIIIa to natural killer cell lipid rafts leads to activation of ERK and enhanced production of interferon-gamma. *Blood.* (2008) 111:4173–83. doi: 10.1182/blood-2007-01-06 8908
201. Cecchetti S, Spadaro F, Lugini L, Podo F, Ramoni C. Functional role of phosphatidylcholine-specific phospholipase C in regulating CD16 membrane expression in natural killer cells. *Eur J Immunol.* (2007) 37:2912–22. doi: 10.1002/eji.200737266
202. Lou Z, Jevremovic D, Billadeau DD, Leibson J. A balance between positive and negative signals in cytotoxic lymphocytes regulates the polarization of lipid rafts during the development of cell-mediated killing. *J Exp Med.* (2000) 191:347–54. doi: 10.1084/jem.191.2.347
203. David A, Fridlich R, Aviram I. The presence of membrane Proteinase 3 in neutrophil lipid rafts and its colocalization with FcgammaRIIIb and cytochrome b558. *Exp Cell Res.* (2005) 308:156–65. doi: 10.1016/j.yexcr.2005.03.034
204. Fernandes MJ, Rollet-Labelle E, Pare G, Marois S, Tremblay ML, Teillaud JL, et al. CD16b associates with high-density, detergent-resistant membranes in human neutrophils. *Biochem J.* (2006) 393(Pt. 1):351–9. doi: 10.1042/BJ20050129
205. Edberg JC, Kimberly R. Modulation of Fc gamma complement receptor function by the glycosyl-phosphatidylinositol-anchored form of Fc gamma RIII. *J Immunol.* (1994) 152:5826–35.
206. Yang H, Jiang H, Song Y, Chen DJ, Shen XJ, Chen JH. Neutrophil CD16b crosslinking induces lipid raft-mediated activation of SHP-2 and affects cytokine expression and retarded neutrophil apoptosis. *Exp Cell Res.* (2018) 362:121–31. doi: 10.1016/j.yexcr.2017.11.009
207. Green JM, Schreiber AD, Brown EJ. Role for a glycan phosphoinositol anchor in Fc gamma receptor synergy. *J Cell Biol.* (1997) 139:1209–17. doi: 10.1083/jcb.139.5.1209
208. Goodridge HS, Reyes CN, Becker CA, Katsumoto TR, Ma J, Wolf AJ, et al. Activation of the innate immune receptor Dectin-1 upon formation of a 'phagocytic synapse'. *Nature.* (2011) 472:471–5. doi: 10.1038/nature10071
209. Xu S, Huo J, Gunawan M, Su IH, Lam K. Activated dectin-1 localizes to lipid raft microdomains for signaling and activation of phagocytosis and cytokine production in dendritic cells. *J Biol Chem.* (2009) 284:22005–11. doi: 10.1074/jbc.M109.009076
210. Mempel TR, Henrickson SE, Von Andrian UH. T-cell priming by dendritic cells in lymph nodes occurs in three distinct phases. *Nature.* (2004) 427:154–9. doi: 10.1038/nature02238
211. Grakoui A, Bromley SK, Sumen C, Davis MM, Shaw AS, Allen M, et al. The immunological synapse: a molecular machine controlling T cell activation. *Science.* (1999) 285:221–7. doi: 10.1126/science.285.5425.221
212. Shaw AS, Dustin ML. Making the T cell receptor go the distance: a topological view of T cell activation. *Immunity.* (1997) 6:361–9. doi: 10.1016/S1074-7613(00)80279-4
213. Viola A, Schroeder S, Sakakibara Y, Lanzavecchia A. T lymphocyte costimulation mediated by reorganization of membrane microdomains. *Science.* (1999) 283:680–2. doi: 10.1126/science.283.5402.680
214. Cambi A, de Lange F, van Maarseveen NM, Nijhuis M, Joosten B, van Dijk EM, et al. Microdomains of the C-type lectin DC-SIGN are portals for virus entry into dendritic cells. *J Cell Biol.* (2004) 164:145–55. doi: 10.1083/jcb.200306112
215. Neumann AK, Thompson NL, Jacobson J. Distribution and lateral mobility of DC-SIGN on immature dendritic cells–implications for pathogen uptake. *J Cell Sci.* (2008) 121(Pt. 5):634–43. doi: 10.1242/jcs.022418
216. Caparros E, Munoz, Sierra-Filardi E, Serrano-Gomez D, Puig-Kroger A, Rodriguez-Fernandez JL, et al. DC-SIGN ligation on dendritic cells results in ERK and PI3K activation and modulates cytokine production. *Blood.* (2006) 107:3950–8. doi: 10.1182/blood-2005-03-1252
217. Guo B, Kato RM, Garcia-Lloret M, Wahl MI, Rawlings DJ. Engagement of the human pre-B cell receptor generates a lipid raft-dependent calcium signaling complex. *Immunity.* (2000) 13:243–53. doi: 10.1016/S1074-7613(00)00024-8
218. Escriba V, Busquets X, Inokuchi J, Balogh G, Torok Z, Horvath I, et al. Membrane lipid therapy: Modulation of the cell membrane composition and structure as a molecular base for drug discovery and new disease treatment. *Prog Lipid Res.* (2015) 59:38–53. doi: 10.1016/j.plipres.2015.04.003
219. Gu L, Saha ST, Thomas J, Kaur M. Targeting cellular cholesterol for anticancer therapy. *FEBS J.* (2019) 286:4192–208. doi: 10.1111/febs.15018
220. Bernardes N, Garizo AR, Pinto SN, Canico B, Perdigao C, Fernandes F, et al. Azurin interaction with the lipid raft components ganglioside GM-1 and caveolin-1 increases membrane fluidity and sensitivity to anti-cancer drugs. *Cell Cycle.* (2018) 17:1649–66. doi: 10.1080/15384101.2018.1489178
221. Zhang J, Li Q, Wu Y, Wang D, Xu L, Zhang Y, et al. Cholesterol content in cell membrane maintains surface levels of ErbB2 and confers a therapeutic vulnerability in ErbB2-positive breast cancer. *Cell Commun Signal.* (2019) 17:15. doi: 10.1186/s12964-019-0328-4
222. Kirsch C, Eckert G, Mueller WE. Statin effects on cholesterol micro-domains in brain plasma membranes. *Biochem Pharmacol.* (2003) 65:843–56. doi: 10.1016/S0006-2952(02)01654-4

223. Zhou Y, Cho KJ, Plowman SJ, Hancock JF. Nonsteroidal anti-inflammatory drugs alter the spatiotemporal organization of Ras proteins on the plasma membrane. *J Biol Chem.* (2012) 287:16586–95. doi: 10.1074/jbc.M112.348490
224. Sharma VK, Nagao M, Rai DK, Mamontov E. Membrane softening by nonsteroidal anti-inflammatory drugs investigated by neutron spin echo. *Phys Chem Chem Phys.* (2019) 21:20211–18. doi: 10.1039/C9CP03767E
225. Hamdan TA, Lang A, Lang KS. The diverse functions of the ubiquitous Fcgamma receptors and their unique constituent, FcRgamma subunit. *Pathogens.* (2020) 9:140. doi: 10.3390/pathogens9020140
226. Pohlmann S, Soilleux EJ, Baribaud F, Leslie GJ, Morris LS, Trowsdale J, et al. DC-SIGNR, a DC-SIGN homologue expressed in endothelial cells, binds to human and simian immunodeficiency viruses and activates infection in trans. *Proc Natl Acad Sci USA.* (2001) 98:2670–5. doi: 10.1073/pnas.051631398
227. Lai WK, Sun J, Zhang J, Jennings A, Lalor F, Hubscher S, et al. Expression of DC-SIGN and DC-SIGNR on human sinusoidal endothelium: a role for capturing hepatitis C virus particles. *Am J Pathol.* (2006) 169:200–8. doi: 10.2353/ajpath.2006.051191
228. Sedmak DD, Davis DH, Singh U, van de Winkel JG, Anderson CL. Expression of IgG Fc receptor antigens in placenta and on endothelial cells in humans. An immunohistochemical study. *Am J Pathol.* (1991) 138:175–81.
229. Pulford K, Ralfkiaer E, MacDonald SM, Erber WN, Falini B, Gatter KC, et al. A new monoclonal antibody (KB61) recognizing a novel antigen which is selectively expressed on a subpopulation of human B lymphocytes. *Immunology.* (1986) 57:71–6.
230. Ishikawa T, Takizawa T, Iwaki J, Mishima T, Ui-Tei K, Takeshita T, et al. Fc gamma receptor IIb participates in maternal IgG trafficking of human placental endothelial cells. *Int J Mol Med.* (2015) 35:1273–89. doi: 10.3892/ijmm.2015.2141
231. Ganesan L, Kim J, Wu Y, Mohanty S, Phillips GS, Birmingham DJ, et al. FcgammaRIIb on liver sinusoidal endothelium clears small immune complexes. *J Immunol.* (2012) 189:4981–8. doi: 10.4049/jimmunol.1202017
232. Peress NS, Fleit HB, Perillo E, Kuljis R, Pezzullo C. Identification of Fc gamma RI, II and III on normal human brain ramified microglia and on microglia in senile plaques in Alzheimer's disease. *J Neuroimmunol.* (1993) 48:71–9. doi: 10.1016/0165-5728(93)90060-C
233. Ulvestad E, Williams K, Vedeler C, Antel J, Nyland H, Mork S, et al. Reactive microglia in multiple sclerosis lesions have an increased expression of receptors for the Fc part of IgG. *J Neurol Sci.* (1994) 121:125–31. doi: 10.1016/0022-510X(94)90340-9
234. Mohamed HA, Mosier DR, Zou LL, Siklos L, Alexianu ME, Engelhardt JI, et al. Immunoglobulin Fc gamma receptor promotes immunoglobulin uptake, immunoglobulin-mediated calcium increase, and neurotransmitter release in motor neurons. *J Neurosci Res.* (2002) 69:110–6. doi: 10.1002/jnr.10271
235. Cremesti AE, Goni FM, Kolesnick R. Role of sphingomyelinase and ceramide in modulating rafts: do biophysical properties determine biologic outcome? *FEBS Lett.* (2002) 531:47–53. doi: 10.1016/S0014-5793(02)03489-0
236. Zajchowski LD, Robbins SM. Lipid rafts and little caves. Compartmentalized signalling in membrane microdomains. *Eur J Biochem.* (2002) 269:737–52. doi: 10.1046/j.0014-2956.2001.02715.x
237. Lichtenberg D, Goni FM, Heerklotz H. Detergent-resistant membranes should not be identified with membrane rafts. *Trends Biochem Sci.* (2005) 30:430–6. doi: 10.1016/j.tibs.2005.06.004
238. Stanly TA, Fritzsche M, Banerji S, Garcia E, Bernardino de la Serna J, Jackson DG, et al. Critical importance of appropriate fixation conditions for faithful imaging of receptor microclusters. *Biol Open.* (2016) 5:1343–50. doi: 10.1242/bio.019943
239. Cheng R, Zhang F, Li M, Wo X, Su YW, Wang W. Influence of fixation and permeabilization on the mass density of single cells: a surface plasmon resonance imaging study. *Front Chem.* (2019) 7:588. doi: 10.3389/fchem.2019.00588

Conflict of Interest: The authors declare that the research was conducted in the absence of any commercial or financial relationships that could be construed as a potential conflict of interest.

frontiers in Cell and Developmental Biology

ORIGINAL RESEARCH
published: 14 July 2020
doi: 10.3389/fcell.2020.00586

The Beauty of Asymmetric Membranes: Reconstitution of the Outer Membrane of Gram-Negative Bacteria

*Laura Paulowski[1,2], Annemarie Donoghue[1,3], Christian Nehls[1], Sabrina Groth[1], Max Koistinen[1], Sven O. Hagge[1], Arne Böhling[1], Mathias Winterhalter[3] and Thomas Gutsmann[1]**

[1] Division of Biophysics, Priority Research Area Infection, Research Center Borstel Leibniz Lung Center, Borstel, Germany, [2] Division of Diagnostic Mycobacteriology, Priority Research Area Infection, National Reference Center for Mycobacteria, Research Center Borstel Leibniz Lung Center, Borstel, Germany, [3] Department of Life Sciences & Chemistry, Jacobs University Bremen, Bremen, Germany

The architecture of the lipid matrix of the outer membrane of Gram-negative bacteria is extremely asymmetric: Whereas the inner leaflet is composed of a phospholipid mixture, the outer leaflet is built up by glycolipids. For most Gram-negative species, these glycolipids are lipopolysaccharides (LPS), for a few species, however, glycosphingolipids. We demonstrate experimental approaches for the reconstitution of these asymmetric membranes as (i) solid supported membranes prepared by the Langmuir-Blodgett technique, (ii) planar lipid bilayers prepared by the Montal-Mueller technique, and (iii) giant unilamellar vesicles (GUVs) prepared by the phase transfer method. The asymmetric GUVs (aGUVs) composed of LPS on one leaflet are shown for the first time. They are characterized with respect to their phase behavior, flip-flop of lipids and their usability to investigate the interaction with membrane active peptides or proteins. For the antimicrobial peptide LL-32 and for the bacterial porin OmpF the specificity of the interaction with asymmetric membranes is shown. The three reconstitution systems are compared with respect to their usability to investigate domain formation and interactions with peptides and proteins.

Keywords: phase transfer, membranes, asymmetry, coupling, lipid flip-flop

OPEN ACCESS

Edited by:
Robert Ernst,
Saarland University, Germany

Reviewed by:
Karin A. Riske,
Federal University of São Paulo, Brazil
Francesco Tadini-Buoninsegni,
University of Florence, Italy

***Correspondence:**
Thomas Gutsmann
tgutsmann@fz-borstel.de

Specialty section:
This article was submitted to Cellular Biochemistry, a section of the journal Frontiers in Cell and Developmental Biology

Received: *04 May 2020*
Accepted: *16 June 2020*
Published: *14 July 2020*

Citation:
Paulowski L, Donoghue A, Nehls C, Groth S, Koistinen M, Hagge SO, Böhling A, Winterhalter M and Gutsmann T (2020) The Beauty of Asymmetric Membranes: Reconstitution of the Outer Membrane of Gram-Negative Bacteria. Front. Cell Dev. Biol. 8:586. doi: 10.3389/fcell.2020.00586

INTRODUCTION

Since the introduction of the fluid mosaic model by SINGER and NICOLSON in 1972, the membrane itself and its unique, complex architecture has remained a central pillar of research today (Singer and Nicolson, 1972). Also in the early 1970s, KORNBERG and MCCONNELL were the first to successfully resolve the kinetics of lipid flip-flop between the individual membrane leaflets (Kornberg and McConnell, 1971). These two important hallmarks in research were essential steps in membrane biophysics. As a result, hitherto, various aspects, such as the molecular dynamics within the membrane, lipid specificity and the composition of the membrane in general, have entered the focus of current research and represent a discipline that combines classical physics, chemistry, biology, and medicine.

Many new insights into lipid membranes and their interaction with peptides and proteins have been gained by reconstituted membranes in biophysical experiments. These systems often accept the limitation that the model membranes usually have a symmetrical lipid architecture. There is a lively discussion about the existence and nature of lateral heterogeneity or domains, also known as lipid rafts, and their importance for the function of membrane processes. However, relatively little is known about the importance of axial heterogeneity or lipid asymmetry in membranes.

Within the manifold functionalities of cell membranes, asymmetry can explain various directed effects. Membrane asymmetry is induced and preserved in the form of variations of the headgroups and the length and degree of saturation of the hydrocarbon tail of the individual membrane components. A group of proteins, the flippases (outer leaflet to inner leaflet translocation of lipids) and floppases (inner leaflet to outer leaflet translocation of lipids) actively maintain the asymmetric lipid distribution (Marquardt et al., 2015; Rivel et al., 2019). Besides the axial heterogeneity referred to as membrane asymmetry, lateral membrane heterogeneity includes aspects such as lipid rafts, the formation of microdomains and lipid sorting. However, protein asymmetry is probably the most frequently investigated form of asymmetry on the cellular level. Surface proteins (that are attached to the membrane) or peripheral proteins (that partially penetrate the lipid bilayer) are often found accumulated on a certain membrane leaflet (Van Meer et al., 2008). Proteins involved in intracellular processes or in cellular defense mechanisms are primarily located on the inner leaflet or outer leaflet, respectively.

In recent years, the very limited range of reconstitution techniques suitable for the production of asymmetric membranes [including Montal-Mueller membranes (Montal and Mueller, 1972) and Langmuir-Blodgett films (Blodgett, 1934; Rinia et al., 1999)] has been supplemented by few but very useful additional techniques. These include the preparation of asymmetric GUVs by the phase transfer method (Pautot et al., 2003) and of smaller liposomes by cyclodextrin-mediated lipid exchange (Cheng and London, 2009). Thus, it is possible to characterize coupling or decoupling of lateral heterogeneity across the lipid bilayer, the effects of lipid asymmetry on protein localization, orientation, and conformation, and the influence of proteins on lipid distribution within a single leaflet and between the two leaflets (Van Meer et al., 2008). Simulations of distinct membrane models, e.g., for cancer and normal membranes, hint to a loss of asymmetry from healthy to unhealthy condition (Rivel et al., 2019). This loss of membrane asymmetry during disease shows the importance of this topic in the development of new drugs and therapeutic approaches.

In this study we focus on the asymmetry of the outer membrane of Gram-negative bacteria as the most asymmetric membrane described so far. We have modeled the asymmetric membrane with LPS being the main component in the bacterial outer leaflet and a phospholipid mixture (PL) as inner leaflet. At this point, it is noteworthy, that unlike eukaryotic membranes, the bacterial membrane has a much higher degree of flexibility, which is due to the packing density of the LPS in the outer leaflet. We modeled the phospholipid-rich inner leaflet from the three main components PE, PG and cardiolipin (CL), in a ratio equivalent to the composition of the cytoplasmic inner membranes (Gutsmann et al., 2015) of bacteria (Cronan and Vagelos, 1972; Osborn et al., 1972; Zachowski, 1993). Gram-negative bacteria feature two major forms of LPS – smooth (S) and rough (R) LPS (Alexander and Rietschel, 2001). Strains with S-form LPS harbor the full core oligosaccharide and O-antigen regions in the outer leaflet contrasting rough mutants expressing the glycolipid without O-antigen and truncated core oligosaccharide. For this project, we designed the outer leaflet with LPS R45 from the deep rough mutant of *Proteus mirabilis* strain R45. This LPS has a nearly conical molecular geometry shaped by full length lipid A and an inner core unit, that is composed of 3-deoxy-D-manno-2-octulsonic acid (Kdo) with a non-stoichiometric (approx. 50%) substitution of L-arabinose at two positions resulting in a reduced negative net charge (−3.0) (Wiese et al., 1998; Howe et al., 2007).

Within the scope of this paper, we elucidate the functions of the two membrane leaflets of LPS/PL membranes to analyze lipid asymmetry in bacterial membranes and to address the influence of this asymmetry on membrane permeability to drugs and small molecules. Therefore, we have chosen a set of biophysical techniques to investigate and compare the properties of free-standing (Montal and Mueller, 1972) and solid supported mono- and bilayers [Langmuir-Blodgett films (Blodgett, 1934)] and GUVs (Pautot et al., 2003). We provide clear evidence, that phase separation in bilayers can be different from the sum of the properties of the individual monolayers. With the help of fluorescence spectroscopy, i.e., dithionite quenching, lipid flip-flop rates were determined. Fluorescence microscopy of both symmetric and asymmetric vesicles showed the formation of LPS/LPS as well as LPS/PL domains within a narrow temperature range. The potency to reconstitute asymmetric membranes and to characterize membrane properties such as the flip-flop of lipids and the phase behavior across the lipid leaflets are essential parts of this work. The connection between phase separation and lipid flip-flop rates are yet not clear understood, but wide time ranges for lipid translocation were already described (Marquardt et al., 2015). The flip-flop rates discussed can range from a few seconds to hours or days depending on the lipid composition, membrane reconstitution system, fluorescent probe or temperature (Rosoff, 1996). In addition to the characterization of asymmetric membranes, we have used them to study their interaction with peptides and proteins. We show that the antimicrobial peptide LL-32 and the bacterial protein OmpF specifically interact with the two sides of asymmetric LPS/PL membranes.

MATERIALS AND METHODS

Chemicals and Buffers

As buffer system, we used 100 mM KCl (potassium chloride), 5 mM $MgCl_2$ (magnesium chloride), and 5 mM HEPES [4-(2-hydroxyethyl)-1-piperazineethanesulfonic acid] adjusted to neutral pH (pH = 7.0) with 1 M KOH (potassium hydroxide) TitriPUR (Merck, Darmstadt, Germany). The buffer was sterile

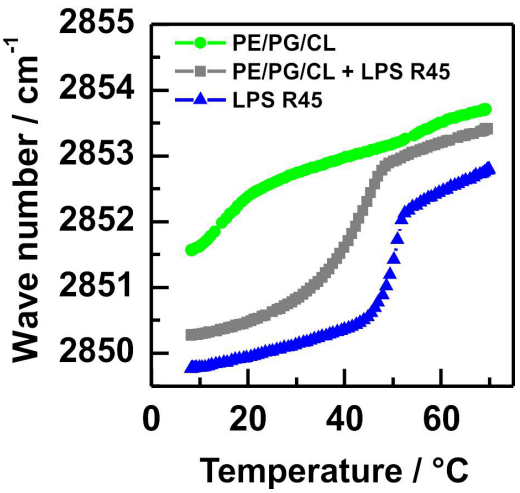

FIGURE 1 | The equimolar mixture of LPS R45 and PL has a phase transition between those of LPS and PL alone. Phase transitions of membranes reconstituted from pure phospholipids (●), pure LPS R45 (▲), and an equimolar mixture of both (■) were recorded in FTIR measurements by measuring the symmetric CH_2-stretching vibrations within a temperature window from 10°C to 70°C. The lipid mixture PE/PG/CL (81:17:2 w/w/w) shows a broad phase transition around 17°C, whereas for the pure LPS R45 a well-defined phase transition at 50°C is detected. The equimolar mixture of both, phospholipids and LPS exhibits a shifted phase transition to lower temperatures (T_m = 42°C) with a slightly less sharp characteristic. All experiments were performed with LPS and lipid concentration of 20 mM in 100 mM KCl, 5 mM $MgCl_2$, 5 mM HEPES at pH 7.0.

filtered using a 0.22 μm pore size filter (ExpressTM PLUS, Millipore, Billerica, MA, United States) and stored at 4°C until use. For fluorescence quenching either KI (potassium iodide) or $Na_2S_2O_4$ (sodium dithionite) was used. All chemicals were purchased from Sigma-Aldrich (Merck, Darmstadt, Germany). For the generation of asymmetric vesicles, pure anhydrous dodecan and a mixture of anhydrous dodecan and silicone oil (AR 200) in a ratio of 99:1 (v/v) was used. All solvents, including chloroform ($CHCl_3$), ethanol (EtOH) and methanol (MeOH) were either purchased from Sigma-Aldrich (Merck, Darmstadt, Germany) or Acros Organics (Thermo Fisher Scientific, Rochester, NY, United States).

Phospholipids and Lipopolysaccharides (LPS)

The inner membrane of Gram-negative bacteria was reconstituted from a PL-mixture composed of L-α-phosphatidylethanolamine from *E. coli* (PE, Avanti 840027P), L-α-phosphatidylglycerol from *E. coli* (PG, Avanti 841188P), and 1',3'-bis[1,2-dioleoyl-*sn*-glycero-3-phospho]-glycerol (DPG, Avanti 710335P) also referred to as 18:1 cardiolipin (CL) in a lipid ratio of 81:17:2. This lipid mixture ratio is originally derived from the phospholipid composition of the inner leaflet of the OM of *Salmonella typhimurium* (Osborn et al., 1972; Shaw, 1974). The lipopolysaccharides used were extracted by the phenol/chloroform/petroleum ether method (Galanos et al., 1969) from a deep rough mutant of *Proteus mirabilis* strain R45. LPS R45 was fluorescently labeled with FITC by binding to the aminoarabinose (Ara4N). All phospholipids were purchased from Avanti (Avanti Polar Lipids Inc., Alabaster, AL, United States) and prepared at stock concentrations of 10 mg/mL in $CHCl_3$ as described in earlier publications. Fluorescence conjugated lipids *N*-(7-nitrobenz-2-oxa-1,3-diazol-4-yl)-1,2-dihexadecanoyl-*sn*-glycero-3-phosphoethanolamine (NBD-PE) and Lissamine^{TM} Rhodamine B 1,2-dihexadecanoyl-*sn*-glycero-3-phosphoethanolamine (Rho-DHPE), were purchased from Life Technologies (Carlsbad, CA, United States). The lipid-dye conjugate FITC-phosphatidylethanolamine (FITC-PE) was purchased from Molecular Probes (Invitrogen GmbH, Darmstadt, Germany).

Peptides and Proteins

The human cathelicidin fragment LL-32 with and without fluorescent Lissamine^{TM} Rhodamine B label were synthesized in-house (Research Center Borstel, Leibniz Lung Center, Germany) in accordance with a standardized solid-phase Fmoc-synthesis protocol at 0.1 mmol scale (Kent, 1988). Peptide synthesis was performed in an automated experimental lapse on preloaded Wang resin on a peptide synthesizer 433A (Applied Biosystems, Carlsbad, CA, United States). The crude peptide was purified by gradient controlled reversed-phase HPLC at 214 nm with MeCN/H_2O supplemented with 0.1% trifluoroacetic acid (TFA, Riedel-de Haën, Seelze, Germany). After chromatographic purification on a Proteo 4 μm 80 Å 4.6 × 250 mm or Gemini Polar C18 4 × 3 mm LC-column, all peptides were lyophilized and further characterized by mass spectrometry. For fluorescence spectroscopy or microscopy, peptide stock solutions of 1 mg/ml in ultrapure water were prepared. All other peptide stocks were dissolved in 0.01% (v/v) TFA at concentrations of 2 mg/ml or 1 mM, respectively. The antimicrobial peptides LL-32 and ^{Rho}LL-32 were used in this study to analyze their interaction with LPS and asymmetric vesicles.

For the expression of OmpF, the expression plasmid pGOmpF harboring the ompF gene of *E. coli* K12 was transformed into *E. coli* strain BL21(DE3)omp8. OmpF was purified as described by Lamichhane et al. (2013) and stored in 0.5% octyl-POE (n-octyl-polyoxyethylene; Alexis Biochemicals, Lausen, Switzerland).

Fourier-Transform Infrared Spectroscopy (FTIR)

FTIR spectroscopy is generally performed on lipid multilayers. Multilayers are obtained by spreading multilamellar vesicles (MLVs). For the reconstitution of phospholipid-LPS MLVs, lipid species and glycolipid species were individually dissolved in a solvent mix composed of $CHCl_3$/MeOH in a volumetric ratio of 9:1 (v/v) with a final concentration of 20 mM. Afterward, the lipids PE, PG, and CL were then mixed in a molar lipid ratio of 81:17:2. Half of this lipid mixture was supplemented with LPS R45 in a 1:1 ratio (v/v). The organic solvent was evaporated under nitrogen and resuspended in buffer (100 mM KCl, 5 mM $MgCl_2$, 5 mM HEPES, pH 7.0) giving again a final concentration of 20 mM. The resulting suspension

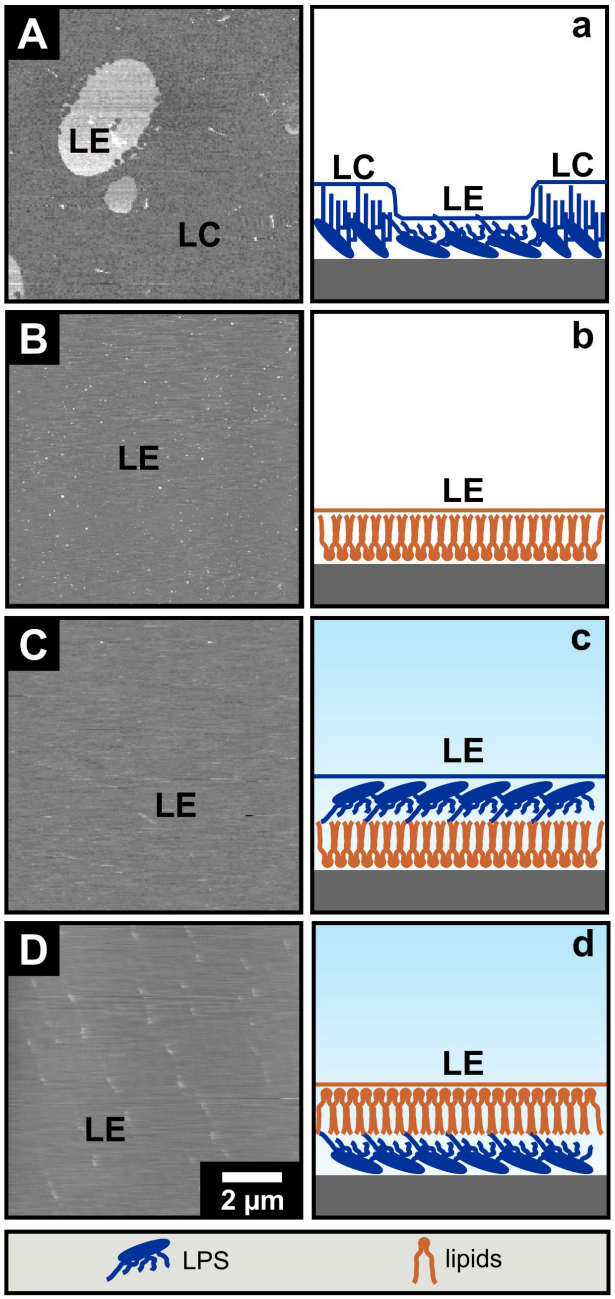

FIGURE 2 | The phase separation of LPS R45 solid supported Langmuir-Blodgett monolayers is not maintained in asymmetric bilayers. Solid supported Langmuir-Blodgett monolayers **(A,B)** were imaged by AFM in air while imaging of Langmuir-Blodgett bilayers **(C,D)** was conducted in buffer. **(A,a)** LPS R45 monolayer; liquid expanded (LE) domains appear higher compared to the liquid condensed (LC) domains in the attractive regime of the AFM AC-mode; **(B,b)** PL (PE:PG:CL; 81:17:2; w/w/w) monolayer; **(C,c)** LPS R45/PL bilayer with the PL adsorbed on the solid support and the LPS R45 oriented to the buffer; and **(D,d)** PL/LPS R45 bilayer with the LPS adsorbed on the solid support and the PL oriented to the buffer. Only the LPS R45 monolayer showed a phase separation. Monolayer formation, Langmuir-Blodgett transfer and AFM imaging were performed in 100 mM KCl, 5 mM $MgCl_2$, 5 mM HEPES buffer at pH 7.0 and T = 21°C. Lateral pressure of the monolayer during transfer to the mica was p = 20 mN/m. AFM height images are shown with a gray scale range of 5 nm.

was sonicated (Branson, Sonifier, Cell disruptor B15) for one minute. MLVs were generated by running all samples through a two-step temperature cycle (30 min at 67°C and 30 min at 4°C), which was repeated three times. To measure the phase transition temperature (T_m) 20 µl of the suspensions were placed between two calcium fluoride (CaF_2) crystals (Korth Kristalle GmbH, Altenholz, Germany) with a 12.5 µm Teflon spacer. The samples were tempered in a temperature range of 10°C to 70°C with a heating rate of 2°C/min and the IR spectra were continuously recorded (IFS-55 spectrometer, Bruker, Karlsruhe, Germany). The phase transition was determined by the shift of the absorbance band of the symmetric stretching vibration of the methylene groups (ν = 2865-2845 cm^{-1}) (Colthup et al., 1990). Experiments were repeated at least two times and representative curves are shown.

Film Balance and Atomic Force Microscopy (AFM)

Lipid monolayers at the air/water interface were prepared by using a film balance. Measurements were performed on a KSV Nima Langmuir-Blodgett trough (Biolin Scientific Inc., Stockholm, Sweden). The temperature of the buffer/subphase was controlled by water circulation (Haake, Karlsruhe, Germany) and set to 21°C. The trough was filled with 65 ml buffer solution. Experiments were performed as follows: lipid solution PE/PG/CL (81:17:2) or LPS R45 solved in $CHCl_3$ or $CHCl_3$/MeOH 9:1 (v/v) were spread onto the surface of the subphase. After an equilibration time of 10 min at zero pressure, a pressure-area-isotherm was recorded by a symmetric compression of the effective film area with a constant compression rate of 10 $mm \cdot min^{-1}$. The monolayers were compressed to a lateral pressure of 20 mN/m which is in the range of the values discussed for the lateral pressure in cell membranes (Marčelja, 1974). The monolayers were equilibrated for 1 h at constant lateral pressure. For AFM measurements, monolayers were transferred onto mica plates according to the Langmuir-Blodgett technique with a pulling speed of 10 µm/s. For bilayer preparation, two individual monolayers were prepared and transferred one by one onto each other. Monolayers were imaged in air with the MFP-3D (Asylum Research, Santa Barbara, CA, United States) in AC-mode using NSG11 B cantilevers with a typical spring constant of 5.5 N/m and a resonance frequency of 150 kHz (NT-MDT, Moscow, Russia). Bilayers were imaged in buffer using CSG 11B cantilevers with a typical spring constant of $k \sim 30$ mN/m and a resonance frequency of $\omega_0 \sim 9.8$ kHz (NT-MDT, Moscow, Russia). For additional fluorescence imaging the LPS monolayer was labeled with 1% NBD-PE. The image processing was performed using the MFP-3D associated software package under IGOR Pro (Lake Oswego, OR, United States).

Free-Standing Membranes

Planar bilayers were prepared according to the Montal-Mueller technique (Montal and Mueller, 1972) as described earlier (Wiese and Seydel, 2000; Gutsmann et al., 2015). Briefly, asymmetric bilayers were formed by opposing two lipid monolayers prepared on aqueous subphases from $CHCl_3$ or $CHCl_3$/MeOH solutions of

the lipids or LPS, respectively, at a small aperture (Ø ~150 μm) in a thin Teflon septum. The inner membrane of Gram-negative bacteria was reconstituted from a PL-mixture composed of PE, PG, and CL in a lipid ratio of 81:17:2. For electrical measurements, planar membranes were voltage-clamped via a pair of Ag/AgCl-electrodes (type IVM E255, Advanced Laboratory Research Inc., Franklin, United States) connected to the head-stage of an L/M-PCA patch-clamp amplifier (List-Medical, Darmstadt, Germany). All measurements were performed in 100 mM KCl, 5 mM $MgCl_2$, 5 mM HEPES at 37°C and a pH-value of 7.0. For the fluorescence micrographs a home build microscope was used which is based on a mercury arc lamp (HBO 103 W/2, Osram, Munich, Germany), a dichroitic mirror (515DRLP, Omega Opticals, Brattleboro, VT, United States), an objective (M Plan APO 50x, Mitutoyo America Corporation, Aurora, IL, United States), two filters (455DF70 and 515ALP, Omega Opticals, Brattleboro, VT, United States), and a CCD-camera (C8484-02, Hamamatsu Photonics Germany GmbH, Herrsching, Germany). Both membrane sides, the PL as well as the LPS layer could be fluorescently labeled by adding 1% the lipid-dye conjugate NBD-PE. The proper bilayer formation was controlled by measuring the membrane current and capacitance. For apertures of about 150 μm the current was below 2 pA and the capacitance above 70 pF.

Preparation of Asymmetric Vesicles

Outer and inner membrane leaflets were prepared in individual approaches and combined in the final centrifugation step. As inner leaflet a lipid mixture consisting of PE/PG/CL (81:17:2) is prepared first. For this purpose, all lipids were dissolved in $CHCl_3$ to a final concentration of 2.5 mg/ml. From this lipid solution, 100 μL were transferred into a 5 mL screw-cap vessel and the solvent was evaporated under a stream of N_2 (2 min/100 μl). After complete evaporation, 2 mL anhydrous dodecane were added to the lipids (final concentration 0.125 mg/mL). The solution was treated with sonication (Branson, Sonifier, Cell disruptor B15) for 30 min and then incubated over night at room temperature (T = 23°C). The next day, 250 μL buffer were added to the same solution and left to stir for 3 h at 300 rpm on a magnetic stirring plate (magnetic stirring fish of 10 × 6 mm). The phospholipids self-assemble as inverted micelles facing the headgroups into the aqueous phase of the small buffer droplets and the fatty acid chains into the hydrophobic dodecane phase. While the inner leaflet preparation is stirred, the outer leaflet preparation is performed: For this, LPS was solved in a mixture of anhydrous dodecane and silicone oil in a volumetric ratio of 99:1 (v/v) giving a final LPS concentration of 0.05 mg/mL. In a 50 mL Falcon® tube (Corning™ CentriStar centrifugation tubes), 1 mL of buffer solution was covered over by 2 mL of the LPS solution. The buffer contained 100 mM KCl, 5 mM $MgCl_2$, 5 mM HEPES (pH 7.0). Because of the phase separation between the buffer and the dodecane:silicone oil the LPS arranged at the phase boundary with the headgroups orientated into the buffer solution and the fatty acid chains into the dodecane. The incubation time was about three hours. Afterward, 150 μL of the phospholipid emulsion from the inner leaflet preparation was gently pipetted on top of the LPS solution and centrifuged (120*g; 10 min; 4°C). The final vesicle solution was removed by a 21 gauge syringe (B. Braun, Sterican®, 21 G x 1 1/2 ‘’) (Pautot et al., 2003). To proof the asymmetry, fluorescent dies were introduced in both leaflets. The LPS leaflet was labeled with 0.5% Rho-DHPE and the PL leaflet with 1% NBD-PE. By adding a fluorescence quencher, e.g., KI, the orientation of the fluorescent label as well as the integrity of the vesicles could be validated.

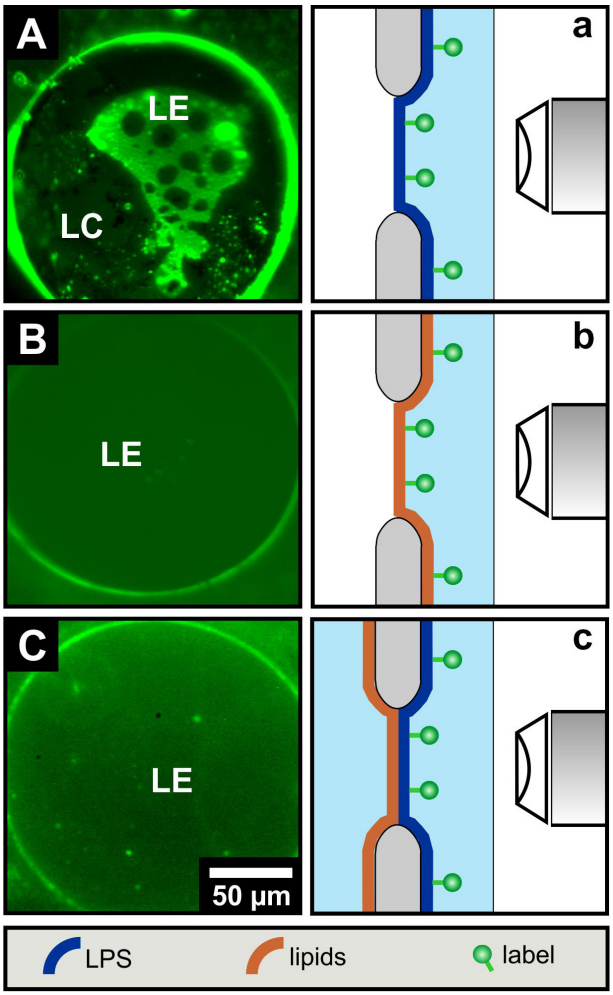

FIGURE 3 | LPS R45 free-standing planar monolayers lose their phase separation upon combination to an LPS R45/PL free-standing bilayer. Fluorescence microscopic images of **(A)** a LPS R45 monolayer, **(B)** a PL (PE:PG:CL; 81:17:2; w/w/w) monolayer, and **(C)** a LPS R45/PL planar bilayer reconstituted over an aperture. For fluorescence labeling of an individual membrane leaflet, the lipid monolayer was supplement with 1% NBD-PE which partitions into the liquid expanded (LE) domains. As with the solid-supported membranes, phase separation in free-standing lipid systems occurred only for the LPS R45 monolayer. Experiments were conducted in 100 mM KCl, 5 mM $MgCl_2$, 5 mM HEPES at pH 7.0 and T = 37°C.

Fluorescence Microscopy

Fluorescence microscopy was performed at 23°C either on a motorized inverted fluorescence microscope (IX-81, Olympus, Tokyo, Japan) or on a Leica TCS SP3 spectral confocal

microscope (Leica Microsystems Heidelberg GmbH, Heidelberg, Germany). For confocal imaging, FITC labels were excited at λ_{Ex} = 488 nm, while the fluorescence emission was recorded from λ_{Em} = 500-550 nm. Vesicles were investigated without further dilution as (i) untreated samples, (ii) samples with added quencher (KI, 0.83 M) and (iii) samples with added quencher plus added peptide (^{Rho}LL-32, 38 nM). In the presence of fluorescently labeled ^{Rho}LL-32 excitation of FITC and Rho channels occurred back-to-back at 488 and 543 nm respectively, while the fluorescence was recorded from 500 to 550 nm and from 580 to 800 nm, respectively. In the recorded micrographs (**Figure 4**) FITC fluorescence was assigned to green color while Rho was assigned to red. To prove the existence of vesicles with quenched fluorescence, pictures with transmitted white light were recorded. For conventional fluorescence microscopy of aGUVs, images were acquired with an UplanSApo100xO oil-immersion objective (Olympus, Hamburg, Germany) in intX mode (intelligent exposure) at 23°C and collected with the software Cell*P (Olympus Soft Imaging Solutions, Münster, Germany). The microscopy images (**Figures 6C,D**) were processed with Fiji (49, 50) (NIH, Bethesda, MD, United States) and subsequent evaluation by fluorescence dye distribution analysis (**Figures 6c,d**).

Fluorescence Spectroscopy

To determine the permeabilization of asymmetric GUVs by the pore forming peptide LL-32 and the protein OmpF aGUVs were prepared of LPS R45 outside and the PL mixture inside, or *vice versa*. In both cases the inner leaflet was labeled with 1% NBD-PE. The fluorescence was measured by a spectrometer (Fluorolog 3, Horiba Jobin Yvon GmbH, Bensheim, Germany). aGUVs (1.5 mL) were used in the concentration obtained after preparation. The first addition after 10 min were 15 µL $Na_2S_2O_4$ (1 M, end conc. 10 mM) or buffer as control. Second addition after 20 min were 15 µL LL-32 (3 mM, end conc. 30 µM), 15 µL OmpF (end conc. 5 µg/mL), or the respective solvent of LL-32 (0.01% TFA) or OmpF (0.004% octyl-POE). Experiments were repeated in three independent experiments (n = 3). Respective curves of the quotient between intensity after peptide/protein addition and intensity after buffer addition are shown.

RESULTS

Characterization of the Phase Behavior of the Individual Components

Fourier transform infrared spectroscopy of symmetric MLVs. First, we characterized the phase behavior of the used lipids and lipid mixtures with the help of FTIR spectroscopy. We studied the induction of conformational changes in the stretching vibrations of the CH_2-groups of the acyl chains over a temperature range from 10°C to 70°C for pure LPS and pure phospholipid membranes as well as a mixture of the two (**Figure 1**). For the pure PL mixture two main transitions at T_{m1} = 15°C and T_{m2} = 50°C were detected. These two phase transitions can correspond to the individual phase transitions of the different components in this lipid mixture (**Figure 1**, green line). However, already at room temperature of 21°C the wave number is around ν = 2852.5 cm^{-1}, which is indicative for an almost fluid phase behavior. The pure LPS R45 of *P. mirabilis* showed a phase

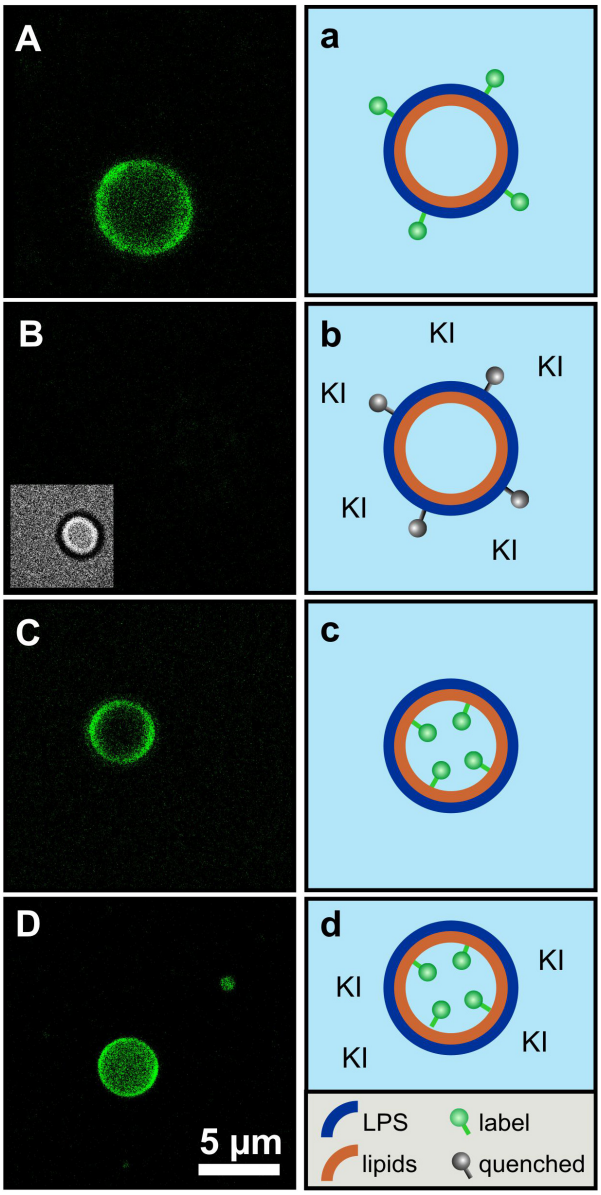

FIGURE 4 | The asymmetry of giant unilamellar LPS R45/PL vesicles is confirmed by leaflet-specific fluorescence quenching with KI. **(A,a)** Asymmetric vesicles with LPS R45 in the outer leaflet and PL (PE:PG:CL; 81:17:2; w/w/w) in the inner leaflet; 5% (w/w) of the LPS R45 molecules in the outer leaflet were fluorescent FITC-LPS R45; **(B,b)** Quenched fluorescence of the vesicles after the addition of KI. The inlet shows the vesicle in phase contrast; **(C,c)** Asymmetric vesicles with LPS R45 in the outer leaflet and PL in the inner leaflet; 2% (w/w) of the PL molecules in the inner leaflet were fluorescent FITC-PE; **(D,d)** Vesicles after the addition of KI. The fluorophores in the inner leaflet were protected from quenching. Experiments were carried out at 25°C in 100 mM KCl, 5 mM $MgCl_2$, 5 mM HEPES buffer at pH 7.0 using a Leica TCS SP3 confocal microscope. Final KI concentration was 0.83 M; Scale bar applies to all images.

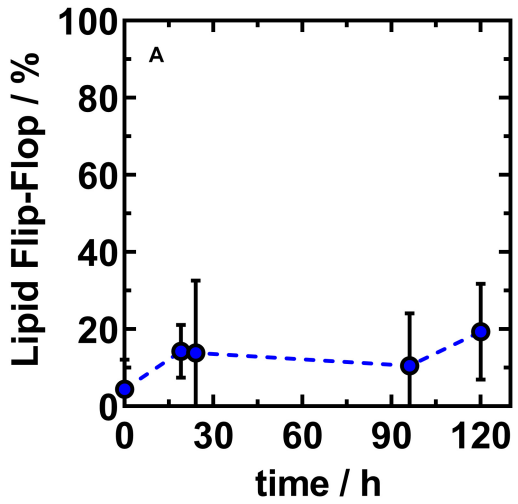

FIGURE 5 | The net lipid translocation into the outer leaflet of asymmetric LPS R45/PL vesicles largely finds a saturation level at a NBD-PE fraction of about 20%. Fraction of NBD-PE found in the outer leaflet of asymmetric vesicles reconstituted from LPS R45 (OL) and PE:PG:CL (IL; 81:17:2; w/w/w). The ability of lipid flip-flop of NBD-PE is monitored over time. Initial flip-flop from inner to outer leaflet occurs fast (1 h) after phase transfer and asymmetric vesicle generation. Asymmetric vesicles with stable outer leaflet composition are achieved approximately 19 h after final preparation. Data shown represent the mean value of three independent experiments ± SD (n = 3).

transition at T_m = 50°C (**Figure 1**, blue line). With an equimolar mixing ratio of PL and LPS only one phase transition ($T_{m,mix}$ = 42°C) was detected, which had a smoother transition in-between the phase transitions of the pure LPS 45 and the PL mixture (**Figure 1**, gray line).

Characterization of Asymmetric LPS/PL Lipid Membranes

AFM imaging of solid supported mono- and bilayers prepared by Langmuir-Blodgett transfer. In order to model biological membranes, one approach is the lipid deposition of Langmuir-Blodgett (LB) films on hydrophilic mica. Therewith solid supported lipid mono- and bilayers are generated in an either symmetric or asymmetric organization. Monolayers were prepared via the Langmuir-Blodgett technique onto the solid support and were subsequently imaged by AFM in air. The liquid expanded domains of an LPS R45 monolayer (**Figure 2A**) appear higher in the height images (Roes et al., 2005). Because of their more flexible fatty acid chains the liquid expanded (LE) domains are about 0.8 nm lower compared to the liquid condensed (LC) domains when imaged in contact mode (**Figure 2a**). The lateral size of the domains depends on the temperature and the lateral pressure. Under the same conditions no phase separation could be observed for the pure PL mixture (**Figure 2B**). To verify this result, a lipid-dye conjugate (1% NBD-PE) was added to the organic phase while preparation of the lipid solution. In doing so, the solid supported monolayer showed a homogenous fluorescence. This shows that the monolayer was in the fluid phase before Langmuir-Blodgett transfer (Roes et al., 2005). In another experiment, a second monolayer is prepared and transferred over the first. Thus, a bilayer is obtained, which can be altered in composition and orientation of the individual membrane components contributing to this bilayer. Bilayers were imaged in buffer. For asymmetric bilayers, two different preparation approaches were followed: The PL-mix is adsorbed on mica first and then coated with the LPS layer so that the LPS-containing layer is aligned toward the buffer (**Figure 2C**) or *vice versa* (**Figure 2D**). In both cases no phase separation was detected. In **Figure 2D** small objects can be seen which originate from free-flowing particles in the buffer. Again, the verification experiment with incorporation of NBD-PE into the bilayers resulted in a homogenous fluorescence distribution across the membrane in both scenarios (data not shown). All experiments were performed at room temperature (approx. 21°C).

Fluorescence microscopy of free-standing planar mono- and bilayers prepared by the Montal-Mueller technique. With the solid supported lipid systems, we could not clarify to what extent the opposite monolayers influence their phase behavior. As solid supports can change the phase behavior of lipid monolayers and bilayers, we have investigated asymmetric free-standing planar lipid bilayers to complement the data obtained so far. LPS R45 as well as the PL mixture were each mixed with 1% NBD-PE with a preference to the fluid phase. This unequally distributed fluorescent-lipid conjugates into the fluid membrane domains leading to an enhanced green fluorescence. The fluorescence dye is excluded from the more rigid membrane areas as those domains appear black. In a first series of experiments only LPS R45 monolayers were reconstituted over the aperture of the Teflon foil and fluorescence images were taken (**Figure 3A**). The physiological body temperature of healthy humans of about 37°C was used for the free-standing membrane experiments to obtain stable LPS R45 monolayers during the process of preparation. At this temperature, a phase separation of the LE and LC domains could be observed. Progressing heating of the monolayer to 42°C (resembling fever) resulted in a fluidization of the monolayer and therewith a phase melting. The original phase separation was lost at 42°C (SI, **Supplementary Figure S1**). This effect was reversible. Compared to the LPS monolayer, both the pure PL monolayer and the full reconstituted asymmetric LPS R45/PL planar bilayer remain in the LE phase showing no domains (**Figures 3B,C**). In **Figure 3C** small objects can be seen which originate from free-flowing particles in the buffer. Even by cooling, it was not possible to reach a temperature at which a phase separation in the bilayer was induced. Temperatures below 25°C led to a loss of membrane stability and thus the asymmetric LPS-containing bilayers ruptured. Further, it was not possible to generate two individual LPS R45 monolayers on one another for the reconstitution of a symmetric free-standing LPS-LPS bilayer. This instability might be due to steric hindrance and spatial arrangement of the hydrocarbon chains of the LPS. Another reason could be the unnatural high rigidity of such a membrane that cannot be compensated by the more fluid PL leaflet. The asymmetric distribution of LPS and PL on both leaflets leads to differences in the Gouy-Chapman, the dipole and the Born potential. These three potentials on both sides of the bilayer sum up to the overall inner membrane potential. In

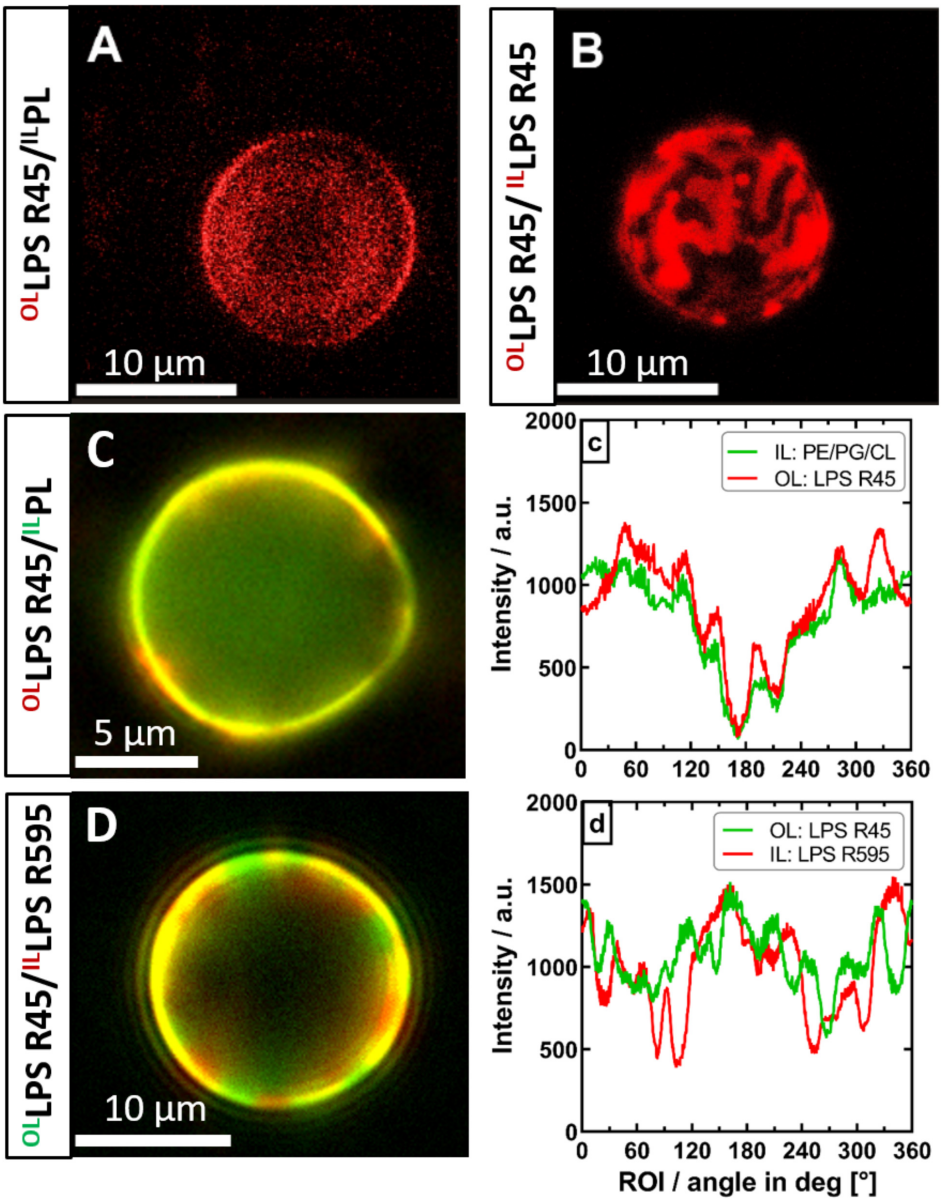

FIGURE 6 | The phase separation of the outer leaflet of asymmetric vesicles is depending on interactions with the inner leaflet. Both asymmetric and symmetric giant unilamellar vesicles were generated by the phase transfer method. **(A)** Asymmetric LPS R45/^{Rho}PL vesicles expose no phase separation (PL refers to PE:PG:CL; 81:17:2; w/w/w). **(B)** Symmetric ^{Rho}LPS R45/^{Rho}LPS R45 vesicles show dominant phase separation in the outer as well as in the inner leaflet (IL), exposing stripe and patch shaped domains. **(C)** Phase separation in asymmetric LPS R45/PL vesicles could not be enforced by lowering divalent cation content. **(c)** Fluorescence dye distribution analysis of IL and outer leaflet (OL). The fluorescent dye conjugates of both leaflets correlate and show an intensity minimum at approx. 180°. **(D)** Asymmetric ^{FITC}LPS R45/^{Rho}LPS R595 vesicles show a dominant phase separation with areas wherein the fatty acid chains of the different LPS types match (yellow) and mismatch (red/green). **(d)** Fluorescence dye distribution analysis of the individual LPS leaflets giving areas of correlation and anti-correlation of the different fluorescence labels. All experiments were run out in 100 mM KCl buffer supplemented with either 5 mM $MgCl_2$ and 5 mM HEPES **(A+B,D)** or 0.5 mM $CaCl_2x2H_2O$ **(C)** at pH 7. Confocal laser scanning microscopy **(A+B)** was performed at 26°C. Images were taken with a Leica SP3. Z-series were performed and compiled for 3D visualization. Inverse fluorescence microscopy was performed at room temperature with an Olympus IX-81.

case of an asymmetric membrane an inner membrane potential difference exists which can be determined by using the inner field compensation (IFC) method. This method provided evidence on a stable asymmetric lipid distribution over the membrane's lifetime of up to two hours (Hagge et al., 2004).

Fluorescence quenching of asymmetric GUVs generated by phase transfer. For an even closer mimicry of the biological system, asymmetric vesicles were designed with a membrane curvature resembling bacterial cells. We used a protocol based on the original method as described by PAUTOT et al.

(Pautot et al., 2003). We were successful to generate asymmetric vesicles with a full LPS outer leaflet and a full PL inner leaflet by the so-called phase transfer method. In addition, our protocol allowed us to generate for the first time inside out asymmetric vesicles with a full PL outer leaflet and a full LPS inner leaflet to gain accessibility from both sides. Furthermore, it is also possible to produce symmetric vesicles consisting of two pure LPS leaflets. The yield of the vesicles generated via phase transfer is significantly lower compared to other vesicle preparation methods. The yield is strongly dependent on the quality of lipid suspension during the preparational process. The vesicle size varies between two and 20 μm in diameter. Different approaches were followed for checking the overall asymmetric distribution: (i) Fluorescent labeled vesicles with LPS R45 containing 5% FITC-LPS R45 in the outer leaflet were prepared. After addition of an aqueous solution of potassium iodide (KI), the fluorescence of the vesicles was quenched due to the accessibility of the fluorophore in the outer leaflet (**Figure 4A**: before addition of KI, **Figure 4B**: after the addition of KI); (ii) In parallel, phase contrast images were taken to check whether the vesicle integrity was disturbed by the addition of or by the KI itself (inlet **Figure 4B**). This proved that the vesicles remained intact and the fluorescence quenching was successful, which demonstrates an exclusive localization of LPS in the outer leaflet. Since KI is classified as permeable to membranes due to its size and substance properties, a further experimental approach was needed. The aim was to test whether the observed effect is due to the outward orientation of the fluorophores or was possibly caused by membrane permeable quencher. Therefore, (iii) asymmetric vesicles with FITC-PE in the inner leaflet were prepared (**Figure 4C**). The addition of KI to the FITC-PE vesicles showed no effect and a continuous, stable fluorescence (**Figure 4D**) which indicates that the membrane integrity is strong and impermeable to the quencher compared to conventional phospholipid-only membranes. This also demonstrates that in a time frame of 5 days no significant amounts of phospholipids flipped from inner to outer leaflet (**Figure 5**). In a few cases, lipid domains could be detected at room temperature (**Figure 6C**), which was not the case for temperatures above 25°C.

After successful confirmation of the asymmetric membrane structure, we wanted to find out if lipid flip-flop in LPS-containing asymmetric vesicles is possible at all. In a further quenching approach, aGUVs that resembled the natural Gram-negative membrane model were prepared. The inner PL layer was additionally enriched with a lipid-dye conjugate of the same lipid species (1% NBD-PE). By means of fluorescence spectroscopy we exposed the prepared aGUVs to sodium dithionite as quencher for a period of up to 5 days. By repeated measurements at different points in time (**Figure 5**) we could confirm that a lipid exchange from the inner PL layer to the outer LPS layer takes place. On the other hand, after 120 h, saturation was reached in which a maximum of ∼20% of the fluorescence-labeled lipid species in the outer layer could be detected due to progressing quenching. The sometimes strongly varying percentages are due to the size distribution of the prepared vesicles, since there is a certain

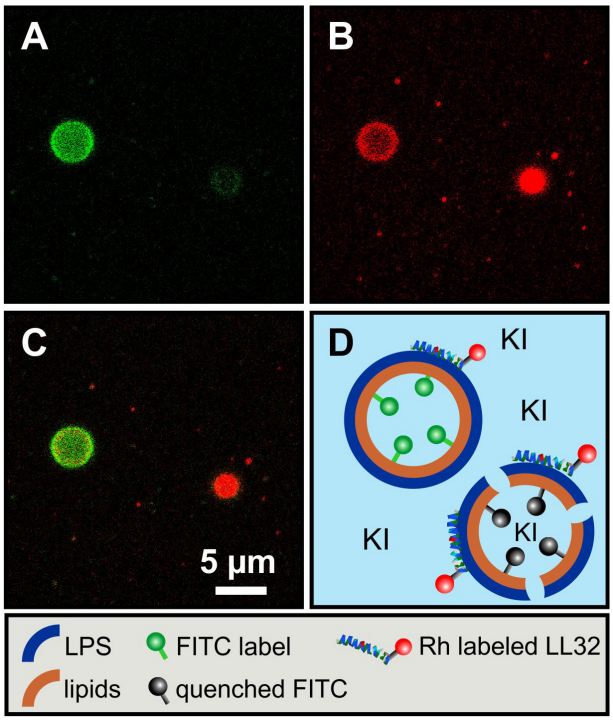

FIGURE 7 | Fluorescence quenching in asymmetric LPS R45/PL vesicles allows the observation of a concentration dependent permeabilization by antimicrobial peptide LL-32. For fluorescent labeling of the vesicles 2% (w/w) of the PL (PE:PG:CL; 81:17:2; w/w/w) in the inner leaflet were fluorescent FITC-PE. Images show the vesicles after incubation with 0.83 M KI and 38 nM ^{Rho}LL32. **(A)** FITC-PE fluorescence; **(B)** ^{Rho}LL-32 fluorescence; **(C)** Superposition of **(A)** and **(B)**; **(D)** Illustration of the experiment. The left vesicle had taken up less ^{Rho}LL-32, remained intact and therefore exhibited unquenched FITC fluorescence from its inner leaflet. The right vesicle had taken up more ^{Rho}LL-32, was permeabilized and partly quenched by invading KI. Experiments were carried out at 25°C in 100 mM KCl, 5 mM $MgCl_2$, 5 mM HEPES at pH 7.0 using a Leica TCS SP3 confocal microscope. Scale bar applies for **(A–C)**.

degree of heterogeneity due to the phase transfer method. The given maximum of 20% shows that if there is a flip-flop it cannot be higher that 20%; however, the decrease in fluorescence can also originate from a general leakage of some of the GUVs. Based on these data, we wanted to understand to what extent there is a connection between the lipid flip-flop and the microscopically visualized phase separation at temperatures below 25°C. More precisely, what happens first: Lipid flip-flop with subsequent phase separation or is there a phase separation already existing after aGUV preparation and the observed lipid flip-flop is created to compensate for other effects, such as membrane rigidity. To answer these questions, however, we looked at aGUVs in natural arrangement (LPS/PL), in inverse arrangement (PL/LPS), and uniform arrangement (LPS/LPS) microscopically. In order to be able to record effects between the individual layers, we used an approach in which both sides of the membrane were mixed with the same lipid-dye conjugate (Rho-DHPE) and an approach in which the inner and outer layers were provided with

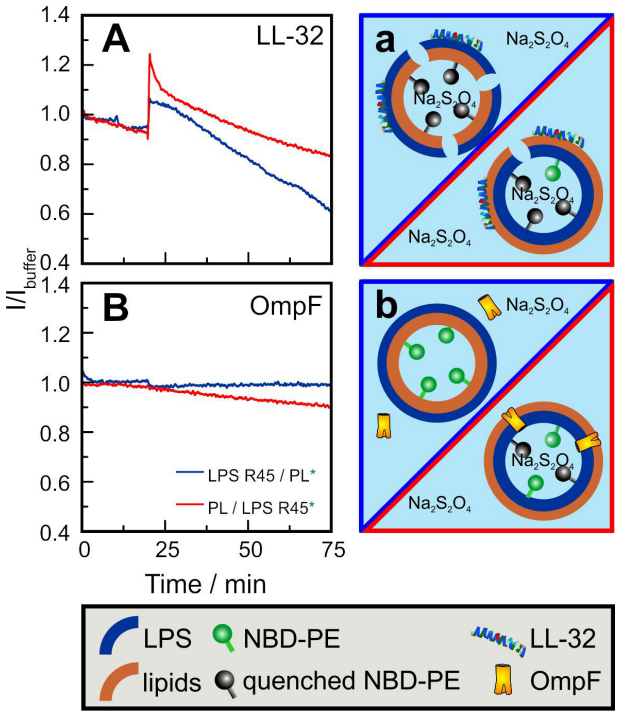

FIGURE 8 | Inner leaflet labeled asymmetric GUVs enable the determination of orientation-sensitive quencher-uptake dynamics through **(A,a)** LL-32 induced lesions and through **(B,b)** bacterial porin OmpF. GUVs prepared by the phase transfer method were composed of LPS R45 on the outer leaflet and the PL mixture (PE:PG:CL; 81:17:2; w/w/w) on the inner leaflet (**A:** blue curves; **a**:blue framing) and *vice versa* (**A:** red curves; **a:** red framing). After 10 min, $Na_2S_2O_4$ was added to a final concentration of 10 mM. **(A)** After 20 min, LL-32 was added to a final concentration of 30 μM. After a first intensity increase because of peptide insertion a decrease because of the quenching of the inner leaflet marker NBD-PE (2%) can be seen. **(B)** After 20 min OmpF was added to a final concentration of 5 μg/ml. Influx of the quencher $Na_2S_2O_4$ only occurs if the PL mixture is faced outward and directly exposed to the protein. Experiments were performed in 100 mM KCl, 5 mM $MgCl_2$, and 5 mM HEPES at pH 7.0 and at T = 37°C.

different dyes (1% NBD-PE and 0.5% Rho-DHPE). **Figure 6** shows the results of those approaches. The structure of the ^{Rho}LPS R45/PL membrane mimicking the natural composition does not show any separation (**Figure 6A**). We see an even fluorescence distribution over the z-stacks of these aGUVs. The situation becomes interesting when uniform ^{Rho}LPS R45/^{Rho}LPS R45 (**Figure 6B**) GUVs are viewed under the microscope: Here, there is a pronounced phase separation within the two layers in a registered manner (**Figure 6B**). At temperatures below 25°C phase separation in LPS/PL membranes could be observed in both leaflets of the ^{Rho}LPS R45/^{NBD}PL in a registered manner (**Figures 6C,c**). To check weather this effect is PL specific we prepared aGUVs composed of LPS extracted from different bacterial strains. Again, a strong phase separation was achieved when LPS layers of different species are prepared against each other (**Figures 6D,d**). We also detected a domain formation, but in an anti-registered manner in the individual layers of ^{NBD}LPS R45/^{Rho}LPS R595 aGUVs (**Figure 6D**).

Interaction of Asymmetric GUVs With Pore-Forming Peptides and Proteins

The usability of asymmetric GUVs to investigate the activity of pore-forming peptides or proteins and the importance of the asymmetric composition is demonstrated in the following by microscopic and spectroscopic experiments.

Fluorescence microscopy of asymmetric GUVs. First, we demonstrate the interaction between the asymmetric vesicles and the fluorescently labeled antimicrobial peptide ^{Rho}LL-32 by using confocal microscopy. This peptide can induce lesions and at higher concentrations it can permeabilize the membrane. We used asymmetric vesicles labeled with FITC-PE in the inner leaflet and added KI to the solution. ^{Rho}LL-32 was added, and the fluorescence of both fluorophores was imaged (**Figure 7**). After peptide addition some vesicles showed a weak fluorescence of ^{Rho}LL-32 and still a strong fluorescence of the inner leaflet (**Figure 7C**, left vesicle). This demonstrates that only a limited number of peptides have attached to the outer lipid leaflet. The required threshold concentration of LL-32 was not reached, which prevented the formation of pores. Due to the lack of pore formation, the quenching molecule was unable to permeate the membrane and thus quench the fluorescence of the inner leaflet. If the concentration of ^{Rho}LL-32 on the surface was higher (**Figure 7C**, right vesicle), the peptides could form pores leading to a permeabilization of the bilayer and a resulting decrease in the fluorescence of the FITC-PE. At higher peptide concentrations the GUVs were destroyed. This confirms that above a certain critical concentration, ^{Rho}LL-32 induces lesions large enough to allow the quencher to access the inside of the vesicles. The absolute peptide concentration can have significant variations within the sample because of the small volumes added on the microscopy slide. Therefore, these data cannot be used to determine the absolute concentration necessary to induce membrane permeabilization. Compared to other experiments the LL-32 concentration of 38 nM was very low.

Fluorescence spectroscopy of asymmetric GUVs. In a second approach, we used fluorescence spectroscopy to show that LL-32 and the porin OmpF interact differently with the different leaflets of the asymmetric GUVs. After the addition of LL-32 to aGUVs with NBD-PE labeled inner leaflet, a quick increase in fluorescence was observed for both membrane compositions LPS R45/PL (natural outside-out orientation) and PL/LPS R45 (inside-out orientation) (**Figure 8A**). This can be caused by the insertion of LL-32 into the lipid bilayer leading to a change in the fluorophore lateral organization, changes of aggregation of LL-32, and of further unknown artefacts. The effect of LL-32 and other fragments of the human cathelicidin on liposomes including the permeabilization and the increase in their diameter as determined by DLS experiments was described in detail before (De Miguel et al., 2019). After this initial step, the fluorescence decreased because of the permeation of the quenching molecules ($Na_2S_2O_4$) into the aGUVs. This effect was more pronounced for membranes in which the LPS R45 was present in the outer leaflet.

Because of the higher number of negative charges in the LPS compared to the PL mixture the interaction with the polycationic LL-32 was stronger and led to a more intensive permeabilization. Opposite to this effect it has been shown that porins intercalate only from the PL side into an asymmetric LPS/PL membrane, but not from the LPS side (Hagge et al., 2002). Exactly this effect was also observed in the presented results (**Figure 8B**). After addition of OmpF to aGUVs composed of LPS R45 on the outer leaflet no change in the fluorescence intensity was detected. Addition to inside-out aGUVs (lipid mixture as outer leaflet) led to a linear decrease in intensity. Unlike LL-32, OmpF molecules did not destabilize the overall membrane integrity, but allowed a continuous permeation of $Na_2S_2O_4$ molecules, which explains the slower decrease in fluorescence.

DISCUSSION

After Singer and Nicolson (1972) published their fluid mosaic model in 1971, M. BRETSCHER discussed the asymmetry in lipid membranes (Bretscher, 1972). Since then, a number of studies have shown how the lipid composition differs in the two leaflets of various membranes, what influence this has on the function (Gupta et al., 2020), localization and orientation of proteins, how asymmetry is established and maintained by active processes and which consequences changes in asymmetry can have. Despite all these advances, relatively little is still known about the underlying molecular processes. In recent years, techniques have been established to reconstitute asymmetric membranes that allow detailed characterization. In 2003, PAUTOT et al. presented a method by which the design of an asymmetric membrane was facilitated by phase transfer of two individual prepared lipid compartments (Pautot et al., 2003). Based on this approach, we developed a protocol that allowed the generation of asymmetric LPS-containing membranes in a size range between 2 μm to 20 μm. This size range resembles the size of living bacteria and enables the microscopic analysis of asymmetric membranes without solid support. For the first time, it was possible to prepare asymmetric vesicles with a pure LPS outer (natural) or even inner leaflet (unnatural) and phospholipids in the opposing leaflet. Furthermore, we can design vesicles composed of LPS on both leaflets with either LPS received from the same origin giving symmetric LPS vesicles with a uniform fatty acid chain distribution or LPS received from different origins giving asymmetric LPS vesicles with a non-uniform fatty acid chain distribution. In this study we used LPS purified from a deep rough mutant of *P. mirabilis* R45. This LPS preparation consists of a natural mixture of different number and length of fatty acids and other non-stoichiometric substituents. Therefore, domain formation driven by the different chemical species can occur. Furthermore, the phospholipids used to reconstitute the inner leaflet are a mixture of naturally occurring lipid species in PE, PG, and CL. The goal of this work was to generate the LPS/PL aGUVs, to compare their properties with those of planar lipid bilayers and solid supported membranes, to characterize their phase behavior, and to use them to analyze the lipid-dependent activity of the antimicrobial peptide LL-32 and the bacterial porin OmpF.

As early as, Brandenburg and Seydel (1990) reported for all enterobacterial LPS a gel to liquid crystalline phase transition occurring within a temperature range from 30°C to 37°C (Brandenburg and Seydel, 1990; Brandenburg et al., 1990) in buffer containing no divalent ions such as magnesium or calcium. The phase transition temperature for the herein used LPS R45 matches with around 35°C the literature values (Howe et al., 2007). Here, we used a buffer containing 5 mM $MgCl_2$. This increases the stability of the membranes, i.e., that of the planar lipid bilayers and it increases the phase transition temperature to 45°C. The PL mixture has a phase transition temperature below 20°C and the mixture of LPS and PL of 40°C (**Figure 1**).

The phase separation in LPS monolayers (**Figures 2A**, **3A**) can be explained easily. At 21°C and a lateral pressure of 20 mN/m most of the LPS molecules on the film balance were in a liquid condensed (LC) phase and some were in the liquid expanded (LE) phase. This led to a phase separation of the molecules (**Figure 2A**). This is in good agreement with the data obtained from the LPS monolayer prepared during the Montal-Mueller reconstitution of a planar membrane at 37°C (**Figure 3A**). The phospholipid molecules in the monolayers were all in the LE phase at 21°C (**Figures 2B**, **3B**) and showed therefore no phase separation. These results are consistent with that obtained from the FTIR experiments using liposomes. Now, the interesting part of the measurements was the behavior of the bilayers. The results of the experiments showed that there was no phase separation of the LPS molecules in asymmetric LPS/PL bilayers on a solid support (**Figures 2C,D**) or prepared as a planar lipid bilayer (**Figure 3C**). The two layers influenced each other by shifting the phase transition temperature of the LPS to lower temperatures. In case of the solid supported bilayers it did not matter whether the LPS or the PL mixture was oriented toward the mica.

By using the phase transfer method to reconstitute asymmetric GUVs, we prepared asymmetric vesicles composed of LPS in the outer and phospholipids in the inner leaflet for the first time. Maktabi et al. (2019) published in 2019 a method to produce asymmetric LPS-containing vesicles as water-in-oil-in-water double emulsions prepared by a microfluidics approach. Attempts to reconstitute asymmetric LPS-containing vesicles by cyclodextrin-catalysis (Doktorova et al., 2018) did not work out so far. We could show that the prepared vesicles were asymmetric and stayed asymmetric for more than 5 days. The average diameters of the prepared vesicles were about 5 μm and therefore they could be used as a good bacterial membrane model in different experimental setups. The size of the aGUVs can be adjusted by modifying the parameters of the preparation of the buffer droplets and by changing the ion concentrations of the buffer. To proof the asymmetry, we determined the potency of potassium iodide to quench the fluorescence of dyes which were in the LPS or in the phospholipid leaflet (**Figure 4**). Using fluorescence quenching, we have shown that the vesicles generated by phase transfer are indeed asymmetric and at the same time impermeable to potassium iodide. In addition, we have successfully demonstrated that the asymmetry remained stable over days. Therefore, we studied the lipid flip-flop rates. Bearing in mind that phospholipid flip-flop strongly depends on headgroups with a smaller dependence on acyl chain length and

that under physiological pH (pH 7.4) flip-flop rates increase in the order of PC < PG < PA < PE, we carried out our experiments on a cuvette scale, measuring the lipid flip-flop of fluorescence-labeled PE. In general, rates measured for PE are at least 10-times greater than those of PC (Rosoff, 1996). In the literature, large activation energies for flip-flop ranging from 38 kcal/mol for the longest acyl chain derivative of PC to 25 kcal/mol for the PE derivatives could be found (Rosoff, 1996). An increase in acyl chain length is linked to reduced phospholipid flip-flop rates whereas acidification, e.g., change in pH from pH 7.4 to 4.0 which is described for phagosome acidification, accelerate lipid flip-flop by 500-fold. The most frequent obstacle in the determination of lipid flip-flop is probably the strong dependence of the insolubility of the polar head groups in the intracellular space or the membrane interior, respectively. The flip-flop rate in our NBD-PE labeled GUVs was below 20% within five days (**Figure 5**). This was the flip-flop of the fluorescently labeled PE which might be reduced compared to unlabeled phospholipids. However, we propose that the flip-flop of the even larger LPS molecules composed of four glucans would not be higher. This is supported by the observation that the FITC-labeled LPS was exclusively in the outer leaflet after five days (data not shown). On a shorter time scale (up to 2 h) we investigated the asymmetry of LPS/PL planar membranes by measuring the inner membrane potential difference by the inner field compensation method (Hagge et al., 2004). Even within the first seconds and minutes the asymmetry of the bilayers was constant.

A decisive property for lipid membranes is the phase behavior and thus the lateral diffusion of lipids and proteins in the membrane. Differences in the lateral diffusion between the two leaflets have been shown by fluorescence imaging microscopy (Gupta et al., 2020). In case of plasma membranes, the diffusion coefficient is higher, and the domain confined diffusion of lipid probes is lower for the inner leaflet as compared to the outer leaflet. We showed that in the asymmetric LPS R45/PL aGUVs no domains were observable at temperatures above 25°C, but below 25°C domains in the outer and inner leaflet appeared in a registered phase (**Figure 6A**). Consequently, the phase transition temperature of around 25°C for asymmetric GUVs does not correspond to that of 42°C for mixed LPS R45/PL liposomes (SUVs). Therefore, we suggested that the inter-leaflet coupling between the LPS R45 leaflet and the PL leaflet is strong. In general, membrane domain registration and anti-registration describe the inter-leaflet domain dynamics, which are mainly determined by the inter-leaflet coupling (Zhang and Lin, 2019). In case of symmetric LPS R45/LPS R45 GUVs a clear registered domain formation could be observed (**Figure 6B**). Interestingly, in case of GUVs composed of LPS R45 on one leaflet and LPS R595 on the other leaflet a clear anti-registration could be observed (**Figure 6D**). Thus, both registration and anti-registration, can occur. Since, the natural LPS preparations are mixtures of different molecules with variations in number and length of the fatty acid chains and differences in the non-stoichiometric substitutions a simple interpretation of these data is not possible. Further experiments using various well-defined preparations will follow. Bossa et al. (2019) suggested that registered domains are not structurally but energetically connected across the bilayer. Furthermore, they define two distinct inter-leaflet coupling mechanisms: (i) a thermodynamically driven one due to the presence of a compositional mismatch between the two leaflets and (ii) a structurally driven one due to the presence of transmembrane proteins. WANG et al. observed in asymmetric vesicles that the inhibition of outer-leaflet ordered-domain formation by inner-leaflet lipids decreased. He explains this by an increased ability of outer-leaflet lipids to form an ordered state by themselves (Wang and London, 2018). From coarse-grained molecular dynamics simulations Fowler et al. (2016) proposed a two-step model in which membranes undergo a shift from an anti-registered phase to registered symmetric phase after bilayer equilibration. In summary, asymmetric LPS-containing bilayers can have registered and/or anti-registered phases of different sizes depending on temperature and lipid composition.

The asymmetry of membranes not only plays a decisive role in the thermodynamic behavior of pure lipid components but can also be decisive in the interaction with peptides and proteins. In many cases, proteins are responsible for the expression of asymmetry or its maintenance. Proteins, such as flippases, floppases, and scramblases influence the asymmetry in a targeted manner, but other proteins can also influence the distribution of lipids. On the other hand, asymmetry can have an influence on the binding, incorporation, orientation and functions of peptides and proteins. We used the polycationic antimicrobial peptide LL-32, which binds in a charge-dependent manner to lipid membranes. Therefore, the interaction with the highly negative charged LPS leaflet should be stronger than with the PL leaflet having a lower surface charge density (Hagge et al., 2006). Furthermore, it has been shown before that the permeabilization is strongly concentration-dependent (De Miguel et al., 2019). Both effects have been perfectly visible using the asymmetric LPS/PL GUVs. The micrographs in **Figure 7** demonstrate the ability to measure the permeabilization of the GUVs by the influx of small quenching molecules such as KI. Only in case of a high enough LL-32 concentration pores or lesions were induced. Fluorescence spectroscopy allowed to integrate the effects over many aGUVs. The addition of LL-32 led to a fast increase of the fluorescence of the lipid-bound dye located in the inner leaflet by reducing the self-quenching caused by an insertion of the peptide into the hydrophobic region of the bilayer (**Figure 8**). After the initial increase, the fluorescence decreased because of an influx of the quenching molecule $Na_2S_2O_4$ into the vesicle. In case of GUVs composed of LPS on the outer leaflet the permeabilization is more pronounced as compared to the one composed of PL on the outer leaflet. Bacterial porins intercalate into lipid membranes depending on the asymmetry of the bilayer. It has been shown for PhoE that the insertion only occurs from the PL side but not from the LPS side of planar lipid bilayers (Hagge et al., 2002). OmpF shows the same behavior using Montal-Mueller membranes (to be published elsewhere). The same effect can be seen in the quenching experiments using the asymmetric GUVs composed of LPS or PL on the outer leaflet. Only in case of PL facing the outer leaflet OmpF addition led to protein insertion into the bilayers inducing influx of the quencher (**Figure 8**).

In summary, asymmetric GUVs are an excellent tool to characterize specific membrane properties and their influence on the interaction with peptides and proteins. It has been shown that asymmetric membranes are more than just the sum of their two halves and that the function of proteins is strongly influenced by the specific lipid asymmetry. Therefore, asymmetric GUVs mimic the outer membrane of Gram-negative bacteria more closely and comprise a unique tool to test and study the lipid-mediated resistance of bacteria.

DATA AVAILABILITY STATEMENT

All datasets presented in this study are included in the article/**Supplementary Material**.

AUTHOR CONTRIBUTIONS

LP and AD contributed equally to the manuscript. AD, MK, LP, and TG designed the experiments. AB performed the AFM experiments. SH performed the Montal-Mueller experiments. AD, SG, and LP prepared asymmetric vesicles. MK and LP conducted the fluorescence microscopy. SG performed the lipid flip-flop and fluorescence spectroscopic experiments. MW contributed reagents and materials. AD prepared the first draft of the manuscript. LP, TG, and CN wrote the manuscript. All authors contributed to the interpretation of primary data and the discussion.

FUNDING

TG, LP, and CN acknowledges funding by the Deutsche Forschungsgemeinschaft (DFG, German Research Foundation) under Germany's Excellence Strategy – EXC 2167-390884018 and the DFG priority program (SPP1580) and by the Phospholipid Research Center, Heidelberg. LP acknowledges funding by the Joachim Herz Foundation under Add-on Fellowship for Interdisciplinary Science.

ACKNOWLEDGMENTS

We thank Larissa Mohr and Kerstin Stephan for their excellent technical assistance and support. We thank our in-house facilities of the Research Center Borstel Leibniz Lung Center for their contribution: Rainer Bartels and Volker Grote for peptide synthesis, Dominik Schwudke and his team for mass spectrometric analysis. Uwe Mammat for LPS cultivation and provision of the strains.

SUPPLEMENTARY MATERIAL

The Supplementary Material for this article can be found online at: https://www.frontiersin.org/articles/10.3389/fcell.2020.00586/full#supplementary-material

REFERENCES

Alexander, C., and Rietschel, E. T. (2001). Bacterial lipopolysaccharides and innate immunity. *J. Endotoxin. Res.* 7, 167–202. doi: 10.1179/096805101101532675

Blodgett, K. B. (1934). Monomolecular films of fatty acids on glass. *J. Am. Chem. Soc.* 56, 495–495. doi: 10.1021/ja01317a513

Bossa, G. V., Gunderson, S., Downing, R., and May, S. (2019). Role of transmembrane proteins for phase separation and domain registration in asymmetric lipid bilayers. *Biomolecules* 9:303. doi: 10.3390/biom9080303

Brandenburg, K., Koch, M. H., and Seydel, U. (1990). Phase diagram of lipid A from *Salmonella* minnesota and *Escherichia coli* rough mutant lipopolysaccharide. *J. Struct. Biol.* 105, 11–21. doi: 10.1016/1047-8477(90)90093-r

Brandenburg, K., and Seydel, U. (1990). Investigation into the fluidity of lipopolysaccharide and free lipid A membrane systems by Fourier-transform infrared spectroscopy and differential scanning calorimetry. *Eur. J. Biochem.* 191, 229–236. doi: 10.1111/j.1432-1033.1990.tb19114.x

Bretscher, M. S. (1972). Asymmetrical lipid bilayer structure for biological membranes. *Nat. New Biol.* 236, 11–12. doi: 10.1038/newbio236011a0

Cheng, H. T., and London, M. E. (2009). Preparation and properties of asymmetric vesicles that mimic cell membranes: effect upon lipid raft formation and transmembrane helix orientation. *J. Biol. Chem.* 284, 6079–6092. doi: 10.1074/jbc.M806077200

Colthup, N. B., Lawrence, H., and Daly, S. E. W. (1990). *Introduction to Infrared and Raman Spectroscopy*, 3rd Edn. Boston, MA: Academic Press.

Cronan, J. E., and Vagelos, P. R. (1972). Metabolism and function of the membrane phospholipids of *Escherichia coli*. *Biochim. Biophys. Acta* 265, 25–60. doi: 10.1016/0304-4157(72)90018-4

De Miguel, C. A. E., Forbrig, J. K., Nehls, C., Paulowski, L., Gutsmann, T., Hildebrandt, P., et al. (2019). The C-Terminal VPRTES Tail of LL-37 influences the mode of attachment to a lipid bilayer and antimicrobial activity. *Biochemistry* 58, 2447–2462. doi: 10.1021/acs.biochem.8b01297

Doktorova, M., Heberle, F. A., Eicher, B., Standaert, R. F., Katsaras, J., London, E., et al. (2018). Preparation of asymmetric phospholipid vesicles for use as cell membrane models. *Nat. Protoc.* 13, 2086–2101. doi: 10.1038/s41596-018-0033-6

Fowler, P. W., Williamson, J. J., Sansom, M. S., and Olmsted, P. D. (2016). Roles of interleaflet coupling and hydrophobic mismatch in lipid membrane phase-separation kinetics. *J. Am. Chem. Soc.* 138, 11633–11642. doi: 10.1021/jacs.6b04880

Galanos, C., Luderitz, O., and Westphal, O. (1969). A new method for the extraction of R lipopolysaccharides. *Eur. J. Biochem.* 9, 245–249. doi: 10.1111/j.1432-1033.1969.tb00601.x

Gupta, A., Korte, T., Herrmann, A., and Wohland, T. (2020). Plasma membrane asymmetry of lipid organization: fluorescence lifetime microscopy and correlation spectroscopy analysis. *J. Lipid Res.* 61, 252–266. doi: 10.1194/jlr.D119000364

Gutsmann, T., Heimburg, T., Keyser, U., Mahendran, K. R., and Winterhalter, M. (2015). Protein reconstitution into freestanding planar lipid membranes for electrophysiological characterization. *Nat. Protoc.* 10, 188–198. doi: 10.1038/nprot.2015.003

Hagge, S. O., de Cock, H., Gutsmann, T., Beckers, F., Seydel, U., and Wiese, A. (2002). Pore formation and function of phosphoporin PhoE of *Escherichia coli* are determined by the core sugar moiety of lipopolysaccharide. *J. Biol. Chem.* 277, 34247–34253. doi: 10.1074/jbc.M201950200

Hagge, S. O., Hammer, M. U., Wiese, A., Seydel, U., and Gutsmann, T. (2006). Calcium adsorption and displacement: characterization of lipid monolayers and their interaction with membrane-active peptides/proteins. *BMC Biochem.* 7:15. doi: 10.1186/1471-2091-7-15

Hagge, S. O., Wiese, A., Seydel, U., and Gutsmann, T. (2004). Inner field compensation as a tool for the characterization of asymmetric membranes and Peptide-membrane interactions. *Biophys. J.* 86, 913–922. doi: 10.1016/S0006-3495(04)74167-3

Howe, J., Andra, J., Conde, R., Iriarte, M., Garidel, P., Koch, M. H., et al. (2007). Thermodynamic analysis of the lipopolysaccharide-dependent resistance of gram-negative bacteria against polymyxin B. *Biophys. J.* 92, 2796–2805. doi: 10.1529/biophysj.106.095711

Kent, S. B. (1988). Chemical synthesis of peptides and proteins. *Annu. Rev. Biochem.* 57, 957–989. doi: 10.1146/annurev.bi.57.070188.004521

Kornberg, R. D., and McConnell, H. M. (1971). Inside-outside transitions of phospholipids in vesicle membranes. *Biochemistry* 10, 1111–1120. doi: 10.1021/bi00783a003

Lamichhane, U., Islam, T., Prasad, S., Weingart, H., Mahendran, K. R., and Winterhalter, M. (2013). Peptide translocation through the mesoscopic channel: binding kinetics at the single molecule level. *Eur. Biophys. J.* 42, 363–369. doi: 10.1007/s00249-012-0885-6

Maktabi, S., Schertzer, J. W., and Chiarot, P. R. (2019). Dewetting-induced formation and mechanical properties of synthetic bacterial outer membrane models (GUVs) with controlled inner-leaflet lipid composition. *Soft Matter* 15, 3938–3948. doi: 10.1039/c9sm00223e

Marčelja, S. (1974). Chain ordering in liquid crystals: II. Structure of bilayer membranes. *Biochim. Biophys. Acta Biomemb.* 367, 165–176.

Marquardt, D., Geier, B., and Pabst, G. (2015). Asymmetric lipid membranes: towards more realistic model systems. *Membranes (Basel)* 5, 180–196. doi: 10.3390/membranes5020180

Montal, M., and Mueller, P. (1972). Formation of bimolecular membranes from lipid monolayers and a study of their electrical properties. *Proc. Natl. Acad. Sci. U.S.A.* 69, 3561–3566. doi: 10.1073/pnas.69.12.3561

Osborn, M. J., Gander, J. E., Parisi, E., and Carson, J. (1972). Mechanism of assembly of the outer membrane of *Salmonella* typhimurium. Isolation and characterization of cytoplasmic and outer membrane. *J. Biol. Chem.* 247, 3962–3972.

Pautot, S., Frisken, B. J., and Weitz, D. A. (2003). Engineering asymmetric vesicles. *Proc. Natl. Acad. Sci. U.S.A.* 100, 10718–10721. doi: 10.1073/pnas.1931005100

Rinia, H. A., Demel, R. A., van der Eerden, J. P., and de Kruijff, B. (1999). Blistering of langmuir-blodgett bilayers containing anionic phospholipids as observed by atomic force microscopy. *Biophys. J.* 77, 1683–1693. doi: 10.1016/S0006-3495(99)77015-3

Rivel, T., Ramseyer, C., and Yesylevskyy, S. (2019). The asymmetry of plasma membranes and their cholesterol content influence the uptake of cisplatin. *Sci. Rep.* 9:5627. doi: 10.1038/s41598-019-41903-w

Roes, S., Seydel, U., and Gutsmann, T. (2005). Probing the properties of lipopolysaccharide monolayers and their interaction with the antimicrobial peptide polymyxin B by atomic force microscopy. *Langmuir* 21, 6970–6978. doi: 10.1021/la048218c

Rosoff, M. (1996). *Vesicles*, Vol. 62. Boca Raton, FL: CRC Press.

Shaw, N. (1974). Lipid composition as a guide to the classification of bacteria. *Adv. Appl. Microbiol.* 17, 63–108. doi: 10.1016/s0065-2164(08)70555-0

Singer, S. J., and Nicolson, G. L. (1972). "The fluid mosaic model of the structure of cell membranes," in *Membranes and Viruses in Immunopathology*, eds S. B. Day and R. A. Good (Washington, DC: American Association for the Advancement of Science), 7–47. doi: 10.1016/b978-0-12-207250-5.50008-7

Van Meer, G., Voelker, D. R., and Feigenson, G. W. (2008). Membrane lipids: where they are and how they behave. *Nat. Rev. Mol. Cell Biol.* 9, 112–124. doi: 10.1038/nrm2330

Wang, Q., and London, E. (2018). Lipid structure and composition control consequences of interleaflet coupling in asymmetric vesicles. *Biophys. J.* 115, 664–678. doi: 10.1016/j.bpj.2018.07.011

Wiese, A., Munstermann, M., Gutsmann, T., Lindner, B., Kawahara, K., Zahringer, U., et al. (1998). Molecular mechanisms of polymyxin B-membrane interactions: direct correlation between surface charge density and self-promoted transport. *J. Membr. Biol.* 162, 127–138. doi: 10.1007/s002329900350

Wiese, A., and Seydel, U. (2000). Electrophysiological measurements on reconstituted outer membranes. *Methods Mol. Biol.* 145, 355–370. doi: 10.1385/1-59259-052-7:355

Zachowski, A. (1993). Phospholipids in animal eukaryotic membranes: transverse asymmetry and movement. *Biochem. J.* 294(Pt 1), 1–14. doi: 10.1042/bj2940001

Zhang, S., and Lin, X. (2019). Lipid acyl chain cis double bond position modulates membrane domain registration/anti-registration. *J. Am. Chem. Soc.* 141, 15884–15890. doi: 10.1021/jacs.9b06977

Conflict of Interest: The authors declare that the research was conducted in the absence of any commercial or financial relationships that could be construed as a potential conflict of interest.

frontiers in Cell and Developmental Biology

ORIGINAL RESEARCH
published: 21 July 2020
doi: 10.3389/fcell.2020.00575

Simulations of Asymmetric Membranes Illustrate Cooperative Leaflet Coupling and Lipid Adaptability

*Madison Blumer[1,2], Sophia Harris[1], Mengzhe Li[1,3], Luis Martinez[1], Michael Untereiner[1,4], Peter N. Saeta[1], Timothy S. Carpenter[5], Helgi I. Ingólfsson[5] and W. F. Drew Bennett[5]**

[1] Harvey Mudd College, Claremont, CA, United States, [2] Scripps College, Claremont, CA, United States, [3] Claremont McKenna College, Claremont, CA, United States, [4] Pomona College, Claremont, CA, United States, [5] Biochemical and Biophysical Systems Group, Biosciences and Biotechnology Division, Lawrence Livermore National Laboratory, Livermore, CA, United States

OPEN ACCESS

Edited by:
Rainer A. Böckmann,
University of Erlangen-Nuremberg, Germany

Reviewed by:
Kristyna Pluhackova,
ETH Zürich, Switzerland
Tomasz Rog,
University of Helsinki, Finland
Matti Javanainen,
Institute of Organic Chemistry and Biochemistry, Academy of Sciences of the Czech Republic (ASCR), Czechia

***Correspondence:**
W. F. Drew Bennett
bennett69@llnl.gov

Specialty section:
This article was submitted to Cellular Biochemistry, a section of the journal Frontiers in Cell and Developmental Biology

Received: 01 February 2020
Accepted: 15 June 2020
Published: 21 July 2020

Citation:
Blumer M, Harris S, Li M, Martinez L, Untereiner M, Saeta PN, Carpenter TS, Ingólfsson HI and Bennett WFD (2020) Simulations of Asymmetric Membranes Illustrate Cooperative Leaflet Coupling and Lipid Adaptability. Front. Cell Dev. Biol. 8:575. doi: 10.3389/fcell.2020.00575

Biological membranes are composed of lipid bilayers that are often asymmetric with regards to the lipid composition and/or aqueous solvent they separate. Studying lipid asymmetry both experimentally and computationally is challenging. Molecular dynamics simulations of lipid bilayers with asymmetry are difficult due to finite system sizes and time scales accessible to simulations. Due to the very slow flip-flop rate for phospholipids, one must first choose how many lipids are on each side of the bilayer, but the resulting bilayer may be unstable (or metastable) due to differing tensile and compressive forces between leaflets. Here we use molecular dynamics simulations to investigate a number of different asymmetric membrane systems, both with atomistic and coarse-grained models. Asymmetries studied include differences in number of lipids, lipid composition (unsaturated and saturated tails and different headgroups), and chemical gradients between the aqueous phases. Extensive analysis of the bilayers' properties such as area per lipid, density, and lateral pressure profiles are used to characterize bilayer asymmetry. We also address how cholesterol (which flip-flops relatively quickly) influences membrane asymmetries. Our results show how each leaflet is influenced by the other and can mitigate the structural changes to the bilayer overall structure. Cholesterol can respond to changes in bilayer asymmetry to alleviate some of the effect on the bilayer structure, but that will alter its leaflet distribution, which in turn affects its chemical potential. Ionic imbalances are shown to have a modest change in bilayer structure, despite large changes in the electrostatic potential. Bilayer asymmetry can also induce a modest electrostatic potential across the membrane. Our results highlight the importance of membrane asymmetry on bilayer properties, the influence of lipid headgroups, tails and cholesterol on asymmetry, and the ability of lipids to adapt to different environments.

Keywords: lipid membrane, membrane asymmetry, molecular dynamic simulations, cholesterol, multiscale modeling

INTRODUCTION

Lipid membranes separate organelles and cells from their exterior environments. Lipids can spontaneously assemble into a bilayer, which is the basic structure of cell membranes. These lipid bilayers function as a selective barrier to molecular entry/exit for the cell and serve as planar platforms for colocalizing various cell machinery. Because of their small scale, complexity and fluid phase behavior, it is difficult to study lipid bilayers directly, particularly *in vivo*. It has been long established that most cellular membranes have an asymmetric distribution of lipids between the inner and outer bilayer leaflets. Quantifying lipid compositions in either leaflet, transleaflet exchange (flip-flop), how cells create and maintain asymmetry, and the biological and physical effects of membrane asymmetry remain open research areas.

There are a number of ways that a membrane can exhibit asymmetry: different numbers of lipids, different types of lipids, asymmetric proteins, and by separating chemically different aqueous compartments. Removing lipids from one leaflet creates a stress in the membrane and can result in membrane curvature. Extreme examples are small unilamellar vesicles, which have high curvature and different numbers of lipids in either leaflet. In cells, regions of high curvature, such as membrane tubules, exosomes, and during vesicle fission/fusion, can results in lipid asymmetry (Callan-Jones et al., 2011; Skotland et al., 2017; Gruenberg, 2020). Cells tightly control the transbilayer distribution of lipids. Mammalian plasma membranes have phosphatidylcholine and sphingomyelin enriched in the outer leaflet and phosphatidylethanolamine and phosphatidylserine enriched in the inner leaflet (Van Meer et al., 2008; Lorent et al., 2020). The localization of cholesterol and rate of flip-flop remains debated (Lange and Steck, 2008; Mondal et al., 2009; Steck and Lange, 2018). Disruption of the membrane asymmetry with phosphatidylserine exposure on the outer leaflet is an important cell signal, for example during apoptosis (Van Meer et al., 2008). *In vivo* this is even more complex, because domains or lipid rafts can cause a heterogenous lipid distribution within the same leaflet. Considerable effort has been spent studying the interplay between lipid phase separation in one leaflet and asymmetric distribution of lipids across the membrane (Collins and Keller, 2008; Perlmutter and Sachs, 2011). A main question is if and how ordered domains enriched in cholesterol and sphingomyelin in the external leaflet can induce domains in the inner leaflet. Complexity is furthered by the active transport of lipids across membranes by transmembrane proteins. Additionally, cells tightly control the ion and osmotic gradients across the membrane with transmembrane protein channels and transporters. Key examples of how cells actively use the electrostatic potential difference are nerve cell propagation and energy production. The situation is even more complex, because the activity of the channels and transporters that create and maintain these asymmetries are in turn affected by their local lipid and ionic environment. Teasing out the interplay between the physicochemical effects of asymmetry and biological processes is ongoing.

Advances in computer simulations of lipid bilayers have made simulating complex and more biologically relevant membranes possible. This is exemplified by recent simulations on a realistic plasma membrane (Marrink et al., 2019), a neuronal membrane (Ingólfsson et al., 2017), bacterial membranes (Khalid et al., 2015), and entire organelles, such as a chromatophore vesicle (Singharoy et al., 2019). While at the outset it seems trivial for one to set up an asymmetric membrane *in silico*, as one can simply place lipids on one side or the other, there are problems that can create artifacts (Park et al., 2015; Huber et al., 2019). Finite system sizes means small bilayer patches are necessary, which can influence asymmetry effects, such as membrane bending. Simulation times that are very short compared to slow lipid movements, such as phospholipid flip-flop (McNamee and McConnell, 1973; Tieleman and Marrink, 2006; Bennett et al., 2009b; Marquardt et al., 2017), can influence simulation results. Including transmembrane proteins that have asymmetric shape further complicates this problem. Therefore, one *can* simulate nearly any asymmetry one chooses, but deciding what is relevant is a more difficult problem. Using the Martini coarse-grained (CG) model (Marrink et al., 2007), it was shown that even completely removing one leaflet (i.e., infinite asymmetry) was possible in relatively short and small simulations due to the strong stabilizing effect of periodic boundary conditions (Esteban-Martín et al., 2009), and slow time scale for phospholipid flip-flop. Another example showed that a CG simulation of a POPC membrane with 15 mol% difference in the number of lipids between leaflets was metastable, and applying a small pressure to break the metastability resulted in a membrane bud forming (Siggel et al., 2019). A transmembrane scramblase protein was then shown to alleviate the asymmetry.

To date most molecular dynamics (MD) simulations of lipid bilayers have been symmetric in the composition of their two leaflets. Many simulations of complex asymmetric bilayers have chosen the composition based on matching the average area per lipid (APL) of symmetric bilayers that represent each of the different desired leaflets (Huber et al., 2019). Recent work by Doktorova and Weinstein (2018) suggest that an asymmetric membrane should be constructed not just so the overall membrane tension is zero but so the tension in each leaflet is zero. Subsequently Hossein and Deserno (2020) showed that differential stress can still exist within membranes with non-zero tension, suggesting a detailed balancing of compositional and lateral stress is needed for balancing the physical effects of asymmetry. There has also been a number of simulations investigating the role of ion and lipid gradients on the transmembrane electrostatic potential (Gurtovenko and Vattulainen, 2007; Gurtovenko and Lyulina, 2014). Large ion imbalances lead to membrane electroporation, where a water filled pore forms across the bilayer, which has also been studied extensively with simulations (Gurtovenko and Vattulainen, 2005; Böckmann et al., 2008; Gurtovenko et al., 2010). MD simulations have also looked at cholesterol in lipid domains and have provided physical insight into domain registration for asymmetric membranes (Perlmutter and Sachs, 2011; Tian et al., 2016). Simulations have shown how liquid-ordered domains

on one leaflet can promote more order in the opposite leaflet (Perlmutter and Sachs, 2011; Tian et al., 2016).

We have conducted a systematic investigation of different types of membranes simulated with multiscale simulation protocols. This work provides detailed physical insights in membrane asymmetry with biological implications as well as interesting technical details for the simulation community. MD simulations using atomistic and CG models of lipid bilayer asymmetry are presented and the bilayers' properties are analyzed and compared. We address a number of asymmetric membrane scenarios: a gradual change in asymmetry, different numbers of lipids, different types of lipid, and ion imbalances, with and without cholesterol. We calculate lipid properties and bilayer properties, including lipid density profiles, electrostatic potentials, lipid order parameters, APL, cholesterol flip-flop and lateral pressure profiles. These results show how changes in lipid asymmetry can have modest to no effect on some membrane properties but rather large changes for other properties, emphasizing when more detailed attention to asymmetry is necessary. By comparing atomistic and CG models, we can assess model and chemical differences and inform future work. Simulations with cholesterol illustrate how lipids that can flip-flop readily can alter the asymmetry and influence the resulting membrane properties.

MATERIALS AND METHODS

Large CG Lipid Membrane Simulations and Setup

We set up the larger CG lipid bilayers with varying degrees of asymmetry using the Martini tool *insane* (Wassenaar et al., 2015). These where simulated at the CG resolution only, contained up to 222 lipids in each leaflet and were run with an asymmetric DPSM (d18:1/18:0-sphingomyelin), POPC (16:0/18:1-PC), and PAPE (16:0/20:4-phosphatidylethanolamine) lipid mixture with a 40/40/20 ratio in the upper leaflet and 10/40/50 in the lower leaflet. Simulations were done with and without a high 50 mol% cholesterol content with lipid count asymmetry ranging from 0 to 35 lipids from the lower leaflet. All simulations were setup with 150 mM NaCl (∼75 beads each) and >15 CG water beads per lipid (∼6700 beads), corresponding to >60 waters per lipid.

Small CG and AA Lipid Membrane Simulation Setup

Systems with up to 64 lipids in each leaflet were setup with DPPC (16:0-PC) and DIPC (18:2-PC) in both leaflets, with 0, 5, or 10 lipids removed from one leaflet (e.g., DPPC_5). Asymmetric membranes with DPPC in one leaflet and DIPC in the other were simulated [DIPC(upper)/DPPC(lower)], and with 5 and 10 lipids removed from the DIPC leaflet (e.g., DPPC_0_DIPC_5). Each system was simulated at the atomistic and CG resolution and with and without ∼30 mol% cholesterol (relative to the upper layer) placed in each leaflet at the start of the simulation (replacing the PC lipid to maintain 64 lipids). Simulations were done with an asymmetric bilayer with DPPE (16:0-PE) in the upper leaflet and DPPC in the lower leaflet (headgroup asymmetry), both with 64 lipids. Additionally, at the CG resolution a larger range of asymmetries for the DIPC(upper)/DPPC(lower) were simulated (see **Supplementary Figure S3**). Each system contained 150 mM NaCl (∼22 beads each) and ∼2000 CG water beads. We set up double bilayer systems by replicating a single bilayer twice in the z-dimension. For asymmetric bilayers we also flipped the bilayer leaflets, so that the upper and lower are on opposite sides for the two bilayers. To create ion imbalances, we simply changed one sodium to a chloride in one water bath and chloride to sodium in the other, leading to a 4e imbalance.

Martini Simulations

We used the Martini CG force field v2.0 (Marrink et al., 2007) and a recent (unpublished) version of cholesterol that updated the shape of the original cholesterol model (Marrink et al., 2007) similar to the updated cholesterol model described in Melo et al. (2015) but without using virtual-sites. A 20 fs time step was used with the leap-frog algorithm and the new-rf Martini simulation parameters (De Jong et al., 2016). Each of the 64 lipids per leaflet simulations was simulated for 2 μs at 333 K and the 222 lipids per leaflet simulations for 10 μs at 320 K, both using the velocity rescale thermostat (Bussi et al., 2007) with a 12 ps time constant. The systems with DPPE were simulated at 340 K to be above the melting temperature for DPPE. Semi-isotropic pressure coupling was used with Berendsen barostat (Berendsen et al., 1984) with 1 bar pressure, a compressibility of 3×10^{-4} bar^{-1}, and a relaxation time of 12 ps. Electrostatics were computed using the reaction-field method, with a dielectric constant of 15 within a 1.1 nm cutoff and infinite beyond the cutoff.

Atomistic Simulations

CHARMM36 lipids (Klauda et al., 2010) with CHARMM specific (Durell et al., 1994; Neria et al., 1996) TIP3P water (Jorgensen et al., 1983) were simulated with GROMACS v5.1.4 (Van Der Spoel et al., 2005; Abraham et al., 2015). The starting structure was taken from the 200 ns frame of the Martini CG model and back mapped to CHARMM36 using the Backward method (Wassenaar et al., 2014). Simulations were then continued using a 2 fs time step, with four replicates of 250 ns, with the final 200 ns from each used for analysis. Lennard-Jones interactions were cut-off after 1.2 nm, with a force-switch-function from 1.0 to 1.2 nm. Long-range electrostatic interactions were calculated with the particle mesh Ewald method (Darden et al., 1993; Essmann et al., 1995). Temperature was maintained at 333 K using the Nose-Hoover thermostat (Martyna et al., 1992) with a time constant of 1 ps. Semi-isotropic pressure coupling was used to maintain a constant pressure of 1 bar lateral and normal to the plane of the bilayer. The Parrinello-Rahman barostat (Parrinello and Rahman, 1981) was used with a compressibility of 4.5×10^{-5} and a coupling constant of 5 ps. Water was constrained with the SETTLE method (Miyamoto and Kollman, 1992), and hydrogens on lipids with P-LINCS (Hess et al., 1997; Hess, 2008).

Simulation Analyses

After the simulations we used a variety of computational methods to analyze the lipid membrane systems. The different analysis

methods use a combination of GROMACS tools, custom Python scripts using MDAnalysis (Michaud-Agrawal et al., 2011; Melcr et al., 2018; Antila et al., 2019). as well as the FATSLiM program (Buchoux, 2016) for APL calculations using Voronoi tessellation and membrane thickness calculations. The atomistic lipid tail order parameter was calculated using:

$$S_{CH} = < 3\ cos^2\ \theta - 1 > /2$$

where θ is the angle between the C-H bond and the normal to bilayer. This was calculated using an analysis script in MDAnalysis (Michaud-Agrawal et al., 2011; Melcr et al., 2018; Antila et al., 2019). Density and electrostatic profiles were calculated with an in-house script using MDAnalysis (Michaud-Agrawal et al., 2011). The electrostatic profile was determined using the method of Sachs et al. (2004), where the partial charge distribution across the membrane is integrated twice to give the electrostatic potential. For electrostatic potentials with asymmetry, we used a double bilayer set-up, allowing the two water chambers to have different ion concentrations.

The lateral pressure profile (LPP) was calculated using a modified version of GROMACS (Vanegas et al., 2014; Torres-Sánchez et al., 2015). The local stress is calculated by post-processing the trajectory file which returns a local stress file for the simulation averaged over the user-selected time range. We used the Goetz-Loetsky force decomposition and a grid spacing of 0.1 nm for atomistic and 0.15 nm for CG simulations. The local stress tensor (σ) is extracted from the binary file using the program tensortools (Vanegas et al., 2014; Torres-Sánchez et al., 2015), the LPP estimated as $(\sigma_{xx} + \sigma_{yy})/2$ and the leaflet surface tension (ST) for the upper and lower leaflet as the integral from the bilayer center of mass to the box end on either side. Note, for asymmetric bilayers the center of mass is not the exact center of the integrated LPP (where either leaflet has equal amplitude but opposite sign) but for the mixture simulated in **Figure 1** the difference was within error of the LPP calculations see upper/lower symmetry in ST (**Figure 1F**).

Cholesterol exhibits the unique ability among the lipids used in this paper to flip from one leaflet to another over the course of a simulation. To investigate the effect of cholesterol mobility on asymmetry, we calculated the number of cholesterol molecules in each leaflet during the CG simulations. We considered cholesterols belonging to each leaflet if the ROH beads were >1.2 nm from the leaflet as defined by MDAnalysis leaflet finder using the non-flip-flopping lipids PO4 beads.

The combined analysis tools and a pipeline for setting up CG simulations is available, as is, on GitHub[1].

RESULTS

CG Membrane Asymmetry

To explore the desired lipid number asymmetry for complex asymmetrical bilayers we systematically simulated the asymmetric DPSM/POPC/PAPE mixture with 40:40:20 lipid ratio in the upper and 10:40:50 ratio in the lower leaflet, both with and without added 50 mol% cholesterol (**Figure 1**). In this mixture the upper leaflet has significantly more lipids with saturated tails (DPSM) and less with high level of unsaturation (PAPE) compared to the lower leaflet. The upper leaflet should therefore want to have a smaller APL than the lower leaflet. In a periodic system with a fixed number of lipids this would translate into a lipid number asymmetry with fewer lipids on the lower leaflet than the upper one. To determine what the number asymmetry should be, we systematically reduced the number of lipids in the lower leaflet, simulating 4–5 repeats at each asymmetry value ranging from 0 to 35 random lipids removed from the lower leaflet (reaching a number asymmetry of ∼16%). For the cholesterol-containing systems, both leaflets start with an equal amount of cholesterol, which then flip-flops between the leaflets. **Figure 1B** shows the cholesterol fraction in the upper and lower leaflets average over the last 2 ms (∼5% of the cholesterol is transitioning or resides in the bilayer middle and is excluded from this analysis). There is a net drive to move cholesterol from the lower leaflet into the upper leaflet, until a leaflet number asymmetry of 31 (14%) where the drive reverses.

Figure 1C shows the APL for systems with (right) and without (left) cholesterol as the number asymmetry increases. The APL increases for the lower leaflet and decreases for the upper leaflet in both systems as lipids are removed from the lower leaflet. The increase in the lower leaflet APL is ∼2% higher in amplitude than the decrease in the upper leaflet APL. For the same systems the bilayer thickness changes very little (∼0.02 nm) with increased asymmetry (**Figure 1D**, note the y-axes narrow range). With enough simulations the trend in thickness change can be picked up showing a reduced bilayer thickness with fewer lipids in both system types, with an interesting initial increase in thickness in the systems without cholesterol.

Figure 1E shows the LPP along the z-axis with increased number asymmetry, where each profile is the average of the 4–5 repeated simulations with a few outliers removed (**Supplementary Figures S1, S2**). For the systems without cholesterol in the upper leaflet (on the left of the LPP plots), the LPP starts with a deeper minimum and a shallower maximum which then reverses as the number asymmetry increases. This is the opposite for the lower leaflet (right side of the LPP plots). For the cholesterol containing systems the trend is less clear due to the lower relative change in the LPP profile and more complex shape. With increased number asymmetry the minimum for the upper leaflet (left side of the LPP plots) reduces in amplitude as well as the central maximum and the opposite holds for the maximum of the lower leaflet (right side of the LPP plots). **Figure 1F** quantifies the ST for each leaflet in all the systems (the integral of the LPP to the bilayer center). Both with and without cholesterol the amplitude and the ST difference between the leaflets reduces as the number asymmetry increases, and then flips sign and increases again. The amplitude in the cholesterol-containing systems is notably smaller in spite of the high range of the LPPs. The zero ST is reached at an asymmetry of 15–16 without cholesterol and 14–15 with cholesterol (**Figure 1C** dashed lines). For comparison asymmetry estimates from the APL ratio of symmetric upper and

[1]https://github.com/llnl-hmc-clinic/Bilayer-Simulation-Pipeline

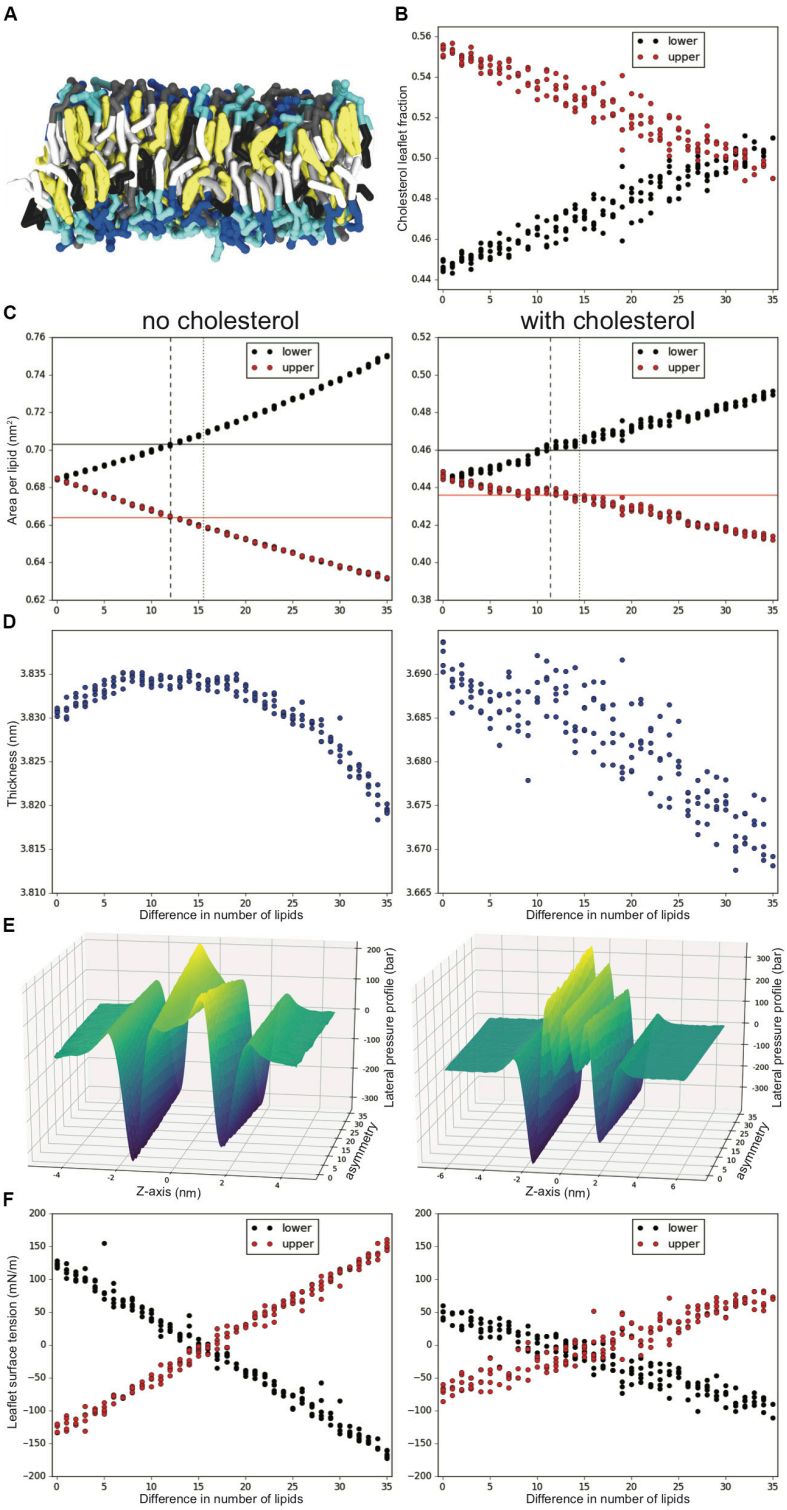

FIGURE 1 | Tuning lipid number asymmetry for an asymmetric DPSM/POPC/PAPE 40:40:20 upper and 10:40:50 lower mixture, with and without 50% cholesterol. **(A)** Snapshot showing a sideview of a simulation with cholesterol and a difference in number asymmetry of 20 lipids. Tails are colored white, gray and black for 0, 1, and 4 double bonds, cholesterol is yellow and the headgroups are gray, blue and cyan for SM, PC and PE, respectively. **(B)** Cholesterol fraction in the upper and lower leaflet of each system. **(C)** Upper and lower leaflet APL for increased lipid number asymmetry. APL for symmetric upper (red) and symmetric lower (black) are shown in solid lines. Suggested number asymmetry value for this mixture from ratio of symmetric simulations and minimal leaflet ST are shown in dashed and dotted lines, respectively. **(D)** Bilayer thickness. **(E)** LPPs averaged over repeat simulations and outliers removed (**Supplementary Figure S1**). **(F)** Upper and lower leaflet ST. All analysis is averaged over the last 2 ms of the 10 ms simulations and there are 4–5 repeats for each lipid number asymmetry value.

symmetric lower simulations give 12.1 (without cholesterol) and 11.4 (with cholesterol) (**Figure 1C** dotted lines).

To address the local effects of leaflet asymmetry in more detail, we compared atomistic and CG simulations of small bilayer patches composed of pure DPPC and pure DIPC. **Figure 2** shows the density plots for the different CG bilayers. For the pure bilayers, a ∼8% (5 lipids) and ∼15% (10 lipids) difference in composition had a negligible effect on the lipid bilayer density. Particularly for the DIPC bilayer, the profiles are nearly identical. We then simulated a mixed bilayer with one leaflet DPPC and the other DIPC. The DIPC(upper)/DPPC(lower) bilayers had substantial changes, with a density in between the pure DPPC and DIPC density profiles (**Figure 2C**). Both leaflets respond in opposite directions, indicating that the DPPC leaflets became more fluid and the DIPC leaflets more structured. Similar to the pure bilayers, changing the number of lipids in the mixed bilayers (removing 5 DIPC), also had little effect on the density.

Table 1 lists the APL for each of the lipids in either the upper or lower leaflet. As expected, the leaflets with fewer lipids have a higher APL, and the ones with more lipids have a lower APL, compared to the pure bilayers. The mixed DIPC(upper)/DPPC(lower) bilayer has an APL in between the pure DPPC and DIPC membranes, as expected from the density profile. **Supplementary Figure S3** plots the APL for the DIPC(upper)/DPPC(lower) bilayers as a function of the number of lipids removed from the DIPC(upper) leaflet. For reference, we also plot the APL for each type of lipid in pure symmetric bilayers (horizontal lines). The vertical line indicates the suggested asymmetry from symmetrical upper/lower leaflet simulations N(upper) = N(lower) × apl (lower)/apl(upper), which gives 51.8, or ∼12 fewer lipids for the DIPC(upper) leaflet.

We tested the effect of adding 30 mol% cholesterol to each of the bilayers. Cholesterol is able to flip-flop on a time scale accessible to CG simulations. This means that cholesterol is able to equilibrate between leaflets and affect the asymmetric bilayers structure. **Supplementary Figure S4** shows how the number of cholesterol molecules changes during the CG simulations. **Supplementary Figure S4A** shows relatively slow exchange of cholesterol in the saturated DPPC bilayer and very fast exchange in the DIPC bilayer. For the asymmetric DIPC(upper)/DPPC(lower) bilayer, the cholesterol molecules concentrate in the DPPC leaflet, depleting the DIPC leaflet. These results match expectations from numerous previous studies on cholesterol flip-flop and chemical potential (Bennett et al., 2009a; Jo et al., 2010; Javanainen and Martinez-Seara, 2019). We note that the final structure at 200 ns was used to start the atomistic simulations. For the atomistic saturated DPPC bilayers, the cholesterol does not undergo flip-flop over the 1 μs of simulation, and rarely for the DIPC bilayer (**Supplementary Figure S5**). For the DPPC_0 system, we know that the cholesterol distribution must be equal, so we picked a frame (175 ns) that has an equal distribution of cholesterol, as opposed to the frame at 200 ns, which has an asymmetric distribution of cholesterol. For the asymmetric membranes, it is not clear that we have the correct distribution of cholesterol, because its chemical potential might be different in the two leaflets. It is not clear that the chemical potential difference between the CG and AA model would be the same, so we chose the frame at the end of the simulation. Future work could incorporate free energy calculations and/or simulate an ensemble of CG frames for AA conversion.

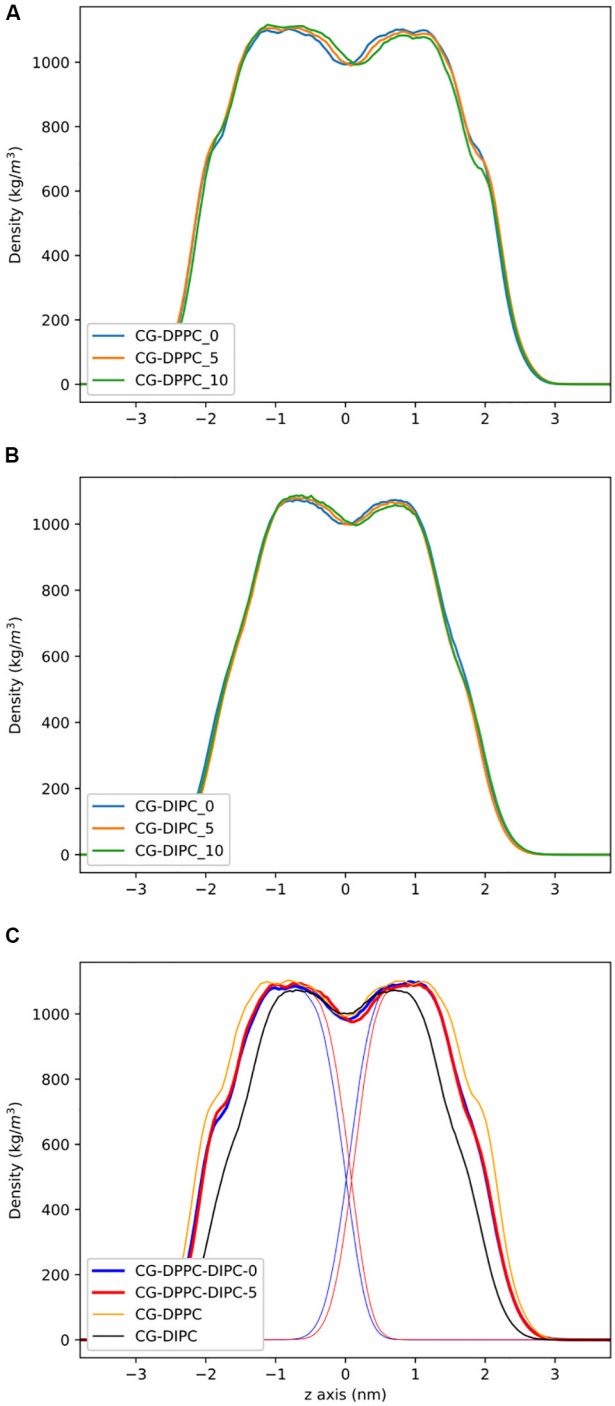

FIGURE 2 | Partial density profiles for the CG lipid bilayers without cholesterol. **(A)** Profiles for DPPC. **(B)** Partial densities for DIPC. **(C)** DIPC(upper)/DPPC(lower) bilayers, with thin lines showing the individual DIPC or DPPC densities.

TABLE 1 | Area per phospholipid for the CG lipid bilayers.

Name	Mol% cholesterol	DPPC (lower)	DPPC (upper)	DIPC (lower)	DIPC (upper)
DPPC_0	0	0.644 (0.001)	0.644 (0.001)		
DPPC_5	0	0.620 (0.002)	0.672 (0.002)		
DPPC_10	0	0.605 (0.001)	0.715 (0.001)		
DIPC_0	0			0.795 (0.001)	0.795 (0.001)
DIPC_5	0			0.768 (0.001)	0.831 (0.001)
DIPC_10	0			0.742 (0.001)	0.878 (0.001)
DPPC_DIPC_0	0	0.702 (0.002)			0.702 (0.002)
DPPC_DIPC_5	0	0.668 (0.001)			0.725 (0.001)
DPPC_DIPC_10	0	0.638 (0.001)			0.755 (0.001)
DPPC_0	30	0.522 (0.001)	0.525 (0.0036)		
DPPC_5	30	0.512 (0.004)	0.521 (0.0073)		
DPPC_10	30	0.512 (0.004)	0.523 (0.0093)		
DIPC_0	30			0.662 (0.002)	0.661 (0.003)
DIPC_5	30			0.649 (0.004)	0.665 (0.005)
DIPC_10	30			0.633 (0.003)	0.673 (0.006)
DPPC_DIPC_0	30	0.494 (0.003)			0.679 (0.004)
DPPC_DIPC_5	30	0.488 (0.003)			0.696 (0.007)

Error is shown in parentheses and units are nm^2.

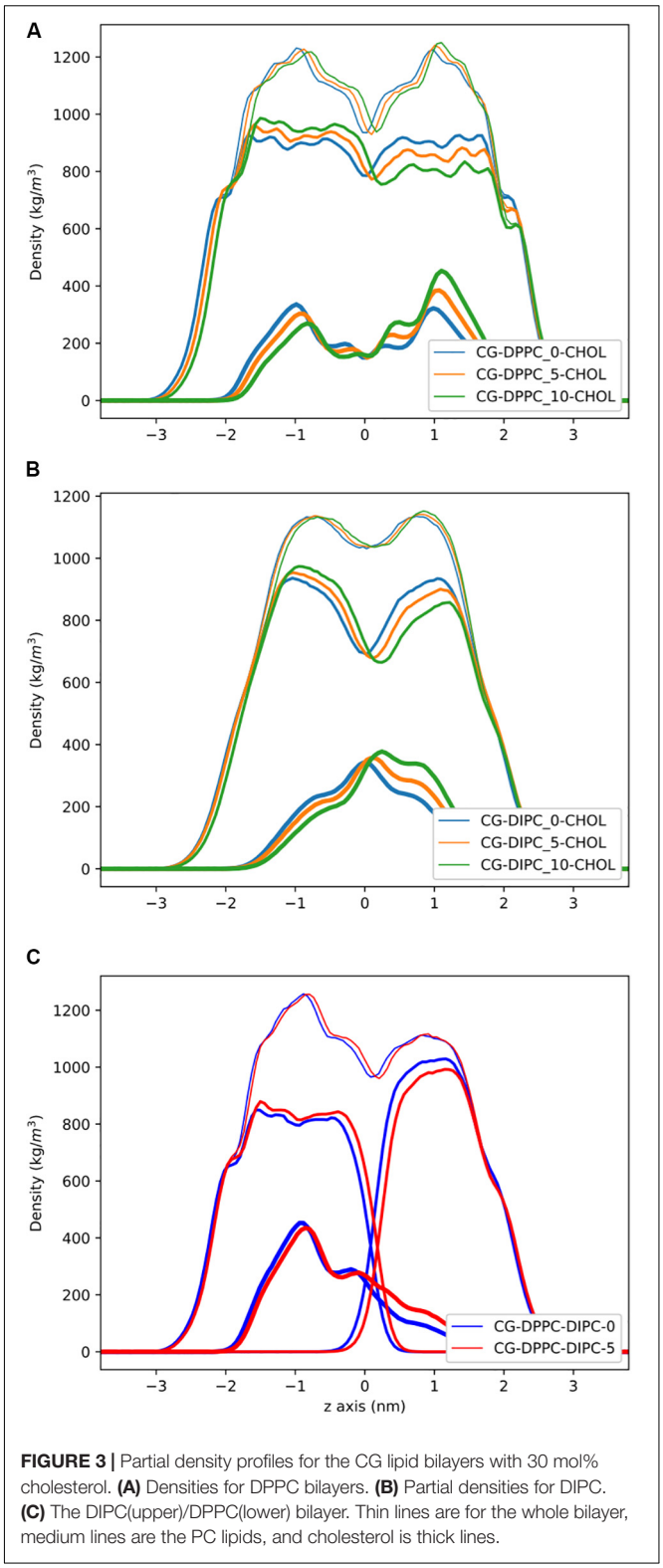

FIGURE 3 | Partial density profiles for the CG lipid bilayers with 30 mol% cholesterol. **(A)** Densities for DPPC bilayers. **(B)** Partial densities for DIPC. **(C)** The DIPC(upper)/DPPC(lower) bilayer. Thin lines are for the whole bilayer, medium lines are the PC lipids, and cholesterol is thick lines.

Figure 3 shows the partial density profiles for the CG bilayers with 30 mol% cholesterol. These profiles show more substantial differences compared to the pure PC bilayers, but the same trends as bilayers without cholesterol. Notably, the DIPC and the DPPC densities have substantial differences compared to the symmetric bilayers, as well as cholesterol, but the overall bilayer density is similar for the asymmetric bilayers. **Figure 3C** illustrates how cholesterol is concentrated in the DPPC leaflet in the DIPC(upper)/DPPC(lower) bilayer. The APL for each CG bilayer are listed in **Table 1** and show very modest changes with respect to the symmetric bilayers. Overall, the APL is much lower than the bilayers without cholesterol, due to cholesterols condensing effect.

Lateral pressure profiles are an important property of lipid membranes, as they show the stress/pressure at each slice through the lipid membrane. **Figure 4** shows the LPPs for the CG model with pure DPPC, pure DIPC, and both with 30 mol% cholesterol. For the pure bilayers, there is a large negative peak at the headgroup region and a shallow peak at the center of the membrane. Removing lipids from one leaflet of the DPPC bilayers has little effect on the height of the lateral pressure peak and trough (**Figure 4A**). There is a shift in the LPPS in the region

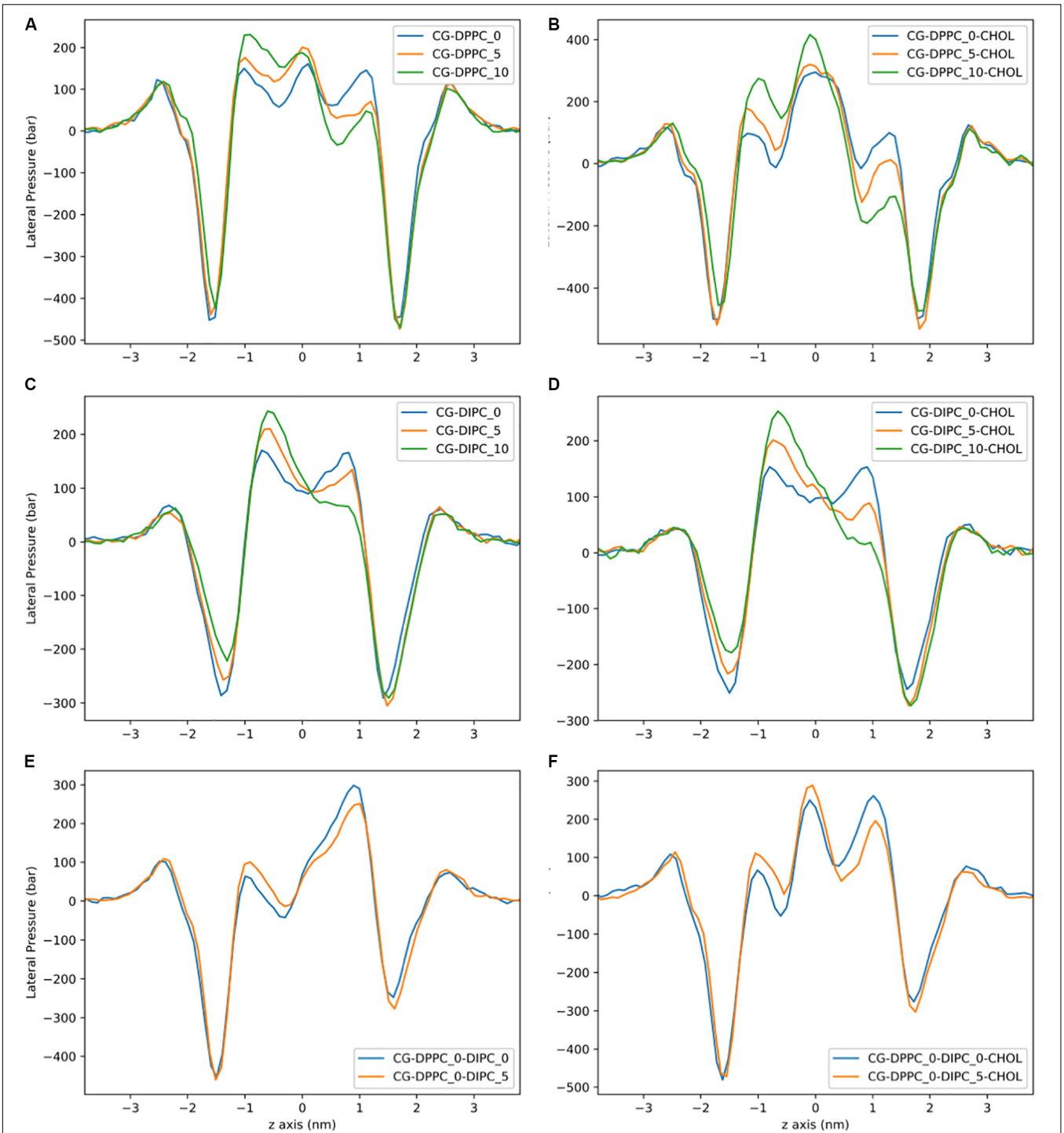

FIGURE 4 | Lateral pressure profiles for CG bilayers with asymmetric number of lipids between leaflets. **(A)** DPPC. **(B)** DPPC:CHOL. **(C)** DIPC. **(D)** DIPC:CHOL. **(E)** DIPC(upper)/DPPC(lower). **(F)** DIPC(upper)/DPPC(lower):CHOL.

corresponding to the middle of the lipid tails. A similar trend is observed for the polyunsaturated DIPC bilayers, although a slight decrease in pressure at the headgroup is also observed (**Figure 4B**). The magnitude of the pressures for the unsaturated DIPC bilayers are substantially lower than the saturated DPPC bilayers. Compared to the pure DPPC bilayers, LPPs for DPPC with 30 mol% cholesterol have a similar trend when removing lipids, but a much lower trough in pressure at the bilayer center (**Figure 4C**). The LPPs for the DIPC bilayers with and without cholesterol are very similar (**Figure 4D** compared to **Figure 4B**).

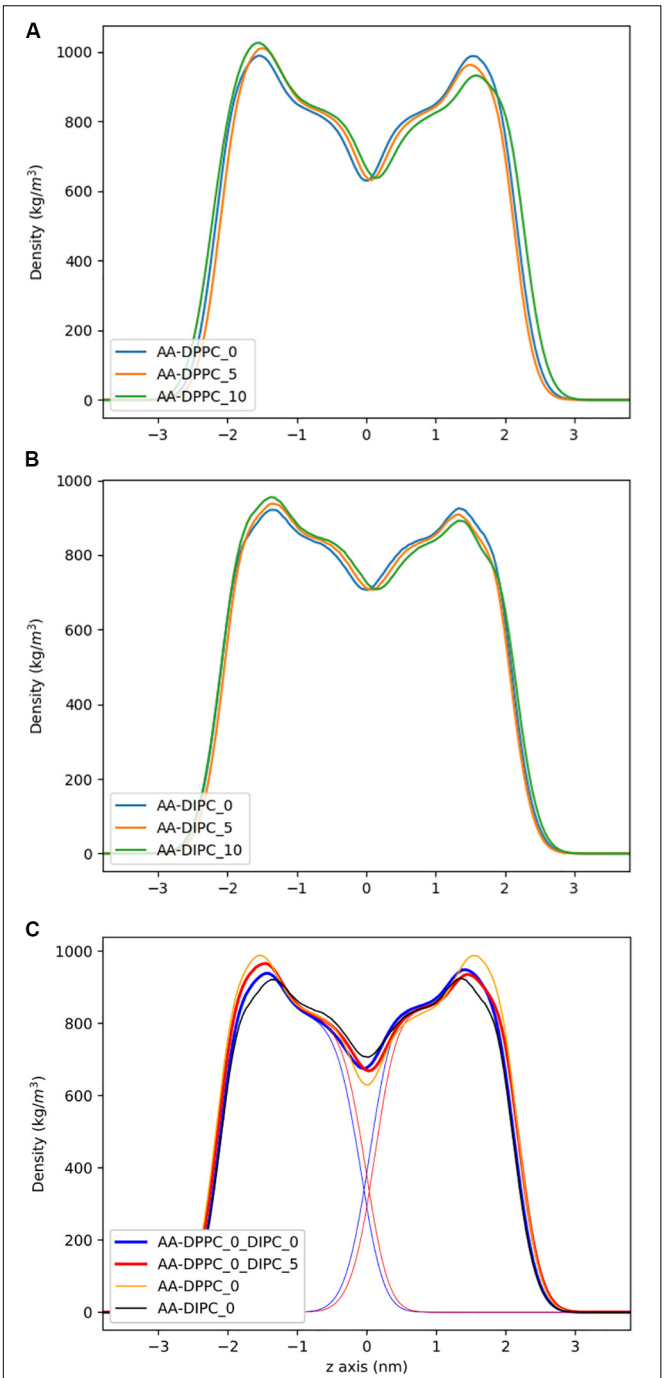

FIGURE 5 | Partial density profiles for the AA bilayers without cholesterol. **(A)** DPPC density profiles. **(B)** DIPC density profiles. **(C)** Asymmetric bilayers with DPPC in one leaflet (lower) and DIPC in the other (upper). Thin lines are for densities for DPPC or DIPC lipids separately.

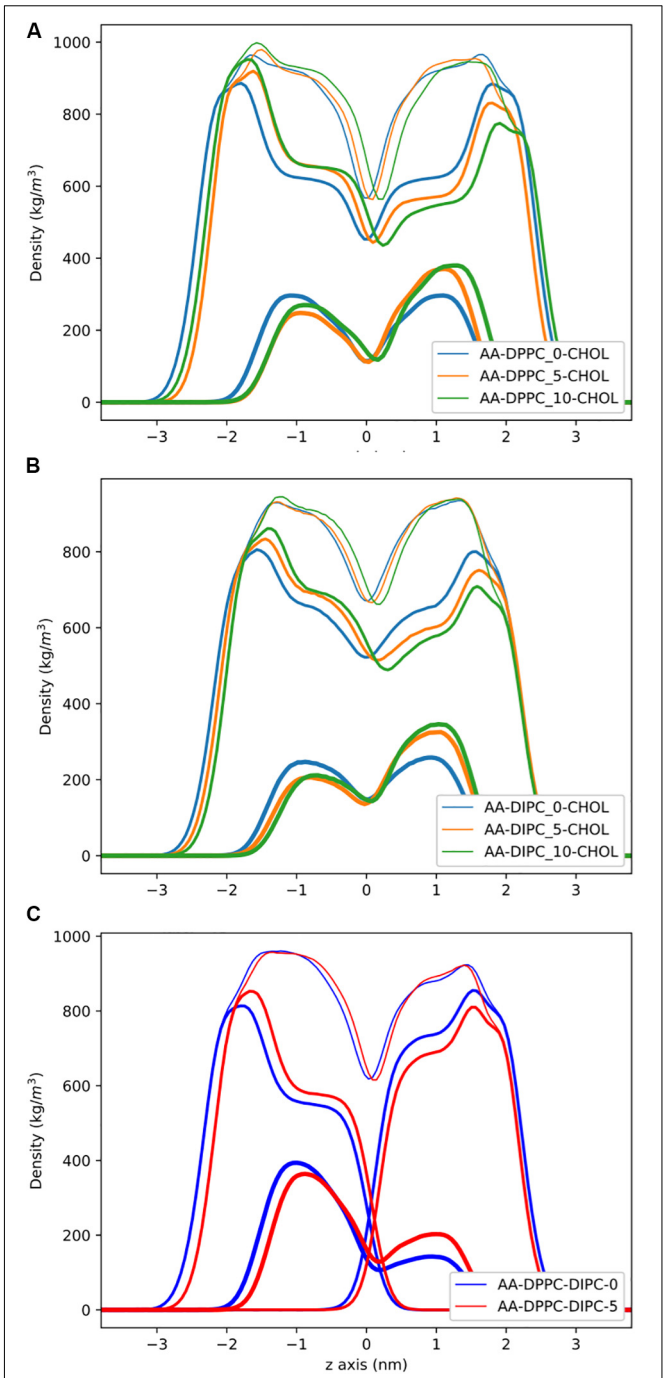

FIGURE 6 | Partial density profiles for the AA lipid bilayers with 30 mol% cholesterol. **(A)** Profiles for DPPC. **(B)** Partial densities for DIPC. **(C)** Bilayers with asymmetric DPPC in one leaflet and DIPC in the other. Thin lines are for the whole bilayer, medium lines are the PC lipids, and cholesterol is thick lines.

AA Membrane Asymmetry

We tested the effect of membrane asymmetry on the structure of atomistic lipid membranes by simulating bilayers with the CHARMM36 lipids (AA). For each system, after 200 ns of CG simulation, the membrane structure was used to back map to an atomistic bilayer, using the Backward method (Wassenaar et al., 2014), and the AA simulation started. **Figure 5** shows the resulting partial density profiles for the phospholipids in the membranes. These profiles show that without cholesterol the

TABLE 2 | Area per phospholipid for the AA bilayers.

Name	Mol% cholesterol	DPPC (lower)	DPPC (upper)	DIPC (lower)	DIPC (upper)
DPPC_0	0	0.623 (0.003)	0.623 (0.002)		
DPPC_5	0	0.602 (0.001)	0.651 (0.001)		
DPPC_10	0	0.583 (0.001)	0.687 (0.001)		
DIPC_0	0			0.721 (0.001)	0.721 (0.001)
DIPC_5	0			0.696 (0.001)	0.753 (0.001)
DIPC_10	0			0.667 (0.002)	0.797 (0.002)
DPPC_DIPC_0	0	0.678 (0.001)			0.678 (0.001)
DPPC_DIPC_5	0	0.646 (0.001)			0.699 (0.001)
DPPC_0	30	0.558 (0.001)	0.529 (0.001)		
DPPC_5	30	0.550 (0.002)	0.534 (0.001)		
DPPC_10	30	0.518 (0.001)	0.561 (0.002)		
DIPC_0	30			0.641 (0.007)	0.632 (0.003)
DIPC_5	30			0.621 (0.006)	0.642 (0.002)
DIPC_10	30			0.620 (0.004)	0.651 (0.024)
DPPC_DIPC_0	30	0.524 (0.003)			0.677 (0.006)
DPPC_DIPC_5	30	0.522 (0.003)			0.675 (0.009)

Error is shown in parentheses and units are nm^2.

bilayer's partial density is modified slightly by relatively large changes in the number of lipids in each leaflet. As expected, the leaflet with fewer lipids resulted in a slightly lower density, and the one with more resulted in a larger density compared to the symmetric bilayers. The differences in density are more pronounced than the CG density differences (**Figure 2**).

The APL was also calculated for each AA lipid bilayer (**Table 2**). The results show a trend expected from the shift in density profiles. By removing lipids in one leaflet, the opposite leaflet compensates, so the APL increases in the leaflet with fewer lipids and decreases in the leaflet with more lipids, compared to the pure bilayer. The DIPC(upper)/DPPC(lower) membrane has an APL in between the pure DPPC and pure DIPC areas per lipid.

Partial density profiles for the AA bilayer with cholesterol are shown in **Figure 6**. Similar to the CG results, we observe substantial differences in the PC lipid density, by removing lipids in one leaflet, but the cholesterol density compensates, and the overall bilayer density has little change. The DIPC(upper)/DPPC(lower) bilayer with cholesterol, shows a substantial concentration of cholesterol in the lower DPPC bilayer, causing a large difference in the overall bilayers density between leaflets. This matches the results from the CG model. The DIPC(upper)/DPPC(lower) bilayer with five fewer lipids in the DIPC bilayer has a similar trend as the pure PC membranes, with cholesterol compensating for asymmetric PC density. This results in very similar overall bilayer densities for the DIPC(upper)/DPPC(lower) bilayer with and without equal number of lipids in either leaflet. The APL for the AA cholesterol membranes (**Table 2**) have the same trends as the CG membranes, with little changes in area when lipids are removed from only one leaflet.

To assess the effect of asymmetry on the individual lipid's structures, we calculated the lipid tail's order parameter. The order parameter is a measure of the membranes ordering, based on the lipid tails alignment with the membrane normal. A value of 0 indicates no ordering and 1 completely ordered. **Figure 7A** shows that the bilayers compensate for the change in number of lipids by the leaflet with more lipids becoming more ordered, and the leaflet with fewer lipids becoming less ordered. **Figure 7B** shows that the DPPC lipids are more ordered with cholesterol, and the effect of asymmetry is reduced. For the 5 DPPC lipid difference, we observe the opposite trend as the other membranes, with the leaflet with more lipids having a slightly lower order parameter, and the one with fewer lipids more ordered. This could be due to an artifact of having the wrong distribution of cholesterol from the starting CG structure, although the difference is quite small. Future work explicitly studying cholesterol's chemical potential would be of interest to properly assess this discrepancy.

We calculated the order parameter for DPPC lipids in the mixed composition membranes (**Figure 7C**). In the DIPC(upper)/DPPC(lower) membrane the DPPC molecules have less order, as they are forced to compensate for the more disordered lipids in the opposite leaflet. We also tested the effect of asymmetric membranes with different headgroups, with DPPC in one leaflet and DPPE in the other. The DPPC in the DPPE(upper)/DPPC(lower) bilayer had high order, with a very similar profile as the DPPC_5 upper leaflet. This illustrates how the leaflets can compensate for the other, with the DPPC becoming more ordered to accommodate the DPPE in the opposite leaflet, with a much lower APL. With 30 mol% cholesterol (**Figure 7D**), there are interesting differences, with the DPPC lipids in the DIPC(upper)/DPPC(lower) mixed membranes having a higher order parameter compared to the pure DPPC bilayer. This is due to the increased concentration of cholesterol in the DPPC leaflet.

The LPPs for the AA bilayers are shown in **Figure 8**. These pressure profiles have large local pressures of hundreds of bars. For the pure DPPC bilayers, there is a very large trough in the pressure at the headgroup region, and a large positive peak at the bilayer center. Removing lipids from one leaflet has an effect on the depth of the trough at the DPPC headgroup region and no effect on the height of the peak at the bilayer center. Similar to the CG model, the biggest change in the pressure profile is observed in the lipid tail region of the DPPC bilayers. Similar behavior is observed for the pure DIPC bilayers (**Figure 8B**), but with less of an effect compared to DPPC. The bilayers with 30 mol%

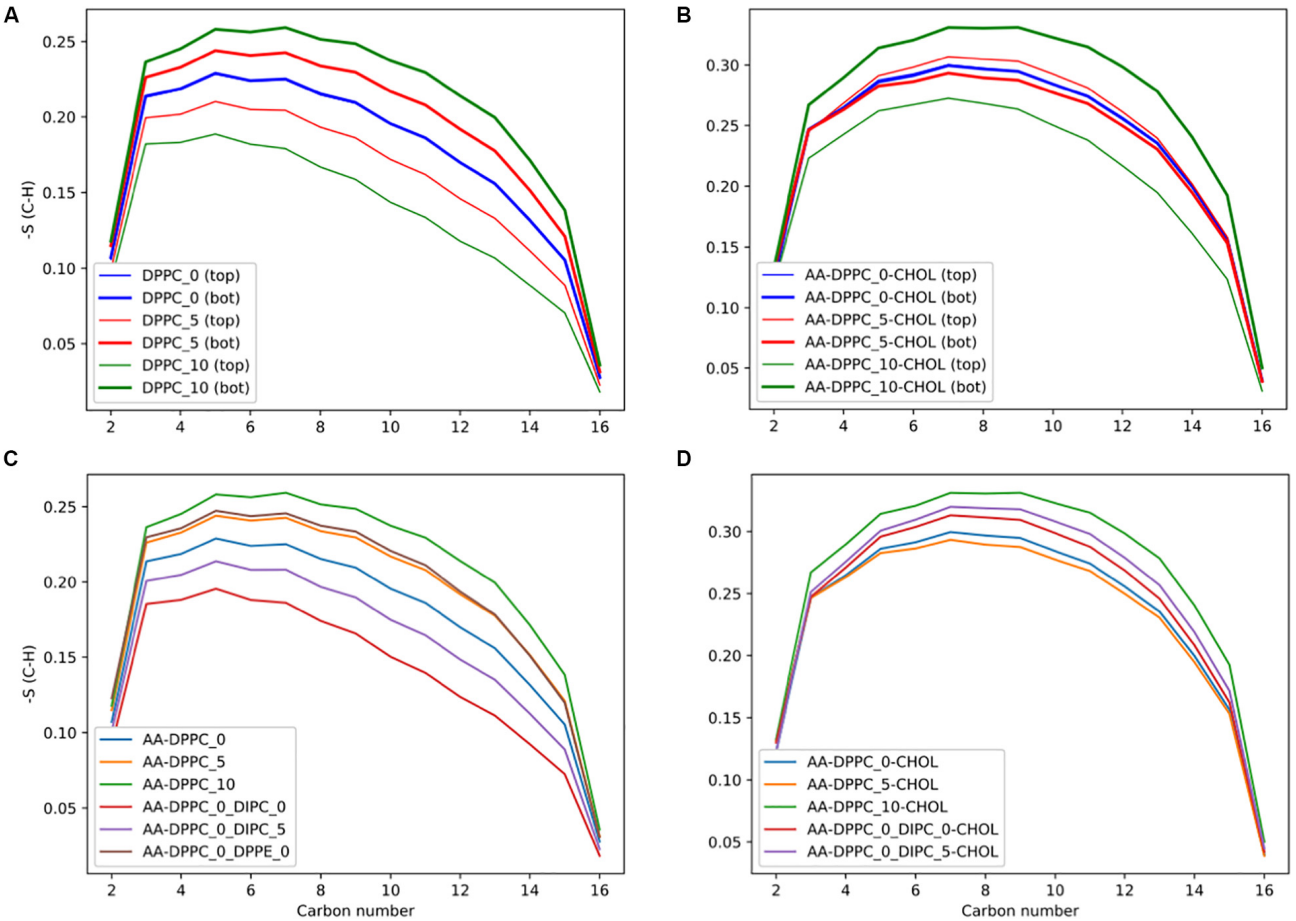

FIGURE 7 | DPPC lipid chain order parameters for the DPPC's *sn*-2 chain. **(A)** Order parameters for the pure DPPC bilayer, comparing the top and bottom leaflets, and **(B)** with 30 mol% cholesterol. **(C)** Comparing order parameters for the top leaflet in the different membranes with compositional asymmetry, and **(D)** with 30 mol% cholesterol.

cholesterol have qualitatively different pressure profiles, with larger pressures, and a second headgroup trough and headgroup peak, compared to the bilayers without cholesterol. This behavior has been observed in other simulations of cholesterol (Shahane et al., 2019). The cholesterol bilayers show a substantial shift in the headgroup region for the asymmetric bilayers. There is also no effect on the magnitude of the pressure peak at the membrane center for asymmetric bilayers.

Ion and Electrostatic Imbalances

The membranes electrostatic potential can have important consequences on many biological functions of membranes and membrane proteins. **Figure 9A** shows the system set-up and the electrostatic potential (**Figure 9B**) across lipid membranes that do not have a charge imbalance. The bilayers have a relatively large positive potential at the bilayer center. The strength of the potential depends on the bilayer structure and composition, with a lower potential for the more disordered, unsaturated bilayers. For symmetric bilayers, the potential is equal to zero on both sides of the membrane. The poly unsaturated DIPC bilayer has a lower potential at the bilayer center compared to the DPPC bilayer. Asymmetric membranes cause the potential to shift between the two aqueous environments, even though both contain 150 mM NaCl, and there is no charge imbalance. Reducing the number of lipids on one side (DPPC_10) causes an increase in potential of ∼100 mV, while having DIPC or DPPE on the other leaflet causes a potential of ∼-70 mV. We also show the electrostatic potential across a Martini DIPC bilayer (**Figure 9B**). The Martini model does not reproduce the positive potential at the membrane center, which is a well-known short coming of the model.

Another source of membrane asymmetry is imbalances in the composition of the aqueous phases that the bilayer separates. Many biological membranes have an electrostatic potential across the bilayer. To investigate this effect, we simulated lipid bilayers with a net charge imbalance (4e) across the membrane. **Figure 9C** shows the electrostatic potential across pure DPPC and pure DIPC lipid bilayers with a 4e charge imbalance. The charge imbalance causes a potential difference of ∼1.2 V across the DPPC bilayer and ∼0.75 V across the DIPC bilayer. This illustrates the importance of the bilayer structure on the electrostatic potential gradients. The relatively large charge imbalance has a small effect on the bilayer structure, as shown

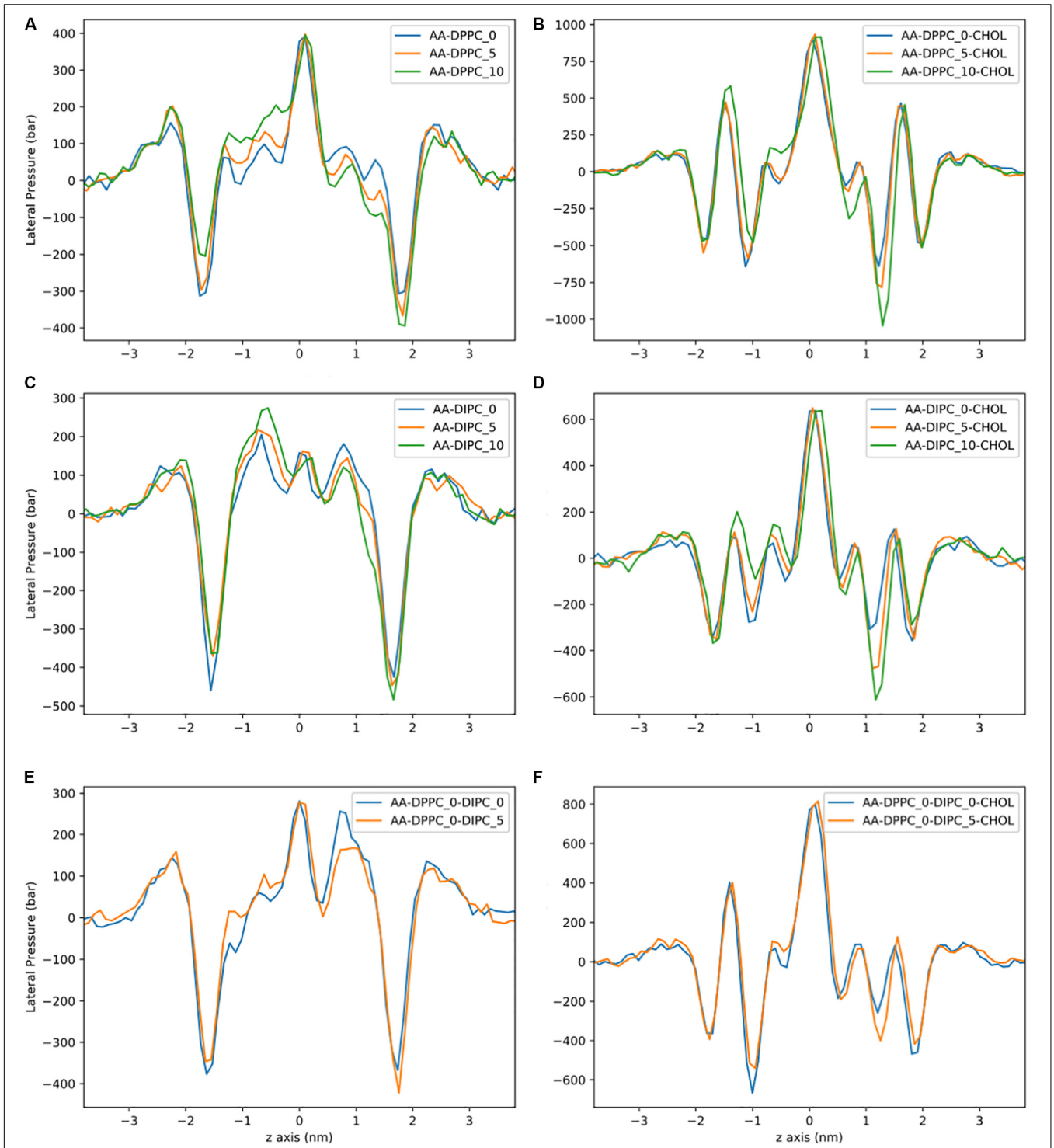

FIGURE 8 | Lateral pressure profiles for AA bilayers with asymmetric number of lipids between leaflets. **(A)** DPPC. **(B)** DPPC:CHOL. **(C)** DIPC. **(D)** DIPC:CHOL. **(E)** DIPC(upper)/DPPC(lower). **(F)** DIPC(upper)/DPPC(lower):CHOL.

by the lateral pressure profile in **Figure 9D**. The APL for DPPC increases to 0.63 from 0.62 nm^2 without a charge imbalance. **Supplementary Figure S6** shows the order parameters for the 4e DPPC bilayer are slightly reduced compared to the pure DPPC bilayer. This modest change in structure is somewhat surprising, given that if we simulated long enough, a pore would likely form across the membrane, to allow the ions to equilibrate between water compartments.

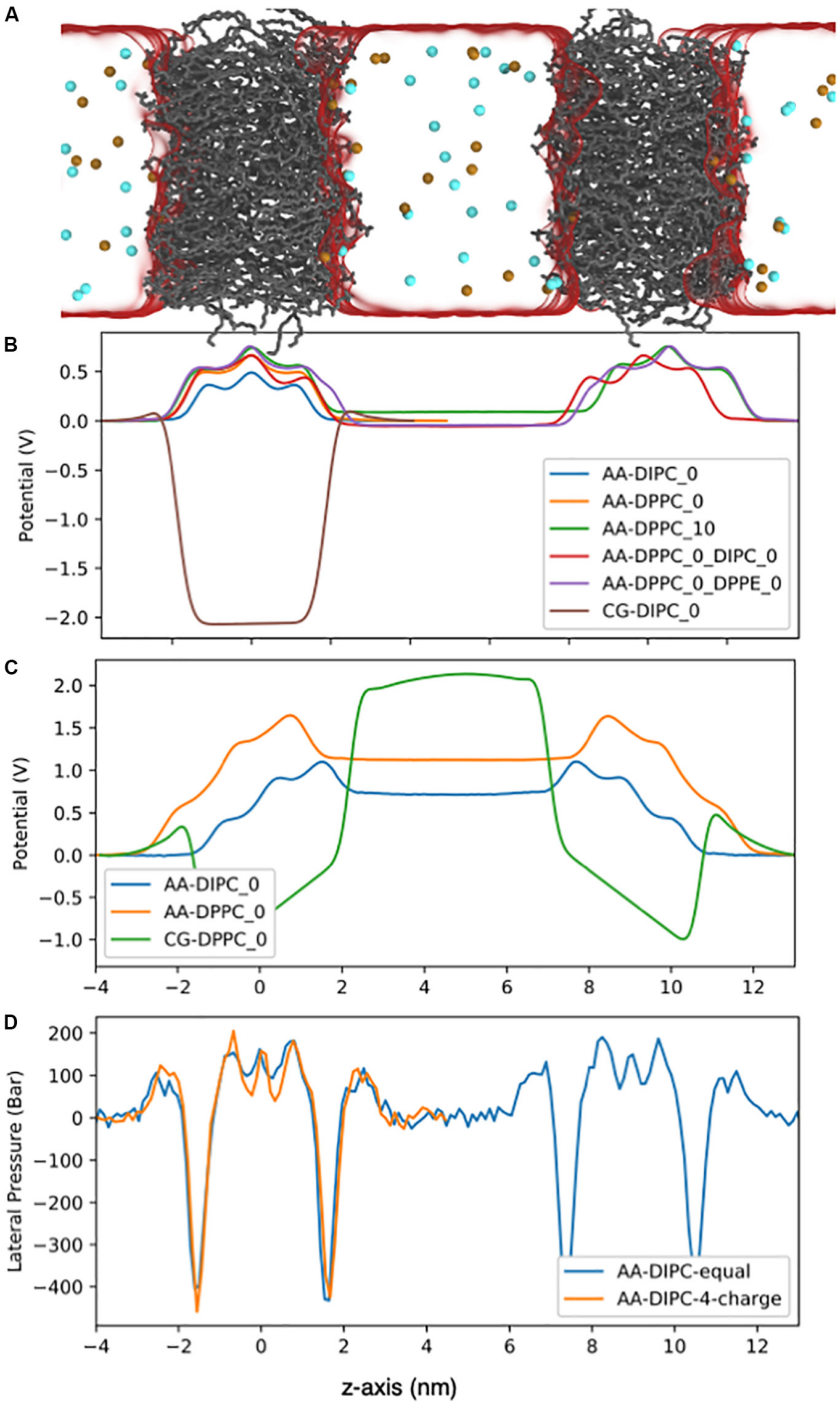

FIGURE 9 | Electrostatic potential for the AA lipid membranes. **(A)** Snapshot of the double bilayer set-up. The DPPC lipids are shown as gray lines, ions are red and blue balls, and water is a translucent surface. **(B)** Bilayers with no charge imbalance between aqueous compartments. The potentials were set to zero on the left side of the bilayer. **(C)** Double bilayer systems with a 4e charge imbalance. Water regions have a flat potential due to conducting counter ions. **(D)** Lateral pressure profile for the DIPC double bilayer with and without a 4e charge imbalance.

DISCUSSION

Biological membranes contain incredible complexity and diversity. While it has long been known that biological membranes contain asymmetry between one side and the other, much remains unknown about the origin, physical effect, biological function, and consequences of its disruption. Here we have investigated a number of different types of membrane

asymmetry using both atomistic and CG models. Our results illustrate how lipid membranes are complex and cooperative aggregates. Changes on one side of the membrane affect the opposite leaflet. In general, the two leaflets attempt to balance asymmetric deviations. For example, if one leaflet becomes more ordered, the opposite leaflet will become more ordered. How the bilayer responds to the asymmetry depends on the composition and chemical structure of its lipids. We chose simulation boxes that were small, to preclude the effect of bilayer bending in response to asymmetry. Future work on the system size dependence of asymmetry would be of interest, or large-scale CG simulations of small unilamellar vesicles with asymmetric lipid distributions.

Here we have used both atomistic and CG simulations to study a number of asymmetric bilayer systems. While there are many detailed insights, the overall trend we observe is the coupling between the bilayers two leaflets. By running extensive simulations for CG systems with 3–4 lipid components and systematically changing the asymmetry, we show that the number lipids in each leaflet can be adjusted to minimize leaflet ST (**Figures 1C,F**). The resulting number asymmetry is somewhat higher than using estimates from the APL of the two symmetric bilayers. This effect had been shown previously (Doktorova and Weinstein, 2018; Hossein and Deserno, 2020), but here we have run extensive CG simulations to characterize the behavior with and without cholesterol. Hossein and Deserno (2020) also showed that in some cases a more complex balance between spontaneous curvature and tension is desired. Because the two leaflets are interacting, they will alter the others elastic properties and therefore shift the packing of the lipids. While this can have important consequences, we also note that many bilayer properties are quite similar over a wide range of asymmetries (**Figure 1D**), suggesting that getting the exact number asymmetry may not seriously impact many simulation results. This effect is also due to the lipid's flexibility, where each leaflet compensates, so the difference between the two leaflets is minimized.

We have also addressed the influence of cholesterol on membrane asymmetry. Cholesterol has been hypothesized to be able to reduce membrane asymmetry by being able to flip quickly from one leaflet to the other and equilibrate membrane stress (Miettinen and Lipowsky, 2019). Our results suggest that for the systems tested here this is true for some properties, such as the overall membrane density and APL, cholesterol can also increase the effect on some other properties, such as the LPP. Cholesterol makes the situation of simulating membrane asymmetry more complicated, because it is able to flip-flop on a time scale easily accessible to CG simulations, but not for AA simulations of long saturated lipids. This is also likely the case for other fast flipping lipids such as fatty acids, ceramides and diacylglycerol (Bennett and Tieleman, 2012; Janke et al., 2014). Cholesterol's distribution is also more complicated because it will be driven by its chemical potential for either leaflet, and its ability to influence the membrane's spontaneous curvature (Allender et al., 2019; Hossein and Deserno, 2020). Considerable work in this area is needed to properly assess lipid distributions, such as free energy methods for determining their relative chemical potential in each leaflet.

By systematically investigating AA and CG models, we are able to compare specific difference for the effect of membrane asymmetry. We find that many of the properties and differences are captured using both levels of detail. While there are substantial differences in the shape and magnitude of the LPPs, many of the changes for asymmetric membranes are similar for the two models. This is crucial for future simulation work using multiscale approaches to study asymmetric membranes. These methods are attractive due to the fast sampling of the CG models, which is necessary for many slow processes involving lipids, and the fine chemical details provided by the AA models. Ensuring that the CG asymmetric lipid distribution matches the AA models is necessary, or the AA simulation will be biased by the initial CG simulation result. The electrostatic potentials for Martini are shown to be opposite to that of AA models, illustrating a fundamental limitation for the model. It is also likely that the large preference of cholesterol for DPPC over DIPC in the asymmetric bilayer could be due to Martini's strong repulsion between cholesterol and poly unsaturated phospholipids. Future work comparing the lipid chemical potentials for both models might help provide more qualitative differences. The overall good agreement between the AA and CG results is promising for large scale multiscale membrane simulations. Future work investigating the effect of proteins inclusion in asymmetric membrane systems would also be of interest. Another aspect of asymmetry for future work are pH gradients, which require more sophisticated computational methods.

We examined how asymmetric ion distributions can affect the membrane structure, as well as how asymmetric lipid distributions influence the electrostatic potential across the membrane. Our results match previous results showing that changes in lipid headgroup can shift the overall membrane electrostatic potential (Gurtovenko and Vattulainen, 2007). We also show that changing the lipid tails can have a substantial effect on the membrane's dipole potential. The fact that lipid distribution influences membrane electrostatic potentials has important implications on numerous biological processes, such as nerve cell activation. Another source of membrane asymmetry is the bilayer separating aqueous compartments with chemical and/or ionic gradients. We show that relatively large electrostatic potentials have a modest effect on the membranes overall structure. This is somewhat surprising, as these membranes are likely to form pores if simulated for long times, so the ions can equilibrate (Gurtovenko and Vattulainen, 2005). These large electrostatic gradients might promote structural fluctuations that promote pore formation, such as water wires across the membrane, which have been shown to be a pre-pore state for pore formation in lipid bilayers (Bennett et al., 2014). Our results also illustrate how changes in lipid tails have a large effect on the electrostatic potential resulting from ionic imbalances. These differences are important for many biological processes, including the activity of voltage-gated ion channels (Bezanilla, 2007), GPCR signaling (Rinne et al., 2015) and the insertion and penetration of charged peptides, such as antimicrobial

peptides (Teixeira et al., 2012) and cell-penetrating peptides (Moghal et al., 2020).

CONCLUSION

Asymmetry in lipid bilayer simulations is a crucial form of complexity in biological systems. Cells create and exploit asymmetry for energy production, signaling, and general transport of molecules. Studying membrane asymmetry in model systems is challenging for experiments and simulations, as this is an inherently non-equilibrium situation. For simulations, finite system sizes and time scales makes membrane asymmetry hard to study. Our results show how changes in number of lipids, lipid headgroups, lipid tails, ionic imbalances, and the effect of cholesterol impact bilayer's structural properties. Overall, we show that CG Martini simulations reproduce the effects observed with AA CHARMM36 simulations. One leaflets structure effects the opposite leaflet, as the individual lipids adapt to their local environment. Fast flip-flop of cholesterol creates additional challenges, for simulating asymmetric membrane simulations. Cholesterol reduces the impact of membrane asymmetry for some structural properties, but can create more imbalance, especially when it has a large preference for lipids in one leaflet over the other. There is much work in the future for membrane simulations of asymmetry, including assessing chemical potential differences and enhanced sampling methods.

DATA AVAILABILITY STATEMENT

The datasets generated for this study are available on request to the corresponding author.

AUTHOR CONTRIBUTIONS

MB, SH, ML, LM, and MU wrote the analysis scripts. PS and HI managed the project. All authors contributed to running simulations, analyzing the result, and conceiving the project.

FUNDING

This work was partially supported by the Laboratory Directed Research and Development at the Lawrence Livermore National Laboratory (18-ERD-035) and performed under the auspices of the U.S. DOE by the Lawrence Livermore National Laboratory under contract DE-AC52-07NA27344. Release LLNL-JRNL-801959.

ACKNOWLEDGMENTS

We thank Fred Streitz for his guidance and support, and Livermore Computing for access to computing time. MB, SH, ML, LM, and MU thank the Harvey Mudd Clinic Program for support.

SUPPLEMENTARY MATERIAL

The Supplementary Material for this article can be found online at: https://www.frontiersin.org/articles/10.3389/fcell.2020.00575/full#supplementary-material

REFERENCES

Abraham, M. J., Murtola, T., Schulz, R., Páll, S., Smith, J. C., Hess, B., et al. (2015). GROMACS: high performance molecular simulations through multi-level parallelism from laptops to supercomputers. *SoftwareX* 1–2, 19–25. doi: 10.1016/j.softx.2015.06.001

Allender, D., Sodt, A., and Schick, M. (2019). Cholesterol-dependent bending energy is important in cholesterol distribution of the plasma membrane. *Biophys. J.* 116, 2356–2366. doi: 10.1016/j.bpj.2019.03.028

Antila, H., Buslaev, P., Favela-Rosales, F., Ferreira, T. M., Gushchin, I., Javanainen, M., et al. (2019). Headgroup structure and cation binding in phosphatidylserine lipid bilayers. *J. Phys. Chem. B* 123, 9066–9079. doi: 10.1021/acs.jpcb.9b06091

Bennett, W. F. D., MacCallum, J. L., Hinner, M. J., Marrink, S. J., and Tieleman, D. P. (2009a). Molecular view of cholesterol flip-flop and chemical potential in different membrane environments. *J. Am. Chem. Soc.* 131, 12714–12720. doi: 10.1021/ja903529f

Bennett, W. F. D., MacCallum, J. L., and Tieleman, D. P. (2009b). Thermodynamic analysis of the effect of cholesterol on dipalmitoylphosphatidylcholine lipid membranes. *J. Am. Chem. Soc.* 131, 1972–1978. doi: 10.1021/ja808541r

Bennett, W. F. D., Sapay, N., and Tieleman, D. P. (2014). Atomistic simulations of pore formation and closure in lipid bilayers. *Biophys. J.* 106, 210–219. doi: 10.1016/j.bpj.2013.11.4486

Bennett, W. F. D., and Tieleman, D. P. (2012). Molecular simulation of rapid translocation of cholesterol, diacylglycerol, and ceramide in model raft and nonraft membranes. *J. Lipid Res.* 53, 421–429. doi: 10.1194/jlr.M022491

Berendsen, H. J., van Postma, J., van Gunsteren, W. F., DiNola, A., and Haak, J. R. (1984). Molecular dynamics with coupling to an external bath. *J. Chem. Phys.* 81, 3684–3690. doi: 10.1063/1.448118

Bezanilla, F. (2007). "Voltage-gated ion channels," in *Biological Membrane Ion Channels*, eds S. H. Chung, O. S. Andersen, and V. Krishnamurthy (Cham: Springer), 81–118. doi: 10.1007/0-387-68919-2_3

Böckmann, R. A., De Groot, B. L., Kakorin, S., Neumann, E., and Grubmüller, H. (2008). Kinetics, statistics, and energetics of lipid membrane electroporation studied by molecular dynamics simulations. *Biophys. J.* 95, 1837–1850. doi: 10.1529/biophysj.108.129437

Buchoux, S. (2016). FATSLiM: a fast and robust software to analyze MD simulations of membranes. *Bioinformatics* 33, 133–134. doi: 10.1093/bioinformatics/btw563

Bussi, G., Donadio, D., and Parrinello, M. (2007). Canonical sampling through velocity rescaling. *J. Chem. Phys.* 126:014101. doi: 10.1063/1.2408420

Callan-Jones, A., Sorre, B., and Bassereau, P. (2011). Curvature-driven lipid sorting in biomembranes. *Cold Spring Harb. Perspect. Biol.* 3:a004648. doi: 10.1101/cshperspect.a004648

Collins, M. D., and Keller, S. L. (2008). Tuning lipid mixtures to induce or suppress domain formation across leaflets of unsupported asymmetric bilayers. *Proc. Natl. Acad. Sci. U.S.A.* 105, 124–128. doi: 10.1073/pnas.0702970105

Darden, T., York, D., and Pedersen, L. (1993). Particle mesh Ewald: an N· log (N) method for Ewald sums in large systems. *J. Chem. Phys.* 98, 10089–10092. doi: 10.1063/1.464397

De Jong, D. H., Baoukina, S., Ingólfsson, H. I., and Marrink, S. J. (2016). Martini straight: boosting performance using a shorter cutoff and GPUs. *Comput. Phys. Commun.* 199, 1–7. doi: 10.1016/j.cpc.2015.09.014

Doktorova, M., and Weinstein, H. (2018). Accurate in silico modeling of asymmetric bilayers based on biophysical principles. *Biophys. J.* 115, 1638–1643. doi: 10.1016/j.bpj.2018.09.008

Durell, S. R., Brooks, B. R., and Ben-Naim, A. (1994). Solvent-induced forces between two hydrophilic groups. *J. Phys. Chem.* 98, 2198–2202. doi: 10.1021/j100059a038

Essmann, U., Perera, L., Berkowitz, M. L., Darden, T., Lee, H., and Pedersen, L. G. (1995). A smooth particle mesh Ewald method. *J. Chem. Phys.* 103, 8577–8593. doi: 10.1063/1.470117

Esteban-Martín, S., Risselada, H. J., Salgado, J., and Marrink, S. J. (2009). Stability of asymmetric lipid bilayers assessed by molecular dynamics simulations. *J. Am. Chem. Soc.* 131, 15194–15202. doi: 10.1021/ja904450t

Gruenberg, J. (2020). Life in the lumen: the multivesicular endosome. *Traffic* 21, 76–93. doi: 10.1111/tra.12715

Gurtovenko, A. A., Anwar, J., and Vattulainen, I. (2010). Defect-mediated trafficking across cell membranes: insights from in silico modeling. *Chem. Rev.* 110, 6077–6103. doi: 10.1021/cr1000783

Gurtovenko, A. A., and Lyulina, A. S. (2014). Electroporation of asymmetric phospholipid membranes. *J. Phys. Chem. B* 118, 9909–9918. doi: 10.1021/jp5028355

Gurtovenko, A. A., and Vattulainen, I. (2005). Pore formation coupled to ion transport through lipid membranes as induced by transmembrane ionic charge imbalance: atomistic molecular dynamics study. *J. Am. Chem. Soc.* 127, 17570–17571. doi: 10.1021/ja053129n

Gurtovenko, A. A., and Vattulainen, I. (2007). Lipid transmembrane asymmetry and intrinsic membrane potential: two sides of the same coin. *J. Am. Chem. Soc.* 129, 5358–5359. doi: 10.1021/ja070949m

Hess, B. (2008). P-LINCS: a parallel linear constraint solver for molecular simulation. *J. Chem. Theory Comput.* 4, 116–122. doi: 10.1021/ct700200b

Hess, B., Bekker, H., Berendsen, H. J., and Fraaije, J. G. (1997). LINCS: a linear constraint solver for molecular simulations. *J. Comput. Chem.* 18, 1463–1472. doi: 10.1002/(sici)1096-987x(199709)18:12<1463::aid-jcc4>3.0.co;2-h

Hossein, A., and Deserno, M. (2020). Spontaneous curvature, differential stress, and bending modulus of asymmetric lipid membranes. *Biophys. J.* 118, 624–642.

Huber, R. G., Carpenter, T. S., Dube, N., Holdbrook, D. A., Ingólfsson, H. I., Irvine, W. A., et al. (2019). "Multiscale modeling and simulation approaches to lipid–protein interactions," in *Lipid-Protein Interactions*, ed. J. Kleinschmidt (Cham: Springer), 1–30. doi: 10.1007/978-1-4939-9512-7_1

Ingólfsson, H. I., Carpenter, T. S., Bhatia, H., Bremer, P.-T., Marrink, S. J., and Lightstone, F. C. (2017). Computational lipidomics of the neuronal plasma membrane. *Biophys. J.* 113, 2271–2280.

Ingólfsson, H. I., Melo, M. N., van Eerden, F. J., Arnarez, C., Lopez, C. A., Wassenaar, T. A., et al. (2014). Lipid organization of the plasma membrane. *J. Am. Chem. Soc.* 136, 14554–14559. doi: 10.1021/ja507832e

Janke, J. J., Bennett, W. D., and Tieleman, D. P. (2014). Oleic acid phase behavior from molecular dynamics simulations. *Langmuir* 30, 10661–10667. doi: 10.1021/la501962n

Javanainen, M., and Martinez-Seara, H. (2019). Rapid diffusion of cholesterol along polyunsaturated membranes via deep dives. *Phys. Chem. Chem. Phys.* 21, 11660–11669. doi: 10.1039/c9cp02022e

Jo, S., Rui, H., Lim, J. B., Klauda, J. B., and Im, W. (2010). Cholesterol flip-flop: insights from free energy simulation studies. *J. Phys. Chem. B* 114, 13342–13348. doi: 10.1021/jp108166k

Jorgensen, W. L., Chandrasekhar, J., Madura, J. D., Impey, R. W., and Klein, M. L. (1983). Comparison of simple potential functions for simulating liquid water. *J. Chem. Phys.* 79, 926–935. doi: 10.1063/1.445869

Khalid, S., Berglund, N. A., Holdbrook, D. A., Leung, Y. M., and Parkin, J. (2015). The membranes of Gram-negative bacteria: progress in molecular modelling and simulation. *Biochem. Soc. Trans.* 43, 162–167. doi: 10.1042/bst20140262

Klauda, J. B., Venable, R. M., Freites, J. A., O'Connor, J. W., Tobias, D. J., Mondragon-Ramirez, C., et al. (2010). Update of the CHARMM all-atom additive force field for lipids: validation on six lipid types. *J. Phys. Chem. B* 114, 7830–7843. doi: 10.1021/jp101759q

Lange, Y., and Steck, T. L. (2008). Cholesterol homeostasis and the escape tendency (activity) of plasma membrane cholesterol. *Prog. Lipid Res.* 47, 319–332. doi: 10.1016/j.plipres.2008.03.001

Lorent, J. H., Levental, K. R., Ganesan, L., Rivera-Longsworth, G., Sezgin, E., Doktorova, M., et al. (2020). Plasma membranes are asymmetric in lipid unsaturation, packing and protein shape. *Nat. Chem. Biol.* 16:710. doi: 10.1038/s41589-020-0564-3

Marquardt, D., Heberle, F. A., Miti, T., Eicher, B., London, E., Katsaras, J., et al. (2017). 1H NMR shows slow phospholipid flip-flop in gel and fluid bilayers. *Langmuir* 33, 3731–3741. doi: 10.1021/acs.langmuir.6b04485

Marrink, S. J., Corradi, V., Souza, P. C., Ingólfsson, H. I., Tieleman, D. P., and Sansom, M. S. (2019). Computational modeling of realistic cell membranes. *Chem. Rev.* 119, 6184–6226. doi: 10.1021/acs.chemrev.8b00460

Marrink, S. J., Risselada, H. J., Yefimov, S., Tieleman, D. P., and De Vries, A. H. (2007). The MARTINI force field: coarse grained model for biomolecular simulations. *J. Phys. Chem. B* 111, 7812–7824.

Martyna, G. J., Klein, M. L., and Tuckerman, M. (1992). Nosé–Hoover chains: the canonical ensemble via continuous dynamics. *J. Chem. Phys.* 97, 2635–2643. doi: 10.1063/1.463940

McNamee, M. G., and McConnell, H. M. (1973). Transmembrane potentials and phospholipid flip-flop in excitable membrane vesicles. *Biochemistry* 12, 2951–2958. doi: 10.1021/bi00740a001

Melcr, J., Martinez-Seara, H., Nencini, R., Kolafa, J., Jungwirth, P., and Ollila, O. S. (2018). Accurate binding of sodium and calcium to a POPC bilayer by effective inclusion of electronic polarization. *J. Phys. Chem. B* 122, 4546–4557. doi: 10.1021/acs.jpcb.7b12510

Melo, M., Ingólfsson, H., and Marrink, S. (2015). Parameters for Martini sterols and hopanoids based on a virtual-site description. *J. Chem. Phys.* 143:243152. doi: 10.1063/1.4937783

Michaud-Agrawal, N., Denning, E. J., Woolf, T. B., and Beckstein, O. (2011). MDAnalysis: a toolkit for the analysis of molecular dynamics simulations. *J. Comput. Chem.* 32, 2319–2327. doi: 10.1002/jcc.21787

Miettinen, M. S., and Lipowsky, R. (2019). Bilayer membranes with frequent flip-flops have tensionless leaflets. *Nano Lett.* 19, 5011–5016. doi: 10.1021/acs.nanolett.9b01239

Miyamoto, S., and Kollman, P. A. (1992). Settle: an analytical version of the SHAKE and RATTLE algorithm for rigid water models. *J. Comput. Chem.* 13, 952–962. doi: 10.1002/jcc.540130805

Moghal, M. M. R., Islam, M. Z., Hossain, F., Saha, S. K., and Yamazaki, M. (2020). Role of membrane potential on entry of cell-penetrating peptide transportan 10 into single vesicles. *Biophys. J.* 118, 57–69. doi: 10.1016/j.bpj.2019.11.012

Mondal, M., Mesmin, B., Mukherjee, S., and Maxfield, F. R. (2009). Sterols are mainly in the cytoplasmic leaflet of the plasma membrane and the endocytic recycling compartment in CHO cells. *Mol. Biol. Cell* 20, 581–588. doi: 10.1091/mbc.e08-07-0785

Neria, E., Fischer, S., and Karplus, M. (1996). Simulation of activation free energies in molecular systems. *J. Chem. Phys.* 105, 1902–1921. doi: 10.1063/1.472061

Park, S., Beaven, A. H., Klauda, J. B., and Im, W. (2015). How tolerant are membrane simulations with mismatch in area per lipid between leaflets? *J. Chem. Theory Comput.* 11, 3466–3477. doi: 10.1021/acs.jctc.5b00232

Parrinello, M., and Rahman, A. (1981). Polymorphic transitions in single crystals: a new molecular dynamics method. *J. Appl. Phys.* 52, 7182–7190. doi: 10.1063/1.328693

Perlmutter, J. D., and Sachs, J. N. (2011). Interleaflet interaction and asymmetry in phase separated lipid bilayers: molecular dynamics simulations. *J. Am. Chem. Soc.* 133, 6563–6577. doi: 10.1021/ja106626r

Rinne, A., Mobarec, J. C., Mahaut-Smith, M., Kolb, P., and Bünemann, M. (2015). The mode of agonist binding to a G protein–coupled receptor switches the effect that voltage changes have on signaling. *Sci. Signal.* 8:ra110. doi: 10.1126/scisignal.aac7419

Sachs, J. N., Crozier, P. S., and Woolf, T. B. (2004). Atomistic simulations of biologically realistic transmembrane potential gradients. *J. Chem. Phys.* 121, 10847–10851.

Shahane, G., Ding, W., Palaiokostas, M., and Orsi, M. (2019). Physical properties of model biological lipid bilayers: insights from all-atom molecular dynamics simulations. *J. Mol. Model.* 25:76. doi: 10.1007/s00894-019-3964-0

Siggel, M., Bhaskara, R. M., and Hummer, G. (2019). Phospholipid scramblases remodel the shape of asymmetric membranes. *J. Phys. Chem. Lett.* 10, 6351–6354. doi: 10.1021/acs.jpclett.9b02531

Singharoy, A., Maffeo, C., Delgado-Magnero, K. H., Swainsbury, D. J., Sener, M., Kleinekathöfer, U., et al. (2019). Atoms to phenotypes: molecular design principles of cellular energy metabolism. *Cell* 179, 1098–1111.

Skotland, T., Sandvig, K., and Llorente, A. (2017). Lipids in exosomes: current knowledge and the way forward. *Prog. Lipid Res.* 66, 30–41. doi: 10.1016/j.plipres.2017.03.001

Steck, T. L., and Lange, Y. (2018). Transverse distribution of plasma membrane bilayer cholesterol: picking sides. *Traffic* 19, 750–760. doi: 10.1111/tra.12586

Teixeira, V., Feio, M. J., and Bastos, M. (2012). Role of lipids in the interaction of antimicrobial peptides with membranes. *Prog. Lipid Res.* 51, 149–177. doi: 10.1016/j.plipres.2011.12.005

Tian, J., Nickels, J., Katsaras, J., and Cheng, X. (2016). Behavior of bilayer leaflets in asymmetric model membranes: atomistic simulation studies. *J. Phys. Chem. B* 120, 8438–8448. doi: 10.1021/acs.jpcb.6b02148

Tieleman, D. P., and Marrink, S.-J. (2006). Lipids out of equilibrium: energetics of desorption and pore mediated flip-flop. *J. Am. Chem. Soc.* 128, 12462–12467. doi: 10.1021/ja0624321

Torres-Sánchez, A., Vanegas, J. M., and Arroyo, M. (2015). Examining the mechanical equilibrium of microscopic stresses in molecular simulations. *Phys. Rev. Lett.* 114:258102.

Van Der Spoel, D., Lindahl, E., Hess, B., Groenhof, G., Mark, A. E., and Berendsen, H. J. (2005). GROMACS: fast, flexible, and free. *J. Comput. Chem.* 26, 1701–1718. doi: 10.1002/jcc.20291

Van Meer, G., Voelker, D. R., and Feigenson, G. W. (2008). Membrane lipids: where they are and how they behave. *Nat. Rev. Mol. Cell Biol.* 9, 112–124. doi: 10.1038/nrm2330

Vanegas, J. M., Torres-Sánchez, A., and Arroyo, M. (2014). Importance of force decomposition for local stress calculations in biomembrane molecular simulations. *J. Chem. Theory Comput.* 10, 691–702. doi: 10.1021/ct4008926

Wassenaar, T. A., Ingólfsson, H. I., Böckmann, R. A., Tieleman, D. P., and Marrink, S. J. (2015). Computational lipidomics with insane: a versatile tool for generating custom membranes for molecular simulations. *J. Chem. Theory Comput.* 11, 2144–2155. doi: 10.1021/acs.jctc.5b00209

Wassenaar, T. A., Pluhackova, K., Böckmann, R. A., Marrink, S. J., and Tieleman, D. P. (2014). Going backward: a flexible geometric approach to reverse transformation from coarse grained to atomistic models. *J. Chem. Theory Comput.* 10, 676–690. doi: 10.1021/ct400617g

Conflict of Interest: The authors declare that the research was conducted in the absence of any commercial or financial relationships that could be construed as a potential conflict of interest.

frontiers in Cell and Developmental Biology

MINI REVIEW
published: 28 July 2020
doi: 10.3389/fcell.2020.00609

T Cell Membrane Heterogeneity Aids Antigen Recognition and T Cell Activation

Megan V. Farrell[1,2†], *Samantha Webster*[1,2†], *Katharina Gaus*[1,2*] *and Jesse Goyette*[1,2*]

[1] EMBL Australia Node in Single Molecule Science, School of Medical Sciences, University of New South Wales, Sydney, NSW, Australia, [2] ARC Centre of Excellence in Advanced Molecular Imaging, University of New South Wales, Sydney, NSW, Australia

T cells are critical for co-ordinating the immune response. T cells are activated when their surface T cell receptors (TCRs) engage cognate antigens in the form of peptide-major histocompatibility complexes (pMHC) presented on the surface of antigen presenting cells (APCs). Large changes in the contact interface between T cells and APCs occur over the course of tens of minutes from the initial contact to the formation of a large-scale junction between the two cells. The mature junction between a T cell and APC is known as the immunological synapse, and this specialized plasma membrane structure is the major platform for TCR signaling. It has long been known that the complex organization of signaling molecules at the synapse is critical for appropriate activation of T cells, but within the last decade advances in microscopy have opened up investigation into the dynamics of T cell surface topology in the immune synapse. From mechanisms mediating the initial contact between T cells and APCs to roles in the organization of molecules in the mature synapse, these studies have made it increasingly clear that local membrane topology has a large impact on signaling processes. This review focuses on the functional consequences of the T cells' highly dynamic and heterogeneous membrane, in particular, how membrane topology leads to the reorganization of membrane proteins on the T cell surface.

Keywords: T cells, microvilli, T cell receptor, membrane curvature, membrane heterogeneity, T cell activation

OPEN ACCESS

Edited by:
Falk Nimmerjahn, University of Erlangen Nuremberg, Germany

Reviewed by:
Jianfeng Chen, Shanghai Institute of Biochemistry and Cell Biology (CAS), China
Raffaella Pippa, Sanford Burnham Prebys Medical Discovery Institute, United States

***Correspondence:**
Katharina Gaus
k.gaus@unsw.edu.au
Jesse Goyette
j.goyette@unsw.edu.au

[†] *These authors have contributed equally to this work*

Specialty section:
This article was submitted to Cellular Biochemistry, a section of the journal Frontiers in Cell and Developmental Biology

Received: *30 April 2020*
Accepted: *19 June 2020*
Published: *28 July 2020*

Citation:
Farrell MV, Webster S, Gaus K and Goyette J (2020) T Cell Membrane Heterogeneity Aids Antigen Recognition and T Cell Activation. Front. Cell Dev. Biol. 8:609. doi: 10.3389/fcell.2020.00609

INTRODUCTION

T cells are integral members of the immune system, in which they mediate adaptive immunity through direct, antigen-specific contact with antigen-presenting cells (APCs). In order to initiate an appropriate immune response, the T cell relies upon external signals communicated to them by proteins on the surface of an APC. The signal given to the T cell determines the effector response, for instance, an APC can trigger the activation of a T cell by presenting peptide antigens on major histocompatibility complexes (pMHC). pMHCs can bind to the T cell receptor (TCR) on the T cell membrane, triggering a signaling cascade through the associated cluster of differentiation 3 (CD3) subunits, which includes recruitment of cytosolic signaling proteins such as the protein kinase zeta-chain-associated protein kinase 70 (Zap70) and phosphorylation of membrane proteins such as the linker for activation of T cells (LAT) (Balagopalan et al., 2015; Courtney et al., 2018).

These events lead to the formation of the immunological synapse, a reorganization of molecular components, membrane proteins, and the actin cytoskeleton, which is characteristic of active T cells. In addition to pMHCs, the APC also presents inhibitory ligands, which bind to cognate

receptors on the T cell and lead to signal termination and inactivation of the T cell (Chen and Flies, 2013). Spatial reorganization of membrane-bound activating and inhibitory receptors is an essential factor for determining the response of a T cell, with inhibitory receptors being shown to be excluded from the area of activating receptor engagement (Choudhuri et al., 2005; Burroughs et al., 2006). Thus, T cells must be equipped to respond to a diverse range of extracellular signals.

The plasma membrane is the major platform for T cell signaling. For this reason, heterogeneities in the T cell membrane can lead to alterations in protein organization and signaling, and therefore, have functional consequences for the T cell. Heterogeneity in the plasma membrane can be caused by multiple different factors. For instance, changes in membrane topology can cause the plasma membrane to decrease the spatial scale on which protein-protein interactions occur in order to promote weak, yet biologically important receptor-ligand interactions (Choudhuri et al., 2005; Stone et al., 2017). Additionally, intracellular processes, such as the reorganization of the actin cytoskeleton, may influence protein diffusion and compartmentalization within the membrane, as well as regulate the nanoscale clustering of certain membrane proteins (Sadegh et al., 2017). Thus, the study of the organization of receptors and other molecules in the plasma membrane, as well as the dynamics of the plasma membrane itself, can reveal novel insights into the activation of T cells and their function as mediators of the adaptive immune system.

In this review we outline general membrane features and discuss how membrane curvature can influence the distribution of proteins on the membrane. This is followed on by an example of how these processes can affect cellular functions. Finally, we discuss how these highly dynamic and heterogeneous membranes can result in functional consequences for T cells, in particular how membrane topology leads to the reorganization of the membrane proteins on the T cell surface.

MEMBRANE FEATURES

Membrane topology encompasses the complex and dynamic system of morphological features present at the surface of the T cell membrane. Morphological features, i.e., protrusions and invaginations, of the T cell membrane are naturally suspected to significantly impact the protein distribution and composition at the membrane and therefore are likely to play some role in intracellular signaling and cell function (Chang et al., 2016; Jung et al., 2016; Razvag et al., 2018, 2019; Ghosh et al., 2020). The localization of signaling proteins to either protrusive or intrusive regions of the cell membrane, or conversely, the segregation of signaling molecules from areas of high membrane curvature suggests a functional relationship between cell surface morphology and subcellular signaling.

The T cell membrane is not spatially homogeneous, and in fact there are several morphological motifs present on the cell surface (**Figure 1**). One major morphological feature of the T cell membrane is the small, cylindrical protrusions which cover the surface of circulating mammalian lymphocytes.

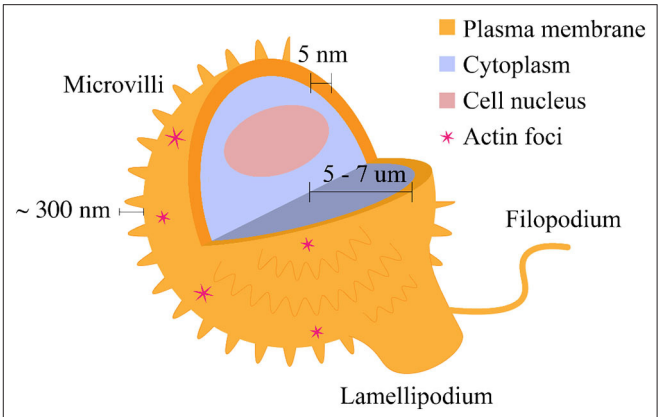

FIGURE 1 | Morphological features of the T cell plasma membrane. The plasma membrane is shaped by the underlying actin cytoskeleton. These morphological features are related to surface protein distribution and consequently, cell signaling. Microvilli cover most of the cell surface and are composed of actin filaments. Lamellipodia and filopodia are related to cell migration and are also composed of actin. Actin foci may be observed in a variety of characteristic shapes (Fritzsche et al., 2017). The features are not depicted to scale.

These lymphocyte microvilli, or invadosome-like protrusions (ILPs) (Sage et al., 2012), are highly dynamic, actin-based structures which have been shown to continuously assemble and disassemble at the cell surface. The first quantitative characterization of lymphocyte microvilli by Majstoravich et al. used scanning electron microscopy to determine that microvilli contain long, parallel bundles of actin filaments (Majstoravich et al., 2004). These bundles are disrupted by treatment with Latrunculin A, which causes actin end-blocking, suggesting continuous actin assembly and reassembly at the cell surface, changing on a time scale of seconds to minutes (Majstoravich et al., 2004). More recently, Kim et al. used a combination of techniques to determine that T cells generate microvillus-originated particles upon T cell stimulation (Kim et al., 2018).

Small lymphocyte microvilli on T cell surfaces may be used as sensory organs to enable the search for pMHCs (Brodovitch et al., 2013). T cells must efficiently survey the surface of APCs for pMHCs in order for TCR recognition to occur and enact a signaling cascade which mounts an adaptive immune system response (Baumgart et al., 2019). Cai et al. explored the role that active surface topology plays in ligand detection. Their results indicate that TCR recognition appears to happen at the same time as surface deformations provide initial contact. However, it is still unclear whether the initial surface deformation contact zones are stable or whether cells continue to survey the surface of the APC after initial contact (Cai et al., 2017). Characterization of microvilli movement on the T cell reveals an apparent fractal distribution on the surface, which would provide consistent coverage across scales (Cai et al., 2017). Microvilli contacts on a supported lipid bilayer imaged with a lattice light-sheet microscope occurred at consistent densities over time. These dynamic, actin-rich adhesion structures may probe APCs during T cell searching. In one study, the intercellular contacts

TABLE 1 | Approximate measurements of T cell membrane features.

Feature	Length	Width	Proposed function	References
Actin foci			Facilitate distal signaling events in T cells, including PLCγ1 activation and subsequent cytoplasmic calcium ion elevation	Kumari et al., 2015; Fritzsche et al., 2017
Vortices[†]	–	500 nm		
Asters/stars[†]	–	2.5–5 μm		
Filopodia	5–7 μm	0.1–0.3 μm	Probe environment and assist with cell migration	Mattila and Lappalainen, 2008; Kim et al., 2018
Lamellipodia	–	0.1–0.2 μm	Promote cell migration and extension	Mattila and Lappalainen, 2008
Microvilli or ILPs	0.3–5 μm	0.2–0.5 μm	Scan and search antigens on APC, perhaps also serve as immunological synaptosomes	Majstoravich et al., 2004; Sage et al., 2012; Cai et al., 2017; Kim et al., 2018

For reference, T cells have a diameter of approximately 6 to 12μm (Rosenbluth et al., 2006).
[†]Actin vortices, asters, and stars are representative of structures which result from actin self-organization at actin foci. Actin vortices may transition into actin stars and asters.

between the T cell and APC were found to consistently precede and support T cell activation as indicated by increased calcium flux. On antigen-pulsed APCs, T cells rapidly fluxed calcium, lost spatial polarity, and arrested migration and under these activating conditions, a dense array of "podo-prints" largely stably (18 min) localized at the periphery of the T cell/APC interface (Linder, 2009; Sage et al., 2012).

In addition to microvilli, other morphological features include filopodia and lamellipodia, which are involved in cell migration and contribute to the regulation of signaling (**Figure 1**). While their contribution to migratory cell processes is closely related, these structures differ in their actin content; lamellipodia are sheet-like protrusions which contain branched actin networks, while filopodia are thin structures with tight, parallel bundles of F-actin (Mattila and Lappalainen, 2008). Fritzsche et al. describe actin foci, another morphological feature present on the T cell membrane. Actin foci may be polymerized into self-organized actin patterns (Fritzsche et al., 2017). These self-organized patterns may take the form of actin vortices, asters, or stars (Fritzsche et al., 2017) and can lead to distal signaling events in T cells, including phospholipase C, gamma 1 (PLCγ1) activation and subsequent cytoplasmic calcium ion elevation (Kumari et al., 2015). **Table 1** provides a summary of the dimensions of the morphological features discussed above.

CURVATURE-DRIVEN REGULATION OF PROTEIN DISTRIBUTION

There is no comprehensive explanation for the mechanisms of interaction between cell morphology and signal transduction. However, cell morphological motifs alone can offer a mechanism for the spatial organization of molecular signals at the subcellular scale through co-localization of proteins and morphological structures. Methods are being developed to detect and identify subcellular morphological motifs as well as calculate relevant parameters such as mean curvature, volume, and surface area of structures such as filopodia, lamellipodia, and microvilli (Driscoll et al., 2019). The data may be acquired through both high resolution light-sheet microscopy techniques and more conventional microscopy techniques.

Previously established membrane curvature-sensing models have relied on specific protein structural motifs such as amphipathic or hydrophobic structure insertion, protein scaffolding, Bin/Amphiphysin/Rvs (BAR), and amphipathic helix insertion, or steric interactions to facilitate energetically favorable binding to the membrane (Callan-Jones and Bassereau, 2013). However, disordered proteins also seem to exhibit curvature-sensing mechanisms when binding to the membrane. Several studies suggest that certain proteins, even those without specific curvature-sensing domains, have the capacity to sense and preferentially localize to sites of distinct curvature on the membrane (Bartels et al., 2010; Larsen et al., 2015; Zhao et al., 2017). Zeno et al. present a model that includes both an entropic and electrostatic mechanism to attempt to explain the ability of disordered proteins to find and bind to structural heterogeneities in the plasma membrane (Zeno et al., 2019). The model suggests that as membrane curvature increases, steric hindrance decreases between the disordered protein and the membrane and chain entropy increases, making it entropically favorable for proteins with a high degree of conformational energy to bind to high curvature locales on the membrane. As the curvature increases, the average distance between anionic membrane lipids and negatively charged amino acid chains also increases making this an electrostatically favorable configuration for proteins with high net negative charge. This model could be used to give a conceptual explanation for why certain surface proteins exhibit curvature preference on the plasma membrane. Another model aims to describe the relationship between membrane curvature and transmembrane protein distribution with a purely thermodynamic approach (Aimon et al., 2014). The membrane is modeled as a thin (quasi-2D) fluid film in which proteins freely diffuse and the addition of each protein to this surface alters the bending energy of the membrane. The protein distribution is then determined through a calculation which minimizes free energy.

The models discussed above all aim to describe the mechanisms through which proteins preferentially distribute themselves on the curved plasma membrane. To add context to these models, we now discuss some mechanisms which create curvature gradients on the plasma membrane, and therefore mediate curvature-driven regulation of protein distribution.

Mechanical forces generate curved membrane surfaces which may facilitate T cell activation. One investigation of the mechanical forces generated upon engagement of the TCR and Lymphocyte function-associated antigen 1 (LFA-1) gave a

quantified description of a force generation sequence upon local bidimensional engagement of the TCR-CD3 complex (Husson et al., 2011). The sequence is described by an initial latency phase, which is followed by a pushing phase and then a pulling phase. During the pushing phase, the cell extended a directional growth toward the APC. The initial growth of the T cell protrusion toward the APC was characterized by a constant growth speed which is comparable to actin polymerization kinetics, while co-engagement of LFA-1 and TCR showed a clear decrease in the protrusion length emitted in the pushing phase. Another study characterized T cell spreading response as a function of substrate rigidity (Wahl et al., 2019). Depending on the surface receptors stimulated, the cellular response may either be biphasic or monotonous. Actin polymerization-generated forces are the basis for this theoretical description of mechanosensitive spreading of T cells. In the authors' proposed model, the biphasic behavior of the driving tensile force depends on high effective bond stiffness and low bond force sensitivity.

The connection between the capacity for curvature-sensing, which many proteins and peptides exhibit, and the membrane surface protein distribution is not yet well-defined. However, structural mechanisms as well as thermodynamic models can now provide insight into the curvature-driven regulation of protein distribution on the plasma membrane. The processes through which this curvature is created may then also play a major role in the membrane curvature/protein distribution relationship. In effect, cellular mechanisms which induce curvature in the plasma membrane could have several nontrivial consequences for cell signaling processes.

MEMBRANE PROTEIN DISTRIBUTION

The mechanism by which cell surface proteins seem to be able to detect changes in membrane curvature is currently a poorly understood phenomenon. However, many studies have shown the redistribution of proteins, such as the TCR, in response to curvature in the cell membrane, particularly favoring localizing on protrusions such as microvilli (Sage et al., 2012; Cai et al., 2017). Protein organization on the T cell membrane has previously been characterized using single molecule localization microscopy (SMLM), showing this spatial reorganization of proteins on the surface of T cells is essential for the TCR triggering, therefore conferring a functional significance for T cells (Pageon et al., 2016).

The redistribution of TCRs into small peripheral bundles observed using SMLM were termed micro- or nano-clusters and have since become a defining feature of T cell activation (**Figure 2A**). This called into question how the reorganization of proteins into spatially heterogeneous clusters on the membrane gives a functional advantage to the cell by facilitating T cell triggering. The answer has been theorized by various activation models. The kinetic proofreading model, together with the induced rebinding model, postulates that the clustering of TCR molecules allows for discrimination between the 10^{-4} lower-levels of antigenic-pMHC to non-stimulating-pMHC molecules, via temporal lags in binding, and rapid rebinding to pMHC molecules (Mckeithan, 1995; Dushek and van der Merwe, 2014; Goyette et al., 2019). Thus, the grouping of TCR complexes into clusters on the membrane may lead to rapid binding and sampling of pMHC by TCR, thereby allowing T cells to maintain sensitivity and discrimination of cognate peptides.

Following the finding that TCR clustering aids activation, further emphasis was placed on the concept that proteins may compartmentalize on the membrane to facilitate biochemical reactions. A combination of imaging approaches revealed that signaling proteins associated with the LAT signalosome form distinct submicrometer-sized physical compartments at the membrane (Su et al., 2016). It was additionally seen that the formation of these LAT compartments may be driven by lipid phase separation (Ditlev et al., 2019). Additionally, bulky phosphatases such as CD45 are sterically excluded from areas of TCR-ligand engagement, thereby shifting the balance toward phosphorylation upon triggering and further strengthening the theory that membrane protein organization facilitates early T cell signaling (Leupin et al., 2000; Chang et al., 2016). This indicates that heterogeneities in the composition of the plasma membrane may be essential for the compartmentalization of proteins and contribute to altered functional outcomes.

Moreover, it has been well-documented using various microscopy techniques, that membrane proteins involved in T cell activation distribute into distinct regions within a "supramolecular activation cluster" (SMAC) and collectively form an immunological synapse with an APC (Monks et al., 1998). By combining this knowledge with TCR microcluster formation, it was hypothesized that these clusters accumulate and stabilize at the middle of the synapse, forming a central hub of activation, with bulky phosphatases pushed to outer areas (Grakoui et al., 1999). Conversely, later studies found that early stage TCR clusters form at the leading edge of an activating T cell and immediately recruit signaling proteins, with later-stage signaling corresponding to the movement of microclusters to the center of the synapse (Bunnell et al., 2002). Furthermore, early TCR signaling molecules such as Zap70 and SLP-76 dissociate from the TCR upon entry into the central area of the SMAC, leading to signal termination (Yokosuka et al., 2005). Collectively, these studies all show that dynamic protein heterogeneity in the membrane can dramatically shift signaling and functional responses.

The organization of proteins into distinct compartments on the membrane was speculated to also facilitate signal termination. Choudhuri et al. showed microvesicles with high levels of TCR molecules budding from the plasma membrane, indicating that the membrane at the central immune synapse has high curvature (Choudhuri et al., 2014). Later studies using live-cell imaging of the T cell-APC interface defined these budded fragments as T cell microvilli-derived particles (TMP), proposing that T cells leave behind TMPs on APC surfaces post-activation (Kim et al., 2018). The relocation of TCR microclusters to the center of the synapse may, therefore, facilitate budding from the membrane, terminating signaling, removing TCR molecules from the T cell surface, and perhaps a means of trans-cellular communication with the APC in the synapse interface in a process termed "trogocytosis" (Kim et al., 2018).

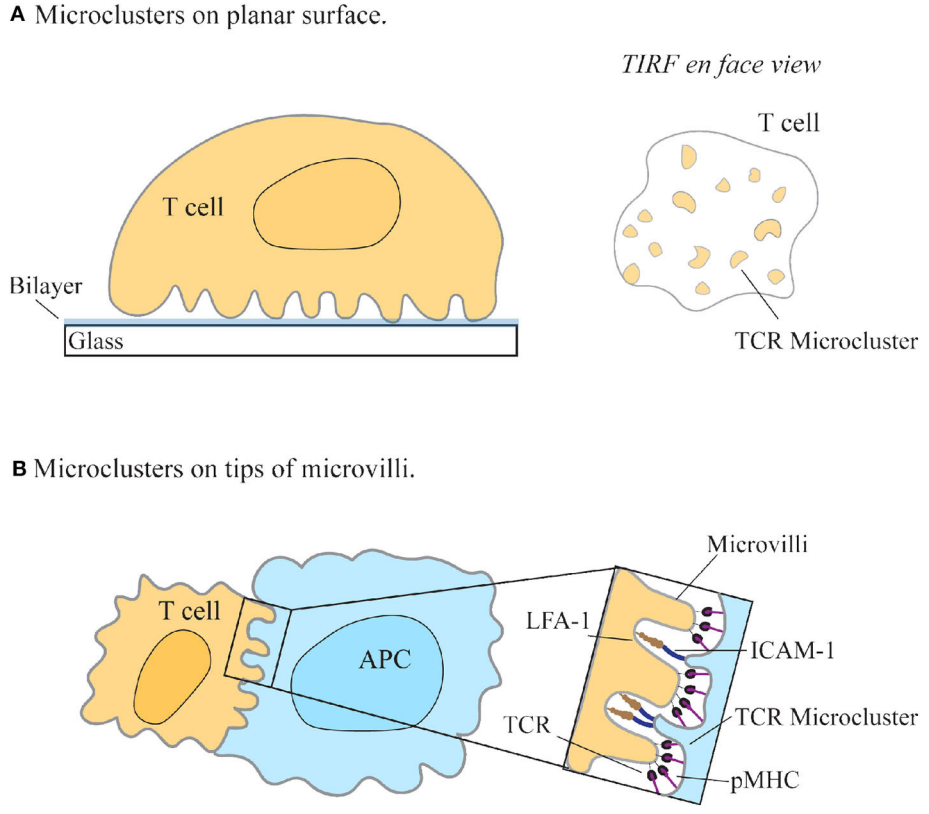

FIGURE 2 | T cell receptor enrichment on microvilli. **(A)** T cell receptors (TCR) seem to redistribute into microclusters upon engagement with a SLB-coated surface using TIRF-microscopy. (**A**, right) *En face* view of the interface between the cell and the coverslip, as seen with TIRF-microscopy. **(B)** Jung et al. found that TCRs preferentially localize to the tips of microvilli on T cells to facilitate searching of antigen presenting cells (APC) for cognate pMHC (Jung et al., 2016). Zoom-in region shows the contact interface with the larger adhesion molecules LFA-1 and ICAM-1 binding at the base and TCR/pMHC interacting at the tips of microvilli (Neve-Oz et al., 2018).

Much of the knowledge of membrane protein distribution and signal regulation of T cells is collected using TIRF microscopy techniques, allowing for the nanoscale detection of membrane proteins. One compromise when imaging nanoscale protein distributions using super-resolution techniques is the necessity for the cell to be immobilized onto planar surfaces, such as antibody-coated glass and supported lipid bilayers (SLB) (**Figure 2A**). Although SLBs allowed for the mobility of ligand-protein interactions and the movement of receptors into clusters, the use of a stiff surface to activate cells may mechanically "frustrate" cells and restrict essential membrane formations, an aspect that must be considered when interpreting data collected from planar surfaces (Sage et al., 2012). Additionally, studying T cells under resting conditions is an essential baseline for understanding the changes T cells undergo upon activation. Recent studies show that many features seen in "resting" T cells may be artifacts of the coating used to adhere these cells onto a surface, consequently causing non-physiological responses (Ponjavic et al., 2018; Rossboth et al., 2018; Santos et al., 2018).

Thus, the use of various light microscopy techniques have indubitably been an asset to understanding how these complex immune cells function, however, these methods are inherently limiting. Therefore, one should consider how these findings may apply to broader three-dimensional interactions between a T cell and an APC.

TOPOLOGY-DRIVEN PROTEIN DISTRIBUTION

In physiological settings, T cells make contact with deformable surfaces and must penetrate the thick glycocalyx present on cells. Therefore, protein distribution may vary when the T cell comes into contact with an APC (and may differ from that in a reconstituted system). For these reasons, focus has shifted recently to taking membrane topological features into consideration when activating and imaging immune cells.

Various imaging approaches facilitated the finding that membrane protein distribution may be linked to cell topography. One such approach is combining variable-angle TIRF (VA-TIRF) with stochastic localization nanoscopy (SLN) to determine the relationship between TCR membrane distribution and T cell microvilli (Jung et al., 2016). Through this method, it was hypothesized that microvilli may facilitate antigen searching by T cells, with a higher density of T cell receptors found at the tips of microvilli, suggesting that this enrichment of TCR molecules

in resting T cells may be a consequence of membrane topological features (Jung et al., 2016) (**Figure 2B**). This supported the observation, using SMLM techniques, that the TCR complex is pre-clustered in quiescent T cells (Lillemeier et al., 2010). A defining feature of T cells is their ability to search the large surface area of APCs for cognate pMHCs; this finding thus suggested an explanation for how the cell may efficiently facilitate this search.

This discovery shed light on the complicated process of APC searching, however, the method microvilli used to search was still largely unclear. Advances in light microscopy, such as the ability to form a light-sheet, led to greater insight into these 3D processes (Huisken et al., 2004). Lattice light-sheet microscopy is used to investigate how T cells utilize their dynamic surface protrusions to interact with large surface areas of APCs and find cognate pMHC. Studies show that this searching is conducted in a quick, efficient manner, with microvilli stabilizing upon the recognition of pMHC (Cai et al., 2017; Fernandes et al., 2019). This led to a greater understanding of how the high density of TCR molecules on the tips of the microvilli carried out the search and what occurred upon recognition of a cognate antigen.

The ILPs observed by Sage et al. when activating T cells with endothelial cells pulsed with antigen (similar in size and dimension to previously described microvilli) were shown to be used by T cells for probing cells for antigens, much like microvilli, penetrating the surface of planar endothelial cells and facilitating trans-endothelial migration in the absence of antigen. This finding is consistent with the theory that TCRs are accumulated on the tips of T cell protrusions and, additionally, they showed that these peripheral protrusions are not only enriched in TCR components but also with the corresponding signaling molecules, such as Zap70, suggesting active signaling occurring in protrusions (Sage et al., 2012).

In order for T cells to penetrate the thick glycocalyx, some mechanical forces must be generated. As mentioned previously, using biomembrane force probes, T cells were shown to undergo directional "pushing" toward the model APC at a rate of growth comparable to actin polymerization kinetics. This indicates that microvilli may need to "reach out" to engage cognate pMHCs (Husson et al., 2011). Given the comparable length of microvilli and width of the glycocalyx (estimated 200–500 nm for endothelial cells), this may be a functional mechanism for the cell to protrude through the glycocalyx to reach its surface ligands (**Table 1**) (Reitsma et al., 2007). Additional works highlighted the role of actin in the spatial and temporal dynamics of T cell signaling at the membrane surface. T cells were shown to generate forces against the interacting surface and actin flow was highlighted as the responsible agent for the mechanical force (Colin-York et al., 2019). This underlines a mechanism by which T cells can maintain signaling from TCR microclusters at the tips of microvilli through the force produced by actin polymerization and, additionally sustaining protein compartmentalization via "molecular clutch" interactions between LAT-associated proteins and actin filaments (Ditlev et al., 2019). Collectively, new insights suggest a dynamic relationship between membrane topology and protein distributions on the T cell surface, a process which may be facilitated by the actin network.

A recent study carried out by Ghosh et al. showed that essential components of TCR signaling are pre-organized on microvilli creating a hub of TCR signaling (Ghosh et al., 2020). This study followed on from previous work using combinational VA-TIRFM and SLN techniques, which revealed pre-clustering of TCR molecules at the tips of microvilli in resting T cells (Jung et al., 2016). They additionally show, using the same approach, that TCR components, the co-stimulating molecule CD2 and the co-receptor CD4 also localize to the microvilli region, with over 90% of molecules within protrusion regions. Microvilli were deemed "hubs" of signaling as the kinase Lck and the signaling adaptor LAT were also localized to microvilli regions, indicating the formation of membrane curvature, in the form of microvilli, promotes signaling from the TCR complexes, thereby facilitating functional consequences (Ghosh et al., 2020). Consistent with previous reports, the phosphatase CD45 was seen to be relatively homogeneously distributed on the T cell membrane, with only ∼30% of CD45 molecules localized within microvilli regions, further promoting T cell activation (Cai et al., 2017; Fernandes et al., 2019).

3D studies have shed light on how T cells recognize antigens amongst a sea of self-peptides, utilizing membrane protrusions rich in TCR molecules as antigen sensors, rapidly searching APCs, stabilizing and signaling upon antigen recognition. Thus, heterogeneities in membrane topology, composition and protein distribution within the T cell membrane are demonstrated to be essential for the regulation of effector functions in T cells.

MEMBRANE HETEROGENEITY AIDS T CELL ACTIVATION

The cell membrane is a complex entity, the movement and curvature of which is influenced dynamically by a range of factors all affecting and responding to each other. Influential factors include lipid compositions, trans-membrane proteins responses, e.g., curvature-sensing proteins, mechanical forces, contacts with extracellular matrices, and cell-cell interactions. The combination of all of these processes has intracellular effects on the cell that lead to alternate cellular responses. In the context of T cells, there are multiple ways in which heterogeneities in the membrane such as these can effect the T cells initial activation, inter-membrane architecture and ultimately signaling and cell responses. Membrane curvature creates an uneven surface, on which the first interactors of an APC will be proteins located at the tips of protrusions. In T cells, many studies mentioned earlier in the review have described how the T cell utilizes this by enriching protrusions with TCR molecules in order to rapidly search APCs for cognate pMHC (Lillemeier et al., 2010; Jung et al., 2016). Following this, pre-clustering and/or ligand-induced TCR clustering has been described to increase the selectivity and sensitivity of the T cell response by facilitating binding to multiple pMHC molecules on the APC and allow for rapid re-binding events to occur due to high local concentrations of TCR molecules on the membrane. This process can enhance the sensitivity of the T cell to rare antigens upon recognition and sustain the signaling response (Goyette et al., 2019). Additionally

to membrane dimensions influencing protein organizations, the converse can also occur. Following TCR triggering, multi-protein complexes form to create a "hub" of signaling. As discussed previously, the LAT signalosome forms in response to TCR triggering (Su et al., 2016). This signalosome is made up of multivalent binding interactions which coagulate into clusters of intracellular signaling proteins and form "islands" of signaling in the membrane, influencing membrane compositions and rapidly signaling intracellularly, resulting in cellular responses (Ditlev et al., 2019).

Interactions between cells can have profound influences on the heterogeneity of the membrane. Steric and other external biophysical factors can alter protein distributions and induce curvature in the membrane, ultimately having an influence on cellular functions. For instance, the relative size and shape of receptors on the T cell surface, and their associated ligands, are well characterized and have functional consequences at contact interfaces. This knowledge allows for the prediction of how close together the T cell membrane must be to the APC membrane in order for contact to occur. For this reason, heterogeneities in the topology of the membrane help to facilitate the ligation of proteins on the T cell surface, which have functional consequences. Dimensional heterogeneities such as these can have functional impacts on T cell recognition. Adhesion molecules, such as CD2, on T cells, bind to their ligands to create a close contact area between the two cell membranes at a distance close enough (∼10 nm) to allow the TCR to bind to the pMHC molecule on the APC, and have been seen to localize to the tips of microvilli (Jung et al., 2016). Additionally, other adhesion molecules, such as LFA-1 and ICAM-1, on T cells and APCs, respectively, create a larger inter-membrane distance (∼37 nm) where surface proteins that make up the lymphocytic glycocalyx (rich in sialic acid), such as CD43 and CD45, are excluded (Springer, 1990; Davis and van der Merwe, 2006; Razvag et al., 2019). This proceeds in limiting the lateral mobility of membrane proteins with large extracellular domains through the creation of a physical barrier. Collectively, this creation of 'tight contact areas' promotes the recognition of antigens by T cells, segregates phosphatases such as CD45 from tight contacts, enriching and laterally trapping them in areas of high local curvature in the membrane, enhancing signaling and sustaining T cell activation (Razvag et al., 2019). Thus, there is dynamic interplay between membrane topology and protein distributions which contribute to the diverse functional outcomes of T cells.

CONCLUSION

The interplay between spatial organization of membrane proteins and membrane topological features, i.e., the characteristic heterogeneities of the T cell membrane, has functional consequences and significantly contributes to the fate of T cells. In this review we have covered research which demonstrates that the membrane has heterogeneous processes which affect T cell function. The dimensions of the morphological features which give the membrane biophysical properties, consequently allowing pre-clustering of proteins on the membrane surface, directly affect the organization of membrane proteins at the T cell/ APC contact interface, and though the study of these "initial" protein distributions is currently an active field of research, there remains the critical question of how these clusters are functionally advantageous and to what extent they increase the selectivity and sensitivity of the T cell. Reorganization of membrane proteins at the immunological synapse comes as a result of ligand-induced clustering, which in turn shapes the membrane itself. Thus, the reciprocal relationship between these classifications of T cell heterogeneity—protein pre-clustering and ligand-induced protein clustering—is that protein pre-clustering, due to biophysical mechanisms which determine the membrane shape, defines the protein distribution at the T cell/APC contact interface, which in turn shapes the membrane itself. We predict that this will continue to be an active area of research as more evidence is discovered to demonstrate the intrinsic relationship between membrane heterogeneity and T cell antigen recognition and subsequent activation.

Although there have been huge advancements in investigating the effect of these membrane heterogeneities on T cell activation in recent years, there are still essential questions, to which, answers are yet to be discovered. Reports of the length of microvilli seem to range from 0.3 to 5 μm (**Table 1**) but is there a functional reason or cause for this variation? Is it simply a matter of standardizing morphological classification? The answer to this may lie in the further characterization and identification of these subcellular morphological motifs, defining criteria such as surface area, volume, and degree of curvature of protrusions seen on the T cell surface. The capacity for curvature-sensing by proteins involved in the initial engagement between the T cell and the APC and the degree to which it affects membrane protein distribution and curvature is also not well-defined. Thus, further investigations are needed to conclude if these surface proteins could amplify or regulate membrane bending. Additionally, it is possible that the formation of these protrusions alters depending on the interacting substrate—these alterations including synthetic activation using coverslips or simply differences in the APC cell type (Sage et al., 2012; Wahl et al., 2019). Furthermore, it has been reported that microvilli aid searching of the APC surface, however, it is still unclear if this searching continues prior to initial contact with a cognate antigen. It also remains unclear whether TCR molecules are pre-clustered at the tips of microvilli, or if clustering occurs upon TCR triggering, as previously described. The answer to these questions lies in further studies, utilizing the recent advances in microscopy, such as high resolution light-sheet microscopy, and continued creative use of conventional techniques to help unveil the hidden intricacies of the T cell/APC interaction interface.

AUTHOR CONTRIBUTIONS

MF and SW wrote the manuscript and created the figures. KG and JG provided guidance and edited the manuscript. All authors contributed to the article and approved the submitted version.

REFERENCES

Aimon, S., Callan-Jones, A., Berthaud, A., Pinot, M., Toombes, G. E., and Bassereau, P. (2014). Membrane shape modulates transmembrane protein distribution. *Dev. Cell* 28, 212–218. doi: 10.1016/j.devcel.2013.12.012

Balagopalan, L., Kortum, R. L., Coussens, N. P., Barr, V. A., and Samelson, L. E. (2015). The linker for activation of T cells (lat) signaling hub: from signaling complexes to microclusters. *J. Biol. Chem.* 290, 26422–26429. doi: 10.1074/jbc.R115.665869

Bartels, T., Ahlstrom, L. S., Leftin, A., Kamp, F., Haass, C., Brown, M. F., et al. (2010). The n-terminus of the intrinsically disordered protein α-synuclein triggers membrane binding and helix folding. *Biophys. J.* 99, 2116–2124. doi: 10.1016/j.bpj.2010.06.035

Baumgart, F., Schneider, M., and Schütz, G. J. (2019). How T cells do the "search for the needle in the haystack." *Front. Phys.* 7:11. doi: 10.3389/fphy.2019.00011

Brodovitch, A., Bongrand, P., and Pierres, A. (2013). T lymphocytes sense antigens within seconds and make a decision within one minute. *J. Immunol.* 191, 2064–2071. doi: 10.4049/jimmunol.1300523

Bunnell, S. C., Hong, D. I., Kardon, J. R., Yamazaki, T., McGlade, C. J., Barr, V. A., et al. (2002). T cell receptor ligation induces the formation of dynamically regulated signaling assemblies. *J. Cell Biol.* 158, 1263–1275. doi: 10.1083/jcb.200203043

Burroughs, N. J., Lazic, Z., and van der Merwe, P. A. (2006). Ligand detection and discrimination by spatial relocalization: a kinase-phosphatase segregation model of TCR activation. *Biophys. J.* 91, 1619–1629. doi: 10.1529/biophysj.105.080044

Cai, E., Marchuk, K., Beemiller, P., Beppler, C., Rubashkin, M. G., Weaver, V. M., et al. (2017). Visualizing dynamic microvillar search and stabilization during ligand detection by T cells. *Science* 356:6338. doi: 10.1126/science.aal3118

Callan-Jones, A., and Bassereau, P. (2013). Curvature-driven membrane lipid and protein distribution. *Curr. Opin. Solid State Mater. Sci.* 17, 143–150. doi: 10.1016/j.cossms.2013.08.004

Chang, V. T., Fernandes, R. A., Ganzinger, K. A., Lee, S. F., Siebold, C., McColl, J., et al. (2016). Initiation of T cell signaling by CD45 segregation at 'close contacts'. *Nat. Immunol.* 17, 574–582. doi: 10.1038/ni.3392

Chen, L., and Flies, D. B. (2013). Molecular mechanisms of t cell co-stimulation and co-inhibition. *Nat. Rev. Immunol.* 13, 227–242. doi: 10.1038/nri3405

Choudhuri, K., Llodrá, J., Roth, E. W., Tsai, J., Gordo, S., Wucherpfennig, K. W., et al. (2014). Polarized release of T-cell-receptor-enriched microvesicles at the immunological synapse. *Nature* 507, 118–123. doi: 10.1038/nature12951

Choudhuri, K., Wiseman, D., Brown, M. H., Gould, K., and van der Merwe, P. A. (2005). T-cell receptor triggering is critically dependent on the dimensions of its peptide-MHC ligand. *Nature* 436, 578–582. doi: 10.1038/nature03843

Colin-York, H., Javanmardi, Y., Skamrahl, M., Kumari, S., Chang, V. T., Khuon, S., et al. (2019). Cytoskeletal control of antigen-dependent T cell activation. *Cell Rep.* 26, 3369–3379. doi: 10.1016/j.celrep.2019.02.074

Courtney, A. H., Lo, W.-L., and Weiss, A. (2018). TCR signaling: mechanisms of initiation and propagation. *Trends Biochem. Sci.* 43, 108–123. doi: 10.1016/j.tibs.2017.11.008

Davis, S. J., and van der Merwe, P. A. (2006). The kinetic-segregation model: TCR triggering and beyond. *Nat. Immunol.* 7, 803–809. doi: 10.1038/ni1369

Ditlev, J. A., Vega, A. R., Köster, D. V., Su, X., Tani, T., Lakoduk, A. M., et al. (2019). A composition-dependent molecular clutch between T cell signaling condensates and actin. *eLife* 8, 1–44. doi: 10.7554/eLife.42695

Driscoll, M. K., Welf, E. S., Jamieson, A. R., Dean, K. M., Isogai, T., Fiolka, R., et al. (2019). Robust and automated detection of subcellular morphological motifs in 3D microscopy images. *Nat. Methods* 16, 1037–1044. doi: 10.1038/s41592-019-0539-z

Dushek, O., and van der Merwe, P. A. (2014). An induced rebinding model of antigen discrimination. *Trends Immunol.* 35, 153–158. doi: 10.1016/j.it.2014.02.002

Fernandes, R. A., Ganzinger, K. A., Tzou, J. C., Jonsson, P., Lee, S. F., Palayret, M., et al. (2019). A cell topography-based mechanism for ligand discrimination by the T cell receptor. *Proc. Natl. Acad. Sci. U.S.A.* 116, 14002–14010. doi: 10.1073/pnas.1817255116

Fritzsche, M., Li, D., Colin-York, H., Chang, V. T., Moeendarbary, E., Felce, J. H., et al. (2017). Self-organizing actin patterns shape membrane architecture but not cell mechanics. *Nat. Commun.* 8:14347. doi: 10.1038/ncomms14347

Ghosh, S., Di Bartolo, V., Tubul, L., Shimoni, E., Kartvelishvily, E., Dadosh, T., et al. (2020). ERM-dependent assembly of T cell receptor signaling and co-stimulatory molecules on microvilli prior to activation. *Cell Rep.* 30, 3434–3447. doi: 10.1016/j.celrep.2020.02.069

Goyette, J., Nieves, D. J., Ma, Y., and Gaus, K. (2019). How does T cell receptor clustering impact on signal transduction? *J. Cell Sci.* 132:jcs226423. doi: 10.1242/jcs.226423

Grakoui, A., Bromley, S. K., Sumen, C., Davis, M. M., Shaw, A. S., Allen, P. M., et al. (1999). The immunological synapse: a molecular machine controlling T cell activation. *Science* 285, 221–227. doi: 10.1126/science.285.5425.221

Huisken, J., Swoger, J., Del Bene, F., Wittbrodt, J., and Stelzer, E. H. K. (2004). Optical sectioning deep inside live embryos by selective plane illumination microscopy. *Science* 305, 1007–1009. doi: 10.1126/science.1100035

Husson, J., Chemin, K., Bohineust, A., Hivroz, C., and Henry, N. (2011). Force generation upon T cell receptor engagement. *PLoS ONE* 6:e19680. doi: 10.1371/journal.pone.0019680

Jung, Y., Riven, I., Feigelson, S. W., Kartvelishvily, E., Tohya, K., Miyasaka, M., et al. (2016). Three-dimensional localization of T-cell receptors in relation to microvilli using a combination of superresolution microscopies. *Proc. Natl. Acad. Sci. U.S.A.* 113, E5916–E5924. doi: 10.1073/pnas.1605399113

Kim, H. R., Mun, Y. V., Lee, K. S., Park, Y. J., Park, J. S., Park, J. H., et al. (2018). T cell microvilli constitute immunological synaptosomes that carry messages to antigen-presenting cells. *Nat. Commun.* 9:3630. doi: 10.1038/s41467-018-06090-8

Kumari, S., Depoil, D., Martinelli R., Judokusomo, E., Carmona, G., Gertler, F. B., et al. (2015). Actin foci facilitate activation of the phospholipase c-γ in primary t lymphocytes via the wasp pathway. *eLife* 4:e04953. doi: 10.7554/eLife.04953.034

Larsen, J. B., Jensen, M. B., Bhatia, V. K., Pedersen, S. L., Bjørnholm, T., Iversen, L., et al. (2015). Membrane curvature enables N-Ras lipid anchor sorting to liquid-ordered membrane phases. *Nat. Chem. Biol.* 11, 192–194. doi: 10.1038/nchembio.1733

Leupin, O., Zaru, R., Laroche, T., Muller, S., and Valitutti, S. (2000). Exclusion of CD45 from the T-cell receptor signaling area in antigen-stimulated T lymphocytes. *Curr. Biol.* 10, 277–280. doi: 10.1016/S0960-9822(00)00362-6

Lillemeier, B. F., Mörtelmaier, M. A., Forstner, M. B., Huppa, J. B., Groves, J. T., and Davis, M. M. (2010). TCR and Lat are expressed on separate protein islands on T cell membranes and concatenate during activation. *Nat. Immunol.* 11, 90–96. doi: 10.1038/ni.1832

Linder, S. (2009). Invadosomes at a glance. *J. Cell Sci.* 122, 3009–3013. doi: 10.1242/jcs.032631

Majstoravich, S., Zhang, J., Nicholson-Dykstra, S., Linder, S., Friedrich, W., Siminovitch, K. A., et al. (2004). Lymphocyte microvilli are dynamic, actin-dependent structures that do not require Wiskott-Aldrich syndrome protein (WASp) for their morphology. *Blood* 104, 1396–1403. doi: 10.1182/blood-2004-02-0437

Mattila, P. K., and Lappalainen, P. (2008). Filopodia: molecular architecture and cellular functions. *Nat. Rev. Mol. Cell Biol.* 9, 446–454. doi: 10.1038/nrm2406

Mckeithan, T. W. (1995). Kinetic proofreading in T-cell receptor signal transduction (protein-tyrosine kinase/major histocompatibility complex/mathematical model). *Immunology* 92, 5042–5046. doi: 10.1073/pnas.92.11.5042

Monks, C. R., Freiberg, B. A., Kupfer, H., Sciaky, N., and Kupfer, A. (1998). Three-dimensional segregation of supramolecular activation clusters in T cells. *Nature* 395, 82–86. doi: 10.1038/25764

Neve-Oz, Y., Sajman, J., Razvag, Y., and Sherman, E. (2018). InterCells: a generic monte-carlo simulation of intercellular interfaces captures nanoscale patterning at the immune synapse. *Front. Immunol.* 9:2051. doi: 10.3389/fimmu.2018.02051

Pageon, S. V., Tabarin, T., Yamamoto, Y., Ma, Y., Nicovich, P. R., Bridgeman, J. S., et al. (2016). Functional role of T-cell receptor nanoclusters in signal initiation and antigen discrimination. *Proc. Natl. Acad. Sci. U.S.A.* 113, 5454–5463. doi: 10.1073/pnas.1607436113

Ponjavic, A., McColl, J., Carr, A. R., Santos, A. M., Kulenkampff, K., Lippert, A., et al. (2018). Single-molecule light-sheet imaging of suspended T cells. *Biophys. J.* 114, 2200–2211. doi: 10.1016/j.bpj.2018.02.044

Razvag, Y., Neve-Oz, Y., Sajman, J., Reches, M., and Sherman, E. (2018). Nanoscale kinetic segregation of TCR and CD45 in engaged microvilli facilitates early T cell activation. *Nat. Commun.* 9:732. doi: 10.1038/s41467-018-03127-w

Razvag, Y., Neve-Oz, Y., Sajman, J., Yakovian, O., Reches, M., and Sherman, E. (2019). T cell activation through isolated tight contacts. *Cell Rep*. 29, 3506–3521.e6. doi: 10.1016/j.celrep.2019.11.022

Reitsma, S., Slaaf, D. W., Vink, H., van Zandvoort, M. A. M. J., and oude Egbrink, M. G. A. (2007). The endothelial glycocalyx: composition, functions, and visualization. *Pflugers Archiv*. 454, 345–359. doi: 10.1007/s00424-007-0212-8

Rosenbluth, M. J., Lam, W. A., and Fletcher, D. A. (2006). Force microscopy of nonadherent cells: a comparison of leukemia cell deformability. *Biophys. J.* 90, 2994–3003. doi: 10.1529/biophysj.105.067496

Rossboth, B., Arnold, A. M., Ta, H., Platzer, R., Kellner, F., Huppa, J. B., et al. (2018). TCRs are randomly distributed on the plasma membrane of resting antigen-experienced T cells. *Nat. Immunol*. 19, 821–827. doi: 10.1038/s41590-018-0162-7

Sadegh, S., Higgins, J. L., Mannion, P. C., Tamkun, M. M., and Krapf, D. (2017). Plasma membrane is compartmentalized by a self-similar cortical actin meshwork. *Phys. Rev. X* 7:011031. doi: 10.1103/PhysRevX.7.011031

Sage, P. T., Varghese, L. M., Martinelli, R., Sciuto, T. E., Kamei, M., Dvorak, A. M., et al. (2012). Antigen recognition is facilitated by invadosome-like protrusions formed by memory/effector T cells. *J. Immunol*. 188, 3686–3699. doi: 10.4049/jimmunol.1102594

Santos, A. M., Ponjavic, A., Fritzsche, M., Fernandes, R. A., De La Serna, J. B., Wilcock, M. J., et al. (2018). Capturing resting T cells: the perils of PLL correspondence. *Nat. Immunol*. 19, 203–205. doi: 10.1038/s41590-018-0048-8

Springer, T. A. (1990). Adhesion receptors of the immune system. *Nature* 346, 425–434. doi: 10.1038/346425a0

Stone, M. B., Shelby, S. A., Núñez, M. F., Wisser, K., and Veatch, S. L. (2017). Protein sorting by lipid phase-like domains supports emergent signaling function in b lymphocyte plasma membranes. *eLife* 6:e19891. doi: 10.7554/eLife.19891

Su, X., Ditlev, J. A., Hui, E., Xing, W., Banjade, S., Okrut, J., et al. (2016). Phase separation of signaling molecules promotes T cell receptor signal transduction. *Science* 352, 595–599. doi: 10.1126/science.aad9964

Wahl, A., Dinet, C., Dillard, P., Nassereddine, A., Puech, P.-H., Limozin, L., et al. (2019). Biphasic mechanosensitivity of T cell receptor-mediated spreading of lymphocytes. *Proc. Natl. Acad. Sci. U.S.A*. 116, 5908–5913. doi: 10.1073/pnas.1811516116

Yokosuka, T., Sakata-Sogawa, K., Kobayashi, W., Hiroshima, M., Hashimoto-Tane, A., Tokunaga, M., et al. (2005). Newly generated T cell receptor microclusters initiate and sustain T cell activation by recruitment of Zap70 and SLP-76. *Nat. Immunol*. 6, 1253–1262. doi: 10.1038/ni1272

Zeno, W. F., Thatte, A. S., Wang, L., Snead, W. T., Lafer, E. M., and Stachowiak, J. C. (2019). Molecular mechanisms of membrane curvature sensing by a disordered protein. *J. Am. Chem. Soc*. 141, 10361–10371. doi: 10.1021/jacs.9b03927

Zhao, W., Hanson, L., Lou, H.-Y., Akamatsu, M., Chowdary, P. D., Santoro, F., et al. (2017). Nanoscale manipulation of membrane curvature for probing endocytosis in live cells. *Nat. Nanotechnol*. 12, 750–756. doi: 10.1038/nnano.2017.98

Conflict of Interest: The authors declare that the research was conducted in the absence of any commercial or financial relationships that could be construed as a potential conflict of interest.

frontiers in Cell and Developmental Biology

ORIGINAL RESEARCH
published: 04 August 2020
doi: 10.3389/fcell.2020.00756

A Quantitative Analysis of Cellular Lipid Compositions During Acute Proteotoxic ER Stress Reveals Specificity in the Production of Asymmetric Lipids

John Reinhard[1,2†], Carsten Mattes[1,2†], Kristina Väth[1,2†], Toni Radanović[1,2], Michal A. Surma[3], Christian Klose[3] and Robert Ernst[1,2]*

[1] Medical Biochemistry and Molecular Biology, Medical Faculty, Saarland University, Homburg, Germany, [2] PZMS, Center for Molecular Signaling, Medical Faculty, Saarland University, Homburg, Germany, [3] Lipotype GmbH, Dresden, Germany

OPEN ACCESS

Edited by:
Fernando Antunes, University of Lisbon, Portugal

Reviewed by:
Guillaume Thibault, Nanyang Technological University, Singapore
Yukio Kimata, Nara Institute of Science and Technology (NAIST), Japan

***Correspondence:**
Robert Ernst
robert.ernst@uks.eu

† These authors have contributed equally to this work

Specialty section:
This article was submitted to Cellular Biochemistry, a section of the journal Frontiers in Cell and Developmental Biology

Received: *06 May 2020*
Accepted: *20 July 2020*
Published: *04 August 2020*

Citation:
Reinhard J, Mattes C, Väth K, Radanović T, Surma MA, Klose C and Ernst R (2020) A Quantitative Analysis of Cellular Lipid Compositions During Acute Proteotoxic ER Stress Reveals Specificity in the Production of Asymmetric Lipids. Front. Cell Dev. Biol. 8:756. doi: 10.3389/fcell.2020.00756

The unfolded protein response (UPR) is central to endoplasmic reticulum (ER) homeostasis by controlling its size and protein folding capacity. When activated by unfolded proteins in the ER-lumen or aberrant lipid compositions, the UPR adjusts the expression of hundreds of target genes to counteract ER stress. The proteotoxic drugs dithiothreitol (DTT) and tunicamycin (TM) are commonly used to induce misfolding of proteins in the ER and to study the UPR. However, their potential impact on the cellular lipid composition has never been systematically addressed. Here, we report the quantitative, cellular lipid composition of *Saccharomyces cerevisiae* during acute, proteotoxic stress in both rich and synthetic media. We show that DTT causes rapid remodeling of the lipidome when used in rich medium at growth-inhibitory concentrations, while TM has only a marginal impact on the lipidome under our conditions of cultivation. We formulate recommendations on how to study UPR activation by proteotoxic stress without interferences from a perturbed lipid metabolism. Furthermore, our data suggest an intricate connection between the cellular growth rate, the abundance of the ER, and the metabolism of fatty acids. We show that *Saccharomyces cerevisiae* can produce asymmetric lipids with two saturated fatty acyl chains differing substantially in length. These observations indicate that the pairing of saturated fatty acyl chains is tightly controlled and suggest an evolutionary conservation of asymmetric lipids and their biosynthetic machineries.

Keywords: UPR, Ire1, lipid bilayer stress, proteotoxic stress, lipidomics, DTT, tunicamycin, asymmetric lipids

INTRODUCTION

Biological membranes are complex assemblies of proteins and lipids forming the boundary of cellular life and compartmentalizing biochemical processes in different organelles (van Meer et al., 2008; Bigay and Antonny, 2012). A major fraction of cellular bioactivity is localized to biological membranes: one third of all proteins and the majority of therapeutic drug targets are either membrane embedded or membrane associated (Uhlén et al., 2015). The interactions, activities, and subcellular localizations of membrane proteins

are modulated by their complex and dynamically regulated environment (Lee, 2004; Phillips et al., 2009; Lorent et al., 2017). The lipidome of a eukaryotic cell comprises hundreds, if not thousands, of lipid species and it can be remodeled upon dietary perturbation, by the growth phase, and in response to external cues such as temperature or nutrient availability (Shevchenko and Simons, 2010; Klose et al., 2012; Casanovas et al., 2015; Han, 2016; Levental et al., 2020). This membrane responsiveness down to the level of individual lipid species is essential to sustain cellular fitness, by maintaining physicochemical membrane properties such as fluidity, permeability, phase behavior, and surface charge density in a regime acceptable for membrane function (Bigay and Antonny, 2012; Sezgin et al., 2017; Ernst et al., 2018; Harayama and Riezman, 2018). Our understanding of these complex remodeling processes, their purposes and the underlying principles, remains rather limited.

The endoplasmic reticulum (ER) is the central hub for membrane biogenesis in eukaryotic cells (van Meer et al., 2008). The vast majority of membrane proteins is targeted to ER-localized machineries for membrane insertion (Aviram and Schuldiner, 2017). Likewise, a major fraction of membrane lipids including sterols, glycerophospholipids, and ceramides is produced in the ER (van Meer et al., 2008). In the past years it became increasingly clear that protein quality control and lipid metabolism are intimately connected both on the cellular and the molecular level (Jonikas et al., 2009; De Kroon et al., 2013; Stordeur et al., 2014; Volmer and Ron, 2015; Fun and Thibault, 2020; Goder et al., 2020).

A prominent example is the unfolded protein response (UPR) (Walter and Ron, 2011). Both an accumulation of unfolded protein in the lumen of the ER and stiffening of the ER membrane due to lipid imbalances serve as activating signals for the UPR (Halbleib et al., 2017; Karagöz et al., 2017; Adams et al., 2019; Preissler and Ron, 2019). How precisely these activating signals from the lumen of the ER and the ER membrane are integrated by the transducers of the UPR is matter of active debate (Volmer and Ron, 2015; Covino et al., 2018; Fun and Thibault, 2020). Once activated, the UPR increases the size of the ER and its folding capacity in order to reestablish ER homeostasis even under adverse conditions (Bernales et al., 2006; Schuck et al., 2009). This is accomplished by a global attenuation of protein production (Walter and Ron, 2011), by upregulating the ER-associated degradation machinery, and by increasing the number of ER chaperones (Cox et al., 1993; Jonikas et al., 2009). At the same time, the UPR induces the expression of a large number of genes involved in membrane-related processes such as lipid biosynthesis, membrane protein sorting, and vesicular traffic (Travers et al., 2000). Unbiased genetic screens and targeted perturbations of lipid metabolism have clearly established the mutual dependency of the UPR and lipid metabolism (Jonikas et al., 2009; Pineau et al., 2009; Schuck et al., 2009; Promlek et al., 2011; Thibault et al., 2012; Surma et al., 2013). Given its central importance for ER homeostasis and cell physiology, it is not surprising that the UPR plays also a crucial role in pathologic processes such as viral infections, neurodegeneration, and cancer (Wang and Kaufman, 2012,Wang and Kaufman, 2014; Hetz et al., 2019). Metabolic diseases associated with chronic UPR signaling such as type II diabetes and non-alcoholic steatohepatitis (Kaufman, 2002; Fonseca et al., 2009) are historically studied with a focus on the role of unfolded, soluble proteins in the ER lumen while the contribution of signals from the ER membrane remains understudied.

The eukaryotic model organism *Saccharomyces cerevisiae* (*S. cerevisiae*) has facilitated the identification of numerous key components of the secretory pathway, lipid metabolism, and the proteostasis network (Novick et al., 1980; Wolf and Schäfer, 2006; Henry et al., 2012; De Kroon et al., 2013). In contrast to metazoans, the UPR in *S. cerevisiae* relies on a single, ER-localized UPR transducer (Kimata and Kohno, 2011): the Inositol-requiring enzyme 1 (Ire1p). It is conserved from yeast to humans and comprises an N-terminal sensor domain facing the ER-lumen, a single transmembrane helix, and cytosolic effector domains with kinase and RNase functions. The formation of dimers and higher oligomers of Ire1p during stress from unfolded proteins or from the ER membrane (Kimata et al., 2007; Korennykh et al., 2009; Halbleib et al., 2017) triggers the *trans*-autophosphorylation of the cytosolic kinase domain and the activation of the adjacent RNase domain. The RNase activity of Ire1p contributes to an unconventional splicing of the *HAC1* mRNA in the cytosol (Cox and Walter, 1996; Mori et al., 1996) thereby facilitating the production of the active transcription factor Hac1p regulating several hundred UPR-target genes.

For studying and assaying the UPR, it is common practice to stress the cells acutely either with dithiothreitol (DTT), a reducing agent interfering with disulfide bridge formation in the ER-lumen, or tunicamycin (TM), a natural inhibitor of the N-linked glycosylation of proteins in the ER (Azim and Surani, 1979). It is generally assumed that DTT and TM exclusively cause proteotoxic ER stress. However, the impact of DTT and TM on the cellular lipid composition has never been systematically tested.

Here, we have studied the impact of DTT or TM on the lipidome of *S. cerevisiae* in both rich and synthetic medium. Serendipitously, we find evidence for a remarkable selectivity of *S. cerevisiae* in the generation and metabolism of highly asymmetric glycerophospholipids with one saturated, medium fatty acyl chain (C10 or C12) and a long, saturated one (C16 or C18). Despite a high overall abundance of unsaturated fatty acyl chains (C16:1 or C18:1), we find an almost exclusive paring of two saturated fatty acyl chains in these asymmetric glycerophospholipids, thereby implying a strong, inherent selectivity of acyl chain pairing. With respect to the UPR, we find that (1) DTT and TM impair cellular growth, (2) the medium has a significant impact on the cellular lipidome thereby potentially tuning the sensitivity of the UPR, (3) DTT at growth-inhibitory concentrations causes a substantial and rapid remodeling of the lipidome in rich medium, and (4) TM under our experimental conditions has only a marginal impact on the cellular lipidome in both synthetic and rich medium. Based on these findings, we provide a guideline to predictably and unambiguously activate the UPR by proteotoxic stress, whilst minimizing potential artifacts from lipid bilayer stress.

MATERIALS AND METHODS

Yeast Strains

Yeasts used were the standard laboratory wild-type *S. cerevisiae* strain BY4741 MATa *his3*Δ1 *leu2*Δ0 *met15*Δ0 *ura3*Δ0 and the *ire1*Δ-derivative BY4741 MATa; *ura3*Δ0; *leu2*Δ0; *his3*Δ1; *met15*Δ0; *YHR079c*::*kan*MX4.

Reagents

Chemicals and solvents of HPLC/LC-MS analytical grade were used. TM (#T7765), DTT (#D0632), and ammonium bicarbonate (#9830) were purchased from Sigma-Aldrich. Ammonium sulfate (#9218) was purchased from Carl Roth.

Media

All media were prepared according to standard protocols (Dymond, 2013). D(+)-Glucose (#HN06, tryptone/peptone (#8952), and yeast extract (#2363) were purchased from Carl Roth. Yeast nitrogen base (YNB) (#CYN0602), agar–agar (#AGA03), and complete supplement mixture (CSM complete) (#DCS0019) were purchased from FORMEDIUM.

Cell Cultivation for Lipidomics

Cells were cultivated under constant agitation at 30°C at 220 rpm, if not stated otherwise. Every lipidomic sample started from an individual, single colony on either yeast peptone dextrose (YPD) or synthetic complete dextrose (SCD) agar plates. A single colony was used to inoculate a pre-culture, which was then cultivated overnight for 21 h in either YPD or SCD liquid medium. The resulting stationary culture was used to inoculate a main culture in fresh medium to a final OD_{600} of 0.1. When the culture reached an OD_{600} of 0.8 ± 0.05, the cells were either stressed with DTT, TM or left untreated. DTT was used at a final concentration 8 mM and 2 mM in YPD and SCD, respectively. TM was used at a final concentration of 1.0 μg/ml and 1.5 μg/ml in YPD and SCD, respectively. After an additional hour of cultivation, 20 OD units of cells were harvested by centrifugation (3,500 × *g*, 5 min, 4°C), and washed three-times with ice-cold 155 mM ammonium bicarbonate supplemented with 10 mM sodium azide in 1.5 ml reaction tubes using quick centrifugation (10.000 × *g*, 20 s, 4°C). The resulting cell pellets were snap-frozen with liquid nitrogen and stored for up to 4 weeks at −80°C. Prior to cell lysis, pellets were thawed on ice and then resuspended in 1 ml 155 mM ammonium bicarbonate. 200 μl zirconia beads were added to the suspension and cells were disrupted by vigorous shaking using a DisruptorGenie for 10 min at 4°C. 500 μl of the resulting lysate was snap-frozen and used for further analysis via shotgun mass spectrometry.

Growth Assay – Acute Stress

Cultures in YPD and SCD were inoculated precisely as described for lipidomic experiments. The density of the culture was monitored over a prolonged period of time by determining the OD_{600} for up to 5 h after they had reached an OD_{600} = 0.8. For determining the doubling time of an exponentially growing culture, all data points with an OD_{600} between 0.2 and 2.5 were considered. The data were fitted to the exponential (Malthusian) growth function using Prism 8 for macOS Version 8.4.1.

Growth Assay – Prolonged Stress

Stationary overnight cultures in YPD were used to inoculate a pre-culture in either YPD or SCD to an OD_{600} of 0.2. The cells were then cultivated for 6 h to reach the exponential growth phase. These cultures were used to inoculate a main culture in a 96-well plate to an OD_{600} of 0.01 using fresh medium (either YPD or SCD) containing different concentrations of DTT. After cultivation for 16 h at 30°C with no agitation, the final OD_{600} was determined after intense mixing of the culture using a microplate reader (Tecan Microplate Reader Spark).

Lipid Extraction for Mass Spectrometry Lipidomics

Mass spectrometry-based lipid analysis was performed by Lipotype GmbH (Dresden, Germany) as described (Ejsing et al., 2009; Klose et al., 2012). Lipids were extracted using a two-step chloroform/methanol procedure (Ejsing et al., 2009). Samples were spiked with internal lipid standard mixture containing: CDP-DAG 17:0/18:1, ceramide 18:1;2/17:0 (Cer), diacylglycerol 17:0/17:0 (DAG), lyso-phosphatidate 17:0 (LPA), lyso-phosphatidylcholine 12:0 (LPC), lyso-phosphatidylethanolamine 17:1 (LPE), lyso-phosphatidylinositol 17:1 (LPI), lyso-phosphatidylserine 17:1 (LPS), phosphatidate 17:0/14:1 (PA), phosphatidylcholine 17:0/14:1 (PC), phosphatidylethanolamine 17:0/14:1 (PE), phosphatidylglycerol 17:0/14:1 (PG), phosphatidylinositol 17:0/14:1 (PI), phosphatidylserine 17:0/14:1 (PS), ergosterol ester 13:0 (EE), triacylglycerol 17:0/17:0/17:0 (TAG), stigmastatrienol, inositolphosphorylceramide 44:0;2 (IPC), mannosyl-inositolphosphorylceramide 44:0;2 (MIPC), mannosyl-di-(inositolphosphoryl)ceramide 44:0;2 ($M(IP)_2C$). After extraction, the organic phase was transferred to an infusion plate and dried in a speed vacuum concentrator. 1st step dry extract was resuspended in 7.5 mM ammonium acetate in chloroform/methanol/propanol (1:2:4, V:V:V) and 2nd step dry extract in 33% ethanol solution of methylamine in chloroform/methanol (0.003:5:1; V:V:V). All liquid handling steps were performed using Hamilton Robotics STARlet robotic platform with the Anti Droplet Control feature for organic solvents pipetting.

MS Data Acquisition

Samples were analyzed by direct infusion on a QExactive mass spectrometer (Thermo Scientific) equipped with a TriVersa NanoMate ion source (Advion Biosciences). Samples were analyzed in both positive and negative ion modes with a resolution of $R_{m/z\ =\ 200}$ = 280000 for MS and $R_{m/z\ =\ 200}$ = 17500 for MSMS experiments, in a single acquisition. MSMS was triggered by an inclusion list encompassing corresponding MS mass ranges scanned in 1 Da increments (Surma et al., 2015). Both MS and MSMS data were combined to monitor EE, DAG, and TAG ions as ammonium adducts; PC as an acetate adduct; and CL, PA,

PE, PG, PI, and PS as deprotonated anions. MS only was used to monitor LPA, LPE, LPI, LPS, IPC, MIPC, $M(IP)_2C$ as deprotonated anions; Cer and LPC as acetate adducts and ergosterol as protonated ion of an acetylated derivative (Liebisch et al., 2006).

MS Data Analysis

Data were analyzed by Lipotype GmbH using an in-house developed lipid identification software based on LipidXplorer (Herzog et al., 2011, 2012). Data post-processing and normalization were performed using an in-house developed data management system. Only lipid identifications with a signal-to-noise ratio > 5, and a signal intensity five-fold higher than in corresponding blank samples were considered for further data analysis.

RESULTS

We investigated the impact of two potent, proteotoxic inducers of ER stress, namely DTT and TM, on cellular growth and the cellular lipid composition. Our ultimate goal was to faithfully induce proteotoxic stress in the lumen of the ER whilst minimizing potential artifacts from aberrant ER lipid compositions.

DTT and TM Inhibit Cellular Growth

We wanted to know the impact of DTT and TM on cellular growth. To this end, we cultivated the *S. cerevisiae* wildtype (WT) strain BY4741 and isogenic *ire1*Δ cells in either rich medium (YPD) or synthetic medium (SCD) to the exponential growth phase. Using these cells, we inoculated fresh cultures in a 96-well plate to an OD_{600} of 0.01 in the respective medium supplemented with various concentrations of DTT and TM. After overnight cultivation, cellular growth was assayed via the OD_{600} (**Figures 1A–D**). Not surprisingly, WT cells are more resistant to DTT- or TM-induced ER stress than *ire1*Δ in both rich and synthetic medium (**Figures 1A–D**). This suggests that UPR-activation via Ire1p contributes to cellular fitness under conditions of prolonged proteotoxic stress. Notably, the choice of the medium affects the growth-inhibitory concentrations of DTT and TM such that higher initial concentrations of DTT are required to inhibit overnight growth in rich medium, while lower concentrations are sufficient in minimal medium

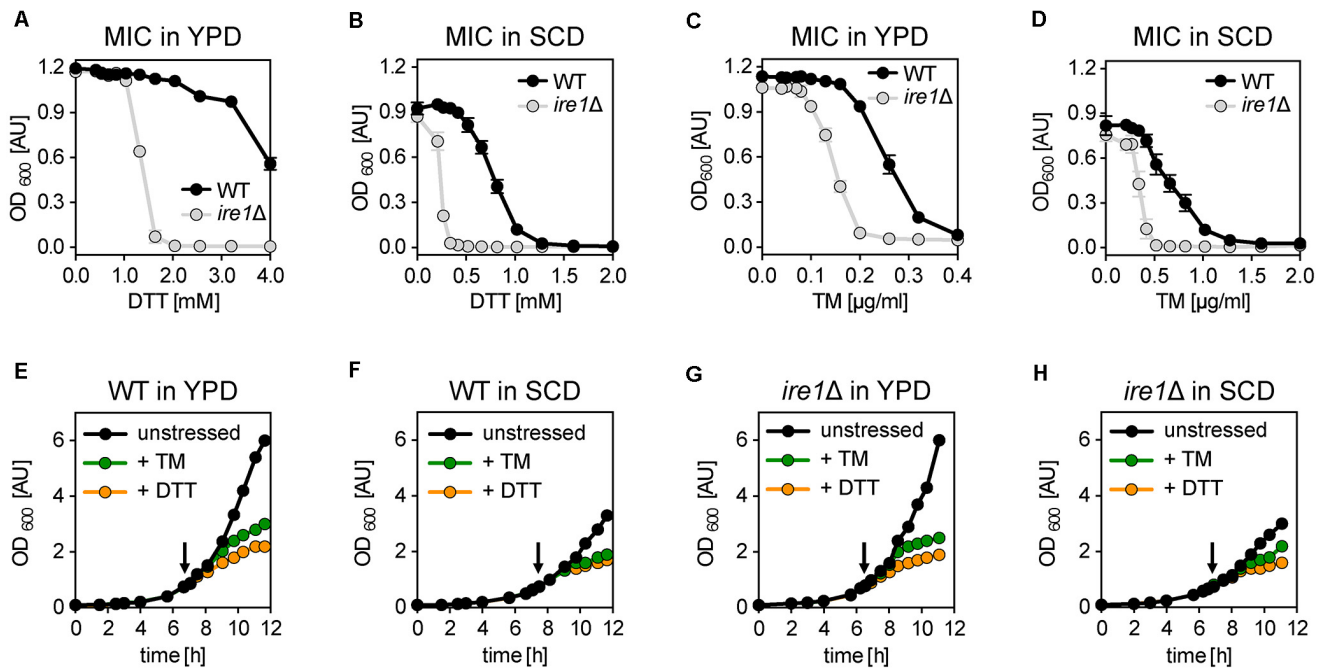

FIGURE 1 | Acute and prolonged ER stress inhibits cellular growth. **(A–D)** Determination of the minimal inhibitory concentration (MIC) of DTT and TM for the indicated strains. An overnight culture of the indicated strains in rich medium (YPD) was used to inoculate a main culture in either YPD **(E)** or SCD **(F)** to an OD_{600} of 0.2. After 6 h of cultivation to reach the exponential growth phase, a fresh culture in a 96-well plate was inoculated to an OD_{600} = 0.01 and adjusted to the indicated, final concentrations of either DTT or TM. After 16 h of cultivation, the OD_{600} as a measure for the overnight growth was plotted against the concentration of the proteotoxic drug. The data in panels **(A–D)** are plotted as the average ± standard deviation (SD) from three independent experiments (n = 3) with technical duplicates. **(E–H)** BY4741 WT and the isogenic *ire1*Δ strain were cultivated in either synthetic (SCD) or rich (YPD) medium at 30°C. The main cultures were inoculated to an OD_{600} of 0.1 from a stationary overnight culture in the respective medium. Cell proliferation is monitored by plotting the OD_{600} against the time of cultivation. At an OD_{600} of 0.80 ± 0.05 the cells were either left untreated (black) or stressed with either TM (green) or DTT (orange). An arrow indicates the time point of drug addition. DTT was used at a final concentration 8 mM and 2 mM in YPD and SCD, respectively. TM was used at a final concentration of 1.0 µg/ml and 1.5 µg/ml in YPD and SCD, respectively. The data in panels **(A–D)** are from a single, representative experiment. Raw data can be found in the **Supplementary Data Sheet 2**.

(**Figures 1A,B**). In contrast, lower concentrations of TM are required to block overnight growth in rich versus synthetic medium (**Figures 1C,D**). The underlying reasons remain unclear. Among other possibilities, the medium might affect the drug *per se* (e.g., DTT oxidation), the uptake and extrusion of the compound, or -via diverse mechanisms- the cellular resistance to proteotoxic stress. Nevertheless, our data help choosing appropriate concentrations to effectively inhibit overnight growth for each medium and both drugs.

Next, we wanted to study the impact of acute ER stress on cellular growth. We cultivated WT cells in rich (YPD) and synthetic (SCD) medium (**Figures 1E,F**) under conditions most commonly used for studying the biology of *S. cerevisiae* (Sherman, 2002). We inoculated liquid cultures to an OD_{600} of 0.1 using stationary, overnight cultures in the respective medium and then followed the cellular growth over time. When the cultures reached an OD_{600} of 0.75 to 0.8, the cells were either left untreated or stressed with DTT or TM at concentrations causing a near-complete inhibition of overnight growth to account for the different dose–response curves in different media (**Figures 1A–D**). Specifically, DTT was used at a concentration of 8 mM and 2 mM, while TM was used at a concentration of 1.0 μg/ml and 1.5 μg/ml in rich and synthetic medium, respectively. Notably, 8 mM of DTT has previously been used to study ER membrane expansion in stressed cells, while 1–2 μg/ml of TM are known to reorganize Golgi traffic and mitochondrial enlargement by activating the UPR (Bernales et al., 2007; Schuck et al., 2009; Hsu et al., 2016; Tran et al., 2019).

Expectedly, we find that unstressed cells grow faster in rich medium (doubling time 86 min) than in synthetic medium (doubling time 107 min) (**Figures 1E,F**), which underscores the previous finding that BY4741 strains requires an additional supplementation of the SCD medium for optimal growth (Hanscho et al., 2012). Furthermore, DTT- and TM-stressed cells grow markedly slower compared to the unstressed cells in both media (**Figures 1E,F**). Consistent with previous observations (Pincus et al., 2010), the reduced rate of growth becomes apparent as early as 1 h after the addition of the stress-inducing agents (**Supplementary Figures S1A,B**). Notably, the impact of DTT is more pronounced than the impact of TM at the given concentrations (**Figures 1E,F**).

Next, we wanted to test if the reduced growth of the stressed cells is due to an activation of the UPR, which is known to peak within 1 h after the addition of DTT or TM to the medium and which largely remodels the cellular transcriptome (Kawahara et al., 1997; Travers et al., 2000; Promlek et al., 2011). Surprisingly, the growth of both stressed and unstressed *ire1*Δ cells was indistinguishable from WT cells in both rich and synthetic medium (**Figures 1E–H** and **Supplementary Figures S1C–H**). This suggests that DTT and TM impair cellular growth during this early phase of stress predominantly via their impact on protein folding and not by processes downstream of UPR activation. The slightly higher potency of DTT to impede cellular growth compared to TM at the given concentrations may reflect the fact that these compounds affect the folding of different sets of proteins: proteins with disulfide bonds in the case of DTT and N-linked glycosylated proteins in the case of TM. Furthermore, DTT can reduce already formed disulfide bonds and is known to directly affect also other cellular processes outside the ER such as the protein import into mitochondria (Mesecke et al., 2005) and protein palmitoylation (Levental et al., 2010). In contrast, TM affects only the glycosylation of freshly synthesized proteins. Our data suggest that the growth inhibition observed in *acutely* stressed cells is independent of UPR activation.

Experimental Outline and Global Insights From Principal Component Analysis

We used shotgun mass spectrometry-based lipidomics to comprehensively and quantitatively dissect the impact of acute proteotoxic stress on the cellular lipid composition. In light of the pronounced impact of DTT and TM on cellular growth, we focused on their immediate effects within 1 h of treatment. We analyzed the lipid composition for six conditions and two different strains each as biological triplicates (**Figure 2A**). A principal component analysis (PCA) of the entire dataset at the level of individual lipid species revealed a close clustering of all samples from WT and *ire1*Δ cells cultivated in SCD, thereby suggesting UPR activity itself has little impact on their lipidomes (**Figure 2B**). In contrast, we observed two clusters for cells cultivated in rich medium. One cluster contained samples from WT and *ire1*Δ cells that were either left untreated or stressed with TM, while the other cluster contained samples from cells that were stressed with DTT at concentrations commonly used for UPR activation. This suggests that DTT causes a substantial remodeling of the lipidome, while TM treatments have a lesser impact on the cellular lipid composition. Not surprisingly, the loadings plot suggests a correlation of specific groups of lipids (**Supplementary Figure S2A**). The total amount of lipids quantified from 1 OD unit of cells (**Supplementary Figure S2B**) and the amount of storage lipids (**Supplementary Figure S2C**) highlight a low variability between replicates and show that storage lipids are more abundant in synthetic (SCD) medium. Storages lipids comprise all triacylglycerol (TAG) species and ergosterol esters.

The Impact of YPD and SCD Medium on the Lipidome of *S. cerevisiae*

For representing this complex dataset, we assorted the identified lipid species to one of four major lipid categories: sterols, sphingolipids (SLs), membrane glycerolipids (MGLs), and storage lipids. MGLs comprise all glycerophospholipids and diacylglycerol (DAG) species (**Figure 3** and **Supplementary Figure S3**). Overall, we find a remarkable impact of the medium on the cellular lipid composition (**Figure 3A**).

Global Impact of the Medium on Sphingolipids

Yeast SLs comprise inositolphosphorylceramide (IPC), mannosyl-inositol phosphorylceramide (MIPC), mannosyl-di-(inositolphosphoryl) ceramide ($M(IP)_2C$), and – less abundantly – ceramides (Cer). With the exception of Cer, all SLs have a significantly lower level in cells cultivated in rich medium compared to cells cultivated synthetic medium

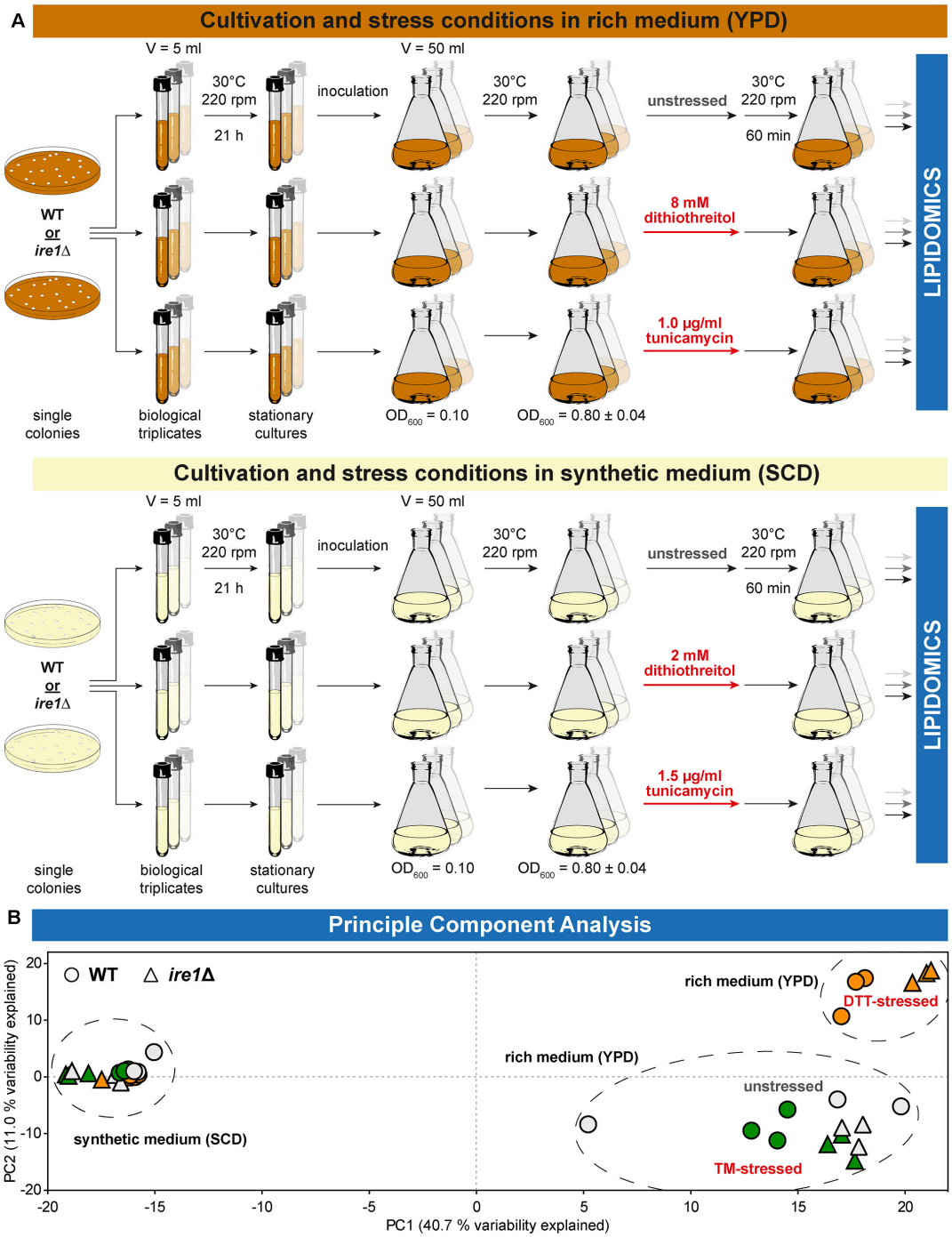

FIGURE 2 | Experimental conditions affecting lipidome variability. **(A)** Overview of the cultivation and stress conditions use for lipidomic analysis. **(B)** A two-dimensional principal component analysis (PCA) of lipid species abundances reveals the degree of variations between different cultivation and stress conditions. Data from BY4741 WT and *ire1*Δ cells are indicated by circles and triangles, respectively. The color of the data points indicates unstressed cells in gray and cells stressed either with DTT (orange) or TM (green). Data from stressed and unstressed cells are indicated red and gray, respectively. PCA reveals that the lipidomes from both stressed and unstressed cells cultivated in synthetic medium (SCD) are very similar. In contrast, DTT induces a characteristic remodeling of the lipidome of both WT and *ire1*Δ cells cultivated in rich medium (YPD).

(**Figure 3A**). The same trend was observed for all SLs in *ire1*Δ cells (**Supplementary Figure S3A**). Thus, the lower level of sphingolipids in YPD-cultured cells is not due to possible differences in basal, constitutive UPR signaling. However, because SLs are concentrated along the secretory pathway and highly abundant in the plasma membrane (van

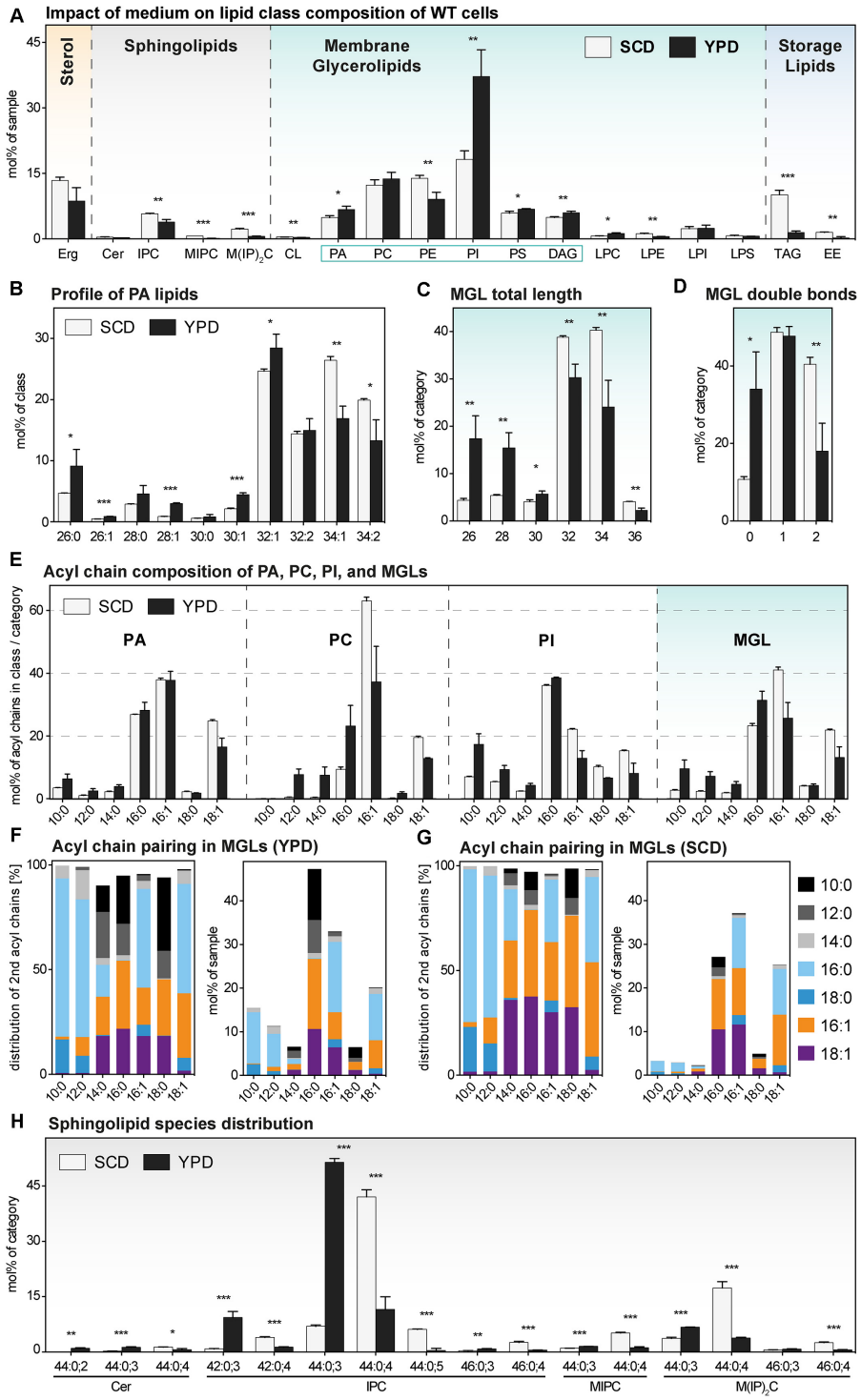

FIGURE 3 | The lipid composition of *S. cerevisiae* WT in different media. A single colony of the BY4741 WT strain was used to inoculate a preculture in either synthetic (SCD) or rich (YPD) medium. After overnight cultivation for 21 h, a fresh culture was inoculated to an OD_{600} of 0.1. When the cells reached an OD_{600} of 0.80 ± 0.05, they were cultivated for one more hour. 20 OD equivalents of these cells were harvested and analyzed by lipid mass spectrometry. The data represented by black and white bars relate to cells cultivated in rich and synthetic medium, respectively [except for panels **(F** and **G)]**. **(A)** Lipid class composition in mol% of all quantified lipids in the sample organized by the categories: sterol (orange), sphingolipids (magenta), membrane glycerolipids (green, classes with two acyl chains highlighted by green box), and storage lipids (blue). Erg, ergosterol; Cer, ceramide; IPC, inositolphosphorylceramide; MIPC, mannosy-IPC; M(IP)2C, mannosyl-di-IPC; CL, cardiolipin; PA, phosphatidic acid; PC, phosphatidylcholine; PE, phosphatidylethanolamine; PI, phosphatidylinositol; PS, phosphatidylserine;

(Continued)

FIGURE 3 | Continued
DAG, diacylglycerol; LPC, lyso-PC; LPE, lyso-PE; LPI, lyso-PI; LPS, lyso-PS; TAG, triacylglycerol; EE, ergosteryl ester. **(B)** Profile of PA lipids in mol% of the class. **(C)** Total length of lipids in a sub-category of membrane glycerolipids (MGLs) including PA, PC, PE, PI, PS, DAG. The total length is given as the sum of carbon atoms in both fatty acyl chains in mol% of this sub-category. **(D)** Total number double bonds in a sub-category of MGLs (PA, PC, PE, PI, PS, DAG) is given as the sum of double bonds in both acyl chains, in mol% of this sub-category. **(E)** The acyl chain composition of PA, PC, PI and of a s sub-category of MGLs (PA, PC, PE, PI, PS, DAG) is normalized either to the individual lipid class or the sub-category and given in mol%. **(F,G)** The pairing of fatty acyl chains in MGLs (PA, PC, PE, PI, PS, DAG) is plotted for cells cultivated in **(F)** rich (YPD) and **(G)** synthetic (SCD) medium. The left panel indicates the pairing of fatty acyl chains in a sub-category of MGLs (PA, PC, PE, PI, PS, DAG) normalized to each particular fatty acyl chain and is given as mol%. The right panel indicates the abundance of acyl chain pairs in the sub-category of MGLs and is given in mol%. **(H)** Profile of sphingolipids in mol% of the category. The least abundant species in each panel are omitted for clarity. Each bar represents the average ± SD from $n = 3$ independent experiments. Statistical significance was tested by an unpaired two-tailed *t*-test using GraphPad Prism, $*p < 0.05$, $**p < 0.01$, $***p < 0.001$.

Meer et al., 2008; Klemm et al., 2009; Hannich et al., 2011; Surma et al., 2011) it is tempting to speculate that cells cultivated in rich medium feature a higher abundance of inner membranes relative to the plasma membrane. In fact, the rapidly growing cells in rich medium have a particularly high demand for membrane biogenesis and both ER size and the rate of membrane lipid production can be controlled independently of UPR signaling (Loewen, 2004; Schuck et al., 2009; Henry et al., 2012).

Global Impact of the Medium on Membrane Glycerolipids

Membrane glycerolipids constitute the most abundant lipid category comprising the lipid classes phosphatidic acid (PA), phosphatidylcholine (PC), phosphatidyl-ethanolamine (PE), phosphatidylinositol (PI), phosphatidylserine (PS), and diacylglycerol (DAG) (Henry et al., 2012; Klose et al., 2012). Less abundant are cardiolipin (CL) and the lyso-lipid derivatives of the major glycerophospholipid classes with one fatty acid (FA) chain. We find that phosphatidylinositol (PI) is by far the most abundant lipid class in both WT and *ire1*Δ cells when cultivated in rich medium (**Figure 3A** and **Supplementary Figure S3A**). However, when cells are cultivated in synthetic medium, PI is much less abundant and found at levels comparable with phosphatidylcholine (PC) and phosphatidylethanolamine (PE) (**Figure 3A** and **Supplementary Figure S3A**). This is particularly relevant when studying the UPR: Ire1p has been identified as inositol-requiring enzyme (Nikawa and Yamashita, 1992), it is activated by inositol-depletion (Promlek et al., 2011), and sensitive to the stiffness of the ER membrane (Halbleib et al., 2017) thereby implying an important role of PI lipids. But not only PI, also the abundance of PE is affected by the choice the medium. PE is significantly less abundant in cells cultivated in rich versus synthetic medium (**Figure 3A**). Again, this is likely to affect the sensitivity and activity of the UPR as aberrant PE-to-PC ratios have been firmly implicated in chronic activation of the UPR in yeast, worms, and mammals (Fu et al., 2011; Thibault et al., 2012; Hou et al., 2014).

Although qualitatively consistent with previous reports (Ejsing et al., 2009; Klose et al., 2012; Surma et al., 2013; Casanovas et al., 2015) our observations also highlight an important caveat for the use of rich medium. Because YPD is not a defined medium (in contrast to the synthetic-defined SCD), its use will inevitably lead to inconsistencies with respect to the lipid composition. As a consequence, it is almost impossible to compare data coming from different laboratories using media from different suppliers or even media batches. It is also impossible to exclude a technical bias as contributing factor for seemingly divergent observations: different procedures for lipid extraction into an organic phase may affect the spectrum of lipids that can be detected, different modes of sample separation and/or detection [such as thin-layer chromatography (TLC), liquid chromatography coupled to mass spectrometry (LC-MS) or the shotgun lipidomics platform used for this study] might bias the detection of some lipids/lipid classes over others. Ideally, the use of internal standards should correct the bias from extraction and detection. Furthermore, only fully quantitative data expressed in absolute units (such as pmol or derived molar fractions) can be compared to each other, as any relative data depend on the experimental setup and reference points applicable only within a given experiment.

Impact of the Medium on Storage Lipids

The choice of the medium has a striking impact on the abundancies of storage lipids. Exponentially growing cells cultivated in rich medium store much less TAGs and EEs than those cultivated in synthetic medium (**Figure 3A**). The same trend is observed in *ire1*Δ cells (**Supplementary Figure S3A**). It is tempting to speculate that rapidly growing cells depend more heavily on the production of membrane lipids than relatively slow growing cells, which can 'afford' to store some lipids for future use. Clearly, the different growth rates in the two media (**Figure 1** and **Supplementary Figure S1**) must be considered in light of the intricate connections between membrane biogenesis, lipid droplet formation, and the UPR (Gaspar et al., 2011; Stordeur et al., 2014; Casanovas et al., 2015). Our data underscore the importance to study the UPR under tightly controlled conditions.

Impact of the Medium on the Lipid Species Level Identifies Asymmetric Lipids

We wanted to know the impact of rich versus synthetic medium on lipid acyl chains and initially focused our attention on the profile of PA lipids (**Figure 3B**). Normally, in *S. cerevisiae*, the fatty acid composition of PA lipids is mostly limited to palmitic (C16:0), palmitoleic (C16:1) and oleic acid (C18:1) with low amounts of shorter fatty acids (Klose et al., 2012). However, the cells cultivated in rich medium exhibited a significantly higher abundance of PA lipids with shorter, saturated acyl chains, as evidenced by the level of PA lipids with a cumulative acyl chain length of C26, C28, and C30

(**Figure 3B**). A combined analysis of all MGLs with two fatty acyl chains (PA, PC, PE, PI, PS, DAG) further highlighted this general and significant shift toward shorter (**Figure 3C**) and more saturated lipid species (**Figure 3D**). Notably, identical trends can be observed for *ire1*Δ cells indicating that a low, basal activation of the UPR does not contribute to this global trend in all MGLs caused by the cultivation in different media (**Supplementary Figures S3B–D**).

We then studied the usage of different fatty acyl chains in PA, PC, and PI in cells cultivated in both rich and synthetic medium (**Figure 3E**) and also calculated the abundance of the different fatty acyl chains in all MGLs (with two fatty acyl chains) (**Figure 3E**). Consistent with previous reports, we find that the distribution of the fatty acyl chains differs between the individual glycerophospholipids classes (**Figure 3E**) (Ejsing et al., 2009; Klose et al., 2012; Casanovas et al., 2015). Strikingly, our data reveal that saturated, medium fatty acyl chains (C10, C12, and C14) are much more prominently found in cells cultivated in rich medium throughout all glycerophospholipid classes (**Figure 3E**). Notably, similar asymmetric lipids with two acyl chains differing substantially in length have only recently been found at high abundance in the lipidome of *Schizosaccharomyces japonicus* (Makarova et al., 2020).

In order to gain more insight in the molecular rules that govern the production of asymmetric lipids, we studied the pairing of fatty acyl chains in MGLs. We found an almost exclusive pairing of saturated, medium fatty acyl chains (C10:0 or C12:0) with longer saturated fatty acyl chains (C16:0 or C18:0) in *S. cerevisiae* (**Figure 3F**; left panel). In fact, we find virtually no pairing of unsaturated fatty acyl chain (C16:1 or C18:1) with medium fatty acyl chains (C10:0 or C12:0). Also when considering the relative abundance of the different fatty acyl chains (C16:0, C16:1 and C18:1 are most abundant), the same, remarkable selectivity for certain pairs of fatty acyl chains becomes clear: medium fatty acyl chains preferentially pair with saturated, but not with unsaturated fatty acyl chains (**Figure 3F**; right panel). YPD is not a fully defined medium and it may contain minor concentrations of short and medium chain fatty acids. In order to test if *S. cerevisiae* can synthesize asymmetric lipids from scratch, we analyzed the acyl chain pairing in cells cultivated in synthetic medium (**Figure 3G**). Again, we found a strong preferential pairing of saturated, medium fatty acyl chains with saturated, long fatty acid chains, but not with unsaturated ones (**Figure 3G**). Our data suggest that tight and evolutionary conserved rules underly the pairing of fatty acyl chains in these highly asymmetric lipids.

A Medium-Dependent Switch in the Species Distribution of Sphingolipids

Another remarkably specific impact of the medium can be observed in the profile of SLs for both WT (**Figure 3H**) and *ire1*Δ cells (**Supplementary Figure S3E**). The most abundant sphingolipid species of cells cultivated in rich medium is IPC 44:0,3 (with three hydroxylations) contributing to more than 50 mol% of all SLs, while IPC 44:0,4 (with four hydroxylations) is much less abundant. In contrast, IPC 44:0;4 is contributing to more than 40 mol% to the pool of SLs and is the most abundant SL species in SCD-cultured cells. The molecular underpinnings of this remarkable shift in the species composition and its physiological relevance remains to be studied in greater detail.

The Impact of DTT and TM on the Lipidome of *S. cerevisiae* in Rich Medium

We wanted to study the impact of DTT and TM on the lipid composition of cells cultivated in both rich medium (**Figure 4**) and synthetic medium (**Figure 5**) and focus our attention on an early time point after 1 h of treatment. As important controls, we also determined the lipid compositions of stressed and unstressed *ire1*Δ cells in both media to test a possible contribution of UPR to changes of the lipidome (**Supplementary Figures S4, S5**).

Consistent with our PCA analysis (**Figure 2B**), we find that the TM-induced stress has barely any impact on the lipid composition of WT cells (**Figure 4A**). This lack-of-impact is best evident when representing difference of abundance between stressed and unstressed cells for each lipid class (**Figure 4B**). There is also barely any impact of TM on the profile of PA lipids (**Figure 4C**), the length distribution of the fatty acyl chains (**Figure 4D**), the degree of saturation (**Figure 4E**), and the species composition of SLs (**Figure 4F**). Notably, this is true for both for WT and *ire1*Δ cells (**Supplementary Figures S4A–F**). These data suggest TM can be used as proteotoxic drug in YPD-cultivated cells without severely affecting the cellular lipid composition.

In contrast to that, DTT at the given concentration has a significant impact on the lipidome of YPD-cultured cells (**Figure 4A**), which is most apparent when plotting the difference of lipid class abundance between stressed and unstressed cells (**Figure 4B**). Clearly, treating the cells for only 1 h with DTT is sufficient to cause a significant and substantial increase of PA in the stressed cells. Given that PA lipids are important signaling lipids involved in regulating membrane biogenesis (Loewen, 2004; Schuck et al., 2009; Henry et al., 2012; Hofbauer et al., 2018), a two-fold increase of the cellular PA level is likely to have broad impact on lipid metabolism and the cellular transcriptome. Intriguingly, treating the cells with DTT induces also a shift in the profile of PA lipids toward a higher average acyl chain length and more unsaturation for both WT (**Figure 4C**) and *ire1*Δ cells (**Supplementary Figure S4C**). While these observations suggest that DTT affects PA lipids either directly (by affecting fatty acid metabolism) or indirectly (by its impact on cellular growth or other means; **Supplementary Figure S1A**), these trends are not pronounced in the wider group of MGLs with two fatty acyl chains – neither for WT nor *ire1*Δ cells (**Figures 4D,E** and **Supplementary Figures S4D,E**). Based on its position in the lipid metabolic network (Henry et al., 2012; Ernst et al., 2016), we speculate that PA is a class of 'early-responding' lipids, which change most readily upon an environmental perturbation, while other MGLs are affected only after prolonged periods of stress.

We also find some impact of ER stress on the profile of SLs of WT and *ire1*Δ cells (**Figure 4F** and **Supplementary Figure S4F**), but these changes are relatively small. The overall similarity of the lipidomic changes observed for WT and *ire1*Δ cells upon DTT treatments, suggest that most DTT impacts on lipid metabolism

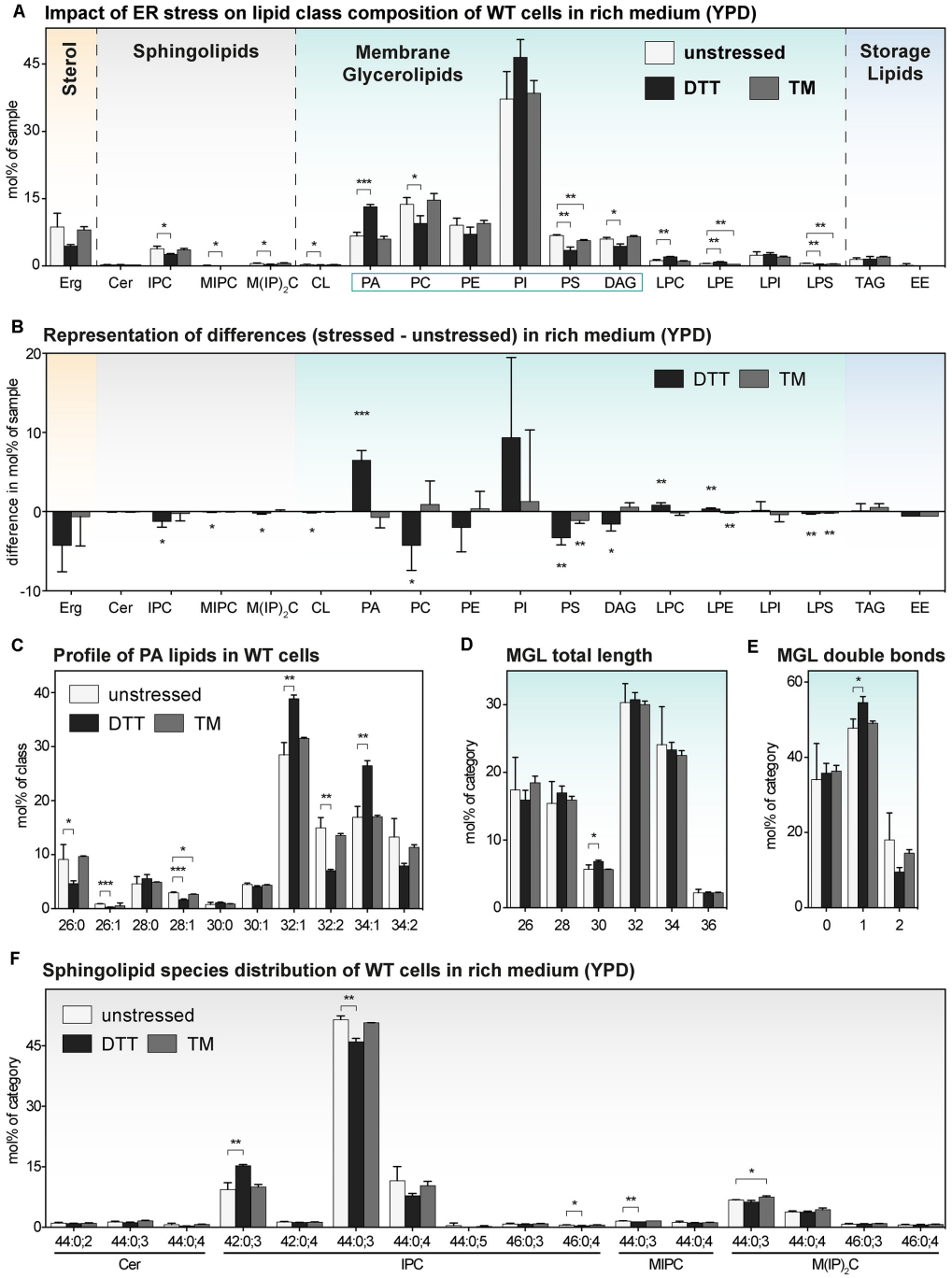

FIGURE 4 | The impact of proteotoxic stress on the lipidome of *S. cerevisiae* WT in rich medium. A single colony of the BY4741 WT strain was used to inoculate a preculture in rich (YPD) medium. After overnight cultivation for 21 h, a fresh culture was inoculated to an OD_{600} of 0.1 and then cultivated to an OD_{600} of 0.80 ± 0.05. The cells were then either left untreated (white bars), stressed by the addition of either with 8 mM DTT (black bars) or 1.0 μg/ml TM (gray bars). After one additional hour of cultivation, 20 OD equivalents of these cells were harvested and analyzed by lipid mass spectrometry. **(A)** Lipid class composition in mol% of all quantified lipids in the sample organized by lipid categories. **(B)** The difference in lipid class abundance in stressed minus unstressed cells highlights the impact of DTT (black) and TM (gray) on the cellular lipid composition in rich medium. The difference in abundance in mol% was calculated by subtracting the abundance in unstressed cells from the abundance in either DTT- or TM-stressed cells under consideration of error propagation. **(C)** Profile of PA lipids in mol% of the class. **(D)** Total length of lipids in a sub-category of MGLs (PA, PC, PE, PI, PS, DAG). The total length is given as the sum of carbon atoms in both fatty acyl chains in mol% of this sub-category. **(E)** Total number double bonds in a sub-category of MGLs (PA, PC, PE, PI, PS, DAG) is given as the sum of double bonds in both acyl chains and represented in mol% of this sub-category. **(F)** Profile of sphingolipids in mol% of this category. The least abundant species are omitted for clarity. Each bar represents the average ± SD from $n = 3$ independent experiments. Statistical significance was tested by an unpaired two-tailed *t*-test using GraphPad Prism, $^{*}p < 0.05$, $^{**}p < 0.01$, $^{***}p < 0.001$.

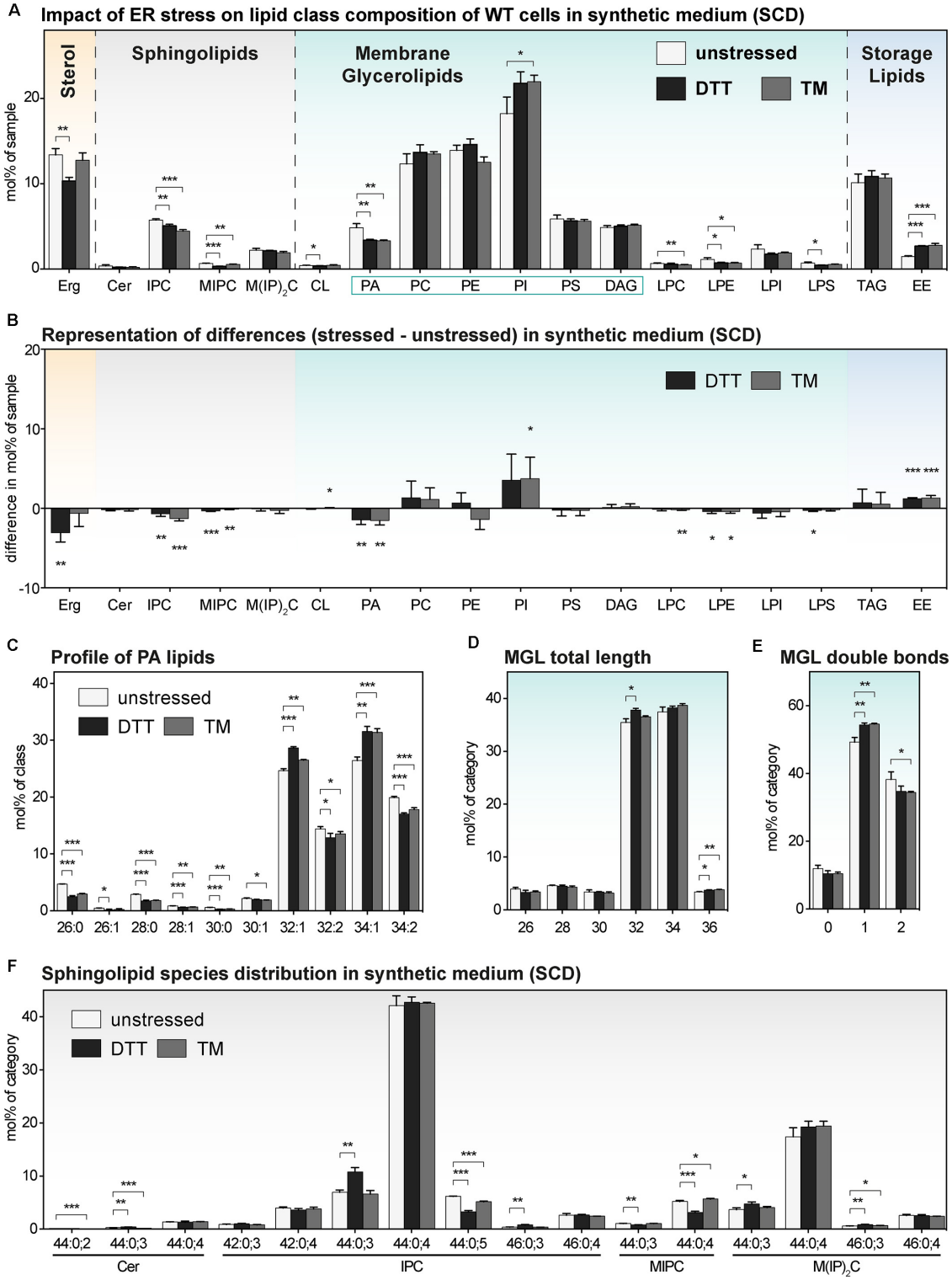

FIGURE 5 | The impact of proteotoxic stress on the lipidome of *S. cerevisiae* WT cultivated in synthetic medium. A single colony of the BY4741 WT strain was used to inoculate a preculture in synthetic medium (SCD). After overnight cultivation for 21 h, a fresh culture was inoculated to an OD_{600} of 0.1 and then cultivated to an OD_{600} of 0.80 ± 0.05. The cells were then either left untreated (white bars), stressed by the addition of either with 8 mM DTT (black bars) or 1.0 μg/ml TM (gray bars). After one additional hour of cultivation, 20 OD equivalents of these cells were harvested and analyzed by lipid mass spectrometry. **(A)** Lipid class composition in mol% of all quantified lipids in the sample organized by lipid categories. **(B)** The difference in lipid class abundance in stressed minus unstressed cells highlights

(Continued)

FIGURE 5 | Continued
the impact of DTT (black) and TM (gray) on the cellular lipid composition in synthetic medium. The difference in abundance in mol% was calculated by subtracting the abundance in unstressed cells from the abundance in either DTT- or TM-stressed cells under consideration of error propagation. **(C)** Profile of PA lipids in mol% of the class. **(D)** Total length of lipids in a sub-category of MGLs (PA, PC, PE, PI, PS, DAG). The total length is given as the sum of carbon atoms in both fatty acyl chains in mol% of this sub-category. **(E)** Total number double bonds in a sub-category of MGLs (PA, PC, PE, PI, PS, DAG) is given as the sum of double bonds in both acyl chains and represented in mol% of this sub-category. **(F)** Profile of sphingolipids in mol% of this category. The least abundant species are omitted for clarity. Each bar represents the average ± SD from $n = 3$ independent experiments. Statistical significance was tested by an unpaired two-tailed *t*-test using GraphPad Prism, $^{*}p < 0.05$, $^{**}p < 0.01$, $^{***}p < 0.001$.

are independently of UPR-signaling, at least under the given conditions (**Figure 4** and **Supplementary Figure S4**).

In summary, we find that even a short cultivation in the presence of DTT induces substantial changes of the cellular lipidome.

The Impact of DTT and TM on the Lipidome of *S. cerevisiae* in Synthetic Medium

We wanted to know the impact of DTT and TM on the lipid composition of *S. cerevisiae* cultivated in synthetic medium. We therefore determined the lipidomes of both stressed and unstressed WT and *ire1*Δ cells (**Figure 5** and **Supplementary Figure S5**). Overall, we find an almost identical lipid class composition for cells stressed either with DTT or TM compared to untreated control cells with only minor changes in the abundance of several lipid classes (**Figures 5A,B** and **Supplementary Figures S5A,B**). While the changes between stressed and unstressed cells are significant, the difference in abundance seems rather moderate (**Figure 5B**). For example, the ∼30% lower level of PA in both DTT- and TM-stressed cells (**Figure 5A**), has most probably a lower impact on cellular physiology than the two-fold increase of PA in DTT-treated cells in rich medium (**Figure 4A**). Other significant, moderate changes are observed for several SLs, Erg, and EEs (**Figure 5A**). We doubt that these lipidome changes are substantial enough to impact on the activity of the UPR via a membrane-based mechanism. This speculation is supported by the observation that proteotoxic stress clearly dominates over membrane-based stress when cells are treated with either DTT or TM for 1 h or less (Promlek et al., 2011).

Beyond the overall very similar lipid class distribution of stressed and unstressed cells cultivated in synthetic medium, we find significant, but minor stress-induced changes in the PA species composition (**Figure 5C**), a similar total fatty acyl chain length in MGLs (**Figure 5D**), a mildly affected degree of lipid saturation (**Figure 5E**), and a largely similar profile of SLs (**Figure 5F**). Again, the lipidomes observed for WT and *ire1*Δ cells are extremely similar. In summary, we find, somewhat surprisingly, that the cellular lipidome is quite 'resistant' to perturbations from DTT- and TM-treatments when cells are treated for 1 h in synthetic medium.

Our lipidomic survey of stressed and unstressed *S. cerevisiae* reveals that TM treatments for 1 h are suitable in both rich and synthetic medium to activate the UPR via proteotoxic stress with only little interference from a perturbed lipid composition. However, more precautions should be taken when using DTT.

DISCUSSION

We have performed a systematic, quantitative analysis of the lipidomic changes associated with acute ER stress caused by the proteotoxic agents DTT and TM. Given the central relevance of the UPR for cellular homeostasis and the adverse effects associated with chronic UPR activation, it is crucial to better understand the signals that underlie prolonged and chronic activation of the UPR in the future.

Recommendations for Studying UPR-Activating Signals

Using *S. cerevisiae* as a model, we highlight the importance of tightly controlled cultivation conditions and quantitative lipid analyses for a more holistic approach toward understanding the interplay of UPR-activating signals. We show that (1) the proteotoxic drugs DTT and TM impair cellular growth, thereby confirming previous observations (Pincus et al., 2010), (2) DTT causes within 1 h of treatment substantial changes of the lipidome of YPD-cultured cells, (3) DTT and TM have only a minor impact on the lipidome of SCD-cultured cells, (4) unstressed WT and *ire1*Δ cells feature virtually identical lipidomes under the tested conditions, thereby suggesting that basal, low-level UPR signaling (or lack of thereof) does not substantially affect the cellular lipid composition. Overall, our data are consistent with the general assumption that TM predominantly causes proteotoxic stress, at least within the first hour of treatment (Promlek et al., 2011). The rapid, DTT-dependent remodeling of the lipidome observed in YPD-cultured cells and the strongly impaired growth of stressed cultures, however, may serve as a warning to carefully interpret data derived from acutely stressed cells. We like to stress that we investigated only the impact of a single concentration for each drug in both media on the cellular lipid composition. It is possible that TM, when used at higher concentrations, might have a more severe impact on the cellular lipid composition. Nevertheless, for studying the UPR and its response to proteotoxic signals with little to no interference from a perturbed lipid metabolism, we suggest (1) the use of defined SCD over ill-defined YPD, (2) the use of TM over DTT, because of its more specific impact on protein folding in the ER, and (3) applying TM or DTT stress for a maximum of 1 h.

Membrane Biogenesis in Rapidly Growing Cells – Competition for Lipid Metabolites

Our systematic lipidomic analyses of WT and *ire1*Δ cells in two different media provides insights into the orchestration

of membrane biogenesis by rapidly growing, eukaryotic cells. Even though rich medium provides a rich supply of nutrients, cells cultivated in this medium do not accumulate substantial amounts of storage lipids during the exponential growth phase (**Figure 3A**). Cells cultivated in synthetic medium, however, accumulate a five times higher level of neutral lipids (TAGs + EEs) although the medium is not as rich (**Figure 3A**). We speculate that these marked differences are at least partly due to the growth rate, which is substantially higher for YPD-cultured cells. This interpretation is consistent with the previous observation that storage lipids are dynamically regulated in a growth-stage dependent fashion (Klose et al., 2012; Kohlwein et al., 2013; Casanovas et al., 2015) and suggests an increased flux of fatty acids into membrane lipids in rapidly growing cells. In fact, the lipid phenotypes associated with a genetically disrupted fatty acid desaturation are more pronounced in YPD-cultured cells (Surma et al., 2013). The global role of the cellular growth rate on lipid metabolism remains to be established in the future.

Along these lines, we also find that the ratio of SLs to MGLs is low in rapidly growing, YPD-cultured cells, but higher in slow-growing SCD-cultured cells (**Figure 3A**). While it is clear that many distinct regulatory circuits of the cell are affected by the composition of the medium, we speculate that the low SL-to-MGL ratio reflects an increased global rate of the lipid biosynthesis in the ER and -as a consequence- a low ratio of plasma membrane-to-ER abundance. Notably, our finding that WT and *ire1*Δ cells feature almost identical lipidomes (**Supplementary Figure S3**) would suggest that ER abundance is controlled independently of the UPR in this case. This is consistent with previous findings that ER proliferation can be uncoupled from the UPR via the Opi1 and Ino2/Ino4 regulatory circuit (Loewen, 2004; Schuck et al., 2009; Henry et al., 2012). Opi1 binding to PA lipids at the ER membrane (Loewen, 2004; Hofbauer et al., 2018) de-represses Ino2/Ino4-regulated genes involved in MGL biosynthesis and tip the balance from storing neutral lipids toward membrane proliferation. In fact, we find an increased level of PA lipids in YPD-cultured cells (**Figure 3A** and **Supplementary Figure S3A**). Our findings fuel that idea that the flux of fatty acids into either membrane or storage lipids is affected by the cellular growth rate, which shall investigated by dedicated experiments in the future.

Revealing Acyl Chain Selectivity in Saturated, Asymmetric Lipids

We were surprised by the high content of saturated lipids in YPD-grown cells (**Figures 3D,E**), which differs from previous studies (Klose et al., 2012; Surma et al., 2013; Casanovas et al., 2015) and which resembles lipid phenotypes observed only in genetically modified *S. cerevisiae* with a disrupted fatty acid desaturation (Pineau et al., 2009; Surma et al., 2013; Ballweg and Ernst, 2017; Budin et al., 2018). The majority of these saturated lipids contain a medium fatty acyl chain (C10:0 or C12:0) paired with a second, long fatty acyl chain (C16:0 or C18:0). Such asymmetric, saturated lipids at even higher abundancies have been recently identified in *Schizosaccharomyces japonicus* (Makarova et al., 2020). The length difference of the two acyl chains may allow for an interdigitation of the acyl chains, which increases lipid packing, whilst maintaining a fluid bilayer (Xu and Huang, 1987; Schram and Thompson, 1995; Makarova et al., 2020). This way, the asymmetric lipids can provide an alternative handle to balance competing demands in the homeostasis of physicochemical membrane properties, e.g., by maintaining membrane barrier function whilst increasing membrane fluidity (Lande et al., 1995; Schram and Thompson, 1995; Radanović et al., 2018). This may become very relevant under conditions when medium-chain fatty acids accumulate in the cell and/or when the desaturation of long-chain fatty acids via the fatty acid desaturase Ole1 becomes limiting (Stukey et al., 1989; Ballweg and Ernst, 2017). How precisely saturated, asymmetric lipids provide a feedback to the production of unsaturated fatty acid via the lipid saturation sensor Mga2 (Covino et al., 2016; Ballweg et al., 2020) is an interesting question for the future. Our finding that asymmetric, saturated lipids can be observed at substantial levels in *S. cerevisiae* suggests that such lipids may play a much wider role than previously anticipated.

The machineries and mechanisms mediating a finely tuned production of asymmetric lipids in *S. cerevisiae* and other fungi are still unknown, but tracking the origin and fate of medium chain fatty acids might help identifying them. Our finding that saturated, asymmetric lipids are produced even upon cultivation in fatty acid-free SCD medium (**Figure 3G**) suggests that at least a significant portion of the esterified medium chain fatty acids originate from *de novo* biosynthesis. The fungal fatty acid synthase produces fatty acids of different lengths determined by the cellular ratio of acetyl-CoA to malonyl-CoA, which are used for priming and fatty acid elongation (Sumper et al., 1969; Okuyama et al., 1979; Heil et al., 2019). It is possible that a different product spectrum of the fatty acid synthase contributes to the production and abundance of asymmetric lipids in *S. cerevisiae*. Intriguingly, a hyper-active mutation in the rate-limiting enzyme for fatty acid biosynthesis leads to an increased production of malony-CoA and increased average fatty acyl chain length in glycerophospholipids (Hofbauer et al., 2014). In line with previous reports (Makarova et al., 2020), we therefore propose that the profile of *de novo* synthesized fatty acids is a major determinant for the abundance of saturated, asymmetric lipids.

Our finding that saturated, medium fatty acyl chain pair almost exclusive with saturated, but not with the more abundant unsaturated fatty acyl chains (**Figures 3E–G**), reveals a remarkable, inherent selectivity in the biosynthesis and metabolism of asymmetric lipids. It will be intriguing to learn about the processes that contribute to this selectivity and to dissect the contribution of fatty acid biosynthesis and activation, acyl transferases, phospholipases, and substrate channeling (Henry et al., 2012; Ernst et al., 2016; Patton-Vogt and de Kroon, 2020). Because the key enzymes of lipid metabolism and the principle mechanisms of membrane adaptivity are conserved throughout evolution (Henry et al., 2012; Ernst et al., 2016), it will be intriguing to test if similarly specific mechanisms of acyl chain pairing are at work in organisms from bacteria to humans.

CONCLUSION

The UPR has been implicated in a wide array of pathologies and is gaining increasing attention as a potential drug target (Hetz et al., 2019). While the fatal consequences of prolonged ER stress have been intensively studied (Tabas and Ron, 2011), the molecular events that cause chronic UPR activation remain poorly characterized. In the future, it will be crucial to develop new tools and assays to better understand the signals that perpetuate ER stress. Only quantitative information on the ER load with unfolded proteins and on the composition of the ER membrane during acute and prolonged ER stress can unambiguously establish the relative importance of signals from the ER lumen and the ER membrane. As a first step in this direction, we have studied the impact of different media and two UPR-activating, proteotoxic drugs on the cellular lipid composition. Our data will provide an important reference point for future endeavors, and has already proven useful for highlighting possible connections between the cellular growth rate, proteotoxic ER stress, and lipid metabolism. Our finding that *S. cerevisiae* produces asymmetric lipids with two saturated acyl chains of different lengths provides evidence for a remarkable specificity in paring of saturated fatty acyl chains.

DATA AVAILABILITY STATEMENT

All datasets presented in this study are included in the article/**Supplementary Material**.

AUTHOR CONTRIBUTIONS

RE conceived and designed the experiments. JR, CM, KV, MS, and CK performed the experiments. JR, CM, KV, and TR analyzed the data. JR, MS, and CK contributed reagents, materials, and analysis tools. JR, CM, TR, and RE wrote the manuscript. All authors contributed to the article and approved the submitted version.

FUNDING

This work was supported by the Volkswagen Foundation (Life?, 93089 to RE), European Commission (ERC-CoG 866011), and the Deutsche Forschungsgemeinschaft (SFB894, 'Ca^{2+} Signals: Molecular Mechanisms and Integrative Functions' and SFB807, 'Transport and Communication across biological membranes' to RE).

ACKNOWLEDGMENTS

The authors would like to thank Ilya Levental, James Sáenz, Maya Schuldiner, and Toon de Kroon for insightful discussions.

SUPPLEMENTARY MATERIAL

The Supplementary Material for this article can be found online at: https://www.frontiersin.org/articles/10.3389/fcell.2020.00756/full#supplementary-material

REFERENCES

Adams, C. J., Kopp, M. C., Larburu, N., Nowak, P. R., and Ali, M. M. U. (2019). Structure and molecular mechanism of ER stress signaling by the unfolded protein response signal activator IRE1. *Front. Mol. Biosci.* 6:11. doi: 10.3389/fmolb.2019.00011

Aviram, N., and Schuldiner, M. (2017). Targeting and translocation of proteins to the endoplasmic reticulum at a glance. *J. Cell Sci.* 130, 4079–4085. doi: 10.1242/jcs.204396

Azim, M., and Surani, H. (1979). Glycoprotein synthesis and inhibition of glycosylation by tunicamycin in preimplantation mouse embryos: compaction and trophoblast adhesion. *Cell* 18, 217–227. doi: 10.1016/0092-8674(79)90370-2

Ballweg, S., and Ernst, R. (2017). Control of membrane fluidity: the OLE pathway in focus. *Biol. Chem.* 398, 215–228. doi: 10.1515/hsz-2016-0277

Ballweg, S., Sezgin, E., Doktorova, M., Covino, R., Reinhard, J., Wunnicke, D., et al. (2020). Regulation of lipid saturation without sensing membrane fluidity. *Nat. Commun.* 11:756. doi: 10.1038/s41467-020-14528-1

Bernales, S., McDonald, K. L., and Walter, P. (2006). Autophagy counterbalances endoplasmic reticulum expansion during the unfolded protein response. *PLoS Biol.* 4:e423. doi: 10.1371/journal.pbio.0040423

Bernales, S., Schuck, S., and Walter, P. (2007). ER-Phagy: selective autophagy of the endoplasmic reticulum. *Autophagy* 3, 285–287. doi: 10.4161/auto.3930

Bigay, J., and Antonny, B. (2012). Curvature, lipid packing, and electrostatics of membrane organelles: defining cellular territories in determining specificity. *Dev. Cell* 23, 886–895. doi: 10.1016/j.devcel.2012.10.009

Budin, I., de Rond, T., Chen, Y., Chan, L. J. G., Petzold, C. J., and Keasling, J. D. (2018). Viscous control of cellular respiration by membrane lipid composition. *Science* 362, 1186–1189. doi: 10.1126/science.aat7925

Casanovas, A., Sprenger, R. R., Tarasov, K., Ruckerbauer, D. E., Hannibal-Bach, H. K., Zanghellini, J., et al. (2015). Quantitative analysis of proteome and lipidome dynamics reveals functional regulation of global lipid metabolism. *Chem. Biol.* 22, 412–425. doi: 10.1016/j.chembiol.2015.02.007

Covino, R., Ballweg, S., Stordeur, C., Michaelis, J. B., Puth, K., Wernig, F., et al. (2016). A eukaryotic sensor for membrane lipid saturation. *Mol. Cell* 63, 49–59. doi: 10.1016/j.molcel.2016.05.015

Covino, R., Hummer, G., and Ernst, R. (2018). Integrated functions of membrane property sensors and a hidden side of the unfolded protein response. *Mol. Cell* 71, 458–467. doi: 10.1016/j.molcel.2018.07.019

Cox, J. S., Shamu, C. E., and Walter, P. (1993). Transcriptional induction of genes encoding endoplasmic reticulum resident proteins requires a transmembrane protein kinase. *Cell* 73, 1197–1206. doi: 10.1016/0092-8674(93)90648-A

Cox, J. S., and Walter, P. (1996). A novel mechanism for regulating activity of a transcription factor that controls the unfolded protein response. *Cell* 87, 391–404. doi: 10.1016/s0092-8674(00)81360-4

De Kroon, A. I. P. M., Rijken, P. J., and De Smet, C. H. (2013). Checks and balances in membrane phospholipid class and acyl chain homeostasis, the yeast perspective. *Prog. Lipid Res.* 52, 374–394. doi: 10.1016/j.plipres.2013.04.006

Dymond, J. S. (2013). *Saccharomyces cerevisiae* growth media. *Methods Enzymol.* 533, 191–204. doi: 10.1016/B978-0-12-420067-8.00012-X

Ejsing, C. S., Sampaio, J. L., Surendranath, V., Duchoslav, E., Ekroos, K., Klemm, R. W., et al. (2009). Global analysis of the yeast lipidome by quantitative shotgun mass spectrometry. *Proc. Natl. Acad. Sci. U.S.A.* 106, 2136–2141. doi: 10.1073/pnas.0811700106

Ernst, R., Ballweg, S., and Levental, I. (2018). Cellular mechanisms of physicochemical membrane homeostasis. *Curr. Opin. Cell Biol.* 53, 44–51. doi: 10.1016/j.ceb.2018.04.013

Ernst, R., Ejsing, C. S., and Antonny, B. (2016). Homeoviscous adaptation and the regulation of membrane lipids. *J. Mol. Biol.* 428, 4776–4791. doi: 10.1016/j.jmb.2016.08.013

Fonseca, S. G., Burcin, M., Gromada, J., and Urano, F. (2009). Endoplasmic reticulum stress in β-cells and development of diabetes. *Curr. Opin. Pharmacol.* 9, 763–770. doi: 10.1016/j.coph.2009.07.003

Fu, S., Yang, L., Li, P., Hofmann, O., Dicker, L., Hide, W., et al. (2011). Aberrant lipid metabolism disrupts calcium homeostasis causing liver endoplasmic reticulum stress in obesity. *Nature* 473, 528–531. doi: 10.1038/nature09968

Fun, X. H., and Thibault, G. (2020). Lipid bilayer stress and proteotoxic stress-induced unfolded protein response deploy divergent transcriptional and non-transcriptional programmes. *Biochim. Biophys. Acta* 1865:158449. doi: 10.1016/j.bbalip.2019.04.009

Gaspar, M. L., Hofbauer, H. F., Kohlwein, S. D., and Henry, S. A. (2011). Coordination of storage lipid synthesis and membrane biogenesis: evidence for cross-talk between triacylglycerol metabolism and phosphatidylinositol synthesis. *J. Biol. Chem.* 286, 1696–1708. doi: 10.1074/jbc.M110.172296

Goder, V., Alanis-Dominguez, E., and Bustamante-Sequeiros, M. (2020). Lipids and their (un)known effects on ER-associated protein degradation (ERAD). *Biochim. Biophys. Acta* 1865:158488. doi: 10.1016/j.bbalip.2019.06.014

Halbleib, K., Pesek, K., Covino, R., Hofbauer, H. F., Wunnicke, D., Hänelt, I., et al. (2017). Activation of the unfolded protein response by lipid bilayer stress. *Mol. Cell* 67, 673–684.e8. doi: 10.1016/j.molcel.2017.06.012

Han, X. (2016). Lipidomics for studying metabolism. *Nat. Rev. Endocrinol.* 12, 668–679. doi: 10.1038/nrendo.2016.98

Hannich, J. T., Umebayashi, K., and Riezman, H. (2011). Distribution and functions of sterols and sphingolipids. *Cold Spring Harb. Perspect. Biol.* 3:a004762. doi: 10.1101/cshperspect.a004762

Hanscho, M., Ruckerbauer, D. E., Chauhan, N., Hofbauer, H. F., Krahulec, S., Nidetzky, B., et al. (2012). Nutritional requirements of the BY series of *Saccharomyces cerevisiae* strains for optimum growth. *FEMS Yeast Res.* 12, 796–808. doi: 10.1111/j.1567-1364.2012.00830.x

Harayama, T., and Riezman, H. (2018). Understanding the diversity of membrane lipid composition. *Nat. Rev. Mol. Cell Biol.* 19, 281–296. doi: 10.1038/nrm.2017.138

Heil, C. S., Wehrheim, S. S., Paithankar, K. S., and Grininger, M. (2019). Fatty acid biosynthesis: chain-length regulation and control. *ChemBioChem* 20, 2298–2321. doi: 10.1002/cbic.201800809

Henry, S. A., Kohlwein, S. D., and Carman, G. M. (2012). Metabolism and regulation of glycerolipids in the yeast Saccharomyces cerevisiae. *Genetics* 190, 317–349. doi: 10.1534/genetics.111.130286

Herzog, R., Schuhmann, K., Schwudke, D., Sampaio, J. L., Bornstein, S. R., Schroeder, M., et al. (2012). Lipidxplorer: a software for consensual cross-platform lipidomics. *PLoS One* 7:e29851. doi: 10.1371/journal.pone.0029851

Herzog, R., Schwudke, D., Schuhmann, K., Sampaio, J. L., Bornstein, S. R., Schroeder, M., et al. (2011). A novel informatics concept for high-throughput shotgun lipidomics based on the molecular fragmentation query language. *Genome Biol.* 12:R8. doi: 10.1186/gb-2011-12-1-r8

Hetz, C., Axten, J. M., and Patterson, J. B. (2019). Pharmacological targeting of the unfolded protein response for disease intervention. *Nat. Chem. Biol.* 15, 764–775. doi: 10.1038/s41589-019-0326-2

Hofbauer, H. F., Gecht, M., Fischer, S. C., Seybert, A., Frangakis, A. S., Stelzer, E. H. K., et al. (2018). The molecular recognition of phosphatidic acid by an amphipathic helix in Opi1. *J. Cell Biol.* 217, 3109–3126. doi: 10.1083/jcb.201802027

Hofbauer, H. F., Schopf, F. H., Schleifer, H., Knittelfelder, O. L., Pieber, B., Rechberger, G. N., et al. (2014). Regulation of gene expression through a transcriptional repressor that senses acyl-chain length in membrane phospholipids. *Dev. Cell* 29, 729–739. doi: 10.1016/j.devcel.2014.04.025

Hou, N. S., Gutschmidt, A., Choi, D. Y., Pather, K., Shi, X., Watts, J. L., et al. (2014). Activation of the endoplasmic reticulum unfolded protein response by lipid disequilibrium without disturbed proteostasis *in vivo*. *Proc. Natl. Acad. Sci. U.S.A.* 111, E2271–E2280. doi: 10.1073/pnas.1318262111

Hsu, J. W., Tang, P. H., Wang, I. H., Liu, C. L., Chen, W. H., Tsai, P. C., et al. (2016). Unfolded protein response regulates yeast small GTPase Arl1p activation at late Golgi via phosphorylation of Arf GEF Syt1p. *Proc. Natl. Acad. Sci. U.S.A.* 113, E1683–E1690. doi: 10.1073/pnas.1518260113

Jonikas, M. C., Collins, S. R., Denic, V., Oh, E., Quan, E. M., Schmid, V., et al. (2009). Comprehensive characterization of genes required for protein folding in the endoplasmic reticulum. *Science* 323, 1693–1697. doi: 10.1126/science.1167983

Karagöz, G. E., Acosta-Alvear, D., Nguyen, H. T., Lee, C. P., Chu, F., and Walter, P. (2017). An unfolded protein-induced conformational switch activates mammalian IRE1. *eLife* 6:e30700. doi: 10.7554/eLife.30700

Kaufman, R. J. (2002). Orchestrating the unfolded protein response in health and disease. *J. Clin. Invest.* 110, 1389–1398. doi: 10.1172/jci16886

Kawahara, T., Yanagi, H., Yura, T., and Mori, K. (1997). Endoplasmic reticulum stress-induced mRNA splicing permits synthesis of transcription factor Hac1p/Ern4p that activates the unfolded protein response. *Mol. Biol. Cell* 8, 1845–1862. doi: 10.1091/mbc.8.10.1845

Kimata, Y., Ishiwata-Kimata, Y., Ito, T., Hirata, A., Suzuki, T., Oikawa, D., et al. (2007). Two regulatory steps of ER-stress sensor Ire1 involving its cluster formation and interaction with unfolded proteins. *J. Cell Biol.* 179, 75–86. doi: 10.1083/jcb.200704166

Kimata, Y., and Kohno, K. (2011). Endoplasmic reticulum stress-sensing mechanisms in yeast and mammalian cells. *Curr. Opin. Cell Biol.* 23, 135–142. doi: 10.1016/j.ceb.2010.10.008

Klemm, R. W., Ejsing, C. S., Surma, M. A., Kaiser, H. J., Gerl, M. J., Sampaio, J. L., et al. (2009). Segregation of sphingolipids and sterols during formation of secretory vesicles at the trans-Golgi network. *J. Cell Biol.* 185, 601–612. doi: 10.1083/jcb.200901145

Klose, C., Surma, M. A., Gerl, M. J., Meyenhofer, F., Shevchenko, A., and Simons, K. (2012). Flexibility of a eukaryotic lipidome - insights from yeast lipidomics. *PLoS One* 7:e35063. doi: 10.1371/journal.pone.0035063

Kohlwein, S. D., Veenhuis, M., and van der Klei, I. J. (2013). Lipid droplets and peroxisomes: key players in cellular lipid homeostasis or a matter of fat-store'em up or burn'em down. *Genetics* 193, 1–50. doi: 10.1534/genetics.112.143362

Korennykh, A. V., Egea, P. F., Korostelev, A. A., Finer-Moore, J., Zhang, C., Shokat, K. M., et al. (2009). The unfolded protein response signals through high-order assembly of Ire1. *Nature* 457, 687–693. doi: 10.1038/nature07661

Lande, M. B., Donovan, J. M., and Zeidel, M. L. (1995). The relationship between membrane fluidity and permeabilities to water, solutes, ammonia, and protons. *J. Gen. Physiol.* 106, 67–84. doi: 10.1085/jgp.106.1.67

Lee, A. G. (2004). How lipids affect the activities of integral membrane proteins. *Biochim. Biophys. Acta* 1666, 62–87. doi: 10.1016/j.bbamem.2004.05.012

Levental, I., Lingwood, D., Grzybek, M., Coskun, Ü., and Simons, K. (2010). Palmitoylation regulates raft affinity for the majority of integral raft proteins. *Proc. Natl. Acad. Sci. U.S.A.* 107, 22050–22054. doi: 10.1073/pnas.1016184107

Levental, K. R., Malmberg, E., Symons, J. L., Fan, Y. Y., Chapkin, R. S., Ernst, R., et al. (2020). Lipidomic and biophysical homeostasis of mammalian membranes counteracts dietary lipid perturbations to maintain cellular fitness. *Nat. Commun.* 11:1339. doi: 10.1038/s41467-020-15203-1

Liebisch, G., Binder, M., Schifferer, R., Langmann, T., Schulz, B., and Schmitz, G. (2006). High throughput quantification of cholesterol and cholesteryl ester by electrospray ionization tandem mass spectrometry (ESI-MS/MS). *Biochim. Biophys. Acta* 1761, 121–128. doi: 10.1016/j.bbalip.2005.12.007

Loewen, C. J. R. (2004). Phospholipid metabolism regulated by a transcription factor sensing phosphatidic acid. *Science* 304, 1644–1647. doi: 10.1126/science.1096083

Lorent, J. H., Diaz-Rohrer, B., Lin, X., Spring, K., Gorfe, A. A., Levental, K. R., et al. (2017). Structural determinants and functional consequences of protein affinity for membrane rafts. *Nat. Commun.* 8:1219. doi: 10.1038/s41467-017-01328-3

Makarova, M., Peter, M., Balogh, G., Glatz, A., MacRae, J. I., Lopez Mora, N., et al. (2020). Delineating the rules for structural adaptation of membrane-associated proteins to evolutionary changes in membrane lipidome. *Curr. Biol.* 30, 367–380.e8. doi: 10.1016/j.cub.2019.11.043

Mesecke, N., Terziyska, N., Kozany, C., Baumann, F., Neupert, W., Hell, K., et al. (2005). A disulfide relay system in the intermembrane space of mitochondria that mediates protein import. *Cell* 121, 1059–1069. doi: 10.1016/j.cell.2005.04.011

Mori, K., Kawahara, T., Yoshida, H., Yanagi, H., and Yura, T. (1996). Signalling from endoplasmic reticulum to nucleus: transcription factor with a basic-leucine zipper motif is required for the unfolded protein-response pathway. *Genes Cells* 1, 803–817. doi: 10.1046/j.1365-2443.1996.d01-274.x

Nikawa, J., and Yamashita, S. (1992). IRE1 encodes a putative protein kinase containing a membrane-spanning domain and is required for inositol phototrophy in Saccharomyces cerevisiae. *Mol. Microbiol.* 6, 1441–1446. doi: 10.1111/j.1365-2958.1992.tb00864.x

Novick, P., Field, C., and Schekman, R. (1980). Identification of 23 complementation groups required for post-translational events in the yeast secretory pathway. *Cell* 21, 205–215. doi: 10.1016/0092-8674(80)90128-2

Okuyama, H., Saito, M., Joshi, V. C., Gunsberg, S., and Wakil, S. J. (1979). Regulation by temperature of the chain length of fatty acids in yeast. *J. Biol. Chem.* 254, 12281–12284.

Patton-Vogt, J., and de Kroon, A. I. P. M. (2020). Phospholipid turnover and acyl chain remodeling in the yeast ER. *Biochim. Biophys. Acta* 1865:158462. doi: 10.1016/j.bbalip.2019.05.006

Phillips, R., Ursell, T., Wiggins, P., and Sens, P. (2009). Emerging roles for lipids in shaping membrane-protein function. *Nature* 459, 379–385. doi: 10.1038/nature08147

Pincus, D., Chevalier, M. W., Aragón, T., van Anken, E., Vidal, S. E., El-Samad, H., et al. (2010). BiP binding to the ER-stress sensor Ire1 tunes the homeostatic behavior of the unfolded protein response. *PLoS Biol.* 8:e1000415. doi: 10.1371/journal.pbio.1000415

Pineau, L., Colas, J., Dupont, S., Beney, L., Fleurat-Lessard, P., Berjeaud, J. M., et al. (2009). Lipid-induced ER stress: synergistic effects of sterols and saturated fatty acids. *Traffic* 10, 673–690. doi: 10.1111/j.1600-0854.2009.00903.x

Preissler, S., and Ron, D. (2019). Early events in the endoplasmic reticulum unfolded protein response. *Cold Spring Harb. Perspect. Biol.* 11:a033894. doi: 10.1101/cshperspect.a033894

Promlek, T., Ishiwata-Kimata, Y., Shido, M., Sakuramoto, M., Kohno, K., and Kimata, Y. (2011). Membrane aberrancy and unfolded proteins activate the endoplasmic reticulum stress sensor Ire1 in different ways. *Mol. Biol. Cell* 22, 3520–3532. doi: 10.1091/mbc.E11-04-0295

Radanović, T., Reinhard, J., Ballweg, S., Pesek, K., and Ernst, R. (2018). An emerging group of membrane property sensors controls the physical state of organellar membranes to maintain their identity. *Bioessays* 40:e1700250. doi: 10.1002/bies.201700250

Schram, V., and Thompson, T. E. (1995). Interdigitation does not affect translational diffusion of lipids in liquid crystalline bilayers. *Biophys. J.* 69, 2517–2520. doi: 10.1016/s0006-3495(95)80122-0

Schuck, S., Prinz, W. A., Thorn, K. S., Voss, C., and Walter, P. (2009). Membrane expansion alleviates endoplasmic reticulum stress independently of the unfolded protein response. *J. Cell Biol.* 187, 525–536. doi: 10.1083/jcb.200907074

Sezgin, E., Levental, I., Mayor, S., and Eggeling, C. (2017). The mystery of membrane organization: composition, regulation and roles of lipid rafts. *Nat. Rev. Mol. Cell Biol.* 18, 361–374. doi: 10.1038/nrm.2017.16

Sherman, F. (2002). Getting started with yeast. *Methods Enzymol.* 350, 3–41. doi: 10.1016/S0076-6879(02)50954-X

Shevchenko, A., and Simons, K. (2010). Lipidomics: coming to grips with lipid diversity. *Nat. Rev. Mol. Cell Biol.* 11, 593–598. doi: 10.1038/nrm2934

Stordeur, C., Puth, K., Sáenz, J. P., and Ernst, R. (2014). Crosstalk of lipid and protein homeostasis to maintain membrane function. *Biol. Chem.* 395, 313–326. doi: 10.1515/hsz-2013-0235

Stukey, J. E., McDonough, V. M., and Martin, C. E. (1989). Isolation and characterization of OLE1, a gene affecting fatty acid desaturation from *Saccharomyces cerevisiae*. *J. Biol. Chem.* 264, 16537–16544.

Sumper, M., Riepertinger, C., Lynen, F., and Oesterhelt, D. (1969). Die Synthese verschiedener Carbonsäuren durch den Multienzymkomplex der Fettsäuresynthese aus Hefe und die Erklärung ihrer Bildung. *Eur. J. Biochem.* 10, 377–387. doi: 10.1111/j.1432-1033.1969.tb00701.x

Surma, M. A., Herzog, R., Vasilj, A., Klose, C., Christinat, N., Morin-Rivron, D., et al. (2015). An automated shotgun lipidomics platform for high throughput, comprehensive, and quantitative analysis of blood plasma intact lipids. *Eur. J. Lipid Sci. Technol* 117, 1540–1549. doi: 10.1002/ejlt.201500145

Surma, M. A., Klose, C., Klemm, R. W., Ejsing, C. S., and Simons, K. (2011). Generic sorting of raft lipids into secretory vesicles in yeast. *Traffic* 12, 1139–1147. doi: 10.1111/j.1600-0854.2011.01221.x

Surma, M. A., Klose, C., Peng, D., Shales, M., Mrejen, C., Stefanko, A., et al. (2013). A lipid E-MAP identifies Ubx2 as a critical regulator of lipid saturation and lipid bilayer stress. *Mol. Cell* 51, 519–530. doi: 10.1016/j.molcel.2013.06.014

Tabas, I., and Ron, D. (2011). Integrating the mechanisms of apoptosis induced by endoplasmic reticulum stress. *Nat. Cell Biol.* 13, 184–190. doi: 10.1038/ncb0311-184

Thibault, G., Shui, G., Kim, W., McAlister, G. C., Ismail, N., Gygi, S. P., et al. (2012). The membrane stress response buffers lethal effects of lipid disequilibrium by reprogramming the protein homeostasis network. *Mol. Cell* 48, 16–27. doi: 10.1016/j.molcel.2012.08.016

Tran, D. M., Ishiwata-Kimata, Y., Mai, T. C., Kubo, M., and Kimata, Y. (2019). The unfolded protein response alongside the diauxic shift of yeast cells and its involvement in mitochondria enlargement. *Sci. Rep.* 9:12780. doi: 10.1038/s41598-019-49146-5

Travers, K. J., Patil, C. K., Wodicka, L., Lockhart, D. J., Weissman, J. S., and Walter, P. (2000). Functional and genomic analyses reveal an essential coordination between the unfolded protein response and ER-associated degradation. *Cell* 101, 249–258. doi: 10.1016/S0092-8674(00)80835-1

Uhlén, M., Fagerberg, L., Hallström, B. M., Lindskog, C., Oksvold, P., Mardinoglu, A., et al. (2015). Tissue-based map of the human proteome. *Science* 347:1260419. doi: 10.1126/science.1260419

van Meer, G., Voelker, D. R., and Feigenson, G. W. (2008). Membrane lipids: where they are and how they behave. *Nat. Rev. Mol. Cell Biol.* 9, 112–124. doi: 10.1038/nrm2330

Volmer, R., and Ron, D. (2015). Lipid-dependent regulation of the unfolded protein response. *Curr. Opin. Cell Biol.* 33, 67–73. doi: 10.1016/j.ceb.2014.12.002

Walter, P., and Ron, D. (2011). The unfolded protein response: from stress pathway to homeostatic regulation. *Science* 334, 1081–1086. doi: 10.1126/science.1209038

Wang, M., and Kaufman, R. J. (2014). The impact of the endoplasmic reticulum protein-folding environment on cancer development. *Nat. Rev. Cancer* 14, 581–597. doi: 10.1038/nrc3800

Wang, S., and Kaufman, R. J. (2012). The impact of the unfolded protein response on human disease. *J. Cell Biol.* 197, 857–867. doi: 10.1083/jcb.201110131

Wolf, D. H., and Schäfer, A. (2006). CPY* and the power of yeast genetics in the elucidation of quality control and associated protein degradation of the endoplasmic reticulum. *Curr. Top. Microbiol. Immunol.* 300, 41–56. doi: 10.1007/3-540-28007-3_3

Xu, H., and Huang, C. H. (1987). Scanning calorimetric study of fully hydrated asymmetric phosphatidylcholines with one acyl chain twice as long as the other. *Biochemistry* 26, 1036–1043. doi: 10.1021/bi00378a009

Conflict of Interest: MS and CK were employed by the company Lipotype GmbH, Dresden.

The remaining authors declare that the research was conducted in the absence of any other commercial or financial relationships that could be construed as a potential conflict of interest.

frontiers in Cell and Developmental Biology

REVIEW
published: 05 August 2020
doi: 10.3389/fcell.2020.00757

Membrane Heterogeneity Controls Cellular Endocytic Trafficking

Gregory M. I. Redpath[1,2†], Verena M. Betzler[3,4], Pascal Rossatti[3,4] and Jérémie Rossy[4,5*†]*

[1] Department of Biochemistry, School of Biomedical Sciences, University of Otago, Dunedin, New Zealand, [2] The ANZAC Research Institute, Concord Repatriation General Hospital, Concord, NSW, Australia, [3] Graduate School for Cellular and Biomedical Sciences, University of Bern, Bern, Switzerland, [4] Biotechnology Institute Thurgau (BITg) at the University of Konstanz, Kreuzlingen, Switzerland, [5] Department of Biology, University of Konstanz, Konstanz, Germany

OPEN ACCESS

Edited by:
Robert Ernst,
Saarland University, Germany

Reviewed by:
Todd R. Graham,
Vanderbilt University, United States
Ora Weisz,
University of Pittsburgh, United States

***Correspondence:**
Gregory M. I. Redpath
gregory.redpath@otago.ac.nz;
gregory.redpath@anzac.edu.au
Jérémie Rossy
jeremie.rossy@bitg.ch

†ORCID:
Gregory M. I. Redpath
orcid.org/0000-0002-1990-6457
Jérémie Rossy
orcid.org/0000-0002-5128-5283

Specialty section:
This article was submitted to Membrane Traffic, a section of the journal Frontiers in Cell and Developmental Biology

Received: 10 April 2020
Accepted: 20 July 2020
Published: 05 August 2020

Citation:
Redpath GMI, Betzler VM, Rossatti P and Rossy J (2020) Membrane Heterogeneity Controls Cellular Endocytic Trafficking. Front. Cell Dev. Biol. 8:757. doi: 10.3389/fcell.2020.00757

Endocytic trafficking relies on highly localized events in cell membranes. Endocytosis involves the gathering of protein (cargo/receptor) at distinct plasma membrane locations defined by specific lipid and protein compositions. Simultaneously, the molecular machinery that drives invagination and eventually scission of the endocytic vesicle assembles at the very same place on the inner leaflet of the membrane. It is membrane heterogeneity – the existence of specific lipid and protein domains in localized regions of membranes – that creates the distinct molecular identity required for an endocytic event to occur precisely when and where it is required rather than at some random location within the plasma membrane. Accumulating evidence leads us to believe that the trafficking fate of internalized proteins is sealed following endocytosis, as this distinct membrane identity is preserved through the endocytic pathway, upon fusion of endocytic vesicles with early and sorting endosomes. In fact, just like at the plasma membrane, multiple domains coexist at the surface of these endosomes, regulating local membrane tubulation, fission and sorting to recycling pathways or to the *trans*-Golgi network via late endosomes. From here, membrane heterogeneity ensures that fusion events between intracellular vesicles and larger compartments are spatially regulated to promote the transport of cargoes to their intracellular destination.

Keywords: endosomal sorting, Rab11, retromer/retriever, clathrin, endophilin, CLIC/GEEC, phosphoinositide, phosphatidylserine

INTRODUCTION

In most situations, cells respond to extracellular stimuli through the binding and activation of cell surface receptors to extracellular ligands. Following activation, receptors are internalized, sorted for degradation or for recycling to regulate the composition, distribution and density of the pool of available receptors at the cell surface and ultimately to modulate the signaling response (Scita and Di Fiore, 2010). While they were first regarded as being part of a constitutive process, it is now well established that the manifold mechanisms that make up cellular trafficking are highly regulated. Determination of when and where events such as packaging of cargoes or scission and fusion of vesicles is central to the regulation of endocytic trafficking and relies greatly on heterogeneity of membranes. Successive models for cell membranes – fluid mosaic (Singer and Nicolson, 1972), lipid rafts (Simons and Ikonen, 1997), picket-fence (Kusumi et al., 2011), or active

composite (Rao and Mayor, 2014) tend toward a perception that membranes are not homogenous mixtures of lipids and proteins, but rather heterogeneous and compartmentalized (Jacobson et al., 2019). The interplay between different lipid species, membrane proteins, local dynamics of actin polymerisation and membrane curvature creates non-homogenous membrane domains that drive and regulate endocytosis, sorting and recycling. In this review, we highlight how at every step of the endocytic pathway, membrane heterogeneity generates specific domains that ultimately regulate cargo fate. We focus on domains constituted of lipid species – phosphoinositides, cholesterol and phosphatidylserine – which most contribute to membrane heterogeneity during intracellular trafficking, yet the concepts we refer to are likely to extend to other lipid species in similar cellular processes.

Phosphoinositides or phosphatidylserine membrane domains can be generated through clustering by Ca^{2+} (Boettcher et al., 2011; Wen et al., 2018) or by BAR domain containing proteins (Saarikangas et al., 2009; Zhao et al., 2013; Picas et al., 2014). Other mechanisms of phosphoinositide clustering are comprehensively described in an excellent recent review (Picas et al., 2016). However, in the context of endocytic trafficking, membrane heterogeneity most often results from the recruitment of membrane remodeling proteins – phospholipid-modifying enzymes, flippases, curvature-inducing proteins or regulators of actin polymerization – by coat proteins, adaptors, or lipids that already define membrane domains with distinct properties. Hence, in this review we consider that heterogenous membrane domains do not dissipate during transitions from one step of the endocytic journey to the next, but rather that endocytic transitions are driven by shedding and recruitment of membrane remodeling proteins.

Heterogeneity is one of the main factors determining where and which type of endocytosis will be triggered. Endocytic events occur in unique membrane domains which then undergo precise changes as they mature to facilitate formation of endosomes (Danson et al., 2013; Boucrot et al., 2015; Nakatsu et al., 2015; Posor et al., 2015). Membrane heterogeneity is propagated further through the endosomal pathway by phosphoinositide metabolism that switches phosphoinositide species throughout the endocytic trafficking process, ultimately regulating every step of the intracellular sorting process that occurs following endocytosis.

Below, we discuss how membrane heterogeneity generates domains that regulate the initiation and progression of clathrin-dependent endocytosis, fast endophilin-mediated endocytosis and clathrin independent carrier/glycosylphosphatidylinositol -anchored protein enriched endocytic compartments (CLIC/GEEC) endocytosis. We address the contribution of different phosphoinositide species and cholesterol, actin and membrane curvature to ensuring the mode of endocytosis remains tightly regulated. We then detail how phosphoinositide and phosphatidylserine membrane domains ensure each cargo progresses through the endosomal sorting steps to its target destination. Ultimately, we propose a model in which phosphoinositide and phosphatidylserine generate membrane heterogeneity either during or immediately following endocytosis and segregates cargoes into defined membrane domains. Therefore, our model implies that the trafficking fate of cargoes is decided at the endocytosis stage, and these domains are maintained throughout their respective sorting pathways until the required cellular destination is reached. In short, this review highlights how at every step of the endocytic pathway, membrane heterogeneity generates specific domains that ultimately regulate cargo fate.

ENDOCYTOSIS

Membrane heterogeneity stands at the center of regulating entry of receptors and cargoes into the cell *via* endocytosis. Endocytosis involves the invagination of the plasma membrane containing the cargo, followed by scission of the invaginated region from the plasma membrane, and eventually the formation of a distinct endocytic vesicle. Endocytosis is segregated into two broad modes- clathrin-dependent and clathrin-independent. Clathrin-dependent endocytosis is the best studied of the two and is defined by the presence of a clathrin coat on the endocytic vesicle. Clathrin-independent endocytosis represents multiple, less defined internalization pathways. Membrane heterogeneity contributes to the selection of the mode of internalization and ultimately regulates how, when and where a cargo enters the cell. It further ensures that clathrin-dependent and -independent endocytosis remain distinct and selective and that the many elements shared exert specific functions in each mode of endocytosis.

Clathrin-Dependent Endocytosis

Clathrin-dependent endocytosis is defined by extrusion of the plasma membrane into an endocytic vesicle surrounded by a clathrin lattice followed by scission from the membrane. Spatial and temporal heterogeneity of phosphoinositide metabolism regulates the timing of each step of clathrin-dependent endocytosis, including clathrin coat nucleation, endocytic pit formation, vesicle scission and clathrin uncoating [extensively reviewed in Mettlen et al. (2018)].

Phosphoinositides are membrane lipid species that are readily modifiable by phosphorylation at the 3, 4, or 5 hydroxyl positions on the inositol ring and represent a major source of membrane heterogeneity within the cell (Schink et al., 2016). In this regard, they are especially important for intracellular trafficking (Wang et al., 2019). For clathrin-dependent endocytosis, heterogeneity mainly results from plasma membrane regions enriched in phosphoinositide 4,5 phosphate [$PI(4,5)P_2$] and displaying high membrane curvature, which together provide the initial impetus for formation of a clathrin coated pit (**Figure 1A**). Asymmetric enrichments of $PI(4,5)P_2$ lead to spontaneous induction of membrane curvature *in vitro* through a mechanism that remains to be elucidated (Shukla et al., 2019). In turn, membrane curvature leads to recruitment and stabilization of a clathrin-lattice at the plasma membrane (**Figure 1B**) (Jost et al., 1998; Cremona et al., 1999). This lattice is further stabilized by formation of actin filaments promoted by direct binding of actin regulatory proteins to areas enriched in

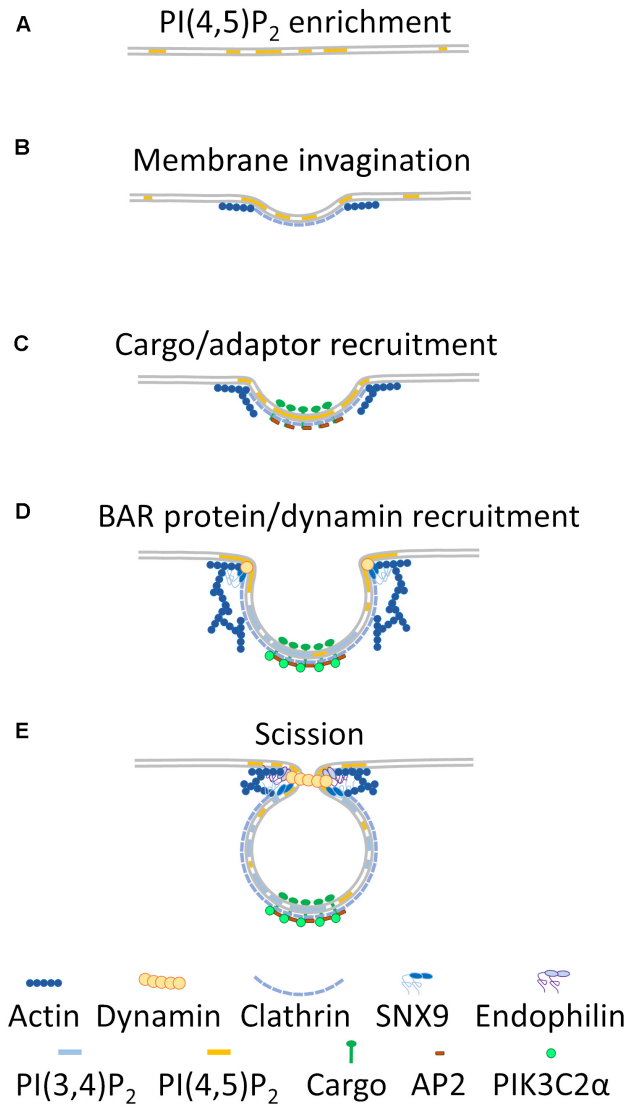

FIGURE 1 | Membrane heterogeneity regulating clathrin-dependent endocytosis. In relatively flat regions of the plasma membrane, $PI(4,5)P_2$ enrichment occurs **(A)**. This enrichment leads to induction of membrane curvature that recruits clathrin and branched actin to the nascent endocytic pit **(B)**. Cargo is enriched within this pit, and AP2 is recruited to the cargo and clathrin coat **(C)**. Further actin branching and extrusion of the clathrin coated pit leads to recruitment of PIK3C2α, which metabolizes $PI(4,5)P_2$ to $PI(3,4)P_2$ around the clathrin coat, while BAR-domain containing proteins and dynamin are recruited to the highly curved neck region of the pit **(D)**. Finally, increased recruitment of BAR-domain containing proteins, branched actin and dynamin to the neck region leads to constriction of the endosome and scission from the plasma membrane **(E)**.

$PI(4,5)P_2$ in the membrane (**Figure 1B**) (Yin and Janmey, 2003; Leyton-Puig et al., 2017). Ligand binding promotes translocation of receptors and cargo to these stabilized clathrin plaques (Leyton-Puig et al., 2017). Localized enrichments in $PI(4,5)P_2$ are therefore required to initiate clathrin-dependent endocytosis and stabilize the clathrin lattice in order to allow cargo entry into the forming endocytic pit.

Recruitment of adaptor proteins to the stabilized clathrin lattice leads to an additional local increase of $PI(4,5)P_2$, further creating a membrane environment distinct from the surrounding plasma membrane (**Figure 1C**) (Krauss et al., 2006). The adaptor protein AP-2 interacts with $PI(4,5)P_2$, which stabilizes it in an open conformation and facilitates cargo and clathrin binding at the forming lattice. Open AP-2 also recruits phosphatidylinositol kinase type-I which generates more $PI(4,5)P_2$ (Krauss et al., 2006; Jackson et al., 2010). Heterogeneity in the plasma membrane resulting from phosphoinositide (PI) enrichment is therefore a crucial step for initiating and stabilizing clathrin endocytic pits.

At this stage, a clathrin pit begins to resemble a 3D endocytic structure being extruded from the plasma membrane, in which a segregation between the endocytic pit and surrounding plasma membrane is evident (**Figures 1B–D**). Rather than being a two-dimensional assembly of proteins on the plasma membrane, the clathrin-coated pit has a strong dimension of curvature that allows the recruitment of membrane curvature-sensing and -inducing BAR-domain containing proteins at the neck of the budding vesicles (**Figure 1D**) (Lo et al., 2017; Schöneberg et al., 2017). This geometric membrane heterogeneity is reinforced by $PI(4,5)P_2$ concentration to the neck region of the pit and facilitates the recruitment of dynamin (**Figure 1D**) (Zheng et al., 1996). Dynamin ultimately exerts a constricting force on the endocytic pit which leads to scission from the plasma membrane (Ferguson et al., 2009).

While clathrin pits progress to fully formed endocytic vesicles, further membrane heterogeneity is created by generation of $PI(3,4)P_2$ around the forming clathrin-coated vesicle (**Figure 1D**) (Posor et al., 2013). PIK3C2α is recruited to the clathrin lattice *via* interactions with clathrin and $PI(4,5)P_2$, where it metabolizes $PI(4,5)P_2$ to $PI(3,4)P_2$ in conjunction with the 5-phosphatases ORCL and synaptojanin-1 (Posor et al., 2013; He et al., 2017; Schöneberg et al., 2017). This distinct phospholipid environment promotes the recruitment and activation of the BAR-domain containing protein SNX9 that interacts with actin-branching activators and dynamin (**Figure 1D**) (Posor et al., 2013; Lo et al., 2017; Schöneberg et al., 2017) and provides constricting force at the neck of the endocytic vesicle (Shin et al., 2008; Ferguson et al., 2009).

The final alteration in membrane heterogeneity in clathrin-dependent endocytosis serves to remove clathrin and adaptor proteins from the endocytic vesicle, ensuring scission from the plasma membrane and entry into the endocytic trafficking pathway. Endophilin is a further BAR-domain containing protein that is recruited to dynamin at the neck of the endocytic vesicle (Perera et al., 2006; Ferguson et al., 2009). Endophilin, as with SNX9 and other BAR-domain containing proteins, can deform membranes to assist dynamin in vesicle scission (**Figure 1E**) (Itoh et al., 2005). Endophilin also directly modifies the membrane composition of the endocytic vesicle by recruiting the 5-phosphatase synaptojanin-1 to the neck region of the vesicle immediately prior to fission. Synaptojanin-1 metabolizes $PI(4,5)P_2$ to PI(4)P, which makes further clathrin and AP-2 binding unfavorable (Perera et al., 2006; Milosevic et al., 2011). Auxilin, which is recruited to

the mature pit by dynamin and binding to enriched PI(4)P, recruits the uncoating chaperone HSC70, ultimately leading to uncoating of the clathrin-adaptor complex from the endocytic vesicle and release of the vesicle into the cell (Massol et al., 2006; Guan et al., 2010). Recruitment of the 5-phosphatase ORCL to the neck of the clathrin-coated pit by SNX9 immediately prior to fission further stimulates vesicle uncoating (Nández et al., 2014).

Key points:

- Clathrin-dependent endocytosis is regulated by membrane heterogeneity at every step.
- $PI(4,5)P_2$ enrichment at the plasma membrane generates membrane curvature and a distinct domain within the plasma membrane, which eventually recruits clathrin.
- $PI(4,5)P_2$ enrichment recruits AP-2 and phosphatidylinositol kinase type-I, further promoting high local $PI(4,5)P_2$ concentration.
- $PI(4,5)P_2$ and clathrin recruit PIK3C2α, which produces $PI(3,4)P_2$, resulting in $PI(3,4)P_2$ enrichment around the clathrin-coated region while leaving PI(4,5)P present in the neck region.
- $PI(4,5)P_2$ in the neck region recruits dynamin, SNX9, endophilin and branched actin, ultimately leading to vesicle scission and uncoating of clathrin from the vesicle.

Clathrin-Independent Endocytosis

Clathrin-independent endocytosis represents multiple endocytic pathways with the common factor being that they do not rely on clathrin. The major difference in the initiation of endocytosis between clathrin-mediated and clathrin-independent endocytosis is the local microenvironment at the site of internalization, making membrane heterogeneity a key determinant of the endocytic mode responsible for internalizing cargo.

Fast Endophilin-Mediated Endocytosis

Endophilin plays an important role in vesicle scission and uncoating and is a central regulator of the fast endophilin-mediated endocytosis pathway (Boucrot et al., 2015). While clathrin-dependent endocytosis occurs across the entire plasma membrane at regions of $PI(4,5)P_2$ enrichment (**Figure 2A**), fast endophilin-mediated endocytosis occurs within $PI(3,4,5)P_3$-rich sites in response to activation of receptors (**Figure 2B**) (Leonard et al., 2008; Boucrot et al., 2015).

CDC42 activity initiates fast endophilin-mediated endocytosis through the recruitment of the BAR-domain containing proteins FBP17 and CIP4, which in turn recruit the 5-phosphatase SHIP2 (Chan Wah Hak et al., 2018). Activated SHIP2 metabolizes $PI(3,4,5)P_3$ to $PI(3,4)P_2$ at the cell leading edge (Pesesse et al., 2001) resulting in the recruitment of lamellipodin and eventually endophilin (Boucrot et al., 2015; Chan Wah Hak et al., 2018). Cycling of CDC42 activation leads to constant assembly/disassembly of membrane patches primed for endophilin recruitment. These are only stabilized if ligand-bound receptors are present, in which case the endophilin-enriched membrane patch proceeds through endocytosis (Chan Wah Hak et al., 2018). Interestingly, in clathrin-dependent endocytosis, endophilin localizes to the highly curved, $PI(4,5)P_2$ enriched neck region of the endocytic vesicle (Perera et al., 2006; Milosevic et al., 2011). During fast endophilin-mediated endocytosis, endophilin is concentrated in a completely different $PI(3,4)P_2$-enriched membrane environment at the leading edge of the cell (Boucrot et al., 2015). This highlights how membrane heterogeneity ultimately controls how one protein can regulate two endocytic modes (**Figures 2A,B**).

In contrast to clathrin-dependent endocytosis where the membrane is held in a defined, rigid conformation by the clathrin coat, endophilin-mediated endocytosis requires a malleable membrane for formation and scission of the vesicle from the plasma membrane. Twenty BAR-domain containing proteins

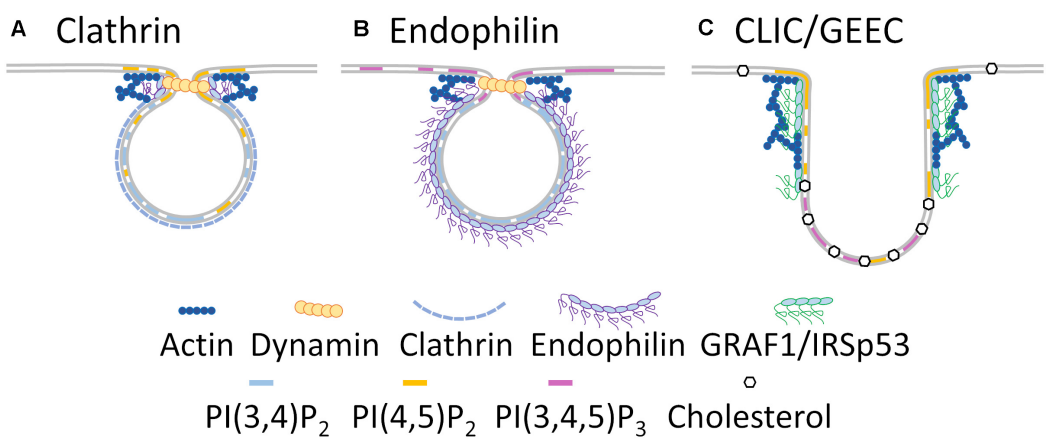

FIGURE 2 | Membrane heterogeneity regulates endocytic specificity. Clathrin dependent endocytosis **(A)** occurs in $PI(3,4)P_2$ and $PI(4,5)P_2$ enriched regions of the plasma membrane and requires endophilin, dynamin and actin recruitment for endosomal scission. Fast endophilin-mediated endocytosis **(B)** occurs in $PI(3,4)P_2$ and $PI(3,4,5)P_3$ enriched regions of polarized membranes, with endophilin likely forming the coat around the endosome, and branched actin and dynamin required for endosomal scission. CLIC/GEEC endocytosis **(C)** occurs in cholesterol, $PI(4,5)P_2$ and $PI(3,4,5)P_3$ enriched regions of the plasma membrane and relies on branched actin and GRAF1/IRSp53 BAR -domain containing proteins for endosomal scission.

have been identified in endophilin-enriched membrane patches thus far, strongly indicating that local membrane bending and remodeling is the critical factor in forming endosomes in fast endophilin-mediated endocytosis (Chan Wah Hak et al., 2018).

Key points:

- Fast endophilin-mediated endocytosis is initiated within $PI(3,4,5)P_3$ areas of the cell.
- CDC42 assembles primed membrane patches for fast endophilin-mediated endocytosis, recruiting BAR-domain proteins and the 5-phosphatase SHIP2.
- If ligand: receptor binding occurs, SHIP2 is activated leading to rapid metabolism of $PI(3,4,5)P_3$ to $PI(3,4)P_2$.
- $PI(3,4)P_2$ enriched patches recruit lamellipodin and endophilin, leading to cargo endocytosis.

CLIC/GEEC Endocytosis

CLIC/GEEC endocytosis is predominantly defined as being a clathrin-independent, dynamin-independent endocytic pathway (Doherty and Lundmark, 2009). Similar to fast endophilin-mediated endocytosis, CLIC/GEEC endocytosis occurs at the leading edge or polarized membranes of the cell in a CDC42 and BAR-domain containing protein dependent manner, and is notable for the formation of pronounced membrane tubules carrying cargo (Howes et al., 2010; Francis et al., 2015; Rossatti et al., 2019). While clathrin-dependent and fast endophilin-mediated endocytosis predominantly regulate receptor internalization, CLIC/GEEC endocytosis regulates receptor internalization (Kumari and Mayor, 2008; Rossatti et al., 2019), toxin uptake (Lundmark et al., 2008; Romer et al., 2010) and fluid-phase endocytosis (Howes et al., 2010).

CLIC/GEEC endocytosis occurs in either $PI(4,5)P_2$ or $PI(3,4,5)P_3$ enriched membranes and relies more on plasma membrane cholesterol than clathrin dependent or fast endophilin mediated endocytosis (**Figure 2C**). The presence of cholesterol within the plasma membrane is also critical for CDC42 activation and subsequent actin polymerisation. Consequently, mild cholesterol depletion abolishes CLIC/GEEC endocytosis while leaving clathrin-dependent endocytosis unperturbed (Chadda et al., 2007). Active CDC42 recruits the BAR-domain containing proteins GRAF-1 and/or IRSp53 and the actin nucleation complex Arp2/3 to the plasma membrane which together induce membrane curvature and tubulation that is characteristic of the CLIC/GEEC pathway (Francis et al., 2015; Sathe et al., 2018). GRAF-1 binds $PI(4,5)P_2$ (Lundmark et al., 2008) while IRSp53 binds $PI(3,4,5)P_3$ and $PI(4,5)P_2$ (Suetsugu et al., 2006), indicating that CLIC/GEEC endocytosis may occur at wider range of membrane environments than fast endophilin-mediated endocytosis, perhaps to account for its role in large-scale membrane turnover (Howes et al., 2010; Francis et al., 2015). CLIC/GEEC endocytosis is also sensitive to local membrane tension, its rate increasing with decreasing membrane tension, *via* the mechanotransducer vinculin (Thottacherry et al., 2018). Phosphatidylserine clustering in the inner leaflet of the plasma membrane is capable of promoting membrane curvature and endocytosis (Hirama et al., 2017). Conversely, cholesterol limits phosphatidylserine clustering in the plasma membrane, preventing spontaneous endocytosis (Hirama et al., 2017; Hirama and Fairn, 2018). However, molecular dynamics simulations indicate cholesterol itself induces membrane curvature and associates with phosphatidylserine in highly curved regions in asymmetric membranes (Yesylevskyy et al., 2013), indicating a complex relationship between cholesterol and phosphatidylserine in endocytosis. We therefore speculate CLIC/GEEC endocytosis may rely on the functional interrelation of cholesterol and phosphatidylserine at the plasma membrane and the interplay of both to induce the local membrane curvature required for endosome formation.

A critical difference between fast endophilin-mediated endocytosis and CLIC/GEEC endocytosis is the lack of dynamin-dependence for vesicle scission off the plasma membrane in the latter. A confluence of BAR-domain containing proteins deforming CLIC/GEEC membrane tubules coupled with tubule constriction by branched actin fibers may provide the physical force needed for endosome scission in the absence of dynamin (Sathe et al., 2018). Cholesterol, in coordination with actin polymerisation, greatly enhances scission of membrane tubules formed during CLIC/GEEC endocytosis (Romer et al., 2010), and is required for CDC42 activation dependent actin polymerisation on $PI(4,5)P_2$-enriched membranes (Chadda et al., 2007). It is likely that cholesterol and $PI(4,5)P_2$ in CLIC/GEEC membrane tubules is an absolute requirement for the recruitment of BAR-domain containing proteins required for scission to release endosomes. Specific membrane heterogeneity – in terms of membrane composition, curvature and tension – is therefore required for not only initiating CLIC/GEEC endocytosis, but also in ensuring scission of CLIC/GEEC endocytic tubules.

Key points:

- CLIC/GEEC endocytosis occurs in cholesterol, $PI(3,4,5)P_3$ or $PI(4,5)P_2$ enriched regions of the cell leading edge or polarized membranes of the cell.
- Cholesterol, in conjunction with phosphatidylserine, may induce the membrane curvature required for initiation of CLIC/GEEC endocytosis.
- CDC42 recruits GRAF1 and IRSp53, which in conjunction with branched actin induce membrane tubulation.
- GRAF1 and IRSp53 can bind $PI(4,5)P_2$ and/or $PI(3,4,5)P_3$, leading to induction of CLIC/GEEC endocytosis in a wide range of membrane patches on the cell leading edge.
- Cholesterol and branched actin are capable of inducing membrane tubule scission, leading to the formation of endocytic carriers in CLIC/GEEC endocytosis.

ENDOSOMAL SORTING

Endocytosed cargoes are sorted via three main routes that result in different fates: (1) recycling to the plasma membrane via retromer/retriever and the *trans*-Golgi network, (2) degradation by the lysosome, or (3) recycling to the plasma membrane *via* Rab11 dependent recycling endosomal pathway (**Figure 3**).

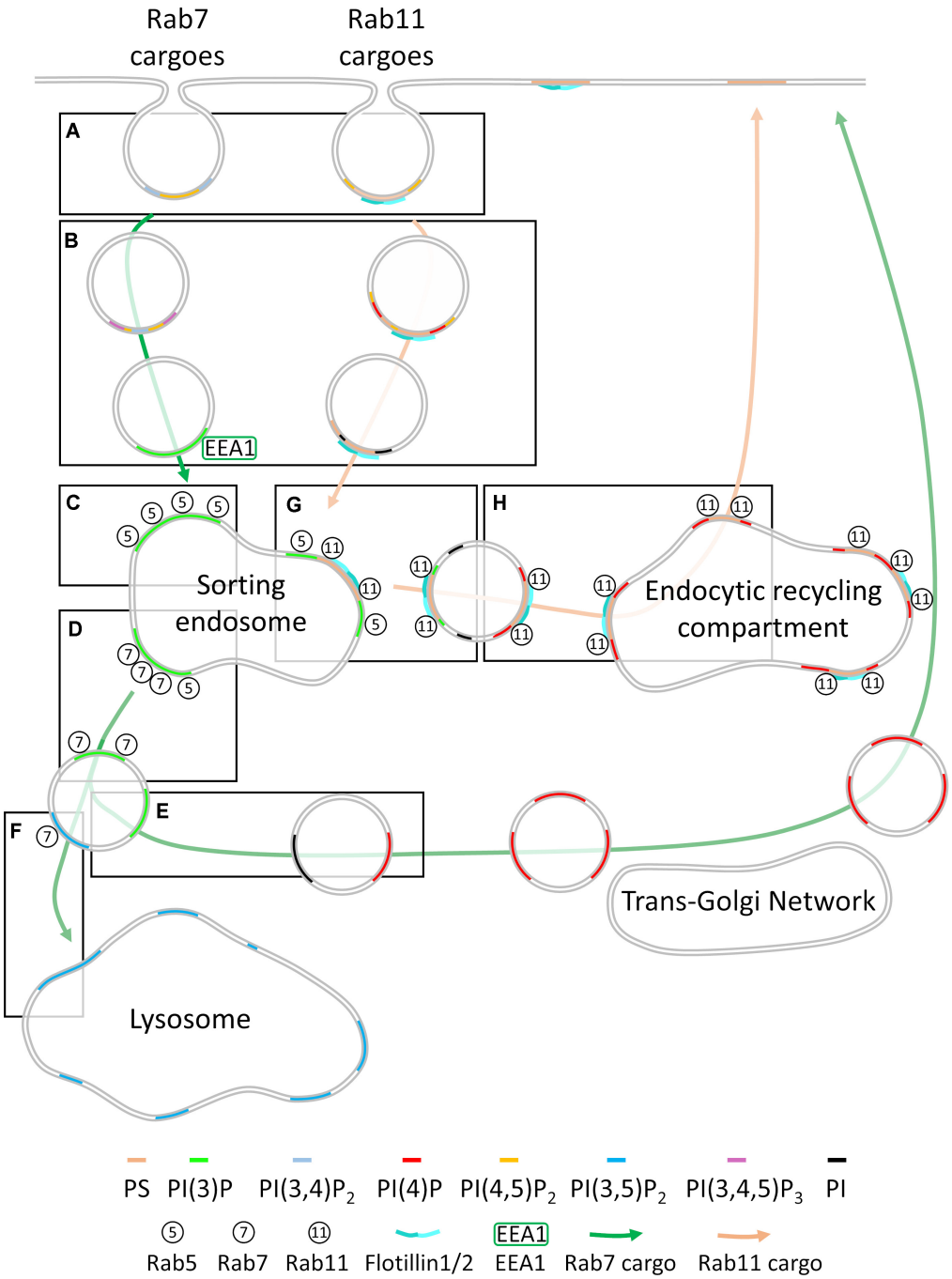

FIGURE 3 | Membrane heterogeneity regulates cargo sorting throughout the endocytic network. **(A)** Cargoes are segregated into endocytic pits containing a specific combination of phosphoinositides (PI, left) or phosphoinositides and phosphatidylserine (PS, right) at the plasma membrane. This ensures cargoes are kept segregated after having been internalized. Endosomes containing only phosphoinositides become enriched in PI(3)P at this point (left) while phosphoinositides on phosphatidylserine containing endosomes are de-phosphorylated **(B)**. Cargo destined for Rab7-dependent trafficking enters the Rab5$^+$ sorting endosome, where it resides in a PI(3)P-enriched membrane domain **(C)**. This PI(3)P enrichment recruits Rab7 and leads to the inactivation of Rab5, maturing into a Rab7$^+$ late endosome **(D)**. PI(4,5)P_2 is generated on the Rab7$^+$ late endosome, allowing recruitment of retromer/retriever/CCC factors that retrieve the cargo, metabolize the PI(4,5)P_2 and PI(3)P to phosphoinositide and PI(4)P, displacing Rab7 and allowing cargo trafficking to the *trans*-Golgi network, where it can be re-secreted to the plasma membrane **(E)**. Rab7-dependent cargoes that are not trafficked to the *trans*-Golgi network are trafficked to the lysosome for degradation **(F)**. Cargoes entering the cell via the phosphatidylserine-enriched endocytic pathway fuse with the Rab5$^+$ sorting endosome, where their membrane domains are enriched in PI(3)P, leading to recruitment of Rab11 and scission from the Rab5$^+$ sorting endosome **(G)**. Following scission, the PI(3)P on the Rab11$^+$ vesicle is metabolized to PI(4)P, allowing fusion with the Rab11$^+$ endocytic recycling compartment and re-delivery to the plasma membrane **(H)**.

Rab7 regulates formation of the late endosome, from which retromer, retriever and COMMD/CCDC22/CCDC93 (CCC)-dependent cargo retrieval and recycling occurs (McNally et al., 2017; Purushothaman et al., 2017; Singla et al., 2019) or from which cargoes are directed to the lysosome for degradation (Guerra and Bucci, 2016). Rab4 is predominantly localized to the Rab5$^+$ sorting endosomal compartment (Sönnichsen et al., 2000) and can regulate cargo transfer into both Rab11 recycling and cellular degradative pathways (McCaffrey et al., 2001; Nag et al., 2018). Little is known about the composition of membranes that recruit Rab4, however. Rab11 regulates trafficking of cargoes to the endocytic recycling compartment for direct recycling to the plasma membrane (Takahashi et al., 2012). Entry into these pathways is regulated by the Rab5$^+$ sorting endosome, which has been historically viewed as where the sorting decisions for the cell are carried out (Jovic et al., 2010; Naslavsky and Caplan, 2018).

Membrane heterogeneity acts as a decisive regulator of each step of the sorting process, from the plasma membrane and throughout the endosomal network. Recent evidence indicates that cargoes are pre-sorted into distinct plasma membrane environments and that the sorting fate of a protein is either determined with the formation of the endocytic coat or immediately following endocytosis (Sigismund et al., 2005, 2008; Lakadamyali et al., 2006; Qian et al., 2007; Leonard et al., 2008; Leren, 2014; Sposini et al., 2017; Redpath et al., 2019). Membrane heterogeneity plays a decisive role in sorting cargoes toward the Rab7 or Rab11 pathways. As cargoes remain segregated following endocytosis (Lakadamyali et al., 2006; Leonard et al., 2008; Franke et al., 2019), we speculate that the membrane lipids of each type of endocytic vesicle could also remain segregated following fusion with the Rab5$^+$ endosome. From here, these distinct membrane domains undergo specific changes in their composition that lead to recruitment of either Rab7 or Rab11. Rab7 leads to recruitment of retromer/retriever complexes for retrograde recycling or of the endosomal sorting complex required for transport (ESCRT) for lysosomal degradation. Recruitment of Rab11 leads to Rab11-dependent recycling (Fairn et al., 2011; Franco et al., 2014; Takatori et al., 2016; Campa et al., 2018; Cullen and Steinberg, 2018; Redpath et al., 2019). SNAREs, the protein complexes responsible for fusing cellular membranes together also reside in specific regions of heterogenous membranes. The role of SNAREs in targeting and fusion of subcellular membranes extend beyond the scope of this review but is extensively is reviewed in Jahn and Scheller (2006) and Dingjan et al. (2018).

Sorting for Retromer/Retriever/CCC-Dependent Recycling or Lysosomal Degradation

Even though the fate of cargoes is presumably determined prior to or during endocytosis, trafficking is required to be highly modular in order to adapt to cellular conditions. As such, trafficking via the Rab5 to Rab7 endocytic pathway can result in either recycling *via* the retromer/retriever pathway or degradation in the lysosome (**Figures 3A–F**) (Guerra and Bucci, 2016). Membrane domains with distinct phosphoinositide contents control entry into and sorting along the Rab5 to Rab7 pathway. Cargoes targeted to this route enter the Rab5$^+$ sorting endosome in PI3P enriched domains distinct from those of Rab11-dependent recycling cargoes, which are enriched in phosphatidylserine (**Figures 3A,B** – left) (Lakadamyali et al., 2006; Leonard et al., 2008; Tanaka et al., 2016). These cargoes remain in the Rab5$^+$ sorting endosomes, which mature into Rab7$^+$ late endosomes. They are then clustered in ESCRT-rich domains within Rab7$^+$ membranes and transported into lysosomes in which they are degraded (Rink et al., 2005). However, depending on the cellular conditions, cargoes typically targeted to the degradative pathway can be redirected for recycling *via* the *trans*-Golgi by the recruitment of the retriever and CCC complexes within subdomains of the Rab7$^+$ endosome (Burd and Cullen, 2014; McNally et al., 2017; Singla et al., 2019).

Following internalization, cargoes addressed to Rab7$^+$ endosomes are segregated from those cargoes destined for Rab11-depenent recycling and rapidly enter EEA1$^+$ compartments on their way to the Rab5$^+$ sorting endosome (Lakadamyali et al., 2006). This step relies on membrane heterogeneity, as residual phosphoinositides from the endocytic pit are metabolized to PI(3)P (Christoforidis et al., 1999). PI(4,5)P_2 on the endosome (either immediately, prior to, or following fission from the plasma membrane) is phosphorylated to PI(3,4,5)P_3 by PI3Kβ (Shin et al., 2005). PI(3,4,5)P_3 is subsequently metabolized to PI(3,4)P_2 and PI(3)P by OCRL and INPP4A/B (Shin et al., 2005; Vicinanza et al., 2011). Residual PI(3,4)P_2 from the endocytic pit is similarly metabolized to PI(3)P (Shin et al., 2005, **Figures 3A,B** – left).

These PI(3)P-positive membranes promote the recruitment of EEA1 which triggers cargo entry into the Rab5$^+$ sorting endosome (Christoforidis et al., 1999; Murray et al., 2016). EEA1 acts as a fusogenic tether (Christoforidis et al., 1999; Murray et al., 2016) and simultaneously binds both PI(3)P and Rab5 to bring PI(3)P$^+$ endosomes together with Rab5$^+$ sorting endosomes (**Figures 3B,C** – left) (Lawe et al., 2002; Murray et al., 2016). EEA1 binding to the membrane of endocytic vesicles after internalization represents a crucial difference in the pre-Rab5$^+$ sorting of Rab11- and Rab7-dependent cargoes. Typically, while epidermal growth factor (EGF) remains associated with EEA1$^+$ vesicles, transferrin either only spuriously interacts with or is rapidly sorted through this population of endocytic vesicles (Leonard et al., 2008). It follows that EEA1 knockdown reduces degradation of EGF-stimulated EGF receptor, while transferrin uptake and recycling is unaffected (Leonard et al., 2008; Navaroli et al., 2012) (**Figure 3B**). Interestingly, our own studies of TCR, another Rab11-dependent recycling cargo, reveals similar short interactions with Rab5$^+$ early endosomes following endocytosis (Redpath et al., 2019), indicating that recycling cargoes may only very transiently interact with early endosomal compartments.

Similarly to EEA1, sorting nexin 15 (SNX15) binds to and promotes the formation of heterogeneous membrane domains to ensure correct sorting of cargoes trafficking toward the lysosome immediately following clathrin-dependent endocytosis (Danson et al., 2013; Flores-Rodriguez et al., 2015). SNX15 can drive entry of EGF into EEA1$^+$ and Rab5$^+$ endosomes through the

simultaneous ability to interact with clathrin and PI(3)P (Danson et al., 2013; Flores-Rodriguez et al., 2015; Chandra et al., 2019). SNX15 also interacts with the ESCRT protein family, which deform membranes for formation of multi-vesicular bodies (a prelude to lysosomal trafficking) (Flores-Rodriguez et al., 2015).

Rab5$^+$ sorting endosomes mature into late endosomes over time by acquiring Rab7 and losing Rab5 (**Figures 3C,D**). This transition relies on membrane heterogeneity, and more specifically on timed and localized enrichment in PI(3)P. Regions of Rab5$^+$ sorting endosome get progressively enriched in PI(3)P, leading to recruitment of Rab7 and inactivation of Rab5 (**Figure 3D**) (Rink et al., 2005). These specific membranes within the Rab5$^+$ endosome have a high PI(3)P content (**Figure 3C**) (Gillooly et al., 2003), either because they result from fusion with EEA1 endosomes or because of Rab5-dependent recruitment of the phosphoinositide-3 kinase VPS34, which generates PI(3)P from PI (Shin et al., 2005). Enlargement of Rab5 endosomes – likely due to continued delivery of cargo-containing endocytic vesicles to the Rab5$^+$ compartment – leads to recruitment of the protein SAND-1/Mon1, which subsequently displaces Rab5 activating factors and recruits Rab7 to the endosome (Poteryaev et al., 2010). High levels of PI(3)P also allow the binding of TBC-2, which is an inhibitor of Rab5 (Law et al., 2017). Once recruited on Rab5$^+$ endosomes, Rab7 acts to negatively regulate further PI(3)P synthesis by recruiting WDR91 (Liu et al., 2016, 2017). Sufficient PI(3)P must, however, remain on the endosome to recruit the Rab7 inactivating factor, Armus for later termination of Rab7 activity (Jaber et al., 2016). Too little PI(3)P generation leads to Rab5 and Rab7 hyperactivation and ultimately defective cargo trafficking to the lysosome (Jaber et al., 2016). Conversely, cargoes fail to leave early endosomes in presence of too high levels of PI(3)P (Liu et al., 2017).

PI(3)P enriched microdomains in the Rab7$^+$ late endosomal membrane are also central to recovering cargoes and circumventing lysosomal degradation for re-delivery to the plasma membrane, directly or through the *trans* Golgi network (**Figure 3D**). Three protein complexes have been identified to stimulate this recovery *via* recognition of specific sequences on the cargo: retromer, retriever and the CCC complex (McNally et al., 2017; Purushothaman et al., 2017; Singla et al., 2019). Retromer and retriever are formed by specific sorting nexin family members and three vacuolar protein sorting (VPS) family subunits. Both retromer and retriever bind the CCC protein complex, which directly regulates endosomal PI(3)P levels (Singla et al., 2019). Retromer is recruited to the Rab7 endosomal membrane *via* direct interaction between Rab7 and the retromer VPS subunits, and PI(3)P binding by the SNX subunits (Rojas et al., 2008). Neither the VPS or SNX subunits of retriever associate with Rab7 or PI(3)P, respectively, despite residing on the same endosomal membrane domains as retromer (McNally et al., 2017). How precisely retriever is targeted to the same membrane domain as retromer is not yet fully understood, however, retriever associates with the CCC complex which itself has PI(3)P binding capacity (McNally et al., 2017). Alongside PI(3)P, PI(4,5)P_2 plays an important role in the recycling of cargos through the retromer/retriever pathway. PI(4,5)P_2 must be generated on the Rab7$^+$ endosomal membrane by the phophoinositide-5 kinase PIPKIγi5 for cargo entry and direct retromer recruitment (Sun et al., 2020). Furthermore, binding of the COMMD1 subunit of the CCC complex to PI(4,5)P_2 is required for cargo recovery to the *trans*-Golgi network (Stewart et al., 2019), providing a potential link between retriever and the PI(3)P/PI(4,5)P_2-enriched membrane domain utilized by retromer for cargo recovery (**Figures 3D,E** – left).

Multiple local phosphoinositide changes in the membrane domains defined by retromer/retriever are required to facilitate cargo transport toward the *trans*-Golgi network (**Figure 3E** – right). Prior to scission from the Rab7$^+$ late endosome, the actin-branching activating complex WASH localizes to the PI(3)P-enriched retrieval subdomains (Gomez and Billadeau, 2009; Cullen and Steinberg, 2018; Singla et al., 2019). Actin polymerization downstream of WASH leads to scission of the retromer membrane domain from the Rab7$^+$ late endosome (Gomez and Billadeau, 2009). After scission, PI(3)P is metabolized to PI by the 3-phosphatase MTMR2, which leads to a reduction in WASH activation and displacement of actin from the retromer/retriever membrane domain (Cao et al., 2007; Singla et al., 2019). Without PI(3)P reduction, actin accumulates on endosomal membranes and cargo degradation is increased while recycling decreases (Bartuzi et al., 2016; Singla et al., 2019). Local membrane composition further contributes to regulate the transport of retromer cargoes toward the *trans*-Golgi network. Following scission from the late endosome, the subunit SNX6 links the retromer membrane domain with the molecular motor dynein, resulting in cargo transport (Hong et al., 2009; Wassmer et al., 2009; Purushothaman et al., 2017). SNX6 then binds enriched PI(4)P membranes in the *trans*-Golgi network, which subsequently causes release of the molecular motor dynein and cargo delivery into the *trans*-Golgi network, from where re-secretion can finally occur (Niu et al., 2013).

Cargoes not recovered from the late endosome by retromer, retriever or the CCC complex are clustered in membrane domains enriched in the ESCRT complex, which initiates their transport to the lysosome for degradation (**Figure 3F**) (Rojas et al., 2008; Bartuzi et al., 2016; McNally et al., 2017; Cullen and Steinberg, 2018). PI(3,5)P_2 is generated from residual PI(3)P by PIK*fyve*, which is critical for maintaining the membrane integrity of late Rab7$^+$ endosomes and lysosomes (Ikonomov et al., 2002, 2006; Bissig et al., 2017). Rab7$^+$ lysosomes represent terminal compartments in which cargoes not destined for recycling are degraded (Humphries et al., 2011). The interaction between Rab7 and PI(3,5)P_2, or how PI(3,5)P_2 recruits other requisite lysosomal proteins is not yet known.

Key points:

- The Rab5/Rab7 endocytic pathway relies on tightly controlled PI(3)P enrichment.
- PI(3)P recruits Rab7 to the Rab5$^+$ sorting endosome and recruits Rab5 inactivating factors.
- PI(3)P recruits retromer/retriever/CCC subunits required to facilitate cargo recovery to the *trans*-Golgi network.
- PI(3)P recruits actin branching factors to facilitate endosomal scission from the late endosome.

- PI(4,5)P is enriched in retromer/CCC-bound membrane domains and is required for cargo recovery.
- Once vesicles targeting the Golgi have left the Rab7$^+$ endosome, PI(3)P is metabolized to PI.
- PI(4)P from the *trans*-Golgi network recruits retromer subunits, resulting in cargo delivery.
- PI(3)P is converted to PI(3,5)P_2 during lysosomal maturation, resulting in cargo degradation.

Sorting for Rab11-Dependent Recycling

Rab11-dependent recycling relies on delivery of endocytic cargoes to the Rab11$^+$ peri-nuclear endocytic recycling compartment, from where they are re-delivered to the plasma membrane (Ullrich et al., 1996; Redpath et al., 2019). The exact mechanism of cargo sorting before and into the Rab11$^+$ recycling endosome is not clearly established or understood in the literature compared to the relatively well-described retromer/retriever-dependent recycling pathway. However, recent studies have begun to reveal a clearer picture. Cargoes destined for Rab11$^+$-dependent recycling can be internalized *via* clathrin-dependent or independent pathways (Ullrich et al., 1996; Compeer et al., 2018). Transferrin and EGF, both internalized via clathrin-dependent endocytosis, are found segregated in the plasma membrane then trafficked via a Rab11 or Rab7-dependent pathways, respectively. This delineation at level of the plasma membrane is clearly of functional importance highlighted by the subsequent divergent sorting into the Rab11 or Rab7 pathways (**Figure 3A** – right) (Lakadamyali et al., 2006; Leonard et al., 2008). Immediately following endocytosis, cargoes endocytosed by clathrin-dependent or independent modes and destined for Rab11-dependent recycling appear to be committed to this fate (Lakadamyali et al., 2006; Leonard et al., 2008; Redpath et al., 2019), supporting the notion that a distinct plasma membrane environment must exist to facilitate sorting of Rab11-dependent recycling cargo early on.

Membrane heterogeneity is modulated *via* phosphoinositide switching on phosphatidylserine-enriched membranes throughout the endocytic pathway and is therefore critical for cargo progression throughout the Rab11-dependent recycling pathway (**Figures 3A,B,G,H** – right). The exact properties of the plasma membrane domains where Rab11-dependent recycling cargoes reside is not yet clearly defined. There is, however, substantial evidence to formulate a speculative model that is centered around phosphatidylserine-enriched membranes. Rab11-family interacting proteins (Rab11-FIPs) bind distinct phosphatidylserine membranes (Baetz and Goldenring, 2014) and link Rab11 to EHDs, dynein, SNAREs, VPS and SNX proteins to facilitate cargo exit from sorting endosomes and re-delivery to the plasma membrane (Naslavsky et al., 2006; Horgan et al., 2010; Solinger et al., 2020). This indicates that phosphatidylserine-enriched membranes are critical for assembling the protein machinery required for Rab11-dependent recycling. Phosphatidylserine attracts specific cargo binding and is present on the cytosolic leaflet of the plasma membrane and throughout the Rab5 to Rab11 endocytic pathway (**Figure 3A** – right) (Yeung et al., 2008; Hirama et al., 2017). Phosphatidylserine is capable of inducing endocytosis without canonical clathrin-dependent or clathrin-independent endocytic regulators, indicating that phosphatidylserine enriched microdomains in the plasma membrane are themselves primed for endocytosis (Hirama et al., 2017). Phosphatidylserine is maintained strictly on the cytoplasmic face of endosomes throughout the entire Rab11$^+$ endocytic recycling pathway, and this enrichment is an absolute requirement for cargo recycling to occur (**Figures 3A,B,G,H**) (Chen et al., 2010; Fairn et al., 2011; Uchida et al., 2011; Lee et al., 2015; Tanaka et al., 2016). Transferrin is processed through the Rab11-dependent recycling route. It co-localizes with phosphatidylserine from the earliest stages of endocytosis, in contrast to EGF which traffics via the Rab5 to Rab7 degradative/recycling pathway and is found only transiently in a subset of phosphatidylserine enriched endosomes (**Figure 3A** – right) (Tanaka et al., 2016). Cargo persistence in phosphatidylserine enriched endosomes could be required from the initiation of endocytosis to ensure sorting into Rab11-positive recycling endosomes. This illustrates that segregation of cargo into phosphatidylserine-enriched membrane domains at the level of the plasma membrane facilitates later sorting into the Rab11-dependent recycling pathway.

Immediately following endocytosis, membrane heterogeneity continues to play a role in determining sorting of cargoes for Rab11-dependent recycling. Tightly regulated dephosphorylation of phosphoinositides in time and space is a critical requirement for Rab11-dependent recycling cargoes. Following clathrin-dependent or -independent endocytosis, the 5-phosphatase ORCL and 4-phosphatase Sac2 are recruited to newly formed endosomes, which sequentially metabolize residual PI(4,5)P_2 from endocytic pit formation to PI(4)P and then PI (**Figure 3B** – right) (Nakatsu et al., 2015). Generation of PI(4)P by Sac2 is required for subsequent sorting of transferrin out of the Rab5$^+$ endosome. By contrast, EGF does not require Sac2 to exit Rab5$^+$ sorting endosomes (Hsu et al., 2015), indicating that heterogeneous generation of PI within the Rab5$^+$ sorting endosome is crucial for cargo discrimination. It has not yet been determined if residual PI(3,4)P_2 from the endocytic pit is metabolized to PI(3)P or PI in endosomes destined for Rab11 recycling.

Cargoes that are sorted from Rab5 to Rab7 stably associate with EEA1$^+$ and Rab5$^+$ endosomes rapidly following endocytosis, while the EEA1$^+$ intermediate is dispensable for transferrin sorting (Leonard et al., 2008; Navaroli et al., 2012). Compared to the Rab5-to-Rab7 cargoes, cargo destined for Rab11-dependent recycling associates only transiently with the Rab5$^+$ sorting endosome (Lakadamyali et al., 2006; Leonard et al., 2008; Redpath et al., 2019). Strikingly, despite this transient association, cargoes eventually sorted to both Rab11$^+$ and Rab7$^+$ compartments can be present within the same Rab5$^+$ endosome (**Figures 3D,G**) (Franke et al., 2019), highlighting incredible heterogeneity in membrane domains within a relatively small intracellular organelle. In contrast to the Rab5 to Rab7 sorting domain, in which PI(3)P generated by VPS34 biogenesis of the Rab5$^+$ endosome facilitates recruitment of Rab7 (Shin et al., 2005), inactive Rab11 is already present on peripheral Rab5$^+$ endosomes and is activated by local generation and enrichment of PI(3)P by PI3K-C2α (**Figure 3G** – left)

(Franco et al., 2014; Campa et al., 2018). Once activated by local PI(3)P enrichment, recruitment of the SNAREs, EHD1, sorting nexins and VPS proteins of the FERARI complex to Rab11 facilitates removal of cargoes from the Rab5$^+$ endosome for subsequent recycling (**Figures 3G,H**) (Campa et al., 2018; Solinger et al., 2020).

There is strong evidence highlighting the need for membrane heterogeneity within the Rab11$^+$ recycling network for cargo progression along the endocytic recycling axis. Activation of Rab11 recruits the phosphatidylinositol 3-phosphatase MTM1 to PI(3)P enriched domains, where it converts PI(3)P to unphosphorylated phosphoinositide (PI), which leads to the rapid dissociation of Rab11$^+$ vesicles from the Rab5$^+$ endosome (**Figure 3G** – right) (Ketel et al., 2016; Campa et al., 2018). PI(3)P enrichment is critical to vesiculation and removal of the Rab11$^+$ domain from the Rab5$^+$ compartment (Campa et al., 2018). PI(3)P further promotes the association of Rab5$^+$ endosomes with fission factors and the microtubule motor dynein – through interactions with the BAR-domain containing protein SNX4 and/or SNX1 and Rebenosyn-5. Rab-FIP5 is central for the interaction of Rab11 with these fission factors, indicating phosphatidylserine enrichment is still required within endosomal membrane to facilitate the Rab5-to-Rab11 sorting events (Baetz and Goldenring, 2014; Campa et al., 2018; Solinger et al., 2020). Dynein provides the force for vesicle fission and delivers the newly formed vesicle to the endocytic recycling compartment (Traer et al., 2007; Horgan et al., 2010). The newly formed vesicular PI is then phosphorylated to PI(4)P by PI4Kα, which leads to delivery of the vesicle to the perinuclear endocytic recycling compartment and to the recruitment of the exocyst machinery required for cargo re-delivery to the plasma membrane (**Figure 3H**) (Ketel et al., 2016). Interestingly, recycling cargoes internalized by both clathrin-dependent and -independent modes ultimately traffic to the endocytic recycling compartment, yet remain segregated within this compartment (Xie et al., 2016), indicating that within the Rab11$^+$ recycling network heterogeneity membrane domains may be required for cargo segregation.

Amongst the rapidly changing and tightly regulated environment of membrane phosphoinositides on Rab11$^+$ endosomes, phosphatidylserine remains enriched and precisely oriented on the cytoplasmic face of recycling cargo membrane domains. Phosphatidylserine is present in the Rab5$^+$ sorting endosome, Rab11$^+$ vesicles and the Rab11$^+$ endocytic recycling compartment (**Figure 3**) (Chen et al., 2010; Baetz and Goldenring, 2014; Lee et al., 2015). Disruption of multiple confirmed or suspected phosphatidylserine flippases or translocases abolishes recycling and leads to accumulation of cargoes in EEA1/Rab5$^+$ early/sorting endosomes, in Rab11$^+$ vesicles and in endocytic recycling compartments (Chen et al., 2010; Lee et al., 2015; Tanaka et al., 2016). Furthermore, cytoplasmic orientation of phosphatidylserine is required for recruitment of the membrane deforming protein EHD1 to the endocytic recycling compartment, where it induces membrane tubulation to allow cargo exit for recycling (Lee et al., 2015; Deo et al., 2018).

Rab11-dependent recycling membrane domains are enriched in the membrane domain organizing proteins: flotillin-1 and flotillin-2 (flotillins hereafter), which regulate the recycling of a wide range of cargoes (Solis et al., 2013; Hülsbusch et al., 2015; Bodrikov et al., 2017; Compeer et al., 2018). Flotillins define cholesterol-rich membrane domains throughout the plasma membrane and endocytic recycling network and require the presence of phosphatidylserine for localization to these domains (Maekawa and Fairn, 2015). Flotillins interact with SNX4 and Rab11 along membrane tubules and within the endocytic recycling compartment, and are required for the sorting of transferrin and the T-cell receptor into Rab11$^+$ endosomes (Solis et al., 2013; Redpath et al., 2019). New data from our group has demonstrated that flotillins interact extremely rapidly with Rab5$^+$ endosomes and then accumulate in Rab11$^+$ endosomes (Redpath et al., 2019). Taken together, we have proposed that flotillins-based domains act as entry doors into the Rab5$^+$-Rab11$^+$ recycling endosomal network. These domains are maintained on Rab5$^+$ endosomes and are unique from the surrounding Rab5$^+$ endosomal membrane. Eventually, they could then facilitate interaction with the FERARI complex of sorting nexins, rabenosyn-5, EHD1, SNAREs, and VPS proteins, dynein and Rab11 to ensure efficient cargo sorting to the recycling endosomal compartment (**Figures 3B,G,H**).

Sorting for Rab11-dependent recycling is clearly critically dependent on membrane heterogeneity. Phosphoinositides are rapidly catabolised, enriched and converted to ensure recruitment of the requisite sorting factors at the correct time; phosphatidylserine is maintained in a strict cytoplasmic orientation throughout this rapidly changing phosphoinositide environment to regulate cargo endocytosis, delivery to and recycling from the Rab11$^+$ endocytic recycling compartment. Finally, membrane-organizing proteins may act to maintain microdomains throughout the Rab11$^+$ recycling network to ensure cargo is efficiently sorted throughout this entire process.

Key points:

- Phosphatidylserine is enriched throughout the Rab11$^+$ endocytic recycling pathway.
- Residual plasma membrane PI(4,5)P is metabolized to PI prior to Rab11 recycling cargo entry into the Rab5$^+$ sorting endosome.
- A localized enrichment of PI(3)P in the Rab5$^+$ sorting endosome activates Rab11.
- The Rab11$^+$ vesicle detaches from the Rab5$^+$ sorting endosome, enriches in PI(4)P and traffics to the endocytic recycling compartment.
- PI(4)P in the endocytic recycling compartment recruits the exocyst complex for re-delivery of recycling vesicles to the plasma membrane.
- Phosphatidylserine in the endocytic recycling compartment recruits EDH1, which induces vesicle scission from Rab11$^+$ endocytic recycling compartment.
- PI(4)P, phosphatidylserine enriched vesicles can then be re-delivered to the plasma membrane.
- Flotillins may maintain phosphatidylserine-enriched microdomains from the plasma membrane and

throughout the endocytic recycling network, facilitating cargo recycling.

Sorting to the APPL Endosome – A Special Case for Signaling

The APPL$^+$ endosome represents a specialized pre-Rab5 endosomal compartment with a unique membrane composition highly enriched in PI that supports continued signaling from receptors internalized by either clathrin-dependent or -independent endocytosis (Lee et al., 2011; Kalaidzidis et al., 2015; Masters et al., 2017; Sposini et al., 2017; Lakoduk et al., 2019). The transition from the endocytic pit to APPL$^+$ endosomes is driven by the conversion of PI(4,5)P_2 to PI by OCRL and INPP5B. Under specific signaling conditions, the 3-phosphatase MTMR2 specifically associates with APPL and, in conjunction with OCRL, can also generate further PI from PI(3,4)P_2 (Erdmann et al., 2007; Franklin et al., 2013). The APPL$^+$ endosome is initially completely devoid of PI(3)P. The substitution of APPL for Rab5 is promoted by acquisition of PI(3)P (Zoncu et al., 2009; Kalaidzidis et al., 2015). Receptors entering the APPL endosome can either be rapidly recycled to the plasma membrane following signaling, or proceed to the Rab5$^+$ sorting endosome (Kalaidzidis et al., 2015; Sposini et al., 2017). Crucially, receptors that typically traffic through alternate pathways, such as the EGF receptor, are re-routed to transit the APPL endosome when additional signaling or rapid recycling is required (Lakoduk et al., 2019). The APPL$^+$ endosome therefore represents a separate endosomal population to those of cargoes directly entering the Rab5 to Rab7 or Rab11 trafficking pathways with a unique membrane composition that supports further receptor signaling following endocytosis.

Membrane Heterogeneity Regulates Targeted Trafficking in Polarized Cells

Membrane heterogeneity also controls sorting along specialized endocytic pathways utilized in cell types with distinct polarized apical and basolateral membranes such as hepatocytes, pancreatic cells and kidney epithelia, and in neurons.

Apical and basolateral membranes in polarized cells both contain PI(4,5)P_2 (Szalinski et al., 2013), while distribution of other phosphoinositides is polarized. PI(3,4)P_2 is enriched in apical membranes, and PI(3,4)P_2 is enriched in basolateral membranes (Román-Fernández et al., 2018). Endocytosis is distinct in apical and basolateral membranes in polarized renal epithelia and hepatocytes (Tuma et al., 1999; Szalinski et al., 2013), with cargoes remaining distinctly separated following internalization, even if targeting the same endocytic compartment (Cerneus and Van Der Ende, 1991). As enrichment in PI(3,4)P_2 facilitates fast endophilin mediated endocytosis (Boucrot et al., 2015; Chan Wah Hak et al., 2018) and PI(3,4,5)P_3 and PI(4,5)P_2 facilitates CLIC/GEEC endocytosis (Suetsugu et al., 2006; Lundmark et al., 2008), we speculate that differences in phosphoinositide content in polarized membranes may facilitate different modes of endocytosis. Following endocytosis, rapid segregation of Rab7-targetted and Rab11-targetted recycling cargoes into EEA1-positive or negative endosomes occurs as in non-polarized cells (Leung et al., 2000).

Similarly, sorting in polarized cells also involves maintenance of specific phosphoinositides on endocytic membrane. Inhibition of PI(3)P synthesis in hepatocytes leads to accumulation of apical plasma membrane proteins into large vacuolar structures following endocytosis (Tuma et al., 1999). At the level of recycling endosomes, Rab11$^+$ compartments receive cargoes both directly from apical and basolateral endocytosis (Thompson et al., 2007). The role of membrane heterogeneity in regulating the passage of cargoes through Rab11$^+$ endosomes in polarized cells is again similar to what we have described for non-polarized cells. Rab11$^+$ endosomes contain PI(4)P and phosphatidylserine in kidney epithelia but little PI(3)P (Gagescu et al., 2000; Román-Fernández et al., 2018) and PI(3)P is required for cargo entry into Rab11$^+$ transcytosis pathways (Hansen et al., 1995). Transcytosis from the Rab11$^+$ recycling endosomal compartment involves the phosphatidylserine binding Rab11-FIP5 protein (Su et al., 2010). Finally, delivery of recycling vesicles to polarized membranes requires PI(4)P enrichment on vesicular membranes, analogous to non-polarized cells (Nguyen et al., 2019).

Neurons use a specialized form of endocytosis called "activity-dependent bulk endocytosis" for rapid retrieval and recycling of synaptic membrane during sustained neurotransmission (Watanabe and Boucrot, 2017). Activity-dependent bulk endocytosis is initiated on PI(4,5)P_2-enriched membranes, similar to clathrin-dependent endocytosis, but utilizing the BAR-domain containing proteins syndapin and endophilin (Clayton and Cousin, 2009). However, it likely that membrane heterogeneity involving phosphoinositide species contribute to provide specificity to this mode of endocytosis.

Following internalization of cargoes, neuronal trafficking and sorting mirrors that of non-polarized cells indicating that membrane heterogeneity has a similar important regulatory role in neuronal sorting. PI(3)P is required for cargo sorting through Rab5$^+$ to Rab7$^+$ endosomes and the lysosome (Morel et al., 2013). Loss of WDR91, a protein required for neuronal development, results in accumulation of PI(3)P on endosomes and defective trafficking of cargoes into Rab7$^+$ endosomes and lysosomes (Liu et al., 2017). Retromer is recruited to Rab7$^+$ endosomes in neurons analogous to non-polarized cells, utilizing the PI(3)P binding VPS29 and is required for regeneration of synaptic vesicles (Singla et al., 2019; Ye et al., 2020). Rab11$^+$ endosomes regulates recycling from activity-dependent bulk endosomes (Kokotos et al., 2018) and are highly enriched in phosphatidylserine (Calderon and Kim, 2008), indicating that the distinct membrane domains that segregate Rab11-dependent recycling cargoes from Rab5-to-Rab7 cargoes are similar between neuronal and non-polarized cells.

INTEGRATION OF ENDOCYTOSIS INTO ENDOSOMAL SUBPOPULATIONS FOR CARGO SORTING

The multiple modes of endocytosis that exist in the cell ultimately result in cargoes being integrated into degradative or recycling pathways (**Figures 2**, **3**). As discussed above, we speculate that this cargo fate decision is made prior to cargo entry into the

endosomal subpopulations that make up the endocytic sorting pathways. The EGF receptor (EGFR), LDL receptor (LDLR) and G-coupled protein receptors (GPCRs) provide broad examples of how the fate of endocytic cargoes fate is determined prior to or during endocytosis and how this eventually conditions the endosomal subpopulation the cargo enters. Interestingly, this cargo fate decision integrates binding of accessory proteins such as ligands or circulating proteins to the receptor cargo with membrane heterogeneity.

EGFR endocytosis is incredibly complex and is therefore still relatively uncharacterized despite decades of intense research. EGFR is recycled to the plasma membrane or degraded in the lysosome dependent on the concentration of EGF present. At low to medium EGF concentrations, EGFR is internalized by clathrin-dependent endocytosis into multiple potential endosomal subpopulations: $AAPL^+$ endosomes for continued signaling and subsequent recycling, autophagosomes for recycling and $EEA1^+$ endosomes for degradation (Leonard et al., 2008; Flores-Rodriguez et al., 2015; Fraser et al., 2019; Lakoduk et al., 2019). At high EGF concentrations or inhibition of clathrin, EGF is taken up independently of clathrin *via* macropinocytosis and delivered to the lysosome for degradation, ensuring signaling is terminated (Ménard et al., 2018). It is important to note that while integration of EGFR into these endosomal subpopulations is broadly EGF concentration dependent, these pathways are unlikely to be mutually exclusive.

Membrane heterogeneity is central to the pathway directing EGFR fate. EGFR can be internalized into the cell *via* clathrin pits of differing compositions, inducing recycling or degradation. In clathrin pits containing AP2, EGFR is recycled whereas in the absence of AP2 it is degraded (Pascolutti et al., 2019). Membrane heterogeneity further regulates clustering of EGFR, which in turn results in differing endocytic sorting fates. At low EGF concentrations, the receptor is in small to non-existent clusters, while at high concentrations the receptor exists in large clusters (Bag et al., 2015). Plasma membrane cholesterol is central to EGF receptor cluster size, and potentially the recruitment of Eps15 to the clathrin coated pits required for EGF receptor recycling (Bag et al., 2015). Phosphatidylserine is responsible for maintaining cholesterol in the cytosolic leaflet of the plasma membrane (Maekawa and Fairn, 2015), and Eps15 and its binding partners involved in interaction with AP2, SGIP1α, and FCHO1 all interact with both phosphatidylserine and $PI(4,5)P_2$ (Uezu et al., 2007; Hollopeter et al., 2014; Wang et al., 2016). Thus, small EGFR clusters at low EGF concentrations are present in phosphatidylserine enriched regions of the plasma membrane that are primed for delivery to the $Rab11^+$ recycling compartment. Macropinocytosis has its own unique phosphoinositide membrane composition (Egami et al., 2014; Maekawa et al., 2014). EGF stimulates the conversion of $PI(4,5)P_2$ to $PI(3,4,5)P_3$ (Araki et al., 2007) following which $PI(3,4,5)P_3$ is sequentially metabolized to $PI(3,4)P_2$, PI(3)P and then PI, with each intermediate phosphoinositide recruiting effectors required for the macropinocytic process (Maekawa et al., 2014). Following uptake by macropinocytosis, EGFR is delivered to the lysosome for degradation (Ménard et al., 2018). Membrane heterogeneity therefore is responsible for delivery of EGFR into the endosomal subpopulations required for its recycling or degradation.

LDLR is exclusively internalized by clathrin-dependent endocytosis in non-atherogenic conditions, following which it can be degraded in the lysosome or recycled via the CCC complex (Bartuzi et al., 2016). In contrast to EGFR, LDLR fate is determined primarily by binding of the circulating protein PCSK9 prior to endocytosis. If present in circulation, PCSK9 binds LDLR at the plasma membrane before it is internalized *via* clathrin mediated endocytosis. When bound to PCSK9, LDLR is cleaved by proteases in the cytoplasmic domain (Tveten et al., 2013), which prevents its recovery from $Rab7^+$ endosomes by the CCC complex for recycling (Bartuzi et al., 2016; Fedoseienko et al., 2018). Therefore, internalized LDLR likely enters a relatively homogenous subpopulation of endosomes, which is determined by PCSK9 binding at the plasma membrane.

GPCRs are well characterized as undergoing clathrin-dependent endocytosis, following which endosomal signaling occurs and the receptors are recycled to the plasma membrane. Interestingly, while the β2-adrenergic receptor (β2AR) and luteinising hormone receptor (LHR) are both internalized by β-arrestin containing clathrin pits, they immediately enter distinct endosomal subpopulations with different recycling rates (Jean-Alphonse et al., 2014; Sposini et al., 2017). β2AR enters $APPL^-$ endosomes, from where relatively slower Rab11-dependent recycling occurs (Puthenveedu et al., 2010; Sposini et al., 2017). By contrast, LHR enters $APPL1^+$ endosomes immediately following endocytosis from where rapid return to the plasma membrane occurs (Jean-Alphonse et al., 2014; Sposini et al., 2017). Crucially, signal sequences in the cytoplasmic tails of the receptors dictate the divergent transit of β2AR and LHR into $APPL1^+$ compartments (Jean-Alphonse et al., 2014). Interestingly, β2AR resides on two distinct membrane domains on vesicles depending on its state of phosphorylation. Non-phosphorylated β2AR resides in "bulk recycling" membrane domains (Vistein and Puthenveedu, 2013; Bowman et al., 2016), from where actin-dependent, Rab11-dependant recycling to the plasma membrane can occur (Puthenveedu et al., 2010). Phosphorylated β2AR recruits the retromer sorting-nexin SNX1 (Bowman et al., 2016) and SNX27 on $EEA1^+$ endosomes (Temkin et al., 2011), prior to the typical retromer interaction on $Rab7^+$ endosomes. Together, these results indicate that in special cases cargoes themselves may modify endosome membrane heterogeneity within a single endosomal subpopulation, enabling modulation of cargo recycling rates in specific circumstances to tune cellular signaling outcomes.

A UNIFYING MODEL FOR MEMBRANE HETEROGENEITY REGULATING CARGO SORTING

The above evidence leads us to present a model for endosomal cargo sorting in which membrane heterogeneity plays a central regulatory role. Decisions on the fate of cargoes are made at the level of endocytic pit formation or rapidly following endocytosis. Cargoes traffic to specific pre-Rab5 endosomes with

distinct membrane compositions: (a) EEA1$^+$ endosomes highly enriched in PI(3)P for trafficking to the Rab7$^+$ late endosome, (b) recycling Rab11$^+$ endosomes with high phosphoinositide and phosphatidylserine content and (c) APPL$^+$ endosomes highly enriched in PI for sustained endosomal signaling. Local membrane composition within each of these compartments immediately following endocytosis plays a central role in recruiting the membrane tubulating proteins, phosphatases, kinases and Rab proteins required to orientate and maintain cargoes in their respective trafficking pathways.

In this model, cargoes destined for the late endosomal pathway enter PI(3)P-enriched, EEA1$^+$ endosomes (**Figure 4A**). EEA1$^+$ recruits Rab5, generating further PI(3)P. This enriched PI(3)P inactivates Rab5 and recruits Rab7. The cargo can now recycle via retromer/retriever/CCC *trans*-Golgi recycling or be degraded in the lysosome. Rab11-dependent recycling cargoes enter the cell into phosphoinositide and phosphatidylserine-enriched endosomes (**Figure 4C**). These endosomes destined for Rab11 recycling fuse with the Rab5$^+$ sorting endosome, where highly spatially restricted generation of PI(3)P occurs, which is then responsible for recruiting Rab11 and sending cargo to the endocytic recycling compartment. Crucially, phosphatidylserine is maintained throughout this cycle. Cargoes that require further signaling following endocytosis are internalized into PI-enriched APPL$^+$ endosomes (**Figure 4B**). The phosphoinositide enrichment prevents recruitment of Rab5, generating a stable platform from which endosomal signaling can occur. Following signaling from APPL$^+$ endosomes, subdomains of the endosome

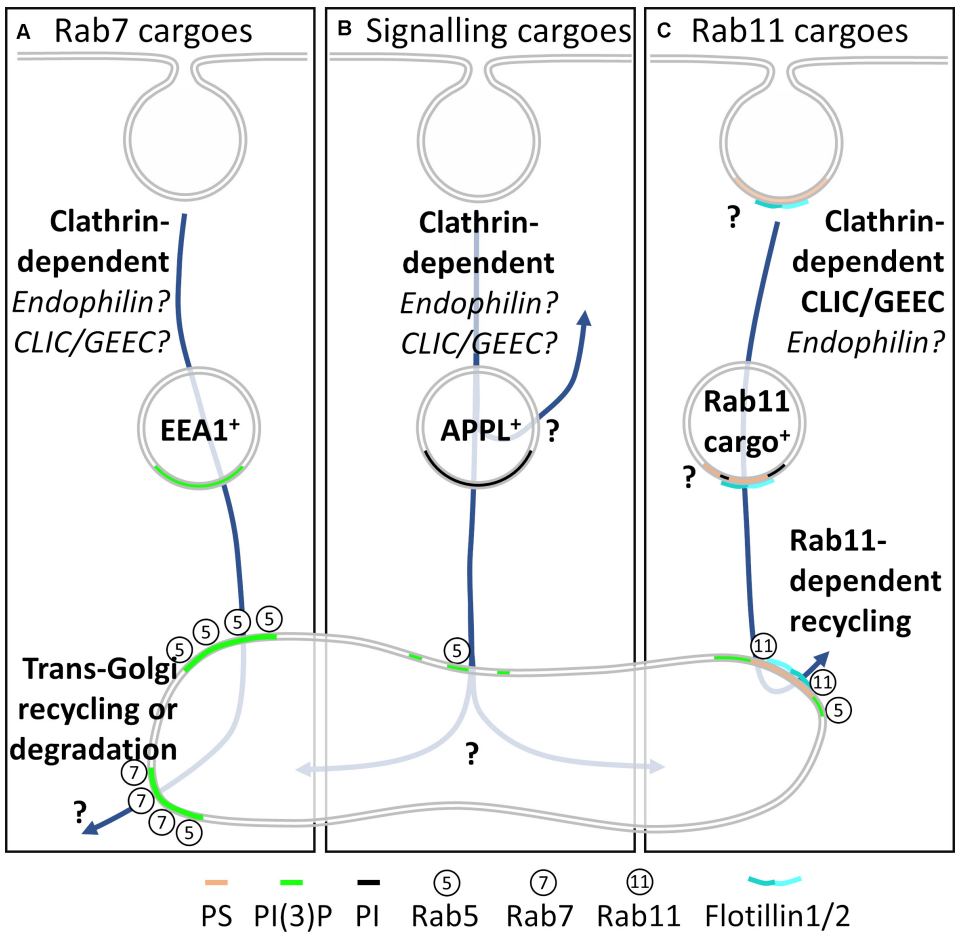

FIGURE 4 | Our model for membrane heterogeneity in endocytic sorting. **(A)** Cargoes destined for *trans*-Golgi recycling or lysosomal degradation enter the cells via clathrin-dependent endocytosis-although fast endophilin-mediated endocytosis and CLIC/GEEC endocytosis may play a role. Endocytic vesicles containing these cargoes acquired EEA1 and are enriched in PI(3)P prior to fusion with the Rab5$^+$ sorting endosome. The microdomains containing these cargoes then mature to Rab7$^+$ endosomes, from where *trans*-Golgi recycling or degradation can occur. **(B)** Cargoes (receptors) from which signaling is still required following endocytosis are internalized into APPL$^+$ endocytic compartments that are enriched in phosphoinositide. Again, fast endophilin-mediated endocytosis and CLIC/GEEC endocytosis may also play roles in cargo delivery. Following signaling from APPL$^+$ compartments, cargoes integrate with the Rab5$^+$ sorting endosome, from where their fate is not well documented. **(C)** Cargoes destined for Rab11-dependent recycling are internalized from phosphatidylserine-enriched regions of the plasma membrane by both clathrin-dependent endocytosis and CLIC/GEEC endocytosis. Fast endophilin-mediated endocytosis may also play a role, and the range of phosphoinositide compositions of this compartment are not yet established. The flotillin membrane organizing protein family organizes the membrane domains on these phosphatidylserine-enriched endosomes, ensuring segregation throughout the sorting pathway.

can acquire Rab5 for cargo entry into the Rab5$^+$ sorting endosome or be recycled directly to the plasma membrane.

For each of these endosomes, the membrane composition immediately following endocytosis controls all further downstream acquisition of proteins and membrane constituents that ultimately control the fate of a cargo. Cargo fate decisions are therefore made at the earliest stages of endocytosis, with membrane heterogeneity enforcing this decision.

REMAINING QUESTIONS AND CONCLUSION

Membrane heterogeneity is a central regulator of cargo endocytosis and sorting. At the center of each mode of endocytosis, a specific membrane environment ensures that endocytosis occurs at a specific time and place within the cell. Immediately following endocytosis, cargoes are segregated into endosomes with specific membrane compositions that dictate whether they ultimately sort into Rab7$^+$ endosomes for recycling or degradation, or Rab11$^+$ endosomes for recycling.

While it is clear membrane heterogeneity is a crucial regulator at each step of the endocytosis and sorting process, questions remain (**Figure 4**). How can heterogenous membrane domains in the same endocytic mode sort for different fates at the level of the plasma membrane? What fates can cargoes endocytosed by clathrin-independent pathways be sorted into, and how does membrane heterogeneity contribute to this? What other membrane lipid species are involved in regulating the endocytic sorting process? Given the nuanced differences in endocytic sorting between polarized and non-polarized cells, do membrane lipids play the same role in polarized trafficking? Do specialized endocytic pathways such as activity-dependent bulk endocytosis and transcytosis segregate cargo utilizing similar lipid microdomains or do specialized domains exist for delivery to specific polarized membranes?

Investigation of the lipid species contributing to membrane heterogeneity have typically relied on biochemical or pharmacological approaches [e.g., cholesterol depletion by methyl-β-cyclodextrin (Chadda et al., 2007), PI(3) kinase inhibition (Boucrot et al., 2015)]; genetic approaches [e.g., PIK3C2α knockout (Franco et al., 2014)]; fixed and live cell imaging studies using fluorescent lipid markers (Ketel et al., 2016) and constitutively active/dominant negative Rab proteins (Liu et al., 2017). While these have provided incredibly useful information on the role of membrane heterogeneity in cellular trafficking, each has limitations. Biochemical and pharmacological approaches carry inevitable off target effects, which have recently been highlighted with methyl-β-cyclodextrin (Hirama and Fairn, 2018). Knockdowns, knockouts and overexpression of constitutively active/dominant negative proteins all have potential unwanted effects. Because of the relatively long-term nature of the protein disruption, compensatory mechanisms can be activated potentially obscuring the results (El-Brolosy and Stainier, 2017). We believe transient optogenetic manipulation of membrane lipids and proteins offers a specific, minimally disruptive method to overcome the majority of the issues observed with biochemical/pharmacological and knockdown/knockout approaches (detailed below).

Genetically encoded biosensors have greatly enhanced our ability visualize the lipid species contributing to plasma membrane and endosomal membrane heterogeneity (Wills et al., 2018). To fully dissect the roles of membrane heterogeneity in endosomal sorting, the generation of biosensors to further lipids enriched in membrane domains will allow a better understanding of their role in endocytosis and trafficking. Further, developing new lipid biosensors that have differing affinities for the same lipid will allow observation of a wider range of cellular events [excellently detailed in Wills et al. (2018)]. Development of nuanced biosensors able to detect protein activation will also provide further advances, with the recent Rab11 biosensor (Campa et al., 2018) providing interesting insights into the role of PI(3)P in the Rab11 recycling pathway.

Advances in light and electron microscopy techniques coupled with lipid biosensors will provide the next leap in understanding of how membrane heterogeneity controls endocytic processes. Optogenetic metabolisers that couple a phosphoinositide phosphatase or kinase to plasma membrane anchors have proven to be extremely effective tools for dissecting functions of various phosphoinositides (Idevall-Hagren et al., 2012; Kakumoto and Nakata, 2013). Further iterations of optogenetic systems have coupled a specific optogenetic metaboliser to a specific subcellular compartment, allowing precise dissection of how a membrane species functions on a single endosomal population, as has been recently performed to investigate the role of PI(4)P on Rab3$^+$ vesicles (Nguyen et al., 2019). Extension of current optogenetic lipid metabolisers to control of other phosphoinositides and membrane species such as cholesterol and phosphatidylserine will allow us to determine precisely their roles in endocytosis and sorting.

Live total internal fluorescence microscopy (TIRF) has provided striking advances of our knowledge of the function plasma membrane lipid species (Ketel et al., 2016). Advances in live cell imaging methodologies beyond TIRF will further advance our understanding of membrane heterogeneity in intracellular populations. We have recently generated methods utilizing single- and two-photon photoactivation of fluorescent proteins to elucidate every step of the T cell receptor endocytic sorting process (Compeer et al., 2018; Redpath et al., 2019). Further, we coupled cargo photoactivation to optogenetic inhibition of Rab proteins (Redpath et al., 2019). Photoactivation of cargo proteins coupled with lipid biosensors, photoactivation of lipid biosensors themselves and coupling of cargo photoactivation with optogenetic activation or inhibition of lipid species, followed by tracking throughout their endocytic routes will undoubtedly advance our knowledge on their role in endocytic sorting.

Finally, this review has focussed on a subset of endocytic processes and endosomal pathways. Each endocytic pathway will have its own unique composition of membrane domains that regulates function, as is the case for clathrin-dependent endocytosis, fast endophilin-mediated endocytosis and CLIC/GEEC endocytosis, and other pathways such as macropinocytosis (Kerr and Teasdale, 2009). Similarly, other endosomal sorting pathways such as polarized apical

and basolateral recycling pathways, transcytosis and synaptic vesicle recycling will have their own endosomal membrane heterogeneity that regulates cargo fate. Further investigation and characterization of the membrane compositions of these endocytic pathways will greatly further our understanding of how cargo trafficking is controlled in the cell.

AUTHOR CONTRIBUTIONS

GR and JR conceived of and wrote the manuscript. GR, VB, PR, and JR prepared the figures. VB and PR provided critical editing and input. All authors contributed to the article and approved the submitted version.

FUNDING

This work was funded in part by grants from the Swiss National Science Foundation (JR-SNSF 31003A_172969), the Thurgauische Stiftung für Wissenschaft und Forschung (JR), the State Secretariat for Education, Research and Innovation, the Deutsche Forschungsgemeinschaft (JR- RO 6238/1-1), and The Royal Society of New Zealand Marsden Fund (GR- UOO1704).

ACKNOWLEDGMENTS

We would like to thank Dr. Nikita Deo for her editing and thoughtful discussions.

REFERENCES

Araki, N., Egami, Y., Watanabe, Y., and Hatae, T. (2007). Phosphoinositide metabolism during membrane ruffling and macropinosome formation in EGF-stimulated A431 cells. *Exp. Cell Res.* 313, 1496–1507. doi: 10.1016/j.yexcr.2007.02.012

Baetz, N. W., and Goldenring, J. R. (2014). Distinct patterns of phosphatidylserine localization within the Rab11a-containing recycling system. *Cell. Logist.* 4:e28680. doi: 10.4161/cl.28680

Bag, N., Huang, S., and Wohland, T. (2015). Plasma membrane organization of epidermal growth factor receptor in resting and ligand-bound states. *Biophys. J.* 109, 1925–1936. doi: 10.1016/j.bpj.2015.09.007

Bartuzi, P., Billadeau, D. D., Favier, R., Rong, S., Dekker, D., Fedoseienko, A., et al. (2016). CCC- and WASH-mediated endosomal sorting of LDLR is required for normal clearance of circulating LDL. *Nat. Commun.* 7:10961. doi: 10.1038/ncomms10961

Bissig, C., Hurbain, I., Raposo, G., and van Niel, G. (2017). PIKfyve activity regulates reformation of terminal storage lysosomes from endolysosomes. *Traffic* 18, 747–757. doi: 10.1111/tra.12525

Bodrikov, V., Pauschert, A., Kochlamazashvili, G., and Stuermer, C. A. O. (2017). Reggie-1 and reggie-2 (flotillins) participate in Rab11a-dependent cargo trafficking, spine synapse formation and LTP-related AMPA receptor (GluA1) surface exposure in mouse hippocampal neurons. *Exp. Neurol.* 289, 31–45. doi: 10.1016/j.expneurol.2016.12.007

Boettcher, J. M., Davis-Harrison, R. L., Clay, M. C., Nieuwkoop, A. J., Ohkubo, Y. Z., Tajkhorshid, E., et al. (2011). Atomic view of calcium-induced clustering of phosphatidylserine in mixed lipid bilayers. *Biochemistry* 50, 2264–2273. doi: 10.1021/bi1013694

Boucrot, E., Ferreira, A. P. A., Almeida-Souza, L., Debard, S., Vallis, Y., Howard, G., et al. (2015). Endophilin marks and controls a clathrin-independent endocytic pathway. *Nature* 517, 460–465. doi: 10.1038/nature14067

Bowman, S. L., Shiwarski, D. J., and Puthenveedu, M. A. (2016). Distinct G protein-coupled receptor recycling pathways allow spatial control of downstream G protein signaling. *J. Cell Biol.* 214, 797–806. doi: 10.1083/jcb.201512068

Burd, C., and Cullen, P. J. (2014). Retromer: a master conductor of endosome sorting. *Cold Spring Harb. Perspect. Biol.* 6:a016774. doi: 10.1101/cshperspect.a016774

Calderon, F., and Kim, H. Y. (2008). Detection of intracellular phosphatidylserine in living cells. *J. Neurochem.* 104, 1271–1279. doi: 10.1111/j.1471-4159.2007.05079.x

Campa, C. C., Margaria, J. P., Derle, A., Del Giudice, M., De Santis, M. C., Gozzelino, L., et al. (2018). Rab11 activity and PtdIns(3)P turnover removes recycling cargo from endosomes. *Nat. Chem. Biol.* 14, 801–810. doi: 10.1038/s41589-018-0086-4

Cao, C., Laporte, J., Backer, J. M., Wandinger-Ness, A., and Stein, M. P. (2007). Myotubularin lipid phosphatase binds the hVPS15/hVPS34 lipid kinase complex on endosomes. *Traffic* 8, 1052–1067. doi: 10.1111/j.1600-0854.2007.00586.x

Cerneus, D. P., and Van Der Ende, A. (1991). Apical and basolateral transferrin receptors in polarized BeWo cells recycle through separate endosomes. *J. Cell Biol.* 114, 1149–1158. doi: 10.1083/jcb.114.6.1149

Chadda, R., Howes, M. T., Plowman, S. J., Hancock, J. F., Parton, R. G., and Mayor, S. (2007). Cholesterol-sensitive Cdc42 activation regulates actin polymerization for endocytosis via the GEEC pathway. *Traffic* 8, 702–717. doi: 10.1111/j.1600-0854.2007.00565.x

Chan Wah Hak, L., Khan, S., Di Meglio, I., Law, A.-L., Lucken-Ardjomande Häsler, S., Quintaneiro, L. M., et al. (2018). FBP17 and CIP4 recruit SHIP2 and lamellipodin to prime the plasma membrane for fast endophilin-mediated endocytosis. *Nat. Cell Biol.* 20, 1023–1031. doi: 10.1038/s41556-018-0146-8

Chandra, M., Chin, Y. K. Y., Mas, C., Feathers, J. R., Paul, B., Datta, S., et al. (2019). Classification of the human phox homology (PX) domains based on their phosphoinositide binding specificities. *Nat. Commun.* 10:1528. doi: 10.1038/s41467-019-09355-y

Chen, B., Jiang, Y., Zeng, S., Yan, J., Li, X., Zhang, Y., et al. (2010). Endocytic sorting and recycling require membrane phosphatidylserine asymmetry maintained by TAT-1/CHAT-1. *PLoS Genet.* 6:e1001235. doi: 10.1371/journal.pgen.1001235

Christoforidis, S., McBride, H. M., Burgoyne, R. D., and Zerial, M. (1999). The Rab5 effector EEA1 is a core component of endosome docking. *Nature* 397, 621–625. doi: 10.1038/17618

Clayton, E. L., and Cousin, M. A. (2009). Quantitative monitoring of activity-dependent bulk endocytosis of synaptic vesicle membrane by fluorescent dextran imaging. *J. Neurosci. Methods* 185, 76–81. doi: 10.1016/j.jneumeth.2009.09.016

Compeer, E. B., Kraus, F., Ecker, M., Redpath, G., Amiezer, M., Rother, N., et al. (2018). A mobile endocytic network connects clathrin-independent receptor endocytosis to recycling and promotes T cell activation. *Nat. Commun.* 9:1597. doi: 10.1038/s41467-018-04088-w

Cremona, O., Di Paolo, G., Wenk, M. R., Lüthi, A., Kim, W. T., Takei, K., et al. (1999). Essential role of phosphoinositide metabolism in synaptic vesicle recycling. *Cell* 99, 179–188. doi: 10.1016/S0092-8674(00)81649-9

Cullen, P. J., and Steinberg, F. (2018). To degrade or not to degrade: mechanisms and significance of endocytic recycling. *Nat. Rev. Mol. Cell Biol.* 19, 679–696. doi: 10.1038/s41580-018-0053-7

Danson, C., Brown, E., Hemmings, O. J., McGough, I. J., Yarwood, S., Heesom, K. J., et al. (2013). SNX15 links clathrin endocytosis to the PtdIns3P early endosome independently of the APPL1 endosome. *J. Cell Sci.* 126, 4885–4899. doi: 10.1242/jcs.125732

Deo, R., Kushwah, M. S., Kamerkar, S. C., Kadam, N. Y., Dar, S., Babu, K., et al. (2018). ATP-dependent membrane remodeling links EHD1 functions to endocytic recycling. *Nat. Commun.* 9:5187. doi: 10.1038/s41467-018-07586-z

Dingjan, I., Linders, P. T. A., Verboogen, D. R. J., Revelo, N. H., Ter Beest, M., and Van Den Bogaart, G. (2018). Endosomal and phagosomal SNAREs. *Physiol. Rev.* 98, 1465–1492. doi: 10.1152/physrev.00037.2017

Doherty, G. J., and Lundmark, R. (2009). GRAF1-dependent endocytosis. *Biochem. Soc. Trans.* 37, 1061–1065. doi: 10.1042/BST0371061

Egami, Y., Taguchi, T., Maekawa, M., Arai, H., and Araki, N. (2014). Small GTPases and phosphoinositides in the regulatory mechanisms of macropinosome formation and maturation: Gtpases and phosphoinositides in macropinocytosis. *Front. Physiol.* 5:374. doi: 10.3389/fphys.2014.00374

El-Brolosy, M. A., and Stainier, D. Y. R. (2017). Genetic compensation: a phenomenon in search of mechanisms. *PLoS Genet.* 13:e1006780. doi: 10.1371/journal.pgen.1006780

Erdmann, K. S., Mao, Y., McCrea, H. J., Zoncu, R., Lee, S., Paradise, S., et al. (2007). A role of the lowe syndrome protein OCRL in early steps of the endocytic pathway. *Dev. Cell* 13, 377–390. doi: 10.1016/j.devcel.2007.08.004

Fairn, G. D., Schieber, N. L., Ariotti, N., Murphy, S., Kuerschner, L., Webb, R. I., et al. (2011). High-resolution mapping reveals topologically distinct cellular pools of phosphatidylserine. *J. Cell Biol.* 194, 257–275. doi: 10.1083/jcb.201012028

Fedoseienko, A., Wijers, M., Wolters, J. C., Dekker, D., Smit, M., Huijkman, N., et al. (2018). The COMMD family regulates plasma LDL levels and attenuates atherosclerosis through stabilizing the CCC complex in endosomal LDLR traffcking. *Circ. Res.* 122, 1648–1660. doi: 10.1161/CIRCRESAHA.117.312004

Ferguson, S., Raimondi, A., Paradise, S., Shen, H., Mesaki, K., Ferguson, A., et al. (2009). Coordinated actions of actin and bar proteins upstream of dynamin at endocytic clathrin-coated pits. *Dev. Cell* 17, 811–822. doi: 10.1016/j.devcel.2009.11.005

Flores-Rodriguez, N., Kenwright, D. A., Chung, P. H., Harrison, A. W., Stefani, F., Waigh, T. A., et al. (2015). ESCRT-0 marks an APPL1-independent transit route for EGFR between the cell surface and the EEA1-positive early endosome. *J. Cell Sci.* 128, 755–767. doi: 10.1242/jcs.161786

Francis, M. K., Holst, M. R., Vidal-Quadras, M., Henriksson, S., Santarella-Mellwig, R., Sandblad, L., et al. (2015). Endocytic membrane turnover at the leading edge is driven by a transient interaction between Cdc42 and GRAF1. *J. Cell Sci.* 128, 4183–4195. doi: 10.1242/jcs.174417

Franco, I., Gulluni, F., Campa, C. C., Costa, C., Margaria, J. P., Ciraolo, E., et al. (2014). PI3K class II α controls spatially restricted endosomal PtdIns3P and Rab11 activation to promote primary cilium function. *Dev. Cell* 28, 647–658. doi: 10.1016/j.devcel.2014.01.022

Franke, C., Repnik, U., Segeletz, S., Brouilly, N., Kalaidzidis, Y., Verbavatz, J. M., et al. (2019). Correlative single-molecule localization microscopy and electron tomography reveals endosome nanoscale domains. *Traffic* 20, 601–617. doi: 10.1111/tra.12671

Franklin, N. E., Bonham, C. A., Xhabija, B., and Vacratsis, P. O. (2013). Differential phosphorylation of the phosphoinositide 3-phosphatase MTMR2 regulates its association with early endosomal subtypes. *J. Cell Sci.* 126, 1333–1344. doi: 10.1242/jcs.113928

Fraser, J., Simpson, J., Fontana, R., Kishi-Itakura, C., Ktistakis, N. T., and Gammoh, N. (2019). Targeting of early endosomes by autophagy facilitates EGFR recycling and signalling. *EMBO Rep.* 20:e47734. doi: 10.15252/embr.201947734

Gagescu, R., Demaurex, N., Parton, R. G., Hunziker, W., Huber, L. A., and Gruenberg, J. (2000). The recycling endosome of Madin-Darby canine kidney cells is a mildly acidic compartment rich in raft components. *Mol. Biol. Cell* 11, 2775–2791. doi: 10.1091/mbc.11.8.2775

Gillooly, D. J., Raiborg, C., and Stenmark, H. (2003). Phosphatidylinositol 3-phosphate is found in microdomains of early endosomes. *Histochem. Cell Biol.* 120, 445–453. doi: 10.1007/s00418-003-0591-7

Gomez, T. S., and Billadeau, D. D. (2009). A FAM21-containing WASH complex regulates retromer-dependent sorting. *Dev. Cell* 17, 699–711. doi: 10.1016/j.devcel.2009.09.009

Guan, R., Han, D., Harrison, S. C., and Kirchhausen, T. (2010). Structure of the PTEN-like region of auxilin, a detector of clathrin-coated vesicle budding. *Structure* 18, 1191–1198. doi: 10.1016/j.str.2010.06.016

Guerra, F., and Bucci, C. (2016). Multiple roles of the small GTPase Rab7. *Cells* 5:34. doi: 10.3390/cells5030034

Hansen, S. H., Olsson, A., and Casanova, J. E. (1995). Wortmannin, an inhibitor of phosphoinositide 3-kinase, inhibits transcytosis in polarized epithelial cells. *J. Biol. Chem.* 270, 28425–28432. doi: 10.1074/jbc.270.47.28425

He, K., Marsland, R., Upadhyayula, S., Song, E., Dang, S., Capraro, B. R., et al. (2017). Dynamics of phosphoinositide conversion in clathrin-mediated endocytic traffic. *Nature* 552, 410–414. doi: 10.1038/nature25146

Hirama, T., and Fairn, G. D. (2018). Induction of spontaneous curvature and endocytosis: unwanted consequences of cholesterol extraction using methyl-β-Cyclodextrin. *Commun. Integr. Biol.* 11, 1–4. doi: 10.1080/19420889.2018.1444306

Hirama, T., Lu, S. M., Kay, J. G., Maekawa, M., Kozlov, M. M., Grinstein, S., et al. (2017). Membrane curvature induced by proximity of anionic phospholipids can initiate endocytosis. *Nat. Commun.* 8:1393. doi: 10.1038/s41467-017-01554-9

Hollopeter, G., Lange, J. J., Zhang, Y., Vu, T. N., Gu, M., Ailion, M., et al. (2014). The membrane-associated proteins FCHo and SGIP are allosteric activators of the AP2 clathrin adaptor complex. *eLife* 3:e03648. doi: 10.7554/eLife.03648

Hong, Z., Yang, Y., Zhang, C., Niu, Y., Li, K., Zhao, X., et al. (2009). The retromer component SNX6 interacts with dynactin p150 Glued and mediates endosome-to-TGN transport. *Cell Res.* 19, 1334–1349. doi: 10.1038/cr.2009.130

Horgan, C. P., Hanscom, S. R., Jolly, R. S., Futter, C. E., and McCaffrey, M. W. (2010). Rab11-FIP3 links the Rab11 GTPase and cytoplasmic dynein to mediate transport to the endosomal-recycling compartment. *J. Cell Sci.* 123, 181–191. doi: 10.1242/jcs.052670

Howes, M. T., Kirkham, M., Riches, J., Cortese, K., Walser, P. J., Simpson, F., et al. (2010). Clathrin-independent carriers form a high capacity endocytic sorting system at the leading edge of migrating cells. *J. Cell Biol.* 190, 675–691. doi: 10.1083/jcb.201002119

Hsu, F. S., Hu, F., and Mao, Y. (2015). Spatiotemporal control of phosphatidylinositol 4-phosphate by Sac2 regulates endocytic recycling. *J. Cell Biol.* 209, 97–110. doi: 10.1083/jcb.201408027

Hülsbusch, N., Solis, G. P., Katanaev, V. L., and Stuermer, C. A. O. (2015). Reggie-1/Flotillin-2 regulates integrin trafficking and focal adhesion turnover via Rab11a. *Eur. J. Cell Biol.* 94, 531–545. doi: 10.1016/j.ejcb.2015.07.003

Humphries, W. H., Szymanski, C. J., and Payne, C. K. (2011). Endo-lysosomal vesicles positive for rab7 and lamp1 are terminal vesicles for the transport of dextran. *PLoS One* 6:e26626. doi: 10.1371/journal.pone.0026626

Idevall-Hagren, O., Dickson, E. J., Hille, B., Toomre, D. K., and De Camilli, P. (2012). Optogenetic control of phosphoinositide metabolism. *Proc. Natl. Acad. Sci. U.S.A.* 109, E2316–E2323. doi: 10.1073/pnas.1211305109

Ikonomov, O. C., Sbrissa, D., Mlak, K., Kanzaki, M., Pessin, J., and Shisheva, A. (2002). Functional dissection of lipid and protein kinase signals of PIKfyve reveals the role of PtdIns 3,5-P2 production for endomembrane integrity. *J. Biol. Chem.* 277, 9206–9211. doi: 10.1074/jbc.M108750200

Ikonomov, O. C., Sbrissa, D., and Shisheva, A. (2006). Localized PtdIns 3,5-P2 synthesis to regulate early endosome dynamics and fusion. *Am. J. Physiol. Cell Physiol.* 291, 393–404. doi: 10.1152/ajpcell.00019.2006

Itoh, T., Erdmann, K. S., Roux, A., Habermann, B., Werner, H., and De Camilli, P. (2005). Dynamin and the actin cytoskeleton cooperatively regulate plasma membrane invagination by BAR and F-BAR proteins. *Dev. Cell* 9, 791–804. doi: 10.1016/j.devcel.2005.11.005

Jaber, N., Mohd-Naim, N., Wang, Z., DeLeon, J. L., Kim, S., Zhong, H., et al. (2016). Vps34 regulates Rab7 and late endocytic trafficking through recruitment of the GTPase-activating protein Armus. *J. Cell Sci.* 129, 4424–4435. doi: 10.1242/jcs.192260

Jackson, L. P., Kelly, B. T., McCoy, A. J., Gaffry, T., James, L. C., Collins, B. M., et al. (2010). A large-scale conformational change couples membrane recruitment to cargo binding in the AP2 clathrin adaptor complex. *Cell* 141, 1220–1229. doi: 10.1016/j.cell.2010.05.006

Jacobson, K., Liu, P., and Lagerholm, B. C. (2019). The lateral organization and mobility of plasma membrane components. *Cell* 177, 806–819. doi: 10.1016/j.cell.2019.04.018

Jahn, R., and Scheller, R. H. (2006). SNAREs - Engines for membrane fusion. *Nat. Rev. Mol. Cell Biol.* 7, 631–643. doi: 10.1038/nrm2002

Jean-Alphonse, F., Bowersox, S., Chen, S., Beard, G., Puthenveedu, M. A., and Hanyaloglu, A. C. (2014). Spatially restricted G protein-coupled receptor activity via divergent endocytic compartments. *J. Biol. Chem.* 289, 3960–3977. doi: 10.1074/jbc.M113.526350

Jost, M., Simpson, F., Kavran, J. M., Lemmon, M. A., and Schmid, S. L. (1998). Phosphatidylinositol-4,5-bisphosphate is required for endocytic coated vesicle formation. *Curr. Biol.* 8, 1399–1404. doi: 10.1016/s0960-9822(98)00022-0

Jovic, M., Sharma, M., Rahajeng, J., and Caplan, S. (2010). The early endosome: a busy sorting station for proteins at the crossroads. *Histol. Histopathol.* 25, 99–112. doi: 10.14670/HH-25.99

Kakumoto, T., and Nakata, T. (2013). Optogenetic control of PIP3: PIP3 is sufficient to induce the actin-based active part of growth cones and is regulated via endocytosis. *PLoS One* 8:e70861. doi: 10.1371/journal.pone.0070861

Kalaidzidis, I., Miaczynska, M., Brewinska-Olchowik, M., Hupalowska, A., Ferguson, C., Parton, R. G., et al. (2015). APPL endosomes are not obligatory endocytic intermediates but act as stable cargo-sorting compartments. *J. Cell Biol.* 211, 123–144. doi: 10.1083/jcb.201311117

Kerr, M. C., and Teasdale, R. D. (2009). Defining macropinocytosis. *Traffic* 10, 364–371. doi: 10.1111/j.1600-0854.2009.00878.x

Ketel, K., Krauss, M., Nicot, A.-S., Puchkov, D., Wieffer, M., Müller, R., et al. (2016). A phosphoinositide conversion mechanism for exit from endosomes. *Nature* 529, 408–412. doi: 10.1038/nature16516

Kokotos, A. C., Peltier, J., Davenport, E. C., Trost, M., and Cousin, M. A. (2018). Activity-dependent bulk endocytosis proteome reveals a key presynaptic role for the monomeric GTPase Rab11. *Proc. Natl. Acad. Sci. U.S.A.* 115, E10177–E10186. doi: 10.1073/pnas.1809189115

Krauss, M., Kukhtina, V., Pechstein, A., and Haucke, V. (2006). Stimulation of phosphatidylinositol kinase type I-mediated phosphatidylinositol (4,5)-bisphosphate synthesis by AP-2μ-cargo complexes. *Proc. Natl. Acad. Sci. U.S.A.* 103, 11934–11939. doi: 10.1073/pnas.0510306103

Kumari, S., and Mayor, S. (2008). ARF1 is directly involved in dynamin-independent endocytosis. *Nat. Cell Biol.* 10, 30–41. doi: 10.1038/ncb1666

Kusumi, A., Suzuki, K. G. N., Kasai, R. S., Ritchie, K., and Fujiwara, T. K. (2011). Hierarchical mesoscale domain organization of the plasma membrane. *Trends Biochem. Sci.* 36, 604–615. doi: 10.1016/j.tibs.2011.08.001

Lakadamyali, M., Rust, M. J., and Zhuang, X. (2006). Ligands for clathrin-mediated endocytosis are differentially sorted into distinct populations of early endosomes. *Cell* 124, 997–1009. doi: 10.1016/j.cell.2005.12.038

Lakoduk, A. M., Roudot, P., Mettlen, M., Grossman, H. M., Schmid, S. L., and Chen, P. H. (2019). Mutant p53 amplifies a dynamin-1/APPL1 endosome feedback loop that regulates recycling and migration. *J. Cell Biol.* 218, 1928–1942. doi: 10.1083/jcb.201810183

Law, F., Seo, J. H., Wang, Z., DeLeon, J. L., Bolis, Y., Brown, A., et al. (2017). The VPS34 PI3K negatively regulates RAB-5 during endosome maturation. *J. Cell Sci.* 130, 2007–2017. doi: 10.1242/jcs.194746

Lawe, D. C., Chawla, A., Merithew, E., Dumas, J., Carrington, W., Fogarty, K., et al. (2002). Sequential roles for phosphatidylinositol 3-phosphate and Rab5 in tethering and fusion of early endosomes via their interaction with EEA1. *J. Biol. Chem.* 277, 8611–8617. doi: 10.1074/jbc.M109239200

Lee, J. R., Hahn, H. S., Kim, Y. H., Nguyen, H. H., Yang, J. M., Kang, J. S., et al. (2011). Adaptor protein containing PH domain, PTB domain and leucine zipper (APPL1) regulates the protein level of EGFR by modulating its trafficking. *Biochem. Biophys. Res. Commun.* 415, 206–211. doi: 10.1016/j.bbrc.2011.10.064

Lee, S., Uchida, Y., Wang, J., Matsudaira, T., Nakagawa, T., Kishimoto, T., et al. (2015). Transport through recycling endosomes requires EHD 1 recruitment by a phosphatidylserine translocase. *EMBO J.* 34, 669–688. doi: 10.15252/embj.201489703

Leonard, D., Hayakawa, A., Lawe, D., Lambright, D., Bellve, K. D., Standley, C., et al. (2008). Sorting of EGF and transferrin at the plasma membrane and by cargo-specific signaling to EEA1-enriched endosomes. *J. Cell Sci.* 121, 3445–3458. doi: 10.1242/jcs.031484

Leren, T. P. (2014). Sorting an LDL receptor with bound PCSK9 to intracellular degradation. *Atherosclerosis* 237, 76–81. doi: 10.1016/j.atherosclerosis.2014.08.038

Leung, S. M., Ruiz, W. G., and Apodaca, G. (2000). Sorting of membrane and fluid at the apical pole of polarized Madin- Darby canine kidney cells. *Mol. Biol. Cell* 11, 2131–2150. doi: 10.1091/mbc.11.6.2131

Leyton-Puig, D., Isogai, T., Argenzio, E., Van Den Broek, B., Klarenbeek, J., Janssen, H., et al. (2017). Flat clathrin lattices are dynamic actin-controlled hubs for clathrin-mediated endocytosis and signalling of specific receptors. *Nat. Commun.* 8:16068. doi: 10.1038/ncomms16068

Liu, K., Jian, Y., Sun, X., Yang, C., Gao, Z., Zhang, Z., et al. (2016). Negative regulation of phosphatidylinositol 3-phosphate levels in early-to-late endosome conversion. *J. Cell Biol.* 212, 181–198. doi: 10.1083/jcb.201506081

Liu, K., Xing, R., Jian, Y., Gao, Z., Ma, X., Sun, X., et al. (2017). WDR91 is a Rab7 effector required for neuronal development. *J. Cell Biol.* 216, 3307–3321. doi: 10.1083/jcb.201705151

Lo, W.-T., Vujièiæ Žagar, A., Gerth, F., Lehmann, M., Puchkov, D., Krylova, O., et al. (2017). A coincidence detection mechanism controls PX-BAR domain-mediated endocytic membrane remodeling via an allosteric structural switch. *Dev. Cell* 43, 522–529.e4. doi: 10.1016/j.devcel.2017.10.019

Lundmark, R., Doherty, G. J., Howes, M. T., Cortese, K., Vallis, Y., Parton, R. G., et al. (2008). The GTPase-activating protein GRAF1 regulates the CLIC/GEEC endocytic pathway. *Curr. Biol.* 18, 1802–1808. doi: 10.1016/j.cub.2008.10.044

Maekawa, M., and Fairn, G. D. (2015). Complementary probes reveal that phosphatidylserine is required for the proper transbilayer distribution of cholesterol. *J. Cell Sci.* 128, 1422–1433. doi: 10.1242/jcs.164715

Maekawa, M., Terasaka, S., Mochizuki, Y., Kawai, K., Ikeda, Y., Araki, N., et al. (2014). Sequential breakdown of 3-phosphorylated phosphoinositides is essential for the completion of macropinocytosis. *Proc. Natl. Acad. Sci. U.S.A.* 111, E978–E987. doi: 10.1073/pnas.1311029111

Massol, R. H., Boll, W., Griffin, A. M., and Kirchhausen, T. (2006). A burst of auxilin recruitment determines the onset of clathrin-coated vesicle uncoating. *Proc. Natl. Acad. Sci. U.S.A.* 103, 10265–10270. doi: 10.1073/pnas.0603369103

Masters, T. A., Tumbarello, D. A., Chibalina, M. V., and Buss, F. (2017). MYO6 regulates spatial organization of signaling endosomes driving AKT activation and actin dynamics. *Cell Rep.* 19, 2088–2101. doi: 10.1016/j.celrep.2017.05.048

McCaffrey, M. W., Bielli, A., Cantalupo, G., Mora, S., Roberti, V., Santillo, M., et al. (2001). Rab4 affects both recycling and degradative endosomal trafficking. *FEBS Lett.* 495, 21–30. doi: 10.1016/S0014-5793(01)02359-6

McNally, K. E., Faulkner, R., Steinberg, F., Gallon, M., Ghai, R., Pim, D., et al. (2017). Retriever is a multiprotein complex for retromer-independent endosomal cargo recycling. *Nat. Cell Biol.* 19, 1214–1225. doi: 10.1038/ncb3610

Ménard, L., Floc'h, N., Martin, M. J., and Cross, D. A. E. (2018). Reactivation of mutant-EGFR degradation through clathrin inhibition overcomes resistance to EGFR tyrosine kinase inhibitors. *Cancer Res.* 78, 3267–3279.

Mettlen, M., Chen, P., Srinivasan, S., Danuser, G., and Schmid, S. L. (2018). Regulation of clathrin-mediated endocytosis. *Annu. Rev. Biochem.* 87, 871–896.

Milosevic, I., Giovedi, S., Lou, X., Raimondi, A., Collesi, C., Shen, H., et al. (2011). Recruitment of endophilin to clathrin-coated pit necks is required for efficient vesicle uncoating after fission. *Neuron* 72, 587–601. doi: 10.1016/j.neuron.2011.08.029

Morel, E., Chamoun, Z., Lasiecka, Z. M., Chan, R. B., Williamson, R. L., Vetanovetz, C., et al. (2013). Phosphatidylinositol-3-phosphate regulates sorting and processing of amyloid precursor protein through the endosomal system. *Nat. Commun.* 4:3250. doi: 10.1038/ncomms3250

Murray, D. H., Jahnel, M., Lauer, J., Avellaneda, M. J., Brouilly, N., Cezanne, A., et al. (2016). An endosomal tether undergoes an entropic collapse to bring vesicles together. *Nature* 537, 107–111. doi: 10.1038/nature19326

Nag, S., Rani, S., Mahanty, S., Bissig, C., Arora, P., Azevedo, C., et al. (2018). Rab4A organizes endosomal domains for sorting cargo to lysosome-related organelles. *J. Cell Sci.* 131:jcs216226. doi: 10.1242/jcs.216226

Nakatsu, F., Messa, M., Nández, R., Czapla, H., Zou, Y., Strittmatter, S. M., et al. (2015). Sac2/INPP5F is an inositol 4-phosphatase that functions in the endocytic pathway. *J. Cell Biol.* 209, 85–95. doi: 10.1083/jcb.201409064

Nández, R., Balkin, D. M., Messa, M., Liang, L., Paradise, S., Czapla, H., et al. (2014). A role of OCRL in clathrin-coated pit dynamics and uncoating revealed by studies of Lowe syndrome cells. *eLife* 3:e02975. doi: 10.7554/eLife.02975

Naslavsky, N., and Caplan, S. (2018). The enigmatic endosome - Sorting the ins and outs of endocytic trafficking. *J. Cell Sci.* 131:jcs216499. doi: 10.1242/jcs.216499

Naslavsky, N., Rahajeng, J., Sharma, M., Joviæ, M., and Caplan, S. (2006). Interactions between EHD Proteins and Rab11-FIP2: a role for EHD3 in Early Endosomal Transport. *Mol. Biol. Cell* 17, 163–177. doi: 10.1091/mbc.e05-05-0466

Navaroli, D. M., Bellvé, K. D., Standley, C., Lifshitz, L. M., Cardia, J., Lambright, D., et al. (2012). Rabenosyn-5 defines the fate of the transferrin receptor following clathrin-mediated endocytosis. *Proc. Natl. Acad. Sci. U.S.A.* 109, E471–E480. doi: 10.1073/pnas.1115495109

Nguyen, P. M., Gandasi, N. R., Xie, B., Sugahara, S., Xu, Y., and Idevall-Hagren, O. (2019). The PI(4)P phosphatase Sac2 controls insulin granule docking and release. *J. Cell Biol.* 218, 3714–3729. doi: 10.1083/jcb.201903121

Niu, Y., Zhang, C., Sun, Z., Hong, Z., Li, K., Sun, D., et al. (2013). PtdIns(4)P regulates retromer-motor interaction to facilitate dynein-cargo dissociation at the trans-Golgi network. *Nat. Cell Biol.* 15, 417–429. doi: 10.1038/ncb2710

Pascolutti, R., Algisi, V., Conte, A., Raimondi, A., Pasham, M., Upadhyayula, S., et al. (2019). Molecularly distinct clathrin-coated pits differentially impact EGFR Fate and signaling. *Cell Rep.* 27, 3049–3061.e6. doi: 10.1016/j.celrep.2019.05.017

Perera, R. M., Zoncu, R., Lucast, L., De Camilli, P., and Toomre, D. (2006). Two synaptojanin 1 isoforms are recruited to clathrin-coated pits at different stages. *Proc. Natl. Acad. Sci. U.S.A.* 103, 19332–19337. doi: 10.1073/pnas.0609795104

Pesesse, X., Dewaste, V., De Smedt, F., Laffargue, M., Giuriato, S., Moreau, C., et al. (2001). The Src Homology 2 Domain Containing Inositol 5-Phosphatase SHIP2 is Recruited to the Epidermal Growth Factor (EGF) Receptor and Dephosphorylates Phosphatidylinositol 3,4,5-Trisphosphate in EGF-stimulated COS-7 Cells. *J. Biol. Chem.* 276, 28348–28355. doi: 10.1074/jbc.M103537200

Picas, L., Gaits-Iacovoni, F., and Goud, B. (2016). The emerging role of phosphoinositide clustering in intracellular trafficking and signal transduction. *F1000Res.* 5:F1000 Faculty Rev-422. doi: 10.12688/f1000research.7537.1

Picas, L., Viaud, J., Schauer, K., Vanni, S., Hnia, K., Fraisier, V., et al. (2014). BIN1/M-Amphiphysin2 induces clustering of phosphoinositides to recruit its downstream partner dynamin. *Nat. Commun.* 5:5647. doi: 10.1038/ncomms6647

Posor, Y., Eichhorn-Gruenig, M., Puchkov, D., Schöneberg, J., Ullrich, A., Lampe, A., et al. (2013). Spatiotemporal control of endocytosis by phosphatidylinositol-3,4-bisphosphate. *Nature* 499, 233–237. doi: 10.1038/nature12360

Posor, Y., Eichhorn-Grünig, M., and Haucke, V. (2015). Phosphoinositides in endocytosis. *Biochim. Biophys. Acta* 1851, 794–804. doi: 10.1016/j.bbalip.2014.09.014

Poteryaev, D., Datta, S., Ackema, K., Zerial, M., and Spang, A. (2010). Identification of the switch in early-to-late endosome transition. *Cell* 141, 497–508. doi: 10.1016/j.cell.2010.03.011

Purushothaman, L. K., Arlt, H., Kuhlee, A., Raunser, S., and Ungermann, C. (2017). Retromer-driven membrane tubulation separates endosomal recycling from Rab7/Ypt7-dependent fusion. *Mol. Biol. Cell* 28, 783–791. doi: 10.1091/mbc.e16-08-0582

Puthenveedu, M. A., Lauffer, B., Temkin, P., Vistein, R., Carlton, P., Thorn, K., et al. (2010). Sequence-dependent sorting of recycling proteins by actin-stabilized endosomal microdomains. *Cell* 143, 761–773. doi: 10.1016/j.cell.2010.10.003

Qian, Y. W., Schmidt, R. J., Zhang, Y., Chu, S., Lin, A., Wang, H., et al. (2007). Secreted PCSK9 downregulates low density lipoprotein receptor through receptor-mediated endocytosis. *J. Lipid Res.* 48, 1488–1498. doi: 10.1194/jlr.M700071-JLR200

Rao, M., and Mayor, S. (2014). Active organization of membrane constituents in living cells. *Curr. Opin. Cell Biol.* 29, 126–132. doi: 10.1016/j.ceb.2014.05.007

Redpath, G. M. I., Ecker, M., Kapoor-Kaushik, N., Vartoukian, H., Carnell, M., Kempe, D., et al. (2019). Flotillins promote T cell receptor sorting through a fast Rab5–Rab11 endocytic recycling axis. *Nat. Commun.* 10:4392. doi: 10.1038/s41467-019-12352-w

Rink, J., Ghigo, E., Kalaidzidis, Y., and Zerial, M. (2005). Rab conversion as a mechanism of progression from early to late endosomes. *Cell* 122, 735–749. doi: 10.1016/j.cell.2005.06.043

Rojas, R., Van Vlijmen, T., Mardones, G. A., Prabhu, Y., Rojas, A. L., Mohammed, S., et al. (2008). Regulation of retromer recruitment to endosomes by sequential action of Rab5 and Rab7. *J. Cell Biol.* 183, 513–526. doi: 10.1083/jcb.200804048

Román-Fernández, Á., Roignot, J., Sandilands, E., Nacke, M., Mansour, M. A., McGarry, L., et al. (2018). The phospholipid PI(3,4)P2 is an apical identity determinant. *Nat. Commun.* 9:5041. doi: 10.1038/s41467-018-07464-8

Romer, W., Pontani, L.-L. L., Sorre, B., Rentero, C., Berland, L., Chambon, V., et al. (2010). Actin dynamics drive membrane reorganization and scission in clathrin-independent endocytosis. *Cell* 140, 540–553. doi: 10.1016/j.cell.2010.01.010

Rossatti, P., Ziegler, L., Schregle, R., Betzler, V. M., Ecker, M., and Rossy, J. (2019). Cdc42 couples T cell receptor endocytosis to GRAF1-mediated tubular invaginations of the plasma membrane. *Cells* 8:1388. doi: 10.3390/cells8111388

Saarikangas, J., Zhao, H., Pykäläinen, A., Laurinmäki, P., Mattila, P. K., Kinnunen, P. K. J., et al. (2009). Molecular mechanisms of membrane deformation by I-BAR domain proteins. *Curr. Biol.* 19, 95–107. doi: 10.1016/J.CUB.2008.12.029

Sathe, M., Muthukrishnan, G., Rae, J., Disanza, A., Thattai, M., Scita, G., et al. (2018). Small GTPases and BAR domain proteins regulate branched actin polymerisation for clathrin and dynamin-independent endocytosis. *Nat. Commun.* 9:1835. doi: 10.1038/s41467-018-03955-w

Schink, K. O., Tan, K.-W., and Stenmark, H. (2016). Phosphoinositides in control of membrane dynamics. *Annu. Rev. Cell Dev. Biol.* 32, 143–171. doi: 10.1146/annurev-cellbio-111315-125349

Schöneberg, J., Lehmann, M., Ullrich, A., Posor, Y., Lo, W.-T., Lichtner, G., et al. (2017). Lipid-mediated PX-BAR domain recruitment couples local membrane constriction to endocytic vesicle fission. *Nat. Commun.* 8:15873. doi: 10.1038/ncomms15873

Scita, G., and Di Fiore, P. P. (2010). The endocytic matrix. *Nature* 463, 464–473. doi: 10.1038/nature08910

Shin, H. W., Hayashi, M., Christoforidis, S., Lacas-Gervais, S., Hoepfner, S., Wenk, M. R., et al. (2005). An enzymatic cascade of Rab5 effectors regulates phosphoinositide turnover in the endocytic pathway. *J. Cell Biol.* 170, 607–618. doi: 10.1083/jcb.200505128

Shin, N., Ahn, N., Chang-Ileto, B., Park, J., Takei, K., Ahn, S. G., et al. (2008). SNX9 regulates tubular invagination of the plasma membrane through interaction with actin cytoskeleton and dynamin 2. *J. Cell Sci.* 121, 1252–1263. doi: 10.1242/jcs.016709

Shukla, S., Jin, R., Robustelli, J., Zimmerman, Z. E., and Baumgart, T. (2019). PIP2 reshapes membranes through asymmetric Desorption. *Biophys. J.* 117, 962–974. doi: 10.1016/j.bpj.2019.07.047

Sigismund, S., Argenzio, E., Tosoni, D., Cavallaro, E., Polo, S., and Di Fiore, P. P. (2008). Clathrin-mediated internalization is essential for sustained EGFR Signaling but dispensable for degradation. *Dev. Cell* 15, 209–219. doi: 10.1016/j.devcel.2008.06.012

Sigismund, S., Woelk, T., Puri, C., Maspero, E., Tacchetti, C., Transidico, P., et al. (2005). Clathrin-independent endocytosis of ubiquitinated cargos. *Proc. Natl. Acad. Sci. U.S.A.* 102, 2760–2765. doi: 10.1073/pnas.0409817102

Simons, K., and Ikonen, E. (1997). Functional rafts in cell membranes. *Nature* 387, 569–572. doi: 10.1038/42408

Singer, S. J., and Nicolson, G. L. (1972). The fluid mosaic model of the structure of cell membranes. *Science* 175, 720–731. doi: 10.1126/science.175.4023.720

Singla, A., Fedoseienko, A., Giridharan, S. S. P., Overlee, B. L., Lopez, A., Jia, D., et al. (2019). Endosomal PI(3)P regulation by the COMMD/CCDC22/CCDC93 (CCC) complex controls membrane protein recycling. *Nat. Commun.* 10:4271. doi: 10.1038/s41467-019-12221-6

Solinger, J. A., Rashid, H. O., Prescianotto-Baschong, C., and Spang, A. (2020). FERARI is required for Rab11-dependent endocytic recycling. *Nat. Cell Biol.* 22, 213–224. doi: 10.1038/s41556-019-0456-5

Solis, G. P., Hülsbusch, N., Radon, Y., Katanaev, V. L., Plattner, H., and Stuermer, C. A. O. (2013). Reggies/flotillins interact with Rab11a and SNX4 at the tubulovesicular recycling compartment and function in transferrin receptor and E-cadherin trafficking. *Mol. Biol. Cell* 24, 2689–2702. doi: 10.1091/mbc.E12-12-0854

Sönnichsen, B., De Renzis, S., Nielsen, E., Rietdorf, J., and Zerial, M. (2000). Distinct membrane domains on endosomes in the recycling pathway visualized by multicolor imaging of Rab4, Rab5, and Rab11. *J. Cell Biol.* 149, 901–913. doi: 10.1083/jcb.149.4.901

Sposini, S., Jean-Alphonse, F. G., Ayoub, M. A., Oqua, A., West, C., Lavery, S., et al. (2017). Integration of GPCR signaling and sorting from very early endosomes via opposing APPL1 mechanisms. *Cell Rep.* 21, 2855–2867. doi: 10.1016/j.celrep.2017.11.023

Stewart, D. J., Short, K. K., Maniaci, B. N., and Burkhead, J. L. (2019). COMMD1 and PtdIns(4,5)P2 interaction maintain ATP7B copper transporter trafficking fidelity in HepG2 cells. *J. Cell Sci.* 132:jcs231753. doi: 10.1242/jcs.231753

Su, T., Bryant, D. M., Luton, F., Vergés, M., Ulrich, S. M., Hansen, K. C., et al. (2010). A kinase cascade leading to Rab11-FIP5 controls transcytosis of the polymeric immunoglobulin receptor. *Nat. Cell Biol.* 12, 1143–1153. doi: 10.1038/ncb2118

Suetsugu, S., Kurisu, S., Oikawa, T., Yamazaki, D., Oda, A., and Takenawa, T. (2006). Optimization of WAVE2 complex-induced actin polymerization by membrane-bound IRSp53, PIP3, and Rac. *J. Cell Biol.* 173, 571–585. doi: 10.1083/jcb.200509067

Sun, M., Luong, G., Plastikwala, F., and Sun, Y. (2020). Control of Rab7a activity and localization through endosomal type Igamma PIP 5-kinase is required for endosome maturation and lysosome function. *FASEB J.* 34, 2730–2748. doi: 10.1096/fj.201901830R

Szalinski, C. M., Guerriero, C. J., Ruiz, W. G., Docter, B. E., Rbaibi, Y., Pastor-Soler, N. M., et al. (2013). PIP5KIβ selectively modulates apical endocytosis in

polarized renal epithelial cells. *PLoS One* 8:e53790. doi: 10.1371/journal.pone.0053790

Takahashi, S., Kubo, K., Waguri, S., Yabashi, A., Shin, H.-W., Katoh, Y., et al. (2012). Rab11 regulates exocytosis of recycling vesicles at the plasma membrane. *J. Cell Sci.* 125, 4049–4057. doi: 10.1242/jcs.102913

Takatori, S., Tatematsu, T., Cheng, J., Matsumoto, J., Akano, T., and Fujimoto, T. (2016). Phosphatidylinositol 3,5-Bisphosphate-Rich Membrane Domains in Endosomes and Lysosomes. *Traffic* 17, 154–167. doi: 10.1111/tra.12346

Tanaka, Y., Ono, N., Shima, T., Tanaka, G., Katoh, Y., Nakayama, K., et al. (2016). The phospholipid flippase ATP9A is required for the recycling pathway from the endosomes to the plasma membrane. *Mol. Biol. Cell* 27, 3883–3893. doi: 10.1091/mbc.E16-08-0586

Temkin, P., Lauffer, B., Jäger, S., Cimermancic, P., Krogan, N. J., and Von Zastrow, M. (2011). SNX27 mediates retromer tubule entry and endosome-to-plasma membrane trafficking of signalling receptors. *Nat. Cell Biol.* 13, 715–723. doi: 10.1038/ncb2252

Thompson, A., Nessler, R., Wisco, D., Anderson, E., Winckler, B., and Sheff, D. (2007). Recycling endosomes of polarized epithelial cells actively sort apical and basolateral cargos into separate subdomains. *Mol. Biol. Cell* 18, 2687–2697. doi: 10.1091/mbc.e05-09-0873

Thottacherry, J. J., Kosmalska, A. J., Kumar, A., Vishen, A. S., Elosegui-Artola, A., Pradhan, S., et al. (2018). Mechanochemical feedback control of dynamin independent endocytosis modulates membrane tension in adherent cells. *Nat. Commun.* 9:4217. doi: 10.1038/s41467-018-06738-5

Traer, C. J., Rutherford, A. C., Palmer, K. J., Wassmer, T., Oakley, J., Attar, N., et al. (2007). SNX4 coordinates endosomal sorting of TfnR with dynein-mediated transport into the endocytic recycling compartment. *Nat. Cell Biol.* 9, 1370–1380. doi: 10.1038/ncb1656

Tuma, P. L., Finnegan, C. M., Yi, J. H., and Hubbard, A. L. (1999). Evidence for apical endocytosis in polarized hepatic cells: Phosphoinositide 3-kinase inhibitors lead to the lysosomal accumulation of resident apical plasma membrane proteins. *J. Cell Biol.* 145, 1089–1102. doi: 10.1083/jcb.145.5.1089

Tveten, K., Strmø, T. B., Berge, K. E., and Leren, T. P. (2013). PCSK9-mediated degradation of the LDL receptor generates a 17 kDa C-terminal LDL receptor fragment. *J. Lipid Res.* 54, 1560–1566. doi: 10.1194/jlr.M034371

Uchida, Y., Hasegawa, J., Chinnapen, D., Inoue, T., Okazaki, S., Kato, R., et al. (2011). Intracellular phosphatidylserine is essential for retrograde membrane traffic through endosomes. *Proc. Natl. Acad. Sci. U.S.A.* 108, 15846–15851. doi: 10.1073/pnas.1109101108

Uezu, A., Horiuchi, A., Kanda, K., Kikuchi, N., Umeda, K., Tsujita, K., et al. (2007). SGIP1α is an endocytic protein that directly interacts with phospholipids and Eps15. *J. Biol. Chem.* 282, 26481–26489. doi: 10.1074/jbc.M703815200

Ullrich, O., Reinsch, S., Urbé, S., Zerial, M., and Parton, R. G. (1996). Rab11 regulates recycling through the pericentriolar recycling endosome. *J. Cell Biol.* 135, 913–924. doi: 10.1083/jcb.135.4.913

Vicinanza, M., Di Campli, A., Polishchuk, E., Santoro, M., Di Tullio, G., Godi, A., et al. (2011). OCRL controls trafficking through early endosomes via PtdIns4,5P 2-dependent regulation of endosomal actin. *EMBO J.* 30, 4970–4985. doi: 10.1038/emboj.2011.354

Vistein, R., and Puthenveedu, M. A. (2013). Reprogramming of G protein-coupled receptor recycling and signaling by a kinase switch. *Proc. Natl. Acad. Sci. U.S.A.* 110, 15289–15294. doi: 10.1073/pnas.1306340110

Wang, H., Lo, W.-T., and Haucke, V. (2019). Phosphoinositide switches in endocytosis and in the endolysosomal system. *Curr. Opin. Cell Biol.* 59, 50–57. doi: 10.1016/J.CEB.2019.03.011

Wang, L., Johnson, A., Hanna, M., and Audhya, A. (2016). Eps15 membrane-binding and -bending activity acts redundantly with Fcho1 during clathrin-mediated endocytosis. *Mol. Biol. Cell* 27, 2675–2687. doi: 10.1091/mbc.E16-03-0151

Wassmer, T., Attar, N., Harterink, M., van Weering, J. R. T., Traer, C. J., Oakley, J., et al. (2009). The retromer coat complex coordinates endosomal sorting and dynein-mediated transport, with carrier recognition by the trans-golgi network. *Dev. Cell* 17, 110–122. doi: 10.1016/j.devcel.2009.04.016

Watanabe, S., and Boucrot, E. (2017). Fast and ultrafast endocytosis. *Curr. Opin. Cell Biol.* 47, 64–71. doi: 10.1016/j.ceb.2017.02.013

Wen, Y., Vogt, V. M., and Feigenson, G. W. (2018). Multivalent cation-bridged PI(4,5)P2 clusters form at very low concentrations. *Biophys. J.* 114, 2630–2639. doi: 10.1016/J.BPJ.2018.04.048

Wills, R. C., Goulden, B. D., and Hammond, G. R. V. (2018). Genetically encoded lipid biosensors. *Mol. Biol. Cell* 29, 1526–1532. doi: 10.1091/mbc.e17-12-0738

Xie, S., Bahl, K., Reinecke, J. B., Hammond, G. R. V., Naslavsky, N., and Caplan, S. (2016). The endocytic recycling compartment maintains cargo segregation acquired upon exit from the sorting endosome. *Mol. Biol. Cell* 27, 108–126. doi: 10.1091/mbc.e15-07-0514

Ye, H., Ojelade, S. A., Li-Kroeger, D., Zuo, Z., Wang, L., Li, Y., et al. (2020). Retromer subunit, vps29, regulates synaptic transmission and is required for endolysosomal function in the aging brain. *eLife* 9:e51977. doi: 10.7554/eLife.51977

Yesylevskyy, S. O., Demchenko, A. P., Kraszewski, S., and Ramseyer, C. (2013). Cholesterol induces uneven curvature of asymmetric lipid bilayers. *Sci. World J.* 2013:965230. doi: 10.1155/2013/965230

Yeung, T., Gilbert, G. E., Shi, J., Silvius, J., Kapus, A., and Grinstein, S. (2008). Membrane phosphatidylserine regulates surface charge and protein localization. *Science* 319, 210–213. doi: 10.1126/science.1152066

Yin, H. L., and Janmey, P. A. (2003). Phosphoinositide regulation of the actin cytoskeleton. *Annu. Rev. Physiol.* 65, 761–789. doi: 10.1146/annurev.physiol.65.092101.142517

Zhao, H., Michelot, A., Koskela, E. V., Tkach, V., Stamou, D., Drubin, D. G., et al. (2013). Membrane-sculpting BAR domains generate stable lipid microdomains. *Cell Rep.* 1213–1223. doi: 10.1016/j.celrep.2013.08.024

Zheng, J., Cahill, S. M., Lemmon, M. A., Fushman, D., Schlessinger, J., and Cowburn, D. (1996). Identification of the binding site for acidic phospholipids on the PH domain of dynamin: implications for stimulation of GTPase activity. *J. Mol. Biol.* 255, 14–21. doi: 10.1006/jmbi.1996.0002

Zoncu, R., Perera, R. M., Balkin, D. M., Pirruccello, M., Toomre, D., and De Camilli, P. (2009). A phosphoinositide switch controls the maturation and signaling properties of APPL endosomes. *Cell* 136, 1110–1121. doi: 10.1016/j.cell.2009.01.032

Conflict of Interest: The authors declare that the research was conducted in the absence of any commercial or financial relationships that could be construed as a potential conflict of interest.

frontiers in Cell and Developmental Biology

REVIEW
published: 05 August 2020
doi: 10.3389/fcell.2020.00684

Cellular Membranes, a Versatile Adaptive Composite Material

Lucas Lamparter[1,2†] *and Milos Galic*[1,2*†]

[1] *Institute of Medical Physics and Biophysics, Faculty of Medicine, University of Münster, Münster, Germany,* [2] *Cells in Motion Interfaculty Centre, University of Müenster, Münster, Germany*

Cellular membranes belong to the most vital yet least understood biomaterials of live matter. For instance, its biomechanical requirements substantially vary across species and subcellular sites, raising the question how membranes manage to adjust to such dramatic changes. Central to its adaptability at the cell surface is the interplay between the plasma membrane and the adjacent cell cortex, forming an adaptive composite material that dynamically adjusts its mechanical properties. Using a hypothetical composite material, we identify core challenges, and discuss how cellular membranes solved these tasks. We further muse how pathological changes in material properties affect membrane mechanics and cell function, before closing with open questions and future challenges arising when studying cellular membranes.

Keywords: composite material, adaptive material, lipid bilayer, plasma membrane, cell cortex

OPEN ACCESS

Edited by:
Falk Nimmerjahn, University of Erlangen-Nuremberg, Germany

Reviewed by:
Congbao Kang, Experimental Drug Development Centre (EDDC), Singapore
Zheng Shi, Rutgers, The State University of New Jersey, United States

***Correspondence:**
Milos Galic
galic@uni-muenster.de

† These authors have contributed equally to this work

Specialty section:
This article was submitted to Cellular Biochemistry, a section of the journal Frontiers in Cell and Developmental Biology

Received: *26 January 2020*
Accepted: *06 July 2020*
Published: *05 August 2020*

Citation:
Lamparter L and Galic M (2020) Cellular Membranes, a Versatile Adaptive Composite Material. Front. Cell Dev. Biol. 8:684. doi: 10.3389/fcell.2020.00684

INTRODUCTION

The cellular membrane is one of the most vital and complex biomaterials in live matter. It is therefore not surprising that it has over the last decades been the subject of extensive studies, giving insights into a fascinating world of regulatory processes that control localization and activity of proteins and lipids in cellular membranes (Singer and Nicolson, 1972; Edidin et al., 1991; Eggeling et al., 2009). These studies established that biomechanical requirements vary across species and subcellular sites, indicative of tremendous diversity and adaptability (Vasanji et al., 2004; van Meer et al., 2008). Yet, despite substantial advancements over the last few decades, we are still lacking a comprehensive understanding of membrane mechanics at the cell surface.

Individual lipids spontaneously self-assemble into a bilayer that is then subject to thermal fluctuations (Faucon et al., 1989), changes in local lipid composition (Estep et al., 1979), and sustained membrane deformations (Baumgart et al., 2003). Besides lipids, cellular membranes further contain proteins that not only influence the local lipid environment (Contreras et al., 2011; Laganowsky et al., 2014) and mechanical membrane properties (Shi et al., 2018), but also render the membrane transmissive to incoming stimuli. These signals can alter, among many others things, membrane potential (Nernst, 1889), shape (Chen et al., 2016; Graber et al., 2017) and lipid composition (Sugimoto et al., 1984). Importantly, signal-induced changes also affect localization and activity of membrane-bound (Carpenter et al., 1978) and cytosolic (Hancock et al., 1989) proteins. One principal target for such signals is the membrane-associated cortical cytoskeleton (Svitkina, 2020). Possibly the most striking of its many features is the ability of the cytoskeleton to generate mechanical push and pull forces (Peskin et al., 1993; Huxley and Simmons, 1971). Hence, by coupling membranes to the adjacent cell cortex yields a composite material that is equally able to sense and respond to external stimuli.

In this review, we will explore the intricate mechanical properties of this adaptive composite material. Readers interested in learning more on signaling across cellular membranes or cytoskeletal mechanics, we refer to the many excellent reviews written elsewhere (Huber et al., 2013;

Lundberg and Borner, 2019; Svitkina, 2020). We begin by defining core mechanical terms, before investigating the material properties of the cell membrane. Next, we show how these properties are affected by its manifold interaction with the cell cortex under physiological and pathophysiological conditions. We conclude by pointing out future challenges toward understanding the mechanical properties of this exciting biomaterial.

FUNDAMENTAL CELL MECHANICS

The plasma membrane and the cortical cytoskeleton jointly form a composite material with unique biomechanical features (Nicolson, 2014). To fully appreciate this elaborate structure, we first need to introduce a number of terms that will repeatedly show up over the following pages. Let's begin by answering what a composite material actually is. This term – originating from manufacturing engineering – depicts two or more connected materials, where the resulting compound exhibits properties that neither of the individual components by itself possesses (Westkämper and Warnecke, 2011). The material properties of the composite are a function of the individual material properties of its components, their geometry and its interface (i.e., the way those materials are connected). Therefore, by changing one of those parameters the overall properties of the composite will be affected. If this happens by design, for instance in response to a stimulus, the material is referred to as an adaptive composite material. For biological membranes, the main components of this composite material are the plasma membrane (PM) that encapsulates the cell, the cell cortex lining the cytosolic site of the PM, and the membrane-cortex-attachment (MCA) that describes the interface connecting PM and cell cortex. In the following, we refer to the composite material emerging from the combination of PM, MCA and cell cortex as "cell surface."

Having introduced the basic terms, we next need to recapitulate the essential material properties. For small strains, any membrane deformation can be regarded as the superposition of three basic types of deformation: pure stretch, shear and bending (**Figure 1A**). A membrane subject to a force acting normal to its edges will experience an extensional stress and an area stretch. The resistance against this stretch is called the stretch modulus K_e. Similarly, a membrane that is subject to forces acting parallel to its edges will experience shear stress, whereby the resistance against the shear deformation is given by the shear modulus K_s. While stretch and shear modulus relate strain to a certain stress, the bending stiffness K_B relates a curvature to a bending moment (i.e., the energy necessary to bend the membrane to its current state). The deformations described so far are purely elastic, and therefore not time dependent. However, biomaterials often exhibit fluid-like behavior, including time dependent plastic deformation. Therefore, we need to introduce a fourth material property, the viscosity η (**Figure 1A**, right). It depicts the resistance of a fluid against shear stress at a specific shear velocity $\frac{du}{dy}$. In contrast to the shear modulus, the viscosity does not relate stress to strain, but to the rate of deformation. By changing one or a combination of these four essential material properties mechanical adaptation can be achieved. Readers interested in learning more about this topic, we refer to work written elsewhere (Kamm and Grodzinsky, 2015).

Finally, let's recapitulate the types of deformations a material can experience. The properties of a material determine its response to a mechanical stimulus. In its most basic form, such a response can be purely elastic or viscous. An elastic material returns to its original shape upon distortion, while a viscous material stays distorted after the load is released. This behavior can be envisioned as a spring (elastic) or dashpot (viscous), respectively (**Figure 1B**). However, many materials display a viscoelastic response, where viscous and elastic properties are coupled. Basic models for such a behavior are the Maxwell and the Kelvin body (**Figure 1C**). In a Maxwell body, elastic and viscous elements are paired in series, thus leading to an elastic response for fast distortions, while slowly applied load is captured in a plastic manner. In contrast, the Kelvin body displays elastic and viscous elements in parallel. Hence, under stress the deformation will over time approach the strain response of the elastic component, whereby it is slowed down by the viscous element. Consequently, the Maxwell body is capable of plastic deformation (i.e., viscoelastic fluid), while the Kelvin body will always return to its original shape when the load is released (i.e., viscoelastic solid). As above, we refer readers interested in this topic to work written elsewhere (Meyers and Chawla, 2010).

ENGINEERING A HYPOTHETICAL BIOMIMETIC MEMBRANE

Inspired by the famous quote "*what I cannot create, I do not understand*" from Richard Feynman, we will attempt on the following pages to conceive a hypothetical biomimetic membrane with the following features: It should reliably separates internal from external space. The boundary should further be flexible, tunable, and able to transiently change its material properties in response to incoming signals. For simplicity and didactic reasons, we designed this as an engineering challenge (**Supplementary Figure S1** and **Supplementary Material**), sequentially expanding the number of requirements (i.e., requested functions) of the hypothetical material. In each section, we begin by musing how such a biomimetic structure could be designed, before exploring in detail how this has been accomplished in biological systems.

The Lipid Bilayer, the Core Module of Cellular Membranes

The most fundamental function of our biomimetic material is to reliably separate the interior from the external environment. To achieve such a continuous barrier in an aqueous solution, a biomimetic material must be able to oppose differences in osmotic and hydrostatic pressure without leakage. Ideally, the material would spontaneously assemble, thus limiting the need for energy and control systems.

In cellular membranes, amphipathic lipids spontaneously self-assemble into a 5–7 nm thick lipid bilayer, with the hydrophobic carbohydrate chains facing toward the inside (Huang and Thompson, 1965). This occurs to minimize the free energy

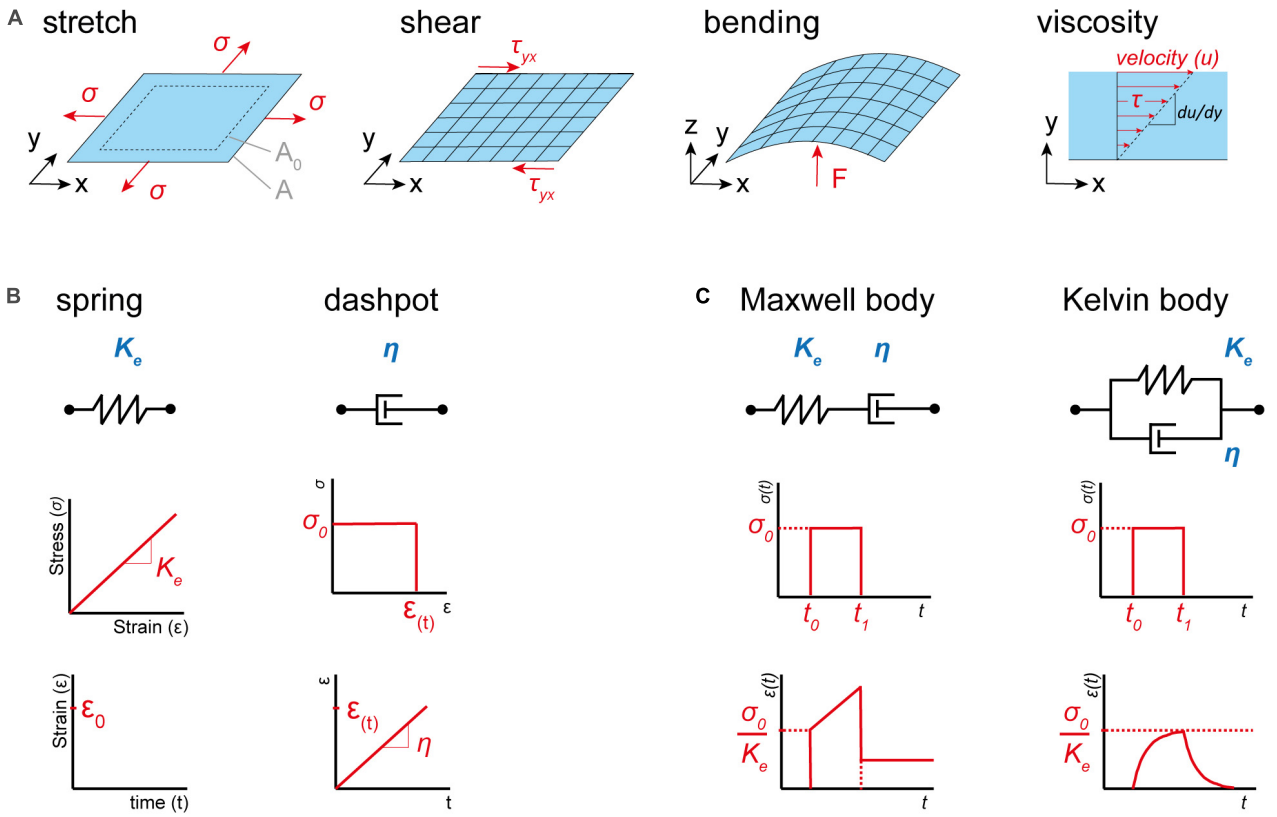

FIGURE 1 | Basic material properties and deformation types. **(A)** From left to right, membrane exposed to uniform extensional stress σ, which is acting normal to its edges, causes an increase of the area (from A_0 to A). Membrane exposed to forces acting parallel to its surface inducing shear stress τ_{yx}. Membrane exposed to a point load (F) acting perpendicular to its surface, which is inducing curvature and therefore a bending moment. Viscosity η, the resistance of a fluid against shear stress τ given at a specific shear velocity $\frac{du}{dy}$. **(B)** Basic properties of a purely elastic (spring, left) and viscous (dashpot, right) material. A purely elastic material always returns to its original state after deformation and exhibits a linear relationship between stress and strain, while a purely viscous material exhibits plastic (permanent) deformations and a linear relationship between stress and shear velocity. **(C)** Models of viscoelastic materials. Maxwell body (left) consisting of a dashpot and a spring in series displays, like a viscoelastic fluid, permanent deformation after the load is removed. Kelvin body (right) returns, like a viscoelastic solid, to its original state when the load is removed. Images adapted from Seidel et al. (2009) and Kamm and Grodzinsky (2015).

of water arising from continuous formation and disassembly of hydrogen bonds (**Figure 2A**, right). Pure lipid bilayers are reported to have a stretch modulus K_e in the range of 100 to 1000 mN/m (Waugh and Evans, 1979), with a value of ∼200 mN/m as most widely accepted (Rawicz et al., 2000). Considering a pure lipid bilayer with a possible areal stretch of 5% (Hallett et al., 1993), and neglecting thermal fluctuation (Evans and Rawicz, 1990), Eq. 2.5 in **Box 1** gives us a rupture tension of 10 mN/m. This value is in accordance to published reports that measured a rupture tensions of 3 to 10 mN/m, depending on the lipid composition of the bilayer (Olbrich et al., 2000). Following Laplace's law.

$$\Delta p = \frac{2N}{R}, \tag{1.1}$$

where N depicts the surface tension and R the principal radius of curvature, we find that the PM can therefore withstand a pressure difference Δp of up to 0.2 bar or 20 kPa assuming a radius of 1 μm before ripping, a remarkable performance given its thickness of only 5–7 nm.

With respect to the material properties mentioned at the beginning of the section, the lipid bilayer already provides excellent stretch resistance. However, it is readily deformed in the presence of forces within the plane (i.e., low shear resistance K_s) or perpendicular to it (i.e., low bending rigidity K_B). Hence, to strengthen the structural integrity of the boundary, and render it tunable, additional support is required.

The Membrane-Cortex Interface Forms a Composite Material

For our hypothetical biomimetic material, the mechanical properties of the hull could be further improved by combining it with a self-assembling scaffold that binds with high affinity to the flexible hull to form a tri-partite composite: hull, supporting scaffold and the connecting glue (**Figure 2B**, left). As one can easily imagine, size, density and rigidity of the scaffold units will directly affect the material properties of the composite. However, these properties equally rely on the assembly pattern of the scaffold along the hull. For instance, scaffolds formed

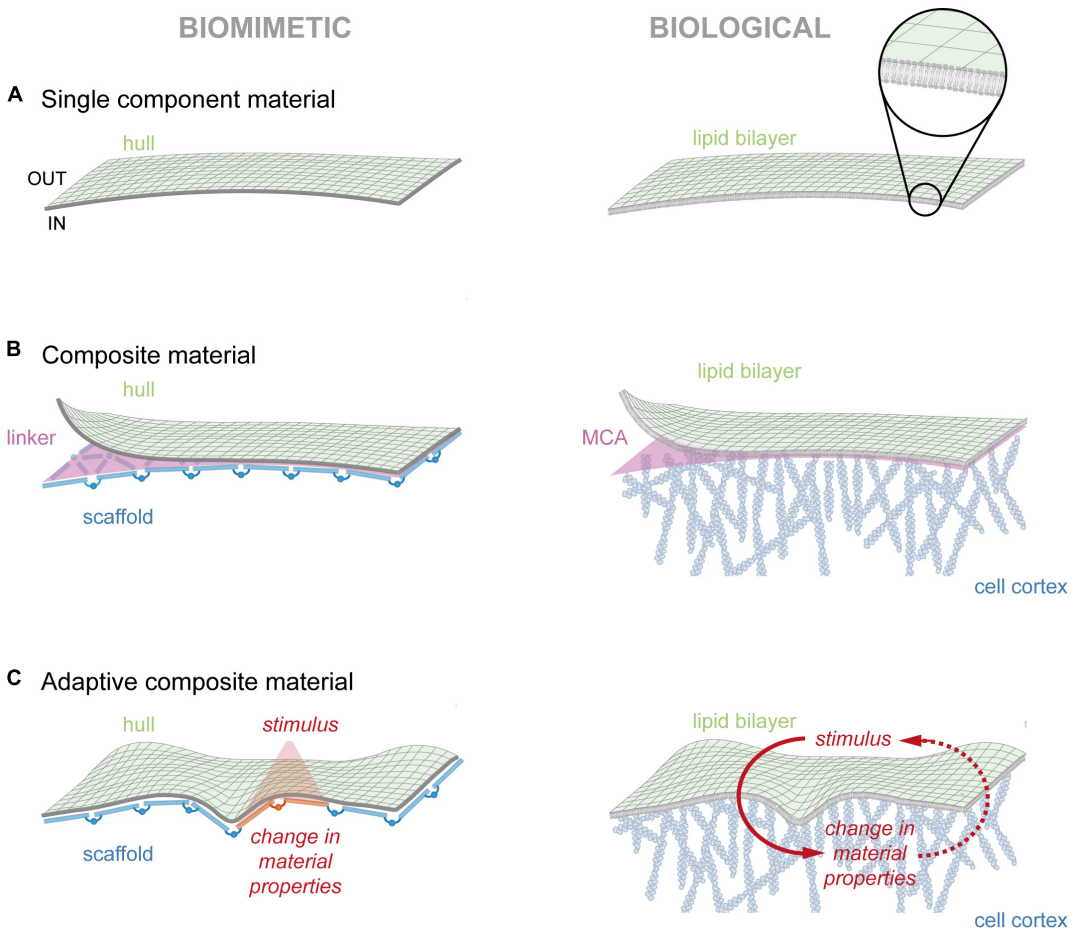

FIGURE 2 | Modules of cellular membrane. **(A)** To the left, hypothetical biomimetic membrane that separates the inside from outside. To the right, the lipid bilayer presents the outermost structure of the cell membrane. Magnification depicts the 5–7 nm thick bilayer composed of individual lipids. **(B)** To the left, hypothetical composite material composed of a flexible hull associated to a rigid scaffold. To the right, the plasma membrane is tightly coupled to the cell cortex, creating a composite material. Individual actin proteins assemble into filaments that are facing the cell membrane with the growing end. **(C)** To the left, hypothetical adaptive composite material that changes material properties upon an external stimulus (red). To the right, the membrane/cortex continuum readily responds to external stimuli (red), reminiscent of an adaptive composite material. Note that changes in actin dynamics can also serve as signal (red, dotted line).

from elongated structures that align along a pre-defined axis will yield polarized (i.e., different) bending moduli along the principal curvatures. In contrast, an omnidirectional assembly of the same structures will produce isotropic mechanical properties. Besides the form of the supporting structure, the spacing between individual subunits also influences the bending stiffness (Naghieh et al., 2018). One such example is agarose gel, which exhibits substantially higher resistance to shear stresses than its primary component water. Hence, by wisely designing the geometry of a supporting structure, or the composition of matrix particles, materials with very diverse mechanical properties may emerge.

A lipid bilayer substantially differs from the cell surface, which is not only stiffer but also displays slower lateral diffusion (Edidin et al., 1991; Shi et al., 2018). This clearly posits the presence of an additional supportive material that interacts with the lipid bilayer. In cells, this composite material is formed through the interaction of the plasma membrane with the cell cortex (**Figure 2B**, right). The cell cortex consist of straight and branched actin filaments that are crosslinked among each other (Mullins et al., 1998), forming a 100–200 nm thick layer at the inner side of the PM (Chugh and Paluch, 2018). In addition to actin, the cell cortex contains, to a lesser degree, intermediate filaments and microtubules (Koning et al., 2008; Singh et al., 2018), providing the ability to exert mechanical forces and change local material properties. Membrane association of the cell cortex is achieved through a specialized protein group, the FERM domain proteins (named after its founding members 4.1 protein, ezrin, radixin, and moesin), which simultaneously bind to lipids and proteins (Chishti et al., 1998). This dynamic interface, also termed membrane-cortex-attachment (Diz-Muñoz et al., 2010), transforms the two separate structures into one composite material. From Eq. 2.2 in **Box 1**, we learn that the energy to buckle a material scales with the thickness cubed. Consequentially, the energy to bend a 200 nm thick cell cortex is orders of magnitude

BOX 1 | Physics at the Cell Surface.

In the following, we consider the cell surface as a plate or shell encapsulating the cytoplasm, following the description by Kamm and Grodzinsky (2015). In general, any deformation can be envisioned as the superposition of three fundamental types of deformation: stretch, bending and shear. Surface tension is defined as the derivation of energy with respect to area, meaning the energy needed to stretch the plate by a certain amount is given by.

$$N = \sigma\, h = \frac{E\, h}{1-\nu}\varepsilon = \frac{E\, h}{2(1-\nu)}\frac{\Delta A}{A_0} = K_e \frac{\Delta A}{A_0}, \tag{2.1}$$

where σ depicts the uniform normal stress, N the in plane tension in force per unit length (N/m), E the elastic modulus (Young's modulus), ν the Poisson ratio, h the plate thickness, ε the strain and K_e the area stretch modulus defined as $K_e = \frac{E\, h}{2(1-\nu)}$. The energy needed to bend a plate of the thickness h in one dimension given by

$$M_x = E_{bend} = -\frac{E\, h^3}{12(1-\nu^2)}\frac{\delta^2 u_z}{\delta x^2} = -K_B \frac{\delta^2 u_z}{\delta x^2}, \tag{2.2}$$

where $\frac{\delta^2 u_z}{\delta x^2}$ depicts the deflection of the plate in z direction and K_B the bending stiffness defined as $K_B = \frac{E\, h^3}{12(1-\nu^2)}$. Elastic materials exhibit resistance against shear deformation arising when the lateral surfaces of the plate are exposed to two different surface tensions. This resistance is given by the shear modulus K_s, with the unit N/m, relating the arising shear force per unit length N_{xy} to the amount of shear deformation, the strain ε_{xy}. The shear force per unit length is the product of the shear stress τ_{xy} times the plate thickness h, which can also be described by the shear modulus G and the shear deformation ε_{xy}. Corresponding to Eq. 2.2 the shear modulus can be expressed by Young's modulus E and the Poisson ratio υ:

$$\sigma_{xy} = \tau_{xy} h = 2G\, \varepsilon_{xy} = \frac{E}{1+\nu}\varepsilon_{xy} = K_s\, \varepsilon_{xy}, \tag{2.3}$$

Considering the cells surrounding, we must apply for thermal fluctuation by adding a random force term $\xi(t)$ and, for the damping of membrane movement by the extracellular fluid, we add a term in form of $\eta_e \frac{\delta u_z}{\delta(t)}$ with the effective viscosity of the surrounding fluid η_e dissipating its energy. Adding thermal fluctuation and energy dissipation due to external fluid damping, neglecting shear stress, yields

$$\Delta p + \xi(t) = K_B\left(\frac{\delta^4 u_z}{\delta x^4} + 2\frac{\delta^4 u_z}{\delta x^2 \delta y^2} + \frac{\delta^4 u_z}{\delta y^4}\right) - N\left(\frac{\delta^2 u_z}{\delta x^2} + \frac{\delta^2 u_z}{\delta y^2}\right) + \eta_e \frac{\delta u_z}{\delta t}, \tag{2.4}$$

which is giving us a more complete picture of the cell membrane behavior. Note that the principle of superposition is only valid for small strains, where linearization is appropriate (e.g., small discretization of time and space). Neglecting all terms except of pressure and surface tension – as it can be appropriate for small curvatures, Eq. 2.4 gives rise to the famous Laplace equation.

$$\Delta p = -N\left(\frac{\delta^2 u_z}{\delta x^2} + \frac{\delta^2 u_z}{\delta y^2}\right) \cong N\left(\frac{1}{R_1} + \frac{1}{R_2}\right). \tag{2.5}$$

Biomaterials often exhibit viscoelastic properties. Therefore, we also have to consider the materials viscosity η. In contrast to the elastic modulus E, the viscosity relates the stress not to the deformation of the material but to the rate of change of the deformation $\frac{d\varepsilon(t)}{dt}$. One way to describe the properties of a viscoelastic solid is the Kelvin-Voigt model (see **Figure 2C**), which can be envisioned by an elastic spring and a viscous damper connected in parallel. The elastic properties of the material are given by the elastic modulus E, and the viscous properties by the viscosity η. The experienced stress σ is then given by

$$\sigma(t) = E\, \varepsilon(t) + \eta \frac{d\varepsilon(t)}{dt}. \tag{2.6}$$

However, the cell surface exhibits the ability of plastic deformation and therefore behaves more like a fluid. Regarding the cell cortex this property arises from the turnover rate of the linking proteins. In contrast to a viscoelastic solid, a viscoelastic fluid can be modeled by a Maxwell body, which can be envisioned by an elastic spring and viscous damper connected in series (see **Figure 2C**). The experienced stress σ is here given by

$$\sigma(t) + \frac{\eta}{E}\frac{\sigma(t)}{dt} = \eta \frac{d\varepsilon(t)}{dt}. \tag{2.7}$$

higher than for a 5–7 nm thin lipid bilayer. Hence, the contribution of the lipid bilayer to the overall cell surface stiffness can be neglected for shape changes at cellular length scales. Intriguingly, the high frequency regime of the fluctuation spectrum of membrane fluctuation assays seems to depend to a large extent on the mechanical properties of the PM (Gárate et al., 2015), suggesting that the membrane is at least partly able to swing freely at small length-scales. Similar high fluctuation modes at the scale of dozens of nanometers were also observed in vesicles (Betz and Sykes, 2012). Thus, the bending stiffness of the cell surface (see **Figure 1A**) is likely dominated by the cell cortex on the cellular level and by a partly unattached PM on sub-micron length scales (Salbreux et al., 2012).

The connection from cell cortex to membrane also affects surface tension (Chugh et al., 2017). The cell membrane is attached to the cortex via linker proteins, which in turn are put under tension by the cortical surface tension N_{cor}, yielding.

$$N_{cor}\frac{2}{R} = \rho_{link} F_{link}, \tag{1.2}$$

where ρ_{link} depicts the linker protein density and F_{link} the force applied by each linker. Using Laplace law (see also **Box 1**, Eq. 2.5), we find.

$$\Delta p = N_{PM}\frac{2}{R} + \rho_{link} F_{link} = (N_{PM} + N_{cor})\frac{2}{R}, \tag{1.3}$$

which means that cell surface tension N_{cell} is the sum of membrane tension N_{PM} and cortical tension N_{cor} (Sens and Plastino, 2015). Let's have a closer look at membrane tension. In a lipid bilayer, local gradients in membrane tension (e.g., induced by rapidly pulling on a tether) equalize over the rest of the membrane in a matter of milliseconds (Shi and Baumgart, 2015), which is reminiscent of a fluid lacking shear stress. This, however, changes as soon as the PM is attached to the cellular cortex. Roughly one quarter of the total PM area is occupied by transmembrane proteins, half of which are connected to the cellular cortex (Bussell et al., 1995). These proteins, if attached to the cell cortex, serve as obstacles that limit membrane flow (u).

$$u = \frac{k}{\eta_{lipid}} \nabla N, \tag{1.4}$$

with Darcy permeability k of a porous medium (i.e., the array of obstacles) and lipid viscosity η_{lipid} (Shi et al., 2018). The lateral permeability k can be described as a function of the area fraction ϕ occupied by the integral proteins and their radius a (Happel, 1959).

$$k \approx -\frac{a^2(1 + \ln(\phi))}{8\phi}. \tag{1.5}$$

Hence, if confined into two dimensions, the flow resistance decreases logarithmically with the distance to the obstacle (rather than exponential). Since the logarithmic function diverges for large distances, the effect will be noticeable no matter how far away from the obstacle we evaluate the system - a phenomenon called the Stokes paradox. The same study further noted that the surface tension of a PM attached to the cell cortex propagate over time in a diffusive manner, given by.

$$\frac{\delta N}{\delta t} = \frac{E\,k}{\eta_{lipid}} \nabla^2 N, \tag{1.6}$$

where E depicts the elastic modulus of the PM and η_{lipid} the viscosity of the lipids (i.e., the fluid's viscosity flowing through these obstacles). Note that Eq. 1.6 exhibits a striking similarity to Fick's second law of diffusion. In their elegant study, Shi and Cohen defined a tension diffusion coefficient D_N

$$D_N = \frac{E\,k}{\eta_{lipid}}, \tag{1.7}$$

yielding

$$\frac{\delta N}{\delta t} = D_N \nabla^2 N. \tag{1.8}$$

Consequently, the cortex bound integral proteins cause local and long lived gradients of membrane tension. It is plausible to envision that cells may locally alter the tension diffusion coefficient through MCA-induced changes in number and position of transmembrane obstacles (i.e., change ϕ). Consistently, recent work showed a positive correlation between membrane-proximal actin density and membrane tension (Bisaria et al., 2020). If and how membrane tension gradients influence cortical tension N_{cor}, and in consequence cell tension N_{cell}, remains elusive.

Finally, let's consider membrane viscosity. PM viscosity differs from the viscosity of a pure lipid bilayer due to the embedded integral membrane proteins (IMPs). For a suspension with no interparticle interactions (i.e., low concentration), the effective viscosity of such a suspension can be approximated by.

$$\mu_e = \mu_0(1 + B\phi), \tag{1.9}$$

where μ_0 is the viscosity of the suspending liquid, ϕ volume fraction of the embedded particles and B a coefficient depending on the particle shape (e.g., spheres, cylinders, disks) (Bird et al., 2007). Hence, it is possible that the attachment, and therefore immobilization of IMPs, may also affect PM viscosity. Despite the existence of some approximations on the effective viscosity (Larson and Higdon, 1986, 1987; Kolodziej, 1988), this complex topic remains unresolved and is beyond the scope of this review (see also **Supplementary Material**). Importantly, the sole plasma membrane exhibits viscous material properties. Attachment of to the PM to the cell cortex (i.e., the cell surface), however, displays a combination of viscous and elastic properties on the cellular length scale (Bausch et al., 1998). This means that on short time scales (i.e., ∼1 s) the cell surface responds like an elastic material, while it shows properties of a viscous material on longer time scales (i.e., 10–100 s). Considering that the cortex consist of interlinked actin filaments, which are subject to continuous turnover of cross-linking proteins and actin filaments, the cell cortex is able to perform plastic deformation reminiscent of a viscoelastic fluid. This behavior can, in its simplest form, be modeled as a Maxwell body (Begemann et al., 2019) described by Eq. 2.7 in **Box 1** (see also **Figure 1C**).

In conclusion, our short survey demonstrates how interactions of membranes with the cell cortex alter the mechanical properties of the PM itself as well as of the cell surface. Yet, despite the versatility in material properties that can be achieved, the resulting composite material at this point still lacks the ability to readily respond to changes from the environment (i.e., adaptive response).

The Cell Surface Is an Adaptive Composite Material

In the form described this far, the composite material will always thrive to adopt the minimal energy state. Strikingly, mechanical properties of membrane and cortex can be separately tuned with high spatial and temporal accuracy, providing the possibility to turn the passive composite into an active material. In our hypothetical composite material, such adaptivity could be achieved by rendering its components sensitive to a transient stimulus (e.g., light, temperature). The response to such a stimulus, which triggers local changes in one (or a combination) of the four essential material properties (**Figure 1A**), yields an adaptive composite material (**Figure 2C**, left).

Following, we will discuss how stimulus-induced transient changes in mechanical properties of membrane or cortex yield an adaptive composite material. We begin with tension. As mentioned above in Eq. 1.3, the tension of the cell surface is the sum of the PM tension and cortex tension, and therefore a

function of the density of linker proteins ρ_{link} and the stretch moduli of the plasma membrane K_e^{PM} and cell cortex K_e^{cor}. These parameters, in turn, rely on the respective elastic moduli E, thickness h, and the Poisson ratio ν (Eq. 2.1, **Box 1**). Hence, signal-induced changes to any of those properties will necessarily influence the cells surface stretch modulus K_e^{cell}. The stretch resistance of the lipid bilayer K_e^{PM}, for instance, arises from energy penalty caused by exposure of the hydrophobic core to the surrounding aqueous solution. It could therefore, in theory, be tuned by changing the membrane lipid composition, which may also effect the membrane thickness h. However, with a modulus of ∼200 mN/m (Rawicz et al., 2000), the lipid bilayer is not a strongly extendable structure, and thus not well suited. Note that most values in literature describe the apparent stretch modulus of the PM, which integrate large scale changes in membrane area originating from membrane undulation, membrane folds, vesicle fusion, the smoothening of membrane fluctuations and other sources (Le Roux et al., 2019). Complementing membrane-based tension, cortex-based tension can be modulated by signal-dependent changes in actin cross-linker density, the MCA (i.e., density of PM-cortex linker proteins ρ_{link}) and cortical myosin (Stewart et al., 2011). In particular, the latter renders the composite material suitable to adaptation on physiological timescales (i.e., order of seconds), whereby lipid composition as well as the cortex geometry (e.g., mesh size) will affect the respective elastic moduli.

Bending Stiffness

As membrane and cortical stiffness critically depend on the length scale, we will consider their contribution separately. The bending stiffness of the PM, which is relevant in the sub-micron regime, depends on the composition of the lipid bilayer (Helfrich, 1973). By changing length and saturation of individual carbohydrate chains, the lipid bilayer thickness, and thereby the bending energy, can be modulated (see Eq. 2.2 in **Box 1**). Adding hydrophobic heads with varying size further renders lipids curvature-sensitive, while differences in charge will influence protein-lipid interactions with peripheral cytosolic proteins (Ebrahimkutty and Galic, 2019; Bassereau et al., 2018). The bending stiffness of the cell cortex, which is relevant in the μm regime, can be influenced by changes to the actin mesh size (depicted by the density of cortex linker proteins) or the thickness of the cortex itself. In addition, signals that change the elastic moduli of both materials (discussed above) will also influence their respective bending rigidities K_B^{PM} and K_B^{cor} (see Eq. 2.2 in **Box 1**).

Shear Resistance and Viscosity

Pure lipid bilayers behave like a fluid void of shear stress (Mofrad and Kamm, 2006). This is not always the case in cellular membranes (Shi et al., 2018). From Eq. 2.3 in **Box 1**, we deduce that all cellular stimuli that influence the shear modulus (and therefore Young's modulus E as well as the Poisson's ratio υ, as discussed above) will also affect the elastic shear stress response of both materials, and therefore also of the cell surface. As the cell cortex as well as the attached PM both exhibit viscoelastic properties, we further have to consider the control variables of the respective viscosities. In case of the cortex, the dominating control variable (i.e., target for adaptive stimuli) are the relative turnover rates of actin and its cross-linkers, as well as the relative mesh size of the cell cortex (Boulbitch et al., 2000; Kasas et al., 2005). Regarding the PM, and recalling the description of Stokes paradox from the previous paragraph, viscosity of the PM could be modulated by signal-induced changes to the total concentration of integral proteins, its spatial distribution (e.g., clustering), and the fraction of cortex bound units.

The findings summarized in this section highlight the manifold strategies for signal-induced changes in individual material properties that render the cell surface an adaptive composite material. How these material properties are changed under pathophysiological conditions is the topic of the following chapter.

FAULTY MATERIAL PROPERTIES CAUSE DISEASE

In any engineered structure, incorporation of faulty materials yields catastrophic consequences for the over-all stability of the object. In cells, such faulty materials manifest as disease. Following, we survey disease arising from individual materials, the resulting composite and its adaptive features, respectively.

As described in the previous section, changes in relative lipid levels within the membrane may not only deplete components involved in signaling, but could also alter its material properties. Mounting evidence exist for changes in lipid balance [e.g., (cholesterol)↑, (sphingomyelin)↑ and (phosphatidylinositol)↓] during aging, but also in lipidosis such as Niemann-Pick disease types A and C (Karten et al., 2002; Arroyo et al., 2014), establishing how mechanical properties of the membrane may be altered in disease.

Intriguingly, faulty materials that lead to disease can also be found in cell cortex proteins. For instance, mutations in smooth muscle α-actin (*ACTA2*), which alter interactions between actin and myosin (Lu et al., 2015), cause vascular disease and stroke (Guo et al., 2009). Mutations in *ACTB*, the gene encoding cytoplasmic β-actin, change actin polymerization dynamics (Hundt et al., 2014), resulting in deafness, cancer and developmental disorders (Procaccio et al., 2006). Mutations in the gene encoding α-actinin-4 (*ACTN4*), an actin cross-linking protein, cause proteinuric kidney disease (Kaplan et al., 2000). Collectively, these few examples illustrate how changes in material properties of cell cortex components yield substantial physiological effects.

Disease can further be traced back to errors of the composite material. As described above, lipid composition determines rigidity and fluidity of membranes. Strikingly, some of these lipids form highly dynamic and heterogeneous membrane nanodomains (Head et al., 2014; Sechi and Wehland, 2000), which can be stabilized to form larger signaling platforms that are associated with actin filaments (Oliferenko et al., 1999; Galic et al., 2012; Begemann et al., 2019). As lipid availability or dynamics is changed in certain disease, the resulting mechanical

properties of the membrane-cortex composite are likely altered in such conditions.

Finally, mutations can also affect the adaptability of the composite. One major family of disease originates from mutations in receptor proteins, which disturb signal-induced changes in material properties of the composite. One such example are G-protein coupled receptors (GPCRs), which alter among others the material properties of the cell cortex (Bhattacharya et al., 2004). Here, mutations cause aberrant signaling by disrupting surface expression (Ward et al., 2012), basal activity (Seifert and Wenzel-Seifert, 2002), or ligand binding (Venkatakrishnan et al., 2013). Furthermore, GPCRs directly interact with lipids, which means that changes in membrane composition or mutations in the lipid-recognition motifs can alter GPCR signaling by changing its stability, subcellular localization or activity (Keri and Barth, 2018; Pucadyil and Chattopadhyay, 2006). Importantly, errors in signal-induced changes in material properties can also be traced back to other receptor families (Jiang and Gonen, 2012; Fruman et al., 2017; Zakany et al., 2020), giving rise to an ever-growing family of membrane-related disease. A second major family of disease that influences the adaptability of the composite material relies on membrane curvature. Here, transiently deformed membrane sections trigger recruitment of curvature-sensitive proteins (Peter et al., 2004) and lipids (Wang et al., 2007; James et al., 2010). Notably, many of the more than 100 known curvature-sensing molecules identified in cells directly alter actin polymerization, thus changing mechanical forces applied to the PM. This dual ability of selected molecules to sense and modify actin-induced PM curvature is important, as it posits the core properties of an adaptive composite material. Consistently, defects of individual force-regulatory feedback loops (e.g., *OPHN1* and *SRGAP2*) result in very specific diseases (Billuart et al., 1998; Charrier et al., 2012).

While by far not complete, these selected examples illustrate how the material properties of individual components critically influence the overall mechanical state of the cell surface – both, in health and disease. How the mechanical properties of this versatile adaptive composite material are measured will be discussed in the next section.

MEASURING MATERIAL PROPERTIES IN CELLULAR MEMBRANES

The picture drawn this far depicts the importance of a functioning interplay between cortex, membrane and MCA. Considering its small scale, separating cell cortex from membranes in living cells is a challenging task (Diz-Muñoz et al., 2018). To gain insights into membrane tension, previous studies have taken advantage of pipets and optical tweezers to measure the force needed to extract a membrane tether from the cell surface (Raucher and Sheetz, 2000). Another approach relies on time-resolved membrane fluctuation spectroscopy (Betz and Sykes, 2012). Here, an optical tweezer is being used to measure membrane deformations rather than to pull tethers. In such measurements, the power spectral density of low-frequency fluctuations drops as tension increases (Betz and Sykes, 2012). Notably, fluctuation spectroscopy can also be used to gain insights into bending rigidity and viscosity of the material (Betz and Sykes, 2012). Quantitative measurements on membrane viscosity can also be acquired using high-throughput single molecule tracking or fluorescence correlation spectroscopy (Barbotin et al., 2019).

Yet, as mentioned above, changes in cortex bound protein spacing will affect membrane fluidity (Cohen and Shi, 2020). Hence, measurements from tether pulling and membrane fluctuation present a convolute of membrane and cell cortex properties (Shi et al., 2018). Thus, while each of these approaches allows exciting novel insights into the mechanical properties of cell membranes, it remains a challenging task to unequivocally dissect the contribution of the individual components of the composite material.

CONCLUSION AND OUTLOOK

Seminal work one pure lipid bilayers, which are the topic of other reviews in this special issue, have substantially contributed to our current understanding of membrane mechanics. Yet recent studies argue that some cellular membranes should be considered an adaptive composite material (Shi et al., 2018; Cohen and Shi, 2020). In this review, we used a hypothetical biomimetic material to elucidate the astounding versatility of cellular membranes. We discussed how small changes in the mechanical properties of individual core modules allow the material to readily adapt its properties, thus fulfilling highly diverse functions, while relying on the same building materials. Strikingly, the composite nature of the cell surface not only allows cellular membranes to rapidly adjust its mechanical properties to the given situation, but also provides explanations to disease and some seemingly contradicting properties of the cell surface. One such example is the need for efficient transport of large objects across the cell cortex, while maintaining structural integrity at all times (Wollman and Meyer, 2012). As mentioned above, the lipid-cortex interface largely relies on non-covalent interactions. In consequence, the cytoskeleton continuously de- and reattaches from the lipid bilayer. These transient detachments not only open up the possibility to readily adjust interactions, but also the ability to transport and fuse vesicles (i.e., large objects) without permanent detachment of the plasma membrane from the underlying cortex.

Using the analogy of a hypothetical biomimetic material we realize that man-made materials still lag far behind its biological counterparts. It is encouraging, however, that this opportunity has been recognized, nucleating a rapidly growing research field (Amaral and Pasparakis, 2019; Chen and Li, 2020). Future advancements into bioinspired and biomimetic material will likely benefit from computational approaches (Sun et al., 2018; Schroer et al., 2020), which allow rapid advancement of theoretical and experimental data of membrane-MCA-cortex dynamics at an ever-increasing spatio-temporal resolution.

AUTHOR CONTRIBUTIONS

Both authors listed have made a substantial, direct and intellectual contribution to the work, and approved it for publication.

FUNDING

This work was supported by funds from the DFG (EXC-1003, CRC1348/A06) and the Faculty of Medicine of the University of Muenster to MG (IMF IGA-121610).

ACKNOWLEDGMENTS

We would like to thank members of the Galic lab for critical feedback and discussion.

SUPPLEMENTARY MATERIAL

The Supplementary Material for this article can be found online at: https://www.frontiersin.org/articles/10.3389/fcell.2020.00684/full#supplementary-material

REFERENCES

Amaral, A. J. R., and Pasparakis, G. (2019). Cell membrane engineering with synthetic materials: applications in cell spheroids, cellular glues and microtissue formation. *Acta Biomater.* 90, 21–36. doi: 10.1016/j.actbio.2019.04.013

Arroyo, A. I., Camoletto, P. G., Morando, L., Sassoe-Pognetto, M., Giustetto, M., van Veldhoven, P. P., et al. (2014). Pharmacological reversion of sphingomyelin-induced dendritic spine anomalies in a Niemann Pick disease type A mouse model. *EMBO Mol. Med.* 6, 398–413. doi: 10.1002/emmm.201302649

Barbotin, A., Galiani, S., Urbanèiè, I., Eggeling, C., and Booth, M. J. (2019). Adaptive optics allows STED-FCS measurements in the cytoplasm of living cells. *Opt. Express* 27, 23378–23395. doi: 10.1364/OE.27.023378

Bassereau, P., Jin, R., Baumgart, T., Deserno, M., Dimova, R., Frolov, V. A., et al. (2018). The 2018 biomembrane curvature and remodeling roadmap. *J. Phys. D Appl. Phys.* 51:343001. doi: 10.1088/1361-6463/aacb98

Baumgart, T., Hess, S. T., and Webb, W. W. (2003). Imaging coexisting fluid domains in biomembrane models coupling curvature and line tension. *Nature* 425, 821–824. doi: 10.1038/nature02013

Bausch, A. R., Ziemann, F., Boulbitch, A. A., Jacobson, K., and Sackmann, E. (1998). Local measurements of viscoelastic parameters of adherent cell surfaces by magnetic bead microrheometry. *Biophys. J.* 75, 2038–2049. doi: 10.1016/S0006-3495(98)77646-5

Begemann, I., Saha, T., Lamparter, L., Rathmann, I., Grill, D., Golbach, L., et al. (2019). Mechanochemical self-organization determines search pattern in migratory cells. *Nat. Phys.* 15, 848–857. doi: 10.1038/s41567-019-0505-9

Betz, T., and Sykes, C. (2012). Time resolved membrane fluctuation spectroscopy. *Soft Matter* 8, 5317–5326. doi: 10.1039/C2SM00001F

Bhattacharya, M., Babwah, A. V., and Ferguson, S. S. G. (2004). Small GTP-binding protein-coupled receptors. *Biochem. Soc. Trans.* 32(Pt 6), 1040–1044. doi: 10.1042/BST0321040

Billuart, P., Bienvenu, T., Ronce, N., Des Portes, V., Vinet, M. C., Zemni, R., et al. (1998). Oligophrenin-1 encodes a rhoGAP protein involved in X-linked mental retardation. *Nature* 392, 923–926. doi: 10.1038/31940

Bird, R. B., Stewart, W. E., and Lightfoot, E. N. (2007). *Transport Phenomena (Rev. 2. ed.)*. Hoboken, NJ: Wiley.

Bisaria, A., Hayer, A., Garbett, D., Cohen, D., and Meyer, T. (2020). Membrane-proximal F-actin restricts local membrane protrusions and directs cell migration. *Science* 368, 1205–1210. doi: 10.1126/science.aay7794

Boulbitch, A., Simson, R., Simson, D. A., Merkel, R., Häckl, W., Bärmann, M., et al. (2000). Shape instability of a biomembrane driven by a local softening of the underlying actin cortex. *Phys. Rev. E Stat. Phys. Plasmas Fluids Relat. Interdiscip. Top.* 62(3 Pt B), 3974–3985. doi: 10.1103/physreve.62.3974

Bussell, S. J., Koch, D. L., and Hammer, D. A. (1995). Effect of hydrodynamic interactions on the diffusion of integral membrane proteins: tracer diffusion in organelle and reconstituted membranes. *Biophys. J.* 68, 1828–1835. doi: 10.1016/S0006-3495(95)80359-0

Carpenter, G., King, L., and Cohen, S. (1978). Epidermal growth factor stimulates phosphorylation in membrane preparations in vitro. *Nature* 276, 409–410. doi: 10.1038/276409a0

Charrier, C., Joshi, K., Coutinho-Budd, J., Kim, J.-E., Lambert, N., Marchena, J., et al. (2012). Inhibition of SRGAP2 function by its human-specific paralogs induces neoteny during spine maturation. *Cell* 149, 923–935. doi: 10.1016/j.cell.2012.03.034

Chen, X., and Li, J. (2020). Bioinspired by cell membranes: functional polymeric materials for biomedical applications. *Mater. Chem. Front.* 4, 750–774. doi: 10.1039/C9QM00717B

Chen, Z., Atefi, E., and Baumgart, T. (2016). Membrane shape instability induced by protein crowding. *Biophys. J.* 111, 1823–1826. doi: 10.1016/j.bpj.2016.09.039

Chishti, A. H., Kim, A. C., Marfatia, S. M., Lutchman, M., Hanspal, M., Jindal, H., et al. (1998). The FERM domain: a unique module involved in the linkage of cytoplasmic proteins to the membrane. *Trends Biochem. Sci.* 23, 281–282. doi: 10.1016/S0968-0004(98)01237-7

Chugh, P., Clark, A. G., Smith, M. B., Cassani, D. A. D., Dierkes, K., Ragab, A., et al. (2017). Actin cortex architecture regulates cell surface tension. *Nat. Cell Biol.* 19, 689–697. doi: 10.1038/ncb3525

Chugh, P., and Paluch, E. K. (2018). The actin cortex at a glance. *J. Cell Sci.* 131:jcs186254. doi: 10.1242/jcs.186254

Cohen, A. E., and Shi, Z. (2020). Do cell membranes flow like honey or jiggle like jello? *BioEssays* 42:e1900142. doi: 10.1002/bies.201900142

Contreras, F.-X., Ernst, A. M., Wieland, F., and Brügger, B. (2011). Specificity of intramembrane protein-lipid interactions. *Cold Spring Harb. Perspect. Biol.* 3:a004705. doi: 10.1101/cshperspect.a004705

Diz-Muñoz, A., Krieg, M., Bergert, M., Ibarlucea-Benitez, I., Muller, D. J., Paluch, E., et al. (2010). Control of directed cell migration in vivo by membrane-to-cortex attachment. *PLoS Biol.* 8:e1000544. doi: 10.1371/journal.pbio.1000544

Diz-Muñoz, A., Weiner, O. D., and Fletcher, D. A. (2018). In pursuit of the mechanics that shape cell surfaces. *Nat. Phys.* 14, 648–652. doi: 10.1038/s41567-018-0187-8

Ebrahimkutty, M. P., and Galic, M. (2019). Receptor-free signaling at curved cellular membranes. *BioEssays* 41:e1900068. doi: 10.1002/bies.201900068

Edidin, M., Kuo, S. C., and Sheetz, M. P. (1991). Lateral movements of membrane glycoproteins restricted by dynamic cytoplasmic barriers. *Science* 254, 1379–1382. doi: 10.1126/science.1835798

Eggeling, C., Ringemann, C., Medda, R., Schwarzmann, G., Sandhoff, K., Polyakova, S., et al. (2009). Direct observation of the nanoscale dynamics of membrane lipids in a living cell. *Nature* 457, 1159–1162. doi: 10.1038/nature07596

Estep, T. N., Mountcastle, D. B., Barenholz, Y., Biltonen, R. L., and Thompson, T. E. (1979). Thermal behavior of synthetic sphingomyelin-cholesterol dispersions. *Biochemistry* 18, 2112–2117. doi: 10.1021/bi00577a042

Evans, E., and Rawicz, W. (1990). Entropy-driven tension and bending elasticity in condensed-fluid membranes. *Phys. Rev. Lett.* 64, 2094–2097. doi: 10.1103/PhysRevLett.64.2094

Faucon, J. F., Mitov, M. D., Méléard, P., Bivas, I., and Bothorel, P. (1989). Bending elasticity and thermal fluctuations of lipid membranes. Theoretical and experimental requirements. *J. Phys.* 50, 2389–2414. doi: 10.1051/jphys:0198900500170238900

Fruman, D. A., Chiu, H., Hopkins, B. D., Bagrodia, S., Cantley, L. C., and Abraham, R. T. (2017). The PI3K pathway in human disease. *Cell* 170, 605–635. doi: 10.1016/j.cell.2017.07.029

Galic, M., Jeong, S., Tsai, F.-C., Joubert, L.-M., Wu, Y. I, Hahn, K. M., et al. (2012). External push and internal pull forces recruit curvature-sensing N-BAR domain proteins to the plasma membrane. *Nat. Cell Biol.* 14, 874–881. doi: 10.1038/ncb2533

Gárate, F., Betz, T., Pertusa, M., and Bernal, R. (2015). Time-resolved neurite mechanics by thermal fluctuation assessments. *Phys. Biol.* 12:66020. doi: 10.1088/1478-3975/12/6/066020

Graber, Z. T., Shi, Z., and Baumgart, T. (2017). Cations induce shape remodeling of negatively charged phospholipid membranes. *Phys. Chem. Chem. Phys.* 19, 15285–15295. doi: 10.1039/c7cp00718c

Guo, D.-C., Papke, C. L., van Tran-Fadulu Regalado, E. S., Avidan, N., Johnson, R. J., Kim, D. H., et al. (2009). Mutations in smooth muscle alpha-actin (ACTA2) cause coronary artery disease, stroke, and Moyamoya disease, along with thoracic aortic disease. *Am. J. Hum. Genet.* 84, 617–627. doi: 10.1016/j.ajhg.2009.04.007

Hallett, F. R., Marsh, J., Nickel, B. G., and Wood, J. M. (1993). Mechanical properties of vesicles. II. A model for osmotic swelling and lysis. *Biophys. J.* 64, 435–442. doi: 10.1016/S0006-3495(93)81384-5

Hancock, J. F., Magee, A. I., Childs, J. E., and Marshall, C. J. (1989). All ras proteins are polyisoprenylated but only some are palmitoylated. *Cell* 57, 1167–1177. doi: 10.1016/0092-8674(89)90054-8

Happel, J. (1959). Viscous flow relative to arrays of cylinders. *AIChE J.* 5, 174–177. doi: 10.1002/aic.690050211

Head, B. P., Patel, H. H., and Insel, P. A. (2014). Interaction of membrane/lipid rafts with the cytoskeleton: impact on signaling and function: membrane/lipid rafts, mediators of cytoskeletal arrangement and cell signaling. *Biochim. Biophys. Acta* 1838, 532–545. doi: 10.1016/j.bbamem.2013.07.018

Helfrich, W. (1973). Elastic properties of lipid bilayers: theory and possible experiments. *Z. Nat. Teil C Biochem. Biophys. Biol. Virol.* 28, 693–703. doi: 10.1515/znc-1973-11-1209

Huang, C., and Thompson, T. E. (1965). Properties of lipid bilayer membranes separating two aqueous phases: determination of membrane thickness. *J. Mol. Biol.* 13, 183–193. doi: 10.1016/S0022-2836(65)80088-2

Huber, F., Schnauß, J., Rönicke, S., Rauch, P., Müller, K., Fütterer, C., et al. (2013). Emergent complexity of the cytoskeleton: from single filaments to tissue. *Adv. Phys.* 62, 1–112. doi: 10.1080/00018732.2013.771509

Hundt, N., Preller, M., Swolski, O., Ang, A. M., Mannherz, H. G., Manstein, D. J., et al. (2014). Molecular mechanisms of disease-related human β-actin mutations p.R183w and p.E364k. *FEBS J.* 281, 5279–5291. doi: 10.1111/febs.13068

Huxley, A. F., and Simmons, R. M. (1971). Proposed mechanism of force generation in striated muscle. *Nature* 233, 533–538. doi: 10.1038/233533a0

James, D. J., Khodthong, C., Kowalchyk, J. A., and Martin, T. F. J. (2010). Phosphatidylinositol 4,5-bisphosphate regulation of SNARE function in membrane fusion mediated by CAPS. *Adv. Enzyme Regul.* 50, 62–70. doi: 10.1016/j.advenzreg.2009.10.012

Jiang, Q.-X., and Gonen, T. (2012). The influence of lipids on voltage-gated ion channels. *Curr. Opin. Struct. Biol.* 22, 529–536. doi: 10.1016/j.sbi.2012.03.009

Kamm, R., and Grodzinsky, A. (2015). *Molecular, Cellular, and Tissue Biomechanics*. Cambridge, MA: Massachusetts Institute of Technology.

Kaplan, J. M., Kim, S. H., North, K. N., Rennke, H., Correia, L. A., Tong, H. Q., et al. (2000). Mutations in ACTN4, encoding alpha-actinin-4, cause familial focal segmental glomerulosclerosis. *Nat. Genet.* 24, 251–256. doi: 10.1038/73456

Karten, B., Vance, D. E., Campenot, R. B., and Vance, J. E. (2002). Cholesterol accumulates in cell bodies, but is decreased in distal axons, of Niemann-Pick C1-deficient neurons. *J. Neurochem.* 83, 1154–1163. doi: 10.1046/j.1471-4159.2002.01220.x

Kasas, S., Wang, X., Hirling, H., Marsault, R., Huni, B., Yersin, A., et al. (2005). Superficial and deep changes of cellular mechanical properties following cytoskeleton disassembly. *Cell Motil. Cytoskeleton* 62, 124–132. doi: 10.1002/cm.20086

Keri, D., and Barth, P. (2018). Reprogramming G protein coupled receptor structure and function. *Curr. Opin. Struct. Biol.* 51, 187–194. doi: 10.1016/j.sbi.2018.07.008

Kolodziej, J. A. (1988). Influence of the porosity of a porous medium on the effective viscosity in Brinkman's filtration equation. *Acta Mech.* 75, 241–254. doi: 10.1007/BF01174638

Koning, R. I., Zovko, S., Bárcena, M., Oostergetel, G. T., Koerten, H. K., Galjart, N., et al. (2008). Cryo electron tomography of vitrified fibroblasts: microtubule plus ends in situ. *J. Struct. Biol.* 161, 459–468. doi: 10.1016/j.jsb.2007.08.011

Laganowsky, A., Reading, E., Allison, T. M., Ulmschneider, M. B., Degiacomi, M. T., Baldwin, A. J., et al. (2014). Membrane proteins bind lipids selectively to modulate their structure and function. *Nature* 510, 172–175. doi: 10.1038/nature13419

Larson, R. E., and Higdon, J. J. L. (1986). Microscopic flow near the surface of two-dimensional porous media. Part 1. Axial flow. *J. Fluid Mech.* 166, 449–472. doi: 10.1017/S0022112086000228

Larson, R. E., and Higdon, J. J. L. (1987). Microscopic flow near the surface of two-dimensional porous media. Part 2. Transverse flow. *J. Fluid Mech.* 178, 119–136. doi: 10.1017/S0022112087001149

Le Roux, A.-L., Quiroga, X., Walani, N., Arroyo, M., and Roca-Cusachs, P. (2019). The plasma membrane as a mechanochemical transducer. *Philos. Trans. R. Soc. Lond. Ser. B Biol. Sci.* 374:20180221. doi: 10.1098/rstb.2018.0221

Lu, H., Fagnant, P. M., Bookwalter, C. S., Joel, P., and Trybus, K. M. (2015). Vascular disease-causing mutation R258C in ACTA2 disrupts actin dynamics and interaction with myosin. *Proc. Natl. Acad. Sci. U.S.A.* 112, E4168–E4177. doi: 10.1073/pnas.1507587112

Lundberg, E., and Borner, G. H. H. (2019). Spatial proteomics: a powerful discovery tool for cell biology. *Nat. Rev. Mol. Cell Biol.* 20, 285–302. doi: 10.1038/s41580-018-0094-y

Meyers, M. A., and Chawla, K. K. (2010). *Mechanical Behavior of Materials*, 2nd Edn. Cambridge, MA: Cambridge University Press.

Mofrad, M. R. K., and Kamm, R. D. (2006). *Cytoskeletal Mechanics: Models and Measurements in Cell Mechanics. Cambridge Texts in Biomedical Engineering*. Cambridge, MA: Cambridge University Press.

Mullins, R. D., Heuser, J. A., and Pollard, T. D. (1998). The interaction of Arp2/3 complex with actin: nucleation, high affinity pointed end capping, and formation of branching networks of filaments. *Proc. Natl. Acad. Sci. U.S.A.* 95, 6181–6186. doi: 10.1073/pnas.95.11.6181

Naghieh, S., Sarker, M., Karamooz-Ravari, M., McInnes, A., and Chen, X. (2018). Modeling of the mechanical behavior of 3d bioplotted scaffolds considering the penetration in interlocked strands. *Appl. Sci.* 8:1422. doi: 10.3390/app8091422

Nernst, W. H. (1889). *The Electromotoric Effectiveness of Ions*. Habilitation Thesis, University of Tübingen, Tübingen.

Nicolson, G. L. (2014). The fluid-mosaic model of membrane structure: still relevant to understanding the structure, function and dynamics of biological membranes after more than 40 years. *Biochim. Biophys. Acta* 1838, 1451–1466. doi: 10.1016/j.bbamem.2013.10.019

Olbrich, K., Rawicz, W., Needham, D., and Evans, E. (2000). Water permeability and mechanical strength of polyunsaturated lipid bilayers. *Biophys. J.* 79, 321–327. doi: 10.1016/S0006-3495(00)76294-1

Oliferenko, S., Paiha, K., Harder, T., Gerke, V., Schwärzler, C., Schwarz, H., et al. (1999). Analysis of Cd44-containing lipid rafts: recruitment of annexin II and stabilization by the actin cytoskeleton. *J. Cell Biol.* 146, 843–854.

Peskin, C. S., Odell, G. M., and Oster, G. F. (1993). Cellular motions and thermal fluctuations: the Brownian ratchet. *Biophys. J.* 65, 316–324. doi: 10.1016/S0006-3495(93)81035-X

Peter, B. J., Kent, H. M., Mills, I. G., Vallis, Y., Butler, P. J. G., Evans, P. R., et al. (2004). Bar domains as sensors of membrane curvature: the amphiphysin BAR structure. *Science* 303, 495–499. doi: 10.1126/science.1092586

Procaccio, V., Salazar, G., Ono, S., Styers, M. L., Gearing, M., Davila, A., et al. (2006). A mutation of beta -actin that alters depolymerization dynamics is associated with autosomal dominant developmental malformations, deafness, and dystonia. *Am. J. Hum. Genet.* 78, 947–960. doi: 10.1086/504271

Pucadyil, T. J., and Chattopadhyay, A. (2006). Role of cholesterol in the function and organization of G-protein coupled receptors. *Prog. Lipid Res.* 45, 295–333. doi: 10.1016/j.plipres.2006.02.002

Raucher, D., and Sheetz, M. P. (2000). Cell spreading and lamellipodial extension rate is regulated by membrane tension. *J. Cell Biol.* 148, 127–136. doi: 10.1083/jcb.148.1.127

Rawicz, W., Olbrich, K. C., McIntosh, T., Needham, D., and Evans, E. (2000). Effect of chain length and unsaturation on elasticity of lipid bilayers. *Biophys. J.* 79, 328–339.

Salbreux, G., Charras, G., and Paluch, E. (2012). Actin cortex mechanics and cellular morphogenesis. *Trends Cell Biol.* 22, 536–545. doi: 10.1016/j.tcb.2012.07.001

Schroer, C. F. E., Baldauf, L., van Buren, L., Wassenaar, T. A., Melo, M. N., Koenderink, G. H., et al. (2020). Charge-dependent interactions of monomeric and filamentous actin with lipid bilayers. *Proc. Natl. Acad. Sci. U.S.A.* 117, 5861–5872. doi: 10.1073/pnas.1914884117

Sechi, A. S., and Wehland, J. (2000). The actin cytoskeleton and plasma membrane connection: ptdins(4,5)P(2) influences cytoskeletal protein activity at the plasma membrane. *J. Cell Sci.* 113(Pt 21), 3685–3695.

Seidel, A., Lepenies, I., Engler, T., Cherif, C., and Zastrau, B. W. (2009). Aspects of creep behavior of textile reinforcements for composite materials. *Open Mater. Sci. J.* 3, 67–79. doi: 10.2174/1874088X00903010067

Seifert, R., and Wenzel-Seifert, K. (2002). Constitutive activity of G-protein-coupled receptors: cause of disease and common property of wild-type receptors. *Naunyn Schmiedeberg's Arch. Pharmacol.* 366, 381–416. doi: 10.1007/s00210-002-0588-0

Sens, P., and Plastino, J. (2015). Membrane tension and cytoskeleton organization in cell motility. *J. Phys.* 27:273103. doi: 10.1088/0953-8984/27/27/273103

Shi, Z., and Baumgart, T. (2015). Membrane tension and peripheral protein density mediate membrane shape transitions. *Nat. Commun.* 6:5974. doi: 10.1038/ncomms6974

Shi, Z., Graber, Z. T., Baumgart, T., Stone, H. A., and Cohen, A. E. (2018). Cell membranes resist flow. *Cell* 175, 1769.e13–1779.e13. doi: 10.1016/j.cell.2018.09.054

Singer, S. J., and Nicolson, G. L. (1972). The fluid mosaic model of the structure of cell membranes. *Science* 175, 720–731. doi: 10.1126/science.175.4023.720

Singh, A., Saha, T., Begemann, I., Ricker, A., Nüsse, H., Thorn-Seshold, O., et al. (2018). Polarized microtubule dynamics directs cell mechanics and coordinates forces during epithelial morphogenesis. *Nat. Cell Biol.* 20, 1126–1133. doi: 10.1038/s41556-018-0193-1

Stewart, M. P., Helenius, J., Toyoda, Y., Ramanathan, S. P., Muller, D. J., and Hyman, A. A. (2011). Hydrostatic pressure and the actomyosin cortex drive mitotic cell rounding. *Nature* 469, 226–230. doi: 10.1038/nature09642

Sugimoto, Y., Whitman, M., Cantley, L. C., and Erikson, R. L. (1984). Evidence that the Rous sarcoma virus transforming gene product phosphorylates phosphatidylinositol and diacylglycerol. *Proc. Natl. Acad. Sci. U.S.A.* 81, 2117–2121. doi: 10.1073/pnas.81.7.2117

Sun, F., Schroer, C. F. E., Xu, L., Yin, H., Marrink, S. J., and Luo, S.-Z. (2018). Molecular dynamics of the association of L-selectin and FERM regulated by PIP2. *Biophys. J.* 114, 1858–1868. doi: 10.1016/j.bpj.2018.02.034

Svitkina, T. M. (2020). Actin cell cortex: structure and molecular organization. *Trends Cell Biol.* 30, 556–565. doi: 10.1016/j.tcb.2020.03.005

van Meer, G., Voelker, D. R., and Feigenson, G. W. (2008). Membrane lipids: where they are and how they behave. *Nat. Rev. Mol. Cell Biol.* 9, 112–124. doi: 10.1038/nrm2330

Vasanji, A., Ghosh, P. K., Graham, L. M., Eppell, S. J., and Fox, P. L. (2004). Polarization of plasma membrane microviscosity during endothelial cell migration. *Dev. Cell* 6, 29–41. doi: 10.1016/s1534-5807(03)00397-6

Venkatakrishnan, A. J., Deupi, X., Lebon, G., Tate, C. G., Schertler, G. F., and Babu, M. M. (2013). Molecular signatures of G-protein-coupled receptors. *Nature* 494, 185–194. doi: 10.1038/nature11896

Wang, W., Yang, L., and Huang, H. W. (2007). Evidence of cholesterol accumulated in high curvature regions: implication to the curvature elastic energy for lipid mixtures. *Biophys. J.* 92, 2819–2830. doi: 10.1529/biophysj.106.097923

Ward, N.-A., Hirst, S., Williams, J., and Findlay, J. B. C. (2012). Pharmacological chaperones increase the cell-surface expression of intracellularly retained mutants of the melanocortin 4 receptor with unique rescuing efficacy profiles. *Biochem. Soc. Trans.* 40, 717–720. doi: 10.1042/BST20110764

Waugh, R., and Evans, E. A. (1979). Thermoelasticity of red blood cell membrane. *Biophys. J.* 26, 115–131. doi: 10.1016/S0006-3495(79)85239-X

Westkämper, E., and Warnecke, H.-J. (2011). *Einführung in die Fertigungstechnik (8., aktualis. u. erw. Aufl., korr. Nachdr)*. Cham: Vieweg + Teubner.

Wollman, R., and Meyer, T. (2012). Coordinated oscillations in cortical actin and Ca2+ correlate with cycles of vesicle secretion. *Nat. Cell Biol.* 14, 1261–1269. doi: 10.1038/ncb2614

Zakany, F., Kovacs, T., Panyi, G., and Varga, Z. (2020). Direct and indirect cholesterol effects on membrane proteins with special focus on potassium channels. *Biochim. Biophys. Acta Mol. Cell Biol. Lipids* 1865:158706. doi: 10.1016/j.bbalip.2020.158706

Conflict of Interest: The authors declare that the research was conducted in the absence of any commercial or financial relationships that could be construed as a potential conflict of interest.

frontiers in Cell and Developmental Biology

ORIGINAL RESEARCH
published: 11 August 2020
doi: 10.3389/fcell.2020.00767

Variations in Plasma Membrane Topography Can Explain Heterogenous Diffusion Coefficients Obtained by Fluorescence Correlation Spectroscopy

Astrid Gesper[1], Stefan Wennmalm[2], Philipp Hagemann[1], Sven-Göran Eriksson[3], Patrick Happel[1†] and Ingela Parmryd[3†]*

[1] RUBION, Ruhr-Universität Bochum, Bochum, Germany, [2] SciLifeLab, Royal Institute of Technology, Stockholm, Sweden, [3] Institute of Biomedicine, University of Gothenburg, Gothenburg, Sweden

OPEN ACCESS

Edited by:
Rainer A. Böckmann,
University of Erlangen-Nuremberg,
Germany

Reviewed by:
Christian Stock,
University of Münster, Germany
Alessandro Alaimo,
University of Trento, Italy
Gerhard J. Schütz,
Vienna University of Technology,
Austria

***Correspondence:**
Ingela Parmryd
ingela.parmryd@gu.se

[†] These authors have contributed equally to this work

Specialty section:
This article was submitted to Cellular Biochemistry, a section of the journal Frontiers in Cell and Developmental Biology

Received: 30 April 2020
Accepted: 21 July 2020
Published: 11 August 2020

Citation:
Gesper A, Wennmalm S, Hagemann P, Eriksson S-G, Happel P and Parmryd I (2020) Variations in Plasma Membrane Topography Can Explain Heterogenous Diffusion Coefficients Obtained by Fluorescence Correlation Spectroscopy. Front. Cell Dev. Biol. 8:767. doi: 10.3389/fcell.2020.00767

Fluorescence correlation spectroscopy (FCS) is frequently used to study diffusion in cell membranes, primarily the plasma membrane. The diffusion coefficients reported in the plasma membrane of the same cell type and even within single cells typically display a large spread. We have investigated whether this spread can be explained by variations in membrane topography throughout the cell surface, that changes the amount of membrane in the FCS focal volume at different locations. Using FCS, we found that diffusion of the membrane dye DiI in the apical plasma membrane was consistently faster above the nucleus than above the cytoplasm. Using live cell scanning ion conductance microscopy (SICM) to obtain a topography map of the cell surface, we demonstrate that cell surface roughness is unevenly distributed with the plasma membrane above the nucleus being the smoothest, suggesting that the difference in diffusion observed in FCS is related to membrane topography. FCS modeled on simulated diffusion in cell surfaces obtained by SICM was consistent with the FCS data from live cells and demonstrated that topography variations can cause the appearance of anomalous diffusion in FCS measurements. Furthermore, we found that variations in the amount of the membrane marker DiD, a proxy for the membrane, but not the transmembrane protein TCRζ or the lipid-anchored protein Lck, in the FCS focal volume were related to variations in diffusion times at different positions in the plasma membrane. This relationship was seen at different positions both at the apical cell and basal cell sides. We conclude that it is crucial to consider variations in topography in the interpretation of FCS results from membranes.

Keywords: diffusion, fluorescence correlation spectroscopy, membrane topography, plasma membrane, scanning ion conductance microscopy

INTRODUCTION

In diffusion studies of membrane molecules with optical techniques, a common assumption is that the membrane is both flat and aligned with the imaging plane. This is a reasonable assumption for supported lipid bilayers (Machan and Hof, 2010), but highly unlikely for biological membranes. The wealth of images from cytoskeletal studies do not show flat cell surfaces and an assumption of flat cell membranes is both surprising and somewhat difficult to justify. Although rarely acknowledged in studies on cells, it has been demonstrated that the global curvature of a membrane will affect diffusion measurements (Holyst et al., 1999; Faraudo, 2002). How we perceive cellular processes like cell signaling, cell adhesion and molecular clustering is also affected by membrane topography (Owen et al., 2013; Parmryd and Onfelt, 2013; Dinic et al., 2015; Jung et al., 2016; Cai et al., 2017).

In the analysis of data from widespread methods employed for diffusion studies of membrane components like fluorescence correlation spectroscopy (FCS), fluorescence recovery after photobleaching (FRAP), and single particle tracking (SPT) it is still assumed that the membrane is locally flat and aligned with the imaging plane. The associated data underpins elaborate membrane models including hop diffusion (Fujiwara et al., 2002), transient anchorage (Chen et al., 2006), and fixed obstacles (Nicolau et al., 2007) to explain non-Brownian diffusion. While it is possible that membrane organization might correspond to these models, non-flat surfaces alone can create the appearance of anomalous diffusion – something we have previously demonstrated for SPT-analysis (Adler et al., 2010, 2019).

In FCS, fluctuations of fluorescence in a focal volume are analyzed and provide information about several parameters including the diffusion coefficient. When FCS is performed in a membrane, the membrane must be flat and perpendicular to the excitation light (**Figure 1A**), for the unmodified and commonly used autocorrelation function to correctly describe the data (Malchus and Weiss, 2010). Whenever these criteria are not met, the rate of diffusion is underestimated since the molecules in the membrane may have traveled much further than assumed while remaining in the focal volume (**Figure 1B**). This has been demonstrated in simulations of folded membranes mimicking the highly convoluted ER and Golgi apparatus (Weiss et al., 2003). Importantly, variations in topography in combination with cells being dynamic could help explain the generally big spread of FCS-measurements for the same cell type.

Scanning ion conductance microscopy (SICM; Hansma et al., 1989) is a non-contact surface scanning technique suitable for imaging the topography of live cells, as reviewed in Happel et al. (2012). In an extensive study covering a wide range of cell types examined live, it was demonstrated that all cell types had extensive topography with ridges, undulations and projections and none could be described as flat (Adler et al., 2010).

More recent developments of FCS including imaging FCS (Krieger et al., 2015) and stimulated emission depletion (STED)-FCS (Mueller et al., 2011) usually are performed at the basal side of cells, i.e., the side in contact with the coverslip. Although the basal side of cell is more restricted in movement than its apical side, topography variations still exist as supported by electron microscopy (Andrews et al., 2008), reflection light microscopy (Barr and Bunnell, 2009), and variable-angle TIRF microscopy (Cardoso Dos Santos et al., 2016).

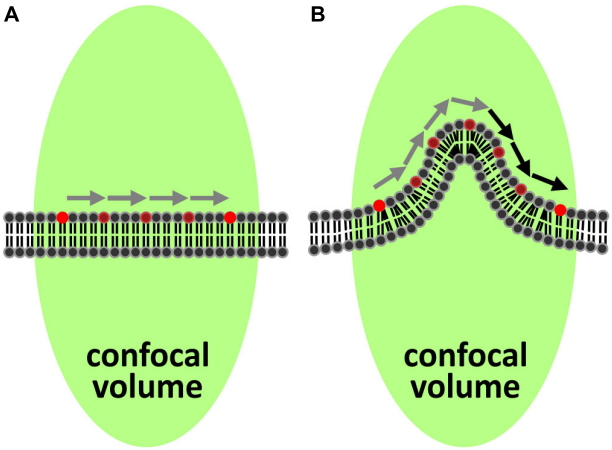

FIGURE 1 | Impact of curved membrane sections on FCS recordings. **(A)** The most common model for analyzing diffusion in two dimensions with FCS assumes a locally flat membrane aligned perpendicular to the optical axis of the excitation beam (green elongated spot). Gray arrows indicate the length of the path from one side of the excitation spot to the other. **(B)** If the membrane is locally curved, the path becomes longer (indicated by the additional black arrows) due to the surplus of membrane within the excitation spot, which leads to longer transit times determined by FCS.

In this study, we used FCS to examine the diffusion and SICM to assess the topography in different parts of the plasma membrane and analyzed the relationship between the two. For this a method to assess the distribution of membrane topographical features was developed. Performing complementary diffusion simulations and FCS modeling, we show how topography rather than anomalous diffusion can explain longer transit times.

MATERIALS AND METHODS

Materials

Glutamine, DMEM, trypsin-EDTA, and penicillin/streptomycin were obtained from GE Healthcare HyClone (Logan, UT, United States). Fetal bovine serum, enzymes, 3-aminopropyltriethoxy silane (TESPA), L-15 and chemicals were from Sigma (St. Louis, MO, United States). DiI-C_{12}, DiD-C_{18}, Lipofectamine 2000 and Gibco Opti-MEM were from Thermo Fisher Scientific (Waltham, MA, United States). High performance, 1.5H, coverslips were from Marienfeld (Lauda-Königshofen, Germany). The colon cancer cell line HT29 was a kind gift of Dr. A. Blokzijl, Uppsala University, Sweden and SW480 cells were from ATCC (Manassas, VA, United States). CD3ζ-EYFP, mouse CD3ζ fused to EYFP via a six aa linker expressed in the pBJ1-Neo plasmid under the CMV-promotor, was from Mark Davis, Stanford University School of Medicine, United States (Krummel et al., 2000). Lck-EGFP, a fusion

protein of mouse Lck and EGFP via a six aa linker expressed in the pcDNA3 under the CMV-promotor, was from Tony Magee, Imperial College London, United Kingdom (Janes et al., 1999). Borosilicate glass (1B100F-4) was from World Precision instruments (Sarasota, FL, United States).

Cell Culture

HT29 and SW480 human colon adenocarcinoma cells were cultured in DMEM supplemented with 10% FCS, 100 U/ml penicillin, 100 μg/ml streptomycin, and 2 mM glutamine. The cells were maintained at 37°C in a humidified incubator under 5% CO_2.

Transfection of Cells

Cells at 40% confluence plated on TESPA-coated 1.5H coverslips mounted in Petri dishes were washed in DMEM supplemented with 10% fetal calf serum. The cells were transfected with CD3ζ-EYFP or Lck-EGFP using Lipofectamin 2000 according to the instructions of the manufacturer.

Cell Staining for FCS

Cells were plated on TESPA-coated No. 1.5 high precision coverslips mounted in Petri dishes 34–40 h before imaging. The cells were washed twice with DMEM and stained with 200 μl 2.5 μg/ml DiD-C_{18} at 37°C for 15 min or 1 ml 2.5 μg/ml DiI-C_{12} at 37°C for 15 min or on ice for 5 min, followed by two washes in DMEM without phenol red. Cells stained on ice were kept on ice until the start of the imaging session.

FCS Setup

Fluorescence correlation spectroscopy measurements were performed on a Zeiss 780 confocal laser scanning microscope equipped for FCS, with a Zeiss water immersion objective, C-Apochromat 40×/1.2 NA. Samples containing DiI were excited at 514 nm or 561 nm and emission was collected between 520–695 nm or 570–695 nm, respectively. Samples containing DiD were excited at 633 nm and emission was collected between 640–695 nm. The 514 nm focus had a beam waist (ω) of 0.22 μm and a volume (V) of 0.36 fl [from measurement of Rhodamine 6G that has a diffusion coefficient (D) of 390 $\mu m^2/s$ (Müller et al., 2008) and adjusted for 22°C, yielding $\tau_D = 30$ μs]. The 561 nm focus had ω = 0.27 μm and V = 0.64 fl (from measurement of Alexa 568 that has D ≈ 400 $\mu m^2/s$, yielding $\tau_D = 45$ μs). The 633 nm focus had $\tau_D = 65$ μs, ω = 0.31 μm, and V = 0.71 fl [from measurement of HiLyte 647 that has D = 296 $\mu m^2/s$ (Wennmalm et al., 2015) and adjusted for 22°C, yielding $\tau_D = 65$ μs]. The 488 nm focus had ω = 0.23 μm and V = 0.36 fl [from measurements of Alexa 488 that has D = 390 $\mu m^2/s$ (Petrasek and Schwille, 2008) and adjusted for 22°C, yielding $\tau_D = 32$ μs].

FCS Measurements

Imaging was performed in 2 ml DMEM without phenol red supplemented with 16 U/ml glucose oxidase and 7000 U/ml catalase. The *z*-position for FCS measurements at the top of the cell, i.e., above the nucleus, was set in imaging mode such that the top of the cell was in the focal plane. This yielded the same result as optimizing the *z*-position for maximum fluorescence intensity during FCS-recording. FCS was recorded during 60–120 s at each position; (1) above the nucleus, (2) above the cytoplasm, i.e., midway between the nucleus and the longest axes of the cell spread on the apical cell side, and (3) at varying positions at the basal cell side. The *z*-position for FCS measurements at the apical cell side midway between the nucleus and the longest axes of the cell spread (above cytoplasm) was set in imaging mode such that the in focus-part of the cell, i.e., the position where FCS was recorded, appeared as a stripe around the upper part of the cell in the center part of the image. In order to verify that any difference in τ_D between the top of the nucleus and above the cytoplasm measurements was not due to false *z*-positioning during the measurements at the latter, a series of control measurements at this position was performed 0.5 μm above and 0.5 μm below the focus of the plasma membrane, as well as in focus.

FCS Analysis

Fluorescence correlation spectroscopy curves were fitted using the Zeiss Zen 2012 software to a model for 2D diffusion of a single diffusion component, without triplet. Only the part of the FCS curve slower than τ = 102 μs was fitted in order to avoid the influence of any blinking processes. In a few cases the fitting indicated the need for a model with more than one diffusion component, and τ_D was then estimated from the half-amplitude of the FCS curve. We chose not to calculate the weighted mean τ_D after fitting to a two-component model because with this approach, in cases when the slower component is very long (several hundreds of ms), the slower component completely dominates the weighted mean τ_D, even when its relative amplitude is small. The initial value of the fluorescence intensity of DiD, DiO, EGFP, and EYFP was estimated from the intensity trace at the start of the FCS measurement, with an error of $\pm\sqrt{I}/2$. For each measurement point, shorter FCS recordings of 4–10 s were repeated to obtain a total measurement time of 60–120 s. Individual 4–10 s measurements were excluded from the analysis if membrane movement or initial photobleaching was present, since these processes distort the FCS curves.

SICM Measurements

The SICM was a home-build setup previously described (Gesper et al., 2017). In brief, the scanning pipette was mounted on a three-way piezo cube (Nanocube, Physik Instrumente, Germany), which was additionally equipped with a stiff shear force piezo (P-111.05, PI Ceramics, Germany) to allow for faster recording. Glass capillaries were made from borosilicate glass with access resistances between 80 and 120 MOhm and filled with Leibovitz (L-15) medium. The estimated pipette inner radii were 22–32 nm. Assuming a half cone opening angle of 7° typical for pipettes pulled with the setting used (Gesper et al., 2017), these pipettes allow a lateral resolution between 66–96 nm. The cells were scanned in L-15 medium. The approach velocity was 100 nm ms^{-1}, the pixelsize 125 nm and the threshold was set to 1%. From scans of flat surfaces (Gesper et al., 2017), we estimate the vertical accuracy of the SICM we used to be in the range of 10 nm.

Analysis of Cell Surface Roughness

Scanning ion conductance microscopy raw data was filtered using a 3 × 3 pixel median filter. Binary masks for each cell were drawn manually to prevent the overlap of masks from neighboring cells. The mask was applied to the slope data of the scan and convolved with a 2D-Gaussian profile with a full width at half maximum (FWHM) of eight pixels and the height was reconstructed to obtain smoothed height data. The coordinates of the highest point of the smoothed height data were selected as the reference point. Using the slope instead of the height directly avoids the impact of inaccuracies in the positioning of the pipette along the slow scanning direction. However, in some cases where a cell was located next to a second cell, this procedure failed. In that case, the height was convolved directly and data containing notable inaccuracies in the positioning of the pipette along the slow scanning direction were omitted from the analysis. The Euclidean distance from every pixel to the reference point was computed and the maximum distance obtained was used to split the pixels into ten groups. The first group comprised pixels with a distance between 0 and 10% of the maximum distance, the second group pixels with a distance between 10 and 20% of the maximum distance and so on. For display, large artifactual topographical features such as tilt of the cell culture dish or steps along the fast scanning direction, most likely introduced by vibrations when retracting the pipette quickly by a large distance at the end of a line, were removed by linewise fitting of a line to a manually selected region of the data and subsequent subtraction of this line from the data. Roughness was calculated from the processed SICM data only along the fast scanning direction to remove the potential impact of inaccuracies in the positioning of the scanning pipette along the slow scanning direction. Seven consecutive pixels (1–7, 2–8, 3–9, ...) along the fast scanning direction were chosen. To remove the general, low-frequency cell shape, a polynomial of fifth degree was fitted to and subsequently subtracted from the data. We then set the roughness of the central, i.e., the fourth, pixel as the root of the mean of the squared deviations from the seven data points.

Simulations and FCS-Modeling

All simulations and FCS-modeling were performed in Matlab, versions 2017a to 2019b. The diffusion of molecules undergoing Brownian diffusion within a convoluted surface was simulated using an algorithm that enables simulation of diffusion in periodic, nodal surfaces (Wohland et al., 2001), and can operate on any surface defined by the function $\varphi(\vec{r}) = 0$. This function was defined by interpolating the data points by cubic splines with the Matlab class *griddedInterpolant*, providing a function $z(x, y)$ that returns the z-coordinate for any (x, y)-coordinate on the interpolated surface.

The gradients $\nabla z(x, y)$ along x- and y-directions of an interpolated set of data points with a pixel size of about 5 nm were computed for every pixel of the interpolated data. The simulation started at a random point $\overrightarrow{r_0}$ with the lateral coordinates (x_0, y_0) drawn from a uniform distribution. The lateral coordinates of the next point, $\overrightarrow{r_1}$, were computed as $x_1 = \cos\left(\nabla z\left(x_0', y_0'\right)\right)_x \Delta x_0 + x_0$ and $y_1 = \cos\left(\nabla z\left(x_0', y_0'\right)\right)_y \Delta y_0 + y_0$. Here, $\left(x_0', y_0'\right)$ indicate the coordinates of a point closest to $\left(x_0, y_0\right)$ that lies on the grid of the previously interpolated data points, $\nabla z\left(x_0', y_0'\right)_x$ indicates the gradient along the x-direction at this data point and Δx_0 indicates a random length drawn from a normal distribution with mean $\mu = 0$ and standard deviation $\sigma = \sqrt{2D\Delta t}$ where D is the diffusion coefficient and Δt the time of one step in the random movement (analogously for y). This implements random movement within the tangential plane at $\left(x_0', y_0'\right)$ with a length of $\sqrt{\Delta x_0^2 + \Delta y_0^2}$. The corresponding z-coordinate was then computed by projecting the point back onto the surface. The procedure was repeated for $\overrightarrow{r_2}$ by using $\overrightarrow{r_1}$ as the previous data point, etc.

The intensities of the simulated fluorescent molecules were calculated using a hypothetical confocal microscope (Qian and Elson, 1991; Holyst et al., 1999; Wohland et al., 2001) with the following optical parameters and the corresponding notations: $\lambda_{Exc} = 570$ nm, wavelength of the excitation light; $\lambda_{Em} = 620$ nm, wavelength of the emitted light; $n = 1.518$, refractive index of the medium; NA $= n \sin\alpha = 1.4$, numerical aperture of the objective, with α denoting the half cone angle of the objective; $M = 1$, magnification of the objective; $R_{ph} = 0.5$ AU, pinhole radius in units of the Airy disk diameter (AU). Note that a magnification of $M = 1$ was used to simplify the calculation of the effect of the pinhole. Calculations were restricted to components that have a position-dependent effect on the intensity such as the confocal pinhole, but omitted photophysical relations such as quantum yield.

The excitation beam was positioned in the center of the investigated area and its z-position was selected as the z-coordinate of the respective pixel. In the following, we use the index S to indicate coordinates with respect to the excitation beam. The intensity I of a molecule at position $\overrightarrow{r_S} = (x_S, y_S, z_S)$ was calculated as $I\left(\overrightarrow{r_S}\right) = \gamma\left(\overrightarrow{r_S}\right)\rho\left(\overrightarrow{r_S}\right)$. Here, $\rho\left(\overrightarrow{r_S}\right)$ describes the effect of the pinhole and $\gamma\left(\overrightarrow{r_S}\right)$ the intensity distribution of the focused laser beam. The latter was approximated as a three-dimensional Gaussian distribution: $\gamma\left(\overrightarrow{r_S}\right) = \left(w_0 w_z^{-1}\right)^2 \exp\left(-2\left(x_S^2 + y_S^2\right) w_z^{-2}\right)$. Here, $w_0 = 0.5\left(\Gamma / \left(2\ln(2)\right)\right)^{1/2}$ is the radius of the beam at intensity $\exp(-2)$ with $\Gamma = \lambda_{Exc}(2\text{NA})^{-1}$ denoting the FWHM of the diffraction limited beam; $w_z = w_0\left(1 + (z_S/z_0)^2\right)$ describes the width of the beam as a function of the z-coordinate with $z_0 = \pi w_0^2/\lambda_{Exc}$ denoting the Rayleigh length of the diffraction limited beam. Note that in practice, z_0 often is larger due to compromises between signal strength and resolution.

The effect of the pinhole was calculated by the following geometrical considerations: The amount of light emitted from a fluorophore and collected by the objective is limited by the half cone angle α of the objective. Hence, the radius R_z of the cone from a molecule located at an arbitrary z_S position is $R_z = R_0 + z_S \tan\alpha$. Here, R_0 is the minimum radius of the cone, which was defined as the resolution limit of the microscope $R_0 = \lambda_{Em}(2\text{NA})^{-1}$. It was assumed that all light that passes the pinhole is detected, hence, the effect of the pinhole can be calculated by determining the area of intersection A between the pinhole and the cone of light emitted from the molecule. For this, let

$d_S = \left(x_S^2 + y_S^2\right)^{1/2}$ denote the distance from the molecule to the optical axis. Due to the symmetry of the system, it is sufficient to consider molecules at positions ($d_S \geq 0, z_S \geq 0$). If the distance d_S of the molecule to the center of the pinhole is larger than the sum of the pinhole radius R_{ph} and the cone radius, the overlapping area $A = 0$. If $R_{ph} \geq R_z$ and $R_z + r_S \leq R_{ph}$, all emitted light passes the pinhole, hence, $A = \pi R_z^2$. If $r_S - R_z \leq -R_{ph}$, the pinhole is completely covered by light, hence, $A = \pi R_{ph}^2$. In all other cases, the pinhole and the cone intersect and we computed the area of intersection ζ of the corresponding circles, hence $A = \zeta\ (R_{ph}, R_z, r_S)$. The effect of the pinhole ρ was computed as $\rho\left(\overrightarrow{r_S}\right) = A\left(\pi R_z^2\right)^{-1}$. To compute the auto-correlation $G(\tau)$ of the sum of the intensities of the single molecules after one simulation step, an adaption of the Matlab multiple *tau* algorithm, that can be found at https://pypi.python.org/pypi/multipletau/, was used. A single-spot FCS model $G(\tau) = N^{-1}\left(1 + (\tau/\tau_D)\right)^{-1}$ was fitted to the autocorrelation data. Here, N is the average number of molecules located in the focus of the excitation beam and τ_D is the average transit time of molecules diffusing through the focus. Fits were performed using Matlab's fit function from the Curve Fitting Toolbox, which implements a linear least squares algorithm.

To obtain the transit times at different positions of the cell membrane, the free diffusion of molecules with a density of ∼10 molecules/μm^2 were simulated five times. The diffusion coefficient used was 0.1 $\mu m^2/\Delta t$ and Δt was selected as 10^{-3} ms. At this readout time, these settings correspond to a diffusion coefficient of 0.1 μm^2/s, a typical diffusion coefficient for plasma membrane proteins (Chojnacki et al., 2017). In a perfectly flat and smooth membrane, this procedure yields transit times approximately 1% larger than expected from the simulated diffusion coefficient with a standard deviation of about 10%.

The selection of positions for diffusion simulations and FCS modeling was arbitrary and only cell surfaces were included. In addition, it was ensured that the corresponding membrane regions did not overlap and thus represented different parts of the plasma membrane.

Assessment of Anomalous Diffusion

To assess apparent anomalous diffusion, FCS was modeled at 14 arbitrarily selected positions at five excitation spot sizes. The FWHM ranged from ∼65 nm, which corresponds to spot sizes obtained by STED-FCS, to ∼300 nm, which corresponds to FCS in the near infrared region. The spot sizes are reported as multiples of the area of the modeled beam described in section "Simulations and FCS-modeling" as used for the previous FCS modeling, referred to as the reference spot size. The model $A \times s^{\alpha}$ was fitted to the mean transit times for the five simulations at each position and spot size. To account for the different uncertainties in the transit time, means for the different spot sizes were weighted by their inverse variance multiplied by the respective mean. In the model, s indicates the size of the excitation spot and A a free scaling factor. For free Brownian diffusion, the relationship between transit time and spot size is directly proportional with $\alpha = 1$. Any deviation of α from 1 indicates anomalous diffusion and in our simulations; the smaller the α the larger the apparent anomalous diffusion. To assess whether the degree of apparent anomalous diffusion was related to the transit time of the reference spot size, the Pearson correlation coefficient between α and the transit time was used.

Statistical Analysis

The τ_D-values from FCS were compared using a paired, two-sided t-test. Using the Anderson–Darling test, it could not be rejected that the data were normally distributed. The roughness was analyzed by linear ANOVA models using the mean of the 90th percentiles of the 10 distance groups of all investigated cells and t-tests were performed on $\log_{10}$-transformed values. For the comparisons of the means of the 90th percentile, a pairwise t-test including the Holm-Bonferroni method to correct for multiple comparisons was used. Whether τ_D-values could be explained by I-values was assessed using multiple linear regression analysis after $\log_{10}$-transformation of the τ_D and I values to make the data less skewed. The effect the variables $\log_{10}(I_{protein})$, $\log_{10}(I_{DiD})$, cell type, protein type, positions for the FCS-measurements and individual cells on $\log_{10}(\tau_D)$ were estimated simultaneously with least squares in a multiple linear regression model with the restriction that the slope was the same for all experiments. In the model all observations were given equal weight.

RESULTS

Cells are never smooth and flat, which we have shown dramatically affects the interpretation of SPT data (Adler et al., 2010, 2019). FCS of membrane components would appear to be equally prone to topographical artifacts and this we set out to investigate.

Diffusion in the Plasma Membrane Appears to Be Faster Above the Nucleus Than Above the Cytoplasm

In FCS, a considerable spread of data from diffusion coefficient measurement of plasma membrane components is commonplace (Ries and Schwille, 2008; Stromqvist et al., 2011). We suspected that variations in the positioning of the excitation beam at the apical side of the plasma membrane could help explaining this variation. To this end we used human colon cancer HT29 cells, an adherent epithelial cell type, that maintain a rounded shape when cultivated on glass or plastic rather than becoming extensively stretched. Epithelial cells, like many other cell types, are rich in topographical features (Adler et al., 2010), but the distribution of these features have not been well characterized. We decided to compare whether there was a difference in diffusion on top of the nucleus and over the center of the cytoplasm (**Figure 2A**). Measurements above the nucleus were performed at the top of the cell (**Figure 2B**) and measurements above the cytoplasm were performed midway between the nucleus and the longest axes of the cell spread. When in focus, this area of the plasma membrane appears as a fluorescent band around the upper part of the cell and this band was positioned in the center part of the image before the FCS measurements (**Figure 2C**). This focusing method allowed us to check after each completed FCS measurement that the plasma membrane remained in focus.

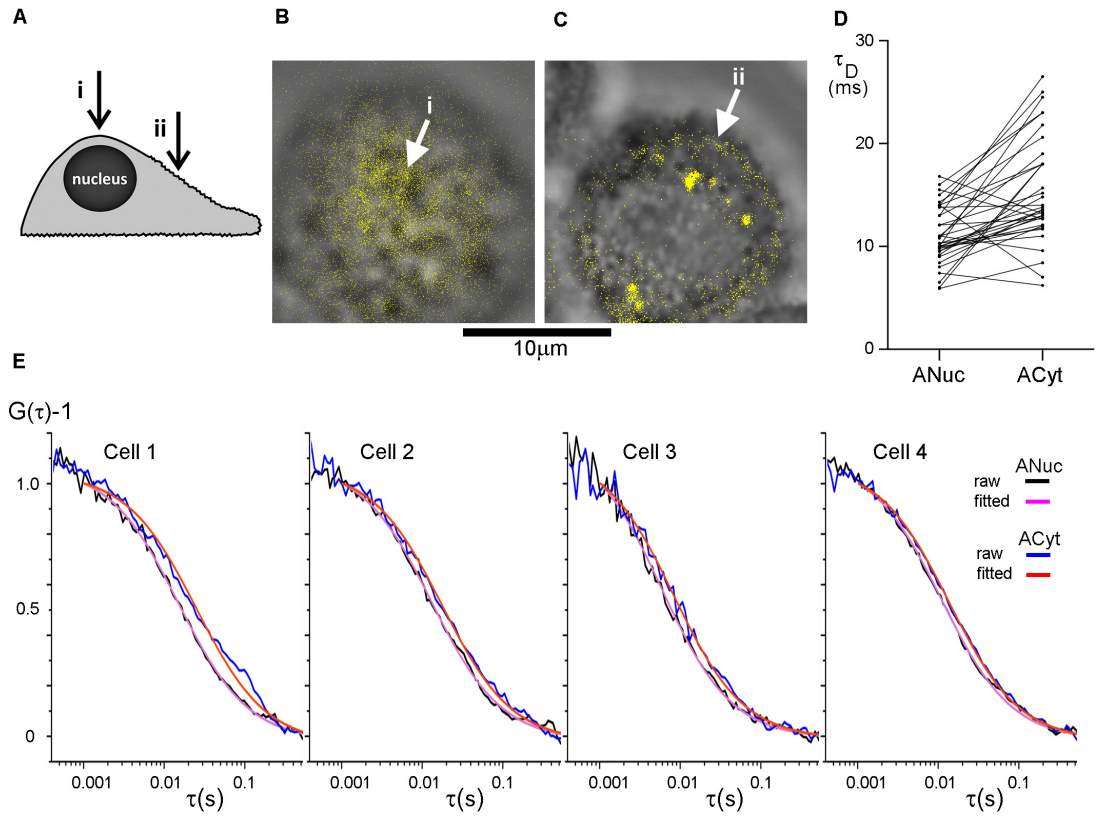

FIGURE 2 | The diffusion in the plasma membrane appears to be faster on top of the nucleus than over the center of the cytoplasm. **(A)** The cells were subjected to FCS measurements at two different positions at their apical side plasma membranes; (i) on top of the nucleus and (ii) midway between the nucleus and the longest axes of the cell spread, above the cytoplasm center (indicated with arrows). HT29 cells stained with DiI imaged at **(B)** the top of the nucleus and **(C)** over the center of the cytoplasm with (i) and (ii) corresponding to panel **(A)**. The DiI-signal in panels **(B,C)** was intensity thresholded and is displayed in false color. Scale bar 10 µm. **(D)** Comparison of the difference in τ_D from the plasma membrane on top of the nucleus and over the center of the cytoplasm. $p = 5.0 \times 10^{-6}$ for a two-tailed, paired *t*-test, and $n = 36$. Values from one cell were excluded from the graph, but not from the analysis, for clarity because its τ_D_values were considerably longer. **(E)** FCS curves from four different HT29 cells. On each cell FCS was measured above the nucleus (experimental curve in black, fitted curve in purple) and over the center of the cytoplasm (experimental curve in blue, fitted curve in red). Curves were fitted to a model assuming one diffusing species starting the fit at $\tau = 102$ µs.

Confocal FCS was used to study the diffusion of DiI-C_{12} in the plasma membrane of HT29 cells. A comparison of the correlation time, τ_D, which is inversely proportional to the diffusion coefficient, suggested that the diffusion in the plasma membrane on top of the nucleus was faster than that over the cytoplasm. Interestingly, minimizing the risk of the internalization of the membrane probe by labeling cells on ice, with the FCS measurements performed immediately after labeling at room temperature, resulted in a similar trend as labeling at 37°C. Therefore, results from both labeling temperatures were pooled in the analysis. The absolute values of τ_D varied considerably from cell to cell, but the difference in τ_D between the two positions was highly significant with τ_D over the cytoplasm being longer than τ_D on top of the nucleus (**Figure 2D**). The difference in τ_D at the two positions is illustrated for four individual cells, fitted with a model for 2D diffusion of a single diffusion component (**Figure 2E**).

To verify that the observed difference in τ_D above the nucleus and above the cytoplasm was not due to incorrect *z*-positioning during the measurements, control measurements 0.5 µm below and above the fluorescence band, i.e., focus in the cytoplasm and outside the cell, respectively, were performed. These measurements confirmed that a one-component-model was appropriate and that false positioning was not causing the difference in τ_D for the two positions. The measurements 0.5 µm above and below focus did not differ significantly from measurements of the plasma membrane in focus, i.e., incorrect *z*-positioning was unlikely to explain the longer τ_D observed above the cytoplasm as compared to that above the nucleus. If we inadvertently had assigned 0.5 µm above the PM as the in focus position, then defocusing by ±0.5 µm should have yielded a 50% increase in τ_D for the +1.0 µm position, and a 20–25% decrease for the 0.0 µm position (Humpolickova et al., 2006).

Cell Surface Roughness Is Unevenly Distributed

To investigate whether the topographic features are inhomogeneously distributed across the cell surface, we imaged living HT29 cells by SICM, one cell measurement is

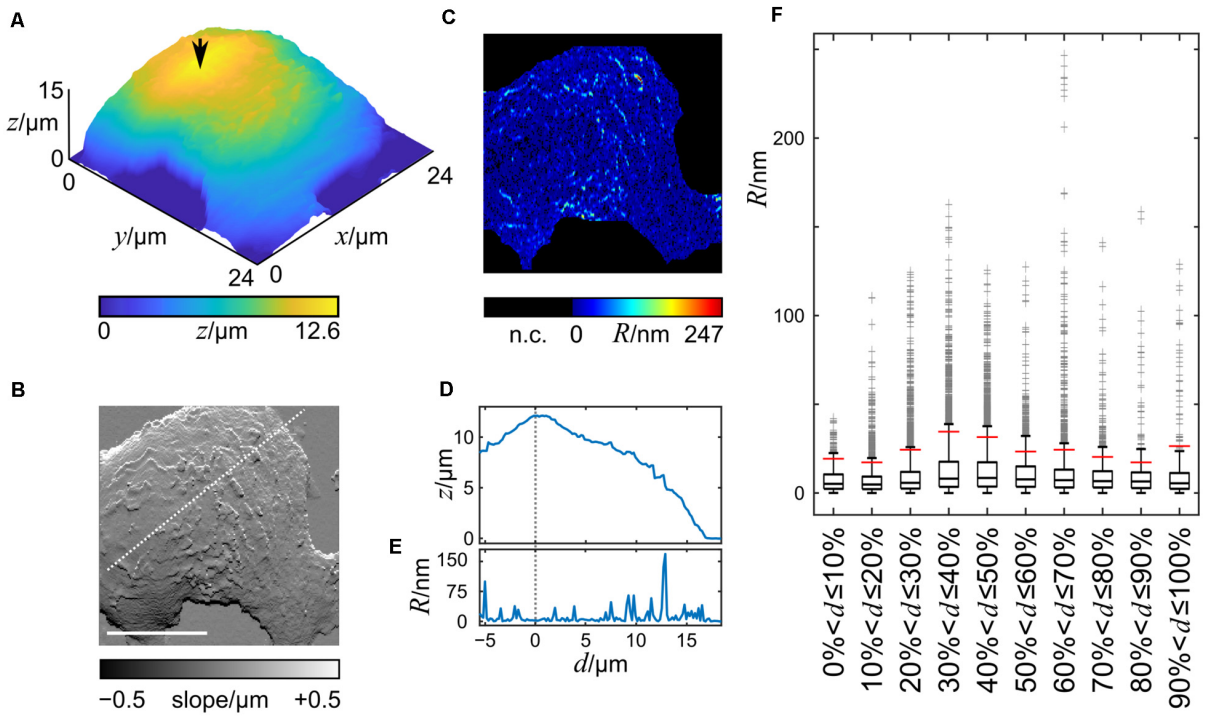

FIGURE 3 | 3D-Height and slope representation of a section of a living HT29 cell imaged by SICM. Height and slope representation of a HT29 cell imaged live by SICM is shown in **(A,B)**. **(C)** Computed roughness of the cell surface. The cell chamber bottom and the steep transitions between the dish and the cell were not considered (n.c.). The arrow in A indicates the position of the reference point. Scale bar in B: 10 µm, also applies to **(C)**. **(D)** Height and **(E)** roughness profiles along the dashed white line shown in **(B)**. The vertical dashed line in **(D,E)** represents the position of the highest point of the nucleus. **(F)** Box plot of the roughness data grouped into 10 equally spaced groups with increasing distance from the reference point. Boxes indicate the lower and upper middle quartile, whiskers data within ± 1.5 inter quartile ranges, gray crosses indicate outliers.

shown in **Figure 3A**. The maximum cell height observed was 12.6 µm and the cell footprint was larger than the scanning frame of 24 × 24 µm. In the slope representation topographic features of the cell membrane are visible (**Figure 3B**), with single protrusions extending approximately 1 µm from the cell's silhouette (**Supplementary Figure 1**). The roughness, calculated as the deviation from the mean height of a 7 × 1 pixel window (875 × 125 nm), after subtracting the cell silhouette, ranged from 0 nm to 247 nm with average of 14.9 ± 38.4 nm and the data were heavily skewed toward higher values (**Figure 3C**). Under these imaging conditions, the roughness of the coated cell culture dish was between 0 and 5 nm.

A profile of the roughness along a line (**Figure 3B**) through a reference point, selected as the highest point of the cell after smoothing (indicated by the arrow in **Figure 3A**), shows that the roughness is not evenly distributed (**Figures 3D,E**). The lowest cell surface roughness is found at the highest part of the cells.

To test whether our finding could be generalized to the entire cell surface, we split the cell surface into ten groups of pixels, the first group comprising pixels with an Euclidean distance between 0 and 10% of the maximum distance from the reference point, the second group comprising pixels between 10% and 20% of the maximum distance, etc. **Figure 3F** shows a box plot of the roughness values of the cell membrane using this grouping. A large number of points exceeded 1.5 inter quartile ranges (IQRs) indicating that the data is skewed toward higher values. Consequently, the difference of the medians was small with the lowest median at 5.0 nm (second group) and the highest at 8.5 nm (fifth group) while the difference of the maxima of the groups was large with values from 41.9 nm (first group) to 247.0 nm (seventh group). The minima of all groups were 0.0 nm.

Since we wanted to test whether extreme roughness values, i.e., the larger topographical features, are distributed inhomogenously across the cell, we chose to investigate the 90th percentile of the roughness data, *R*90, indicated by the red vertical bars in **Figure 3F**.

The grouping procedure described above was applied to 31 cells (**Supplementary Figure 2**) and the corresponding *R*90-values were analyzed. The *R*90 means of groups 4–9, i.e., away from the nucleus were significantly larger than that of group 1 at the top of the nucleus (**Figure 4**). The *p*-values adjusted for multiple comparisons are provided in **Supplementary Table 1**.

FCS Modeled on Simulated Diffusion in Experimentally Obtained Cell Surface Support FCS Data From Live Cells

To investigate whether the inhomogeneous distribution of the topographical features would have an effect on FCS measurements, we simulated free diffusion in the sections of

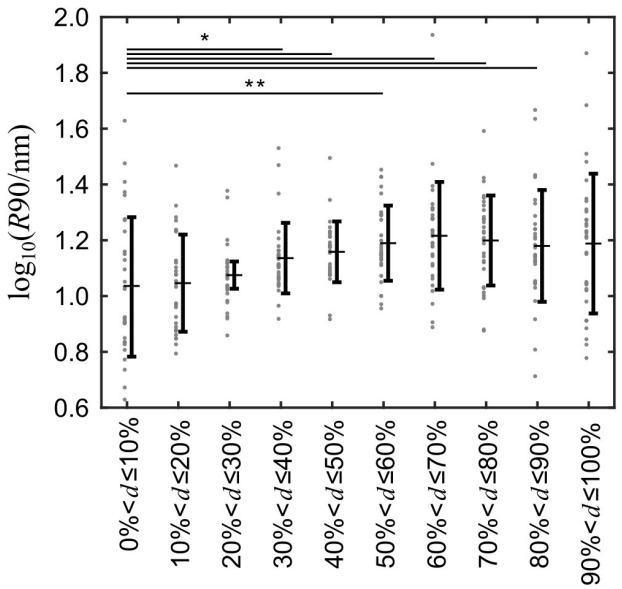

FIGURE 4 | Surface roughness is unevenly distributed over the cell surface and greater away from than at the top of the cells. The cell membrane roughness of 31 different cells was recorded and grouped into 10 evenly spaced groups relative to the spatial dimension of each cell and the log-transformed means of the 90th percentile of the roughness data in each group was compared with a paired *t*-test. Gray dots indicate the 90th percentile of the cell surface roughness for every cell, horizontal bars with whiskers indicate the mean ± standard deviation. $^{*}p < 0.05$; $^{**}p < 0.01$ versus Group 1.

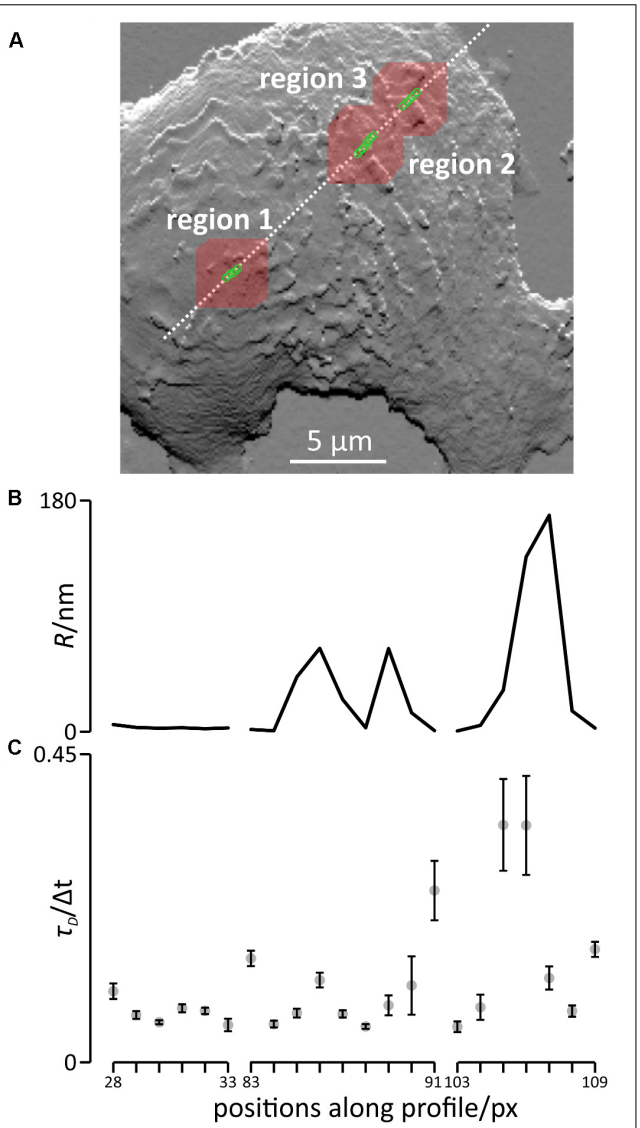

FIGURE 5 | Simulation of diffusion and modeled FCS recordings in the apical part of the membrane of living cells. **(A)** Positions of the modeled FCS recordings (green circles) and areas in which diffusion was simulated (red squares around each green circles) superimposed on the slope plot of the topography of the plasma membrane (**Figure 3B**). **(B)** Roughness of the cell membrane at the positions of the modeled FCS recordings. **(C)** Transit times presented as means ± SD, $n = 5$.

the cell shown in **Figure 3A** and modeled FCS-recordings at three different regions along the profile shown in **Figures 3B–D**. The respective regions are highlighted in **Figure 5A**, the red areas indicate the sections of the cell in which diffusion was simulated. The first region was located at the highest point of the cell and comprised a smooth area of the plasma membrane, the second region comprised an area of the plasma membrane containing two sections of higher roughness located in close proximity, and the third region comprised an area of the plasma membrane containing the maximum roughness observed along the profile (**Figure 5B**).

The results of the modeled FCS recordings are shown in **Figure 5C** and the corresponding auto-correlation curves are shown in **Supplementary Figure 3**. Note that we provide the resulting correlation times, τ_D, in units of Δt, the time of a single simulation step. In region one, the results of the modeled FCS recording only varied slightly if the position was slightly shifted, yielding transit times ranging from 0.055 ± 0.009 Δt at position 33 to 0.104 ± 0.011 Δt at position 28, a 1.9 fold difference. In region 2, the shortest transit time was 0.052 ± 0.003 Δt at position 88, the longest transit time was 0.251 ± 0.043 Δt (position 91), almost a 4.8 fold difference. In region 3 (bottom panel), the shortest transit time was 0.052 ± 0.008 Δt (position 103), the longest transit time was 0.347 ± 0.067 Δt (position 105), a 6.7 fold difference. In summary, shifting the position slightly has a huge impact in regions rich in topographical features or with high topography differences.

To assess whether even larger differences in the observed transit times could be found, we simulated diffusion and modeled FCS recordings at 14 additional arbitrarily selected positions spread over the cell surface (**Supplementary Figure 4**). The resulting transit times ranged from 0.040 ± 0.003 Δt to 0.121 ± 0.012 Δt. Overall, the transit times observed for diffusion in this particular cell varied by factor of approximately 6.7. When simulating diffusion on ten arbitrarily selected positions on a

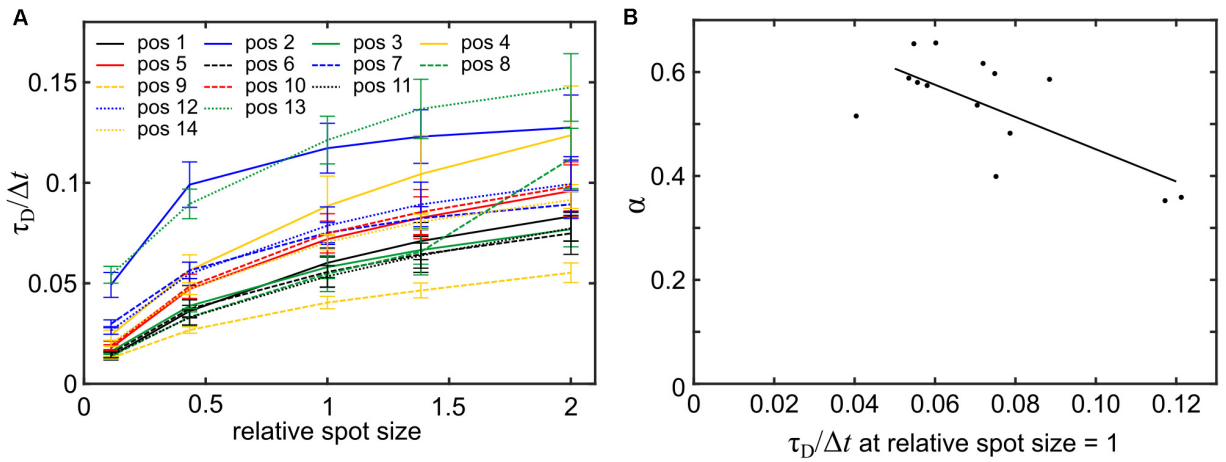

FIGURE 6 | Modeling spot size variation FCS reports topography-induced apparent anomalous diffusion. **(A)** Mean transit times (±SD, $n = 5$) for varying spot sizes. Spot sizes are presented as multiples of the area of the reference spot size (FWHM of ∼200 nm) used in **Figure 5C**. **(B)** Scatter plot of the parameter α obtained from fitting the model $A \times s^{\alpha}$ to the data in panel **(A)** and the transit time at the reference spot size. The Pearson correlation coefficient for the two variables was −0.70 ($p = 0.0044$).

second cell using the same parameters, we found a variation by a factor of 3.2 (**Supplementary Figure 5**).

Next, we assessed whether plasma membrane topography could lead to the erroneous reporting of anomalous diffusion in FCS as it does in SPT (Adler et al., 2010). To this end, spot size variation FCS was modeled at the 14 arbitrarily selected positions shown in **Supplementary Figure 4A**. At all positions, the relationship between spot size and transit time was non-linear, indicative of anomalous diffusion (**Figure 6A**). The model $A \times s^{\alpha}$, with s representing the excitation spot size, A representing the transit time obtained from modeling FCS with the reference spot size and α representing an estimate of the degree of anomalous diffusion was fitted to the data. The α-values ranged from 0.35 ± 0.14 to 0.65 ± 0.08 (errors indicate the 95% confidence interval) and the mean of the α-values was 0.53 ± 0.10 (errors indicate standard deviation). As anticipated, a higher degree of anomalous diffusion was found at positions that showed a higher transit time when modeling FCS at the reference spot size (**Figure 6B**). In summary, we found that more convoluted membrane sections lead to larger overestimations of the transit times accompanied by a higher degree of apparent anomalous diffusion.

Variations of the Amount of a Membrane Marker in the FCS Focal Volume Can Explain Variations in τ_D

Given the topography variations of cells, the amount of membrane in the FCS focal volume will differ, which could explain the large variations in τ_D observed for membrane proteins (Stromqvist et al., 2011). Previously, counting of molecules in the FCS focal volume has been used to account for global membrane curvature (Honigmann et al., 2014). We reasoned that the topography variation should be reflected in the fluorescence intensity of a membrane marker at the start of a FCS-measurement and could be used to determine the contribution of topography to the variation in τ_D for a membrane protein. To this end, we stained HT29 cells transfected with the transmembrane plasma membrane protein CD3ζ linked to EYFP and SW480 cells or Jurkat T cells transfected with Lck-EGFP. All three cell types were labeled with DiD. We first investigated whether the intensity of the protein constructs themselves could explain the variations in τ_D. Interestingly, we found that the initial intensities of EGFP and EYFP could not explain variations in τ_D for the protein constructs (**Figure 7A**). Using multiple linear regression analysis, we found a relationship between τ_D for the proteins and the initial intensity of DiD (**Figure 7B**). Neither the position in the plasma membrane at which the FCS measurements were performed, i.e., the bottom of the cells, above the nucleus, or above the center of the cytoplasm, nor the cell or protein type had a statistically significant effect. However, the relationship between τ_D and I_{DiD} was as expected not perfect, meaning that not all of the variability in τ_D for the two proteins could be accounted for by variations in the amount of membrane in the focal volume.

DISCUSSION

The plasma membrane is a compartment where several fundamental biological processes take place, e.g., cell adhesion, endo- and exocytosis and signaling via receptors that recognize extracellular ligands. It is therefore important to understand plasma membrane dynamics of which the diffusion modes of its components play a prominent role. FCS is a powerful method for studying diffusion, but in plasma membrane studies it is known to report data with a big spread both within and between cells for the same membrane protein (Schwille et al., 1999; Ries and Schwille, 2008; Stromqvist et al., 2011). Reasons for this include membrane undulations and misalignment of the membrane and the focal volume (Milon et al., 2003;

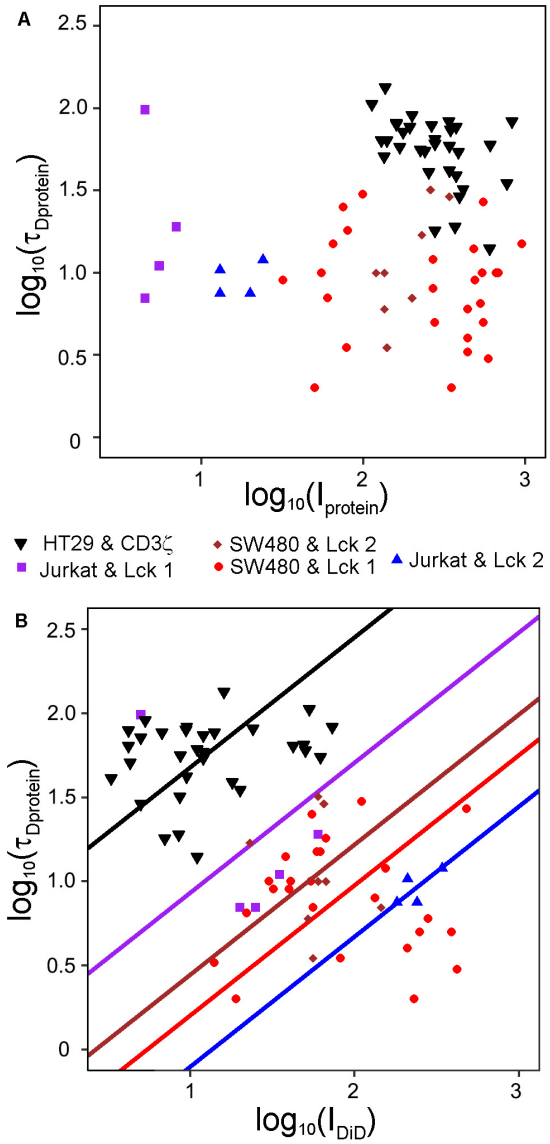

FIGURE 7 | Variations in τ_D for plasma membrane proteins can be explained by the membrane density in the focal volume. τ_D and I at the start of FCS measurement were determined for DiD-labeled SW480 and Jurkat T cells transfected with Lck-EGFP or HT29 cells transfected with CD3ζ-EYFP. The FCS measurements were conducted in the plasma membrane above the top of the nucleus, above the cytoplasm midway between the top of the nucleus and the cell edge in the direction the cell had stretched the most and at the basal cell side in touch with the coverslip. Curves were fitted to a model assuming one diffusing species starting the fit at $\tau = 102$ µs. Scatter plots of **(A)** $\log_{10}(\tau_D)$ versus $\log_{10}$(I) for the proteins and **(B)** $\log_{10}(\tau_D)$ for the proteins versus $\log_{10}$(I) for DiD. The values from five different experiments are displayed with different symbols. The lines in B were fitted with least squares in a multiple linear regression model where $\log_{10}(\tau_D)$ was the dependent variable and $\log_{10}$ (I_{DiD}) was the independent variable. The mean value of $\log_{10}$ τ_D conditioned by $\log_{10}$ I shifted between the different experiments, modeled by indicator variables. Random effects for different cells within each experiment were included in the model, but not in the graph. The model had the restriction that all experiments should have the same slope, which was estimated to be 0.77. The variable $\log_{10}(I_{DiD})$ was statistically significant ($p = 0.0092$), but $\log_{10}(I_{protein})$ was not significant ($p = 0.16$) and therefore no lines were fitted in **(A)**. R^2 for the model was 0.83.

Malchus and Weiss, 2010). Membrane undulations are large-scale membrane fluctuations that result in changes in membrane topography but, importantly, the undulating membrane is considered to be smooth. However, using live cell SICM it has been demonstrated that the plasma membrane is far from smooth (Gorelik et al., 2003; Adler et al., 2010). The topography of the plasma membrane is the result of an interplay between turgor pressure, the cytoskeleton, the plasma membrane and the glycocalix (Shurer et al., 2019). We therefore suspected that local topography variations could play a prominent role in explaining the large spread observed in FCS results.

We show that in HT29 cells diffusion in the plasma membrane as determined by FCS appears to be slower in plasma membrane segments that are located above the cytoplasm than in segments located on top of the nucleus. Using SICM we also found more pronounced topographical features in areas of the plasma membrane not overlying the nucleus in this cell type. Hence, we found that longer transit times coincided with regions richer in topographical features indicating a causal relationship.

To analyze the size and occurrence of topographical features, we transferred a measure used in the material sciences to biology: The surface roughness. Mainly, lamellar structures were observed on the cells investigated by SICM. Lamellar structures are smooth in the direction parallel to their fronts, and abrupt height changes only occur at the front of the lamella. Since the size of the window used to compute the surface roughness was smaller than the observed lamellar structures, high roughness values were only observed at the fronts of the lamellar structures. This was considered by analyzing the 90th percentile of the roughness data after grouping the roughness data according to their distance from the nucleus. We found that the 90th percentile of groups away from the nucleus was significantly higher than the 90th percentile of the group located on top of the nucleus. Importantly, the distribution of topographical features differs from cell to cell emphasizing the importance of establishing the local topography where the FCS measurement is being conducted.

According to the FCS diffusion law, the diffusion behavior of plasma membrane components can be extracted if FCS is performed at different focal volume sizes (Wawrezinieck et al., 2005; Schneider et al., 2018) or *z*-planes (Humpolickova et al., 2006). If the relationship between the focal volume and the transit time deviates from linearity the diffusion is considered anomalous, explained by diffusion barriers or trapping in the form of transient binding, or partitioning to membrane nanodomains (Winkler et al., 2017). Topography is generally not considered as a cause for anomalous diffusion but our results strongly suggest that its consideration is highly relevant as does a recent study (Gupta et al., 2020). As outlined above, the effect of the membrane topography on the transit times is dependent of the FCS focal volume and could therefore account for a non-linear relationship with the measured diffusion coefficient. In particular, considering membrane topography is important when interpreting high-resolution FCS recordings using STED-FCS instruments, where the focal volumes can be reduced to tens of nanometers (Eggeling et al., 2009; Honigmann et al., 2014; Benda et al., 2015; Sezgin et al., 2019), as we showed by modeling spot size variation FCS.

To assess whether differences in experimental FCS data are caused by an uneven distribution of topographical features in the plasma membrane, concurrent recording of both variables would be useful. However, an instrument combining SICM and FCS recordings has yet to be developed, but correlated SICM and fluorescence measurements have been performed, even with super-resolution microscopy methods (Gorelik et al., 2002; Hagemann et al., 2018). An alternative approach is to use the intensity of a membrane marker as a proxy for membrane volume within the FCS focal volume. As we demonstrate, intensity variations of the membrane marker can, to a large extent, but not fully, explain variations in transit times of membrane proteins. This we observed in three different cell lines – two adenocarcinoma colon cancer cell types that are adherent and Jurkat T cells that grow in suspension and for two different proteins – the Src-family lipid anchored Lck and the transmembrane CD3ζ subunit of the T cell receptor. Moreover, the fluorescence intensity in the focal volume could explain differences in transit times regardless of the position in the plasma membrane; the basal side or the apical side either on top of the nucleus or the cytoplasm. Any difference remaining between positions when topography has been accounted for could be due to anomalous diffusion caused by the proteins interacting with other plasma membrane components and/or domains of the plasma membrane like ordered membrane domains. However, the interpretation is complicated by topographical features themselves being able to cause anomalous diffusion both in the form of sub- and superdiffusion (Adler et al., 2019).

The plasma membrane contains two co-existing liquid phases – the more loosely packed liquid disordered (ld) phase and the more tightly packed liquid ordered (lo) phase, of which the latter forms ordered membrane nanodomains known as lipid rafts. A basic requirement for a membrane probe used to report variations in membrane topography is that it distributes randomly in the bulk membrane and co-existing membrane nanodomains and does not show preferential partitioning. Partition studies are generally performed in model membranes with well separated ld- and lo-phases and in those the short acyl chain DiI (C_{16} and lower) probes display a preference for ld-phase whereas for the longer chain DiI (C_{18} and higher) probes the lipid composition determines their phase preference (Baumgart et al., 2007). However, the composition and asymmetry of the plasma membrane are not well represented by these model membranes and the difference between any co-existing phases in the plasma membrane is much smaller (Sezgin et al., 2012; Dinic et al., 2013; Fujimoto and Parmryd, 2016). It is therefore reasonable to assume that the fluorescence intensity of probes used in this study, DiI-C_{12} and DiD-C_{18}, are good proxies for the amount of membrane present in the FCS focal volume.

Interestingly, in contrast to DiD-C_{18}, the two protein constructs, Lck-EGFP and TCRζ-EYFP, did not prove to be good proxies for the amount of plasma membrane in the focal volume. The reason could be because they both are enriched in ordered membrane nanodomains and hence may not be homogenously distributed (Kabouridis et al., 1997; Dinic et al., 2015). Moreover, neither Lck nor TCRζ are exclusively plasma membrane proteins. Two days past transfection, the protein constructs well represent the distribution of the endogenous proteins, which are both found in intracellular membranes in addition to the plasma membrane. Since the elongated focal volume extends into the cytoplasm, endosomes, and vesicles are likely to be included and cause an overestimation of the fluorescence intensity in the plasma membrane. The diffusion from such vesicles is accounted for in the subsequent FCS analysis, but in practice it is difficult to account for the fraction of the fluorescence originating from the vesicles. The membrane markers, on the other hand, were added to the cells just before the FCS recordings were made and hence the label was primarily found in the plasma membrane.

Theoretical studies have concluded that membrane curvature *per se* will slow down the diffusion of membrane proteins since it influences the packing in the two leaflets and hence the interaction between the protein and the lipids (Gov, 2006; Yoshigaki, 2007; Kabbani et al., 2017). This should also be considered as an explanation for variations in τ_D, since close to endless combinations of curvature in the focal volume are possible for the same membrane area. In addition, thermal fluctuations, resulting in membrane undulations, may contribute to variations in τ_D and even more to the total fluorescence intensity (Reister and Seifert, 2005; Ries and Schwille, 2008; Machan and Hof, 2010).

To estimate the potential impact of the topographical features of the membrane on FCS data, we modeled FCS recordings on these structures with a hypothetical microscope operating at the resolution limit. Under these conditions, we found differences in the transit times of up to sevenfold with slight variations in the position of the excitation beam. However, this number may vary between cells since we found a variation around three in a second cell. In our experimental data, we observed differences of up to threefold in the plasma membrane above the nucleus and cytoplasm for the same cells, in line with the simulations. These variations could be, and probably have been, misinterpreted as anomalous diffusion. It is important to keep in mind that SICM is a surface scanning method and thus better at reporting membrane protrusions than invaginations. Moreover, lateral membrane folding will be missed by SICM. The amount of membrane modeled from the SICM measurements therefore is likely to be an underestimate of the amount of plasma membrane. A reasonable assumption would then be that we should find larger differences in the experimental rather than simulated FCS. However, in practice, resolution is often sacrificed to obtain a better signal-to-noise ratio. A larger focal volume, as used in the FCS experiments compared with the simulations, averages over a larger volume and therefore the impact of vertical topographical features is reduced. This effect we observed when modeling spot size variation FCS based on the SICM data.

By simulating diffusion and modeling FCS recordings, we found a relationship between the plasma membrane roughness and the transit times in FCS recordings supporting the experimental findings. We also showed that an increase in the transit time of up to factor of seven due to differences in membrane topography is possible in FCS recordings at different plasma membrane positions of a single cell. However, we could not use the roughness values to predict the transit times of FCS. There are two reasons for this. Firstly, this is an effect of the window of 7×1 pixels, selected to compute the roughness, being smaller than the focal volume modeled to probe the fluorescence

intensity. However, we selected this window size since it allowed processing of the data without correcting for inaccuracies along the slow scanning direction, which are a common problem in scanning probe microscopy (Voigtländer, 2015), ensuring that no artificial topographic features are introduced by the correction procedure. Secondly, different topographies can produce the same roughness value, but might lead to different FCS transit times, i.e., the exact topography affects the transit times.

By modeling spot size variation FCS we have shown that topography deviations from a flat and smooth plasma membrane will report anomalous diffusion. Thus FCS, when topography is not considered, can easily be misinterpreted as anomalous diffusion. Our data demonstrate a large cell-to-cell and within cell variation of the plasma membrane topography and hence it needs to be assessed for each cell in order to avoid the over reporting of anomalous diffusion.

In conclusion, we have demonstrated that topography variations can to a large extent explain differences in FCS measurements of plasma membrane components, exemplified by comparisons in diffusion above the nucleus and cytoplasm. To estimate the effect of topography on the diffusion of a protein, a membrane marker can be used, but the marker is a proxy for the membrane area and a given area can be folded in many different ways that in turn alter the transit times. It is not possible to generalize how topography varies in different positions in the cell since both inter and intra cell variations are substantial. Whenever a cell treatment is reported to affect the diffusion of a plasma membrane molecule or the molecule is reported to undergo anomalous diffusion, it needs to be ascertained that changes in the membrane topography are not the underlying cause of the findings.

DATA AVAILABILITY STATEMENT

The implementation of the simulation, the code to model the FCS recordings as well as the code to compute the autocorrelation is available at https://github.com/RUBION-Nanoscopy/FCS-simulation.

AUTHOR CONTRIBUTIONS

AG, SW, PaH, and IP designed and performed the experiments. PaH wrote the simulation and modeling software. AG and PhH performed the simulations. S-GE performed the statistical modeling. All authors analyzed the data. IP and PaH drafted the manuscript and conceived the idea. All authors contributed to the article and approved the submitted version.

FUNDING

This work was supported by grants to PaH from the German Research Foundation (411517989) and the Volkswagen Foundation (88390) and to IP from the Swedish Research Council (2015–04764) and Magnus Bergvall's Foundation.

ACKNOWLEDGMENTS

We thank Dr. Jan Saras for assistance with cell culture and transfections. FCS was performed at the FCS-Advanced Light Microscopy facility, SciLifeLab, Stockholm. We thank Irmgard Dietzel-Meyer, Thomas Günther-Pomorski, and Wolfgang Schuhmann for sharing their equipment.

SUPPLEMENTARY MATERIAL

The Supplementary Material for this article can be found online at: https://www.frontiersin.org/articles/10.3389/fcell.2020.00767/full#supplementary-material

REFERENCES

Adler, J., Shevchuk, A. I., Novak, P., Korchev, Y. E., and Parmryd, I. (2010). Plasma membrane topography and interpretation of single-particle tracks. *Nat. Methods* 7, 170–171. doi: 10.1038/nmeth0310-170

Adler, J., Sintorn, I. M., Strand, R., and Parmryd, I. (2019). Conventional analysis of movement on non-flat surfaces like the plasma membrane makes Brownian motion appear anomalous. *Commun. Biol.* 2:12.

Andrews, N. L., Lidke, K. A., Pfeiffer, J. R., Burns, A. R., Wilson, B. S., Oliver, J. M., et al. (2008). Actin restricts FcepsilonRI diffusion and facilitates antigen-induced receptor immobilization. *Nat. Cell Biol.* 10, 955–963. doi: 10.1038/ncb1755

Barr, V. A., and Bunnell, S. C. (2009). Interference reflectace microscopy. *Curr. Protoc. Cell Biol.* 45, 4.23.21–24.23.19.

Baumgart, T., Hunt, G., Farkas, E. R., Webb, W. W., and Feigenson, G. W. (2007). Fluorescence probe partitioning between Lo/Ld phases in lipid membranes. *Biochim. Biophys. Acta* 1768, 2182–2194. doi: 10.1016/j.bbamem.2007.05.012

Benda, A., Ma, Y., and Gaus, K. (2015). Self-calibrated line-scan STED-FCS to quantify lipid dynamics in model and cell membranes. *Biophys. J.* 108, 596–609. doi: 10.1016/j.bpj.2014.12.007

Cai, E., Marchuk, K., Beemiller, P., Beppler, C., Rubashkin, M. G., Weaver, V. M., et al. (2017). Visualizing dynamic microvillar search and stabilization during ligand detection by T cells. *Science* 356:eaal3118. doi: 10.1126/science.aal3118

Cardoso Dos Santos, M., Deturche, R., Vezy, C., and Jaffiol, R. (2016). Topography of cells revealed by variable-angle total internal reflection fluorescence microscopy. *Biophys. J.* 111, 1316–1327. doi: 10.1016/j.bpj.2016.06.043

Chen, Y., Thelin, W. R., Yang, B., Milgram, S. L., and Jacobson, K. (2006). Transient anchorage of cross-linked glycosyl-phosphatidylinositol-anchored proteins depends on cholesterol, Src family kinases, caveolin, and phosphoinositides. *J. Cell Biol.* 175, 169–178. doi: 10.1083/jcb.200512116

Chojnacki, J., Waithe, D., Carravilla, P., Huarte, N., Galiani, S., Enderlein, J., et al. (2017). Envelope glycoprotein mobility on HIV-1 particles depends on the virus maturation state. *Nat. Commun.* 8:545.

Dinic, J., Ashrafzadeh, P., and Parmryd, I. (2013). Actin filaments attachment at the plasma membrane in live cells cause the formation of ordered lipid domains. *Biochim. Biophys. Acta* 1828, 1102–1111. doi: 10.1016/j.bbamem.2012.12.004

Dinic, J., Riehl, A., Adler, J., and Parmryd, I. (2015). The T cell receptor resides in ordered plasma membrane nanodomains that aggregate upon patching of the receptor. *Sci. Rep.* 5:10082.

Eggeling, C., Ringemann, C., Medda, R., Schwarzmann, G., Sandhoff, K., Polyakova, S., et al. (2009). Direct observation of the nanoscale dynamics of membrane lipids in a living cell. *Nature* 457, 1159–1162. doi: 10.1038/nature07596

Faraudo, J. (2002). Diffusion equation on curved surfaces. I. Theory and application to biological membranes. *J. Chem. Phys.* 116, 5831–5841. doi: 10.1063/1.1456024

Fujimoto, T., and Parmryd, I. (2016). Interleaflet coupling, pinning, and leaflet asymmetry-major players in plasma membrane nanodomain formation. *Front. Cell Dev. Biol.* 4:155. doi: 10.3389/fcell.2016.00155

Fujiwara, T., Ritchie, K., Murakoshi, H., Jacobson, K., and Kusumi, A. (2002). Phospholipids undergo hop diffusion in compartmentalized cell membrane. *J. Cell Biol.* 157, 1071–1081.

Gesper, A., Hagemann, P., and Happel, P. (2017). A low-cost, large field-of-view scanning ion conductance microscope for studying nanoparticle-cell membrane interactions. *Nanoscale* 9, 14172–14183. doi: 10.1039/c7nr04306f

Gorelik, J., Shevchuk, A., Ramalho, M., Elliott, M., Lei, C., Higgins, C. F., et al. (2002). Scanning surface confocal microscopy for simultaneous topographical and fluorescence imaging: application to single virus-like particle entry into a cell. *Proc. Natl. Acad. Sci. U.S.A.* 99, 16018–16023. doi: 10.1073/pnas.252458399

Gorelik, J., Shevchuk, A. I., Frolenkov, G. I., Diakonov, I. A., Lab, M. J., Kros, C. J., et al. (2003). Dynamic assembly of surface structures in living cells. *Proc. Natl. Acad. Sci. U.S.A.* 100, 5819–5822. doi: 10.1073/pnas.1030502100

Gov, N. S. (2006). Diffusion in curved fluid membranes. *Phys. Rev. E Stat. Nonlin. Soft. Matter. Phys.* 73:041918.

Gupta, A., Phang, I. Y., and Wohland, T. (2020). To hop or not to hop: exceptions in the FCS diffusion law. *Biophys. J.* 118, 2434–2447. doi: 10.1016/j.bpj.2020.04.004

Hagemann, P., Gesper, A., and Happel, P. (2018). Correlative stimulated emission depletion and scanning ion conductance microscopy. *ACS Nano.* 12, 5807–5815. doi: 10.1021/acsnano.8b01731

Hansma, P. K., Drake, B., Marti, O., Gould, S. A., and Prater, C. B. (1989). The scanning ion-conductance microscope. *Science* 243, 641–643. doi: 10.1126/science.2464851

Happel, P., Thatenhorst, D., and Dietzel, I. D. (2012). Scanning ion conductance microscopy for studying biological samples. *Sensors* 12, 14983–15008. doi: 10.3390/s121114983

Holyst, R., Plewczynski, D., Aksimentiev, A., and Burdzy, K. (1999). Diffusion on curved, periodic surfaces. *Phys. Rev.* 60, 302–307. doi: 10.1103/physreve.60.302

Honigmann, A., Mueller, V., Ta, H., Schoenle, A., Sezgin, E., Hell, S. W., et al. (2014). Scanning STED-FCS reveals spatiotemporal heterogeneity of lipid interaction in the plasma membrane of living cells. *Nat. Commun.* 5:5412.

Humpolickova, J., Gielen, E., Benda, A., Fagulova, V., Vercammen, J., Vandeven, M., et al. (2006). Probing diffusion laws within cellular membranes by Z-scan fluorescence correlation spectroscopy. *Biophys. J.* 91, L23–L25.

Janes, P. W., Ley, S. C., and Magee, A. I. (1999). Aggregation of lipid rafts accompanies signaling via the T cell antigen receptor. *J. Cell Biol.* 147, 447–461. doi: 10.1083/jcb.147.2.447

Jung, Y., Riven, I., Feigelson, S. W., Kartvelishvily, E., Tohya, K., Miyasaka, M., et al. (2016). Three-dimensional localization of T-cell receptors in relation to microvilli using a combination of superresolution microscopies. *Proc. Natl. Acad. Sci. U.S.A.* 113, E5916–E5924.

Kabbani, A. M., Woodward, X., and Kelly, C. V. (2017). Revealing the effects of nanoscale membrane curvature on lipid mobility. *Membranes* 7:60. doi: 10.3390/membranes7040060

Kabouridis, P. S., Magee, A. I., and Ley, S. C. (1997). S-acylation of LCK protein tyrosine kinase is essential for its signalling function in T lymphocytes. *EMBO J.* 16, 4983–4998. doi: 10.1093/emboj/16.16.4983

Krieger, J. W., Singh, A. P., Bag, N., Garbe, C. S., Saunders, T. E., Langowski, J., et al. (2015). Imaging fluorescence (cross-) correlation spectroscopy in live cells and organisms. *Nat. Protoc.* 10, 1948–1974. doi: 10.1038/nprot.2015.100

Krummel, M. F., Sjaastad, M. D., Wulfing, C., and Davis, M. M. (2000). Differential clustering of CD4 and CD3zeta during T cell recognition. *Science* 289, 1349–1352. doi: 10.1126/science.289.5483.1349

Machan, R., and Hof, M. (2010). Lipid diffusion in planar membranes investigated by fluorescence correlation spectroscopy. *Biochim. Biophys. Acta* 1798, 1377–1391. doi: 10.1016/j.bbamem.2010.02.014

Malchus, N., and Weiss, M. (2010). Elucidating anomalous protein diffusion in living cells with fluorescence correlation spectroscopy-facts and pitfalls. *J. Fluoresc.* 20, 19–26. doi: 10.1007/s10895-009-0517-4

Milon, S., Hovius, R., Vogel, H., and Wohland, T. (2003). Factors influencing fluorescence correlation spectroscopy measurements on membranes: simulations and experiments. *Chem. Phys.* 288, 171–186. doi: 10.1016/s0301-0104(03)00018-1

Mueller, V., Ringemann, C., Honigmann, A., Schwarzmann, G., Medda, R., Leutenegger, M., et al. (2011). STED nanoscopy reveals molecular details of cholesterol- and cytoskeleton-modulated lipid interactions in living cells. *Biophys. J.* 101, 1651–1660. doi: 10.1016/j.bpj.2011.09.006

Müller, C. B., Loman, A., Pacheco, V., Koberling, F., Willbold, D., Richtering, W., et al. (2008). Precise measurement of diffusion by multi-color dual-focus fluorescence correlation spectroscopy. *Europhys. Lett.* 83:46001. doi: 10.1209/0295-5075/83/46001

Nicolau, D. V. Jr., Hancock, J. F., and Burrage, K. (2007). Sources of anomalous diffusion on cell membranes: a monte carlo study. *Biophys. J.* 92, 1975–1987. doi: 10.1529/biophysj.105.076869

Owen, D. M., Williamson, D. J., Boelen, L., Magenau, A., Rossy, J., and Gaus, K. (2013). Quantitative analysis of three-dimensional fluorescence localization microscopy data. *Biophys. J.* 105, L05–L07.

Parmryd, I., and Onfelt, B. (2013). Consequences of membrane topography. *FEBS J.* 280, 2775–2784. doi: 10.1111/febs.12209

Petrasek, Z., and Schwille, P. (2008). Precise measurement of diffusion coefficients using scanning fluorescence correlation spectroscopy. *Biophys. J.* 94, 1437–1448. doi: 10.1529/biophysj.107.108811

Qian, H., and Elson, E. L. (1991). Analysis of confocal laser-microscope optics for 3-D fluorescence correlation spectroscopy. *Appl. Opt.* 30, 1185–1195.

Reister, E., and Seifert, U. (2005). Lateral diffusion of a protein on a fluctuating membrane. *Europhys. Lett.* 71, 859–865. doi: 10.1209/epl/i2005-10139-6

Ries, J., and Schwille, P. (2008). New concepts for fluorescence correlation spectroscopy on membranes. *Phys. Chem. Chem. Phys.* 10, 3487–3497.

Schneider, F., Waithe, D., Galiani, S., Bernardino de la Serna, J., Sezgin, E., and Eggeling, C. (2018). Nanoscale spatiotemporal diffusion modes measured by simultaneous confocal and stimulated emission depletion nanoscopy imaging. *Nano Lett.* 18, 4233–4240. doi: 10.1021/acs.nanolett.8b01190

Schwille, P., Korlach, J., and Webb, W. W. (1999). Fluorescence correlation spectroscopy with single-molecule sensitivity on cell and model membranes. *Cytometry* 36, 176–182. doi: 10.1002/(sici)1097-0320(19990701)36:3<176::aid-cyto5>3.0.co;2-f

Sezgin, E., Levental, I., Grzybek, M., Schwarzmann, G., Mueller, V., Honigmann, A., et al. (2012). Partitioning, diffusion, and ligand binding of raft lipid analogs in model and cellular plasma membranes. *Biochim. Biophys. Acta* 1818, 1777–1784. doi: 10.1016/j.bbamem.2012.03.007

Sezgin, E., Schneider, F., Galiani, S., Urbancic, I., Waithe, D., Lagerholm, B. C., et al. (2019). Measuring nanoscale diffusion dynamics in cellular membranes with super-resolution STED-FCS. *Nat. Protoc.* 14, 1054–1083.

Shurer, C. R., Kuo, J. C., Roberts, L. M., Gandhi, J. G., Colville, M. J., Enoki, T. A., et al. (2019). Physical principles of membrane shape regulation by the glycocalyx. *Cell* 177, 1757–1770.

Stromqvist, J., Johansson, S., Xu, L., Ohsugi, Y., Andersson, K., Muto, H., et al. (2011). A modified FCCS procedure applied to Ly49A-MHC class I cis-interaction studies in cell membranes. *Biophys. J.* 101, 1257–1269. doi: 10.1016/j.bpj.2011.06.057

Voigtländer, B. (2015). *Artifacts in SPM In Scanning Probe Microscopy, NanoScience and Technology*. Berlin: Springer.

Wawrezinieck, L., Rigneault, H., Marguet, D., and Lenne, P. F. (2005). Fluorescence correlation spectroscopy diffusion laws to probe the submicron cell membrane organization. *Biophys. J.* 89, 4029–4042. doi: 10.1529/biophysj.105.067959

Weiss, M., Hashimoto, H., and Nilsson, T. (2003). Anomalous protein diffusion in living cells as seen by fluorescence correlation spectroscopy. *Biophys. J.* 84, 4043–4052. doi: 10.1016/s0006-3495(03)75130-3

Wennmalm, S., Chmyrov, V., Widengren, J., and Tjernberg, L. (2015). Highly sensitive FRET-FCS detects amyloid beta-peptide oligomers in solution at

physiological concentrations. *Anal. Chem.* 87, 11700–11705. doi: 10.1021/acs.analchem.5b02630

Winkler, P. M., Regmi, R., Flauraud, V., Brugger, J., Rigneault, H., Wenger, J., et al. (2017). Transient nanoscopic phase separation in biological lipid membranes resolved by planar plasmonic antennas. *ACS Nano.* 11, 7241–7250. doi: 10.1021/acsnano.7b03177

Wohland, T., Rigler, R., and Vogel, H. (2001). The standard deviation in fluorescence correlation spectroscopy. *Biophys. J.* 80, 2987–2999. doi: 10.1016/s0006-3495(01)76264-9

Yoshigaki, T. (2007). Theoretically predicted effects of Gaussian curvature on lateral diffusion of membrane molecules. *Phys. Rev.* 75:041901.

Conflict of Interest: The authors declare that the research was conducted in the absence of any commercial or financial relationships that could be construed as a potential conflict of interest.

frontiers in Cell and Developmental Biology

ORIGINAL RESEARCH
published: 04 September 2020
doi: 10.3389/fcell.2020.531229

Transport Properties of Gramicidin A Ion Channel in a Free-Standing Lipid Bilayer Filled With Oil Inclusions

*Harvey Tawfik, Sevde Puza, Ralf Seemann and Jean-Baptiste Fleury**

Experimental Physics and Center for Biophysics, Universität des Saarlandes, Saarbrücken, Germany

Ion channels are key proteins in mammalian cell membranes. They have a central role in the physiology of excitable cells such as neurons, muscle, and heart cells. They also play a crucial role in kidney physiology. The gramicidin ion channel is one of the most studied ion channels, in particular it was intensively employed to investigate the lipid–protein interactions in model cell membranes. For example, even though the sequence of gramicidin is extremely hydrophobic, its motion is impaired in membrane bilayer, i.e., it does not rapidly flip to the other membrane leaflet, and low channel activity were observed when gramicidin is added asymmetrically to only one leaflet of a model cell membrane. In this article, we study the transport properties of gramicidin channel in a heterogeneous model membrane. Using microfluidics, we are forming freestanding bilayers as model cell membranes including heterogeneous domains that are created by oil inclusions. The presence of oil inclusions is then demonstrated by measuring the bilayer capacity via a patch-clamp amplifier and fluorescent confocal inspection. Based on electrophysiological and optical measurements Gramicidin A (gA) ion channels are dispersed into the buffer phases on both side of the formed lipid bilayer and insert spontaneously into the bilayer upon formation. The presence of functional Gramicidin A is then demonstrated by measuring conductivity signals. Based on electrophysiological and optical measurements, we explore the consequence of the presence of these oil inclusions on the functionality of incorporated gA ion channels. For low oil concentration, we measure a decrease of gA transport properties due to the reduction of the bilayer tension. For large oil concentration, we measure a saturation of gA transport properties due to an increase of the bilayer thickness.

Keywords: lipid bilayer, gramicidin, oil, ion channel, conduction

OPEN ACCESS

Edited by:
Falk Nimmerjahn,
University of Erlangen–Nuremberg, Germany

Reviewed by:
Todd R. Graham,
Vanderbilt University, United States
Leslie Climer,
Baylor University, United States

***Correspondence:**
Jean-Baptiste Fleury
jean-baptiste.fleury@physik.uni-saarland.de

Specialty section:
This article was submitted to Membrane Traffic, a section of the journal Frontiers in Cell and Developmental Biology

Received: *31 January 2020*
Accepted: *14 August 2020*
Published: *04 September 2020*

Citation:
Tawfik H, Puza S, Seemann R and Fleury J-B (2020) Transport Properties of Gramicidin A Ion Channel in a Free-Standing Lipid Bilayer Filled With Oil Inclusions. Front. Cell Dev. Biol. 8:531229. doi: 10.3389/fcell.2020.531229

INTRODUCTION

Biomembranes are composed of a wide range of biomolecules: lipids, proteins, and cholesterol that are important in several membrane-mediated processes. Functional ion channels formed by transmembrane proteins have a key role in the transport processes of living cells. As example, they have a crucial role in the physiology of excitable cells like neurons, muscle, cardiac cells and in the physiology of kidneys (Kuo and Ehrlich, 2012).

Ion channels enable the transport of small molecules, like ions through bilayer, while protein-free lipid bilayer is impermeable to ionic charges (Miyamoto and Thompson, 1966). Eukaryotic ion channels are pore-forming proteins that allow the flow of ions across membranes, either plasma membranes or the membranes of intracellular organelles (Armstrong, 1975; Hille, 2001; Alexander et al., 2011; Inanobe and Kurachi, 2014). Many ion channels such as most Na, K, Ca and some Cl channels are gated by voltage but others such as certain K and Cl channels, TRP channels, ryanodine receptors and IP_3 receptors are relatively voltage-insensitive and are gated by second messengers and other intracellular or extracellular mediators. Bacterial ion channels are infecting the host cell to create a bacterial pore, which is eventually damaging host tissues and leading to cells lysis (Armstrong, 1975; Martinac et al., 2008).

Transport properties of bacterial pore ion channels embedded in artificial lipid bilayer have been intensively studied in the past years (Koprowski and Kubalski, 2001; Funakoshi et al., 2006; Bayley et al., 2008; Peraro and van der Goot, 2016; Heo et al., 2019). The obtained results reflect that some particular bacterial channels, like α-hemolysin (Funakoshi et al., 2006; Bayley et al., 2008; Heo et al., 2019), present many advantages compared to mammalian ion channels for model membranes. One of the most studied examples of this type of ion channel is α-hemolysin, a bacterial protein from E-Coli, which is water soluble and which inserts spontaneously into a lipid bilayer that is containing PC phospholipids (Lakey et al., 1994; Diabate et al., 2015; Peraro and van der Goot, 2016). In contrast to mammalian channel proteins, α-hemolysin proteins are easy to synthesize in large quantities and they are water soluble in their monomeric state. Moreover, in their monomeric state, they are spontaneously inserting and diffusing into an artificial lipid bilayer and eventually forming a bacterial ion channel pore by self-assembly (Funakoshi et al., 2006; Bayley et al., 2008; Peraro and van der Goot, 2016; Heo et al., 2019). α-hemolysin pores are composed by 6, or more monomeric proteins (Song et al., 1996). The final pore diameter is depending of the number of individual protein units composing the bacterial-complex. Inorganic monovalent ions, such as potassium or sodium can travel through these pores freely via diffusion (Watanabe et al., 2014). Another example of a highly studied ion channel is Gramicidin A (gA) that consist of a dimeric structure, made of two helices (parallel and anti-parallel) that self-assemble to form a pore protein-complex (Cross et al., 1999). gA can be dispersed in buffer, and like hemolysin, can spontaneously insert into lipid bilayer before diffusing and forming a pore in the bilayer by self-assembly. Here, the self-assembly differs from hemolysin, as each gA monomer occupies only one leaflet of the bilayer, thus it needs two monomers face-to-face to form an ion channel (Cross et al., 1999; Acharya et al., 2013). Such a gA ion channel also enables inorganic monovalent ions, as potassium or sodium to freely travel through these pores via diffusion (Cross et al., 1999). In low doses gA can be used as antibiotic medications against gram-positive bacteria (Urry, 1971; Van Epps, 2006; Wang et al., 2012; Lum et al., 2017). As gA forms only pores that consist of dimers, these pores have a constant diameter, in contrast to hemolysin that can form pores with different diameter and therefore present different transport properties (Ketchem et al., 1993; Lum et al., 2017).

As mentioned previously, lipid bilayer has been employed, intensively, to characterize the conducting properties of gA pores via electrical measurements (Montal and Mueller, 1972). Such planar lipid bilayer is consisting of two separated lipid monolayers stabilized by a solvent is referred to as a Black Lipid Membrane (BLM) (Oiki, 2012). Advantages of the BLM methods over lipid vesicles are the possibility of electrophysiological measurements and the exchange of chemical reagents without the need of tedious vesicle handling and manipulation (Montal and Mueller, 1972; Oiki, 2012; Khangholi et al., 2020). One of the recent approaches with this technique, the droplet interface bilayer (DIB), has been specifically developed to produce a solvent-free lipid bilayer having a rich lipid composition (Bayley et al., 2008). This method also enables a rapid membrane characterization, drug screening, and ion channel recordings, whereas the possibility of having a continuous flow surrounding the bilayer in the DIB technique is somehow limited (Bayley et al., 2008). Thus, many miniaturized apparatuses have been developed, such as microfluidic devices, to overcome the drawbacks of all the previous techniques (Funakoshi et al., 2006). Moreover, the formation of lipid bilayers in microfluidic devices presents the advantage of changing the buffer around the bilayer while enabling good optical and electrophysiological access without using an undesired solvent (typically oil), which is essential for various biotechnological purposes (Heo et al., 2019; Khangholi et al., 2020). However, the properties of these pores in heterogeneous membrane are not known (Cross et al., 1999; Kourie et al., 2002; Acharya et al., 2013).

In this article, we study the transport properties of gA ion channels in heterogeneous membranes. Our heterogeneous membranes consist of a lipid bilayer filled with nanoscopic oil inclusions. It results that this type of heterogeneous bilayer possesses a substantial dynamic heterogeneity due to the diffusion of single oil molecules, or due to the self-organization of nanoscopic oil inclusions (Yang et al., 2016). As oil inclusion, we consider the case of silicone oil (SiAR20 Sigma-Aldrich) which is known to be present in lipid bilayer without forming large scale inclusions (micrometer and larger) (Claudeta et al., 2016). The presence of nanoscopic oil inclusions in our system was confirmed by highly sensitive electrophysiological measurements and confocal fluorescence microscopy. It is in particular of great interest for physicists studying ion channel protein in DiB system (Bayley et al., 2008), because in such systems a massive amount of silicone oil (until 50%) is needed to stabilize the formed lipid bilayer. Thus, it is relevant to investigate if the usage of large silicone oil concentration could affect the transport properties of an ion channel protein.

Behind these physical aspects, studying the influence of silicone oil inclusion in model membranes is also of biological relevance. Indeed, as silicone oils may contaminate the ocean as pollutant, it can be absorbed by algae, plankton, fish or plants (Nendza, 2007). Silicone oil is, also, commonly used in cosmetics and fast food as an anti-foaming agent (Bergeron et al., 1997; Erickson, 2015). Even if silicone oil is typically considered as

biologically inert, we investigate its influence on the transport properties of gA ion channels (Bergeron et al., 1997; Erickson, 2015). Moreover, we think that the case of oil spills may not be relevant directly for marine organism, as it is an antibiotic. But it may raises questions for other ion channel proteins with a dimeric structure present in their membrane in presence of an oil pollutant.

Using microfluidics, we are forming a model cell membrane including possible nanodomains consisting of silicone oil inclusions. We explore the consequence of the presence of these oil inclusions on the functionality of incorporated gA ion channel. Our model cell membrane is a free-standing lipid bilayer formed by contacting two aqueous fingers in a microfluidic chip surrounded by an oil phase that contains lipids. Upon pushing the aqueous fingers into the microfluidic device their interfaces get decorated with a lipid monolayer and eventually zip to form a bilayer when the monolayers contact each other (Vargas et al., 2014). The gA ion channels are dispersed into the aqueous buffer phases, on both side of the formed lipid bilayer and insert spontaneously into the bilayer upon bilayer formation. The presence of functional gA channels is demonstrated by measuring conductivity signals via a patch-clamp amplifier. We repeat this study by varying the concentration of silicone oil inside the bilayer. Thus, we explore the effect of silicone oil nano-domains on the conductive properties of gA pores.

EXPERIMENTAL

Material and Methods

1,2-Dioleoyl-sn-glycero-3-phosphocholine (DOPC) were bought from Avanti Polar Lipids. DOPC is used because it is one of the most common phospholipids present in human cells (Heo et al., 2019). The silicone oil (SiAR20) and squalene oil were purchased from Sigma-Aldrich. Ultra-pure water was obtained by filtration using a filtration system from Thermo Fisher. PDMS184 was purchased from Dow Corning. Gramicidin A and all other chemical, like salts: LiCl, NaCl, KCl, RbCl, CsCl, were purchased from Sigma-Aldrich. 0.1 M solute solution were prepared by dispersing the salt directly in pure water and under mechanical steering with 1 nM of gA.

Microfluidic Chips Design and Fabrication

A detailed description of the microfluidic design and fabrication is provided in the **Supplementary Material**. Two types of chips were produced: a 2D and a 3D microfluidic chips were produced. The 2D microfluidic chip allows the production of a lipid bilayer with a vertical orientation. The 3D microfluidic chip allows the production of a lipid bilayer with a horizontal orientation.

Surface Tension Measurements and Membrane Tension Calculation

Measurements of the surface tension γ were done applying the pendant drop technique using a commercial device (OCA 20, data physics). A droplet of the respective electrolyte solution was dispensed from a needle immersed in a cuvette that is filled with the studied lipid/oil composition containing also gA at a concentration of 1 nM. Different concentrations of silicone (0%, 0.1%, 0.3%, 5%, and 10%) were used to extract its effect on the surface tension (**Table 1**). The corresponding membrane tension Γ for each buffer/oil/lipid composition (5 mg/ml lipid concentration), can be calculated from these surface tension (**Table 1**) using the following equation $\Gamma = 2\gamma \cos\theta$, where θ is the contact angle extracted from optical micrographs as indicated in **Figure 1** (Bibette et al., 1999).

Electrophysiological Measurements

All measurements were done using a Patch Clamp amplifier (EPC 10 from Heka-Electronics). Two homemade Ag/AgCl electrodes were prepared by chlorination of ultra-clean Ag wires with diameter of 150 μm. The chlorination was achieved by immersing the two Ag wires in sodium hypochlorite solution (Merck, Germany) for about 30 min while applying a potential difference of a few volts. After chlorination; Ag wires turned into reference Ag/AgCl electrodes and we connected both of them to the probe of the patch amplifier. The two electrodes were inserted into the microfluidic chip via the two inlets of the aqueous phase, a few hundred microns away from the lipid bilayer. As excitation signal, we used a sinusoidal wave at a frequency of 10 kHz and an amplitude of up to 50 mV.

Formation of a Lipid Bilayer With Vertical Orientation

Before introducing the aqueous solution inside the chip, first the lipid/oil mixture (5 mg/ml lipid concentration) was injected into the chip and let there at rest for about 1 h to ensure complete hydrophobicity of the microfluidic channels. Then the aqueous solutions were injected in the chip through the inlets using a homemade hydrostatic pressure control consisting of two plastic syringes filled with the aqueous solution hanging on a laboratory stand while both can be moved up and down in small steps. The two syringes are open at their top, which enables adding ions, proteins or any other cargos. During the slow advancement of the two electrolyte fingers inside the microfluidic chip, both water/oil surfaces are decorated with lipid molecules; forming eventually two lipid monolayers. Once the two aqueous fingers appear close to the gap of the x-junction, we lower the height of both plastic syringes to slow down their advancement. When both aqueous fingers reached the gap region, they touch each other and shortly after form a lipid bilayer membrane (**Figure 1**; Vargas et al., 2014; Khangholi et al., 2020).

TABLE 1 | Measurements of the water/(Squalene-SiAR20) interface interfacial tension in presence of 5 mg/ml DOPC as function of silicone oil concentration in the surrounding squalene oil.

Si AR20 (vol%)	0	0.1	0.30	5	10
γ (mN/m)	8 ± 0.2	0.88 ± 0.07	0.72 ± 0.07	0.70 ± 0.07	0.71 ± 0.07
θ (°)	40 ± 1	28.5 ± 1	25.5 ± 1	25.5 ± 1	25.5 ± 1
Γ (mN/m)	12.2 ± 0.1	1.55 ± 0.1	1.29 ± 0.1	1.26 ± 0.1	1.28 ± 0.1

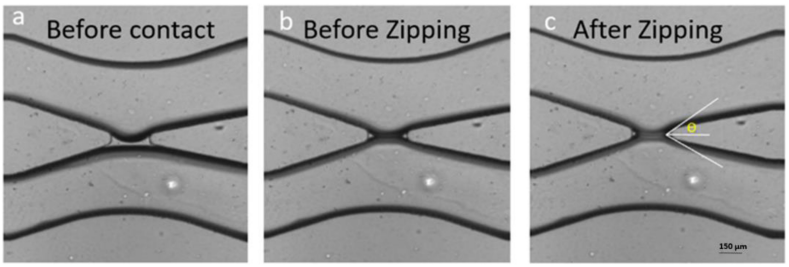

FIGURE 1 | Formation of a bilayer lipid membrane (DOPC) in a microfluidic device. **(a)** The two interfaces of the buffer fingers in the top and bottom channel are decorated by lipid monolayers but are still separated by a thin oil layer present in the gap. **(b)** The two monolayers were brought in contact by microfluidic manipulation and touch each other but did not yet form a lipid bilayer. **(c)** After formation a bilayer the conductivity can be measured by electrophysiological measurements and the contact angle θ can be obtained optically.

Formation of a Lipid Bilayer With Horizontal Orientation

All the lipid-oil mixtures are prepared with a concentration of 5 mg/mL in squalene oil. The lipids are dissolved in squalene via magnetic steering and let at 45°C for 3–4 h until completely dissolved. The free-standing bilayer formation method is based on a variant of the DIB method (Bayley et al., 2008). Two buffer fingers are dispersed in an oil-lipid phase. As the lipid molecules are amphiphilic, they are similar to a surfactant and they are covering each water-oil interface. Our chip is designed to position the two buffer fingers close to each other and only separated by an oil-lipid sandwich. The thickness of this oil-lipid phase is approximately a few tenths of micrometers. As the PDMS chip is porous it drains the oil phase separating the two buffer phases, which eventually brings the two lipid monolayers in contact to from a lipid bilayer. Experimentally, we perform this by filling the bottom microchannel by buffer first. The complete adsorption of squalene by PDMS walls varies between 1 and 2 h depending on the volume of lipid-oil mixture introduced to the system. After absorption of the oil, the lipid-oil sandwich becomes thinner and the lipid bilayer formation visually starts to be visible by the observation of a circle at the middle of the aperture between the two microfluidic channels.

Single Channel Analysis

For Single channel analysis (**Figure 6**), Gramicidin A (Sigma-Aldrich) was added into both aqueous phases surrounding a bilayer. The concentration of gA was 1 nM and the buffer solutions contained 1 M NaCl to enable electrophysiological measurements of the expected ion channels. After letting the system equilibrate for 15–20 min to form a stable bilayer, the bilayer was caught with a micropipette. To investigate the conductive properties of possibly formed pores, a silver chloride electrode connected to a patch-clamp setup was inserted into the micropipette (EPC10 – HEKA Germany). Using the single channel analysis mode, we recorded the current through the voltage-clamped membrane. Only after dispersing gA into the aqueous phases, an unitary amplitude of ≈2.8 pA is recorded, see **Figure 6** (solid black line). This value is characteristic for gA pores under the used experimental conditions. As a control test, this experiment was repeated, yet adding 5×10^{-3} M of calcium chloride ($CaCl_2$) into the buffer phases. The presence of divalent ions, such as calcium, is known to block the conductive properties of gA, when inserted in planar lipid bilayers. The presence of the divalent ion $CaCl_2$ blocked the conductive property of gA, inserted into a bilayer (as expected).

RESULTS AND DISCUSSION

We will first discus the transport properties of Gramicidin A pores without silicone oil and subsequently their altered transport properties in presence of silicone oil inclusions.

Transport Properties of an Oil-Free Lipid Bilayer With Gramicidin A Pores

From an electrical point of view, a pure lipid bilayer is equivalent to a dielectric, which makes it impermeable to charged molecules or ions (Miyamoto and Thompson, 1966). This is demonstrated by measuring the specific capacitance (~ 3.7 mF.m^{-2} for DOPC; Vargas et al., 2014) of the bilayer formed in our microfluidic chip (**Figure 1**). Also, no significant current could be measured as function of an applied voltage, as long this voltage is below the well-known threshold voltage inducing electroporation. After dispersing gA monomers at both sides of the bilayer and waiting ∼10 min, electrophysiological measurements reveal a collapse of the capacitance signal and a current signal could be measured that is linearly dependent on the applied constant voltage (**Figure 2**). These characteristic signals demonstrate the successful reconstitution of gA ion pores in our oil-free free-standing lipid bilayer. Additionally, this type of pore is known to be blocked in presence of divalent calcium ions. Correspondingly, a few minutes after dispersing 20 mM $CaCl_2$ buffer phase around the bilayer containing gA, we measured an increase of the capacitance signal close to the value obtained for a pure lipid bilayer and a simultaneous collapse of the current signal across the formed bilayer.

After this basic test that demonstrates the functionality of the gA pores inserted in our free-standing bilayer, we determine the transport properties of these pores for the following monovalent ions: Li^+, Na^+, K^+, Rb^+, Cs^+ in a way that these measurements could be compared. For that we first produced a lipid bilayer

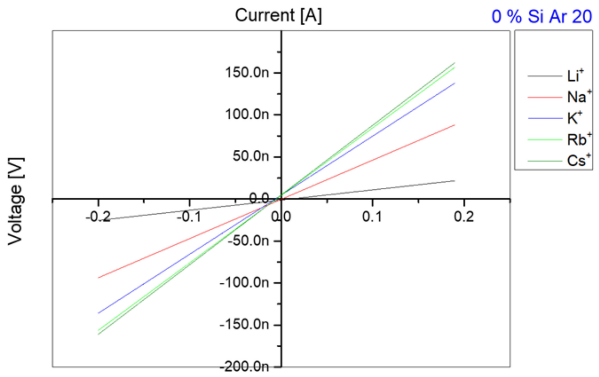

FIGURE 2 | Current-voltage measurements for different ions crossing through gA ion channels inserted in a DOPC bilayer in absence of Si-oil. According to the atomic weight, the transfer velocity through gA ion channels is increasing with increase in atomic weight until reaching Rb^+ and Cs^+ which have a very close transfer rate and sometimes rates for Rb^+ are faster than for Cs^+.

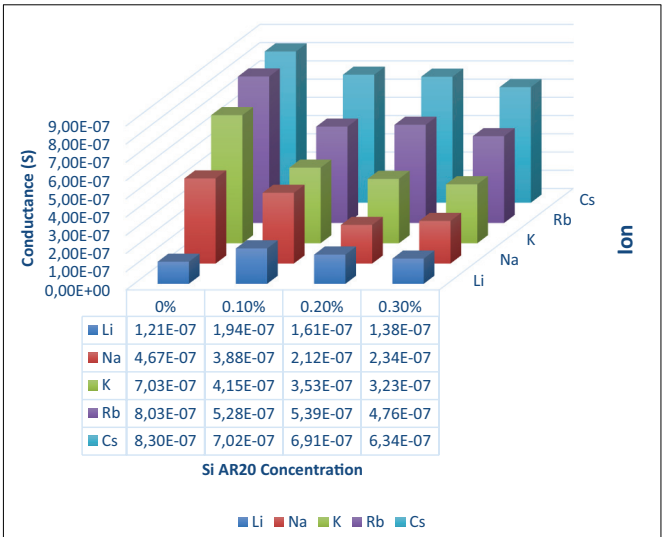

FIGURE 3 | DOPC bilayer conductance measured in presence of gA ion pores for five different monovalent ions (Li, Na, K, Rb, and Cs) and four different silicone oil (Si AR20) concentrations up to 0.3 vol% in squalene oil. For this fairly low Si-oil concentration, we can notice that Li^+ has the lowest conductance in all oil compositions, while Rb^+ and Cs^+ have the highest conductance. In general, there is a decrease in conductance for all ions after the addition of Si AR20 except for Li^+ which has the lowest conductance. The most pronounced decrease in conductivity for increasing concentration of SiAR20 is observed for K^+. Each point was on obtain on ~100 measurements.

as describe in section "Single Channel Analysis," with a buffer that contains 1 nM of gA monomers and 100 mM of the respective salt. After 10 min of stabilization, we exchanged the buffer phase around the bilayer and replaced it with a buffer containing the desired ion types (for example Na^+/Cl^-) and without proteins. It is important to note, that this exchange of buffer is conducted using microfluidic pressure pumps whereas the lipid bilayer do not break during this procedure. Moreover, even the bilayer area stays about constant during this process and no noticeable change could be observed optically. After inserting the gA pores and adjusting the desired ion concentration, we measured a series of 10 characteristic current-voltage curves for each ion type and plotted the averaged results, as exemplary shown in **Figure 2**. The slope of each curve in **Figure 2** is equal to the conductance of the bilayer, as plotted in **Figure 3**. Once such a measurement series is completed, we changed again the buffer phase around the bilayer containing another type of ionic charges. This protocol is repeated until we measured the current-voltage properties of the bilayer containing gA pores for the following five type of monovalent ions: Li^+, Na^+, K^+, Rb^+, Cs^+. It results that for the same applied voltage we measured different fluxes for the different monovalent charges, respectively bilayer conductivities. In particular we obtained conductivities $[Cs^+] > [Rb^+] > [K^+] > [Na^+] > [Li^+]$ for the same studied Si-oil free lipid bilayer (**Figure 3**), which corresponds to the characteristic diffusion rate of these monovalent cationic charges through gA pores as reported in literature (Sandblom et al., 1977; Eisenman et al., 1978; Latorre and Miller, 1983).

Transport Properties of Gramicidine A Pores Inserted in an Oil Containing Lipid Bilayer

To form a bilayer that contains silicone oil inclusions, we just mix a certain percentage of silicone oil to the squalene oil before forming a lipid bilayer. When the water-oil interfaces of the aqueous fingers coated with lipid molecules are brought into

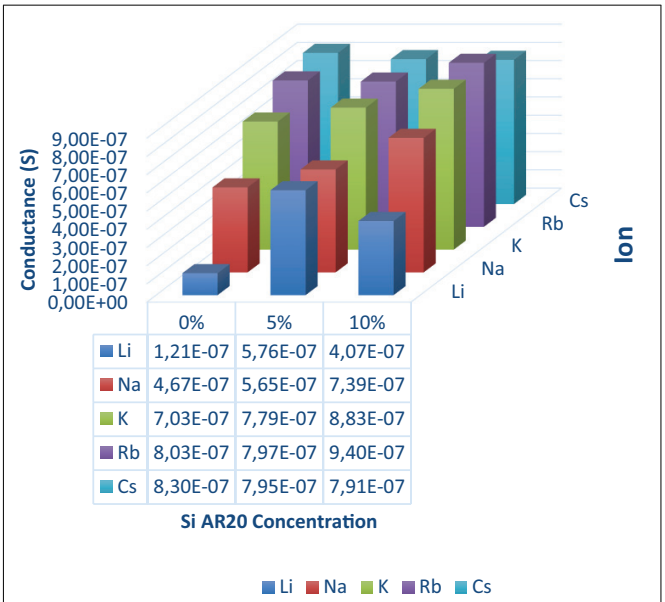

FIGURE 4 | Conductance of a DOPC bilayer in presence of gA ion pores measured for five different monovalent ions (Li, Na, K, Rb, and Cs) and three different silicone oil (Si AR20) concentration up to 10 vol% in squalene oil. For this range of large Si-oil concentrations we can notice that Li^+ has the lowest conductance in all oil compositions, while Rb^+ and Cs^+ have the largest conductance. In general, there is an increase in conductance for all ions after the addition of Si AR20 except in Li^+ which has the lowest conductance. Each point was on obtain on ~100 measurements.

contact in such a surrounding oil phase, they form a bilayer containing some silicone oil as the dewetting process forming a bilayer is in general unable to expulse the silicone oil molecules completely. It results that this is a simple method to obtain a bilayer that contains some silicone oil molecules. The resulting trapped amount of oil is not easy to measure, but we can guess that the amount of trapped oil is proportional to the percentage of silicone oil that is originally contained in the squalene oil.

Adding (0.1–0.3%) silicone oil in a lipid bilayer affects the physical properties of this bilayer in several ways. The bilayer tension is affected by the presence of silicone oil. It is known that silicone oil stabilizes lipid bilayer by reducing the corresponding bilayer tension (Thiam et al., 2012; Guo et al., 2018). Measurements of the surface tension of a lipid coated water-(Squalene – silicone oil) oil interface and calculations of the bilayer tension based on the optically obtained bilayer contact angle θ (cf. **Figure 1**), confirm a drastic reduction of the bilayer tension (**Table 1**) and thus an increase of bilayer thickness (Goulian et al., 1998). However, it is commonly believed that silicone oil is weakly inserting into the lipid bilayer for this range of silicone oil concentration (Guo et al., 2018). In fact, a weak presence of silicone oil can be demonstrated via fluorescence inspection by confocal microscopy (**Figure 4**). Using an oil tracer (BODIPY), the presence of an oil is demonstrated by measuring a weak fluorescent signal in our lipid bilayer (**Figure 5**; Heo et al., 2019). Inspecting our bilayer, the shape of individual oil inclusions could not be characterized, which means that individual inclusions must be smaller than the lateral resolution of about 250 nm and can therefore not be resolved by confocal microscopy. This means that we have nano-inclusions and certainly no micro-inclusions. It is important to note that without the presence of silicone oil, no fluorescent signal is visible into the bilayer (Heo et al., 2019).

Adding (5–10%) silicone oil molecules in our lipid bilayer, we do not measure a change of surface tension compared to (0.1–0.3%) silicone oil (**Table 1**). This means that the membrane tension stays constant despite the increased silicone oil inclusions in our lipid bilayer. However, comparing specific capacitance measurements ($\sim$ 3.7 mF.m^{-2} of a protein-free DOPC bilayer to the value of $\sim$ 3 mF.m^{-2} for 10 vol% silicone oil reveal an increase by about $\sim$1 nm), which corresponds to an increase about $\sim$20% of the bilayer thickness. The presence of silicone oil is also clearly visible via fluorescence inspection (**Figure 5**) for 5% and 10%vol. Interestingly, individual oil inclusions could not be resolved which means that individual inclusions must be smaller than the lateral resolution of about 250 nm and can therefore not be seen. These electrophysiological and optical results indicate that silicone oil inserts strongly into the bilayer core at these

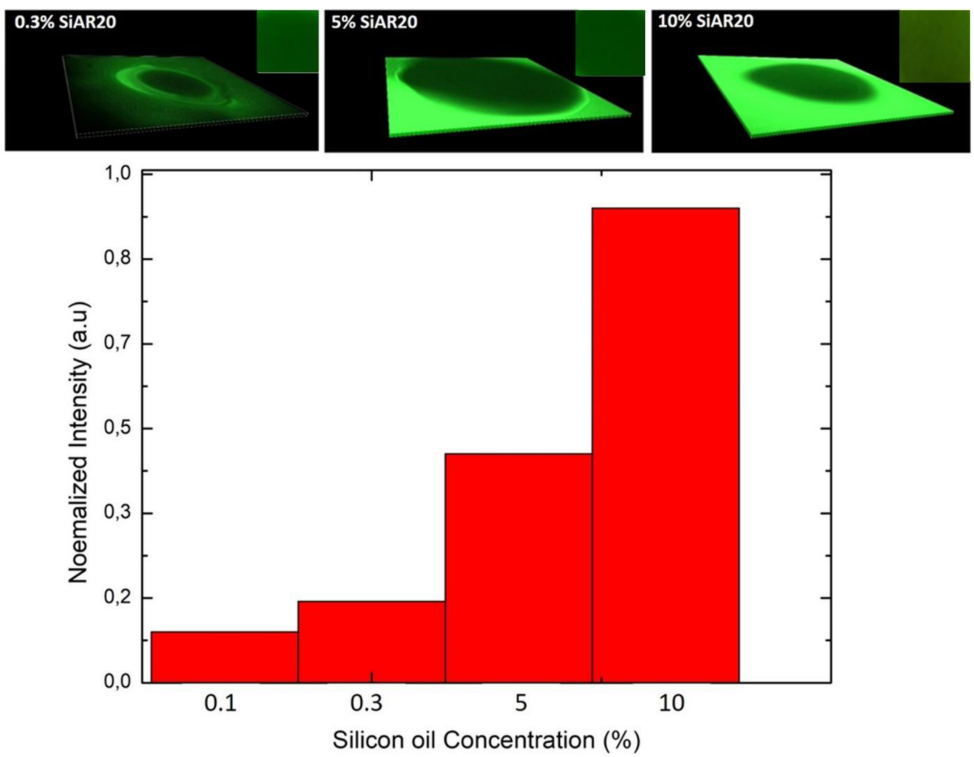

FIGURE 5 | Upper row: 3D representation of a fluorescence inspection of a horizontal free-standing DOPC bilayer with a confocal microscope; inset shows a region of interest of the bilayer from the top view. The silicone oil is labeled with BODIPY and the bilayer picture is obtained after its zipping. The highly fluorescence region of the green area indicates the squalene/silicone oil reservoir. The green signal with a less intense fluorescence in the middle shows the bilayer region for a define concentration of silicone oil. **Lower row:** Normalized intensity signals averaged over the bilayer region of interest after normalized their intensity signal in respect to the strongest signal.

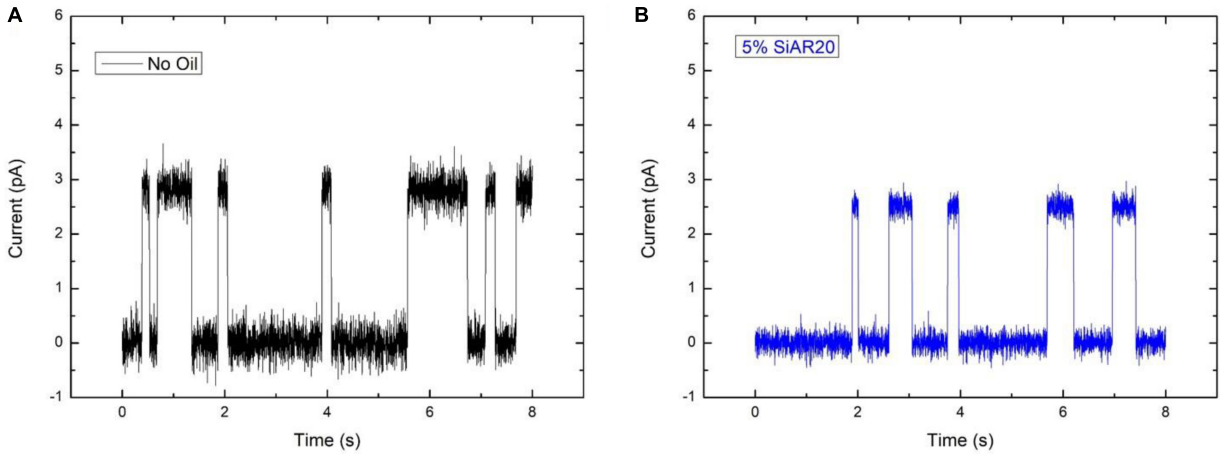

FIGURE 6 | Ionic conductance of a single gA pore embedded in a DOPC bilayer, **(A)** without silicone oil and **(B)** with 5 vol% silicone oil AR20 in the squalene phase. The buffer contains 1 M NaCl, the applied potential difference across the bilayer is 200 mV, T = 25°C. The conduction of gA without Si-oil in **(A)** is around 2.8 pA and **(B)** around 2.5 pA in the presence of Si-oil. Measurements present, here, are a short measurements on hundreds of reproducible single jumps.

large Si-oil concentrations. Thus, we can safely assume that the bilayer thickness increases for (5–10%) silicone oil in comparison to small silicone oil concentrations of (0.1–0.3%).

Now, we can measure the transport properties of gA pores as function of the nature of the ionic charges (Li^+, Na^+, K^+, Rb^+, Cs^+). To measure the different transport properties of gA for these ions, we follow the procedure described in section "Single Channel Analysis," with a buffer that contains gA monomers. Then, after ∼10 min, we exchanged the buffer phase around the bilayer by a buffer containing one type of ionic charges (for example Na^+/Cl^-) and no proteins. Then we measured a series of 10 characteristic current-voltage curves and plot the average results, as shown in **Figure 2**. Once this step is conducted, we changed again the buffer phase around the bilayer with another type of ionic charges and repeat the same measurement for this type of ionic charge. These measurements were repeated for fairly small silicone oil concentrations of 0.1 vol%, 0.2 vol%, and 0.3 vol% and we measured a transport rate through gA pores that is following the relation $[Cs^+] > [Rb^+] > [K^+] > [Na^+] > [Li^+]$ like in a bilayer without silicone oil (**Figure 3**). Compared to the case without silicone oil, the ionic transport rate seems to be reduced when adding a little silicone oil. This point could be understood as a reduction of pore conductivity due to a decrease of membrane tension from ∼8 to ∼1 mN/m that is accompanied with an increase in bilayer thickness. Because the thickness of a gA dimer is less than the thickness of a relaxed bilayer (when the bilayer is not under tension), a gA dimer locally compresses the bilayer (Goulian et al., 1998). However, when the bilayer is under high tension, i.e., bilayer tension >4 mN/m, the bilayer thickness becomes close to the extension of a gA dimer. Therefore, it is easier to form gA pores and so the bilayer conductivity is increased (Goulian et al., 1998).

If the amount of silicone oil is raised to larger concentrations, of 5 vol% or 10 vol%, the measured transport rates are no more respecting the characteristic transport rate dependence for ions across gA pores. For those large silicone oil concentration of 5 vol% and above, we even obtained a conductance that is about equal for $[Cs^+] \sim [Rb^+] \sim [K^+]$, which is characteristic for a saturation of the channel via, maybe, a single-file transport of these cations (Finkelstein and Andersen, 1981). We can even suppose that the reduction of membrane tension due to inserted silicone oil, is reducing the pore size and facilitates the saturation of the gA ion pore via a possible single-file transport (Finkelstein and Andersen, 1981; Goulian et al., 1998). To test this hypothesis, we performed single-channel analysis for a DOPC bilayer containing gA ion pores without silicone oil, and with 5 vol% silicone oil in the surrounding squalene phase (following the method describe by Hähl et al., 2017) (**Figure 6**). It results that these measurements reveal a slight reduction of a single-channel conduction from ∼2.8 pA for a bilayer without oil inclusions to ∼2.5 pA in presence of silicone oil (**Figure 6**), with $r^2 = \frac{l.\Delta I}{\pi GCU}$ (where r is the pore diameter, l is the length of the channel, ΔI is the step increase in current, G is the molar conductivity, C is the concentration, and U is the applied voltage). This fact could be understood as a reduction of the pore radius due to an increase of the bilayer thickness which is facilitating the possibility of single-file cation transport (Lundbaek and Andersen, 1994; Goulian et al., 1998; Lundbaek et al., 2010).

CONCLUSION

We studied the transport properties of Gramicidin A in a heterogeneous lipid bilayer that was fabricated using a microfluidic scheme. We studied how silicone inclusions are affecting the transport properties of gA. It results that without silicone oil, the gA pores exhibit the transport properties reported in the literature. However, with increasing silicone oil inclusion (0.1–0.3) vol% in the bilayer, the transport properties of gA pores embedded in these bilayers is reduced with respect to their standard behavior. For the largest silicone oil concentration tested (5 vol% and above), the conductivity seems to saturate on a

increase level and we even obtain about equal transport properties for $[Cs^+] \sim [Rb^+] \sim [K^+]$, which is characteristic of a saturation of the gA channel via, maybe, a single-file transport of these cations. We suppose that this effect is due the reduction of membrane tension that is induced by the presence of silicone oil that is increasing the bilayer thickness, which is reducing the pore size and thus facilitate the channel saturation. This hypothetic channel pore reduction is supported by single-channel analysis performed in presence of 5 vol% silicone oil. Thus, even that we demonstrated that silicone oil can affect the transport properties of ion channels. The oil quantities needed to perturb the ion channel transport remarkably, are too high to be considered as biologically relevant.

DATA AVAILABILITY STATEMENT

The datasets generated for this study are available on request to the corresponding author.

AUTHOR CONTRIBUTIONS

HT, SP, and J-BF performed the measurements. RS and J-BF directed the research. J-BF designed the research. All authors contributed to the article and approved the submitted version.

FUNDING

All the authors acknowledge funding from SFB1027 (DFG-Project B4).

SUPPLEMENTARY MATERIAL

The Supplementary Material for this article can be found online at: https://www.frontiersin.org/articles/10.3389/fcell.2020.531229/full#supplementary-material

REFERENCES

Acharya, S., Portman, A., Salazar, C., and Schmidt, J. J. (2013). Hydrogel-stabilized droplet bilayers for high speed solution exchange. *Sci. Rep.* 3:3139. doi: 10.1038/srep03139

Alexander, S. P. H., Mathie, A., and Peters, J. A. (2011). Ion channels. *Br. J. Pharmacol.* 164, 137–174. doi: 10.1111/j.1476-5381.2011.01649_5.x

Armstrong, C. M. (1975). Ionic pores, gates, and gating currents. *Q. Rev. Biophys.* 7, 179–210. doi: 10.1017/s0033583500001402

Bayley, H., Cronin, B., Heron, A., Holden, M. A., Hwang, W. L., Syeda, R., et al. (2008). Droplet interface bilayers. *Mol. Biosyst.* 4, 1191–1208. doi: 10.1039/b808893d

Bergeron, V., Cooper, P., Fischer, C., Giermanska-Kahn, J., Langevin, D., Pouchelon, A., et al. (1997). Polydimethylsiloxane (PDMS)-based antifoams. *Coll. Surf. A Physicochem. Eng. Asp.* 122, 103–120. doi: 10.1016/S0927-7757(96)03774-0

Bibette, J., Calderon, F. L., and Poulin, P. (1999). Emulsions: basic principles. *Rep. Prog. Phys.* 62:969. doi: 10.1088/0034-4885/62/6/203

Claudeta, C., In, M., and Massiera, G. (2016). Method to disperse lipids as aggregates in oil for bilayers production. *Eur. Phys. J.* 39:9. doi: 10.1140/epje/i2016-16009-6

Cross, T., Arseniev, A., Cornell, B., Davis, J. H., Killian, J. A., Koeppe, R. E. II, et al. (1999). Gramicidin channel controversy — revisited. *Nat. Struct. Mol. Biol.* 6, 610–611. doi: 10.1038/10650

Diabate, M., Munro, P., Garcia, E., Jacquel, A., Michel, G., Obba, S., et al. (2015). *Escherichia coli* α-hemolysin counteracts the anti-virulence innate immune response triggered by the rho GTPase activating toxin CNF1 during bacteremia. *PLoS Pathog.* 11:e1004732. doi: 10.1371/journal.ppat.1004732

Eisenman, G., Sandblom, J., and Neher, E. (1978). Ionic selectivity, saturation and block in gramicidin A channels: CS, Rb, K, Na, Li, Tl, H, and effects of anion binding. *Biophys. J.* 22, 307–340. doi: 10.1016/S0006-3495(78)85491-5

Erickson, M. D. (2015). *Book: Deep Frying: Chemistry, Nutrition, and Practical Applications*. Champaign: AOCS Press.

Finkelstein, A., and Andersen, O. S. (1981). The gramicidin a channel: a review of its permeability characteristics with special reference to the single-file aspect of transport. *J. Membrain Biol.* 59, 155–171. doi: 10.1007/BF01875422

Funakoshi, K., Hiroaki, S., and Takeuchi, S. (2006). Lipid bilayer formation by contacting monolayers in a microfluidic device for membrane protein analysis. *Analyt. Chem.* 78, 8169–8174. doi: 10.1021/ac0613479

Goulian, M., Mesquita, O. N., Fygenson, D. K., Nielsen, C., Andersen, O. S., and Libchaber, A. (1998). Gramicidin channel kinetics under tension. *Biophys. J.* 74, 328–337. doi: 10.1016/S0006-3495(98)77790-2

Guo, Y., Werner, M., Seemann, R., Baulin, V. A., and Fleury, J.-B. (2018). Tension-induced translocation of an ultrashort carbon nanotube through a phospholipid bilayer. *ACS. Nano* 12, 12042–12049. doi: 10.1021/acsnano.8b04657

Hähl, H., Vargas, J. N., Griffo, A., Laaksonen, P., Szilvay, G., Lienemann, M., et al. (2017). Pure protein bilayers and vesicles from native fungal hydrophobins. *Adv. Mater.* 29:1602888. doi: 10.1002/adma.201602888

Heo, P., Ramakrishnan, S., Coleman, J., Rothman, J. E., Fleury, J.-B., and Pincet, F. (2019). Highly reproducible physiological asymmetric membrane with freely diffusing embedded proteins in a 3D-Printed microfluidic setup. *Small* 15:21. doi: 10.1002/smll.201900725

Hille, B. (2001). *Ion Channel of Excitable Membranes*, 3rd Edn, Sunderland, MA: Sinauer Associates.

Inanobe, A., and Kurachi, Y. (2014). Membrane channels as integrators of G-protein-mediated signaling. *Biochim. Biophys. Acta Biomembr.* 1838, 521–531. doi: 10.1016/j.bbamem.2013.08.018

Ketchem, R. R., Hu, W., and Cross, T. A. (1993). High-resolution conformation of gramicidin A in a lipid bilayer by solid-state NMR. *Science* 10:5127. doi: 10.1126/science.7690158

Khangholi, N., Seemann, R., and Fleury, J.-B. (2020). Simultaneous measurement of surface and bilayer tension in a microfluidic chip. *Biomicrofluidics* 14:024117. doi: 10.1063/1.5137810

Koprowski, P., and Kubalski, A. (2001). Bacterial ion channels and their eukaryotic homologues. *Bioessays* 23, 1148–1158. doi: 10.1002/bies.10017

Kourie, J. I., Culverson, A. L., Farrelly, P. V., Henry, C. L., and Laohachai, K. N. (2002). Heterogeneous amyloid-formed ion channels as a common cytotoxic mechanism. *Cell Biochem. Biophys* 36, 191–207. doi: 10.1385/CBB:36:2-3:191

Kuo, I. Y., and Ehrlich, B. E. (2012). Ion channels in renal disease. *Chem. Rev.* 112, 6353–6372. doi: 10.1021/cr3001077

Lakey, J. H., van der Goot, F. G., and Pattus, F. (1994). All in the family: the toxic activity of pore-forming toxins. *Toxicology* 87, 85–108. doi: 10.1016/0300-483x(94)90156-2

Latorre, R., and Miller, C. (1983). Conduction and selectivity in potassium channels. *J. Membrain Biol.* 71, 11–30. doi: 10.1007/BF01870671

Lum, K., Ingólfsson, H. I., Koeppe, R. E., and Andersen, O. S. (2017). Exchange of gramicidin between lipid bilayers: implications for the mechanism of channel formation. *Biophys. J.* 113, 1757–1767. doi: 10.1016/j.bpj.2017.08.049

Lundbaek, J. A., and Andersen, O. S. (1994). Lysophospholipids modulate channel function by altering the mechanical properties of lipid bilayers. *J. Gen. Physiol.* 104, 645–673. doi: 10.1085/jgp.104.4.645

Lundbaek, J. A., Koeppe, R. E., and Andersen, O. S. (2010). Amphiphile regulation of ion channel function by changes in the bilayer spring constant. *Proc. Natl. Acad. Sci. U.S.A.* 107, 15427–15430. doi: 10.1073/pnas.1007455107

Martinac, B., Saimi, Y., and Kung, C. (2008). Ion channels in microbes. *Physiol. Rev.* 88, 1449–1490. doi: 10.1152/physrev.00005.2008

Miyamoto, V. K., and Thompson, T. E. (1966). Some electrical properties of lipid bilayer membranes. *J. Coll. Interf. Sci.* 25, 16–25. doi: 10.1016/0021-9797(67)90005-7

Montal, M., and Mueller, P. (1972). Formation of bimolecular membranes from lipid monolayers and a study of their electrical properties. *Proc. Natl. Acad. Sci. U.S.A.* 69:3561. doi: 10.1073/pnas.69.12.3561

Nendza, M. (2007). Hazard assessment of silicone oils (polydimethylsiloxanes, PDMS) used in antifouling/foul release products in the marine environment. *Mar. Pollut. Bull.* 54, 1190–1196. doi: 10.1016/j.marpolbul.2007.04.009

Oiki, S. (2012). "Planar lipid bilayer method for studying channel molecules," in *Patch Clamp Techniques, Protocols Handbooks*, ed. Y. Okada (Tokyo: Springer).

Peraro, M., and van der Goot, F. (2016). Pore-forming toxins: ancient, but never really out of fashion. *Nat. Rev. Microbiol.* 14, 77–92. doi: 10.1038/nrmicro.2015.3

Sandblom, J., Eisenman, G., and Neher, E. (1977). Ionic selectivity, saturation and block in gramicidin A channels. *J. Membrain Biol.* 31, 383–417. doi: 10.1007/BF01869414

Song, L., Hobaugh, M. R., Shustak, C., Cheley, S., Bayley, H., and Gouaux, J. E. (1996). Structure of staphylococcal alpha-hemolysin, a heptameric transmembrane pore. *Science* 274, 1859–1866. doi: 10.1126/science.274.5294.1859

Thiam, A. R., Bremond, N., and Bibette, J. (2012). From stability to permeability of adhesive emulsion bilayers. *Langmuir* 28, 6291–6298. doi: 10.1021/la3003349

Urry, D. W. (1971). The gramicidin A transmembrane channel: a proposed pi(L,D) helix. *Proc. Natl. Acad. Sci. U.S.A.* 68, 672–676. doi: 10.1073/pnas.68.3.672

Van Epps, H. L. (2006). René dubos: unearthing antibiotics. *J. Exp. Med.* 203:259. doi: 10.1084/jem.2032fta

Vargas, J. N., Seemann, R., and Fleury, J. B. (2014). Fast membrane hemifusion via dewetting between lipid bilayers. *Soft Matter.* 10, 9293–9299. doi: 10.1039/C4SM01577K

Wang, F., Qin, L., Pace, C. J., Wong, P., Malonis, R., and Gao, J. (2012). Solubilized gramicidin A as potential systemic antibiotics. *Chembiochemistry* 13, 51–55. doi: 10.1002/cbic.201100671

Watanabe, R., Soga, N., Fujita, D., Tabata, K. V., Yamauchi, L., Kim, S. H., et al. (2014). Arrayed lipid bilayer chambers allow single-molecule analysis of membrane transporter activity. *Nat. Commun.* 5:4519. doi: 10.1038/ncomms5519

Yang, S., Lim, S., Kiessling, V., Kwon, I., and Tamm, L. K. (2016). Site-specific fluorescent labeling to visualize membrane translocation of a myristoyl switch protein. *Sci. Rep.* 6:32866. doi: 10.1038/srep32866

Conflict of Interest: The authors declare that the research was conducted in the absence of any commercial or financial relationships that could be construed as a potential conflict of interest.

frontiers in Cell and Developmental Biology

METHODS
published: 21 October 2020
doi: 10.3389/fcell.2020.573230

Addressing Differentiation in Live Human Keratinocytes by Assessment of Membrane Packing Order

Danuta Gutowska-Owsiak[1,2], Ewa I. Podobas[3,4], Christian Eggeling[2,5,6], Graham S. Ogg[2] and Jorge Bernardino de la Serna[2,7]**

[1] University of Gdansk, Intercollegiate Faculty of Biotechnology of University of Gdansk and Medical University of Gdansk, Gdansk, Poland, [2] Medical Research Council Human Immunology Unit, National Institute for Health Research Oxford Biomedical Research Centre, Medical Research Council Weatherall Institute of Molecular Medicine, University of Oxford, Oxford, United Kingdom, [3] Institute of Biochemistry and Biophysics, Polish Academy of Sciences, Warsaw, Poland, [4] Faculty of Biology, Institute of Genetics and Biotechnology, University of Warsaw, Warsaw, Poland, [5] Institute of Applied Optics and Biophysics, Friedrich-Schiller-University Jena, Jena, Germany, [6] Leibniz Institute of Photonic Technologies e.V., Jena, Germany, [7] Faculty of Medicine, National Heart and Lung Institute, Imperial College London, London, United Kingdom

OPEN ACCESS

Edited by:
Robert Ernst,
Saarland University, Germany

Reviewed by:
Yoshikazu Uchida,
Northern California Institute for Research and Education, United States
Kandice Levental,
University of Virginia, United States

***Correspondence:**
Danuta Gutowska-Owsiak
danuta.gutowska-owsiak@ug.edu.pl
Jorge Bernardino de la Serna
j.bernardino-de-la-serna@imperial.ac.uk

Specialty section:
This article was submitted to Cellular Biochemistry, a section of the journal Frontiers in Cell and Developmental Biology

Received: 16 June 2020
Accepted: 15 September 2020
Published: 21 October 2020

Citation:
Gutowska-Owsiak D, Podobas EI, Eggeling C, Ogg GS and Bernardino de la Serna J (2020) Addressing Differentiation in Live Human Keratinocytes by Assessment of Membrane Packing Order. Front. Cell Dev. Biol. 8:573230. doi: 10.3389/fcell.2020.573230

Differentiation of keratinocytes is critical for epidermal stratification and formation of a protective *stratum corneum*. It involves a series of complex processes leading through gradual changes in characteristics and functions of keratinocytes up to their programmed cell death via cornification. The *stratum corneum* is a relatively impermeable barrier, comprised of dead cell remnants (corneocytes) embedded in lipid matrix. Corneocyte membranes are comprised of specialized lipids linked to late differentiation proteins, contributing to the formation of a stiff and mechanically strengthened layer. To date, the assessment of the progression of keratinocyte differentiation is only possible through determination of specific differentiation markers, e.g., by using proteomics-based approaches. Unfortunately, this requires fixation or cell lysis, and currently there is no robust methodology available to study keratinocyte differentiation in living cells in real-time. Here, we explore new live-cell based approaches for screening differentiation advancement in keratinocytes, in a "calcium switch" model. We employ a polarity-sensitive dye, Laurdan, and Laurdan general polarization function (GP) as a reporter of the degree of membrane lateral packing order or condensation, as an adequate marker of differentiation. We show that the assay is straightforward and can be conducted either on a single cell level using confocal spectral imaging or on the ensemble level using a fluorescence plate reader. Such systematic quantification may become useful for understanding mechanisms of keratinocyte differentiation, such as the role of membrane in homogeneities in stiffness, and for future therapeutic development.

Keywords: keratinocyte differentiation, cornification, membrane heterogeneity, spectral imaging, high throughput, membrane stiffness, Laurdan fluorescence

INTRODUCTION

The epidermis, in the form of a stratified and desquamating tissue is a fascinating feature of many organisms; it retains very distinct characteristics which enable it to exert function, shielding us from external threats and preventing fluid evaporation. An understanding is emerging on how these unique features contribute to the important protective role of the epidermis; these lessons

are learned both from a physiological setting and through the perspective of skin diseases. For example, keratinocyte differentiation and cornification are essential for prevention of allergic diathesis by forming a functional skin barrier (Kubo et al., 2012; Flohr et al., 2014; Horimukai et al., 2014; Venkataraman et al., 2014). Cornification encompasses a series of processes leading to the programmed keratinocyte death, which results in formation of a cellular remnant known as "corneocyte." Corneocytes, embedded in a lipid-enriched matrix (Eckhart et al., 2013) provide mechanical hardness, while the lipids support elastic properties of the *stratum corneum*. In addition, at the cellular level, the lamellar organization of lipids and their lateral packing properties prevent evaporation (Iwai et al., 2012; Janssens et al., 2012; Narangifard et al., 2018), forming a seal over the moisture trapped in the *stratum corneum*. This phenomenon is achieved by high abundance of hydrophilic compounds, known as Natural Moisturizing Factor (NMF).

Multiple processes take place during the cornification advancement in the epidermis; these occur simultaneously both at the organellar and molecular levels (**Figure 1**). The characteristics of progression in keratinocyte differentiation *in vitro* are reflected by multiple morphological changes (i.e., related to the cell shape and adherence) and distinct organellar transformations). For instance, the appearance and maturation of keratohyalin granules (KHGs) (Gutowska-Owsiak et al., 2018), nuclear condensation and extrusion (Gdula et al., 2013; Rogerson et al., 2018), cytoskeleton collapse (Gutowska-Owsiak et al., 2018), and alterations in mitochondria (Ipponjima et al., 2020); in some of those events, autophagy has been shown to be involved (Akinduro et al., 2016). At the molecular level, shifts in cytokeratin expression have been documented (keratin 5, keratin 14 are progressively replaced with keratin 1 and keratin 10) while additional proteins are upregulated, e.g., involucrin and transglutaminase as well as the markers of late differentiation, defined by the expression of late envelope proteins (e.g., involucrin, filaggrin, loricrin) (Marshall et al., 2001; Candi et al., 2005, 2016; Sandilands et al., 2009; Eckhart et al., 2013). These differentiation-dependent proteins contribute to barrier strengthening by incorporation into the insoluble cornified envelope (CE; also known as cornified cell envelope, CCE) or by supporting the hydration of the stratum corneum (Kezic et al., 2009).

Along with the expression of protein markers and organellar changes, an overall increase in cell stiffness can be observed (Plasencia et al., 2007; Janssens et al., 2012; Wennberg et al., 2018). This stiffness is a consequence of two main processes; the formation of a rigid, protein-based CE and extensive lipid remodeling leading to specialized lipid profile adaptation (Ponec et al., 1987; Schmidt et al., 1991; López et al., 2007). Specifically, the high phospholipid and cholesterol content is gradually replaced by a predominance of ceramides and saturated triglycerides (Ponec et al., 1988), especially in conditions where stratification is supported. These lipid composition variations lead to more ordered membrane packing (Janssens et al., 2012), higher stiffness and consequently, changes in the relative lateral heterogeneity properties of the plasma membrane (Bernardino de la Serna et al., 2016). This selection has specific functional properties; the ceramides and free fatty acids provide attachment points for the CE proteins (Behne et al., 2000; López et al., 2007; Akiyama, 2017) and a scaffold to replace the plasma membrane by a corneocyte lipid envelope (CLE), which links CE with the lipids of the intercellular matrix (Elias et al., 2014). It is believed that ceramide enrichment displaces the balance between ordered and disordered regions to support membrane heterogeneity, where higher order regions work as docking molecular anchors supporting the CLE function and ultimately, stabilizing the CE structure. Regulation of ceramide synthesis is mediated via peroxisome proliferator-activated receptor (PPAR) pathways (Chon et al., 2015) associated with keratinocyte differentiation (Mao-Qiang et al., 2004); disturbances in these pathways result in clinical manifestations (Akiyama, 2017).

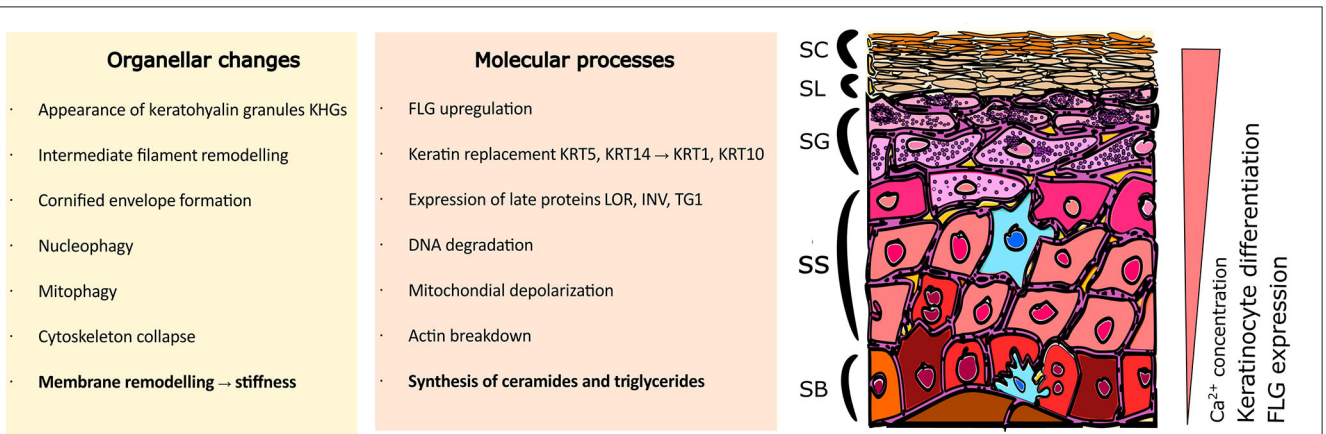

FIGURE 1 | Organellar and molecular changes in keratinocytes during the differentiation process. Stratified epidermis consists of multiple layers of epidermal keratinocytes characterized by increasing advancement of cell differentiation. Cells undergo extensive organellar and molecular alterations as they gradually move to the upper layers. Where SC, Stratum Corneum; SL, Stratum Lucidum; SG, Stratum Granulosum; SS, Stratum Spinosum; SB, Stratum Basale; FLG, filaggrin; KRT5, keratin 5; KRT14, keratin 14; KRT1, keratin 1; KRT10, keratin 10; LOR, loricrin; INV, involucrin; TG1, transglutaminase 1.

To date, no robust experimental readout for the assessment of differentiation advancement in live primary keratinocytes in real-time is available. Protein-targeted detection methods, such as the expression quantification by proteomics-based approaches, as well as other commonly used, e.g., immunostaining or western blot, require cell permeabilization or lysis and are only suitable for end-point measurements.

Previous studies have revealed the gel nature of the membranes in the stratum corneum (Plasencia et al., 2007). Here, we built upon the known lipid profile variation and ceramide enrichment during keratinocyte differentiation; we hypothesized that lipid lateral packing and order increase can be used as a hallmark for quantitative assessment of live-cell cornification advancement. For this purpose, we took advantage of the lipophilic polarity-sensitive membrane dye Laurdan, purposely designed by Weber and Farris (1979) to encompass an electron-donor and electron-acceptor, which displays large solvent-dependent fluorescence shifts. Laurdan ubiquitously distributes at the plane of the plasma membrane, regardless of its lipid lateral packing properties, and is oriented parallel with the phospholipid's hydrophobic tails in membranes. Moreover, its emission spectra and location are independent of phospholipid head groups and notably, indirectly report about the relative packing order by sensing the degree of water penetration in its vicinity (Parasassi et al., 1990, 1994, 1997; Bagatolli et al., 1998, 1999); the studies showed that Laurdan could sense the well-known phase transition from fluid to gel at 41C in in 1,2-dipalmitoyl-sn-glycero-3-phosphocholine (DPPC) bilayers. Most of these environmentally-sensitive probes display an increase in charge separation when excited in polar solvents resulting in a larger dipolar moment (Lakowicz, 1999); the penetration of water molecules into a bilayer formed of loosely packed lipids allow more rotational and translational freedom to the probe, yielding an emission shift toward longer wavelengths. On the contrary, the probe emission shifts toward the blue when its motion is more restricted due to sensing a *milieu* with lesser water content. Ratiometrically measuring the emission intensities at 440 and 490 nm renders the Laurdan "general polarization index" (GP), which allows relative quantification of the membrane order or degree of lipid lateral packing (Parasassi et al., 1990, 1997; Sezgin et al., 2015). This method has been used in visualizing native membrane microdomains in planar supported bilayers, giant unilamellar vesicles (de la Serna et al., 2009; Bernardino de la Serna et al., 2013) and in living cells (Gaus et al., 2003; Owen et al., 2011; Carugo et al., 2017; Gutowska-Owsiak et al., 2018; Bernabé-Rubio et al., 2019).

Even though the membrane order can only be measured indirectly, and being aware that the stiffness of a membrane influences can be in principle characterized by fluorescence polarization or fluorescence anisotropy, in this paper we introduced membrane lateral packing order as a readout for keratinocyte differentiation advancement. Using single-cell based confocal spectral imaging or a fluorescence plate reader for high-throughput screening of cellular ensembles we utilize the Laurdan general polarization index assessment of membrane order as an efficient readout for determination of the progression of keratinocyte differentiation in living cells.

MATERIALS AND METHODS

Human Keratinocyte Culture and Calcium Switch

Normal human epidermal keratinocytes (NHEKs) were purchased from Lonza (Lonza, Basel, Switzerland, neonatal, pooled) and cultured in keratinocyte KBM-2 media (Lonza, Basel, Switzerland) at conditions supporting proliferation ($[Ca2+] = 0.06$ mM) and subcultured by accutase treatment (Sigma Aldrich, Dorset, United Kingdom). To promote terminal differentiation, calcium switch was performed by adjusting calcium level do the final concentration of $[Ca2+] = 1.5$ mM for a period of 24 h before immunofluorescent labeling. To adjust to the desired calcium concentration a calcium switch was conducted over a period of 24 h by replacing the culture media with media adjusted to the desired calcium concentration by adding CaCl2 (Sigma Aldrich, Dorset, United Kingdom sigma).

Recombinant Filaggrin

The expression plasmid was constructed using a SLIC method. Briefly, the nucleotide sequence encoding 7th FLG domain with N-terminal 6-His-tagged SUMO protein sequence was cloned into pET28 vector using BamHI i XhoI restrictions sites. The construct was transformed into *E. coli* BL21-CodonPlus-RIL and propagated in LB liquid media with antibiotics, followed by autoinduction media (Formedium AIM- Super Broth) for 48 h at 18°C. The cells were sonicated in lysis buffer (10 mM Tris pH 8, 150 mM NaCl, 10 mM imidazole) with protease inhibitors cocktail. The purification procedure was performed on an ÄKTA^{TM}Xpress chromatography system. Lysate was loaded on Ni-NTA Agarose column (Qiagen). On-column cleavage by SUMO protease (4 μg/1 ml) was carried out in elution buffer (10 mM Tris pH 8, 150 mM NaCl, 300 mM imidazole) for 8 h at 10°C. The protein was purified by desalting and on Ni-NTA Agarose columns. Flow though fractions were loaded into a Superdex 200 column (GE Healthcare) and analyzed by SDS-PAGE; protein identification was carried out by MALDI-TOF MS.

Fluorescent Antibody Staining and Confocal Microscopy Imaging

NHEKs were grown and calcium-switched in eight-well cell culture slides (Beckton Dickinson), fixed and permeabilized by neat acetone. Blocking was carried out in freshly made blocking buffer (5% FCS, Sigma-Aldrich, Gillingham, Dorset, United Kingdom; 2% BSA, Sigma-Aldrich, Gillingham, Dorset, United Kingdom in PBS). For the primary antibody anti-filaggrin antibody (mouse monoclonal 15C10 from Leica Biosystems, Milton Keynes, United Kingdom) and anti-keratin 14 (clone EPR1612 from GeneTex, Irvine, CA, United States) were used; specificity of the antibody was verified prior with both recombinant human FLG and on epidermal lysates (**Supplementary Figure 1**). The staining was followed by secondary antibody labeling (anti-mouse Alexa 488 and anti-rabitt Alexa 568 Life Technologies/ThermoFisher Scientific, Waltham, MA, United States), all carried out in PBS. To visualize nuclei NucBlue reagent (Hoechst,

Life Technologies/ThermoFisher Scientific, Waltham, MA, United States) was used. The cover-slides were mounted with Mowiol-488 (Sigma-Aldrich, Gillingham, Dorset, United Kingdom).

Imaging acquisition was carried out on a Zeiss 780 inverted confocal microscope (Zeiss, Jena, Germany), by recording 2D images or 3D z-stacks. We used 488 nm excitation line and detected from 500–550nm. Images were postprocessed using Zen Software (Zeiss, Jena, Germany) and ImageJ National Institutes of Health, Bethesda, MD, United States).

Immunocytochemistry

Cells were grown in culture slides (BD Biosciences, San Jose, CA, United States) until 80% confluent, and were subjected to calcium switch for 24 h. The staining was conducted with anti-E-cadherin antibody (Biolegend, San Diego, CA, United States). An EnVision+ DAB polymer immunohistochemistry system (Dako) was used for both for visualization.

Intracellular Western Blot

Intracellular filaggrin and keratin-14 detection was carried out on cells cultured on 96 well plates that were used for the high throughput Laurdan screen, following data acquisition on the plate reader. Briefly, the cells were washed in PBS and fixed in 3.7% formaldehyde; 0.1% Triton X-100 was used for permeabilization and 2% BSA was used for blocking. Anti-filaggrin clone FLG01 (Abcam, Cambridge, United Kingdom) was verified with rhFLG and on epidermal lysate (by WB) as above. Anti-filaggrin FLG01 and anti-keratin 14 (clone EPR1612 from GeneTex, Irvine, California, United States) were diluted in Odyssey blocking buffer (Lincoln, NE, United States) and incubated for 2 h. After extensive wash (0.1% Tween 20) secondary antibodies (IRDye goat anti-mouse 800 and goat anti-rabbit 680; Li-Cor, Lincoln, NE, United States) were used for 1 h incubation. The data were acquired on Li-Cor Odyssey Scanner and analyzed in Image Studio software and statistical significance was determined by one-way ANOVA test with Tukey's multiple comparison.

Quantification of Membrane Order by Spectral Imaging

Spectral imaging of the different membrane samples was performed on a Zeiss LSM 780 confocal microscope equipped with a 32-channel GaAsP detector array. Excitation laser at 405 nm was used and the lambda detection range was set between 415 and 691 nm, and intervals set at 8.9 nm for the individual detection channels. This permitted the coverage of the whole spectrum with the 32 detection channels. The images were saved in .lsm file format and analyzed with a custom plug-in compatible with Fiji/ImageJ, as described later. Selection of regions of interest was done using ImageJ and the quantification of the GP index from these regions was done as explained below.

Quantification of Plasma Membrane Order in Plate Reader

Measurements of the plasma membrane stiffness were carried out on live NHEKs monolayers, employing either a fluorometer (CLARIOstar, BMG LABTECH, Ortenberg, Germany) or optical microscopy using spectral imaging on a Zeiss 780 inverted microscope. We used an environmental polarity sensitive probe, 6-dodecanoyl-2-dimethylamino naphthalene (Laurdan; Sigma Aldrich). Briefly, for the fluorimetric assessment by the plate reader, cells were seeded out on a 96-well glass-bottom plate (Greiner, Stonehouse, UK). Cell membrane labeling with Laurdan was obtained by 5 to 10 min incubation with 5 μL of a solution in dimethyl sulfoxide (DMSO, Sigma Aldrich) and Phosphate Buffer Saline pH 7.4 (PBS, Sigma Aldrich), DMSO/PBS 1:3 v/v, at a final Laurdan concentration of 0.5 μM at room temperature; afterwards, cells were washed with PBS.

Fluorescence emission of Laurdan was exciting at 374 nm and recorded over its whole spectrum from 405 to 600 nm. The intensity of emission wavelengths at 440 ± 10 nm and 490 ± 10 nm was used to obtain the GP values. The experiments were done in triplicates employing 3 different cell batches; the fluorescence values observed were an average out of minimum 25 flashes. Additionally, for imaging purposes we added phenol-free L-15 cell media (Leibovitz, Lonza). Samples were prepared and imaged on an 8-well glass-bottom chamber #1.5 (Ibidi, Planegg/Martinsried, Germany).

Generalized Polarization Index (GP)

Calculation of GP value was carried out as:

$$GP = \frac{I_{440} - I_{490}}{I_{440} + I_{490}}$$

where I_{440} and I_{490} correspond to the emission intensities of Laurdan at 440 and 490 nm, respectively, using 380 nm excitation wavelength. Values of GP vary from 1 to −1, where higher numbers reflect lower fluidity or higher lateral lipid order, whereas lower numbers indicate increasing fluidity. The GP measurements on live keratinocyte monolayers at different calcium concentrations (from [Ca2+] = 0.06 to 5 mM) were on one hand performed on a micro plate fluorescence reader (CLARIOstar, BMG LABTECH), with Laurdan fluorescence emission excited at 374 nm and recorded from 405 to 600 nm. The emission intensities at 440 and 490 ± 10 nm were used to obtain the GP values according to the above equation. On the other hand, confocal spectral imaging on live NHEKs at calcium concentrations [Ca2+] = 0.06 and 1.5 mM was performed on a Zeiss LSM 780 confocal microscope equipped with a 32-channel GaAsP detector array. Fluorescence of Laurdan was excited at 405 nm and detected between 415 and 691 nm. The images were then analyzed using a custom plug-in compatible with Fiji/ImageJ, as previously described 2 using a gamma variate fit of the spectra. A frequency histogram of the GP values was generated in Origin Pro (Oregon, United States), which disclosed two populations, one with high GP values representing the plasma membrane fraction and one with low GP values revealing the cytosolic fraction (e.g., from organelles). A fit of a double Gaussian distribution to the distribution allowed determining average GP values as well as standard deviations of both populations. In contrast, the plate reader measurements gave an average value over both populations. For both plate reader and spectral imaging $n = 3$ biological replicate were

performed, while from each keratinocyte monolayer a minimum of 25 plate reader recordings or 15 confocal images (spectral images) were acquired and analyzed.

For the calculation of the GP index employing spectral imaging and rendering a GP map, we used a purposed-coded plug-in published elsewhere (Sezgin et al., 2015) and available at https://github.com/dwaithe/GP-plugin). Briefly, the plugin has in-built the GP general polarization formula and the discrete intensity values around the peak maxima (i.e., 440, and 490 nm) are obtained from a fitting to the spectrum obtained per pixel and extracting the values around these peak maxima from the nearest wavelength intervals. This methodology produces a spatial GP map representing the GP value for each pixel of the image. The outputs from these pixels are then exported into OriginPro (OriginLab, Oregon, United States) to produce the normalized frequency counts histograms per GP value. Every image pseudo-color representation has a corresponding custom look-up-table (LUT) matching the highest and lowest GP value obtained from the data.

RESULTS

Assessment of Membrane Order in Live Human Epidermal Keratinocytes at a Single-Cell Level

Previously, we extensively characterized the coordinated role of actin scaffolds and filaggrin granule formation during differentiation of normal human epidermal keratinocytes (NHEKs) (Gutowska-Owsiak et al., 2018). Specifically, we monitored filaggrin and actin at different calcium concentrations and described and quantified the distribution of these supramolecular assemblies in cornification. We noted that membrane molecular packing was following an interesting condensation pattern. Therefore, we decided to further investigate this and develop a fast, robust, and easy method to assess cornification development by quantifying lipid order in NHEKs. For this purpose, we used a "calcium switch" model of keratinocyte differentiation, whereby differentiation is induced by addition of calcium (Bikle et al., 2012), reflecting physiological changes observed during epidermal stratification (Menon et al., 1985). In this model a dramatic increase of filaggrin-positive granule accumulation in the cytosol and around the nucleus with higher calcium concentrations can be observed (**Figure 2A**). Furthermore, we observe expected changes in additional markers of keratinocyte differentiation (keratin 14 expression and formation of cellular junction), assessed by E-cadherin staining localization (Owens et al., 2000; Charest et al., 2009) as shown in **Figures 2B,C**, respectively. Combined, all these hallmark features span through the entire thickness of a live epidermis, i.e., represent early, intermediate and late differentiation stages of keratinocyte differentiation (keratin-14, adherens junction formation, and filaggrin, respectively) validate the assay as a suitable model to investigate keratinocyte differentiation. In order to characterize the lipid lateral packing properties in NHEK membranes, we directly labeled undifferentiated cells grown at low calcium level ([Ca2+] = 0.06 mM) with Laurdan. Next, we carried out spectral imaging by confocal microscopy to address changes in membrane stiffness reported by the quantification of the Laurdan general polarization (GP) index. This solvatochromic probe reports on the extent of water relaxation processes in its direct proximity in local molecular environment (**Figure 2D**). The additional advantage of Laurdan is that this dye only fluoresces when incorporated into a membrane environment, hence the GP index is unaffected by the minimal amount of Laurdan which is not associated to membranes. In cells, it is known that the overall internal organelle membrane composition differs from the plasma membrane (Bernardino de la Serna et al., 2016). Plasma membrane lipids have been reported to be more tightly packed and this is clearly demonstrated in **Figure 2E** GP pseudo-color map, where the plasma membrane display a redder color, indicative of a higher degree of condensation or more densely packed membranes in comparison to the intracellular membranes. Since our aim for this study was to develop a high throughput method to report on keratinocyte differentiation, we wanted to ensure that the overall quantification of the GP index would unambiguously report on the degree of cellular lipid lateral condensation, in a similar fashion to the quantification performed at the plasma membrane only. For this purpose, we compared the GP index population distribution and gaussian fit of a whole cell (**Figure 2E**-1) with the GP of the internal membranes (**Figure 2E**-2) and with the GP of the plasma membrane (**Figure 2E**-3). The distribution of GP values of the whole cell yielded two distinct gaussians: one with lower GP values, mostly distributed in the internal organelles and reflecting more fluid membranes (see **Figure 2E** in blue-green color; GP = −0.09); and the other with higher values, mainly localized at the plasma membrane, indicating higher degree of lateral packing (see **Figure 2E** in yellow-orange color; GP = 0.26). The values for the lower and higher GPs obtained from the whole cell, did not substantially differ from the lower GP values of the cytosolic membrane component and the higher of the plasma membrane component. This indicates that resolving the GP index distribution in cell membranes is sufficient to successfully characterize the lipid order heterogeneity.

Laurdan General Polarization Index Increases During *in vitro* Keratinocyte Differentiation

Next, we tested whether confocal spectral imaging would show membrane order changes in live NHEKs during keratinocyte differentiation at a single cell level *in vitro*. Since a very steep calcium gradient in the epidermis (Menon et al., 1985, 1992; Elias et al., 1998, 2002; Ahn et al., 1999) is thought to be the main factor promoting differentiation and stratification *in vivo* (Hennings et al., 1980; Dale et al., 1983; Pillai et al., 1990), this model directly relates to skin physiology. Initially, we validated our assay by simultaneous determination of the differentiation progression in the cells using proteomics (end point assessment). Here, we used the ratio between the expression of a late differentiation marker (filaggrin) and keratin 14, which is predominantly expressed by undifferentiated keratinocytes of lower epidermal layers,

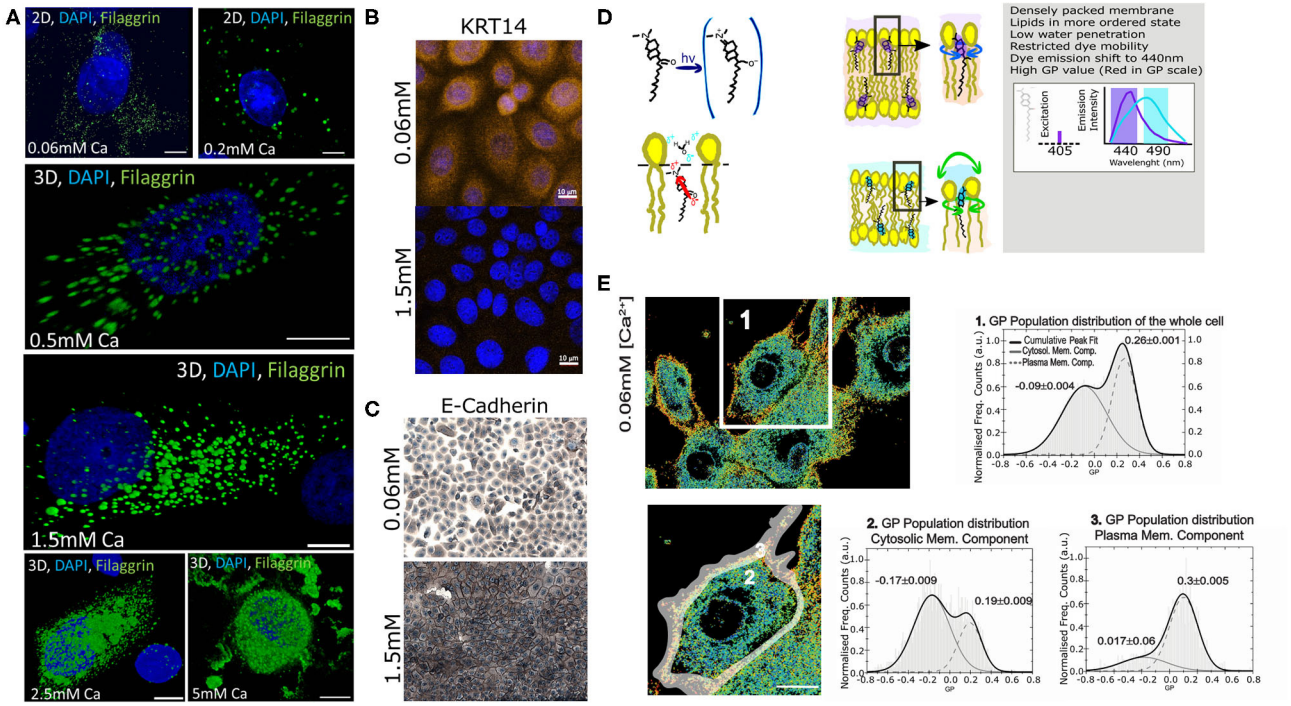

FIGURE 2 | Assessment of the membrane order and stiffness in live normal human epithelial keratinocytes (NHEKs) by LAURDAN polarization sensing dye. **(A)** Detection of filaggrin-containing keratohyalin granules (KHGs) induced in primary normal human epidermal keratinocytes upon calcium switch by immunofluorescence ([Ca2+] = 5 mM to [Ca2+] = 2.5 mM); where Chromatin stained with DAPI is shown in Blue, and Filaggrin in green; scale bar 10 μm; **(B)** expression of keratin-14 and **(C)** E-cadherin staining to assess the formation of cellular junctions during calcium-induced differentiation; **(D)** A cartoon representing Laurdan chemical structure, its positioning within membranes and a description of its biophysical and fluorescence spectral properties. Loosely packed lipids and high water content promote unrestricted Laurdan mobility, resulting in dye emission shift representing fluid membrane state while dense lipid packing and lower water penetration restrict free movement of the dye, resulting in reflecting of shorter wavelengths; differences in LAURDAN emission reflects increased order of the lipids and is detected by a shift in emission wavelength (right panel). This results in an increase in the value of General Polarization (GP). **(E)** Pseudo-color scale represents the increase of a gradual shift from fluid (blue) to stiff (red) membrane. Representative GP images as determined from 2D scanning confocal spectral imaging on live undifferentiated NHEKS [Ca2+] = 0.06 mM; overview (upper panel, scale bar 5 μm) and magnified (lower panel, gray-shaded area: selection for plasma membrane part) of area marked by a white box. Pseudo-color scale: blue to red shift represent increase from low to high GP values. Frequency histograms of GP pixel values from areas of images marked by the respective number 1–3: (1) averaging over a whole cell; (2) cytosolic membranes fraction; and (3) plasma membrane fraction. The histograms were fit by a double-Gaussian (black line, with peak values, and their accuracy from the fit stated) to outline the plasma membrane (right peaks) and cytosolic (left peaks) fraction. Analysis from 3 different cell batches, and a minimum of 5 cells per batch; Statistical GP values obtained were −0.15+/−0.03 and 0.29+/−0.03 at cytosolic membranes and plasma membrane, respectively; the analysis of the whole cell yielded a double peak pit centered at a low GP −0.1+/−0.04 of and at a high GP of 0.21+/−0.05.

including in the basal layer characterized by high proliferation rates (**Figure 3A**). The increase of the filaggrin/keratin 14 ratio indicates keratinocytes advancing in their differentiation process.

Next, using spectral imaging we investigated whether quantifying the GP index in live NHEKs in our validated differentiation model would yield differences that could be confidently used to assess cornification by the means of membrane order quantification. Specifically, we exposed NHEKs to increasing calcium level for 24 h, labeled them with Laurdan and determined GP imaging maps and GP index population distributions. The GP maps in **Figure 3B** confirmed the overall cellular membrane state, showing a decrease in fluid membranes overall and an increase in more ordered membranes. Moreover, the histograms showed a clear and significant response of the membrane packing readout in both the low and high GP value with increased calcium concentration. For instance, from 0.06 mM to 1.5 mM Ca^{2+} the whole population distribution is shifted toward higher GP values: from −0.06 to 0.05 and from 0.26 to 0.45 for the low and high GP, respectively. Interestingly, the highest calcium concentration (5 mM) shows complete disruption of the cells and their membranes. Plasma membrane stiffness and thus GP values increased with calcium concentration throughout the tested range (0.06–5 mM). Given this, we concluded that GP values hold as a robust readout for determination of differentiation stages of keratinocytes at the single live-cell level.

High Throughput GP Index Quantification Assay to Determine Progression of Differentiation in Live Keratinocytes

Once we demonstrated that the GP index is a suitable reporter of cell membrane order without the need to obtain values exclusively from the plasma membrane, we progressed further in

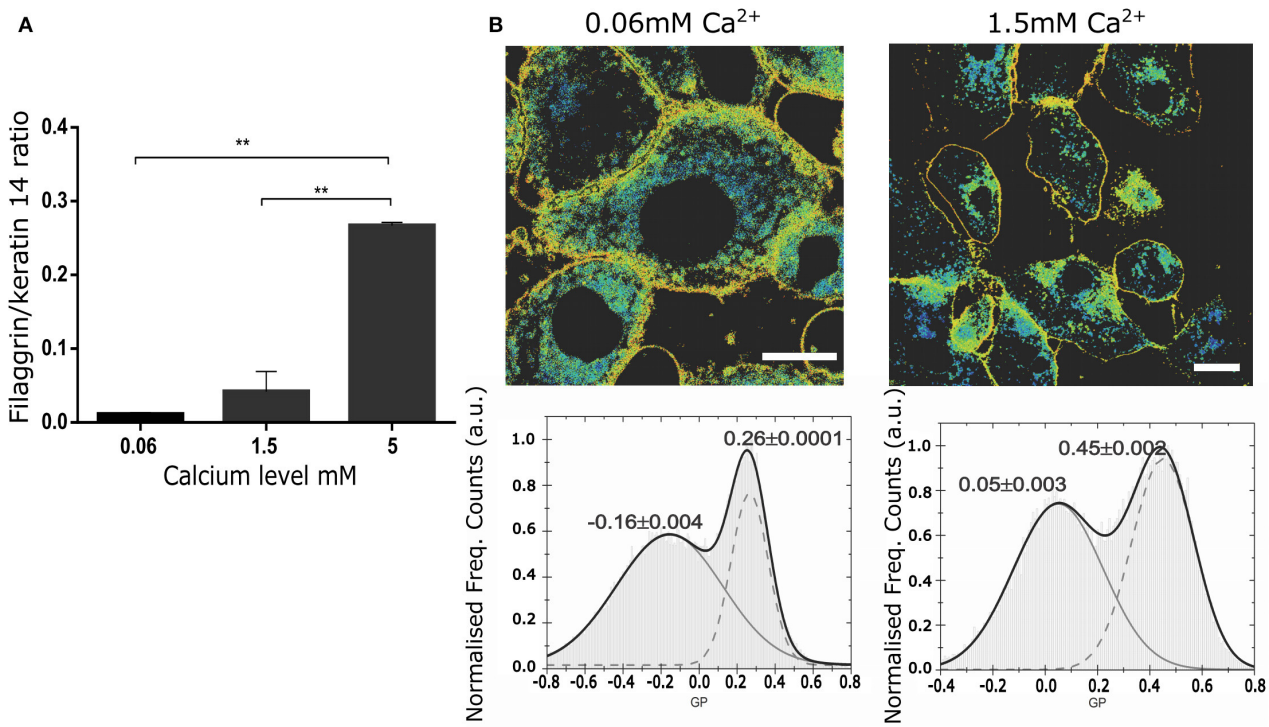

FIGURE 3 | Changes in the membrane stiffness during *in vitro* keratinocyte differentiation assessed by LAURDAN live imaging at the level of a single cell. **(A)** Representation of the keratinocyte differentiation advancement by assessment of filaggrin/keratin 14 ratio in intracellular western blot assay in the cells used for LAURDAN assay; representative of 2 separate NHEK batches, assay carried out in duplicates; **(B)** GP images (upper panels) and histograms of GP pixel values (lower panels, from whole image) for increasing calcium levels ($[Ca^{2+}] = 0.06$ mM (left), 1.5 mM (right)). The histograms were fit by a double-Gaussian (black line, with peak values and their accuracy from the fit stated) to outline the increase in GP and thus stiffness for the plasma membrane fraction (right peaks) and an indifferent change for the cytosolic fraction (left peaks). Representative example from 3 different cell batches, and a minimum of 5 cells per batch. Statistical membrane GP values obtained were 0.21+/−0.03 and 0.34+/−0.05 for $[Ca^{2+}] = 0.06$ and 1.5 mM, respectively; scale bar 5 μm.

our aim of developing an inexpensive and robust methodology to asses keratinocyte differentiation with a high throughput readout and analysis. For this, we tested whether calculating the GP index at the cell-ensemble level, rather than at the single-cell, would yield corresponding results. Hence, we reproduced the previous experimental set up, but employing a plate reader instead of a confocal microscope. This assay provided average GP values from whole cell populations within sub-second time frames. In these experiments we determined GP values representative of all cell membranes, i.e., calculating the average over both the cytoplasmic and cytosolic membrane fractions. This new approach allowed us to test multiple calcium concentrations faster and in a larger field of view; ultimately allowing access to a more robust statistical analysis. A caveat to this approach is the fact that the readout is an average of the fluorescence spectra detected from an ensemble of keratinocytes within a cell monolayer. To further test whether this could be a set-back to our method, we ran the samples in parallel in a plate under a confocal microscope and in a plate reader (**Figure 4A**). Notably, using the same cell populations as imaged on the confocal microscope (the plate format fitted both the microscopy setup and the fluorescent reader) we could still observe a gradual increase of the Laurdan GP values along with the progression of keratinocyte differentiation in our calcium switch model (**Figure 4B**). The low error bars along with the short measurement times highlight the plate reader assay as a robust high-throughput readout to assess keratinocyte differentiation.

DISCUSSION

Epidermis consists of multiple layers of keratinocytes which represent different stages of progression of terminal differentiation. Successful and complete differentiation is critical for the functional characteristics of the skin, and affects their permeability, antimicrobial, and mechanical properties. While the cells gradually progress, their characteristics change dramatically; this results in differential cell reactivity and outcomes in functionally distinct keratinocyte populations. To date there are no specific tools available to trace the progression of keratinocyte differentiation *in vitro* in real-time or to precisely determine differentiation advancement stage of these cells while preserving cell viability; at neither single-cell nor population level. Such an assessment modality would be beneficial, however, as it would enable the determination of the dependence between the cell reactivity and functional outcomes of the advancement in their differentiation program. Furthermore, a plate reader format could provide an efficient tool for scaling up into a high-throughput assay. Similarly, given that several skin diseases

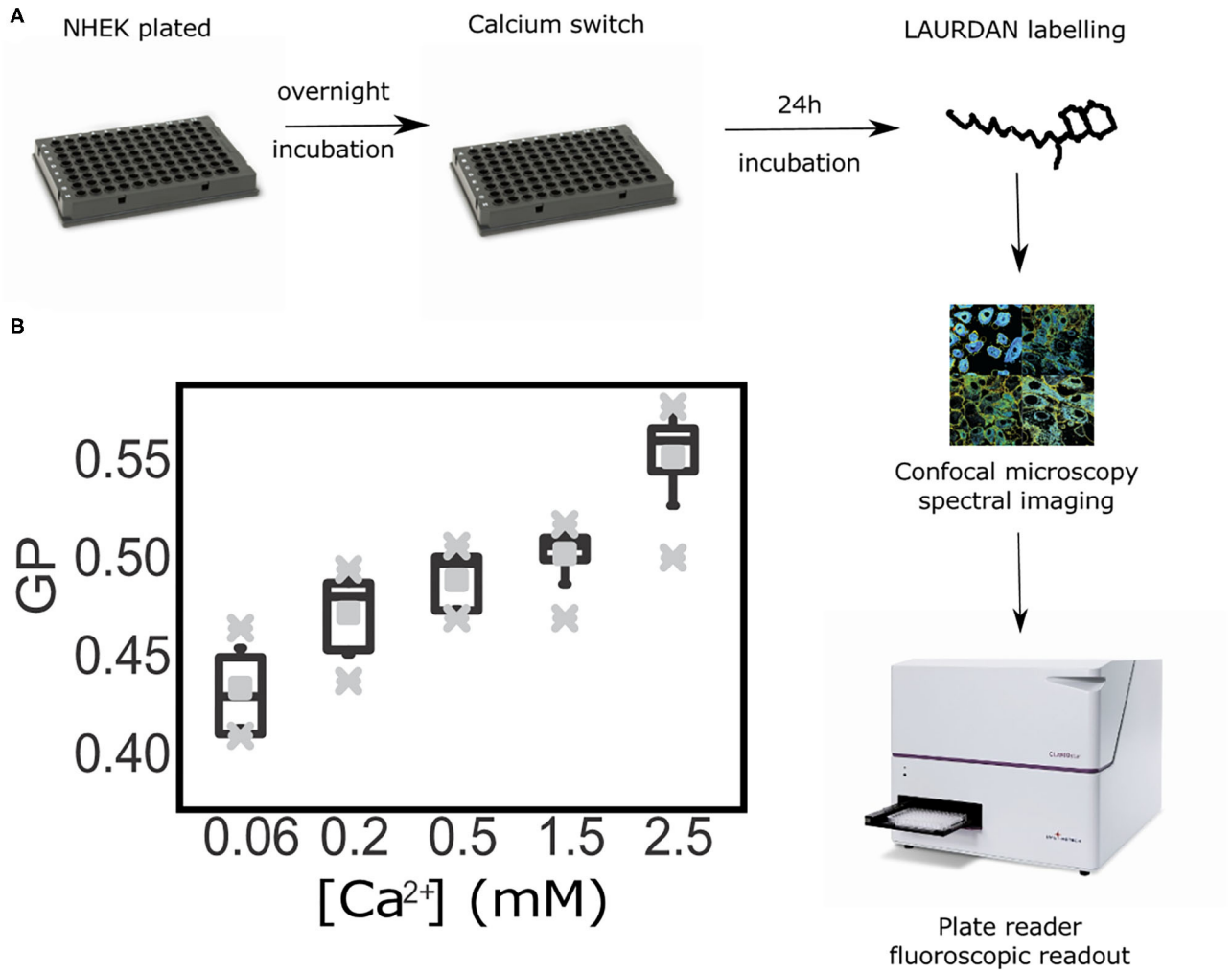

FIGURE 4 | High throughput assessment of Laurdan General Polarization (GP) in living keratinocytes at the population level by a fluorescent plate readout. **(A)** Workflow diagram: primary keratinocytes were seeded and calcium-switched in a range of calcium concentrations ([Ca2+] = 0.06 mM to [Ca2+] = 2.5 mM) at confluence. Twenty four hour after cells were LAURDAN-stained live and GP values were obtained by confocal immunofluorescence readout and fluorescence spectroscopy on a plate reader. **(B)** Whiskers-box plot of the distribution of GP values, with average (middle vertical black lines), the standard deviations (error bars), and the outlier ranges (gray crosses).

have been found to show a degree of delayed or abnormal epidermal differentiation and resulting insufficiency in the skin barrier function (Kubo et al., 2012; Eyerich et al., 2018), there is an unmet need for robust and validated techniques which could be used to propose new diagnostic and therapeutic options. Our study provides an inexpensive and effective methodology to assess keratinocyte differentiation and has implications to both basic and applied research, e.g., in drug testing. However, it is important to note that while our assay may be used to determine the GP value and make assumptions with regards to the membrane stiffness across a spectrum of calcium concentrations, the cells grown at calcium levels of 5 mM or above may no longer be viable, likely due to differentiation-dependent cell death and not suitable for downstream analysis. Another important aspect to consider is the fact the Laurdan GP is not an absolute, but relative value; the values are indicative of a process of differentiation, where clearly the order in the cellular membranes increases upon higher calcium levels. As shown, absolute value differences in the analyses can be attributed to (i) the lower sensitivity of the plate reader compared to the microscope detectors; (ii) the excitation power and wavelength (in a LED vs. laser-based for the microscope); and (iii) the difference in the cellular organization (ensemble of cells, where cell-cell attachments influence the membrane fluidity, vs. single-cell visualization under the microscope).

Lipid membrane remodeling and resulting changes in the polarity can be employed to measure the degree of membrane condensation by utilizing fluorescent lipophilic probes such as Laurdan, where emission spectra and solvent-polarity dependence report on lipid lateral packing. The readout of the

Laurdan fluorescence and GP index can be used to provide information regarding membrane heterogeneity, which allows for the estimation of the membrane stiffness and fluidity. Furthermore, lack of the apparent Laurdan toxicity and the sub-second readout time of the plate reader allowed us to study changes in keratinocyte stiffness and progression of differentiation over time. It is important to note that the GP index is not an absolute measure of fluidity, but an indirect and relative estimate. Therefore, GP values may differ from study to study. For instance, very precise measurements at room temperature of GP in gradually laterally compressed monolayers of the di-saturated lipid DPPC (1,2-dipalmitoyl-sn-glycero-3-phosphocholine), a lipid with a transition temperature of 41°C, lead to GP values between 0.25 and 0.4 (Brewer et al., 2010) at lateral pressures, similar to those experienced in a lipid bilayer in the liquid order phase (de la Serna et al., 2009; Bernardino de la Serna et al., 2013). However, when DPPC is compressed further to reach a gel state (e.g., a phase that has only been reported in skin membranes or model membranes) the GP value still reaches values below 0.5. Therefore, the values reported here for highly densely packed membranes of are in good agreement with the increase of the membrane order (de la Serna et al., 2009; Gutowska-Owsiak et al., 2018).

In this study we demonstrated that Laurdan general polarization (GP) index can be used as an effective tool to determine keratinocyte differentiation advancement and progression in live keratinocytes at both single-cell and population level, within a cell monolayer and with an option for high-throughput assessment. Laurdan has been previously used in experiments with porcine skin to determine penetration of liposomes (Carrer et al., 2008). Assessment of Laurdan emission in these studies showed a decrease of the GP value with the increased skin depth, from *stratum corneum* through to the dermis, including a progressive decrease at the level of the epidermis; this is in line with data presented here. While we utilized Laurdan to assess differentiation process in epidermal keratinocytes specifically, we anticipate that this methodology may be also potentially successfully used with other cell types, which undergo lipid remodeling during differentiation or maturation (Reynier et al., 1991; Wong et al., 2018).

In summary, we designed and validated a Laurdan-based assay which enables for a precise determination of differentiation advancement stage in living keratinocytes, by the assessment of changes in membrane stiffness. Due to the lack of apparent cytotoxicity, this *in vitro* assay may also be used to trace differentiation over time, either at the level of a single cell or scaled up for high throughput measurements.

DATA AVAILABILITY STATEMENT

The raw data supporting the conclusions of this article will be made available by the authors, without undue reservation.

AUTHOR CONTRIBUTIONS

DG-O and JBS designed and performed the experiments, carried out the data processing and analysis, discussed, prepared, and wrote the manuscript. EIP carried out experiments. CE and GO supervised the work, helped with analysis, discussed, prepared, and wrote the manuscript. All authors contributed to the article and approved the submitted version.

FUNDING

DG-O and GO are grateful for the support from the Medical Research Council (UK) and the NIHR Oxford Biomedical Research Centre. DG-O also acknowledged funding from the European Union's Horizon 2020 research and innovation programme under the Marie Skłodowska-Curie grant agreement no. 665778 coordinated by the National Science Centre, under the Polonez project number 2016/23/P/NZ6/04056 and Foundation for Polish Science (FNP) under the First TEAM project number POIR.04.04.00-00-21FA/16-00, and the British Skin Foundation. EIP was supported by the Preludium (2013/09/N/NZ6/02405) and the Etiuda Programs funded by the National Science Centre of Poland. JBS acknowledges support from a Marie Curie Career Integration Grant (PCIG13-GA-2013-618914). CE acknowledges support from the Wolfson Imaging Centre Oxford (Christoffer Lagerholm), the Wolfson Foundation (18272), the Medical Research Council (MC_UU_12010/unit programmes G0902418 and MC_UU_12025), MRC/BBSRC/ESPRC (Grant No. MR/K01577X/1), the Wellcome Trust [104924/14/Z/14, 100262Z/12/Z, 098274/Z/12/Z, and Strategic Award 091911 (107457/Z/15/Z, Advanced Micron Bioimaging Unit)], the Deutsche Forschungsgemeinschaft (Collaborative Research Center 1278, Research unit 1905, Jena Excellence Cluster Balance of the Microverse), and internal University of Oxford funding (EPA Cephalosporin Fund and John Fell Fund).

ACKNOWLEDGMENTS

We are grateful to Prof. Wojciech Bal for his support to EIP and the study.

SUPPLEMENTARY MATERIAL

The Supplementary Material for this article can be found online at: https://www.frontiersin.org/articles/10.3389/fcell.2020.573230/full#supplementary-material

Supplementary Figure 1 | Validation of anti-filaggrin antibodies used in the study. Western blot assessment of the antibody specificity for FLG01 and 15C10 antibodies used in the study. **(A)** Blotting against recombinant human FLG protein; **(B)** Blotting against epidermal lysates.

REFERENCES

Ahn, S. K., Hwang, S. M., Jiang, S. J., Choi, E. H., and Lee, S. H. (1999). The changes of epidermal calcium gradient and transitional cells after prolonged occlusion following tape stripping in the murine epidermis. *J. Invest. Dermatol.* 113, 189–195. doi: 10.1046/j.1523-1747.1999.00650.x

Akinduro, O., Sully, K., Patel, A., Robinson, D. J., Chikh, A., McPhail, G., et al. (2016). Constitutive autophagy and nucleophagy during epidermal differentiation. *J. Invest. Dermatol.* 136, 1460–1470. doi: 10.1016/j.jid.2016.03.016

Akiyama, M. (2017). Corneocyte lipid envelope (CLE), the key structure for skin barrier function and ichthyosis pathogenesis. *J. Dermatol. Sci.* 88, 3–9. doi: 10.1016/j.jdermsci.2017.06.002

Bagatolli, L. A., Gratton, E., and Fidelio, G. D. (1998). Water dynamics in glycosphingolipid aggregates studied by LAURDAN fluorescence. *Biophys. J.* 75, 331–341. doi: 10.1016/S0006-3495(98)77517-4

Bagatolli, L. A., Parasassi, T., Fidelio, G. D., and Gratton, E. (1999). A model for the interaction of 6-lauroyl-2-(N,N-dimethylamino)naphthalene with lipid environments: implications for spectral properties. *Photochem. Photobiol.* 70, 557–564. doi: 10.1562/0031-8655(1999)070<0557:AMFTIO>2.3.CO;2

Behne, M., Uchida, Y., Seki, T., de Montellano, P. O., Elias, P. M., and Holleran, W. M. (2000). Omega-hydroxyceramides are required for corneocyte lipid envelope (CLE) formation and normal epidermal permeability barrier function. *J. Invest. Dermatol.* 114, 185–192. doi: 10.1046/j.1523-1747.2000.00846.x

Bernabé-Rubio, M., Bosch-Fortea, M., García, E., de la Serna, J. B., and Alonso, M. A. (2019). The ciliary membrane of polarized epithelial cells stems from a midbody remnant-associated membrane patch with condensed nanodomains. *bioRxiv* 667642. doi: 10.1101/667642

Bernardino de la Serna, J., Hansen, S., Berzina, Z., Simonsen, A. C., Hannibal-Bach, H. K., Knudsen, J., et al. (2013). Compositional and structural characterization of monolayers and bilayers composed of native pulmonary surfactant from wild type mice. *Biochim. Biophys. Acta* 1828, 2450–2459. doi: 10.1016/j.bbamem.2013.07.008

Bernardino de la Serna, J., Schütz, G. J., Eggeling, C., and Cebecauer, M. (2016). There is no simple model of the plasma membrane organization. *Front Cell Dev. Biol.* 4:106. doi: 10.3389/fcell.2016.00106

Bikle, D. D., Xie, Z., and Tu, C.-L. (2012). Calcium regulation of keratinocyte differentiation. *Expert Rev. Endocrinol. Metab.* 7, 461–472. doi: 10.1586/eem.12.34

Brewer, J., de la Serna, J. B., Wagner, K., and Bagatolli, L. A. (2010). Multiphoton excitation fluorescence microscopy in planar membrane systems. *Biochim. Biophys. Acta* 1798, 1301–1308. doi: 10.1016/j.bbamem.2010.02.024

Candi, E., Knight, R. A., Panatta, E., Smirnov, A., and Melino, G. (2016). Cornification of the skin: a non-apoptotic cell death mechanism. *eLS* 1–10. doi: 10.1002/9780470015902.a0021583.pub2

Candi, E., Schmidt, R., and Melino, G. (2005). The cornified envelope: a model of cell death in the skin. *Nat. Rev. Mol. Cell Biol.* 6, 328–340. doi: 10.1038/nrm1619

Carrer, D. C., Vermehren, C., and Bagatolli, L. A. (2008). Pig skin structure and transdermal delivery of liposomes: a two photon microscopy study. *J. Control. Release* 132, 12–20. doi: 10.1016/j.jconrel.2008.08.006

Carugo, D., Aron, M., Sezgin, E., Bernardino de la Serna, J., Kuimova, M. K., Eggeling, C., et al. (2017). Modulation of the molecular arrangement in artificial and biological membranes by phospholipid-shelled microbubbles. *Biomaterials* 113, 105–117. doi: 10.1016/j.biomaterials.2016.10.034

Charest, J. L., Jennings, J. M., King, W. P., Kowalczyk, A. P., and García, A. J. (2009). Cadherin-mediated cell–cell contact regulates keratinocyte differentiation. *J. Invest. Dermatol.* 129, 564–572. doi: 10.1038/jid.2008.265

Chon, S. H., Tannahill, R., Yao, X., Southall, M. D., and Pappas, A. (2015). Keratinocyte differentiation and upregulation of ceramide synthesis induced by an oat lipid extract via the activation of PPAR pathways. *Exp. Dermatol.* 24, 290–295. doi: 10.1111/exd.12658

Dale, B. A., Haugen Scofield, J. A., Hennings, H., Stanley, J. R., and Yuspa, S. H. (1983). Identification of filaggrin in cultured mouse keratinocytes and its regulation by calcium. *J. Invest. Dermatol.* 81 (1 Suppl), S90–S95. doi: 10.1111/1523-1747.ep12540769

de la Serna, J. B., Orädd, G., Bagatolli, L. A., Simonsen, A. C., Marsh, D., Lindblom, G., et al. (2009). Segregated phases in pulmonary surfactant membranes do not show coexistence of lipid populations with differentiated dynamic properties. *Biophys. J.* 97, 1381–1389. doi: 10.1016/j.bpj.2009.06.040

Eckhart, L., Lippens, S., Tschachler, E., and Declercq, W. (2013). Cell death by cornification. *Biochim. Biophys. Acta* 1833, 3471–3480. doi: 10.1016/j.bbamcr.2013.06.010

Elias, P. M., Brown, B. E., Crumrine, D., Feingold, K. R., and Ahn, S. K. (2002). Origin of the epidermal calcium gradient: regulation by barrier status and role of active vs passive mechanisms. *J. Invest. Dermatol.* 119, 1269–1274. doi: 10.1046/j.1523-1747.2002.19622.x

Elias, P. M., Gruber, R., Crumrine, D., Menon, G., Williams, M. L., Wakefield, J. S., et al. (2014). Formation and functions of the corneocyte lipid envelope (CLE). *Biochim. Biophys. Acta* 1841, 314–318. doi: 10.1016/j.bbalip.2013.09.011

Elias, P. M., Nau, P., Hanley, K., Cullander, C., Crumrine, D., Bench, G., et al. (1998). Formation of the epidermal calcium gradient coincides with key milestones of barrier ontogenesis in the rodent. *J. Invest. Dermatol.* 110, 399–404. doi: 10.1046/j.1523-1747.1998.00151.x

Eyerich, S., Eyerich, K., Traidl-Hoffmann, C., and Biedermann, T. (2018). Cutaneous barriers and skin immunity: differentiating a connected network. *Trends Immunol.* 39, 315–327. doi: 10.1016/j.it.2018.02.004

Flohr, C., Perkin, M., Logan, K., Marrs, T., Radulovic, S., Campbell, L. E., et al. (2014). Atopic dermatitis and disease severity are the main risk factors for food sensitization in exclusively breastfed infants. *J. Invest. Dermatol.* 134, 345–350. doi: 10.1038/jid.2013.298

Gaus, K., Gratton, E., Kable, E. P. W., Jones, A. S., Gelissen, I., Kritharides, L., et al. (2003). Visualizing lipid structure and raft domains in living cells with two-photon microscopy. *Proc. Natl. Acad. Sci. U.S.A.* 100, 15554–15559. doi: 10.1073/pnas.2534386100

Gdula, M. R., Poterlowicz, K., Mardaryev, A. N., Sharov, A. A., Peng, Y., Fessing, M. Y., et al. (2013). Remodeling of three-dimensional organization of the nucleus during terminal keratinocyte differentiation in the epidermis. *J. Invest. Dermatol.* 133, 2191–2201. doi: 10.1038/jid.2013.66

Gutowska-Owsiak, D., de La Serna, J. B., Fritzsche, M., Naeem, A., Podobas, E. I., Leeming, M., et al. (2018). Orchestrated control of filaggrin–actin scaffolds underpins cornification. *Cell Death Dis.* 9:412. doi: 10.1038/s41419-018-0407-2

Hennings, H., Michael, D., Cheng, C., Steinert, P., Holbrook, K., and Yuspa, S. H. (1980). Calcium regulation of growth and differentiation of mouse epidermal cells in culture. *Cell* 19, 245–254. doi: 10.1016/0092-8674(80)90406-7

Horimukai, K., Morita, K., Narita, M., Kondo, M., Kitazawa, H., Nozaki, M., et al. (2014). Application of moisturizer to neonates prevents development of atopic dermatitis. *J. Allergy Clin. Immunol.* 134, 824–830.e826. doi: 10.1016/j.jaci.2014.07.060

Ipponjima, S., Umino, Y., Nagayama, M., and Denda, M. (2020). Live imaging of alterations in cellular morphology and organelles during cornification using an epidermal equivalent model. *Sci. Rep.* 10:5515. doi: 10.1038/s41598-020-62240-3

Iwai, I., Han, H., den Hollander, L., Svensson, S., Ofverstedt, L. G., Anwar, J., et al. (2012). The human skin barrier is organized as stacked bilayers of fully extended ceramides with cholesterol molecules associated with the ceramide sphingoid moiety. *J. Invest. Dermatol.* 132, 2215–2225. doi: 10.1038/jid.2012.43

Janssens, M., van Smeden, J., Gooris, G. S., Bras, W., Portale, G., Caspers, P. J., et al. (2012). Increase in short-chain ceramides correlates with an altered lipid organization and decreased barrier function in atopic eczema patients. *J. Lipid Res.* 53, 2755–2766. doi: 10.1194/jlr.P030338

Kezic, S., Kammeyer, A., Calkoen, F., Fluhr, J. W., and Bos, J. D. (2009). Natural moisturizing factor components in the stratum corneum as biomarkers of filaggrin genotype: evaluation of minimally invasive methods. *Br. J. Dermatol.* 161, 1098–1104. doi: 10.1111/j.1365-2133.2009.09342.x

Kubo, A., Nagao, K., and Amagai, M. (2012). Epidermal barrier dysfunction and cutaneous sensitization in atopic diseases. *J. Clin. Invest.* 122, 440–447. doi: 10.1172/JCI57416

Lakowicz, J. R. (1999). *Principles of Fluorescence Spectroscopy*. New York, NY: Plenum Publishers. Available online at: https://www.springer.com/gp/book/9780387312781#aboutBook

López, O., Cócera, M., Wertz, P. W., López-Iglesias, C., and de la Maza, A. (2007). New arrangement of proteins and lipids in the stratum corneum cornified envelope. *Biochim. Biophys. Acta.* 1768, 521–529. doi: 10.1016/j.bbamem.2006.11.023

Mao-Qiang, M., Fowler, A. J., Schmuth, M., Lau, P., Chang, S., Brown, B. E., et al. (2004). Peroxisome-proliferator-activated receptor (PPAR)-gamma activation stimulates keratinocyte differentiation. *J. Invest. Dermatol.* 123, 305–312. doi: 10.1111/j.0022-202X.2004.23235.x

Marshall, D., Hardman, M. J., Nield, K. M., and Byrne, C. (2001). Differentially expressed late constituents of the epidermal cornified envelope. *Proc. Natl. Acad. Sci. U.S.A.* 98, 13031–13036. doi: 10.1073/pnas.231489198

Menon, G. K., Elias, P. M., Lee, S. H., and Feingold, K. R. (1992). Localization of calcium in murine epidermis following disruption and repair of the permeability barrier. *Cell Tissue Res.* 270, 503–512. doi: 10.1007/BF00645052

Menon, G. K., Grayson, S., and Elias, P. M. (1985). Ionic calcium reservoirs in mammalian epidermis: ultrastructural localization by ion-capture cytochemistry. *J. Invest. Dermatol.* 84, 508–512. doi: 10.1111/1523-1747.ep12273485

Narangifard, A., den Hollander, L., Wennberg, C. L., Lundborg, M., Lindahl, E., Iwai, I., et al. (2018). Human skin barrier formation takes place via a cubic to lamellar lipid phase transition as analyzed by cryo-electron microscopy and EM-simulation. *Exp. Cell Res.* 366, 139–151. doi: 10.1016/j.yexcr.2018.03.010

Owen, D. M., Rentero, C., Magenau, A., Abu-Siniyeh, A., and Gaus, K. (2011). Quantitative imaging of membrane lipid order in cells and organisms. *Nat. Protoc.* 7, 24–35. doi: 10.1038/nprot.2011.419

Owens, D. W., Brunton, V. G., Parkinson, E. K., and Frame, M. C. (2000). E-cadherin at the cell periphery is a determinant of keratinocyte differentiation *in vitro*. *Biochem. Biophys. Res. Commun.* 269, 369–376. doi: 10.1006/bbrc.2000.2292

Parasassi, T., De Stasio, G., d'Ubaldo, A., and Gratton, E. (1990). Phase fluctuation in phospholipid membranes revealed by Laurdan fluorescence. *Biophys. J.* 57, 1179–1186. doi: 10.1016/S0006-3495(90)82637-0

Parasassi, T., Di Stefano, M., Loiero, M., Ravagnan, G., and Gratton, E. (1994). Cholesterol modifies water concentration and dynamics in phospholipid bilayers: a fluorescence study using laurdan probe. *Biophys. J.* 66 (3 Pt. 1), 763–768. doi: 10.1016/S0006-3495(94)80852-5

Parasassi, T., Gratton, E., Yu, W. M., Wilson, P., and Levi, M. (1997). Two-photon fluorescence microscopy of laurdan generalized polarization domains in model and natural membranes. *Biophys. J.* 72, 2413–2429. doi: 10.1016/S0006-3495(97)78887-8

Pillai, S., Bikle, D. D., Mancianti, M. L., Cline, P., and Hincenbergs, M. (1990). Calcium regulation of growth and differentiation of normal human keratinocytes: modulation of differentiation competence by stages of growth and extracellular calcium. *J. Cell. Physiol.* 143, 294–302. doi: 10.1002/jcp.1041430213

Plasencia, I., Norlén, L., and Bagatolli, L. A. (2007). Direct visualization of lipid domains in human skin stratum corneum's lipid membranes: effect of pH and temperature. *Biophys. J.* 93, 3142–3155. doi: 10.1529/biophysj.106.096164

Ponec, M., Kempenaar, J., Weerheim, A., and Boonstra, J. (1987). Differentiation of human keratinocytes: changes in lipid synthesis, plasma membrane lipid composition, and 125I-EGF binding upon administration of 25-hydroxycholesterol and mevinolin. *J. Cell. Physiol.* 133, 358–364. doi: 10.1002/jcp.1041330221

Ponec, M., Weerheim, A., Kempenaar, J., Mommaas, A. M., and Nugteren, D. H. (1988). Lipid composition of cultured human keratinocytes in relation to their differentiation. *J. Lipid Res.* 29, 949–961.

Reynier, M., Sari, H., d'Anglebermes, M., Kye, E. A., and Pasero, L. (1991). Differences in lipid characteristics of undifferentiated and enterocytic-differentiated HT29 human colonic cells. *Cancer Res.* 51, 1270–1277.

Rogerson, C., Bergamaschi, D., and O'Shaughnessy, R. F. L. (2018). Uncovering mechanisms of nuclear degradation in keratinocytes: a paradigm for nuclear degradation in other tissues. *Nucleus* 9, 56–64. doi: 10.1080/19491034.2017.1412027

Sandilands, A., Sutherland, C., Irvine, A. D., and McLean, W. H. (2009). Filaggrin in the frontline: role in skin barrier function and disease. *J. Cell Sci.* 122 (Pt. 9), 1285–1294. doi: 10.1242/jcs.033969

Schmidt, R., Parish, E. J., Dionisius, V., Cathelineau, C., Michel, S., Shroot, B., et al. (1991). Modulation of cellular cholesterol and its effect on cornified envelope formation in cultured human epidermal keratinocytes. *J. Invest. Dermatol.* 97, 771–775. doi: 10.1111/1523-1747.ep12486720

Sezgin, E., Waithe, D., Bernardino de la Serna, J., and Eggeling, C. (2015). Spectral imaging to measure heterogeneity in membrane lipid packing. *Chemphyschem* 16, 1387–1394. doi: 10.1002/cphc.201402794

Venkataraman, D., Soto-Ramírez, N., Kurukulaaratchy, R. J., Holloway, J. W., Karmaus, W., Ewart, S. L., et al. (2014). Filaggrin loss-of-function mutations are associated with food allergy in childhood and adolescence. *J. Allergy Clin. Immunol.* 134, 876–882.e874. doi: 10.1016/j.jaci.2014.07.033

Weber, G., and Farris, F. J. (1979). Synthesis and spectral properties of a hydrophobic fluorescent probe: 6-propionyl-2-(dimethylamino)naphthalene. *Biochemistry.* 14, 3075–3078. doi: 10.1021/bi00581a025

Wennberg, C. L., Narangifard, A., Lundborg, M., Norlén, L., and Lindahl, E. (2018). Structural transitions in ceramide cubic phases during formation of the human skin barrier. *Biophys. J.* 114, 1116–1127. doi: 10.1016/j.bpj.2017.12.039

Wong, M., Xu, G., Park, D., Barboza, M., and Lebrilla, C. B. (2018). Intact glycosphingolipidomic analysis of the cell membrane during differentiation yields extensive glycan and lipid changes. *Sci. Rep.* 8:10993. doi: 10.1038/s41598-018-29324-7

Conflict of Interest: The authors declare that the research was conducted in the absence of any commercial or financial relationships that could be construed as a potential conflict of interest.

frontiers in Physiology

ORIGINAL RESEARCH
published: 23 October 2020
doi: 10.3389/fphys.2020.578868

Serotonin Alters the Phase Equilibrium of a Ternary Mixture of Phospholipids and Cholesterol

Oskar Engberg[1], Anna Bochicchio[2†], Astrid F. Brandner[2], Ankur Gupta[3], Simli Dey[3], Rainer A. Böckmann[2], Sudipta Maiti[3] and Daniel Huster[1,3]**

[1] Institute for Medical Physics and Biophysics, University of Leipzig, Leipzig, Germany, [2] Computational Biology, Department of Biology, Friedrich-Alexander University Erlangen-Nürnberg, Erlangen, Germany, [3] Department of Chemical Sciences, Tata Institute of Fundamental Research, Mumbai, India

Unsaturated and saturated phospholipids tend to laterally segregate, especially in the presence of cholesterol. Small molecules such as neurotransmitters, toxins, drugs etc. possibly modulate this lateral segregation. The small aromatic neurotransmitter serotonin (5-HT) has been found to bind to membranes. We studied the lipid structure and packing of a ternary membrane mixture consisting of palmitoyl-oleoyl-phosphatidylcholine, palmitoyl-sphingomyelin, and cholesterol at a molar ratio of 4/4/2 in the absence and in the presence of 5-HT, using a combination of solid-state ^{2}H NMR, atomic force microscopy, and atomistic molecular dynamics (MD) simulations. Both NMR and MD report formation of a liquid ordered (L_o) and a liquid disordered (L_d) phase coexistence with small domains. Lipid exchange between the domains was fast such that single component ^{2}H NMR spectra are detected over a wide temperature range. A drastic restructuring of the domains was induced when 5-HT is added to the membranes at a 9 mol% concentration relative to the lipids. ^{2}H NMR spectra of all components of the mixture showed two prominent contributions indicative of molecules of the same kind residing both in the disordered and the ordered phase. Compared to the data in the absence of 5-HT, the lipid chain order in the disordered phase was further decreased in the presence of 5-HT. Likewise, addition of serotonin increased lipid chain order within the ordered phase. These characteristic lipid chain order changes were confirmed by MD simulations. The 5-HT-induced larger difference in lipid chain order results in more pronounced differences in the hydrophobic thickness of the individual membrane domains. The correspondingly enlarged hydrophobic mismatch between ordered and disordered phases is assumed to increase the line tension at the domain boundary, which drives the system into formation of larger size domains. These results not only demonstrate that small membrane binding molecules such as neurotransmitters have a profound impact on essential membrane properties. It also suggests a mechanism by which the interaction of small molecules with membranes can influence the function of membrane proteins and non-cognate receptors. Altered membrane properties may modify lateral sorting of membrane protein, membrane protein conformation, and thus influence their function as suspected for neurotransmitters, local anesthetics, and other small drug molecules.

Keywords: ^{2}H NMR spectroscopy, molecular dynamics simulation, domain size, raft mixture, line tension

OPEN ACCESS

Edited by:
Fabio Fernandes, University of Lisbon, Portugal

Reviewed by:
Erdinc Sezgin, Karolinska Institutet (KI), Sweden
Luis M. S. Loura, University of Coimbra, Portugal

***Correspondence:**
Sudipta Maiti
maiti@tifr.res.in
Daniel Huster
daniel.huster@medizin.uni-leipzig.de

†Present address:
Anna Bochicchio, Schrödinger GmbH, Mannheim, Germany

Specialty section:
This article was submitted to Membrane Physiology and Membrane Biophysics, a section of the journal Frontiers in Physiology

Received: *01 July 2020*
Accepted: *06 October 2020*
Published: *23 October 2020*

Citation:
Engberg O, Bochicchio A, Brandner AF, Gupta A, Dey S, Böckmann RA, Maiti S and Huster D (2020) Serotonin Alters the Phase Equilibrium of a Ternary Mixture of Phospholipids and Cholesterol. Front. Physiol. 11:578868. doi: 10.3389/fphys.2020.578868

INTRODUCTION

Small molecules of a molecular weight of less than 1 kDa play key roles in various important processes in biology as receptor agonists or antagonists, (neuro)transmitters, toxins, defense agents against predation and many others (Stockwell, 2004). Also, most pharmaceuticals are small molecules (Scott et al., 2016). Typically, the mode of action of these compounds is well described by orthosteric binding to their target proteins (Weis and Kobilka, 2018). More recently, also allosteric regulation pathways leading to functional selectivity have been described through which small molecules interact with their targets (Macpherson and Anastasiou, 2017). Both biologically and pharmacologically active compounds are often lipophilic and, especially when administered in relatively high dose that can reach a few mol% (Bruns et al., 2000), may unspecifically interact with the cellular membrane (Postila et al., 2016; Josey et al., 2020; Turnbulla et al., 2020). Binding of small lipophilic molecules to membranes is described by a partition equilibrium and can lead to substantial accumulation of the respective compound. In this way, the membrane represents a reservoir for these molecules. As the dimensionality of the diffusion of these compounds is reduced from three in solution to two on the membrane surface, membrane partitioning of small molecules leads to an increase in their effective concentration by a factor of ∼1,000 which is increasing the probability of binding to a cognate receptors (Sargent and Schwyzer, 1986; Brunsveld et al., 2009; Posttila and Róg, 2020).

Small molecules such as neurotransmitters often strongly interact with membranes and lipids (Peters et al., 2013; Postila et al., 2016; Josey et al., 2020; Posttila and Róg, 2020). This has several important consequences as lipids are involved in many physiological processes such as the regulation of synapse development and plasticity, presynaptic vesicle release, regulation of receptors, and cofactors of proteins in the form of non-annular lipids (Huster, 2014; Posttila and Róg, 2020). The interaction of these compounds with various lipid species may lead to alterations in lipid spontaneous curvature and dynamics, membrane hydrophobic thickness and lipid packing density, and/or membrane domain structure. All these properties will in turn influence the structure and function of membrane proteins and ultimately their biological function (Soubias and Gawrisch, 2012; Brown, 2017; Posttila and Róg, 2020). For instance, the action of general anesthetics is related to either direct binding to postsynaptic ligand-gated ion channels (Nury et al., 2011) or indirectly modulating the membrane properties which affects these proteins (Cantor, 1997; Griepernau et al., 2007; Griepernau and Böckmann, 2008; Jerabek et al., 2010; Weizenmann et al., 2012). Such effects are discussed to be crucial also for other membrane proteins giving rise to various side effects of our current drugs.

The physicochemical properties of membranes and their modulation through binding of small molecules have been studied for decades using in particular spectroscopic tools (Scheidt and Huster, 2008; Mouritsen and Bagatolli, 2015; Naito et al., 2018). Spectroscopic methods have been developed to study lipid chain and headgroup conformation and dynamics as well as the lateral organization of the lipids and the membrane domain structure in complex lipid mixtures (Leftin and Brown, 2011; Cebecauer et al., 2018). In particular for the latter, solid-state ^{2}H NMR spectroscopy represents a useful technique (Veatch et al., 2007; Bartels et al., 2008; Bunge et al., 2008; Engberg et al., 2020). Deuteration of individual lipids in a particular mixture allows determining the phase state of the membrane and the local environment a given lipid species experiences. Even the relative proportion of a given lipid species in a given phase can be exactly determined if it partitions into more than one phase (Stahlberg et al., 2015; Yasuda et al., 2015; Engberg et al., 2020). Furthermore, from the ^{2}H NMR order parameter, the chain length and cross-sectional area of the lipid chains can be determined as well as the average number of *gauche* isomers within the chains (Petrache et al., 2000; Vogel et al., 2009; Shaikh et al., 2015). Thereby, the deuteration of lipids introduces minimal perturbation of the samples and their thermotropic phase behavior (Veatch et al., 2007; Bartels et al., 2008; Bunge et al., 2008). Furthermore, if lipids are subject to slow exchange between two phases, which occurs when the domains are large (i.e., μm size), two component ^{2}H NMR spectra are observed (Veatch et al., 2007; Engberg et al., 2019). In contrast, if the domain size is small, lateral lipid diffusion is responsible for a fast exchange of molecules between the two environments allowing to detect NMR spectra consisting of only one (averaged) spectral component.

In addition to spectroscopic methods, molecular dynamics simulations have become an indispensable tool in the description of phospholipid membranes and their interaction with peptides, proteins, or drugs from the atomistic length scale to tens of nanometers and on the pico- to microsecond timescale (Pluhackova and Böckmann, 2015; Marrink et al., 2019; Chen et al., 2020). While the access to (spontaneous) lipid domain formation in simulations was initially restricted to coarse-grained methodologies [e.g., the MARTINI model (de Jong et al., 2013)] at the cost of modified thermodynamics of membranes, atomistic simulations caught up: lipid force fields (see, e.g., Pluhackova et al., 2016; Sandoval-Perez et al., 2017), improved algorithms and computer speed allow for the study of chemical (Sodt et al., 2014; Javanainen et al., 2017) and physical (Murtola et al., 2006; Kirsch and Böckmann, 2019) nanodomain formation. The combination of NMR and other experimental methods with MD simulations have yielded important insight into the structure and dynamics of lipid membranes and their interaction with small molecules (Feller et al., 1999, 2002; Sodt et al., 2014; Vogel et al., 2014, 2016; Doktorova et al., 2020).

Here, we report in detail how the small neurotransmitter serotonin (5-hydroxytryptamine, 5-HT) interacts with a raft model membrane composed of monounsaturated palmitoyl-oleoyl-phosphatidylcholine (POPC), palmitoyl-sphingomyelin (PSM), and cholesterol (Chol). 5-HT is an important neurotransmitter and signaling molecule in the human body. The serotonergic system is a major target for psychotropic drugs. 5-HT can reach very high concentrations of up to 270 mM in synaptic vesicles (Bruns et al., 2000; Balaji et al., 2005). Also efficient binding of 5-HT to lipid membranes has been reported (Peters et al., 2013; Josey et al., 2020). In particular, the influence of 5-HT on the lipid packing properties

and the membrane domain structure was of interest. 5-HT has been known to partition into the lipid water interface of model membranes altering membrane structure and lipid packing (Yau et al., 1998; Peters et al., 2013). The octanol/water partition coefficient (log P) of 5-HT has been determined to be between 0.56 and 0.73 indicating its lipophilic potential (Postila et al., 2016; Turnbulla et al., 2020). Indeed, also MD simulations hinted to its membrane binding preference, 84% of the 5-HT was found membrane-bound (Postila et al., 2016). We applied a combination of experimental ^{2}H NMR spectroscopy and atomistic MD simulations to describe the preference of 5-HT for differently ordered lipid membrane domains and its domain-specific influence on the membrane structure and dynamics. We used a lipid mixture consisting of POPC, PSM, and Chol at a 4:4:2 molar ratio mimicking the composition of the extracellular leaflet of eukaryotic plasma membranes.

MATERIALS AND METHODS

Materials

Cholesterol (Chol), 1-palmitoyl-2-oleoyl-*sn*-glycero-3-phosphocholine (POPC), 1-palmitoyl-d_{31}-2-oleoyl-*sn*-glycero-3-phosphocholine (POPC-d_{31}), *N*-palmitoyl-D-erythro-sphingosylphosphorylcholine (PSM), *N*-palmitoyl-d_{31}-D-erythro-sphingosylphosphorylcholine (PSM-d_{31}), and sphingomyelin from chicken egg (egg SM) of highest quality were purchased from Avanti Polar Lipids (Alabaster, AL, United States). 5-HT and 5-HT -d_4 was purchased from Merck (Darmstadt, Germany). Cholesterol-d_6 was purchased from Cambridge Isotope Laboratories, Inc. (Tewksbury, MA, United States). All other chemicals were of the highest purity with the exception of organic solvents, which were of spectroscopic grade.

Sample Preparation

Lipids were dissolved in chloroform/methanol (2:1) and 5-HT was dissolved in methanol. Aliquots of all components were mixed. Subsequently, the organic solvents were evaporated in a rotary evaporator. The lipid film was dissolved in cyclohexane followed by freezing in liquid nitrogen and overnight lyophilization, which resulted in a fluffy powder. The samples were hydrated to 50 wt% using aqueous buffer (20 mM K_2PO_4, 100 mM NaCl, 0.1 mM EGTA, pH 7.4) followed by 10 freeze-thaw cycles between liquid nitrogen and a 40°C water bath for equilibration. Finally, the samples were transferred to 4 mm NMR rotors and sealed for ^{2}H NMR measurements.

Planar supported lipid bilayers were prepared for AFM experiments by mixing aliquots of POPC, egg SM, and Chol and dissolving them in chloroform, which was evaporated under an Argon flux and the lipid film was dried under vacuum for 24 h. The lipid film was rehydrated in water to a final concentration of 2.5 mg/ml. The lipid suspension was then vortexed vigorously and extruded using a 50 nm pore diameter polycarbonate membrane. 50 μL of this extruded lipid dispersion and 250 μL of ∼13 mM of $CaCl_2{\cdot}2H_2O$ was deposited on freshly cleaved mica previously glued on to a glass coverslip affixed to a liquid cell and incubated for 1 h at 60°C in a water bath and slowly cooled to room temperature. Samples were rinsed extensively with deionized water to remove non-fused vesicles.

Solid-State NMR Spectroscopy

^{2}H NMR spectra of the multilamellar vesicles were acquired on a Bruker 750 Avance I NMR spectrometer using a double channel solids probe equipped with a 5 mm solenoid coil operating at a resonance frequency of 115.1 MHz for ^{2}H. For signal acquisition, the phase-cycled quadrupolar echo sequence (Davis et al., 1976) with two π/2 pulses of 2.5–4 μs length separated by a 30 μs delay was used. The spectral width was ±250 kHz. Measurements were carried out between 20 and 50°C with a temperature increment of 2 K. All analysis and parameters calculated from the NMR spectra was performed in programs written in the Mathcad software (MathSoft, Cambridge, MA, United States) as described before (Huster et al., 1998). ^{2}H NMR lineshape simulations were performed as described in Stahlberg et al. (2015). In brief, time domain data were simulated as free induction decays (FID) for *i* superimposed Pake doublets each scaled by an order parameter S_{CDi} according to:

$$FID\,(t) = \sum_{i=1}^{N}\left(\left(\int_{\theta=0}^{90^\circ} d\theta \cos\left(\frac{3}{4}\chi \cdot \frac{1}{2}\left(3\cos^2\theta - 1\right)\cdot S_{CDi}\cdot t\right)\cdot \sin\theta\right) \cdot \exp\left(t \cdot LB_i \cdot \pi\right)\right). \quad (1)$$

In Eq. 1, *LB* is the line broadening factor, χ = 167 kHz is the quadrupolar coupling constant for the C-^{2}H bond, and θ the angle for powder averaging, which was incremented by 0.00625°. The FID was calculated as a function of time (*t*) for n data points using $t = n \cdot DW$, with a dwell time (DW) of 1 μs.

AFM Force Indentation

AFM force measurements (Butt and Franz, 2002; Chiantia et al., 2006; Sullan et al., 2013) were acquired using the NanoWizard II system (JPK Instruments, Berlin, Germany), mounted on an Axiovert Inverted Microscope (Zeiss, Germany). The deflection sensitivity, resonance frequencies (both in air and in water) and resultant spring constant were measured via thermal noise method. The cantilever used for all the force experiments had a resonance frequency of 10–20 kHz and a spring constant of 0.025–0.035 N/m. These values remained the same before and after the experiments. AFM experiments were performed on mica glued to the glass surface on a liquid cell, and the bilayer was hydrated till the experiment was completed. The total z-piezo displacement was 1.0 μm, and the speed both for approach and retraction were kept at 0.5 μm/s. In the non-contact region, the AFM tip approaches the top surface of the bilayer where the force remains constant. As it touches the bilayer surface at the contact point, the force gradually increases, this is followed by a sudden breakthrough of the bilayer which appears as a "kink" in the smooth force-distance curve. The value at which this occurs is the indentation force. Subsequently, the tip reaches the solid mica support. All the experiments were carried out at many different positions on the bilayer in the absence and in the

presence of 5.8 mM 5-HT. All breakthrough force curves were analyzed using the JPK data processing software. The indentation force values were extracted from each approach curve, and were plotted as a histogram.

Molecular Dynamics Simulations

Simulation setup of the different membranes and in-depth analysis of the structure and dynamics of the domains spontaneously formed are described in detail in the companion paper to this article (Bochicchio et al., 2020). In brief: we conducted 10 μs long atomistic MD simulations [CHARMM36 force field (Klauda et al., 2010)] of POPC/PSM/Chol (4/4/2) mixtures in absence and presence of 9 mol% 5-HT. Spontaneously formed disordered and ordered phases were distinguished by virtue of a Hidden Markov Model using the lipid tail order [director order parameter (Yankova et al., 2012)] as observable for the definition of the putative ordered, disordered, and intermediate ordered states.

RESULTS

5-HT Modifies the Domain Structure of the POPC/PSM/Chol (4/4/2) Mixture as Revealed by ^{2}H Solid-State NMR Spectroscopy

The phase behavior of the ternary POPC/PSM/Chol (4/4/2, mol/mol/mol) mixture in the absence and in the presence of 5-HT was studied using ^{2}H NMR over a temperature range from 20 to 50°C using a temperature increment of 2 K. In three independent preparations, each component of the mixture was ^{2}H labeled and the respective ^{2}H NMR spectra are shown in **Supplementary Figure 1**. Thus, the full thermotropic phase behavior of each lipid component of the mixture was recorded.

Figure 1 displays the ^{2}H NMR spectra of each ^{2}H-labeled component of the POPC/PSM/Chol mixture in the absence (left spectra in black) and in the presence of 9 mol% 5-HT (right spectra in color). In the absence of 5-HT, very typical ^{2}H NMR spectra characteristic of POPC forming a liquid disordered (L_d) phase as indicated by the smaller quadrupolar splittings and PSM forming a liquid ordered (L_o) phase as characterized by the larger quadrupolar splittings are obtained in agreement with the literature (Veatch et al., 2007; Bartels et al., 2008; Bunge et al., 2008; Soni et al., 2009; Bosse et al., 2019). The ^{2}H NMR spectra of all lipid components show just one set of quadrupolar splittings for each chain methylene and methyl groups suggesting that the majority of the POPC molecules on the one hand and the PSM and cholesterol molecules on the other resides in the L_d and L_o phases, respectively (Veatch et al., 2007; Bunge et al., 2008). Previous microscopy work has demonstrated that L_o and L_d domains are found for this mixture (Veatch and Keller, 2003). The ^{2}H NMR spectra of the Chol-d_6 also feature just one quadrupolar splitting for each deuteron. These measured quadrupolar splittings agree with an upright orientation of the sterol in the membrane undergoing axially symmetric reorientations about its long axis as analyzed in detail before (Dufourc et al., 1984).

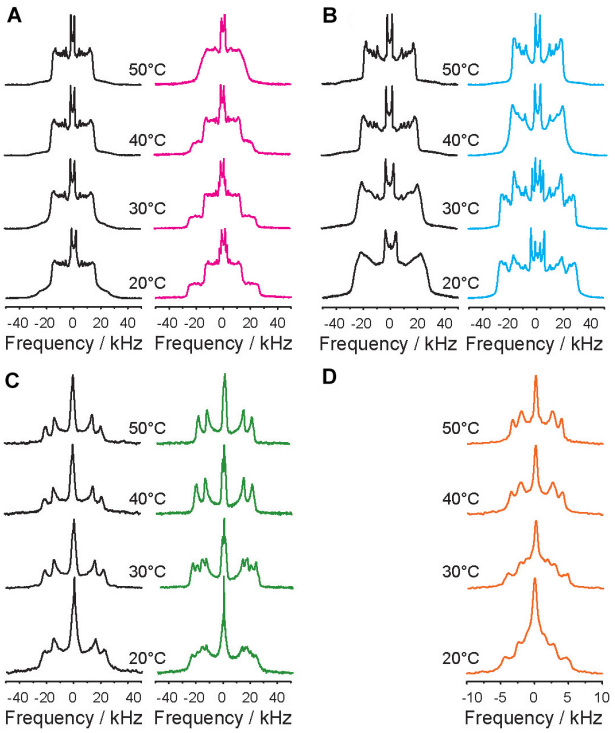

FIGURE 1 | Temperature dependence of the ^{2}H NMR spectra of a ternary POPC/PSM/Chol mixture (molar ratio 4/4/2) hydrated to 50 wt% aqueous buffer (K_2PO_4 20 mM, 100 mM NaCl, 0.1 mM EGTA, pH 7.4) in the absence (black spectra in the left columns) and in the presence of 9 mol% 5-HT (colored spectra in the right columns) at various temperatures as indicated. **(A–D)** ^{2}H NMR spectra were recorded for each component of the mixture: **(A)** POPC-d_{31}, **(B)** PSM-d_{31}, **(C)** Chol-d_6, **(D)** 5-HT-d_4.

NMR investigations have also revealed that specific lipid molecules while significantly enriched in one phase are not exclusively found in just one phase (Veatch et al., 2007; Bartels et al., 2008; Bunge et al., 2008). This means that individual PSM and Chol molecules also partition into the L_d phase and some POPC is found in the L_o phase (Yasuda et al., 2015). The exchange of the lipids between the two phases is limited by lateral diffusion (Huster et al., 1998). Thus, if the domains are small, lipids can quickly exchange between the two environments. In such a case, only one averaged NMR signal is detected for each lipid species. In the terminology suggested by Feigenson and coworkers, such domains would be referred to as "nanodomains" (Usery et al., 2017). It has been estimated that on the NMR time scale, small domains would have a diameter on the order of less than about 25 nm (Huster et al., 1998). If domains are large, then the exchange of the molecules between the two environments is slow and the obtained NMR spectra consist of two contributions, one from each environment. For ^{2}H NMR spectra of lipids with perdeuterated lipid chains, one observes two Pake spectra for each deuterated lipid segment (Veatch et al., 2007; Bartels et al., 2008; Bunge et al., 2008). Such large domains would be referred to

as "macrodomains" (Usery et al., 2017). In the absence of 5-HT, all recorded NMR spectra only featured one component, suggesting that the domains are small such that lipids of the same species can rapidly exchange between L_o and L_d phases. Consequently, rapid lateral lipid diffusion averages the NMR signals.

The presence of 5-HT at a concentration of 9 mol% induced a drastic restructuring of the domains of the mixture. In a certain temperature range, the ^{2}H NMR spectra of each component of the POPC/PSM/Chol/5-HT (4/4/2/1) mixture can be conclusively interpreted as the superposition of two NMR signals for each molecular segment (**Figure 1**, spectra highlighted in color). This indicates that each component of the mixture is found in two different chemical environments and that the exchange of the molecules between these environments is slow. With regard to a lipid membrane with a given domain structure, this means that the domains are very large and the lateral lipid diffusion is too slow to allow for a significant exchange between the phases. It is remarkable that the ^{2}H NMR spectra of all components of the mixture showed these two contributions with unique sets of quadrupolar splittings each. Even the 5-HT molecules displayed distinct two component NMR spectra. ^{2}H NMR spectra with two contributions were observed over a broad temperature range from 20–48°C for POPC, 20–38°C for PSM and cholesterol, and 20–36°C for the 5-HT. Each phase of the respective component is characterized by a unique set of quadrupolar splittings (**Figure 1**). At temperatures higher than 46°C, the ^{2}H NMR spectra of the POPC component are exchange broadened, indicative of critical fluctuations (Veatch et al., 2007), while for PSM, Chol, and 5-HT well resolved ^{2}H NMR spectra with just one set of quadrupolar splittings are detected indicating fast exchange of lipids as in the absence of 5-HT.

The compositions of these phase states and the individual structural parameters of the lipid chains of each component of the mixture were analyzed in detail for the ^{2}H NMR spectra recorded at 30°C. To this end, numerical simulations of the ^{2}H NMR spectral lineshapes were carried out (Stahlberg et al., 2015), which are shown in **Figure 2** along with the enlarged NMR spectra of each component of the mixture in the presence and in the absence of 5-HT. While the ^{2}H NMR spectrum of the POPC component indicates fast exchange between molecules in small domains in the absence of 5-HT, the presence of 9 mol% (relative to all lipids) 5-HT causes a significant restructuring of the mixture. Two sets of quadrupolar splittings detected for each POPC segment suggest that the molecule partitions into two domains of relatively large size. The POPC molecules experience a significantly different chain packing in both environments. The exchange of lipids between these pools is too slow to allow for an averaging between the two environments. The two different components of the ^{2}H NMR powder spectra correspond to lipids in a much more ordered and a more disordered phase (Veatch et al., 2007). For a quantitative analysis of the observed phenomena, numerical simulations of all ^{2}H NMR spectra provide structural information on the individual lipid environments.

From these simulations, the lipid chain order parameters of the molecules in each phase could be calculated and are displayed in **Figure 3**. In the absence of 5-HT, the POPC molecules display an order parameter profile as typical for the L_d state

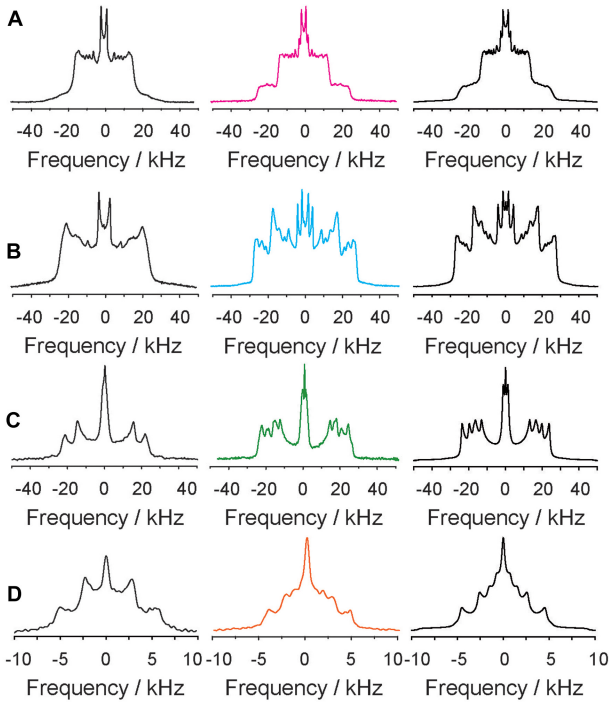

FIGURE 2 | ^{2}H NMR spectra of deuterated POPC-d_{31} **(A)** PSM-d_{31} **(B)**, Chol-d_6 **(C)**, and 5-HT-d_4 **(D)** of the POPC/PSM/Chol mixture (molar ratio 4/4/2) mixture in the absence (left column) and in the presence of 9 mol% 5-HT (middle column) at a temperature of 30°C. Note that the ^{2}H NMR spectrum shown in the left column of panel **(D)** was acquired for 5-HT in pure POPC membranes. The right column shows numerical simulations of the ^{2}H NMR spectra.

(Bunge et al., 2008). In the presence of 5-HT, we clearly observed two lipid phases. In the first phase (referred to as phase I), the POPC molecules had somewhat lower order parameters than in the absence of 5-HT (**Figure 3**). In the second phase (referred to as phase II) the POPC molecules showed much higher order parameters compared to the absence of 5-HT (**Figure 3**). From these order parameter profiles, the projected chain lengths ($\langle L \rangle$) can be estimated according to analytical models developed by the Brown laboratory (Petrache et al., 2000). These chain lengths are plotted in the insets of **Figure 3**. In the absence of 5-HT, the *sn*-1 chain of POPC is relatively disordered with a projected length of 13.2 Å, which means that it contains on average 5.8 *gauche* conformers as typical for an L_d phase. This number is calculated considering that each *gauche* defect reduces the average length of an all-*trans* chain by 1.1 Å (Feller et al., 2002). In the presence of 5-HT, the relative proportion of POPC in each individual phase can be determined from the NMR line shape simulation. 60% of the POPC is found in a more disordered state (phase I), where each acyl chain has an average length of 12.7 Å and is characterized by 6.4 *gauche* defects, while 40% of the POPC is found in a much more ordered state (phase II, $\langle L \rangle$ = 15.5 Å) with only 3.6 *gauche* defects per chain. Such parameters are characteristic of a L_o phase state.

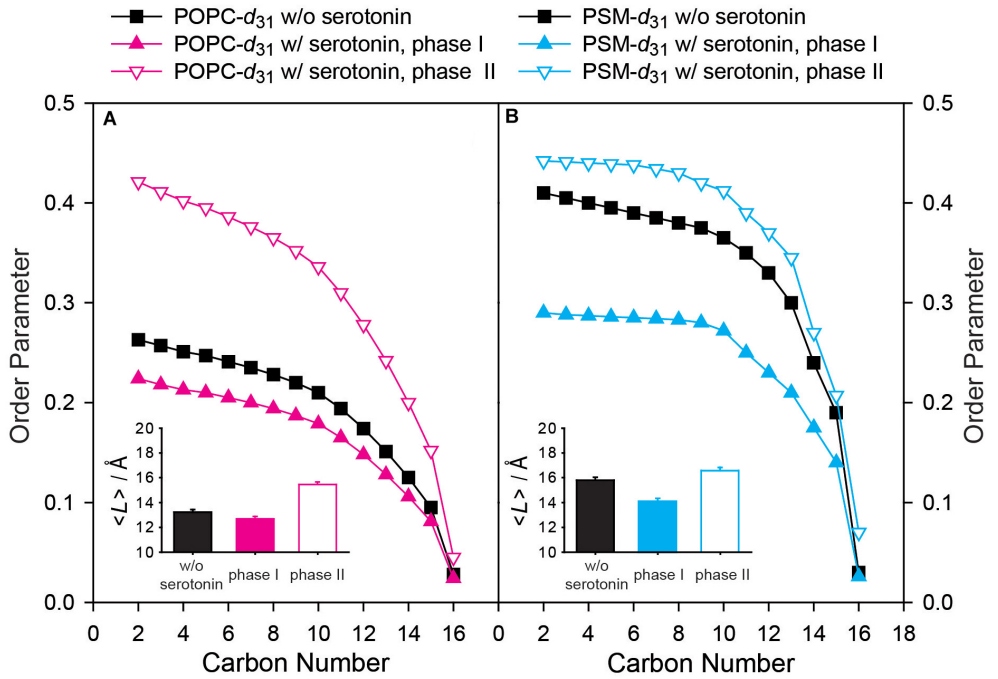

FIGURE 3 | Experimental order parameter profiles and average chain length of **(A)** POPC-d_{31} and **(B)** PSM-d_{31} in a POPC/PSM/Chol (4/4/2) mixture in the absence and in the presence of 9 mol% 5-HT determined from ^{2}H NMR experiments carried out at a temperature of 30°C. In the presence of 5-HT, two phases with distinctly different order parameters are observed. Phase I represents a disordered and phase II an ordered phase. The insets show the projected average chain length $\langle L \rangle$ of the palmitoyl chain of POPC or PSM in the absence (black bars) and in the presence of 9 mol% 5-HT (phase I filled colored bars, phase II empty colored bars). The error bars in the insets represent the error estimate of the chain length determination from ^{2}H NMR spectra (Holte et al., 1996).

Next, we analyzed the ^{2}H NMR spectra of the PSM component of the mixture (**Figure 2B**). Characteristic ^{2}H NMR spectra for the L_o phase state were recorded in the absence of 5-HT and the chain order parameters of PSM-d_{31} are shown in **Figure 3B**. Under these conditions, the palmitoyl chain of PSM is highly ordered ($\langle L \rangle$= 15.8 Å) and contains on average 3.2 *gauche* defects. As for the case of POPC, in the presence of 5-HT, the ^{2}H NMR spectra of the PSM lipids also showed the superposition of two spectral components suggesting that the lipids were organized in two environments of unique properties with only slow exchange. The chain order parameters for PSM were calculated from the ^{2}H NMR spectrum and are shown in **Figure 3B**. Compared to the case without 5-HT, we find PSM molecules to reside within a much more disordered phase I as well as in a somewhat more ordered phase II. The disordered phase contains 37% of the PSM molecules and is characterized by lipid chains of an average length of 14.1 Å that feature on average 4.5 *gauche* defects, which is more typical of the L_d phase. In contrast, 63% of the PSM molecules formed the more ordered phase II which displays highly ordered chains with an average length of 16.6 Å corresponding to only 2.2 *gauche* defects characteristic for a highly ordered phase state.

The addition of 5-HT to the mixture also led to a segregation of cholesterol into two distinctly different chemical environments. We observed 22% of the cholesterol with somewhat smaller quadrupolar splittings suggesting that it partitioned into the more disordered phase I. In contrast, the majority of the Chol (78%) partitioned to the more ordered phase II. As the ratio between the individual quadrupolar splittings for each site on the molecule did not change, we conclude that the tumbling amplitude of the cholesterol in the more disordered phase I is increased (Dufourc et al., 1984), while it is slightly decreased in the more ordered phase II in agreement with the looser and tighter lipid packing in each phase, respectively.

Finally, ^{2}H NMR spectra of deuterated 5-HT-d_4 were analyzed. In 5-HT-d_4, the two methylene groups in the sidechain of 5-HT are labeled. We obtained rather narrow ^{2}H NMR spectra (**Figure 2D**) indicating high mobility of the molecule when partitioned into the membranes. In pure POPC bilayers, we could resolve one Pake doublet for each deuterated site (**Supplementary Figure 2**). In the POPC/PSM/Chol (4/4/2) membrane, again two sets of quadrupolar splittings were observed for each site characteristic for a 5-HT localization in the more disordered phase I and the more ordered phase II. From the ^{2}H NMR lineshape simulations we estimated that about 28% of the 5-HT showed a more disordered ^{2}H NMR spectrum while 65% of the spectral intensity expressed a slightly higher state of order. About 7% of serotonin is isotropic and presumably not bound to the membrane. Although plausible, from this analysis it cannot be concluded that 28% of the 5-HT is bound to the disordered phase I and 65% of it to the ordered phase II. Both fractions of the molecule show high mobility indicating that 5-HT moves fast undergoing large amplitude motions.

In order to investigate how these molecular changes in lipid chain packing induced by 5-HT alter the mesoscopic

and mechanical properties of the membrane, we carried out AFM indentation force measurements on supported POPC/egg-SM/Chol bilayers of the same mixing ratio (Butt and Franz, 2002; Chiantia et al., 2006; Sullan et al., 2013). The force of indentation (or breakthrough force) is the force required to rupture the bilayer locally and provide the estimation of the membrane's stiffness. We compared the breakthrough force of the bilayer in the absence and in the presence of 5.8 mM serotonin incubated for 1 h. The representative breakthrough force distribution is shown in **Supplementary Figure 3**. The analysis showed that 5-HT binding increases the indentation force by about 44%, which is interpreted as an increase in membrane stiffness.

Given the very intriguing impact of 5-HT on the phase behavior of the POPC/PSM/Chol (4/4/2) mixture, we also conducted the same set of experiments in equimolar POPC/PSM mixtures in the absence of cholesterol as the sterol represents the most crucial player in membrane domain formation (Brown and London, 1998). In a POPC/PSM/5-HT (5/5/1) molar mixture, we observed single component ^{2}H NMR spectra for each phospholipid of the mixture at various temperatures (**Supplementary Figure 4**). The POPC-d_{31} of the mixture is found in a disordered and the PSM-d_{31} in an ordered state; the chain order parameters of both components are fairly different suggesting demixing of the two phospholipids (**Supplementary Figure 4** and **Figure 5**). But the ^{2}H NMR spectra of each phospholipid only show one component each. This indicates that Chol is indeed the key component for the observed alterations of the domain structure of the lipid mixture in the presence of 5-HT and 5-HT alone cannot induce the restructuring of the domains as observed for the raft mixture in presence of cholesterol.

Analysis of the Phase State of the POPC/PSM/Chol (4/4/2) Mixture in the Absence and in the Presence of 9 mol% 5-HT Using Molecular Dynamics Simulations

We also carried out MD simulations of the same mixture in the absence and in the presence of 5-HT, which yielded a wealth of information on the interaction of the neurotransmitter with the mixed membranes. Methods and further results of the MD simulation are discussed in detail in the companion paper to this article (Bochicchio et al., 2020). Here, we focus on the analysis of the serotonin-dependent chain order parameters of both POPC and PSM. The order parameters of either lipid species in the mixed membrane determined from the MD simulation are displayed in **Figure 4**.

First, it is important to discuss characteristic differences between the experimental ^{2}H NMR order parameters and those determined from the MD simulations. (i) Experimentally, only the order parameters of the perdeuterated *sn*-1 chain of POPC or palmitoyl chain of PSM can be observed as only lipids with this deuteration scheme are available. In contrast, from the MD simulation, also the order parameters of the *sn*-2 chains of POPC and the sphingosine moiety of PSM are readily accessible as shown in **Figures 4B,D**. (ii) While the chain order parameter profiles determined by experiment gradually decrease from the glycerol backbone toward the end of the chains, the order parameter profiles determined from the MD feature a low order parameter for the C-2 segment, an order increase for the subsequent carbons toward the middle of the chain and an order decrease again toward the chain ends. The reason for this difference is the lacking assignments in the experimental ^{2}H NMR spectra. Since lipids with perdeuterated chains are used in the experiment, the assignment of an order parameter to the respective carbon position in the chain is not available due to the superposition of Pake doublets in the experimental ^{2}H NMR spectra. By convention (Davis, 1983), the order parameter, determined from the largest quadrupolar splitting is assigned to the C-2 position in the chain, the next lower order parameter to the C-3 position and so forth. In contrast, in the MD, the exact assignment of a given order parameter to its respective carbon atom in the chain is absolutely clear. Therefore, only the MD simulation reports the correct ordering of the individual hydrocarbon order parameters along the acyl chain. (iii) The *sn*-2 chain order parameters of the oleoyl moiety are very low in the middle of the chain due to the orientation of the double bond that results in an orientation close to the magic angle (54.7°) between the C-^{2}H bond vectors and the membrane normal. This is also seen for the *trans* double bond in the sphingosine backbone of PSM providing very low order parameters for the C-4/5 segments.

Close inspection of the MD order parameter profiles revealed several interesting details. In the absence of 5-HT, POPC molecules were found in both ordered and disordered domains characterized by corresponding order parameters (**Figures 4A,B**). Upon the addition of 5-HT to the solvent phase of the simulation system, the order parameters of POPC in the ordered state remained relatively similar, while the POPC molecules in the disordered phase displayed significantly decreased order parameters (after the establishment of an equilibrium between membrane-bound and free 5-HT). These features were observed for both chains. For PSM, a similar situation was encountered (**Figures 4C,D**). In the absence of 5-HT, PSM was found in both more ordered and disordered phases. Upon addition of 5-HT, the order parameters profiles of the ordered phase II remain approximately constant while the order parameters of the disordered phase I decreased rather drastically. Again, this effect was observed both for the palmitoyl and the sphingosine chains.

For comparison of the absolute order parameters determined from experiment and from simulation illustrated in **Figure 5**, only the average over the *sn*-1 chain of POPC or the acyl chain of PSM could be considered due to the assignment problem of ^{2}H NMR. Inspection of **Figure 5** shows that the chain order parameters determined from the experiment and the simulation agreed slightly better for PSM than for POPC. Overall, the pronounced alterations that 5-HT induced on chain order were by and large reproduced in the simulation. For POPC, the experimental order parameters were generally lower than those from the MD simulation. In very good agreement with the experiment, the difference between the order parameters of phase I (disordered phase) and phase II (ordered phase) increased in presence of 5-HT. Furthermore, the MD also confirmed that

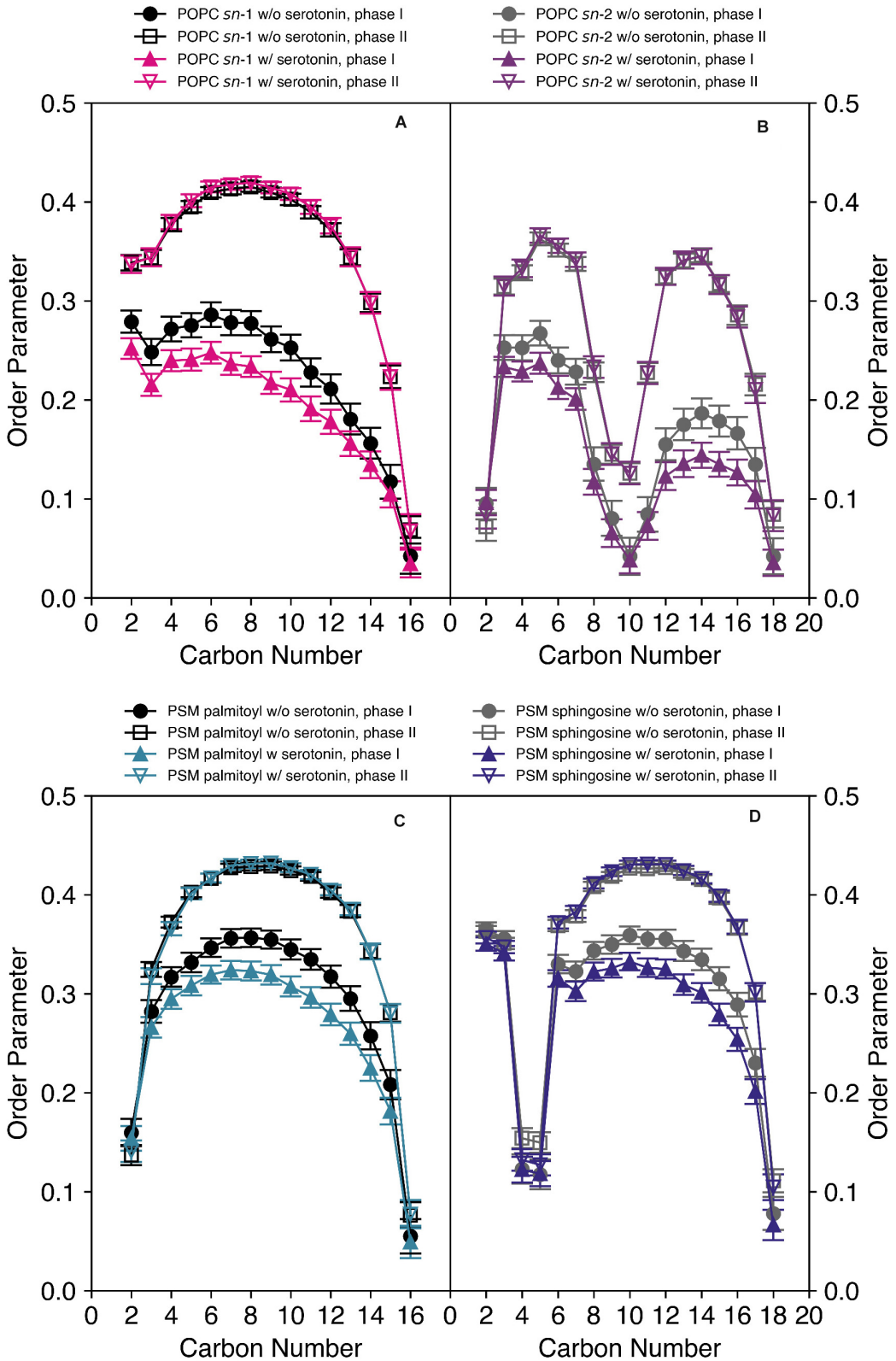

FIGURE 4 | Order parameter profiles of POPC-d_{31} **(A,B)** and PSM-d_{31} **(C,D)** in a POPC/PSM/Chol (4/4/2) mixture in the absence and in the presence of 9 mol% 5-HT determined from a MD simulation at a temperature of 30°C. Upon the addition of 5-HT, an increased difference in the order parameters between the two phases was observed. I indicates the disordered and II the ordered phase or domain.

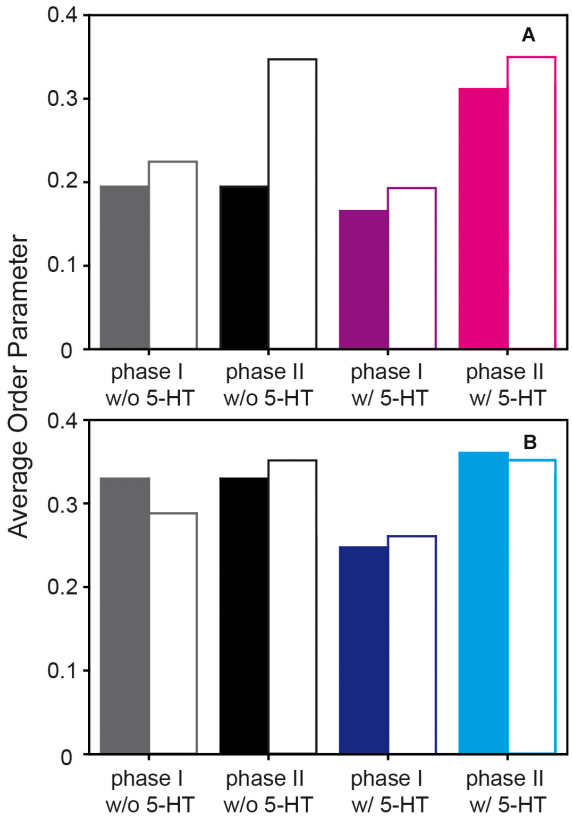

FIGURE 5 | Comparison of the average order parameters of the *sn*-1 chain of POPC **(A)** and the acyl chain of PSM **(B)** in a POPC/PSM/Chol (4/4/2) mixture in the presence and in the absence of 5-HT determined by ^{2}H NMR experiments (filled bars) and the MD simulations (open bars). Note that in the absence of 5-HT only one averaged lipid phase is observed experimentally and the same bars are reported.

even in the absence of 5-HT, each lipid species partitioned into ordered and disordered domains (phases I and II, respectively) with pronounced order differences.

DISCUSSION

Ternary lipid mixtures of an unsaturated phospholipid, sphingomyelin (SM) and cholesterol are subject to a complex phase behavior giving rise to a multitude of domain sizes and shapes depending on temperature, lipid chemistry, molecular mixing ratio, hydration level etc. (Baumgart et al., 2003; Rosetti et al., 2017). There is agreement that SM and Chol are predominantly found in the L_o phase, while the unsaturated phospholipid forms the L_d phase (Pike, 2006). However, these phases are not "pure" as SM and Chol are found as well in the L_d phase and the unsaturated phospholipid in the L_o state (Yasuda et al., 2015). Although these phenomena are best described by fluctuations of the lipid distribution (Veatch et al., 2007), in equilibrium a steady lipid distribution is achieved.

In the current work, we observed the striking result that the small aromatic neurotransmitter 5-HT that partitions into the lipid water interface of the membrane can drastically restructure a heterogeneous lipid mixture consisting of POPC/PSM/Chol at a 4/4/2 molar ratio. Binding of 5-HT to these membranes (i) leads to a restructuring of the domain sizes in the lipid membrane, in which (ii) the lipids form much larger domains with more pronounced ordered and disordered characteristics compared to the L_o and L_d states observed in the absence of 5-HT. (iii) Each component of the mixture is found to be present in both phases at different proportions. These phenomena are not induced by 5-HT-binding exclusively to one domain, as (iv) 5-HT is found to partition into both the disordered and the ordered lipid phases. These results were found at a 5-HT concentration of 9 mol% relative to the lipids in the mixture. This number corresponds to the membrane partitioning of 5-HT when lipid vesicles are incubated with 5 mM serotonin in solution, which is reasonably representative of the broad range of serotonin concentrations that physiological membranes are exposed to (S. Dey and S. Maiti, unpublished).

How can a small membrane binding neurotransmitter induce such a remarkable restructuring of the equilibrium domain structure of the ternary membrane mixture? In understanding these interesting results it is useful first to recall Gibbs phase rule which states that the number of degrees of freedom for a system with a fixed number of phases increases when the number of components of the mixture increases (Rosetti et al., 2017). As 5-HT binds to the lipid molecules, it can be considered a component of the system which consequently increases its degrees of freedom. On a more molecular level, critical phenomena at the phase boundary as well as contributions from lateral tension, line tension, bending resistance, dipole interaction, and normal pressure differences have to be considered (Baumgart et al., 2003). The line tension is pronounced to be the decisive factor that determines the size of the domains in heterogeneous membranes (Baumgart et al., 2003; Rosetti et al., 2017; Usery et al., 2017; Tsai and Feigenson, 2019). Line tension describes the interfacial energy at the edge of the membrane domains. This parameter is critically influenced by the hydrophobic mismatch between lipid chains at the interface between coexisting phases. This is exemplified by the exchange of monounsaturated PLs to di-unsaturated symmetric PCs in saturated PL/cholesterol-containing bilayers, leading to hydrophobic mismatch and therefore nanosized domains to become micro sized domains as detected in both confocal microscopy (Usery et al., 2017) and ^{2}H NMR (Nyholm et al., 2019). Our experimental results show that binding of 5-HT to both the L_o and L_d phases alters the lipid chain order of both phospholipids rather drastically. Both our experimental and MD simulation results show that the disordered phases become more disordered. The NMR experiments further revealed a more ordered L_o phase upon binding of 5-HT (**Figure 3** and **Figure 5**). Taken together, the hydrophobic mismatch between the lipid molecules in the two phases increases, which is supposed to increase the line tension at the phase boundary (Tsai and Feigenson, 2019; Huang et al., 2020). This effect provides the driving force for the restructuring of the domain size in the presence of 5-HT (Usery et al., 2017; Huang et al., 2020). This simple argument can explain why 5-HT binding to the lipid

mixture increases the domain size as experimentally observed. Furthermore, 5-HT introduces an additional dipole moment into the membrane, which may also influence domain size (Usery et al., 2017).

On a molecular level, the question remains how neurotransmitter binding can on the one hand increase the order of the PSM in L_o phase and at the same time decrease the order of POPC in the L_d phase. In asking what are the molecular mechanisms by which 5-HT exerts its pronounced effects on lipid chain order, we looked into the details of 5-HT binding to the lipid molecules in either phase state. Several experimental and MD simulation studies have determined the distribution of 5-HT (Peters et al., 2013; Josey et al., 2020) or other indole derived small molecules (Yau et al., 1998) in the membrane. As observed for other small aromatic compounds (Scheidt et al., 2004; Siarheyeva et al., 2006; Weizenmann et al., 2012), 5-HT prefers an interface localization within the lipid bilayer that comprises the headgroup, glycerol, and upper chain region of the membrane in agreement with experimental studies (Dey et al., 2020; Josey et al., 2020) and MD simulations (Peters et al., 2013). Such an interface location was also confirmed in our MD simulations as discussed in detail in the companion paper (Bochicchio et al., 2020). Interestingly, in our MD simulation, a bimodal distribution of 5-HT parallel to the membrane normal was observed (**Supplementary Figure 6**): some of the 5-HT was found associated with the lipid headgroups and some was localized more deeply in the upper chain region of the lipid membrane (Dey et al., 2020). We analyzed if there was a correlation between the depth of 5-HT penetration into the membrane and the phase state of the respective domain in the MD data. This analysis revealed that 5-HT penetrates more deeply into disordered L_d membrane domains while a more superficial association of 5-HT with the lipid headgroups is primarily observed in the L_o phase (**Supplementary Figure 6A**). From the MD simulation of the ternary lipid mixture, we determined the number of contacts between 5-HT and the lipids in the L_o and the L_d phase revealing that 53.0% of the total 5-HT is associated with the L_d and 16.4% with the L_o phase at 30°C. However, there was a significant difference in the distribution of the 5-HT along the membrane normal: in the L_o phase, only 7.3% of the lipid contacts of 5-HT occurred with the glycerol/upper lipid chain segments while 92.7% were in contact with the lipid headgroups. In contrast, in the L_d phase, 29.2% of the 5-HT contacts were observed with the glycerol/upper chain region and 73.1% with the headgroup. This increased number of contacts of 5-HT with the glycerol/upper chain segments of L_d phase lipids and with the headgroup of L_o phase lipids was confirmed by MD simulations of 5-HT binding to pure L_o and L_d phases, respectively [**Supplementary Figures 6B,C**; for details see companion paper (Bochicchio et al., 2020)].

Our results suggest that 5-HT, bound to the glycerol upper chain region of the L_d phase lipids, causes a decrease in the lipid chain order parameters. 5-HT molecules penetrate the glycerol/upper chain segments and thus decrease the packing density in the membrane providing more free volume in the lower chain region which is occupied by larger amplitude motions of the chain segments causing lower order parameters in the more disordered phase. In contrast, 5-HT that is bound to the lipid headgroup region may have a tendency to decrease the repulsive forces between the lipid headgroups. 5-HT may intercalate between negatively charged phosphate groups thus leading to an increase in lipid chain packing density expressed by higher chain order parameters of the more ordered phases. Such resulting area compression in lipid membranes has been reported previously for membranes interacting with anionic polyelectrolytes in the presence of divalent cations or positively charged lipids (Huster et al., 1999, 2000). Also, interactions between 5-HT and the lipid's phosphate groups have been described in previous MD simulations (Peters et al., 2013). Taken together, the formation of the more disordered phase I and the more ordered phase II of the ternary mixture observed in the presence of 5-HT is likely the consequence of the different insertion depths into and binding strengths to the L_o and L_d membrane phases as analyzed from corresponding MD simulations of 5-HT binding to pure L_d (POPC/PSM/Chol, molar ratio 69/23/8) and L_o (POPC/PSM/Chol, molar ratio 8/61/31) ternary membrane compositions (see **Supplementary Figure 6**). For the L_o phase, two localized regions were found with maxima either inside the membrane headgroup region or in a diffusive adsorption layer on the membrane surface (**Supplementary Figure 6**). In contrast, only one broader binding region embedded more deeply within the membrane is seen for the L_d phase. In turn, the increased acyl chain order within phase II is suggested to be related to the preferred 5-HT binding to the lipid headgroup region as well as to the increased domain sizes that allowed to distinguish different phases for PC lipids within the NMR spectra only in the presence of 5-HT. However, while the simulations do show a decreased ordering within the disordered phase and a more distinguished phase separation (see also companion manuscript), a direct effect of 5-HT on the acyl chain order within the ordered phase could not be seen. This observation is possibly related to the limited size of the studied membrane patches as well as slow processes in phase formation beyond the simulation time scale of 10 μs. It appears that the 5-HT-induced increase of the lipid chain order, and the intimately coupled phase separation well beyond a length scale of ten nanometer, are relevant for rendering the membrane stiffer in the presence of 5-HT as observed in the AFM measurements (**Supplementary Figure 3**).

Phase separation phenomena as observed in lipid membranes and raft models are always related to both the temperature of a specific preparation relative to the main phase transition temperature of the lipid species in the mixture and its specific cholesterol content (Veatch et al., 2007; Sodt et al., 2014). In that regard, the ^{2}H NMR spectra of DOPC/DPPC-d_{62}/Chol mixtures at varying compositions, reported by the Gawrisch and Keller labs, are particularly informative (Veatch et al., 2007). For instance, phase pure ^{2}H NMR spectra of the L_o and the L_d phases at 20°C were reported for 4/1 DOPC/DPPC-d_{62} mixtures in the presence of 40 or 15% Chol, respectively. Furthermore, ^{2}H NMR spectra indicative L_d/L_o phase coexistence as observed here in the presence of 5-HT were reported for an equimolar DOPC/DPPC-d_{62} mixture in the presence of 15% Chol. In addition, L_d/L_o phase coexistence by ^{2}H NMR has also been

observed in SM/Chol bilayers with different di-unsaturated phospholipids, e.g., 14:1, 18:1, 20:1-PC at the same molar lipid ratio of unsaturated PC/SM/Chol 4/4/2 as used in our study (Nyholm et al., 2019). We did not observe any 5-HT-induced alteration of the phase composition of POPC/PSM membranes in the absence of Chol (**Supplementary Figure 4** and **Figure 5**), so it is clear that cholesterol is the major factor in the observed phenomena. This is related to the preferential interaction of cholesterol with saturated chains and the fact that the cone shaped Chol strongly influences membrane curvature. Interestingly, simulations performed at temperatures between 21 and 30°C of the POPC/PSM/Chol mixture further suggest a serotonin-induced change in domain composition: Addition of 5-HT led to a cholesterol content of the disordered phase decreased by 14–29% (see Table 3 in Bochicchio et al., 2020). Thus, the differential 5-HT binding results in a modified interaction network at the membrane interface leading to the observed remodeling of the membrane domain composition, size, and structure. By 5-HT binding to the upper chain region, the favorable interactions between Chol and the saturated lipid chains (Huster et al., 1998; Almeida et al., 2005; Tsamaloukas et al., 2006; Frazier et al., 2007; Scheidt et al., 2013) are perturbed potentially contributing to the observed restructuring of the membrane domains.

In conclusion, we report that the small neurotransmitter 5-HT binds to biologically relevant membrane models and induces a significant restructuring of its domain size. By modulating membrane properties, sorting of membrane proteins may be influenced impacting their structure and dynamics (Huang et al., 2020). For G protein-coupled receptors, secondary structure adaptation to the membrane hydrophobic thickness (Soubias et al., 2008) as well as alterations in the dynamical behavior in various membrane compositions (Thomas et al., 2015) have been reported. Essential membrane properties such as chain length and unsaturation critically influence the function of rhodopsin (Litman and Mitchell, 1996). Thus, 5-HT and small molecule binding to lipid membranes can have a profound influence on the function of non-cognate receptors by regulating their conformational equilibrium. The study suggests that a complex interplay between the lipids of the membrane with neurotransmitters binding from the aqueous phase can alter the function of membrane proteins through alterations in membrane hydrophobic thickness and membrane domain size in the biological system (Postila et al., 2016).

DATA AVAILABILITY STATEMENT

The original contributions presented in the study are included in the article/**Supplementary Material**, further inquiries can be directed to the corresponding authors.

AUTHOR CONTRIBUTIONS

SM and DH designed the research. OE did all experimental work using NMR spectroscopy. AG and SD did the AFM experiments. AB and RB carried out MD simulations. OE and DH analyzed the ^{2}H NMR spectra and performed lineshape simulations. AG, SD, and SM analyzed the AFM measurements. AB, AFB, and RB analyzed the MD simulations. DH wrote the manuscript with contributions from all coauthors. All authors contributed to the article and approved the submitted version.

FUNDING

DH acknowledges funding by the Deutsche Forschungsgemeinschaft (DFG, German Research Foundation) through SFB 1423, project number 421152132, subproject A02. RB acknowledges support through the SFB 1027, *Physical modeling of non-equilibrium processes in biological systems*. SM acknowledges support of the Department of Atomic Energy, Government of India, provided under project no. RTI4003. OE acknowledges support by the Sigrid Juselius Foundation, and Ruth and Nils-Erik Stenbäck's Foundation. We acknowledge support from Leipzig University for Open Access Publishing.

ACKNOWLEDGMENTS

Helpful discussions with Prof. Dr. Jürgen Arnhold about 5-HT peroxidation and with Prof. Dr. Roland Winter about membrane domain size are gratefully acknowledged.

SUPPLEMENTARY MATERIAL

The Supplementary Material for this article can be found online at: https://www.frontiersin.org/articles/10.3389/fphys.2020.578868/full#supplementary-material

REFERENCES

Almeida, P. F., Pokorny, A., and Hinderliter, A. (2005). Thermodynamics of membrane domains. *Biochim. Biophys. Acta* 1720, 1–13. doi: 10.1016/j.bbamem.2005.12.004

Balaji, J., Desai, R., Kaushalya, S. K., Eaton, M. J., and Maiti, S. (2005). Quantitative measurement of serotonin synthesis and sequestration in individual live neuronal cells. *J. Neurochem.* 95, 1217–1226. doi: 10.1111/j.1471-4159.2005.03489.x

Bartels, T., Lankalapalli, R. S., Bittman, R., Beyer, K., and Brown, M. F. (2008). Raftlike mixtures of sphingomyelin and cholesterol investigated by solid-state ^{2}H NMR spectroscopy. *J. Am. Chem. Soc.* 130, 14521–14532. doi: doi.org/10.1021/ja801789t

Baumgart, T., Hess, S., and Webb, W. W. (2003). Imaging coexisting fluid domains in biomembrane models coupling curvature and line tension. *Nature* 425, 821–824. doi: 10.1038/nature02013

Bochicchio, A., Brandner, A. F., Engberg, O., Huster, D., and Böckmann, R. A. (2020). Spontaneous membrane nanodomain formation in the absence or presence of the neurotransmitter serotonin. *Front. Cell. Dev. Biol.* 11.

Bosse, M., Sibold, J., Scheidt, H. A., Patalag, L. J., Kettelhoit, K., Ries, A., et al. (2019). Shiga toxin binding alters lipid packing and the domain structure of

Gb3-containing membranes: a solid-state NMR study. *Phys. Chem. Chem. Phys.* 21, 15630–15638. doi: 10.1039/C9CP02501D

Brown, D. A., and London, E. (1998). Functions of lipid rafts in biological membranes. *Annu. Rev. Cell Dev. Biol.* 14, 111–136. doi: 10.1146/annurev.cellbio.14.1.111

Brown, M. F. (2017). Soft matter in lipid-protein interactions. *Annu. Rev. Biophys.* 46, 379–410. doi: 10.1146/annurev-biophys-070816-033843

Bruns, D., Riedel, D., Klingauf, J., and Jahn, R. (2000). Quantal release of serotonin. *Neuron* 28:220.

Brunsveld, L., Waldmann, H., and Huster, D. (2009). Membrane binding of lipidated Ras peptides and proteins — the structural point of view. *Biochim. Biophys. Acta* 1788, 273–288. doi: 10.1016/j.bbamem.2008.08.006

Bunge, A., Müller, P., Stöckl, M., Herrmann, A., and Huster, D. (2008). Characterization of the ternary mixture of sphingomyelin, POPC, and cholesterol: support for an inhomogeneous lipid distribution at high temperatures. *Biophys. J.* 94, 2680–2690. doi: 10.1529/biophysj.107.112904

Butt, H.-J., and Franz, V. (2002). Rupture of molecular thin films observed in atomic force microscopy. *I. Theory. Phys. Rev. E.* 66, 031601.

Cantor, R. S. (1997). The lateral pressure profile in membranes: a physical mechanism of general anesthesia. *Biochemistry* 36, 2339–2344. doi: 10.1021/bi9627323

Cebecauer, M., Amaro, M., Juriewicz, P., Sarmento, M. J., Šachl, R., Cwiklik, L., et al. (2018). Membrane lipid nanodomains. *Chem. Rev.* 118, 11259–11297.

Chen, C. H., Melo, M. C., Berglund, N., Khan, A., de la Fuente-Nunez, C., Ulmenschneider, J. P., et al. (2020). Understanding and modelling the interactions of peptides with membranes: from partitioning to self-assembly. *Curr. Opin. Struct. Biol.* 61, 160–166. doi: 10.1016/j.sbi.2019.12.021

Chiantia, S., Ries, J., Kahya, N., and Schwille, P. (2006). Combined AFM and two-focus SFCS study of raft-exhibiting model membranes. *ChemPhysChem* 7, 2409–2418. doi: 10.1002/cphc.200600464

Davis, J. H. (1983). The description of membrane lipid conformation, order and dynamics by ^{2}H NMR. *Biochim. Biophys. Acta* 737, 117–171. doi: 10.1016/0304-4157(83)90015-1

Davis, J. H., Jeffrey, K. R., Bloom, M., Valic, M. I., and Higgs, T. P. (1976). Quadrupolar echo deuteron magnetic resonance spectroscopy in ordered hydrocarbon chains. *Chem. Phys. Lett.* 42, 390–394. doi: 10.1016/0009-2614(76)80392-2

de Jong, D. H., Singh, G., Bennett, W. F., Arnarez, C., Wassenaar, T. A., Schäfer, L. V., et al. (2013). Improved parameters for the martini coarse-grained protein force field. *J. Chem. Theory Comput.* 9, 687–697.

Dey, S., Surendran, D., Engberg, O., Gupta, A., Fanibunda, S. E., Das, A., et al. (2020). Receptor-independent membrane mediated pathways of serotonin action. *bioRxiv*. [Preprint]. doi: 10.1101/2020.07.01.177451

Doktorova, M., Kucerka, N., Kinnun, J. J., Pan, J., Marquardt, D., Scott, H. L., et al. (2020). Molecular structure of sphingomyelin in fluid phase bilayers determined by the joint analysis of small-angle neutron and X-ray scattering data. *J. Phys. Chem. B.* 124, 5186–5200. doi: 10.1021/acs.jpcb.0c03389

Dufourc, E. J., Parish, E. J., Chitrakorn, S., and Smith, C. P. (1984). Structural and dynamical details of cholesterol-lipid interaction as revealed by deuterium NMR. *Biochemistry* 23, 6062–6071. doi: 10.1021/bi00320a025

Engberg, O., Kovacik, A., Pullmannová, P., Juhaščik, M., Opálka, L., Huster, D., et al. (2020). The sphingosine and acyl chains of ceramide [NS] show very different structure and dynamics challenging our understanding of the skin barrier. *Angew. Chem. Int. Ed.* 59, 17383–17387. doi: 10.1002/anie.202003375

Engberg, O., Scheidt, H. A., Nyholm, T. K. M., Slotte, J. P., and Huster, D. (2019). Membrane localization and lipid interactions of common lipid-conjugated fluorescence probes. *Langmuir* 35, 11902–11911. doi: 10.1021/acs.langmuir.9b01202

Feller, S. E., Gawrisch, K., and MacKerell, A. D. Jr. (2002). Polyunsaturated fatty acids in lipid bilayers: intrinsic and environmental contributions to their unique physical properties. *J. Am. Chem. Soc.* 124, 318–326. doi: 10.1021/ja011834o

Feller, S. E., Huster, D., and Gawrisch, K. (1999). Interpretation of NOESY cross-relaxation rates from molecular dynamics simulations of a lipid bilayer. *J. Am. Chem. Soc.* 121, 8963–8964. doi: 10.1021/ja991456n

Frazier, M. L., Wright, J. R., Pokorny, A., and Almeida, P. F. (2007). Investigation of domain formation in sphingomyelin/cholesterol/POPC mixtures by fluorescence resonance energy transfer and Monte Carlo simulations. *Biophys. J.* 92, 2422–2433. doi: 10.1529/biophysj.106.100107

Griepernau, B., and Böckmann, R. A. (2008). The influence of 1-alkanols and external pressure on the lateral pressure profiles of lipid bilayers. *Biophys. J.* 95, 5766–5778. doi: 10.1529/biophysj.108.142125

Griepernau, B., Leis, S., Schneider, M. F., Sikor, M., Steppich, D., and Böckmann, R. A. (2007). 1-Alkanols and membranes: a story of attraction. *Biochim. Biophys. Acta* 1768, 2899–2913. doi: 10.1016/j.bbamem.2007.08.002

Holte, L. L., Separovic, F., and Gawrisch, K. (1996). Nuclear magnetic resonance investigations of hydrocarbon chain packing in bilayers of polyunsaturated phospholipids. *Lipids* 31, S199–S203.

Huang, J., Hiraki, S., and Feigenson, G. W. (2020). Calculation of lquid-disordered/liquid-ordered line tension from pairwise lipid interactions. *J. Phys. Chem. B.* 124, 4949–4959. doi: 10.1021/acs.jpcb.0c03329

Huster, D. (2014). Solid-state NMR spectroscopy to study protein-lipid interactions. *Biochim. Biophys. Acta* 1841, 1146–1160.

Huster, D., Arnold, K., and Gawrisch, K. (1998). Influence of docosahexaenoic acid and cholesterol on lateral lipid organization in phospholipid membranes. *Biochemistry* 37, 17299–17308. doi: 10.1021/bi980078g

Huster, D., Dietrich, U., Gutberlet, T., Gawrisch, K., and Arnold, K. (2000). Lipid matrix properties in cationic membranes interacting with anionic polyelectrolytes - a solid state NMR approach. *Langmuir* 16, 9225–9232. doi: 10.1021/la000620d

Huster, D., Paasche, G., Dietrich, U., Gutberlet, T., Zschörnig, O., Gawrisch, K., et al. (1999). Investigation of phospholipid area compression induced by calcium-mediated dextran sulfate interaction. *Biophys. J.* 77, 879–887. doi: 10.1016/s0006-3495(99)76939-0

Javanainen, M., Martinez-Seara, H., and Vattulainen, I. (2017). Nanoscale membrane domain formation driven by cholesterol. *Sci. Rep.* 7:1143.

Jerabek, H., Pabst, G., Rappolt, M., and Stockner, T. (2010). Membrane-mediated effect on ion channels induced by the anesthetic drug ketamine. *J. Am. Chem. Soc.* 132, 7990–7997. doi: 10.1021/ja910843d

Josey, B. P., Heinrich, F., Silin, V., and Lösche, M. (2020). Association of model neurotransmitters with lipid bilayer membranes. *Biophys. J.* 118, 1044–1057. doi: 10.1016/j.bpj.2020.01.016

Kirsch, S. A., and Böckmann, R. A. (2019). Coupling of membrane nanodomain formation and enhanced electroporation near phase transition. *Biophys. J.* 116, 2131–2148. doi: 10.1016/j.bpj.2019.04.024

Klauda, J. B., Venable, R. M., Freites, J. A., O'Connor, J. W., Tobias, D. J., Mondragon-Ramirez, C., et al. (2010). Update of the CHARMM all-atom additive force field for lipids: validation on six lipid types. *J. Phys. Chem. B.* 114, 7830–7843. doi: 10.1021/jp101759q

Leftin, A., and Brown, M. F. (2011). An NMR database for simulations of membrane dynamics. *Biochim. Biophys. Acta* 1808, 818–839. doi: 10.1016/j.bbamem.2010.11.027

Litman, B. J., and Mitchell, D. C. (1996). A role for phospholipid polyunsaturation in modulating membrane protein function. *Lipids* 31, S193–S197.

Macpherson, J. A., and Anastasiou, D. (2017). Allosteric regulation of metabolism in cancer: endogenous mechanisms and considerations for drug design. *Curr. Opin. Biotechnol.* 48, 102–110. doi: 10.1016/j.copbio.2017.03.022

Marrink, S. J., Corradi, V., Souza, P. C. T., Ingólfsson, H. I., Tieleman, D. P., and Sansom, M. S. P. (2019). Computational modeling of realistic cell membranes. *Chem. Rev.* 119, 6184–6226. doi: 10.1021/acs.chemrev.8b00460

Mouritsen, O. G., and Bagatolli, L. A. (2015). Lipid domains in model membranes: a brief historical perspective. *Essays Biochem.* 57, 1–19. doi: 10.1042/bse0570001

Murtola, T., Róg, T., Falck, E., Karttunen, M., and Vattulainen, I. (2006). Transient ordered domains in single-component phospholipid bilayers. *Phys. Rev. Lett.* 97:238102.

Naito, A., Matsumori, N., and Ramamoorthy, A. (2018). Dynamic membrane interactions of antibacterial and antifungal biomolecules, and amyloid peptides, revealed by solid-state NMR spectroscopy. *Biochim. Biophys. Acta* 1862, 307–323. doi: 10.1016/j.bbagen.2017.06.004

Nury, H., van Renterghem, C., Weng, Y., Tran, A., Baaden, M., Dufresne, V., et al. (2011). X-ray structures of general anaesthetics bound to a pentameric ligand-gated ion channel. *Nature* 469, 428–431. doi: 10.1038/nature09647

Nyholm, T. K. M., Engberg, O., Hautala, V., Tsuchikawa, H., Lin, K. L., Murata, M., et al. (2019). Impact of acyl chain mismatch on the formation and properties of sphingomyelin-cholesterol domains. *Biophys. J.* 117, 1577–1588. doi: 10.1016/j.bpj.2019.09.025

Peters, G. H., Wang, C., Cruys-Bagger, N., Velardez, G. F., Madsen, J. J., and Westh, P. (2013). Binding of serotonin to lipid membranes. *J. Am. Chem. Soc.* 135, 2164–2171.

Petrache, H. I., Dodd, S. W., and Brown, M. F. (2000). Area per lipid and acyl length distributions in fluid phosphatidylcholines determined by ^{2}H NMR spectroscopy. *Biophys. J.* 79, 3172–3192. doi: 10.1016/s0006-3495(00)76551-9

Pike, L. J. (2006). Rafts defined: a report on the keystone symposium on lipid rafts and cell function. *J. Lipid Res.* 47, 1597–1598. doi: 10.1194/jlr.e600002-jlr200

Pluhackova, K., and Böckmann, R. A. (2015). Biomembranes in atomistic and coarse-grained simulations. *J. Phys. Condens. Matter.* 27:323103. doi: 10.1088/0953-8984/27/32/323103

Pluhackova, K., Kirsch, S. A., Han, J., Sun, L., Unruh, T., and Böckmann, R. A. (2016). A critical comparison of biomembrane force fields: structure and dynamics of model DMPC, POPC, and POPE bilayers. *J. Phys. Chem. B.* 120, 3888–3903. doi: 10.1021/acs.jpcb.6b01870

Postila, P. A., Vattulainen, I., and Róg, T. (2016). Selective effect of cell membrane on synaptic neurotransmission. *Sci. Rep.* 6:19345.

Posttila, P. A., and Róg, T. (2020). A perspective: active role of lipids in neurotransmitter dynamics. *Mol. Neurobiol.* 57, 910–925. doi: 10.1007/s12035-019-01775-7

Rosetti, C. M., Mangiarotti, A., and Wilke, N. (2017). Sizes of lipid domains: what do we know from artificial lipid membranes? What are the possible shared features with membrane rafts in cells? *Biochim. Biophys. Acta* 1859, 789–802. doi: 10.1016/j.bbamem.2017.01.030

Sandoval-Perez, A., Pluhackova, K., and Böckemann, A. (2017). Critical comparison of biomembrane force fields: protein-lipid interactions at the membrane interface. *J. Chem. Theory Comput.* 13, 2310–2321. doi: 10.1021/acs.jctc.7b00001

Sargent, D. F., and Schwyzer, R. (1986). Membrane lipid phase as catalyst for peptide-receptor interactions. *Proc. Natl. Acad. Sci. U.S.A.* 83, 5774–5778. doi: 10.1073/pnas.83.16.5774

Scheidt, H. A., and Huster, D. (2008). The interaction of small molecules with phospholipid membranes studied by ^{1}H NOESY NMR under magic-angle spinning. *Acta Pharmacol. Sin.* 29, 35–49. doi: 10.1111/j.1745-7254.2008.00726.x

Scheidt, H. A., Meyer, T., Nikolaus, J., Baek, D. J., Haralampiev, I., Thomas, L., et al. (2013). Cholesterol's aliphatic side chain structure modulates membrane properties. *Angew. Chem. Int. Ed.* 52, 12848–12851. doi: 10.1002/anie.201306753

Scheidt, H. A., Pampel, A., Nissler, L., Gebhardt, R., and Huster, D. (2004). Investigation of the membrane localization and distribution of flavonoids by high-resolution magic angle spinning NMR spectroscopy. *Biochim. Biophys. Acta* 1663, 97–107. doi: 10.1016/j.bbamem.2004.02.004

Scott, D. E., Bayly, A. R., Abell, C., and Skidmore, J. (2016). Small molecules, big targets: drug discovery faces the protein-protein interaction challenge. *Nat. Rev. Drug Discov.* 15, 533–550. doi: 10.1038/nrd.2016.29

Shaikh, S. R., Kinnun, J. J., Leng, X., Williams, J. A., and Wassall, S. R. (2015). How polyunsaturated fatty acids modify molecular organization in membranes: insight from NMR studies of model systems. *Biochim. Biophys. Acta* 1848, 211–219. doi: 10.1016/j.bbamem.2014.04.020

Siarheyeva, A., Lopez, J. J., and Glaubitz, C. (2006). Localization of multidrug transporter substrates within model membranes. *Biochemistry* 45, 6203–6211. doi: 10.1021/bi0524870

Sodt, A. J., Sandar, M. L., Gawrisch, K., Pastor, R. W., and Lyman, E. (2014). The molecular structure of the liquid-ordered phase of lipid bilayers. *J. Am. Chem. Soc.* 136, 725–732. doi: 10.1021/ja4105667

Soni, S. P., Ward, J. A., Sen, S. E., Feller, S. E., and Wassall, S. R. (2009). Effect of trans unsaturation on molecular organization in a phospholipid membrane. *Biochemistry* 48, 11097–11107. doi: 10.1021/bi901179r

Soubias, O., and Gawrisch, K. (2012). The role of the lipid matrix for structure and function of the GPCR rhodopsin. *Biochim. Biophys. Acta* 1818, 234–240. doi: 10.1016/j.bbamem.2011.08.034

Soubias, O., Niu, S. L., Mitchell, D. C., and Gawrisch, K. (2008). Lipid-rhodopsin hydrophobic mismatch alters rhodopsin helical content. *J. Am. Chem. Soc.* 130, 12465–12471. doi: 10.1021/ja803599x

Stahlberg, S., Skolova, B., Madhu, P. K., Vogel, A., Vavrova, K., and Huster, D. (2015). Probing the role of the ceramide acyl chain length and sphingosine unsaturation in model skin barrier lipid mixtures by 2H solid-state NMR spectroscopy. *Langmuir* 31, 4906–4915. doi: 10.1021/acs.langmuir.5b00751

Stockwell, B. R. (2004). Exploring biology with small organic molecules. *Nature* 432, 846–854. doi: 10.1038/nature03196

Sullan, R. M. A., Shi, W., Chan, H., Li, J. K., and Walker, G. C. (2013). Mechanical stability of phase-segregated multicomponent lipid bilayers enhanced by PS-*b*-PEO diblock copolymers. *Soft Matter* 9, 6245–6253. doi: 10.1039/c3sm50855b

Thomas, L., Kahr, J., Schmidt, P., Krug, U., Scheidt, H. A., and Huster, D. (2015). The molecular dynamics of the G protein-coupled neuropeptide Y2 receptor in monounsaturated membranes investigated by solid-state NMR spectroscopy. *J. Biomol. NMR.* 61, 347–359. doi: 10.1007/s10858-014-9892-5

Tsai, W. C., and Feigenson, G. W. (2019). Lowering line tension with high cholesterol content induces a transition from macroscopic to nanoscopic phase domains in model biomembranes. *Biochim. Biophys. Acta* 1861, 478–485. doi: 10.1016/j.bbamem.2018.11.010

Tsamaloukas, A., Szadkowska, H., and Heerklotz, H. (2006). Nonideal mixing in multicomponent lipid/detergent systems. *J. Phys. Condens. Matter* 18, S1125–S1138.

Turnbulla, S., Turnbull, S., Lee, B. Y., and Leonenko, Z. (2020). The effects of melatonin, serotonin, tryptophan and NAS on the biophysical properties of DPPC monolayers. *Biochim. Biophys. Acta* 1862:183363. doi: 10.1016/j.bbamem.2020.183363

Usery, R. D., Enoki, T. A., Wickramasinghe, S. P., Weiner, M. D., Tsai, W. C., Kim, M. B., et al. (2017). Line tension controls liquid-disordered + liquid-ordered domain size transition in lipid bilayer. *Biophys. J.* 112, 1431–1443. doi: 10.1016/j.bpj.2017.02.033

Veatch, S. L., and Keller, S. L. (2003). Separation of liquid phases in giant vesicles of ternary mixtures of phospholipids and cholesterol. *Biophys. J.* 85, 3074–3083. doi: 10.1016/s0006-3495(03)74726-2

Veatch, S. L., Soubias, O., Keller, S. L., and Gawrisch, K. (2007). Critical fluctuations in domain-forming lipid mixtures. *Proc. Natl. Acad. Sci. U.S.A.* 104, 17650–17655. doi: 10.1073/pnas.0703513104

Vogel, A., Reuther, G., Weise, K., Triola, G., Nikolaus, J., Tan, K. T., et al. (2009). The lipid modifications of Ras that sense membrane environments and induce local enrichment. *Angew. Chem. Int. Ed.* 48, 8784–8787. doi: 10.1002/anie.200903396

Vogel, A., Scheidt, H. A., Baek, D. J., Bittman, R., and Huster, D. (2016). Structure and dynamics of the aliphatic cholesterol side chain in membranes as studied by (2)H NMR spectroscopy and molecular dynamics simulation. *Phys. Chem. Chem. Phys.* 18, 3730–3738. doi: 10.1039/c5cp05084g

Vogel, A., Scheidt, H. A., Feller, S. E., Metso, J., Badeau, R. M., Tikkanen, M. J., et al. (2014). The orientation and dynamics of estradiol and estradiol oleate in lipid membranes and HDL disc models. *Biophys. J.* 107, 114–125. doi: 10.1016/j.bpj.2014.04.060

Weis, W. I., and Kobilka, B. K. (2018). The molecular basis of G protein-coupled receptor activation. *Annu. Rev. Biochem.* 87, 897–919. doi: 10.1146/annurev-biochem-060614-033910

Weizenmann, N., Huster, D., and Scheidt, H. A. (2012). Interaction of local anesthetics with lipid bilayers investigated by ^{1}H MAS NMR spectroscopy. *Biochim. Biophys. Acta* 1818, 3010–3018. doi: 10.1016/j.bbamem.2012.07.014

Yankova, T. S., Bobrovsky, A. Y., and Vorobiev, A. K. (2012). Order parameters <P2>, <P4>, and <P6> of aligned nematic liquid-crystalline polymer as determined by numerical simulation of electron paramagnetic resonance spectra. *J. Phys. Chem. B.* 116, 6010–6016. doi: 10.1021/jp301170b

Yasuda, T., Tsuchikawa, H., Murata, M., and Matsumori, N. (2015). Deuterium NMR of raft model membranes reveals domain-specific order profiles and compositional distribution. *Biophys. J.* 108, 2502–2506. doi: 10.1016/j.bpj.2015.04.008

Yau, W. M., Wimley, W. C., Gawrisch, K., and White, S. H. (1998). The preference of tryptophan for membrane interfaces. *Biochemistry* 37, 14713–14718. doi: 10.1021/bi980809c

Conflict of Interest: The authors declare that the research was conducted in the absence of any commercial or financial relationships that could be construed as a potential conflict of interest.

frontiers in Cell and Developmental Biology

ORIGINAL RESEARCH
published: 26 October 2020
doi: 10.3389/fcell.2020.579388

Lipid Dynamics in Membranes Slowed Down by Transmembrane Proteins

Lisa Ebersberger[1], *Torben Schindler*[1], *Sonja A. Kirsch*[2], *Kristyna Pluhackova*[2], *Alexandra Schambony*[3], *Tilo Seydel*[4], *Rainer A. Böckmann*[2] *and Tobias Unruh*[1,5]*

[1] Physics Department, Institute for Crystallography and Structural Physics, Friedrich-Alexander-Universität Erlangen-Nürnberg, Erlangen, Germany, [2] Computational Biology, Department Biology, Friedrich-Alexander-Universität Erlangen-Nürnberg, Erlangen, Germany, [3] Department Biology, Chair of Developmental Biology, Friedrich-Alexander-Universität Erlangen-Nürnberg, Erlangen, Germany, [4] Science Division, Institut Laue-Langevin, Grenoble, France, [5] Physics Department, Center for Nanoanalysis and Electron Microscopy (CENEM) and Interdisciplinary Center for Nanostructured Films (IZNF), Friedrich-Alexander-Universität Erlangen-Nürnberg, Erlangen, Germany

Lipids and proteins, as essential components of biological cell membranes, exhibit a significant degree of freedom for different kinds of motions including lateral long-range mobility. Due to their interactions, they not only preserve the cellular membrane but also contribute to many important cellular functions as e.g., signal transport or molecular exchange of the cell with its surrounding. Many of these processes take place on a short time (up to some nanoseconds) and length scale (up to some nanometers) which is perfectly accessible by quasielastic neutron scattering (QENS) experiments and molecular dynamics (MD) simulations. In order to probe the influence of a peptide, a transmembrane sequence of the transferrin receptor (TFRC) protein, on the dynamics of 1,2-dimyristoyl-*sn*-glycero-3-phosphocholine (DMPC) large unilamellar vesicles (LUVs) on a nanosecond time scale, high-resolution QENS experiments and complementary MD simulations have been utilized. By using different scattering contrasts in the experiment (chain-deuterated lipids and protonated lipids, respectively), a model could be developed which allows to examine the lipid and peptide dynamics separately. The experimental results revealed a restricted lipid lateral mobility in the presence of the TFRC transmembrane peptides. Also the apparent self-diffusion coefficient of the lateral movement of the peptide molecules could be determined quantitatively for the probed short-time regime. The findings could be confirmed very precisely by MD simulations. Furthermore, the article presents an estimation for the radius of influence of the peptides on the lipid long-range dynamics which could be determined by consistently combining results from experiment and simulation.

Keywords: quasielastic neutron scattering, lipid dynamics, protein dynamics, lipid-protein interactions, MD simulations, membrane domains

OPEN ACCESS

Edited by:
Brian Storrie, University of Arkansas for Medical Sciences, United States

Reviewed by:
Judith Peters, Université Grenoble Alpes, France
Thomas Hellweg, Bielefeld University, Germany

***Correspondence:**
Tobias Unruh
tobias.unruh@fau.de

Specialty section:
This article was submitted to Membrane Traffic, a section of the journal Frontiers in Cell and Developmental Biology

Received: *02 July 2020*
Accepted: *22 September 2020*
Published: *26 October 2020*

Citation:
Ebersberger L, Schindler T, Kirsch SA, Pluhackova K, Schambony A, Seydel T, Böckmann RA and Unruh T (2020) Lipid Dynamics in Membranes Slowed Down by Transmembrane Proteins. Front. Cell Dev. Biol. 8:579388. doi: 10.3389/fcell.2020.579388

1. INTRODUCTION

The interactions between lipids and proteins in biological membranes play an important role in e.g., cellular signal transport as well as the exchange of molecules or ions between the cell and the cellular environment. A lateral long-range mobility of these membrane components is an essential precondition for many cellular functions, which are initialized by dimerization, formation of

lipid-protein-complexes and membrane rafts (Hirsch-Kauffmann et al., 2009). Thereby, membrane dynamics cover a large range of length and time scales. Many biological relevant processes take place on the nanometer length scale (Ramadurai et al., 2009; Busch et al., 2010) and at short times of a few nanoseconds. Consequently, it is not surprising that the complementary methods, quasielastic neutron scattering (QENS) experiments and molecular dynamics (MD) simulations, which cover these short time (from picoseconds up to several nanoseconds) and length (from Ångstrøm up to nanometers) scales, are perfectly suited to observe dynamical processes in membranes (Heller et al., 1993; Niemelä et al., 2010; Jeon et al., 2012; Pluhackova and Böckmann, 2015; Pluhackova et al., 2016b; Lautner et al., 2017; Srinivasan et al., 2019).

Early QENS studies revealed fast localized motions of lipid molecules over short distances (nanometers) and times (a few tens of picoseconds) (Tabony and Perly, 1991; König et al., 1992). These motions differ significantly from the slower long-range diffusion observed by macroscopic methods as e.g., fluorescence recovery after photobleaching (FRAP) (Axelrod et al., 1976; Almeida et al., 1992) or single particle tracking (SPT) (Hsieh et al., 2014). In order to explain these discrepancies, Galla et al. (1979) assigned the concept of the free volume theory (Cohen and Turnbull, 1959; Turnbull and Cohen, 1961, 1970) which originates from glass physics to membranes. They assumed to observe a shaking of lipid molecules in their cage of neighboring lipid molecules in the short-time regime of QENS measurements. The first step of a long-range diffusive motion was thereby explained by the hopping of a lipid molecule out of its cage position between the nearest lipid neighbors into a neighbored vacancy created by thermal heterogeneities (Vaz and Almeida, 1991; Almeida et al., 1992). For many years this so-called free volume theory was able to successfully explain the discrepancies between the diffusion coefficients measured by microscopic and macroscopic methods, respectively. Doubts about the simple mechanistic interpretation of the free volume theory aroused, when realizing by MD simulations and experimental studies that molecular jumps into vacancies could not be observed and neighbored lipid molecules perform highly correlated motions over distances up to the nanometer range (Ayton and Voth, 2004; Gambin et al., 2006; Rheinstädter et al., 2008; Roark and Feller, 2009; Busch, 2012).

In this respect, a new approach to explain the differences between short and long-term dynamics of membrane components was provided by MD simulations. Falck et al. (2008) used atomistic MD simulations of 1,2-dipalmitoyl-*sn*-glycero-3-phosphocholine (DPPC) bilayers in the liquid-crystalline phase and examined the movements of individual lipids in the bilayer, as well as the movements of their neighboring lipid molecules, as a function of time. It was observed, that always when an individual lipid molecule moves very fast into a certain direction its neighboring molecules move essentially into the same direction leading to lipid clusters drifting into the same direction for a certain time. These clusters form, persist for a short time [up to nanoseconds (Falck et al., 2008; Busch et al., 2010)], disintegrate, and randomly rearrange to show up somewhere else again. The resulting movement is referred to as collective flow-like motions of the lipid molecules in a membrane.

Such flow-like lipid motions could also be detected by QENS experiments. Busch et al. (2010); Busch (2012) studied pure multilamellar 1,2-dimyristoyl-*sn*-glycero-3-phosphocholine (DMPC) phospholipid membranes in the liquid-crystalline phase by using various instrumental time resolutions and thus observation times (on the pico to nanosecond time scale). The experiment revealed that the experimentally determined flow velocities match those from the simulation (Busch, 2012). The influence of small molecules as additives and the shape of the phospholipid layer (lamellar, vesicular, monolayers) on the lipid short-time dynamics has also been studied (Busch and Unruh, 2011a; Busch et al., 2012; Pluhackova et al., 2015). At short observation times the collective flow-like motions of the membrane lipids resemble the atomic and molecular movements in liquids (Kegel and van Blaaderen, 2000; Angelini et al., 2011; Cisneros et al., 2011; Zhang et al., 2011; Morhenn et al., 2012, 2013).

Furthermore, Armstrong et al. (2010, 2011) used QENS to study the pico- to nanosecond dynamics of DMPC lipid molecules in D_2O-hydrated single as well as multilamellar lipid bilayers on silicon wafers. Thereby, a large length scale from 1.3 Å up to 22 Å was covered, which corresponds to about 3 lipid to lipid distances. Their results indicated a continuous diffusion of the lipid molecules, which changed at distances, shorter than the nearest neighbor distance (< 2.37 Å), into short-range flow-like ballistic motions.

While lipid dynamics in membranes is fairly well-understood, the short-time motions of proteins and peptides, respectively, also their influence on lipid dynamics are still unclear despite their relevance for initiating cellular processes. On one hand, various neutron scattering studies are published about antimicrobial peptides as e.g., the bee venom melittin (Sharma et al., 2015, 2016a; Buck et al., 2018) or the so-called Alzheimer peptide amyloid-β (Buchsteiner et al., 2010, 2012; Barrett et al., 2016; Rai et al., 2016) as well as about amyloid fibrils of α-Synuclein (Fujiwara et al., 2019) (Parkinson's disease), which all three tend to damage cell membranes. On the other hand very little is known about the short-time transmembrane dynamics of proteins and peptides in membranes. Niemelä et al. (2010) used MD simulations to study the dynamics of a single Kv1.2 protein embedded in a 1-palmitoyl-2-oleoyl-*sn*-glycero-3-phosphocholine (POPC) lipid bilayer in the liquid-crystalline phase. They observed a kind of transient complex formed by the protein and its neighboring lipids which diffuses laterally in the plane of the membrane. The direct neighboring lipids move together with the protein but are not directly bound to the protein. Diffusion coefficients could be determined for the direct neighboring lipids ($D \approx 0.6 \cdot 10^{-8}$ cm^2/s), the other lipids ($D \approx 9 \cdot 10^{-8}$ cm^2/s) and the protein itself ($D \approx 0.3 \cdot 10^{-8}$ cm^2/s). In the simulation, the protein significantly influenced the dynamics of the surrounding lipids at a distance of about 1–2 nm around the protein. But proteins do not only influence lipid dynamics in their vicinity, they also influence the dynamics of proteins in their neighborhood. MD simulations of a transmembrane receptor CXCR4 have

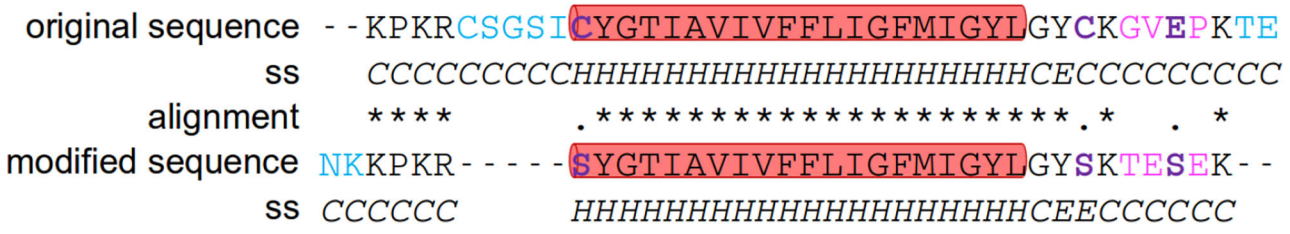

FIGURE 1 | Transferrin transmembrane sequence. Comparison and alignment of the original and the here utilized sequences of the transferrin peptide as well as the prediction of their secondary structure. Sequence alignment was done on the ExPASy webpage using the tool SIM (Miller and Huang, 1991). In order to guide the eye the insertions or deletions are colored blue, substitutions for unsimilar residues are colored magenta and substitutions for similar residues in purpleblue and highlighted in bold. The secondary structure of the peptides was determined using PEP2D (http://crdd.osdd.net/raghava/pep2d/index.html). The part of the peptide predicted to be helical was highlighted by a red background.

shown that while individual proteins slow down lipids they speed up the dynamics of surrounding proteins prior their dimerization. The fact that this fastening was most significant at low cholesterol concentrations indicate a fascinating complexity in the mutual influence of membrane components on their dynamic properties (Pluhackova et al., 2016b).

In this contribution we present a combined QENS experiment and MD simulation study of the influence of a peptide, more precisely a transmembrane sequence of the transferrin receptor (TFRC) protein, on the dynamics of DMPC lipids in large unilamellar vesicles (LUVs) in the liquid crystalline phase. TFRC plays an important role in the transport of iron into the cell (Moos and Morgan, 2000) as well as in the regulation of the cell iron balance (Gatter et al., 1983; Ponka and Lok, 1999). The receptors, coupled with apotransferrin, accumulate in special membrane areas and can deliver the iron ions to the cell by receptor-mediated endocytosis (Harding et al., 1983). To enable protein accumulation in certain membrane areas, the proteins must be mobile in the lateral plane of the membrane. In order to observe the protein dynamics, vesicles with chain-deuterated DMPC-d54 were studied by QENS in addition to the DMPC lipid vesicles both with and without 6 mol % of the TFRC peptide. This allowed the experimental determination of the lateral self-diffusion coefficient of lipid molecules in absence and presence of the TFRC peptides but also the calculation of the self-diffusion coefficient of the TFRC peptides. Finally, we introduce an estimation of the radius of the peptide influence on the lipid dynamics. Our experimental results of TFRC in DMPC membranes coincide with the findings of Kv1.2 protein embedded in POPC by MD simulations supporting the formation of transient complexes formed by the proteins and its neighboring lipids (Niemelä et al., 2010).

2. MATERIALS AND METHODS

2.1. Materials

Dry DMPC (1,2-dimyristoyl-*sn*-glycero-3-phosphocholine) powder was purchased from Lipoid GmbH (≥ 98%, Ludwigshafen, Germany). Dry chain-deuterated DMPC-d54 powder was purchased from Avanti Polar Lipids, Inc (>99%, Alabama, United States). The transmembrane sequence of the transferrin receptor (KPKRC SGSIC YGTIAVIVFFLIGFMIGYLGY C KGVEP KTE) turned out to be highly hydrophobic and could not be purified. Thus, the C- and N-termini were slightly modified (NKKPKRS YGTIAVIVFFLIGFMIGYLGY SKTESEK) to increase the solubility and enable purification to ≥ 85% by PSL GmbH (Heidelberg, Germany). The sequence of the transmembrane helix (TMH) was conserved except for a small replacement at its N terminus of a cysteine for a serine, which did not result in a change of the hydrophobic properties of the transmembrane helix. In **Figure 1**, both, the original and the modified sequence are displayed in order to elucidate the differences. Thereby, the total hydrophobicity of the peptide reduced from 0.653 to 0.460 [as determined by HELIQUEST (Gautier et al., 2008)] and the charge increased from +3 to +4. Charged residues, which act as membrane anchors and ensure a stable transmembrane orientation, were still present on both ends of the peptide and additionally the transmembrane domain was mostly unchanged. These conditions should ensure, that the transmembrane orientation is supposed to be preserved for the new sequence. Potentially, the aggregation behavior of the peptides could be influenced by the deletion of the patch of the polar residues (5-CSGSI-9), however, a peptide aggregation was not observed on the simulation time scale (**Figure 2** bottom). This peptide was used for the experiments reported here. Additionally, for vesicle preparation, chloroform ($CHCl_3$, ≥ 99%) from Carl Roth GmbH (Karlsruhe, Germany) and deuterated water (D_2O, ≥ 99.9%) from Euriso-Top (Saarbrücken, Germany) was utilized.

2.2. Sample Preparation

Two samples containing pure lipid vesicles (DMPC and DMPC-d54, respectively) and two analogous samples with additional 6 mol % (with respect to the lipid concentration) of the TFRC peptide sequence were prepared.

For the lipid vesicle preparation, 20 mg chloroform ($CHCl_3$) were added to 1 mg dry phospholipid powder. The solution was vortexed for at least 3 min until a macroscopically transparent liquid phase formed. The solvent was removed by using a rotary evaporator yielding a lipid film at the surface of the round bottom flask. To remove remaining traces of the solvent, the flask was evacuated for at least 12 h. Subsequently, the dry lipid film was

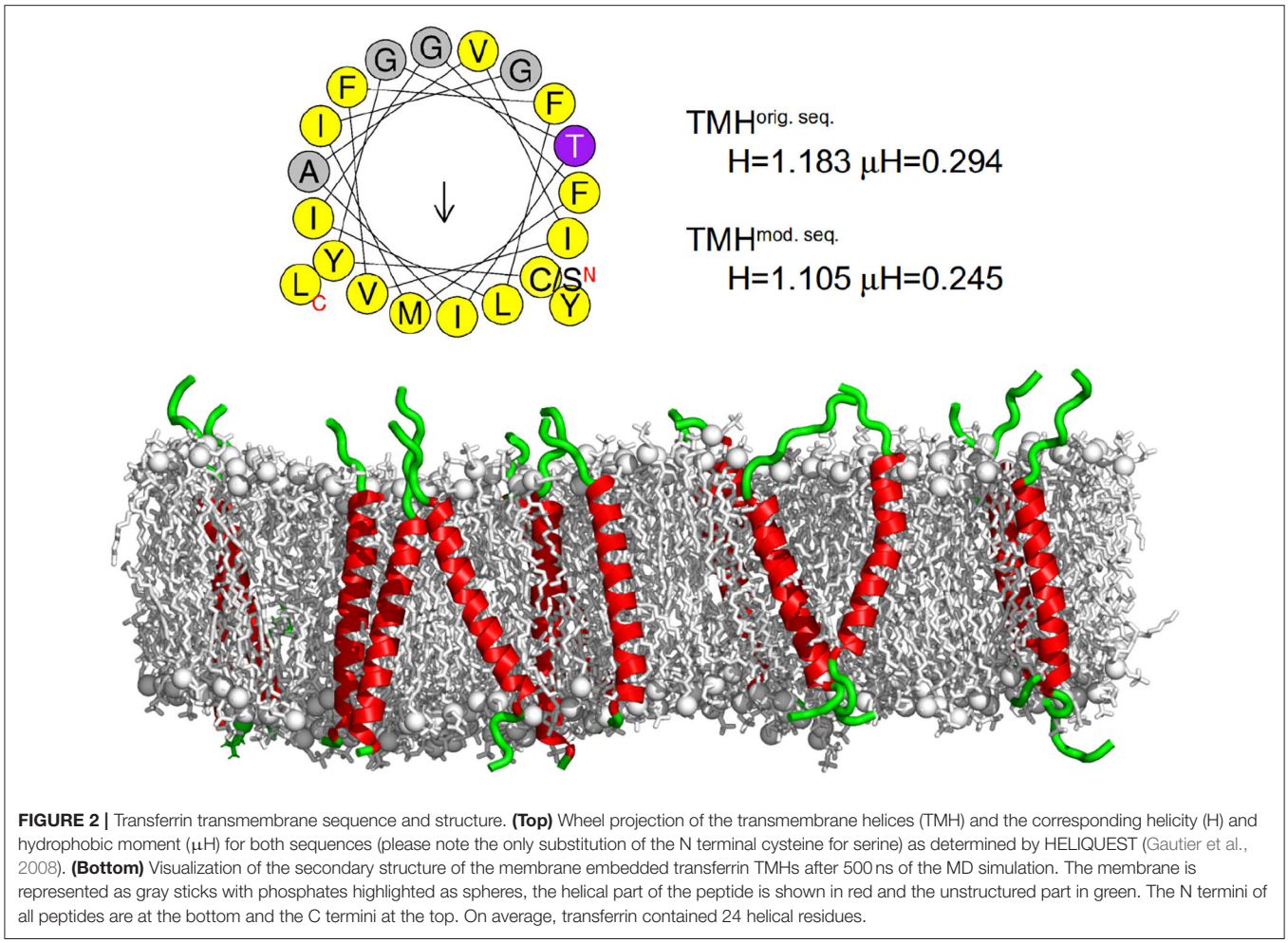

FIGURE 2 | Transferrin transmembrane sequence and structure. **(Top)** Wheel projection of the transmembrane helices (TMH) and the corresponding helicity (H) and hydrophobic moment (μH) for both sequences (please note the only substitution of the N terminal cysteine for serine) as determined by HELIQUEST (Gautier et al., 2008). **(Bottom)** Visualization of the secondary structure of the membrane embedded transferrin TMHs after 500 ns of the MD simulation. The membrane is represented as gray sticks with phosphates highlighted as spheres, the helical part of the peptide is shown in red and the unstructured part in green. The N termini of all peptides are at the bottom and the C termini at the top. On average, transferrin contained 24 helical residues.

hydrated with 90 wt % D_2O relative to the lipid weight at T = 40 °C and vortexed for 3 min. The lipid-water-mixture was stored in a hot cabinet at 40°C for 2 h to enable swelling of the lipid. Finally, three freeze-thaw cycles were performed by alternately storing the sample for 10 min at −20°C in a fridge and for 15 min at 50°C in the hot cabinet.

LUVs were produced by 21 repeated extrusion cycles using an extruder from Avestin Europe GmbH (Mannheim, Germany) and 1 ml syringes from Hamilton Germany GmbH (Gräfelfing, Germany). During the extrusion process, the extruder was placed on a heating plate (at 50°C) to ensure that the temperature of the lipid-water-mixture remains above the gel/fluid phase transition temperature. For the extrusion a filter with a pore diameter of 100 nm was used yielding LUVs with diameters of about 120 nm (determined by photon correlation spectroscopy, PCS). For preparing lipid-peptide vesicles, the 6 mol % of peptide relative to the lipid concentration was added as a powder to the lipid vesicle solution. The amount of 6 mol % of TFRC was chosen to guarantee a sufficient scattering contribution of the peptides and therefore enable to study not only the influence of peptides on the lipid dynamics but also the peptide dynamics itself.

2.3. Quasielastic Neutron Scattering

QENS experiments (Lautner et al., 2015) were performed at the backscattering spectrometer IN16B (Frick et al., 2010; Henning et al., 2011) at Institut Laue-Langevin (ILL) in Grenoble, France. For the experiments, an instrumental resolution (full width at half maximum) of ΔE = 0.75 μeV, an elastic wavelength of 6.271 Å [Si(111)], and a sinus Doppler velocity profile with a maximum speed of 4.55 m/s was chosen. During the measurement, the sample temperature was controlled and set to 310 K using a cryofurnace. Approximately 1 ml of sample was needed to fill the hollow cylindrical aluminum container with a gap distance of 0.2 mm. The corresponding effective sample thickness of about 0.63 mm has been demonstrated to result in experimental data with negligible multiple scattering effects (Busch and Unruh, 2011b). Each sample as well as pure D_2O and the empty can was measured for 5 h. For determination of instrument resolution and detector sensitivity, a vanadium foil with a thickness of 0.2 mm placed inside another aluminum hollow cylinder sample holder was measured for 5 h.

The raw data were treated using the program LAMP (LAMP, 2018) for summing up consecutive measurement files, normalizing to primary beam intensity, and removing defect

detector signals. For sample, vanadium, and D_2O measurements, absorption correction and subtraction of the empty can measurement were performed, respectively. The intensity of the vanadium elastic line was integrated, corrected for the Debye-Waller factor, and used for normalization of the detector sensitivities. The corrected spectra were converted to scattering functions $S(Q, \omega)$ while binning the energy transfer data to equidistant steps of 0.1 μeV. Finally, the D_2O spectrum scaled according to the amount of D_2O in the sample was subtracted from the sample data.

For data analysis the program FABADA (Pardo et al., 2011, 2014) has been used which is based on a Bayesian analysis. This program performs a convolution of a theoretical model function with the experimental instrument resolution function when fitting the parameters of the model function to the experimental data. The algorithm performed 1,000,000 cycles with an automatic adjustment of the step size every 100,000 cycles with a convergence factor of 0.66. The advantage of the Monte Carlo based approach is that the probability distribution function (PDF) of the figure of merit (here χ^2) is determined for each optimization allowing to identify the quality of two models with respect to each other.

The theoretical model function describes the molecular dynamics in pure lipid vesicles by localized slow and fast intramolecular motions and a long-range mobility (Bée, 1988; Busch et al., 2010; Busch, 2012). The long-range mobility can be either described by a Lorentzian $L(\Gamma_{\text{lipid}}, \omega)$ characterizing a diffusive lipid motion or by a Gaussian $G(\sigma_{\text{lipid}}, \omega)$ describing a flow-like motion. The fast localized motion has been found to be too fast to be distinguished from a constant contribution c to $S(Q, \omega)$ within the narrow dynamic range of the measurement whereas the slow localized motion is characterized by the Lorentzian half width at half maximum (HWHM) Γ_s. For diffusive long-range motions, the scattering function $S_{\text{diff}}(Q, \omega)$ can be modeled as

$$S_{\text{diff}}(Q,\omega) = a(Q) \cdot L(\Gamma_{\text{lipid}}, \omega) \otimes \left[A_s(Q) \cdot \delta(\omega) + (1 - A_s(Q)) \cdot L(\Gamma_s, \omega)\right] + c \ , \quad (1)$$

with delta functions $\delta(\omega)$, the Lorentzians

$$L(\Gamma_{\text{s, lipid}}, \omega) = \frac{1}{\pi} \cdot \frac{\Gamma_{\text{s, lipid}}}{\Gamma^2_{\text{s, lipid}} + \omega^2} \ , \quad (2)$$

the elastic incoherent structure factor (EISF) $A_s(Q)$ of the respective slow localized motion, and a prefactor $a(Q)$ containing the Debye-Waller factor. The EISF provides insight into the amplitude and geometry of the localized motion (Busch et al., 2010). From the HWHM $\Gamma_{\text{lipid}}(Q) = \hbar D Q^2$ the apparent self-diffusion coefficient D of the lipids can be calculated. It characterizes the lateral motion of the lipid molecules within the membrane within the observation time given by the resolution of the spectrometer.

Accordingly, for a flow-like motion, the scattering function $S_{\text{flow}}(Q, \omega)$ can be modeled as

$$S_{\text{flow}}(Q,\omega) = a(Q) \cdot G(\sigma_{\text{lipid}}, \omega) \otimes \left[A_s(Q) \cdot \delta(\omega) + (1 - A_s(Q)) \cdot L(\Gamma_s, \omega)\right] + c \ , \quad (3)$$

with the Gaussian

$$G(\sigma_{\text{lipid}}, \omega) = \frac{1}{\sigma_{\text{lipid}}\sqrt{2\pi}} \exp\left[-\frac{\omega^2}{2\sigma^2_{\text{lipid}}}\right] \ , \quad (4)$$

the standard deviation $\sigma_{\text{lipid}} = \hbar v_0 Q$, and the most probable flow velocity v_0.

For vesicles with incorporated peptides, the peptide dynamics is modeled by a fast localized motion, reflecting CH_3 group rotations and other fast internal movements and a long-range diffusive motion [Lorentzian $L(\Gamma_{\text{peptide}}, \omega)$]. It is assumed that the peptide spans both membrane leaflets which should lead to slower long-range self-diffusion compared to the lipid molecules as well as disturbing and not participating in the collective lipid molecular flows within the single lipid monolayers.

Combining the additive scattering functions of the lipid (assuming flow-like long-range motion) and peptide diffusion leads to

$$\begin{aligned} S_{\text{flow}}(Q,\omega) = {} & p \cdot b(Q) \cdot L(\Gamma_{\text{peptide}}, \omega) \otimes \left[B_s(Q) \cdot \delta(\omega) + (1 - B_s(Q)) \cdot L(\Gamma_{\text{s,peptide}}, \omega)\right] + \\ & (1-p) \cdot a(Q) \cdot G(\sigma_{\text{lipid}}, \omega) \otimes \left[A_s(Q) \cdot \delta(\omega) + (1 - A_s(Q)) \cdot L(\Gamma_{\text{s,lipid}}, \omega)\right] + c. \end{aligned} \quad (5)$$

The leading coefficients p and $(1 - p)$ represent the scattering contributions of the peptides and lipids, respectively. $B_s(Q)$ represents the EISF of the peptides and $b(Q)$ denotes a coefficient for the local peptide motion according to $a(Q)$ for the lipids. All localized internal motions that are too fast to be distinguished from a scattering contribution constant in Q are summed in constant c.

For long-range lipid diffusion one gets accordingly.

$$\begin{aligned} S_{\text{diff}}(Q,\omega) = {} & p \cdot b(Q) \cdot L(\Gamma_{\text{peptide}}, \omega) \otimes \left[B_s(Q) \cdot \delta(\omega) + (1 - B_s(Q)) \cdot L(\Gamma_{\text{s,peptide}}, \omega)\right] + \\ & (1-p) \cdot a(Q) \cdot L(\Gamma_{\text{lipid}}, \omega) \otimes \left[A_s(Q) \cdot \delta(\omega) + (1 - A_s(Q)) \cdot L(\Gamma_{\text{s,lipid}}, \omega)\right] + c. \end{aligned} \quad (6)$$

2.4. Molecular Dynamics Simulations

Molecular dynamics (MD) simulations of a DMPC phospholipid bilayer with and without 6 mol% of the TFRC transmembrane sequence, respectively, were performed using the software package GROMACS (van der Spoel et al., 2005; Pronk et al., 2013) and the CHARMM36 force field (Klauda et al., 2010; Best et al., 2012). The pure DMPC membrane was simulated for 300 ns and mixed DMPC/TRFC systems for 500 ns. The simulated box sizes amount to 15 × 15 × 9 nm (DMPC bilayers) and 15 × 15 × 8 nm (DMPC/TFRC bilayer), respectively, containing either 790 DMPC molecules (pure DMPC system) or 576 (768) DMPC molecules plus 36 (16) TFRC transmembrane peptides which corresponds to a ratio of 16 and 48 lipids per peptide molecule, respectively. The systems were equilibrated at 310 K meeting the temperatures of the corresponding QENS experiments. A

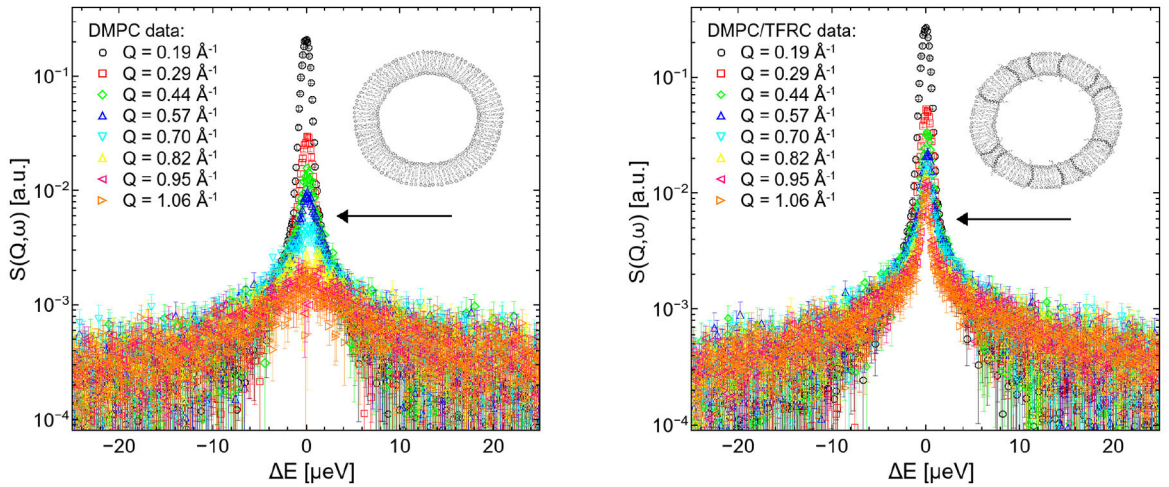

FIGURE 3 | QENS spectra of DMPC **(left)** and DMPC/TFRC **(right)** LUVs plotted for different *Q*-values.

detailed description of the parameters and simulation setups can be found in Pluhackova et al. (2016a) and Sandoval-Perez et al. (2017), respectively.

For the determination of the lipid and peptide self-diffusion coefficients, the mean square displacement (MSD) of the lipid and peptide atoms, respectively, was calculated as a function of time. To compute the MSD, the simulations were splitted into time intervals of 60ns. The linear range of the MSD vs. time curve was selected (2–5 ns) and the diffusion coefficient was determined from the slope of the corresponding linear regression line (Böckmann et al., 2003).

3. RESULTS

3.1. Lipid and Peptide Dynamics Within DMPC and DMPC-d54 LUVs

In order to study the lipid and peptide dynamics in bilayers, LUVs consisting of DMPC and chain-deuterated DMPC-d54, respectively, were measured in the fluid phase, each with and without 6 mol% of TFRC. The deuterated DMPC-d54 was chosen to reduce the scattering signal of the lipids to study the peptide dynamics. Since the peptide diffusion was expected to be rather slow, the QENS experiments were performed at the backscattering spectrometer IN16B which provides a high energy resolution ($\Delta E_{\mathrm{FWHM}} \approx 0.75\,\mu\mathrm{eV}$) corresponding to an observation time t_{obs} of about 5 ns.

QENS spectra of pure DMPC and DMPC/TFRC LUVs are visualized in **Figure 3**. Comparing the broadening of the elastic line for corresponding Q-values with the pure DMPC LUVs, it can be observed that the peptide loaded LUVs (right panel) exhibit a significantly reduced line width. This clearly indicates a slowdown of the overall molecular dynamics in the peptide loaded vesicles. The question arises whether this slowdown can be attributed solely to the slow peptide dynamics or whether the presence of the peptides also induces a reduction of the lateral dynamics of the lipid molecules.

To answer this question, it is necessary to test if the lipid long-range motions exhibit either a diffusive or a flow-like behavior on the studied time-scale. For this purpose the QENS data for pure DMPC and deuterated DMPC-d54 lipids haven been analyzed.

The left hand plot of **Figure 4** represents the QENS spectra of the measurement of pure DMPC LUVs fitted with the flow model (cf. Equation 3) for $Q = 0.29\,\mathrm{Å}^{-1}$. The best fit to the data is plotted (red line) including the individual additive components of Equation (3). Three additional spectra for $Q = 0.29\,\mathrm{Å}^{-1}$, $Q = 0.57\,\mathrm{Å}^{-1}$, and $Q = 0.95\,\mathrm{Å}^{-1}$ are displayed in the right hand panel of **Figure 4** with the corresponding best fits. The model of flow-like motions correctly describes the data over the whole observed *Q*-range. The same applies for the model of diffusive movements. The long-range lipid dynamics in DMPC LUVs can therefore be modeled by both, flow-like and diffusive motions. For a better comparison of the fit results, the respective PDFs of the two models are displayed in the **Figure 5** with the corresponding standard deviations and half-widths of the DMPC and DMPC-d54 spectra. From the PDFs it is obvious that the model of diffusive motions fits the DMPC and the DMPC-d54 data better than the flow model. For both sample systems, the maximum and the center of mass of the PDF is found for the diffusive model at smaller χ^2. From this result, it is concluded that for an observation time as short as $t_{\mathrm{obs}} \approx 5\,\mathrm{ns}$ the lipid long-range motion is described best by a diffusion process.

The results of the calculated most probable velocities as well as the apparent self-diffusion coefficients obtained from the fits to the data described above are listed in **Table 1**. From the data it can be extracted that the deuteration of the lipid chains has no influence on the long-range dynamics of the lipids molecules. This applies to both tested models, the diffusion and the flow model (Equations 1 and 3). The calculated diffusion coefficients for lipid molecules in both, pure DMPC and DMPC-d54 vesicles, amount to about $20 \cdot 10^{-8}\,\mathrm{cm}^2/\mathrm{s}$. Diffusion coefficients of nearly

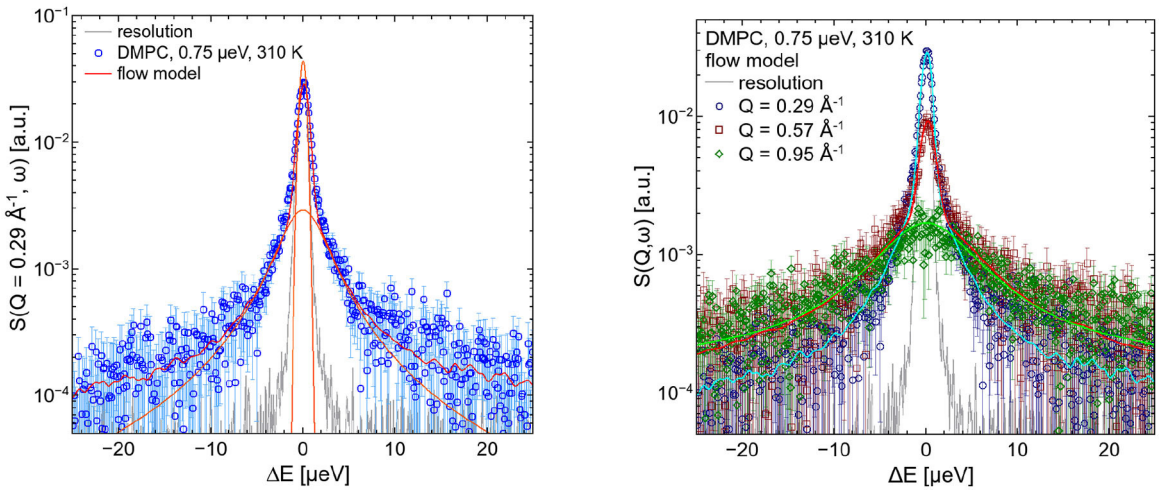

FIGURE 4 | QENS spectra of DMPC LUVs. The experimental data for $Q = 0.29\,\text{Å}^{-1}$ are plotted in the left panel as blue diamonds. The best fit of the flow model (Equation 3, red) and the corresponding additive components of the fit are visualized (orange). In the right panel, three spectra and corresponding best fits are displayed for $Q = 0.29\,\text{Å}^{-1}$, $Q = 0.57\,\text{Å}^{-1}$, and $Q = 0.95\,\text{Å}^{-1}$. The instrumental resolution is plotted in gray.

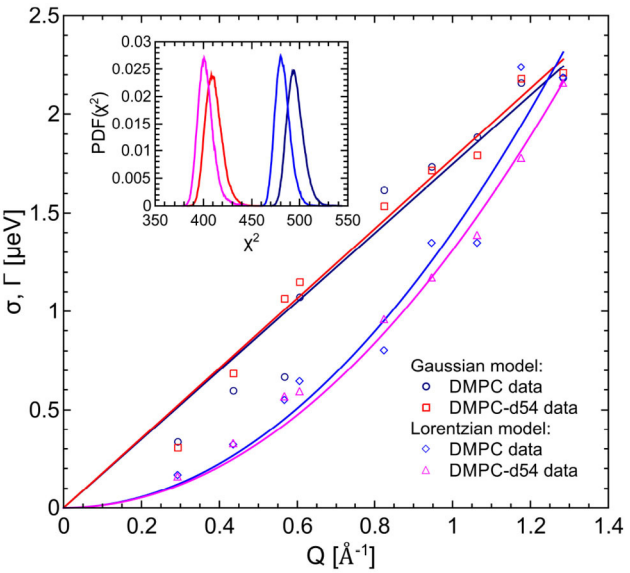

FIGURE 5 | PDFs as a function of χ^2 for the fit model of the respective DMPC (blue) and DMPC-d54 (red) data. The diffusion (Lorentzian) model better represents the long-range lipid dynamics which can be seen by the PDF maxima at smaller χ^2-values. Furthermore, the standard deviations and HWHM are plotted as functions of Q.

TABLE 1 | Results of the neutron backscattering measurements of DMPC and chain-deuterated DMPC-d54 vesicles, with and without the respective amount of 6 mol% of TFRC.

	DMPC	DMPC-d54	DMPC/TFRC	DMPC-d54/TFRC
Lipid v_0 [m/s]	0.27	0.27	0.13	0.13
TFRC D [cm^2/s]	–	–	$0.4{\cdot}10^{-8}$	$0.5{\cdot}10^{-8}$
Lipid D [cm^2/s]	$21{\cdot}10^{-8}$	$20{\cdot}10^{-8}$	$8{\cdot}10^{-8}$	$8{\cdot}10^{-8}$
TFRC D [cm^2/s]	–	–	$0.5{\cdot}10^{-8}$	$0.5{\cdot}10^{-8}$

The resulting parameters for using Equation (5) (flow model for the lipids, upper two rows) and Equation (6) (diffusion model for the lipids, lower two rows). The long range diffusion of the peptide sequence is hardly affected by neither the evaluation model nor the deuteration of the lipids.

comparable systems are found to be more than two times the value presented here. In a system of multilamellar DMPC bilayers at 303 K, measured at an instrumental resolution of about 4 μeV, the calculated diffusion coefficients for the lipid molecules was found to be $44 \cdot 10^{-8}$ cm^2/s (Busch et al., 2010). Another system of DMPC lipid vesicles at 310 K (instrumental resolution of about 3.4 μeV) indicated a diffusion coefficient of about $50 \cdot 10^{-8}$ cm^2/s (Sharma et al., 2016b). It has to be clarified, that diffusion coefficients determined by measurements at different neutron scattering instruments, and thus different instrumental resolutions, are not directly comparable. But it is known, that with decreasing instrumental resolution, and therefore increasing observation times, the diffusion coefficients tend to slow down (Barrett et al., 2016; Lautner et al., 2017). However, the reported DMPC diffusion coefficient of $20 \cdot 10^{-8}$ cm^2/s in this article is still more than two times the long-range diffusion coefficient of macroscopic measurements [e.g., FRAP $8.4 \cdot 10^{-8}$ cm^2/s (Cevc, 1993)].

For the evaluation of the QENS data of the peptide loaded LUVs the corresponding flow (Equation 5) and diffusion (subsection 2.3) models for the lipid motion have been used. For DMPC LUVs (6 mol% TFRC), the scattering contribution of the peptide with respect to the total scattering of the sample is about 20%. For the chain-deuterated DMPC-d54 LUVs, this scattering contribution amounts to almost 50%. The respective PDFs as functions of χ^2 are displayed in **Figure 6** for each model (Gaussian and Lorentzian) and for both, the DMPC/TFRC

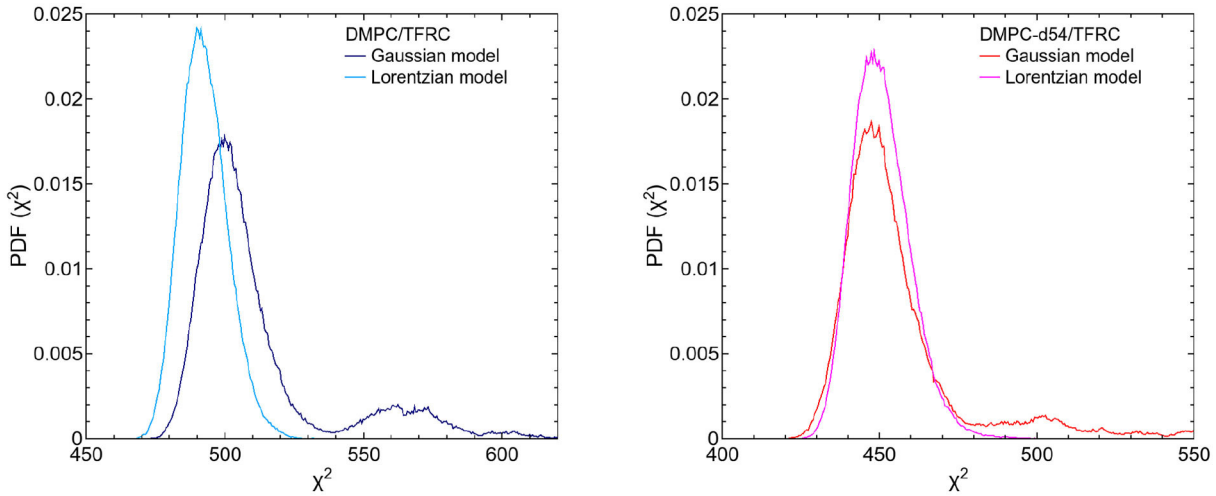

FIGURE 6 | PDFs as a function of χ^2 for both fit models (Gaussian and Lorentzian model) of the respective DMPC/TFRC (light blue/dark blue) (left figure) and DMPC-d54/TFRC (magenta/red) (right figure) data. Regarding the DMPC/TFRC data, the diffusion (Lorentzian) model, again, slightly better represents the long-range lipid dynamics compared to the flow (Gaussian) model.

data as well as the DMPC-d54/TFRC data. A careful analysis of both data sets allowed the extraction of the peptide dynamics. The DMPC/TFRC spectra are plotted for different Q-values in **Figure 7** with fitting curves for both analytical models. The σ-values of the lipid long-range flow motion resulting from the analysis of the QENS data of pure DMPC LUVs and DMPC/TFRC LUVs with the flow model are plotted as a function of Q in the left hand panel of **Figure 8**. In the right hand part of this figure the Γ-values of the lipid long-range diffusive motion acquired from the analysis with the diffusion model for the same samples are plotted as a function of Q^2. From the slopes of the respective linear regression to the data, the most probable velocities v_0 and the self-diffusion coefficients D of the lipids in the presence of peptides and the D-values for the peptides have been determined and are summarized in **Table 1**.

The results clearly indicate that the long-range lipid dynamics is more than halved in presence of TFRC peptides compared to the lipid mobility in pure lipid vesicles. The most probable velocity of lateral lipid motions slows down from 0.27 to 0.13 m/s in the presence of the peptides and the observed apparent self-diffusion coefficient decreases from $21 \cdot 10^{-8}$ to $8 \cdot 10^{-8}$ cm^2/s. Although it has been demonstrated above that the lipid diffusion model represents the data slightly better than the flow model, both pictures essentially characterize the long-range lipid motion consistently well. A reduced lipid mobility in the presence of the TFRC peptide results for both models. It is assumed that the transmembrane peptides are hindered in their diffusion not only by their larger mass compared to the lipids but also by the anchoring in both membrane leaflets. Thus, a certain amount of lipid molecules neighbored to the peptides is likely to also be hindered in their long-range mobility which leads to the decrease of their self-diffusion coefficient.

It is remarkable that no difference in the results for the DMPC and chain-interpreted DMPC-d54 dynamics could be detected (cf. **Table 1**). It is also interesting that the relatively small scattering contribution of the peptides of about 20% in the non-deuterated DMPC vesicles is already sufficient to analyze the peptide dynamics satisfactorily. The self-diffusion coefficient of the peptides could be determined and amounts to $D_{\text{peptide}} = 0.5 \cdot 10^{-8}$ cm^2/s. This value is about 40 times smaller than the self-diffusion coefficients of the lipids and supports the interpretation of the observed reduced lipid long-range mobility in presence of TFRC. The observed small value of the self-diffusion coefficient of the peptide is not only independent of the model used to describe the lipid long-range motion but also of the contrast variation by deuteration of the lipid chains. This illustrates very nicely the excellent reproducibility and reliability of the QENS measurements.

These results demonstrate for the first time, that QENS combined with an observation time of $t_0 \approx 5$ ns is capable to determine the self-diffusion coefficient of TFRC in a DMPC membrane. In comparison, the diffusion of TFRC peptides has been studied before by other methods like FRAP and SPT. Srivastava and Petersen (1998) studied the lateral diffusive motion of labeled TFRC monomers in 3T3 fibroblasts as well as in HEp2 carcinoma cells by using FRAP experiments at 298 K. The resulting TFRC diffusion coefficients in 3T3 amounts to $0.68 \pm 2.1 \cdot 10^{-8}$ cm^2/s and in HEp2 $0.29 \pm 1.3 \cdot 10^{-8}$ cm^2/s, respectively. Thereby, a free Brownian motion of the proteins can be observed in the lateral plane of the membrane as long as their mobility is not hindered by interactions with slower membrane components or immobile molecules. The diffusion coefficient of TFRC has also been determined by SPT measurements in a plasma membrane (Sako and Kusumi, 1994, 1995). A value of $\sim 10^{-9}$ cm^2/s has been reported.

In conclusion, it can be stated that the values for the self-diffusion coefficient of the TFRC peptide observed by QENS on short time scales are in the same range as those observed

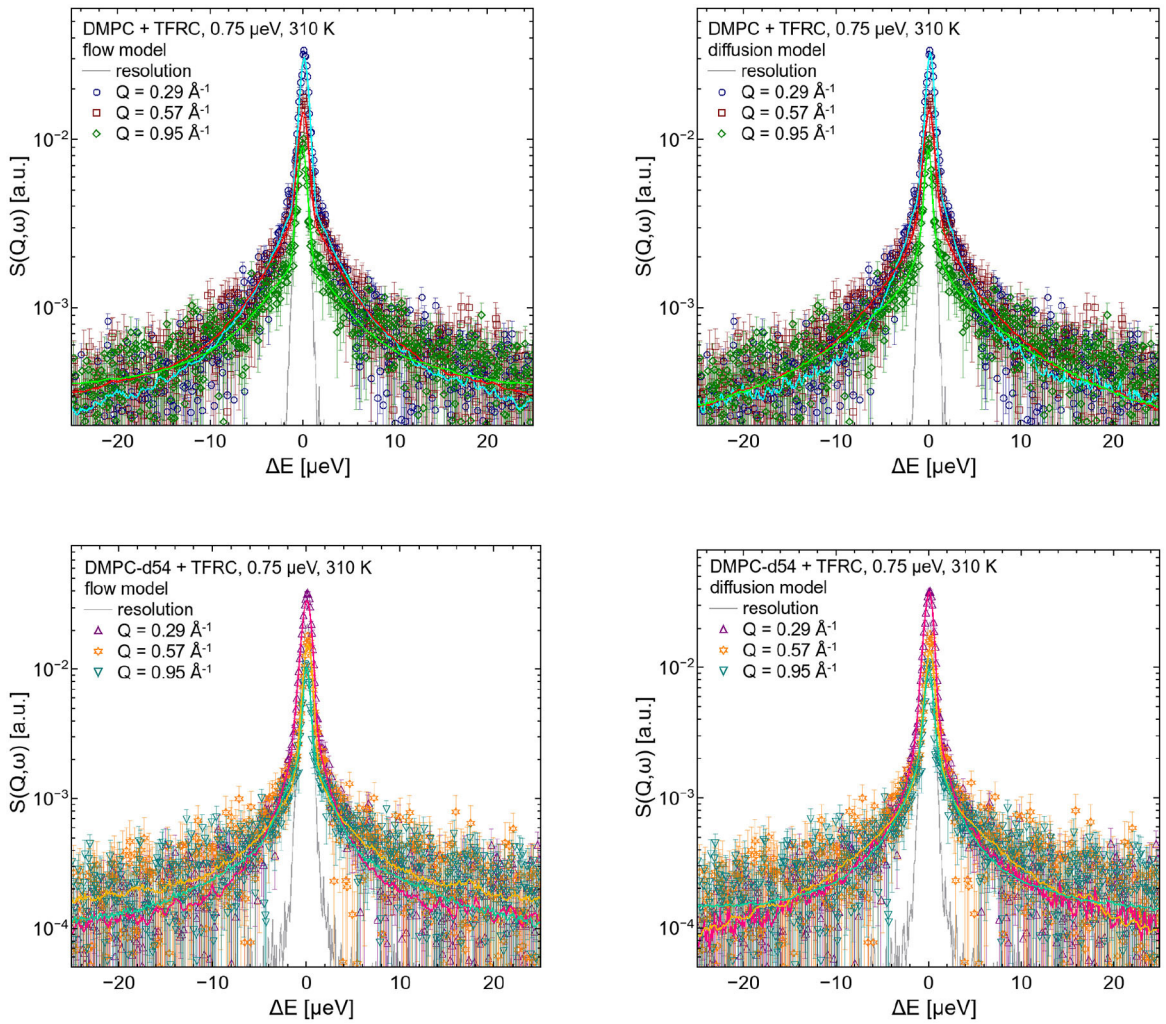

FIGURE 7 | QENS spectra of DMPC/TFRC LUV dispersions for $Q = 0.29\,\text{Å}^{-1}$, $Q = 0.57\,\text{Å}^{-1}$, and $Q = 0.95\,\text{Å}^{-1}$. In the left hand figures, the DMPC/TFRC LUV data (colored symbols) are displayed including the best fits of the flow model (colored lines, top: DMPC, bottom: DMPC-d54). In the right hand figure the same data and corresponding best fits of the diffusion model are visualized. The instrumental resolution is plotted as gray line in all panels.

by FRAP and SPT under similar conditions on extended time scales. Obviously, the long-range mobility of the peptide reaches its long-time diffusion limit already within an observation time as short as 5 ns.

3.2. Complementing the QENS Results by MD Simulations

A more detailed analysis of the QENS data can be achieved using the results of MD simulations which in turn can be validated by a comparison with QENS data. Thus, state-of-the-art MD simulations have been performed for DMPC lipid bilayers with 2, 6 mol%, and without TFRC. The self-diffusion coefficients of the DMPC lipids and the peptides have been determined. The corresponding results are listed in **Table 2**. The diffusion coefficients of the lipids are in excellent agreement with the respective QENS results. This holds for pure DMPC membranes ($D_{\text{QENS, DMPC}} = 21 \cdot 10^{-8}\,\text{cm}^2/\text{s}$) and for DMPC membranes loaded with 6 mol% TFRC ($D_{\text{QENS, DMPC, TFRC}} = 8 \cdot 10^{-8}\,\text{cm}^2/\text{s}$).

However, in the MD simulation the transmembrane peptides exhibit a significantly faster lateral diffusion than observed experimentally ($D_{\text{QENS, TFRC}} = 0.5 \cdot 10^{-8}\,\text{cm}^2/\text{s}$). The low peptide mobility observed experimentally in the peptide-dense system (6 mol% TFRC) suggests peptide-lipid domain formation as a possible reason for this discrepancy. A corresponding formation of TFRC clusters has been reported before by Srivastava and Petersen (1998). The formation of domains with large peptide concentration is unlikely to be observed in atomistic MD simulations on the submillisecond timescale. On the basis of the QENS data, such a domain formation can, however, not easily be distinguished from the more local demixing of the lipids around each peptide in the membrane as assumed by our QENS data fitting model.

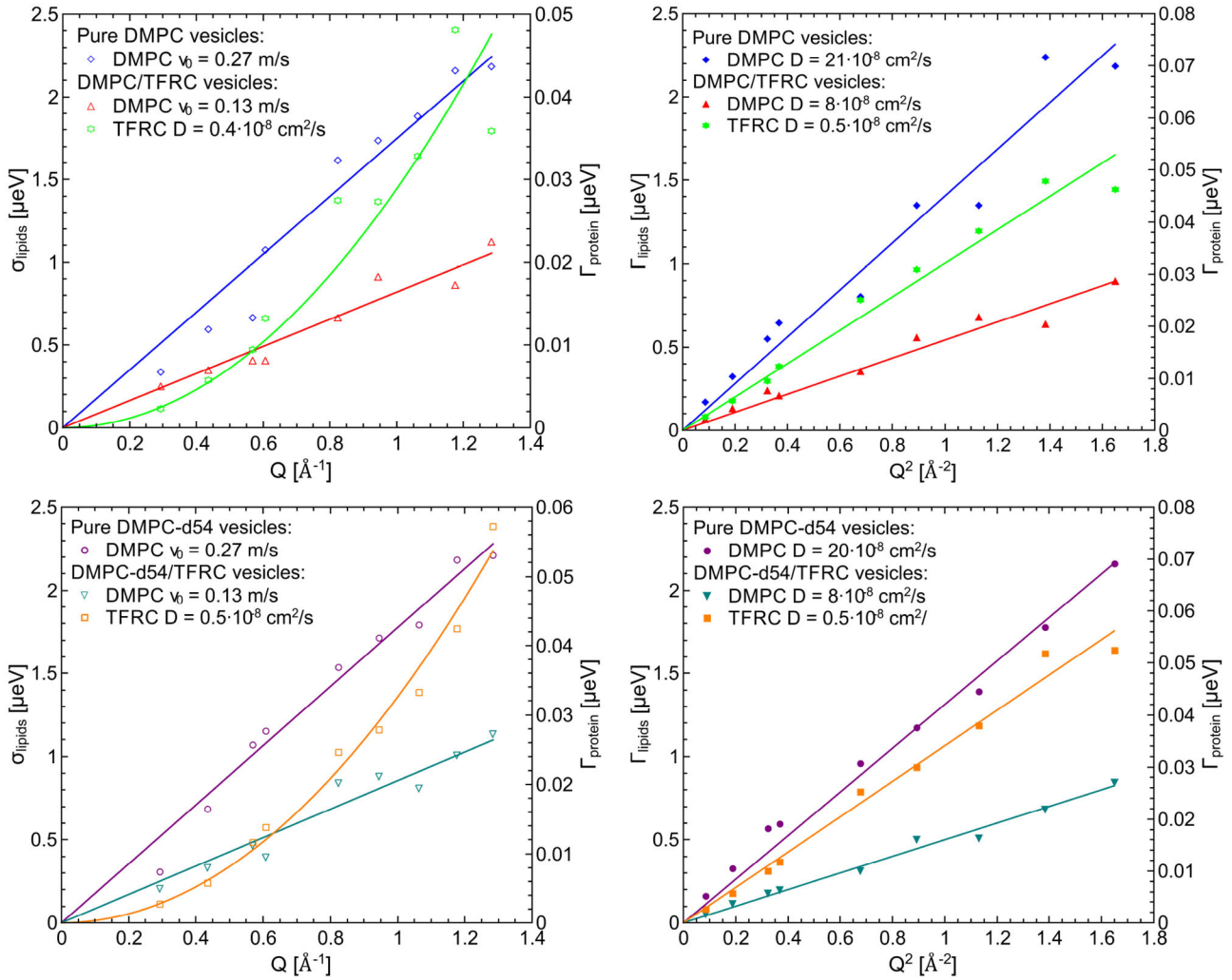

FIGURE 8 | Left figures (lipid flow model): σ-values for the lipid flow motion resulting from QENS data of pure DMPC LUVs and DMPC/TFRC LUVs (top) as well as DMPC-d54 LUVs and DMPC-d54/TFRC LUVs (bottom) and Γ-values of the diffusive motion of the TFRC peptide sequence (green and orange curves, right scale) as a function of Q, right figures (lipid diffusion model): Γ-values for the lipid and the peptide, respectively, of the same samples as a function of Q^2.

TABLE 2 | Lateral molecular self-diffusion coefficients of DMPC and TFRC derived from MD simulations of DMPC lipid membranes with 2, 6 mol%, and without TFRC, respectively.

	Pure DMPC	DMPC with 2 mol% TFRC		DMPC with 6 mol% TFRC	
		DMPC	TFRC	DMPC	TFRC
D [cm^2/s]	$18.95 \cdot 10^{-8}$ $\pm 0.09 \cdot 10^{-8}$	$13.30 \cdot 10^{-8}$ $\pm 0.06 \cdot 10^{-8}$	$6.02 \cdot 10^{-8}$ $\pm 0.15 \cdot 10^{-8}$	$7.89 \cdot 10^{-8}$ $\pm 0.04 \cdot 10^{-8}$	$3.98 \cdot 10^{-8}$ $\pm 0.07 \cdot 10^{-8}$

3.3. Lipid-Peptide Interaction Length

The self-diffusion coefficients determined by QENS characterize the average mobility of the corresponding molecular species. To which degree is the dynamics of lipid molecules influenced by the peptide? Up to what distance does the peptide influence the lipid dynamics? In order to estimate this averaged interaction radius of the peptide influence on the lipid dynamics, the flow model represented by Equation (5) has been extended by replacing the scattering function of the lipid motions by two additional terms:

$$\begin{aligned} S_{\text{flow}}(Q,\omega) = {} & p \cdot b(Q) \cdot L(\Gamma_{\text{peptide}},\omega) \otimes \left[B_{\text{s}}(Q) \cdot \delta(\omega) \right. \\ & \left. + (1 - B_{\text{s}}(Q)) \cdot L(\Gamma_{\text{s,peptide}},\omega)\right] + \\ & (1-p) \cdot l \cdot a(Q) \cdot G(\sigma_{\text{lipid},1},\omega) \otimes \left[A_{\text{s}}(Q) \cdot \delta(\omega) \right. \\ & \left. + (1 - A_{\text{s}}(Q)) \cdot L(\Gamma_{\text{s,lipid}},\omega)\right] + \\ & (1-p) \cdot (1-l) \cdot a(Q) \cdot G(\sigma_{\text{lipid},2},\omega) \otimes \left[A_{\text{s}}(Q) \cdot \delta(\omega) \right. \\ & \left. + (1 - A_{\text{s}}(Q)) \cdot L(\Gamma_{\text{s,lipid}},\omega)\right] + c\,. \end{aligned} \tag{7}$$

The first of these additive terms (second term in Equation 7) describes the proportion l of non-interacting lipids. The parameters of this term are adopted from the fits to the QENS

data of pure DMPC vesicles. The second term represents the proportion $(1 - l)$ of lipids with dynamics slowed down by interaction with the peptide. The parameters describing the peptide dynamics within this term were fixed to the values of the previous results. A fit to the data allows to determine the proportion l of the affected lipids and their average velocity v_0 by using $\sigma_{\mathrm{lip},2} = \hbar v_0 Q$. The diffusion model (subsection 2.3) can be extended analogously by replacing the Gaussians $G(\sigma_{\mathrm{lipid},1}, \omega)$ and $G(\sigma_{\mathrm{lipid},2}, \omega)$ in Equation (7) by the corresponding Lorentzians $L(\Gamma_{\mathrm{lipid},1}, \omega)$ and $L(\Gamma_{\mathrm{lipid},2}, \omega)$. In order to calculate a lipid-peptide interaction length, both, the Gaussian and the Lorentzian model for the lipid dynamics were tested. In both analysis, the protein dynamics were described by the Lorentzian model. The corresponding PDFs of the fits are displayed as a function of χ^2 in **Figure 9**.

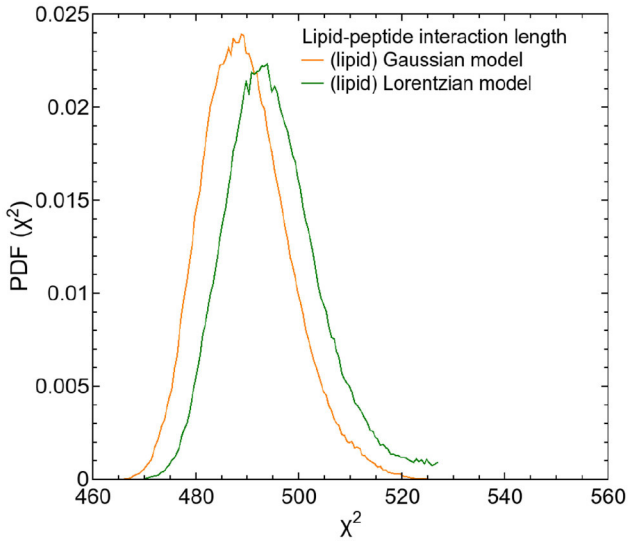

FIGURE 9 | PDFs as a function of χ^2 for both fit models of the respective DMPC/TFRC data. The PDF of the fit of the Gaussian model is displayed in orange, the one of the Lorentzian model is displayed in green.

The extended models can nicely be fitted to the QENS data. The results of both tested models indicate that the dynamics of about 80% of the lipids are influenced by the peptides and exhibit a reduced lateral long-range dynamics. Assuming an effective area $A_{\mathrm{DMPC}} \approx 60\,\text{Å}^2$ of a DMPC molecule and an effective area $A_{\mathrm{TFRC}} \approx 66\,\text{Å}^2$ of a TFRC peptide in the membrane as calculated from our MD atomistic structures, an average peptide-lipid interaction radius between 1 and 1.5 nm around the peptide can be estimated. Based on this knowledge, the peptide-lipid interaction length has been visualized by a schematic representation of a single lipid layer in top view in **Figure 10**. In the scheme it becomes obvious that the dynamics of nearest lipid neighbors of a peptide but also some second next neighbors are influenced by the peptide. Beyond that, at the relatively high peptide concentration of 6 mol% most of the lipids are within the peptide-lipid interaction radius of about 1.5 nm (cf. **Figure 11A**).

In order to further quantify the interaction radius of TFRC, an additional 500 ns atomistic MD simulation of a DMPC/TFRC system has been performed at a reduced TFRC density of 2 mol%. Despite the smaller peptide concentration, the lipid diffusion coefficient was reduced by about 30% with respect

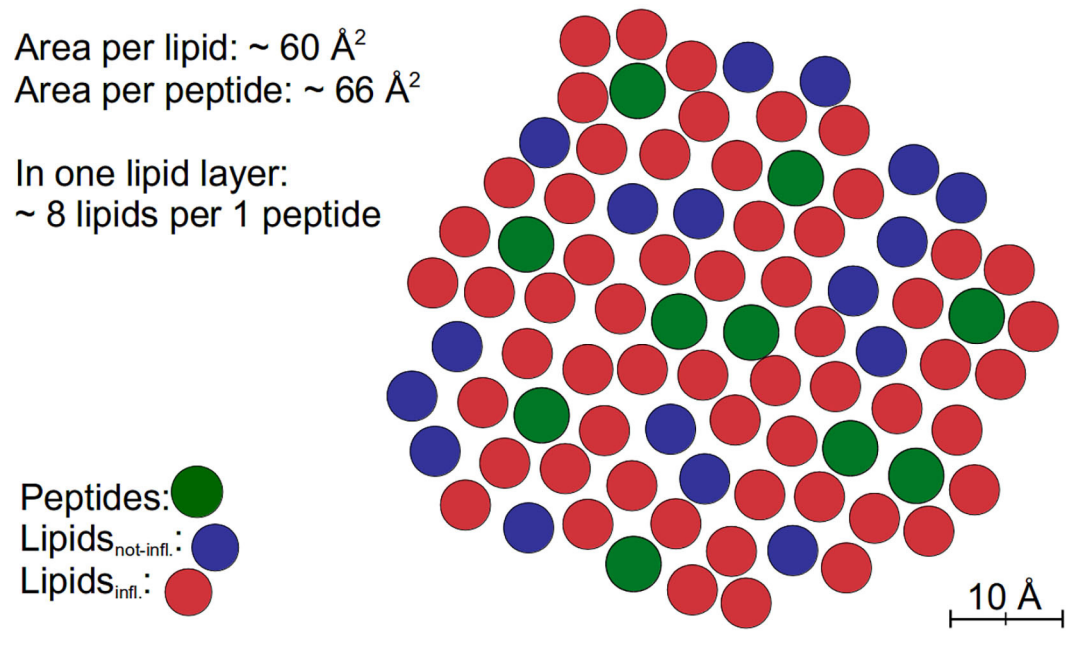

FIGURE 10 | Schematic representation of a fraction of a lipid layer with peptides in top view. The peptides are colored green, the lipids interacting with the peptides ($\mathrm{Lipids_{infl.}}$) are labeled red, and other lipids ($\mathrm{Lipids_{not\text{-}infl.}}$) are labeled blue.

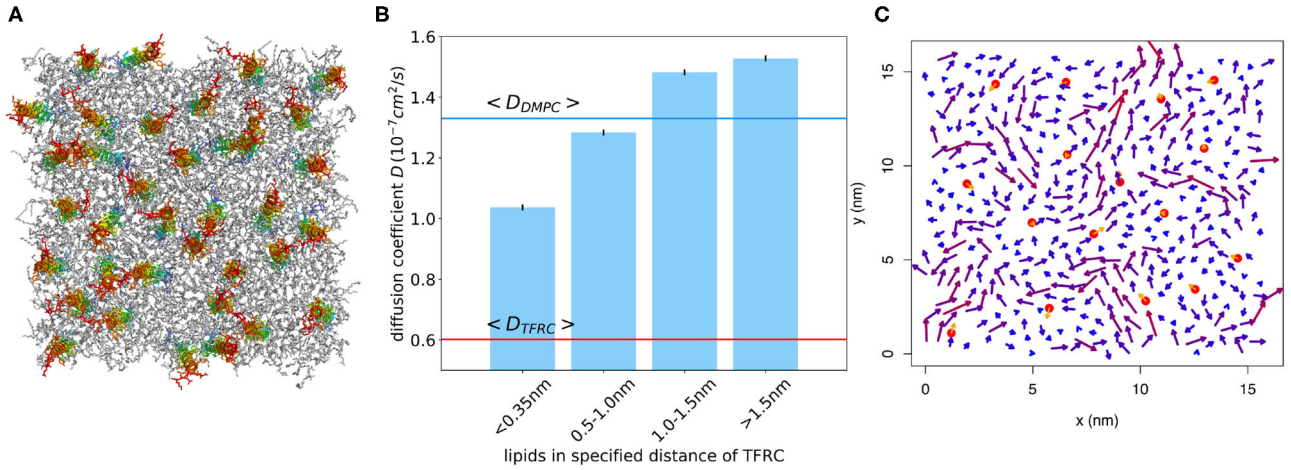

FIGURE 11 | (A) Snapshot of atomistic MD simulation of a DMPC/TFRC system at 6 mol% TFRC after 500 ns equilibration (lipids in gray, peptides colored). **(B)** Lipid diffusion coefficient for different distances from the peptide for the system at 2 mol% TFRC. The diffusion coefficient was determined from time windows of 10 ns length. For comparison, the average lipid and TFRC diffusion coefficients are displayed as blue and red horizontal lines, respectively. **(C)** The arrows represent the peptide (orange) and lipid (blueish) average molecular center of mass velocity for a selected time window of 10 ns, respectively. Lipids in the vicinity of a peptide move considerably slower on average.

to the pure DMPC (cf. **Table 2**). The mobility of the lipids in close vicinity (phosphate within distance $d < 0.35$ nm) of the peptides was found to be drastically reduced (**Figure 11B**). For short times ($t < 10$ ns) lipids within the first shells moved together with the transmembrane peptides (**Figure 11C**). Overall, the simulations confirm an interaction radius of 1–1.5 nm around transmembrane peptides. A similar interaction radius was reported before for the Kv1.2 protein (Niemelä et al., 2010).

4. CONCLUSION

QENS experiments and MD simulations have been performed to study the long-range molecular motions (covering several lipid-lipid distances) within a DMPC membrane loaded with TFRC peptides in transmembrane orientation. The results demonstrate that QENS is capable to separately explore the lipid and peptide long-range motions and to quantify both the peptide lateral self-diffusion coefficient and its influence on the lipid long-range mobility. The calculated self-diffusion coefficients for the lipids are in excellent agreement with the results of state-of-the-art MD simulations and other experimental investigations. The significantly lower diffusion coefficients for TFRC as compared to our simulations further hints to the formation of peptide-rich domains harboring also most of the lipids ($\sim$ 80%) that are characterized by slow dynamics and possibly also increased ordering. Using a consistent fitting model for the QENS data, it was possible to determine the peptide-lipid interaction length within the membrane to be about 1–1.5 nm. This finding is in perfect agreement with results from MD simulations of TFRC molecules embedded in a DMPC bilayer.

DATA AVAILABILITY STATEMENT

The raw data supporting the conclusions of this article will be made available by the authors, without undue reservation.

AUTHOR CONTRIBUTIONS

LE performed the QENS measurements, did the data analysis, and wrote the manuscript. TSc helped during the QENS experiments. SK and KP performed the MD simulations and analysis. AS contributed with help on TFRC selection, preparation, and purification. TSe supported us during the QENS measurements and provided data reduction. RB helped with MD simulation data analysis. TU supported with QENS data interpretation. RB and TU contributed to manuscript writing and organized financial support. All authors did proof reading of the manuscript.

ACKNOWLEDGMENTS

We acknowledge support by the Research Training Group 1962/1, Dynamic Interactions at Biological Membranes—from Single Molecules to Tissue, the Cluster of Excellence Engineering of Advanced Materials, and the Collaboration Research Center SFB 1027 Physical modeling of non-equilibrium processes in biological systems all funded by the Deutsche Forschungsgemeinschaft (DFG). We gratefully acknowledge the Institut Laue-Langevin (ILL) for granting beamtime and travel support, as well as the RRZE for computing time.

REFERENCES

Almeida, P. F. F., Vaz, W. L. C., and Thompson, T. E. (1992). Lateral diffusion in the liquid phases of dimyristoylphosphatidylcholine/cholesterol lipid bilayers: a free volume analysis. *Biochemistry* 31, 6739–6747. doi: 10.1021/bi00144a013

Angelini, T. E., Hannezo, E., Trepat, X., Marquez, M., Fredberg, J. J., and Weitz, D. A. (2011). Glass-like dynamics of collective cell migration. *Proc. Natl. Acad. Sci. U.S.A.* 108, 4714–4719. doi: 10.1073/pnas.1010059108

Armstrong, C. L., Kaye, M. D., Zamponi, M., Mamontov, E., Tyagi, M., Jenkins, T., et al. (2010). Diffusion in single supported lipid bilayers studied by quasi-elastic neutron scattering. *Soft Matter* 6, 5864–5867. doi: 10.1039/c0sm00637h

Armstrong, C. L., Trapp, M., Peters, J., Seydel, T., and Rheinstädter, M. C. (2011). Short range ballistic motion in fluid lipid bilayers studied by quasi-elastic neutron scattering. *Soft Matter* 7, 8358–8362. doi: 10.1039/c1sm05691c

Axelrod, D., Koppel, D. E., Schlessinger, J., Elson, E., and Webb, W. W. (1976). Mobility measurements by analysis of fluorescence photobleaching recovery kinetics. *Biophys. J.* 16, 1055–1069. doi: 10.1016/S0006-3495(76)85755-4

Ayton, G. S., and Voth, G. A. (2004). Mesoscopic lateral diffusion in lipid bilayers. *Biophys. J.* 87, 3299–3311. doi: 10.1529/biophysj.104.047811

Barrett, M. A., Trapp, M., Lohstroh, W., Seydel, T., Ollivier, J., Ballauff, M., et al. (2016). Alzheimer's peptide amyloid-β, fragment 22–40, perturbs lipid dynamics. *Soft Matter* 12, 1444–1451. doi: 10.1039/C5SM02026C

Bée, M. (1988). *Quasielastic Neutron Scattering*. Bristol: Adam Hilger IOP Publishing Ltd.

Best, R. B., Zhu, X., Shim, J., Lopes, P. E. M., Mittal, J., Feig, M., et al. (2012). Optimization of the additive CHARMM all-atom protein force field targeting improved sampling of the backbone phi, psi and side-chain chi1 and chi2 dihedral angles. *J. Chem. Theory Comput.* 8, 3257–3273. doi: 10.1021/ct300400x

Böckmann, R. A., Hac, A., Heimburg, T., and Grubmüller, H. (2003). Effect of sodium chloride on a lipid bilayer. *Biophys. J.* 85, 1647–1655. doi: 10.1016/S0006-3495(03)74594-9

Buchsteiner, A., Hauß, T., Dante, S., and Dencher, N. A. (2010). Alzheimer's disease amyloid-β peptide analogue alters the ps-dynamics of phospholipid membranes. *Biochim. Biophys. Acta* 1798, 1969–1976. doi: 10.1016/j.bbamem.2010.06.024

Buchsteiner, A., Hauß, T., and Dencher, N. A. (2012). Influence of amyloid-β peptides with different lengths and amino acid sequences on the lateral diffusion of lipids in model membranes. *Soft Matter* 8, 424–429. doi: 10.1039/C1SM06823G

Buck, Z. N., Torres, J., Miskowiec, A., Mamontov, E., Kaiser, H., Hansen, F. Y., et al. (2018). Effect of melittin on water diffusion and membrane structure in DMPC lipid bilayers. *Europhys. Lett.* 123:18002. doi: 10.1209/0295-5075/123/18002

Busch, S. (2012). *The pico- to nanosecond dynamics of phospholipid molecules* (Ph.D. thesis). München: Technische Universität München.

Busch, S., Pardo, L. C., Smuda, C., and Unruh, T. (2012). The picosecond dynamics of the phospholipid dimyristoylphosphatidylcholine in mono- and bilayers. *Soft Matter* 8, 3576–3585. doi: 10.1039/c2sm07380c

Busch, S., Smuda, C., Pardo, L. C., and Unruh, T. (2010). Molecular mechanism of long-range diffusion in phospholipid membranes studied by quasielastic neutron scattering. *J. Am. Chem. Soc.* 132, 3232–3233. doi: 10.1021/ja907581s

Busch, S., and Unruh, T. (2011a). The influence of additives on the nanoscopic dynamics of the phospholipid dimyristoylphosphatdycholine. *Biochim. Biophys. Acta* 1808, 199–208. doi: 10.1016/j.bbamem.2010.10.012

Busch, S., and Unruh, T. (2011b). The slow short-time motions of phospholipid molecules with a focus on the influence of multiple scattering and fitting artefacts. *J. Phys. Condens. Matter* 23:254205. doi: 10.1088/0953-8984/23/25/254205

Cevc, C. (1993). *Phospholipids Handbook*. London: Taylor & Francis Inc.

Cisneros, L. H., Kessler, J. O., Ganguly, S., and Goldstein, R. E. (2011). Dynamics of swimming bacteria: transition to directional order at high concentration. *Phys. Rev. E* 83:061907. doi: 10.1103/PhysRevE.83.061907

Cohen, M. H., and Turnbull, D. (1959). Molecular transport in liquids and glasses. *J. Chem. Phys.* 31, 1164–1169. doi: 10.1063/1.1730566

Falck, E., Róg, T., Karttunen, M., and Vattulainen, I. (2008). Lateral diffusion in lipid membranes through collective flows. *J. Am. Chem. Soc.* 130, 44–45. doi: 10.1021/ja7103558

Frick, B., Mamontov, E., van Eijck, L., and Seydel, T. (2010). Recent backscattering instrument developments at the ILL and SNS. *Z. Phys. Chem.* 224:33. doi: 10.1524/zpch.2010.6091

Fujiwara, S., Kono, F., Matsuo, T., Sugimoto, Y., Matsumoto, T., Narita, A., et al. (2019). Dynamic properties of human α-synuclein related to propensity to amyloid fibril formation. *J. Mol. Biol.* 431, 3229–3245. doi: 10.1016/j.jmb.2019.05.047

Galla, H.-J., Hartmann, W., Theilen, U., and Sackmann, E. (1979). On two-dimensional passive random walk in lipid bilayers and fluid pathways in biomembranes. *J. Membr. Biol.* 48, 215–236. doi: 10.1007/BF01872892

Gambin, Y., Lopez-Esparza, R., Reffay, M., Sierecki, E., Gov, N. S., Genest, M., et al. (2006). Lateral mobility of proteins in liquid membranes revisited. *Proc. Natl. Acad. Sci. U.S.A.* 103, 2098–2102. doi: 10.1073/pnas.0511026103

Gatter, K. C., Brown, G., Trowbridge, I. S., Woolston, R.-E., and Mason, D. Y. (1983). Transferrin receptors in human tissues: their distribution and possible clinical relevance. *J. Clin. Pathol.* 36, 539–545. doi: 10.1136/jcp.36.5.539

Gautier, R., Douguet, D., Antonny, B., and Drin, G. (2008). HELIQUEST: a web server to screen sequences with specific α-helical properties. *Bioinformatics* 24, 2101–2102. doi: 10.1093/bioinformatics/btn392

Harding, C., Heuser, J., and Stahl, P. (1983). Receptor-mediated endocytosis of transferrin and recycling of the transferrin receptor in rat reticulocytes. *J. Cell Biol.* 97, 329–339. doi: 10.1083/jcb.97.2.329

Heller, H., Schaefer, M., and Schulten, K. (1993). Molecular dynamics simulation of a bilayer of 200 lipids in the gel and in the liquid crystal phase. *J. Phys. Chem.* 97, 8343–8360. doi: 10.1021/j100133a034

Henning, M., Frick, B., and Seydel, T. (2011). Optimum velocity of a phase-space transformer for cold-neutron backscattering spectroscopy. *J. Appl. Cryst.* 44:467. doi: 10.1107/S0021889811013227

Hirsch-Kauffmann, M., Schweiger, M., and Schweiger, M.-R. (2009). *Biologie und molekulare Medizin für Mediziner und Naturwissenschaftler*. Stuttgart: Georg Thieme Verlag KG.

Hsieh, C.-L., Spindler, S., Ehrig, J., and Sandoghdar, V. (2014). Tracking single particles on supported lipid membranes: multimobility diffusion and nanoscopic confinement. *J. Phys. Chem. B* 118, 1545–1554. doi: 10.1021/jp412203t

Jeon, J.-H., Monne, H. M.-S., Javanainen, M., and Metzler, R. (2012). Anomalous diffusion of phospholipids and cholesterols in a lipid bilayer and its origins. *Phys. Rev. Lett.* 109:188103. doi: 10.1103/PhysRevLett.109.188103

Kegel, W. K., and van Blaaderen, A. (2000). Direct observation of dynamical heterogeneities in colloidal hard-sphere suspensions. *Science* 287, 290–293. doi: 10.1126/science.287.5451.290

Klauda, J. B., Venable, R. M., Freites, J. A., O'Connor, J. W., Tobias, D. J., Mondragon-Ramirez, C., et al. (2010). Update of the CHARMM all-atom additive force field for lipids: validation on six lipid types. *J. Phys. Chem. B* 114, 7830–7843. doi: 10.1021/jp101759q

König, S., Pfeiffer, W., Bayerl, T., Richter, D., and Sackmann, E. (1992). Molecular dynamics of lipid bilayers studied by incoherent quasi-elastic neutron scattering. *J. Phys. II* 24, 1589–1615. doi: 10.1051/jp2:1992100

LAMP (2018). *LAMP—Large Array Manipulation Program*. Available online at: https://www.ill.eu/de/users/support-labs-infrastructure/software-scientific-tools/lamp/

Lautner, L., Pluhackova, K., Barth, N. K. H., Seydel, T., Lohstroh, W., Böckmann, R. A., et al. (2017). Dynamic processes in biological membrane mimics revealed by quasielastic neutron scattering. *Chem. Phys. Lipids* 206, 28–42. doi: 10.1016/j.chemphyslip.2017.05.009

Lautner, L., Schindler, T., Seydel, T., and Unruh, T. (2015). *ENS Study of the Influence of Transmembrane Proteins on the Dynamics of Phospholipid Vesicles*. Grenoble: Institut Laue-Langevin (ILL). doi: 10.5291/ILL-DATA.9-13-598

Miller, W., and Huang, X. (1991). A time-efficient, linear-space local similarity algorithm. *Adv. Appl. Math.* 12, 337–357. doi: 10.1016/0196-8858(91)90017-D

Moos, T., and Morgan, E. H. (2000). Transferrin and transferrin receptor function in brain barrier systems. *Cell. Mol. Neurobiol.* 20, 77–95. doi: 10.1023/A:1006948027674

Morhenn, H., Busch, S., Meyer, H., Richter, D., Petry, W., and Unruh, T. (2013). Collective intermolecular motions dominate the picosecond dynamics of short polymer chains. *Phys. Rev. Lett.* 111:173003. doi: 10.1103/PhysRevLett.111.173003

Morhenn, H., Busch, S., and Unruh, T. (2012). Chain dynamics in a hexadecane melt as seen by neutron scattering and identified by molecular dynamics simulations. *J. Phys. Condens. Matter* 24:375108. doi: 10.1088/0953-8984/24/37/375108

Niemelä, P. S., Miettinen, M. S., Monticelli, L., Hammaren, H., Bjelkmar, P., Murtola, T., et al. (2010). Membrane proteins diffuse as dynamic complexes with lipids. *J. Am. Chem. Soc.* 132, 7574–7575. doi: 10.1021/ja101481b

Pardo, L. C., Rovira-Esteva, M., and Busch, S. (2014). *FABADA: Fitting Algorithm for Bayesian Analysis od DAta—Manual*. Available online at: https://gcm.upc.edu/members/luis-carlos/manual_fabada

Pardo, L. C., Rovira-Esteva, M., Busch, S., Ruiz-Martin, M., and Tamarit, J. (2011). FABADA: a Fitting Algorithm for Bayesian Analysis of DAta. *J. Phys. Conf. Ser.* 325:012006. doi: 10.1088/1742-6596/325/1/012006

Pluhackova, K., and Böckmann, R. A. (2015). Biomembranes in atomistic and coarse-grained simulations. *J. Phys. Condens. Matter* 27:323103. doi: 10.1088/0953-8984/27/32/323103

Pluhackova, K., Gahbauer, S., Kranz, F., Wassenaar, T. A., and Böckmann, R. A. (2016b). Dynamic cholesterol-conditioned dimerization of the G protein coupled chemokine receptor type 4. *PLoS Comp. Biol.* 12:e1005169. doi: 10.1371/journal.pcbi.1005169

Pluhackova, K., Kirsch, S. A., Han, J., Sun, L., Jiang, Z., Unruh, T., et al. (2016a). A critical comparison of biomembrane force fields: structure and dynamics of model DMPC, POPC, and POPE bilayers. *J. Phys. Chem. B* 120, 3888–3903. doi: 10.1021/acs.jpcb.6b01870

Pluhackova, K., Morhenn, H., Lautner, L., Lohstroh, W., Nemkovski, K. S., Unruh, T., et al. (2015). Extension of the LOPLS-AA force field for alcohols, esters, and monoolein bilayers and its validation by neutron scattering experiments. *J. Phys. Chem. B* 119, 15287–15299. doi: 10.1021/acs.jpcb.5b08569

Ponka, P., and Lok, C. N. (1999). The transferrin receptor: role in health and disease. *Int. J. Biochem. Cell Biol.* 31, 1111–1137. doi: 10.1016/S1357-2725(99)00070-9

Pronk, S., Páll, S., Schulz, R., Larsson, P., Bjelkmar, P., Apostolov, R., et al. (2013). GROMACS 4.5, a high-throughput and highly parallel open source molecular simulation toolkit. *Bioinformatics* 29, 845–854. doi: 10.1093/bioinformatics/btt055

Rai, D. K., Sharma, V. K., Anunciado, D., O'Neill, H., Mamontov, E., Urban, V., et al. (2016). Neutron scattering studies of the interplay of amyloid β peptide(1-40) and an anionic lipid 1,2-dimyristoyl-sn-glycero-3-phosphoglycerol. *Sci. Rep.* 6:30983. doi: 10.1038/srep30983

Ramadurai, S., Holt, A., Krasnikov, V., van den Bogaart, G., Killian, J. A., and Poolman, B. (2009). Lateral diffusion of membrane proteins. *J. Am. Chem. Soc.* 131, 12650–12656. doi: 10.1021/ja902853g

Rheinstädter, M. C., Das, J., Flenner, E., Brüning, B., Seydel, T., and Kosztin, I. (2008). Motional coherence in fluid phospholipid membranes. *Phys. Rev. Lett.* 101:248106. doi: 10.1103/PhysRevLett.101.248106

Roark, M., and Feller, S. E. (2009). Molecular dynamics simulation study of correlated motions in phospholipid bilayer membranes. *J. Phys. Chem. B* 113, 13229–13234. doi: 10.1021/jp902186f

Sako, Y., and Kusumi, A. (1994). Compartmentalized structure of the plasma membrane for receptor movements as revealed by a nanometer-level motion analysis. *J. Cell Biol.* 125, 1251–1264. doi: 10.1083/jcb.125.6.1251

Sako, Y., and Kusumi, A. (1995). Barriers for lateral diffusion of transferrin receptor in the plasma membrane as characterized by receptor dragging by laser tweezers: fence versus tether. *J. Cell Biol.* 129, 1559–1574. doi: 10.1083/jcb.129.6.1559

Sandoval-Perez, A., Pluhackova, K., and Böckmann, R. A. (2017). A critical comparison of biomembrane force fields: protein-lipid interactions at the membrane interface. *J. Chem. Theory Comput.* 13, 2310–2321. doi: 10.1021/acs.jctc.7b00001

Sharma, V. K., Mamontov, E., Anunciado, D. B., O'Neill, H., and Urban, V. S. (2015). Effect of antimicrobial peptide on the dynamics of phosphocholine membrane: role of cholesterol and physical state of bilayer. *Soft Matter* 11:6755. doi: 10.1039/C5SM01562F

Sharma, V. K., Mamontov, E., Tyagi, M., Qian, S., Rai, D. K., and Urban, V. S. (2016a). Dynamical and phase behavior of a phospholipid membrane altered by an antimicrobial peptide at low concentration. *J. Phys. Chem. Lett.* 7, 2394–2401. doi: 10.1021/acs.jpclett.6b01006

Sharma, V. K., Mamontov, E., Tyagi, M., and Urban, V. S. (2016b). Effect of α-tocopherol on the microscopic dynamics of dimyristoylphosphatidylcholine membrane. *J. Phys. Chem. B* 120, 154–163. doi: 10.1021/acs.jpcb.5b10417

Srinivasan, H., Sharma, V. K., Mitra, S., García Sakai, V., and Mukhopadhyay, R. (2019). Dynamical landscape in DODAB membrane system: MD simulation and neutron scattering studies. *Phys. B* 562, 55–58. doi: 10.1016/j.physb.2018.12.013

Srivastava, M., and Petersen, N. O. (1998). Diffusion of transferrin receptor clusters. *Biophys. Chem.* 75, 201–211. doi: 10.1016/S0301-4622(98)00206-3

Tabony, J., and Perly, B. (1991). Quasielastic neutron scattering measurements of fast local translational diffusion of lipid molecules in phospholipid bilayers. *Biochim. Biophys. Acta* 1063, 67–72. doi: 10.1016/0005-2736(91)90354-B

Turnbull, D., and Cohen, M. H. (1961). Free-volume model of the amorphous phase: glass transition. *J. Chem. Phys.* 34, 120–125. doi: 10.1063/1.1731549

Turnbull, D., and Cohen, M. H. (1970). On the free-volume model of the liquid-glass transition. *J. Chem. Phys.* 52, 3038–3041. doi: 10.1063/1.1673434

van der Spoel, D. J., Lindahl, E., Hess, B., Groenhof, G., Mark, A. E., and Berendsen, H. J. C. (2005). GROMACS: fast, flexible, and free. *J. Comput. Chem.* 26, 1701–1718. doi: 10.1002/jcc.20291

Vaz, W. L., and Almeida, P. F. (1991). Microscopic versus macroscopic diffusion in one-component fluid phase lipid bilayer membranes. *Biophys. J.* 60, 1553–1554. doi: 10.1016/S0006-3495(91)82190-7

Zhang, Z., Yunker, P. J., Habdas, P., and Yodh, A. G. (2011). Cooperative rearrangement regions and dynamical heterogeneities in colloidal glasses with attractive versus repulsive interactions. *Phys. Rev. Lett.* 107:208303. doi: 10.1103/PhysRevLett.107.208303

Conflict of Interest: The authors declare that the research was conducted in the absence of any commercial or financial relationships that could be construed as a potential conflict of interest.

frontiers in Cell and Developmental Biology

ORIGINAL RESEARCH
published: 03 November 2020
doi: 10.3389/fcell.2020.590158

High-Precision Protein-Tracking With Interferometric Scattering Microscopy

Richard W. Taylor[1,2†], *Cornelia Holler*[1,2†], *Reza Gholami Mahmoodabadi*[1,2], *Michelle Küppers*[1,2,3], *Houman Mirzaalian Dastjerdi*[1,2,4], *Vasily Zaburdaev*[2,5], *Alexandra Schambony*[1,2,5] *and Vahid Sandoghdar*[1,2,3*]

[1] Max Planck Institute for the Science of Light, Erlangen, Germany, [2] Max-Planck-Zentrum für Physik und Medizin, Erlangen, Germany, [3] Department of Physics, Friedrich Alexander University Erlangen-Nuremberg, Erlangen, Germany, [4] Department of Computer Science, Friedrich Alexander University Erlangen-Nuremberg, Erlangen, Germany, [5] Department of Biology, Friedrich Alexander University Erlangen-Nuremberg, Erlangen, Germany

OPEN ACCESS

Edited by:
Robert Ernst,
Saarland University, Germany

Reviewed by:
Erdinc Sezgin,
Karolinska Institutet (KI), Sweden
Edward Lyman,
University of Delaware, United States

***Correspondence:**
Vahid Sandoghdar
vahid.sandoghdar@mpl.mpg.de

[†] *These authors have contributed equally to this work*

Specialty section:
This article was submitted to Membrane Traffic, a section of the journal Frontiers in Cell and Developmental Biology

Received: *31 July 2020*
Accepted: *05 October 2020*
Published: *03 November 2020*

Citation:
Taylor RW, Holler C, Mahmoodabadi RG, Küppers M, Dastjerdi HM, Zaburdaev V, Schambony A and Sandoghdar V (2020) High-Precision Protein-Tracking With Interferometric Scattering Microscopy. Front. Cell Dev. Biol. 8:590158. doi: 10.3389/fcell.2020.590158

The mobility of proteins and lipids within the cell, sculpted oftentimes by the organization of the membrane, reveals a great wealth of information on the function and interaction of these molecules as well as the membrane itself. Single particle tracking has proven to be a vital tool to study the mobility of individual molecules and unravel details of their behavior. Interferometric scattering (iSCAT) microscopy is an emerging technique well-suited for visualizing the diffusion of gold nanoparticle-labeled membrane proteins to a spatial and temporal resolution beyond the means of traditional fluorescent labels. We discuss the applicability of interferometric single particle tracking (iSPT) microscopy to investigate the minutia in the motion of a protein through measurements visualizing the mobility of the epidermal growth factor receptor in various biological scenarios on the live cell.

Keywords: interferometric scattering microscopy, iSCAT, iSPT, single particle tracking, live cell imaging, membrane organization, epidermal growth factor receptor

1. INTRODUCTION

All cells are enclosed by an outer plasma membrane and, in addition, eukaryotic cells are commonly compartmentalized by internal membranes into cell organelles, to generate specialized functional entities. The plasma membrane acts as a barrier, transport, and communication platform between the cell and its environment that separates the interior of the cell from its surroundings, controls the flux of ions and nutrients and mediates sending and sensing of signals to and from the cell. These multiple functions of the membrane are enabled by its complex composition of phospholipids, sphingo- and glycolipids, cholesterol, and proteins.

The plasma membrane is also a carefully regulated and highly dynamic structure which sculpts the mobility of the proteins and lipids of which it is composed (Krapf, 2018; Jacobson et al., 2019). Our view on the organizational motifs of the plasma membrane has expanded greatly over the last few decades following much investigation and advances in single-particle imaging microscopies. Present wisdom informs that the plasma membrane is organized over many length scales (Destainville et al., 2008; Krapf, 2018; Jacobson et al., 2019), with motifs including cellular domains such as cell-cell contact sites or the apical surface of epithelial cells being strictly separated from the basolateral surface of the membrane by cell-cell adhesion molecules. In addition, other

motifs include cytoskeletal actin-mesh induced microscale compartmentalization (Fujiwara et al., 2002, 2016; Jaqaman and Grinstein, 2012), nanoscale transient raft domains (Pike, 2006; Jacobson et al., 2007; Sezgin et al., 2017), and molecular-level crowding from protein-protein interactions (Jin and Verkman, 2007; Dix and Verkman, 2008).

These organizational motifs provide a mechanism for spatial and temporal control of the lipids and proteins by hierarchically restricting their freedom of movement. Doing so allows for regions of specific composition and hence dedicated function which is required for a diverse array of physiological processes such as signal transduction, directed transport across a membrane or cell-cell-communication (Destainville et al., 2008; Krapf, 2018). In signaling, one requires the formation of nanoscale signaling domains which comprise selected proteins. By transiently confining respective proteins, these domains are believed to regulate signaling events by changing the local concentration of proteins and as a consequence modulating efficient protein-protein interactions. In contrast, they also have the capacity to prevent signaling altogether in the absence of a stimulus through exclusionary segregation of the membrane components (Krapf, 2018).

The ability to track the motion of proteins within the membrane on the one hand provides insights on the paths a particular protein takes during the period of observation and on the other indirectly reveals obstacles, boundaries, or accelerators that affect its mobility. One thus stands to gain further insight into the functionality and structure of the membrane by observing the lateral mobility of membrane proteins as these molecules serve as ideal probes for this complex environment. Unsurprisingly, tracking protein mobility has been an important target of research over the last decades, with numerous optical techniques having been developed to meet this challenge (Jaqaman and Grinstein, 2012). Studies at the single molecule level have shown to be extremely fruitful since they allow for direct visualization of the behavior of individual molecules and their molecular interactions, no matter how rare or infrequent, without fear of being lost to an ensemble observation.

Single particle tracking (SPT) of protein and lipid mobility has proven to be an exceptionally valuable and productive technique in this effort to decipher the interactions that constitute the organizing principles of the membrane (Alcor et al., 2009; Kusumi et al., 2014; Manzo and Garcia-Parajo, 2015; Shen et al., 2017; Ye et al., 2019). SPT microscopy is typically accomplished by localizing the position of the membrane molecule through attachment of an optical label, be the label a fluorescent molecule (Wieser and Schütz, 2008; Albrecht et al., 2015), quantum dot (Pinaud et al., 2010; Clausen and Lagerholm, 2013), or nanoparticle (Kusumi et al., 1993; Fujiwara et al., 2002). The purpose is then to reveal the path taken in the membrane by the molecule as detected at various temporal resolutions depending on the method of choice. While low temporal resolution can provide only partial information about the motion of the molecule without revealing the fine details of its diffusion, imaging with high frame rates effectively visualizes the molecular trajectories resultant from fast and short-lived interactions within the membrane.

Fluorescence-based labels have been enormously popular for single-molecule imaging since they enable precise distinction between signal and background during imaging. However, fluorescence imposes several important limitations which restrict how well one can track the mobility of a membrane molecule. Firstly, the finite rate by which light is emitted from the fluorophore limits how well the position of the labeled protein can be determined. For a molecule to emit a fluorescence photon, an electron within the molecule must become promoted into a higher energy level through absorption of a photon. On relaxation of the electron, a fluorescent photon is emitted, with the whole process taking several nanoseconds. The rate at which the label can emit photons is a critical quantity in SPT as the measured number of photons determines directly the precision to which the location of an emitter can be determined (Thompson et al., 2002; Deschout et al., 2014). Since the emission rate is depending on the excitation lifetime, one therefore finds that for nanosecond lifetimes the best attainable resolutions are on the order of tens of nanometers per millisecond of recording.

In addition, fluorescent dyes are vulnerable to several processes that result in the emission of no light which is naturally detrimental for tracking microscopies. Firstly, photochemical processes can occur which alter the wavelength needed for the emitter to become excited or to fluoresce, known as *photobleaching*. Secondly, it is possible for the electron within the fluorophore to become temporarily trapped in a transient state that is dark to the illumination wavelength, a process commonly referred to as *blinking*. Owing to these issues, there have been many efforts to investigate mechanisms for label-free imaging of bio-membranes (Mashaghi et al., 2014).

The desire to gain an ever greater insight into the precise mobility of single molecules within the membrane has motivated the search for alternative optical labels that can offer improved spatial and temporal resolutions in SPT microscopy. Scattering is an attractive alternative because it does not encounter the critical limitations previously described for fluorophores. Furthermore, the permanence of scattering also enables for the scattering label to be tracked for an essentially endless period, limited only by the sample itself, and so opening the possibility to watch entire biological processes in a complete uninterrupted fashion.

The first experiments that showed the potential for scattering labels were pioneered as far back as the late 1980s (De Brabander et al., 1986, 1988; Geerts et al., 1987). These efforts laid the foundation for the seminal investigations by Kusumi et al. whose high-speed single particle measurements revealed the existence of diffusion barriers within the plasma membrane and founded the concept of compartmentalized organization of the membrane itself (Kusumi et al., 1993, 2005; Fujiwara et al., 2002).

The challenge faced in performing SPT microscopy with nanoparticle labels is that the scattering signal is comparatively small and accompanied by a large imaging background from the remaining sample which must be tackled. Interferometric scattering (iSCAT) microscopy is an emerging technique which confronts these issues directly (Lindfors et al., 2004; Taylor and Sandoghdar, 2019; Taylor et al., 2019; Young and Kukura, 2019). With iSCAT, it recently has been shown to be possible to track the

diffusion of labeled proteins on the membrane of artificial and live cells (Spindler et al., 2016; Huang et al., 2017a; de Wit et al., 2018; Taylor et al., 2019; Mazaheri et al., 2020) with nanometric precision in all *three-dimensions* with microsecond temporal resolution (Taylor et al., 2019; Mahmoodabadi et al., 2020). The recent advances of interferometric SPT (iSPT) is further spurring new efforts to understand and model the plasma membrane (Lyman et al., 2018).

In this work, we show how iSCAT microscopy is highly suited for investigating the mobility of a transmembrane signaling protein to fine detail within the live cell membrane. We chose the epidermal growth factor receptor (EGFR) as a candidate since EGFR is a prototypical receptor tyrosine kinase belonging to the ErbB family and is a key regulator of cell proliferation, growth, survival, and differentiation in mammalian cells (Oda et al., 2005). EGFR is an 1,186 amino acid single-pass transmembrane glycoprotein that binds and is activated by ligands of the Epidermal Growth Factor (EGF)-family with 11 known members in humans (Roskoski, 2014).

In its inactive state, EGFR is mostly residing and traveling within the plasma membrane either as a monomer or as pre-formed but inactive dimers, with the ability to continuously switch between these two states (Chung et al., 2010). To be primed for signaling, however, EGFR must be in the dimerised state in order to become active after EGF ligand binding. Signaling is initiated by autophosphorylation of the intracellular part of the receptor, which constitutes binding interfaces for signaling proteins from which the signal is further transduced along the signaling cascade. Once activated, EGFR becomes rapidly endocytosed and continues signaling in endocytic compartments until the receptors either are returning to the inactive state and recycled back to the membrane or become degraded via the lysosomal pathway (Linggi and Carpenter, 2006; Sorkin and Goh, 2009; Arteaga and Engelman, 2014; Roskoski, 2014; Tomas et al., 2014; Kovacs et al., 2015; Freed et al., 2017).

Since EGFR signaling strongly depends on receptor mobility as outlined above and aberrant signaling of EGFR is associated with various cancers by promoting oncogenic signaling, this receptor has been widely investigated as a model system to explore how the nanoscale organization of the plasma membrane affects signaling function (Oda et al., 2005; Erazo-Oliveras et al., 2018). For this reason, EGFR has also served as a model membrane protein for numerous SPT microscopies (Kusumi et al., 1993; Sako et al., 2000; Abulrob et al., 2010; Chung et al., 2010; Bag et al., 2015; Liu et al., 2016).

Here, we show how the high spatial and temporal resolution of iSPT can be used to uncover fine details in the trajectories of an EGFR in scenarios such as diffusion in the membrane as well as applicability in investigating processes such as endocytosis and trafficking. We discuss several methods for statistical quantification of single particle trajectories that take advantage of the high temporal resolution to reveal detailed information about protein mobility in the membrane such as nanoscale sub-diffusion and confinement events. We first begin by introducing the principle of iSPT microscopy and in particular how three-dimensional (3D) nanometric particle localization is accomplished.

2. iSPT ON THE LIVE CELL

2.1. SPT Microscopy: Interferometric Scattering vs. Fluorescence

In fluorescence-based SPT, one follows the molecule of interest by detecting the light emitted by an attached fluorescent label. Since the light emitted by the label is shifted to a longer wavelength than that used for excitation, one can exclusively detect the labeled protein through the use of convenient wavelength-selective filters. This detection strategy has proven enormously successful, with single-molecule sensitivity now being something widely accessible to many laboratories.

However, the aforementioned inconsistent and low number of photons emitted through fluorescence curtails the resolution and fidelity by which one may identify the position of the target molecule. This problem is further compounded with the presence of detection noise which is often of a similar intensity to the weak probe signal.

Light scattering is an alternative optical process to fluorescence which overcomes many of these difficulties. In light scattering, the incoming light briefly couples to the electrons in the material before being swiftly re-radiated away. For this reason, whilst not all materials can fluoresce, all are able to scatter light. Moreover, light scattering is not vulnerable to the processes of blinking and bleaching as encountered with fluorescence.

One advantage of light scattering is that the interaction between the photon and the electron is near-instantaneous. For a metal nanoparticle, such as gold, this interaction can be as fast as 10 fs and hence one can generate a million scattered photons in the same time it would take to generate a single fluorescence photon.

The process of light scattering also has the crucial property of being coherent, a feature not shared by fluorescence. In being coherent, the light scattered by the particle retains the same temporal signature as the illuminating light, meaning they share the same phase difference throughout time. Hence, two light beams can be meaningfully added together in an optical process known as interference. The advantage in interfering two optical beams together is that if one of the beams is weak in amplitude—for example as occurs with nanoscale scattering, then one can boost the effective amplitude of this weak signal by mixing with a stronger coherent companion beam. Oftentimes one can boost the weak scattered signal far above the level of normal detection noise, thus offering exquisite detection sensitivities. Microscopies that harness this detection principle are described under the umbrella term "interferometric microscopies," and in particular iSCAT is a technique that has been developed to optimize the sensitivity for the detection of nanoparticulate matter.

We can express the interferometric detection of scattered light via the following equation:

$$I_{\mathrm{det}} = (\mathbf{E}_{\mathrm{ref}} + \mathbf{E}_{\mathrm{sca}})^2 = |\mathbf{E}_{\mathrm{ref}}|^2 + |\mathbf{E}_{\mathrm{sca}}|^2 + 2|\mathbf{E}_{\mathrm{ref}}||\mathbf{E}_{\mathrm{sca}}|\cos(\theta)\,, \quad (1)$$

where I_{det}, is the light incident upon our detector, $\mathbf{E}_{\mathrm{sca}}$ the electric field of the scattered light of the sample and $\mathbf{E}_{\mathrm{ref}}$ is the companion beam with which we interfere the scattered light. In practice this

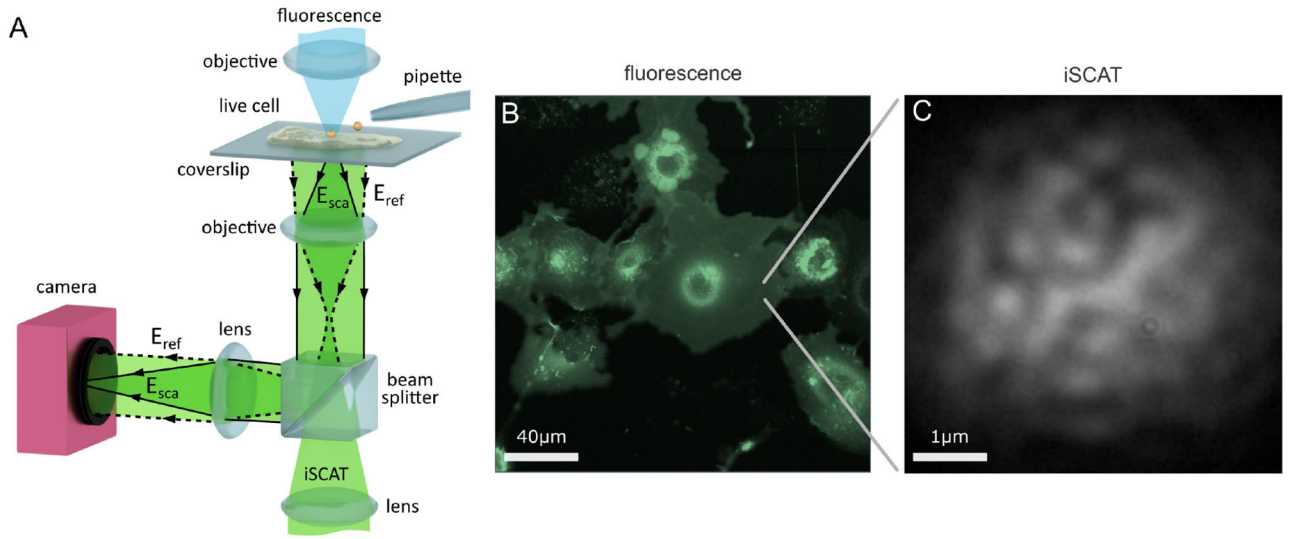

FIGURE 1 | Imaging the live cell with iSCAT microscopy. **(A)** Schematic of a wide-field reflection iSCAT microscope which incorporates a micropipette and a confocal fluorescence imaging channel. **(B)** A complementary macroscopic confocal fluorescence image of COS-7 cells transfected to over-express the EGFR-EGFP protein. **(C)** A raw widefield iSCAT image of the COS-7 membrane from the region highlighted in **(B)**.

beam, referred to as the "reference" beam, can be obtained from a reflection of the illuminating beam in the optical path, which we discuss further in the following section. The key component of Equation (1) is the cross-term where one sees the multiplication of the scattered and reference fields to create a product with an overall larger intensity.

The phase term $\cos(\theta)$ determines the contrast of the interference term with respect to the bright signal of the reference intensity and the exact phase difference is determined by many contributions including the material of the scatter, the imaging arrangement and sample geometry (Mahmoodabadi et al., 2020).

2.2. iSCAT Microscopy on the Live Cell

A popular modality for iSCAT microscopy is the wide-field reflection arrangement shown in **Figure 1A**, where the sample is illuminated by a wide beam, and the reference beam (labeled $\mathbf{E}_{ref}$) with which the sample-scattered light ($\mathbf{E}_{sca}$) interferes originates from the portion of this incident illumination which back-reflects off the sample-bearing glass coverslip.

A key advantage of iSCAT microscopy is that the high sensitivity of detection permits imaging with excellent signal-to-noise levels even at extremely high speeds, with framerates in the range of 100–1,000,000 frames per second (fps) reported in the investigation of membrane diffusion (Lin et al., 2014; Spindler et al., 2016; Wu et al., 2016; Huang et al., 2017a; de Wit et al., 2018; Reina et al., 2018; Taylor et al., 2019). For imaging protein mobility on live cells, high framerates are particularly important in order to observe transient nanoscale molecular interactions which occur at swift milli- to microsecond time scales that may otherwise be not observable at lower framerates (Ritchie et al., 2005). Illumination intensities required for these high framerates are typically in the order of $I = 1-10\,\mathrm{kWcm}^{-2}$, which are compatible with live cell imaging (Wäldchen et al., 2015).

In this work, we perform our investigations upon live HeLa and COS-7 cells. HeLa cells are an adherent, epithelial cell line derived from human cervix tissue and COS-7 cells are an adherent but fibroblast-like cell line that originate from the kidney tissue of the African Green Monkey. On HeLa, we track the endogenous EGFR whereas on COS-7 we track exogenous EGFR. In the latter case, this is achieved by transfecting the COS-7 cells with a plasmid encoding EGFR which increases the level of EGFR expressed within the cell. We link the EGFR plasmid with the enhanced green fluorescent protein (EGFP) to yield the fusion protein construct EGFR-EGFP which then allows us to visualize successful transfection through the fluorescence signal of EGFP. An asset of iSCAT microscopy is that it is fully compatible with fluorescence imaging (Kukura et al., 2009), and so one can incorporate conventional fluorescence microscopies and labeling strategies to assist with investigation on live cells.

We introduce a scanning confocal fluorescence channel from above the sample, shown in **Figure 1A**, to provide a macroscopic overview image of the live cell sample, as shown in **Figure 1B**. iSCAT microscopy may also be performed in parallel to confocal fluorescence imaging, and **Figure 1C** presents an image of a portion of the lower cell membrane viewed with iSCAT microscopy. The nature of iSCAT microscopy, particularly in this back-reflection scheme, produces interferometric images of the cell membrane that show a characteristic speckle pattern as shown in **Figure 1C**.

2.3. On Labeling in iSPT

The universality by which all materials scatter light results in their ability to be detected in iSCAT microscopy, provided appropriate care is taken to mitigate optical noise associated with the detection of light. In particular, it indeed has been shown to be possible with iSCAT microscopy to detect individual proteins

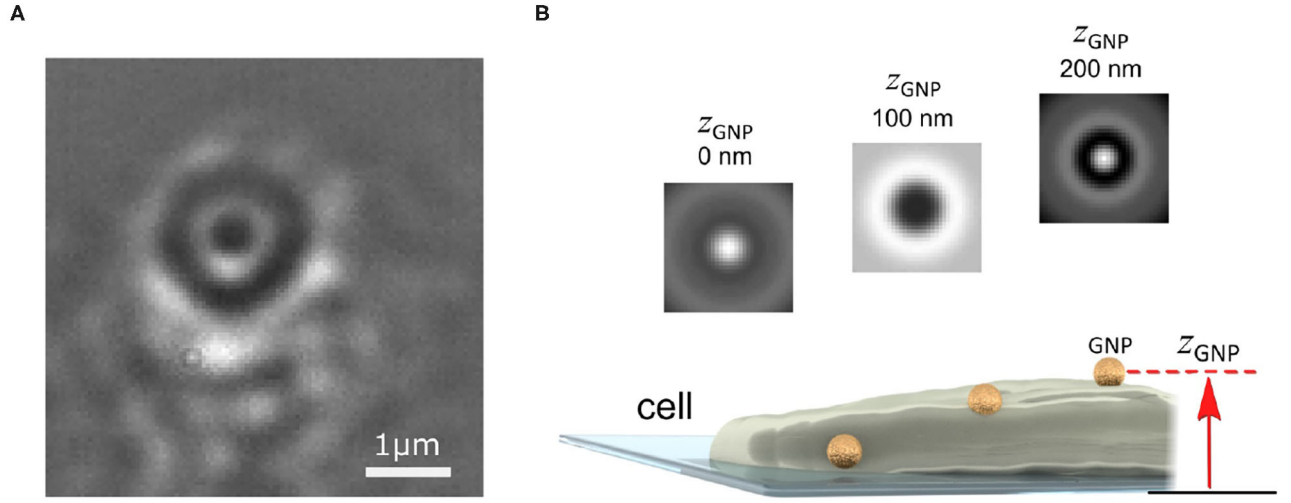

FIGURE 2 | Imaging and localizing a GNP probe in 3D with iSPT. **(A)** Background-corrected iSCAT image of the COS-7 cell membrane with a bound GNP probe (diameter 48 nm). The GNP appears as a series of black and white rings from the iPSF. The distinctive ring pattern depends on the height of the GNP probe above the coverslip and also its position relative to the objective focus. **(B)** Schematic illustrating how the height of the GNP probe enables determination of its axial position: as the GNP diffuses on the membrane, a change in the height of the GNP above the coverslip produces a distinct iPSF which can be used to determine the height of the GNP z_{GNP}.

directly without the need for any label when observed in isolation upon glass coverslips (Piliarik and Sandoghdar, 2014; McDonald et al., 2018; Young et al., 2018).

In tracking lipids and proteins when incorporated into a membrane, it is necessary to invoke use of a label to identify the molecule of interest and to render it distinct. Just as one can use a fluorescent label, one can equally use a strongly scattering nanoparticle as well as a label. Gold nanoparticles (GNPs) are widely used owing to their excellent scattering efficiency and bio-compatibility. As with fluorescence labeling, use of a colloidal label can potentially introduce artifacts that affect the diffusion under study, and these issues are addressed later in the discussion section.

2.4. 3D Localization With iSPT Microscopy

In iSPT, one images the light scattered by the GNP-labeled protein. However, since the remaining cell and its constituents also scatter light, they also produce a signal which we refer to as the imaging background. To localize the GNP-labeled protein in any given frame, it is first necessary to isolate this probe signal out of the imaging background.

Removal of the imaging background of the cell is, in general, challenging (Taylor and Sandoghdar, 2019). This is because firstly the scattered light has the same wavelength as the illumination and sample background and so simple wavelength-selective filtering is not possible. Secondly, the cell background is dynamic and fluctuating in nature, and consists of features with fine details of a similar size and shape to the probe signal. This dynamism stems from the fluctuating composition and morphology of the membrane and the cell interior, which is then observed as a random speckle-like pattern with temporal fluctuations in intensity, as illustrated in **Figure 1C**.

Several strategies have recently been reported which address this problem of removing the interferometric imaging background of the cell (Cheng and Hsieh, 2017; de Wit et al., 2018). One strategy exploits the difference between the highly symmetric circular pattern of the imaged gold probe and the "random" pattern of the cell background speckle (Taylor et al., 2019). **Figure 2A** presents an image of the plasma membrane of a COS-7 cell, where a single GNP has become bound to the membrane. As the nanoparticle is smaller than the optical diffraction limit, in imaging the GNP, especially interferometrically, one sees not an image of the particle but instead a series of rings of alternating contrast referred to as the interferometric point spread function (iPSF) (Mahmoodabadi et al., 2020). By using a circularly-symmetric feature extraction algorithm, the probe iPSF can be read from one frame of the video (Taylor et al., 2019; Mahmoodabadi et al., 2020).

The imaging background, however, should not necessarily be viewed as a nuisance, rather it can also provide useful information. For example, the interferometric image of the cell can indicate sample creep and drift which are important parameters to quantify and correct for in wanting to reliably interpret single particle trajectories (Taylor et al., 2019). Once the probe iPSF has been isolated from the background, one can then determine to nanometric precision the 3D position of the probe. The lateral (x-y) position is found by determining the center of the symmetric iPSF, which can be accomplished through a variety of means such as by finding the center of symmetry (Parthasarathy, 2012), or through fitting of a two-dimensional Gaussian intensity function or an interferometric diffraction-based model which describes the iPSF exactly (Mahmoodabadi et al., 2020).

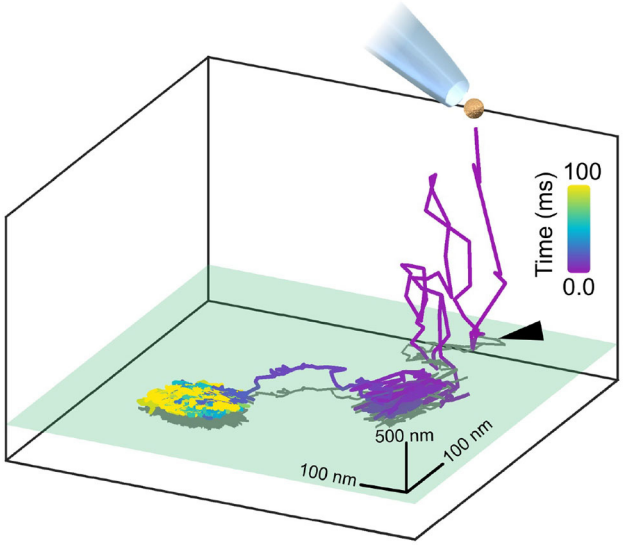

FIGURE 3 | Watching *in situ* the moment a GNP lands upon the plasma membrane. A GNP, once pipetted toward the COS-7 cell, is tracked axially over a range of 2 μm whilst it diffuses in the culture medium before coming to land upon the cell membrane, with the initial point of contact with the membrane marked with a black arrow. The axial plane of the cell membrane is represented in green and a two-dimensional projection of the trajectory is plotted in gray. The whole landing event lasted approximately 100 ms and was recorded at 30,000 fps. The GNP used here was positively-charged so as to immediately and readily bind non-specifically to the negatively-charged cell membrane for the purpose of illustration.

To determine the height of the GNP above the coverslip (z_{GNP}), one exploits the information encoded within the alternating contrast of the iPSF ring pattern, which is a distinctive feature of iSPT (Mahmoodabadi et al., 2020). **Figure 2B** illustrates several iPSFs for a GNP that is diffusing over a region of the cell membrane which raises its height. The distinctiveness of the iPSF and the good sensitivity by which it can be measured enables nanometrically-precise lateral and axial localization. One can determine the relative change in height by direct calibration of the central contrast of the iPSF (Jacobsen et al., 2007), or by machine-learning assisted clustering of the iPSF (Taylor et al., 2019) or by direct fitting of the iPSFs to a model specifically describing iPSF formation (Mahmoodabadi et al., 2020).

2.5. Watching *in situ* Landing of a GNP Probe on the Membrane With iSPT

To provide an illustration of 3D nanometric iSPT of a GNP probe, we present **Figure 3**, wherein we track the landing of a GNP probe upon the cell membrane. To observe the labeling step is an important ability in interferometric particle tracking as one is able to ensure that indeed it is the GNP probe which is being observed but also one is able to know when the probe-protein interaction began which is especially important for investigating time-dependent processes.

Figure 3 demonstrates the *in situ* binding of a pipetted GNP probe to the plasma membrane, visualized through the 3D trajectory. Here in this example, for illustration we use a positively-charged GNP which readily binds to the negatively-charged plasma membrane. It should be noted that in this case, binding to the plasma membrane is purely electrostatic and not representing any particular lipid or protein motion in the membrane. Here, the GNP is tracked axially over a range of two microns where it is then seen to initially interact with the membrane, break loose before then ultimately becoming permanently attached.

2.6. Describing the Erratic Mobility of Proteins

If one watches the path taken by an individual protein as it navigates through the environment of the cell, one sees the protein takes steps that are seemingly random in length and direction. This behavior is driven by ever-present random fluctuations in the environment of the protein and is referred to as diffusion. When the mobility of a particle is driven by thermal fluctuations and otherwise unencumbered, we refer to the mobility of the particle as being Brownian or "normal."

When normal diffusion is enhanced or restricted by an external influence, for example, by a variety of geometric and steric interactions, then the diffusion becomes anomalous. Such anomalous diffusion encapsulates two regimes of mobility that are in many regards polar opposites. Anomalous diffusion, wherein the mobility is enhanced by the presence of phases of persistent motion, for example by the application of an external driving force, or complex velocity flow, is referred to as *super-diffusion*. Conversely, one can have *sub-diffusion*, where the dispersal process happens slower than in the case of normal diffusion, with a sub-linear scaling of the MSD (Montroll and Lebowitz, 1976; Bouchaud and Georges, 1990; Isichenko, 1992; Metzler and Klafter, 2000). In the plasma membrane, sub-diffusion may arise from various biological mechanisms such as interactions with the organizational elements of the membrane, for example between cytoskeletal barriers, molecular crowding, or binding interactions between membrane molecules (Saxton, 1994, 1996; Jin and Verkman, 2007; Dix and Verkman, 2008; Jacobson et al., 2019). Determining the mechanistic origin of sub-diffusion in the cell is challenging, and remains an active area of research (Saxton and Jacobson, 1997; Saxton, 2012) with recent efforts presenting statistical frameworks to characterize and discriminate between different membrane models (Weber et al., 2012; Renner et al., 2017; Woringer et al., 2020).

Mean Square Displacement Analysis of Membrane Mobility

The general diffusive nature of membrane protein mobility implies that it is impossible to predict how the protein will proceed from one step to the next as the process is essentially random. Nonetheless, various statistical models have been proposed to interpret these random walks in order to describe any characteristic properties they may have (Metzler et al., 2014; Meroz and Sokolov, 2015). One immediate characterization is, for example, whether the walk exhibits normal or anomalous behavior, which may be an important indicator of function in the case of a transmembrane protein.

One of the most widespread means of analysis is that of the Mean Square Displacement (MSD) where one examines the time-dependent character of the diffusive walk to quantify whether the walk is normal or anomalous, and if it is anomalous, to which degree. We can express the MSD as:

$$\mathrm{MSD}(\tau) = \Gamma_\alpha \tau^\alpha \tag{2}$$

where τ represents an interval of time within the trajectory, Γ_α is a coefficient of proportionality and α is the temporal exponent (time-dependence) that we seek in order to quantify the nature of the diffusive walk. A protein undergoing unencumbered Brownian diffusion is characterized by a MSD which is linear in time, i.e., $\alpha = 1$, which is so-called "normal" diffusion and $\Gamma_{\alpha=1} = D$ is just the diffusion constant. For a diffusing protein that is not truly free, i.e., being subject to additional influences beyond thermal fluctuations, then the diffusion can be anomalous and $\alpha \neq 1$. An $\alpha > 1$ describes super-diffusion, and occurs, for example, in instances where the protein is being specifically guided along a certain path such as which occurs in intracellular transport. An $\alpha < 1$ denotes the hindered mobility of sub-diffusion, and for diffusion measured in the plasma membrane a typical value of $\alpha = 0.7$ is characteristic by conventional ensemble MSD analysis (Saxton and Jacobson, 1997). With careful analysis of the MSD and temporal exponent, one can hence characterize the diffusive character of the membrane protein within the local membrane environment.

To compute the MSD, one calculates how the average distance walked squared for a given interval of time depends on how long the time interval is. To obtain a reliable measure of the time-dependence of the walk one requires a sufficient number of recordings to give an average that is statistically robust (Kepten et al., 2013, 2015; Vestergaard, 2016). One method is to build an average out of many similar trajectories from separate measurements. Alternatively one may take a single sufficiently long trajectory and subdivide it into shorter pieces which are then averaged together. The former approach is known as a *ensemble average* and the latter is referred to as a *time-average*. A diffusive system in which these two approaches are equivalent is said to be *ergodic*. The plasma membrane of the cell is an example of a system that can exhibit weak ergodicity breaking which is a behavior chiefly originating out of inhomogenous confinement and stalling of the diffusing protein in the membrane (Metzler et al., 2014). As a consequence, these two approaches can not generally be assumed to be equivalent.

In our work presented here, we accumulate a sufficient number of frames from a very short window in time, typically representing just a small fragment of the complete trajectory. We then roll the MSD analysis incrementally across the whole trajectory and thus build up a measure of how the temporal exponent is changing throughout the trajectory. Doing so allows one to visualize how the mobility is evolving in time as the diffusing protein encounters new and differing obstacles and environments (Taylor et al., 2019). This contrasts with conventional MSD analysis where one considers all points in a trajectory at once (see **Supplementary Material 1**).

The rolling window time-averaged MSD is given by:

$$\mathrm{MSD}_i(\tau) = \left\langle \left(r(t_j+\tau) - r(t_j)\right)^2 \right\rangle_i = \Gamma_{\alpha_i} \tau^{\alpha_i} + \sigma_{xy}, \tag{3}$$

where i denotes the index of the temporal window wherein the MSD is to be computed, $r(t_j)$ is the x-y position of the protein at a time t_j, where t_j represents points in time belonging within the window and $\langle \ldots \rangle$ denotes the calculation of an average. The temporal exponent which characterizes the time-dependence of the MSD within the given window i is denoted by α_i.

The microsecond imaging resolution of iSPT allows one to quantify the time-dependence of the protein mobility to millisecond resolution when employing the rolling time-average. One, however, must also be careful when analysing trajectories recorded at high-frame rates. Firstly, in general, one must always account for the error introduced by the localization precision for each specific trajectory point (σ_{xy}) in the computation of the MSD as an omission of this uncertainty would lead to underestimation of the respective temporal exponent (Martin et al., 2002). When imaging at high framerates in particular, it is possible that the step taken by the protein between two pairs of frames is comparable to, if not smaller than, the certainty with which the start and end positions are able to be known. In such cases, when performing the analysis one must be careful to avoid use of these frame pairs to avoid erroneous calculation of α_i.

Directional Correlation Analysis

A complementary means to quantitatively identify the presence of obstacles and barriers to diffusion or directed transport is to look for correlation in the direction in which any two steps are taken. In the case of free diffusion, one would expect no correlation in the walked trajectory as the process is essentially random with no memory. In the presence of obstacles, however, one would expect the occurrence of recoil or "knock-back" upon collision with said obstacles. In the case of directional transport, one would expect a prevalence of a certain direction, i.e., a positive correlation. Directional correlation analysis seeks to quantify the occurrence of such collisions by considering the angular correlation between two steps, and seeing if this is a meaningfully repeated occurrence.

The directional correlation is calculated by first considering two steps taken by the diffusing probe. The first step, $\Delta\overrightarrow{r}_1$, is the vectorial displacement between two frames separated in time by τ: $\Delta\overrightarrow{r}_1 = r(t+\tau) - r(t)$, where here we take $\tau = 5$ frames. The second step begins where step $\Delta\overrightarrow{r}_1$ ended, and also occurs over an equal time interval, i.e., $\Delta\overrightarrow{r}_2 = r(t+2\tau) - r(t+\tau)$. The cosine of the angle between these two steps is then computed, thus giving an expression for their angular correlation. As with the MSD, this calculation is repeated for all pairs of steps that occur within a smaller window (i) of the whole trajectory so that changes in the directional correlation can be identified over the course of the trajectory. Formally, we calculate the directional correlation C_i for the vectorial steps $\Delta\overrightarrow{r}_1$ and $\Delta\overrightarrow{r}_2$ via the following (Weeks and Weitz, 2002; Munder et al., 2016):

$$C_i = \left\langle \frac{\Delta\overrightarrow{r_1}}{|\Delta\overrightarrow{r_1}|} \cdot \frac{\Delta\overrightarrow{r_2}}{|\Delta\overrightarrow{r_2}|} \right\rangle_i \tag{4}$$

where $|\ldots|$ denotes the magnitude of the vectorial step and as before, the average is computed for all pairs in the i^{th} window. A truly random process possesses no overall angular correlation between any pairs of steps, and so $C = 0$. A positive directional correlation would imply the diffusing probe exhibits some persistent motion and a negative correlation suggests persistent knock-back or deflection.

3. TRACKING EGFR ON THE LIVE CELL WITH iSPT

3.1. Labeling the Receptor

In our investigation to label the EGFR, we functionalize GNPs of 48 nm diameter with EGF to produce an EGF-GNP probe that specifically binds to the EGFR. To do so, we use streptavidin-coated GNPs and EGF probes with attached biotin molecules. The strong chemical bond between streptavidin and biotin serves as the linker between the GNP and the EGF ligand. A micropipette is then used to deliver small quantities of the EGF-GNPs to the immediate vicinity of the cell under investigation. This introduces the distinct advantage of setting a clear start point in which the probe is known to begin to interact with the membrane, which is important for biological processes stimulated by probe binding. The permanence of the scattering signal from the GNP probe along with the ability of iSPT to track nanoparticles in 3D over an extended axial range permits observation of the labeling process prior to immediate tracking of the mobility of the labeled protein. Once the functionalized GNP has bound the receptor we refer to this complex as "EGFR-GNP."

3.2. Anomalous Mobility on the Plasma Membrane

In **Figure 4**, we present an example of a typical trajectory following the labeling of the EGFR with an EGF-GNP probe. This trajectory was recorded on the lamellapodium of a COS-7 cell at a framerate of 30,000 frames per second for a duration of 8.3 s (250,000 trajectory points). The *x-y* projection of the trajectory is plotted in **Figure 4A**. The axial information of the trajectory reveals diffusion on a locally-flat but slowly curving surface expected from the lamellapodium, depicted in **Figure 4B**.

The extended period of observation shows the frequent occurrence of the probe revisiting the same regions of the membrane as well as navigating through distinct patches with differing sparsity of trajectory points. One must express care in interpreting the trajectories by visual inspection, and thus we defer to quantification by MSD and directional correlation analysis.

We first begin by calculating the whole-trajectory MSD, shown in **Figure 4C**. When presented on a log-log scale, shown in the inset of **Figure 4C**, the plot becomes linear and the gradient gives the temporal exponent which typifies the *whole* trajectory. By using the rolling-window MSD we are able to explore the "microscopic" changes in the diffusional character of the trajectory in time. The temporal exponent of diffusion is plotted in **Figures 4D,E**. Additional information on the determination of α_i is presented in **Supplementary Material 2**. Here we use a rolling window of length of 1,000 frames, corresponding to a window with temporal duration $T_w = 33$ ms, and find the temporal exponent to be fairly robust against the size of the window length, shown in **Supplementary Material 3**. Generally, the trajectory has a global mean value of $\alpha_i = 0.7 \pm 0.1$ confirming indeed the diffusion is anomalous. Inspection of the rolling value reveals a distribution in the value of α_i, which appears to be region-specific, with some portions of the walk encountering strong confinement with $\alpha_i \approx 0.5$. In comparing the directional correlation, **Figures 4F,G**, to their respective temporal correlation partner, we find strong agreement between both methods of analysis with the same temporal fluctuations and spatial distribution evident in both. The mean directional correlation value for the trajectory, $C = -0.2 \pm 0.1$ implies deflection and knock-back of varying strength. In tandem, both α and C suggest that the sub-diffusion occurring in the trajectory results from the obstructed random walk of the EGFR-GNP, and that this interaction is locally heterogeneous.

The origin for the heterogeneous environment encountered by the EGFR protein—which manifests in the anomalous trajectory of the protein—is multifold. Whilst it is beyond the scope of this work to give a comprehensive account of all the known means of interaction, it is nonetheless interesting to consider some of the core principles of membrane organization that readily affect EGFR. To that end we might begin with the role played by the substructure and compartmentalization of the plasma membrane itself. Kusumi and co-workers first proposed that the membrane is partitioned into compartments, sometimes doubly so, by the underlying actin cytoskeleton which thus acts as a diffusive barrier to membrane proteins, with compartment side lengths in the range $L = 40$–800 nm depending on the cell type (Kusumi et al., 1993, 2005, 2012; Fujiwara et al., 2002, 2016). These compartments, which frustrate free diffusion, appear to render useful biological function. For example, monomeric proteins tend to be able to pass the compartment boundaries more easily via a process known as "hopping" or "hop-diffusion," whereas dimeric or oligomeric forms of the protein tend to remain confined (Kusumi et al., 2012). As a result, such compartments may enrich or exclude multimeric proteins and thus constitute functional platforms in e.g., signaling or adhesion.

It is interesting to reflect upon the fact that our understanding of the important role membrane compartmentalization plays upon diffusion was borne out of the early pioneering work of Kusumi and co-workers more than two decades ago. By using one of the earliest realizations of iSPT microscopy which granted them sufficient temporal resolution, membrane compartmentalization, and "hop-diffusion" could be inferred through careful analysis of the trajectories of membrane proteins. With the recent progress in improved detection sensitivity, spatio-temporal resolution, and precision from the ever-expanding iSCAT and iSPT microscopy community (Piliarik and Sandoghdar, 2014; Huang et al., 2017a; Young et al., 2018; Taylor et al., 2019), it is an exciting prospect to revisit and explore the role membrane compartmentalization plays on protein mobility with renewed experimental and theoretical vigor (Lyman et al., 2018).

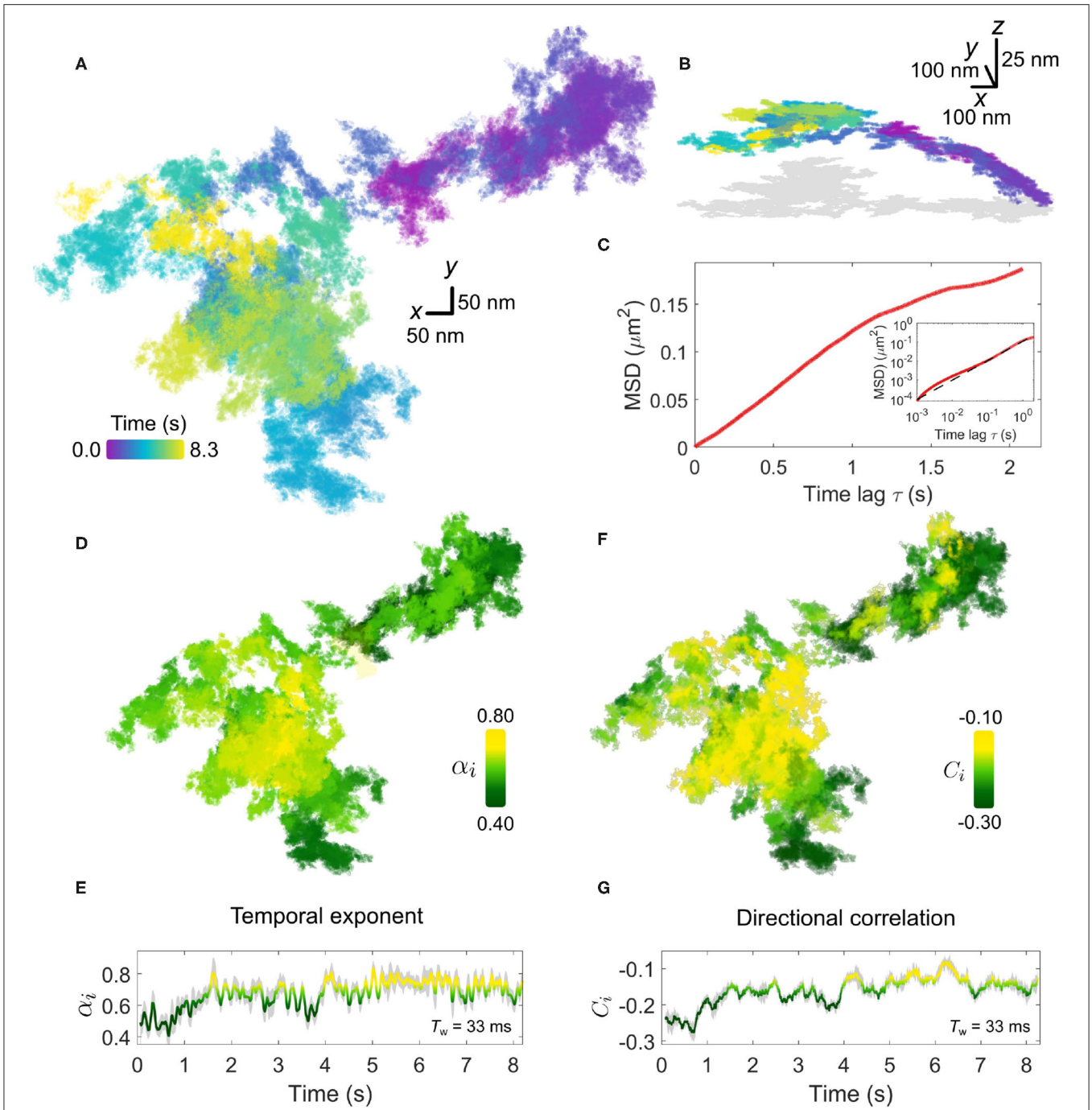

FIGURE 4 | Anomalous EGFR diffusion in the plasma membrane revealed by high-speed iSPT. **(A)** A typical EGFR-GNP trajectory recorded with 30,000 frames per second for a duration of 8.3 s on a COS-7, here shown as *x-y* plane. **(B)** The trajectory from **(A)** viewed in 3D, revealing global curvature. The 2D projection is depicted in gray. **(C)** The whole-trajectory MSD. Inset shows the same plot but on a log-log scale with a linear slope as a guide to the eye. **(D)** The rolling temporal exponent of diffusion α_i for the trajectory for an incrementally sliding window of 1,000 frames ($T_w = 33$ ms), represented by the color scale, mapped onto the *x-y* trajectory. **(E)** The temporal exponent plotted as a function of time. **(F)** Similar to **(D)**, the rolling directional correlation C_i is mapped onto the *x-y* trajectory and also expressed as a function of time **(G)**. The gray shadow in **(E,G)** show the bounds of uncertainty in calculation of each respective quantity.

We next consider an additional example of membrane diffusion similar to **Figure 4**, shown in **Figure 5**, where the lateral trajectory (**Figure 5A**) shows again a heterogeneity and sparsity in the walked path as well as clear re-visiting of domains as opposed to the continued visiting of new membrane areas. Performing the MSD (**Figures 5B,C**) and directional correlation

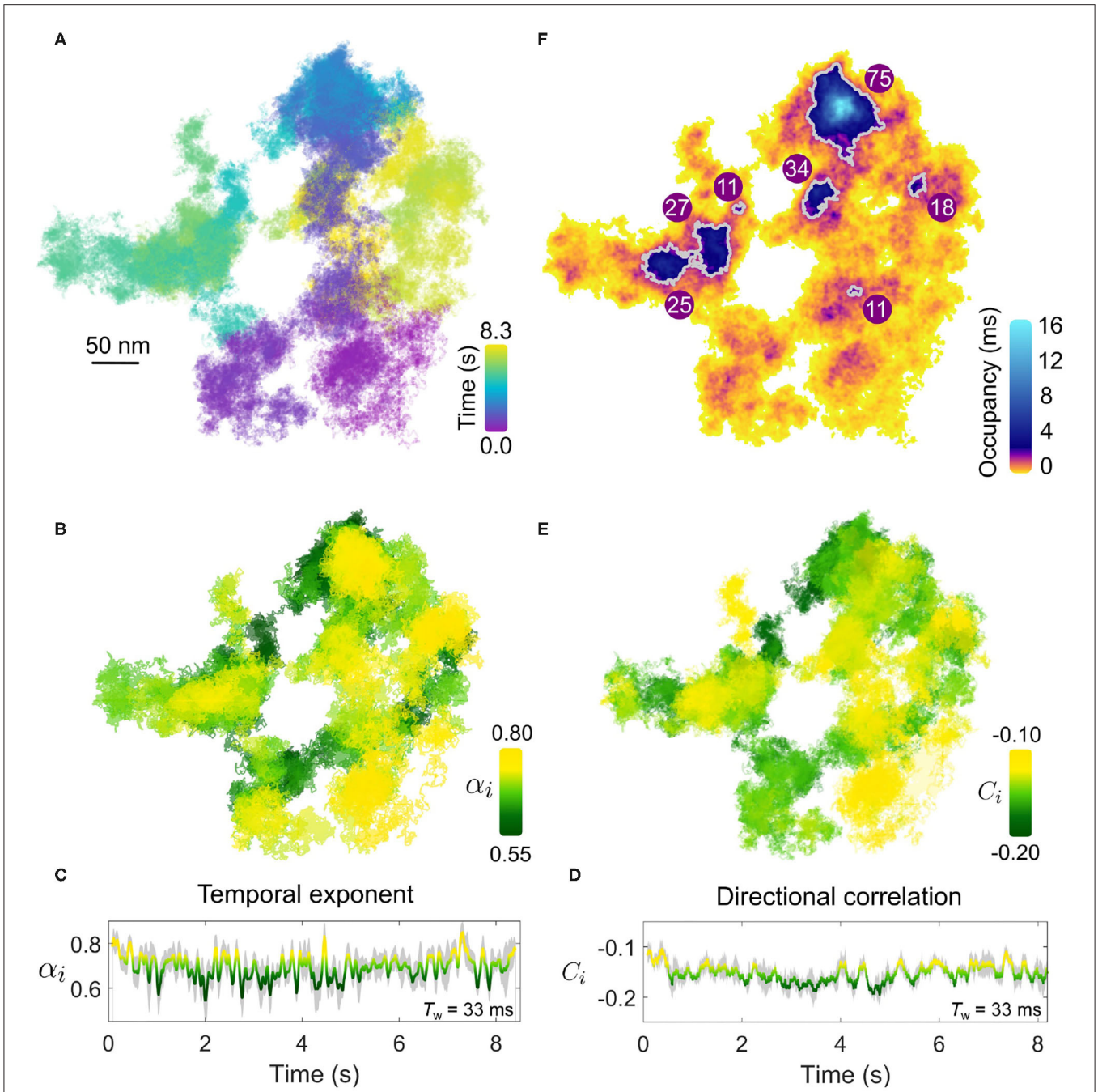

FIGURE 5 | Confining patches within an anomalous walk. **(A)** The EGFR-GNP trajectory projected in x-y plane recorded at 30,000 fps over 8.3 s on a COS-7 cell. **(B)** The temporal exponent of diffusion is plotted for the trajectory as the color-scale over the trajectory showing the spatial distribution. **(C)** The temporal exponent of diffusion plotted as a function of time. **(D)** The directional correlation is also plotted as a function of time. **(E)** Directional correlation plotted over the corresponding position in the trajectory and time. **(F)** The density of trajectory points across the space of the trajectory is plotted as an ATOM map where color denotes the occupancy of each 2D areal bin of size $4 \times 4\ nm^2$. Patches of extra-ordinary occupancy are outlined in gray as a guide to the eye. The numbers plotted represent the equivalent circular diameter in nm of the outlined patches.

analysis (**Figures 5D,E**) upon this trajectory for again a window of 1,000 frames ($T_w = 33$ ms) reveals interesting features. Firstly, we observe again strong heterogeneity in α and C throughout the trajectory that is region-specific but not necessarily always the same through the course of time of the measurement. In particular, the temporal exponent shows a strong variance in value but generally is centered around $\alpha = 0.7$. Interestingly, the directional correlation shows general agreement in trend with

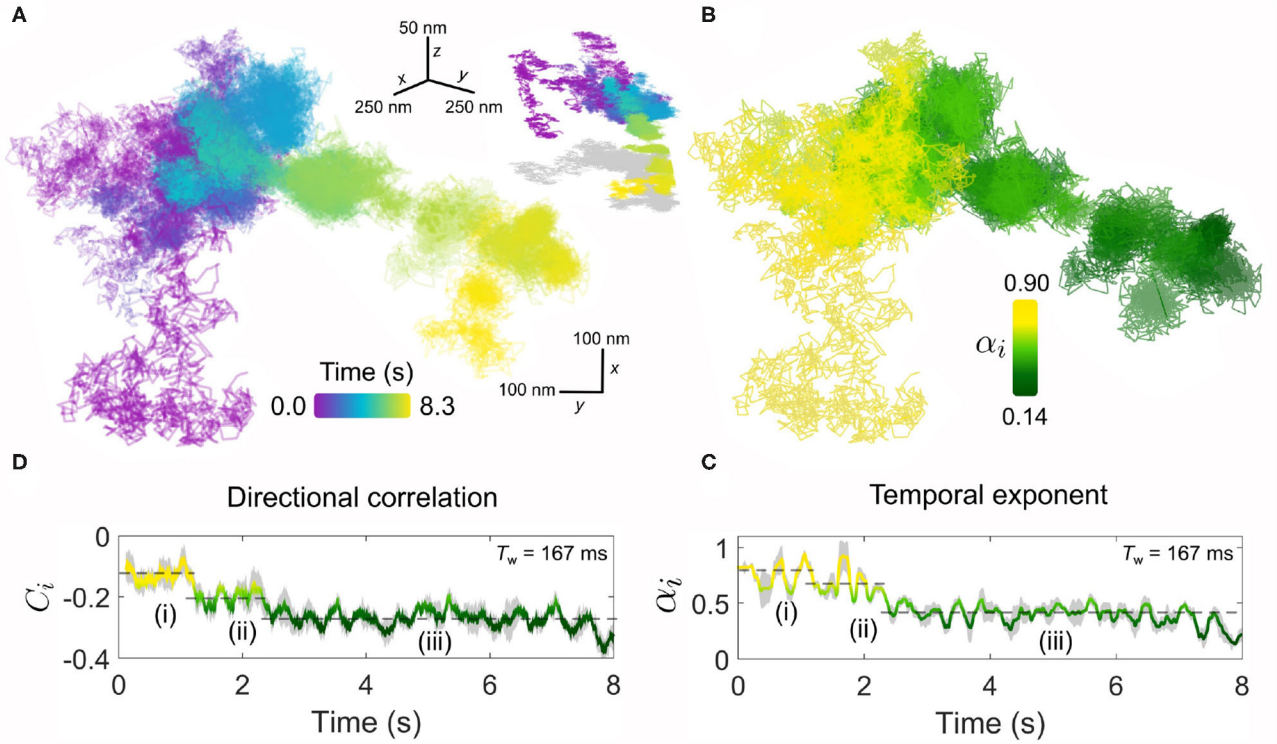

FIGURE 6 | The endurance of iSPT imaging enables visualization of dynamic, time-evolving processes. **(A)** An exemplar trajectory of a EGFR-GNP on a HeLa cell is plotted for a measurement over 8.3 s recorded at 6,000 fps. Inset: the 3D trajectory of the *x*-*y* projection shown in **(A)**, with a 2D "shadow" projection plotted in gray. **(B)** The temporal exponent of the trajectory presented in **(A)** plotted spatially over the trajectory positions. **(C)** Temporal exponent plotted as an explicit function of time. **(D)** The corresponding directional correlation of the trajectory is also plotted as a function of time. Both temporal exponent and directional correlation use a sliding window of 1,000 frames ($T_w = 167$ ms) and the dashed lines guide the eye to the three distinct phases of diffusive behavior, labeled (i)–(iii).

the temporal exponent, and is also suggesting "knock-back." But unlike the example of **Figure 4**, there is weaker correspondence between the sharp changes in the degree of sub-diffusion and the step correlations. Since these two forms of analysis probe different aspects of the EGFR-GNP trajectory this is entirely plausible. One possible interpretation is that the labeled EGFR-protein is slowed down within a "sticky" sub-domain because then the distance traveled in time, quantified by α_i, would show sub-diffusion, whilst if no immediate barrier or boundary is encountered no correlation in steps would be evident. Here we define sticky to mean orders of magnitude longer residency than typically observed from the surrounding membrane, here longer than 1 ms.

Furthermore, visual inspection also reveals the presence of patch domains consisting of a higher density of trajectory points. The presence of nanodomains on the membrane, where one believes that diffusion of a transmembrane protein becomes transiently arrested, is of great interest. The high temporal resolution of iSPT permits us to visualize the presence of domains where the EGFR-GNP becomes confined by simply dividing the *x*-*y* trajectory into 2D bins and counting the occupancy of each bin. Such a plot we refer to as the accumulated total occupancy map (ATOM) (Taylor et al., 2019). Confining domains would consist of a higher population of trajectory points than non-confining, sparse regions. **Figure 5F** presents the ATOM plot for the trajectory for an areal bin size of $4\times4\,\text{nm}^2$. Here we use a highly non-linear color scheme to denote the occupancy to elucidate the wide range in residence times. We calculate the residence time by multiplying the total number of trajectory points per bin by the exposure time of one frame. The ATOM plot of **Figure 5F** displays several clear patches of extended residency with a mean equivalent circular diameter in nanometers illustrated on each prominent patch outlined in gray. Such regions of extended residency might represent favorable biochemical, structural, or morphological features of the cell membrane, although lacking further information one can only speculate on the nature of such features.

One advantage of iSPT for investigating membrane processes is the ability to observe the EGFR-GNP for an extended, in principle indefinite, period owing to the absence of photo-degradation of the GNP probe. Coupled with the high temporal resolution and the sliding window analysis one can therefore monitor cellular processes in which the EGFR-GNP is involved, as reflected through marked changes in its diffusional behavior.

Figure 6 presents such an example for diffusion occurring on the plasma membrane. Inspecting the lateral trajectory **Figure 6A** reveals an apparent change in the diffusion which in time becomes progressively more spatially confined, with

eventually a concerted directional motion replacing the random-like exploration of the membrane. Examining the 3D projection of the trajectory (shown in the inset of **Figure 6A**), one sees the latter directed phase of the diffusion carries the EGFR-GNP down and away from the region of initial confinement. These distinct changes also manifest clearly in the kinetic parameters of the trajectory. For example, the temporal exponent (**Figures 6B,C**) confirms a stark transition from a nearly-free like diffusion ($\alpha_i = 0.9$) in the first several seconds of observation that quickly transitions into a strongly confined mode ($\alpha_i = 0.4$) that is maintained until the end of observation. Our sliding window analysis explores the diffusive nature to time lags bounded within the window length, here $T_w = 167$ ms, and thus we discover that within this phase the EGFR-GNP is strongly confined. These observations are similarly reflected in the directional correlation which displays persistent recoil from a confining obstacle and identifies three stages of the trajectories evolution, marked (i)–(iii).

Such a change in the diffusional behavior of EGFR shown here is evocative of processes such as the binding of the EGFR-EGF complex to the actin skeleton beneath the membrane. The actin-binding domain located on the EGFR (Den Hartigh et al., 1992) can guide association with the cytoskeleton. This interaction has been shown to lead to an oriented transport by the flow of the skeleton accompanied by a decrease in diffusion (de Bruin et al., 2007), since remodeling of cortical actin is an active and important organizational motif for membrane molecules (Gowrishankar et al., 2012).

3.3. Confined Diffusion on the Plasma Membrane

Aside from sub-diffusion which still explores sufficiently large regions of the membrane, another mode observed is a diffusion where the probe moves very little from its original position and thus is often classified as being confined. These modes of diffusion are also interesting to investigate since restriction in the mobility of a membrane protein is an especially important aspect of membrane organization and a means to regulate function of signaling proteins such as EGFR.

In **Figure 7**, we present two examples of diffusion which is markedly confined within a spatial domain of approximately $100 \times 100\,\text{nm}^2$. The confined nature of the diffusion is most visually apparent when one compares the lateral trajectories of **Figures 7A,D** with that of **Figure 4A** which was recorded for the same duration and framerate. The temporal exponent of the diffusion, shown in **Figures 7B,E** for a sliding window length of 1,000 frames ($T_w = 33$ ms) similarly confirms the strong confinement of the EGFR with a consistent average value of $\alpha = 0.6$ observed for both confined examples, although the trajectory of **Figure 7A** shows slightly larger variance.

Here, in this example the diffusion occurs within a limited spatial region and within the apparent boundary of this region the entire space is repeatedly explored by the EGFR-GNP. This then opens the interesting possibility to examine the spatial occupancy of the trajectory through the ATOM plot wherein the frequent sampling of the membrane environment through our high-resolution tracking might reveal information about any structures influencing the EGFR-GNP diffusion. The ATOM plots for trajectories shown in **Figures 7A,D** are plotted in **Figures 7C,F**, respectively for an areal 2D bin of $4 \times 4\,\text{nm}^2$. Inspection of the occupancy elucidated in the ATOM maps reveals distinct patches and heterogeneous patches of particularly long confinement. In **Figure 7B**, we identify a patch of ≈ 25 nm diameter as well as intermediate structures, typically located centrally, with also circular-like structures. In **Figure 7F**, we find numerous patches of extended occupation which are not homogeneous, but appear perforated with holes, suggesting regions of partial exclusion. Inspection also suggests the presence of circular-structures of a similar mean size of 25 nm, possibly pointing toward structures in the membrane the EGFR-GNP is interacting with whilst confined within the corral.

Another important example of confinement of a diffusing protein which occurs on the plasma membrane is that of confinement into "pits" or "bowls" that are often associated with endocytosis of membrane proteins. For example, it is known that one route for EGFR internalization is through clathrin-mediated endocytosis, where clathrin assembles a bowl-like structure to envelope the portion of the membrane to be internalized.

In **Figures 8A,B**, we present an example of an EGFR-GNP trajectory, seen from two perspectives, recorded at 20,000 fps over 1.0 s, and a second example in **Figure 8C** recorded at 30,000 fps over 3.2 s. Both examples show a 3D trajectory which reveals the EGFR-GNP is confined to the surface of a 3D bowl, with both examples presenting a bowl with an approximate diameter of 350 nm. The bowl morphology is most apparent when one interpolates through all the trajectory points to render an effective smooth surface, shown in **Figure 8D**.

In previous work, we observed the trajectory of the EGFR-GNP within such a bowl that suggested a persistent rotation of the probe around the center of mass of the bowl. We denote the angular position of the probe with ϕ, shown schematically in **Figure 8D**, and plot the angular position as a function of time for the trajectories of **Figures 8A,C** in **Figures 8E,F**, respectively. In these angular plots, the radial extent denotes time, and in doing so one sees a back and forth rotation in **Figure 8E**, as reported previously (Taylor et al., 2019). It should be noted however, that not all bowl-like confinements necessarily exhibit this clear and persistent rotational motion. **Figure 8F** presents an example where no coherent rotational motion is seen, instead the probe was able to diffuse more erratically about the entire surface, but with occupancy favoring the lower regions of the bowl.

Given that EGFR is known to be internalized via clathrin mediated endocytosis and the similarity these EGFR-GNP bowl-trajectories bear with such pits, a potential biological origin is identified. It stands as an exciting line of future inquiry, however, to affirm the role these pits play in the EGFR membrane biology. Furthermore, one can identify whether the EGFR-GNP probe is mobile within a static membrane bowl, or whether the probe is bound to the membrane and the whole bowl itself undergoes rotation or alternatively whether a combination of the two is at play. Nonetheless, these measurements demonstrate the potential for iSPT to provide new avenues for deeper nanoscopic insight into established membrane biology.

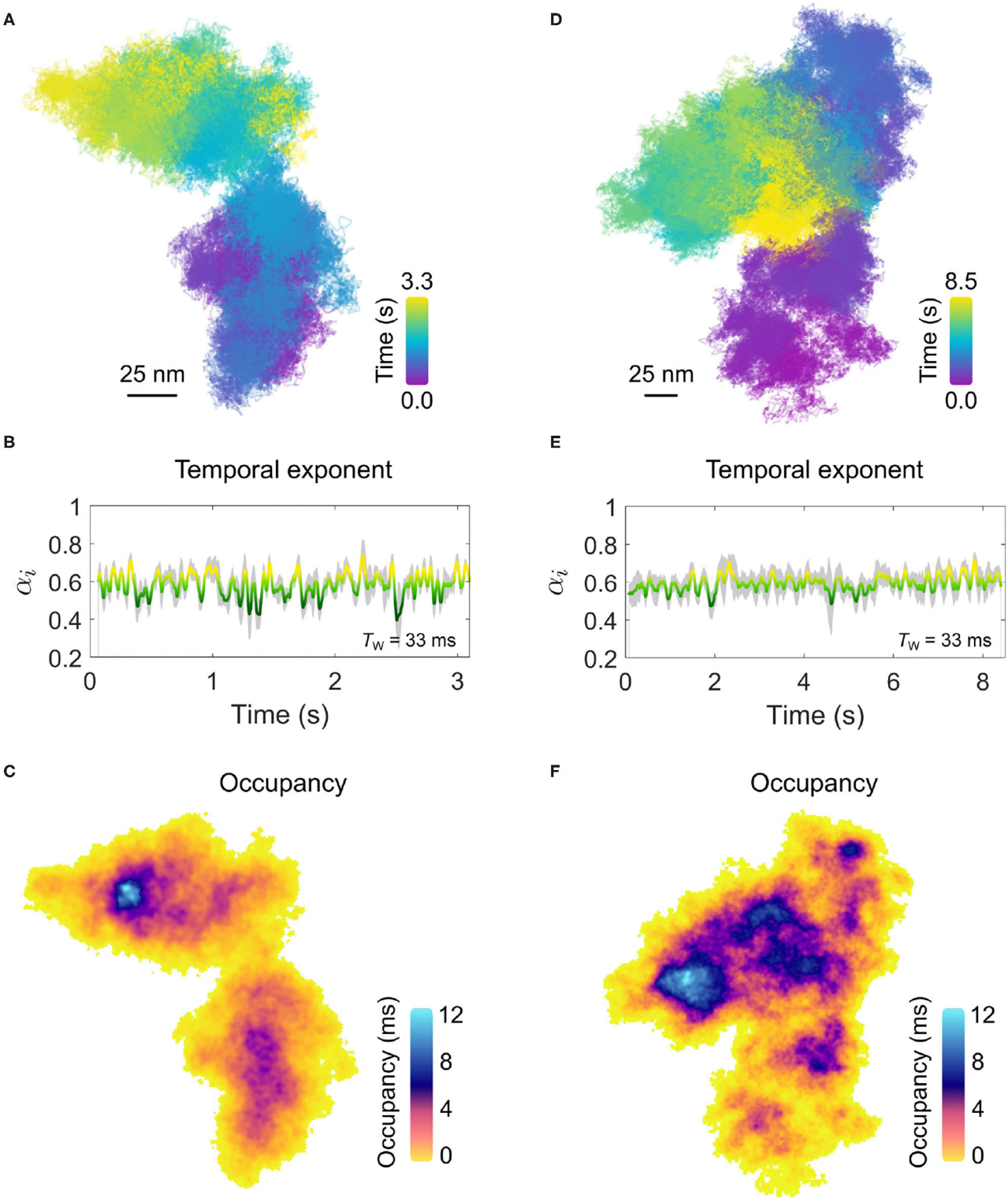

FIGURE 7 | Confinement on the plasma membrane of a COS-7 cell. **(A)** The trajectory for an example of confined EGFR-GNP diffusion on a COS-7 cell is presented. The imaging framerate of 30,000 fps for a total of 3.3 s gives a total of 100,000 trajectory points. **(B)** The temporal exponent for the trajectory in **(A)** with an averaging window of $T_w = 33$ ms. **(C)** The respective ATOM plot for the trajectory of **(A)** is presented in **(C)**. The areal bin size is 4×4 nm^2 and patches of extra-ordinary residence are reflected in the non-uniform color scale encoding total occupation time. **(D)** The trajectory for a second example of confined membrane diffusion, recorded at the same framerate as **(A)**, but for 8.5 s, giving a total of 250,000 recordings. **(E)** The corresponding temporal exponent for the trajectory in **(D)** with an averaging window of $T_w = 33$ ms. **(F)** The ATOM plot for the trajectory of **(D)**, with an areal bin size is 4×4 nm^2.

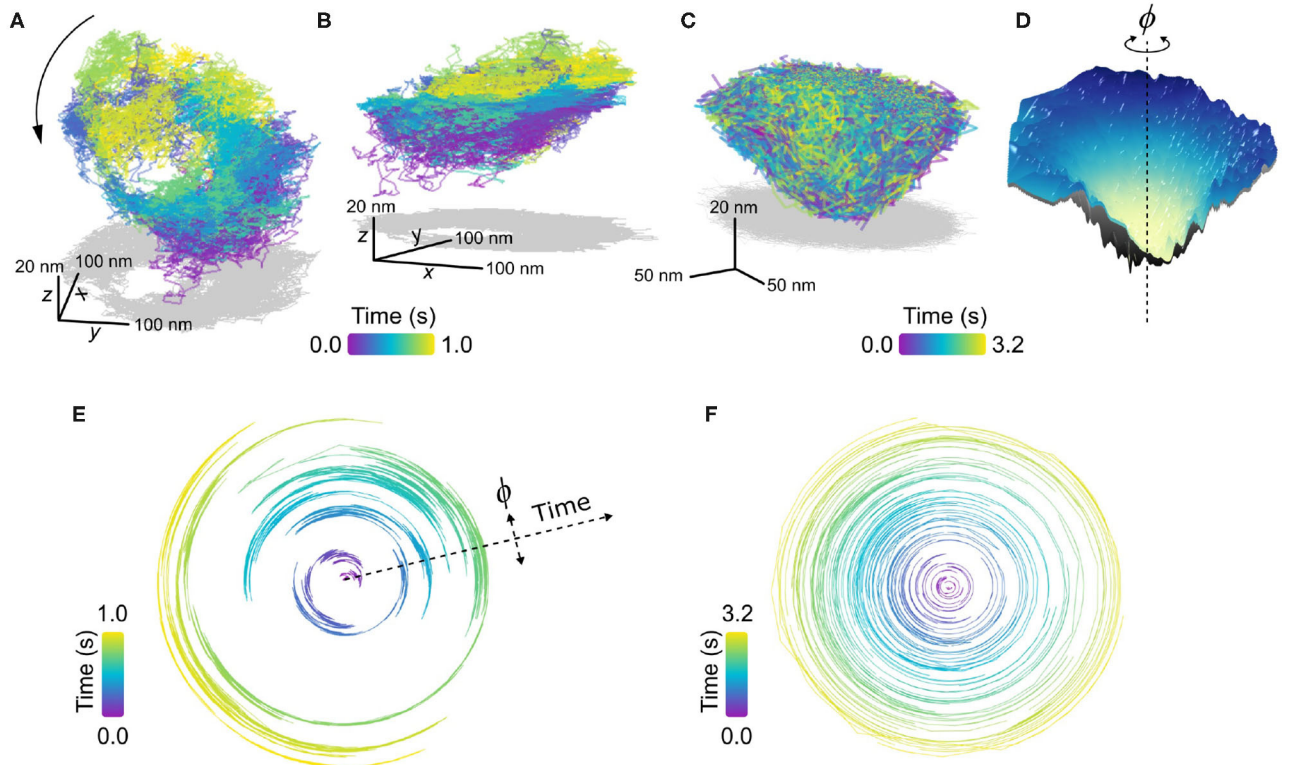

FIGURE 8 | Confinement into bowl/pit-like on the plasma membrane. **(A,B)** Trajectory of a confined EGFR-GNP on a HeLa cell displaying a tilted "bowl" or "pit"-like morphology, as seen from two perspectives. The trajectory was recorded at 20,000 fps for 1.0 s. Gray plots represents the 2D projection. **(C)** A second exemplary trajectory of a pit-like confinement, recorded at 30,000 fps for 3.2 s on a COS-7 cell. **(D)** An interpolated smooth surface of elucidating the pit topology from **(C)**, with the center of rotation marked with a dashed line. **(E)** Angular trajectory of the EGFR-GNP about the center of the bowl from **(A)**, where the radial position denotes time. **(F)** Angular trajectory of the EGFR-GNP about the center of the bowl from **(C)**.

3.4. Directed Motion

A final example of another interesting mode of protein mobility is that of motion in a single concerted direction, as shown in **Figure 9**. In the cellular context, such directed motion is typically due to active transport processes mediated by motor proteins that move organelles and endocytosed vesicles along the intracellular network of cytoskeletal filaments (Caspi et al., 2000; Verhey et al., 2011; Granger et al., 2014). We might suppose in the examples shown in **Figure 9** that EGFR-GNP is internalized within a vesicle inside of the cell, and is being trafficked within the cellular corpus.

In **Figure 9A**, we consider an example recorded at 10,000 fps wherein one sees a concerted diffusion along a given direction for several seconds that is then followed by a reverse walk and then a change in direction near orthogonal to the previous. Inspection of the trajectory in 3D reveals in fact that the second leg of the walk lies above the first, suggesting a switch in the track along which the walk occurs. The typical track width is seen to be around 20 nm.

A trajectory with such a persistent directionality is described as being super-diffusive as the time-dependence of the MSD as $\alpha > 1$. In **Figure 9B**, we present the macroscopic MSD computed by taking the complete trajectory at once, and find $\alpha = 1.98$, which one can visualize through the upward curving slope of the MSD. The inset of **Figure 9B** presents the same MSD plotted on a log-log scale wherein on can see clearly the super-diffusive transport behavior manifest over longer time scales ($\tau > 0.01\,s$) and at shorter time scales ($\tau > 0.01$ s) a more sub-diffusive time-dependence is apparent. We can explore this sub-diffusive aspect of the trajectory more closely by considering the rolling temporal exponent, shown in **Figure 9C**, for a temporal window of $T_w = 100$ ms. Here, one sees the temporal exponent fluctuates around $\alpha \approx 0.54$. One can anticipate such 'confined'-like behavior in the short-time diffusion since the EGFR-GNP is likely confined to a vesicle which itself is tethered to the intracellular filament. Over longer timescales the processive mobility begins to emerge, reflected in the increasing value in α.

A second example, of super-diffusive mobility is presented in **Figure 9D** for a trajectory recorded at 1,000 fps over 30 s observation time. In this example, a strongly linear track with a mean width of 10 nm is evident. Careful analysis of such trajectories shown in **Figures 9A,D** allows us to not only identify the diffusive mode of transport but other important characteristics such as the velocity, step size and dwell time associated with the specific motor proteins which traffic cargo along these filaments within the cell. Taking into consideration that here we monitor the movement of EGFR most likely

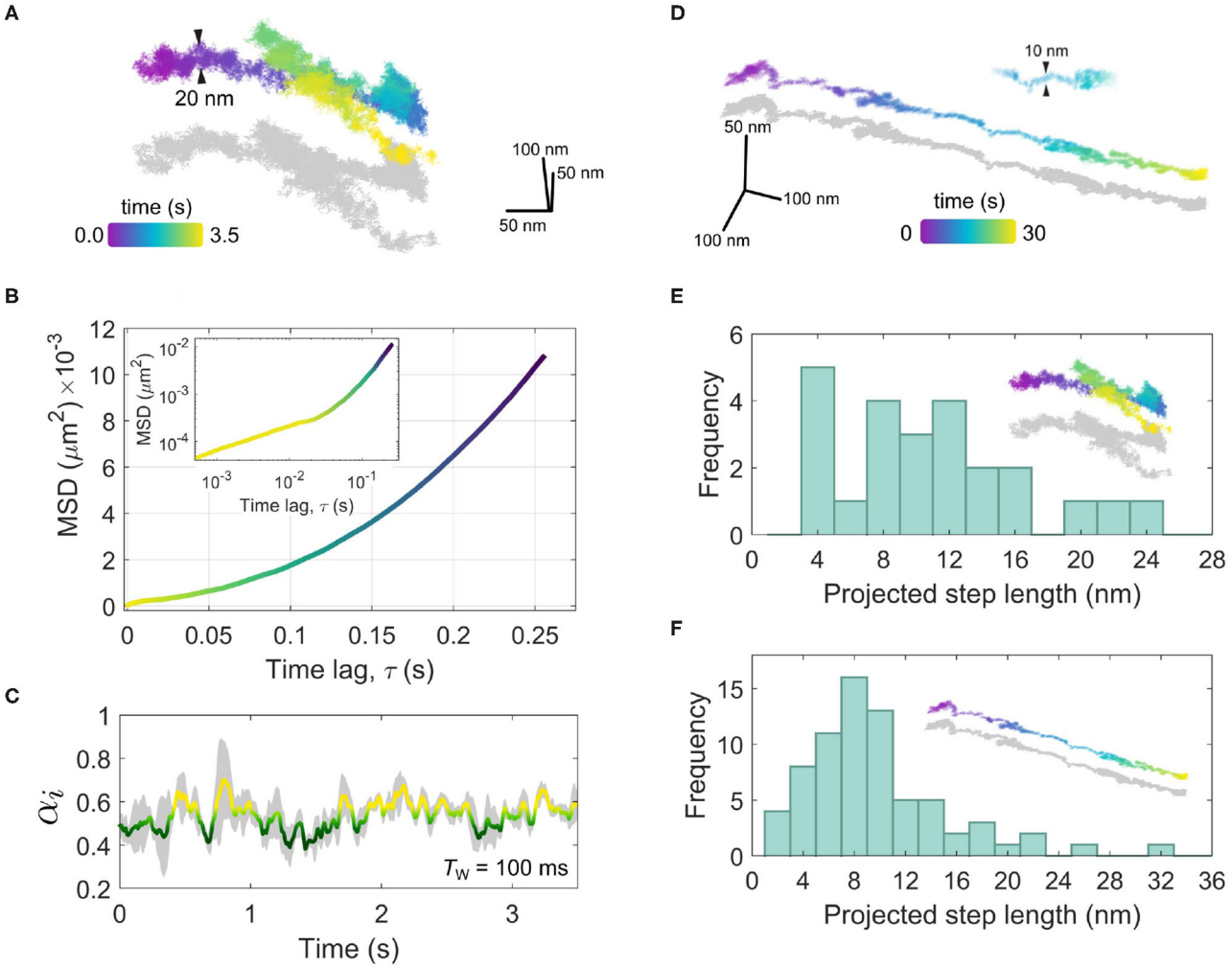

FIGURE 9 | Directed motion of the EGFR-GNP probe. **(A)** A trajectory recorded at 10,000 fps for 3.5 s showing a concerted linear trafficking of the EGFR-GNP probe on a HeLa cell. The typical width of the trajectory track is 20 nm. **(B)** The MSD of the trajectory from **(A)**, showing super-diffusive mobility. The inset is the same MSD plotted on a log-log scale. **(C)** The temporal exponent of the trajectory from **(A)** for a rolling window of $T_W = 100$ ms. **(D)** A second example of a 3D trajectory showing directed motion, recorded at 1,000 fps for a duration of 30 s. The width of the track is approximately 10 nm. **(E)** A histogram of prominent steps projected into the direction of travel, from the trajectory in **(A)**. **(F)** A histogram of prominent steps projected onto the direction of travel, taken the trajectory shown in **(D)**.

trapped in an intracellular vesicle, the inspection of these features of *in vivo* transport is fraught with complications and nuanced interpretation. In addition to active transport, velocity and step size will be affected by indirect movements such as polymerization or depolymerization of the filament it is attached to. Moreover, one must be mindful of the region within the cell where the EGFR-GNP is being tracked. If the filament is not lying flat to the coverslip, for example being located near the nucleus and orientated randomly, then what one observes in 2D is a projection of the true trajectory and hence it is not an accurate representation of the true step size. In iSCAT one can capture the 3D position so such a problem can be remedied. However, since the trajectories in **Figure 9** appear near-parallel to the focal plane, one can assume this skew is not significant in these recordings. Whilst it is beyond the scope of this work to draw specific conclusions as to the behavior exhibited in **Figure 9**, it is nonetheless interesting to inspect what iSPT can provide in exploring *in vivo* transport and the issues surrounding it.

To inspect the occurrence of a preferred step length in the trajectories of **Figures 9A,D** we define a linear axis that lies through the global direction of travel and onto this we project each individual step. We then may compute the accumulated distance walked by summing all projected steps and by using a peak-finding algorithm we can extract positions separating prominent steps along the walk. **Figure 9E** presents a histogram of the prominent projected steps from the trajectory shown in **Figure 9A** (denoted by the inset) wherein one sees a preference for steps with an approximate integer multiple of 4 nm, most of which in a range up to 24 nm.

In **Figure 9F**, a similar step-size histogram is given for the trajectory of **Figure 9D**. In this latter example one also sees a similar distribution, but now with a stronger bias toward steps of $\approx$ 8 nm.

Elucidation of the step size associated with specific motor proteins has been the subject of numerous *in vitro* experiments wherein individual filaments and single motor proteins are investigated under pristine conditions (e.g., Hirakawa et al., 2000; Köhler et al., 2003; Leduc et al., 2007; Ali et al., 2011; Hundt et al., 2016). Whilst much of these investigations to quantify the step size have been done with fluorescence microscopies, recent efforts have harnessed the improved resolution of iSPT to identify the exact stepping mechanism of single myosin V (Ortega Arroyo et al., 2014; Andrecka et al., 2015), also *in vitro*, which has remained a long standing matter of debate. The tracking and interpretation of transport mediated by motor proteins *in vivo* within the living cell is a much more complex scenario, since it can involve more than just one transport mechanism. Various studies have, for example, revealed a switch of the transporting motor protein species such as from myosin, which travels on actin filaments to kinesin, which travels upon microtubules (Provance et al., 2008; Kapitein et al., 2013). Additionally, these motor proteins not only alternate when transporting cargo, but can also be attached to the vesicle at the same time, requiring cooperative and even coordinated interactions (Gross et al., 2002; Levi et al., 2006; Ali et al., 2011). Furthermore, sub-division of the anticipated characteristic steps sizes can occur, as observed in *in vitro* experiments with kinesin (Leduc et al., 2007) and in live cells with myosin II (Fujita et al., 2019).

The step sizes and track widths of the trajectories in **Figure 9** are in the range of step sizes reported for common molecular motor proteins including kinesin, myosin II, myosin V, and VI in analogous *in vitro* and live cell measurements (Yildiz et al., 2003; Ökten et al., 2004; Leduc et al., 2007; Pierobon et al., 2009; Ali et al., 2011; Fujita et al., 2019) and in good agreement with the widths of 7 nm of single actin filaments and 25 nm of microtubules (Cooper, 2000). Therefore, these trajectories likely represent examples of active transport within the cell. However, lacking further information one may only speculate as to the molecular origin of these observed step sizes since the step size alone is not a distinctive characteristic of a particular motor protein and may be affected by interactions, cooperative and antagonistic effects in a living cell. One also has to consider that most of the *in vivo* and *in vitro* studies measure step size by labeling the motor protein itself, while we, in contrast, see the stepping behavior of the transported cargo.

To address the issue of intracellular transport more conclusively, one requires further investigation with a larger sample size to draw a more robust statistical analysis as well as measurement which harnesses fluorescence-based labeling to identify and visualize intracellular filaments and motor proteins in parallel with the iSPT tracking. Nonetheless, these initial efforts and recent similar *in vivo* iSPT tracking of cytoplasmatic vesicle transport (Huang et al., 2017b) demonstrate that iSPT is well-suited to investigate the nanoscopic minutia of intracellular transport events in living cells.

DISCUSSION: iSPT FOR INVESTIGATION OF MOBILITY WITHIN THE LIVE CELL

iSPT Microscopy

iSPT microscopy over the past few years has demonstrated great potential for new avenues of investigation into membrane diffusion, whether on synthetic or live cell membranes, owing to its high detection sensitivity affording fast and precise particle tracking. The power of the technique lies in the exploitation of interference between the light scattered by the probe and that which naturally reflects off the sample coverslip. For this reason iSPT, and more generally iSCAT microscopy, does not require any special equipment, save for a suitably fast camera to achieve high imaging rates. This makes iSCAT microscopy easy to implement on existing microscopes, including commercial fluorescence microscopes, and as both microscopies are mutually compatible (Kukura et al., 2009) they can also be performed in parallel. This is particularly important in live cell imaging where fluorescent labeling is useful for identifying specific cell and membrane components and features.

Phototoxicity

One important issue in live cell imaging is the role of photodamage associated with high laser intensities commonly associated with high-resolution microscopies (Laissue et al., 2017). The threshold for potential cell damage depends on the particular cells in use as well as the particular aspect of the membrane and cell biology under investigation (Wäldchen et al., 2015). We have demonstrated previously one can achieve high framerate and accurate tracking of EGFR-GNP probes on HeLa cells using illumination powers that are tolerable for cell viability (Taylor et al., 2019), being on the order of no more than 10 kWcm^{-2}. In general, using illumination wavelengths toward the red end of the spectrum (beginning around 600 nm) appears to be the most compatible for preserving cell viability. One asset of iSCAT microscopy is that, unlike fluorescence, one has complete flexibility in choice of the wavelength used and thus it is possible to perform iSCAT microscopies at wavelengths that preserve cell health whilst also maintaining high framerate imaging and good signal-to-noise ratio.

Influence of the Probe

An issue often raised in SPT is to what extent the probe influences the diffusive process and membrane biology under investigation. The label, depending on its geometry and functionalization introduces multivalent binding, non-specific binding as well as the physical size adding steric hindrances to the crowded membrane environment. The latter of which is an important consideration for colloidal probes particularly used for iSPT. In addition, because the localization precision now can approach the few-nm length scale, the influence of the GNP-to-ligand linker becomes of interest, in particular, its length and flexibilty, and how these might affect the accuracy in localization of the associated protein. Many of these questions are not fully answered, but recent studies have investigated these issues of multi-valent labeling and efforts to control it (Reina et al., 2018; Liao et al., 2019), as well as the influence of colloidal probe size

(Ritchie et al., 2005; Clausen and Lagerholm, 2011; Etoc et al., 2018). In the case of the latter, the size of the probe may not have significant effects on diffusion within the cell as one would have initially assumed.

Similarly, in previous work, we also found the use of 48 nm EGF-GNP probes seemingly did not impair the EGFR signaling pathway or uptake via clathrin-mediated endocytosis (Taylor et al., 2019). To fully address this matter, one must systematically explore membrane diffusion for colloidal probes of differing sizes, as it has been recently demonstrated for synthetic membranes (Liao et al., 2019). Usage of smaller colloidal probes on the live cell membrane is challenging solely due to the dynamic speckle background which presents the biggest hurdle to overcome. However, new methods for background modeling and subtraction in interferometric microscopies are constantly being proposed (Cheng and Hsieh, 2017; Taylor et al., 2019; Lin et al., 2020; Mahmoodabadi et al., 2020), and so it is realistic that the challenge posed by the cell background will be met within the near future.

CONCLUSION AND OUTLOOK

iSPT microscopy stands as a promising technique to expand the frontiers of investigation into single molecule diffusion and membrane organization. The high resolution visualization of protein mobility in 3D provides a wealth of information hitherto inaccessible through conventional fluorescence microscopies. When coupled with complementary techniques such as super-resolution fluorescence and correlative electron microscopies, one is presented with an impressive tool box that could help addressing long standing questions regarding dynamic membrane organization such as the size, lifetime, and diffusive properties of membrane raft domains. In this work we have focused on demonstrating the applicability of high-resolution iSPT microscopy on the live cell, and as such rather than providing an exhaustive study into the membrane biology of the receptor. We remark that each of the phenomena discussed herein warrants an extended investigation of its own to fully characterize and explain the behaviors observed.

Furthermore, more broadly, iSCAT microscopy is an emergent and rapidly growing technique that is finding increasing applications in nanoscale biology, with aims ranging from label-free detection and mass-determination of single proteins and complexes, to the detection of viruses and vesicles as well as live cell imaging. Recent interdisciplinary efforts to model the iPSF as well as to address dynamic speckle background through machine learning opens new paths to exciting live-cell applications. This will allow the use of smaller scattering probes, multiple distinct scattering labels for co-labeling investigations as well as being able to perform imaging and iSPT over extended axial ranges within deeply scattering tissues.

MATERIALS AND METHODS

Widefield iSCAT Microscopy

Laser light from a supercontinuum white-light laser (NKT Photonics) was filtered down to $\lambda_{iSCAT} = 550 \pm 15$ nm through a Varia filter box. An 100x oil-immersion (NA = 1.4) objective was used to give a field of view of $5 \times 5 \mu m^2$, which was then imaged onto 128x128 pixels of a high-speed camera (Vision Research, Phantom, Miro LAB 3a10).

In practice, illumination can be from any coherent light source, for gold nanoparticles green light is optimal. The illumination is unpolarized to minimize polarization artifacts which can arise for high-NA imaging. The objective is oil-immersion to maximize collection efficiency.

Confocal Fluorescence Imaging

A Zeiss LSM 800 was used with a water-dipping objective (40x), and modified to accommodate an iSCAT microscope underneath. A wavelength of 650 nm was chosen to avoid overlapping with the wide-field iSCAT imaging wavelength and to mitigate potential damage to live cells.

Cell Culturing and Fluorescent Labeling

HeLa and COS-7 cells were grown in DMEM (Gibco Invitrogen) supplemented with 10% fetal calf serum (FCS, Life Technologies) in a humidified atmosphere at 37°C and 5% CO_2. For measurement, HeLa cells were plated onto a glass-bottomed sample dish (Ibidi GmBH) and grown to 70% confluency. Before measurement, each dish was rinsed twice with warmed PBS-BSA solution, serum starved for several hours and rinsed again with warmed PBS-BSA. Imaging was done in Leibovitz's L-15 Medium (1.5 ml Gibco, Invitrogen).

For tracking over-expressed EGFR on COS-7 cells, cells were counted and 90,000 cells per dish were seeded. The next day, medium was replaced by 3 ml fresh DMEM and the Lipofectamine 3000 transfection mix was added (prepared according to the manufacturer's protocol, ThermoFisher). [Details: 4.6 μl Lipofectamine 3000, 2 μg plasmid DNA (EGFR-EGFP, addgene #32751) and 4 μl P3000 Reagent]. For imaging, cells were rinsed twice with DPBS and 3 ml of pre-warmed Leibovitz's L-15 medium (without phenol red, ThermoFisher) were added.

When placed on the microscope, each culture was held at 37°C by a home-built objective heater. A micropipette (Piezo Drill Tip, Eppendorf) was used to deliver 10 μl of the EGF–GNPs to a local region of the culture, with observation beginning immediately thereafter.

Gold Nanoparticle Probes

GNPs with a diameter of 48 nm were functionalized with monoclonal anti-biotin (British Biocell International), and GNPs with diameters of 20 nm, functionalized with streptavidin (British Biocell International), were conjugated at a molar ratio of 1:1 with biotinylated EGF (ThermoFisher) at a concentration of 0.66 nM. PBS was used as a buffer. The solution containing EGF–GNP was agitated for several hours at 37°C to assist conjugation, purified through centrifugation and diluted up to a final concentration of 0.1 nM. Cationic GNPs with diameter 50 nm were purchased from Nanopartz Inc. (item CC11-50-POS-DIH-50-1) and diluted to a ratio 1:100 in water.

DATA AVAILABILITY STATEMENT

The raw data supporting the conclusions of this article will be made available by the authors, without undue reservation.

AUTHOR CONTRIBUTIONS

RT and CH made iSCAT and fluorescence measurements. RT performed data analysis. CH prepared the live cell materials. RM and HD developed background correction routines for the iSCAT images. MK developed the combination of confocal fluorescence and iSCAT microscopy. VZ supervised interpretation and analysis of the data. AS supervised biological preparation and data interpretation. VS conceived and supervised the project. RT, CH, VZ, and AS wrote the manuscript. All authors discussed the results and commented on the manuscript.

FUNDING

This project was funded by an Alexander von Humboldt professorship, the Max Planck Society and the Research and Training Grant 1962 (Dynamic Interactions at Biological Membranes) of the German Research Foundation. RT acknowledges an Alexander von Humboldt fellowship. AS was also supported by grants from the German Research Foundation (grant nos. SCHA965/6-2 and SCHA965/9-1).

ACKNOWLEDGMENTS

The authors wish to thank Jennifer Lühr for assisting with the development of GNP pipetting, Moritz Grob, and David Albrecht for careful reading of the manuscript and insightful comments, Simone Ihloff for assistance with the culturing of cells, Navid Bonakdar, Maksim Schwab, Oliver Bittel, and Lothar Meier for designing and fabricating the sample heating system.

SUPPLEMENTARY MATERIAL

The Supplementary Material for this article can be found online at: https://www.frontiersin.org/articles/10.3389/fcell.2020.590158/full#supplementary-material

REFERENCES

Abulrob, A., Lu, Z., Baumann, E., Vobornik, D., Taylor, R., Stanimirovic, D., et al. (2010). Nanoscale imaging of epidermal growth factor receptor clustering: effects of inhibitors. *J. Biol. Chem.* 285, 3145–3156. doi: 10.1074/jbc.M109.073338

Albrecht, D., Winterflood, C. M., and Ewers, H. (2015). Dual color single particle tracking via nanobodies. *Methods Appl. Fluoresc.* 3:024001. doi: 10.1088/2050-6120/3/2/024001

Alcor, D., Gouzer, G., and Triller, A. (2009). Single-particle tracking methods for the study of membrane receptors dynamics. *Eur. J. Neurosci.* 30, 987–997. doi: 10.1111/j.1460-9568.2009.06927.x

Ali, M. Y., Kennedy, G. G., Safer, D., Trybus, K. M., Sweeney, H. L., and Warshaw, D. M. (2011). Myosin Va and Myosin VI coordinate their steps while engaged in an *in vitro* tug of war during cargo transport. *Proc. Natl. Acad. Sci. U.S.A.* 108, E535-E541. doi: 10.1073/pnas.1104298108

Andrecka, J., Arroyo, J. O., Takagi, Y., de Wit, G., Fineberg, A., MacKinnon, L., et al. (2015). Structural dynamics of myosin 5 during processive motion revealed by interferometric scattering microscopy. *eLife* 4:e05413. doi: 10.7554/eLife.05413

Arteaga, C. L., and Engelman, J. A. (2014). ErbB receptors: from oncogene discovery to basic science to mechanism-based cancer therapeutics. *Cancer Cell* 25, 282–303. doi: 10.1016/j.ccr.2014.02.025

Bag, N., Huang, S., and Wohland, T. (2015). Plasma membrane organization of epidermal growth factor receptor in resting and ligand-bound states. *Biophys. J.* 109, 1925–1936. doi: 10.1016/j.bpj.2015.09.007

Bouchaud, J.-P., and Georges, A. (1990). Anomalous diffusion in disordered media: statistical mechanisms, models and physical applications. *Phys. Rep.* 195, 127–293. doi: 10.1016/0370-1573(90)90099-N

Caspi, A., Granek, R., and Elbaum, M. (2000). Enhanced diffusion in active intracellular transport. *Phys. Rev. Lett.* 85, 5655–5658. doi: 10.1103/PhysRevLett.85.5655

Cheng, C.-Y., and Hsieh, C.-L. (2017). Background estimation and correction for high-precision localization microscopy. *ACS Photon.* 4, 1730–1739. doi: 10.1021/acsphotonics.7b00238

Chung, I., Akita, R., Vandlen, R., Toomre, D., Schlessinger, J., and Mellman, I. (2010). Spatial control of egf receptor activation by reversible dimerization on living cells. *Nature* 464, 783–787. doi: 10.1038/nature08827

Clausen, M., and Lagerholm, C. (2011). The probe rules in single particle tracking. *Curr. Protein Pept. Sci.* 12, 699–713. doi: 10.2174/138920311798841672

Clausen, M. P., and Lagerholm, B. C. (2013). Visualization of plasma membrane compartmentalization by high-speed quantum dot tracking. *Nano Lett.* 13, 2332–2337. doi: 10.1021/nl303151f

Cooper, G. M. (2000). *The Cell: A Molecular Approach, 2nd Edn.* Structure and Organization of Actin Filaments. Sunderland, MA: Sinauer Associates (2000). Available online at: https://www.ncbi.nlm.nih.gov/books/NBK9908/

De Brabander, M., Geuens, G., Nuydens, R., Moeremans, M., and De Mey, J. (1986). Microtubule-dependent intracellular motility investigated with nanometer particle video ultramicroscopy (nanovid ultramicroscopy). *Ann. N. Y. Acad. Sci.* 466, 666–668. doi: 10.1111/j.1749-6632.1986.tb38448.x

De Brabander, M., Nuydens, R., Geerts, H., and Hopkins, C. (1988). Dynamic behavior of the transferrin receptor followed in living epidermoid carcinoma (a431) cells with nanovid microscopy. *Cell Motil. Cytoskel.* 9, 30–47. doi: 10.1002/cm.970090105

de Bruin, K., Ruthardt, N., Von Gersdorff, K., Bausinger, R., Wagner, E., Ogris, M., et al. (2007). Cellular dynamics of EGF receptor-targeted synthetic viruses. *Mol. Ther.* 15, 1297–1305. doi: 10.1038/sj.mt.6300176

de Wit, G., Albrecht, D., Ewers, H., and Kukura, P. (2018). Revealing compartmentalized diffusion in living cells with interferometric scattering microscopy. *Biophys. J.* 114, 2945–2950. doi: 10.1016/j.bpj.2018.05.007

Den Hartigh, J. C., van Bergen en Henegouwen, P. M. P., Verkleij, A. J., and Boonstra, J. (1992). The EGF receptor is an actin-binding protein. *J. Cell Biol.* 119, 349–355. doi: 10.1083/jcb.119.2.349

Deschout, H., Zanacchi, F. C., Mlodzianoski, M., Diaspro, A., Bewersdorf, J., Hess, S. T., et al. (2014). Precisely and accurately localizing single emitters in fluorescence microscopy. *Nat. Methods* 11:253. doi: 10.1038/nmeth.2843

Destainville, N., Dumas, F., and Salomé, L. (2008). What do diffusion measurements tell us about membrane compartmentalisation? Emergence of the role of interprotein interactions. *J. Chem. Biol.* 1, 37–48. doi: 10.1007/s12154-008-0005-3

Dix, J. A., and Verkman, A. S. (2008). Crowding effects on diffusion in solutions and cells. *Annu. Rev. Biophys.* 37, 247–263. doi: 10.1146/annurev.biophys.37.032807.125824

Erazo-Oliveras, A., Fuentes, N. R., Wright, R. C., and Chapkin, R. S. (2018). Functional link between plasma membrane spatiotemporal dynamics, cancer

biology, and dietary membrane-altering agents. *Cancer Metastasis. Rev.* 37, 519–544. doi: 10.1007/s10555-018-9733-1

Etoc, F., Balloul, E., Vicario, C., Normanno, D., Liße, D., Sittner, A., et al. (2018). Non-specific interactions govern cytosolic diffusion of nanosized objects in mammalian cells. *Nat. Mater.* 17, 740–746. doi: 10.1038/s41563-018-0120-7

Freed, D. M., Bessman, N. J., Kiyatkin, A., Salazar-Cavazos, E., Byrne, P. O., Moore, J. O., et al. (2017). EGFR ligands differentially stabilize receptor dimers to specify signaling kinetics. *Cell* 171, 683–695. doi: 10.1016/j.cell.2017.09.017

Fujita, K., Ohmachi, M., Ikezaki, K., Yanagida, T., and Iwaki, M. (2019). Direct visualization of human myosin ii force generation using DNA origami-based thick filaments. *Commun. Biol.* 2, 1–11. doi: 10.1038/s42003-019-0683-0

Fujiwara, T., Ritchie, K., Murakoshi, H., Jacobson, K., and Kusumi, A. (2002). Phospholipids undergo hop diffusion in compartmentalized cell membrane. *J. Cell Biol.* 157, 1071–1082. doi: 10.1083/jcb.200202050

Fujiwara, T. K., Iwasawa, K., Kalay, Z., Tsunoyama, T. A., Watanabe, Y., Umemura, Y. M., et al. (2016). Confined diffusion of transmembrane proteins and lipids induced by the same actin meshwork lining the plasma membrane. *Mol. Biol. Cell* 27, 1101–1119. doi: 10.1091/mbc.E15-04-0186

Geerts, H., De Brabander, M., Nuydens, R., Geuens, S., Moeremans, M., De Mey, J., et al. (1987). Nanovid tracking: a new automatic method for the study of mobility in living cells based on colloidal gold and video microscopy. *Biophys. J.* 52, 775–782. doi: 10.1016/S0006-3495(87)83271-X

Gowrishankar, K., Ghosh, S., Saha, S., Rumamol, C., Mayor, S., and Rao, M. (2012). Active remodeling of cortical actin regulates spatiotemporal organization of cell surface molecules. *Cell* 149, 1353–1367. doi: 10.1016/j.cell.2012.05.008

Granger, E., McNee, G., Allan, V., and Woodman, P. (2014). The role of the cytoskeleton and molecular motors in endosomal dynamics. *Semin. Dev. Cell Biol.* 31, 20–29. doi: 10.1016/j.semcdb.2014.04.011

Gross, S. P., Tuma, M. C., Deacon, S. W., Serpinskays, A. S., Reilein, A. R., and Gelfand, V. I. (2002). Interactions and regulation of molecular motors in xenopus melanophores. *J. Cell Biol.* 156, 855–865. doi: 10.1083/jcb.200105055

Hirakawa, E., Higuchi, H., and Toyoshima, Y. Y. (2000). Processive movement of single 22s dynein molecules occurs only at low ATP concentrations. *Proc. Natl. Acad. Sci. U.S.A.* 97, 2533–2537. doi: 10.1073/pnas.050585297

Huang, Y.-F., Zhuo, G.-Y., Chou, C.-Y., Lin, C.-H., Chang, W., and Hsieh, C.-L. (2017a). Coherent brightfield microscopy provides the spatiotemporal resolution to study early stage viral infection in live cells. *ACS Nano* 11, 2575–2585. doi: 10.1021/acsnano.6b05601

Huang, Y.-F., Zhuo, G.-Y., Chou, C.-Y., Lin, C.-H., and Hsieh, C.-L. (2017b). Label-free, ultrahigh-speed, 3D observation of bidirectional and correlated intracellular cargo transport by coherent brightfield microscopy. *Nanoscale* 9, 6567–6574. doi: 10.1039/C7NR00604G

Hundt, N., Steffen, W., Pathan-Chhatbar, S., Taft, M. H., and Manstein, D. J. (2016). Load-dependent modulation of non-muscle myosin-2a function by tropomyosin 4.2. *Sci. Rep.* 6:20554. doi: 10.1038/srep20554

Isichenko, M. B. (1992). Percolation, statistical topography, and transport in random media. *Rev. Mod. Phys.* 64:961. doi: 10.1103/RevModPhys.64.961

Jacobsen, V., Klotzsch, E., and Sandoghdar, V. (2007). "Chapter 9: Interferometric detection and tracking of nanoparticles," in *Nano Biophotonics: Science and Technology, Vol. 3*, eds H. Masuhara, S. Kawata, and F. Tokunaga (Amsterdam: Elsevier), 143–159. doi: 10.1016/S1574-0641(07)80014-3

Jacobson, K., Liu, P., and Lagerholm, B. C. (2019). The lateral organization and mobility of plasma membrane components. *Cell* 177, 806–819. doi: 10.1016/j.cell.2019.04.018

Jacobson, K., Mouritsen, O. G., and Anderson, R. G. (2007). Lipid rafts: at a crossroad between cell biology and physics. *Nat. Cell Biol.* 9, 7–14. doi: 10.1038/ncb0107-7

Jaqaman, K., and Grinstein, S. (2012). Regulation from within: the cytoskeleton in transmembrane signaling. *Trends Cell Biol.* 22, 515–526. doi: 10.1016/j.tcb.2012.07.006

Jin, S., and Verkman, A. (2007). Single particle tracking of complex diffusion in membranes: simulation and detection of barrier, raft, and interaction phenomena. *J. Phys. Chem. B* 111, 3625–3632. doi: 10.1021/jp067187m

Kapitein, L. C., van Bergeijk, P., Lipka, J., Keijzer, N., Wulf, P. S., Katrukha, E. A., et al. (2013). Myosin-V opposes microtubule-based cargo transport and drives directional motility on cortical actin. *Curr. Biol.* 23, 828–834. doi: 10.1016/j.cub.2013.03.068

Kepten, E., Bronshtein, I., and Garini, Y. (2013). Improved estimation of anomalous diffusion exponents in single-particle tracking experiments. *Phys. Rev. E* 87:052713. doi: 10.1103/PhysRevE.87.052713

Kepten, E., Weron, A., Sikora, G., Burnecki, K., and Garini, Y. (2015). Guidelines for the fitting of anomalous diffusion mean square displacement graphs from single particle tracking experiments. *PLoS ONE* 10:e117722. doi: 10.1371/journal.pone.0117722

Köhler, D., Ruff, C., Meyhöfer, E., and Bähler, M. (2003). Different degrees of lever arm rotation control myosin step size. *J. Cell Biol.* 161, 237–241. doi: 10.1083/jcb.200212039

Kovacs, E., Zorn, J. A., Huang, Y., Barros, T., and Kuriyan, J. (2015). A structural perspective on the regulation of the epidermal growth factor receptor. *Annu. Rev. Biochem.* 84, 739–764. doi: 10.1146/annurev-biochem-060614-034402

Krapf, D. (2018). Compartmentalization of the plasma membrane. *Curr. Opin. Cell Biol.* 53, 15–21. doi: 10.1016/j.ceb.2018.04.002

Kukura, P., Ewers, H., Müller, C., Renn, A., Helenius, A., and Sandoghdar, V. (2009). High-speed nanoscopic tracking of the position and orientation of a single virus. *Nat. Methods* 6, 923–927. doi: 10.1038/nmeth.1395

Kusumi, A., Fujiwara, T. K., Chadda, R., Xie, M., Tsunoyama, T. A., Kalay, Z., et al. (2012). Dynamic organizing principles of the plasma membrane that regulate signal transduction: commemorating the fortieth anniversary of singer and Nicolson's fluid-mosaic model. *Annu. Rev. Cell Dev. Biol.* 28, 215–250. doi: 10.1146/annurev-cellbio-100809-151736

Kusumi, A., Nakada, C., Ritchie, K., Murase, K., Suzuki, K., Murakoshi, H., et al. (2005). Paradigm shift of the plasma membrane concept from the two-dimensional continuum fluid to the partitioned fluid: high-speed single-molecule tracking of membrane molecules. *Annu. Rev. Biophys. Biomol. Struct.* 34, 351–378. doi: 10.1146/annurev.biophys.34.040204.144637

Kusumi, A., Sako, Y., and Yamamoto, M. (1993). Confined lateral diffusion of membrane receptors as studied by single particle tracking (nanovid microscopy). Effects of calcium-induced differentiation in cultured epithelial cells. *Biophys. J.* 65, 2021–2040. doi: 10.1016/S0006-3495(93)81253-0

Kusumi, A., Tsunoyama, T. A., Hirosawa, K. M., Kasai, R. S., and Fujiwara, T. K. (2014). Tracking single molecules at work in living cells. *Nat. Chem. Biol.* 10, 524–532. doi: 10.1038/nchembio.1558

Laissue, P. P., Alghamdi, R. A., Tomancak, P., Reynaud, E. G., and Shroff, H. (2017). Assessing phototoxicity in live fluorescence imaging. *Nat. Methods* 14, 657–661. doi: 10.1038/nmeth.4344

Leduc, C., Ruhnow, F., Howard, J., and Diez, S. (2007). Detection of fractional steps in cargo movement by the collective operation of kinesin-1 motors. *Proc. Natl. Acad. Sci. U.S.A.* 104, 10847–10852. doi: 10.1073/pnas.0701864104

Levi, V., Serpinskaya, A. S., Gratton, E., and Gelfand, V. I. (2006). Organelle transport along microtubules in xenopus melanophores: evidence for cooperation between multiple motors. *Biophys. J.* 90, 318–327. doi: 10.1529/biophysj.105.067843

Liao, Y.-H., Lin, C.-H., Cheng, C.-Y., Wong, W. C., Juo, J.-Y., and Hsieh, C.-L. (2019). Monovalent and oriented labeling of gold nanoprobes for the high-resolution tracking of a single-membrane molecule. *ACS Nano* 13, 10918–10928. doi: 10.1021/acsnano.9b01176

Lin, S., He, Y., Li, H., Zhang, P., and Chen, X.-W. (2020). Multiscale modeling and analysis of interferometric scattering microscopy. *arXiv [Preprint]*. Available online at: https://arxiv.org/abs/2004.10575 (accessed May 30, 2020).

Lin, Y.-H., Chang, W.-L., and Hsieh, C.-L. (2014). Shot-noise limited localization of single 20 nm gold particles with nanometer spatial precision within microseconds. *Opt. Exp.* 22, 9159–9170. doi: 10.1364/OE.22.009159

Lindfors, K., Kalkbrenner, T., Stoller, P., and Sandoghdar, V. (2004). Detection and spectroscopy of gold nanoparticles using supercontinuum white light confocal microscopy. *Phys. Rev. Lett.* 93:037401. doi: 10.1103/PhysRevLett.93.037401

Linggi, B., and Carpenter, G. (2006). ErbB receptors: new insights on mechanisms and biology. *Trends Cell Biol.* 16, 649–656. doi: 10.1016/j.tcb.2006.10.008

Liu, Y.-L., Perillo, E. P., Liu, C., Yu, P., Chou, C.-K., Hung, M.-C., et al. (2016). Segmentation of 3d trajectories acquired by tsunami microscope: an application to EGFR trafficking. *Biophys. J.* 111, 2214–2227. doi: 10.1016/j.bpj.2016.09.041

Lyman, E., Hsieh, C.-L., and Eggeling, C. (2018). From dynamics to membrane organization: experimental breakthroughs occasion a "modeling manifesto." *Biophys. J.* 115, 595–604. doi: 10.1016/j.bpj.2018.07.012

Mahmoodabadi, R. G., Taylor, R. W., Kaller, M., Spindler, S., Mazaheri, M., Kasaian, K., et al. (2020). Point spread function in interferometric scattering microscopy (iSCAT). part i: aberrations in defocusing and axial localization. *Opt. Exp.* 28, 25969–25988. doi: 10.1364/OE.401374

Manzo, C., and Garcia-Parajo, M. F. (2015). A review of progress in single particle tracking: from methods to biophysical insights. *Rep. Prog. Phys.* 78:124601. doi: 10.1088/0034-4885/78/12/124601

Martin, D. S., Forstner, M. B., and Käs, J. A. (2002). Apparent subdiffusion inherent to single particle tracking. *Biophys. J.* 83, 2109–2117. doi: 10.1016/S0006-3495(02)73971-4

Mashaghi, A., Mashaghi, S., Reviakine, I., Heeren, R. M., Sandoghdar, V., and Bonn, M. (2014). Label-free characterization of biomembranes: from structure to dynamics. *Chem. Soc. Rev.* 43, 887–900. doi: 10.1039/C3CS60243E

Mazaheri, M., Ehrig, J., Shkarin, A., Zaburdaev, V., and Sandoghdar, V. (2020). Ultrahigh-speed imaging of rotational diffusion on a lipid bilayer. *Nano Lett.* 20, 7213–7219. doi: 10.1021/acs.nanolett.0c02516

McDonald, M. P., Gemeinhardt, A., König, K., Piliarik, M., Schaffer, S., Völkl, S., et al. (2018). Visualizing single-cell secretion dynamics with single-protein sensitivity. *Nano Lett.* 18, 513–519. doi: 10.1021/acs.nanolett.7b04494

Meroz, Y., and Sokolov, I. M. (2015). A toolbox for determining subdiffusive mechanisms. *Phys. Rep.* 573, 1–29. doi: 10.1016/j.physrep.2015.01.002

Metzler, R., Jeon, J.-H., Cherstvy, A. G., and Barkai, E. (2014). Anomalous diffusion models and their properties: non-stationarity, non-ergodicity, and ageing at the centenary of single particle tracking. *Phys. Chem. Chem. Phys.* 16, 24128–24164. doi: 10.1039/C4CP03465A

Metzler, R., and Klafter, J. (2000). The random walk's guide to anomalous diffusion: a fractional dynamics approach. *Phys. Rep.* 339, 1–77. doi: 10.1016/S0370-1573(00)00070-3

Montroll, E. W., and Lebowitz, J. (1976). *Studies in Statistical Mechanics*. North-Holland Publishing Company.

Munder, M. C., Midtvedt, D., Franzmann, T., Nuske, E., Otto, O., Herbig, M., et al. (2016). A pH-driven transition of the cytoplasm from a fluid-to a solid-like state promotes entry into dormancy. *eLife* 5:e09347. doi: 10.7554/eLife.09347

Oda, K., Matsuoka, Y., Funahashi, A., and Kitano, H. (2005). A comprehensive pathway map of epidermal growth factor receptor signaling. *Mol. Syst. Biol.* 1:2005.0010. doi: 10.1038/msb4100014

Ökten, Z., Churchman, L. S., Rock, R. S., and Spudich, J. A. (2004). Myosin VI walks hand-over-hand along actin. *Nat. Struct. Mol. Biol.* 11, 884–887. doi: 10.1038/nsmb815

Ortega Arroyo, J., Andrecka, J., Spillane, K., Billington, N., Takagi, Y., Sellers, J., et al. (2014). Label-free, all-optical detection, imaging, and tracking of a single protein. *Nano Lett.* 14, 2065–2070. doi: 10.1021/nl500234t

Parthasarathy, R. (2012). Rapid, accurate particle tracking by calculation of radial symmetry centers. *Nat. Methods* 9:724. doi: 10.1038/nmeth.2071

Pierobon, P., Achouri, S., Courty, S., Dunn, A. R., Spudich, J. A., Dahan, M., et al. (2009). Velocity, processivity, and individual steps of single myosin v molecules in live cells. *Biophys. J.* 96, 4268–4275. doi: 10.1016/j.bpj.2009.02.045

Pike, L. J. (2006). Rafts defined: a report on the keystone symposium on lipid rafts and cell function. *J. Lipid Res.* 47, 1597–1598. doi: 10.1194/jlr.E600002-JLR200

Piliarik, M., and Sandoghdar, V. (2014). Direct optical sensing of single unlabelled proteins and super-resolution imaging of their binding sites. *Nat. Commun.* 5, 1–8. doi: 10.1038/ncomms5495

Pinaud, F., Clarke, S., Sittner, A., and Dahan, M. (2010). Probing cellular events, one quantum dot at a time. *Nat. Methods* 7, 275–285. doi: 10.1038/nmeth.1444

Provance, D. W., Addison, E. J., Wood, P. R., Chen, D. Z., Silan, C. M., and Mercer, J. A. (2008). Myosin-VB functions as a dynamic tether for peripheral endocytic compartments during transferrin trafficking. *BMC Cell Biol.* 9:44. doi: 10.1186/1471-2121-9-44

Reina, F., Galiani, S., Shrestha, D., Sezgin, E., de Wit, G., Cole, D., et al. (2018). Complementary studies of lipid membrane dynamics using iSCAT and super-resolved fluorescence correlation spectroscopy. *J. Phys. D Appl. Phys.* 51:235401. doi: 10.1088/1361-6463/aac04f

Renner, M., Wang, L., Levi, S., Hennekinne, L., and Triller, A. (2017). A simple and powerful analysis of lateral subdiffusion using single particle tracking. *Biophys. J.* 113, 2452–2463. doi: 10.1016/j.bpj.2017.09.017

Ritchie, K., Shan, X.-Y., Kondo, J., Iwasawa, K., Fujiwara, T., and Kusumi, A. (2005). Detection of non-brownian diffusion in the cell membrane in single molecule tracking. *Biophys. J.* 88, 2266–2277. doi: 10.1529/biophysj.104.054106

Roskoski, R. Jr. (2014). The ErBb/HER family of protein-tyrosine kinases and cancer. *Pharmacol. Res.* 79, 34–74. doi: 10.1016/j.phrs.2013.11.002

Sako, Y., Minoghchi, S., and Yanagida, T. (2000). Single-molecule imaging of egfr signalling on the surface of living cells. *Nat. Cell Biol.* 2, 168–172. doi: 10.1038/35004044

Saxton, M. J. (1994). Anomalous diffusion due to obstacles: a Monte Carlo study. *Biophys. J.* 66, 394–401. doi: 10.1016/S0006-3495(94)80789-1

Saxton, M. J. (1996). Anomalous diffusion due to binding: a Monte Carlo study. *Biophys. J.* 70, 1250–1262. doi: 10.1016/S0006-3495(96)79682-0

Saxton, M. J. (2012). Wanted: a positive control for anomalous subdiffusion. *Biophys. J.* 103, 2411–2422. doi: 10.1016/j.bpj.2012.10.038

Saxton, M. J., and Jacobson, K. (1997). Single-particle tracking: applications to membrane dynamics. *Annu. Rev. Biophys.* 26, 373–399. doi: 10.1146/annurev.biophys.26.1.373

Sezgin, E., Levental, I., Mayor, S., and Eggeling, C. (2017). The mystery of membrane organization: composition, regulation and roles of lipid rafts. *Nat. Rev. Mol.* 18:361. doi: 10.1038/nrm.2017.16

Shen, H., Tauzin, L. J., Baiyasi, R., Wang, W., Moringo, N., Shuang, B., et al. (2017). Single particle tracking: from theory to biophysical applications. *Chem. Rev.* 117, 7331–7376. doi: 10.1021/acs.chemrev.6b00815

Sorkin, A., and Goh, L. K. (2009). Endocytosis and intracellular trafficking of ErbBs. *Exp. Cell Res.* 315, 683–696. doi: 10.1016/j.yexcr.2008.07.029

Spindler, S., Ehrig, J., König, K., Nowak, T., Piliarik, M., Stein, H. E., et al. (2016). Visualization of lipids and proteins at high spatial and temporal resolution via interferometric scattering (iSCAT) microscopy. *J. Phys. D Appl. Phys.* 49:274002. doi: 10.1088/0022-3727/49/27/274002

Taylor, R. W., Mahmoodabadi, R. G., Rauschenberger, V., Giessl, A., Schambony, A., and Sandoghdar, V. (2019). Interferometric scattering microscopy reveals microsecond nanoscopic protein motion on a live cell membrane. *Nat. Photon.* 13, 480–487. doi: 10.1038/s41566-019-0414-6

Taylor, R. W., and Sandoghdar, V. (2019). "Interferometric scattering (iSCAT) microscopy and related techniques," in *Label-Free Super-Resolution Microscopy* ed V. Astratov (Cham:Springer), 25–65. doi: 10.1007/978-3-030-21722-8_2

Thompson, R. E., Larson, D. R., and Webb, W. W. (2002). Precise nanometer localization analysis for individual fluorescent probes. *Biophys. J.* 82, 2775–2783. doi: 10.1016/S0006-3495(02)75618-X

Tomas, A., Futter, C. E., and Eden, E. R. (2014). EGF receptor trafficking: consequences for signaling and cancer. *Trends Cell. Biol.* 24, 26–34. doi: 10.1016/j.tcb.2013.11.002

Verhey, K. J., Kaul, N., and Soppina, V. (2011). Kinesin assembly and movement in cells. *Annu. Rev. Biophys.* 40, 267–288. doi: 10.1146/annurev-biophys-042910-155310

Vestergaard, C. L. (2016). Optimizing experimental parameters for tracking of diffusing particles. *Phys. Rev. E* 94:022401. doi: 10.1103/PhysRevE.94.022401

Wäldchen, S., Lehmann, J., Klein, T., Van De Linde, S., and Sauer, M. (2015). Light-induced cell damage in live-cell super-resolution microscopy. *Sci. Rep.* 5:15348. doi: 10.1038/srep15348

Weber, S. C., Thompson, M. A., Moerner, W. E., Spakowitz, A. J., and Theriot, J. A. (2012). Analytical tools to distinguish the effects of localization error, confinement, and medium elasticity on the velocity autocorrelation function. *Biophys. J.* 102, 2443–2450. doi: 10.1016/j.bpj.2012.03.062

Weeks, E. R., and Weitz, D. (2002). Properties of cage rearrangements observed near the colloidal glass transition. *Phys. Rev. Lett.* 89:095704. doi: 10.1103/PhysRevLett.89.095704

Wieser, S., and Schütz, G. J. (2008). Tracking single molecules in the live cell plasma membrane-do's and don't's. *Methods* 46, 131–140. doi: 10.1016/j.ymeth.2008.06.010

Woringer, M., Izeddin, I., Favard, C., and Berry, H. (2020). Anomalous subdiffusion in living cells: bridging the gap between experiments and realistic models through collaborative challenges. *Front. Phys.* 8:134. doi: 10.3389/fphy.2020.00134

Wu, H.-M., Lin, Y.-H., Yen, T.-C., and Hsieh, C.-L. (2016). Nanoscopic substructures of raft-mimetic liquid-ordered membrane domains revealed by high-speed single-particle tracking. *Sci. Rep*. 6:20542. doi: 10.1038/srep 20542

Ye, Z., Wang, X., and Xiao, L. (2019). Single-particle tracking with scattering-based optical microscopy. *Anal. Chem*. 91, 15327–15334. doi: 10.1021/acs.analchem.9b02760

Yildiz, A., Forkey, J. N., McKinney, S. A., Ha, T., Goldman, Y. E., and Selvin, P. R. (2003). Myosin V walks hand-over-hand: single fluorophore imaging with 1.5-nm localization. *Science* 300, 2061–2065. doi: 10.1126/science.10 84398

Young, G., Hundt, N., Cole, D., Fineberg, A., Andrecka, J., Tyler, A., et al. (2018). Quantitative mass imaging of single biological macromolecules. *Science* 360, 423–427. doi: 10.1126/science.aar 5839

Young, G., and Kukura, P. (2019). Interferometric scattering microscopy. *Annu. Rev. Phys. Chem*. 70, 301–322. doi: 10.1146/annurev-physchem-050317-021247

Conflict of Interest: The authors declare that the research was conducted in the absence of any commercial or financial relationships that could be construed as a potential conflict of interest.

frontiers in Cell and Developmental Biology

ORIGINAL RESEARCH
published: 16 November 2020
doi: 10.3389/fcell.2020.581016

Understanding the Functional Properties of Lipid Heterogeneity in Pulmonary Surfactant Monolayers at the Atomistic Level

Juho Liekkinen[1†], *Berta de Santos Moreno*[2†], *Riku O. Paananen*[3], *Ilpo Vattulainen*[1,4,5*], *Luca Monticelli*[6*], *Jorge Bernardino de la Serna*[2*] and *Matti Javanainen*[4,7*]

[1] Department of Physics, University of Helsinki, Helsinki, Finland, [2] National Heart & Lung Institute, Faculty of Medicine, Imperial College London, London, United Kingdom, [3] Helsinki Eye Lab, Ophthalmology, University of Helsinki and Helsinki University Hospital, Helsinki, Finland, [4] Computational Physics Laboratory, Tampere University, Tampere, Finland, [5] MEMPHYS – Centre for Biomembrane Physics, Odense, Denmark, [6] Molecular Microbiology and Structural Biochemistry (MMSB), UMR 5086 CNRS & University of Lyon, Lyon, France, [7] Institute of Organic Chemistry and Biochemistry of the Czech Academy of Sciences, Prague, Czechia

Pulmonary surfactant is a complex mixture of lipids and proteins lining the interior of the alveoli, and constitutes the first barrier to both oxygen and pathogens as they progress toward blood circulation. Despite decades of study, the behavior of the pulmonary surfactant at the molecular scale is poorly understood, which hinders the development of effective surfactant replacement therapies, useful in the treatment of several lung-related diseases. In this work, we combined all-atom molecular dynamics simulations, Langmuir trough measurements, and AFM imaging to study synthetic four-component lipid monolayers designed to model protein-free pulmonary surfactant. We characterized the structural and dynamic properties of the monolayers with a special focus on lateral heterogeneity. Remarkably, simulations reproduce almost quantitatively the experimental data on pressure-area isotherms and the presence of lateral heterogeneities highlighted by AFM. Quite surprisingly, the pressure-area isotherms do not show a plateau region, despite the presence of liquid-condensed nanometer-sized domains at surface pressures larger than 20 mN/m. In the simulations, the liquid-condensed domains were small and transient, but they did not coalesce to yield a separate phase. They were only slightly enriched in DPPC and cholesterol, and their chemical composition remained very similar to the overall composition of the monolayer membrane. Instead, they differed from liquid-expanded regions in terms of membrane thickness (in agreement with AFM data), diffusion rates, as well as acyl chain packing and orientation. We hypothesize that such lateral heterogeneities are crucial for lung surfactant function, as they allow both efficient packing, to achieve low surface tension, and sufficient fluidity, critical for rapid adsorption to the air–liquid interface during the breathing cycle.

Keywords: pulmonary surfactant, lipid monolayer, molecular dynamics simulation, pressure-area isotherm, atomic force microscopy, heterogeneity, membrane domain

OPEN ACCESS

Edited by:
Rainer A. Böckmann, University of Erlangen Nuremberg, Germany

Reviewed by:
Alexander Jackson Sodt, National Institutes of Health (NIH), United States
Jacek Korchowiec, Jagiellonian University, Poland

***Correspondence:**
Matti Javanainen
matti.javanainen@gmail.com
Ilpo Vattulainen
ilpo.vattulainen@helsinki.fi
Luca Monticelli
luca.monticelli@inserm.fr
Jorge Bernardino de la Serna
j.bernardino-de-la-serna@imperial.ac.uk

[†] *These authors have contributed equally to this work*

Specialty section:
This article was submitted to Cellular Biochemistry, a section of the journal Frontiers in Cell and Developmental Biology

Received: *07 July 2020*
Accepted: *16 October 2020*
Published: *16 November 2020*

Citation:
Liekkinen J, de Santos Moreno B, Paananen RO, Vattulainen I, Monticelli L, Bernardino de la Serna J and Javanainen M (2020) Understanding the Functional Properties of Lipid Heterogeneity in Pulmonary Surfactant Monolayers at the Atomistic Level. Front. Cell Dev. Biol. 8:581016. doi: 10.3389/fcell.2020.581016

1. INTRODUCTION

The integrity of the alveolar gas-blood barrier is crucial for effective gas exchange and health, filtering of undesirable components, and response to inhaled hazard. At the same time, it develops tolerance mechanisms to attenuate immunopathology. The alveoli are continuously exposed to inhaled micro- and nanosized pathogens, which are normally rapidly eliminated with the help of the immune system. Immune responses in the alveoli must be tightly regulated to prevent excessive inflammation and tissue damage. Inappropriate or excessive immune responses cause the development of systemic airway inflammation, as in the Acute Respiratory Distress Syndrome (ARDS) (Ware and Matthay, 2000). ARDS is the major cause of respiratory failure affecting millions of people annually, and it is also a main cause of death in many viral infections, such as in severe acute respiratory syndrome coronavirus 1 (SARS-CoV-1), and in the current SARS-CoV-2 which causes the coronavirus disease 2019 (COVID-19) (Xu et al., 2020).

The alveolar epithelium is coated by pulmonary surfactant, that is a delicate membranous proteolipid film that maintains normal lung function. Pulmonary surfactant forms a monolayer, which lines the alveolar epithelium and is synthesized and secreted by epithelial alveolar type 2 cells. Pulmonary surfactant is the most permeable interface of the human body exposed to the environment, presenting the first respiratory barrier against inhaled foreign matter and microorganisms. It is a lipoprotein complex comprising approximately 90 weight-% lipid of which phosphatidylcholine (PC) is the principal component. Importantly, the pulmonary surfactant is exceptionally rich in dipalmitoylphosphatidylcholine (DPPC) with a high main transition temperature (T_m). Other major lipid components involve PCs with an unsaturated chain, phosphatidylglycerol (PG), and cholesterol (Goerke, 1998). As to protein content, the pulmonary surfactant contains four specific surfactant proteins (SP-A, SP-B, SP-C, and SP-D) of which SP-A and SP-D are innate immune defense proteins, whereas SP-B and SP-C together with the phospholipids are crucial in sustaining the very low surface tension needed to avoid alveolar collapse, oedema, and lack of oxygenation (Possmayer et al., 2010).

Basic cellular and molecular biology research has suggested that early pulmonary surfactant dysfunction contributes to the high morbidity of coronaviruses (Xu et al., 2020). The ability to reduce the surface tension of pulmonary surfactant can be compromised due to decreased concentration of surfactant phospholipids and proteins, altered phospholipid composition, proteolysis, and/or protein inhibition, as well as oxidative inactivation of lipids and proteins (Postle et al., 1999; Taeusch et al., 2005; Zasadzinski et al., 2005; Dushianthan et al., 2014). Variations of these dysfunctional mechanisms have been reported in child and adult patients with ARDS. For instance, pulmonary surfactant metabolism studies in adult ARDS patients showed altered surfactant lipid composition: DPPC content was decreased, whereas the fractions of the surface tension-inactive unsaturated species were increased (Amigoni et al., 2017). Moreover, both the total amounts of PC and PG were decreased (Amigoni et al., 2017). Therefore, the possibility that early surfactant replacement therapy could be beneficial in preventing progression of disease severity is encouraging, given the established harmless profile of the pulmonary surfactant. Even though it is mainly indicated for prematurely born babies, surfactant replacement therapy has also been used in adult ARDS studies (Walmrath et al., 1996, 2002; Gunther et al., 2002; Moller et al., 2003). This method (Echaide et al., 2017), where exogenous surfactant is supplied into the lungs, is currently being tested in clinical trials to treat COVID-19 infected patients that require ventilator support (Grocott, 2020; Lewis, 2020). Accordingly, for the development of efficient surfactant replacements, we require a better understanding of the roles of the pulmonary surfactant components in lung mechanics.

Pulmonary surfactant forms a network of complex biological self-assembling morphologies lining the alveoli. The distinctive structure formed by the pulmonary surfactant is a monolayer at the gas-alveolar epithelium liquid interface. In addition to lateral packing in the monolayer at the liquid-air interface, a fraction of the pulmonary surfactant is also likely folded from the interface into lipid bilayers or multilayers in the aqueous subphase (Baoukina et al., 2007a), acting as lipid reservoirs (Pérez-Gil, 2008; Parra and Pérez-Gil, 2015). This monolayer is repeatedly compressed and expanded during breathing cycles without hysteresis—a property that can only be withheld by a material with very peculiar viscoelastic properties (Andreassen et al., 2010; Steimle et al., 2011). These reservoirs have also been suggested to participate in oxygen transfer from the inhaled air to circulation (Olmeda et al., 2010). It has been shown that the pulmonary surfactant monolayers and membranes exhibit phase behavior that is believed to play roles in lung mechanics; tight packing of lipids with saturated lipid chains promotes its ability to lower surface tension, whereas lipids with unsaturated chains increase pulmonary surfactant fluidity and thus allow for its rapid adsorption to the air–water interface (Bernardino de la Serna et al., 2004, 2013a,b; Casals and Cañadas, 2012). Moreover, the phase behavior is also considered to regulate the functions of the surfactant proteins (Pérez-Gil, 2008; Bernardino de la Serna et al., 2009). However, the biophysical implications of the phase behavior are poorly understood, and a molecular view of the molecular organization would be extremely helpful in understanding the roles of different lipids and surfactant proteins in lung functionality enabled by pulmonary surfactant.

When compressed under the T_m of the corresponding membrane, single-component monolayers transition from a two-dimensional gas phase into a loosely packed and dynamic liquid-expanded (L_E) phase. Further compression takes the monolayer to a brittle liquid-condensed (L_C) phase, which eventually collapses, excreting matter into the aqueous subphase (Kaganer et al., 1999; Baoukina et al., 2008; Brewer et al., 2010). The L_E-L_C transition takes place through the formation of a coexistence phase characterized by a plateau in a surface pressure-area isotherm, which is manifested as observable domains (Klopfer and Vanderlick, 1996; Mansour and Zografi, 2007; Javanainen et al., 2017a).

The behavior of native pulmonary surfactant monolayers is quite different from such model systems. Still, fluorescence and Brewster angle microscopy reported visible domains in

monolayers formed from lipid fractions of the pulmonary surfactant (Discher et al., 1999; Bernardino de la Serna et al., 2013a). These domains were suggested to be highly enriched in DPPC (Discher et al., 1999). Domains were also detected in vesicles created from the pulmonary surfactant, and also in the presence of the surfactant proteins (Bernardino de la Serna et al., 2004, 2013a). However, the surface pressure-area isotherms measured for pulmonary surfactant lipid fractions were not found to contain a plateau of any sort (Discher et al., 1999). Thus, the monolayer did not entirely transition to the L_C phase at any pressure, indicating that no L_E-L_C coexistence was present either. Presumably, the observed domains did not present an equilibrium phase. Indeed, the composition of the pulmonary surfactant seems to be adjusted so that the mixture is barely fluid at body temperature (Bernardino de la Serna et al., 2004; Suri et al., 2012), which can lead to distinct behavior of its lipid components. By doping the pulmonary surfactant lipid fraction with additional DPPC, the T_m can be gradually increased, and a coexistence plateau becomes eventually visible (Discher et al., 1999). These observations suggest that the behavior of the pulmonary surfactant may be characterized by transient heterogeneity arising from critical fluctuations (Nielsen et al., 2000), where the behavior of each lipid type is determined by its T_m value.

These research topics are difficult to study at the molecular level due to the limited resolution of available experimental techniques. Molecular simulations are often helpful in resolving such aspects down to the atomistic level (Enkavi et al., 2019). However, previous simulation studies on multi-component monolayers are relatively scarce (Baoukina et al., 2007a,b, 2008, 2012, 2014; Baoukina and Tieleman, 2011) with only a few studies performed using atomistic models (Javanainen et al., 2010; Olzyńska et al., 2020). While previous simulations have generated a lot of insight to better understand the behavior of surfactant monolayers, they have been haunted by the insufficiently accurate description of the physical behavior of the lipids at the interface, that, in turn, was largely due to insufficient quality of water models in describing phenomena at water-monolayer-air interfacial regions (Baoukina et al., 2007b; Vega and De Miguel, 2007; Lamberg and Ollila, 2015; Javanainen et al., 2017a). Moreover, The description of the driving forces behind membrane heterogeneity in often used coarse-grained Martini model is limited (Davis et al., 2013).

To overcome these limitations and provide a detailed and accurate picture of the molecular-level organization of surfactant monolayers, we used extensive state-of-the-art all-atom molecular dynamics (MD) simulations of model systems, validated with experimental Langmuir trough data. The composition of our model monolayers was chosen to match the composition of the protein-free pulmonary surfactant (Bernardino de la Serna et al., 2013a). These model systems were simulated at various compression states and temperatures, matching the conditions used in experiments. By using our recently developed protocol for performing simulations of lipid monolayers at the air–water interface, Javanainen et al. (2017a) and Paananen et al. (2019) we were able to reach quantitative agreement with experimental surface pressure-area isotherms. Our simulations predict the presence of lateral heterogeneity characterized by domain formation, which we confirmed by atomic force microscopy (AFM) imaging. Upon compression, we found the appearance of transient L_C-like domains. Upon further compression these domains were found to aggregate to form large ordered regions. Thanks to the atomistic detail available in the simulations, we were able to draw conclusions as to the physical and chemical properties of the nanoscale domains. Interestingly, simulations predict that the domains are not substantially enriched by any lipid type, indicating that the peculiar viscoelastic properties of the pulmonary surfactant arise from the collective behavior of the mixture rather than from the features of its individual lipid components. Our findings help understand lung mechanics and are valuable in the development of strategies to tackle lung conditions, while also paving the methodological way for future studies of the pulmonary surfactant.

2. METHODS

2.1. Atomistic Molecular Dynamics Simulations

Until recently, the poor description of surface tension by the commonly used water models (Chen and Smith, 2007; Vega and De Miguel, 2007) has prevented quantitative simulation studies of lipid monolayers at the air–water interface. However, very recently we demonstrated that a combination of the four-point OPC water model (Izadi et al., 2014) and the CHARMM36 lipid model (Klauda et al., 2010) reproduces experimental surface pressure-area isotherms in single-component 1-palmitoyl-2-oleoylphosphatidylcholine (POPC) and DPPC monolayers (Javanainen et al., 2017a), and the agreement is largely quantitative. In this study, we extend this approach to quaternary lipid monolayers whose composition was chosen to match the composition of the protein-free pulmonary surfactant (Goerke, 1998) as accurately as possible. In practice, our systems contained 60 mol% DPPC, 20 mol% POPC, 10 mol% 1-palmitoyl-2-oleoylphosphatidylglycerol (POPG), and 10 mol% cholesterol. The systems were set up as follows. Two monolayers, separated by a water slab and each containing 169 lipids were first set up at an area per lipid (APL) equal to 50 Å^2. Next, these monolayers were either expanded or compressed during a 10 ns simulation to an average APL value of 100 or 40 Å^2, respectively, using the `MOVINGRESTRAINT` and `CELL` keywords in the PLUMED 2.2 package (Tribello et al., 2014). Structures at a total of 17 APL values were extracted and used as initial structures for the production monolayer simulations in the NVT ensemble for 1 μs each. All simulations were performed at both 298 and 310 K, and additional repeats as well as larger simulations of up to 3,042 lipids were performed to provide further validation for the results.

The CHARMM36 model for phospholipids (Klauda et al., 2010) and cholesterol (Lim et al., 2011) was used together with the four-point OPC water model (Izadi et al., 2014). The simulations were performed with the version 5.1.x of the

GROMACS simulation package (Abraham et al., 2015), and the recommended simulation parameters for the CHARMM36 force field (Lee et al., 2015) were used to reproduce realistic monolayer behavior (Javanainen et al., 2017a). Details on the simulation setups and on the simulation methodology are provided in the **Supplementary Material**.

2.2. Analyses of MD Simulations

2.2.1. Surface Pressure-Area Isotherms

Monolayer behavior was characterized and compared to experiments using surface pressure-area isotherms. Monolayer surface pressure π at an APL of A was calculated as $\pi(A) = \gamma_0 - \gamma(A)$, where γ and γ_0 are the surface tensions of the monolayer-covered and plain air-water interfaces, respectively. Here, the surface tensions are obtained from the pressure components along the monolayer plane ($P_L = \left(P_{xx} + P_{yy}\right)/2$) and normal to it ($P_N = P_{ZZ}$) as $\gamma = L_z \times (P_N - P_L)/2$, where L_z is the simulation box size normal to the monolayer plane, and a factor of two indicates the presence of two air–water interfaces in the simulation box. The values were obtained with the `gmx energy` tool provided with GROMACS (Abraham et al., 2015).

2.2.2. Monolayer Isothermal Compressibility

The values for the monolayer isothermal compressibility modulus (C_s^{-1}) were calculated from the surface pressure-area isotherms for both the simulated and measured systems as $C_s{}^{-1} = -A\frac{d\pi}{dA}$, where A is the area per molecule at a given pressure and $\frac{d\pi}{dA}$ is the slope of the surface pressure-area isotherm. The derivatives were calculated using Matlab from a piecewise smoothing spline fitted to the isotherms. Smoothing parameters of 0.01 and 0.25 were used for the fit to the simulated and measured data, respectively. With these values, the fit was well within the error bars of the original data, while allowing to avoid unphysical jumps in the compressibility modulus.

2.2.3. Detection of Monolayer Domains

Domains packed like in the L_C phase were detected by clustering lipid chains and cholesterols based on their packing in the monolayer plane. The 10th carbons in the lipid chains and the C14 atom in cholesterol ring were included in the clustering that used the DBSCAN algorithm (Ester et al., 1996). The chosen atoms in the lipid chains capture well the hexagonal packing in ordered structures (Javanainen et al., 2017b), and the C14 carbon of cholesterol resides at the same depth. This carbon is part of both the five-member (D) and six-member (C) rings. For DBSCAN, we used a cut-off of 0.71 nm and a minimum neighbor count of 6. The cut-off was set to the distance at which the first minimum appears in the radial distribution function of the clustered atoms. The clusters were considered to be part of the L_C-like domain. This clustering was performed on conformations separated by 1 ns. The L_C-like fraction, number of individual clusters, and the largest cluster size were extracted for each conformation. All these quantities were then averaged over the trajectory independently for both monolayers in the simulation system. Their average values are reported, whereas the differences in the values extracted for the two monolayers serve as error estimates. Pattern-matching was used to find all residence events in the L_C clusters. These times were histogrammed and fitted with a power law with an exponent of b.

2.2.4. Contact Fraction

Lateral demixing of lipids with unsaturated and saturated chains was quantified by the contact fraction. Following Domański et al. (2012), we defined the contact fraction as $f_{mix} = c_{US-S}/(c_{US-US} + c_{US-S})$, where c_{US-S} is the number of contacts between the lipids with an unsaturated chain (POPC and POPG) and the lipids with saturated chains (DPPC). For a contact, the phosphorus atoms of the lipids had to be within 1.1 nm from each other. We extracted contact data using the `gmx mindist` tool every 1 ns and calculated the average values over the last 500 ns of the simulations for both monolayers. We plot the mean of these two average values, whereas their difference serves as an error estimate.

2.2.5. Cholesterol Clusters

Cholesterol molecules were considered to be part of a cholesterol cluster if they were in contact with at least one other cholesterol molecule. We used a cut-off of 0.94 nm based on the first minimum in the cholesterol-cholesterol radial distribution function. All residence events were used in the calculation of the probability distribution of cholesterol cluster sizes. The distances were measured from the centers of mass of the cholesterol molecules.

2.2.6. Diffusion Coefficients

Diffusion coefficients were calculated to characterize monolayer dynamics and to detect changes in monolayer packing. The diffusion coefficients were extracted from center-of-mass (COM) trajectories. The motion of lipids with respect to the movement of the monolayer as a whole was analyzed to eliminate possible artifacts due to monolayer drift. The diffusion coefficients were extracted from linear fits to time- and ensemble-averaged mean-squared displacement at lag times between 10 and 100 ns. Two values were extracted—one from each monolayer—and averaged, and their difference served as an error estimate. The GROMACS tool `gmx msd` was used, and the COM trajectories were generated using `gmx traj`.

2.2.7. Monolayer Thickness

Monolayer thickness was used to couple AFM height profiles of heterogeneous membranes to the lateral packing within the domains. This thickness was estimated from density profiles calculated for each lipid type along the monolayer normal (z) using the GROMACS tool `gmx density`. These profiles were aligned at the phosphorus peak of DPPC, and the lipid was set to begin and end at z values where its density crossed 5% of its maximum value.

2.2.8. Lipid Chain Tilt

Lipid chain tilt was used to characterize persistent L_C-like packing in the monolayers. The tilt angle of lipid chains was calculated as the angle between the z axis and the vector joining the 1st and 16th carbons in the fatty acid chains of phospholipids using the GROMACS tool `gmx gangle`. The angle distributions were averaged over both chains and both

monolayers, and the distributions were fitted with a Gaussian. The location of its maximum and the variance were used as the mean tilt angle and its error estimate, respectively.

2.3. Langmuir Trough Measurements

2.3.1. Langmuir–Wilhelmy Compression Isotherms

By means of a specially designed ribbon Langmuir–Wilhelmy trough (NIMA Technology, UK), compression isotherm assays were performed and surface pressures as a function of molecular area were obtained at constant temperature, as described previously (Dohm et al., 2010). The lipid mixture was identical to that employed in the simulations (see above). The employed Langmuir–Wilhelmy trough has a maximum area of 312 cm^2 and a minimum of 54 cm^2 and instead of the canonical rigid barriers uses a continuous Teflon-coated ribbon that by moving symmetrically reduces the available area in the aqueous surface, and therefore compresses the confined sample to carry out the compression isotherm. The pressure is recorded using an electronic pressure sensor and a piece of cellulose and employing the Wilhelmy plate technique, with an estimated error of ± 1 mN/m among different isotherms, that were assessed at least in triplicate at 298 K. The compression isotherm displayed in **Figure 1** shows the first compression of 44.1 nmol of a DPPC/POPC/POPG/Chol mixture of mimetic surfactant monolayer, spread on a saline solution containing 150 mM NaCl. After placing the lipid mixture onto the aqueous subphase surface, the generated lipid layer was left to equilibrate for 10 min, so the solvents could evaporate, and the lipids organize and disperse at the interface. Thereafter, the narrowest area was achieved by compressing the monolayer at a constant speed of 150 cm^2/min. This compression speed was set to reflect the functional quality of the assessed surfactant, by recapitulating as much as possible the dynamic context of native pulmonary surfactant in the human organism, and allow reaching the highest surface pressure possible.

2.3.2. Surface Dilatational Rheology

We again used a lipid composition identical to the one in simulations (see above). All these lipids were obtained from Avanti Polar Lipids (Alabaster, AL). Lipids were spread in 2 mM chloroform solution on the surface of a deionized water subphase (Milli-Q, Millipore, Bedford, MA) in a Langmuir trough (KSV Minitrough, Espoo, Finland) with a platinum Wilhelmy plate. The dilatational rheology of the monolayer was studied using the oscillating barrier method. The film was first compressed to the desired surface pressure, after which sinusoidal area compressions with an amplitude of 1% were performed at a frequency of 10, 50, 100, or 200 mHz and the changes in surface pressure in response to the oscillations were recorded. This allowed us to determine the surface dilatational modulus, ($E = -\mathrm{d}\Pi/\mathrm{d}\ln A$), whose real part represents the elastic modulus, and imaginary part the viscous modulus. In the limit of slow oscillations, the elastic modulus corresponds to the compressibility modulus introduced earlier. Each measurement was repeated two times, and an average dilatational modulus was calculated over frequency, since the magnitude of the dilatational modulus was found to be constant with respect to frequency, although the ratio of compressibility to viscous moduli decreased upon increasing frequency. All measurements were conducted at room temperature (297 K).

2.4. Atomic Force Microscopy Imaging

2.4.1. Langmuir–Blodgett Transferred Monolayers

Lipid monolayers were transferred onto mica as described in Brown et al. (2011). The transfer ratio was equal to 1, i.e., no compression or expansion of the monolayer took place during the transfer. For the monolayer preparation, the sample was spread at 298 K onto the air–water interface until the minimum surface pressure of ∼0–1 mN/m was observed. After 10 min of monolayer equilibration, the film was compressed until the desired surface pressure was reached (from 15 to 45 mN/m, in 5 mN/m steps), at a compression speed of 50 cm^2/min. Before the transfer was started, the film was again equilibrated for 5 min at constant pressure. The monolayers were finally deposited in a freshly cleaved muscovite mica substrate (Plano GmbH, Wetzlar, Germany) that had been previously submerged. The lifting device—to which the mica substrate was fixed—was raised in the vertical plane out of the buffered aqueous subphase at a speed of 10 mm/min at constant pressure. In all experiment modalities three independent experiments were carried out, as a minimum, and up to 10 images were taken and analyzed.

2.4.2. Atomic Force Microscopy

Langmuir–Blodgett supported monolayers' topographical images were taken using an atomic force microscope (JPK NanoWizard, JPK Instruments, Berlin, Germany), employing in both cases Silicon-SPM cantilevers (Nanosensors, NanoWorld AG, Neuchatel, Switzerland). The AC mode in air was selected for monolayers. The scan rate was ∼1 Hz for all AFM images. At least three different supported monolayer systems were assessed, and each sample was imaged on a minimum of three different positions. Image processing of AFM data was done using the SPIP software package as in Bernardino de la Serna et al. (2013a) (Image Metrology, Hørsholm, Denmark).

3. RESULTS

3.1. Monolayers Display Lateral Heterogeneity Without a Coexistence Plateau

Surface pressure-area isotherm is a key quantity representing monolayer behavior at the air–water interface, and it is readily extracted from both Langmuir trough measurements and computer simulations. These isotherms for the quaternary pulmonary surfactant lipid monolayers at 298 and 310 K are shown in **Figure 1**.

The isotherms from experiments and simulations are in nearly quantitative agreement. No plateau indicating L_C/L_E coexistence was visible in the experimental isotherm, and the isothermal compressibility modulus extracted from these isotherms (see **Supplementary Figure 16**) remained well below the value of 250 mN/m, typically assigned to the L_C phase, suggesting that the monolayers remained in the L_E phase.

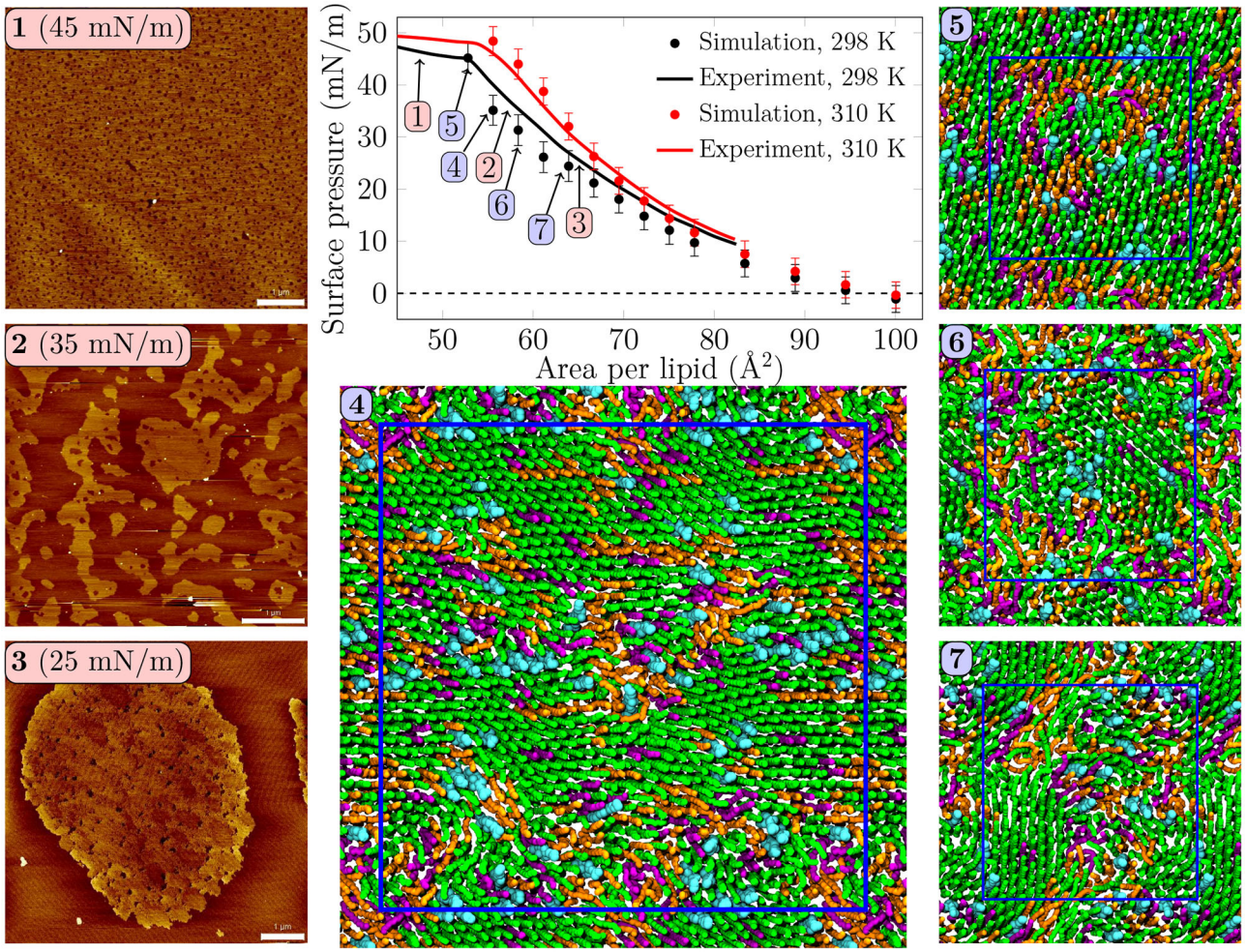

FIGURE 1 | Surface pressure—area isotherms from simulations and experiments, with AFM images and simulation snapshots taken from selected surface pressures at 298 K. Scale bar 1 μm. At 25 mN/m, **(3)** one can identify small irregularly shaped domains with visible nanostructures inside the domains. At 35 mN/m, **(2)** the domains start to fuse and lose their rounded shapes. In the collapse plateau at 45 mN/m, **(1)** the domains are no longer visible in the AFM images, and some lipids are squeezed out from the monolayer film. Clearly visible transient or persistent heterogeneity can also be observed in the simulation snapshots **(4–7)** of monolayers at different surface pressures. Here, **(4)** was extracted from a 4-fold larger monolayer than **(5–7)**. Only the data points below the experimental collapse pressure are shown in the isotherm, whereas all simulated points with all of the independent repetitions are shown in **Supplementary Figure 1**.

Still, our AFM measurement displayed heterogeneity in lipid packing. The AFM images taken at 298 K (**Figure 1**, panels **1–3**, and **Supplementary Figures 2–5**) revealed surface pressure-dependent formation of a heterogeneous monolayer with thinner and thicker regions. Starting from low surface pressure (higher APL), at 25 mN/m (**Figure 1**, panel **3**) the observed domains were rounded yet irregular in shape. The insides of these domains are heterogeneous with visible nanostructures, indicated also by our height profile studies of the domains (see **Figure 2**, **Supplementary Figures 6–9**). Similar heterogeneity was also evident in the simulations (**Figure 1**, panels **4–7**), where domains were readily seen at surface pressures above 25 mN/m, or at APL below 65 Å^2 at 298 K. No L_C/L_E coexistence plateau was observed in the simulated isotherms either (**Figure 1**, **Supplementary Figure 1**), and the isothermal compressibility modulus also followed the experimental values reasonably well (**Supplementary Figure 16**). Moreover, independent replica simulations at selected APLs, as well as additional simulations of larger monolayer systems confirmed that the initial monolayer configuration and the finite-size effects did not affect the extracted values of surface pressure (**Supplementary Figure 1**) nor the presence of heterogeneities. Still, the lipid organization in the larger systems is most likely affected by their initial configurations, as lipids do not have time to sample the whole monolayer during the simulation timescale. Therefore, we did not consider the larger monolayer systems in further analyses. The movies at doi: 10.6084/m9.figshare.12612317 as well as the additional snapshots of the simulated monolayers at 298 and 310 K given in **Supplementary Figures 10, 11**, respectively, clearly demonstrate heterogeneity in lateral organization.

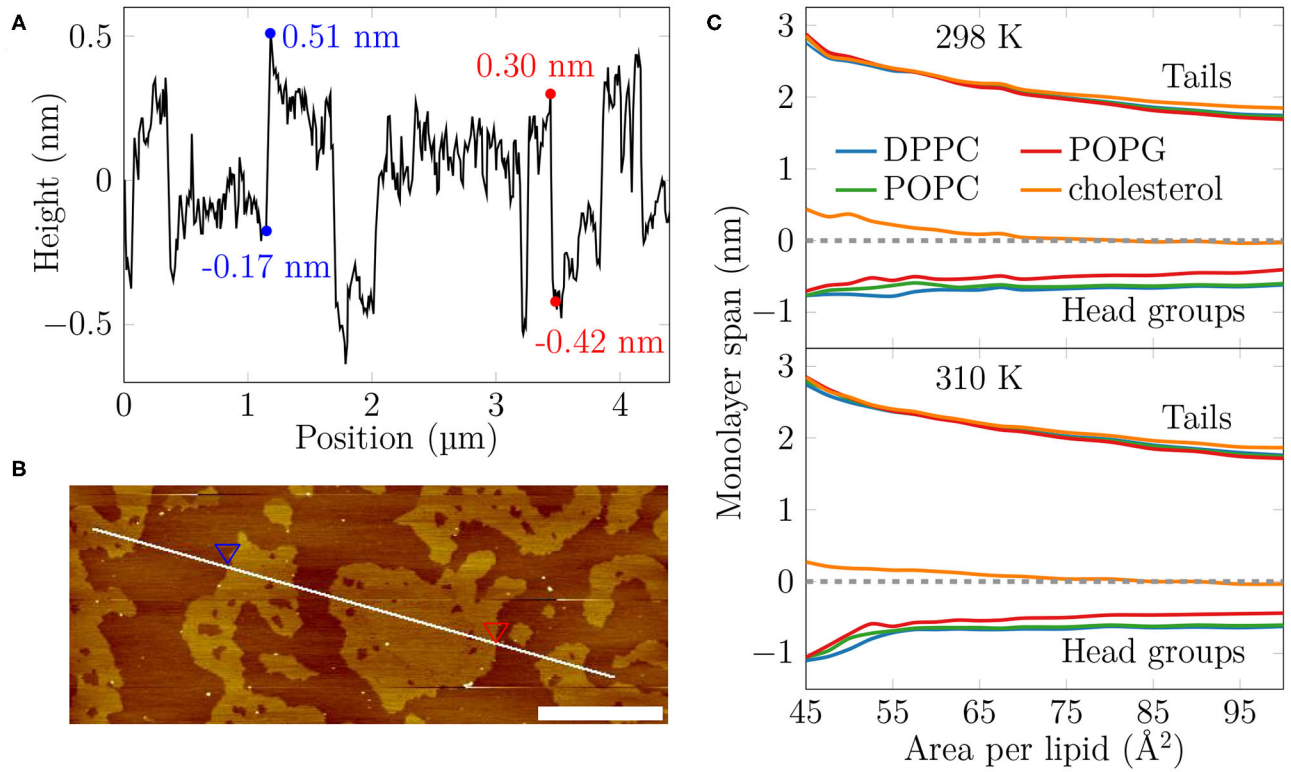

FIGURE 2 | The AFM height profile at 35 mN/m at 298 K and the average monolayer thickness calculated from the simulations. **(A)** The AFM height profile results show a difference of approximately 0.7 nm at the border of the two phases at the selected positions. By considering the average height of the phases and averaging over all boundaries captured in the profile, the average thickness difference is similar, at 0.52 ± 0.15 nm. **(B)** The path of the measurement. Two points marked with the blue and red triangles indicate selected positions at the border of the L_C- and L_E-like regions. The scale bar at the lower right corner equals to 1 µm. **(C)** The average thickness of the monolayer in the simulations. The dashed line indicates the position of maximum of phosphorus density of DPPC. The lines indicate the span of lipids from tails to head groups. At each extreme, the line shows the location where the lipid density drops below 5% of its maximum value.

Based on our simulations at 298 K (**Figure 2C**), the monolayers at APLs equal to 47.5–50 Å^2 (corresponding to the very packed state with major regions in an L_C-like arrangement) and 90–100 Å^2 (corresponding to the L_E phase) extend approximately 2.5 nm and 1.7–1.8 nm toward the air phase, respectively, calculated from the plane defined by the DPPC phosphorus atoms (see section 2). This difference of 0.6–0.7 nm matches well the differences in height profile observed in our AFM experiments at surface pressures below monolayer collapse (**Figures 2A,B**, **Supplementary Figures 6, 7**), indicating that the measured thicker and thinner regions in the monolayers would correspond to L_C- and L_E-like regions, respectively. The thickness difference of these two regions in simulations is highlighted in **Supplementary Figure 17**.

The extent of the L_C-like region grows as the surface pressure of the monolayer is increased, as would also be expected during a proper phase coexistence region (Javanainen et al., 2017a), although the surface pressure does not remain constant here based on the isotherms shown in **Figure 1**. From AFM figures, at 35 mN/m (**Figure 1**, image **2**) the L_C domains seem to fuse together to form more irregular shapes, but the overall heterogeneity is clearly visible. Here, the coalescence of the domains was likely also limited by the slow diffusion within the compressed monolayers. Indeed, our simulations predict that compression from a state with APL equal to 80 Å^2 to the one with APL equal to 50 Å^2 slows lipid diffusion by 1–2 orders of magnitude (**Figure 3A**). The nanostructures within the domains correspond to the L_C-like ones measured at 25 mN/m (see **Supplementary Material**). At 45 mN/m (**Figure 1**, image **1** below APL 55 Å^2) and 55 mN/m (**Supplementary Figure 5**) we have already reached the monolayer equilibrium collapse plateau seen in the experimental surface pressure-area isotherms (Mansour and Zografi, 2007). It should be noted that the monolayers in the alveoli are expected to reach surface tension values close to 0 mN/m (corresponding to surface pressure of ∼70 mN/m). However, in experiments this is only achieved by very rapid compression (Crane and Hall, 2001), or by the use of bubble surfactometer methods (Schurch et al., 1989). In the collapse region, the domains are completely merged with a continuous network of small holes, forming a sponge-like collapsed structure at the boundary of the air-liquid interface. Further on, the protruding regions seen in the AFM images at surface pressures above the collapse plateau are collapsed material, excluded from the interfacial film

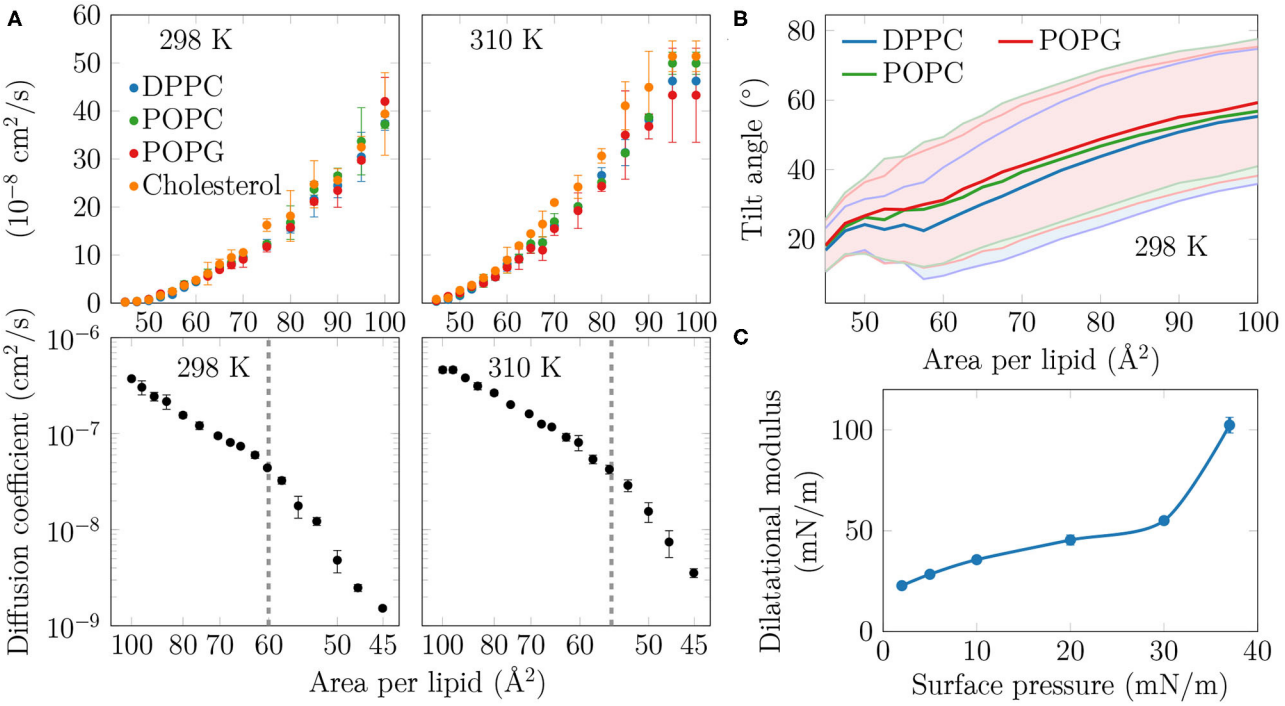

FIGURE 3 | (A) Diffusion coefficients *D* of the lipids in the monolayers. Top row: The diffusion coefficients, shown in linear scale as a function of APL, show no signs of a phase transition at either studied temperature. Bottom row: *D*, in logarithmic scale, shown as a function of 1/APL displays two slopes with a crossover at APL≈60 Å^2 (298 K) or ≈55 Å^2 (310 K), highlighted with a dashed gray line. **(B)** Tilt angles of the phopsholipid chains in the monolayers at 298 K. The shaded areas, bordered by dim lines, show the standard deviation. Data for 310 K is provided in **Supplementary Figure 12**. **(C)** Dilatational modulus of the monolayer as a function of surface pressure at 297 K.

into the water phase. This is verified by the height profiles (**Supplementary Figure 9**), which show height differences of up to 10 nm, which is clearly above the difference observed in the simulations between monolayers at different APLs (**Figure 2C**). Increasing the temperature to 310 K in the simulations renders the monolayer more fluid and the heterogeneity is visible at surface pressures above 30 mN/m, or APL below 60 Å^2 (**Supplementary Figure 11**).

Concluding, both AFM measurements and computer simulations revealed lateral heterogeneity in a broad range of APL values, despite the lack of a plateau in the surface pressure-area isotherm. Together, simulations and AFM imaging suggest that the structure of these domains resembles the L_C phase.

3.2. Condensed Nanodomains Affect the Structural and Dynamic Properties of the Monolayer

As no coexistence plateau is observed in the isotherms obtained from experiments and simulations, it is worth asking whether the heterogeneity observed by AFM and simulations manifests itself in some other monolayer properties. To this end, we measured the dilatational modulus of the monolayer at various surface pressures using the oscillating barrier approach. As shown in **Figure 3C**, we observe little change in this modulus up to a surface pressure of 30 mN/m. This signals that the monolayer area can be changed relatively easily, possibly due to a rapid reorganization of lipids in the membrane plane. However, beyond 30 mN/m—corresponding roughly to APL equal to 60 Å^2 based on the isotherms in **Figure 1**—the modulus grows rapidly. This indicates that there are structural changes in the monolayer, perhaps due to the formation of continuous or percolating ordered regions.

On the simulation side, we analyzed the diffusion of lipids at different APLs. The diffusion coefficients, *D*, are shown in the top row of **Figure 3A**. The curves demonstrate what seems to be a continuous and smooth increase in diffusion coefficient with increasing APL. However, as shown in the bottom row of **Figure 3A**, a plot of log(*D*) vs. 1/APL does not reveal a single slope, as expected for monolayers without a plateau in the pressure–area isotherm, such as DLPC at 294 K (Peters and Beck, 1983; Mangiarotti et al., 2014). Instead, we observed two distinct slopes with crossovers at 60 and 55 Å^2 for DPPC at 298 and 310 K, respectively. The presentation of the diffusion data used herein is based on the idea that the diffusion of lipids depends on their degree of packing. This presentation resembles that used to interpret diffusion in terms of the free volume theory (Almeida et al., 1992). However, due to various issues in applying this theory to diffusion in lipid monolayers (Javanainen et al., 2010), we refrain from interpreting the diffusion data further within this framework. Yet, we acknowledge a clear change in the trend of the APL-dependence of diffusion coefficients.

Let us move on to a structural property extracted from the simulations. The tilt angle distributions at 310 K, shown in **Supplementary Figure 12**, show a continuous increase in the chain tilt upon increasing area. However, as show in **Figure 3B**, at 298 K and between APLs of 45 and 60 Å^2, the chains remain tilted at an angle of ∼25°. A similar tilt angle of ∼25° was also reported for DPPC monolayers in the L_C phase using both X-ray diffraction (Lee et al., 2002) and vibrational sum frequency generation spectroscopy (Ma and Allen, 2007). This indicates that at 298 K, the monolayer retains regions of L_C-like packing with a characteristic chain tilt until relatively large APL values, and this structural feature is coupled to a diffusion mode that differs from that observed at larger APL values. It is worth noting that the long-range orientational order of the tilted L_C-like domains (Moy et al., 1986) is also clearly evident in **Figure 1**.

Concluding, in both experiments and simulations we systematically observe a a sudden change in monolayer properties at a certain compression level, despite the isotherms showing no coexistence plateau.

3.3. Condensed Domains Display Little Enrichment in DPPC and Cholesterol

With the presence of L_C-like domains evident in both simulations and experiments, we next use the simulation data to study the composition of the domains. The leftmost panels in **Figure 4A** show the fraction of phospholipid chains and cholesterols in L_C-like domains obtained from clustering analyses (see section 2). Examples of the results of the clustering algorithm at different APL values are shown in **Supplementary Figure 14**. The data are resolved by lipid type and shown in a cumulative manner so that the total L_C-like fraction can be read from **Figure 4A**. At low APL values, almost the entire monolayer is part of the L_C-like region, yet the excluded lipids can still be readily compressed, resulting in a compressibility modulus that is lower than values associated with the L_C phase. At the other end, at large APL only few transient clusters of a few lipids are observed. Still, more than half of the phospholipid chains and cholesterol molecules are part of an L_C-like domain up to APL values of ∼65 Å^2. These results naturally depend on the parameters used for the clustering algorithm, as demonstrated in **Supplementary Figure 15**. Still, our choice of cutoff based on the first minimum in the radial distribution function of the clustered particles (see section 2) provides results at the extreme APL values that are intuitively expected. Interestingly, temperature has little effect on the calculated L_C fractions, since very similar domain compositions are extracted from the simulations at room and body temperatures.

It is clear from **Figure 4A** that DPPC with its two saturated chains makes up the majority of the L_C-like regions, regardless of the surface pressure and temperature. This is natural, since DPPC is also the most prevalent lipid type in our simulations. For a more detailed look into the composition of the L_C-like domains, we plot the fraction of lipids in these regions in the right panels of **Figure 4A**. Here, the dashed lines highlight the overall fractions of the different components in the system. At very low APL, essentially the entire monolayer is detected by the clustering algorithm to be part of a L_C-like region, and therefore the fractions of lipids in this region agree with their fractions in the system. However, at intermediate APLs between 50 and 80 Å^2, DPPC is present in the L_C-like domain slightly more than expected by its fraction in the system. The fraction of POPC within the L_C-like regions is fairly constant over all APLs, whereas those of POPG and cholesterol change more noticeably while moving toward larger APLs; the fraction of POPG decreases while that of cholesterol increases in the shrinking and more transient L_C-like regions. Indeed, at large APLs, cholesterol seems to be a key player in the formation of condensed lipid clusters.

It seems somewhat counter-intuitive that the L_C-like domains have so little preference for any lipid type. However, stable L_C and L_E phases exist in monolayers made of a single lipid type (Javanainen et al., 2017a). We analyzed whether the lipid types underwent lateral demixing during the simulation. The mean contact fractions between lipids with unsaturated and saturated chains in all simulations are shown in **Figure 4B**. The dashed line at 0.66 represents ideal mixing of DPPC with the lipids with unsaturated chains (POPC and POPG). It is evident from **Figure 4B** that there is generally little preference for lipid demixing, yet at smaller APL values there is a small tendency for DPPC lipids to reside with other DPPC molecules. The APL values below which lipid mixing deviates from ideal behavior are again close to 55 and 60 Å^2, where rapid changes in the APL-dependence of many quantities were observed in the last section. Curiously, temperature has again very little effect on this demixing. Finally, it is worth pointing out that we also studied the time evolution of the contact fractions of the systems at different APL values but found no systematic tendency for any of the monolayers to demix during the simulation time.

We also studied whether cholesterol has a tendency to cluster in the monolayers. The probability of a cholesterol to be in a cluster of a given size is shown in the left panel in **Figure 4C** for the simulations at 298 K, whereas the data for simulations at 310 K are given in **Supplementary Figure 13**. The right panel shows the sum of probabilities with $n \geq 2$, corresponding to the probability that a cholesterol molecule is part of a cluster with at least one other cholesterol molecule.

It is evident from **Figure 4C** that all distributions peak at 1, indicating that most cholesterol molecules are on average not in contact with other cholesterol molecules. Still, the probability of a cholesterol to be in a cluster with size larger than one is ∼20% in all monolayers (right panel in **Figure 4C**). Curiously, at APLs 65 Å^2 and larger, clusters of more than 5 cholesterol molecules sometimes appear. Still, the probability of cholesterol clusters larger than one shows no clear dependence on APL, although not surprisingly, the chance of finding cholesterol clusters is highest in the monolayers with the smallest APLs.

To analyze the distribution of the domains in the monolayer, we show in **Figure 5A** the number of condensed clusters as well as the fraction of the system occupied by the largest cluster. Between APLs of 45 and 60 Å^2 the size of the largest cluster drops steeply from a coverage of ∼80% of the lipids to a mere ∼10%. At the same time, the number of L_C clusters increases from a few to 15–20, and these maxima are reached at an APL equal to 60 Å^2

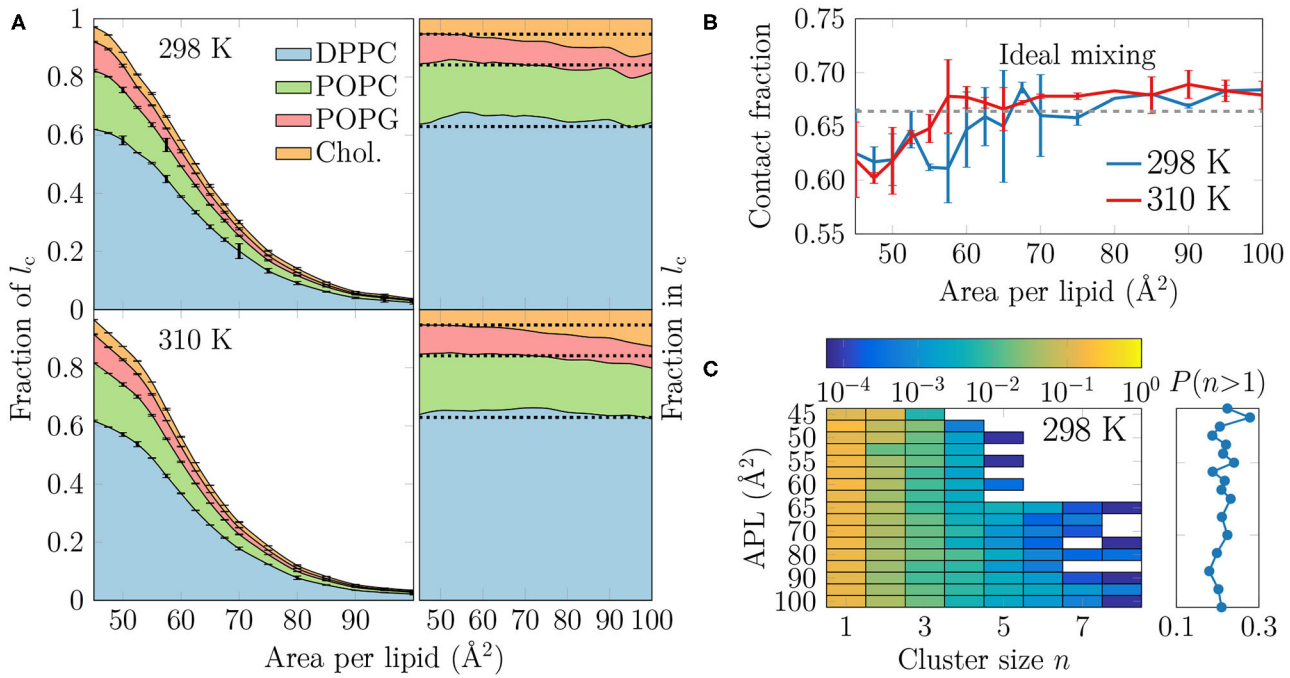

FIGURE 4 | (A) The extent and composition of the L_C-like regions. On the left, the fraction of phospholipid chains and cholesterols in the L_C-like regions is shown for all lipid types. These curves sum to the total fraction of the L_C-like region. The error bars show the differences calculated for the two monolayers in the simulation system. On the right, the fraction of lipids that make up the L_C-like regions at different APLs, i.e., in this plot the curves always sum to 1. The dashed lines show the values expected based on the overall monolayer lipid composition. **(B)** Mean contact fraction during the last 500 ns between DPPC and the lipids with unsaturated chains (POPC and POPG). Ideal mixing is highlighted by a dashed line at 0.66, whereas values smaller than that indicate a preference to demix. **(C)** Left: 2-dimensional probability distributions of cholesterol molecules residing in a cluster with at least one other cholesterol at all simulated APLs at 298 K. Note that the color bar is in logarithmic scale. Right: The sum of probabilities of $n > 1$, i.e., the probability for cholesterol to be in a cluster with size larger than one molecule. Data for simulations at 310 K are given in **Supplementary Figure 13**.

(298 K) or slightly smaller (310 K). These APL values agree well with those at which changes in trends as a function of APL were observed in many properties in the previous section. The melting of the largest cluster is coupled to the formation of many smaller clusters. Upon an increase in APL beyond 60 Å^2, the number of clusters begins to decrease again, until only a few are detected in the pure L_E phase. Moreover, these few are very small, since the largest one occupies only 2% of the lipids, or less, indicating that it is likely a false positive due to density fluctuations and the used clustering algorithm. It is also noteworthy that at 298 K and between 45 and 70 Å^2, there are slightly fewer domains as compared to the case at 310 K. However, the largest domain at 298 K is respectively larger in this interval of APLs.

To evaluate whether the observed domains are transient or long-lived, we analyzed the distributions of residence time of the lipid chains in the L_C-like regions. The residence time distributions for selected monolayers are shown in **Figure 5C**. These distributions clearly show power law scaling, i.e., the probability P of a binding time τ follows $P(\tau) = a \times \tau^b$. In the log-log scale, we extracted exponents b from a linear fit, and these exponents are shown in **Figure 5B**. The larger in absolute value of b, the faster the distribution decays, *i.e.* the less lipids reside for extended times in the L_C-like clusters. The exponents decrease upon increasing APL indicating that the residence times of lipids in the L_C-like regions decrease. At an APL of 50 Å^2, there are more than 100 events where a lipid stays in the L_C-like domain for more than 100 ns, and some lipids stay there throughout the entire simulation. Interestingly, the exponents start to rapidly decay at APLs of 60 Å^2 (298 K) or 55 Å^2 (310 K), indicating that long-lived domains are replaced by more dynamic heterogeneity. These APL values, again, agree well with those at which significant changes are observed in other monolayer properties (see previous section). At APLs smaller than 55 Å^2, the distributions at the two temperatures are very similar due to the large extent of the L_C-like regions, whereas there are clear differences in the APL range between 55 and 75 Å^2. Namely, the residence times for monolayers at 298 K are drastically longer. At areas above 75 Å^2, the L_C-like clusters are extremely dynamic and the longest residence times do not reach much over 10 ns regardless of the temperature.

4. DISCUSSION

We first extracted surface pressure-area isotherms from simulations and experiments. As these isotherms did not display a coexistence plateau, we performed AFM experiments that demonstrated the presence of sub-micrometer sized domains (**Figure 1**, **Supplementary Figures 2–5**). The height profiles (**Figure 2B**, **Supplementary Figures 6–9**) and the thickness profiles obtained from our simulations (**Figure 2C**) indicated

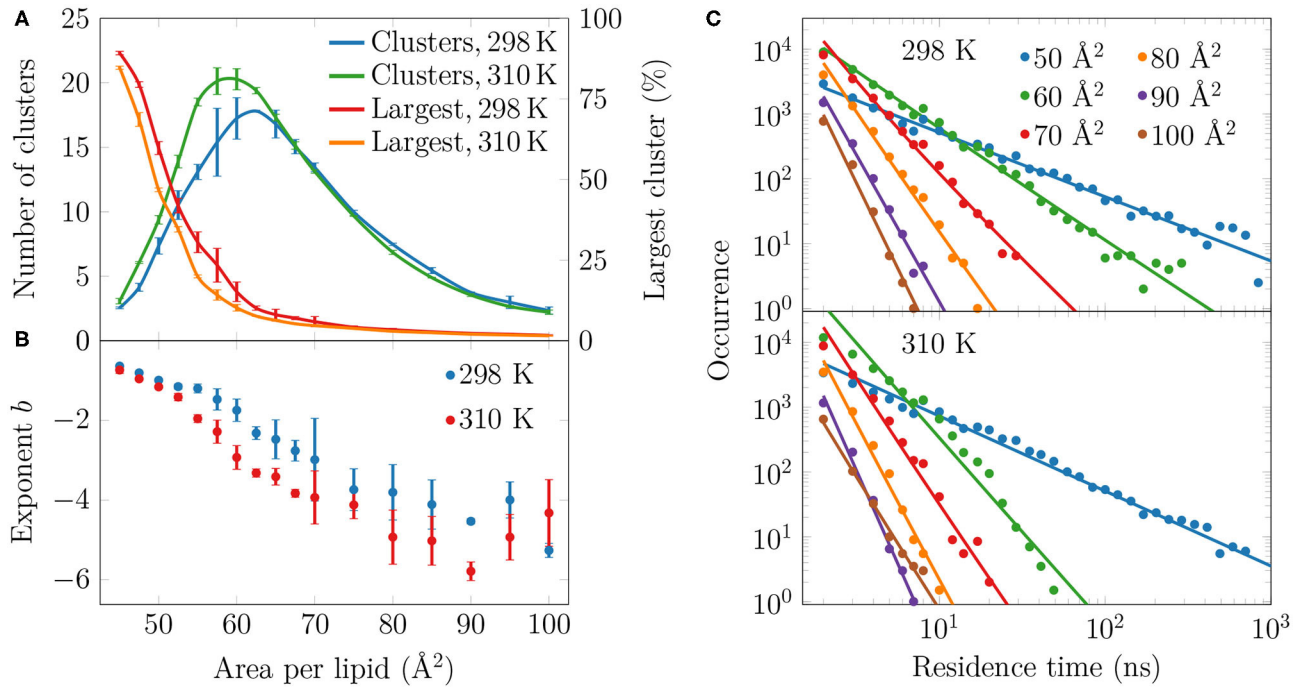

FIGURE 5 | Spatial and temporal extent of the L_C-like regions. **(A)** The numbers of clusters in monolayers at 298 and 310 K are shown in green and blue, respectively, whereas the largest clusters in these systems are indicated red and orange, respectively. **(B)** The exponents b of the fits in the form of $P(\tau) = a \times \tau^b$ to the residence time distributions in **(C)**. The error bars show the differences calculated for the two monolayers in the simulation system. **(C)** The lifetime distributions of the L_C-like domains for both 298 K (top) and 310 K (bottom). The solid lines show the power law fits.

that the domains resemble the L_C phase with hexagonal tail organization, whereas the remainder of the monolayer is in the L_E phase. A detailed investigation of the atomistic simulation data on the condensed domains showed that at large APL (>60 Å^2) these domains consisted of transient, isolated islands. As long as the condensed domains are "cushioned" by the surrounding L_E phase, the macroscopic properties of the monolayer such as dilatational/compressibility modulus resemble those of the L_E phase. Here, the domain morphology likely plays a minor effect. Interestingly, a similar observation emerged from a recent coarse-grained simulation study on the elastic properties of lipid bilayers (Eid et al., 2020); it was shown indeed that, in the presence of phase separation, bilayer elastic properties (including both the bending modulus and the area compressibility modulus) are close to the values calculated for the softer component. The present investigation extends the previous conclusion to monolayers not showing proper phase separation, but still presenting structural heterogeneity in the form of dynamic nano-sized domains. At smaller APL (<60 Å^2) the condensed domains become stable and form a continuous meshwork, which explains the sudden increase in rigidity of the monolayer indicated by the change in the dilatational modulus in Langmuir trough measurements (**Figure 3C**). The shift from transient to stable condensed domains was also accompanied by a change in the lateral diffusion dynamics in the monolayer, as well as in the lipid mixing properties (**Figure 4B**) and in the lifetimes of the L_C-like domains (**Figure 5**).

Stable phase separation has also been reported, employing fluorescence microscopy and AFM, in pulmonary surfactant extract bilayer (Bernardino de la Serna et al., 2004) and monolayer membranes (Bernardino de la Serna et al., 2013a), whose behavior was similar when the monolayer was compressed to a pressure of ∼30 mN/m. The monolayer phase behavior is naturally more complex of the two, as it is strongly affected by lateral pressure, as highlighted by AFM experiments (Bernardino de la Serna et al., 2013a). Importantly, the AFM images measured for monolayers from lung surfactant extracts [compare **Figure 1** with Bernardino de la Serna et al. (2013a)] are very similar to those obtained for our synthetic monolayers. This suggests that our quaternary lipid mixture captures the central features of the phase behavior of the entire complex pulmonary surfactant, suggesting a minor role of surfactant proteins in this respect. Lateral heterogeneity plays a major role in lung mechanics, as pulmonary surfactant needs to possess certain viscoelastic properties in order to decrease the surface tension to low levels upon compression, and at the same time maintain its ability to spread rapidly at the air–water interface, and fold away from the interface to form lipid reservoirs in the aqueous subphase when the lateral pressure exceeds a certain threshold.

The role of DPPC in the pulmonary surfactant has been pictured to reduce surface tension exclusively by forming condensed domains (Discher et al., 1999). This conclusion was drawn from experiments on calf pulmonary surfactant extracts

that displayed large flower-shaped DPPC-rich L_C-like domains. However, these experiments were performed at 293 K, i.e., 17 K lower than the physiologically relevant body temperature, which can have a major effect on phase behavior near a phase transition. In contrast, our simulations indicate that at room and physiological temperatures, DPPC is only slightly enriched in the L_C-like domains. Based on such results, we hypothesize that the role of DPPC is to act—together with cholesterol—as a nucleation center for the formation of domains into which lipids with unsaturated chains can also merge. This is further evidenced by our analyses on domain compositions and lifetimes, which suggests that lipids in monolayers have little tendency to undergo phase separation based on the saturation level of their acyl chains (**Figure 4**).

In terms of fluidity, POPG has been suggested to be a key player (Hook et al., 1984), in addition to its role in protein-lipid interactions (Pérez-Gil, 2008; Liekkinen et al., 2020). We observed that bulk L_E regions are indeed enriched in POPG. Still, the fluidity is not due to POPG alone, since all the lipid components display fairly similar diffusion coefficients across APL values (**Figure 3**). Additionally, we observed that cholesterol has a slight tendency to induce ordered clusters at large APLs, whereas the cholesterols themselves show little tendency to cluster together.

The fact that the spatial heterogeneity was dynamic and dictated by different packing ("physical separation") instead of the nature of the lipid species ("chemical separation"), suggests that the pulmonary surfactant has specific and collective viscoelastic properties that cannot be derived from the behavior of its components in a straightforward manner. These dynamic properties will be further clarified in our future work. This picture is drastically different from that obtained in similar mixtures using the coarse-grained Martini model: Baoukina et al. observed a plateau in the pressure-area isotherm for a monolayer that underwent "chemical" separation into very distinct phases (Baoukina et al., 2012). Thus, the absence of a plateau in experimental isotherms is in line with the domains visible in AFM images not being compositionally very different from the bulk parts of the monolayer. Moreover, our earlier studies (Bernardino de la Serna et al., 2009, 2013a) have indicated similar "physical separation" of lipids into observable co-existing L_E and L_C-like regions that have matching diffusion properties, indicating that the chemical compositions of the phases can remain similar in heterogeneous systems. Our simulations also indicate that the behavior of the monolayers is in general very similar at room and body temperature at the studied surface pressures below 50 mN/m. This is not very surprising, as both temperatures fall below the T_m of DPPC. In addition to these well-balanced viscoelastic properties of the pulmonary surfactant, the observed heterogeneity likely plays a role in regulating the function of surfactant proteins (Pérez-Gil, 2008; Bernardino de la Serna et al., 2009).

Computer simulations have become an indispensable tool in biological soft matter research due to their ability to probe small time and length scales (Enkavi et al., 2019). Traditionally, reproducing surface pressure-area isotherms in classical molecular dynamics simulations has been challenging, and—unlike here—the isotherms in earlier studies were often shifted artificially to match the experimental ones (Baoukina et al., 2007b; Huynh et al., 2014). This signals that, in previous simulation studies of pulmonary surfactant monolayers, the descriptions of the physics at the interface was inadequate due to inadequate water models (Baoukina et al., 2007b; Lamberg and Ollila, 2015). The simulation approach used in the present work largely overcomes these issues through a combination of recently developed simulation models and simulation parameters (Klauda et al., 2010; Izadi et al., 2014; Javanainen et al., 2017a). It is worth noting that the majority of atomistic water models also feature significant errors in air–water surface tension (Chen and Smith, 2007; Vega and De Miguel, 2007), and that OPC provides not only an accurate description of the surface tension, but also of many key properties of water (Izadi et al., 2014). As such performance is not achievable using three-site models (Izadi and Onufriev, 2016), and since the 4-point OPC water does not compromise the behavior of CHARMM36 lipids (Javanainen et al., 2017a), this combination should perhaps be adopted more widely.

The only apparent deviations between the current simulation model and experiment appear at small APLs, where a monolayer collapse plateau is observed in the experimental isotherms at above 45 mN/m and 50 mN/m surface pressures (with areas below 52 and 54 $Å^2$) at 298 and 310 K, respectively. This equilibrium collapse pressure is in the ballpark measured for numerous single-component monolayers (Mansour and Zografi, 2007). In the simulations at 298 and 310 K, the systems remain stable above the experimental equilibrium collapse pressures of phospholipid monolayers (Lee et al., 2001; Mansour and Zografi, 2007), which likely results from the fact that the simulated monolayer is kinetically trapped in a metastable state and its collapse is limited by the system size and its periodic nature. This limitation has two implications. On the one hand, it hinders studies of the formation of bilayer folds upon high lateral compression, i.e., during collapse. For such studies, the qualitative picture provided by the MARTINI model (Marrink et al., 2007) is likely sufficient (Baoukina et al., 2007a, 2008, 2014). On the other hand, the atomistic simulations might model well the non-equilibrium situation in the lungs, where monolayer collapse is prevented by rapid compression, and surface pressures can thus reach very high values (Crane and Hall, 2001). Experimentally, achieving such metastable states requires a specific Langmuir trough or the use of captive bubble surfactometer (Schürch et al., 1998; Crane et al., 1999).

One obvious question that arises is whether our AFM observations of sub-micrometer-sized domains are compatible with the nanoscopic and fairly transient domains detected in our simulations. This is a general problem in atomistic simulations, including those dealing with lipid bilayers that often compare heterogeneity between a simulation system with a few hundred lipids to experimental data obtained on phase-separating systems, where the phases would coalesce in any size scale if given enough time (Sodt et al., 2014). For us

the situation is slightly more favorable, as the length scales in our simulations and experiments are only 1–3 orders of magnitude apart. Line tension, i.e., the penalty of creating a domain boundary, dictates domain shapes (Bernardino de la Serna et al., 2004). The non-circular domain shapes observed by AFM indicate a fairly small line tension, which is also supported by the fact that small and independent domains do not coalesce—as would eventually happen in the case of phase separation. This is in line with the short lifetimes of domains observed in our simulations (**Figure 5C**). Based on the simulations, we hypothesize that the L_C-like domains are highly dynamic in monolayers at the air–water interface, but much less dynamic when the samples are transferred onto a mica substrate for AFM measurements. Nevertheless, the heterogeneity observed by AFM is not an artifact of the immobilization, as heterogeneity was also detected in the dilatational modulus of monolayers measured in the Langmuir trough (**Figure 3C**). Finally, it is worth again noting that the domains visible in our simulations are limited by the simulation box size, despite representing the state-of-the-art in this regard. Our control simulations with more lipids (see section 2) result in similar behavior, thus suggesting that the observed heterogeneity does not arise due to finite-size effects. The surface pressures were also unchanged by the change in simulation box size (**Supplementary Figure 1**). Still, the domain morphologies are likely dependent on the system size, and unfortunately proper lateral mixing of lipids is not feasible in the larger monolayers with atomistic simulations, nor in the smaller monolayer when most of the monolayer is part of the L_C-like regions. For the two key functions—the viscoelastic properties of the surfactant and phase-dependent protein functions (Bernardino de la Serna et al., 2004, 2009, 2013a,b; Pérez-Gil, 2008; Casals and Cañadas, 2012)—the domain morphology is likely not very important. The domain lifetimes extracted from simulations are likely dependent on the domain sizes, and thus also system sizes, since escaping a core of a larger domain takes more time. Unfortunately, extrapolating these lifetimes to microscopic scales is not straightforward.

Our study highlights that, despite the absence of a coexistence plateau in the surface pressure-area isotherm, heterogeneity at the nanometer scale—undetectable by fluorescence or Brewster angle microscopies—should be detected by experimental approaches other than AFM. The surface dilatational rheology measurements using an oscillating barrier readily observed a major change in the dilatational modulus at an APL where the heterogeneities begin to appear (**Figure 3C**). Lipid diffusion analyzed from the simulations also revealed a change in the trend at this crossover APL. As monolayer phase transitions are readily detected in experiments that probe lipid diffusion (Peters and Beck, 1983), such experiments could also detect smaller scale heterogeneity. Finally, lipid tilt measured from our simulations (**Figure 3B**) revealed a persistent tilt angle of 25° up to the crossover APL, and this behavior should be captured by either X-ray diffraction (Lee et al., 2002) or vibrational sum frequency generation spectroscopy methods (Ma and Allen, 2007).

5. CONCLUSIONS

Using a combination of Langmuir trough experiments, AFM imaging, and atomistic molecular dynamics simulations, we demonstrated that a synthetic quaternary lipid mixture is able to qualitatively reproduce the key features of the phase behavior of the native pulmonary surfactant extracts. Under a large range of compression levels, thicker L_C-like domains appear in the otherwise thinner L_E-phase monolayer. These domains are dynamic and only slightly enriched in DPPC with two saturated chains. We demonstrated that despite there not being a visible phase transition to the L_C phase, some monolayer properties change significantly at well-defined values of area per lipid, and this crossover value is consistent between numerous quantities. Moreover, since these properties should be readily measurable using experimental methods, our study also guides experimental work on detecting heterogeneities in biofilms.

Synthetic pulmonary surfactants mimicking the properties of the full functional surfactant are continuously investigated (Walther et al., 2019). A critical aspect is to find a proper lipid composition mixture. Our results highlight how already a few key lipid components of the pulmonary surfactant display small domains, resembling the behavior of surfactant extracts (Bernardino de la Serna et al., 2013a). The lipid mixture is able to pack in a dynamic manner, thus enabling efficient surface tension reduction while maintaining sufficient fluidity. This behavior might also be crucial for the function of surfactant proteins, as has been investigated in other molecular simulations with multilipid components (Robichaud et al., 2019), which we will focus on in our future work.

Our approach, combining the CHARMM36 force field with the four-point OPC water model, enables atomistic studies of lipid structures at the air–water interfaces in the complex pulmonary surfactant, allowing for studies of the physiologically important processes in the lung at a detail difficult to achieve experimentally. By integrating experimental data with molecular simulations, we provide, for the first time, a quantitatively accurate, unprecedented picture of the structural and dynamic properties of a realistic model of lung surfactant, under physiologically relevant conditions.

DATA AVAILABILITY STATEMENT

The datasets presented in this study can be found in online repositories. The names of the repository/repositories and accession number(s) can be found in the article/**Supplementary Material**.

AUTHOR CONTRIBUTIONS

MJ, LM, and IV designed the simulations. JL performed all simulations under the supervision of MJ and IV. JL and MJ analyzed the simulations. JB designed the isotherm and AFM experiments and analyzed the data. BS performed these experiments under the supervision of JB. RP designed, performed, and analyzed the surface dilatational rheology experiments. JL and MJ wrote the first draft of the manuscript. All

authors contributed to manuscript revision, read, and approved the submitted version.

FUNDING

JL and IV thank the Sigrid Juselius Foundation and the Academy of Finland (Centre of Excellence program) for financial support. IV also thanks the HiLIFE (Helsinki Institute of Life Science) Fellow program. RP thanks the Mary and Georg C. Ehrnrooth Foundation, the Eye and Tissue Bank Foundation, the Evald and Hilda Nissi Foundation and the Biomedicum Helsinki Foundation for financial support. LM acknowledges funding by the Institut national de la santé et de la recherche médicale (INSERM). MJ thanks the Emil Aaltonen Foundation for funding. BS and JB acknowledge funding from the Bill and Melinda Gates Foundation, Grant No. INV-016631.

ACKNOWLEDGMENTS

We thank CSC–IT Center for Science (Espoo, Finland) for computing resources.

SUPPLEMENTARY MATERIAL

The Supplementary Material for this article can be found online at: https://www.frontiersin.org/articles/10.3389/fcell.2020.581016/full#supplementary-material

REFERENCES

Abraham, M., Murtola, T., Schulz, R., Páll, S., Smith, J., Hess, B., et al. (2015). GROMACS: high performance molecular simulations through multi-level parallelism from laptops to supercomputers. *SoftwareX* 1–2, 19–25. doi: 10.1016/j.softx.2015.06.001

Almeida, P. F., Vaz, W. L., and Thompson, T. (1992). Lateral diffusion in the liquid phases of dimyristoylphosphatidylcholine/cholesterol lipid bilayers: a free volume analysis. *Biochemistry* 31, 6739–6747. doi: 10.1021/bi00144a013

Amigoni, A., Pettenazzo, A., Stritoni, V., and Circelli, M. (2017). Surfactants in acute respiratory distress syndrome in infants and children: past, present and future. *Clin. Drug Invest.* 37, 729–736. doi: 10.1007/s40261-017-0532-1

Andreassen, S., Steimle, K. L., Mogensen, M. L., Bernardino de la Serna, J., Rees, S., and Karbing, D. S. (2010). The effect of tissue elastic properties and surfactant on alveolar stability. *J. Appl. Physiol.* 109, 1369–1377. doi: 10.1152/japplphysiol.00844.2009

Baoukina, S., Mendez-Villuendas, E., and Tieleman, D. P. (2012). Molecular view of phase coexistence in lipid monolayers. *J. Am. Chem. Soc.* 134, 17543–17553. doi: 10.1021/ja304792p

Baoukina, S., Monticelli, L., Amrein, M., and Tieleman, D. P. (2007a). The molecular mechanism of monolayer-bilayer transformations of lung surfactant from molecular dynamics simulations. *Biophys. J.* 93, 3775–3782. doi: 10.1529/biophysj.107.113399

Baoukina, S., Monticelli, L., Marrink, S. J., and Tieleman, D. P. (2007b). Pressure-area isotherm of a lipid monolayer from molecular dynamics simulations. *Langmuir* 23, 12617–12623. doi: 10.1021/la702286h

Baoukina, S., Monticelli, L., Risselada, H. J., Marrink, S. J., and Tieleman, D. P. (2008). The molecular mechanism of lipid monolayer collapse. *Proc. Natl. Acad. Sci. U.S.A.* 105, 10803–10808. doi: 10.1073/pnas.0711563105

Baoukina, S., Rozmanov, D., Mendez-Villuendas, E., and Tieleman, D. P. (2014). The mechanism of collapse of heterogeneous lipid monolayers. *Biophys. J.* 107, 1136–1145. doi: 10.1016/j.bpj.2014.05.053

Baoukina, S., and Tieleman, D. (2011). Lung surfactant protein SP-B promotes formation of bilayer reservoirs from monolayer and lipid transfer between the interface and subphase. *Biophys. J.* 100, 1678–1687. doi: 10.1016/j.bpj.2011.02.019

Bernardino de la Serna, J., Hansen, S., Berzina, Z., Simonsen, A. C., Hannibal-Bach, H. K., Knudsen, J., et al. (2013a). Compositional and structural characterization of monolayers and bilayers composed of native pulmonary surfactant from wild type mice. *BBA-Biomembranes* 1828, 2450–2459. doi: 10.1016/j.bbamem.2013.07.008

Bernardino de la Serna, J., Oradd, G., Bagatolli, L. A., Simonsen, A. C., Marsh, D., Lindblom, G., et al. (2009). Segregated phases in pulmonary surfactant membranes do not show coexistence of lipid populations with differentiated dynamic properties. *Biophys. J.* 97, 1381–1389. doi: 10.1016/j.bpj.2009.06.040

Bernardino de la Serna, J., Pérez-Gil, J., Simonsen, A. C., and Bagatolli, L. A. (2004). Cholesterol rules: direct observation of the coexistence of two fluid phases in native pulmonary surfactant membranes at physiological temperatures. *J. Biol. Chem.* 279, 40715–40722. doi: 10.1074/jbc.M404648200

Bernardino de la Serna, J., Vargas, R., Picardi, V., Cruz, A., Arranz, R., Valpuesta, J. M., et al. (2013b). Segregated ordered lipid phases and protein-promoted membrane cohesivity are required for pulmonary surfactant films to stabilize and protect the respiratory surface. *Faraday Discuss.* 161, 535–548; discussion 563-589. doi: 10.1039/C2FD20096A

Brewer, J., Bernardino de la Serna, J., Wagner, K., and Bagatolli, L. A. (2010). Multiphoton excitation fluorescence microscopy in planar membrane systems. *BBA-Biomembranes* 1798, 1301–1308. doi: 10.1016/j.bbamem.2010.02.024

Brown, N. J., Dohm, M. T., Bernardino de la Serna, J., and Barron, A. E. (2011). Biomimetic N-terminal alkylation of peptoid analogues of surfactant protein C. *Biophys. J.* 101, 1076–1085. doi: 10.1016/j.bpj.2011.04.055

Casals, C., and Ca nadas, O. (2012). Role of lipid ordered/disordered phase coexistence in pulmonary surfactant function. *BBA-Biomembranes* 1818, 2550–2562. doi: 10.1016/j.bbamem.2012.05.024

Chen, F., and Smith, P. E. (2007). Simulated surface tension of common water models. *J. Chem. Phys.* 126:221101. doi: 10.1063/1.2745718

Crane, J. M., and Hall, S. B. (2001). Rapid compression transforms interfacial monolayers of pulmonary surfactant. *Biophys. J.* 80, 1863–1872. doi: 10.1016/S0006-3495(01)76156-5

Crane, J. M., Putz, G., and Hall, S. B. (1999). Persistence of phase coexistence in disaturated phosphatidylcholine monolayers at high surface pressures. *Biophys. J.* 77, 3134–3143. doi: 10.1016/S0006-3495(99)77143-2

Davis, R. S., Sunil Kumar, P., Sperotto, M. M., and Laradji, M. (2013). Predictions of phase separation in three-component lipid membranes by the MARTINI force field. *J. Phys. Chem. B* 117, 4072–4080. doi: 10.1021/jp4000686

Discher, B. M., Schief, W. R., Vogel, V., and Hall, S. B. (1999). Phase separation in monolayers of pulmonary surfactant phospholipids at the air-water interface: composition and structure. *Biophys. J.* 77, 2051–2061. doi: 10.1016/S0006-3495(99)77046-3

Dohm, M. T., Brown, N. J., Seurynck-Servoss, S. L., Bernardino de la Serna, J., and Barron, A. E. (2010). Mimicking SP-C palmitoylation on a peptoid-based sp-b analogue markedly improves surface activity. *BBA-Biomembranes* 1798, 1663–1678. doi: 10.1016/j.bbamem.2010.04.012

Domański, J., Marrink, S. J., and Schäfer, L. V. (2012). Transmembrane helices can induce domain formation in crowded model membranes. *BBA-Biomembranes* 1818, 984–994. doi: 10.1016/j.bbamem.2011.08.021

Dushianthan, A., Goss, V., Cusack, R., Grocott, M. P., and Postle, A. D. (2014). Altered molecular specificity of surfactant phosphatidycholine synthesis in patients with acute respiratory distress syndrome. *Respir. Res.* 15:128. doi: 10.1186/s12931-014-0128-8

Echaide, M., Autilio, C., Arroyo, R., and Pérez-Gil, J. (2017). Restoring pulmonary surfactant membranes and films at the respiratory surface. *BBA-Biomembranes* 1859, 1725–1739. doi: 10.1016/j.bbamem.2017.03.015

Eid, J., Razmazma, H., Jraij, A., Ebrahimi, A., and Monticelli, L. (2020). On calculating the bending modulus of lipid bilayer membranes from buckling simulations. *J. Phys. Chem. B.* 29, 6299–6311. doi: 10.1021/acs.jpcb.0c04253

Enkavi, G., Javanainen, M., Kulig, W., Róg, T., and Vattulainen, I. (2019). Multiscale simulations of biological membranes: the challenge to understand

biological phenomena in a living substance. *Chem. Rev*. 119, 5607–5774. doi: 10.1021/acs.chemrev.8b00538

Ester, M., Kriegel, H.-P., Sander, J., and Xu, X. (1996). "A density-based algorithm for discovering clusters in large spatial databases with noise," in *KDD, Vol. 96*, (Portland, OR), 226–231.

Goerke, J. (1998). Pulmonary surfactant: functions and molecular composition. *BBA-Mol. Basis. Dis*. 1408, 79–89. doi: 10.1016/S0925-4439(98)00060-X

Grocott, M. P. (2020). *A Clinical Trial of Nebulized Surfactant for the Treatment of Moderate to Severe COVID-19 (COVSurf)*. ClinicalTrials.gov identifier NCT04362059.

Gunther, A., Schmidt, R., Harodt, J., Schmehl, T., Walmrath, D., Ruppert, C., et al. (2002). Bronchoscopic administration of bovine natural surfactant in ARDS and septic shock: impact on biophysical and biochemical surfactant properties. *Eur. Respir. J*. 19, 797–804. doi: 10.1183/09031936.02.00243302

Hook, G., Spalding, J., Ortner, M., Tombropoulos, E., and Chignell, C. (1984). Investigation of phospholipids of the pulmonary extracellular lining by electron paramagnetic resonance. The effects of phosphatidylglycerol and unsaturated phosphatidylcholines on the fluidity of dipalmitoyl phosphatidylcholine. *Biochem. J*. 223, 533–542. doi: 10.1042/bj2230533

Huynh, L., Perrot, N., Beswick, V., Rosilio, V., Curmi, P. A., Sanson, A., et al. (2014). Structural properties of POPC monolayers under lateral compression: computer simulations analysis. *Langmuir* 30, 564–573. doi: 10.1021/la4043809

Izadi, S., Anandakrishnan, R., and Onufriev, A. V. (2014). Building water models: a different approach. *J. Phys. Chem. Lett*. 5, 3863–3871. doi: 10.1021/jz501780a

Izadi, S., and Onufriev, A. V. (2016). Accuracy limit of rigid 3-point water models. *J. Chem. Phys*. 145:074501. doi: 10.1063/1.4960175

Javanainen, M., Lamberg, A., Cwiklik, L., Vattulainen, I., and Ollila, O. S. (2017a). Atomistic model for nearly quantitative simulations of Langmuir monolayers. *Langmuir* 34, 2565–2572. doi: 10.1021/acs.langmuir.7b02855

Javanainen, M., Martinez-Seara, H., and Vattulainen, I. (2017b). Nanoscale membrane domain formation driven by cholesterol. *Sci. Rep*. 7, 1–10. doi: 10.1038/s41598-017-01247-9

Javanainen, M., Monticelli, L., Bernardino de la Serna, J., and Vattulainen, I. (2010). Free volume theory applied to lateral diffusion in Langmuir monolayers: atomistic simulations for a protein-free model of lung surfactant. *Langmuir* 26, 15436–15444. doi: 10.1021/la102454m

Kaganer, V. M., Möhwald, H., and Dutta, P. (1999). Structure and phase transitions in langmuir monolayers. *Rev. Mod. Phys*. 71:779. doi: 10.1103/RevModPhys.71.779

Klauda, J. B., Venable, R. M., Freites, J. A., OšConnor, J. W., Tobias, D. J., Mondragon-Ramirez, C., et al. (2010). Update of the CHARMM all-atom additive force field for lipids: validation on six lipid types. *J. Phys. Chem. B* 114, 7830–7843. doi: 10.1021/jp101759q

Klopfer, K., and Vanderlick, T. (1996). Isotherms of dipalmitoylphosphatidylcholine (DPPC) monolayers: features revealed and features obscured. *J. Colloid. Interface Sci*. 182, 220–229. doi: 10.1006/jcis.1996.0454

Lamberg, A., and Ollila, O. S. (2015). Comment on "Structural properties of POPC monolayers under lateral compression: computer simulations analysisŠŠ. *Langmuir* 31, 886–887. doi: 10.1021/la5025845

Lee, J., Cheng, X., Swails, J. M., Yeom, M. S., Eastman, P. K., Lemkul, J. A., et al. (2015). CHARMM-GUI input generator for NAMD, GROMACS, AMBER, OpenMM, and CHARMM/OpenMM simulations using the CHARMM36 additive force field. *J. Chem. Theory Comput*. 12, 405–413. doi: 10.1021/acs.jctc.5b00935

Lee, K. Y. C., Gopal, A., von Nahmen, A., Zasadzinski, J. A., Majewski, J., Smith, G. S., et al. (2002). Influence of palmitic acid and hexadecanol on the phase transition temperature and molecular packing of dipalmitoylphosphatidylcholine monolayers at the air-water interface. *J. Chem. Phys*. 116, 774–783. doi: 10.1063/1.1420730

Lee, S., Kim, D. H., and Needham, D. (2001). Equilibrium and dynamic interfacial tension measurements at microscopic interfaces using a micropipet technique. 2. Dynamics of phospholipid monolayer formation and equilibrium tensions at the water-air interface. *Langmuir* 17, 5544–5550. doi: 10.1021/la0103261

Lewis, J. (2020). *London's Exogenous Surfactant Study for COVID19 (LESSCOVID)*. ClinicalTrials.gov identifier NCT04375735.

Liekkinen, J., Enkavi, G., Javanainen, M., Olmeda, B., Pérez-Gil, J., and Vattulainen, I. (2020). Pulmonary surfactant lipid reorganization induced by the adsorption of the oligomeric surfactant protein B complex. *J. Mol. Biol*. 432, 3251–3268. doi: 10.1016/j.jmb.2020.02.028

Lim, J. B., Rogaski, B., and Klauda, J. B. (2011). Update of the cholesterol force field parameters in CHARMM. *J. Phys. Chem. B* 116, 203–210. doi: 10.1021/jp207925m

Ma, G., and Allen, H. C. (2007). Condensing effect of palmitic acid on DPPC in mixed Langmuir monolayers. *Langmuir* 23, 589–597. doi: 10.1021/la061870i

Mangiarotti, A., Caruso, B., and Wilke, N. (2014). Phase coexistence in films composed of DLPC and DPPC: a comparison between different model membrane systems. *BBA-Biomembranes* 1838, 1823–1831. doi: 10.1016/j.bbamem.2014.02.012

Mansour, H. M., and Zografi, G. (2007). Relationships between equilibrium spreading pressure and phase equilibria of phospholipid bilayers and monolayers at the air-water interface. *Langmuir* 23, 3809–3819. doi: 10.1021/la063053o

Marrink, S. J., Risselada, H. J., Yefimov, S., Tieleman, D. P., and De Vries, A. H. (2007). The MARTINI force field: coarse grained model for biomolecular simulations. *J. Phys. Chem. B* 111, 7812–7824. doi: 10.1021/jp071097f

Moller, J. C., Schaible, T., Roll, C., Schiffmann, J. H., Bindl, L., Schrod, L., et al. (2003). Treatment with bovine surfactant in severe acute respiratory distress syndrome in children: a randomized multicenter study. *Intensive Care Med*. 29, 437–446. doi: 10.1007/s00134-003-1650-1

Moy, V. T., Keller, D., Gaub, H., and McConnell, H. (1986). Long-range molecular orientational order in monolayer solid domains of phospholipid. *J. Phys. Chem*. 90, 3198–3202. doi: 10.1021/j100405a030

Nielsen, L. K., Bjørnholm, T., and Mouritsen, O. G. (2000). Critical phenomena: fluctuations caught in the act. *Nature* 404:352. doi: 10.1038/35006162

Olmeda, B., Villén, L., Cruz, A., Orellana, G., and Pérez-Gil, J. (2010). Pulmonary surfactant layers accelerate O_2 diffusion through the air-water interface. *BBA-Biomembranes* 1798, 1281–1284. doi: 10.1016/j.bbamem.2010.03.008

Olzyńska, A., Delcroix, P., Dolejšová, T., Krzaczek, K., Korchowiec, B., Czogalla, A., et al. (2020). Properties of lipid models of lung surfactant containing cholesterol and oxidized lipids: a mixed experimental and computational study. *Langmuir* 36, 1023–1033. doi: 10.1021/acs.langmuir.9b02469

Paananen, R. O., Javanainen, M., Holopainen, J. M., and Vattulainen, I. (2019). Crystalline wax esters regulate the evaporation resistance of tear film lipid layers associated with dry eye syndrome. *J. Phys. Chem. Lett*. 10, 3893–3898. doi: 10.1021/acs.jpclett.9b01187

Parra, E., and Pérez-Gil, J. (2015). Composition, structure and mechanical properties define performance of pulmonary surfactant membranes and films. *Chem. Phys. Lipids* 185, 153–175. doi: 10.1016/j.chemphyslip.2014.09.002

Pérez-Gil, J. (2008). Structure of pulmonary surfactant membranes and films: the role of proteins and lipid-protein interactions. *BBA-Biomembranes* 1778, 1676–1695. doi: 10.1016/j.bbamem.2008.05.003

Peters, R., and Beck, K. (1983). Translational diffusion in phospholipid monolayers measured by fluorescence microphotolysis. *Proc. Natl. Acad. Sci. U.S.A*. 80, 7183–7187. doi: 10.1073/pnas.80.23.7183

Possmayer, F., Hall, S. B., Haller, T., Petersen, N. O., Zuo, Y. Y., Bernardino de la Serna, J., et al. (2010). Recent advances in alveolar biology: some new looks at the alveolar interface. *Respir. Physiol. Neurobiol*. 173(Suppl.), S55-ŰS64. doi: 10.1016/j.resp.2010.02.014

Postle, A. D., Mander, A., Reid, K. B., Wang, J. Y., Wright, S. M., Moustaki, M., et al. (1999). Deficient hydrophilic lung surfactant proteins A and D with normal surfactant phospholipid molecular species in cystic fibrosis. *Am. J. Respir. Cell. Mol. Biol*. 20, 90–98. doi: 10.1165/ajrcmb.20.1.3253

Robichaud, N. A., Khatami, M. H., Saika-Voivod, I., and Booth, V. (2019). All-atom molecular dynamics simulations of dimeric lung surfactant protein B in lipid multilayers. *Int. J. Mol. Sci*. 20:3863. doi: 10.3390/ijms20163863

Schurch, S., Bachofen, H., Goerke, J., and Possmayer, F. (1989). A captive bubble method reproduces the *in situ* behavior of lung surfactant monolayers. *J. Appl. Phys*. 67, 2389–2396. doi: 10.1152/jappl.1989.67.6.2389

Schürch, S., Green, F. H., and Bachofen, H. (1998). Formation and structure of surface films: captive bubble surfactometry. *BBA-Mol. Basis Dis*. 1408, 180–202. doi: 10.1016/S0925-4439(98)00067-2

Sodt, A. J., Sandar, M. L., Gawrisch, K., Pastor, R. W., and Lyman, E. (2014). The molecular structure of the liquid-ordered phase of lipid bilayers. *J. Am. Chem. Soc*. 136, 725–732. doi: 10.1021/ja4105667

Steimle, K. L., Mogensen, M. L., Karbing, D. S., Bernardino de la Serna, J., and Andreassen, S. (2011). A model of ventilation of the healthy human lung. *Comput. Methods Programs Biomed.* 101, 144–155. doi: 10.1016/j.cmpb.2010.06.017

Suri, L. N., McCaig, L., Picardi, M. V., Ospina, O. L., Veldhuizen, R. A., Staples, J. F., et al. (2012). Adaptation to low body temperature influences pulmonary surfactant composition thereby increasing fluidity while maintaining appropriately ordered membrane structure and surface activity. *BBA-Biomembranes* 1818, 1581–1589. doi: 10.1016/j.bbamem.2012.02.021

Taeusch, H. W., Bernardino de la Serna, J., Pérez-Gil, J., Alonso, C., and Zasadzinski, J. A. (2005). Inactivation of pulmonary surfactant due to serum-inhibited adsorption and reversal by hydrophilic polymers: experimental. *Biophys. J.* 89, 1769–1779. doi: 10.1529/biophysj.105.062620

Tribello, G. A., Bonomi, M., Branduardi, D., Camilloni, C., and Bussi, G. (2014). PLUMED 2: new feathers for an old bird. *Comput. Phys. Commun.* 185, 604–613. doi: 10.1016/j.cpc.2013.09.018

Vega, C., and De Miguel, E. (2007). Surface tension of the most popular models of water by using the test-area simulation method. *J. Chem. Phys.* 126:154707. doi: 10.1063/1.2715577

Walmrath, D., Grimminger, F., Pappert, D., Knothe, C., Obertacke, U., Benzing, A., et al. (2002). Bronchoscopic administration of bovine natural surfactant in ards and septic shock: impact on gas exchange and haemodynamics. *Eur. Respir. J.* 19, 805–810. doi: 10.1183/09031936.02.00243402

Walmrath, D., Gunther, A., Ghofrani, H. A., Schermuly, R., Schneider, T., Grimminger, F., et al. (1996). Bronchoscopic surfactant administration in patients with severe adult respiratory distress syndrome and sepsis. *Am. J. Respir, Crit. Care Med.* 154, 57–62. doi: 10.1164/ajrccm.154.1.8680699

Walther, F. J., Gordon, L. M., and Waring, A. J. (2019). Advances in synthetic lung surfactant protein technology. *Expert Rev. Respir. Med.* 13, 499–501. doi: 10.1080/17476348.2019.1589372

Ware, L. B., and Matthay, M. A. (2000). The acute respiratory distress syndrome. *N. Engl. J. Med.* 342, 1334–1349. doi: 10.1056/NEJM200005043421806

Xu, Z., Shi, L., Wang, Y., Zhang, J., Huang, L., Zhang, C., et al. (2020). Pathological findings of COVID-19 associated with acute respiratory distress syndrome. *Lancet Respir. Med.* doi: 10.1016/S2213-2600(20)30076-X

Zasadzinski, J. A., Alig, T., Alonso, C., Bernardino de la Serna, J., Perez-Gil, J., and Taeusch, H. W. (2005). Inhibition of pulmonary surfactant adsorption by serum and the mechanisms of reversal by hydrophilic polymers: theory. *Biophys. J.* 89, 1621–1629. doi: 10.1529/biophysj.105.062646

Conflict of Interest: The authors declare that the research was conducted in the absence of any commercial or financial relationships that could be construed as a potential conflict of interest.

frontiers in Cell and Developmental Biology

REVIEW
published: 19 November 2020
doi: 10.3389/fcell.2020.580814

Membrane Heterogeneity Beyond the Plasma Membrane

Hong-Yin Wang[1†], Deepti Bharti[1,2†] and Ilya Levental[1]*

[1] Department of Molecular Physiology and Biological Physics, University of Virginia, Charlottesville, VA, United States,
[2] National Institute of Technology, Rourkela, India

The structure and organization of cellular membranes have received intense interest, particularly in investigations of the raft hypothesis. The vast majority of these investigations have focused on the plasma membrane of mammalian cells, yielding significant progress in understanding membrane heterogeneity in terms of lipid composition, molecular structure, dynamic regulation, and functional relevance. In contrast, investigations on lipid organization in other membrane systems have been comparatively scarce, despite the likely relevance of membrane domains in these contexts. In this review, we summarize recent observations on lipid organization in organellar membranes, including endoplasmic reticulum, Golgi, endo-lysosomes, lipid droplets, and secreted membranes like lung surfactant, milk fat globule membranes, and viral membranes. Across these non-plasma membrane systems, it seems that the biophysical principles underlying lipid self-organization contribute to lateral domains.

Keywords: membrane domain, lipid raft, organelle, Golgi, endoplasmic reticulum

OPEN ACCESS

Edited by:
Rainer A. Böckmann, University of Erlangen–Nuremberg, Germany

Reviewed by:
Iztok Urbancic, Institut "Jožef Stefan" (IJS), Slovenia
Leonel Malacrida, Universidad de la República, Uruguay
Erwin London, Stony Brook University, United States

****Correspondence:***
Ilya Levental
ilya.levental@uth.tmc.edu;
il2sy@virginia.edu

[†] These authors have contributed equally to this work

Specialty section:
This article was submitted to Cellular Biochemistry, a section of the journal Frontiers in Cell and Developmental Biology

Received: *07 July 2020*
Accepted: *02 October 2020*
Published: *19 November 2020*

Citation:
Wang H-Y, Bharti D and Levental I (2020) Membrane Heterogeneity Beyond the Plasma Membrane. Front. Cell Dev. Biol. 8:580814. doi: 10.3389/fcell.2020.580814

INTRODUCTION

The exquisite complexity and capability of biology are enabled largely by physical and/or biochemical compartmentalization. A predominant mechanism for biological compartmentalization is provided by lipid membranes, which partition intracellular space into membrane-bound organelles. Further, these membranes themselves can be compartmentalized into functional, lateral subdomains (Garcia-Parajo et al., 2014). The most well-studied example of such membrane subdomains is the so-called membrane rafts. In the present manuscript, "raft" describes lipid-driven, relatively ordered assemblies of lipids and proteins typically associated with the mammalian plasma membrane (PM) (Lingwood and Simons, 2010). Such domains result from preferential associations between cholesterol, sphingolipids, and other saturated lipids that produce a tightly packed lipid environment different from, and coexisting with, less tightly packed, non-raft membrane regions (Levental I. et al., 2020). In living cells, these effects are believed to produce nanoscopic, dynamic domains whose specific properties (sizes, lifetimes) are highly context-dependent. These domains have been implicated in various physiological roles, most notably signaling (Simons and Toomre, 2000) and membrane trafficking (Simons and Ikonen, 1997; Schuck and Simons, 2004), although their general function can be summarized as lateral sorting of proteins, which could facilitate or inhibit their interactions with other biomolecules (Lorent et al., 2017). There is also a growing body of evidence supporting similar membrane domains in prokaryotes, which may depend on sterol-analogous molecules like hopanoids

(Saenz et al., 2012; Saenz et al., 2015; Belin et al., 2018) or exogenous sterols scavenged from other organisms (Huang and London, 2016). This work has been expertly reviewed elsewhere (Lopez and Koch, 2017) and will not be discussed in detail here.

The raft phenomenon has been studied extensively, with much of that attention focused on functional domains of the PM. The reasons for this inordinate attention to PM rafts are both historical and practical. The raft concept was originally proposed to explain the unique sterol- and sphingolipid-enriched composition of the apical PM in epithelial cells (van Meer et al., 1987). In this context, self-assembly of raft-preferring lipids and proteins would aid in the sorting of PM-destined components in the trans-Golgi apparatus. Thus, a reasonable assumption would be that the PM is raft-rich. Functionally, the PM is the site for exchanging material and signals between cells and extracellular environments; thus, many interesting and important biological events are involved. Compositionally, the PM contains high levels of cholesterol (up to 40% mol; Levental et al., 2016, 2017; Lorent et al., 2020) and sphingolipids (10%; Symons et al., 2020), which tend to promote the formation of ordered raft domains (Jacobson et al., 2007). Finally and perhaps most significantly, the PM is large, relatively flat, and easily accessible for external labeling and manipulation, making it the most experimentally convenient membrane of the cell.

Despite these valid reasons for attention on mammalian PM domains, it is possible, if not likely, that similar principles of self-organization can drive membrane domains in other cell membranes. Lipids in other cell membranes have properties that tend to cause favorable interactions between various subclasses, leading to lateral heterogeneity. Examples of such properties include (a) acyl chain saturation, with relatively saturated lipids tending to pack together into ordered solid or liquid domains; (b) cholesterol abundance, with cholesterol interacting preferentially with relatively saturated lipids; (c) headgroup charge, with polyvalent cations or proteins capable of ionic cross-linking (Wang et al., 2002; Yeung et al., 2008; Levental et al., 2009); (d) specific headgroup chemistries driving self-association (Wang and Silvius, 2003; Sodt et al., 2015) and/or lipid-protein interactions (Ewers et al., 2010). Therefore, it is tempting to predict that membrane domains may also be present in organellar membranes beyond the PM.

Accumulating evidence indeed strongly suggests, and sometimes directly shows, the presence of lipid domains in various organelles. In this review, we summarize observations of lipid domains found in non-PM membranes, including subcellular organelles [endoplasmic reticulum (ER), Golgi, endosomes, lysosomes, and lipid droplets (LDs)] and non-cellular structures [milk fat and lung surfactant (LS)] (**Figure 1**). Where applicable, we also discuss the functional relevance of these domains in cellular physiology, with examples from a viral infection of mammalian cells to organelle inheritance in yeast. Although some clues suggest the possibility of lipid domains in nuclear (Cascianelli et al., 2008; Ramamurthy et al., 2018) and mitochondrial membranes (Garofalo et al., 2015), we have not focused on these organelles here. Notably, the lipid domains we reviewed here include not only liquid-ordered (Lo) domains or lipid rafts but also mechanisms of membrane compartmentalization based on solid domains or gel phases. These examples illustrate that the basic biophysical rules of membrane organization are applicable and physiologically relevant across living membrane systems.

LIPID DOMAINS OF THE ENDOPLASMIC RETICULUM

The ER is the largest cellular membrane system, consisting of a contiguous network of membrane tubes and sheets that comprises the cell's center for lipid metabolism (Shibata et al., 2006). Although cholesterol is produced in the ER, it is rapidly transported out into other organelles, partly through active machinery present at membrane contact sites (Lev, 2012; Mesmin et al., 2013; Phillips and Voeltz, 2016). For that reason, the ER stores only ∼0.5–1% of the cell's total cholesterol (Lange et al., 1999), comprising ∼3–5% of all ER lipids (Radhakrishnan et al., 2008). Due to such low cholesterol levels and low levels of saturated sphingolipids, the ER membrane is believed to be mostly disordered (Maxfield and Tabas, 2005; van Meer et al., 2008). Despite this generalization, some observations suggest that functional lipid nanodomains can exist in the ER under certain conditions.

Lipid Domains at Endoplasmic Reticulum Exit Sites

Membrane protein transport from the ER to the Golgi requires binding to the Sec24 subunit of the coat protein complex II vesicle coat. However, glycosylphosphatidylinositol (GPI)-anchored proteins cannot directly bind to Sec24 because they lack a cytosolic domain. Instead, the P24-P23 protein complex, which can bind to Sec24D, acts as a cargo receptor to mediate the export of GPI-anchored proteins like CD59 or the folate receptor (Bonnon et al., 2010). Because fully processed GPI-anchored proteins typically bear saturated acyl chains (Levental et al., 2010a), there is some suggestion that such GPI-anchor rich exit sites may be related to lipid raft domains on the ER membrane (Bonnon et al., 2010). Consistent with this notion, CD59 and P24-P23 are enriched in detergent-resistant membranes, the biochemical correlate of raft association (Bonnon et al., 2010). Cholesterol depletion disrupts the interaction between CD59 and P24-P23 and thus reduces the export of CD59 to Golgi, whereas the trafficking of non-raft proteins like transferrin receptor and ER–Golgi intermediate compartment-53 is not affected. The results indicate that functional lipid rafts at the ER membrane can assist GPI-anchored proteins in transporting to Golgi.

Evidence for Lipid Domains at Inter-Organelle Contact Sites

Mitochondria-associate membranes (MAMs) are ER subdomains that play crucial roles in inter-organellar crosstalk between ER and mitochondria required for the homeostasis of both organelles. It has been suggested that these MAMs also have unique lipid compositions that resemble

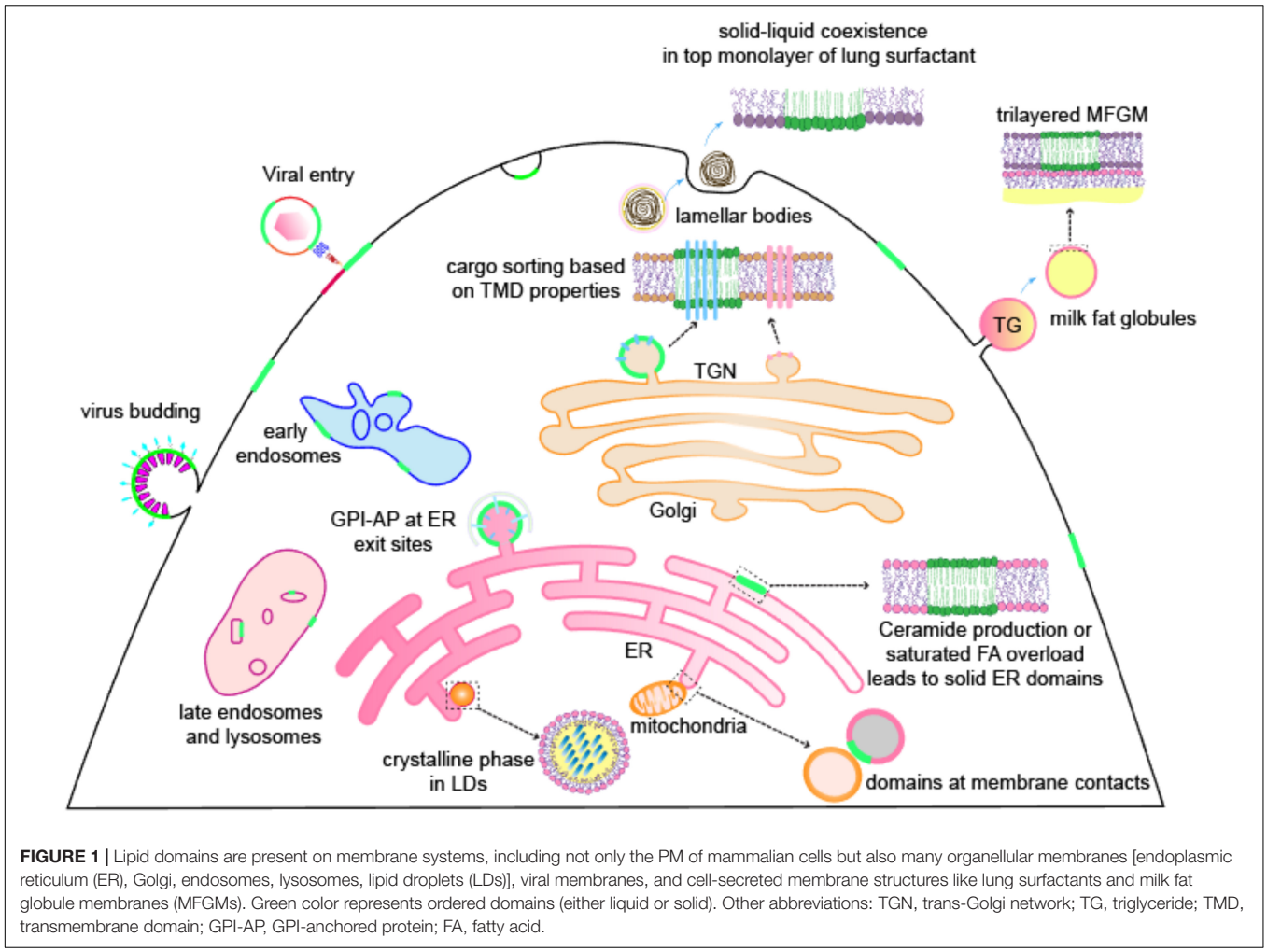

FIGURE 1 | Lipid domains are present on membrane systems, including not only the PM of mammalian cells but also many organellular membranes [endoplasmic reticulum (ER), Golgi, endosomes, lysosomes, lipid droplets (LDs)], viral membranes, and cell-secreted membrane structures like lung surfactants and milk fat globule membranes (MFGMs). Green color represents ordered domains (either liquid or solid). Other abbreviations: TGN, trans-Golgi network; TG, triglyceride; TMD, transmembrane domain; GPI-AP, GPI-anchored protein; FA, fatty acid.

lipid rafts (Garofalo et al., 2016). Indeed, cholesterol and glycosphingolipids appear to be concentrated at the MAMs and potentially required for MAM formation (Sano et al., 2009; Hayashi and Fujimoto, 2010; Garofalo et al., 2016). Such MAM lipid domains may play key functional roles in regulating autophagy, recruiting autophagy-related molecules to the MAM region to facilitate autophagosome formation (Garofalo et al., 2016).

The presence of lipid microdomains at inter-organelle contacts was also recently strikingly supported by observations of large intracellular vesicles induced by hypotonic swelling of adherent cells. This procedure results in the formation of large vesicles derived from various organelles, including ER, mitochondria, endosomes, and lysosomes (although not peroxisomes or LDs) (King et al., 2020). ER-derived vesicles showed microscopically observable phase separation below room temperature, revealed by segregation between disorder-preferring protein Sec61β and order-preferring GPI-anchored protein. Interestingly, these ordered domains appeared solid-like in their physical state, as their proteins were practically immobile as measured by fluorescence recovery after photobleaching (FRAP) (King et al., 2020). Notably, such ordered domains were particularly concentrated at ER contact sites with the PM, endosomes, LDs, and mitochondria, whereas relatively disordered domains formed contacts with lysosomes and peroxisomes. These micron-sized ordered domains at ER-mitochondria contact sites are consistent with the implications of raft nanodomains at ER-MAMs (Garofalo et al., 2016). Altogether, these observations suggest a putative role for ordered membrane microdomains in maintaining contacts responsible for inter-organellar lipid transfer. It is tempting to speculate on the lipid composition of the domains in the organelles in contact with the ER and the possibility that organellar contacts are mediated by apposing ordered domains; the unconventional large intracellular vesicle method may provide a tool to investigate such organization in intracellular membranes (Bag et al., 2020).

Gel-Like Domains in the Endoplasmic Reticulum

Much of the above discussion has focused on lipid rafts, which are defined in part by being in the Lo state. However, membrane lipids can also form non-liquid ordered domains, most notably the two-dimensional crystalline phase knows as the gel phase, or solid-ordered (So) phase. The So phase is similar to the Lo phase in its high degree of lipid order but distinguished by the negligibly low translational diffusivity of membrane components

(van Meer et al., 2008). This state is driven by very tight packing between saturated phospholipids, uninterrupted by sterols. Such functional solid nanodomains have been observed in the ER membrane of budding yeast (Clay et al., 2014). Such domains appear to behave as regulated membrane diffusion barriers for the cortical ER membrane at the neck of a nascent bud, the precursor of the daughter cell in dividing *Saccharomyces cerevisiae*. The function of these diffusion barriers is to retain misfolded or otherwise aberrant proteins in the mother cell, thus protecting the daughter cell from noxious ER stress. These domains are likely composed of sphingolipids, as these are the major saturated lipids in yeast, and inhibition of sphingolipid synthesis pathways (but not other lipids, including glycerolipid, lipid-linked oligosaccharide, and ergosterol) impaired diffusion barrier formation. Because inhibition of ergosterol did not abolish the diffusion barrier, the domains are probably So, rather than Lo. Importantly, such domains can serve as selective barriers to membrane inheritance: the long chains of sphingolipids, especially in an ordered state, present a relatively thick lipid bilayer, which tends to exclude membrane proteins with short transmembrane domains (TMDs) due to hydrophobic mismatch (Clay et al., 2014). This mechanism may be related to aging and renewal of yeast cells, as a perturbation of the diffusion barrier can lead to aberrant inheritance of membrane proteins from mother to daughter cells (Singh et al., 2017) and resulting reduction in culture lifetimes. Although the exact physical state of these diffusion-restrictive domains is not yet clearly defined, lipidomic, and biophysical studies should help resolve the composition and properties of these essential nanodomains.

Consistent with ordered nanodomains in yeast ER, large-scale lipid domains have been observed in mammalian ER under conditions of perturbed metabolism and lipid synthesis (Shen et al., 2017). Feeding HeLa cells with deuterated fatty acids allows observation of the products of lipid metabolism in the ER membrane with minimal perturbation using stimulated Raman scattering microscopy (Shen et al., 2017). Feeding saturated fatty acid increased the synthesis and accumulation of tightly packed saturated lipids, which, without the fluidizing effect of cholesterol, induced large So-like domains in the ER membrane. The domains excluded lipid dyes that partition into fluid membranes and ER membrane proteins and exhibited detergent resistance, low diffusivity, high conformational order, and high domain stability. As expected, large So domains are not compatible with normal cellular physiology and led to cytotoxicity, likely related to induced ER stress (Halbleib et al., 2017). Interestingly, feeding saturated fatty acids, together with their unsaturated counterparts (e.g., the fish oil component docosahexaenoic acid), eliminated solid domain formation and decreased cytotoxicity. These results are consistent with recent findings that maintaining the fluidity of the ER membrane is an essential homeostatic mechanism in mammalian cells (Levental K. R. et al., 2020). Micron-sized protein-free domains were also observed on ER membranes of central nervous system cells from hypothermic ground squirrels during hibernation (Azzam et al., 2000). These domains are reversible after body temperature rises. Whether these domains are related to So domains is worth further investigation.

Regulation of Membrane Physical State in Endoplasmic Reticulum

The physical state of the ER (e.g., fluidity, lipid packing, membrane thickness, curvature) must be carefully regulated to fulfill its versatile functions. The ER membranes must be fluid and compliant to accommodate nascent membrane proteins with diverse physical properties (Sharpe et al., 2010) but may require local regions to facilitate protein sorting or export (Bonnon et al., 2010; Clay et al., 2014). Perturbations to membrane fluidity can cause deleterious ER stress and result in cytotoxicity (Covino et al., 2016; Ernst et al., 2016; Halbleib et al., 2017; Shen et al., 2017; Levental K. R. et al., 2020). To maintain ER membrane homeostasis, cells use various "sense-and-response" regulators that combine sensitivity to membrane physical properties with a signaling module capable of feedback control (Covino et al., 2018). An archetypal example is Mga2, which sensitively detects aberrant lipid packing density of the ER membrane and responds by upregulating production of the desaturase enzyme that produces unsaturated lipids (Ballweg et al., 2020). Similarly, an overly thick ER membrane can induce the clustering of Ire1, activating the membrane stress response to maintain protein and lipid homeostasis (Halbleib et al., 2017). These and other mechanisms work in parallel to sense and regulate ER membrane biophysical properties and thereby ensure ER membrane homeostasis (Covino et al., 2018).

SORTING OUT THE GOLGI

Unlike the ER, which is a continuous network with a thin and readily deformable membrane to allow facile insertion of nascent membrane proteins, the Golgi apparatus is a polarized organelle composed of stacked cisternae functionally compartmentalized into cis-, medial-, and trans-Golgi (Boncompain and Weigel, 2018). The major functions of the Golgi complex are to process proteins received from the ER (via posttranslational modifications like glycosylation) and sort them for export to various cellular destinations (PM, endolysosomes, etc.). Due to the diversity of cargos, no single sorting model is likely to explain the trafficking rates and destinations of most membrane-bound proteins. Several different sorting models have been proposed, including selective vesicle trafficking, cisternal maturation, domain partitioning, and others, and it is likely that combinations, or possibly even all of these, are required for optimal Golgi function (Boncompain and Weigel, 2018). Irrespective of the specific sorting models, the importance of lipids and lipid domains in cargo sorting at the trans-Golgi network (TGN) has been well recognized (von Blume and Hausser, 2019). The inositide lipid PI4P is specifically enriched at the TGN (Weixel et al., 2005), where its generation drives cholesterol and ceramide transport from ER to Golgi through lipid transfer proteins oxysterol-binding protein (Mesmin et al., 2013) and ceramide transport protein (Hanada et al., 2003), respectively. Accumulation of ceramide leads to the production of sphingomyelin and other sphingolipids in the Golgi (D'Angelo et al., 2013), particularly the TGN, where their interactions with the accumulating cholesterol may potentiate the formation of raft domains (Simons and Ikonen, 1997; Schuck and Simons, 2004).

Another mechanism to enrich rafts in the Golgi is their specific exclusion from Golgi-to-ER retrograde carriers mediated by coat protein complex I (Brugger et al., 2000).

Such Golgi raft domains have been heavily implicated in protein sorting to the PM in non-polarized cells (Yoshimori et al., 1996; Diaz-Rohrer et al., 2014a) and, more specifically, to the apical PM in polarized epithelial cells (Simons and Ikonen, 1997; Paladino et al., 2004; Schuck and Simons, 2004; Surma et al., 2012). In this model, proteins destined for the PM (rich in raft-forming lipids; Gerl et al., 2012; Levental et al., 2016; Symons et al., 2020) are sorted at the TGN via their affinity for ordered membrane domains. These ordered membranes are then extracted from the TGN to form carrier vesicles rich in raft lipids and proteins, which are delivered as a bundle to the PM. Evidence supporting this raft-mediated mechanism is that cholesterol extraction or impaired sphingolipid synthesis reduces apical transport in epithelial cells (Hansen et al., 2000; Lipardi et al., 2000). Direct evidence of raft involvement in Golgi-mediated PM sorting has also been obtained by isolating a specific class of PM-directed vesicles in yeast. Vesicles marked by a raft-associated protein were enriched in sphingolipid and ergosterol and had more tightly packed membranes than membranes of the Golgi or parallel carrier vesicles (Klemm et al., 2009; Surma et al., 2011). In addition to their ability to sort lipids and proteins, raft domains may facilitate the budding of the vesicles due to the accumulation of line tension at the phase boundary between the raft and non-raft regions (Vind-Kezunovic et al., 2008; Surma et al., 2012).

Raft-based sorting in membrane traffic relies on proteins' preferential partitioning to ordered membrane domains. This partitioning relies on biophysical differences between membrane domains: raft domains are relatively thick and tightly packed, whereas more disordered domains are thinner and less packed. Thus, thicker raft bilayers favor the incorporation of proteins with long TMDs (Diaz-Rohrer et al., 2014b; Lorent and Levental, 2015). Consistently, bioinformatic analysis of single-pass transmembrane proteins revealed that PM proteins generally have longer hydrophobic sections compared with Golgi resided proteins (Sharpe et al., 2010). Experimentally, shortening the length of the PM-resident transmembrane helix leads to intracellular retention of proteins (Munro, 1995; Diaz-Rohrer et al., 2014b). Together, these observations reveal that the length of a protein's TMD is an important factor for cargo sorting at the TGN (Dukhovny et al., 2009). Similarly, other factors that determine a protein's association with raft domains (TMD surface area, palmitoylation; Levental et al., 2010b) are also correlated with PM localization (Lorent et al., 2017). A recent finding shows that soluble protein cargo lipoprotein lipase can also be sorted into sphingomyelin-rich secretory vesicles through binding to an integral membrane protein Syndecan-1, which depends on its TMD length to target sphingomyelin-rich domains (Sundberg et al., 2019). Finally, we recently observed that the biophysical asymmetry of the PM might be a determinant of protein sorting, with structurally asymmetric TMDs accumulating at the PM (Lorent et al., 2020). This observation suggests the possibility of "asymmetric domains" in the Golgi membrane that warrant future investigations. Notably, raft domains in the Golgi have yet to be directly observed and characterized, with the size and morphology of this organelle hindering unambiguous observations.

SHUTTLING THROUGH THE ENDO-LYSOSOMAL SYSTEM

Endosomes and lysosomes organize the sorting, recycling, and degradation of PM membrane components internalized via endocytosis. Endocytosis involves numerous mechanistically parallel pathways, several of which have been associated with raft domains, including caveolae (Parton and Richards, 2003), clathrin-independent carriers (Kirkham and Parton, 2005), and GPI-enriched endocytic compartments (Sabharanjak et al., 2002). After endocytosis, these vesicles coalesce together and fuse with preexisting early endosomes, which are likely rich in cholesterol and sphingomyelin because of their origin at the PM. As these vesicles mature into late endosomes and lysosomes, their abundance of cholesterol and sphingolipids is reduced (Tharkeshwar et al., 2017), although evidence from detergent resistance and electron microscopy suggests that microdomains are still present in late endosomes (Sobo et al., 2007) and lysosomes (Simons and Gruenberg, 2000). One hypothesis for the depletion of cholesterol and sphingolipids in later stages of the endocytic pathway is that the raft components are recycled back to PM. Consistent with this notion, raft lipids are indeed enriched in recycling compartments and intermediates (Gagescu et al., 2000; Diaz-Rohrer et al., 2014a). Similarly, TMD constructs with high raft affinity localize at the PM, whereas mutations that reduce raft affinity lead to accumulation in late endosomes and lysosomes (Diaz-Rohrer et al., 2014b). Interestingly, it was recently suggested that cholesterol might be transferred from endosomes to phagosomes, in a membrane microdomain-dependent process of phagosome maturation (Rai et al., 2016). These ordered membrane domains in phagosomes act as a platform to recruit a team of dynein molecules, microtubule motors that drive phagosomes toward lysosomes for degradation.

Perhaps because of the unique lipid composition of the lysosome, some of the clearest microscopic evidence for raft domains in living cells comes from studies of the vacuole in yeast, which is analogous to the mammalian lysosome. While in the logarithmic phase, the yeast vacuole appears microscopically homogenous. In striking contrast, vacuoles of yeast grown to stationary phase show micron-sized coexisting liquid domains with distinct ergosterol abundances (Toulmay and Prinz, 2013). The depletion of ergosterol abolishes the formation of these domains, suggesting that they are sterol-dependent (Toulmay and Prinz, 2013; Tsuji et al., 2017). Later observations confirmed that these domains bear key biophysical hallmarks of ordered–disordered liquid phase separation, including domain coalescence and temperature-dependent, reversible demixing (Rayermann et al., 2017). The functions of these coexisting domains are not completely understood, although they may be involved in nutrient signaling or lipid transport at interorganellar contact sites (Murley et al., 2017), as discussed above. Finally, as domains can promote membrane bending (Hamada et al.,

2007), phase separation could facilitate lipophagy through inward budding after binding to LDs (Seo et al., 2017). Thus, direct observations reveal large, ordered domains in live cells. The broad analogy between yeast vacuoles and mammalian lysosomes suggests that large-scale lipid phase separation may also be possible in mammalian cells under some conditions.

STRUCTURE IN THE FAT–LIPID PHASES IN LIPID DROPLETS

Lipid droplets are often misconceived as structureless and relatively inert fat particles, when in fact, these organelles are vital for cellular homeostasis via energy storage and detoxification of free fatty acids. Although not directly related to ordered membrane domains, LDs present some fascinating biophysical features worth brief consideration. Droplets are typically spherical intracellular organelles 0.1–100 μm in diameter. Their major structural feature is a large core of neutral lipids (primarily triglycerides, but also cholesterol esters) surrounded by a phospholipid monolayer derived from the ER (Thiam et al., 2013). LDs are generated by a gradual accumulation of neutral lipids in the hydrophobic core of the ER membrane, until a critical threshold is exceeded, causing a dilation of the hydrophobic core into a "lens domain" (Chapman et al., 2019). This lens expands until the droplet buds off the ER facilitated by fat-inducing transmembrane proteins 1 and 2. Recent observations revealed that under certain metabolic scenarios, the core of LD transitions from a disordered liquid to a smectic liquid-crystal with clear long-range order observable by cryogenic electron microscopy (Mahamid et al., 2019). These experimental observations can be well described by a phase diagram that predicts a phase transition between liquid and liquid-crystal phases under near-physiological conditions due to the presence of cholesterol esters (Shimobayashi and Ohsaki, 2019). The crystallization of the droplet core due to excess sterol esters may have pathogenic significance in the case of non-alcoholic steatohepatitis (Ioannou et al., 2019) and atherosclerosis (Lada et al., 2002). Interestingly, in analogy to LDs, low-density lipoprotein particles were also reported to show reversible liquid crystalline phase transitions at varying temperatures and lipid compositions (Deckelbaum et al., 1977; Sherman et al., 2003).

FUNCTION OF LIPID DOMAINS IN VIRAL ASSEMBLY

Enveloped viruses, including important pathogens like human immunodeficiency virus (HIV), influenza, Ebola, and coronaviruses, are encapsulated by a lipid membrane originating from the membranes of host cells during virus budding. In many of these cases, the viruses bud from the PM with an envelope relatively rich in cholesterol and sphingolipids, suggesting the possibility of raft involvement in membrane assembly (Ono and Freed, 2001). Indeed, the PMs of HIV and influenza are highly enriched in raft-associated lipids, even compared with the PM from which they bud (Brugger et al., 2006; Gerl et al., 2012), indicating that these viruses bud from raft-like regions of the PM, and thus, raft domains may exist in virus membrane envelope.

The involvement of raft domains in HIV assembly and budding was recently supported by an exciting set of microscopic studies relying on validated lipid and protein probes for membrane domains (Podkalicka and Bassereau, 2019; Sengupta et al., 2019). The nascent viral buds specifically recruited raft lipid probes like fluorescent cholesterol and sphingomyelin and lipidated proteins, while excluding markers of disordered domains (Sengupta et al., 2019). The observations also suggested that rather than budding at preexisting raft domains on PM, ordered domains were recruited and assembled actively after binding the HIV matrix protein Gag to the mammalian PM, consistent with previous studies (Ono and Freed, 2001). Gag is known to interact with the PM via binding to the charged phosphoinositide lipids PIP2 (Ono et al., 2004), which may couple with sphingolipid-rich outer leaflet (Lorent et al., 2020) to produce a transbilayer ordered domain. Similar coupling behavior has also been inferred between inner leaflet PS with long saturated acyl chains and outer leaflet GPI-anchored proteins (Raghupathy et al., 2015). Considering PS is also enriched in the HIV membrane (Lorizate et al., 2013), it is possible that enrichment of PS at the assembly site could further enhance coupling between the two leaflets to facilitate domain formation. Furthermore, the myristoyl chain in Gag protein may enhance its interaction with PIP2 and PS with saturated chains and stabilize raft domains.

The precise roles of membrane domains in viral function have not been completely resolved; however, several possibilities have been suggested by experimental evidence. First, similar to protein sorting in eukaryote membrane traffic, rafts may function as sorting platforms for selective incorporation/exclusion of viral proteins. Consistent with this notion, many viral envelope proteins are posttranslationally palmitoylated, including those of influenza (Kordyukova et al., 2008; Engel et al., 2010), HIV (Bhattacharya et al., 2004), the severe acute respiratory syndrome-related coronavirus (Petit et al., 2007), and Chikungunya (Zhang et al., 2019). Such palmitoylation would help target these viral proteins to PM rafts, as posttranslational palmitoylation has been established as a crucial signal for the recruitment of proteins to ordered domains (Levental et al., 2010b). It has been demonstrated that the ordered environment of the viral membrane stabilizes and affects the conformation of some envelope glycoproteins (Salimi et al., 2020), suggesting that rafts can both recruit and regulate viral protein function. Another important possibility is that the presence of a large membrane domain could promote the outward curvature required for the generation of a viral bud (Chazal and Gerlier, 2003). Moreover, the unique lipid composition of viral envelopes may promote their stability in cold air (Polozov et al., 2008), facilitating transmission. Consistently, the extraction of cholesterol from HIV and other viruses inactivated viral infectivity (Graham et al., 2003). Finally, raft domains on the viral envelope may play an essential role in the membrane fusion required for viral entry into infected cells. It was observed that the HIV fusion protein

gp41 preferentially attaches to the interface between ordered and disordered domains on the host membrane, perhaps due to the line energy present at this interface. The boundaries between the raft and non-raft domains on both the viral and host membranes are energetically costly, and this energy could be reduced by membrane fusion, potentially providing an energetic driver for viral entry (Yang et al., 2016, 2017).

PULMONARY SURFACTANT

Lung surfactant is a thin film of lipids and proteins at the surface of alveoli secreted by type II alveolar epithelial cells. The main function of LS is to reduce the surface tension at the air–alveoli interface and thereby protect alveoli from collapse during the rapid area compression–expansion involved in the breathing cycle (Perez-Gil, 2008). Surfactant deficiency, e.g., in premature neonates, can result in neonatal respiratory distress syndrome, which can be treated by administrating exogenous surfactant, consisting of lamella-forming mixtures of phospholipids, cholesterol, and proteins (Andersson et al., 2017). Lipids account for ∼90% of LS dry weight, with the most abundant being dipalmitoylphosphatidylcholine (40–70%) and cholesterol (10%) (Veldhuizen et al., 1998). The composite structures (lipid monolayer at the air/liquid interface, overlying multiple bilayers; Follows et al., 2007) and phase behaviors of LS are believed to be critical for its function. Neutron scattering experiments revealed multilamellar stacks that appear to be in the disordered phase at physiological temperature (Follows et al., 2007). This is somewhat surprising considering the high concentration of fully saturated lipids may be expected to form gel phases below 40°C. Although a membrane composed solely of pure So phase can efficiently reduce surface tension (Veldhuizen et al., 1998), it would not be as effective in the dynamic environment, experiencing rapid changes in shape and area. Thus, other unsaturated phospholipids and cholesterol are included in LS to provide essential fluidity and flexibility. These mixtures tend to form a variety of structures, including coexisting ordered and disordered domains (Casals and Canadas, 2012). This phase separation may facilitate the bending of LS films to provide membrane reservoirs for compression–expansion during respiration (Casals and Canadas, 2012). Moreover, various LS proteins partition differently into these lipid domains, or the domain interface, to stabilize the complex LS structures (Canadas et al., 2020). Ultimately, although the exact structure and dynamical properties of native LS are not yet fully elucidated, it is likely that lipid domains play an important role in maintaining key biophysical properties. Whether such domains may also play roles in molecular signaling, gas exchange, or other LS processes should also be explored.

MILK FAT GLOBULE MEMBRANE

Mammalian milk is rich in lipids packaged in the form of fat globules surrounded by a milk fat globule membrane (MFGM). The MFGM is an unusual tri-layer, whose inner monolayer is comprised of polar phospholipids and proteins surrounding a core of neutral triglycerides. This typical LD-like configuration is then surrounded by an outer bilayer, presumably acquired during extrusion of the LD-like fat globule through the apical surface of mammary epithelial cells (Lopez et al., 2010). The specific lipid composition of this unusual membrane differs somewhat among various mammalian species; however, it is broadly composed of approximately equimolar PE, PC, and sphingomyelin, with a relatively high abundance of cholesterol (chol/SM ∼ 3) (Et-Thakafy et al., 2017). Consistent with this composition and its origin in the apical PM of epithelial cells, the MFGM separates into coexisting ordered and disordered membrane domains over a large temperature range that includes physiologically relevant temperatures (Lopez et al., 2010; Et-Thakafy et al., 2017). Atomic force microscopy showed that these domains were different by approximately ∼1 nm in height (Murthy et al., 2016), consistent with the expected differences between ordered and disordered phases (Heberle et al., 2020). Domains with morphology reminiscent of both liquid (circular) and solid (jagged and irregular) phases are observable under various conditions, so it is not yet clear what determines the precise nature of the ordered phase. The physiological purpose of this phase coexistence is also not understood. It has been suggested that milk components can be antimicrobial, protecting against food-borne antigens. In this context, it is possible that the phase-separated MFGM could act as a "sink" for an unproductive fusion of viruses (Yang et al., 2016).

CONCLUSION AND OUTLOOK

The presence of lipid domains on non-PM membrane systems is fully consistent with, and a logical extension of, the lipid raft hypothesis. The evidence above combines to strongly support the relevance of lipid domains in various biological membranes, highlighting a general principle of membrane compartmentalization regulating various biological processes. The underlying biophysical insights generated from the intensive interest in PM lipid rafts are equally applicable to non-PM membrane systems. The experimental challenges of studying intracellular membranes have been a formidable barrier to a detailed understanding of their structure and organization: such membranes are not accessible to external labels or manipulations; organelles are often small and have a variety of complex shapes (tubules, folds, etc.); and various membranes are tightly packed inside the cells making unambiguous identification difficult. However, several methods have been recently developed that allow observations of large-scale domains, such as enlarging organelles through hypotonic swelling or fatty acid feeding (Shen et al., 2017; King et al., 2020). In parallel, the continuing advances in microscopic and spectroscopic technologies, and novel membrane sensitive probes (Klymchenko, 2017), are pushing toward the necessary temporal and spatial resolutions for unambiguous detection of membrane

domains (Stone and Veatch, 2015; Sezgin et al., 2017, 2019; Stone et al., 2017). Novel technologies such as label-free Raman microscopy (Shen et al., 2017) and cryoEM imaging of membrane properties (Heberle et al., 2020) are opening doors to dissect membrane domains with minimal perturbations inaccessible with typical fluorescence microscopy. Finally and most importantly, lateral heterogeneity is likely a widespread phenomenon across various biological membranes, prompting more directed attention to non-PM systems that have the potential to extend our understanding of the structure and function of living membranes.

AUTHOR CONTRIBUTIONS

All authors listed have made a substantial, direct and intellectual contribution to the work, and approved it for publication.

FUNDING

Funding for this work was provided by the NIH/National Institute of General Medical Sciences (GM114282, GM124072, GM120351, and GM134949), the Volkswagen Foundation (grant 93091), and the Human Frontiers Science Program (RGP0059/2019). All authors have no competing interests.

REFERENCES

Andersson, J. M., Grey, C., Larsson, M., Ferreira, T. M., and Sparr, E. (2017). Effect of cholesterol on the molecular structure and transitions in a clinical-grade lung surfactant extract. *Proc. Natl. Acad. Sci. U.S.A.* 114, E3592–E3601. doi: 10.1073/pnas.1701239114

Azzam, N. A., Hallenbeck, J. M., and Kachar, B. (2000). Membrane changes during hibernation. *Nature* 407, 317–318. doi: 10.1038/35030294

Bag, N., Ramezani, M., Holowka, D. A., and Baird, B. A. (2020). Bringing light to ER contacts and a new phase in organelle communication. *Proc. Natl. Acad. Sci. U.S.A.* 117, 9668–9670. doi: 10.1073/pnas.2003620117

Ballweg, S., Sezgin, E., Doktorova, M., Covino, R., Reinhard, J., Wunnicke, D., et al. (2020). Regulation of lipid saturation without sensing membrane fluidity. *Nat. Commun.* 11:756. doi: 10.1038/s41467-020-14528-1

Belin, B. J., Busset, N., Giraud, E., Molinaro, A., Silipo, A., and Newman, D. K. (2018). Hopanoid lipids: from membranes to plant-bacteria interactions. *Nat. Rev. Microbiol.* 16, 304–315. doi: 10.1038/nrmicro.2017.173

Bhattacharya, J., Peters, P. J., and Clapham, P. R. (2004). Human immunodeficiency virus type 1 envelope glycoproteins that lack cytoplasmic domain cysteines: impact on association with membrane lipid rafts and incorporation onto budding virus particles. *J. Virol.* 78, 5500–5506. doi: 10.1128/JVI.78.10.5500-5506.2004

Boncompain, G., and Weigel, A. V. (2018). Transport and sorting in the Golgi complex: multiple mechanisms sort diverse cargo. *Curr. Opin. Cell Biol.* 50, 94–101. doi: 10.1016/j.ceb.2018.03.002

Bonnon, C., Wendeler, M. W., Paccaud, J. P., and Hauri, H. P. (2010). Selective export of human GPI-anchored proteins from the endoplasmic reticulum. *J. Cell Sci.* 123, 1705–1715. doi: 10.1242/jcs.062950

Brugger, B., Glass, B., Haberkant, P., Leibrecht, I., Wieland, F. T., and Krausslich, H. G. (2006). The HIV lipidome: a raft with an unusual composition. *Proc. Natl. Acad. Sci. U.S.A.* 103, 2641–2646. doi: 10.1073/pnas.0511136103

Brugger, B., Sandhoff, R., Wegehingel, S., Gorgas, K., Malsam, J., Helms, J. B., et al. (2000). Evidence for segregation of sphingomyelin and cholesterol during formation of COPI-coated vesicles. *J. Cell Biol.* 151, 507–518. doi: 10.1083/jcb.151.3.507

Canadas, O., Olmeda, B., Alonso, A., and Perez-Gil, J. (2020). Lipid-protein and protein-protein interactions in the pulmonary surfactant system and their role in lung homeostasis. *Int. J. Mol. Sci.* 21:3708. doi: 10.3390/ijms21103708

Casals, C., and Canadas, O. (2012). Role of lipid ordered/disordered phase coexistence in pulmonary surfactant function. *Biochim. Biophys. Acta* 1818, 2550–2562. doi: 10.1016/j.bbamem.2012.05.024

Cascianelli, G., Villani, M., Tosti, M., Marini, F., Bartoccini, E., Magni, M. V., et al. (2008). Lipid microdomains in cell nucleus. *Mol. Biol. Cell* 19, 5289–5295. doi: 10.1091/mbc.e08-05-0517

Chapman, K. D., Aziz, M., Dyer, J. M., and Mullen, R. T. (2019). Mechanisms of lipid droplet biogenesis. *Biochem. J.* 476, 1929–1942. doi: 10.1042/BCJ20180021

Chazal, N., and Gerlier, D. (2003). Virus entry, assembly, budding, and membrane rafts. *Microbiol. Mol. Biol. Rev.* 67, 226–237. doi: 10.1128/MMBR.67.2.226-237.2003

Clay, L., Caudron, F., Denoth-Lippuner, A., Boettcher, B., Frei, S. B., Snapp, E. L., et al. (2014). A sphingolipid-dependent diffusion barrier confines ER stress to the yeast mother cell. *eLife* 3:e01883. doi: 10.7554/eLife.01883

Covino, R., Ballweg, S., Stordeur, C., Michaelis, J. B., Puth, K., Wernig, F., et al. (2016). A eukaryotic sensor for membrane lipid saturation. *Mol. Cell* 63, 49–59. doi: 10.1016/j.molcel.2016.05.015

Covino, R., Hummer, G., and Ernst, R. (2018). Integrated functions of membrane property sensors and a hidden side of the unfolded protein response. *Mol. Cell* 71, 458–467. doi: 10.1016/j.molcel.2018.07.019

D'Angelo, G., Uemura, T., Chuang, C. C., Polishchuk, E., Santoro, M., Ohvo-Rekila, H., et al. (2013). Vesicular and non-vesicular transport feed distinct glycosylation pathways in the Golgi. *Nature* 501, 116–120. doi: 10.1038/nature12423

Deckelbaum, R. J., Shipley, G. G., and Small, D. M. (1977). Structure and interactions of lipids in human plasma low density lipoproteins. *J. Biol. Chem.* 252, 744–754.

Diaz-Rohrer, B. B., Levental, K. R., and Levental, I. (2014a). Rafting through traffic: membrane domains in cellular logistics. *Biochim. Biophys. Acta Biomembr.* 1838, 3003–3013. doi: 10.1016/j.bbamem.2014.07.029

Diaz-Rohrer, B. B., Levental, K. R., Simons, K., and Levental, I. (2014b). Membrane raft association is a determinant of plasma membrane localization. *Proc. Natl. Acad. Sci. U.S.A.* 111, 8500–8505. doi: 10.1073/pnas.1404582111

Dukhovny, A., Yaffe, Y., Shepshelovitch, J., and Hirschberg, K. (2009). The length of cargo-protein transmembrane segments drives secretory transport by facilitating cargo concentration in export domains. *J. Cell Sci.* 122, 1759–1767. doi: 10.1242/jcs.039339

Engel, S., Scolari, S., Thaa, B., Krebs, N., Korte, T., Herrmann, A., et al. (2010). FLIM-FRET and FRAP reveal association of influenza virus haemagglutinin with membrane rafts. *Biochem. J.* 425, 567–573. doi: 10.1042/BJ20091388

Ernst, R., Ejsing, C. S., and Antonny, B. (2016). Homeoviscous adaptation and the regulation of membrane lipids. *J. Mol. Biol.* 428, 4776–4791. doi: 10.1016/j.jmb.2016.08.013

Et-Thakafy, O., Guyomarc'h, F., and Lopez, C. (2017). Lipid domains in the milk fat globule membrane: dynamics investigated in situ in milk in relation to temperature and time. *Food Chem.* 220, 352–361. doi: 10.1016/j.foodchem.2016.10.017

Ewers, H., Romer, W., Smith, A. E., Bacia, K., Dmitrieff, S., Chai, W., et al. (2010). GM1 structure determines SV40-induced membrane invagination and infection. *Nat. Cell Biol.* 12, 11–18. doi: 10.1038/ncb1999

Follows, D., Tiberg, F., Thomas, R. K., and Larsson, M. (2007). Multilayers at the surface of solutions of exogenous lung surfactant: direct observation by neutron reflection. *Biochim. Biophys. Acta* 1768, 228–235. doi: 10.1016/j.bbamem.2006.10.004

Gagescu, R., Demaurex, N., Parton, R. G., Hunziker, W., Huber, L. A., and Gruenberg, J. (2000). The recycling endosome of Madin-Darby canine kidney cells is a mildly acidic compartment rich in raft components. *Mol. Biol. Cell* 11, 2775–2791. doi: 10.1091/mbc.11.8.2775

Garcia-Parajo, M. F., Cambi, A., Torreno-Pina, J. A., Thompson, N., and Jacobson, K. (2014). Nanoclustering as a dominant feature of plasma membrane organization. *J. Cell Sci.* 127, 4995–5005. doi: 10.1242/jcs.146340

Garofalo, T., Manganelli, V., Grasso, M., Mattei, V., Ferri, A., Misasi, R., et al. (2015). Role of mitochondrial raft-like microdomains in the regulation of cell apoptosis. *Apoptosis* 20, 621–634. doi: 10.1007/s10495-015-1100-x

Garofalo, T., Matarrese, P., Manganelli, V., Marconi, M., Tinari, A., Gambardella, L., et al. (2016). Evidence for the involvement of lipid rafts localized at the ER-mitochondria associated membranes in autophagosome formation. *Autophagy* 12, 917–935. doi: 10.1080/15548627.2016.1160971

Gerl, M. J., Sampaio, J. L., Urban, S., Kalvodova, L., Verbavatz, J. M., Binnington, B., et al. (2012). Quantitative analysis of the lipidomes of the influenza virus envelope and MDCK cell apical membrane. *J. Cell Biol.* 196, 213–221. doi: 10.1083/jcb.201108175

Graham, D. R., Chertova, E., Hilburn, J. M., Arthur, L. O., and Hildreth, J. E. (2003). Cholesterol depletion of human immunodeficiency virus type 1 and simian immunodeficiency virus with beta-cyclodextrin inactivates and permeabilizes the virions: evidence for virion-associated lipid rafts. *J. Virol.* 77, 8237–8248. doi: 10.1128/JVI.77.15.8237-8248.2003

Halbleib, K., Pesek, K., Covino, R., Hofbauer, H. F., Wunnicke, D., Hanelt, I., et al. (2017). Activation of the unfolded protein response by lipid bilayer stress. *Mol. Cell* 67, 673–684.e8. doi: 10.1016/j.molcel.2017.06.012

Hamada, T., Miura, Y., Ishii, K., Araki, S., Yoshikawa, K., Vestergaard, M., et al. (2007). Dynamic processes in endocytic transformation of a raft-exhibiting giant liposome. *J. Phys. Chem. B* 111, 10853–10857. doi: 10.1021/jp075412+

Hanada, K., Kumagai, K., Yasuda, S., Miura, Y., Kawano, M., Fukasawa, M., et al. (2003). Molecular machinery for non-vesicular trafficking of ceramide. *Nature* 426, 803–809. doi: 10.1038/nature02188

Hansen, G. H., Niels-Christiansen, L. L., Thorsen, E., Immerdal, L., and Danielsen, E. M. (2000). Cholesterol depletion of enterocytes. Effect on the Golgi complex and apical membrane trafficking. *J. Biol. Chem.* 275, 5136–5142. doi: 10.1074/jbc.275.7.5136

Hayashi, T., and Fujimoto, M. (2010). Detergent-resistant microdomains determine the localization of sigma-1 receptors to the endoplasmic reticulum-mitochondria junction. *Mol. Pharmacol.* 77, 517–528. doi: 10.1124/mol.109.062539

Heberle, F. A., Doktorova, M., Scott, H. L., Skinkle, A., Waxham, M. N., and Levental, I. (2020). Direct label-free imaging of nanodomains in biomimetic and biological membranes by cryogenic electron microscopy. *Proc. Natl. Acad. Sci. U.S.A.* 117, 19943–19952. doi: 10.1073/pnas.2002200117

Huang, Z., and London, E. (2016). Cholesterol lipids and cholesterol-containing lipid rafts in bacteria. *Chem. Phys. Lipids* 199, 11–16. doi: 10.1016/j.chemphyslip.2016.03.002

Ioannou, G. N., Landis, C. S., Jin, G. Y., Haigh, W. G., Farrell, G. C., Kuver, R., et al. (2019). Cholesterol crystals in hepatocyte lipid droplets are strongly associated with human nonalcoholic steatohepatitis. *Hepatol. Commun.* 3, 776–791. doi: 10.1002/hep4.1348

Jacobson, K., Mouritsen, O. G., and Anderson, R. G. (2007). Lipid rafts: at a crossroad between cell biology and physics. *Nat. Cell Biol.* 9, 7–14. doi: 10.1038/ncb0107-7

King, C., Sengupta, P., Seo, A. Y., and Lippincott-Schwartz, J. (2020). ER membranes exhibit phase behavior at sites of organelle contact. *Proc. Natl. Acad. Sci. U.S.A.* 117, 7225–7235. doi: 10.1073/pnas.1910854117

Kirkham, M., and Parton, R. G. (2005). Clathrin-independent endocytosis: new insights into caveolae and non-caveolar lipid raft carriers. *Biochim. Biophys. Acta* 1746, 349–363. doi: 10.1016/j.bbamcr.2005.11.005

Klemm, R. W., Ejsing, C. S., Surma, M. A., Kaiser, H. J., Gerl, M. J., Sampaio, J. L., et al. (2009). Segregation of sphingolipids and sterols during formation of secretory vesicles at the trans-Golgi network. *J. Cell Biol.* 185, 601–612. doi: 10.1083/jcb.200901145

Klymchenko, A. S. (2017). Solvatochromic and fluorogenic dyes as environment-sensitive probes: design and biological applications. *Acc. Chem. Res.* 50, 366–375. doi: 10.1021/acs.accounts.6b00517

Kordyukova, L. V., Serebryakova, M. V., Baratova, L. A., and Veit, M. (2008). S acylation of the hemagglutinin of influenza viruses: mass spectrometry reveals site-specific attachment of stearic acid to a transmembrane cysteine. *J. Virol.* 82, 9288–9292. doi: 10.1128/JVI.00704-08

Lada, A. T., Willingham, M. C., and St Clair, R. W. (2002). Triglyceride depletion in THP-1 cells alters cholesteryl ester physical state and cholesterol efflux. *J. Lipid Res.* 43, 618–628.

Lange, Y., Ye, J., Rigney, M., and Steck, T. L. (1999). Regulation of endoplasmic reticulum cholesterol by plasma membrane cholesterol. *J. Lipid Res.* 40, 2264–2270.

Lev, S. (2012). Nonvesicular lipid transfer from the endoplasmic reticulum. *Cold Spring Harbor Perspect. Biol.* 4:a013300. doi: 10.1101/cshperspect.a013300

Levental, I., Christian, D. A., Wang, Y. H., Madara, J. J., Discher, D. E., and Janmey, P. A. (2009). Calcium-dependent lateral organization in phosphatidylinositol 4,5-bisphosphate (PIP2)- and cholesterol-containing monolayers. *Biochemistry* 48, 8241–8248. doi: 10.1021/bi9007879

Levental, I., Grzybek, M., and Simons, K. (2010a). Greasing their way: lipid modifications determine protein association with membrane rafts. *Biochemistry* 49, 6305–6316. doi: 10.1021/bi100882y

Levental, I., Levental, K. R., and Heberle, F. A. (2020). Lipid rafts: controversies resolved, mysteries remain. *Trends Cell Biol.* 30, 341–353. doi: 10.1016/j.tcb.2020.01.009

Levental, I., Lingwood, D., Grzybek, M., Coskun, U., and Simons, K. (2010b). Palmitoylation regulates raft affinity for the majority of integral raft proteins. *Proc. Natl. Acad. Sci. U.S.A.* 107, 22050–22054. doi: 10.1073/pnas.1016184107

Levental, K. R., Lorent, J. H., Lin, X., Skinkle, A. D., Surma, M. A., Stockenbojer, E. A., et al. (2016). Polyunsaturated lipids regulate membrane domain stability by tuning membrane order. *Biophys. J.* 110, 1800–1810. doi: 10.1016/j.bpj.2016.03.012

Levental, K. R., Malmberg, E., Symons, J. L., Fan, Y. Y., Chapkin, R. S., Ernst, R., et al. (2020). Lipidomic and biophysical homeostasis of mammalian membranes counteracts dietary lipid perturbations to maintain cellular fitness. *Nat. Commun.* 11:1339. doi: 10.1038/s41467-020-15203-1

Levental, K. R., Surma, M. A., Skinkle, A. D., Lorent, J. H., Zhou, Y., Klose, C., et al. (2017). omega-3 polyunsaturated fatty acids direct differentiation of the membrane phenotype in mesenchymal stem cells to potentiate osteogenesis. *Sci. Adv.* 3:eaao1193. doi: 10.1126/sciadv.aao1193

Lingwood, D., and Simons, K. (2010). Lipid rafts as a membrane-organizing principle. *Science* 327, 46–50. doi: 10.1126/science.1174621

Lipardi, C., Nitsch, L., and Zurzolo, C. (2000). Detergent-insoluble GPI-anchored proteins are apically sorted in fischer rat thyroid cells, but interference with cholesterol or sphingolipids differentially affects detergent insolubility and apical sorting. *Mol. Biol. Cell* 11, 531–542. doi: 10.1091/mbc.11.2.531

Lopez, C., Madec, M.-N., and Jimenez-Flores, R. (2010). Lipid rafts in the bovine milk fat globule membrane revealed by the lateral segregation of phospholipids and heterogeneous distribution of glycoproteins. *Food Chem.* 120, 22–33. doi: 10.1016/j.foodchem.2009.09.065

Lopez, D., and Koch, G. (2017). Exploring functional membrane microdomains in bacteria: an overview. *Curr. Opin. Microbiol.* 36, 76–84. doi: 10.1016/j.mib.2017.02.001

Lorent, J. H., Diaz-Rohrer, B., Lin, X., Spring, K., Gorfe, A. A., Levental, K. R., et al. (2017). Structural determinants and functional consequences of protein affinity for membrane rafts. *Nat. Commun.* 8:1219. doi: 10.1038/s41467-017-01328-3

Lorent, J. H., and Levental, I. (2015). Structural determinants of protein partitioning into ordered membrane domains and lipid rafts. *Chem. Phys. Lipids* 192, 23–32. doi: 10.1016/j.chemphyslip.2015.07.022

Lorent, J. H., Levental, K. R., Ganesan, L., Rivera-Longsworth, G., Sezgin, E., Doktorova, M., et al. (2020). Plasma membranes are asymmetric in lipid unsaturation, packing and protein shape. *Nat. Chem. Biol.* 16, 644–652. doi: 10.1038/s41589-020-0529-6

Lorizate, M., Sachsenheimer, T., Glass, B., Habermann, A., Gerl, M. J., Krausslich, H. G., et al. (2013). Comparative lipidomics analysis of HIV-1 particles and their producer cell membrane in different cell lines. *Cell. Microbiol.* 15, 292–304. doi: 10.1111/cmi.12101

Mahamid, J., Tegunov, D., Maiser, A., Arnold, J., Leonhardt, H., Plitzko, J. M., et al. (2019). Liquid-crystalline phase transitions in lipid droplets are related to cellular states and specific organelle association. *Proc. Natl. Acad. Sci. U.S.A.* 116, 16866–16871. doi: 10.1073/pnas.1903642116

Maxfield, F. R., and Tabas, I. (2005). Role of cholesterol and lipid organization in disease. *Nature* 438, 612–621. doi: 10.1038/nature04399

Mesmin, B., Bigay, J., Moser, J., von Filseck, S., Lacas-Gervais, G. D., and Antonny, B. (2013). A four-step cycle driven by PI(4)P hydrolysis directs sterol/PI(4)P exchange by the ER-Golgi tether OSBP. *Cell* 155, 830–843. doi: 10.1016/j.cell.2013.09.056

Munro, S. (1995). An investigation of the role of transmembrane domains in Golgi protein retention. *Embo J.* 14, 4695–4704. doi: 10.1002/j.1460-2075.1995.tb00151.x

Murley, A., Yamada, J., Niles, B. J., Toulmay, A., Prinz, W. A., Powers, T., et al. (2017). Sterol transporters at membrane contact sites regulate TORC1 and TORC2 signaling. *J. Cell Biol.* 216, 2679–2689. doi: 10.1083/jcb.201610032

Murthy, A. V. R., Guyomarc'h, F., and Lopez, C. (2016). The temperature-dependent physical state of polar lipids and their miscibility impact the topography and mechanical properties of bilayer models of the milk fat globule membrane. *Biochim. Biophys. Acta* 1858, 2181–2190. doi: 10.1016/j.bbamem.2016.06.020

Ono, A., Ablan, S. D., Lockett, S. J., Nagashima, K., and Freed, E. O. (2004). Phosphatidylinositol (4,5) bisphosphate regulates HIV-1 Gag targeting to the plasma membrane. *Proc. Natl. Acad. Sci. U.S.A.* 101, 14889–14894. doi: 10.1073/pnas.0405596101

Ono, A., and Freed, E. O. (2001). Plasma membrane rafts play a critical role in HIV-1 assembly and release. *Proc. Natl. Acad. Sci. U.S.A.* 98, 13925–13930. doi: 10.1073/pnas.241320298

Paladino, S., Sarnataro, D., Pillich, R., Tivodar, S., Nitsch, L., and Zurzolo, C. (2004). Protein oligomerization modulates raft partitioning and apical sorting of GPI-anchored proteins. *J. Cell Biol.* 167, 699–709. doi: 10.1083/jcb.200407094

Parton, R. G., and Richards, A. A. (2003). Lipid rafts and caveolae as portals for endocytosis: new insights and common mechanisms. *Traffic* 4, 724–738. doi: 10.1034/j.1600-0854.2003.00128.x

Perez-Gil, J. (2008). Structure of pulmonary surfactant membranes and films: the role of proteins and lipid-protein interactions. *Biochim. Biophys. Acta* 1778, 1676–1695. doi: 10.1016/j.bbamem.2008.05.003

Petit, C. M., Chouljenko, V. N., Iyer, A., Colgrove, R., Farzan, M., Knipe, D. M., et al. (2007). Palmitoylation of the cysteine-rich endodomain of the SARS-coronavirus spike glycoprotein is important for spike-mediated cell fusion. *Virology* 360, 264–274. doi: 10.1016/j.virol.2006.10.034

Phillips, M. J., and Voeltz, G. K. (2016). Structure and function of ER membrane contact sites with other organelles. *Nat. Rev. Mol. Cell Biol.* 17, 69–82. doi: 10.1038/nrm.2015.8

Podkalicka, J., and Bassereau, P. (2019). How membrane physics rules the HIV envelope. *Nat. Cell Biol.* 21, 413–415. doi: 10.1038/s41556-019-0312-7

Polozov, I. V., Bezrukov, L., Gawrisch, K., and Zimmerberg, J. (2008). Progressive ordering with decreasing temperature of the phospholipids of influenza virus. *Nat. Chem. Biol.* 4:248. doi: 10.1038/nchembio.77

Radhakrishnan, A., Goldstein, J. L., McDonald, J. G., and Brown, M. S. (2008). Switch-like control of SREBP-2 transport triggered by small changes in ER cholesterol: a delicate balance. *Cell Metab.* 8, 512–521. doi: 10.1016/j.cmet.2008.10.008

Raghupathy, R., Anilkumar, A. A., Polley, A., Singh, P. P., Yadav, M., Johnson, C., et al. (2015). Transbilayer lipid interactions mediate nanoclustering of lipid-anchored proteins. *Cell* 161, 581–594. doi: 10.1016/j.cell.2015.03.048

Rai, A., Pathak, D., Thakur, S., Singh, S., Dubey, A. K., and Mallik, R. (2016). Dynein clusters into lipid microdomains on phagosomes to drive rapid transport toward lysosomes. *Cell* 164, 722–734. doi: 10.1016/j.cell.2015.12.054

Ramamurthy, B., Cohen, S., Canales, M., and Coffman, F. D. (2018). Three-dimensional cellular raman analysis: evidence of highly ordered lipids within cell nuclei. *J. Histochem. Cytochem.* 66, 889–902. doi: 10.1369/0022155418794125

Rayermann, S. P., Rayermann, G. E., Cornell, C. E., Merz, A. J., and Keller, S. L. (2017). Hallmarks of reversible separation of living, unperturbed cell membranes into two liquid phases. *Biophys. J.* 113, 2425–2432. doi: 10.1016/j.bpj.2017.09.029

Sabharanjak, S., Sharma, P., Parton, R. G., and Mayor, S. (2002). GPI-anchored proteins are delivered to recycling endosomes via a distinct cdc42-regulated, clathrin-independent pinocytic pathway. *Dev. Cell* 2, 411–423. doi: 10.1016/S1534-5807(02)00145-4

Saenz, J. P., Grosser, D., Bradley, A. S., Lagny, T. J., Lavrynenko, O., Broda, M., et al. (2015). Hopanoids as functional analogues of cholesterol in bacterial membranes. *Proc. Natl. Acad. Sci. U.S.A.* 112, 11971–11976. doi: 10.1073/pnas.1515607112

Saenz, J. P., Sezgin, E., Schwille, P., and Simons, K. (2012). Functional convergence of hopanoids and sterols in membrane ordering. *Proc. Natl. Acad. Sci. U.S.A.* 109, 14236–14240. doi: 10.1073/pnas.1212141109

Salimi, H., Johnson, J., Flores, M. G., Zhang, M. S., O'Malley, Y., Houtman, J. C., et al. (2020). The lipid membrane of HIV-1 stabilizes the viral envelope glycoproteins and modulates their sensitivity to antibody neutralization. *J. Biol. Chem.* 295, 348–362. doi: 10.1074/jbc.RA119.009481

Sano, R., Annunziata, I., Patterson, A., Moshiach, S., Gomero, E., Opferman, J., et al. (2009). GM1-ganglioside accumulation at the mitochondria-associated ER membranes links ER stress to Ca(2+)-dependent mitochondrial apoptosis. *Mol. Cell* 36, 500–511. doi: 10.1016/j.molcel.2009.10.021

Schuck, S., and Simons, K. (2004). Polarized sorting in epithelial cells: raft clustering and the biogenesis of the apical membrane. *J. Cell Sci.* 117, 5955–5964. doi: 10.1242/jcs.01596

Sengupta, P., Seo, A. Y., Pasolli, H. A., Song, Y. E., Johnson, M. C., and Lippincott-Schwartz, J. (2019). A lipid-based partitioning mechanism for selective incorporation of proteins into membranes of HIV particles. *Nat. Cell Biol.* 21, 452–461. doi: 10.1038/s41556-019-0300-y

Seo, A. Y., Lau, P. W., Feliciano, D., Sengupta, P., Gros, M. A. L., Cinquin, B., et al. (2017). AMPK and vacuole-associated Atg14p orchestrate mu-lipophagy for energy production and long-term survival under glucose starvation. *eLife* 6:e21690. doi: 10.7554/eLife.21690

Sezgin, E., Schneider, F., Galiani, S., Urbancic, I., Waithe, D., Lagerholm, B. C., et al. (2019). Measuring nanoscale diffusion dynamics in cellular membranes with super-resolution STED-FCS. *Nat. Protoc.* 14, 1054–1083. doi: 10.1038/s41596-019-0127-9

Sezgin, E., Schneider, F., Zilles, V., Urbancic, I., Garcia, E., Waithe, D., et al. (2017). Polarity-sensitive probes for superresolution stimulated emission depletion microscopy. *Biophys. J.* 113, 1321–1330. doi: 10.1016/j.bpj.2017.06.050

Sharpe, H. J., Stevens, T. J., and Munro, S. (2010). A comprehensive comparison of transmembrane domains reveals organelle-specific properties. *Cell* 142, 158–169. doi: 10.1016/j.cell.2010.05.037

Shen, Y., Zhao, Z., Zhang, L., Shi, L., Shahriar, S., Chan, R. B., et al. (2017). Metabolic activity induces membrane phase separation in endoplasmic reticulum. *Proc. Natl. Acad. Sci. U.S.A.* 114, 13394–13399. doi: 10.1073/pnas.1712555114

Sherman, M. B., Orlova, E. V., Decker, G. L., Chiu, W., and Pownall, H. J. (2003). Structure of triglyceride-rich human low-density lipoproteins according to cryoelectron microscopy. *Biochemistry* 42, 14988–14993. doi: 10.1021/bi0354738

Shibata, Y., Voeltz, G. K., and Rapoport, T. A. (2006). Rough sheets and smooth tubules. *Cell* 126, 435–439. doi: 10.1016/j.cell.2006.07.019

Shimobayashi, S. F., and Ohsaki, Y. (2019). Universal phase behaviors of intracellular lipid droplets. *Proc. Natl. Acad. Sci. U.S.A.* 116, 25440–25445. doi: 10.1073/pnas.1916248116

Simons, K., and Gruenberg, J. (2000). Jamming the endosomal system: lipid rafts and lysosomal storage diseases. *Trends Cell Biol.* 10, 459–462. doi: 10.1016/S0962-8924(00)01847-X

Simons, K., and Ikonen, E. (1997). Functional rafts in cell membranes. *Nature* 387, 569–572. doi: 10.1038/42408

Simons, K., and Toomre, D. (2000). Lipid rafts and signal transduction. *Nat. Rev. Mol. Cell Biol.* 1, 31–39. doi: 10.1038/35036052

Singh, P., Ramachandran, S. K., Zhu, J., Kim, B. C., Biswas, D., Ha, T., et al. (2017). Sphingolipids facilitate age asymmetry of membrane proteins in dividing yeast cells. *Mol. Biol. Cell* 28, 2712–2722. doi: 10.1091/mbc.e17-05-0335

Sobo, K., Chevallier, J., Parton, R. G., Gruenberg, J., and van der Goot, F. G. (2007). Diversity of raft-like domains in late endosomes. *PLoS One* 2:e391. doi: 10.1371/journal.pone.0000391

Sodt, A. J., Pastor, R. W., and Lyman, E. (2015). Hexagonal substructure and hydrogen bonding in liquid-ordered phases containing palmitoyl sphingomyelin. *Biophys. J.* 109, 948–955. doi: 10.1016/j.bpj.2015.07.036

Stone, M. B., Shelby, S. A., Nunez, M. F., Wisser, K., and Veatch, S. L. (2017). Protein sorting by lipid phase-like domains supports emergent signaling function in B lymphocyte plasma membranes. *eLife* 6:e19891. doi: 10.7554/eLife.19891

Stone, M. B., and Veatch, S. L. (2015). Steady-state cross-correlations for live two-colour super-resolution localization data sets. *Nat. Commun.* 6:7347. doi: 10.1038/ncomms9319

Sundberg, E. L., Deng, Y., and Burd, C. G. (2019). Syndecan-1 mediates sorting of soluble lipoprotein lipase with sphingomyelin-rich membrane in the golgi apparatus. *Dev. Cell* 51, 387–398. doi: 10.1016/j.devcel.2019.08.014

Surma, M. A., Klose, C., Klemm, R. W., Ejsing, C. S., and Simons, K. (2011). Generic sorting of raft lipids into secretory vesicles in yeast. *Traffic* 12, 1139–1147. doi: 10.1111/j.1600-0854.2011.01221.x

Surma, M. A., Klose, C., and Simons, K. (2012). Lipid-dependent protein sorting at the trans-Golgi network. *Biochim. Biophys. Acta* 1821, 1059–1067. doi: 10.1016/j.bbalip.2011.12.008

Symons, J. L., Cho, K. J., Chang, J. T., Du, G., Waxham, M. N., Hancock, J. F., et al. (2020). Lipidomic atlas of mammalian cell membranes reveals hierarchical variation induced by culture conditions, subcellular membranes, and cell lineages. *Soft. Matter*. doi: 10.1039/D0SM00404A. [Epub ahead of print].

Tharkeshwar, A. K., Trekker, J., Vermeire, W., Pauwels, J., Sannerud, R., Priestman, D. A., et al. (2017). A novel approach to analyze lysosomal dysfunctions through subcellular proteomics and lipidomics: the case of NPC1 deficiency. *Sci. Rep.* 7:41408. doi: 10.1038/srep41408

Thiam, A. R., Farese, R. V. Jr., and Walther, T. C. (2013). The biophysics and cell biology of lipid droplets. *Nat. Rev. Mol. Cell Biol.* 14, 775–786. doi: 10.1038/nrm3699

Toulmay, A., and Prinz, W. A. (2013). Direct imaging reveals stable, micrometer-scale lipid domains that segregate proteins in live cells. *J. Cell Biol.* 202, 35–44. doi: 10.1083/jcb.201301039

Tsuji, T., Fujimoto, M., Tatematsu, T., Cheng, J., Orii, M., Takatori, S., et al. (2017). Niemann-Pick type C proteins promote microautophagy by expanding raft-like membrane domains in the yeast vacuole. *eLife* 6:e25960. doi: 10.7554/eLife.25960

van Meer, G., Stelzer, E. H., Wijnaendts-van-Resandt, R. W., and Simons, K. (1987). Sorting of sphingolipids in epithelial (Madin-Darby canine kidney) cells. *J. Cell Biol.* 105, 1623–1635. doi: 10.1083/jcb.105.4.1623

van Meer, G., Voelker, D. R., and Feigenson, G. W. (2008). Membrane lipids: where they are and how they behave. *Nat. Rev. Mol. Cell Biol.* 9, 112–124. doi: 10.1038/nrm2330

Veldhuizen, R., Nag, K., Orgeig, S., and Possmayer, F. (1998). The role of lipids in pulmonary surfactant. *Biochim. Biophys. Acta* 1408, 90–108. doi: 10.1016/S0925-4439(98)00061-1

Vind-Kezunovic, D., Nielsen, C. H., Wojewodzka, U., and Gniadecki, R. (2008). Line tension at lipid phase boundaries regulates formation of membrane vesicles in living cells. *Biochim. Biophys. Acta* 1778, 2480–2486. doi: 10.1016/j.bbamem.2008.05.015

von Blume, J., and Hausser, A. (2019). Lipid-dependent coupling of secretory cargo sorting and trafficking at the trans-Golgi network. *FEBS Lett.* 593, 2412–2427. doi: 10.1002/1873-3468.13552

Wang, J., Gambhir, A., Hangyas-Mihalyne, G., Murray, D., Golebiewska, U., and McLaughlin, S. (2002). Lateral sequestration of phosphatidylinositol 4,5-bisphosphate by the basic effector domain of myristoylated alanine-rich C kinase substrate is due to nonspecific electrostatic interactions. *J. Biol. Chem.* 277, 34401–34412. doi: 10.1074/jbc.M203954200

Wang, T. Y., and Silvius, J. R. (2003). Sphingolipid partitioning into ordered domains in cholesterol-free and cholesterol-containing lipid bilayers. *Biophys. J.* 84, 367–378. doi: 10.1016/S0006-3495(03)74857-7

Weixel, K. M., Blumental-Perry, A., Watkins, S. C., Aridor, M., and Weisz, O. A. (2005). Distinct Golgi populations of phosphatidylinositol 4-phosphate regulated by phosphatidylinositol 4-kinases. *J. Biol. Chem.* 280, 10501–10508. doi: 10.1074/jbc.M414304200

Yang, S. T., Kiessling, V., and Tamm, L. K. (2016). Line tension at lipid phase boundaries as driving force for HIV fusion peptide-mediated fusion. *Nat. Commun.* 7:11401. doi: 10.1038/ncomms11401

Yang, S. T., Kreutzberger, A. J. B., Kiessling, V., Ganser-Pornillos, B. K., White, J. M., and Tamm, L. K. (2017). HIV virions sense plasma membrane heterogeneity for cell entry. *Sci. Adv.* 3:e1700338. doi: 10.1126/sciadv.1700338

Yeung, T., Gilbert, G. E., Shi, J., Silvius, J., Kapus, A., and Grinstein, S. (2008). Membrane phosphatidylserine regulates surface charge and protein localization. *Science* 319, 210–213. doi: 10.1126/science.1152066

Yoshimori, T., Keller, P., Roth, M. G., and Simons, K. (1996). Different biosynthetic transport routes to the plasma membrane in BHK and CHO cells. *J. Cell Biol.* 133, 247–256. doi: 10.1083/jcb.133.2.247

Zhang, N., Zhao, H., and Zhang, L. (2019). Fatty acid synthase promotes the palmitoylation of chikungunya virus nsP1. *J. Virol.* 93, e1747–e1718. doi: 10.1128/JVI.01747-18

Conflict of Interest: The authors declare that the research was conducted in the absence of any commercial or financial relationships that could be construed as a potential conflict of interest.

frontiers in Immunology

ORIGINAL RESEARCH
published: 27 November 2020
doi: 10.3389/fimmu.2020.590121

Maturation of Monocyte-Derived DCs Leads to Increased Cellular Stiffness, Higher Membrane Fluidity, and Changed Lipid Composition

*Jennifer J. Lühr[1,2,3], Nils Alex[4], Lukas Amon[1], Martin Kräter[3,5], Markéta Kubánková[3,5], Erdinc Sezgin[6,7], Christian H. K. Lehmann[1], Lukas Heger[1], Gordon F. Heidkamp[1,8], Ana-Sunčana Smith[9], Vasily Zaburdaev[3,10,11], Rainer A. Böckmann[12], Ilya Levental[13], Michael L. Dustin[14], Christian Eggeling[7,15,16], Jochen Guck[3,5] and Diana Dudziak[1,11,17,18]**

[1] Laboratory of Dendritic Cell Biology, Department of Dermatology, Friedrich-Alexander University Erlangen-Nürnberg (FAU), University Hospital Erlangen, Erlangen, Germany, [2] Nano-Optics, Max-Planck Institute for the Science of Light, Erlangen, Germany, [3] Max-Planck-Zentrum für Physik und Medizin, Erlangen, Germany, [4] Department of Physics, Friedrich-Alexander University Erlangen-Nürnberg (FAU), Erlangen, Germany, [5] Biological Optomechanics, Max-Planck Institute for the Science of Light, Erlangen, Germany, [6] Science for Life Laboratory, Department of Women's and Children's Health, Karolinska Institutet, Stockholm, Sweden, [7] MRC Human Immunology Unit, Weatherall Institute of Molecular Medicine, John Raddcliffe Hospital, University of Oxford, Oxford, United Kingdom, [8] Roche Innovation Center Munich, Roche Pharmaceutical Research and Early Development, pRED, Munich, Germany, [9] PULS Group, Department of Physics, IZNF, Friedrich-Alexander University Erlangen-Nürnberg (FAU), Erlangen, Germany, [10] Mathematics in Life Sciences, Department of Biology, Friedrich-Alexander University Erlangen-Nürnberg (FAU), Erlangen, Germany, [11] Medical Immunology Campus Erlangen, Erlangen, Germany, [12] Computational Biology, Department of Biology, Friedrich-Alexander University Erlangen-Nürnberg (FAU), Erlangen, Germany, [13] McGovern Medical School, The University of Texas Health Science Center, Houston, TX, United States, [14] Kennedy Institute of Rheumatology, University of Oxford, Oxford, United Kingdom, [15] Institute for Applied Optics and Biophysics, Friedrich-Schiller University Jena, Jena, Germany, [16] Leibniz Institute of Photonic Technologies e.V., Jena, Germany, [17] Deutsches Zentrum Immuntherapie (DZI), Erlangen, Germany, [18] Comprehensive Cancer Center Erlangen-European Metropolitan Area of Nuremberg (CCC ER-EMN), Erlangen, Germany

OPEN ACCESS

Edited by:
Cheol-Heui Yun,
Seoul National University, South Korea

Reviewed by:
Ole Jørgen Bjarnason Landsverk,
Oslo University Hospital, Norway
Ken Shortman,
Walter and Eliza Hall Institute of Medical Research, Australia

***Correspondence:**
Diana Dudziak
diana.dudziak@uk-erlangen.de

Specialty section:
This article was submitted to Molecular Innate Immunity, a section of the journal Frontiers in Immunology

Received: 31 July 2020
Accepted: 15 October 2020
Published: 27 November 2020

Citation:
Lühr JJ, Alex N, Amon L, Kräter M, Kubánková M, Sezgin E, Lehmann CHK, Heger L, Heidkamp GF, Smith A-S, Zaburdaev V, Böckmann RA, Levental I, Dustin ML, Eggeling C, Guck J and Dudziak D (2020) Maturation of Monocyte-Derived DCs Leads to Increased Cellular Stiffness, Higher Membrane Fluidity, and Changed Lipid Composition. Front. Immunol. 11:590121. doi: 10.3389/fimmu.2020.590121

Dendritic cells (DCs) are professional antigen-presenting cells of the immune system. Upon sensing pathogenic material in their environment, DCs start to mature, which includes cellular processes, such as antigen uptake, processing and presentation, as well as upregulation of costimulatory molecules and cytokine secretion. During maturation, DCs detach from peripheral tissues, migrate to the nearest lymph node, and find their way into the correct position in the net of the lymph node microenvironment to meet and interact with the respective T cells. We hypothesize that the maturation of DCs is well prepared and optimized leading to processes that alter various cellular characteristics from mechanics and metabolism to membrane properties. Here, we investigated the mechanical properties of monocyte-derived dendritic cells (moDCs) using real-time deformability cytometry to measure cytoskeletal changes and found that mature moDCs were stiffer compared to immature moDCs. These cellular changes likely play an important role in the processes of cell migration and T cell activation. As lipids constitute the building blocks of the plasma membrane, which, during maturation, need to adapt to the environment for migration and DC-T cell interaction, we performed an unbiased high-throughput lipidomics screening to identify the lipidome of moDCs. These

analyses revealed that the overall lipid composition was significantly changed during moDC maturation, even implying an increase of storage lipids and differences of the relative abundance of membrane lipids upon maturation. Further, metadata analyses demonstrated that lipid changes were associated with the serum low-density lipoprotein (LDL) and cholesterol levels in the blood of the donors. Finally, using lipid packing imaging we found that the membrane of mature moDCs revealed a higher fluidity compared to immature moDCs. This comprehensive and quantitative characterization of maturation associated changes in moDCs sets the stage for improving their use in clinical application.

Keywords: cell mechanics, cellular stiffness, lipids, lipidomics, monocyte-derived dendritic cells, maturation, low-density lipoprotein, cholesterol

INTRODUCTION

Dendritic cells (DCs) are very important professional antigen-presenting cells of the immune system (1). They are distributed throughout the body including lymphohematopoietic tissues such as the lymph nodes, thymus, tonsils, or spleen, but can also be found in barrier tissues such as the skin, brain, or mucosa (2, 3). DCs act as sentinels and form a bridge between innate and adaptive immunity (4). Upon recognition of pathogenic antigens, DCs upregulate costimulatory molecules and chemokine receptors, secrete cytokines, and migrate into secondary lymphoid organs (5–7). During these maturation steps, DCs process the acquired antigens and present small peptides in the major histocompatibility complex (MHC; in humans: human leucocyte antigen HLA) binding groove. T cells that recognize these peptide:MHC complexes in an inflammatory context — possibly correlating to the peptide-dependent flexibility of the peptide:MHC complex (8) — become activated and undergo proliferative responses, finally leading to immunity. In dependency of the DC subset that is presenting the antigen as well as the cytokine milieu, naïve T cells differentiate into different sets of T effector cells (9–12). Besides, DCs play also a pivotal role in regulating peripheral tolerance in the steady-state, as they are able to present self-antigens in a non-inflammatory environment and thus activate regulatory $CD4^+$ T cells and induce a non-responsive state in T effector cells (1, 13, 14). Due to their exceptional ability to orchestrate T cell responses, DCs represent ideal targets for immunotherapeutic approaches (1, 2, 15–17).

In general, DCs are distinguished into conventional DCs type 1 (cDC1), type 2 (cDC2), and plasmacytoid DCs (3, 16, 18–20). While these populations are present under both, homeostatic and inflammatory conditions, the development of a cell population from monocytes sharing key phenotypic and functional characteristics with cDCs has been described exclusively in an inflammatory milieu *in vivo* (21). This population is regularly referred to as monocyte-derived DCs (moDCs), inflammatory DCs, or Tip DCs in the literature (16, 22, 23). In contrast to cDCs, monocytes exhibit a high frequency in human blood rendering them an interesting tool for the generation of vast moDC numbers for autologous cell transfer approaches (23–25). Further, the combination of robustness, functional parallels to primary DCs, and availability emphasize the application of moDCs as a model system to gain a general overview in new aspects of DC biology (26, 27).

The *in vitro* differentiation of moDCs from monocytes in the presence of granulocyte-macrophage colony-stimulating factor (GM-CSF) and interleukin-4 (IL-4) was established over two decades ago and allows for the generation of large amounts of moDCs (24, 28, 29). Following cultivation, moDCs can be matured *via* various stimuli including the application of agonistic αCD40 antibodies, TLR ligands (including LPS, (TLR4 ligand), poly (I:C) (TLR3 ligand), CpG (TLR9 ligand)), or cytokine cocktails (such as the classical maturation cocktail comprising IL-1β, PGE_2, IL-6, and TNFα) (29, 30). Mature moDCs share a multitude of features with primary DCs in peripheral blood including a typical stellate morphology, high expression of MHC I and MHC II, and the ability of antigen presentation.

The principle of cell-based therapy using moDCs for self-vaccination against incurable tumors was established several years ago (23). *Ex vivo* loading of *in vitro* generated moDCs from patients using antigenic peptides, soluble proteins, tumor lysates, or RNA/DNA in combination with adjuvants to establish fully mature moDCs was applied to treat different solid tumor entities in otherwise incurable patients (2, 15, 31–35). Even though moDC-based therapies increased the life expectancy of certain types of cancer patients, the response rate is still lower than desired (15, 36–39). For DC vaccination, it is crucial that injected moDCs migrate into draining lymph nodes to meet their corresponding T lymphocytes. Several studies in melanoma patients revealed that after intradermal injection, only 2–4% of the moDCs reached the lymph nodes (40, 41). After intravenous injection in mice, it has been found that bone marrow-derived DCs were accumulating in vascularized organs such as spleen, lung, kidneys, and liver instead of migrating into lymph nodes (42, 43). This could be caused by virtue of inappropriate mechanical and cellular properties that might affect the microcirculation (44). Even after intranodal injections in melanoma patients, moDCs were found mostly nonviable and also less mature when accumulating in the lymph nodes (41, 45). This was reflected by insufficient immune responses and poor prognosis for the cancer patients (39). Thus, it will be important to better understand cell migration capacities and the circulation

of cells in the lymphatic system and in blood for improving of moDC-based immunotherapies and induced T cell responses.

Cell migration is a key component for the function of DCs. In peripheral tissues, patrolling primary DCs sample their environment for antigens (immature DCs) and upregulate the C-C chemokine receptor 7 (CCR7) upon envisaging danger signals. Depending on the further activation status, migration speed might increase, enabling the DCs to travel into the draining lymph nodes to activate T cells (5, 46–48). Migration is an active process relying on actin and microtubule cytoskeleton remodeling that is accompanied with mechanical cellular changes (49). Pioneer work to address dynamics of the cytoskeleton during DC migration demonstrated that migration is dependent on non-muscular myosinIIA contractility generating the force for movement of bone marrow-derived DCs in confined microenvironments such as microfabricated channels (50–52). Further, active remodeling of the actin cytoskeleton and its regulatory proteins is a highly dynamic process including the maturation of DCs, antigen uptake by plasma membrane vesicle internalization to endo- and lysosomal compartments, antigen processing and presentation, recycling of MHC molecules, and DC-T cell interactions at the immunological synapse (48, 53–56). Various methods for analyses are available to measure mechanical properties of a cell such as atomic force microscopy, magnetic or optical forces, particle tracking microrheology, or traction force microscopy (57, 58). In contrast to the listed methods, the recently developed microfluidic lab-on-chip system, so-called real-time deformability cytometry, allows for high-throughput measurements of single cells in suspension to understand the processes linking cell mechanics with cell function (59).

All these steps also involve active membrane remodeling. Biomembranes provide a multitude of functions for cells as they establish a biological barrier to the extracellular environment and thus control the movement of molecules into and out of cells. The best-studied cellular membrane is the plasma membrane that consists of a lipid bilayer, which is tightly packed with various transmembrane proteins (60, 61). The distribution of different lipid species allows for the formation of functional microdomains, so-called lipid rafts (62–64). Distinct combinations of lipids, such as sterols and sphingolipids, with membrane proteins are essential in the processes of endocytosis, signal transduction, and many other membrane functions (62–65). The majority of mammalian plasma membranes are formed by glycerophospholipids, glycolipids, and sterols. i) The first group consists of amphipathic molecules, which share a common glycerol backbone and contain a phosphate group (66). This polar head group can be modified leading to the formation of different phospholipids: phosphatidylcholine (PC), phosphatidylethanolamine (PE), phosphatidylserine (PS), phosphatidylinositol (PI), and phosphatidic acid (PA). ii) Next, the major forms of sphingolipids are composed of sphingomyelin (SM) and glycosphingolipids (66). iii) Sterols constitute the third most abundant group of membrane lipids. One representative is cholesterol that is enriched in the plasma membrane where it interacts with sphingolipids. Therefore, cholesterol is able to modify the fluidity and structure of the membrane (67). Interestingly, asymmetrical distribution of lipids between the two lipid monolayers has been described to facilitate signaling into the cell and regulation of cellular processes (66). However, the multitude of different lipids and their complex function in cell homeostasis are poorly understood. Recently, a new high-throughput and sensitive mass spectrometry method has been introduced to quantitatively characterize the lipid composition of cells (lipidome) by lipidomics analysis (68, 69).

Since the lipid composition and therefore the formation of functional membrane microdomains and cytoskeletal changes facilitating DC migration might orchestrate the execution of a variety of DC tasks, we hypothesized that the maturation of DCs induces changes in the cytoskeleton as well as in the membrane properties. DCs might need some robustness to withstand mechanical forces including shear stress during circulation and migration into secondary lymphoid organs and while maintaining flexibility for cognate T cell interaction. Here, we show, to our knowledge for the first time, that mature moDCs exhibited a higher stiffness than immature moDCs due to changes in the cytoskeleton as measured by real-time deformability cytometry analyses. In order to gain more knowledge on global lipid changes in moDCs during maturation, as these are linked to membrane changes, we performed an unbiased high-throughput lipidomics screening of multiple donors. Our data demonstrate that moDCs undergo a great conversion of the overall lipid composition. Further, the identified lipid changes were associated with the serum lipid levels of moDC donors indicating an important role of LDL and cholesterol for DCs and the resulting immune responses. By investigating the plasma membrane using lipid packing imaging, we found that mature moDCs increased their membrane fluidity. Thus, we propose that the DC maturation process has an impact on the stiffness of moDCs and on membrane properties, both potentially contributing to efficient emigration and settlement of DCs in new tissue environments such as lymph nodes or tumors and mediating the consequent interaction with T cells.

MATERIALS AND METHODS

Generation of Monocyte-Derived Dendritic Cells

Leucocyte reduction cones from ten healthy donors were obtained from the Department of Transfusion Medicine and Haemostaseology in Erlangen. From all donors, donor-matched serum was collected (see 2.3). Samples were received under local ethical committee approvals (Ethikkommission der Friedrich-Alexander-Universität Erlangen-Nürnberg), and informed written consents were obtained in accordance with the Declaration of Helsinki.

Monocyte-derived DCs (moDCs) were generated as described before (70, 71). Briefly, the blood of anonymous and healthy donors was diluted with RPMI1640 (Sigma). Peripheral blood mononuclear cells (PBMCs) were isolated by density centrifugation using Human Pancoll (ρ = 1.077 g/ml; PanBiotech). After centrifugation, the interphase containing

PBMCs was collected and washed twice with RPMI1640. 5×10^7 cells were adhered to γ-Globulin (50 ng/ml, Sigma) coated tissue culture dishes (TC-treated cell culture dish, 100 mm; BD Falcon) and incubated for 1 h at 37°C, 5% CO_2, and 96% rH. The medium, containing the non-adherent fraction, was removed and 10 ml DC-medium (RPMI1640 containing 100 U/ml penicillin, 100 µg/ml streptomycin, 2 mM L-glutamine, 10 mM HEPES, and 2% human sera type AB (Lonza)) was added to the cells and incubated overnight at 37°C, 5% CO_2, and 96% rH. On the next day, the medium was replaced with DC-medium containing 800 U/ml GM-CSF (Peprotech) and 50 U/ml IL-4 (Peprotech). On day 3 and day 5, a total of 4 ml fresh DC-medium supplemented with 800 U/ml GM-CSF and 50 U/ml IL-4 or 400 U/ml GM-CSF and 25 U/ml IL-4 was added, respectively. To analyze immature as well as mature moDCs, a maturation cocktail consisting of 13.2 ng/ml IL-1β (Peprotech), 1,000 U/ml IL-6 (Peprotech), 10 ng/ml TNFα (Peprotech), and 1 µg/ml PGE_2 (Sigma) was added to one half of the cells for 24 h on day 6. On day 7, immature as well as mature cells were harvested. As fully differentiated moDCs are detaching from the culture dish when using the above described maturation protocol, the use of EDTA or cell scrapers is not needed. Thus, for mature moDCs the supernatant, which is containing mature cells, was harvested. Immature moDCs also detach from the bottom of the culture dish. However, they are more adhesive, requiring careful rinsing of the dish with the above layered medium. Afterwards, moDCs were stained for FACS analysis, cell sorting, or real-time deformability cytometry measurements.

FACS Analysis and Cell Sorting of moDCs

On day 7, immature and mature moDCs were harvested and 5×10^5 or 1×10^6 cells were stained for FACS analysis or cell sorting, respectively. For FACS analysis, CD11c-PE/Cy7 (3.9, BioLegend), HLA-DR-BV605 (L243, BioLegend), CD83-A647 (HB15e, BioLegend), DEC205-PE (MG38, BD Bioscience), and DC-SIGN-FITC (CD209, DCN46, BD Bioscience) antibodies in PBS/2% human sera or the respective isotype controls (IgG1-A647 (MOPC-21, BioLegend), mouse IgG2b-PE (MPC-11, BioLegend), and mouse IgG2b-FITC (eBM2b, eBioscience)) were applied to the cells for 15 min on ice in the dark. After washing, the cells were resuspended in PBS/2% human sera + 0.1 µg/ml 4′,6-diamidino-2-phenylindole and acquired using a 5-laser line BD LSRFortessa.

For cell sorting, moDCs were harvested and stained with an antibody cocktail consisting of the following antibodies in PBS/2% human sera for 20 min on ice: HLA-DR-BV510 (L243, BioLegend), CD83-PE (HB15e, BioLegend), CD86-FITC (2331 (FUN-1), BD Biosciences), CD11b-PE/Cy5 (M1/70, BioLegend), CD11c-PE/Cy7 (3.9, BioLegend), CD14-Alexa700 (HCD14, BioLegend). After washing, cells were resuspended in PBS/2% human sera + 0.1 µg/ml 4′,6-diamidino-2-phenylindole and cell sorted using a BD FACSAria II cell sorter into immature ($CD83^-$ $CD86^{low}$) and mature ($CD83^+CD86^{high}$) moDCs. 4.5×10^5 cells of each population were sorted, washed with PBS and 3,000 cells/µl were cryopreserved at −80°C until they were sent to Lipotype for lipidomics analysis.

Serum Samples

In addition to leucocyte reduction cones, each 7.5 ml blood of ten donors was obtained in serum tubes from the Department of Transfusion Medicine and Haemostaseology in Erlangen. After coagulation, the blood was centrifuged at 3,000xg for 10 min without brake and the serum was used for analyzing lipid content. Cholesterol, low-density lipid-cholesterol (LDL-cholesterol), high-density lipid-cholesterol (HDL-cholesterol), triglycerides, lipoprotein a, and lipase were measured in the Department of Clinical Chemistry in the Central Laboratory in Erlangen, the serum was stored at 4°C until measurement. Free fatty acids and beta-hydroxybutyrate were analyzed in the Clinical Laboratory of the Paediatric Clinic in Erlangen. Therefore, serum samples were kept on ice until measurement since free fatty acids are not stable.

Cell Mechanics Measurements Using Real-Time Fluorescence and Deformability Cytometry

Real-time fluorescence and deformability cytometry measurements were performed on moDCs as described previously (59, 72). Briefly, immature and mature moDCs were harvested on day 7 of culture. First, 1×10^6 cells were stained with the antibodies CD83-PE and HLA-DR-FITC for 10 min at RT to ensure that only immature ($CD83^{low}$) or mature ($CD83^{high}$) cells were taken into account during the measurement. After washing moDCs with PBS/2% human sera, the supernatant was aspirated, and cells were resuspended in PBS supplemented with 0.5% (w/v) methylcellulose (Sigma Aldrich) to increase medium viscosity. The sample was flushed through a microfluidic channel constriction 20 µm x 20 µm in cross section by applying a constant flow rate of 0.16 µl/sec. An image of every measured cell was taken by a high-speed camera and beside other parameters, cell deformability and projected area (cell size) were calculated. Data analysis was performed using the software ShapeOut (Zellmechanik Dresden) and gating for an area ratio between 1 and 1.05 as well as an area gate between 90 to 600 µm² were used to exclude wrongly detected events and debris, respectively. Furthermore, moDCs were gated into immature ($CD83^{low}$) and mature ($CD83^{high}$) cell populations. Statistical analyses were carried out using 1D linear mixed model that incorporates fixed effect parameters and random effects to analyze differences between cell subsets and replicate variances, respectively. p-values were determined by a likelihood ratio test, comparing the full model with a model lacking the fixed effect term.

Lipidomics Analyses

Lipid Extraction for Mass Spectrometry Lipidomics

Mass spectrometry-based lipid analysis was performed by Lipotype GmbH (Dresden, Germany) as described (73). Lipids were extracted from 1.2×10^5 to 2.3×10^5 sorted immature and mature moDCs from 10 donors using a two-step chloroform/methanol procedure (69). Samples were spiked with internal lipid standard mixture containing: cardiolipin 16:1/15:0/15:0/15:0 (CL), ceramide 18:1;2/17:0 (Cer), diacylglycerol 17:0/17:0 (DAG), hexosylceramide 18:1;2/12:0 (HexCer), lyso-phosphatidate 17:0 (LPA), lyso-phosphatidylcholine 12:0

(LPC), lyso-phosphatidylethanolamine 17:1 (LPE), lyso-phosphatidylglycerol 17:1 (LPG), lyso-phosphatidylinositol 17:1 (LPI), lyso-phosphatidylserine 17:1 (LPS), phosphatidate 17:0/17:0 (PA), phosphatidylcholine 17:0/17:0 (PC), phosphatidylethanolamine 17:0/17:0 (PE), phosphatidylglycerol 17:0/17:0 (PG), phosphatidylinositol 16:0/16:0 (PI), phosphatidylserine 17:0/17:0 (PS), cholesterol ester 20:0 (CE), sphingomyelin 18:1;2/12:0;0 (SM), and triacylglycerol 17:0/17:0/17:0 (TAG). After extraction, the organic phase was transferred to an infusion plate and dried in a speed vacuum concentrator. The first-step dry extract was resuspended in 7.5 mM ammonium acetate in chloroform/methanol/propanol (1:2:4, V:V:V) and the second-step dry extract in 33% ethanol solution of methylamine in chloroform/methanol (0.003:5:1; V:V:V). All liquid handling steps were performed using the Hamilton Robotics STARlet robotic platform with the Anti Droplet Control feature for the pipetting of organic solvents.

Mass Spectrometry Data Acquisition in Lipidomics Analysis

Samples were analyzed by direct infusion on a QExactive mass spectrometer (Thermo Scientific) equipped with a TriVersa NanoMate ion source (Advion Biosciences). Samples were analyzed in both, positive and negative ion modes with a resolution of $R_{m/z = 200}$ = 280,000 for mass spectrometry and $R_{m/z = 200}$ = 17,500 for tandem mass spectrometry experiments, in a single acquisition. Tandem mass spectrometry was triggered by an inclusion list encompassing corresponding mass spectrometry mass ranges scanned in 1 Da increments (74). Both, mass spectrometry and tandem mass spectrometry data were combined to monitor cholesterol ester (CE), diacylglycerol (DAG), and triacylglycerol (TAG) ions as ammonium adducts; phosphatidylcholine (PC), phosphatidylcholine ether (PC O-), as acetate adducts; and cardiolipin (CL), phosphatidate (PA), phosphatidylethanolamine (PE), phosphatidylethanolamine ether (PE O-), phosphatidylglycerol (PG), phosphatidylinositol (PI), and phosphatidylserine (PS) as deprotonated anions. Mass spectrometry only was used to monitor lyso-phosphatidate (LPA), lyso-phosphatidylethanomlamine (LPE), lyso-phosphatidylethanolamine ether (LPE O-), lyso-phosphatidylinositol (LPI), and lyso-phosphatidylserine (LPS) as deprotonated anions; ceramide (Cer), hexoslylceramide (HexCer), sphingomyelin (SM), lyso-phosphatidylcholine (LPC), and lyso-phosphatidylcholine-ether (LPC O-) as acetate adducts.

Analyses of Lipidomics Data

Data were analyzed by Lipotype with in-house developed lipid identification software based on LipidXplorer (75, 76). Data post-processing and normalization were performed by Lipotype using an in-house developed data management system. Only lipid identifications with a signal-to-noise ratio >5, and a signal intensity 5-fold higher than in corresponding blank samples were considered for further data analysis. Extended raw data of lipidomics analysis is provided in the **Supplementary Material**. Exploratory analysis of lipidomics data was performed and visualized using R software (version 4.0.1, ×64, Linux, library gplots). Clusters in the standardized data were identified by means of two-way hierarchical clustering, where distances between data points were measured using Pearson's correlation coefficient ρ as d=(1-ρ)/2 and the linkage criterion was chosen as minimal average distance between clusters. Principal component analysis (PCA) was used for feature extraction and dimensionality reduction.

Lipid Packing Imaging

In order to perform lipid packing imaging, immature and mature moDCs (day 7) were spiked with a final concentration of 0.4 µM with Di-4-ANEPPDHQ (ThermoFisher) and subsequently incubated for 5 min on ice (77). In the next step, cells were washed with PBS. RPMI1640 without phenol red and serum was applied to the cells and the solution was transferred into 8-well chamber slides for imaging. The spectral imaging was performed using a Zeiss LSM780 confocal microscope equipped with a 40×, 1.2NA objective, and a 32-channel GaAsP detector array. Fluorescence excitation of Di-4-ANEPPDHQ was set to 488 nm and the lambda detection range was set between 500 and 700 nm. The values of the 32 channels were analyzed within the ImageJ plug-in "Stacks-T functions-Intensity vs. Time Monitor". To calculate generalized polarization (GP) values, one has to define the wavelengths λ_{Ld} and λ_{Lo} of maximum emission of a probe in a reference liquid-disordered (Ld) and liquid-ordered (Lo) membrane environment. The wavelengths λ = 650 nm as maximum wavelength in disordered membraned (red shifted) and λ = 560 nm as maximum wavelength in the gel phase (blue shifted) were used as described previously (77–79).

$$GP = \frac{I_{560} - I_{650}}{I_{560} + I_{650}}$$

Statistics

Statistical significances were either calculated within paired t-test, or ANOVA using GraphPad Prism 5. Not significant (n.s.) $p>0.05$, $^{*}p<0.05$, $^{**}p \leq 0.01$, $^{***}p \leq 0.001$.

RESULTS

moDC Maturation Changes Mechanical Properties

A variety of cellular changes occur during the maturation of moDCs, such as upregulation of costimulatory molecules, CCR7-dependent migration, or a decrease of phagocytosis. We hypothesized that DCs need to change their cell mechanics when they mature as they emigrate from the peripheral tissue to move into the nearest lymph node, where they present the uptaken and processed antigens to T cells. These mechanical changes are dependent on cytoskeleton modifications (80). Therefore, to first investigate the mechanical properties of DCs, we focused on the model system of monocyte-derived DCs, which we generated from plastic-enriched peripheral

blood monocytes cultured with GM-CSF and IL-4. On day 6, we incubated the cells with a maturation cocktail containing IL-1β, PGE_2, IL-6, and TNFα (mature moDCs) or left the cells untreated (immature moDCs). moDCs were stained for DC-specific surface markers to perform flow cytometry as well as cell sorting. Our flow cytometry data ensured the generation of double positive $CD11c^+HLA\text{-}DR^+$ moDCs (**Figure 1A**) and demonstrated the upregulation of the surface markers HLA-DR, DEC205 (Ly75, CD205), and CD83 as well as down regulation of the marker DC-specific ICAM3-grabbing non-integrin (DC-SIGN, CD209) in mature moDCs (**Figure 1B**). Thus, our protocols allowed for moDCs differentiation and maturation.

To investigate the cell mechanical properties of immature and mature moDCs, we employed real-time fluorescence deformability cytometry measurements. This is a high-throughput method for the mechanical characterization of single cells in which a laminar flow in a 300 µm long microfluidic channel applies hydrodynamic forces to cells. Thus, immature and mature moDCs were generated and directly applied without further DC enrichment. As high speed imaging and processing allows for real-time recording of deformation and size (projected area) (59), contour detection of moDCs in the 300 µm long channel at the region of interest revealed that the cells got deformed on a microsecond timescale (**Figure 1C**). Furthermore, real-time deformability cytometry was found to be highly sensitive to cytoskeletal changes (80). Depending on the cell size different forces are exerted. To analyze the retrieved data, a full numerical model was applied that decouples size and deformation to quantitatively relate cell deformation to mechanical parameters (81, 82). Therefore, we calculated for all donors the Young's modulus (elastic modulus E), which is inversely correlating with the degree of deformation, as a measure for cellular stiffness. Our data revealed that immature moDCs had a mean Young's modulus of 0.573 ± 0.154 kPa, whereas mature moDCs were stiffer with a modulus of 0.799 ± 0.260 kPa (**Figures 1D, E**). Moreover, we also found a large variation in cell size in between the donors in our experiment. However, there was a slight trend towards larger immature moDCs. Taken together, our results suggest that mature moDCs exhibit a higher cell cortex stiffness than immature moDCs and that the overall cell mechanics changed during maturation.

Shotgun Lipidomics Approach Identifies Lipid Composition Changes During moDC Maturation

Beside changes in the actin/myosin cytoskeleton compartment (50, 83, 84), we hypothesized that also alterations in the overall lipid contents might contribute to the maturation process of moDCs. To retrieve unbiased information about all lipid changes during moDC maturation, we performed a shotgun lipidomics analysis. Therefore, immature and mature moDCs of ten healthy blood donors were generated, FACS-sorted into $HLA\text{-}DR^+CD11c^+$ cells, and cryopreserved. In addition, serum samples of the same donors were collected at the time of leucocyte apheresis for further analysis of lipids in the blood (see below, **Figure 2A**). In total, 830 lipids were detected by shotgun lipidomics mass spectrometry. Data post-processing and normalization were performed by the company Lipotype using an in-house developed data management system. Only lipids with an intensity 5-fold above the noise in mass spectrum and 5-fold above the intensity in blank samples were included in the analysis. Raw data from lipidomics analysis is provided in the **Supplementary Material**. Our data revealed that the total amount of cellular lipids did not change significantly after moDC maturation as immature moDCs and mature moDCs exhibited either 7,498 ± 1,870 pmol or 7,385 ± 600 pmol of total lipids, respectively (**Figure 2B**).

Thus, we next asked whether immature and mature moDCs, while having similar total lipid content, exhibit differences in the composition from individual lipid species. Therefore, we performed a two-way hierarchical clustering analysis using R software. Using this method, the clusters are built without any bias from the bottom up, starting with individual samples, calculating their pairwise distance and forming a cluster of the two closest samples. This process of calculating distances and pairing the closest clusters is repeated, forming larger and larger clusters until eventually the two remaining clusters are linked. The hierarchy is represented as dendrogram indicating which clusters are linked at which level. For the cluster analysis of lipidomics data we applied the Pearson correlation coefficient ρ as distance measure ($d=(1-\rho)/2$). At each step, the two clusters with minimal average distance were linked (average linkage clustering). Having performed this analysis, the data displays a clear separation of immature moDCs from mature moDCs at the highest level, which translates as follows: The average correlation of lipid compositions between immature and mature moDCs is lower than the average correlations within both clusters. Looking beyond the top-level clustering, we made another interesting observation: Within both the immature moDC and mature moDC clusters, sub-clusters have been formed separating donors 1, 2, 5, 6, 7, and 8 from donors 3, 4, 9, and 10 (**Figure 2C**).

The split of donors into two groups hints at the existence of another variable besides maturation status that contributes to the lipid distribution. To further investigate this phenomenon, we next performed principal component analyses (PCA) to reduce the complexity of the data set. Thus, the number of degrees of freedom was narrowed down by linear combination of different characteristics into principal components (PCs). Focusing on the PCs with the largest eigenvalues (i.e. PC1 and PC2) allows for the visualization of the multi-dimensional data in a two-dimensional graph (**Figures 2D–G**). Integrating our metadata including sex, serum lipid content (see below), and maturation status of the moDCs, we found that the maturation status demonstrated the highest impact to explain the variance within the data sets (PC1, 41.3%, PC2, 24.0%) (**Figures 2D–G**). Furthermore, our data demonstrated that gender had no significant impact on the data structure.

To investigate which other components might be masked in the PCA of the lipidomics screen, we started correlation analyses applying clinical parameters of the donors. Therefore, we

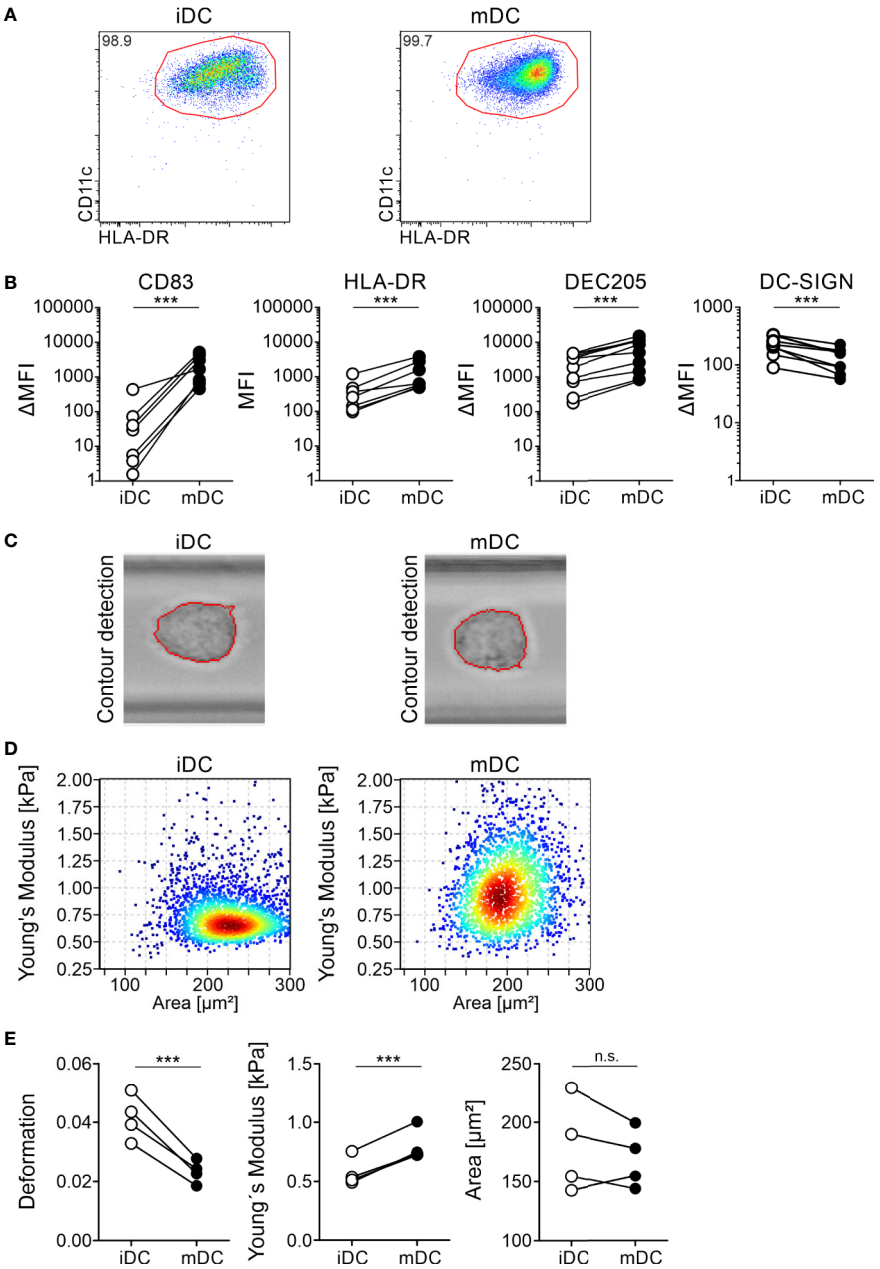

FIGURE 1 | Differential protein surface expression and cell mechanics of immature and mature moDCs. moDCs were generated from monocytes of healthy donors within seven days in cell culture in the presence of GM-CSF and IL-4. On day 6 half of the cells were activated using a maturation cocktail consisting of PGE_2, TNFα, IL-1β, and IL-6. On day 7 immature (iDC) and mature (mDC) moDCs were harvested and 5×10^5 cells were stained for FACS analysis with the antibodies CD11c-PE/Cy7 (1:100), HLA-DR-BV605 (1:100), CD83-A647 (1:100), and CD86-PE (1:100), or respective isotype controls. Cells were recorded using BD LSRFortessa and analyzed using FlowJo software. **(A)** Gating of double positive $CD11c^+HLA\text{-}DR^+$ immature and mature moDCs. Depicted is the gating of one representative donor. **(B)** Paired scatter plots of expression of activation markers CD83 and HLA-DR on immature and mature moDCs as well as the DC markers DEC205 and DC-SIGN. Median fluorescence intensity ΔMFI results of the MFI of antibodies against CLRs minus MFI of the corresponding isotype controls. Statistical significances were calculated using paired t-test (n≥10). Not significant (n.s.) $p>0.05$, *$p<0.05$, **$p \leq 0.01$, ***$p \leq 0.001$. **(C–E)** Real-time fluorescence deformability cytometry of immature (iDC) and mature (mDC) moDCs. moDCs were generated as described before. On day 7, immature and mature moDCs were harvested and 1×10^6 cells were stained for real-time fluorescence deformability cytometry analysis with the antibodies CD83-PE (1:100) and HLA-DR-FITC (1:50). Real-time fluorescence deformability cytometry of immature and mature moDCs from one representative donor (n = 4). **(C)** Phase-contrast images of one representative immature and mature cell with contour detection showing deformation of moDCs. **(D)** Young's modulus with (elastic modulus E) of immature and mature moDCs of the same representative donor as in **(C)**. **(E)** Paired scatter plots of deformation, Young's modulus and cell size (area) of all donors. Statistical significances were calculated using linear mixed model (n = 4). Not significant (n.s.) $p>0.05$, *$p<0.05$, **$p \leq 0.01$, ***$p \leq 0.001$.

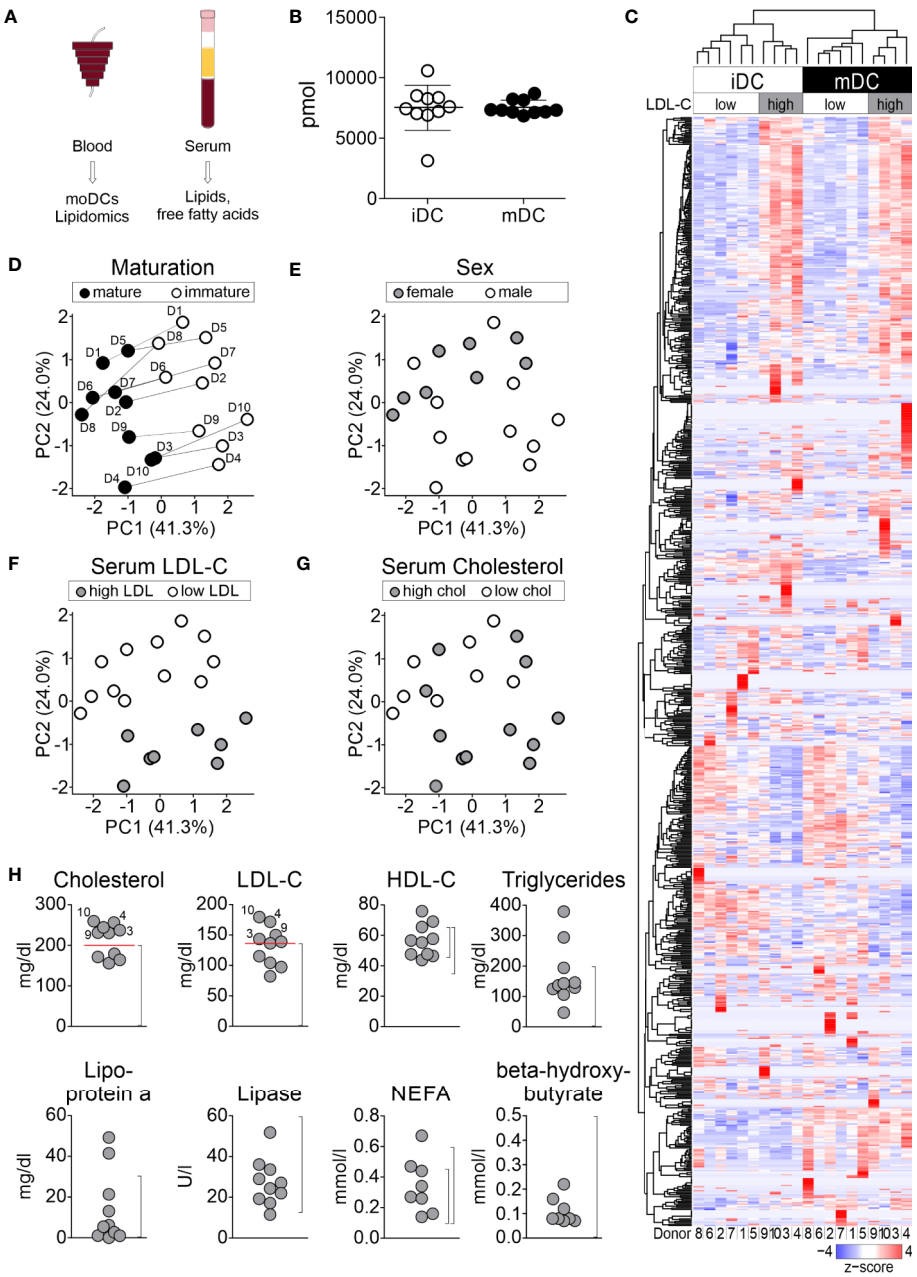

FIGURE 2 | Lipid analyses of moDCs. moDCs were generated as described before. Immature and mature moDCs of ten healthy blood donors were sorted by flow cytometry and shotgun lipidomics analysis of 1.2×10^5 to 2.3×10^5 cells using mass spectrometry was performed by Lipotype Dresden. **(A)** Workflow for lipid analyses. **(B)** Global lipid content of immature and mature moDCs of all donors. The total amount of lipids was calculated by summing the pmol values of the individual lipids belonging to each donor. Values represent the mean of ten biological replicates. **(C)** 830 different lipids were detected, which make up the dendrogram on the left hand side of graph. Each column represents one sample: white indicates immature moDCs, while black depicts mature moDCs. The lipid amounts of cells have been normalized and scaled to a minimum of –4 and maximum of 4. Hierarchical clustering was performed using average linkage, where the distance between clusters has been calculated using Pearson's correlation coefficient ρ (d=(1-ρ)/2). Principal component analysis (PCA) for identification of **(D)** maturation, **(E)** sex, **(F)** serum LDL-C, and **(G)** serum cholesterol-dependent lipid composition of moDCs. Lipid species mol% values per sample were used as input data and further analyzed using R software. Shown are the two principal components (PCs) that had the highest contribution to the variance within the data set. PC1: 41.3%, PC2: 24.0%. **(H)** Analysis of lipids and fatty acids for determination of overall serum lipid profile. Dot plots of serum lipid levels from blood donors for cholesterol (normal rage (NR): <200 mg/dl), low-density lipoprotein (LDL-C, NR: <140 mg/dl), high-density lipoprotein (HDL-C, NR female: 45–65 mg/dl, NR male: 35–65 mg/dl), triglycerides (NR: <200 mg/dl), lipoprotein a (NR: 0–30 mg/dl), lipase (NR: 13–60 U/L), non-esterified amino acids (NEFA, NR female: 0.10–0.45 mmol/L, NR male: 0.10–0.60 mmol/L), and β-hydroxybutyrate (NR: <0.5 mmol/L). Normal ranges for each lipid or fatty acid are indicated in brackets. Analyzed donors n = 10 (same donors as for lipidomics).

analyzed the serum of the donors, from whom the moDC cultures were originally generated. In total, eight parameters were assessed, including cholesterol, LDL-cholesterol (LDL-C), HDL-cholesterol (HDL-C), triglycerides, lipoprotein a, lipase, non-essential fatty acids (NEFA), and beta-hydroxybutyrate. Upon visualization of the normal range, we found that 4 out of 10 donors could be classified as high LDL-C donors (>140 mg/dl, donors 3, 4, 9, and 10) and 6 out of 10 into low LDL-C donors (<140 mg/dl, donors 1, 2, 5, 6, 7, and 8). Another group could be determined, in which 6 out of 10 donors displayed a high total cholesterol (further mentioned as cholesterol) content >200 mg/dl (donors 3, 4, 5, 7, 9, 10) and 4 out of 10 had a low total cholesterol content <200 mg/dl (donors 1, 2, 6, 8) (**Figure 2H**). When we now used these parameters and overlaid them in the PCA analysis (**Figures 2D–G**), we found that the lipid changes of differentiated moDCs were directly correlating with the originally obtained serum lipid levels of LDL-C and cholesterol (**Figures 2D, F**) in that high serum LDL-C donors clearly separated from the other blood donors, indicating that serum LDL-C levels preserved lipid characteristics, independently from the maturation status of moDCs.

Further, the correlation with total cholesterol levels in the sera revealed a similar impact on the overall lipid composition of cells for high LDL-C and high cholesterol donors (donors 3, 4, 9, and 10). Interestingly, donors 5 and 7 displayed high cholesterol levels, but low LDL-C serum levels, and were thus not clearly correlating in the PCA analysis. For all other measured serum lipid levels, values of lipids were fluctuating between the donors (**Figure 2H**). Taken together, our data indicate that not only the maturation itself determines the lipid composition of moDCs, but also the serum LDL-C level influences the lipid composition, even after 7 days of controlled cell culture.

Lipid Class Composition Shifts After Maturation of moDCs

We next assessed lipid class differences in moDCs after maturation. The quantified lipid species were grouped into storage lipids (triacylglycerol and cholesterol ester) and membrane lipids (sphingolipids, glycerophospholipids), which differ in their biological function and structure (66, 85, 86). Our hierarchical cluster analysis of combined lipids revealed that membrane lipids were significantly increased in ceramide (Cer) and hexosylceramide (HexCer), as well as in phosphatidylcholine (PC) in mature moDCs. In contrast, sphingomyelin (SM), phosphatidylcholine ether (PC O-), phosphatidylethanolamine (PE), and phosphatidylglycerol (PG) content decreased after moDC maturation (**Figures 3** and **4A, B**). Moreover, when we investigated the storage lipids in more detail, we found a statistically significant increase of triacylglycerol (TAG) in mature moDCs (**Figures 3** and **4C**). On the other hand, the messenger lipids lyso-phosphatidylcholine (LPC), lyso-phosphatidylethanolamine ether (LPE O-), lyso-phosphatidylethanolamine (LPE), lyso-phosphatidylinositol (LPI), lyso-phosphatidylglycerol (LPG), and lyso-phosphatidate (LPA) showed no significant change of relative abundance after maturation (**Figures 3** and **4D**). All values of lipid class mol% are further shown in **Table 1**. Thus, we conclude that moDCs exhibit an overall shift of membrane and storage lipids upon maturation.

Maturation Leads to a Reduction of Plasma Membrane Lipid Packing in Mature moDCs

As mature moDCs were stiffer than immature cells, we aimed to understand whether the plasma membrane of moDCs might still provide interaction flexibility. To address this question, we performed lipid packing imaging. To this end, immature and mature moDCs (day 7) were stained with a membrane-embedded polarity-sensitive dye Di-4-ANEPPDHQ, whose emission spectrum is dependent on the molecular order of the immediate membrane environment (79). Polarity in biomembranes generally represents the hydration level of the bilayer and therefore the order of membranes (87, 88). Spectral imaging was performed utilizing a Zeiss LSM780 confocal microscope equipped with a 32-channel GaAsP detector array and the relative order of lipids (lipid packing) in the membrane of moDCs was analyzed for their general polarization (GP) value (77). We found that mature moDCs (0.082 ± 0.008) displayed a significantly lower GP value than immature moDCs (0.101 ± 0.006) (**Figure 5**). Thus, our data suggest that mature moDCs harbor a higher fluidity and therefore a higher polarity of the plasma membrane based on the content of water.

Overall, our lipidomics screening together with measurements of the mechanical properties revealed that the higher stiffness of mature moDCs is accompanied by an increase in membrane fluidity, thus potentially providing the plasticity required for immunological processes including the formation of an immunological synapse in mature antigen-presenting DCs.

DISCUSSION

As the maturation of DCs is a highly complex process that involves various changes at the global cellular level (5, 89), we here aimed to investigate whether the DC maturation process also influences the cell mechanics of DCs as well as the global lipid composition and consequently, membrane properties. We hypothesized that the mechanical properties of DCs might change upon maturation in order to detach form peripheral tissues, to migrate into lymph nodes, and to withstand mechanical and shear stress during this process. We further postulated that changes in lipid content in plasma membrane or general cellular lipid content, might contribute to the adaption of the cells associated with maturation processes. We here demonstrate by real-time deformability cytometry analyses that the cellular stiffness of moDCs is increased after the process of maturation. The observed changes upon moDC maturation in cellular mechanics were accompanied by a remodeling of the total lipidome. Beside these changes, the LDL content of the donor's serum was associated with a strong effect on the total lipid composition of moDCs. Moreover, our data display higher

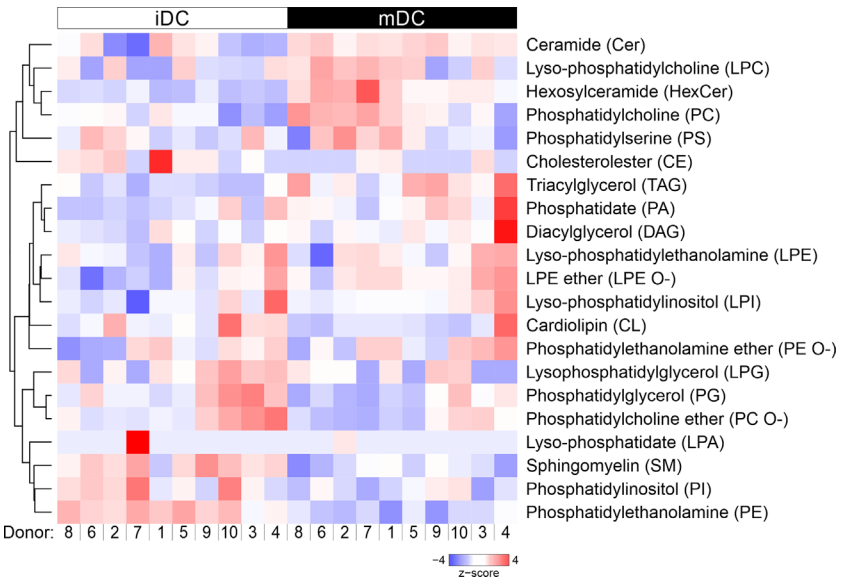

FIGURE 3 | Hierarchical clustering of lipid classes. Mass spectrometric analysis of total lipid composition of immature and mature moDCs was conducted. Here, lipid species were grouped into 20 different lipid classes, which resulted in the dendrogram on the left hand side. Each column represents one sample: white indicates immature moDCs, whereas black depicts mature moDCs. The order of donors follows the clustering from **Figure 2C**. The lipid amounts of cells have been normalized and scaled to a minimum of −4 and maximum of 4. Hierarchical clustering of lipid classes was performed using average linkage, where the distance between clusters has been calculated using Pearson's correlation coefficient ρ (d=(1-ρ)/2).

TABLE 1 | pmol values of lipid classes of immature and mature moDCs.

Class	Immature	Mature	Immature_sd	Mature_sd	Aov_pval
CE	0.122	0.082	0.097	0.015	0.507
Cer	0.151	0.212	0.068	0.013	0.012
CL	0.593	0.507	0.121	0.139	0.157
DAG	0.398	0.552	0.111	0.286	0.130
HexCer	0.050	0.138	0.019	0.051	6.76E-05
LPA	0.046	0.007	0	0	
LPC	0.013	0.018	0.006	0.007	0.186
LPE	0.008	0.009	0.003	0.003	0.411
LPE O-	0.006	0.008	0.003	0.002	0.073
LPG	0.011	0.009	0.002	0.002	0.209
LPI	0.036	0.038	0.013	0.009	0.793
PA	0.054	0.086	0.045	0.062	0.297
PC	44.614	46.612	1.529	2.005	0.022
PC O-	7.169	6.202	1.155	0.878	0.049
PE	9.381	8.075	0.403	0.480	3.47E-06
PE O-	13.324	13.577	0.631	0.635	0.384
PG	0.556	0.442	0.111	0.097	0.025
PI	7.718	7.025	0.684	0.472	0.017
PS	6.821	6.835	0.513	0.843	0.965
SM	8.255	7.391	0.454	0.424	3.49E-04
TAG	0.783	2.253	0.499	1.125	0.001

plasma membrane fluidity that is related to the increased phosphatidylcholine (PC) and decreased sphingomyelin (SM) lipid content upon maturation.

As it was suggested that the cortex is connected to the actin cytoskeleton beneath the plasma membrane and plays a central role in cellular shape control (90), we first performed mechanical phenotyping experiments to investigate into the overall cell mechanics of moDCs during maturation. We used real-time deformability cytometry since this method is able to quantitatively analyze cell material properties such as cell stiffness and was found to be sensitive to cytoskeletal alterations (80). As it is still unknown where and how these maturation processes takes place, we investigated immature and mature (24h stimulation with maturation cocktail) moDCs that represent two definite time points of the maturation status of cells. Here, we identified that the overall cell mechanics of moDCs has changed. These data are suggesting that mature moDCs displayed a higher overall stiffness than immature moDCs (**Figure 1**). Our findings are consistent with recent data received from applying atomic force microscopy measurements on murine bone marrow-derived dendritic cells and primary DCs from murine spleens (53). However, although atomic force microscopy is a sophisticated method to characterize mechanical properties of cells, an advantage of real-time deformability cytometry is the high-throughput. Furthermore, atomic force microscopy requires the attachment of cells to a surface, potentially influencing their mechanical properties. Thus, deformability cytometry provides a more cell autonomous measurement as the cells are fully suspended in solution. From our experiments, we speculate that the increased stiffness of mature moDCs might help the cells to travel through different constrictions in lymphatic vessels in a fast manner on their way to the lymph nodes and to increase their robustness with respect to the shear stress during migration processes. This would be consistent with interesting data of Barbier et al., which indicate that mature murine bone marrow-derived DCs are able

to squeeze through small 3D microchannels at high speed (91). Inversely, our data suggest that immature moDCs appeared to be less stiff, suggesting that they need this higher flexibility of their cytoskeleton to sense, embrace fragments, and uptake antigens in peripheral tissues. This is in accordance to findings by Heuzé and Vargas, in which micropinocytosis or endocytosis have been suggested to be dependent on the membrane-cytoskeletal interface including alternating phases of low and high motility in the immature state (92). Although the cell size differences were not statistically significant, the smaller size of mature moDCs might have an effect on the overall cell mechanics such as cellular robustness and migration (**Figure 1E**).

As important antigen-presenting cells, the main function of DCs is the activation of T cells. Previous results indicated that the induction of T cell activation and profound proliferation needs a prolonged contact of the T cell with an antigen-presenting cell (93, 94). This process is supported by the formation of a so-called immunological synapse (95, 96). Indeed, it was suggested that the cellular mechanics also play an important role in the formation of a synapse. This was in line with the fact that the cytoskeleton of DCs was found to be rearranged after stimulation leading to the relocation of filamentous actin to the site of the immunological synapse (54, 97–99). Blumenthal et al. further showed that the increase in cortical stiffness of mature bone marrow-derived DCs is also due to the actin cytoskeleton modulation (53). As we agreed that a higher stiffness of maturing moDCs is useful to increase resistance to shear stress during the process of DC migration and by providing physical resistance to the pushing and pulling forces exerted by the interacting T cell, we wondered how the higher stiffness of mature moDCs matches the formation of an immunological synapse and the interaction with T cells, a cellular process that needs a high membrane flexibility (100). Thus, we measured the order of the plasma membrane using lipid packing imaging. Complementing the cell mechanics studies, where mature moDCs were stiffer than immature cells, our data revealed that mature moDCs exhibited a lower GP value than immature cells, suggesting a more disordered membrane (**Figure 5**). In general, mature DCs have to be stiff in order to fully activate T cells, controlled by the cortical cytoskeleton (53); however, the order of the plasma membrane is independent from cortical stiffness and might be more fluid with a higher diffusion capacity to rearrange molecules that are important for the initiation of the immunological synapse. This was also in accordance with data from Ayee et al. who demonstrated that an increase in the rigidity and lipid packing of the membrane does not translate into an increase in the overall stiffness of the cellular cortex. On the contrary, it appears that there is an inverse relationship between lipid order of the membrane bilayer and the global stiffness that is dominated by the cortical cytoskeleton (101). The lipid packing of moDCs was a highly interesting finding as the membrane fluidity seems to be uncoupled from the overall stiffness of the cell. In agreement, Blanchard et al. suggested that the two properties of cell deformability and membrane fluidity might play complementary roles in immune cells (102).

Besides cytoskeleton and molecular changes, such as upregulation of costimulatory molecules, lipids might also influence the DC's function during maturation. Lipids play a fundamental role in cell homeostasis and regulation and have diverse functions. They form biological membranes, where they are directly involved in intracellular trafficking, membrane compartmentalization, and the interaction or function of membrane proteins. Further, lipids can act as signaling components themselves (66, 85). Here, we performed high-throughput shotgun lipidomics to investigate the lipidome of immature and mature moDCs of ten different healthy donors. To our knowledge, this is the first study investigating the lipidome of human moDCs. In total, 830 lipids were analyzed. Noteworthy, the total lipid amount did not change during maturation (**Figure 2B**). Since we could not detect differences in the quantity of lipids, we were further investigating the lipid quality. By comparing all lipid species in the hierarchical cluster analysis, we found that mature moDCs clustered away from immature moDCs (**Figure 2C**). From these data we concluded that the maturation status of the cells had the highest impact among all factors (comprising gender and serum lipid content) on the global lipid composition of moDCs. In addition, subclusters within the maturation dependent clusters indicated a second component influencing the global moDC lipid composition.

To corroborate the findings from hierarchical clustering and to reduce the complexity of lipidomics data, we further performed PCA. Our results clearly revealed that the maturation status separated the donors into groups of immature and mature moDCs (**Figures 2D–G**). Therefore, we analyzed the clinical parameters of the beforehand obtained serum samples of the same donors (which was taken 7 days before the moDC lipidomics analysis). Although not unexpected but still surprising, we found that the serum lipids were fluctuating between individual donors (**Figure 2H**) most likely owed to time points of thrombocyte apheresis and eating habits, life style, and genetic predispositions (103, 104). Furthermore, when we overlaid our metadata with the PCA data, we found that independent of the moDC maturation status, serum LDL-C (and to a lower extent also cholesterol levels) clustered the donors into two different groups: those with high LDL-C and those with low LDL-C serum levels. This was a very intriguing result, since the lipid composition of low and high LDL-C donors is conserved after seven days in cell culture that are needed for the generation of moDCs. This might indicate an imprinting effect of the serum lipid levels on the immune cells including moDCs. As cholesterol homeostasis has a pivotal function in regulating immune cells and since an accumulation of cholesterol in the cell membrane of moDCs has been suggested to enhance MHC II-dependent antigen presentation and $CD4^+$ T-cell activation (105), further analyses of high and low LDL-C donors might help to elucidate whether changed lipid serum levels also have an impact DC-mediated immune responses.

When we investigated all lipid classes in more detail (**Figures 3**, **4**), we found that the membrane sphingolipid ceramide (Cer) showed a significantly higher lipid content in mature moDCs. Ceramide is formed under all conditions of cellular stress and plays a role in signal transduction as lipid second messenger (85, 106). Moreover, ceramide might also be involved in the inhibition of

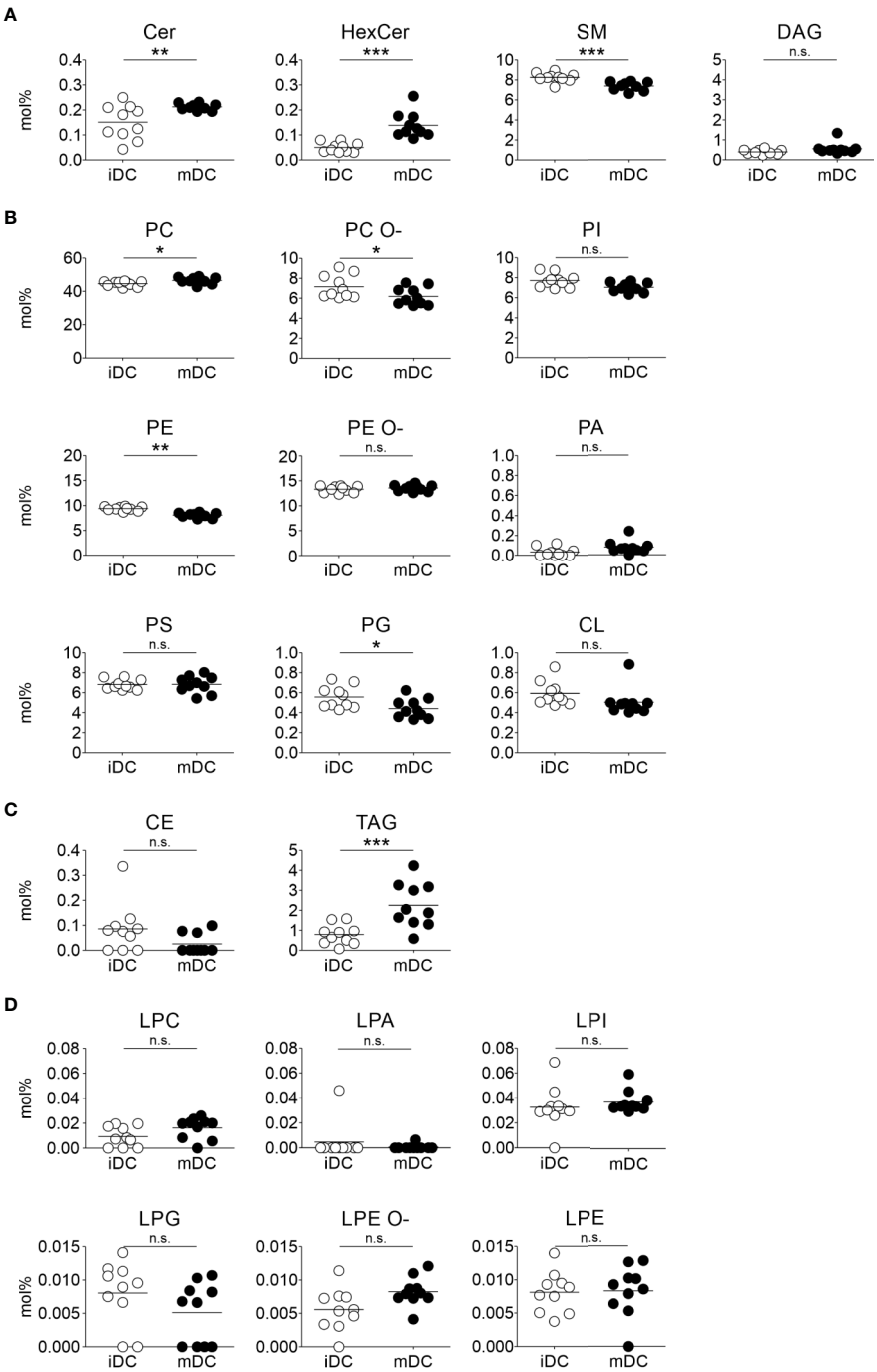

FIGURE 4 | Lipid class changes upon maturation of moDCs. Mass spectrometric analysis of total lipid composition of immature and mature moDCs was carried out. Scatter plots demonstrate lipid class amounts for immature and mature moDCs of all donors. The amount of a lipid class (mol%) is calculated by summing the pmol values of the individual lipids belonging to each class. The class amount was then normalized to total lipid content. Horizontal lines represent mean values of the biological replicates. Content of membrane lipids is divided in **(A)** sphingolipids and glycerolipids, and **(B)** glycerophospholipids. **(C)** Lipid content of storage lipids and **(D)** messenger lipids in immature and mature moDCs. Statistical significances were calculated using ANOVA ($n \geq 10$). Not significant (n.s.) $p > 0.05$, *$p < 0.05$, **$p \leq 0.01$, ***$p \leq 0.001$.

antigen uptake upon DC maturation (107). Strikingly, ceramide-enriched membranes are ideal to sort proteins and to provide an environment for spatial organization of receptors. In fact, ceramide-dependent receptor clustering was already shown for CD40 and CD40 ligand pairs in moDCs and interestingly, these molecules are involved in the formation of the immunological synapse (108–110). Altogether, this supports the notion that the increase of ceramide upon maturation might help moDCs to form

an immunological synapse with T cells with regard to stability and a prolonged contact of DCs with T cells (109, 111).

The increase of ceramide was accompanied by a decrease of sphingomyelin (SM) in mature moDCs due to their closely linked metabolism, as ceramide constitutes the backbone for sphingomyelin. Sphingomyelin is found in membranes and associates with proteins and cholesterol in membrane rafts, which display more ordered membrane parts (62, 112). This behavior is also in accordance with our lipid packing analysis, since a higher sphingomyelin level in immature moDCs is associated with a stiffer membrane (**Figure 5**). In addition, sphingomyelin seems to interact with caveolae that form compartments for endo- and exocytosis in the plasma membrane (113, 114). Thus, sphingomyelin might also play a role for antigen uptake, which explains its higher levels in immature moDCs. Interesting lipidomics data from Santinha et al. suggest a correlation between sphingomyelin and ceramide that appears upon differentiation of DCs and that influences the immunomodulatory properties of DCs including T cell activation (115).

The most prominent lipid in the cell and especially in membranes is phosphatidylcholine (PC). The relative abundance was increasing during maturation of moDCs. In particular, phosphatidylcholine synthesis is required to stabilize the surface of so-called lipid droplets (or lipid bodies) in tissues, where triacylglycerols (TAG) are stored (85). Accordingly, triacylglycerol levels were also significantly increased following maturation of moDCs. This was an interesting finding as triacylglycerol represents an energy storage and might thus play an important role in the metabolism of DCs. Our finding is consistent with previously shown data that triacylglycerol and lipid droplets are accumulating after activation of myeloid cells, indicating an influence on the metabolism of DCs after TLR stimulation (116–118). Overall, lipids accomplish complex functions in DCs, depending on the maturation state of the cell.

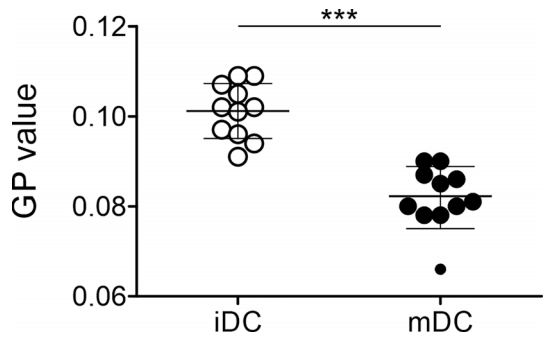

FIGURE 5 | Differential lipid order of plasma membrane of immature and mature moDCs. Lipid packing imaging of immature and mature moDCs was performed. Therefore, cells were spiked with a final concentration of 0.4 µM with Di-4-ANEPPDHQ. The spectral imaging was performed using a Zeiss LSM780 confocal microscope equipped with a 32-channel GaAsP detector array. Fluorescence excitation of Di-4-ANEPPDHQ was set to 488 nm and the lambda detection range was set between 500 and 700 nm. The values of the 32 channels were analyzed within the ImageJ plug-in "Stacks-T functions-Intensity vs. Time Monitor". To calculate generalized polarization (GP) values, the wavelengths λ = 650 nm as maximum wavelength in disordered membraned (red shifted) and λ = 560 nm as maximum wavelength in the gel phase (blue shifted) were used as described previously (77, 78).

$$GP = \frac{I_{560} - I_{650}}{I_{560} + I_{650}}$$

Statistical significances were calculated using paired t-test ($n \geq 10$). Not significant (n.s.) $p > 0.05$, *$p < 0.05$, **$p \leq 0.01$, ***$p \leq 0.001$.

The observed lipid class shift of immature to fully mature moDCs might depend on several processes. One of these processes could be the remodeling of cellular membranes, as it is well known that the maturation process induces the transport and fusion of MHC II containing vesicles to the plasma membrane (119). Further, processes such as metabolic changes occur during DC maturation, in which a switch from oxidative phosphorylation to glycolysis might influence the lipid biosynthesis (120, 121). Thereby, one could speculate that a *de novo* synthesis of fatty acids might induce a shift of the lipid composition during maturation of moDCs. Future experiments will be necessary to evaluate the exact mechanism how the observed shift of the lipid composition is mediated. This might be possible by cell fractionations to isolate membrane-containing compartments of immature and mature moDCs followed by lipidomics.

Although *ex vivo* generated moDCs are widely used for immunotherapeutic approaches (17, 23, 25, 34, 37) – their efficacy in including desired anti-tumor responses still needs to be improved (15, 23, 38). For example, the efficiency of tumor antigen loaded matured moDCs to migrate and settle into lymph nodes is not fully accomplished, since the majority of moDCs does not reach the lymph node (122). In addition, also the immunosuppressive microenvironment of tumors might interfere with the efficacy of the moDC therapy, especially in regard to their capability to induce or to reactivate tumor T cell responses (123). The aspect, that cholesterol impacts on the function of our immune system was recently described for NK cells (124). Interestingly, as serum LDL-C levels seem to influence the lipid composition, irrespective from the maturation status of moDCs, further studies will be necessary to evaluate the initiation of immune responses from moDCs of high and low serum LDL-C donors that might impact T cell and DC activation, or DC migration. For future immunotherapeutic approaches, the cellular and/or serum lipid content of patients could serve as a biomarker to identify patients who are suitable for therapy using autologous cells transfer. In addition, real-time deformability cytometry might help to evaluate the moDC quality before application in cancer patients.

In vitro generated moDCs are not fully comparable to primary steady-state DC subsets present in the body (125); instead, they rather resemble the cells that appear during an inflammatory response *in vivo* (21, 126, 127). Moreover, human inflammatory DCs display conserved gene signatures with moDCs and present a distinct subset of DCs (21). Thus, future experiments need to be performed comparing moDCs and primary DC subsets for lipid content and cell mechanical properties. Primary DCs or *in vitro* expanded primary DCs (naturally occurring DCs) constitute the next generation of DC therapy. However, it is still unclear which particular DC subset

might be used for different immunotherapeutic approaches (128). Thus, moDCs as well as these next generation DC vaccines might serve as combinatorial therapeutics for immune checkpoint inhibitors (128–131).

In conclusion, our study provides the first major observations for maturation dependent changes of moDCs using cutting-edge techniques such as real-time deformability cytometry as well as shotgun lipidomics analysis. Future experiments are needed to fully link the cell function, mediated by the cytoskeleton, to the increased cell stiffness within mature moDCs. Furthermore, the changes in lipid composition and in membrane properties of moDCs need follow-up studies to understand how they might influence the immune response initiated by moDCs. Additionally, this study provides the rationale to consider the easy accessible parameters of cellular deformation and serum lipid content as potential future biomarkers allowing for suitability prediction of a given patient for autologous cell transfer therapy. Our results are just the beginning in understanding the bigger picture of moDC maturation where each of the changes of cellular properties might contribute to multiple functions.

DATA AVAILABILITY STATEMENT

The raw data supporting the conclusions of this article will be made available by the authors, without undue reservation. Lipidomics raw data are included in the **Supplementary Material**.

ETHICS STATEMENT

The studies involving human participants were reviewed and approved by Ethikkommission der Friedrich-Alexander-Universität Erlangen-Nürnberg. The patients/participants provided their written informed consent to participate in this study.

AUTHOR CONTRIBUTIONS

JL performed the experiments with participation by LH, GH, MKr, MKu, and ES. NA and CL analyzed lipidomics data. LH, LA, and CL contributed to the review of the manuscript. LA, CL, and DD contributed to the data analysis and interpretation as well as discussions. JL and DD designed the study, JL, LA, and DD wrote the manuscript, and CL, LH, GH, MKr, MKu, ES, A-SS, VZ, RB, IL, MD, CE, and JG critically revised the manuscript. All authors contributed to the article and approved the submitted version.

FUNDING

This work was partly supported by grants from the German Research Foundation [Deutsche Forschungsgemeinschaft (DFG)] to DD (CRC1181-TPA7, DU548/5-1), to DD, RB, and A-SS (RTG1962); the Emerging Fields Initiative BIG-THERA of the Friedrich-Alexander University Erlangen-Nürnberg to DD and A-SS; Erlanger Leistungsbezogene Anschubfinanzierung und Nachwuchsförderung (ELAN) (DE-17-09-15-1-Heger) to LH; Interdisziplinäres Zentrum für Klinische Forschung (IZKF) (IZKF-A80) to DD; Wellcome and Kennedy Trust for Rheumatology Research (PRF 100262Z/12/Z) to MD. ES is supported by SciLifeLab fellow program. CE acknowledges imaging support by the Wolfson Imaging Centre – Oxford, and funding by the Wolfson Foundation, the EPA Cephalosporin Fund, MRC (Grant No. MC_UU_12010/unit programs G0902418 and MC_UU_12025), the Wellcome Trust (Grant No. 104924/14/Z/14 and Strategic Award 091911 (Micron)), MRC/BBSRC/EPSRC (Grant No. MR/K01577X/1), the John Fell Fund, state of Thuringia (Thüringer Aufbaubank (TAB)), the Deutsche Forschungsgemeinschaft (Research unit 1905, Jena Excellence Cluster "Balance of the Microverse" and Collaborative Research Center 1278) and the Jena Center of Soft Matter.

ACKNOWLEDGMENTS

We thank S. Beck and N. Eissing for technical support. We are grateful for cell-sorting support especially by M. Mroz and D. Schönhöfer (Core Unit Cell Sorting and Immunomonitoring). We thank the Department of Transfusion Medicine of the University Hospital Erlangen. We thank the members of the Dudziak laboratory for their critical comments. Parts of this manuscript were adapted from PhD theses of JL and LA. We thank Dr. Parsch from Central Laboratory, and the Clinical Laboratory of the Paediatric Clinic in Erlangen for measurements of serum samples.

SUPPLEMENTARY MATERIAL

The Supplementary Material for this article can be found online at: https://www.frontiersin.org/articles/10.3389/fimmu.2020.590121/full#supplementary-material

REFERENCES

1. Banchereau J, Steinman R. Dendritic Cells and and the control of immunity. *Nature* (1998) 392(6673):245–52. doi: 10.1038/32588
2. Steinman RM, Banchereau J. Taking dendritic cells into medicine. *Nature* (2007) 449(7161):419–26. doi: 10.1038/nature06175
3. Heidkamp GF, Sander J, Lehmann CHK, Heger L, Eissing N, Baranska A, et al. Human lymphoid organ dendritic cell identity is predominantly dictated by ontogeny, not tissue microenvironment. *Sci Immunol* (2016) 1 (6):eaai7677. doi: 10.1126/sciimmunol.aai7677
4. Steinman R, Inaba K. Immunogenicity: role of dendritic cells. *BioEssays* (1989) 10(5):145–52. doi: 10.1002/bies.950100503
5. Dalod M, Chelbi R, Malissen B, Lawrence T. Dendritic cell maturation: functional specialization through signaling specificity and transcriptional programming. *EMBO J* (2014) 33(10):1104–16. doi: 10.1002/embj.201488027

6. Cella M, Sallusto F, Lanzavecchia A. Origin, maturation and antigen presenting function of dendritic cells. *Curr Opin Immunol* (1997) 9(1):10–6. doi: 10.1016/S0952-7915(97)80153-7
7. Steinman RM. Dendritic cells: understanding immunogenicity. *Eur J Immunol* (2007) 37 Suppl 1:S53–60. doi: 10.1002/eji.200737400
8. Pöhlmann T, Böckmann RA, Grubmüller H, Uchanska-Ziegler B, Ziegler A, Alexiev U. Differential peptide dynamics is linked to major histocompatibility complex polymorphism. *J Biol Chem* (2004) 279 (27):28197–201. doi: 10.1074/jbc.C400128200
9. Tscharke DC, Croft NP, Doherty PC, La Gruta NL. Sizing up the key determinants of the CD8(+) T cell response. *Nat Rev Immunol* (2015) 15 (11):705–16. doi: 10.1038/nri3905
10. Lanzavecchia A, Sallusto F. Regulation of T cell immunity by dendritic cells. *Cell* (2001) 106(3):263–6. doi: 10.1016/S0092-8674(01)00455-X
11. Dudziak D, Kamphorst AO, Heidkamp GF, Buchholz VR, Trumpfheller C, Yamazaki S, et al. Differential antigen processing by dendritic cell subsets in vivo. *Science* (2007) 315(5808):107–11. doi: 10.1126/science.1136080
12. den Haan JMM, Lehar SM, Bevan MJ. Cd8+ but Not Cd8– Dendritic Cells Cross-Prime Cytotoxic T Cells in Vivo. *J Exp Med* (2000) 192(12):1685–96. doi: 10.1084/jem.192.12.1685
13. Steinman RM, Hawiger D, Nussenzweig MC. Tolerogenic dendritic cells. *Annu Rev Immunol* (2003) 21:685–711. doi: 10.1146/annurev.immunol.21.120601.141040
14. Yamazaki S, Dudziak D, Heidkamp GF, Fiorese C, Bonito AJ, Inaba K, et al. $CD8^+CD205^+$ Splenic Dendritic Cells Are Specialized to Induce Foxp3+ Regulatory T Cells. *J Immunol* (2008) 181(10):6923–33. doi: 10.4049/jimmunol.181.10.6923
15. Lehmann CH, Heger L, Heidkamp GF, Baranska A, Lühr JJ, Hoffmann A, et al. Direct Delivery of Antigens to Dendritic Cells via Antibodies Specific for Endocytic Receptors as a Promising Strategy for Future Therapies. *Vaccines (Basel)* (2016) 4(2). doi: 10.3390/vaccines4020008
16. Amon L, Lehmann CHK, Baranska A, Schoen J, Heger L, Dudziak D. Chapter Two - Transcriptional control of dendritic cell development and functions. In: C Lhuillier, L Galluzzi, editors. *International Review of Cell and Molecular Biology*. Cambridge, MA, United States; San Diego, CA, United States; Oxford, United Kingdom; London, United Kingdom: Academic Press (2019). p. 55–151. doi: 10.1016/bs.ircmb.2019.10.001
17. Dörrie J, Schaft N, Schuler G, Schuler-Thurner B. Therapeutic Cancer Vaccination with Ex Vivo RNA-Transfected Dendritic Cells—An Update. *Pharmaceutics* (2020) 12(2). doi: 10.3390/pharmaceutics12020092
18. Merad M, Ginhoux F, Collin M. Origin, homeostasis and function of Langerhans cells and other langerin-expressing dendritic cells. *Nat Rev Immunol* (2008) 8(12):935–47. doi: 10.1038/nri2455
19. Dzionek A, Fuchs A, Schmidt P, Cremer S, Zysk M, Miltenyi S, et al. BDCA-2, BDCA-3, and BDCA-4: three markers for distinct subsets of dendritic cells in human peripheral blood. *J Immunol* (2000) 165(11):6037–46. doi: 10.4049/jimmunol.165.11.6037
20. Guilliams M, Ginhoux F, Jakubzick C, Naik SH, Onai N, Schraml BU, et al. Dendritic cells, monocytes and macrophages: a unified nomenclature based on ontogeny. *Nat Rev Immunol* (2014) 14(8):571–8. doi: 10.1038/nri3712
21. Segura E, Touzot M, Bohineust A, Cappuccio A, Chiocchia G, Hosmalin A, et al. Human Inflammatory Dendritic Cells Induce Th17 Cell Differentiation. *Immunity* (2013) 38(2):336–48. doi: 10.1016/j.immuni.2012.10.018
22. Serbina NV, Salazar-Mather TP, Biron CA, Kuziel WA, Pamer EG. TNF/iNOS-Producing Dendritic Cells Mediate Innate Immune Defense against Bacterial Infection. *Immunity* (2003) 19(1):59–70. doi: 10.1016/S1074-7613(03)00171-7
23. Schuler G. Dendritic cells in cancer immunotherapy. *Eur J Immunol* (2010) 40(8):2123–30. doi: 10.1002/eji.201040630
24. Lutz MB, Schuler G. Immature, semi-mature and fully mature dendritic cells: which signals induce tolerance or immunity? *Trends Immunol* (2002) 23(9):445–9. doi: 10.1016/S1471-4906(02)02281-0
25. Amon L, Hatscher L, Heger L, Dudziak D, Lehmann CHK. Harnessing the Complete Repertoire of Conventional Dendritic Cell Functions for Cancer Immunotherapy. *Pharmaceutics* (2020) 12(7). doi: 10.3390/pharmaceutics12070663
26. Guilliams M, Henri S, Tamoutounour S, Ardouin L, Schwartz-Cornil I, Dalod M, et al. From skin dendritic cells to a simplified classification of human and mouse dendritic cell subsets. *Eur J Immunol* (2010) 40(8):2089–94. doi: 10.1002/eji.201040498
27. Heger L, Hofer TP, Bigley V, de Vries IJM, Dalod M, Dudziak D, et al. Subsets of CD1c+ DCs: Dendritic Cell Versus Monocyte Lineage. *Front Immunol* (2020) 11(2575). doi: 10.3389/fimmu.2020.559166
28. Romani N, Gruner S, Brang D, Kampgen E, Lenz A, Trockenbacher B, et al. Proliferating dendritic cell progenitors in human blood. *J Exp Med* (1994) 180(1):83–93. doi: 10.1084/jem.180.1.83
29. Sallusto F, Lanzavecchia A. Efficient presentation of soluble antigen by cultured human dendritic cells is maintained by granulocyte/macrophage colony-stimulating factor plus interleukin 4 and downregulated by tumor necrosis factor alpha. *J Exp Med* (1994) 179(4):1109–18. doi: 10.1084/jem.179.4.1109
30. Tacken PJ, Figdor CG. Targeted antigen delivery and activation of dendritic cells in vivo: steps towards cost effective vaccines. *Semin Immunol* (2011) 23 (1):12–20. doi: 10.1016/j.smim.2011.01.001
31. Gross S, Erdmann M, Haendle I, Voland S, Berger T, Schultz E, et al. Twelve-year survival and immune correlates in dendritic cell–vaccinated melanoma patients. *JCI Insight* (2017) 2(8). doi: 10.1172/jci.insight.91438
32. Palucka K, Banchereau J. Cancer immunotherapy via dendritic cells. *Nat Rev Cancer* (2012) 12(4):265–77. doi: 10.1038/nrc3258
33. Figdor CG, de Vries IJ, Lesterhuis WJ, Melief CJ. Dendritic cell immunotherapy: mapping the way. *Nat Med* (2004) 10(5):475–80. doi: 10.1038/nm1039
34. Tacken PJ, de Vries IJ, Torensma R, Figdor CG. Dendritic-cell immunotherapy: from ex vivo loading to in vivo targeting. *Nat Rev Immunol* (2007) 7(10):790–802. doi: 10.1038/nri2173
35. Benteyn D, Heirman C, Bonehill A, Thielemans K, Breckpot K. mRNA-based dendritic cell vaccines. *Expert Rev Vaccines* (2015) 14(2):161–76. doi: 10.1586/14760584.2014.957684
36. Melero I, Gaudernack G, Gerritsen W, Huber C, Parmiani G, Scholl S, et al. Therapeutic vaccines for cancer: an overview of clinical trials. *Nat Rev Clin Oncol* (2014) 11(9):509–24. doi: 10.1038/nrclinonc.2014.111
37. Thurner B, Haendle I, Röder C, Dieckmann D, Keikavoussi P, Jonuleit H, et al. Vaccination with Mage-3a1 Peptide–Pulsed Mature, Monocyte-Derived Dendritic Cells Expands Specific Cytotoxic T Cells and Induces Regression of Some Metastases in Advanced Stage IV Melanoma. *J Exp Med* (1999) 190(11):1669–78. doi: 10.1084/jem.190.11.1669
38. Hopewell EL, Cox C. Manufacturing Dendritic Cells for Immunotherapy: Monocyte Enrichment. *Mol Ther Methods Clin Dev* (2020) 16:155–60. doi: 10.1016/j.omtm.2019.12.017
39. Bol KF, Schreibelt G, Rabold K, Wculek SK, Schwarze JK, Dzionek A, et al. The clinical application of cancer immunotherapy based on naturally circulating dendritic cells. *J Immunother Cancer* (2019) 7(1):109. doi: 10.1186/s40425-019-0580-6
40. Verdijk P, Aarntzen EHJG, Lesterhuis WJ, Boullart ACI, Kok E, van Rossum MM, et al. Limited Amounts of Dendritic Cells Migrate into the T-Cell Area of Lymph Nodes but Have High Immune Activating Potential in Melanoma Patients. *Clin Cancer Res* (2009) 15(7):2531. doi: 10.1158/1078-0432.CCR-08-2729
41. Lesterhuis WJ, de Vries IJM, Schreibelt G, Lambeck AJA, Aarntzen EHJG, Jacobs JFM, et al. Route of Administration Modulates the Induction of Dendritic Cell Vaccine–Induced Antigen-Specific T Cells in Advanced Melanoma Patients. *Clin Cancer Res* (2011) 17(17):5725. doi: 10.1158/1078-0432.CCR-11-1261
42. Mullins DW, Sheasley SL, Ream RM, Bullock TNJ, Fu Y-X, Engelhard VH. Route of Immunization with Peptide-pulsed Dendritic Cells Controls the Distribution of Memory and Effector T Cells in Lymphoid Tissues and Determines the Pattern of Regional Tumor Control. *J Exp Med* (2003) 198 (7):1023–34. doi: 10.1084/jem.20021348
43. Dudda JC, Simon JC, Martin S. Dendritic Cell Immunization Route Determines $CD8^+$ T Cell Trafficking to Inflamed Skin: Role for Tissue Microenvironment and Dendritic Cells in Establishment of T Cell-Homing Subsets. *J Immunol* (2004) 172(2):857. doi: 10.4049/jimmunol.172.2.857
44. Tietze S, Kräter M, Jacobi A, Taubenberger A, Herbig M, Wehner R, et al. Spheroid Culture of Mesenchymal Stromal Cells Results in

Morphorheological Properties Appropriate for Improved Microcirculation. *Adv Sci (Weinheim Baden-Wurttemberg Germany)* (2019) 6(8):1802104–1802104. doi: 10.1002/advs.201802104
45. de Vries IJM, Lesterhuis WJ, Barentsz JO, Verdijk P, van Krieken JH, Boerman OC, et al. Magnetic resonance tracking of dendritic cells in melanoma patients for monitoring of cellular therapy. *Nat Biotechnol* (2005) 23(11):1407–13. doi: 10.1038/nbt1154
46. Vargas P, Maiuri P, Bretou M, Sáez PJ, Pierobon P, Maurin M, et al. Innate control of actin nucleation determines two distinct migration behaviours in dendritic cells. *Nat Cell Biol* (2016) 18(1):43–53. doi: 10.1038/ncb3284
47. Maiuri P, Rupprecht J-F, Wieser S, Ruprecht V, Bénichou O, Carpi N, et al. Actin Flows Mediate a Universal Coupling between Cell Speed and Cell Persistence. *Cell* (2015) 161(2):374–86. doi: 10.1016/j.cell.2015.01.056
48. Bretou M, Kumari A, Malbec O, Moreau HD, Obino D, Pierobon P, et al. Dynamics of the membrane–cytoskeleton interface in MHC class II-restricted antigen presentation. *Immunol Rev* (2016) 272(1):39–51. doi: 10.1111/imr.12429
49. Guck J. Some thoughts on the future of cell mechanics. *Biophys Rev* (2019) 11(5):667–70. doi: 10.1007/s12551-019-00597-0
50. Faure-André G, Vargas P, Yuseff M-I, Heuzé M, Diaz J, Lankar D, et al. Regulation of Dendritic Cell Migration by CD74, the MHC Class II-Associated Invariant Chain. *Science* (2008) 322(5908):1705–10. doi: 10.1126/science.1159894
51. Lämmermann T, Bader BL, Monkley SJ, Worbs T, Wedlich-Söldner R, Hirsch K, et al. Rapid leukocyte migration by integrin-independent flowing and squeezing. *Nature* (2008) 453(7191):51–5. doi: 10.1038/nature06887
52. Chabaud M, Heuzé ML, Bretou M, Vargas P, Maiuri P, Solanes P, et al. Cell migration and antigen capture are antagonistic processes coupled by myosin II in dendritic cells. *Nat Commun* (2015) 6(1):7526. doi: 10.1038/ncomms9122
53. Blumenthal D, Avery L, Chandra V, Burkhardt JK. T cell priming is enhanced by maturation-dependent stiffening of the dendritic cell cortex. *bioRxiv* (2020) 680132. doi: 10.7554/eLife.55995.sa2
54. Al-Alwan MM, Rowden G, Lee TDG, West KA. Cutting Edge: The Dendritic Cell Cytoskeleton Is Critical for the Formation of the Immunological Synapse. *J Immunol* (2001) 166(3):1452. doi: 10.4049/jimmunol.166.3.1452
55. Huang Y, Biswas C, Klos Dehring DA, Sriram U, Williamson EK, Li S, et al. The Actin Regulatory Protein HS1 Is Required for Antigen Uptake and Presentation by Dendritic Cells. *J Immunol* (2011) 187(11):5952–63. doi: 10.4049/jimmunol.1100870
56. Graham DB, Osborne DG, Piotrowski JT, Gomez TS, Gmyrek GB, Akilesh HM, et al. Dendritic Cells Utilize the Evolutionarily Conserved WASH and Retromer Complexes to Promote MHCII Recycling and Helper T Cell Priming. *PLoS One* (2014) 9(6):e98606. doi: 10.1371/journal.pone.0098606
57. Moeendarbary E, Harris AR. Cell mechanics: principles, practices, and prospects. *Wiley Interdiscip Rev Syst Biol Med* (2014) 6(5):371–88. doi: 10.1002/wsbm.1275
58. Darling EM, Di Carlo D. High-Throughput Assessment of Cellular Mechanical Properties. *Annu Rev Biomed Eng* (2015) 17(1):35–62. doi: 10.1146/annurev-bioeng-071114-040545
59. Otto O, Rosendahl P, Mietke A, Golfier S, Herold C, Klaue D, et al. Real-time deformability cytometry: on-the-fly cell mechanical phenotyping. *Nat Methods* (2015) 12(3):199–202. doi: 10.1038/nmeth.3281
60. Gerle C. Essay on Biomembrane Structure. *J Membr Biol* (2019) 252(2):115–30. doi: 10.1007/s00232-019-00061-w
61. Henderson R, Unwin PNT. Three-dimensional model of purple membrane obtained by electron microscopy. *Nature* (1975) 257(5521):28–32. doi: 10.1038/257028a0
62. Simons K, Ikonen E. Functional rafts in cell membranes. *Nature* (1997) 387 (6633):569–72. doi: 10.1038/42408
63. Sezgin E, Levental I, Mayor S, Eggeling C. The mystery of membrane organization: composition, regulation and roles of lipid rafts. *Nat Rev Mol Cell Biol* (2017) 18(6):361–74. doi: 10.1038/nrm.2017.16
64. Levental I, Veatch SL. The Continuing Mystery of Lipid Rafts. *J Mol Biol* (2016) 428(24, Part A):4749–64. doi: 10.1016/j.jmb.2016.08.022
65. Simons K, Gerl MJ. Revitalizing membrane rafts: new tools and insights. *Nat Rev Mol Cell Biol* (2010) 11:688. doi: 10.1038/nrm2977
66. van Meer G, Voelker DR, Feigenson GW. Membrane lipids: where they are and how they behave. *Nat Rev Mol Cell Biol* (2008) 9(2):112–24. doi: 10.1038/nrm2330
67. Wu W, Shi X, Xu C. Regulation of T cell signalling by membrane lipids. *Nat Rev Immunol* (2016) 16(11):690–701. doi: 10.1038/nri.2016.103
68. Shevchenko A, Simons K. Lipidomics: coming to grips with lipid diversity. *Nat Rev Mol Cell Biol* (2010) 11(8):593–8. doi: 10.1038/nrm2934
69. Ejsing CS, Sampaio JL, Surendranath V, Duchoslav E, Ekroos K, Klemm RW, et al. Global analysis of the yeast lipidome by quantitative shotgun mass spectrometry. *Proc Natl Acad Sci* (2009) 106(7):2136. doi: 10.1073/pnas.0811700106
70. Heger L, Balk S, Lühr JJ, Heidkamp GF, Lehmann CHK, Hatscher L, et al. CLEC10A Is a Specific Marker for Human CD1c+ Dendritic Cells and Enhances Their Toll-Like Receptor 7/8-Induced Cytokine Secretion. *Front Immunol* (2018) 9(744). doi: 10.3389/fimmu.2018.00744
71. Thurner B, Röder C, Dieckmann D, Heuer M, Kruse M, Glaser A, et al. Generation of large numbers of fully mature and stable dendritic cells from leukapheresis products for clinical application. *J Immunol Methods* (1999) 223(1):1–15. doi: 10.1016/S0022-1759(98)00208-7
72. Rosendahl P, Plak K, Jacobi A, Kraeter M, Toepfner N, Otto O, et al. Real-time fluorescence and deformability cytometry. *Nat Methods* (2018) 15 (5):355–8. doi: 10.1038/nmeth.4639
73. Sampaio JL, Gerl MJ, Klose C, Ejsing CS, Beug H, Simons K, et al. Membrane lipidome of an epithelial cell line. *Proc Natl Acad Sci* (2011) 108(5):1903. doi: 10.1073/pnas.1019267108
74. Surma MA, Herzog R, Vasilj A, Klose C, Christinat N, Morin-Rivron D, et al. An automated shotgun lipidomics platform for high throughput, comprehensive, and quantitative analysis of blood plasma intact lipids. *Eur J Lipid Sci Technol* (2015) 117(10):1540–9. doi: 10.1002/ejlt.201500145
75. Herzog R, Schwudke D, Schuhmann K, Sampaio JL, Bornstein SR, Schroeder M, et al. A novel informatics concept for high-throughput shotgun lipidomics based on the molecular fragmentation query language. *Genome Biol* (2011) 12(1):R8. doi: 10.1186/gb-2011-12-1-r8
76. Herzog R, Schuhmann K, Schwudke D, Sampaio JL, Bornstein SR, Schroeder M, et al. LipidXplorer: A Software for Consensual Cross-Platform Lipidomics. *PLoS One* (2012) 7(1):e29851. doi: 10.1371/journal.pone.0029851
77. Amaro M, Reina F, Hof M, Eggeling C, Sezgin E, et al. Laurdan and Di-4-ANEPPDHQ probe different properties of the membrane. *J Phys D: Appl Phys* (2017) 50(13):134004–4. doi: 10.1088/1361-6463/aa5dbc
78. Owen DM, Rentero C, Magenau A, Abu-Siniyeh A, Gaus K. Quantitative imaging of membrane lipid order in cells and organisms. *Nat Protoc* (2012) 7 (1):24–35. doi: 10.1038/nprot.2011.419
79. Sezgin E, Waithe D, Bernardino de la Serna J, Eggeling C. Spectral imaging to measure heterogeneity in membrane lipid packing. *Chemphyschem* (2015) 16(7):1387–94. doi: 10.1002/cphc.201402794
80. Golfier S, Rosendahl P, Mietke A, Herbig M, Guck J, Otto O. High-throughput cell mechanical phenotyping for label-free titration assays of cytoskeletal modifications. *Cytoskeleton* (2017) 74(8):283–96. doi: 10.1002/cm.21369
81. Mietke A, Otto O, Girardo S, Rosendahl P, Taubenberger A, Golfier S, et al. Extracting Cell Stiffness from Real-Time Deformability Cytometry: Theory and Experiment. *Biophys J* (2015) 109(10):2023–36. doi: 10.1016/j.bpj.2015.09.006
82. Mokbel M, Mokbel D, Mietke A, Träber N, Girardo S, Otto O, et al. Numerical Simulation of Real-Time Deformability Cytometry To Extract Cell Mechanical Properties. *ACS Biomater Sci Eng* (2017) 3(11):2962–73. doi: 10.1021/acsbiomaterials.6b00558
83. Burns S, Thrasher AJ. Dendritic Cells: The Bare Bones of Immunity. *Curr Biol* (2004) 14(22):R965–7. doi: 10.1016/j.cub.2004.10.044
84. Garrett WS, Chen L-M, Kroschewski R, Ebersold M, Turley S, Trombetta S, et al. Developmental Control of Endocytosis in Dendritic Cells by Cdc42. *Cell* (2000) 102(3):325–34. doi: 10.1016/S0092-8674(00)00038-6
85. LIPID MAPS®. *The LIPID MAPS® Lipidomics Gateway*. (2020). Available at: https://www.lipidmaps.org/.
86. Fahy E, Subramaniam S, Murphy RC, Nishijima M, Raetz CRH, Shimizu T, et al. Update of the LIPID MAPS comprehensive classification system for

lipids. *J Lipid Res* (2009) 50(Supplement):S9–14. doi: 10.1194/jlr.R800095-JLR200
87. Sánchez SA, Gunther G. *Modern Research and Educational Topics in Microscopy: Applications in biology and medicine, Band 1Ausgabe 3 von (Microscopy Series)*. In: Méndez-Vilas A., Díaz J. editors. Formatex (2007). p. 1007–14.
88. Parasassi T, Krasnowska EK, Bagatolli L, Gratton E. Laurdan and Prodan as Polarity-Sensitive Fluorescent Membrane Probes. *J Fluoresc* (1998) 8 (4):365–73. doi: 10.1023/A:1020528716621
89. Mellman I. Dendritic Cells: Master Regulators of the Immune Response. *Cancer Immunol Res* (2013) 1(3):145. doi: 10.1158/2326-6066.CIR-13-0102
90. Salbreux G, Charras G, Paluch E. Actin cortex mechanics and cellular morphogenesis. *Trends Cell Biol* (2012) 22(10):536–45. doi: 10.1016/j.tcb.2012.07.001
91. Barbier L, Sáez PJ, Attia R, Lennon-Duménil A-M, Lavi I, Piel M, et al. Myosin II Activity Is Selectively Needed for Migration in Highly Confined Microenvironments in Mature Dendritic Cells. *Front Immunol* (2019) 10 (747). doi: 10.3389/fimmu.2019.00747
92. Heuzé ML, Vargas P, Chabaud M, Le Berre M, Liu Y-J, Collin O, et al. Migration of dendritic cells: physical principles, molecular mechanisms, and functional implications. *Immunol Rev* (2013) 256(1):240–54. doi: 10.1111/imr.12108
93. Lindquist RL, Shakhar G, Dudziak D, Wardemann H, Eisenreich T, Dustin ML, et al. Visualizing dendritic cell networks in vivo. *Nat Immunol* (2004) 5 (12):1243–50. doi: 10.1038/ni1139
94. Shakhar G, Lindquist RL, Skokos D, Dudziak D, Huang JH, Nussenzweig MC, et al. Stable T cell–dendritic cell interactions precede the development of both tolerance and immunity in vivo. *Nat Immunol* (2005) 6(7):707–14. doi: 10.1038/ni1210
95. Grakoui A, Bromley SK, Sumen C, Davis MM, Shaw AS, Allen PM, et al. The immunological synapse: a molecular machine controlling T cell activation. *Science* (1999) 285(5425):221–7. doi: 10.1126/science.285.5425.221
96. Dustin ML. The immunological synapse. *Cancer Immunol Res* (2014) 2 (11):1023–33. doi: 10.1158/2326-6066.CIR-14-0161
97. Malinova D, Fritzsche M, Nowosad CR, Armer H, Munro PM, Blundell MP, et al. WASp-dependent actin cytoskeleton stability at the dendritic cell immunological synapse is required for extensive, functional T cell contacts. *J Leukoc Biol* (2016) 99(5):699–710. doi: 10.1189/jlb.2A0215-050RR
98. Bufi N, Saitakis M, Dogniaux S, Buschinger O, Bohineust A, Richert A, et al. Human Primary Immune Cells Exhibit Distinct Mechanical Properties that Are Modified by Inflammation. *Biophys J* (2015) 108(9):2181–90. doi: 10.1016/j.bpj.2015.03.047
99. Leithner A, Altenburger LM, Hauschild R, Assen F, Rottner K, Stradal TEB, et al. Dendritic cell actin dynamics controls T cell priming efficiency at the immunological synapse. *bioRxiv* (2020) 2020.06.13.150045. doi: 10.1101/2020.06.13.150045
100. Gérard A, Beemiller P, Friedman RS, Jacobelli J, Krummel MF. Evolving immune circuits are generated by flexible, motile, and sequential immunological synapses. *Immunol Rev* (2013) 251(1):80–96. doi: 10.1111/imr.12021
101. Ayee MA, Levitan I. Paradoxical impact of cholesterol on lipid packing and cell stiffness. *Front Biosci (Landmark Ed)* (2016) 21:1245–59. doi: 10.2741/4454
102. Blanchard GJ, Busik JV. Interplay between Endothelial Cell Cytoskeletal Rigidity and Plasma Membrane Fluidity. *Biophys J* (2017) 112(5):831–3. doi: 10.1016/j.bpj.2017.01.013
103. Shephard RJ, Cox M, West C. Some factors influencing serum lipid levels in a working population. *Atherosclerosis* (1980) 35(3):287–300. doi: 10.1016/0021-9150(80)90127-6
104. Heller DA, de Faire U, Pedersen NL, Dahlen G, McClearn GE. Genetic and Environmental Influences on Serum Lipid Levels in Twins. *New Engl J Med* (1993) 328(16):1150–6. doi: 10.1056/NEJM199304223281603
105. Bonacina F, Coe D, Wang G, Longhi MP, Baragetti A, Moregola A, et al. Myeloid apolipoprotein E controls dendritic cell antigen presentation and T cell activation. *Nat Commun* (2018) 9(1):3083. doi: 10.1038/s41467-018-05322-1
106. Goñi FM, Alonso A. Biophysics of sphingolipids I. Membrane properties of sphingosine, ceramides and other simple sphingolipids. *Biochim Biophys Acta (BBA) - Biomembr* (2006) 1758(12):1902–21. doi: 10.1016/j.bbamem.2006.09.011
107. Sallusto F, Nicolò C, De Maria R, Corinti S, Testi R. Ceramide Inhibits Antigen Uptake and Presentation by Dendritic Cells. *J Exp Med* (1996) 184 (6):2411–6. doi: 10.1084/jem.184.6.2411
108. Zhang Y, Li X, Becker KA, Gulbins E. Ceramide-enriched membrane domains—Structure and function. *Biochim Biophys Acta (BBA) - Biomembr* (2009) 1788(1):178–83. doi: 10.1016/j.bbamem.2008.07.030
109. Grassmé H, Jendrossek V, Bock J, Riehle A, Gulbins E. Ceramide-Rich Membrane Rafts Mediate CD40 Clustering. *J Immunol* (2002) 168(1):298–307. doi: 10.4049/jimmunol.168.1.298
110. Vidalain PO, Azocar O, Servet-Delprat C, Rabourdin-Combe C, Gerlier D, Manié S. CD40 signaling in human dendritic cells is initiated within membrane rafts. *EMBO J* (2000) 19(13):3304–13. doi: 10.1093/emboj/19.13.3304
111. Alonso A, Goñi FM. The Physical Properties of Ceramides in Membranes. *Annu Rev Biophys* (2018) 47(1):633–54. doi: 10.1146/annurev-biophys-070317-033309
112. Bochicchio A, Brandner AF, Engberg O, Huster D, Böckmann RA. Spontaneous Membrane Nanodomain Formation in Absence and Presence of the Neurotransmitter Serotonin. *Front Cell Dev Biol* (2020). doi: 10.3389/fcell.2020.601145
113. Slotte JP, Ramstedt B. The functional role of sphingomyelin in cell membranes. *Eur J Lipid Sci Technol* (2007) 109(10):977–81. doi: 10.1002/ejlt.200700024
114. Slotte JP. Biological functions of sphingomyelins. *Prog Lipid Res* (2013) 52 (4):424–37. doi: 10.1016/j.plipres.2013.05.001
115. Santinha DR, Marques DR, Maciel EA, Simoes CS, Rosa S, Neves BM, et al. Profiling changes triggered during maturation of dendritic cells: a lipidomic approach. *Anal Bioanal Chem* (2012) 403(2):457–71. doi: 10.1007/s00216-012-5843-8
116. den Brok MH, Raaijmakers TK, Collado-Camps E, Adema GJ. Lipid Droplets as Immune Modulators in Myeloid Cells. *Trends Immunol* (2018) 39(5):380–92. doi: 10.1016/j.it.2018.01.012
117. Rosas-Ballina M, Guan XL, Schmidt A, Bumann D. Classical Activation of Macrophages Leads to Lipid Droplet Formation Without de novo Fatty Acid Synthesis. *Front Immunol* (2020) 11(131). doi: 10.3389/fimmu.2020.00131
118. Bougnères L, Helft J, Tiwari S, Vargas P, Chang BH-J, Chan L, et al. A Role for Lipid Bodies in the Cross-presentation of Phagocytosed Antigens by MHC Class I in Dendritic Cells. *Immunity* (2009) 31(2):232–44. doi: 10.1016/j.immuni.2009.06.022
119. Leone DA, Rees AJ, Kain R. Dendritic cells and routing cargo into exosomes. *Immunol Cell Biol* (2018) 96(7):683–93. doi: 10.1111/imcb.12170
120. Wculek SK, Khouili SC, Priego E, Heras-Murillo I, Sancho D. Metabolic Control of Dendritic Cell Functions: Digesting Information. *Front Immunol* (2019) 10(775). doi: 10.3389/fimmu.2019.00775
121. Everts B, Amiel E, van der Windt GJW, Freitas TC, Chott R, Yarasheski KE, et al. Commitment to glycolysis sustains survival of NO-producing inflammatory dendritic cells. *Blood* (2012) 120(7):1422–31. doi: 10.1182/blood-2012-03-419747
122. de Vries IJM, Krooshoop DJEB, Scharenborg NM, Lesterhuis WJ, Diepstra JHS, van Muijen GNP, et al. Effective Migration of Antigen-pulsed Dendritic Cells to Lymph Nodes in Melanoma Patients Is Determined by Their Maturation State. *Cancer Res* (2003) 63(1):12.
123. Belderbos RA, Aerts JGJV, Vroman H. Enhancing Dendritic Cell Therapy in Solid Tumors with Immunomodulating Conventional Treatment. *Mol Ther Oncolytics* (2019) 13:67–81. doi: 10.1016/j.omto.2019.03.007
124. Michelet X, Dyck L, Hogan A, Loftus RM, Duquette D, Wei K, et al. Metabolic reprogramming of natural killer cells in obesity limits antitumor responses. *Nat Immunol* (2018) 19(12):1330–40. doi: 10.1038/s41590-018-0251-7
125. Robbins SH, Walzer T, Dembélé D, Thibault C, Defays A, Bessou G, et al. Novel insights into the relationships between dendritic cell subsets in human and mouse revealed by genome-wide expression profiling. *Genome Biol* (2008) 9(1):R17. doi: 10.1186/gb-2008-9-1-r17
126. Lutz MB, Strobl H, Schuler G, Romani N. GM-CSF Monocyte-Derived Cells and Langerhans Cells As Part of the Dendritic Cell Family. *Front Immunol* (2017) 8(1388). doi: 10.3389/fimmu.2017.01388

127. Sabado RL, Balan S, Bhardwaj N. Dendritic cell-based immunotherapy. *Cell Res* (2017) 27(1):74–95. doi: 10.1038/cr.2016.157
128. Garg AD, Coulie PG, Van den Eynde BJ, Agostinis P. Integrating Next-Generation Dendritic Cell Vaccines into the Current Cancer Immunotherapy Landscape. *Trends Immunol* (2017) 38(8):577–93. doi: 10.1016/j.it.2017.05.006
129. De Keersmaecker B, Claerhout S, Carrasco J, Bar I, Corthals J, Wilgenhof S, et al. TriMix and tumor antigen mRNA electroporated dendritic cell vaccination plus ipilimumab: link between T-cell activation and clinical responses in advanced melanoma. *J Immunother Cancer* (2020) 8(1): e000329. doi: 10.1136/jitc-2019-000329
130. Helft J, Anjos-Afonso F, van der Veen AG, Chakravarty P, Bonnet D, Reis e Sousa C. Dendritic Cell Lineage Potential in Human Early Hematopoietic Progenitors. *Cell Rep* (2017) 20(3):529–37. doi: 10.1016/j.celrep.2017.06.075
131. Anselmi G, Vaivode K, Dutertre C-A, Bourdely P, Missolo-Koussou Y, Newell E, et al. Engineered niches support the development of human dendritic cells in humanized mice. *Nat Commun* (2020) 11(1):2054–4. doi: 10.1038/s41467-020-15937-y

Conflict of Interest: The authors declare that the research was conducted in the absence of any commercial or financial relationships that could be construed as a potential conflict of interest.

frontiers in Cell and Developmental Biology

ORIGINAL RESEARCH
published: 30 November 2020
doi: 10.3389/fcell.2020.601145

Spontaneous Membrane Nanodomain Formation in the Absence or Presence of the Neurotransmitter Serotonin

Anna Bochicchio[1†‡], *Astrid F. Brandner*[1†], *Oskar Engberg*[2], *Daniel Huster*[2,3] *and Rainer A. Böckmann*[1*]

[1] *Computational Biology, Department Biology, Friedrich-Alexander University Erlangen-Nürnberg, Erlangen, Germany,* [2] *Institute for Medical Physics and Biophysics, University of Leipzig, Leipzig, Germany,* [3] *Department of Chemical Sciences, Tata Institute of Fundamental Research, Mumbai, India*

OPEN ACCESS

Edited by:
Jorge Bernardino De La Serna, Imperial College London, United Kingdom

Reviewed by:
Matti Javanainen, Academy of Sciences of the Czech Republic (ASCR), Czechia
Tomasz Rog, University of Helsinki, Finland

***Correspondence:**
Rainer A. Böckmann
rainer.boeckmann@fau.de

[†] *These authors have contributed equally to this work*

[‡] ***Present address:***
Anna Bochicchio, Schrödinger GmbH, Mannheim, Germany

Specialty section:
This article was submitted to Cellular Biochemistry, a section of the journal Frontiers in Cell and Developmental Biology

Received: *31 August 2020*
Accepted: *06 November 2020*
Published: *30 November 2020*

Citation:
Bochicchio A, Brandner AF, Engberg O, Huster D and Böckmann RA (2020) Spontaneous Membrane Nanodomain Formation in the Absence or Presence of the Neurotransmitter Serotonin. Front. Cell Dev. Biol. 8:601145. doi: 10.3389/fcell.2020.601145

Detailed knowledge on the formation of biomembrane domains, their structure, composition, and physical characteristics is scarce. Despite its frequently discussed importance in signaling, e.g., in obtaining localized non-homogeneous receptor compositions in the plasma membrane, the nanometer size as well as the dynamic and transient nature of domains impede their experimental characterization. In turn, atomistic molecular dynamics (MD) simulations combine both, high spatial and high temporal resolution. Here, using microsecond atomistic MD simulations, we characterize the spontaneous and unbiased formation of nano-domains in a plasma membrane model containing phosphatidylcholine (POPC), palmitoyl-sphingomyelin (PSM), and cholesterol (Chol) in the presence or absence of the neurotransmitter serotonin at different temperatures. In the ternary mixture, highly ordered and highly disordered domains of similar composition coexist at 303 K. The distinction of domains by lipid acyl chain order gets lost at lower temperatures of 298 and 294 K, suggesting a phase transition at ambient temperature. By comparison of domain ordering and composition, we demonstrate how the domain-specific binding of the neurotransmitter serotonin results in a modified domain lipid composition and a substantial downward shift of the phase transition temperature. Our simulations thus suggest a novel mode of action of neurotransmitters possibly of importance in neuronal signal transmission.

Keywords: membrane domains, neurotransmitter, serotonin, liquid-disordered domain, molecular dynamics simulation, ordered domains

1. INTRODUCTION

Domain formation in biomembranes is thought to be essential for many biological processes as it may promote the localization of e.g., receptors in a specific sector of the membrane. Thereby, membrane domains facilitate as well the assembly or co-localization of different biological macromolecules by delimiting the accessible two-dimensional space on the membrane surface. Examples include immunological synapse formation (Grakoui et al., 1999; Davis and Dustin, 2004), or GPCR signaling related to dimerization (Gahbauer and Böckmann, 2016, 2020). Membrane domains are defined here as membrane regions confined in space and time,

distinguished by membrane composition and/or physico-chemical characteristics from their surroundings (Cebecauer et al., 2018; Kirsch and Böckmann, 2019). These domains have sizes ranging from a few nanometers covering in the order of 10–20 molecules only to more macroscopic domain sizes of a few hundred nanometers (see e.g., Cebecauer et al., 2018). In particular the direct visualization and characterization of small domains is experimentally limited to super-resolution methods such as stimulated emission depletion fluorescence correlation spectroscopy (STED) (Eggeling et al., 2009; Sezgin et al., 2017), interferometric scattering detection (iSCAT) (De Wit et al., 2015; Taylor et al., 2019), or atomic force microscopy (AFM) (Tokumasu et al., 2003; Shan and Wang, 2015). Further experimental evidence for small nanodomains was collected applying Förster resonance energy transfer (FRET) to model membranes (De Almeida et al., 2005; Petruzielo et al., 2013; Koukalová et al., 2017). Other nanoscopic information on membrane domains was achieved using X-ray scattering (SAXS, WAXS) (Sun et al., 2017), neutron scattering (SANS, QENS) (Pencer et al., 2007), or ^{2}H NMR (Veatch et al., 2007; Bartels et al., 2008; Bunge et al., 2008; Engberg et al., 2016; Bosse et al., 2019). However, while nanometer spatial resolution could be collected for a number of different model membrane compositions (see Cebecauer et al., 2018 for a comprehensive review), the sub-microsecond and typically as well sub-millisecond dynamics is masked by the limited temporal resolution of the above advanced microscopy techniques, or relies on model assumptions.

The *gap in temporal resolution* was in parts virtually closed—and sometimes also blurred—by the progress in molecular dynamics (MD) simulations during the past two decades. In particular the so-called coarse-grained (CG) simulations characterized by condensation of the degrees of freedom by introduction of super-atoms or super-beads enabled the study of spontaneous domain formation in biomembrane models. The popular MARTINI model provided a first molecular view on domain formation of model membranes with fully saturated and polyunsaturated phospholipids as well as cholesterol, with well distinguished ordered ("raft" domain, or L_O) and disordered domains (L_D) (Risselada and Marrink, 2008) and has since then been applied in studies on domain formation for various scenarios (Friess et al., 2018; Lin et al., 2018; Bandara et al., 2019). Thereby, frequently little heterogeneity in the composition of individual domains emerged as a characteristics of coarse-grained simulations that is related to the coarsened lipid structure. That is, differences in lipids such as acyl chain length and degree of saturation may at CG resolution easily be exaggerated consequently resulting in pronounced domain separations. In addition, while CG simulations enable for long simulations (micro- to millisecond timescale) coupled to an enhanced dynamics of the membrane constituents (Marrink et al., 2007), the coarsening also affects membrane thermodynamics: The change in degrees of freedom results in a shifted balancing of enthalpy and entropy and thus possibly in a change of temperature-dependency e.g., in domain formation. Nonetheless, CG simulations are in many cases the method of choice to develop a molecular view on domain formation and domain structure.

The experimentally best characterized membrane domains are the sphingomyelin (SM) and sterol-enriched domains that compartmentalize cellular processes (Simons and Ikonen, 1997; Pike, 2006). The size of these domains initially coined *membrane rafts* was given as 10–200 nm (Pike, 2006). More recent experimental studies on model membranes containing phosphatidylcholine (PC), SM, and cholesterol at varying concentrations pointed to domain sizes between approximately 5 and 40 nm (Feigenson and Buboltz, 2001; Pathak and London, 2011, 2015; Koukalová et al., 2017; Saitov et al., 2020). Frequently, these domains were discussed in the context of ordered (L_O) domains introduced early for phosphatidylcholine-cholesterol systems (Hjort Ipsen et al., 1987) and taken as model systems for rafts in cellular membranes. However, based on a combination of Monte Carlo simulations with FRET and z-scan FCS experiments, Koukalová et al. (2017) could show that SM and cholesterol driven nanodomains adopt a fluid and disordered L_D-like state with large amounts of PC lipids maintaining domain fluidity. These more dynamic domains were suggested as models of nanometer-sized heterogeneities or nanocompartments in biomembranes. A first atomistic-resolution picture of a SM-PC-Chol lipid bilayer from atomistic MD simulations was gained in 2015: A differential interaction pattern of Chol with SM and PC lipids was reported using experiment-derived compositions for L_O and L_D domains (Sodt et al., 2015). The L_O-domain was described by a locally hexagonal substructure. Recently, also a *spontaneous* L_O:L_D phase separation was reported for DPPC:DOPC:Chol mixtures (Gu et al., 2020), accompanied by a significant partitioning of Chol to both ordered and disordered domains. In this study, the authors employed the Slipids force field (Jämbeck and Lyubartsev, 2012) shown earlier to perform well also close to the phase transition of PC bilayers (Pluhackova et al., 2016). A spontaneous phase separation or domain formation for sphingomyelin-containing PC membranes was, to our knowledge, not yet reported from atomistic simulations. According to Gibbs (1878), the word *phase* is used here synonymously for domains differing in composition or physical state observed for systems in thermodynamical equilibrium.

Membrane phase or domain formation is not only subject to changes in temperature, pressure, external fields, and lipid composition, but as well to (local) exposure to xenobiotics or endogenous molecules. Of particular interest is the interaction of neurotransmitters with membranes. These are released to the synaptic cleft in response to a signal. Their concentration in synaptic vesicles is as high as 270 mM (Bruns et al., 2000), suggesting a concentration of similar order within the synaptic cleft following exocytosis. Binding of serotonin (5-HT) to lipids would result in formation of a 2-dimensional neurotransmitter (NT) reservoir subject to 2D NT diffusion. Membrane binding drastically enlargens the receptor-neurotransmitter encounter rate and probably facilitates NT entry to membrane-buried receptor ligand-binding sites (Postila and Róg, 2020). A low pH and a high calcium level would in turn impede serotonin association within presynaptic vesicles (Mokkila et al., 2017). In a companion paper to this manuscript we describe by

means of ^{2}H NMR spectroscopy that addition of serotonin to a POPC/PSM/Chol mixture induces increased differences in the lipid acyl chain order between ordered and disordered membrane domains (Engberg et al., 2020). However, detailed knowledge on the interaction with and preference of serotonin (and other neurotransmitters) for plasma membrane (models) displaying L_O and L_D phases is lacking, albeit forming an important cornerstone in the understanding of the role of membranes for neurotransmitter dynamics and possibly linked neurological diseases.

The interaction of the neurotransmitter serotonin with simple phosphocholine lipid bilayers has been described before by means of atomistic MD simulations: Peters et al. (2013) analyzed the interaction of serotonin with single-component 1,2-dipalmitoyl-*sn*-glycero-3-phosphocholine (DPPC) and 1,2-dioleoyl-*sn*-glycero-3-phosphocholine (DOPC) for both charged and neutral forms of serotonin ($pK_a = 9.97$ for primary amino group) on the 100 ns timescale. A protonation-dependent binding orientation of serotonin was reported, with the charged amine interacting with the lipid phosphate moiety and the deprotonated serotonin adopting a reversed orientation with the primary amine pointing toward the membrane core. The cationic serotonin form was independently used to investigate the effect of lipid acyl chain unsaturation (Azouzi et al., 2017): Serotonin was shown to preferentially bind to lipids with unsaturation on both chains. Here, however, both the hydroxyl group as well as the charged amino group of serotonin were seen to interact with the interfacial lipid headgroup region, in disagreement with the orientations reported by Peters et al. (2013), independent of the particular protonation state. Another simulation study addressed the binding of different neurotransmitters to model membranes mimicking intra- and extracellular membrane leaflets. The protonated form of serotonin was found to bind to both membrane compositions, albeit at a higher degree to the anionic intracellular membrane mimic (Postila and Róg, 2020). A charged serotonin was as well used in a simulation-based activation study of the 5-HT_{3A} serotonin receptor (Guros et al., 2020). Whether serotonin is indeed charged when bound to lipid membranes has to our knowledge not been studied. Also, little is known about differences in interaction patterns of neurotransmitters with ordered or disordered membrane domains, or lipid rafts.

Here, employing atomistic molecular dynamics simulations on the 10 μs timescale, we study the spontaneous formation of ordered and disordered domains for POPC/PSM/Chol mixtures at a molar ratio of 4:4:2 as a model for the extracellular leaflet of plasma membranes in the absence or presence of the neurotransmitter serotonin. The lipid composition was chosen to be in the L_D/L_O coexistence region at similar temperatures as studied here, as observed using ^{2}H NMR (Bartels et al., 2008; Engberg et al., 2016), EPR (Ionova et al., 2012), and fluorescence measurements (De Almeida et al., 2003; Veatch and Keller, 2005). Concomitant zeta potential measurements on vesicles of the same composition suggest that serotonin stays deprotonated, i.e., uncharged within the membrane. Overall, we observed an enhanced binding of serotonin to the L_D domain resulting in changes in L_D composition, decreased phase transition temperature, and enhanced dissemination of this phase.

2. MATERIALS AND METHODS

2.1. Molecular Dynamics Simulations

We conducted 4–10 μs long atomistic simulations of POPC:PSM:cholesterol bilayers at a molar ration of 4:4:2 (mixed $L_{O/D}$ system), 8:61:31 (L_O system), and 69:23:8 (L_D system) in the absence or presence of 10 mol% serotonin (5-HT). The simulations were performed at a temperature of 303 K (L_O, L_D, $L_{O/D}$) and at 294 and 298 K ($L_{O/D}$). The lipid compositions for the L_O and L_D systems were selected according to a FRET-based phase diagram for a brain SM:DOPC:cholesterol composition using the tie line ends (Enoki et al., 2018) and a corresponding simulation study (Sodt et al., 2015). Similar tie line end compositions for L_D and L_O phases were reported for the ternary POPC:PSM:cholesterol system (De Almeida et al., 2003; Ionova et al., 2012). A summary of the simulated systems is provided in **Table 1**.

5-HT has two pH-sensitive groups: the primary amino group (NH_2) and an aromatic hydroxyl moiety (OH) (**Figure 5A**), with pKa values of 9.97 and 10.73, respectively (Peters et al., 2013). Hence, serotonin in aqueous environment at neutral pH is cationic. However, the low dielectric constant environment ($\epsilon_r \approx 2$ in the membrane hydrophobic core; Böckmann et al., 2008) inside the membrane could favor the neutral form of 5-HT, as suggested by the measured zeta potential of vesicles in the presence of 5-HT (see below). Since the binding preference to lipid bilayers was shown before for both the charged and the neutral forms of serotonin (Peters et al., 2013), we here modeled only the neutral form of serotonin as the assumed prevalent form of membrane-bound serotonin.

Bilayer systems were initially set up using the CHARMM-GUI web service (Lee et al., 2016). The total number of lipids in each system was between 508 and 510, and the lipids were solvated with at least 38 TIP3P waters per lipid, a salt concentration of 0.15 M NaCl, and an initial box size of $\sim 11 \times 11 \times 9.8\,\text{nm}^3$. Serotonin molecules were added to the water phase of the systems at random orientation, and at a minimum distance of 2 nm from the lipid headgroups using the *gmx insert-molecules* tool implemented in GROMACS 2019 (Abraham et al., 2015). All the simulations were performed with the GROMACS 2019 software suite (Abraham et al., 2015) together with the CHARMM36 force field (Klauda et al., 2010). Serotonin parameters (**Supplementary File 1**) were generated with the CHARMM general force field (CGenFF) v4.0 (MacKerell et al., 1998; Vanommeslaeghe et al., 2010, 2012; Vanommeslaeghe and MacKerell, 2012) using the ParamChem web server v2.2.0 (CGenFF, 2020).

Each system was minimized, heated, and equilibrated and then integrated under NPT conditions using a Nosé-Hoover thermostat (Nosé, 1984; Hoover, 1985), and a Parrinello-Rahman barostat (Parrinello and Rahman, 1981) with a compressibility of $4.5 \times 10^{-5}\,\text{bar}^{-1}$. The integration timestep was set to 2 fs, and bonds to hydrogens were constrained with the LINCS algorithm (Hess et al., 1997). Long-range electrostatics were

TABLE 1 | Simulated systems.

System composition	Molar ratio	Temperature (K)	Duration (μs)	Number of lipids	Number of 5-HT	phase
POPC:PSM:Chol	8:61:31	303	4	510	0	L_O
POPC:PSM:Chol:5-HT	8:61:31:10	303	6	510	51	L_O
POPC:PSM:Chol	69:23:8	303	4	508	0	L_D
POPC:PSM:Chol:5-HT	69:23:8:10	303	5	508	51	L_D
POPC:PSM:Chol	40:40:20	294	8	510	0	$L_{O/D}$
		298	10	510	0	$L_{O/D}$
		303	10	510	0	$L_{O/D}$
POPC:PSM:Chol:5-HT	40:40:20:10	294	10	510	51	$L_{O/D}$
		298	10	510	51	$L_{O/D}$
		303	10	510	51	$L_{O/D}$

computed using particle-mesh Ewald (Darden et al., 1993) with a tolerance of 10^{-6}, 4th-order spline interpolation, and a maximal mesh size of 0.12 nm; van der Waals interactions were shifted smoothly to zero between 1.0 and 1.2 nm.

2.2. Data Analysis

Unless noted otherwise, the last 3 μs of each trajectory were used for the analyses, with frames taken every 1 ns. The analyses were performed using custom scripts involving the Scipy (Virtanen et al., 2020), Numpy (Oliphant, 2015), scikit-learn (Pedregosa et al., 2011), and MDAnalysis (Michaud-Agrawal et al., 2011) python packages. The HMM analysis was implemented based on the hmmlearn python library. Visualization and snapshot representation was done with VMD v 1.9.4 (Humphrey et al., 1996).

2.3. Analysis Protocol for Lipids Order States and Domains

In the $L_{O/D}$ coexistence systems, the state of the lipids was determined using a hidden Markov model (HMM) analysis, similar to the approach of Park and Im (2019). We decided not to use the local lipid composition as emission signal (Sodt et al., 2014; Gu et al., 2020) but rather the lipid order: Lipid chains and cholesterol orientation time series, quantified through the director order parameter $P2$ (Yankova et al., 2012), were used as observables to define three hidden states: putative L_O, L_D, and an intermediate ordered state. Briefly, the director order parameter is defined as $P2 = 1/2\langle 3cos^2\alpha - 1\rangle$, where α is the angle between the membrane normal and the end-to-end vector of the hydrophobic part of cholesterol or the hydrophobic tail of phospholipids. For phospholipids, $|P2|$ was calculated as the average of both tails. The parameters of the model are the probabilities of each hidden state to have a certain $P2$ order, and the probabilities for a hidden state to stay or to change to the other one in a one-time step. The primary assumption is that the probability of the observable emission states, for each lipid type can be decomposed into those from high and lower order states and approximated by a combination of two normal distributions $N(P2|\mu_{L/O}, \sigma_{L/O})$, with means μ_L, μ_O and standard deviations σ_L, σ_O (Park and Im, 2019). This was possible for all the lipid types in the simulated systems.

As in Park and Im (2019), we trained a simple discrete HMM consisting of nine emission states, assigned by partitioning the observable space into nine subspaces (0,…,8). The lowest and highest emission states are assigned when $P2 < \mu_L$ and $P2 > \mu_O$, respectively. The intermediate transition states $i (i = 1, \ldots, 7)$ are assigned when $\mu_L + (i-1)\Delta P2 \leq P2 \leq \mu_L + i\Delta P2$, where $\Delta P2 = (\mu_O - \mu_L)/7$. For the low and high hidden ordered states, the initial emission probability matrix was set up making use of the integrals of the normal distributions over the subspace of the observables. For the intermediate ordered state, we considered integrals over a normal distribution with variance $\mu_I = (\sigma_L\mu_O + \sigma_O\mu_L)/(\sigma_O + \sigma_L)$, and $\sigma_L = \min[|\mu_O - \mu_I|, |\mu_L - \mu_I|]/3$ to ensure that the intermediate states initial emission probabilities are localized within 3σ between the upper, μ_O, and the lower, μ_L, bounds (Park and Im, 2019). Given these initial set of parameters, the Baum-Welch algorithm (Baum et al., 1970; Rabiner, 1989) was used to find the maximum likelihood estimate of the parameters given as input the time series of the emission states for each lipid type in a given leaflet. Once the HMM parameters are determined, the most likely order state sequence for each lipid was determined by the Viterbi algorithm (Viterbi, 1967).

For better comparison of the hidden ordered, disordered, and intermediate states between simulations with/without serotonin and between simulations at different temperatures ($L_{O/D}$ systems), the emission states and the initial transition and emission probabilities were based on the POPC/PSM/Chol 4:4:2 simulation at 303 K.

Time-weighted histograms were computed to analyze the dynamical properties of the assigned ordered/disordered hidden states to POPC and PSM lipids. This analysis was performed on the last 3 μs of the $L_{O/D}$ system at 303 K with and without serotonin.

2.4. Calculation of Deuterium Order Parameters

Deuterium order parameters were calculated at each position along the aliphatic chains of POPC and PSM according to

$$S_{CH} = 1/2\langle 3cos^2\theta - 1\rangle \quad (1)$$

where θ is the angle between the C-H bond and the membrane normal (taken to align with z, while the bilayer is in the xy-plane). Angular brackets denote an average over all sampled configurations. The order parameters were calculated by first averaging over time separately for each lipid in the system and then calculating the average and the standard error of the mean over the different lipids.

The lipids are divided into three populations for the calculation based on the HMM analysis.

2.5. Density Probability Distributions

Density probability distributions of water, lipids headgroups glycerol (POPC) and sphingosine backbones (PSM), and serotonin centers of mass along the bilayer normal, z, with respect to the bilayer center were computed for the last microsecond using the *gmx density* GROMACS 2019 tool (Abraham et al., 2015). The profiles of serotonin were not symmetrized as unsymmetrized profiles provide a useful check on convergence.

2.6. Potential of Mean Force (PMF)

Potential of mean force profiles of serotonin's center of mass were calculated from the last μs of the trajectory according to $F(z) = -k_BTlnp(z)$. $p(z)$ is the probability of finding serotonin at position z, and z is the position along the bilayer normal with respect to the membrane center, T is the absolute temperature, and k_B the Boltzmann constant. The probability density $p(z)$ was estimated using a Gaussian mixture model (Glodek et al., 2013; Bochicchio et al., 2018).

2.7. Serotonin-Bilayer Absorption and Serotonin Orientation

Serotonin absorption and association with the bilayer was determined using its hydroxyl oxygen atom z-position along the bilayer normal. The bilayer was divided into a headgroup and a hydrophobic core region based on the density probability distributions of selected groups of the phospholipids and the sphingolipids along the bilayer normal, as described above. Specifically, the headgroup region was assigned as the region between the choline and the glycerols z-positional probability distribution, the hydrophobic core as the region corresponding to the hydrocarbon chains.

Serotonin orientation in the bilayer-associated states was analyzed in terms of its indole group orientation. Two angles, θ and α were used to define the indole orientation according to a reference coordinate system depicted in **Figure 5**. The z-axis is perpendicular to the indole rings system, bisecting both the benzene and the pyrrole rings. The x-axis bisects the plane of the benzene ring, and the y-axis is orthogonal to the x- and z- axes. θ is the angle between the z-axis and the bilayer normal, and α defines the angle between the x-axis and the projection of the bilayer normal in the x-y plane. A θ value of 90° corresponds to an indole orientation with its plane on average parallel to the bilayer normal. α values of $\sim$ 120° degrees and $\sim$ 310° correspond to an indole orientation in which the hydroxyl oxygen atom is oriented toward the water phase. The percentage of serotonin residing within the hydrophobic core or the headgroup region was determined by calculating the relative number of contacts of serotonin's center of mass and the phosphate groups or the lipid acyl chains, respectively.

2.8. Area Compressibility (K_A)

The instantaneous area per lipid $A_l(t)$ for the bilayers was calculated as the area of the simulation cell A divided by the number of lipids per leaflet. This assumes that undulations are small so the difference in projected and local areas is negligible. The area compressibility K_A is evaluated from:

$$K_A = \frac{k_BT\langle A\rangle}{\langle \delta A^2\rangle} = A\left(\frac{d\gamma}{dA}\right)_T \quad (2)$$

Where $\langle A\rangle$ is the average total area, $\langle \delta A^2\rangle$ is the mean square fluctuation, k_B the Boltzmann constant, and T the temperature. The estimation of the standard error was performed using the block average method (Allen and Tildesley, 2017), with blocks of 10 ns (L_D) to 150 ns (L_O), corresponding to twice the correlation time of the time series fluctuations, estimated from the normalized correlation function of the average total area fluctuations.

2.9. Membrane Bending Modulus (K_C)

The bilayer bending modulus, K_C, was determined using the method developed by Watson et al. (2012), which allows reliable estimates of K_C to be extracted from simulations of modestly sized boxes. This method analyzes the spectral thermal fluctuations of the lipid director vector field $\hat{\boldsymbol{n}}$. The lipid director is a vector pointing from the lipid head to tail and serves as a mean to quantify the lipid orientation. The theoretical prediction for the power spectrum of the longitudinal component of $\hat{\boldsymbol{n}}$ reads:

$$S(q) = \langle |\, \hat{n}_q^{\parallel}\,|^2\rangle = \frac{k_BT}{K_Cq^2}. \quad (3)$$

Deviations from Equation (3) are observed only over wavelengths shorter than 3 bilayer thicknesses (Watson et al., 2012). Previous simulations have shown that simulations with 288 lipids only are sufficient to determine K_C (Levine et al., 2014). For an in-depth description of the method, the reader is referred to Watson et al. (2012) and Levine et al. (2014).

2.10. Materials

Cholesterol (Chol), 1-palmitoyl-2-oleoyl-sn-glycero-3-phosphocholine (POPC), N-palmitoyl-D-erythro-sphingosylphosphorylcholine (PSM) of highest quality were purchased from Avanti Polar Lipids (Alabaster, AL, USA). 5-HT was purchased from Merck (Darmstadt, Germany). All other chemicals were of highest purity with exception of organic solvents which were of spectroscopic grade.

2.11. Lipid Sample Preparation and Zeta Potential Measurements

Lipids were mixed in organic solvents at the molar ratio POPC/PSM/Chol 4/4/2 and evaporated at 40° C in a rotary evaporator. Afterwards the lipids were hydrated at 40° C for 30 min using K_2PO_4 buffer (20 mM K_2PO_4, 100 mM NaCl, 0.1 mM EGTA pH 7.4 in Milli-Q water), freeze thawed and finally extruded through two 100 nm polycarbonate filters at 40° C to make unilamellar vesicles (LUV). Lipid samples were diluted from a LUV stock solution to a concentration of 0.3 mM for the zeta potential measurements. Concentration of 5-HT in the samples varied between 0 and 10 mM. Serotonin was added externally from a K_2PO_4 buffer (12.5 mM 5-HT, 20 mM K_2PO_4, 100 mM NaCl, 0.1 mM EGTA pH 7.4 in Milli-Q water). The samples were measured at 25° C after 10 min incubation after externally adding 5-HT. Zeta potential was measured using a Zeta potential analyzer (Brookhaven) with 10 runs and 10 cycles.

3. RESULTS

The spontaneous formation of biomembrane domains was addressed in atomistic MD simulations for a POPC/PSM/Chol mixture (4:4:2, $L_{O/D}$ system) in the absence or presence of serotonin at three different temperatures (294, 298, and 303 K, each 8–10 μs). In addition, for comparison of the domain characteristics and quantitative binding analysis of serotonin, MD simulations of previously *in silico* characterized L_O and L_D domain compositions (Sodt et al., 2015) were employed as well. Convergence of the different systems was evaluated by monitoring the (overall) area per lipid and the number of lipid-lipid contacts for the different species (**Supplementary Figures 1–3**). The bilayer area equilibrated within $\approx$ 1 μs with a small drift to smaller areas in particular for the $L_{O/D}$ system at low temperature (294 K). Similarly, we observe small drifts in the number of lipid-lipid contacts as a measure of the formation of differently composed domains. Here, we thus focus on the initial steps of domain formation in ternary mixtures containing spingomyelin in the presence or absence of the neurotransmitter serotonin, domain composition, and domain influence on the mechanical membrane properties. The simulation system size and simulation length (10 μs) does not allow to conclude on the formation of large domains beyond 10 nm. Also domain compositions and sizes analyzed below may likely further slowly adapt on the 100 μs to millisecond timescale.

Membrane domain formation was analyzed using a Hidden Markov Model (HMM) employing P2 order parameter-distinguished emission states (see section 2 for details). For an unambigous assignment and for quantitative comparison of systems with/without serotonin as well as for comparison of simulations at different temperatures, the emission states were defined based on the $L_{O/D}$ simulation at 303 K.

3.1. Serotonin Charge

As a measure of the charge of serotonin bound to phospholipid membranes we determined the zeta potential for a POPC/PSM/Chol (4:4:2) mixture in the absence or presence of varying concentrations of serotonin. The zeta potential (see **Table 2**) was hardly affected even for high serotonin concentrations and varied between −0.1 and −4.5 mV, suggesting that serotonin preferentially binds in an uncharged i.e., deprotonatated form to the membrane. Also for pure POPC membranes no effect of serotonin on the zeta potential could be seen (data not shown). Accordingly, serotonin was chosen uncharged in all simulations.

3.2. Spontaneous Nanodomain Formation in Sphingomyelin-Rich PC Membranes

Membrane domain formation was monitored for the $L_{O/D}$ simulation (POPC/PSM/Chol 4:4:2 mixture). The HMM analysis revealed spontaneously formed ordered, sphingomyelin-enriched domains (referred to as L_O domain, see **Figure 1** for snapshots) that include between 48% of all lipids (303 K) and 60% (294 K, compare **Table 3**). At 303 K, the L_O domains contained $\approx$ 43% PSM, 34% POPC, and 23% Chol while the composition of the more disordered L_D domain changed hardly with respect to the overall 4:4:2 composition (see **Table 3**). Interestingly, the L_I domain (including lipids in intermediate ordered state) is observed to be enriched in POPC (52%). That is, the sphingomyelin-enriched L_O domains are surrounded by PC-enriched intermediate regions that transition into a more mixed POPC/PSM L_D domain. That indeed coexisting domains are formed is clearly discernible from representative snapshots displayed in **Figure 2** (see also corresponding movies in the **Supplementary Material**): In particular at 303 K, larger regions of disordered domains formed that display a more loose lipid packing. In contrast, the POPC/PSM/Chol system at 294 K is mostly found in its ordered state (i.e., *yellow*) with only small more disordered patches, however at a comparably high lipid packing density. These differences in the formation of loosely packed L_D domains are as well reflected in the average area per lipid. At 294 K, the area per lipid is $\approx$ 53 Å^2 and increases to $\approx$ 56.5 Å^2 at 303 K (**Supplementary Figure 1**, area per lipid excluding cholesterol). The observed spontaneous formation of domains differing in composition and physical characteristics suggests that the domains approximate corresponding coexistent phases in thermodynamic equilibrium.

In the presence of serotonin, the phase characteristics between L_D and L_O differed more significantly. Even at 294 K, a larger disordered domain is formed, lipids in disordered state now account for 26% of all lipids (18% w/o serotonin). Also, the domain composition changed upon addition of serotonin, in particular a significant change in the PC content is observed: While the PC and PSM content in the absence of serotonin is similar for the L_D domain, addition of serotonin led to a significant enrichment of PC within the disordered domain at all investigated temperatures (e.g., from 39 to 48% at 303 K, **Table 3**). These phase changes are coupled to preferential binding of 5-HT to L_D-phase membrane domains (*triangles* in **Figure 2**, lower panel) as discussed in more detail below.

To further assess the dynamical domain properties we analyzed the lifetime of POPC and PSM lipids within the

TABLE 2 | Zeta potential of a POPC/PSM/Chol 4/4/2 membrane for different serotonin concentrations.

Serotonin concentration	0 mM	0.1 mM	0.25 mM	0.5 mM	1 mM	5 mM	10 mM
Zeta potential (mV)	−4.48	−1.39	−2.46	−4.2	−2.13	−0.09	−0.71
Std. Error	2.43	2.62	2.02	0.58	1.03	1.24	2.25
Ser:lipid molar ratio	0	0.33	0.83	1.67	3.33	16.67	33.33

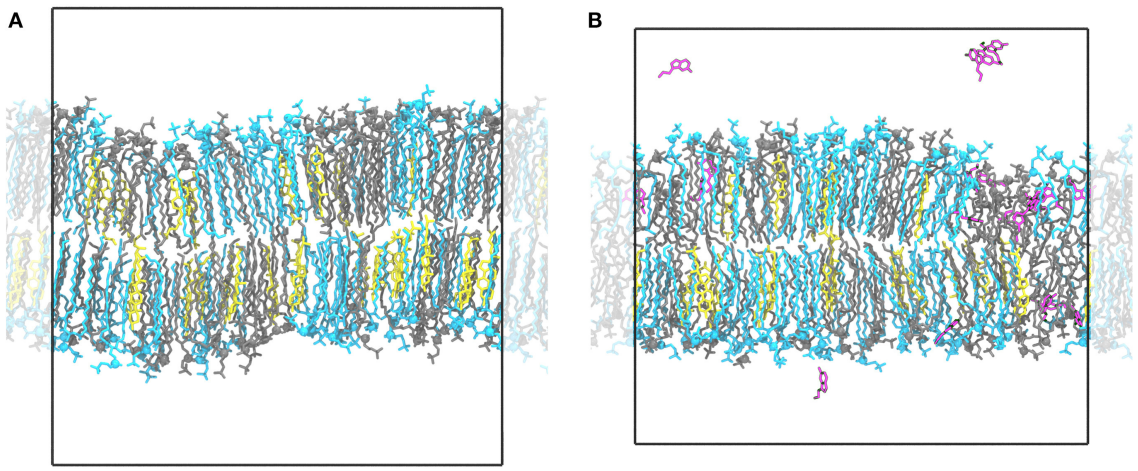

FIGURE 1 | Ordered and disordered membrane domains. Shown are snapshots of the L_d/L_o membrane (POPC:PSM:Chol at 4:4:2) at 294 K without **(A)** and with serotonin **(B)**. In the absence of serotonin, the membrane is overall highly ordered with ≈ 60% of all lipids assigned to the ordered HMM state. In the presence of serotonin, larger disordered and diluted, serotonin-enriched lipid domains emerge suggesting a serotonin-induced phase transition. POPC lipids are depicted as *blue* sticks, PSM lipids in *gray*, cholesterol molecules in *yellow*, and serotonin molecules in *magenta*. Water molecules are omitted for clarity.

TABLE 3 | Phase distribution for Chol, POPC, and PSM lipids in the $L_{O/D}$ system. Standard errors are given in parenthesis.

System		Lipid	303 K			298 K			294 K		
			% L_O	% L_D	%*Int*	% L_O	% L_D	%*Int*	% L_O	% L_D	%*Int*
$L_{O/D}$	w/o 5-HT	POPC	34(2)	39(4)	52(4)	40(2)	30(4)	49(4)	41(2)	28(5)	47(4)
	+ 5-HT		30(2)	46(3)	49(3)	37(2)	38(3)	49(4)	39(2)	37(3)	47(4)
	w/o 5-HT	PSM	43(2)	42(3)	32(4)	40(2)	47(4)	34(4)	41(2)	44(4)	33(4)
	+ 5-HT		43(2)	40(3)	33(4)	41(2)	43(3)	33(4)	41(2)	42(3)	33(4)
	w/o 5-HT	Chol	23(2)	19(3)	16(3)	21(2)	22(3)	17(3)	18(1)	28(4)	19(4)
	+ 5-HT		26(2)	14(2)	18(3)	22(2)	19(3)	18(3)	20(2)	20(3)	20(4)
Domain distribution in %			48(4)	26(3)	25(2)	53(4)	23(3)	24(2)	60(5)	18(4)	22(2)
		+ 5-HT	42(3)	36(3)	22(2)	46(4)	30(3)	26(2)	53(3)	26(2)	21(2)

ordered and disordered hidden states for the $L_{O/D}$ system at 303 K with and without serotonin. In the absence of serotonin, POPC lipid lifetimes showed two clearly distinct populations for ordered and disordered state lipids (**Supplementary Figure 4A**). The time-weighted distributions were fitted by a double exponential and yield lifetimes of 17 and 51 ns for lipids in the disordered state as compared to 32 and 118 ns for lipids in the ordered state (fits performed on initial 300 ns). Addition of serotonin resulted in a significant stabilization of lipids within the disordered state, the lifetimes for the L_D lipids increased to 20 and 99 ns (**Supplementary Figure 4B**). Note, however, that the lifetimes are expected to change for longer simulation times with increasing domain sizes. This effect is clearly seen in the number of disordered state lipids with lifetimes beyond 300 ns that is substantially increased in the presence of serotonin with increasing L_D membrane domain sizes. In contrast, the lifetimes of PSM lipids in disordered and ordered states were not significantly affected by addition of serotonin on the short timescale (**Supplementary Figure 5**). Similar to POPC, the number of PSM lipids that were stabilized within the disordered state increased. These results are in line with the observed preferential binding of serotonin molecules to the L_D phase of membranes (see below).

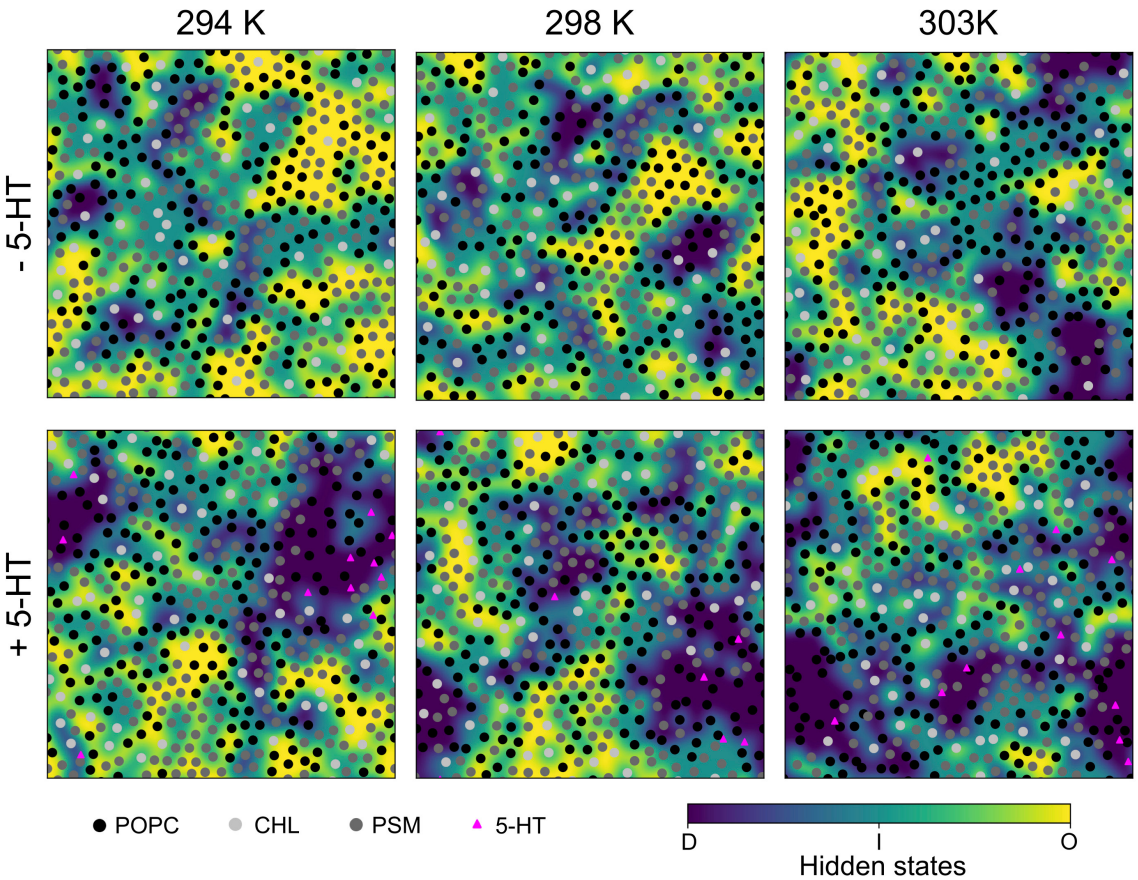

FIGURE 2 | Last snapshots of HMM-assigned lipid order states. A Hidden Markov Model was used to assign ordered ("O," *yellow*), disordered ("D," *violet*), and intermediate ("I," *light blue*) states to lipids based on their P2 order parameters as emission states. The emission states and initial probabilities were derived from the $L_{O/D}$ system at 303 K. The lipid center of mass positions are marked by shaded circles, the positions of bound serotonin by triangles.

3.3. Phase-Dependent Lipid Order

The lipid acyl chain order provides information on the degree of ordering in ordered and disordered membrane domains. The deuterium order parameters for L_O and L_D phases as determined from the HMM differed substantially for the POPC/PSM/Chol (4:4:2) lipid membranes at 303 K, the average POPC *sn-1*-chain order $\langle|S_{CH}|\rangle$ being 0.347 ± 0.008 for the L_O phase and 0.224 ± 0.014 for the L_D phase (see **Figures 3**, **4**). The difference in lipid order diminishes for decreasing temperatures, the L_D *sn-1*-chain order increases to 0.294 ± 0.017 at 294 K while the L_O *sn-1*-order stays approximately constant (0.367 ± 0.006). The comparably high order for lipids assigned a disordered state by the HMM at low temperature is related to the small L_D domain size and hence increased packing density of the lipids (compare **Figure 2**). That is, lipids in more disordered state are embedded in an overall highly ordered environment. A comparison to ^{2}H NMR at 303 K shows a substantially increased POPC *sn-1* order for the $L_{O/D}$ system in the simulations (Engberg et al., 2020). This discrepancy is probably related to an overall shift of the transition temperature to larger values observed for different atomistic force fields (Pluhackova et al., 2016).

The order parameters within the differently ordered domains of the mixed system at 303 K thereby agree well with the palmitoyl chain order determined for pure L_D and L_O systems with compositions equaling those of a previous simulation study (Sodt et al., 2014). Related to the different composition of these 1-phase systems—with POPC:PSM:Chol composition in L_O at 8:61:31 and L_D at 69:23:8—the difference between the average deuterium order parameters for L_O and L_D of POPC is comparable to the $L_{O/D}$ system with $\langle|S_{CH}|\rangle_O = 0.376 \pm 0.009$ and $\langle|S_{CH}|\rangle_D = 0.255 \pm 0.042$.

Upon addition of serotonin, a strong decrease of the lipid acyl chain order is observed for the disordered domains (for both POPC and PSM) at *all* studied temperatures. In contrast, the order within the L_O domains was hardly affected by serotonin (see **Figure 4**). While in the absence of serotonin, truly disordered domains are observed only above 298 K, addition of serotonin results in large disordered and loosely packed domains even at 294 K. That is, the serotonin-lipid interaction partially disrupts the lipid packing. The increased disorder of L_D domains as well as their increased size also

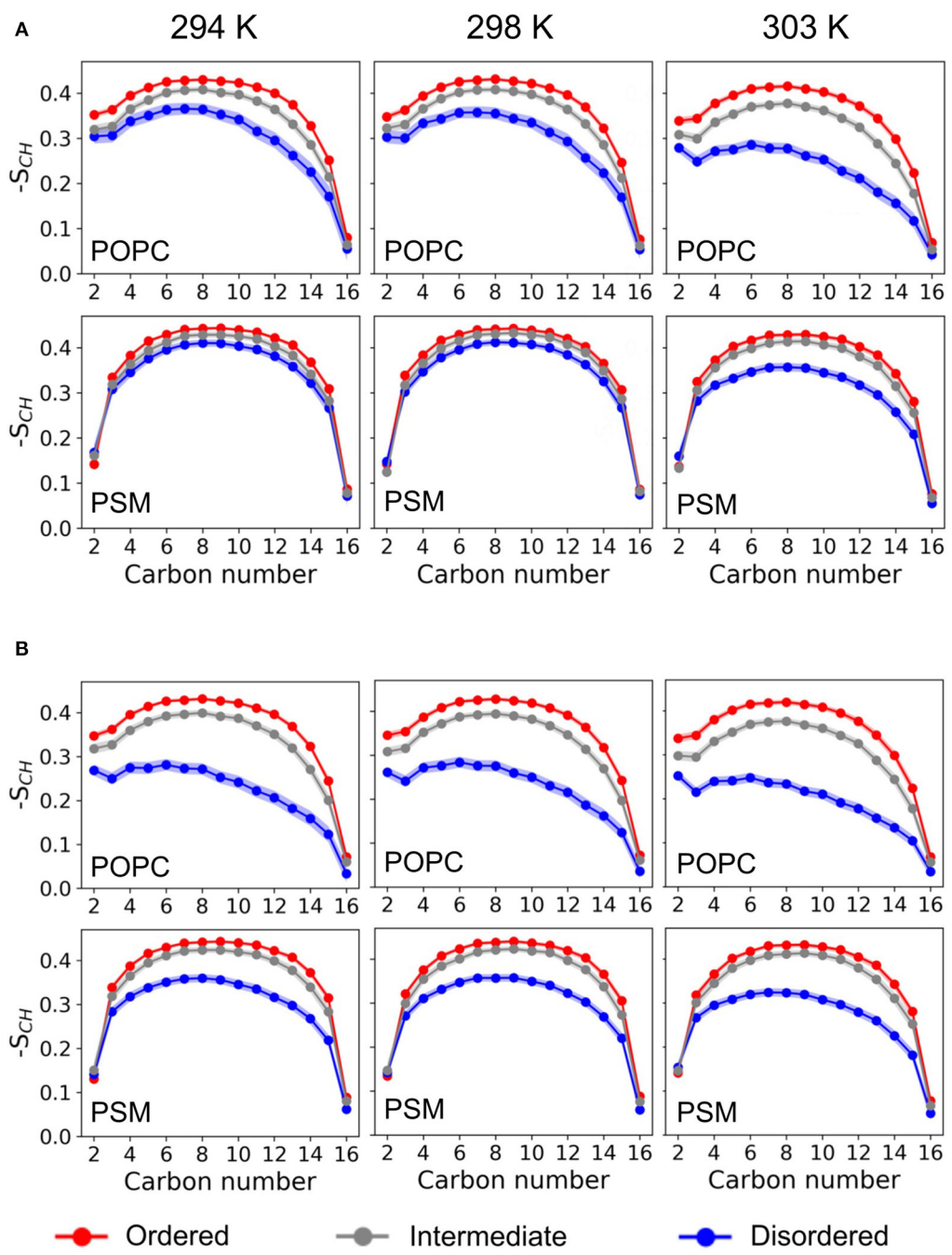

FIGURE 3 | Deuterium order parameter profiles. Shown are the deuterium order parameter profiles for the palmitoyl-chains of POPC (it sn-1) and PSM in the $L_{O/D}$ system at different temperatures for the different HMM-assigned membrane phases (ordered, disordered, intermediate) and without **(A)** or with **(B)** serotonin.

affect the lipid area: At 303 K, the average lipid area is increased by ≈ 5% with respect to the serotonin-free case (**Supplementary Figure 1**).

Our results thus suggest a significant serotonin-induced decrease in the phase transition temperature for the POPC/PSM/Chol mixture.

3.4. Serotonin-Lipid Interaction

At simulation start, serotonin was added to the solvent phase of each system at random positions at a lipid:serotonin ratio of approximately 10:1 (in total 51 serotonin molecules, see **Table 1**). Spontaneous binding of serotonin to lipids was distinguished into binding to either the hydrophobic core region or to the

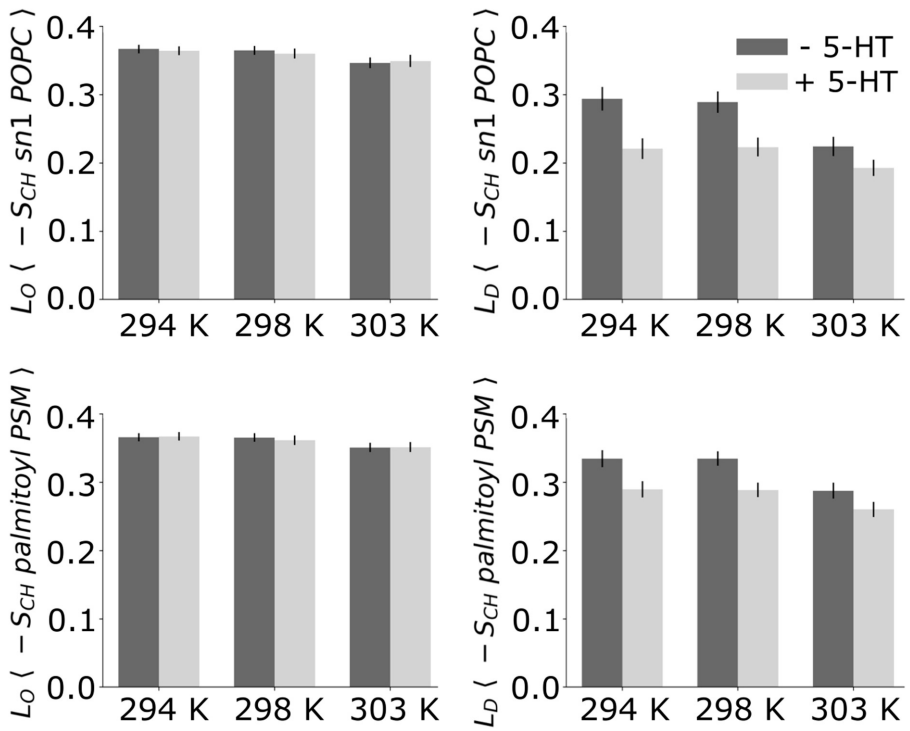

FIGURE 4 | Average deuterium order parameters. Given are the deuterium order parameters averaged over the palmitoyl chain of POPC **(Top)** and the palmitoyl chain of PSM **(Bottom)** without (*dark bars*) and with serotonin (*light bars*).

polar lipid headgroup region. For the pre-assembled L_O phase (POPC:PSM:Chol at a concentration of 8:61:31) binding almost exclusively occurred to the lipid headgroup region (**Figure 5**). In turn, 21 and 17% of all serotonin molecules bound to the hydrophobic core region of membranes with predefined L_D composition or the $L_{O/D}$ membrane, respectively. Also within the $L_{O/D}$ membrane, we observed preferential binding of serotonin to the disordered membrane domains (compare **Figure 1** and **Figure 2**).

The different adsorption modalities of serotonin concerning the membrane phases are well described by the position probability distribution profiles of its center of mass compared to that of selected lipid and cholesterol segments, and water, as well as by the potential of mean force (PMF) profiles. The profiles are shown in **Figure 6** and the selected lipids groups are reported therein. The profiles for the phospholipid atoms and water molecules resemble the features that are generally observed in PC-rich bilayers, i.e., broad phosphate and choline distribution profiles, and penetration of water molecules into the lipid headgroup region including cholesterol hydroxyl groups. All the profiles clearly show that serotonin is able to penetrate the bilayer, irrespective of the membrane phase. For the L_O-system, the highest probability for 5-HT is within the lipid headgroup region, that is, between the choline group and the glycerol/amine backbones. More than 50% of the serotonin remains in the solvent phase, only $\approx$ 3% are able to reach the carbon chains. An interesting density drop at the interface between water and the headgroup region is observed. It corresponds to a small but significant free energy barrier in the PMF profile (**Figure 6**) at the position of the choline group of PSM. In the PC-rich L_D system, serotonin penetrates on average deeper into the membrane. For the $L_{O/D}$ phase the profile is broadened. The same tendency is indicated by the PMF data as well.

The generally broad 5-HT profiles reflect the mobility of the solute in the membranes. An analysis of the orientation of serotonin bound to the membranes is reported in **Figure 5**. We characterize the orientational distribution of 5-HT by attaching a local coordinate frame (**Figure 5**) to its indole group. The bilayer is symmetric under rotations about the bilayer normal, so two angles suffice to characterize the indole distribution: θ, the angle between the z axis of the indole and the bilayer normal; and α, the angle that is assumed when the bilayer normal is projected into the molecular x-y plane (compare section 2). **Figure 5** shows the probability density of the indoles along these two axes. When bound to the headgroup region, serotonin shows broad orientational distributions for all the considered systems (*right panel*). However, orientations with $\theta = 50^o$ or $\theta = 135^o$ are preferred. This can be related to a tendency to form cation-pi stacking interactions with the choline headgroups, experimentally observed for indoles binding to PC lipids (Gaede et al., 2005).

The 5-HT orientation becomes restricted only when it reaches the glycerol backbone and enters the bilayer hydrophobic core (**Figure 5**, *left panel*). The orientation is dominated by structures

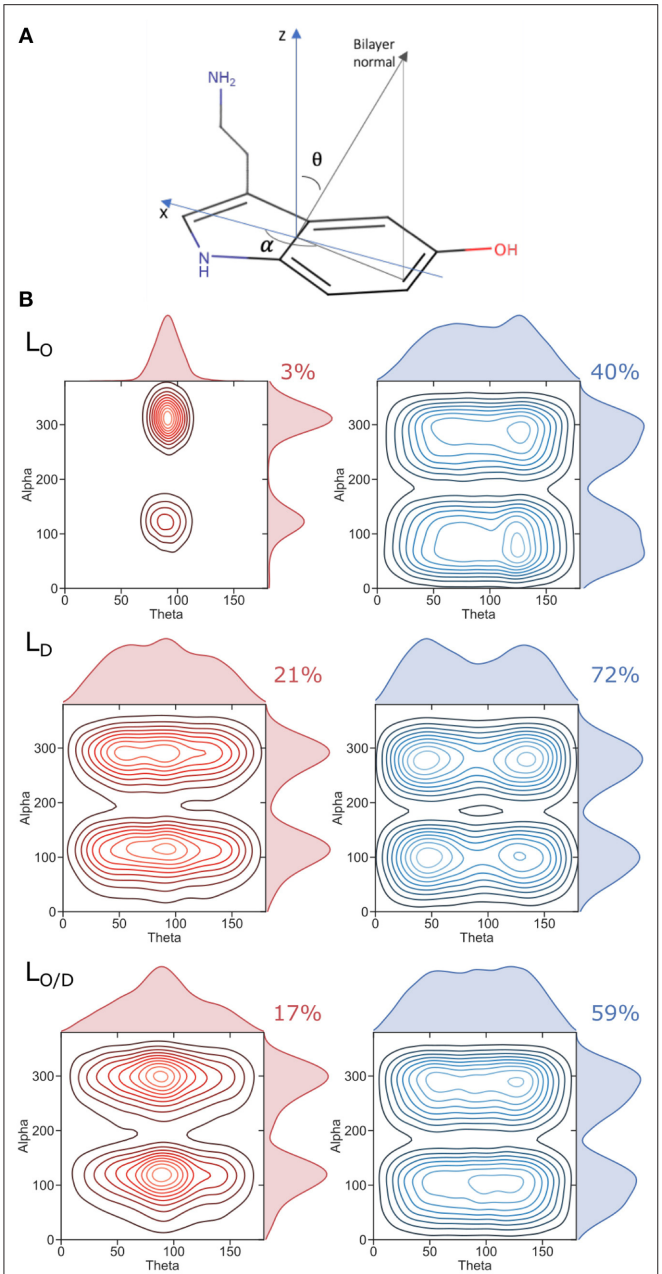

FIGURE 5 | Serotonin orientation in the bilayer. **(A)** Axis framework used to define the orientation of serotonin. **(B)** Plots showing the population of observed angles used to describe the orientation of serotonin for the respective phases (L_O, L_D, $L_{O/D}$). Red plots (left) correspond to serotonin molecules residing in the hydrophobic core of the bilayer, whereas blue plots (right) correspond to those located within the lipid headgroup region. The percentages of serotonin residing at the hydrophobic core of the bilayer or within the headgroups is also reported.

with θ near 90°—indicating that the molecular plane of the indole is orthogonal to the plane of the bilayer. This is particularly the case for serotonin binding to the L_O system, while a much broader profile is observed for the L_D and the mixed $L_{O/D}$ systems (see **Figure 5**). The same preferred orientation for the neutral form of serotonin was already observed by Peters et al. (2013) in a previous MD simulation study employing POPC, DOPC, and DPPC membranes. These maxima occur at α values of 120 and 300°. In the former orientation, the hydroxyl group is oriented toward the water phase, and the aliphatic amino group points to the center of the bilayer. In the latter orientation, the molecule is rotated by 180° corresponding to serotonin binding to the lower membrane leaflet (with reference to the coordinate system in **Figure 5A**). That is, for 5-HT embedded within the L_O domains, the carbon chain aligns to the lipid acyl chains.

These results, together with the huge PMF barrier of > 7 kcal/mol in the membrane's interior (**Figure 6**), suggest a very small permeability for this solute, despite high partitioning into the membrane.

3.5. Membranes Mechanical Properties

The bending modulus K_C is arguably the single most important quantity in membrane biophysics (Watson et al., 2012) and determines the membrane's ability to resist bending in a number of biologically relevant processes such as membrane fusion (Liu et al., 2006), membrane trafficking of molecules (McMahon and Gallop, 2005), and endocytosis (Chernomordik et al., 1995). As such, larger values of K_C correspond to greater rigidity of the bilayers. The area compressibility modulus, K_A, quantifies the response of the membrane area to tension, which under physiological conditions may arise from various perturbations including the addition of small molecules to the membrane.

To our knowledge, no experimental data—area compressibility and bending modulus—are available for the lipid bilayer compositions studied in this work. Hence, a direct comparison of our results to experiment is difficult. However, for the L_D system (see **Table 4**) the average area per lipid (*APL*) is in good agreement with a previous simulation for the same composition (Sodt et al., 2015), however well below the APL reported for pure POPC bilayers in experiment (Kučerka et al., 2011) and simulations (Pluhackova et al., 2016). This decreased APL arises due to the condensing effect in particular of cholesterol. In addition, the area compressibility modulus, K_A, and the bending rigidity, K_C, are in line with previous studies of pure PC bilayers at 303 K, reporting $K_A = 180 - 330$ mN/m (Binder and Gawrisch, 2001), and $K_C = 9 - 13 \times 10^{-20}$ J (Binder and Gawrisch, 2001).

Extremely large K_A values for mixtures of PSM-Chol (1,718 mN/m) with respect to those of POPC-PSM mixtures (781 mN/m) have been experimentally reported by Needham and Nunn (1990), and related to an additional effect of PSM to decrease area fluctuations, possibly related to the tendency of SM to form intermolecular hydrogen bonds with cholesterol (Henriksen et al., 2004). In line with this observation, we observed a similarly large area compressibility of $K_A \approx$2,140 mN/m for the PSM-rich L_O system (61% PSM, 8% Chol). The average area per lipid for this system is also in full agreement with that reported for the same composition by Sodt et al. (2015). Our values for the bending rigidity of the L_D system of $K_C \approx 13.4 \times 10^{-20}$ J are in good agreement with experimental values for PC systems (Nagle, 2017). As the

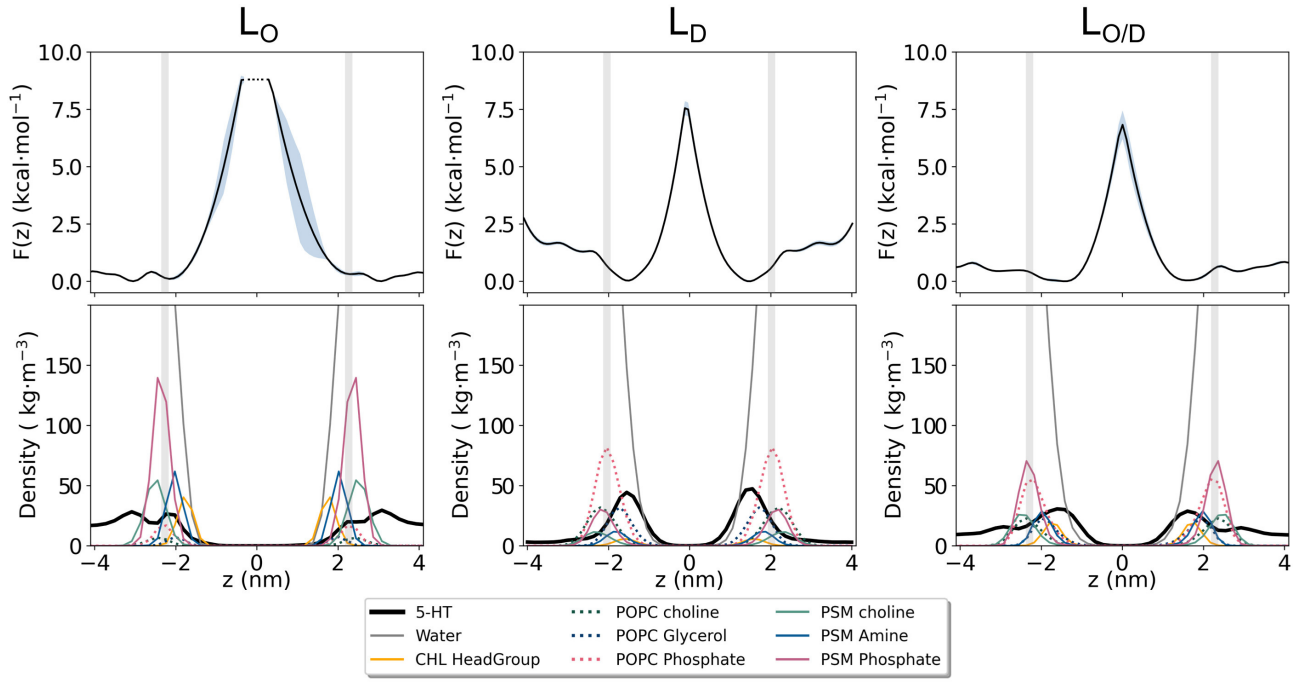

FIGURE 6 | Potential of Mean Force (PMF) for serotonin binding to lipid membranes. Shown is the potential of mean force **(Top)** as estimated from the serotonin density along the membrane normal *z* for the L_O, L_D, and $L_{O/D}$ phase membranes **(Bottom)**.

TABLE 4 | Averaged physical properties of the membrane in the different systems: bending constant (K_C [$10^{-20}J$]), area per lipid (*APL* [^{2}]), and lipid area compressibility (K_A [mN/m]). Standard errors are given in parenthesis.

		303 K			298 K			294 K		
System		K_C	*APL*	K_A	K_C	*APL*	K_A	K_C	*APL*	K_A
$L_{O/D}$	w/o 5-HT	13.0 (0.3)	45.1 (0.1)	552 (3)	10.4 (0.4)	42.8 (0.1)	705 (3)	12.2 (0.4)	42.2 (0.1)	1274 (1)
	+ 5-HT	10.6 (0.4)	47.5 (0.1)	417 (2)	9.2 (0.3)	45.4 (0.1)	543 (2)	9.1 (0.3)	44.9 (0.1)	529 (5)
L_O	w/o 5-HT	24.6 (0.8)	40.4 (0.1)	2143 (2)						
	+ 5-HT	23.3 (0.7)	40.5 (0.1)	2140 (3)						
L_D	w/o 5-HT	13.4 (0.4)	55.3 (0.1)	266 (0.7)						
	+ 5-HT	11.2 (0.4)	57.8 (0.1)	222 (0.4)						

experimental values vary and computational reports on Chol and PSM effect on K_C values in PC membranes are lacking, a more quantitative validation for this and the other systems is hampered.

Serotonin absorption and binding to the membrane has a strong effect on all the calculated physical observables. The data show a 16%, and 12 − 18% decrease in the bending modulus K_C for the L_D system and $L_{O/D}$ systems upon serotonin binding, respectively, as reported in **Table 4**. Such an effect, together with an increase in the average area per lipid and a strong decrease in K_A, indicate substantial membrane softening upon neurotransmitter binding. Little or no change is observed for the pure L_O phase (**Table 4**), as expected from the observed low serotonin absorption.

4. DISCUSSION

Plasma membranes are rich in phosphatidylcholines, cholesterol, and sphingomyelin. In this study, we provide an atomistic view on membrane domain formation of a ternary POPC/PSM/Chol lipid bilayer as a model for plasma membranes. Employing atomistic MD simulations, we trace the initial steps of the formation of (nano-)domains differing in composition, structure, and ordering i.e., dynamics, and mechanics, starting from a random mixture of the membrane constituents. Additionally, we demonstrate that a high neurotransmitter concentration may heavily affect the equilibrium between disordered and ordered lipid membrane domains by preferential binding to L_D-domains.

In the ternary mixture, domains characterized by a substantial difference in lipid acyl chain order are formed only above

298 K. Interestingly, and despite the excellent agreement of these different acyl chain orders with those of simulations of systems with predefined compositions for ordered and disordered domains (see also Sodt et al., 2015), changes in domain composition are less distinct on the 10 μs timescale. That is, the ratios of PSM or POPC do not significantly differ between the differently ordered domains. This finding that composition lags behind ordering is most likely partly related to the limited size of the domains formed on the accessible timescale. It is important to note that ordered lipid domains (L_O) were defined in literature as domains containing lipids with extended and ordered acyl chains similar to the gel phase or L_β-phase, and at the same time display a high mobility more similar to the disordered L_D-phase (Brown and London, 1998; Polozov and Gawrisch, 2006). This rather counterintuitive characteristics, high order combined with high mobility, was supported by pulsed field NMR spectroscopy revealing a lipid diffusion coefficient that differs by only a factor of approximately 3–10 between ordered and disordered phases (Filippov et al., 2004; Orädd et al., 2005; Scheidt et al., 2005). Oppositely, experimental studies showed a comparable fluidity of ordered and gel phases using fluorescence probes (M'Baye et al., 2008). While the simulations yield a large acyl chain order, the lipid diffusion differs substantially between the ordered and disordered phases: The POPC diffusion coefficient within the L_D-phase is $4.1 \cdot 10^{-8} cm^2/s$ and is lowered by a factor of $\approx$ 25 within the ordered phase (diffusion coefficients analyzed for the predefined L_O- and L_D-phases, see also Pluhackova et al., 2016). Possibly, the different timescales between NMR (several ms) and MD (nanoseconds) impede the comparison. We speculate that, due to the long timescale, NMR may partly average the dynamics of lipids exchanging between ordered and disordered phases and thereby yield an efficient enhanced diffusion.

Most simulation studies dealing with serotonin assumed a protonated amine group of serotonin in agreement with the reported pK_a of 9.97. However, binding of the neurotransmitter to lipid membranes with a low dielectric constant (decreasing from $\approx$ 78 in the solvent to $\epsilon_r \approx 2$ within the membrane hydrophobic core; Böckmann et al., 2008) as well as altered hydration properties may substantially shift the pK_a (Narzi et al., 2008; Sandoval et al., 2016). A recent experimental study addressing the association of serotonin to model lipid bilayers revealed a nonspecific binding of the neurotransmitter at physiologically relevant concentrations (Josey et al., 2020). In the same work, neutron reflectometry results favored a model with deep penetration of serotonin into the bilayer, with its long axis oriented along the membrane normal. A protonated serotonin is at variance with the latter configuration since either the polar hydroxyl group or the charged amine would need to protrude into the hydrocarbon core region of the membrane. This indirect hint to a deprotonated membrane-bound form of serotonin is strongly supported by our zeta potential measurements on lipid vesicles displaying a largely serotonin-independent potential. Accordingly, our simulation study on the influence of serotonin on membrane domain formation focused on the deprotonated i.e., uncharged form of serotonin.

Addition of the neurotransmitter led to a significant downward shift of the phase transition temperature, thereby resulting in clearly distinguished ordered and disordered phases now even at 294 K. This phase shift is induced by preferential binding of serotonin to the domains containing mostly lipids in disordered state, enhancing thereby the fluidity of these domains. This is in agreement with a shift of the main phase transition temperature to lower temperatures reported before for DMPC upon addition of serotonin (Seeger et al., 2007) and similarly for ethanol (Griepernau et al., 2007). However, in the former study the shift induced by 3 mM serotonin was below 1 K. The L_D domains under the influence of the bound neurotransmitters are characterized by an enhanced ratio of phosphatidylcholines, an increased area per lipid, as well as a drastic reduction in the bending modulus and the area compressibility. The latter findings are in apparent contradiction to a companion manuscript (Engberg et al., 2020) reporting in particular ^{2}H NMR and AFM indentation experiments on the same ternary biomembrane models. In this work, an increased intendation force was required to rupture the membrane in presence of serotonin and interpreted as an increase in membrane stiffness. These opposing findings, a decreased bending modulus and area compressibility on the nano-scale and an increased membrane stiffness on the AFM scale, may be reconciled assuming that serotonin induces the formation of larger domains as supported by our ^{2}H NMR experiments (Engberg et al., 2020). Additionally, serotonin induces a more pronounced disorder of the L_D domains (this work and ^{2}H NMR; Engberg et al., 2020) as well as a more pronounced order of the L_O domains (^{2}H NMR). The latter may be explained by changed domain compositions as observed in the simulations displaying an increased PC content of the L_D domains and a thus likely decreased PC content for (larger) ordered domains and thereby increased ordering. Interestingly, in good agreement with our simulation data, a recent work reports a significant softening of lipid bilayers containing POPC/POPG/Chol (1:1:1) by serotonin (Dey et al., 2020).

In summary, the initial steps of the spontaneous lateral segregation of a plasma membrane model containing POPC/PSM/Chol (4:4:2) is observed on the microsecond timescale. Despite small differences in compositions, formed nano-domains display a huge difference in order resembling those for PC-rich disordered and PSM/Chol-enriched raft-like ordered domains. The neurotransmitter serotonin reshapes in particular the disordered membrane domains resulting in a PC-enrichment and a decreased membrane elasticity and probably in increased membrane domain sizes as suggested by comparison to ^{2}H NMR (Engberg et al., 2020). These changes in membrane structure, domain formation and domain size, and membrane dynamics will probably among others affect receptor sorting and oligomerization in plasma membranes (Gahbauer and Böckmann, 2020), as well as membrane stability, and related permeability and pore formation (Kirsch and Böckmann, 2016, 2019). A possibly similar mechanism was recently revealed for inhalation anesthetics that were shown to increase the size

of ganglioside (GM1) rafts and to change the localization of the phospholipase D2 to GM1-enriched domains (Pavel et al., 2020).

Regarding its action as neurotransmitter, our results suggest a fast binding of serotonin to the postsynaptic membrane following synaptic vesicle fusion and thereby a fast and efficient mechanism for neurotransmitter removal from the synaptic cleft (Postila et al., 2016). The preferential binding of serotonin to L_D-domains with a concomitant change in composition, ordering, and reduced phase transition temperature likely as well alters the membrane lateral pressure profile as reported before also for ethanol (Griepernau and Böckmann, 2008). A changed membrane pressure may in turn be hypothesized to shift the equilibrium between activated/non-activated receptor configurations if assuming different cross-sectional areas for different receptor activation states (Cantor, 1997a,b, 1998). In addition, high concentrations of membrane-bound neurotransmitters would result in efficient binding to membrane-buried receptor binding sites.

DATA AVAILABILITY STATEMENT

The raw data supporting the conclusions of this article will be made available by the authors, without undue reservation.

AUTHOR CONTRIBUTIONS

RB designed the research. ABo setup and carried out the simulations. ABo and ABr analyzed the simulations. OE performed the zeta potential measurements and analysis. RB wrote the paper with contributions from all coauthors. All authors contributed to the article and approved the submitted version.

FUNDING

RB acknowledges support by the German Science Foundation (DFG) within the SFB1027, Physical Modeling of Non-Equilibrium Processes in Biological Systems (project C6). DH acknowledges funding by the DFG through SFB1423, project number 421152132, subproject A02. OE acknowledges support by the Sigrid Juselius Foundation and Ruth and Nils-Erik Stenbäck's Foundation. Computing time was provided by the Computing Center Erlangen (RRZE).

SUPPLEMENTARY MATERIAL

The Supplementary Material for this article can be found online at: https://www.frontiersin.org/articles/10.3389/fcell.2020.601145/full#supplementary-material

REFERENCES

Abraham, M. J., Murtola, T., Schulz, R., Páll, S., Smith, J. C., Hess, B., et al. (2015). GROMACS: High performance molecular simulations through multi-level parallelism from laptops to supercomputers. *SoftwareX* 1–2, 19–25. doi: 10.1016/j.softx.2015.06.001

Allen, M. P., and Tildesley, D. J. (2017). *Computer Simulation of Liquids*. Oxford: Oxford University Press. doi: 10.1093/oso/9780198803195.001.0001

Azouzi, S., Santuz, H., Morandat, S., Pereira, C., Côté, F., Hermine, O., et al. (2017). Antioxidant and membrane binding properties of serotonin protect lipids from oxidation. *Biophys. J.* 112, 1863–1873. doi: 10.1016/j.bpj.2017.03.037

Bandara, A., Panahi, A., Pantelopulos, G. A., Nagai, T., and Straub, J. E. (2019). Exploring the impact of proteins on the line tension of a phase-separating ternary lipid mixture. *J. Chem. Phys.* 150:204702. doi: 10.1063/1.5091450

Bartels, T., Lankalapalli, R. S., Bittman, R., Beyer, K., and Brown, M. F. (2008). Raftlike mixtures of sphingomyelin and cholesterol investigated by solid-state 2H NMR spectroscopy. *J. Am. Chem. Soc.* 130, 14521–14532. doi: 10.1021/ja801789t

Baum, L. E., Petrie, T., Soules, G., and Weiss, N. (1970). A maximization technique occurring in the statistical analysis of probabilistic functions of Markov chains. *Ann. Math. Stat.* 41, 164–171. doi: 10.1214/aoms/1177697196

Binder, H., and Gawrisch, K. (2001). Effect of unsaturated lipid chains on dimensions, molecular order and hydration of membranes. *J. Phys. Chem. B* 105, 12378–12390. doi: 10.1021/jp010118h

Bochicchio, A., Krepl, M., Yang, F., Varani, G., Sponer, J., and Carloni, P. (2018). Molecular basis for the increased affinity of an RNA recognition motif with re-engineered specificity: a molecular dynamics and enhanced sampling simulations study. *PLoS Comput. Biol.* 14:e1006642. doi: 10.1371/journal.pcbi.1006642

Böckmann, R. A., De Groot, B. L., Kakorin, S., Neumann, E., and Grubmüller, H. (2008). Kinetics, statistics, and energetics of lipid membrane electroporation studied by molecular dynamics simulations. *Biophys. J.* 95, 1837–1850. doi: 10.1529/biophysj.108.129437

Bosse, M., Sibold, J., Scheidt, H. A., Patalag, L. J., Kettelhoit, K., Ries, A., et al. (2019). Shiga toxin binding alters lipid packing and the domain structure of Gb3-containing membranes: a solid-state NMR study. *Phys. Chem. Chem. Phys.* 21, 15630–15638. doi: 10.1039/C9CP02501D

Brown, D. A., and London, E. (1998). Structure and origin of ordered lipid domains in biological membranes. *J. Membr. Biol.* 164, 103–114. doi: 10.1007/s002329900397

Bruns, D., Riedel, D., Klingauf, J., and Jahn, R. (2000). Quantal release of serotonin. *Neuron* 28, 205–220. doi: 10.1016/S0896-6273(00)00097-0

Bunge, A., Müller, P., Stöckl, M., Herrmann, A., and Huster, D. (2008). Characterization of the ternary mixture of sphingomyelin, POPC, and cholesterol: support for an inhomogeneous lipid distribution at high temperatures. *Biophys. J.* 94, 2680–2690. doi: 10.1529/biophysj.107.112904

Cantor, R. S. (1997a). The lateral pressure profile in membranes: a physical mechanism of general anesthesia. *Biochemistry* 36, 2339–2344. doi: 10.1021/bi9627323

Cantor, R. S. (1997b). Lateral pressures in cell membranes: a mechanism for modulation of protein function. *J. Phys. Chem. B* 101, 1723–1725. doi: 10.1021/jp963911x

Cantor, R. S. (1998). The lateral pressure profile in membranes: a physical mechanism of general anesthesia. *Toxicol. Lett.* 100–101, 451–458. doi: 10.1016/S0378-4274(98)00220-3

Cebecauer, M., Amaro, M., Jurkiewicz, P., Sarmento, M. J., Šachl, R., Cwiklik, L., et al. (2018). Membrane lipid nanodomains. *Chem. Rev.* 23, 11259–11297. doi: 10.1021/acs.chemrev.8b00322

CGenFF (2020). *CGenFF Home*.

Chernomordik, L., Kozlov, M. M., and Zimmerberg, J. (1995). Lipids in biological membrane fusion. *J. Membr. Biol.* 146, 1–14. doi: 10.1007/BF00232676

Darden, T., York, D., and Pedersen, L. (1993). Particle mesh Ewald: an Nlog(N) method for Ewald sums in large systems. *J. Chem. Phys.* 98, 10089–10092. doi: 10.1063/1.464397

Davis, D. M., and Dustin, M. L. (2004). What is the importance of the immunological synapse? *Trends Immunol.* 25, 323–327. doi: 10.1016/j.it.2004.03.007

De Almeida, R. F., Fedorov, A., and Prieto, M. (2003). Sphingomyelin/phosphatidylcholine/cholesterol phase diagram: boundaries and composition of lipid rafts. *Biophys. J.* 85, 2406–2416. doi: 10.1016/S0006-3495(03)74664-5

De Almeida, R. F., Loura, L. M., Fedorov, A., and Prieto, M. (2005). Lipid rafts have different sizes depending on membrane composition: a time-resolved fluorescence resonance energy transfer study. *J. Membr. Biol.* 346, 1109–1120. doi: 10.1016/j.jmb.2004.12.026

De Wit, G., Danial, J. S., Kukura, P., and Wallace, M. I. (2015). Dynamic label-free imaging of lipid nanodomains. *Proc. Natl. Acad. Sci. U.S.A.* 112, 12299–12303. doi: 10.1073/pnas.1508483112

Dey, S., Surendran, D., Engberg, O., Gupta, A., Fanibunda, S. E., Das, A., et al. (2020). Receptor-independent membrane mediated pathways of serotonin action. *bioRxiv*. 1–18. doi: 10.1101/2020.07.01.177451

Eggeling, C., Ringemann, C., Medda, R., Schwarzmann, G., Sandhoff, K., Polyakova, S., et al. (2009). Direct observation of the nanoscale dynamics of membrane lipids in a living cell. *Nature* 457, 1159–1162. doi: 10.1038/nature07596

Engberg, O., Bochicchio, A., Brandner, A. F., Gupta, A., Dey, S., Böckmann, R. A., et al. (2020). Serotonin alters the phase equilibrium of a ternary mixture of phospholipids and cholesterol. *Front. Physiol.* 11:1389. doi: 10.3389/fphys.2020.578868

Engberg, O., Hautala, V., Yasuda, T., Dehio, H., Murata, M., Slotte, J. P., et al. (2016). The affinity of cholesterol for different phospholipids affects lateral segregation in bilayers. *Biophys. J.* 111, 546–556. doi: 10.1016/j.bpj.2016.06.036

Enoki, T. A., Heberle, F. A., and Feigenson, G. W. (2018). FRET detects the size of nanodomains for coexisting liquid-disordered and liquid-ordered phases. *Biophys. J.* 114, 1921–1935. doi: 10.1016/j.bpj.2018.03.014

Feigenson, G. W., and Buboltz, J. T. (2001). Ternary phase diagram of dipalmitoyl-pc/dilauroyl-pc/cholesterol: nanoscopic domain formation driven by cholesterol. *Biophys. J.* 80, 2775–2788. doi: 10.1016/S0006-3495(01)76245-5

Filippov, A., Orädd, G., and Lindblom, G. (2004). Lipid lateral diffusion in ordered and disordered phases in raft mixtures. *Biophys. J.* 86, 891–896. doi: 10.1016/S0006-3495(04)74164-8

Friess, M. D., Pluhackova, K., and Böckmann, R. A. (2018). Structural model of the mIgM B-Cell receptor transmembrane domain from self-association molecular dynamics simulations. *Front. Immunol.* 9:2947. doi: 10.3389/fimmu.2018.02947

Gaede, H. C., Yau, W.-M., and Gawrisch, K. (2005). Electrostatic contributions to indole- lipid interactions. *J. Phys. Chem. B* 109, 13014–13023. doi: 10.1021/jp0511000

Gahbauer, S., and Böckmann, R. A. (2016). Membrane-mediated oligomerization of G protein coupled receptors and its implications for GPCR function. *Front. Physiol.* 7:494. doi: 10.3389/fphys.2016.00494

Gahbauer, S., and Böckmann, R. A. (2020). Comprehensive characterization of lipid-guided g protein-coupled receptor dimerization. *J. Phys. Chem. B* 124, 2823–2834. doi: 10.1021/acs.jpcb.0c00062

Gibbs, J. W. (1878). On the equilibrium of heterogeneous substances. *Trans. Connect. Acad. Arts Sci.* 3, 108–248; 343–524. doi: 10.2475/ajs.s3-16.96.441

Glodek, M., Schels, M., and Schwenker, F. (2013). Ensemble Gaussian mixture models for probability density estimation. *Comput. Stat.* 28, 127–138. doi: 10.1007/s00180-012-0374-5

Grakoui, A., Bromley, S. K., Sumen, C., Davis, M. M., Shaw, A. S., Allen, P. M., et al. (1999). The immunological synapse: a molecular machine controlling T cell activation. *Science* 285, 221–227. doi: 10.1126/science.285.5425.221

Griepernau, B., and Böckmann, R. A. (2008). The influence of 1-alkanols and external pressure on the lateral pressure profiles of lipid bilayers. *Biophys. J.* 95, 5766–5778. doi: 10.1529/biophysj.108.142125

Griepernau, B., Leis, S., Schneider, M. F., Sikor, M., Steppich, D., and Böckmann, R. A. (2007). 1-alkanols and membranes: a story of attraction. *Biochim. Biophys. Acta* 1768, 2899–2913. doi: 10.1016/j.bbamem.2007.08.002

Gu, R. X., Baoukina, S., and Peter Tieleman, D. (2020). Phase separation in atomistic simulations of model membranes. *J. Am. Chem. Soc.* 142, 2844–2856. doi: 10.1021/jacs.9b11057

Guros, N. B., Balijepalli, A., and Klauda, J. B. (2020). Microsecond-timescale simulations suggest 5-HT-mediated preactivation of the 5-HT3A serotonin receptor. *Proc. Natl. Acad. Sci. U.S.A.* 117, 405–414. doi: 10.1073/pnas.1908848117

Henriksen, J., Rowat, A. C., and Ipsen, J. H. (2004). Vesicle fluctuation analysis of the effects of sterols on membrane bending rigidity. *Eur. Biophys. J.* 33, 732–741. doi: 10.1007/s00249-004-0420-5

Hess, B., Bekker, H., Berendsen, H. J. C., and Fraaije, J. G. E. M. (1997). LINCS: A linear constraint solver for molecular simulations. *J. Comput. Chem.* 18, 1463–1472. doi: 10.1002/(SICI)1096-987X(199709)18:12<1463::AID-JCC4>3.0.CO;2-H

Hjort Ipsen, J., Karlström, G., Mourtisen, O. G., Wennerström, H., and Zuckermann, M. J. (1987). Phase equilibria in the phosphatidylcholine-cholesterol system. *Biochim. Biophys. Acta* 905, 162–172. doi: 10.1016/0005-2736(87)90020-4

Hoover, W. G. (1985). Canonical dynamics: equilibrium phase-space distributions. *Phys. Rev. A* 31, 1695–1697. doi: 10.1103/PhysRevA.31.1695

Humphrey, W., Dalke, A., and Schulten, K. (1996). VMD: visual molecular dynamics. *J. Mol. Graph.* 14, 27–28, 33–38. doi: 10.1016/0263-7855(96)00018-5

Ionova, I. V., Livshits, V. A., and Marsh, D. (2012). Phase diagram of ternary cholesterol/palmitoylsphingomyelin/palmitoyloleoyl-phosphatidylcholine mixtures: spin-label EPR study of lipid-raft formation. *Biophys. J.* 102, 1856–1865. doi: 10.1016/j.bpj.2012.03.043

Jämbeck, J. P. M., and Lyubartsev, A. P. (2012). Derivation and systematic validation of a refined all-atom force field for phosphatidylcholine lipids. *J. Phys. Chem. B* 116, 3164–3179. doi: 10.1021/jp212503e

Josey, B. P., Heinrich, F., Silin, V., and Lösche, M. (2020). Association of model neurotransmitters with lipid bilayer membranes. *Biophys. J.* 118, 1044–1057. doi: 10.1016/j.bpj.2020.01.016

Kirsch, S. A., and Böckmann, R. A. (2016). Membrane pore formation in atomistic and coarse-grained simulations. *Biochim. Biophys. Acta* 1858, 2266–2277. doi: 10.1016/j.bbamem.2015.12.031

Kirsch, S. A., and Böckmann, R. A. (2019). Coupling of membrane nanodomain formation and enhanced electroporation near phase transition. *Biophys. J.* 116, 2131–2148. doi: 10.1016/j.bpj.2019.04.024

Klauda, J. B., Venable, R. M., Freites, J. A., O'Connor, J. W., Tobias, D. J., Mondragon-Ramirez, C., et al. (2010). Update of the CHARMM all-atom additive force field for lipids: validation on six lipid types. *J. Phys. Chem. B* 114, 7830–7843. doi: 10.1021/jp101759q

Koukalová, A., Amaro, M., Aydogan, G., Gröbner, G., Williamson, P. T., Mikhalyov, I., et al. (2017). Lipid driven nanodomains in giant lipid vesicles are fluid and disordered. *Sci. Rep.* 7, 1–12. doi: 10.1038/s41598-017-05539-y

Kučerka, N., Nieh, M. P., and Katsaras, J. (2011). Fluid phase lipid areas and bilayer thicknesses of commonly used phosphatidylcholines as a function of temperature. *Biochim. Biophys. Acta* 1808, 2761–2771. doi: 10.1016/j.bbamem.2011.07.022

Lee, J., Cheng, X., Swails, J. M., Yeom, M. S., Eastman, P. K., Lemkul, J. A., et al. (2016). CHARMM-GUI input generator for NAMD, GROMACS, AMBER, openMM, and CHARMM/openMM simulations using the CHARMM36 additive force field. *J. Chem. Theory Comput.* 12, 405–413. doi: 10.1021/acs.jctc.5b00935

Levine, Z. A., Venable, R. M., Watson, M. C., Lerner, M. G., Shea, J.-E., Pastor, R. W., et al. (2014). Determination of biomembrane bending moduli in fully atomistic simulations. *J. Am. Chem. Soc.* 136, 13582–13585. doi: 10.1021/ja507910r

Lin, X., Gorfe, A. A., and Levental, I. (2018). Protein partitioning into ordered membrane domains: Insights from simulations. *Biophys. J.* 114, 1936–1944. doi: 10.1016/j.bpj.2018.03.020

Liu, J., Kaksonen, M., Drubin, D. G., and Oster, G. (2006). Endocytic vesicle scission by lipid phase boundary forces. *Proc. Natl. Acad. Sci. U.S.A.* 103, 10277–10282. doi: 10.1073/pnas.0601045103

MacKerell, A. D., Bashford, D., Bellott, M., Dunbrack, R. L., Evanseck, J. D., Field, M. J., et al. (1998). All-atom empirical potential for molecular modeling and dynamics studies of proteins. *J. Phys. Chem. B* 102, 3586–3616. doi: 10.1021/jp973084f

Marrink, S. J., Risselada, H. J., Yefimov, S., Tieleman, D. P., and De Vries, A. H. (2007). The MARTINI force field: Coarse grained model for biomolecular simulations. *J. Phys. Chem. B* 111, 7812–7824. doi: 10.1021/jp071097f

M'Baye, G., Mély, Y., Duportail, G., and Klymchenko, A. S. (2008). Liquid ordered and gel phases of lipid bilayers: fluorescent probes reveal close fluidity but different hydration. *Biophys. J.* 95, 1217–1225. doi: 10.1529/biophysj.107.127480

McMahon, H. T., and Gallop, J. L. (2005). Membrane curvature and mechanisms of dynamic cell membrane remodelling. *Nature* 438, 590–596. doi: 10.1038/nature04396

Michaud-Agrawal, N., Denning, E. J., Woolf, T. B., and Beckstein, O. (2011). MDAnalysis: A toolkit for the analysis of molecular dynamics simulations. *J. Comput. Chem.* 32, 2319–2327. doi: 10.1002/jcc.21787

Mokkila, S., Postila, P. A., Rissanen, S., Juhola, H., Vattulainen, I., and Róg, T. (2017). Calcium assists dopamine release by preventing aggregation on the inner leaflet of presynaptic vesicles. *ACS Chem. Neurosci.* 8, 1242–1250. doi: 10.1021/acschemneuro.6b00395

Nagle, J. F. (2017). Experimentally determined tilt and bending moduli of single-component lipid bilayers. *Chem. Phys. Lipids* 205, 18–24. doi: 10.1016/j.chemphyslip.2017.04.006

Narzi, D., Siu, S. W. I., Stirnimann, C. U., Grimshaw, J. P. A., Glockshuber, R., Capitani, G., et al. (2008). Evidence for proton shuffling in a thioredoxin-like protein during catalysis. *J. Membr. Biol.* 382, 978–986. doi: 10.1016/j.jmb.2008.07.061

Needham, D., and Nunn, R. S. (1990). Elastic deformation and failure of lipid bilayer membranes containing cholesterol. *Biophys. J.* 58, 997–1009. doi: 10.1016/S0006-3495(90)82444-9

Nosé, S. (1984). A molecular dynamics method for simulations in the canonical ensemble. *Mol. Phys.* 52, 255–268. doi: 10.1080/00268978400101201

Oliphant, T. E. (2015). *Guide to NumPy, 2nd Edn*. North Charleston, SC: CreateSpace Independent Publishing Platform.

Orädd, G., Westerman, P. W., and Lindblom, G. (2005). Lateral diffusion coefficients of separate lipid species in a ternary raft-forming bilayer: a Pfg-NMR multinuclear study. *Biophys. J.* 89, 315–320. doi: 10.1529/biophysj.105.061762

Park, S., and Im, W. (2019). Analysis of lipid order states and domains in lipid bilayer simulations. *J. Chem. Theory Comput.* 15, 688–697. doi: 10.1021/acs.jctc.8b00828

Parrinello, M., and Rahman, A. (1981). Polymorphic transitions in single crystals: a new molecular dynamics method. *J. Appl. Phys.* 52, 7182–7190. doi: 10.1063/1.328693

Pathak, P., and London, E. (2011). Measurement of lipid nanodomain (Raft) formation and size in sphingomyelin/POPC/cholesterol vesicles shows TX-100 and transmembrane helices increase domain size by coalescing preexisting nanodomains but do not induce domain formation. *Biophys. J.* 101, 2417–2425. doi: 10.1016/j.bpj.2011.08.059

Pathak, P., and London, E. (2015). The effect of membrane lipid composition on the formation of lipid ultrananodomains. *Biophys. J.* 109, 1630–1638. doi: 10.1016/j.bpj.2015.08.029

Pavel, M. A., Petersen, E. N., Wang, H., Lerner, R. A., and Hansen, S. B. (2020). Studies on the mechanism of general anesthesia. *Proc. Natl. Acad. Sci. U.S.A.* 117, 13757–13766. doi: 10.1073/pnas.2004259117

Pedregosa, F., Varoquaux, G., Gramfort, A., Michel, V., Thirion, B., Grisel, O., et al. (2011). Scikit-learn: machine learning in python. *J. Mach. Learn. Res.* 12, 2825–2830.

Pencer, J., Mills, T. T., Kucerka, N., Nieh, M. P., and Katsaras, J. (2007). Small-angle neutron scattering to detect rafts and lipid domains. *Methods Mol. Biol.* 398, 231–244. doi: 10.1007/978-1-59745-513-8_16

Peters, G. H., Wang, C., Cruys-Bagger, N., Velardez, G. F., Madsen, J. J., and Westh, P. (2013). Binding of serotonin to lipid membranes. *J. Am. Chem. Soc.* 135, 2164–2171. doi: 10.1021/ja306681d

Petruzielo, R. S., Heberle, F. A., Drazba, P., Katsaras, J., and Feigenson, G. W. (2013). Phase behavior and domain size in sphingomyelin-containing lipid bilayers. *Biochim. Biophys. Acta* 1828, 1302–1313. doi: 10.1016/j.bbamem.2013.01.007

Pike, L. J. (2006). Rafts defined: a report on the keystone symposium on lipid rafts and cell function. *J. Lipid Res.* 47, 1597–1598. doi: 10.1194/jlr.E600002-JLR200

Pluhackova, K., Kirsch, S. A., Han, J., Sun, L., Jiang, Z., Unruh, T., et al. (2016). A critical comparison of biomembrane force fields: Structure and dynamics of model DMPC, POPC, and POPE bilayers. *J. Phys. Chem. B* 120, 3888–3903. doi: 10.1021/acs.jpcb.6b01870

Polozov, I. V., and Gawrisch, K. (2006). Characterization of the liquid-ordered state by proton MAS NMR. *Biophys. J.* 90, 2051–2061. doi: 10.1529/biophysj.105.070441

Postila, P. A., and Róg, T. (2020). A perspective: active role of lipids in neurotransmitter dynamics. *Mol. Neurobiol.* 57, 910–925. doi: 10.1007/s12035-019-01775-7

Postila, P. A., Vattulainen, I., and Róg, T. (2016). Selective effect of cell membrane on synaptic neurotransmission. *Sci. Rep.* 6, 1–10. doi: 10.1038/srep19345

Rabiner, L. R. (1989). A tutorial on hidden Markov models and selected applications in speech recognition. *Proc. IEEE* 77, 257–286. doi: 10.1109/5.18626

Risselada, H. J., and Marrink, S. J. (2008). The molecular face of lipid rafts in model membranes. *Proc. Natl. Acad. Sci. U.S.A.* 105, 17367–17372. doi: 10.1073/pnas.0807527105

Saitov, A., Akimov, S. A., Galimzyanov, T. R., Glasnov, T., and Pohl, P. (2020). Ordered lipid domains assemble via concerted recruitment of constituents from both membrane leaflets. *Phys. Rev. Lett.* 124:108102. doi: 10.1103/PhysRevLett.124.108102

Sandoval, A., Eichler, S., Madathil, S., Reeves, P. J., Fahmy, K., and Böckmann, R. A. (2016). The molecular switching mechanism at the conserved D(E)RY otif in class-A GPCRs. *Biophys. J.* 111, 79–89. doi: 10.1016/j.bpj.2016.06.004

Scheidt, H. A., Huster, D., and Gawrisch, K. (2005). Diffusion of cholesterol and its precursors in lipid membranes studied by 1h pulsed field gradient magic angle spinning NMR. *Biophys. J.* 89, 2504–2512. doi: 10.1529/biophysj.105.062018

Seeger, H. M., Gudmundsson, M. L., and Heimburg, T. (2007). How anesthetics, neurotransmitters, and antibiotics influence the relaxation processes in lipid membranes. *J. Phys. Chem. B* 111, 13858–13866. doi: 10.1021/jp075346b

Sezgin, E., Levental, I., Mayor, S., and Eggeling, C. (2017). The mystery of membrane organization: composition, regulation and roles of lipid rafts. *Nat. Rev. Mol. Cell Biol.* 18, 361–374. doi: 10.1038/nrm.2017.16

Shan, Y., and Wang, H. (2015). The structure and function of cell membranes examined by atomic force microscopy and single-molecule force spectroscopy. *Chem. Soc. Rev.* 44, 3617–3638. doi: 10.1039/C4CS00508B

Simons, K., and Ikonen, E. (1997). Functional rafts in cell membranes. *Nature* 387, 569–572. doi: 10.1038/42408

Sodt, A. J., Pastor, R. W., and Lyman, E. (2015). Hexagonal substructure and hydrogen bonding in liquid-ordered phases containing palmitoyl sphingomyelin. *Biophys. J.* 109, 948–955. doi: 10.1016/j.bpj.2015.07.036

Sodt, A. J., Sandar, M. L., Gawrisch, K., Pastor, R. W., and Lyman, E. (2014). The molecular structure of the liquid-ordered phase of lipid bilayers. *J. Am. Chem. Soc.* 136, 725–732. doi: 10.1021/ja4105667

Sun, H. Y., Wu, F. G., Li, Z. H., Deng, G., Zhou, Y., and Yu, Z. W. (2017). Phase behavior of a binary lipid system containing long- and short-chain phosphatidylcholines. *RSC Adv.* 7, 5715–5724. doi: 10.1039/C6RA24961B

Taylor, R. W., Mahmoodabadi, R. G., Rauschenberger, V., Giessl, A., Schambony, A., and Sandoghdar, V. (2019). Interferometric scattering microscopy reveals microsecond nanoscopic protein motion on a live cell membrane. *Nat. Photon.* 13, 480–487. doi: 10.1038/s41566-019-0414-6

Tokumasu, F., Jin, A. J., Feigenson, G. W., and Dvorak, J. A. (2003). Nanoscopic lipid domain dynamics revealed by atomic force microscopy. *Biophys. J.* 84, 2609–2618. doi: 10.1016/S0006-3495(03)75066-8

Vanommeslaeghe, K., Hatcher, E., Acharya, C., Kundu, S., Zhong, S., Shim, J., et al. (2010). CHARMM General Force Field: a force field for drug-like molecules compatible with the CHARMM all-atom additive biological force fields. *J. Comput. Chem.* 31, 671–690. doi: 10.1002/jcc.21367

Vanommeslaeghe, K., and MacKerell, A. D. (2012). Automation of the CHARMM General Force Field (CGenFF) I: bond perception and atom typing. *J. Chem. Inf. Model.* 52, 3144–3154. doi: 10.1021/ci300363c

Vanommeslaeghe, K., Raman, E. P., and MacKerell, A. D. (2012). Automation of the CHARMM General Force Field (CGenFF) II: assignment of bonded parameters and partial atomic charges. *J. Chem. Inf. Model.* 52, 3155–3168. doi: 10.1021/ci3003649

Veatch, S. L., and Keller, S. L. (2005). Miscibility phase diagrams of giant vesicles containing sphingomyelin. *Phys. Rev. Lett.* 94, 3–6. doi: 10.1103/PhysRevLett.94.148101

Veatch, S. L., Soubias, O., Keller, S. L., and Gawrisch, K. (2007). Critical fluctuations in domain-forming lipid mixtures. *Proc. Natl. Acad. Sci. U.S.A.* 104, 17650–17655. doi: 10.1073/pnas.0703513104

Virtanen, P., Gommers, R., Oliphant, T. E., Haberland, M., Reddy, T., Cournapeau, D., et al. (2020). SciPy 1.0: fundamental algorithms for scientific computing in Python. *Nat. Methods* 17, 261–272. doi: 10.1038/s41592-019-0686-2

Viterbi, A. (1967). Error bounds for convolutional codes and an asymptotically optimum decoding algorithm. *IEEE Trans. Inform. Theor.* 13, 260–269. doi: 10.1109/TIT.1967.1054010

Watson, M. C., Brandt, E. G., Welch, P. M., and Brown, F. L. H. (2012). Determining biomembrane bending rigidities from simulations of modest size. *Phys. Rev. Lett.* 109:028102. doi: 10.1103/PhysRevLett.109.028102

Yankova, T. S., Bobrovsky, A. Y., and Vorobiev, A. K. (2012). Order parameters $< p2 >$, $< p4 >$, and $< p6 >$ of aligned nematic liquid-crystalline polymer as determined by numerical simulation of electron paramagnetic resonance spectra. *J. Phys. Chem. B* 116, 6010–6016. doi: 10.1021/jp301170b

Conflict of Interest: The authors declare that the research was conducted in the absence of any commercial or financial relationships that could be construed as a potential conflict of interest.

frontiers in Physiology

REVIEW
published: 04 December 2020
doi: 10.3389/fphys.2020.574371

Recent Advances and Prospects in the Research of Nascent Adhesions

Bernd Henning Stumpf[1], *Andreja Ambriović-Ristov*[2], *Aleksandra Radenovic*[3] *and Ana-Sunčana Smith*[1,4]*

[1] PULS Group, Institute for Theoretical Physics, Interdisciplinary Center for Nanostructured Films, Friedrich-Alexander-Universität Erlangen-Nürnberg, Erlangen, Germany, [2] Laboratory for Cell Biology and Signalling, Division of Molecular Biology, Ruđer Bošković Institute, Zagreb, Croatia, [3] Laboratory of Nanoscale Biology, École Polytechnique Fédérale de Lausanne, Lausanne, Switzerland, [4] Group for Computational Life Sciences, Division of Physical Chemistry, Ruđer Bošković Institute, Zagreb, Croatia

Nascent adhesions are submicron transient structures promoting the early adhesion of cells to the extracellular matrix. Nascent adhesions typically consist of several tens of integrins, and serve as platforms for the recruitment and activation of proteins to build mature focal adhesions. They are also associated with early stage signaling and the mechanoresponse. Despite their crucial role in sampling the local extracellular matrix, very little is known about the mechanism of their formation. Consequently, there is a strong scientific activity focused on elucidating the physical and biochemical foundation of their development and function. Precisely the results of this effort will be summarized in this article.

Keywords: nascent adhesions, focal adhesions, integrin activation, integrin clustering, superresolution microscopy, modeling

OPEN ACCESS

Edited by:
Robert Ernst,
Saarland University, Germany

Reviewed by:
Alf Honigmann,
Max Planck Institute of Molecular Cell Biology and Genetics, Max Planck Society (MPG), Germany
Bramanandam Manavathi,
University of Hyderabad, India

***Correspondence:**
Ana-Sunčana Smith
smith@physik.fau.de;
asmith@irb.hr

Specialty section:
This article was submitted to Membrane Physiology and Membrane Biophysics, a section of the journal Frontiers in Physiology

Received: *19 July 2020*
Accepted: *09 November 2020*
Published: *04 December 2020*

Citation:
Henning Stumpf B, Ambriović-Ristov A, Radenovic A and Smith A-S (2020) Recent Advances and Prospects in the Research of Nascent Adhesions. Front. Physiol. 11:574371. doi: 10.3389/fphys.2020.574371

1. INTRODUCTION

Integrin-mediated adhesion of cells and the associated mechanosensing is of monumental importance for the physiology of nearly any cell type (Kechagia et al., 2019; Samaržija et al., 2020). Upon integrin activation, it often proceeds through the maturation of nascent adhesions (NAs) to focal adhesions (FAs) (**Figure 1**), which are transient supramolecular assemblies, connecting a cell to the extracellular matrix or another cell. NAs typically contain around 50 integrins (Changede et al., 2015), and show a high turnover rate, with lifetimes of a bit over a minute (Choi et al., 2008). FAs, which arise upon the maturation of NAs by recruitment of numerous proteins to their cytoplasmic tails, form multimolecular integrin adhesion complexes. FAs are establishing the linkage between the extracellular matrix (ECM) and the actin cytoskeleton (Winograd-Katz et al., 2014). However, another cytoskeletal element, microtubules, also plays an important role in adhesion and regulates the turnover of adhesion sites (Bouchet et al., 2016; Chen et al., 2018).

While the FAs have been studied extensively in the last decades (Geiger et al., 2009; Parsons et al., 2010; Geiger and Yamada, 2011; Wehrle-Haller, 2012; Cooper and Giancotti, 2019; Green and Brown, 2019), the smaller characteristic size of ∼100 nm diameter makes NAs significantly more elusive (Changede et al., 2015). Studies of NAs require single molecule localization microscopy (SMLM) techniques to image below the diffraction limit of conventional light microscopy, and, furthermore, need to account for the short characteristic lifetime of few minutes (Changede et al., 2015). The resulting scarcity of data associated with NAs makes the theoretical modeling very difficult.

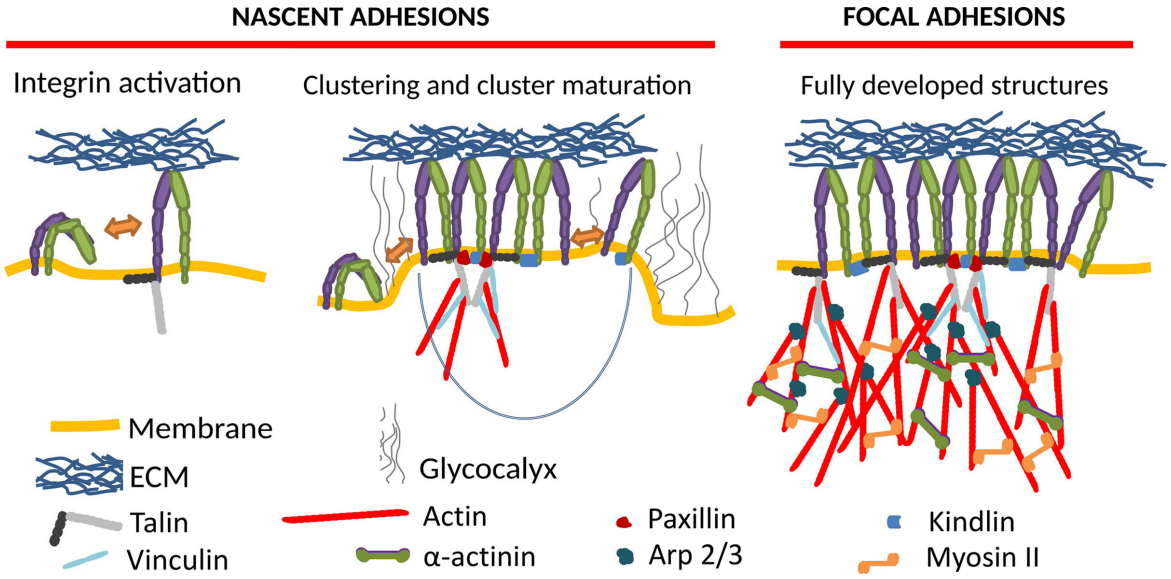

FIGURE 1 | Formation of integrin mediated cell adhesion structures requires integrin activation **(left)**, which induces macromolecular clustering into nascent adhesions **(middle)**, which upon maturation grow into focal adhesions **(right)**. The key molecular players in this process are schematically represented as shown in the legend.

In our current understanding, the NA formation follows three major steps (Sun et al., 2014). First, integrins activate, going from a state of low to high affinity, potentially through a conformational change. This can be induced by the binding of activating proteins like talin or kindlin (Cluzel et al., 2005; Humphries et al., 2007; Saltel et al., 2009; Ye et al., 2013; Ellis et al., 2014; Changede et al., 2015), or by binding to a ligand (Barczyk et al., 2010). In the second step, the integrins cluster into NAs, which show similar structures on substrates of different rigidities (Changede et al., 2015), and are not reliant on myosin II (MII) activity (Choi et al., 2008; Bachir et al., 2014; Oakes et al., 2018). Finally, these clusters are either disassembled, or they mature into FAs and possibly further into fibrillar adhesions.

Despite the efforts leading to our current understanding, the determinants of NA formation, turnover, or maturation, as well as their role in mechanosensing and signaling, are far from being fully resolved. However, the past two decades witnessed the emergence of several novel optical imaging techniques, technological advances in protein engineering and mass spectrometry analysis, as well as the expansion of theoretical modeling that now allow the investigation of protein organization of NAs at the nanoscale. Motivated by these perspectives, we here attempted to recapture recent advances in the field, while identifying open questions which we believe will be addressed in future research.

2. THE KEY MOLECULAR PLAYERS IN NASCENT ADHESIONS

Nascent adhesion revolves around the formation of integrin-ligand contacts between the cell and the extracellular matrix. Integrins are cell adhesion proteins capable of sensing the mechanical properties of the cell environment and providing signals necessary for a number of cell functions including proliferation, and migration (Horton et al., 2015; Cooper and Giancotti, 2019; Green and Brown, 2019; Humphries et al., 2019; Michael and Parsons, 2020). In humans, this broad range of functionalities is maintained by 24 integrin heterodimers (Shimaoka and Springer, 2003) built from 18 α- and 8 β-subunits forming a headpiece and two legs (Xiong, 2001). Several combinations of α and β subunits forming a heterodimer are possible (Hynes, 2002; Campbell and Humphries, 2011). However, only integrins assembled as heterodimers in the endoplasmic reticulum are expressed on the cell surface. Therefore, the composition of the plasma membrane integrin repertoire cannot be reliably predicted by the mRNA expression levels (Hynes, 2002) of integrin subunits. Integrin expression can be regulated by modulating their internalization and recycling, which contributes to the dynamic remodeling of adhesion (Moreno-Layseca et al., 2019).

Most integrins promiscuously bind to several ligands. Furthermore, their interactions are also extremely redundant, as different integrins bind to the same ligand (Humphries et al., 2006). Therefore, the 24 heterodimers are broadly categorized by their specificity to the ECM as (i) Arg-Gly-Asp receptors, binding to fibronectin, fibrinogen, and thrombospondin, (ii) laminin receptors, (iii) collagen receptors, and finally (iv) leukocyte-specific receptors binding to different cell surface receptors such as intercellular adhesion molecule and some ECM proteins (Humphries et al., 2006; Takada et al., 2007; Barczyk et al., 2010). Additional ligands relevant in the immunological context are the intercellular adhesion molecules, immunoglobulin superfamily members present on inflamed endothelium, and antigen-presenting cells. From the four groups, however, only the first three are considered to contribute to NAs.

Integrin binding and clustering is promoted by, and contributes to the formation of multimolecular integrin adhesion complexes involving up to 2,400 proteins together termed adhesome. The composition of integrin adhesion complexes have been first analyzed for cells seeded on fibronectin (Zaidel-Bar et al., 2007; Kuo et al., 2011; Schiller et al., 2011; Byron et al., 2015; Jones et al., 2015), identifying 60 core proteins involved in the fibronectin-induced meta adhesome, termed the consensus adhesome (Horton et al., 2015). One particularly important family of molecules within the consensus adhesome are the so-called adaptor proteins which bind to the cytoplasmic tails of integrins and bridge to the actin-based cytoskeleton. There are four potential axes that link integrins to actin, all implicated in different stages of NA formation, namely (i) integrin-linked kinase-particularly interesting new cysteine-histidine rich protein-1-kindlin, (ii) focal adhesion kinase (FAK)-paxillin, (iii) talin-vinculin and (iv) α-actinin-zyxin-vasodilator-stimulated phosphoprotein (Winograd-Katz et al., 2014; Horton et al., 2015, 2016; Humphries et al., 2019). Interestingly, some adaptors, such as talin, also coordinate the microtubule cytoskeleton at adhesion sites through the interaction with KANK proteins (KN motif and ankyrin repeat-containing proteins) (Bouchet et al., 2016; Sun et al., 2016; Chen et al., 2018; Paradžik et al., 2020), which was shown to stimulate FA turnover (Stehbens and Wittmann, 2012). How early this connection is established and the implication to NAs is still unresolved.

A lot of detail regarding integrin structure and interactions with adaptor proteins is obtained from molecular dynamics simulations, which starting with the seminal works on conformational changes in activation (Puklin-Faucher et al., 2006), addressed integrin unfolding (Chen et al., 2011), differences in integrin transmembrane domains (TMDs) (Pagani and Gohlke, 2018), talin-integrin interactions also regarding the surrounding lipids (Kalli et al., 2017), and interactions with other proteins (Shams and Mofrad, 2017).

Most integrin-related research, nevertheless, involves studies of mature adhesions, particularly in the context of the relation between the integrin adhesion and the cell physiology. This relation revolves around signaling involves a number of kinases, phosphatases, guanine nucleotide exchange factors, GTPase activating proteins, and GTPases (Horton et al., 2016). From the perspective of NAs, they so far have been discussed in the context of the physiology of the FAs. However, with the recently initiated debate that NAs may themselves act as signaling platforms, new perspectives in targeting NA-associated processes emerge. However, harnessing these possibilities requires detailed knowledge of the sensory role of NAs, their dynamic behavior, and their regulation, which are all still poorly understood.

3. THE ONSET OF NASCENT ADHESION: INTEGRIN ACTIVATION

Activation is the first step in the formation of NAs and is associated both with a change in integrin affinity and the binding of integrins to extracellular ligands (Calderwood, 2004). Activation as a term is also used to signify the switch to the extended-open (EO) conformation, which is, with the bent-closed (BC) and the extended-closed states, one of three major integrin conformations (Luo et al., 2007). All three conformations may be specific to one or more ligands, with affinity being conformation dependent (Wang et al., 2018), Often though, the activated EO state is the one with the highest binding affinity (Li J. et al., 2017). For example, prior to activation, the BC state is the most common conformation of $\alpha5\beta1$ in the K562 chronic myelogenous leukemia cell line, making up for around 99.76% of the population (Li J. et al., 2017). Simultaneously, the extended-closed and EO states contribute with 0.09 and 0.15%, respectively. However, $\alpha5\beta1$ and $\alpha4\beta1$ in the EO state have a 4,000–6,000 fold and a 600–800 fold higher affinity for a ligand compared to the BC state (Li and Springer, 2018). Notably, these affinities are measured for ligands in solution, where they do not induce integrin clustering (Cluzel et al., 2005).

The changes of conformation may be introduced by thermodynamic fluctuations of the integrin (Sun et al., 2019) or strong membrane deformations (Gingras and Ginsberg, 2020), but the switch is most often induced by the very association of integrins with ligands, adaptor proteins or Mn^{2+}. However, Mn^{2+} may induce integrin conformations that can be different from physiological ones (Ye et al., 2012). In the cellular environment, the process within which integrins adopt the high affinity state is cast into two major activation models (Wang et al., 2018), the so-called outside-in, where the activation results from binding to extracellular ligands (Barczyk et al., 2010; Park and Goda, 2016), and inside-out, induced by cytoplasmic factors such as adaptor proteins (Ye et al., 2010; Calderwood et al., 2013), for example, by talin (Cluzel et al., 2005; Saltel et al., 2009; Park and Goda, 2016) (**Figure 2**).

A number of cell-related studied addressed inside-out activation. It is now established that already talin head domain is sufficient to activate integrins (Calderwood et al., 1999) and synergizes with kindlin (Ma et al., 2008; Bledzka et al., 2012; Calderwood et al., 2013). This combination may promote binding to multivalent ligands (Ye et al., 2013). However, there seems to be a competition between talin and kindlin, as the overexpression of kindlin-1 and kindlin-2 can both enhance and reduce integrin activation by talin head domain, depending on the integrin type (Harburger et al., 2009). In other cases, kindlin overexpression showed only a small effect compared to talin head domain (Shi et al., 2007; Ma et al., 2008; Ye et al., 2010, 2012, 2013).

Outside-in activation has been extensively studied both in cell and cell-mimetic systems. As pointed out already in the seventies, and then again by more recent work, the microenvironment of the plasma membrane and cell glycocalyx may play a significant role in the regulation of the receptor affinity for ligands (Bell, 1978; Dembo et al., 1988; Bihr et al., 2012; Fenz et al., 2017). Namely, the membrane, by its elasticity and fluctuations can induce switches from low to high affinity states (**Figure 3**), even without changing the actual conformation of the proteins binding the ligands (Fenz et al., 2011; Kim et al., 2020). This mechanism of regulation of affinity was originally suggested by theoretical modeling (Bihr et al., 2012), and was demonstrated

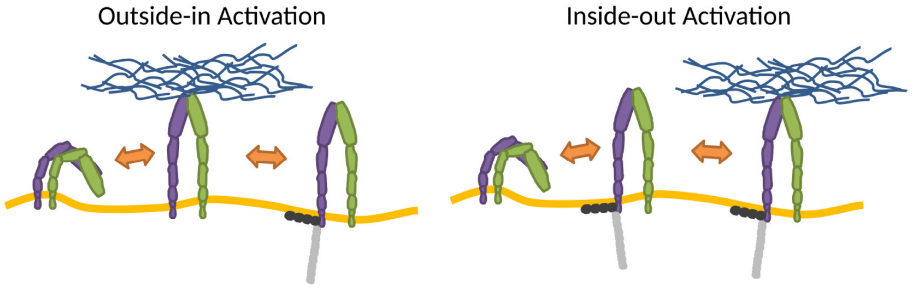

FIGURE 2 | Mechanisms of integrin activation. In the outside-in activation, extracellular factors activate the integrin (Barczyk et al., 2010; Park and Goda, 2016), subsequently stabilized by binding adaptor proteins to the cytoplasmic tail. In the inside-out activation, binding of cytoplasmic factors induces activation (Ye et al., 2010; Calderwood et al., 2013), which primes the integrin for ECM binding. Integrins also stochastically switch between conformations.

for a variety of membrane associated ligand-receptor pairs (Bihr et al., 2015; Fenz et al., 2017). It relies on the modulation of membrane fluctuations in activating cells, and the expulsion of the glycocalyx. However, although this mechanism should be particularly relevant for the formation of NAs, its role for integrin binding remains to be shown explicitly. Preliminary hints for the role of this mechanism come from mimetic system where a liposome bind to a bilayer by the establishment of integrin-Arg-Gly-Asp bonds (Goennenwein et al., 2003; Smith et al., 2008; Streicher et al., 2009). The strength of adhesion and the number of formed integrin-Arg-Gly-Asp constructs depended sensitively on integrin density and mobility, hence the capacity to bind in proximity of an existing bond. This suggests that the membrane indeed mediates correlations and affects the integrin binding rates.

Binding of ligands allows for anchoring of integrins and the exertion of forces. Interestingly, recent work showed that even after the links with the cytoskeleton are fully established, most integrins existed in a state of near-mechanical equilibrium (Tan et al., 2020). This corroborates the idea that retractive actomyosin force is presumably acting only in FAs and not so much in NAs. However, the polymerization of actin in the cytoskeleton couples to the membrane fluctuations, which furthermore couples to the integrin bonds. Consequently, the unbinding rate of the receptor in a particular conformation is directly affected (Bihr et al., 2012), but also the free energy of BC, extended-closed and EO states may change. The importance of this effect was highlighted in the model of Li and Springer (2017), who find a sigmoidal dependence of activation probability with respect to the applied force, where activation here signifies binding of both ligand and adaptor protein. This resulted in full activation of all integrins over few pN for a wide range of adaptor protein concentrations, permitting a quick response to mechanical stimuli. Comparable behavior was found in fibroblasts, which reinforce early integrin adhesions $\leq$ 5 s under load by binding additional integrins (Strohmeyer et al., 2017). However, in this case the force was not applied to the integrin themselves but to the apical membrane of the cell. The response of this system can thus be similar to integrin decorated vesicles subject to pulling force, where the reinforcement was also observed as part of the thermodynamic response of the entire system (Smith et al., 2008).

Recent experiments revealed that upon mechanical stretching (2 to 5%) FA integrin $\beta 3$ displacements closely followed the substrate's elastic displacements (Massou et al., 2020). Such behavior revealed that most stationary integrins inside and outside of FAs remained connected to fibronectin. Moreover, the same platform allowed to investigate whether proteins mediating a dynamic mechanical coupling of integrins to F-actin follow or deviate from integrins' elastic behavior (Massou et al., 2020). Massou et al. concluded that the spatiotemporal force fluctuation in FAs probably emerges from the heterogeneous tensional/connective states of proteins at the nanoscale (Massou et al., 2020).

The response of individual integrins to local force has to be considered also in the context of the catch-bond effect. Namely, unlike slip bonds, which subject to force show an increase in the unbinding rate (Bell, 1978), catch bonds are stabilized by force (Dembo et al., 1988). So far, in the case of integrins, both behaviors were found for different force regimes, which lead to the introduction of the term catch-slip bond. The latter was observed for example for $\alpha_5\beta_1$ (Kong et al., 2009), $\alpha_4\beta_1$ (Choi et al., 2014), and $\alpha_L\beta_2$ (Chen et al., 2010). In the case of $\alpha_5\beta_1$, catch bond formation seemed to involve the headpiece, but not integrin extension (Kong et al., 2009).

Other distinct mechanisms that, similarly to catch bonds, strengthen integrin attachments in a force dependent manner are cyclic mechanical reinforcement (Kong et al., 2013), and the so called dynamic catch (Fiore et al., 2014). In cyclic mechanical reinforcement, an increase of bond lifetime occurs over several loading-unloading cycles. In dynamic catch, the force response is regulated synergistically by the binding of an additional co-receptor to form a trimolecular complex with the integrin and the common ligand. In mimetic, actin free systems, cyclic application of force also resulted in bond-strengthening (Smith et al., 2008), which was shown to emerge from a thermodynamic response of the integrin ensemble. Application of a pulling force (Smith and Seifert, 2005) induced a regrouping of bonds from sparse configurations to clusters in which cooperative response is allowed (strengthening each bond on average), and a new thermodynamic state is established (Smith et al., 2008).

Despite all these efforts and insights, since the sequence of binding events in a cell is not yet fully established, activation

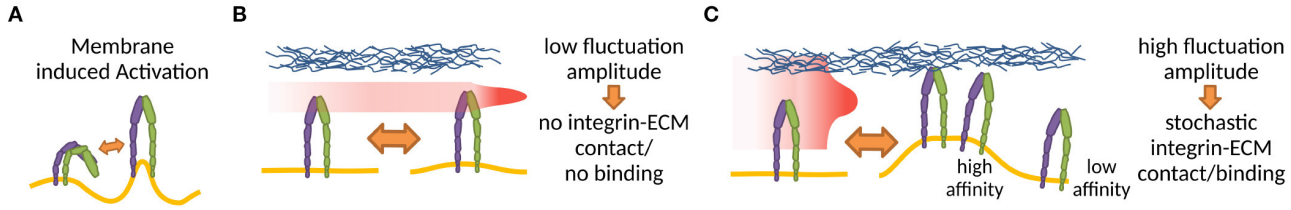

FIGURE 3 | (A) Membrane deformations, for example through curvature or thickness changes, can disrupt integrin TMD interactions, increasing fluctuation induced affinity modulation (Gingras and Ginsberg, 2020). **(B,C)** The amount of interaction of an integrin with a ligand presenting counterpart effectively alters the integrin binding affinity (Schmidt et al., 2012; Fenz et al., 2017) in a membrane fluctuation and therefore also glycocalyx dependent manner. The red area in **(B,C)** shows the positional distribution of the integrin head as a result of membrane fluctuations. The small fluctuations in **(B)** result in no integrin-ECM contact, whereas the high fluctuations in **(C)** result in stochastic integrin-ECM contacts, allowing stochastic binding and creating high affinity regions around the initial bond.

is still heavily studied. As elaborated above, various possibilities for activation are available, but to what extend the cell relies on the different mechanisms remains to be clarified. Due to the stochastic nature of molecular binding, different types of activation could take place simultaneously on the cell surface. Upregulating certain molecular players then only changes the probability for observing a certain pathway. How is the whole process regulated? Does the cell choose to shift the balance toward a particular activation mechanism, and if so why and how are just some of the questions which will need to be answered in the future.

4. FORMATION OF INTEGRIN CLUSTERS

Clustering of integrins (**Figure 4**), with and without the help of adaptor proteins and independent of F-actin (Cluzel et al., 2005) and MII activity (Choi et al., 2008), builds the second step of NA formation. Understanding of this process is greatly facilitated by the emergence of super-resolution microscopy (SR) techniques. The latter provide optical images with spatial resolutions below the diffraction limit of light of the order of $\sim$ 100 nm (Sigal et al., 2018). Therefore, it should be possible to resolve the dynamic nanoscale organization of NAs and the force transduction across individual components within FAs. However, quantitative investigations of NAs are still lacking. The main reason is that existing SMLM techniques require cluster analysis tools, which have been developed for relatively simple cases, such as membrane protein clusters without strong heterogeneity in size, shape, and density (Nicovich et al., 2017; Nieves and Owen, 2020). Several studies have addressed this by designing novel approaches to investigate the inner architecture of NAs and FAs, such as one based on the expectation-maximization of a Gaussian mixture (EMGM) (Deschout et al., 2017). The imagining was carried out on specifically bio-functionalized substrates, on which ordered patterns of nanoscale adhesive spots were provided (Arnold et al., 2004). Such substrates have already been used to probe the behavior of FAs on the nanoscale (Geiger et al., 2009; Schvartzman et al., 2011). In this way, the spatial organization of FA binding sites is precisely controlled, ensuring that the observed substructures are not substrate artifacts. Application of this improved EMGM method on the photoactivated localization microscopy (PALM) data showed that FAs are composed of structures with areas between 0.01 and 1 μm^2, containing 10 to 100 localizations, and exhibiting strong eccentricities (**Figure 5**). This approach is very promising for studies of NAs, and may in future provide new insights in the cluster formation.

So far, however, various nanoscale distributions have been observed for integrins. Clusters as small as 2–3 integrins were reported using electron microscopy (Li, 2003), while clusters observed in SMLM range from tens to hundreds of molecules. Some of the first application of SR techniques yielded 100 nm large NAs, containing on average 50 integrins (Changede et al., 2015). This data is contrasted by a more recent work with improved EMGM method used on PALM data, when it was determined that FAs cover areas between 0.01 and 1 μm^2. Using EMGM, localization uncertainties, an important and unavoidable aspect of any SMLM experiment, could be corrected, showing that the assemblies contained 10 to 100 localizations, and exhibited strong eccentricities (Deschout et al., 2017). Notably, most existing SMLM clustering methods ignored this effect, which can lead to substantial overestimation of the size of identified localization structures.

While the dynamic behavior of NAs is still an open problem, it is nevertheless clear that clusters allow for quick rebinding after bond failure (Bihr et al., 2012; Sun et al., 2019), and the control over maturation or disassembly (Schmidt et al., 2015). Furthermore, clusters could serve as platforms for rigidity sensing (Wolfenson et al., 2016), however it is still unclear which point in the process of NA assembly corresponds to the onset of signaling.

In the absence of detailed microscopy studies, even the necessary conditions for the formation of these meta-stable aggregates are unclear. Some studies report that integrin activation is indispensable for clustering (Cluzel et al., 2005), promoting the nucleation of new structures (Saltel et al., 2009). These results are contrasted by experimental findings that show both active and inactive integrin nanoclusters in FAs (Spiess et al., 2018), obtained using extended state specific antibodies that co-localized with talin, kindlin-2 and vinculin. The existence of inactive clusters could suggest the affinity for ligands in the inactive states is sufficiently large to promote nucleation of domains, although with smaller probability than in the active

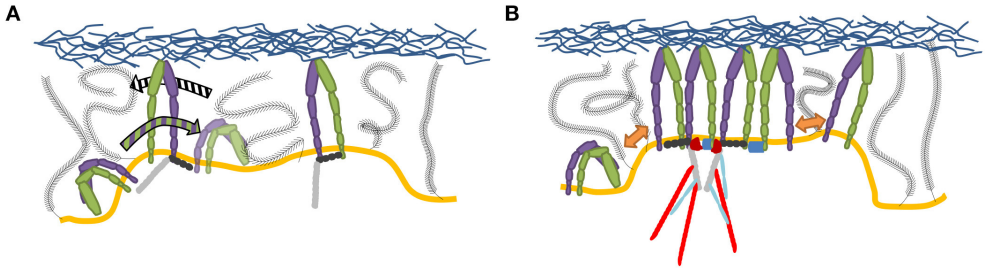

FIGURE 4 | Current picture of integrin clustering. **(A)** Initial liganded integrins create a region with increased integrin binding probability, by membrane and glycocalyx deformation, which effectively attracts integrins while pushing out the glycocalyx. **(B)** Clustering is further amplified by multivalent ligands, dimerizing adaptor proteins, established scaffolding structures through cytoplasmic factors as well as TMD interactions (Gingras and Ginsberg, 2020).

state. Alternatively, one could conclude that ligand binding is not necessary for clustering, although it is possible that ligand bound states preceded cluster formation.

With mobile ligands, on the other hand, Mn^{2+} activated integrins formed small adhesion domains, which significantly increased in size if integrins themselves were maintaining lateral mobility prior to establishing bonds (Smith et al., 2008). In this case, the clustering of bound integrins was mediated by the deformed membrane. The nature and magnitude of these forces could be clearly elucidated (Janeš et al., 2019), and were proposed to play an important role in the cluster nucleation and growth (Bihr et al., 2012). Given that these types of interactions are not protein specific, they should also be seen in other ligand-receptor systems. Indeed, correlations in membrane dynamics and topography with cell spreading was reported recently in several studies of cell adhesions (Perez et al., 2008; Pierres et al., 2008; Lam Hui et al., 2012), and systematically in reconstituted passive systems based on giant unilamellar vesicles (Smith and Sackmann, 2009), including those involving integrins (Goennenwein et al., 2003; Smith et al., 2008; Streicher et al., 2009). However, this mechanism remains to be directly confirmed for integrins in the cellular context.

Most of membrane-related mechanisms include the existence of the cellular glycocalyx implicitly (Bruinsma et al., 2000; Smith and Sackmann, 2009), which was indeed found to play an important role in integrin clustering (Paszek et al., 2014). The compression and consequent expulsion of glycocalyx, by the formation of the initial bond primes the surroundings for further interactions. Concomitantly the membrane deforms toward the ligand (Janeš et al., 2019), creating a microenvironment in which the additional bonds have a much higher likelihood to form (Bihr et al., 2015; Fenz et al., 2017) (**Figures 4**, **6B**). The tension on the bond furthermore increases their lifetimes (Kong et al., 2009), in a synergistic fashion. These effects can be further strengthened by membrane thermal (Helfrich, 1978) and active fluctuations (Turlier and Betz, 2018), which adds to the portfolio of forces acting on NAs, the latter being regulators of adhesion formation (Li and Springer, 2017; Strohmeyer et al., 2017; Oakes et al., 2018).

While the interplay between these many factors contributing to the NA formation in its early stages is not yet fully understood, there is a consensus that integrin activation increases binding to anchored, clustered ligands. Specifically, strong increase in the number of spreading cells was found for a basic pattern of 4 ligands at $\sim$ 60 nm distance compared to 3 ligands at the same density (Schvartzman et al., 2011). If formation of NAs is seen as nucleation process, this result would suggest that the critical number of bonds to achieve a stable adhesion domain is around three, which well corresponds to theoretical predictions (Bihr et al., 2012). A similar result was confirmed by an agent-based model (Jamali et al., 2013), where large agglomerates of ligands provide the largest integrin clusters.

Simulations can also account for the competition between ligand binding and clustering different integrin types, as demonstrated on the example of β_1 and β_3. Closely spaced multivalent ligands promoted clusters of more than two integrins. Weak lateral intra-integrin interactions allowed transient dimer interactions with switching partners (Brinkerhoff and Linderman, 2005) but they also led to smaller number of integrins in the cluster (Bidone et al., 2019).

One scenario suggests that the link between integrin activation and clustering emerges from the lateral interactions between tails of TMDs (Li, 2003; Mehrbod and Mofrad, 2013; Ye et al., 2014). However, limited size of NAs (Changede et al., 2015; Changede and Sheetz, 2017) requires further regulation of such interactions. Moreover, the necessary activation energy between TMDs also seems too high to overcome without help (Mehrbod and Mofrad, 2013). In addition, the TMD could not drive the clustering in Mn^{2+} activated integrins, without ligands present (Cluzel et al., 2005).

Besides ligands, a number of adaptor proteins have been involved in cluster formation. The most prominent examples are kindlin (Ye et al., 2013; Changede et al., 2015) and talin (particularly its head domain) (Cluzel et al., 2005; Saltel et al., 2009; Calderwood et al., 2013; Changede et al., 2015), that have been already implicated in integrin activation (Moser et al., 2008; Zhang et al., 2008; Ye et al., 2013; Theodosiou et al., 2016). Both kindlin (Kammerer et al., 2017; Li H. et al., 2017) and talin (Golji and Mofrad, 2014) have a capacity for dimerization. For example, talin rod, which, using its integrin binding site, can rescue clustering in talin depleted cells (Changede et al., 2015). However, the efficiency of talin rod fragments was found to be inferior to

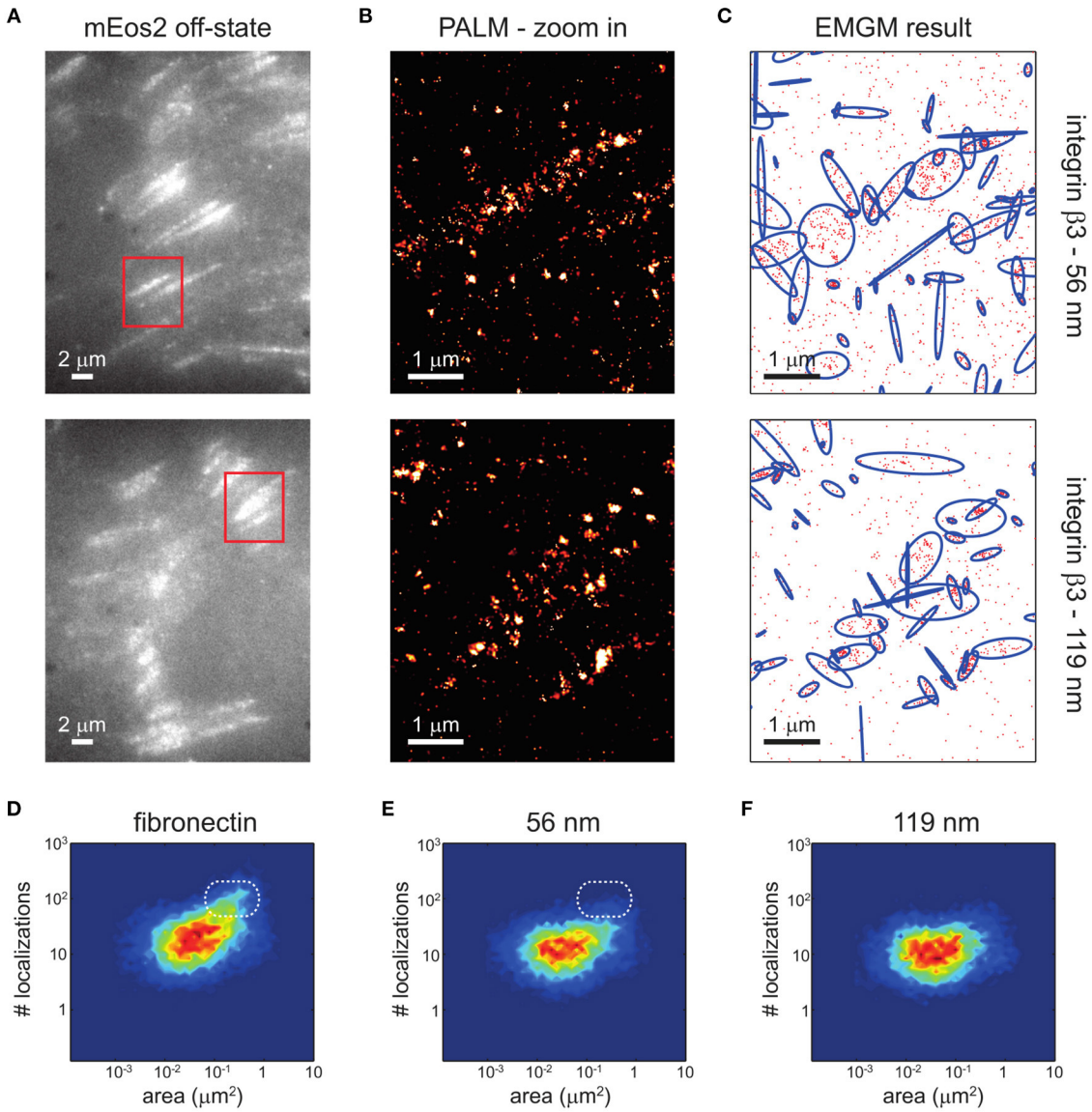

FIGURE 5 | EMGM analysis of PALM data of integrin $\beta 3$ on nanopatterned substrates. **(A)** Shown here are summed TIRF images of the mEos2 off-state of fixed REF cells expressing integrin $\beta 3$ labeled with mEos2, growing on nanopatterned substrates with 56- or 119-nm spacing between the AuNPs. **(B)** Shown here are zoom-in PALM images corresponding to the red rectangles in **(A)**. **(C)** Given here is the result of the EMGM analysis of the PALM data shown in **(B)**. The red dots symbolize the localizations,and the blue ellipses symbolize the 2σ error ellipses of the mixture components. **(D–F)** Given here is the result of the EMGM analysis of PALM data corresponding to different REF cells ($n = 10$). The number of localizations in each mixture component is shown as a function of the area of its 2σ error ellipse, for **(D)** fibronectin-coated substrates, **(E)** nanopatterned substrates with 56-nm spacing, and **(F)** nanopatterned substrates with 119-nm spacing. The dashed white rounded rectangles in **(D,E)** are visual guides. [Figure and figure caption reproduced from (Deschout et al., 2017), figure reference omitted]. Reprinted from Biophysical Journal, 113, Hendrik Deschout, Ilia Platzman, Daniel Sage, Lely Feletti, Joachim P. Spatz, Aleksandra Radenovic, Investigating Focal Adhesion Substructures by Localization Microscopy, 2508-2518, Copyright (2017), with permission from Elsevier.

the full length talin (Saltel et al., 2009). This points to a possible synergy between dimerization and binding the monovalent, and even more so for multivalent ligands with larger stoichiometries (**Figures 4B**, **6A**), which can be perfectly well-understood on the basis of cooperative binding within the membrane.

These potentially complex stoichiometries are, however, a challenge for SMLM. Complex photo-physics of interacting fluorophores can lead to over-counting of molecules at a given location (Annibale et al., 2011a). This complicates the accurate determination of protein stoichiometries from the data. It is, however, possible to estimate the number of labeled-proteins contained in a single cluster (Annibale et al., 2011b; Baumgart et al., 2016; Spahn et al., 2016; Pike et al., 2019), but more accurate quantifications are needed and their accuracy demands further validation. A recently developed supervised machine-learning approach to cluster

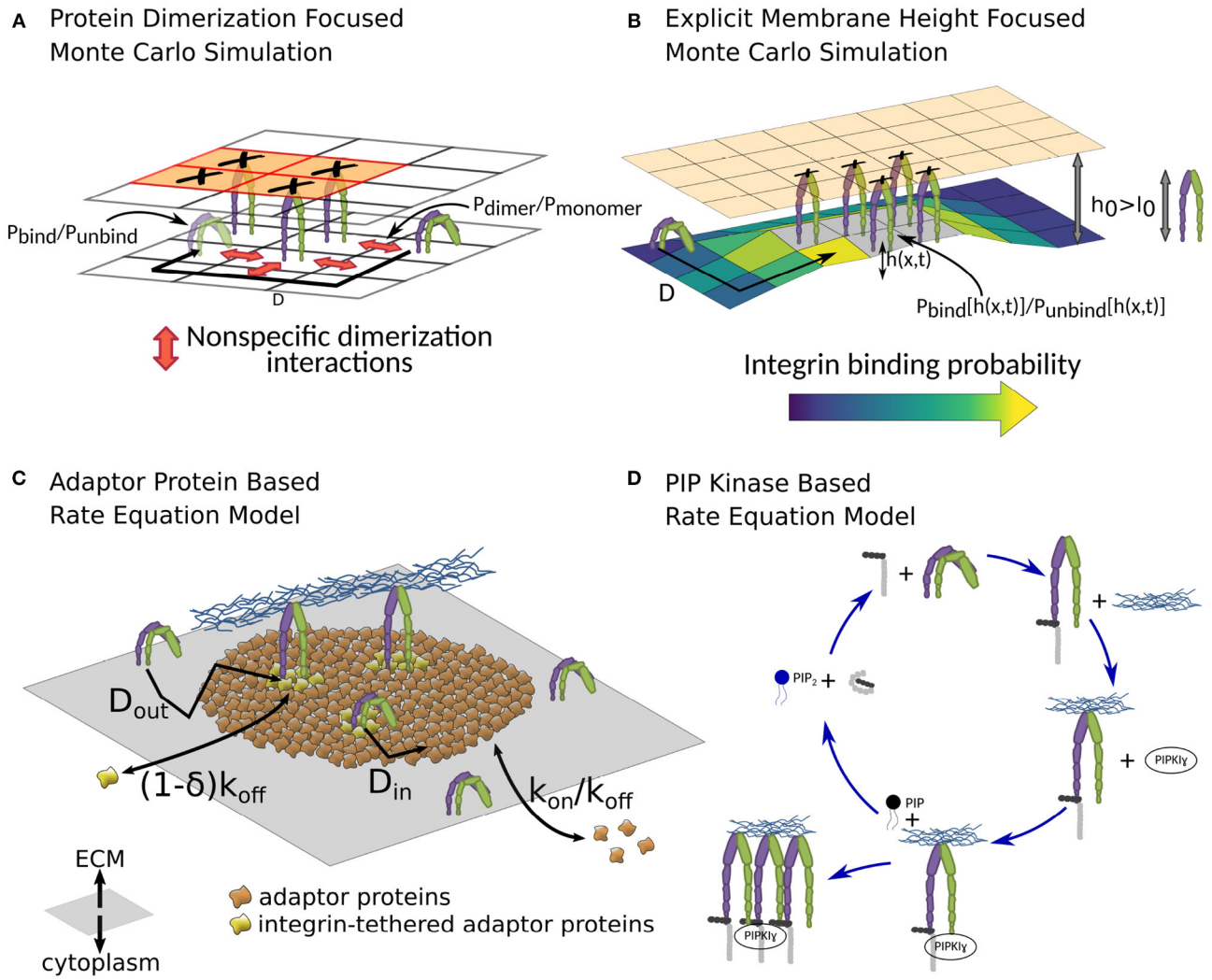

FIGURE 6 | Different theoretical models of the NA formation. **(A)** In the Monte Carlo simulation by Brinkerhoff and Linderman, dimerization interactions between integrins, as well as spatial ligand distribution patterns are studied (Brinkerhoff and Linderman, 2005). They find that clustered ligand islands can increase integrin clustering, as dimerization interactions between immobile, ligand-bound integrins and mobile, unbound integrins can guide the latter toward unoccupied spots on the same ligand island. The lattice shown here is simplified compared to the one used in the publication for illustration purposes. **(B)** The coarse-grained Monte Carlo simulation in Fenz et al. (2017) allows a detailed look at one source of spatial integrin interaction, namely membrane and glycocalyx deformations (Fenz et al., 2017). Repulsions between cell and substrate, stemming among others from the shape and size of glycocalyx proteins, can result in a mismatch between the equilibrium separation of the two surfaces h_0 and the combined size of integrin and ligand l_0. The initial bond formation therefore has to be accompanied by a membrane deformation, imposing an additional energy cost. After initial bond formation, however, the surrounding membrane is already partly deformed, reducing the energy cost of forming additional integrin-ligand bonds, which can locally increase the rate of bond formation by several magnitudes, as well as stabilize these bonds against dissolution. **(C)** MacKay and Khadra employ rate equations to study the NA formation (MacKay and Khadra, 2019). Here the NA is defined not by their integrin content, but solely by an area of cytoplasmic adaptor proteins, which, through stochastic binding and unbinding, build the backbone of the NA, the so-called adhesion plaque. Integrins inside the plaque can bind with the surrounding adaptor proteins, which stabilizes them against unbinding, allowing a sustained or even growing NA. **(D)** In the rate equation model by Welf et al., the growth of NAs is driven by the PIP2-talin interaction. A feedback loop between PIP2 generation, subsequent release of talin autoinhibition, which, in turn, activates further integrins, can result in a sudden increase in bound integrins after the initial bond formation (Welf et al., 2012).

analysis can be an interesting candidate to cope effectively with NAs sample heterogeneity (Williamson et al., 2020). It was successfully applied on data of the C-terminal Src kinase and the adaptor PAG in primary human T cell immunological synapses (Williamson et al., 2020), but was not yet tested for talin-integrin complexation or even more generally on NA data.

Talin rod has an additional property important for the formation of NAs, namely it possesses a binding site for vinculin. Vinculin is a cytoskeletal protein with binding sites, besides talin, for actin, α-actinin, and lipids and it is usually associated with the force transmission. However, recently it was found that the talin rod domain is available to vinculin in a force-independent manner upon

the release of talin autoinhibition (Dedden et al., 2019; Atherton et al., 2020). This would suggest that vinculin could play a role in NAs even before the cytoskeletal forces are involved.

The integration of vinculin could be facilitated by $PI(4,5)P_2$. This phospholipid regulates talin-integrin interactions at the level of the membrane. Its association with the β_3 units opens a binding site for the integrin on the talin head, hence controlling the talin auto-inhibition. Furthermore, the $PI(4,5)P_2$ interaction with the integrin creates a salt bridge toward the membrane that prevents the close interactions of the α and β subunits. Therefore, the integrin remains in an activated, clustering-competent state (Cluzel et al., 2005; Saltel et al., 2009; Dedden et al., 2019). Consistently with these findings, sequestering of $PI(4,5)P_2$ diminishes the formation of clusters (Cluzel et al., 2005).

One more protein strongly investigated in the context of integrin-clustering is α-actinin (Sun et al., 2014). It is microfilament protein necessary for the attachment of actin. Both positive and negative effects were demonstrated for β_1 and β_3 integrins, respectively (Roca-Cusachs et al., 2013; Shams and Mofrad, 2017), which could relate to an integrin crosstalk strategy (Bharadwaj et al., 2017). However, its role in clustering is still debated (Theodosiou et al., 2016).

This large number of molecular players involved through various interactions poses a significant challenge for comprehending the formation of NAs. A promising approach that can address this diversity is theoretical modeling based on rate equations (Zhu and Williams, 2000; Schwarz et al., 2006; Li et al., 2010; Walcott and Sun, 2010; Harland et al., 2011). An early attempt focused purely on the talin-PIP2 interaction (**Figure 6D**) and is therefore limited in scope (Welf et al., 2012). However, more recently, emulating the formation of entire NAs has been attempted (MacKay and Khadra, 2019). In the latter case, a higher emphasis is set on the crosslinking function of adaptor proteins (**Figure 6C**). The model reproduces some features found in experiments, for example the limited area of NA, even at high integrin density. It also predicts unliganded clusters. Actually, the model defines NAs as plaques of adaptor proteins and not as integrin clusters. Integrins stabilize the plaque but are not required, which allows for the possibility of preclustering adaptor proteins in the absence of integrins.

5. CLUSTER DISASSEMBLY OR MATURATION

Clustering of NAs into FAs or disassembly is the last step in the NA life time. The fate of NAs depends on the cell type, protein composition, and mechanical properties of the substrate (Parsons et al., 2010), as well as the attachment to the actin cytoskeleton and both MII isoforms (Vicente-Manzanares et al., 2007).

Most NAs disassemble when the lamellipodium moves past them (Choi et al., 2008) following one of several competing ways of NA disassembly, as discussed in the literature (Gardel et al., 2010). Particularly, well-studied is the role of the non-receptor tyrosine kinase FAK that is known to regulate adhesion disassembly (Webb et al., 2004), possibly through talin proteolysis (Lawson and Schlaepfer, 2012). In addition, FAK might be inhibited at the leading edge of the lamellipodium through interactions with Arp2/3, a protein complex that is related to the actin branching (Swaminathan et al., 2016). Because the regulation of rearrangements of the actin cytoskeleton is crucial for filopodia extension (He et al., 2017) and lamellipodia formation (Small et al., 2002), FAK is implicated in the spatial control of the advance of the leading edge and the NA disassembly. This regulation is facilitated by the binding of FAK to paxillin, which is also recruited by kindlin (Humphries et al., 2007; Böttcher et al., 2017; Zhu et al., 2019), to further control the adhesion turnover (Shan et al., 2009; Choi et al., 2011). Interestingly enough, vinculin, can impede the FAK-paxillin interaction (Subauste et al., 2004), while FAK may play a role in recruiting talin to NA sites (Lawson and Schlaepfer, 2012; Lawson et al., 2012), as well as Arp2/3 (Lawson and Schlaepfer, 2012). As FAK also plays an important role in signaling (Swaminathan et al., 2016), it is difficult to unravel the precise dynamical interactions in NAs.

Another simple way to dissolve NAs is by offering soluble ligands (Cluzel et al., 2005). The latter either exhibit a lateral pressure on the NA site or they compete for the integrin upon stochastic unbinding (Smith et al., 2006). Since the 3D affinity of soluble ligands is always larger than the 2D affinity of surface-confined ligands, the cluster becomes unstable.

Alternative to disassembling is the sequential maturation of NAs into FAs, and in some cases, to centrally positioned fibrillar adhesions enriched in tensin and integrin $\alpha5\beta1$ (Iwamoto and Calderwood, 2015). The inhomogeneous structure of these assemblies were observed already over a decade ago using PALM for imaging FA proteins (Betzig et al., 2006). Just 1 year later, Shroff et al. used dual-color PALM to determine the ultrastructural relationship between different pairs of FA proteins (Shroff et al., 2007). The consensus today is that integrins bind via talin and other adaptor proteins with the actin cytoskeleton, allowing MII generated forces to act on the clusters (Yu et al., 2011). Under force the bonds strengthen, and tilt in the direction of the retrograde actin flow (Nordenfelt et al., 2017). The reinforcement of integrin assemblies is further promoted by the recruitment of vinculin (Huang et al., 2017), the crosslinking by myosins (Burridge and Guilluy, 2016), and the exposure of force-dependent cryptic binding sites (Ciobanasu et al., 2014; Yao et al., 2015, 2016) that allow for the attachment of other adhesome proteins. Finally, through mature adhesions, force is propagated from the ECM to the actin cytoskeleton over the unfolding talin that permits vinculin binding (Asaro et al., 2019), resulting in a strong signaling cascade and mechanoresponse along the adhesome, that regulates a number of physiological processes in cells.

6. CHALLENGES AND PERSPECTIVES IN THE FIELD OF NASCENT ADHESIONS

As presented in the above discussion, many molecular players contributing to the formation of NAs have been identified,

and their mutual interplay have been established, although further investigation of specific interactions is necessary. For example, very little is known about the crosstalk between integrins of the same and different types, recently reported for early adhesions (Bharadwaj et al., 2017; Strohmeyer et al., 2017; Diaz et al., 2020; Samaržija et al., 2020). However, new research avenues in studying molecular interactions in NAs can emerge only from advances in the development of robust quantitative colocalization analysis (Levet et al., 2019). This needs to be accompanied by progress in genome editing and novel protein labeling strategies that could enable quantitative SR. So far, only very few colocalizations of active integrins with talin and kindlin (Spiess et al., 2018) and vinculin and talin (Xu et al., 2018) could be observed. This can be either a technical issue, associated with protein expression, probe photophysics, and the limited choice of labeling pairs and fluorophores. It could also point to unknown integrin regulators (Spiess et al., 2018), and hidden interactions that remain to be revealed. For this purpose, molecular dynamics simulations will become increasingly important as they provide unmatched details in competing binding interactions (e.g., Mehrbod and Mofrad, 2013). With appropriate level of coarse-graining, larger complexes and slower structural changes are coming within reach of molecular dynamics simulations, which now can explicitly address integrin activation and clustering.

Probably, however, the most acute issue is the spatiotemporal evolution of NAs and the role of complex stoichiometries. Namely, the dynamics of NAs is subject of intense debate as the constitutive clusters could be either stationary or showing stochastic transient immobilization (Spiess et al., 2018). This problem is very closely related to the sensory capacity of NAs and the onset of signaling, that are equally understood. Resolution of these open questions requires new techniques that can deal with the fast molecular turnover within NAs. However, this is still a significant challenge for the single molecule localization microscopy (Orré et al., 2019) such as PALM (Betzig et al., 2006), stochastic optical reconstruction microscopy (Rust et al., 2006) or super-resolution optical fluctuation imaging (Dertinger et al., 2009). First promising insights into the dynamics of NAs nevertheless were provided by the single particle tracking PALM (Inavalli et al., 2019), which revealed integrin cycling between free diffusion and immobilization, while transient interaction with talins promoted integrin activation and immobilization (Rossier et al., 2012). Further studies of integrin dynamics will require techniques such that can operate at micro second-time scales with 1 nm precision of molecules located few nanometers apart. An example of such a method is minimal photon fluxes nanoscopy (Balzarotti et al., 2017), although other approaches are starting to appear and will need to be employed in the research of NAs.

Another challenge in studies of NAs is the impact of force. Although not strictly related to actomyosin activity, forces on integrin complexes arise due to the spacial confinement of the molecular players and result in load-dependent competition for binding partners. Different sources of forces may play a role in NA formation, prior to their maturation into FAs. Specifically, the glycocalyx and the membrane are anticipated to generate relatively strong tensions and direct stochastic forces on the individual integrins and the clusters (Paszek et al., 2014; Li and Springer, 2017; Strohmeyer et al., 2017; Sengupta and Smith, 2018). The understanding of these effects relies on the development of force sensors (Tan et al., 2020), and techniques which combine the force application with SR. Furthermore, given the intrinsically non-equilibrium and noisy setting, theoretical support in formulating and validating the appropriate hypothesis on the role of confinement is necessary.

A particularly useful tool in the research of integrin adhesion so far have been functionalized substrates (Goennenwein et al., 2003; Schvartzman et al., 2011; Liu et al., 2014; Changede et al., 2019). Manipulation of stiffness, spatial coordination and mobility of binders allowed to provide mechanical cues which could be exploited to resolve the response of different cell models. Based on this long standing success, it is expected that patterned substrate will continue to play an important role in studies of NAs. Especially interesting should be their combination with specifically designed cell models that express different types of integrins on the plasma membrane surface.

Furthermore, these substrates could be very successfully combined with reconstituted systems. The latter serve as an ideal bridge between the biological complexity and theoretical modeling. Reconstituted systems, typically based on giant lipid vesicles, were instrumental in elucidating the role of mechanical properties of binders, as the role of the receptor and ligand density and mobility in the cell recognition process (Smith and Sackmann, 2009). Furthermore, vesicle-substrate adhesion was successfully used to study the physical mechanisms that regulate ligand-receptor binding, including the role of stochastic membrane deformations, fluctuations and composition, as well the steric repulsion role of the glycocalyx (Sengupta and Smith, 2018). However, the simplicity of these assemblies may not represent the appropriate biological complexity of NAs. To circumvent that issue, more recently droplet-stabilized giant unilamellar vesicles were designed that can be sequentially loaded with talin and kindlin (Weiss et al., 2018). These systems show great potential for the studies of NAs, and could be used to drive the development and validation of theoretical models and simulations used to describe the growth process.

At the current stage, most theoretical models that attempt to capture the formation of NAs account for the molecular complexity of the system, but capture the bio-mechanical context only implicitly, if at all. There is also another class of models that is capable of resolving the stochastic nature of NA formation and the forces acting on the bonds with relatively high level of detail, but they are nearly void of molecular information. Future efforts are likely to bring closer these two distinct families of approaches, with the aim of providing a more reliable foundation that is required to capture the development of NAs in a predictive manner.

Finally, it is a hope that the lessons learned in the studies of NAs may be useful in the context of other integrin-based structures. For example, in hemidesmosomes, linked to the internal keratin intermediate filament network, $\alpha 6\beta 4$ integrins mediate adhesion of epithelial cells to the underlying

basement membrane (Walko et al., 2015). In reticular adhesions, which serve to maintain the attachment of cells to the extracellular matrix during mitotic rounding and division, $\alpha V\beta 5$ integrins, clathrin and endocytic adaptors also form adhesive complexes (Grove et al., 2014; Elkhatib et al., 2017; Leyton-Puig et al., 2017; Lock et al., 2018, 2019). Currently, it is not known whether these different types of adhesion have precursor structures analogous to NAs. However, it is highly likely that tools, methods and approaches developed in studies of NAs may prove to be useful in these potentially different settings.

In closing, we strongly believe that joint advances in SR, the development of model systems and technology for manipulations of proteins, as well as theoretical approaches are required to further propel our understanding in molecular mechanisms of integrin organization, stoichiometry and dynamics at the nanoscale. This will not only allow us to rationalize the observed phenomena, but also gain important concepts and tools that can be used to resolve the physiological role of integrin based structures, but can be further applied beyond the NA research.

Integrin involvement in pathological conditions is mostly the consequence of changes in the expression, either up- or down-regulation. Prominent examples here are tumorigenesis but also the response to chemo- or radiotherapy (Cooper and Giancotti, 2019). Therefore, integrin repertoire changes are an active target for drug development in tumors with the potential to inhibit metastasis, as well as to overcame resistance to chemotherapy or radiotherapy. However, despite convincing experimental evidence that demonstrates the capacity of integrin inhibitors and monoclonal antibodies to contribute to inhibition of cancer progression, metastasis, or boost therapeutic effects, no integrin-targeting drugs have been registered as anti-cancer drug (Desgrosellier and Cheresh, 2010; Seguin et al., 2015; Dickreuter and Cordes, 2017; Hamidi and Ivaska, 2018; Alday-Parejo et al., 2019; Cooper and Giancotti, 2019). Integrins are, nonetheless, used as targets in the prevention of blood clots during the opening of blood vessels in the heart (Tam et al., 1998), multiple sclerosis (Polman et al., 2006) and Crohn's disease (Gordon et al., 2001; Rosario et al., 2017). Furthermore, since the accumulation of disorganized ECM is modulated by several integrin heterodimers via activation of latent transforming growth factor-β, the selected integrins are considered as promising therapeutic targets for fibrosis (Kim et al., 2018). Besides integrin up- or down-regulation, integrin mutations are also associated with some diseases like junctional epidermolysis bullosa, caused by mutations in either integrin subunit of integrin $\alpha 6\beta 4$ forming hemidesmosomes or integrin $\alpha 3$, which pairs with $\beta 1$, forming FAs (McGrath, 2015; Walko et al., 2015). Furthermore, integrin related diseases may also be caused by impaired activation as observed on platelets and leukocytes (Alon and Etzioni, 2003). Integrins are also involved in bacterial (Hoffmann et al., 2011) and viral infections, either in attachment or internalization (Hussein et al., 2015), thus representing possible target molecules to combat infectious diseases.

AUTHOR CONTRIBUTIONS

BH conceived and wrote the first draft of the manuscript under the supervision of A-SS. All authors contributed to the writing of the final paper.

FUNDING

A-SS and BH thank the joint German Science Foundation and the French National Research Agency project SM 289/8-1, AOBJ: 652939, and the Excellence Cluster: Engineering of Advanced Materials at FAU Erlangen for support. AA-R thanks the Croatian Science Foundation (Grant IP-2019-04-1577 to AA-R). We also acknowledge support by the DFG Research Training Group 1962, Dynamic Interactions at Biological Membranes. AR acknowledges the support of the Max Planck-EPFL Center for Molecular Nanoscience and Technology.

ACKNOWLEDGMENTS

This article was previously made available on arXiv:2007.13368 (Stumpf et al., 2020).

REFERENCES

Alday-Parejo, B., Stupp, R., and Rüegg, C. (2019). Are integrins still practicable targets for anti-cancer therapy? *Cancers* 11:978. doi: 10.3390/cancers11070978

Alon, R., and Etzioni, A. (2003). LAD-III, a novel group of leukocyte integrin activation deficiencies. *Trends Immunol.* 24, 561–566. doi: 10.1016/j.it.2003.08.001

Annibale, P., Vanni, S., Scarselli, M., Rothlisberger, U., and Radenovic, A. (2011a). Identification of clustering artifacts in photoactivated localization microscopy. *Nat. Methods* 8, 527–528. doi: 10.1038/nmeth.1627

Annibale, P., Vanni, S., Scarselli, M., Rothlisberger, U., and Radenovic, A. (2011b). Quantitative photo activated localization microscopy: unraveling the effects of photoblinking. *PLoS ONE* 6:e22678. doi: 10.1371/journal.pone.0022678

Arnold, M., Cavalcanti-Adam, E. A., Glass, R., Blümmel, J., Eck, W., Kantlehner, M., et al. (2004). Activation of integrin function by nanopatterned adhesive interfaces. *ChemPhysChem* 5, 383–388. doi: 10.1002/cphc.200301014

Asaro, R. J., Lin, K., and Zhu, Q. (2019). Mechanosensitivity occurs along the adhesome's force train and affects traction stress. *Biophys. J.* 117, 1599–1614. doi: 10.1016/j.bpj.2019.08.039

Atherton, P., Lausecker, F., Carisey, A., Gilmore, A., Critchley, D., Barsukov, I., et al. (2020). Relief of talin autoinhibition triggers a force-independent association with vinculin. *J. Cell Biol.* 219, 1–16. doi: 10.1083/jcb.201903134

Bachir, A. I., Zareno, J., Moissoglu, K., Plow, E. F., Gratton, E., and Horwitz, A. R. (2014). Integrin-associated complexes form hierarchically with variable stoichiometry in nascent adhesions. *Curr. Biol.* 24, 1845–1853. doi: 10.1016/j.cub.2014.07.011

Balzarotti, F., Eilers, Y., Gwosch, K. C., Gynnå, A. H., Westphal, V., Stefani, F. D., et al. (2017). Nanometer resolution imaging and tracking of fluorescent molecules with minimal photon fluxes. *Science* 355, 606–612. doi: 10.1126/science.aak9913

Barczyk, M., Carracedo, S., and Gullberg, D. (2010). Integrins. *Cell Tissue Res.* 339, 269–280. doi: 10.1007/s00441-009-0834-6

Baumgart, F., Arnold, A. M., Leskovar, K., Staszek, K., Fölser, M., Weghuber, J., et al. (2016). Varying label density allows artifact-free analysis of membrane-protein nanoclusters. *Nat. Methods* 13, 661–664. doi: 10.1038/nmeth.3897

Bell, G. I. (1978). Models for the specific adhesion of cells to cells. *Science* 200, 618–627. doi: 10.1126/science.347575

Betzig, E., Patterson, G. H., Sougrat, R., Lindwasser, O. W., Olenych, S., Bonifacino, J. S., et al. (2006). Imaging intracellular fluorescent proteins at nanometer resolution. *Science* 313, 1642–1645. doi: 10.1126/science.1127344

Bharadwaj, M., Strohmeyer, N., Colo, G. P., Helenius, J., Beerenwinkel, N., Schiller, H. B., et al. (2017). αV-class integrins exert dual roles on $\alpha5\beta1$ integrins to strengthen adhesion to fibronectin. *Nat. Commun.* 8:14348. doi: 10.1038/ncomms14348

Bidone, T. C., Skeeters, A. V., Oakes, P. W., and Voth, G. A. (2019). Multiscale model of integrin adhesion assembly. *PLoS Comput. Biol.* 15:e1007077. doi: 10.1371/journal.pcbi.1007077

Bihr, T., Seifert, U., and Smith, A.-S. (2012). Nucleation of ligand-receptor domains in membrane adhesion. *Phys. Rev. Lett.* 109:258101. doi: 10.1103/PhysRevLett.109.258101

Bihr, T., Seifert, U., and Smith, A.-S. (2015). Multiscale approaches to protein-mediated interactions between membranes-relating microscopic and macroscopic dynamics in radially growing adhesions. *N. J. Phys.* 17:083016. doi: 10.1088/1367-2630/17/8/083016

Bledzka, K., Liu, J., Xu, Z., Perera, H. D., Yadav, S. P., Bialkowska, K., et al. (2012). Spatial coordination of kindlin-2 with talin head domain in interaction with integrin β cytoplasmic tails. *J. Biol. Chem.* 287, 24585–24594. doi: 10.1074/jbc.M111.336743

Böttcher, R. T., Veelders, M., Rombaut, P., Faix, J., Theodosiou, M., Stradal, T. E., et al. (2017). Kindlin-2 recruits paxillin and Arp2/3 to promote membrane protrusions during initial cell spreading. *J. Cell Biol.* 216, 3785–3798. doi: 10.1083/jcb.201701176

Bouchet, B. P., Gough, R. E., Ammon, Y.-C., van de Willige, D., Post, H., Jacquemet, G., et al. (2016). Talin-KANK1 interaction controls the recruitment of cortical microtubule stabilizing complexes to focal adhesions. *eLife* 5:e18124. doi: 10.7554/eLife.18124.022

Brinkerhoff, C. J., and Linderman, J. J. (2005). Integrin dimerization and ligand organization: key components in integrin clustering for cell adhesion. *Tissue Eng.* 11, 865–876. doi: 10.1089/ten.2005.11.865

Bruinsma, R., Behrisch, A., and Sackmann, E. (2000). Adhesive switching of membranes: experiment and theory. *Phys. Rev. E* 61, 4253–4267. doi: 10.1103/PhysRevE.61.4253

Burridge, K., and Guilluy, C. (2016). Focal adhesions, stress fibers and mechanical tension. *Exp. Cell Res.* 343, 14–20. doi: 10.1016/j.yexcr.2015.10.029

Byron, A., Askari, J. A., Humphries, J. D., Jacquemet, G., Koper, E. J., Warwood, S., et al. (2015). A proteomic approach reveals integrin activation state-dependent control of microtubule cortical targeting. *Nat. Commun.* 6:6135. doi: 10.1038/ncomms7135

Calderwood, D. A. (2004). Integrin activation. *J. Cell Sci.* 117, 657–666. doi: 10.1242/jcs.01014

Calderwood, D. A., Campbell, I. D., and Critchley, D. R. (2013). Talins and kindlins: partners in integrin-mediated adhesion. *Nat. Rev. Mol. Cell Biol.* 14, 503–517. doi: 10.1038/nrm3624

Calderwood, D. A., Zent, R., Grant, R., Rees, D. J. G., Hynes, R. O., and Ginsberg, M. H. (1999). The talin head domain binds to integrin β subunit cytoplasmic tails and regulates integrin activation. *J. Biol. Chem.* 274, 28071–28074. doi: 10.1074/jbc.274.40.28071

Campbell, I. D., and Humphries, M. J. (2011). Integrin structure, activation, and interactions. *Cold Spring Harbor Perspect. Biol.* 3:a004994. doi: 10.1101/cshperspect.a004994

Changede, R., Cai, H., Wind, S. J., and Sheetz, M. P. (2019). Integrin nanoclusters can bridge thin matrix fibres to form cell-matrix adhesions. *Nat. Mater.* 18, 1366–1375. doi: 10.1038/s41563-019-0460-y

Changede, R., and Sheetz, M. (2017). Integrin and cadherin clusters: a robust way to organize adhesions for cell mechanics. *Bioessays* 39:e201600123. doi: 10.1002/bies.201600123

Changede, R., Xu, X., Margadant, F., and Sheetz, M. P. (2015). Nascent integrin adhesions form on all matrix rigidities after integrin activation. *Dev. Cell* 35, 614–621. doi: 10.1016/j.devcel.2015.11.001

Chen, N.-P., Sun, Z., and Fässler, R. (2018). The Kank family proteins in adhesion dynamics. *Curr. Opin. Cell Biol.* 54, 130–136. doi: 10.1016/j.ceb.2018.05.015

Chen, W., Lou, J., Hsin, J., Schulten, K., Harvey, S. C., and Zhu, C. (2011). Molecular dynamics simulations of forced unbending of integrin $\alpha V\beta3$. *PLoS Comput. Biol.* 7:e1001086. doi: 10.1371/journal.pcbi.1001086

Chen, W., Lou, J., and Zhu, C. (2010). Forcing switch from short- to intermediate- and long-lived states of the αA domain generates LFA-1/ICAM-1 catch bonds. *J. Biol. Chem.* 285, 35967–35978. doi: 10.1074/jbc.M110.155770

Choi, C. K., Vicente-Manzanares, M., Zareno, J., Whitmore, L. A., Mogilner, A., and Horwitz, A. R. (2008). Actin and α-actinin orchestrate the assembly and maturation of nascent adhesions in a myosin II motor-independent manner. *Nat. Cell Biol.* 10, 1039–1050. doi: 10.1038/ncb1763

Choi, C. K., Zareno, J., Digman, M. A., Gratton, E., and Horwitz, A. R. (2011). Cross-correlated fluctuation analysis reveals phosphorylation-regulated paxillin-FAK complexes in nascent adhesions. *Biophys. J.* 100, 583–592. doi: 10.1016/j.bpj.2010.12.3719

Choi, Y. I., Duke-Cohan, J. S., Chen, W., Liu, B., Rossy, J., Tabarin, T., et al. (2014). Dynamic control of $\beta1$ integrin adhesion by the plexinD1-sema3E axis. *Proc. Natl. Acad. Sci. U.S.A.* 111, 379–384. doi: 10.1073/pnas.1314209111

Ciobanasu, C., Faivre, B., and Le Clainche, C. (2014). Actomyosin-dependent formation of the mechanosensitive talin-vinculin complex reinforces actin anchoring. *Nat. Commun.* 5:3095. doi: 10.1038/ncomms4095

Cluzel, C., Saltel, F., Lussi, J., Paulhe, F., Imhof, B. A., and Wehrle-Haller, B. (2005). The mechanisms and dynamics of $\alpha v\beta3$ integrin clustering in living cells. *J. Cell Biol.* 171, 383–392. doi: 10.1083/jcb.200503017

Cooper, J., and Giancotti, F. G. (2019). Integrin signaling in cancer: mechanotransduction, stemness, epithelial plasticity, and therapeutic resistance. *Cancer Cell* 35, 347–367. doi: 10.1016/j.ccell.2019.01.007

Dedden, D., Schumacher, S., Kelley, C. F., Zacharias, M., Biertümpfel, C., Fässler, R., et al. (2019). The architecture of talin1 reveals an autoinhibition mechanism. *Cell* 179, 120.e13–131.e13. doi: 10.1016/j.cell.2019.08.034

Dembo, M., Torney, D. C., Saxman, K., and Hammer, D. (1988). The reaction-limited kinetics of membrane-to-surface adhesion and detachment. *Proc. R. Soc. Lond. Ser. B. Biol. Sci.* 234, 55–83. doi: 10.1098/rspb.1988.0038

Dertinger, T., Colyer, R., Iyer, G., Weiss, S., and Enderlein, J. (2009). Fast, background-free, 3D super-resolution optical fluctuation imaging (SOFI). *Proc. Natl. Acad. Sci. U.S.A.* 106, 22287–22292. doi: 10.1073/pnas.0907866106

Deschout, H., Platzman, I., Sage, D., Feletti, L., Spatz, J. P., and Radenovic, A. (2017). Investigating focal adhesion substructures by localization microscopy. *Biophys. J.* 113, 2508–2518. doi: 10.1016/j.bpj.2017.09.032

Desgrosellier, J. S., and Cheresh, D. A. (2010). Integrins in cancer: biological implications and therapeutic opportunities. *Nat. Rev. Cancer* 10, 9–22. doi: 10.1038/nrc2748

Diaz, C., Neubauer, S., Rechenmacher, F., Kessler, H., and Missirlis, D. (2020). Recruitment of $\alpha\ v\ \beta_3$ integrin to $\alpha_5\ \beta_1$ integrin-induced clusters enables focal adhesion maturation and cell spreading. *J. Cell Sci.* 133:jcs232702. doi: 10.1242/jcs.232702

Dickreuter, E., and Cordes, N. (2017). The cancer cell adhesion resistome: mechanisms, targeting and translational approaches. *Biol. Chem.* 398, 721–735. doi: 10.1515/hsz-2016-0326

Elkhatib, N., Bresteau, E., Baschieri, F., Rioja, A. L., van Niel, G., Vassilopoulos, S., et al. (2017). Tubular clathrin/AP-2 lattices pinch collagen fibers to support 3D cell migration. *Science* 356:eaal4713. doi: 10.1126/science.aal4713

Ellis, S. J., Lostchuck, E., Goult, B. T., Bouaouina, M., Fairchild, M. J., López-Ceballos, P., et al. (2014). The talin head domain reinforces integrin-mediated adhesion by promoting adhesion complex stability and clustering. *PLoS Genet.* 10:e1004756. doi: 10.1371/journal.pgen.1004756

Fenz, S. F., Bihr, T., Schmidt, D., Merkel, R., Seifert, U., Sengupta, K., et al. (2017). Membrane fluctuations mediate lateral interaction between cadherin bonds. *Nat. Phys.* 13, 906–913. doi: 10.1038/nphys4138

Fenz, S. F., Smith, A.-S., Merkel, R., and Sengupta, K. (2011). Inter-membrane adhesion mediated by mobile linkers: effect of receptor shortage. *Soft Matter* 7, 952–962. doi: 10.1039/C0SM00550A

Fiore, V. F., Ju, L., Chen, Y., Zhu, C., and Barker, T. H. (2014). Dynamic catch of a Thy-1-$\alpha5\beta1$+syndecan-4 trimolecular complex. *Nat. Commun.* 5:4886. doi: 10.1038/ncomms5886

Gardel, M. L., Schneider, I. C., Aratyn-Schaus, Y., Waterman, C. M., Aratyn-Schaus, Y., and Waterman, C. M. (2010). Mechanical integration of actin and adhesion dynamics in cell migration. *Annu. Rev. Cell Dev. Biol.* 26, 315–333. doi: 10.1146/annurev.cellbio.011209.122036

Geiger, B., Spatz, J. P., and Bershadsky, A. D. (2009). Environmental sensing through focal adhesions. *Nat. Rev. Mol. Cell Biol.* 10, 21–33. doi: 10.1038/nrm2593

Geiger, B., and Yamada, K. M. (2011). Molecular architecture and function of matrix adhesions. *Cold Spring Harb. Perspect. Biol.* 3:a005033. doi: 10.1101/cshperspect.a005033

Gingras, A. R., and Ginsberg, M. H. (2020). Signal transduction: physical deformation of the membrane activates integrins. *Curr. Biol.* 30, R397–R400. doi: 10.1016/j.cub.2020.02.068

Goennenwein, S., Tanaka, M., Hu, B., Moroder, L., and Sackmann, E. (2003). Functional incorporation of integrins into solid supported membranes on ultrathin films of cellulose: impact on adhesion. *Biophys. J.* 85, 646–655. doi: 10.1016/S0006-3495(03)74508-1

Golji, J., and Mofrad, M. R. (2014). The talin dimer structure orientation is mechanically regulated. *Biophys. J.* 107, 1802–1809. doi: 10.1016/j.bpj.2014.08.038

Gordon, F. H., Lai, C. W., Hamilton, M. I., Allison, M. C., Srivastava, E. D., Fouweather, M. G., et al. (2001). A randomized placebo-controlled trial of a humanized monoclonal antibody to α4 integrin in active Crohn's disease. *Gastroenterology* 121, 268–274. doi: 10.1053/gast.2001.26260

Green, H. J., and Brown, N. H. (2019). Integrin intracellular machinery in action. *Exp. Cell Res.* 378, 226–231. doi: 10.1016/j.yexcr.2019.03.011

Grove, J., Metcalf, D. J., Knight, A. E., Wavre-Shapton, S. T., Sun, T., Protonotarios, E. D., et al. (2014). Flat clathrin lattices: stable features of the plasma membrane. *Mol. Biol. Cell* 25, 3581–3594. doi: 10.1091/mbc.e14-06-1154

Hamidi, H., and Ivaska, J. (2018). Every step of the way: integrins in cancer progression and metastasis. *Nat. Rev. Cancer* 18, 533–548. doi: 10.1038/s41568-018-0038-z

Harburger, D. S., Bouaouina, M., and Calderwood, D. A. (2009). Kindlin-1 and -2 directly bind the C-terminal region of β integrin cytoplasmic tails and exert integrin-specific activation effects. *J. Biol. Chem.* 284, 11485–11497. doi: 10.1074/jbc.M809233200

Harland, B., Walcott, S., and Sun, S. X. (2011). Adhesion dynamics and durotaxis in migrating cells. *Phys. Biol.* 8:015011. doi: 10.1088/1478-3975/8/1/015011

He, K., Sakai, T., Tsukasaki, Y., Watanabe, T. M., and Ikebe, M. (2017). Myosin X is recruited to nascent focal adhesions at the leading edge and induces multi-cycle filopodial elongation. *Sci. Rep.* 7:13685. doi: 10.1038/s41598-017-06147-6

Helfrich, W. (1978). Steric interaction of fluid membranes in multilayer systems. *Z. Naturforschung A* 33:305. doi: 10.1515/zna-1978-0308

Hoffmann, C., Ohlsen, K., and Hauck, C. R. (2011). Integrin-mediated uptake of fibronectin-binding bacteria. *Eur. J. Cell Biol.* 90, 891–896. doi: 10.1016/j.ejcb.2011.03.001

Horton, E. R., Astudillo, P., Humphries, M. J., and Humphries, J. D. (2016). Mechanosensitivity of integrin adhesion complexes: role of the consensus adhesome. *Exp. Cell Res.* 343, 7–13. doi: 10.1016/j.yexcr.2015.10.025

Horton, E. R., Byron, A., Askari, J. A., Ng, D. H. J., Millon-Frémillon, A., Robertson, J., et al. (2015). Definition of a consensus integrin adhesome and its dynamics during adhesion complex assembly and disassembly. *Nat. Cell Biol.* 17, 1577–1587. doi: 10.1038/ncb3257

Huang, D. L., Bax, N. A., Buckley, C. D., Weis, W. I., and Dunn, A. R. (2017). Vinculin forms a directionally asymmetric catch bond with F-actin. *Science* 357, 703–706. doi: 10.1126/science.aan2556

Humphries, J. D., Byron, A., and Humphries, M. J. (2006). Integrin ligands at a glance. *J. Cell Sci.* 119, 3901–3903. doi: 10.1242/jcs.03098

Humphries, J. D., Chastney, M. R., Askari, J. A., and Humphries, M. J. (2019). Signal transduction via integrin adhesion complexes. *Curr. Opin. Cell Biol.* 56, 14–21. doi: 10.1016/j.ceb.2018.08.004

Humphries, J. D., Wang, P., Streuli, C., Geiger, B., Humphries, M. J., and Ballestrem, C. (2007). Vinculin controls focal adhesion formation by direct interactions with talin and actin. *J. Cell Biol.* 179, 1043–1057. doi: 10.1083/jcb.200703036

Hussein, H. A. M., Walker, L. R., Abdel-Raouf, U. M., Desouky, S. A., Montasser, A. K. M., and Akula, S. M. (2015). Beyond RGD: virus interactions with integrins. *Arch. Virol.* 160, 2669–2681. doi: 10.1007/s00705-015-2579-8

Hynes, R. O. (2002). Integrins. *Cell* 110, 673–687. doi: 10.1016/S0092-8674(02)00971-6

Inavalli, V. V. G. K., Lenz, M. O., Butler, C., Angibaud, J., Compans, B., Levet, F., et al. (2019). A super-resolution platform for correlative live single-molecule imaging and STED microscopy. *Nat. Methods* 16, 1263–1268. doi: 10.1038/s41592-019-0611-8

Iwamoto, D. V., and Calderwood, D. A. (2015). Regulation of integrin-mediated adhesions. *Curr. Opin. Cell Biol.* 36, 41–47. doi: 10.1016/j.ceb.2015.06.009

Jamali, Y., Jamali, T., and Mofrad, M. R. (2013). An agent based model of integrin clustering: exploring the role of ligand clustering, integrin homo-oligomerization, integrin-ligand affinity, membrane crowdedness and ligand mobility. *J. Comput. Phys.* 244, 264–278. doi: 10.1016/j.jcp.2012.09.010

Janeš, J. A., Stumpf, H., Schmidt, D., Seifert, U., and Smith, A.-S. (2019). Statistical mechanics of an elastically pinned membrane: static profile and correlations. *Biophys. J.* 116, 283–295. doi: 10.1016/j.bpj.2018.12.003

Jones, M. C., Humphries, J. D., Byron, A., Millon-Frémillon, A., Robertson, J., Paul, N. R., et al. (2015). Isolation of integrin-based adhesion complexes. *Curr. Protoc. Cell Biol.* 66, 9.8.1–9.8.15. doi: 10.1002/0471143030.cb0908s66

Kalli, A. C., Rog, T., Vattulainen, I., Campbell, I. D., and Sansom, M. S. P. (2017). The integrin receptor in biologically relevant bilayers: insights from molecular dynamics simulations. *J. Memb. Biol.* 250, 337–351. doi: 10.1007/s00232-016-9908-z

Kammerer, P., Aretz, J., and Fässler, R. (2017). Lucky kindlin: a cloverleaf at the integrin tail. *Proc. Natl. Acad. Sci. U.S.A.* 114, 9234–9236. doi: 10.1073/pnas.1712471114

Kechagia, J. Z., Ivaska, J., and Roca-Cusachs, P. (2019). Integrins as biomechanical sensors of the microenvironment. *Nat. Rev. Mol. Cell Biol.* 20, 457–473. doi: 10.1038/s41580-019-0134-2

Kim, J., Lee, J., Jang, J., Ye, F., Hong, S. J., Petrich, B. G., et al. (2020). Topological adaptation of transmembrane domains to the force-modulated lipid bilayer is a basis of sensing mechanical force. *Curr. Biol.* 30, 1614.e5–1625.e5. doi: 10.1016/j.cub.2020.02.028

Kim, K. K., Sheppard, D., and Chapman, H. A. (2018). TGF-β1 signaling and tissue fibrosis. *Cold Spring Harb. Perspect. Biol.* 10:a022293. doi: 10.1101/cshperspect.a022293

Kong, F., García, A. J., Mould, A. P., Humphries, M. J., and Zhu, C. (2009). Demonstration of catch bonds between an integrin and its ligand. *J. Cell Biol.* 185, 1275–1284. doi: 10.1083/jcb.200810002

Kong, F., Li, Z., Parks, W. M., Dumbauld, D. W., García, A. J., Mould, A. P., et al. (2013). Cyclic mechanical reinforcement of integrin-ligand interactions. *Mol. Cell* 49, 1060–1068. doi: 10.1016/j.molcel.2013.01.015

Kuo, J.-C., Han, X., Hsiao, C.-T., Yates III, J. R., and Waterman, C. M. (2011). Analysis of the myosin-II-responsive focal adhesion proteome reveals a role for β-Pix in negative regulation of focal adhesion maturation. *Nat. Cell Biol.* 13, 383–393. doi: 10.1038/ncb2216

Lam Hui, K., Wang, C., Grooman, B., Wayt, J., and Upadhyaya, A. (2012). Membrane dynamics correlate with formation of signaling clusters during cell spreading. *Biophys. J.* 102, 1524–1533. doi: 10.1016/j.bpj.2012.02.015

Lawson, C., Lim, S. T., Uryu, S., Chen, X. L., Calderwood, D. A., and Schlaepfer, D. D. (2012). FAK promotes recruitment of talin to nascent adhesions to control cell motility. *J. Cell Biol.* 196, 223–232. doi: 10.1083/jcb.201108078

Lawson, C., and Schlaepfer, D. (2012). Integrin adhesions. *Cell Adhes. Migrat.* 6, 302–306. doi: 10.4161/cam.20488

Levet, F., Julien, G., Galland, R., Butler, C., Beghin, A., Chazeau, A., et al. (2019). A tessellation-based colocalization analysis approach for single-molecule localization microscopy. *Nat. Commun.* 10:2379. doi: 10.1038/s41467-019-10007-4

Leyton-Puig, D., Isogai, T., Argenzio, E., van den Broek, B., Klarenbeek, J., Janssen, H., et al. (2017). Flat clathrin lattices are dynamic actin-controlled hubs for clathrin-mediated endocytosis and signalling of specific receptors. *Nat. Commun.* 8:16068. doi: 10.1038/ncomms16068

Li, H., Deng, Y., Sun, K., Yang, H., Liu, J., Wang, M., et al. (2017). Structural basis of kindlin-mediated integrin recognition and activation. *Proc. Natl. Acad. Sci. U.S.A.* 114, 9349–9354. doi: 10.1073/pnas.1703064114

Li, J., and Springer, T. A. (2017). Integrin extension enables ultrasensitive regulation by cytoskeletal force. *Proc. Natl. Acad. Sci. U.S.A.* 114, 4685–4690. doi: 10.1073/pnas.1704171114

Li, J., and Springer, T. A. (2018). Energy landscape differences among integrins establish the framework for understanding activation. *J. Cell Biol.* 217, 397–412. doi: 10.1083/jcb.201701169

Li, J., Su, Y., Xia, W., Qin, Y., Humphries, M. J., Vestweber, D., et al. (2017). Conformational equilibria and intrinsic affinities define integrin activation. *EMBO J.* 36, 629–645. doi: 10.15252/embj.201695803

Li, R. (2003). Activation of integrin alphaIIbbeta3 by modulation of transmembrane helix associations. *Science* 300, 795–798. doi: 10.1126/science.1079441

Li, Y., Bhimalapuram, P., and Dinner, A. R. (2010). Model for how retrograde actin flow regulates adhesion traction stresses. *J. Phys. Cond. Matter* 22:194113. doi: 10.1088/0953-8984/22/19/194113

Liu, Y., Medda, R., Liu, Z., Galior, K., Yehl, K., Spatz, J. P., et al. (2014). Nanoparticle tension probes patterned at the nanoscale: impact of integrin clustering on force transmission. *Nano Lett.* 14, 5539–5546. doi: 10.1021/nl501912g

Lock, J. G., Baschieri, F., Jones, M. C., Humphries, J. D., Montagnac, G., Strömblad, S., et al. (2019). Clathrin-containing adhesion complexes. *J. Cell Biol.* 218, 2086–2095. doi: 10.1083/jcb.201811160

Lock, J. G., Jones, M. C., Askari, J. A., Gong, X., Oddone, A., Olofsson, H., et al. (2018). Reticular adhesions are a distinct class of cell-matrix adhesions that mediate attachment during mitosis. *Nat. Cell Biol.* 20, 1290–1302. doi: 10.1038/s41556-018-0220-2

Luo, B.-H., Carman, C. V., and Springer, T. A. (2007). Structural basis of integrin regulation and signaling. *Ann. Rev. Immunol.* 25, 619–647. doi: 10.1146/annurev.immunol.25.022106.141618

Ma, Y.-Q., Qin, J., Wu, C., and Plow, E. F. (2008). Kindlin-2 (Mig-2): a co-activator of β3 integrins. *J. Cell Biol.* 181, 439–446. doi: 10.1083/jcb.200710196

MacKay, L., and Khadra, A. (2019). Dynamics of mechanosensitive nascent adhesion formation. *Biophys. J.* 117, 1057–1073. doi: 10.1016/j.bpj.2019.08.004

Massou, S., Nunes Vicente, F., Wetzel, F., Mehidi, A., Strehle, D., Leduc, C., et al. (2020). Cell stretching is amplified by active actin remodelling to deform and recruit proteins in mechanosensitive structures. *Nat. Cell Biol.* 22, 1011–1023. doi: 10.1038/s41556-020-0548-2

McGrath, J. A. (2015). Recently identified forms of epidermolysis bullosa. *Ann. Dermatol.* 27:658. doi: 10.5021/ad.2015.27.6.658

Mehrbod, M., and Mofrad, M. R. K. (2013). Localized lipid packing of transmembrane domains impedes integrin clustering. *PLoS Comput. Biol.* 9:e1002948. doi: 10.1371/journal.pcbi.1002948

Michael, M., and Parsons, M. (2020). New perspectives on integrin-dependent adhesions. *Curr. Opin. Cell Biol.* 63, 31–37. doi: 10.1016/j.ceb.2019.12.008

Moreno-Layseca, P., Icha, J., Hamidi, H., and Ivaska, J. (2019). Integrin trafficking in cells and tissues. *Nat. Cell Biol.* 21, 122–132. doi: 10.1038/s41556-018-0223-z

Moser, M., Nieswandt, B., Ussar, S., Pozgajova, M., and Fässler, R. (2008). Kindlin-3 is essential for integrin activation and platelet aggregation. *Nat. Med.* 14, 325–330. doi: 10.1038/nm1722

Nicovich, P. R., Owen, D. M., and Gaus, K. (2017). Turning single-molecule localization microscopy into a quantitative bioanalytical tool. *Nat. Protoc.* 12, 453–460. doi: 10.1038/nprot.2016.166

Nieves, D. J., and Owen, D. M. (2020). Analysis methods for interrogating spatial organisation of single molecule localisation microscopy data. *Int. J. Biochem. Cell Biol.* 123:105749. doi: 10.1016/j.biocel.2020.105749

Nordenfelt, P., Moore, T. I., Mehta, S. B., Kalappurakkal, J. M., Swaminathan, V., Koga, N., et al. (2017). Direction of actin flow dictates integrin LFA-1 orientation during leukocyte migration. *Nat. Commun.* 8:2047. doi: 10.1038/s41467-017-01848-y

Oakes, P. W., Bidone, T. C., Beckham, Y., Skeeters, A. V., Ramirez-San Juan, G. R., Winter, S. P., et al. (2018). Lamellipodium is a myosin-independent mechanosensor. *Proc. Natl. Acad. Sci. U.S.A.* 115, 2646–2651. doi: 10.1073/pnas.1715869115

Orré, T., Rossier, O., and Giannone, G. (2019). The inner life of integrin adhesion sites: from single molecules to functional macromolecular complexes. *Exp. Cell Res.* 379, 235–244. doi: 10.1016/j.yexcr.2019.03.036

Pagani, G., and Gohlke, H. (2018). On the contributing role of the transmembrane domain for subunit-specific sensitivity of integrin activation. *Sci. Rep.* 8:5733. doi: 10.1038/s41598-018-23778-5

Paradžik, M., Humphries, J. D., Stojanović, N., Nestić, D., Majhen, D., Dekanić, A., et al. (2020). KANK2 links αVβ5 focal adhesions to microtubules and regulates sensitivity to microtubule poisons and cell migration. *Front. Cell Dev. Biol.* 8:125. doi: 10.3389/fcell.2020.00125

Park, Y. K., and Goda, Y. (2016). Integrins in synapse regulation. *Nat. Rev. Neurosci.* 17, 745–756. doi: 10.1038/nrn.2016.138

Parsons, J. T., Horwitz, A. R., and Schwartz, M. A. (2010). Cell adhesion: integrating cytoskeletal dynamics and cellular tension. *Nat. Rev. Mol. Cell Biol.* 11, 633–643. doi: 10.1038/nrm2957

Paszek, M. J., DuFort, C. C., Rossier, O., Bainer, R., Mouw, J. K., Godula, K., et al. (2014). The cancer glycocalyx mechanically primes integrin-mediated growth and survival. *Nature* 511, 319–325. doi: 10.1038/nature13535

Perez, T. D., Tamada, M., Sheetz, M. P., and Nelson, W. J. (2008). Immediate-early signaling induced by e-cadherin engagement and adhesion. *J. Biol. Chem.* 283, 5014–5022. doi: 10.1074/jbc.M705209200

Pierres, A., Benoliel, A.-M., Touchard, D., and Bongrand, P. (2008). How cells tiptoe on adhesive surfaces before sticking. *Biophys. J.* 94, 4114–4122. doi: 10.1529/biophysj.107.125278

Pike, J. A., Khan, A. O., Pallini, C., Thomas, S. G., Mund, M., Ries, J., et al. (2019). Topological data analysis quantifies biological nano-structure from single molecule localization microscopy. *Bioinformatics.* 36, 1614–1621. doi: 10.1093/bioinformatics/btz788

Polman, C. H., O'Connor, P. W., Havrdova, E., Hutchinson, M., Kappos, L., Miller, D. H., et al. (2006). A randomized, placebo-controlled trial of natalizumab for relapsing multiple sclerosis. *N. Engl. J. Med.* 354, 899–910. doi: 10.1056/NEJMoa044397

Puklin-Faucher, E., Gao, M., Schulten, K., and Vogel, V. (2006). How the headpiece hinge angle is opened: new insights into the dynamics of integrin activation. *J. Cell Biol.* 175, 349–360. doi: 10.1083/jcb.200602071

Roca-Cusachs, P., del Rio, A., Puklin-Faucher, E., Gauthier, N. C., Biais, N., and Sheetz, M. P. (2013). Integrin-dependent force transmission to the extracellular matrix by -actinin triggers adhesion maturation. *Proc. Natl. Acad. Sci. U.S.A.* 110, E1361–E1370. doi: 10.1073/pnas.1220723110

Rosario, M., Dirks, N. L., Milch, C., Parikh, A., Bargfrede, M., Wyant, T., et al. (2017). A review of the clinical pharmacokinetics, pharmacodynamics, and immunogenicity of vedolizumab. *Clin. Pharmacokinet.* 56, 1287–1301. doi: 10.1007/s40262-017-0546-0

Rossier, O., Octeau, V., Sibarita, J.-B., Leduc, C., Tessier, B., Nair, D., et al. (2012). Integrins β1 and β3 exhibit distinct dynamic nanoscale organizations inside focal adhesions. *Nat. Cell Biol.* 14, 1057–1067. doi: 10.1038/ncb2588

Rust, M. J., Bates, M., and Zhuang, X. (2006). Sub-diffraction-limit imaging by stochastic optical reconstruction microscopy (STORM). *Nat. Methods* 3, 793–796. doi: 10.1038/nmeth929

Saltel, F., Mortier, E., Hytönen, V. P., Jacquier, M.-C., Zimmermann, P., Vogel, V., et al. (2009). New PI(4,5)P2- and membrane proximal integrin-binding motifs in the talin head control β3-integrin clustering. *J. Cell Biol.* 187, 715–731. doi: 10.1083/jcb.200908134

Samaržija, I., Dekanić, A., Humphries, J. D., Paradžik, M., Stojanović, N., Humphries, M. J., et al. (2020). Integrin crosstalk contributes to the complexity of signalling and unpredictable cancer cell fates. *Cancers* 12:1910. doi: 10.3390/cancers12071910

Schiller, H. B., Friedel, C. C., Boulegue, C., and Fässler, R. (2011). Quantitative proteomics of the integrin adhesome show a myosin II-dependent recruitment of LIM domain proteins. *EMBO Rep.* 12, 259–266. doi: 10.1038/embor.2011.5

Schmidt, D., Bihr, T., Fenz, S., Merkel, R., Seifert, U., Sengupta, K., et al. (2015). Crowding of receptors induces ring-like adhesions in model membranes. *Biochim. Biophys. Acta Mol. Cell Res.* 1853, 2984–2991. doi: 10.1016/j.bbamcr.2015.05.025

Schmidt, D., Bihr, T., Seifert, U., and Smith, A.-S. (2012). Coexistence of dilute and densely packed domains of ligand-receptor bonds in membrane adhesion. *Europhys. Lett.* 99:38003. doi: 10.1209/0295-5075/99/38003

Schvartzman, M., Palma, M., Sable, J., Abramson, J., Hu, X., Sheetz, M. P., et al. (2011). Nanolithographic control of the spatial organization of cellular adhesion receptors at the single-molecule level. *Nano Lett.* 11, 1306–1312. doi: 10.1021/nl104378f

Schwarz, U. S., Erdmann, T., and Bischofs, I. B. (2006). Focal adhesions as mechanosensors: the two-spring model. *Biosystems* 83, 225–232. doi: 10.1016/j.biosystems.2005.05.019

Seguin, L., Desgrosellier, J. S., Weis, S. M., and Cheresh, D. A. (2015). Integrins and cancer: regulators of cancer stemness, metastasis, and drug resistance. *Trends Cell Biol*. 25, 234–240. doi: 10.1016/j.tcb.2014.12.006

Sengupta, K., and Smith, A.-S. (2018). *Adhesion of Biological Membranes*. Cham: Springer International Publishing. doi: 10.1007/978-3-030-00630-3_18

Shams, H., and Mofrad, M. R. K. (2017). α-actinin induces a kink in the transmembrane domain of β3-integrin and impairs activation via talin. *Biophys. J*. 113, 948–956. doi: 10.1016/j.bpj.2017.06.064

Shan, Y., Yu, L., Li, Y., Pan, Y., Zhang, Q., Wang, F., et al. (2009). Nudel and FAK as antagonizing strength modulators of nascent adhesions through paxillin. *PLoS Biol*. 7:e1000116. doi: 10.1371/journal.pbio.1000116

Shi, X., Ma, Y.-Q., Tu, Y., Chen, K., Wu, S., Fukuda, K., et al. (2007). The MIG-2/integrin interaction strengthens cell-matrix adhesion and modulates cell motility. *J. Biol. Chem*. 282, 20455–20466. doi: 10.1074/jbc.M611680200

Shimaoka, M., and Springer, T. A. (2003). Therapeutic antagonists and conformational regulation of integrin function. *Nat. Rev. Drug Discov*. 2, 703–716. doi: 10.1038/nrd1174

Shroff, H., Galbraith, C. G., Galbraith, J. A., White, H., Gillette, J., Olenych, S., et al. (2007). Dual-color superresolution imaging of genetically expressed probes within individual adhesion complexes. *Proc. Natl. Acad. Sci. U.S.A*. 104, 20308–20313. doi: 10.1073/pnas.0710517105

Sigal, Y. M., Zhou, R., and Zhuang, X. (2018). Visualizing and discovering cellular structures with super-resolution microscopy. *Science* 361, 880–887. doi: 10.1126/science.aau1044

Small, J., Stradal, T., Vignal, E., and Rottner, K. (2002). The lamellipodium: where motility begins. *Trends Cell Biol*. 12, 112–120. doi: 10.1016/S0962-8924(01)02237-1

Smith, A.-S., Lorz, B. G., Seifert, U., and Sackmann, E. (2006). Antagonist-induced deadhesion of specifically adhered vesicles. *Biophys. J*. 90, 1064–1080. doi: 10.1529/biophysj.105.062166

Smith, A.-S., and Sackmann, E. (2009). Progress in mimetic studies of cell adhesion and the mechanosensing. *ChemPhysChem* 10, 66–78. doi: 10.1002/cphc.200800683

Smith, A.-S., and Seifert, U. (2005). Force-induced de-adhesion of specifically bound vesicles: strong adhesion in competition with tether extraction. *Langmuir* 21, 11357–11367. doi: 10.1021/la051303f

Smith, A.-S., Sengupta, K., Goennenwein, S., Seifert, U., and Sackmann, E. (2008). Force-induced growth of adhesion domains is controlled by receptor mobility. *Proc. Natl. Acad. Sci. U.S.A*. 105, 6906–6911. doi: 10.1073/pnas.0801706105

Spahn, C., Herrmannsdörfer, F., Kuner, T., and Heilemann, M. (2016). Temporal accumulation analysis provides simplified artifact-free analysis of membrane-protein nanoclusters. *Nat. Methods* 13, 963–964. doi: 10.1038/nmeth.4065

Spiess, M., Hernandez-Varas, P., Oddone, A., Olofsson, H., Blom, H., Waithe, D., et al. (2018). Active and inactive β1 integrins segregate into distinct nanoclusters in focal adhesions. *J. Cell Biol*. 217, 1929–1940. doi: 10.1083/jcb.201707075

Stehbens, S., and Wittmann, T. (2012). Targeting and transport: how microtubules control focal adhesion dynamics. *J. Cell Biol*. 198, 481–489. doi: 10.1083/jcb.201206050

Streicher, P., Nassoy, P., Bärmann, M., Dif, A., Marchi-Artzner, V., Brochard-Wyart, F., et al. (2009). Integrin reconstituted in GUVs: a biomimetic system to study initial steps of cell spreading. *Biochim. Biophys. Acta Biomemb*. 1788, 2291–2300. doi: 10.1016/j.bbamem.2009.07.025

Strohmeyer, N., Bharadwaj, M., Costell, M., Fässler, R., and Müller, D. J. (2017). Fibronectin-bound $\alpha5\beta1$ integrins sense load and signal to reinforce adhesion in less than a second. *Nat. Mater*. 16, 1262–1270. doi: 10.1038/nmat5023

Stumpf, H., Ambriović-Ristov, A., Radenovic, A., and Smith, A.-S. (2020). Recent advances and prospects in the research of nascent adhesions. *arXiv[Preprint].arXiv:2007.13368*.

Subauste, M. C., Pertz, O., Adamson, E. D., Turner, C. E., Junger, S., and Hahn, K. M. (2004). Vinculin modulation of paxillin-FAK interactions regulates ERK to control survival and motility. *J. Cell Biol*. 165, 371–381. doi: 10.1083/jcb.200308011

Sun, Z., Costell, M., and Fässler, R. (2019). Integrin activation by talin, kindlin and mechanical forces. *Nat Cell Biol*. 21, 25–31. doi: 10.1038/s41556-018-0234-9

Sun, Z., Lambacher, A., and Fässler, R. (2014). Nascent adhesions: from fluctuations to a hierarchical organization. *Curr. Biol*. 24, R801–R803. doi: 10.1016/j.cub.2014.07.061

Sun, Z., Tseng, H.-Y., Tan, S., Senger, F., Kurzawa, L., Dedden, D., et al. (2016). Kank2 activates talin, reduces force transduction across integrins and induces central adhesion formation. *Nat. Cell Biol*. 18, 941–953. doi: 10.1038/ncb3402

Swaminathan, V., Fischer, R. S., and Waterman, C. M. (2016). The FAK-Arp2/3 interaction promotes leading edge advance and haptosensing by coupling nascent adhesions to lamellipodia actin. *Mol. Biol. Cell* 27, 1085–1100. doi: 10.1091/mbc.E15-08-0590

Takada, Y., Ye, X., and Simon, S. (2007). The integrins. *Genome Biol*. 8:215. doi: 10.1186/gb-2007-8-5-215

Tam, S. H., Sassoli, P. M., Jordan, R. E., and Nakada, M. T. (1998). Abciximab (ReoPro, Chimeric 7E3 Fab) demonstrates equivalent affinity and functional blockade of glycoprotein IIb/IIIa and α v β 3 integrins. *Circulation* 98, 1085–1091. doi: 10.1161/01.CIR.98.11.1085

Tan, S. J., Chang, A. C., Anderson, S. M., Miller, C. M., Prahl, L. S., Odde, D. J., et al. (2020). Regulation and dynamics of force transmission at individual cell-matrix adhesion bonds. *Sci. Adv*. 6:eaax0317. doi: 10.1126/sciadv.aax0317

Theodosiou, M., Widmaier, M., Böttcher, R. T., Rognoni, E., Veelders, M., Bharadwaj, M., et al. (2016). Kindlin-2 cooperates with talin to activate integrins and induces cell spreading by directly binding paxillin. *eLife* 5:e10130. doi: 10.7554/eLife.10130

Turlier, H., and Betz, T. (2018). "Fluctuations in active membranes," in *Physics of Biological Membranes*, eds P. Bassereau and P. Sens (Cham: Springer International Publishing), 581–619. doi: 10.1007/978-3-030-00630-3_21

Vicente-Manzanares, M., Zareno, J., Whitmore, L., Choi, C. K., and Horwitz, A. F. (2007). Regulation of protrusion, adhesion dynamics, and polarity by myosins IIA and IIB in migrating cells. *J. Cell Biol*. 176, 573–580. doi: 10.1083/jcb.200612043

Walcott, S., and Sun, S. X. (2010). A mechanical model of actin stress fiber formation and substrate elasticity sensing in adherent cells. *Proc. Natl. Acad. Sci. U.S.A*. 107, 7757–7762. doi: 10.1073/pnas.0912739107

Walko, G., Castañón, M. J., and Wiche, G. (2015). Molecular architecture and function of the hemidesmosome. *Cell Tissue Res*. 360, 529–544. doi: 10.1007/s00441-015-2216-6

Wang, S., Wu, C., Zhang, Y., Zhong, Q., Sun, H., Cao, W., et al. (2018). Integrin $\alpha4\beta7$ switches its ligand specificity via distinct conformer-specific activation. *J. Cell Biol*. 217, 2799–2812. doi: 10.1083/jcb.201710022

Webb, D. J., Donais, K., Whitmore, L. A., Thomas, S. M., Turner, C. E., Parsons, J. T., et al. (2004). FAK-Src signalling through paxillin, ERK and MLCK regulates adhesion disassembly. *Nat. Cell Biol*. 6, 154–161. doi: 10.1038/ncb1094

Wehrle-Haller, B. (2012). Structure and function of focal adhesions. *Curr. Opin. Cell Biol*. 24, 116–124. doi: 10.1016/j.ceb.2011.11.001

Weiss, M., Frohnmayer, J. P., Benk, L. T., Haller, B., Janiesch, J.-W., Heitkamp, T., et al. (2018). Sequential bottom-up assembly of mechanically stabilized synthetic cells by microfluidics. *Nat. Mater*. 17, 89–96. doi: 10.1038/nmat5005

Welf, E. S., Naik, U. P., and Ogunnaike, B. A. (2012). A spatial model for integrin clustering as a result of feedback between integrin activation and integrin binding. *Biophys. J*. 103, 1379–1389. doi: 10.1016/j.bpj.2012.08.021

Williamson, D. J., Burn, G. L., Simoncelli, S., Griffié, J., Peters, R., Davis, D. M., et al. (2020). Machine learning for cluster analysis of localization microscopy data. *Nat. Commun*. 11:1493. doi: 10.1038/s41467-020-15293-x

Winograd-Katz, S. E., Fässler, R., Geiger, B., and Legate, K. R. (2014). The integrin adhesome: from genes and proteins to human disease. *Nat. Rev. Mol. Cell Biol*. 15, 273–288. doi: 10.1038/nrm3769

Wolfenson, H., Meacci, G., Liu, S., Stachowiak, M. R., Iskratsch, T., Ghassemi, S., et al. (2016). Tropomyosin controls sarcomere-like contractions for rigidity sensing and suppressing growth on soft matrices. *Nat. Cell Biol*. 18, 33–42. doi: 10.1038/ncb3277

Xiong, J.-P. (2001). Crystal structure of the extracellular segment of integrin $\alpha V\beta3$. *Science* 294, 339–345. doi: 10.1126/science.1064535

Xu, L., Braun, L. J., Rönnlund, D., Widengren, J., Aspenström, P., and Gad, A. K. B. (2018). Nanoscale localization of proteins within focal adhesions indicates discrete functional assemblies with selective force-dependence. *FEBS J*. 285, 1635–1652. doi: 10.1111/febs.14433

Yao, M., Goult, B. T., Chen, H., Cong, P., Sheetz, M. P., and Yan, J. (2015). Mechanical activation of vinculin binding to talin locks talin in an unfolded conformation. *Sci. Rep*. 4:4610. doi: 10.1038/srep04610

Yao, M., Goult, B. T., Klapholz, B., Hu, X., Toseland, C. P., Guo, Y., et al. (2016). The mechanical response of talin. *Nat. Commun.* 7:11966. doi: 10.1038/ncomms11966

Ye, F., Hu, G., Taylor, D., Ratnikov, B., Bobkov, A. A., McLean, M. A., et al. (2010). Recreation of the terminal events in physiological integrin activation. *J. Cell Biol.* 188, 157–173. doi: 10.1083/jcb.200908045

Ye, F., Kim, C., and Ginsberg, M. H. (2012). Reconstruction of integrin activation. *Blood* 119, 26–33. doi: 10.1182/blood-2011-04-292128

Ye, F., Kim, S.-J., and Kim, C. (2014). Intermolecular transmembrane domain interactions activate integrin αIIbβ3. *J. Biol. Chem.* 289, 18507–18513. doi: 10.1074/jbc.M113.541888

Ye, F., Petrich, B. G., Anekal, P., Lefort, C. T., Kasirer-Friede, A., Shattil, S. J., et al. (2013). The mechanism of kindlin-mediated activation of integrin αIIbβ3. *Curr. Biol.* 23, 2288–2295. doi: 10.1016/j.cub.2013.09.050

Yu, C.-h., Law, J. B. K., Suryana, M., Low, H. Y., and Sheetz, M. P. (2011). Early integrin binding to Arg-Gly-Asp peptide activates actin polymerization and contractile movement that stimulates outward translocation. *Proc. Natl. Acad. Sci. U.S.A.* 108, 20585–20590. doi: 10.1073/pnas.1109485108

Zaidel-Bar, R., Itzkovitz, S., Ma'ayan, A., Iyengar, R., and Geiger, B. (2007). Functional atlas of the integrin adhesome. *Nat. Cell Biol.* 9, 858–867. doi: 10.1038/ncb0807-858

Zhang, X., Jiang, G., Cai, Y., Monkley, S. J., Critchley, D. R., and Sheetz, M. P. (2008). Talin depletion reveals independence of initial cell spreading from integrin activation and traction. *Nat. Cell Biol.* 10, 1062–1068. doi: 10.1038/ncb1765

Zhu, C., and Williams, T. E. (2000). Modeling concurrent binding of multiple molecular species in cell adhesion. *Biophys. J.* 79, 1850–1857. doi: 10.1016/S0006-3495(00)76434-4

Zhu, L., Liu, H., Lu, F., Yang, J., Byzova, T. V., and Qin, J. (2019). Structural basis of paxillin recruitment by kindlin-2 in regulating cell adhesion. *Structure* 27, 1686.e5–1697.e5. doi: 10.1016/j.str.2019.09.006

Conflict of Interest: The authors declare that the research was conducted in the absence of any commercial or financial relationships that could be construed as a potential conflict of interest.

Advantages of publishing in Frontiers

OPEN ACCESS
Articles are free to read for greatest visibility and readership

FAST PUBLICATION
Around 90 days from submission to decision

HIGH QUALITY PEER-REVIEW
Rigorous, collaborative, and constructive peer-review

TRANSPARENT PEER-REVIEW
Editors and reviewers acknowledged by name on published articles

Frontiers
Avenue du Tribunal-Fédéral 34
1005 Lausanne | Switzerland

Visit us: www.frontiersin.org
Contact us: frontiersin.org/about/contact

REPRODUCIBILITY OF RESEARCH
Support open data and methods to enhance research reproducibility

DIGITAL PUBLISHING
Articles designed for optimal readership across devices

FOLLOW US
@frontiersin

IMPACT METRICS
Advanced article metrics track visibility across digital media

EXTENSIVE PROMOTION
Marketing and promotion of impactful research

LOOP RESEARCH NETWORK
Our network increases your article's readership